

Challenges and Advances
in Computational Chemistry and Physics 22
Series Editor: Jerzy Leszczynski

Remi Chauvin
Christine Lepetit
Bernard Silvi
Esmail Alikhani *Editors*

Applications of Topological Methods in Molecular Chemistry

 Springer

Challenges and Advances in Computational Chemistry and Physics

Volume 22

Series editor

Jerzy Leszczynski
Department of Chemistry and Biochemistry
Jackson State University, Jackson, MS, USA

This book series provides reviews on the most recent developments in computational chemistry and physics. It covers both the method developments and their applications. Each volume consists of chapters devoted to the one research area. The series highlights the most notable advances in applications of the computational methods. The volumes include nanotechnology, material sciences, molecular biology, structures and bonding in molecular complexes, and atmospheric chemistry. The authors are recruited from among the most prominent researchers in their research areas. As computational chemistry and physics is one of the most rapidly advancing scientific areas such timely overviews are desired by chemists, physicists, molecular biologists and material scientists. The books are intended for graduate students and researchers.

More information about this series at <http://www.springer.com/series/6918>

Remi Chauvin · Christine Lepetit
Bernard Silvi · Esmail Alikhani
Editors

Applications of Topological Methods in Molecular Chemistry

 Springer

Editors

Remi Chauvin
LCC-CNRS
Toulouse
France

Bernard Silvi
Laboratoire de Chimie Théorique
Paris
France

Christine Lepetit
LCC-CNRS
Toulouse
France

Esmail Alikhani
CNRS/UPM
MONARIS UMR 8233 (LADIR + LM2N)
Paris
France

Challenges and Advances in Computational Chemistry and Physics
ISBN 978-3-319-29020-1 ISBN 978-3-319-29022-5 (eBook)
DOI 10.1007/978-3-319-29022-5

Library of Congress Control Number: 2016930542

© Springer International Publishing Switzerland 2016

This work is subject to copyright. All rights are reserved by the Publisher, whether the whole or part of the material is concerned, specifically the rights of translation, reprinting, reuse of illustrations, recitation, broadcasting, reproduction on microfilms or in any other physical way, and transmission or information storage and retrieval, electronic adaptation, computer software, or by similar or dissimilar methodology now known or hereafter developed.

The use of general descriptive names, registered names, trademarks, service marks, etc. in this publication does not imply, even in the absence of a specific statement, that such names are exempt from the relevant protective laws and regulations and therefore free for general use.

The publisher, the authors and the editors are safe to assume that the advice and information in this book are believed to be true and accurate at the date of publication. Neither the publisher nor the authors or the editors give a warranty, express or implied, with respect to the material contained herein or for any errors or omissions that may have been made.

Printed on acid-free paper

This Springer imprint is published by SpringerNature
The registered company is Springer International Publishing AG Switzerland

This volume is dedicated to the memory of Professor Oleg Valerievich Shishkin (1966–2014) SSI “Institute for Single Crystals”, National Academy of Sciences of Ukraine, Kharkiv 61001, Ukraine and to his lifelong passion for chemistry and especially the topological analysis of intermolecular interactions in crystals.

Contents

1	Topological Approaches of the Bonding in Conceptual Chemistry	1
	Bernard Silvi, M. Esmail Alikhani, Christine Lepetit and Remi Chauvin	
Part I Topological Methods: Definition, State of the Art and Prospects		
2	On Quantum Chemical Topology	23
	Paul L.A. Popelier	
3	Localization-Delocalization Matrices and Electron Density-Weighted Adjacency/Connectivity Matrices: A Bridge Between the Quantum Theory of Atoms in Molecules and Chemical Graph Theory	53
	Chérif F. Matta, Ismat Sumar, Ronald Cook and Paul W. Ayers	
4	Extending the Topological Analysis and Seeking the Real-Space Subsystems in Non-Coulombic Systems with Homogeneous Potential Energy Functions.	89
	Shant Shahbazian	
5	Exploring Chemistry Through the Source Function for the Electron and the Electron Spin Densities	101
	Carlo Gatti, Ahmed M. Orlando, Emanuele Monza and Leonardo Lo Presti	
6	Emergent Scalar and Vector Fields in Quantum Chemical Topology	131
	A. Martín Pendás, E. Francisco, A. Gallo Bueno, J.M. Guevara Vela and A. Costales	

7	Topology of Quantum Mechanical Current Density Vector Fields Induced in a Molecule by Static Magnetic Perturbations . . .	151
	P. Lazzeretti	
8	Topological Analysis of the Fukui Function	227
	P. Fuentealba, C. Cardenas, R. Pino-Rios and W. Tiznado	
9	Topological Tools for the Study of Families of Reaction Mechanisms: The Fundamental Groups of Potential Surfaces in the Universal Molecule Context	243
	Paul G. Mezey	
10	Quantum Chemical Topology Approach for Dissecting Chemical Structure and Reactivity	257
	Juan Andrés, Lourdes Gracia, Patricio González-Navarrete and Vicent S. Safont	
Part II Topological Methods for the Characterization of π-Electron Delocalization and Aromaticity		
11	Paradise Lost—π-Electron Conjugation in Homologs and Derivatives of Perylene	297
	Ivan Gutman and Slavko Radenković	
12	Rules of Aromaticity	321
	Ferran Feixas, Eduard Matito, Jordi Poater and Miquel Solà	
13	Localized Structures at the Hückel Level, a Hückel-Derived Valence Bond Method	337
	Yannick Carissan, Nicolas Goudard, Denis Hagebaum-Reignier and Stéphane Humbel	
14	Magnetic Properties of Conjugated Hydrocarbons from Topological Hamiltonians	361
	Jean-Paul Malrieu, Nicolas Ferré and Nathalie Guihéry	
Part III Topological Methods for the Characterization of Weak Bonding Interactions		
15	What Can Be Learnt from a Location of Bond Paths and from Electron Density Distribution	399
	Sławomir J. Grabowski	
16	Following Halogen Bonds Formation with Bader's Atoms-in-Molecules Theory	435
	Vincent Tognetti and Laurent Joubert	

17	Charge Transfer in Beryllium Bonds and Cooperativity of Beryllium and Halogen Bonds. A New Perspective.	461
	Kateryna Mykolayivna Lemishko, Giovanni Bistoni, Leonardo Belpassi, Francesco Tarantelli, M. Merced Montero-Campillo and Manuel Yáñez	
18	A Complete NCI Perspective: From New Bonds to Reactivity	491
	Christophe Narth, Zeina Maroun, Roberto A. Boto, Robin Chaudret, Marie-Laure Bonnet, Jean-Philip Piquemal and Julia Contreras-García	
19	Diversity of the Nature of the Nitrogen-Oxygen Bond in Inorganic and Organic Nitrites in the Light of Topological Analysis of Electron Localisation Function (ELF)	529
	Slawomir Berski and Agnieszka J. Gordon	
20	Quantum Chemical Topology in the Field of Quasirelativistic Quantum Calculations	553
	Mohamed Amaouch, Eric Renault, Gilles Montavon, Nicolas Galland and Julien Pilmé	
	Index	583

Chapter 1

Topological Approaches of the Bonding in Conceptual Chemistry

Bernard Silvi, M. Esmail Alikhani, Christine Lepetit and Remi Chauvin

Abstract Though almost a century old, Lewis's theory of chemical bonding remains at the heart of the understanding of chemical structure. In spite of their basic discrete nature, Lewis's structures (topological 0-manifolds) continue to lend themselves to sophisticated treatments leading to valuable results in terms of topological analysis of chemical properties. The bonding topology is however not only defined, but also refined by direct consideration of the nuclear geometry, itself determined by the configuration of the embedding electron cloud. During the last century, the theory has thus been complemented by the mesomery concept, by the Linnett's double quartet scheme and by the VSEPR/LCP models. These models rely on an assumed spatial disposition of the electrons which does not take the quantum mechanical aspects into account. These models are reexamined by investigation of the topological 1-manifolds generated by the gradient field of potential functions featuring the electron cloud configuration, such as the electron

B. Silvi (✉)

Laboratoire de Chimie Théorique, Sorbonne Universités UPMC, Univ Paris 06, UMR 7616, case courrier 137, 4 place Jussieu, 75005 Paris, France
e-mail: silvi@lct.jussieu.fr

M. Esmail Alikhani

MONARIS, UMR 8233 CNRS/UPMC, Sorbonne Universités, UPMC Univ. Paris 06, MONARIS, UMR 8233, Université Pierre et Marie Curie, CC 49, 4 place Jussieu, 75252 Paris, France
e-mail: esmail.alikhani@upmc.fr

M. Esmail Alikhani

CNRS, MONARIS, UMR 8233, Université Pierre et Marie Curie, 4 place Jussieu, case courrier 49, 75252 Paris Cedex 05 France

C. Lepetit · R. Chauvin (✉)

CNRS, LCC (Laboratoire de Chimie de Coordination), 205 route de Narbonne, BP 44099, 31077 Toulouse Cedex 4 France
e-mail: remi.chauvin@lcc-toulouse.fr

C. Lepetit

e-mail: christine.lepetit@lcc-toulouse.fr

C. Lepetit · R. Chauvin

Université de Toulouse, UPS, INPT, 31077 Toulouse Cedex 4 France

© Springer International Publishing Switzerland 2016

R. Chauvin et al. (eds.), *Applications of Topological Methods in Molecular Chemistry*, Challenges and Advances in Computational Chemistry and Physics 22, DOI 10.1007/978-3-319-29022-5_1

density or electron localization function (ELF). In this chapter, we reexamine these models in order to escape from the quantum mechanical dilemma and we show how topological analyzes enable to recover these models.

1.1 Introduction

Chemistry thinks the matter as being made of atoms linked one to another by bonds. This description has been initiated in the first half of the XIXth century by John Dalton [1] who drew caloric forces between bonded atoms. It was consistently improved all along the century with the introduction of many fundamental concepts. The concept of isomerism, proposed by Berzélius in order to account for structural differences between species having the same stoichiometry but different properties, has been addressed by Alexander Crum Brown [2, 3]. The concept of valence due to Frankland and Kolbe which gives a rationale to the bonding connectivity between atoms, has been an important step ahead in the development of structural chemistry where the important contributions of Kekulé, Kolbe, Couper, Butlerov, Lods Schmidt, Crum Brown, Hofmann, Le Bel and Van't Hoff yield the contemporary representations. The emerging picture of a molecule is, therefore, that of a discrete network where the nodes are occupied by the elemental atoms. The possible valences of the elements are given by their position in the Periodic Table. In this respect, the determination of the structural formulas of the possible isomers corresponding to a given stoichiometry appears to be first a discrete topology problem (before being a geometry problem for the particular case of stereoisomers), which can be mathematically formalized within the framework of finite graph theory [4].¹ In this context, a bridge spanning the traditional gap between chemistry and mathematics was early recognized by the mathematician James J. Sylvester. In his benchmark article “Chemistry and Algebra” [5], 21 years after Kekulé on carbon tetravalence [6] and 41 years before Lewis on “The Atom and the Molecule” [7], he gave a tribute to Frankland while stating: “It may not be wholly without interest to some of the readers of NATURE to be made acquainted with an analogy that has recently forcibly impressed me between branches of human knowledge apparently so dissimilar as modern chemistry and modern algebra (...). I hardly ever take up Dr. Frankland’s exceedingly valuable “Notes for Chemical Students”, which are drawn up exclusively on the basis of Kekulé’s exquisite conception of valence, without deriving suggestions for new researches in the theory of algebraical forms”. And farther: “Every (quantic) invariant and co-variant thus becomes expressible by a graph precisely identical with a Kekulean diagram or chemicograph”. The invariant and co-variant are here assignable to a set of atoms of given valences and a set of bonds, respectively.

¹The concept of infinite graph applicable to non-covalent molecular materials being less directly fruitful because of the ambiguity in the definition of the eigenvalue spectrum.

The physical meaning of the bonding edges of the graph was however unknown. Nevertheless, it rapidly appeared to Berzélius that electric rather than caloric forces were accountable for the bonding [8], this idea was further reformulated by Laming [9] in a fully atomistic fashion accounting for Faraday's electrochemical equivalent. Laming's hypotheses anticipate the atomic electronic shell structure half a century before Joseph John Thomson's discovery of the electron:

a mass of electrical matter, or electricity, may be regarded as composed of electrical atoms, just as a mass of ordinary matter contains ordinary atoms; and thus the sphere of electricity which surrounds an ordinary atom will consist of a number of electrical atoms arranged in concentric strata. The number of electrical atoms belonging to a given ordinary atom may be assumed to be such as to complete its external spherical stratum, or, on the contrary, it may be such as to leave that external spherical stratum more or less imperfect.

A few years after Thomson's discovery of the electron, G. N. Lewis proposed in a memorandum dated March 28, 1902 [7], his cubic atomic model in which the vertices are occupied or not by electrons according to the element's column in the Periodic Table. In this way, he established a direct link between electrons and the concept of valence which provides a foundation to Abegg's valence and counter-valence law [10]. It is worth noting that these different atomic models have been conceived on the only basis of chemical arguments. Moreover, Lewis atom is closer to nowadays representations than Thomson's 1904 plum-pudding model [11]. Lewis's atom in molecule is composed of a kernel grouping the nucleus and the inner shell electrons and an outer shell, the valence shell. The atom tends to have an even number of electrons in its valence shell and especially eight electrons which are symmetrically arranged at the corner of a cube. The atomic shells of two bonded atoms mutually interpenetrate and therefore electrons may belong to the valence shells of two bonded atoms. Lewis emphasized the concept of electron pair as the cornerstone of molecular structure and proposed to write the formulas of chemical compounds by using atomic symbols surrounded by a number of dots corresponding to the number of electrons in the atomic shell. In spite of its simplicity, Lewis' approach is remarkably efficient and remains fundamental for basic chemical education. Although Lewis' model explains the structure of a majority of molecular species, it fails, for example, to account for the hexagonal structure of benzene or for the paramagnetism of dioxygen. Whereas Huggins' attempt to understand benzene by a single Lewis structure yielded chimerical representations [12], the concept of mesomerism, pioneered by Ingold [13, 14], which considers a weighted superposition of structures has been very successful with this respect and therefore constitutes an important complement to Lewis's model. In order to be able to treat dioxygen, Linnert modified the original Lewis model by splitting the initial octet into two sets of four electrons, one having one spin quantum number and the other the opposite value [15, 16].

Until this point, a molecule has been formally described from a set of N nodes (nuclei) by three features only: a labelling (composition: stoichiometry, brutto formula), a topology (connection: bonding skeleton), and a topography (constitution: Lewis structures, resulting from the application of the labelling on the topology).

Nevertheless a “molecular structure” is also defined by a geometry (disposition, i.e. Cram-Dreiding structures) [17]. As the smallest constituent of a—pure substance in French, the Lavoisier’s language—a molecule is assigned to a particular molecular structure corresponding to an equilibrium geometry and corresponding energy (as ultimately determined by iterative resolution of the Schrödinger equation), and to a temperature-dependent chemical potential (as determined from the Boltzmann distribution of states) [18].

In a first attempt to go from topology to geometry, the spatial extension of the bonding and non bonding pairs has been accounted for by the model of Sidgwick and Powell [19] involving both shared and unshared groups having the same size which is uniquely determined by the type of spatial arrangement considered. Gillespie and Nyholm have substantially improved this model explaining the arrangement of the pairs around of a given centre as due to the exclusion principle [20]. The repulsion depends on the type of pairs considered, for example a lone pair is more repulsive than a bonding pair, and on the electronegativity of the ligands. In the earliest version of the Valence Shell Electron Pair Repulsion (VSEPR) model [21], the valence pairs are considered as points on a sphere the arrangement of which is found by maximizing the least distance between any pair of points. The points on a sphere were replaced in a first time by tangent spherical electronic domains attracted by the central positive core and further by ellipsoid, “pear” and “egg” shaped domains of different sizes [22]. Electron pair domains are defined as a charge cloud which occupies a given region of space and excludes other pairs from this region as a consequence of the Pauli exclusion principle. This electron pair domain version of VSEPR emphasizes the shape and size of the domains rather than the magnitude of their mutual repulsion. In addition to bond and lone pair domains, Gillespie considers single electron domains which are expected to be smaller than an electron pair domain [23]. The VSEPR model is very successful in predicting qualitatively the shape of molecules. It enables to understand many features of the molecular geometry in a qualitative fashion.

The Lewis’ and VSEPR models are finally simple to understand and to apply, they provide very convincing explanations of the molecular structure and suffer few exceptions. They have consequently acquired a central place in chemical education. Both rely on the hypothesis of the formation of individualized localized electron pairs which is not an experimental fact and which remains questionable from a strict theoretical point of view. Beyond covalence, actually, the nature of the interactions between atoms (i.e. the “absolute edge weight” of the molecular graph, see below) can indeed be appraised on a purely phenomenological basis (“sharing and pairing” of formal “electronic” quanta) [24].

The aim of this chapter is to give the consistency between the following chapters gathered in this Volume. It consists in an introduction of the topological analysis methods which enable the recovery of the different concepts used in the chemical description of the matter in the spirit of Lewis’ model as well as to go deeper into their contents. After a reminder of the links between chemistry and topology introducing the two types of discrete and continuous topological approaches, the general spirit of these approaches is presented in the subsequent sections.

1.2 Chemistry and Topology

Many authors, among whom the authors of the following chapters of this volume, have addressed the relevance of various aspects of topology in chemistry (see for example: Ayers et al. [25]). From the abstract mathematical standpoint, however, a topology is defined within the framework of set theory: given a set X , a topology T on X is a family of parts of X , called open sets, i.e. a subset of $P(X) = 2^X$, such that:

- (i) the empty set and X are open sets;
- (ii) any union of open sets is an open set;
- (iii) the intersection of any finite number of open sets is an open set.

The (X, T) couple is called a topological space on X . If X is a metric space (endowed with a distance), the canonical topology is defined from the corresponding open balls of X (each of them being defined by a center and a radius). A topological space (X, T) is a topological manifold if it is separated and locally euclidean, i.e. every point in X admits an open neighborhood homeomorphic to \mathbb{R}^n : n is unique and defines the dimension of X , then referred to as a nD -manifold.

Within the chemical context, the “molecular space” is the $3D$ space filled with electrons and punctual nuclei restricting or straining the euclidean topology depending of the electron model. The molecular space is thus either:

- the *discrete* $0D$ -manifold of the Lewis’ graph embedded in the $3D$ euclidean space with an approximate or optimized nuclear geometry. The topology is the one induced by the canonical graph distance.
- or the *continuous* $1D$ -manifold generated by a sufficiently regular potential function $V(\mathbf{r})$ (electron density, ELF, MESP, see below) through its gradient field $\nabla V(\mathbf{r})$ straining the $3D$ space for some particle moving through geodesics according to the least action principle and Euler-Lagrange equations (see Sect. 1.4.2.1). The corresponding topology can be regarded as a generalization of the graph topology for a continuous set of vertices: two points in \mathbb{R}^3 define a generalized edge if they are on the same gradient path of V . The distance between two points is either infinite if the points do not ly on the same path, or equal to the length of the gradient arc between the two points if the points are on the same path (the gradient paths are actually oriented and thus formally define generalized edges of directed graphs). The open balls of the metric topology are therefore arcs of gradient paths, where a neighborhood of any wandering point is homeomorphic to a neighborhood of the tangent space defined by the gradient direction in the dual space.

Application of the gradient dynamical system theory allows delineation of non-overlapping basins forming a partition of the molecular space in \mathbb{R}^3 from which the basin adherences are removed. This partition defines a topology (unions of basin interiors completed by the empty set), which is metric in the Lewis’ sense (the connectivity between basins being related to their synapticity), and which is also a

sigma-algebra.² The measure of the basin-derived measurable sets can be the absolute value of the corresponding integral of V .

The two types of approaches are addressed in the following chapters, and respective general prerequisites are shortly presented in the following sections.

1.3 Discrete Chemical Topology: Chemical Bonding and Graph Theory

Within the context of chemistry [26, 27], a molecule is primarily described by a discrete molecular graph $G = (V, E)$, where V is the finite set of vertices corresponding to atomic nodes, and E is the set of edges corresponding to two-center bonds.³ Therefore, the natural topology of the molecule is the one defined by the edge set E through the canonical metric of G , where the distance $d_G(u, v)$ between two vertices u and v is the smallest number of consecutive edges (shortest path) between them.

Topological comparison between molecular graphs is addressed through either combinatorial analysis or spectral analysis.

Combinatorial analysis of graphs allows the definition of graph invariants (not depending on the numbering of the nodes), called topological indices, lending themselves to the search for empirical relationships with physico-chemical properties. This approach first proposed by Wiener in 1949, initiated the today widely addressed investigation field of *Quantitative Structure-Activity Relationships* (QSAR).

The main Wiener index is a global quantitative index of the graph topology [28] defined as the sum of all the distances of the unordered pairs of vertices:

$$W(G) = \sum_{\{u,v\} \subset V} d_G(u, v) \quad (1.1)$$

A related index is the Wiener Polarity Index:

$$W_P(G) = \gamma_G(3) \quad (1.2)$$

²In the mathematical sense, *metric* does not mean *measurable*. Though the spirits of the definitions are tightly related, a topological space (X, T) , even metric, is indeed not a measurable space a priori. The smallest σ -algebra of X containing the topology T is the Borel algebra A_B serving to define all the measurable subsets of X including all the open sets: only (X, A_B) is a measurable space. Reminder: a σ -algebra of X is a part A of $P(X)$, the elements of which are called *measurable sets*, such that:

- i. $X \in A$ (or $\emptyset \in A$);
- ii. $\forall A \in A, X \setminus A \in A$ (A is closed under complementation);
- iii. $\forall \{A_1, A_2, A_3, \dots\} \subset A, A_1 \cup A_2 \cup A_3 \cup \dots \in A$ (A is closed under countable unions).

³if multi-center bonds are considered, the molecular graph is replaced by a molecular hyper-graph.

where $\gamma_G(k)$ denotes the number of unordered pairs of vertices $\{u, v\}$ such that $d_G(u, v) = k$.

The relevance of W and W_P was illustrated by an accurate correlation between the boiling point (bp) of alkanes and the values of these indices for the corresponding graphs:

$$bp = aW + bW_P + c \quad (1.3)$$

where a, b, c are constants for a given group of isomers C_nH_{2n+2} :

$$\Delta bp \approx 98/n^2 \Delta W + 5.5 \Delta W_P \quad (1.4)$$

Many other topological indices can be defined, calculated by direct inspection of molecular graphs, and used in QSAR analysis.

Spectral graph theory allows extraction of more concealed quantitative features of graphs, such as the so-called “graph energy” [29]. It is based on the diagonalization of the adjacency matrix of G (or the corresponding Hessian matrix). As the adjacency matrix of G features the Hamiltonian of a Lewis’ molecular model, spectral graph theory is the mathematical foundation of the Hückel Molecular Orbital (HMO) method, the eigenvalues corresponding to orbital energies and the eigenvectors to mono-electronic orbitals spanned by a basis set of atomic orbitals bound to each of the constituting atoms.

Beyond these practical applications, abstract spectral graph theory has also been essential in the appraisal of the long-lasting concept of chemical “aromaticity”, namely the influence of the cyclic character of electron delocalization on the molecular energy. Many indices of aromaticity based on various criteria (energetic-structural, magnetic, electronic) have been proposed as approximates of the exact measure of aromaticity. The latter was however proposed as early as 1976, when Gutman et al. on one hand [30], and Aihara on the other hand [31], simultaneously proposed the definition of the Topological Resonance Energy (TRE) by subtracting the contributions of the cyclic components of the graph from the total graph energy. Nevertheless, the quite abstract and complicated process, based on the Sachs’s theorem [32, 33] missed a chemical interpretation and did not draw the attention of the chemists’ community. It was not until recently that indirect and direct chemical interpretations of TRE were disclosed, the key being the simultaneous consideration of the Möbius- and Hückel-types of the cyclic molecule [34, 35].

The Lewis’ molecular graph remains however somewhat arbitrary, because it relies on the decision whether any two edges are bonded or not. It corresponds to the case of a transferable (uniform) resonance integral β° which is constant, and normalized to $\beta^\circ = 1$, for all pair of atoms connected by an edge. In the same way the HMO theory can be generalized to heteroatomic structures by assigning variable Coulomb integrals depending on the atoms occupying given vertices, a β -variable HMO model allows a more accurate description of the molecules. The molecular graph is therefore edge-weighted, e.g. by Coulson-type equations relating the bond distances to the bond orders, and the corresponding resonance integral β featuring

the variable interaction between the atoms. The most general molecular graph is therefore an edge- and vertex-weighted version of the complete graph of G , with β values possibly tending to zero for pairs of “almost non-bonded” atoms. This generalization allowed the definition of the adiabatic TRE versus the usual TRE referred to as the vertical TRE [35].

Finally, graph theory not only remains a powerful analysis tool for direct interpretation of molecular properties, but is also a systematic synthesis tool for the description of molecular structures. In the same way the electronic properties are accurately described by a weighted superposition of mesomeric forms (or valence bond structures), the underlying structure is completely described by a series of line graphs. Following Estrada, indeed [36], whereas the covalent connectivity (Lewis structure) is described by a vertex-weighted graph G , the 2D-geometry (bond distances) described by the corresponding edge-weighted graph is equivalently described by the corresponding vertex-weighted line graph $L^1(G)$. Pursuing in the same spirit, the local 3D-geometry (bond angles) is described by the vertex-weighted second line graph $L^2(G)$, and the global 3D-geometry (torsion angles) by the vertex-weighted third line graph $L^3(G)$. A molecule is therefore fully described by the series of its vertex-weighted line graphs $L^n(G)$.

1.4 Continuous Chemical Topology: Chemical Bonding and Functional Analysis

1.4.1 *Intuitive Bonding Chemical Concepts and Quantum Mechanics*

For almost a century Quantum Mechanics is the physical theory which describes the interaction between particles, such as electrons and nuclei in molecules, and therefore enables the quantitative exact predictions of observables. The reduction of chemistry to physics corresponds to the mechanistic working program of Dirac [37]:

The underlying physical laws necessary for the mathematical theory of a large part of physics and the whole of chemistry are thus completely known, and the difficulty is only that the exact application of these laws leads to equations much too complicated to be soluble.

Although the predictive power of Quantum Mechanics is unquestionable, its ability to provide explanations has been questioned from an epistemological point of view by Thom [38]. As neither atoms in molecules nor bonding and non bonding pairs are defined in terms of quantum mechanical observables, the bridges linking the intuitive chemical approach to Quantum Mechanics are built either by interpreting the approximate molecular wave functions or on the basis of the statistical interpretation of Quantum Mechanics. In the latter approach, the analysis of

electron density of probability functions and more generally density of property functions enables a step-by-step recognition of the chemical objects showing that “Chemistry emerges from Quantum Mechanics” [39].

The one-electron density, $\rho(\mathbf{r})$, expresses the probability of finding one electron in a volume element centered at \mathbf{r} , the remaining electrons being anywhere. It is a fundamental physical property measured in coherent X-ray scattering experiments or calculated with quantum chemical methods. It is involved in very important theorems such as the electrostatic expression of the Hellmann-Feynman theorem [40–43] which enables the calculation of the forces on nuclei and the Hohenberg-Kohn theorem [44] which is at the root of the Density Functional Theory (DFT). The one electron density can be written as the sum of the spin contributions:

$$\rho(\mathbf{r}) = \rho_\alpha(\mathbf{r}) + \rho_\beta(\mathbf{r}) \quad (1.5)$$

where $\rho_\alpha(\mathbf{r})$ and $\rho_\beta(\mathbf{r})$ are the probabilities of finding one electron with respectively α and β spins in the volume element centered at \mathbf{r} . The integration of the one-electron density over the whole space yields the number of electrons of the system:

$$\int \rho(\mathbf{r})d\mathbf{r} = \int \rho_\alpha(\mathbf{r})d\mathbf{r} + \int \rho_\beta(\mathbf{r})d\mathbf{r} = N_\alpha + N_\beta = N \quad (1.6)$$

The pair function $\Pi(\mathbf{r}, \mathbf{r}')$ expresses the probability of finding one electron in the volume element centered at \mathbf{r} and an other in that centered at \mathbf{r}' . It has four spin components, namely $\Pi_{\alpha\alpha}(\mathbf{r}, \mathbf{r}')$, $\Pi_{\alpha\beta}(\mathbf{r}, \mathbf{r}')$, $\Pi_{\beta\alpha}(\mathbf{r}, \mathbf{r}')$ and $\Pi_{\beta\beta}(\mathbf{r}, \mathbf{r}')$ and is normalized to $N(N - 1)$ when ordered pairs are considered [45].

Consider first the concept of atom in molecule. Several definitions can be proposed which depend upon choices such as the nature of the space, the required properties of the atom in the molecule. Richard Bader’s definition is based on (i) a space filling non overlapping partition of the density and (ii) on the fulfillment of an energy decomposition requirement: the electronic energy of the molecule is the sum of atomic and interatomic contributions having a definite value. Condition (i) can be written as:

$$\sum_A \int_{\Omega_A} \rho(\mathbf{r})d\mathbf{r} = \sum_A \bar{N}_A = N \quad (1.7)$$

where Ω_A is the region of space occupied by atom A and N the number of electrons of the molecule, whereas condition (ii) implies:

$$E = \sum_A E_A + \sum_A \sum_{<B} E_{AB} \quad (1.8)$$

Making use of the Hohenberg-Kohn theorem [44], the contributions appearing in Eq. 1.8 have the following expression:

$$\begin{aligned}
 E_A &= T_A[\rho(\mathbf{r})] + \int_{\Omega_A} \int_{\Omega_A} \frac{\rho(\mathbf{r})\rho(\mathbf{r}')}{|\mathbf{r} - \mathbf{r}'|} d\mathbf{r}d\mathbf{r}' + \int_{\Omega_A} v_A(\mathbf{r})\rho(\mathbf{r})d\mathbf{r} \\
 E_{AB} &= \int_{\Omega_A} \int_{\Omega_B} \frac{\rho(\mathbf{r})\rho(\mathbf{r}')}{|\mathbf{r} - \mathbf{r}'|} d\mathbf{r}d\mathbf{r}' + \int_{\Omega_A} v_B(\mathbf{r})\rho(\mathbf{r})d\mathbf{r} + \int_{\Omega_B} v_A(\mathbf{r})\rho(\mathbf{r})d\mathbf{r}
 \end{aligned} \tag{1.9}$$

where $T_A[\rho(\mathbf{r})]$ is the kinetic energy of atom A and $v_A(\mathbf{r})$ the contribution of atom A to the external potential, in other words $v_A(\mathbf{r}) = \frac{-Z_A}{|\mathbf{r} - \mathbf{R}_A|}$ where Z_A is the charge of the nucleus of atom A at position \mathbf{R}_A . All potential energy contributions have definite values, but this is not the case of the kinetic energy $T_A[\rho(\mathbf{r})]$. The latter should be calculated by integrating the kinetic energy density over the volume Ω_A . The kinetic energy density $T(\mathbf{r})$ is a density of property. A density of property, say, $\rho_W(\mathbf{r})$ is a local function such as:

$$\int \rho_W(\mathbf{r})d\mathbf{r} = \langle \Psi | \hat{W}(\mathbf{r}, \mathbf{p}) | \Psi \rangle \tag{1.10}$$

where $\hat{W}(\mathbf{r}, \mathbf{p})$ is the one electron operator associated to the property. The density of property is obtained:

$$\rho_W(\mathbf{r}) = \int \hat{W}(\mathbf{p})F(\mathbf{r}, \mathbf{p})d\mathbf{p} \tag{1.11}$$

where $F(\mathbf{r}, \mathbf{p})$ is the joint distribution of position and momentum. Although joint distributions are not defined in Quantum Mechanics, it is possible to introduce so-called phase-space quasi distributions, such as the Wigner function [46], in order to get an expression which yields the proper expectation value of the operator when integrated over all space. They are built by applying correspondence rules. They do not fulfill the requirement of uniqueness [47] but satisfy the marginal distributions:

$$\begin{aligned}
 \int F(\mathbf{r}, \mathbf{p})d\mathbf{p} &= \rho(\mathbf{r}) \\
 \int F(\mathbf{r}, \mathbf{p})d\mathbf{r} &= \rho(\mathbf{p})
 \end{aligned} \tag{1.12}$$

For an operator which only depends upon the position coordinates, it follows from Eq. 1.12 that the density of property is just the product of this operator by the electron density function. The kinetic density operator $\hat{K} = \frac{\mathbf{p}^2}{2m}$ depending on p , the kinetic energy density $T(\mathbf{r})$, appears to be the sum of two contributions. the first one

$$T_s(\mathbf{r}) = \frac{1}{2} |\nabla \Psi|^2 \quad (1.13)$$

is called the definite positive kinetic energy density, it is always positive and yields the expectation value of the kinetic energy when integrated over all space. For stationary states, the second contribution vanishes. For a stationary state this latter contribution is the Laplacian of the electron density multiplied by an arbitrary constant as a consequence of the non-uniqueness of the joint quasi distribution [48, 49]. The condition for a definite integrated kinetic energy density is that the integral of $\nabla^2 \rho(\mathbf{r})$ vanishes which happens when the integration is performed over the whole space or, according to the divergence theorem, if the bounding surface is a zero flux surface:

$$\int_{\Omega} \nabla^2 \rho(\mathbf{r}) d\mathbf{r} = \oint_S \mathbf{n}(\mathbf{r}) \cdot \nabla \rho(\mathbf{r}) d\mathbf{s} = 0 \quad (1.14)$$

where $\mathbf{n}(\mathbf{r})$ denotes a unit vector normal to $S(\mathbf{r})$ at point \mathbf{r} . Since the atomic volumes Ω are bounded by zero-flux surfaces of $\nabla \rho(\mathbf{r})$, they are identified as the basins of the gradient dynamical system of the electron density function.

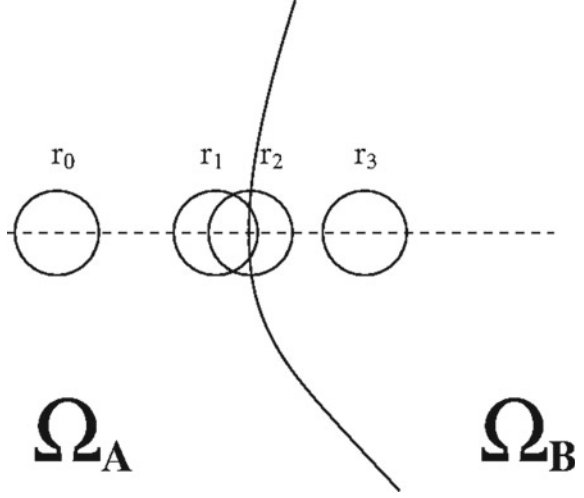
The same strategy of falsification can be applied to the electronic domains of Gillespie in order to find their boundaries. According to the definition “charge cloud which occupies a given region of space and excludes other pairs from this region” one expects that the following hypotheses are verified in the case of two different domains Ω_A and Ω_B :

1. $\rho_\alpha(\mathbf{r}) = \rho_\beta(\mathbf{r}) = \frac{1}{2} \rho(\mathbf{r})$
2. $\Pi_{\sigma\sigma'}(\mathbf{r}, \mathbf{r}') \approx \frac{1}{4} \rho(\mathbf{r}) \rho(\mathbf{r}')$ for $\sigma \neq \sigma'$
3. $\Pi_{\sigma\sigma}(\mathbf{r}, \mathbf{r}') \sim 0$. for $\mathbf{r}, \mathbf{r}' \in \Omega_A$ or $\mathbf{r}, \mathbf{r}' \in \Omega_B$
4. $\Pi_{\sigma\sigma}(\mathbf{r}, \mathbf{r}') = \rho_\sigma(\mathbf{r}) \rho_\sigma(\mathbf{r}') \approx \frac{1}{4} \rho(\mathbf{r}) \rho(\mathbf{r}')$ for \mathbf{r}, \mathbf{r}' in different domains.

where σ and σ' stand for α or β . In order to find the bounding surface we measure the probability $N_{||}(\mathbf{r})$ of finding a same spin pair a in finite sampling volume $V(\mathbf{r}_i)$ around a point at position \mathbf{r}_i chosen such as $\int_{V(\mathbf{r}_i)} \rho(\mathbf{r}) d\mathbf{r}$, is equal to an arbitrary small value n_V . Let now the sampling volume move along a normal to the bounding surface as displayed on Fig. 1.1. When $V(\mathbf{r}_i)$ is entirely in Ω_A or Ω_B , $N_{||}(\mathbf{r}_i) = 0$ such as at positions \mathbf{r}_0 and \mathbf{r}_3 , at positions \mathbf{r}_1 or \mathbf{r}_2 it straddles the bounding surface so:

$$V(\mathbf{r}_i) = V(\mathbf{r}_i) \cap \Omega_A + V(\mathbf{r}_i) \cap \Omega_B \quad (1.15)$$

Fig. 1.1 Sampling volume in the neighbourhood of the bounding surface of two pair domains



and

$$N_{\parallel}(\mathbf{r}_i) = \int_{V(\mathbf{r}_i) \cap \Omega_A} \rho_x(\mathbf{r}) d\mathbf{r} \int_{V(\mathbf{r}_i) \cap \Omega_B} \rho_x(\mathbf{r}') d\mathbf{r}' + \int_{V(\mathbf{r}_i) \cap \Omega_A} \rho_\beta(\mathbf{r}) d\mathbf{r} \int_{V(\mathbf{r}_i) \cap \Omega_B} \rho_\beta(\mathbf{r}') d\mathbf{r}' = \frac{1}{2} n_A (n_V - n_A) \quad (1.16)$$

with $n_A = \int_{V(\mathbf{r}_i) \cap \Omega_A} \rho(\mathbf{r}) d\mathbf{r}$. The maximum of $N_{\parallel}(\mathbf{r}_i)$ occurs at position \mathbf{r}_2 when the reference point belongs to the bounding surface, which is therefore a zero flux surface of $\nabla N_{\parallel}(\mathbf{r}_i)$. The spin pair composition $c_\pi(\mathbf{r})$ [50] and the Electron Localization Indicators (ELI) for same spin pairs $\Upsilon_\omega^\sigma(\mathbf{r}_i)$ [51] and opposite pairs $\Upsilon_\omega^{\alpha\beta}(\mathbf{r}_i)$ [52] have been introduced instead of $N_{\parallel}(\mathbf{r}_i)$ in order to remove the arbitrary choice of n_V and size dependence problems. These functions were introduced by their authors for two main reasons: on the one hand support the gradient dynamical system analysis of the electron localization function (ELF) of Becke and Edgecombe [53] designed in order to identify “localized electronic groups in atomic and molecular systems” and on the other hand enable the generalization of ELF to post Hartree-Fock wave functions. The ELF kernel provides an excellent analytical approximation of the spin pair composition and ELI functions.

An other definition of the electron domains is based on the hypothesis that the variance $\sigma^2(\bar{N}(\Omega))$ of their populations $\bar{N}(\Omega) = \int_\Omega \rho(\mathbf{r}) d\mathbf{r}$ should be minimal with respect to a variation of the domain boundaries. The minimization of the variance with respect to the domain volumes implies that the variational equation

$$\frac{\delta \sigma^2(\bar{N}(\Omega))}{\delta V(\Omega)} = 0 \quad (1.17)$$

should be satisfied. This equation can be written in terms of a surface integral

$$\frac{\delta\sigma^2(\bar{N}(\Omega))}{\delta V(\Omega)} = \oint_{S(\Omega)} \mathbf{n} \cdot \nabla\eta(\mathbf{r})ds = 0 \quad (1.18)$$

in which $\eta(\mathbf{r})$ is a scalar function for which the bounding surface $S(\Omega)$ is a zero flux surface. The determination of $\eta(\mathbf{r})$ from the expression of $\sigma^2(\bar{N}(\Omega))$ is hampered by the fact that it involves a six dimensional integral [54]. Paul W. Ayers has introduced the local covariance measure function to minimize the Frobenius norm of the covariance matrix of the domain populations and shown that this function can be approximated by the ELF [55].

1.4.2 Applications of the Gradient Dynamical System Partitioning

The gradient dynamical system theory appears to be a method of choice for partitioning the molecular space into non overlapping volumes on the basis of energetic or statistical criteria.

1.4.2.1 Short Mathematical Overview

This mathematical theory provides a partition of the space which is analogous to the more familiar partition made in hydrology in river basins delimited by watersheds. It relies on the study of a local function $V(\mathbf{r})$ called the *potential* function. The potential function carries the physical or chemical information e.g. the electron density, the ELF (see below), or even the electrostatic potential [56–58]. In the cases treated in the present book, the potential function is required to be defined at any point of a manifold which is either \mathbb{R}^3 for molecules or the unit cell for periodic systems. Moreover the first and second derivatives with respect to the point coordinates must be defined for any point. Its gradient $\nabla V(\mathbf{r})$ forms a vector field bounded on the manifold and determines two kinds of points: on the one hand are the *wandering points* corresponding to $\nabla V(\mathbf{r}_w) \neq 0$. and on the other hand are the *critical points* for which $\nabla V(\mathbf{r}_c) = 0$. A critical point is characterized by the *index* I_p , the number of positive eigenvalues of the second derivatives matrix (the Hessian matrix). There are four kinds of critical points in \mathbb{R}^3 :

- (i) attractors of index 0, also denoted $(3, -3)$ critical points, which are the local maxima of the potential function,
- (ii) saddle points of index 1 or $(3, -1)$,
- (iii) saddle points of index 2 or $(3, 1)$,
- (iv) repellers of index 3 or $(3, 3)$ which are the local minima.

The number of critical points satisfies the Poincaré-Hopf formula:

$$\sum_P (-1)^{I_P} = \chi(M) \quad (1.19)$$

in which the sum is performed over the critical points, I_P is the index of the critical point labelled by P and $\chi(M)$ is the Euler characteristic of the manifold on which the gradient field is bound, i.e. 1 for a molecule, 0 for a periodic system.

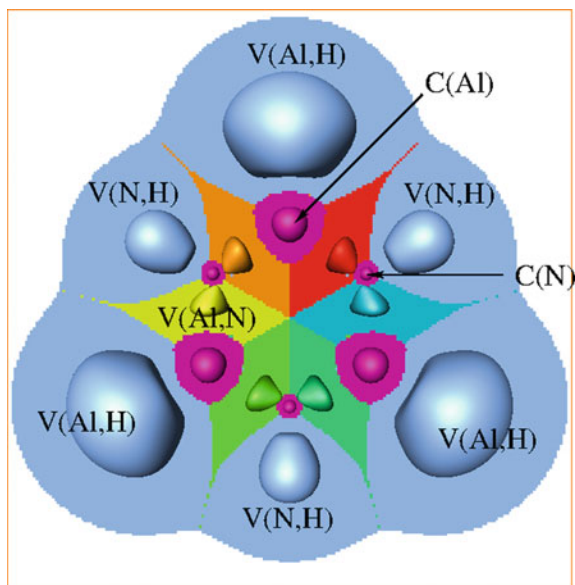
The formal analogy with a velocity field (i.e. $\nabla V(\mathbf{r}) = d\mathbf{r}/dt$) enables to build trajectories by integrating over the time variable. Each trajectory starts in the neighborhood of a point (or set of points) called the α -limit for which $\nabla V(\mathbf{r}) = 0$ and ends in the neighborhood of another point (or set of points) called the ω -limit for which also $\nabla V(\mathbf{r}) = 0$. Except for asymptotic behaviors, the α and ω -limits are critical points. The set of trajectories having a given critical point as ω -limit is called the stable manifold of this critical point whereas its unstable manifold is the set of trajectories for which it is a α -limit. The stable manifold of a critical point of index 0 (a local maximum or *attractor*) is the *basin* of the attractor, that of a critical point of index larger than 0 is a *separatrix*: it is the boundary between basins.

1.4.3 The Basins of the Electron Density and of the ELF

The large maxima of the electron density are expected and are found at the nuclear positions \mathbf{R}_A . These points are ω -limits for the trajectories of $\nabla\rho(\mathbf{r})$, in this sense they are attractors of the gradient field although they are not critical points for the exact density because the nuclear cusp condition makes $\nabla\rho(\mathbf{R}_A)$ not defined. The stable manifold of the nuclear attractors are the *atomic basins*. The non-nuclear attractors occur in metal clusters [59–62], bulk metals [63] and between homonuclear groups at internuclear distances far away from the equilibrium geometry [64]. In the Quantum Theory of Atoms in Molecules (QTAIM) an atom is defined as the union of a nucleus and of the electron density of its atomic basin. It is an open quantum system for which a Lagrangian formulation of quantum mechanics [65–70] enables the derivation of many theorems such as the virial and hypervirial theorems [71]. As the QTAIM atoms are not overlapping, they cannot share electron pairs and therefore the Lewis’s model is not consistent with the description of the matter provided by QTAIM.

The analysis of ELF yields a partition into core and valence basins which “correspond to the qualitative electron pair domains of the VSEPR model and have the same geometry as the VSEPR domains” [72]. The core basins, labeled as C(A) where A is the atomic symbol of the element, surround nuclei with atomic charge $Z > 2$. For a given atom, their number varies with the number of core shell of the element and also with the local symmetry in the molecule. They are usually

Fig. 1.2 Map of the ELF basins in the molecular plane of $\text{Al}_3\text{N}_3\text{H}_3$ and $\text{ELF} = 0.085$ isosurface. The molecule is bounded by the $\rho(\mathbf{r}) = \times 10^{-5}$ isosurface. Color code: magenta = core, light blue = bonded hydrogens, other colors = Al–N bonds

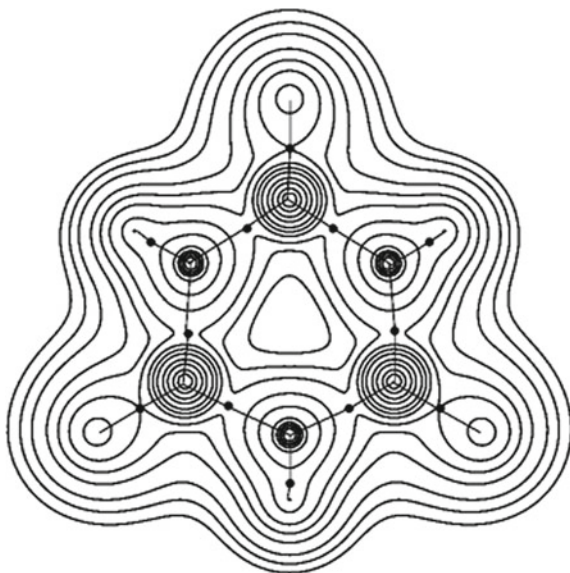


gathered in a single “super-bassin”, although it may be interesting to consider the basins of the external core shells, the subvalence basins, to explain geometrical features [73, 74]. The map of the ELF basins of $\text{Al}_3\text{N}_3\text{H}_3$ in the molecular plane is displayed in Fig. 1.2. The valence basins are organized around the core basins represented in magenta with which they share a boundary. The adopted nomenclature to label the valence basins is $V(\text{A},\text{B},\dots)$ where A,B,... are the atomic symbols of the atomic cores having a boundary with the considered valence basin. There are 3 $V(\text{Al},\text{H})$, 3 $V(\text{N},\text{H})$ and six $V(\text{Al},\text{N})$ valence basins corresponding to the Al–H, N–H and Al–N bonds. The $V(\text{Al},\text{H})$ and $V(\text{N},\text{H})$ basins encompass the proton and are therefore the valence shells of the hydrogen atoms. The valence shell of each aluminum atom is composed by the two $V(\text{Al},\text{N})$ basins and the $V(\text{Al},\text{H})$ located around the Al core whereas the nitrogen valence shells involve two $V(\text{Al},\text{N})$ and $V(\text{N},\text{H})$ basins. A valence basin may belong to the valence shell of one or several atomic valence shells. The synaptic order of a valence basin is the number of atomic valence shell to which it belongs. There are therefore monosynaptic basins $V(\text{A})$, disynaptic $V(\text{A},\text{B})$ and higher polysynaptic basins, $V(\text{A}, \text{B}, \text{C}, \dots)$.

1.4.4 Molecular Graphs and Chemical Structure

The concept of molecular graph introduced by Bader [75, 76] refers to the set of the unstable manifolds of the saddle points of index 1, called *bond critical points* (BCPs) in the case of the analysis of the one electron density. The unstable

Fig. 1.3 Density isocontours and molecular graph of $\text{Al}_3\text{N}_3\text{H}_6$. The BCP's are represented by ●



manifold of a BCP is called *bond path* as it is the union of the two trajectories linking the nuclear attractors of two adjacent interacting atoms. Figure 1.3 shows the molecular graph of $\text{Al}_3\text{N}_3\text{H}_6$ which clearly corresponds to the standard bonding network.

The molecular graph, built from the gradient field critical points, provides a complete representation of the bonding in a molecule accounting for the bonds, the lone pairs and their organization around the cores. It is obtained following the recipe of Krokidis et al. [77] which yields rather intricate patterns around the core basins. In fact ELF molecular graphs have been introduced in the context of the study of the bonding along a reaction pathway because they provide a clear synthetic picture of the topology at each stage of the reaction.

In general the gradient field depends upon a set of parameters, for example the nuclear coordinates in the case of the electron density and ELF fields calculated with the Born-Oppenheimer approximation. These parameters are called *control parameters* and the topology of the gradient field expressed by its critical points and their connectivity may change with the control space parameters. The set of points of the control parameter space for which a given topology is preserved is called a *structural stability domain*. In a reaction the system visits different stability domains which link the structure of the reactants to that of the products. At the turning points at which the system goes from one structural stability domain to another some of the critical points change of type, or become wandering points. In any case the Poincaré-Hopf relation must be satisfied. This evolution can be described in terms of bifurcation catastrophes [78] in the sense of René Thom [79]. In the framework of the electron density analysis, the study of reaction is limited to few types of reactions (isomerizations, cyclizations) because the $\nabla\rho(\mathbf{r})$ field enables to

distinguish chemically bonded atoms from non bonded pairs (for a diatomic molecule the Poincaré-Hopf relation imposes a BCP at any internuclear distance). The process of the creation-annihilation of electronic domains, as depicted by ELF, has been formalized in the Bonding Evolution Theory (BET) of Krokidis et al. [77]. This method has been widely applied to investigate organic chemistry reaction mechanisms [80–86].

1.5 Conclusion

In the following nineteen chapters, the relevance of topology in chemistry is addressed.

The first section presents the latest methodological advances in the topological analysis of molecular structure and reactivity. The first four chapters by Paul L. A. Popelier, Shant Shahbazian, Carlo Gatti et al. and Cherif F. Matta et al, deal with the most recent developments and extensions of the topological analysis of the electron density (QTAIM). In particular, a direct link between QTAIM and chemical graph theory is provided by the localization-delocalization and electron density-weighted connectivity matrices described by Chérif F. Matta et al.. The chapter by Ángel Martín Pendás et al. highlights emergent interests in forgotten scalar and vector fields for topological analyses within the gradient dynamical system theory. The current density vector field is more specifically considered by Paolo Lazeretti, while the Fukui function gradient field, enabling the definition of the chemically reactive regions of a molecule and thus providing a measure of the chemical reactivity, is envisaged by Patricio Fuentealba et al. Other topological tools relevant for the analysis of chemical reactivity and reaction mechanisms, are discussed in the next two chapters by Paul Mezey and Juan Andrés et al. respectively.

The second section focuses on applications of topological analysis for the characterization of π -electron delocalization and aromaticity. The chemical graph theory approach is here shown to remain more topical than ever. In spite of the development of advanced quantum chemical tools beyond Hartree-Fock, DFT or multi-configurational methods, a direct understanding of computational results often requires recourse to the methods of graph theory or Hückel Molecular Orbitals (HMOs). While aromaticity is certainly one of the “most basic topological concept” in chemistry (specific effect of the cyclic character of π -systems in molecules), it has long suffered from a lack of clear-cut definition. The merit of the discrete graph theory level is first illustrated by Ivan Gutman and Slavko Radenkovic delineating the scope of approaches based on the counting of Kekulé structure types for the prediction of the “observable aromatic character” of benzenoids, in particular around the perylene family. From a more general standpoint, Miquel Solà et al. address the relevance of the basic “counting rules of aromaticity” in a systematic manner. The main application of graph theory in quantum chemistry is the use of the adjacency matrix as a Hückel Hamiltonian. Within this context,

Stéphane Humbel et al. give a survey of their Hückel-derived Valence Bond methods for the mesomeric description of π -conjugated systems through localized Lewis structures, while presenting their friendly HuLiS freeware. In a more specific prospect, Jean-Paul Malrieu, et al. show that the topological Hückel mono-electronic Hamiltonian and Hubbard bi-electronic Hamiltonian provide valuable tools for the study of magnetic properties of open-shell π -conjugated hydrocarbons.

The last section is devoted to applications of various topological methods for the characterization of particular weak bonds or interactions. The case of hydrogen and halogen bonding is addressed in the first three chapters by Slavomir Grabowski, Laurent Joubert and Vincent Tognetti, and Manuel Yañez et al. respectively. The characterization of non-covalent interactions is then reviewed by Julia Contreras-Garcia et al. The diversity of nitrogen-oxygen bonds is illustrated by Sławomir Berski and Agnieszka J. Gordon. Finally, relativistic effects on bonding schemes such as the charge-shift bonding character of actinide oxides are examined by Julien Pilmé et al. through combined ELF and QTAIM topological analyses.

In a whole, the volume gives a selected but topical overview of the value of topological methods for an improved understanding of chemical structure and reactivity. It thus outlines the prospects while providing inspiration for future developments in this field.

References

1. Dalton J (1808) New system of chemical philosophy. R. Bickerstaff, London
2. Brown AC (1864) Trans Roy Soc Edinb 23:707
3. Brown AC (1865) J Chem Soc 18:230
4. Babaev EV (1999) Chemical topology: introduction and fundamentals. In: Bonchev D, Rouvray R (eds). Gordon and Breach, Reading, pp 167–264
5. Sylvester JJ (1878) Nature 17:284
6. Kekulé von Stardonitz FA (1857) Annalen der Chemie und Pharmacie 106:129
7. Lewis GN (1916) J Am Chem Soc 38:762
8. Berzélius JJ (1819) *Essai sur la théorie des proportions chimiques et sur l'influence chimique de l'électricité, par J. J. Berzélius, ... Traduit du suédois sous les yeux de l'auteur et publié par lui-même*. Méquignon-Marvis, Paris
9. Laming R (1845) Phil Mag 27:420
10. Abegg A, Anorg Z (1904) Chem 39:330
11. Thomson JJ (1904) Phil Mag 7:237
12. Huggins ML (1922) Science 55:679
13. Ingold CK (1922) J Chem Soc 121:1133
14. Ingold CK (1933) J Chem Soc 143:1120
15. Linnett JW (1961) J Am Chem Soc 83:2643
16. Linnett JW (1964) The electronic structure of molecules. A new approach. Methuen, London
17. Maraval V, Chauvin R (2007) New J Chem 31:1853
18. Chauvin R (1996) J Math Chem 19:147
19. Sidgwick NV, Powell HM (1940) Proc Roy Soc A 176:153
20. Gillespie RJ, Nyholm RS (1957) Quart Rev Chem Soc 11:339
21. Gillespie RJ (1963) J Chem Educ 40:295
22. Gillespie RJ (1991) Chem Soc Rev 21:59

23. Gillespie RJ, Robinson EA (1996) *Angew Chem Int Ed Engl* 35:495
24. Lepetit C, Maraval V, Canac Y, Chauvin R (2016) *Coord Chem Rev.*308:59
25. Ayers PL, Boyd RJ, Bultinck P, Caffarel M, Carbó-Dorca R, Causá M, Cioslowski J, Contreras-García J, Cooper DL, Coppens P, Gatti C, Grabowsky S, Lazzaretti P, Macchi P, Martín Pendás A, Popelier PL, Ruedenberg K, Rzepa H, Savin A, Sax A, Schwarz WE, Shhabbazian S, Silvi B, Solà M, Tsirelson V (2015) *Comput Theor Chem* 1053(2). Special Issue: Understanding structure and reactivity from topology and beyond
26. Diudea MV, Gutman I, Lorentz J (1999) *Molecular topology*. Nova Science, Huntington, New York
27. Restrepo G, Villaveces JL (2012) *Int J Phil Chem* 18:3
28. Wiener H (1947) *J Am Chem Soc* 69:17
29. Gutman I (1978) *Ber Math Stat Sect Forschungszentrum Graz* 103:1
30. Gutman I, Milun M, Trinajstić N (1976) *Croat Chem Acta* 48:87
31. Aihara J (1976) *J Am Chem Soc* 98:2750
32. Sachs H (1962) *Publ Math (Debrecen)* 9:270
33. Heilmann O, Lieb E (1972) *Commun Math Phys* 25:190
34. Chauvin R, Lepetit C, Fowler PW, Malrieu JP (2010) *Phys Chem Chem Phys* 12:5295
35. Chauvin R, Lepetit C (2013) *Phys Chem Chem Phys* 15:3855
36. Estrada E (2000) *Chem Phys Lett* 319:713
37. Dirac PAM (1929) *Proc Roy Soc A* 123:714
38. Thom R (1993) *Prédire n'est pas expliquer*. Flammarion, Paris
39. Popelier PLA (2007) *Faraday Discuss* 135:3
40. Hellmann H (1937) *Einführung in die Quantenchemie*. Franz Deuticke, Leipzig and Vienna
41. Feynman RP (1939) *Phys Rev* 56:340
42. Hurley AC (1954) *Proc Roy Soc A*
43. Hurley AC (1954) *Proc Roy Soc A* 226(1165):179
44. Hohenberg P, Kohn W (1964) *Phys Rev* 136:B864
45. McWeeny R (1989) *Methods of molecular quantum mechanics*, 2nd edn. Academic Press, London
46. Wigner E (1932) *Phys Rev* 40(5):749
47. Shewell JR (1959) *Am J Phys* 27:16
48. Cohen L (1966) *J Math Phys* 7:781
49. Cohen L (1979) *J. Chem. Phys.* 70:788
50. Silvi B (2003) *J Phys Chem A* 107:3081
51. Kohout M, Pernal K, Wagner FR, Grin Y (2004) *Theor Chem Acc* 112:453
52. Kohout M, Pernal K, Wagner FR, Grin Y (2005) *Theor Chem Acc* 113:287
53. Becke AD, Edgecombe KE (1990) *J Chem Phys* 92:5397
54. Silvi B, Fourré I, Alikhani E (2005) *Monatsh Chem* 136:855
55. Ayers PW (2005) *J Chem Sci* 117:441
56. Gadre SR, Shirsat RN (2000) *Electrostatics of atoms and molecules*. Universities Press, Hyderabad
57. Balanarayan P, Gadre SR (2003) *J Chem Phys* 119:5037
58. Espinosa E, Lecomte C, Molins E (1999) *Chem Phys Lett* 300:745
59. Cao WL, Gatti C, MacDougall PJ, Bader RFW (1987) *Chem Phys Lett* 141:380
60. Gatti C, Fantucci P, Pacchioni G (1987) *Theor Chim Acta (Berlin)* 72:433
61. Cioslowski J (1990) *J Phys Chem* 94:5496
62. Mei C, Edgecombe KE, Smith VH Jr, Heilingbrunner A (1993) *Int J Quant Chem* 48:287
63. Silvi B, Gatti C (2000) *J Phys Chem A* 104:947
64. Martín Pendás A, Blanco MA, Costales A, Mori Sánchez P, Luaña V (1999) *Phys Rev Lett* 83:1930
65. Bader RFW (1990) *Atoms in molecules: a quantum theory*. Oxford Univ Press, Oxford
66. Bader RFW (1994) *Phys Rev B* 49:13348
67. Bader RFW (2001) *Theor Chem Acc* 105:276
68. Bader RFW (2005) *Monatsh Chem* 136:819

69. Bader RFW (2007) *J Phys Chem A* 111:7966
70. Bader RFW (2007) The quantum theory of atoms. In: Matta CF, Boyd RJ (eds) *Molecules: from solid state to dna and drug design*. Wiley, New York, pp 37–59
71. Srebrenik S, Bader RFW (1975) *J Chem Phys* 63(9):3945
72. Gillespie RJ, Robinson EA (2007) *J Comput Chem* 28:87
73. Gillespie RJ, Noury S, Pilmé J, Silvi B (2004) *Inorg Chem* 43:3248
74. de Courcy B, Pedersen LG, Parisel O, Gresh N, Silvi B, Pilmé J, Piquemal JP (2010) *J Chem Theory Comput* 6:1048
75. Bader RFW, Anderson SG, Duke AJ (1979) *J Am Chem Soc* 101:1389
76. Bader RFW, Nguyen-Dang TT, Tal Y (1981) *Rep Prog Phys* 44:893
77. Krokidis X, Noury S, Silvi B (1997) *J Phys Chem A* 101:7277
78. Tal Y, Bader RFW, Erkkü J (1980) *Phys Rev A* 21:1
79. Thom R (1972) *Stabilité Structurale et morphogénèse*. Interditions, Paris
80. Berski S, Andrés J, Silvi B, Domingo L (2003) *J Phys Chem A* 107:6014
81. Polo V, Andres J, Castillo R, Berski S, Silvi B (2004) *Chem Eur J* 10:5165
82. Santos JC, Andrés J, Aizman A, Fuentealba P, Polo V (2005) *J Phys Chem A* 109(16):3687
83. Berski S, Andrés J, Silvi B, Domingo LR (2006) *J Phys Chem A* 110:13939
84. Andrés J, Berski S, Domingo LR, Polo V, Silvi B (2011) *Curr Org Chem* 15:3566
85. Andrés J, Berski S, Domingo LR, González-Navarrete P (2012) *J Comput Chem* 33:748
86. González-Navarrete P, Domingo LR, Andrés J, Berski S, Silvi B (2012) *J Comput Chem* 33:2400

Part I
**Topological Methods: Definition, State
of the Art and Prospects**

Chapter 2

On Quantum Chemical Topology

Paul L.A. Popelier

Abstract Quantum Chemical Topology (QCT) is a branch of theoretical chemistry that uses the language of dynamical systems (e.g. attractor, basin, homeomorphism, gradient path/phase curve, separatrix, critical points) to partition chemical systems and characterise them via associated quantitative properties. This methodology can be applied to a variety of quantum mechanical functions, the oldest and most documented one being the electron density. We define and discuss the topological atom, and justify the name topology. Then we define the quantum atom without reference to the topological atom. Subsequently, it turns out that each topological atom is a quantum atom, a property that enables the construction of a topologically inspired force field called QCTFF. We briefly discuss the four primary energy contributions governing this force field under development, and how the machine learning method kriging captures the variation in these energies due to geometrical change. Finally, in a more philosophical style, we advocate falsification in the area of chemical interpretation by means of quantum mechanical tools, introducing the concept of a *non-question*.

2.1 Introduction

Recently a chapter on the “Quantum Theory of Atoms in Molecules (QTAIM)” [1] was commissioned by editors Frenking and Shaik for their book on fundamental aspects of chemical bonding. This detailed and lengthy chapter has meanwhile been published [2], and features alongside authoritative chapters on alternative approaches such as EDA, NBO, Valence Bond, conceptual DFT, Block-localised

P.L.A. Popelier (✉)
Manchester Institute of Biotechnology (MIB), 131 Princess Street,
Manchester M1 7DN, UK
e-mail: pla@manchester.ac.uk

P.L.A. Popelier
School of Chemistry, University of Manchester, Oxford Road,
Manchester M13 9PL, UK

wavefunctions, ELF and high-resolution X-ray crystallography. The spirit of that book combined an educational style with an awareness of current scientific boundaries, while avoiding too many equations in the main text, as requested by the editors. That chapter managed to deliver added value in explaining QTAIM again, by means of an alternative angle of exposition, different to that in other sources [3–7]. Moreover, an historic narrative was given there, as well as a discussion of topological energy partitioning. The current chapter selects and re-explains elements from that document, with the new didactic example of HCN, justifies the name of Quantum Chemical Topology (QCT) (which encompasses and supersedes QTAIM), outlines the current state of affairs in a novel QCT-based protein force field, and briefly invites the community to start falsifying interpretative methods (QCT and non-QCT) in case studies where the outcome would make a difference.

The term Quantum Chemical Topology (QCT) was first coined [8] in 2003, and the first dedicated symposium took place in 2013, in Mexico City. Footnote 19 in the paper that coined QCT, gave a detailed justification for this name and it is helpful to quote part of this footnote, with a few modifications: “...The use of the acronym QCT does not downplay the physics behind “Atoms in Molecules” (AIM) by referring to the topology language as the central idea behind it. Instead, the name QCT seeks to capture better what this approach is about. The term (QT) AIM is widely used but is actually too narrow because, strictly speaking, it only makes sense as a term if one analyses the electron density topologically. Only then does one recover an atom in a molecule. A topological analysis of the Laplacian of the electron density (which is part of AIM) or the topology of the electron localization function (ELF), for example, does not yield atoms in molecules. However, they can both be put under the umbrella of QCT since they share the central topological idea. Also, returning to the electron density, one could use the topological analysis to recover molecules inside van der Waals complexes, an important idea in intermolecular forces. Again, as a name, AIM would not describe this result. The name QCT also invites any future developments based on a topological analysis of other 3D or higher-dimensional scalar functions.” This view was elaborated in Sect. 2.2 of a chapter [9] published in 2005, and updated again in the introduction of a paper [10] in 2009, and finally in Box 8.1 in Chap. 8 of the aforementioned book [2] edited by Frenking and Shaik.

The current book should be the right habitat to start thinking more in terms of falsification when interpreting a chemical phenomenon. Unfortunately, not many papers directly and critically compare methods. The papers that do so, however, often terminate with diplomatic and almost vague conclusions. This status quo perhaps adds to the prevailing notion that all methods are equivalent in quality and predictive value. They can all be used at the same time, in spite of their known pitfalls, and even if their results contradict each other. Such view is echoed in Hoffmann’s statement that “any rigorous definition of a chemical bond is bound to be impoverishing” and also in his advice “that one should have fun with the fuzzy richness of the idea”. Such an attitude perpetuates discussions, without prospect of them ever being resolved. Is this really the fate of interpretative theoretical chemistry? Or should one strive for conceptual hygiene? Is chemistry really this

hopelessly complicated universe preventing chemists to ever discover the right tools to give them solid insight in this universe? Interpretative methods urgently need to make predictions that are falsifiable: one method is wrong and the other is right. Or is asking for such binary resolution naïve? Or is calling for this binary clarity a step towards doing better science? This chapter will give a few examples of interpretations disagreeing and thereby setting the scene for falsification.

2.2 The Topological Atom

Surely everyone can agree that there are atoms inside molecules, in the same way that there are living cells inside an animal or a plant. Molecules are not novel aggregates of electrons and nuclei but are rather constructions based on pre-organised entities called atoms. Similarly, an animal is not a totally new form of life but instead built from specialised cells that each represent pre-organised (more elementary) matter such as proteins, lipids, carbohydrates and nucleotides. Several energy production mechanisms inside a unicellular creature are the same as in the cell of an animal. In a loosely similar vein, atoms largely retain their energy in going from an isolated state in the gas phase to an existence inside a molecule. The near-preservation of atoms is exactly what chemistry is about as a science: the study of how atoms change when interacting with other atoms. Therefore it is important that an atom inside a molecule is defined and calculated such that it does a good job in not changing too much while going from the gas phase to the molecule. It is then that one recovers a truly chemical atom rather than a physical atom. The chemist recovers an atom that allows her, or more modernly him, to insulate how the atom interacts with other atoms rather than being distracted by how that atom was built from scratch (i.e. electrons and the nucleus). Only physics is interested in building the atom from its constituents. Chemistry focuses on the small changes an atom undergoes as it interacts with other atoms, small compared to the energy changes involved in building an atom from electrons and a nucleus (all brought together from infinity).

The question is now *how* to define an atom inside a molecular system and this is where opinions differ, perhaps unfortunately. No experiment helps in settling the contentious question of how to define an atom, and even if there was such an experiment then the interpretation of its measured signal would probably be equally contentious. Hence, it appears that an answer to a prime question of chemistry—what is an atom in a molecule?—can only be tackled theoretically. An important guide to value the theoretical proposals on what an atom inside a molecule actually is, is the energetic transferability of that atom. In other words, how much does the energy of a given atom change as it is transferred from one atomic environment to another one? We will come back to energy transferability in Sect. 2.3.

In this section we focus on the molecular electron density and its shape. We seek a theoretical proposal to define an atom inside a molecule, based on the internal differences in the molecular density. In doing so, we avoid introducing a reference

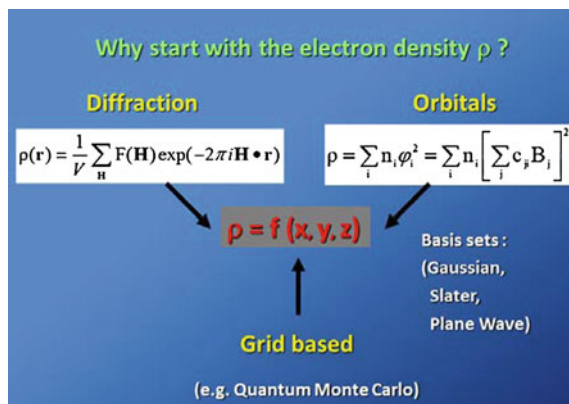


Fig. 2.1 The electron density ρ is a three-dimensional function that can be obtained from three different routes: X-ray diffraction (i.e. crystallography), SCF-LCAO-MO (or “orbitals”) and a method without orbitals where the electron density is known only in given grid points. A method that defines an atom at the level of ρ has the advantage that its definition is independent on how the electron density was obtained

density and this minimality obeys Occam’s razor. This principle of parsimony in assumptions is a quality gauge while assessing theories and models. The fewer parameters a model or theory possesses, while explaining the same number of observed phenomena, the more powerful it is. As a result, the more minimal models are preferable to the more elaborate ones. If experiment does not come to the aid of ranking theoretical proposals by their merit, then Occam’s razor does.

After this philosophical but also strategic interlude we are ready to inspect the electron density of a simple pilot system, the HCN molecule, which is linear. However, we first ask why the electron density is a good starting point to look for an atom in a molecule. Figure 2.1 summarises the argument: the electron density, denoted $\rho(\mathbf{r})$, is independent from the route by which it was generated. In other words, the electron density is an “information platform” describing in detail how electrons distribute themselves in a molecule regardless of the route in which this information was obtained. Figure 2.1 shows three main routes from which the electron density can be acquired.

First, $\rho(\mathbf{r})$ can be obtained from experiment, that is, X-ray crystallography. Routine crystallography only uses local parts of a system’s electron density, namely those at the core of each atom, from which crystallography determines each nuclear position. High-resolution crystallography [11] goes further and collects data on the valence electron density with an eye on measuring chemical features such as bonds and lone pairs. From the 1970s onwards this was done by introducing an artificial reference electron density, which was subtracted from the target electron density, in order to eliminate the huge electron density peaks near the nuclei. This reference density consists of a mere superposition of spherically averaged atomic densities, thereby not allowing any hybridisation to develop and thus missing any chemical

features. As a result, this difference density (technically known as the deformation density) contains all the chemical features. Although a simple and innocent looking approach, the exact form of the reference density is a concern. Different results can be obtained for different choices made in constructing the deformation density. However, there is a more minimal way forward, which avoids such choices in the first place.

Occam's razor proposes to use the molecular electron density as its own reference. Subtracting this density from itself returns a zero density everywhere, which is of course useless but introducing the gradient achieves what is required. The gradient represents an internal difference, via its definition as a derivative, which contains the difference of two function values, each evaluated at two points infinitesimally close to each other. At a given point, the gradient vector contains local information on how the function (in the case the electron density) changes internally. We wonder how the information obtained by the reference-free introspection can be revealed. The key to this goal is simply plotting a succession of gradient vectors, as shown in Fig. 2.2.

The gradient path that results from the primitive construction shown in Fig. 2.2 is all one needs to reveal the internal structure of the electron density. A bundle of gradient paths, called the gradient vector field, naturally exposes two fundamental features a chemist wants to extract from the electron density: the atom and the bond. Figure 2.3 illustrates this for a simple molecule: hydrogen cyanide.

Figure 2.3 clearly shows how a gradient path is everywhere orthogonal to a contour line of constant electron density. This statement is equivalent to the fact that the gradient path traverses the electron density in the direction of maximum ascent. As a result a gradient path also has a direction: its trajectories contain "earlier" points and "later" points in space. The question is now if it has a beginning and an ending. The answer is affirmative to both parts of the question. In fact, the origin and terminus of a gradient path have something in common: they are points where

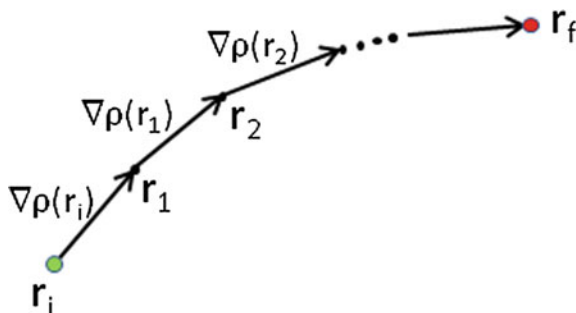


Fig. 2.2 In its most elementary construction a gradient path can be seen as a succession of infinitely short gradient vectors. Starting at r_i the gradient vector evaluated at this point is followed over a very short stretch, reaching r_1 , where the gradient is re-evaluated and again followed very briefly. This resulting broken line becomes a gradient vector in the continuous limit, ultimately terminating in point r_f .

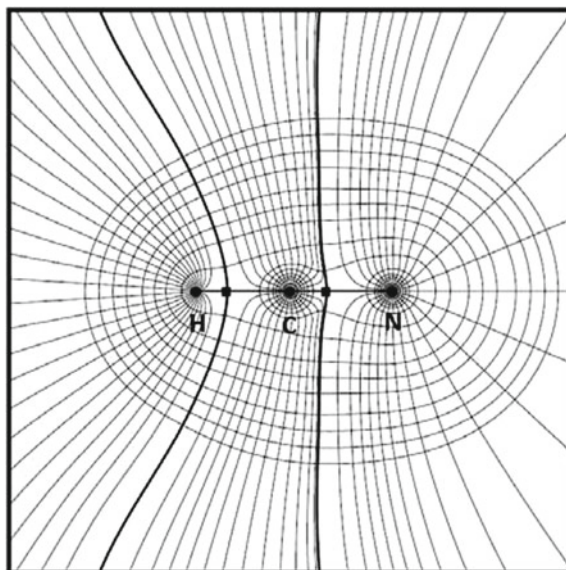


Fig. 2.3 Electron density contour plot of $\text{HC}\equiv\text{N}$ superimposed to its gradient vector field, which consists of an infinite multitude of gradient paths, here represented by a few dozen paths originating at infinity and terminating at the respective nuclei. A special bundle of gradient paths starts at infinity and ends up at the little squares, which are bond critical points. From each bond critical point emerge two gradient paths, each of which is attracted to a different nucleus. This pair of gradient paths is called the atomic interaction line, or in this case of a local energy minimum, the bond path. The carbon is placed at the origin and the bold square box marks the -6 a.u. and $+6$ a.u. horizontal and vertical boundaries of the plot. The electron density values of the contour lines are 1×10^{-n} , 2×10^{-n} , 4×10^{-n} and 8×10^{-n} au where n starts at -3 and increases with unity increments

the gradient vanishes. *Such a point is called a critical point.* Points \mathbf{r}_i and \mathbf{r}_f in Fig. 2.3 are critical points. By deduction all points at infinity are critical points. In three-dimensions there are four types of (non-degenerate) critical points.

Figure 2.3 shows two types of critical points: the maximum and the bond critical point. The maximum is an attractor for an infinite number of gradient paths originating at infinity. *Each such set of gradient paths forms a topological atom.* The bond critical point is a saddle point in that it is a maximum in two directions only (rather than three) and a minimum in the remaining direction. The latter direction is the molecular axis. Indeed, a gradient path originates at the bond critical point and terminates at one of the nuclear maxima. A second gradient path originates at the bond critical point but at the opposite side, and is attracted to the other nuclear maximum at that side. This pair of gradient paths is called an atomic attraction line [12]. When the forces on all nuclei vanish, as is the case for a local energy minimum, then the atomic interaction line becomes a bond path. The set of all bond paths occurring a molecule (or molecular complex) is called a molecular graph. A graph is a mathematical structure that models pairwise relations between objects,

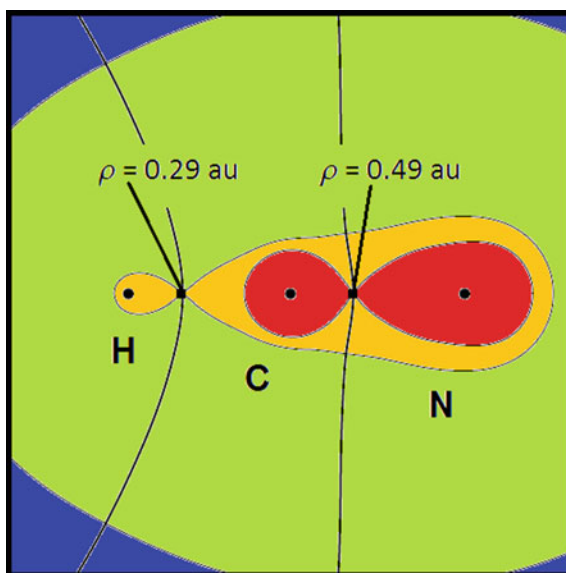
which in this case are atoms. Such a relation is robust under moderate geometric deviations (shrinking and elongation) from the local energy minimum geometry.

It should be pointed out that a gradient path can always be characterised and classified by the *types* of the two critical points that it manifestly connects. This was done exhaustively [13] and for the first time in 2003. This classification focuses on how many gradient paths can originate from a source critical point and how many gradient paths can terminate at the sink critical point.

The attentive reader may ask how a gradient can originate at a critical point if, at that point, the gradient vanishes and hence the gradient path construction of Fig. 2.2 collapses at \mathbf{r}_i . In other words, if there is no gradient there is no directional guidance. This is true but, in practice, the gradient path starts from a position infinitesimally close to the bond critical point, in a direction given by the relevant eigenvector of the Hessian of ρ evaluated at the bond critical point. At that new point the gradient does not vanish. The meaning of the bond critical point is still a matter of debate but an explanation of it, not given in the original literature by what Bader et al., will be given just below.

Let us look again at $\text{HC} \equiv \text{N}$ and fix the value of the electron density at 0.001 a.u. Figure 2.4 show the contour associated with this value, which can be taken as the practical edge of the molecule when in the gas phase. Note that when a molecule is part of a condensed phase then there is no need for such a practical edge; the whole molecule will then be topologically bounded, by a surface that is parameter-free, as explained below. The $\rho = 0.001$ a.u. contour is the boundary between the blue region ($\rho < 0.001$ a.u.) and the green region (0.001 a.u. $< \rho < 0.29$ a.u.). If the electron density is increased beyond 0.29 a.u. then the hydrogen atom becomes disconnected from the rest of the molecule. In other words, this hydrogen, while still being inside

Fig. 2.4 The atomic disconnection process in $\text{HC} \equiv \text{N}$. Each bond critical point (*little black square*) marks the contact point between two adjacent atoms



the molecule, is now completely enclosed by its own contour lines (not shown). The value of 0.29 a.u. is special because it is that at the bond critical point between *H* and *C*. While increasing the electron density starting from 0.001 a.u., the value of 0.29 a.u. is the highest electron density for which the hydrogen is still attached to the rest of the molecule. For any higher value the contours encompassing the whole molecule become disconnected. The same disconnection process occurs when ρ increases above 0.49 a.u., which of course is the electron density at the second bond critical point. It is then that *C* and *N* also become disconnected. Now, all three atoms in $\text{HC}\equiv\text{N}$ are fully encircled by their own contours. Overall, this process shows that bond critical points are “contact points” between certain atoms. *A bond critical point between two given atoms represents the transition point of them being connected or disconnected.* When connected, they are encompassed by the same contours. When disconnected, the respective atoms have their own “atomic” contours.

It is clear that topological atoms are non-overlapping. This is an important property that has attractive consequences in the area of intermolecular forces, where the thinking is dominated by overlapping molecules. The second important feature of topological atoms is that there are no gaps between the atoms. As a consequence, every point in space belongs to a topological atom; there is no “empty” (i.e. unallocated) space. The absence of the void has consequences for how one thinks about pockets in enzymes, including active sites and allosteric sites. The familiar ball-and-stick, or even “helix/turn/sheet ribbon” representation of the protein modelling world, gives the impression that there is empty space. A molecular view according to topological atoms challenges [14] this impression. Instead, if a ligand enters an enzymatic pocket, it will have to deform a host of topological atoms, each of which has an energy cost. Steric hindrance then becomes a more gradual and continuous concept as opposed to the simple on-off picture that van der Waals radii give. In other words, whereas traditional atoms act as billiard balls, topological atoms behave like sponges.

Figure 2.5 gives a three-dimensional view of the topological partitioning of the pilot molecule. The vertical solid lines appearing in Figs. 2.3 and 2.4 now show

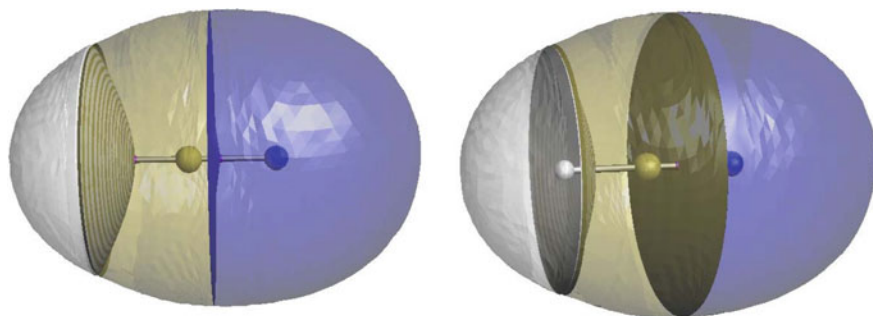


Fig. 2.5 Two views of the same three-dimensional representation of the three topological atoms (grey *H*, gold *C*, blue *N*) in $\text{HC}\equiv\text{N}$. The interatomic surfaces are bundles of gradient paths originating at infinity and terminating at a bond critical point (little bright purple sphere)

their full 3D extent as so-called *interatomic surfaces*. These surfaces are the sharp boundaries between atoms inside a molecule. Because a molecule is simply the union of its topological atoms the boundary between molecules is also sharp. Hence, a molecule in condensed matter is fully bounded by interatomic surfaces, which are parameter free. The use of molecular contour surfaces of constant electron density (e.g. $\rho = 0.001$ a.u.) is artificial and exists for practical (i.e. visualisation) purposes only. Note that a molecule in the gas phase, alone in the Universe, is a fiction: sooner or later one will find another molecule far away that still shares a topological boundary with the original “isolated” molecule.

The hydrogen cyanide molecule, $\text{H}-\text{C}\equiv\text{N}$, can be isomerised to hydrogen isocyanide, $\text{H}-\text{N}^+\equiv\text{C}^-$, by tilting the hydrogen over the carbon and gradually rotating it to the right. Eventually, this hydrogen ends up at the right hand side of a new linear arrangement, which can also be written as $\text{C}^- \equiv \text{N}^+ - \text{H}$ for easy comparison with $\text{H}-\text{C}\equiv\text{N}$. At some sharp transition point during the rotation of hydrogen, the atomic interaction line flips over: where it originally connected H and C , it then connects H and N . This means that the connectivity of the atoms suddenly changes, which is a topological feature. This is an example of a so-called conflict mechanism.

We now ask in which way(s) the name topology is appropriate for what we have discovered. Topology is the mathematical study of shapes and topological spaces. It is an area of mathematics concerned with the properties of space that are preserved under continuous deformations including stretching and bending. Avoiding precise mathematical terms, one can define topology as the study of qualitative properties of certain objects that are invariant under continuous transformations. For example, Euler’s work on the Königsberg bridge problem was one of the earliest topological studies. He showed it was impossible to find a route through the city of Königsberg that crosses each of the seven bridges exactly once. This solution only depended on which bridges are *connected* to which islands and riverbanks. In other words, only connectivity mattered, not the length of the bridges or the distances between them. This work also marked the beginning of graph theory and thereby establishes a link between topology and graph theory. In general, the motivation behind topology is that some geometric problems do not depend on the exact shape of the objects involved, but rather on the way they are put together. How does this way of thinking apply to the analysis of the electron density discussed above?

The keyword “topology” was first used [15] in the expression “quantum topology” by Bader et al. in 1979. Unfortunately, this name is already taken by a branch of mathematics that connects quantum mechanics with low-dimensional topology, which has little to do with Bader et al. developed and which culminated in QCT. In any event, the name “quantum topology” was inspired by a paper [16] by Collard and Hall published in 1977. These authors were the first to use the Poincaré-Hopf theorem, which links the respective numbers of each of the four possible types of critical points to the so-called Euler characteristic. The latter is a purely topological concept and hence justifies the name topology. The Euler characteristic is an application of *algebraic topology*, one of the four branches of topology, which uses tools from abstract algebra to study topological spaces. Collard and Hall also pointed out that the analysis of the discontinuous change in

the topological characteristics of a molecular charge distribution resulting from the continuous change in its nuclear coordinates is given by *catastrophe theory* [17]. This theory is a branch of *bifurcation theory* in the study of *dynamical systems*. In turn, bifurcation theory is the mathematical study of changes in the qualitative or topological structure of a family of vector fields. A second branch of topology called *differential topology*, which is the field dealing with differentiable functions on differentiable manifolds and which is closely related to differential geometry, also applies to QCT. In fact, as early as 1996, a differential geometry study [18] appeared on the Gaussian curvature of interatomic surfaces. Differential topology also makes use of the Poincaré-Hopf theorem, and hence the two branches of topology overlap. Finally, we mention that there are two remaining branches in topology, called *geometric topology* and *general topology*. The first branch, which includes knot theory, is the study of manifolds and maps between them, particularly embeddings of one manifold into another. This branch does not appear to have been applied as of yet in QCT. The second branch (general topology, also known as point-set topology) establishes the foundational aspects of topology (point-set topology, compactness and connectedness etc.). It deals with the basic set-theoretic definitions and constructions used in topology, and thereby underpins the three other branches (differential, geometric and algebraic topology).

Figure 2.6 shows an example of a 2D dynamical system that has nothing to do with quantum mechanics but shows key features of QCT. The equations state how the time derivative (dot signifies d/dt) varies as a function of the position in (x, y) space, as a non-linear function of x and y. A particle at position (x, y) will travel

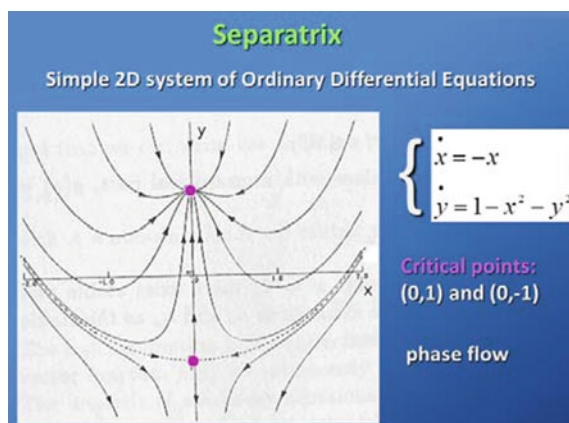


Fig. 2.6 Simple system of two ordinary differential equations, which shows a separatrix (*dashed line*) and two critical points (*pink*). This topological object separates the basin dominated by the attractor critical point (0, 1) (*top*). The second critical point shown is a saddle-type critical point, at which the separatrix trajectories (*dashed line*) terminate. The collection of trajectories (*phase flow*) can be seen as the paths followed by imagined particles travelling in time. The superscripted dots in the equations signify differentiation with respect to time

with a direction and magnitude given by the vector $(-x, 1-x^2-y^2)$. The resulting trajectories form the phase flow in Fig. 2.6, which is reminiscent of the gradient vector field of the electron density of a diatomic molecule with one nucleus shown (at the attractor critical point $(0, 1)$). The second critical point shown lies at point $(0, -1)$ and clearly has a qualitatively different flow pattern locally. This critical point is both a maximum and a minimum, depending on the direction of approach to it, and is reminiscent of a bond critical point. The two dashed trajectories lines that terminate at this critical point form a separatrix, which is reminiscent of an interatomic surface.

A non-exhaustive list of quantum mechanical functions that have hitherto been partitioned includes the electron density $\rho(\mathbf{r})$ (the analysis of which started with Ref. [19]), its Laplacian $\nabla^2\rho(\mathbf{r})$ (started off with Refs. [20, 21] and studied for the first time in terms of the full topology in Refs. [13, 22, 23]), the nuclear potential $V_{\text{nuc}}(\mathbf{r})$ (studied [24] already in 1980 but the first elaborate and self-contained study [10] appeared only 30 years later), the electron localization function (ELF) [25] (started with Ref. [26] and reviewed in Ref. [27]), the electrostatic potential [28] (started with thorough but stubbornly named “topographic” instead of topological studies [29, 30] and continued with more modern work [31–34]), the virial field [35], the magnetically induced molecular current distributions (started with [36]), the intracule density (started with Ref. [37]), the Ehrenfest force field (topology first investigated [38] in 2012 and then improved [39] in 2015), and finally the topological energy partitioning (Coulomb potential energy partitioning started with [40] and culminated into the theory of Interacting Quantum Atoms (IQA) [41] (see below), leading to energetic underpinning for the topological expression of chemical bonding [42]) By bundling all these QCT studies under the umbrella of the topology, the combined method is strengthened and can start competing with the more traditional interpretative method of quantum chemistry [43–49]. This competition should be seen in the light of falsification.

At the end of Sect. 2.2 it is useful to pause and muse about the character of the topology as an instrument to study Nature. The language of dynamical systems, which is rooted in topology, is at the heart of QCT. A hallmark of QCT’s partitioning is its binary character: a point in space belongs to a QCT subspace or not. Whereas non-QCT approaches allow for more gradual transitions from one subspace (e.g. an atom) to another, QCT works with step functions. The 3D step function defines a finite-volume subspace that remains well defined under (possibly large) geometrical deformations. Topology does allow for large deformations in the geometry of the objects it defines while still characterising them by the same invariant measures. However, once beyond a certain degree of deformation, the topological object changes. The suddenness of this change makes some researchers uncomfortable. The comfort of a gradual change may look appealing but then one can ask if this is a false comfort. Can a world view with only gradual change make any clear decision on what is A and what is B ? Or should one not care about being able to make this decision? Or can one make the decision at the price of introducing a parameter? But is then the problem of state allocation (i.e. making the aforementioned decision) not simply deferred to fixing a parameter value?

The topology, even with its abrupt decisions, focuses on the essence of a system in the same way that a phase diagram does. A molecular system can be in the liquid state or the solid state, and the transition between these two states is abrupt (in the limit of an infinitely large system). A phase diagram shares the characteristics of a topologically partitioned space: it has sharp boundaries and it ignores the geometrical details of the system. Indeed, a phase diagram looks beyond the exact positions of the atoms in the molecules that make up a system; the atoms can vibrate while the molecules can translate and rotate. In the same way, QCT looks beyond the exact trajectories of the gradient paths but focuses on their connectivities, which are robust over large deformations of the gradient paths themselves. A topological atom is then analogous to a phase. This is an example of how Nature itself apparently imposes binary structures onto reality: it makes sense to say that a piece of matter is either a liquid or a solid and the boundary between the two is sharp.

There are more examples of sharp compartmentalisation in Nature. One of the deepest examples is the architecture of thermodynamics, which discerns the system and the surroundings. It is essential to the theoretical and practical functioning of thermodynamics that a point in space either belongs to the system or to the surroundings. Any fuzzy partitioning or delay in decision would paralyse any thermodynamic calculations or predictions. Secondly, Life itself, this most complex of structures, has organised and evolved under the very existence of sharp boundaries. Due to its small size, a cell membrane is a relatively sharp boundary between the cytoplasm and the extracellular space. Of course, the boundaries are open (under the control of specialised proteins in the cell's lipid membrane). The boundaries of a topological atom are also open in that electrons can swirl through them. A topological atom is a pattern, comparable to the shape of water as it rapidly cascades over a rock in a river. From a distance, the water appears standing still in a barely fluctuating shape but of course the water itself streams through the pattern. Thirdly, at a higher level, human societies have also carved up the Earth's space in non-overlapping subspaces with sharp boundaries, called countries. When a territory is not allocated to a single clear "attractor" such as China, Pakistan or India, as in the case of Kashmir, then a dispute arises, proving the inherent human nature of partitioning land into non-overlapping sections. Further examples of binary statuses are found in the legal atmosphere where one is either alive or dead, married or not, or guilty or innocent. The question then remains why Chemistry is not the right locale to propose non-overlapping partitioning. What is so intrinsically fuzzy about atoms and electron densities that would prevent sharp boundaries? Is life or human society perhaps less fuzzy?

At the very end of this section on the topological atom, and on the wider topological approach with its fundamental characteristics and consequences, we put the topology to rest and look at energy instead. Energy is a quantum mechanical observable and the main question is how it can be partitioned. This is the topic of the next section, where we forget about the gradient vector field of the electron density, at least at the start.

2.3 The Quantum Atom

Energy is as important as the electron density. The Schrödinger equation presents the energy and the wave function as prime quantities, joined at the hip and being of equal status. For each eigenvalue (energy), there is an eigenfunction (wave function) and they both come as an inseparable pair. Because the electron density immediately derives from the wave function, the molecular electron density and the molecule's energy are also twinned. Hence, because this electron density is of prime importance due to the first Hohenberg-Kohn theorem, energy shares this importance. Indeed, energy is in charge of the way a molecular system behaves and understanding it is therefore crucial. Phenomena, such as steric hindrance, ultimately reduce to energy considerations, even if sterics appear irreducible intuitively (based on daily life experience). The natural way to understand something (at least in the Western tradition of doing science) is to study its parts. Such an approach calls for the spatial partitioning of energy.

The key question is how to define a molecular *fragment* that has a well-defined kinetic energy. This question is attacked by starting with *local* kinetic energy, which is the kinetic energy at a particular point *per unit volume*. This quantity is thus a kinetic energy *density*, which when integrated over a volume, gives the kinetic energy of the electrons in that volume. The kinetic energy of a molecular fragment is then obtained from a 3D integral of the kinetic energy density over the volume of that fragment. However, there is a practical problem in that there is no “the” kinetic energy density; at best, there is “a” kinetic energy density. We write “at best” because if one starts from the quasiprobability distribution function the quantum mechanical treatment of kinetic energy, partitioned or not, is actually problematic. Local kinetic energy is then ambiguous. However, within the paradigm that Anderson et al. [50] call the “Laplacian family of local kinetic energies”, the deduction below is valid [51].

Although there are an infinite number [52] of expressions for the kinetic energy density, it is sufficient to choose only two possible expressions to develop this deduction [53], as given by Eqs. 2.1 and 2.2,

$$\mathbf{K}(\mathbf{r}) = -\frac{1}{4}N \int d\tau' [\psi^* \nabla^2 \psi + \psi \nabla^2 \psi^*] \quad (2.1)$$

$$\mathbf{G}(\mathbf{r}) = \frac{1}{2}N \int d\tau' \nabla \psi^* \cdot \nabla \psi \quad (2.2)$$

where N is the total number of electrons in the system, ψ the system's N -electron wave function, and $\int d\tau'$ signifies integration over all electrons except one. Note that the electron spin is not considered here. It is easy to show that the two kinetic energy densities, $\mathbf{K}(\mathbf{r})$ and $\mathbf{G}(\mathbf{r})$, are linked via the Laplacian of the electron density, $\nabla^2 \rho$, or

$$\mathbf{K}(\mathbf{r}) = \mathbf{G}(\mathbf{r}) - \frac{1}{4} \nabla^2 \rho(\mathbf{r}) \quad (2.3)$$

The Laplacian of the electron density vanishes when integrated over whole space or

$$\int_{\text{whole space}} dV \nabla^2 \rho(\mathbf{r}) = 0 \quad (2.4)$$

Integrating both sides of Eq. 2.3 over whole space then gives a unique value of the molecule's kinetic energy,

$$\mathbf{K}(\text{molecule}) = \mathbf{G}(\text{molecule}) = \mathbf{T}(\text{molecule}) \quad (2.5)$$

where T expresses *the* kinetic energy regardless of whether it was calculated from $\mathbf{K}(\mathbf{r})$ or $\mathbf{G}(\mathbf{r})$. Because a single molecule in the gas phase occupies whole space, one indeed recovers the kinetic energy of the molecule by integration over whole space. This energy is well-defined because it is unique: indeed, both $\mathbf{K}(\mathbf{r})$ and $\mathbf{G}(\mathbf{r})$ give the same answer.

The main question is now if this same unique result can also be obtained for a molecular *fragment*. Let us consider the subspace of an *arbitrary* fragment, denoted \oplus . For such an arbitrary subspace in 3D space we find that

$$\int_{\oplus} dV \nabla^2 \rho(\mathbf{r}) \neq 0 \quad (2.6)$$

From this equation and integration over both sides of Eq. 2.3, one deduces that

$$\mathbf{K}(\oplus) \neq \mathbf{G}(\oplus) \quad (2.7)$$

Hence, we do not obtain a unique kinetic energy for an arbitrary subspace. However, if we can find a *special* subspace Ω such that

$$\int_{\Omega} dV \nabla^2 \rho(\mathbf{r}) = 0 \quad (2.8)$$

then it makes sense to speak of a unique and hence well-defined kinetic energy $\mathbf{T}(\Omega)$ associated with such a special subspace,

$$\mathbf{K}(\Omega) = \mathbf{G}(\Omega) = \mathbf{T}(\Omega) \quad (2.9)$$

An atom that occupies such a special subspace Ω , and thereby obeys Eq. 2.9, is called a *quantum atom*. At this moment we do not worry about what this quantum atom looks like nor about how many possible such atoms there are. The only matter

we are interested in is whether the topological atom is also a quantum atom. A way to find out is to reformulate Eq. 2.9 using Gauss’s divergence theorem, which yields

$$\int_{\Omega} dV \nabla^2 \rho(\mathbf{r}) = \int_{\partial\Omega} dS \nabla \rho(\mathbf{r}) \cdot \mathbf{n}(\mathbf{r}) = 0 \quad (2.10)$$

where $\partial\Omega$ is the boundary of Ω . Equation (2.10) shows how a volume integral over Ω is equal to a surface integral over $\partial\Omega$. Now we focus on the integrand of the surface integral and also look at the gradient vector field in Fig. 2.3. The interatomic surface $\partial\Omega$, separating H and C for example, is a surface that consists of gradient paths. Hence the normal to this surface, denoted $\mathbf{n}(\mathbf{r})$, is orthogonal to a gradient path at any point belonging to this surface including the bond critical point, or

$$\nabla \rho(\mathbf{r}) \cdot \mathbf{n}(\mathbf{r}) = 0 \quad \forall \mathbf{r} \in \partial\Omega \quad (2.11)$$

If Eq. 2.11 is true then Eq. 2.10 is also true. *Thus a topological atom is a quantum atom.* Note that, unlike Bader et al. do we claim the reverse, which is that each quantum atom is also a topological atom. In fact, we now know that this statement is not correct. So, in summary, all topological atoms are quantum atoms but not all possible quantum atoms are topological atoms [54]. Therefore, any criticism [50] against the orthodox version of QTAIM which is the one propagated by Bader, does not apply to the approach presented here. In other words, we do not insist that the topological atoms are the *only* quantum atoms. We have deliberately introduced and justified topological atoms on their own merit, independently from quantum mechanics. They are indeed remarkable and attractive objects, and one can ask why not more scientific disciplines use the elegant idea of partitioning by gradient vector field subspace (called *basin* in short).

It is important to properly appreciate the result obtained above (Eq. 2.9) as a “gateway” to a fully quantum-mechanically based force field. Traditional force fields ignore kinetic energy, or more precisely, they do not explicitly account for it. However, kinetic energy is a physical quantity and cannot be switched off; it does influence the behaviour of atoms in a system and hence must somehow be incorporated in a force field or what one could call a “rapid energy predictor”. A traditional force field only mimics the effect of kinetic energy, and only indirectly, by including it in a Morse-like potential, for example. Such a methodology does not isolate the kinetic energy in an atomic way. Instead, it lumps the behaviour of the kinetic energy of two interacting atoms into *bond-based* parameters. QCT offers a completely different route, one where the parameterisation is atom-based. Moreover, this novel parameterisation recognises the explicit existence of kinetic energy, at atomic level. That a topological atom offers this route, by virtue of being a quantum atom (with a well-defined kinetic energy) is enticing. In the next section we give a very brief outline of the QCT force field strategy.

2.4 Towards a QCT Protein Force Field

2.4.1 Topological Energy Partitioning

An early and important result in the development of QTAIM was that an atom in a molecule has its own (atomic) virial theorem. This means that, for any given topological atom, there is a (simple) relation between the kinetic energy of this atom and its potential energy. This in turn means that the potential energy of an atom (i.e. interacting with itself and all remaining atoms) can be trivially calculated from the atom's kinetic energy (which we already know to be well defined). As a further consequence, the total energy of an atom (which is the sum of kinetic and potential energy) can be calculated from the kinetic energy alone. The sum of all total atomic energies forming a molecule then yields the total energy of that molecule. However, all of this is only true if the forces on the atomic nuclei vanish. If not, one is left with a residual virial term consisting of nuclear position vectors dotted into non-vanishing forces on the nuclei. Partitioning the latter (molecular) quantity over the respective atoms has always been a problem, until in 2001 the potential energy of an atom was calculated [40] independently from the kinetic energy.

The calculation of the interatomic electrostatic potential energy V_{elec} involves a six-dimensional integral, over the volume of each of the two topological atoms A and B , or

$$V_{elec}^{AB} = \int_{\Omega_A} d\mathbf{r}_1 \int_{\Omega_B} d\mathbf{r}_2 \frac{\rho_{tot}(\mathbf{r}_1)\rho_{tot}(\mathbf{r}_2)}{r_{12}} \quad (2.12)$$

where the *total* charge density, $\rho_{tot}(\mathbf{r})$, is the sum of the nuclear charge density and minus the electron density $-\rho(\mathbf{r})$ (i.e. electronic and hence corrected by a minus sign catering for the negative electronic charge), while r_{12} is the distance between two infinitesimal pieces of charge density [40]. This work was further developed with the calculation of non-Coulomb interaction energies [55, 56].

The use of Eq. 2.12 implies that the condition of vanishing forces no longer restricts the topological partitioning of the molecular energy into intra- and inter-atomic contributions. This advance led to the development of Interacting Quantum Atoms (IQA) [41], which since its implementation in AIMALL [57] has become an increasingly popular tool in the armoury of interpretative quantum chemical tools. A second and parallel development from the advance in the aforementioned 2001 paper [40] is that of a quantum mechanical force field based on the energies associated with topological atoms (at any nuclear configuration and including non-stationary points on the potential energy surface). This is indeed what our lab started doing, initially much focusing on multipolar electrostatics, under the acronym QCTFF (Quantum Chemical Topology Force Field) [9, 58–60]. There is sustained and consistent evidence [61] that multipole moments are more accurate and realistic than point charges. In spite of the latter's inherent and well

documented limitations some researchers are still looking (e.g. Ref. [62]) for the “magic point charge” that accurately reproduces the molecular electrostatic potential, even if that point charge is then just a mathematical number without any connection to the physical process of charge transfer. We believe that the atomic monopole is primarily a measure of charge transfer; at long range this monopole becomes increasingly representative of the electrostatic potential that this atom generates.

Applying the Laplace multipole expansion leads to

$$V_{elec}^{AB} = \sum_{l_A l_B m_A m_B} T_{l_A l_B m_A m_B} Q_{l_A m_A} Q_{l_B m_B} \quad (2.13)$$

where $Q_{\ell m}$ represents the m -th component of a rank ℓ atomic multipole moment, while T is a purely geometrical interaction tensor. The convergence properties of this series expansion have been thoroughly studied [63–67] by our lab. There are three conceptual and technical advantages associated with QCT multipole moments. They are more compact than Cartesian multipole moments, avoiding redundancies, they demonstrate good convergence at short-range, and they escape penetration effects (and hence damping functions) due to their non-overlapping nature.

Note that V_{elec}^{AB} consists of 4 contributions, exhausting the purely electronic and nuclear contribution on both A and B (i.e. $4 = 2 \times 2$) that is, the electron-electron Coulomb energy $V_{ee,coul}^{AB}$, the electron-nucleus attraction (potential) energy, denoted V_{en}^{AB} , its dual V_{en}^{BA} , and the nucleus-nucleus repulsion, V_{nn}^{AB} . When added, these terms lead to the full electrostatic interaction between two atoms A and B , V_{elec}^{AB} , or

$$V_{elec}^{AB} = V_{ee,coul}^{AB} + V_{en}^{AB} + V_{en}^{BA} + V_{nn}^{AB} \quad (2.14)$$

The electron-nucleus attraction energy is calculated as a three-dimensional integral,

$$V_{en}^{AB} = -Z_B \int_{\Omega_A} d\mathbf{r} \frac{\rho(\mathbf{r})}{r_{1B}} \quad (2.15)$$

where r_{1B} is the distance between an electron inside the volume of atom A and the nucleus of atom B . This calculation can also be performed if $A = B$, which features in the intra-atomic energy discussed below.

The energy $V_{ee,coul}^{AB}$ can be related to the second-order reduced matrix, $\rho_2(\mathbf{r}_1, \mathbf{r}_2)$. To understand how exactly, one needs to know the fine structure of $\rho_2(\mathbf{r}_1, \mathbf{r}_2)$, or

$$\rho_2(\mathbf{r}_1, \mathbf{r}_2) = \rho_2^{coul} + \rho_2^{exch} + \rho_2^{corr} = \rho(\mathbf{r}_1)\rho(\mathbf{r}_2) - \rho_1(\mathbf{r}_1, \mathbf{r}_2)\rho_1(\mathbf{r}_2, \mathbf{r}_1) + \rho_2^{corr}(\mathbf{r}_1, \mathbf{r}_2) \quad (2.16)$$

where the first term refers to the quantum-mechanically uncorrelated Coulomb-like pair density, the second term to the Fock-Dirac exchange (which is dominated by and associated with the Fermi hole), while the third term is at least an order of magnitude smaller [41, 68] than the second term, and connected with the Coulomb hole. The energy quantity V_{ee}^{AB} is associated with the whole of $\rho_2(\mathbf{r}_1, \mathbf{r}_2)$, collecting the three types of interactions that electrons experience when interacting with each other. Each term in Eq. 2.16 is associated with a type of potential energy, so that the corresponding fine-structure of V_{ee}^{AB} automatically follows,

$$\begin{aligned}
 V_{ee}^{AB} &= \int_{\Omega_A} d\mathbf{r}_1 \int_{\Omega_B} d\mathbf{r}_2 \frac{\rho_2(\mathbf{r}_1, \mathbf{r}_2)}{r_{12}} \\
 &= \int_{\Omega_A} d\mathbf{r}_1 \int_{\Omega_B} d\mathbf{r}_2 \frac{\rho(\mathbf{r}_1)\rho(\mathbf{r}_2)}{r_{12}} - \int_{\Omega_A} d\mathbf{r}_1 \int_{\Omega_B} d\mathbf{r}_2 \frac{\rho_1(\mathbf{r}_1, \mathbf{r}_2)\rho_1(\mathbf{r}_2, \mathbf{r}_1)}{r_{12}} + \int_{\Omega_A} d\mathbf{r}_1 \int_{\Omega_B} d\mathbf{r}_2 \frac{\rho_2^{corr}(\mathbf{r}_1, \mathbf{r}_2)}{r_{12}} \\
 &= V_{ee,coul}^{AB} + V_{ee,exch}^{AB} + V_{ee,corr}^{AB}
 \end{aligned} \tag{2.17}$$

The second term in Eq. 2.17 represents the exchange delocalisation energy, $V_{ee,exch}^{AB}$, which is (already) present at Hartree-Fock level. This term teases out the interaction that keeps bonded atoms together. The degree to which atoms are bonded can be estimated by a non-energy measure, which is typically a quantum-mechanical bond order. QCT offers such a measure [69]. However, it was shown by our lab [56] that this bond order is only the first term of the multipolar expansion of $V_{ee,exch}^{AB}$. Hence, the latter quantity contains more information than a bond order. However, in the construction of QCTFF, the route of expanding $V_{ee,exch}^{AB}$ as so-called *exchange moments* was abandoned because they have an imprint of the molecular orbitals they are derived from. This imprint hampers transferability. The energy quantity $V_{ee,exch}^{AB}$ can remain unexpanded because it drops off so quickly with distance [70] in saturated systems, which proteins largely are. However, multipole moments are essential in the representation of electrostatics because this type of interaction drops off more slowly than V_{elec}^{AB} . Therefore the number of non-negligible V_{elec}^{AB} values is much larger than the number of $V_{ee,exch}^{AB}$ values. The trouble with this observation is the rapidly increase in the number of possible distances between *A* and *B*. In other words, atoms that are further apart can appear in more possible configurations than atoms that are closer to each other. This is why it is undesirable to calculate all possible $1, n$ ($n > 4$) V_{elec}^{AB} interactions. A multipole series succeeds in avoiding the calculation of all these V_{elec}^{AB} interactions. The series separates a geometrically entangled (since r_{12} involves simultaneously \mathbf{r}_1 and \mathbf{r}_2) energy quantity into single atom quantities, i.e. multipole moments. This separation enables the calculation of the interatomic interaction to be free of large geometric variations. Conversely, short-range interactions (1, 2; 1, 3 and 1, 4) are geometrically much more constrained and hence would not benefit that much from multipole moments. This is why it is alright to *not* expand the electrostatic energy V_{elec}^{AB} at short range.

The third term in Eq. 2.17 completes the discussion on the three types of electron-electron energy contributions. The quantity $V_{ee,corr}^{AB}$ covers the effect of dynamic correlation and hence dispersion. It is absent at Hartree-Fock level or $V_{ee,corr}^{AB} = 0$.

$$V_{ee,corr}^{AB} = \sum_{j=1}^{n_G} \sum_{k=1}^j \sum_{l=1}^{n_G} \sum_{m=1}^l d_{jklm} \int_{\Omega_A} d\mathbf{r}_1 \int_{\Omega_B} d\mathbf{r}_2 \frac{1}{r_{12}} G_j(\mathbf{r}_1 - \mathbf{R}_j) G_k(\mathbf{r}_1 - \mathbf{R}_k) G_l(\mathbf{r}_2 - \mathbf{R}_l) G_m(\mathbf{r}_2 - \mathbf{R}_m) \quad (2.18)$$

where d_{jklm} are 4-index coefficients that we have extracted from the computer program GAUSSIAN, G_p is the p -th Gaussian primitive centered on \mathbf{R}_p and n_G is the number of primitives. The number of d-coefficients rapidly increases with the number of primitives, in particular as $\frac{1}{4}[n_G(n_G + 1)]^2$. Hence truncation schemes must be devised and I/O optimised.

The energy contribution $V_{ee,corr}^{AB}$ was calculated for the first time [71] as late as 2015, for the four simple case studies of H_2 , N_2 , H_2O and CO , operating on CCSD/cc-pVDZ wave functions obtained by the program MOLPRO. The effect of dynamic correlation is dual: an increase in the magnitude of the nucleus-electron attraction energy, and a decrease in the electronic repulsion. Representing dispersion accurately and consistently within the QCT framework (rather than by a bolt-on [72]) is important for future-proof success in the modelling of the conjugated residues (imidazole, phenol, indole and benzyl) of the four aromatic amino acids [73]. This streamlined approach will avoid penetration effects, which the non-overlapping topological atoms naturally preclude. Hence, there is no need for damping functions in QCTFF. It appears that satisfactory expressions for damping functions are problematic in view of the complexity of atom typing [74]. The dynamic correlation part of QCTFF is currently under investigation in lab (in connection with the program GAUSSIAN). Figure 2.7 summarises the three types of interatomic energy contributions of QCTFF.

The remaining energy contribution is intra-atomic in nature, denoted E_{intra} , and measures the intrinsic stability of an atom. It cannot be written as “V” because this symbol is reserved for potential energy only and the atomic “self-energy” [40] also contains kinetic energy, which is well-defined for a topological atom, as clearly argued above. Broadly speaking, E_{intra} features in (and indeed may control) rotation barriers, steric hindrance, the anomeric effect, the gauche effect or other stereo-electronic effects. We note that in typical potentials, such as the Lennard-Jones potential, repulsion is formulated as an *inter*-atomic effect, whereas within QCT, steric “interaction” is a *mono*-atomic property. The full consequence of this philosophical difference still needs to be worked out because it already appears to have an impact on the way we should think about “steric clashes”. Some support against the traditional view that steric effects are due to precise one-to-one interaction, and hence in favour of the QCT view, comes from a non-QCT angle.

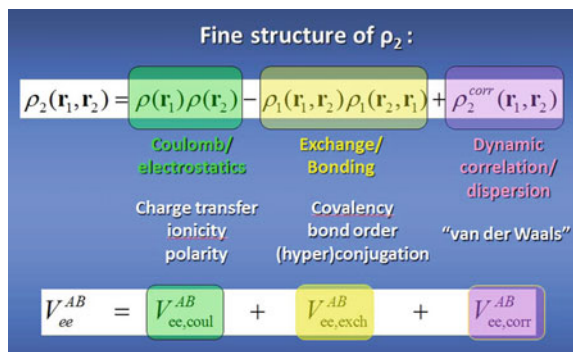


Fig. 2.7 Overview of the three types of inter-atomic energy contributions: Coulomb, exchange and correlation, each with the specific chemical insight they offer

Weinhold, who pioneered the natural bond orbital (NBO) method, writes in a paper [75] dating from 1997: “A persistent theme of this work is that steric exchange repulsion is not simply a sum of pairwise interactions between two electron pairs, but rather a complex function of the entire N-electron distribution. The pattern of orbital energy changes due to exchange repulsion is more complex than a simple “atom–atom repulsion” picture would suggest.” The contribution E_{intra} has indeed an imprint of the whole molecule, although it has a practical cut-off, which we call the atomic horizon (see next paragraph and energetic transferability between tri- and penta-peptides).

Setting $A = B$ in Eqs. 2.15 and 2.17 allows one to write the intra-atomic energy of topological atom A as

$$E_{intra}^A = T^A + V_{ee}^{AA} + V_{en}^{AA} \quad (2.19)$$

where T^A is its kinetic energy. The intra-atomic energy E_{intra}^A is the energy that a single atom possesses inside a system, regardless of whether this system is a single molecule or a cluster of molecules (including even ions). Work from our lab (to be published in *Molecular Physics* 2016) shows that an oxygen, nitrogen or carbon has the same energy, within maximum 2.3 kJmol^{-1} , when appearing in a tri-peptide (three amino acids) compared to appearing in a penta-peptide, with these peptides’ common nuclear skeleton in the same configuration. This energetic transferability was observed in seven test cases, i.e. the homo-oligopeptides of Ala, Ser, Thr, Gly, Val, Leu and Ile. This high degree of energetic transferability is an asset to QCT. Transferability has also been detected [76] in terms of atomic charges by those who develop alternative partitioning schemes (such as the Hirshfeld partitioning [77] scheme and all its variants).

2.4.2 Machine Learning

The final strand of QCTFF to discuss briefly is the way atomic properties (both intra- and inter-) are predicted from the coordinates of the nuclei surrounding the atom of interest. In general, this mapping is so complex that it needs a machine learning method, and one that can handle high-dimensional spaces, given the large number of coordinates that influence the atom of interest. Kriging [78] is such a method. Originating in geostatistics, Kriging is a powerful interpolation technique that can capture the behaviour of an output as a function of many inputs, using a relatively small amount of data points. In its infancy [79] it succeeded in predicting where the best location for a mine would be in a two-dimensional landscape, based on measurements of a precious material (originally gold but could be diamond, oil, uranium or any ore) at various locations in this landscape. The basic idea of Kriging is to predict the value of a function at a given point by computing a weighted average of the known values of the function in the neighborhood of the point. An accessible account of the details of Kriging as used within the QCTFF context has been given elsewhere [80].

Here we highlight one key idea, namely that of maximising the likelihood L , which has not been clarified in that previous account [80]. To fix thoughts, let us start with a simple example: a coin is being tossed thrice. If the coin is fair, then the probability to observe head up, (denoted p_H), is one half, that is $p_H = 0.5$. Equally, the probability of observing tail denoted p_T is one half, or $p_T = 0.5$. The probability to observe head up twice and then tail (HHT) is $p_{HHT} = p_H p_H p_T = p_H^2 (1-p_H) = 0.125$. An equivalent way of saying this is to reverse this statement: the likelihood L that the coin was fair (i.e. $p_H = 0.5$), given the observation of two heads being up (HHT), is one eighth, i.e. $L = 0.125$. This is formally written as follows:

$$L(p_H = 0.5|HHT) = 0.125 \quad (2.20)$$

In summary, the likelihood L is a function returning the probability of observed outcomes (e.g. HHT), given a parameter value (i.e. p_H). We now ask ourselves how the likelihood $L = p_H^2(1-p_H)$ can be maximised. Mathematically this is easy: calculus tells us that $dL/dp_H = d/dp_H [p_H^2(1-p_H)] = 2p_H - 3p_H^2$, which vanishes when $p_H = 2/3$. A plot, or a quick calculation of the second derivative, tells us that $p_H = 2/3$ is indeed a maximum, at which point $L = 4/27$. The result that $p_{H, \max L} = 2/3$ can be intuitively understood by stating that the coin is biased towards heads up, by a factor 2 over tail up. Indeed, with such a bias, the probability of the observed outcomes HHT, given $p_H = 2/3$, is maximal. How does all this help understanding a key aspect behind Kriging?

Kriging uses the same strategy of maximising the likelihood: it finds the parameters θ_h and p_h ($h = 1, 2, \dots, d$) in the so-called Gram matrix \mathbf{R} ,

$$R_{ij} = \exp \left[- \sum_{h=1}^d \theta_h |x_h^i - x_h^j|^{p_h} \right] \quad \theta_h > 0, \quad 0 < p_h \leq 2 \quad (2.21)$$

such that the likelihood L of the Kriging model, given the observed data points y^i ,

$$L(\boldsymbol{\theta}, \mathbf{p}, \mu, \sigma | y^i; i = 1, 2, \dots, N) \sim \exp \left[- \frac{(\mathbf{y} - \mathbf{1}\mu)^T \mathbf{R}^{-1} (\mathbf{y} - \mathbf{1}\mu)}{2\sigma^2} \right] \quad (2.22)$$

is maximal, where σ^2 is the process variance, $\mathbf{1}$ is a column vector of ones, and μ models the global trend of the observable \mathbf{y} . The observations are fixed (i.e. atomic properties = output and coordinates of surrounding nuclei = input) but the parameters are being varied such that what we observed becomes maximally likely. How this maximisation is achieved is beyond the scope of this intentionally non-technical text but this is a very important active research topic in our lab.

We refer the interested reader to the literature [51, 73, 80–86] for the use of Kriging in the construction of QCTFF. Here we can only afford three general remarks. Firstly, we know that three of the four types of energy contributions described above can be Kriged successfully for all 20 amino acids, cholesterol, small carbohydrates and small water clusters (also in the presence of a cation) and a few pilot systems (NMA, ethanol, water, etc.). Proof-of-concept of successful Kriging of the dynamic correlation energy contribution still needs to be obtained but we do not expect any fundamental problems.

Secondly, the term “successful” needs to be qualified. The performance of a Kriging model is validated by an external test set of molecular configurations. This is where we display the full performance of a Kriging model over the *whole* test set, by means of a so-called S-curve. From the latter one can read off which percentage of test configurations scores an energy prediction error up to any desired value. For example, if this value is set to 4 kJmol⁻¹ (referring the old-fashioned and arbitrary unit of kcalmol⁻¹) then 70 % of test configurations containing all local energy minima found in the Ramachandran map of the doubly-capped amino acid isoleucine, return an error of less than 4 kJmol⁻¹. While the mean error over all 200 test configurations is 3.3 kJmol⁻¹, there is a small percentage (~2 %) of test configurations that have errors just over 10 kJmol⁻¹. While this behavior is typical, matters are worse for cysteine where only 50 % return an error of less than 4 kJmol⁻¹, while the average is 5.3 kJmol⁻¹ and just over 10 % have an error within the interval 10–20 kJmol⁻¹. The reported errors are all purely electrostatic and involve all interactions of the type 1, 4 and higher. This is a rather severe test because it involves short-range interactions, switching on all multipole moments up to the hexadecapole moment. The average of mean errors over all 20 amino acids is 4.2 kJmol⁻¹, while the worse values are for cysteine, alanine and arginine, all at 5.3 kJmol⁻¹. The best mean error is 2.8 kJmol⁻¹ for tyrosine.

Thirdly, the kriging method covers all polarisation effects, but without introducing polarisabilities. The QCTFF method focuses on the end result of the

polarisation process, not the process itself. As a result, when used in a molecular dynamics simulation, QCTFF renders immediately the energies of all atoms in response to a given nuclear configuration. There is no need to iteratively converge towards a self-consistent field at each simulation step.

2.5 An Invitation to Falsification

As announced in the Introduction there is a need for more falsification in the area of chemical interpretation by means of quantum mechanical tools. In a first stage contradictions need to be spotted: when are two methods providing (semi)-quantitatively or qualitatively different interpretations? The second stage is more challenging: how can an experiment judge one interpretation to be right and the other wrong? A valiant but strongly disputed [87] example of this kind of scientific activity was published [88] in 2009 where it was claimed that experiment could disprove QTAIM's interpretation of an attractive interaction between the two hydrogens in the bay region of phenanthrene.

With regards to the second stage, one could broaden the decision process, not through experiment, but by teasing out a clash with a theoretical principle or another theoretical interpretation that is more firmly established. For example, a number of electronegativity scales all agree that boron is a very electropositive element. One may then ask how it is possible that a population analysis allocates a negative net charge to boron. Yet this happens. For example, in 1995 Siegbahn allocated a net charge $-0.26e$ to boron in $(\text{BH}_3\text{NH}_3)_2$ using the Mulliken population analysis. Of course the QTAIM charge of boron is emphatically positive. Another candidate for a falsifiable case study is that of 1, 2-difluoroethene, which was discussed in a 2009 publication [89] comparing the IQA method (i.e. QCT) with the non-QCT method EDA and NBO, in connection with interpreting stereo-electronic effects. IQA rules that there is significant FF' delocalisation in the *cis* isomer, which is "not easily found in NBO" according to the article. This is a fine example of one method spotting an effect and the other not. The challenge is to exploit this difference, either via an experiment that can confirm one or the other method, or demonstrate that guidance (in synthesis for example) is more reliable by one method than by the other.

A final example is that of diborane. A pivotal question is: can QTAIM and hence QCT extract a Lewis diagram from a given molecular wave function? A very recent study, published [70] in 2013, set out to answer precisely this question, and the answer is yes. It is possible by inspecting motives in calculated V_{exch}^{AB} values, and this 2013 work systematically investigated V_{exch}^{AB} values, for all atom-atom interactions in 31 small covalent molecules (including ions) and 3 van der Waals complexes. For the first time, clear clusters were revealed in the values of V_{exch}^{AB} , clusters separated by almost an order of magnitude in energy, starting with hundreds of kilojoules per mole, and decreasing in a stepwise manner to less than

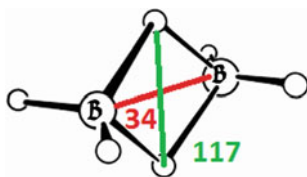


Fig. 2.8 A ball-and-stick diagram of diborane, B_2H_6 , endowed with numerical values of $-V_{xc}^{AB}$ in kJmol^{-1} . The unlabelled disks represent hydrogen atoms

0.1 kJmol^{-1} . This quantitative information reveals where to draw the lines in a Lewis diagram.

A useful example illustrating this success is that of diborane, B_2H_6 , which at one time was controversial in terms of its Lewis structure. Figure 2.8 shows a ball-and-stick diagram of B_2H_6 , endowed with $| -V_{xc}^{AB} |$ values (in kJmol^{-1} and for HF/6-311G(d,p) wave functions). The two largest (absolute) values are 385 and 222 kJmol^{-1} , corresponding to the covalent bonds BH_{term} and BH_{bridge} , respectively. They provide the “sticks” of the molecular graph, which was controversial until 1951. We note that Pauling got the structure wrong while Longuet-Higgins got it right. The next strongest interaction is that between the bridging hydrogens (117 kJmol^{-1}) (green in Fig. 2.8), which is three times larger than the value between the two borons (34 kJmol^{-1}) (red in Fig. 2.8).

In a private communication, Roald Hoffmann spontaneously pointed out that the HH interaction is something new to him and that there is some BB bonding in B_2H_6 is easier to understand. The latter assertion followed from his explanation of a MO diagram. Here we have a clear example of two theories (QCT and MO) stating qualitatively different things. Again, the challenge is to find an experiment that could settle this contradiction.

In closing this section, it is helpful to philosophise a little more, in order to contemplate if the suggested falsification is useful or even possible. Let us start with a simple and clear but ridiculous example (plucked from reality). A reality TV celebrity said that she thought that the sun and the moon were the same object. Sure: when the sun has gone down then it is time for the moon to appear a bit later on. A casual observer may not have a problem with this view. In fact, contemporary political correctness and encouragement of diversity in personal views may even support this assertion. Her “theory” can be adhered to for a long time until one evening, a less casual and alert observer (hopefully herself) sees a red sun at dusk *at the same time* as the moon, and both objects and *clearly separated* in the sky, almost at opposite ends in fact. Such special evenings exist and this one “experiment” kills off the old theory. In summary, at the edge of our knowledge, competing theories (e.g. sun = moon and sun \neq moon) coexist. However, one crucial observation can banish one theory to the history books while promoting the other to build on and use for asking the next exciting question. It is important that a decision is obtained as to which theory is right because otherwise, any planning on how to put a person on the moon is clearly futile, just as an example. To recap briefly with a

now serious example, Alan Guth's inflation theory is really at the edge of our collective human knowledge. This theory predicts the existence of gravitational waves but they have never been detected with certainty (in spite of a premature announcement in 2014). A momentous multi-year, multi-team data collection project set up on the South Pole, can still not decide if gravitational waves exist or not. The signal could be due only to galactic dust. It remains important to settle this question for once or for all. Falsification is needed to make true progress.

The main question is now if the process of falsification (whether smoothly controlled or erratic is not important) is relevant for the interpretation of chemical phenomena. Is the above analysis of the two examples discussed too simple? Does the mechanism of falsification apply to theoretical interpretative chemistry? I believe it does but we should be aware of one more notion. Let us discuss what I call the *non-question*, again starting with an example.

How can we come to grips with the particle-wave duality? Is there an experiment that can decide, for once and for all, if a quantum object is either a particle or a wave? The textbook answer is no: the quantum object is both. But then we ask why this question cannot be settled. In fact, there are enough experiments that decide in favour of a wave, while others decide in favour of a particle. How can this be? A way out is suggesting that the wave-particle question is a *non-question*. *A non-question is a question that cannot be settled one way or the other because it makes a fundamentally wrong assumption.* The problem here, however, is that it is not clear which assumption exactly. But there are several clear examples of non-questions. One is "what is north of the North Pole?", another is "What came first: the chicken of the egg?" The latter cannot be solved because it ignores what really happened in evolution: a pre-chicken "lays" a pre-egg and so on. As one moves back in time the distinction between the two becomes problematic and the question actually dissolves. This chicken-egg "question" is a non-question because it wrongly assumes that one can project a binary end point of evolution onto the very beginning of this evolution. Such a false projection is clearer in a typical child-like question such as "why does a tree not weep if it is chopped down?" Well, one needs a pretty highly developed nervous system in order to weep, a system that the tree clearly lacks. Again, this is a simple example, perhaps ludicrous to adults, but unfortunately spilling over to the world of some adults who believe plants feel pain.

Of course, one should be open to new initially mysterious phenomena, such as X-rays killing living cells. Clearly, X-rays do not emerge from the wonderfully mature edifice of classical mechanics. But one should beware of the non-question. One can spend a life time thinking about the question of the beginning and end of a thing until someone shows that this thing is actually circular. This then means that the wrong image has been projected onto an object, giving rise to a natural and innocent question, which turns out to be a vicious non-question. Imagine if this thing is the Universe. One will then have wasted a life time thinking about this question because it actually turned out to be a non-question. The earlier one spots a non-question, the earlier one can ask the real question. This transition is a major

advance: perhaps from childhood into adulthood, from deluded or blinkered adult to informed adult, from scientist in a desert to scientist in an oasis.

As a community, we should increase the effort in spotting non-questions. Maybe “how aromatic is this compound?” is a non-question. In order to save time and focus on the real question I advocated [90] to carry out bottom-up research and focus on the emergence of patterns of primary quantities (closely linked to the Schrödinger equation). If aromaticity is captured some way along this bottom-up approach then this concept is lucky, as it were, and will survive. Those that spotted this property, more than a century ago, at high and intuitive level, without knowing about quantum chemistry, will then be vindicated. But if aromaticity falls apart into two or more new concepts, or even worse, evaporates altogether, then that is progress. We have then turned the non-question into a question and we can then re-explore the complex world of chemical phenomena armoured with more powerful insight.

2.6 Conclusion

Quantum Chemical Topology has a long and rich history of about four decades. It started with an innocuous paper [19] in 1972, which however marked the birth of a completely novel way of thinking about how to partition and characterise a quantum mechanical system. That the topological atom, which can exist in its own right, is also a quantum atom, makes it possible to build a force field using these atoms. Perhaps this force field is better “called a rapid energy predictor” because it overhauls the architecture of traditional force fields and probes deeper into the quantum mechanics that underpin them. Finally, we point out the need for falsification of theoretical interpretative tools and theories. Experimentalists need more reliable and predictive guidance from theoretical interpretation. If methods contradict each other there is an opportunity to establish one method as the way forward. However, one should beware of the non-question.

Acknowledgments I thank the EPSRC for the award of an Established Career Fellowship.

References

1. Bader RFW (1991) A quantum-theory of molecular-structure and its applications. *Chem Rev* 91:893–928
2. Popelier PLA (2014) The quantum theory of atoms in molecules. In: Frenking G, Shaik S (eds) *The nature of the chemical bond revisited*, Chapter 8. Wiley, pp 271–308
3. Bader RFW (1985) Atoms in molecules. *Acc Chem Res* 18:9–15
4. Bader RFW (1990) *Atoms in molecules. A quantum theory*. Oxford Univ. Press, Oxford, Great Britain
5. Popelier PLA (2000) *Atoms in molecules. An introduction*. Pearson Education, London

6. Matta CF, Boyd RJ (2007) The quantum theory of atoms in molecules. From solid state to DNA and drug design. Wiley, Weinheim
7. Popelier PLA (2012) Quantum chemical topology: on descriptors, potentials and fragments. In: Banting L, Clark T (eds) Drug design strategies: computational techniques and applications, vol 20, Chapter 6. Roy Soc Chem, pp 120–163
8. Popelier PLA, Aicken FM (2003) Atomic properties of amino acids: computed atom types as a guide for future force field design. *Chem Phys Chem* 4:824–829
9. Popelier PLA (2005) Quantum chemical topology: on bonds and potentials. In: Wales DJ (ed) Structure and bonding, intermolecular forces and clusters, vol 115. Springer, Heidelberg, pp 1–56
10. Popelier PLA, Brémond ÉAG (2009) Geometrically faithful homeomorphisms between the electron density and the bare nuclear potential. *Int J Quant Chem* 109:2542–2553
11. Koritsanszky TS, Coppens P (2001) Chemical applications of X-ray charge-density analysis. *Chem Rev* 1583–1627
12. Bader RFW, Essen H (1984) The characterization of atomic interactions. *J Chem Phys* 80:1943–1960
13. Malcolm NOJ, Popelier PLA (2003) An improved algorithm to locate critical points in a 3D scalar field as implemented in the program MORPHY. *J Comp Chem* 24:437–442
14. Popelier PLA (2012) New insights in atom-atom interactions for future drug design. *Curr Top Med Chem* 12:1924–1934
15. Bader RFW, Anderson SG, Duke AJ (1979) Quantum topology of molecular charge distributions. 1. *J Am Chem Soc* 101:1389–1395
16. Collard K, Hall GG (1977) Orthogonal trajectories of the electron density. *Int J Quant Chem* 12:623–637
17. Thom R (1975) Structural stability and morphogenesis; english ed. Benjamin: Reading, MA
18. Popelier PLA (1996) On the differential geometry of interatomic surfaces. *Can J Chem* 74:829–838
19. Bader RFW, Beddall PM (1972) Virial field relationship for molecular charge distributions and the spatial partitioning of molecular properties. *J. Chem. Phys.* 56:3320–3329
20. Bader RFW, MacDougall PJ, Lau CDH (1984) Bonded and nonbonded charge concentrations and their relation to molecular-geometry and reactivity. *J Am Chem Soc* 106:1594–1605
21. Bader RFW, Gillespie RJ, MacDougall PJ (1988) A physical basis for the VSEPR model of molecular geometry. *J Am Chem Soc* 110:7329–7336
22. Popelier PLA (2000) On the full topology of the Laplacian of the electron density. *Coord Chem Rev* 197:169–189
23. Malcolm NOJ, Popelier PLA (2003) The full topology of the Laplacian of the electron density: scrutinising a physical basis for the VSEPR model. *Faraday Discuss* 124:353–363
24. Tal Y, Bader RFW, Erkkü J (1980) Structural homeomorphism between the electron density and the nuclear potential of a molecular system. *Phys Rev A* 21:1–11
25. Becke AD, Edgecombe KE (1990) A simple measure of electron localization in atomic and molecular systems. *J Chem Phys* 92:5397–5403
26. Silvi B, Savin A (1994) Classification of chemical bonds based on topological analysis of electron localization functions. *Nature(London)* 371:683–686
27. Polo V, Andres J, Berski S, Domingo LR, Silvi B (2008) Understanding reaction mechanisms in organic chemistry from catastrophe theory applied to the electron localization function topology. *J Phys Chem A* 112:7128–7136
28. Naray-Szabo G, Ferenczy GG (1995) Molecular electrostatics. *Chem Rev* 95:829–847
29. Gadre SR, Kulkarni SA, Shrivastava IH (1992) Molecular electrostatic potentials: a topographical study. *J Chem Phys* 96:5253–5261
30. Gadre SR, Shrivastava IH (1991) Shapes and sizes of molecular anions via topographical analysis of electrostatic potential. *J Chem Phys* 94:4384–4391
31. Balanarayan P, Gadre SR (2003) Topography of molecular scalar fields. I. algorithm and poincare-hopf relation. *J Chem Phys* 119:5037–5043

32. Balanarayan P, Kavathekar R, Gadre SR (2007) electrostatic potential topography for exploring electronic reorganizations in 1,3 dipolar cycloadditions. *J Phys Chem A* 111:2733–2738
33. Aray Y, Rodriguez J, Coll S, Rodriguez-Arias EN, Vega D (2005) Nature of the lewis acid sites on molybdenum and ruthenium sulfides: an electrostatic potential study. *J Phys Chem B* 109:23564–23570
34. Tsirelson VG, Avilov AS, Lepeshov GG, Kulygin AK, Stahn J, Pietsch U, Spence JCH (2001) Quantitative analysis of the electrostatic potential in rock-salt crystals using accurate electron diffraction data. *J Phys Chem B* 105:5068–5074
35. Keith TA, Bader RFW, Aray Y (1996) Structural homeomorphism between the electron density and the virial field. *Int J Quant Chem* 57:183–198
36. Keith TA, Bader RFW (1993) Topological analysis of magnetically induced molecular current distributions. *J Chem Phys* 99:3669–3682
37. Cioslowski J, Liu GH (1999) Topology of electron-electron interactions in atoms and molecules. II. The correlation cage. *J Chem Phys* 110:1882–1887
38. Pendas AM, Hernandez-Trujillo J (2012) The Ehrenfest force field: topology and consequences for the definition of an atom in a molecule. *J Chem Phys* 137:134101
39. Dillen J (2015) The Topology of the Ehrenfest force density revisited. a different perspective based on slater-type orbitals jan. *J Comput Chem*. doi:[10.1002/jcc.23869](https://doi.org/10.1002/jcc.23869)
40. Popelier PLA, Kosov DS (2001) Atom-atom partitioning of intramolecular and intermolecular Coulomb energy. *J Chem Phys* 114:6539–6547
41. Blanco MA, Pendas AM, Francisco E (2005) Interacting quantum atoms: a correlated energy decomposition scheme based on the quantum theory of atoms in molecules. *J Chem Theor Comput* 1:1096–1109
42. Pendas AM, Francisco E, Blanco MA, Gatti C (2007) Bond paths as privileged exchange channels. *Chem Eur J* 13:9362–9371
43. Webster B (1990) *Chemical bonding theory*. Blackwell, Oxford
44. Reed AE, Curtiss LA, Weinhold F (1988) Intermolecular interactions from a natural bond orbital, donor-acceptor viewpoint. *Chem Rev* 88:899–926
45. Stone AJ (1981) Distributed multipole analysis, or how to describe a molecular charge-distribution. *Chem Phys Lett* 83:233–239
46. Mulliken RS (1955) Electronic population analysis on LCAO-MO molecular wave functions. *I J Chem Phys* 23:1833–1840
47. Pearson RG (2007) Applying the concepts of density functional theory to simple systems. *Int J Quant Chem* 108:821–826
48. Kovacs A, Esterhuysen C, Frenking G (2005) The nature of the chemical bond revisited: an energy-partitioning analysis of nonpolar bonds. *Chem Eur J* 11:1813–1825
49. McWeeny R (1992) *Methods of molecular quantum mechanics*, 2nd edn. Academic Press, SanDiego
50. Anderson JSM, Ayers PW, Hernandez JIR (2010) How ambiguous is the local kinetic energy? *J Phys Chem A* 114:8884–8895
51. Fletcher TL, Kandathil SM, Popelier PLA (2014) The prediction of atomic kinetic energies from coordinates of surrounding atoms using kriging machine learning. *Theor Chem Acc* 133 (1499):1–10
52. Cohen L (1978) Local kinetic energy in quantum mechanics. *J Chem Phys* 70:788–799
53. Bader RFW, Preston HJT (1969) The kinetic energy of molecular charge distributions and molecular stability. *Int J Quant Chem* 3:327–347
54. Nasertayoob P, Shahbazian S (2008) Revisiting the foundations of quantum theory of atoms in molecules (QTAIM): the variational procedure and the zero-flux conditions. *Int J Quant Chem* 108:1477–1484
55. Rafat M, Popelier PLA (2007) Atom-atom partitioning of total (super)molecular energy: the hidden terms of classical force fields. *J Comput Chem* 28:292–301

56. Rafat M, Popelier PLA (2007) Topological atom-atom partitioning of molecular exchange energy and its multipolar convergence. In: Matta CF, Boyd RJ (eds) *Quantum theory of atoms in molecules*, vol 5. Wiley, Weinheim, pp 121–140
57. AIMAll: Todd A, Keith TK (2014) Gristmill software, overland Park KS, USA, (aim.tkgristmill.com)
58. Popelier PLA (2012) Quantum chemical topology: knowledgeable atoms in peptides. *AIP Conf Proc* 1456:261–268
59. Popelier P, Rafat M, Devereux M, Liem SY, Leslie M (2005) Towards a force field via quantum chemical topology. *Lect Series Comput Comput Sci* 4:1251–1255
60. Popelier PLA (2012) A generic force field based on quantum chemical topology. In: Gatti C, Macchi P (eds) *Modern charge-density analysis*, vol 14. Springer, Germany, pp 505–526
61. Cardamone S, Hughes TJ, Popelier PLA (2014) Multipolar electrostatics. *Phys Chem Chem Phys* 16:10367–10387
62. Ivanov MV, Talipov MR, Timerghazin QD (2015) Genetic algorithm optimization of point charges in force field development: challenges and insights. *J Phys Chem A* 119:1422–1434
63. Rafat M, Popelier PLA (2006) A convergent multipole expansion for 1,3 and 1,4 Coulomb interactions. *J Chem Phys* 124(144102):1–7
64. Rafat M, Popelier PLA (2007) Long range behaviour of high-rank topological multipole moments. *J Comput Chem* 28:832–838
65. Popelier PLA, Joubert L, Kosov DS (2001) Convergence of the electrostatic interaction based on topological atoms. *J Phys Chem A* 105:8254–8261
66. Yuan Y, Mills MJL, Popelier PLA (2014) Multipolar electrostatics for proteins: atom-atom electrostatic energies in crambin. *J Comp Chem* 35:343–359
67. Solano CJF, Pendás AM, Francisco E, Blanco MA, Popelier PLA (2010) Convergence of the multipole expansion for 1,2 Coulomb interactions: the modified multipole shifting algorithm. *J Chem Phys* 132:194110
68. Pendas AM, Francisco E, Blanco MA (2006) Binding energies of first row diatomics in the light of the interacting quantum atoms approach. *J Phys Chem A* 110:12864–12869
69. Angyan JG, Loos M, Mayer I (1994) Covalent bond orders and atomic valence indices in the topological theory of atoms in molecules. *J Phys Chem* 98:5244–5248
70. Garcia-Revilla M, Francisco E, Popelier PLA, Martín-Pendas AM (2013) Domain-averaged exchange correlation energies as a physical underpinning for chemical graphs. *Chem Phys Chem* 14:1211–1218
71. Chávez-Calvillo R, García-Revilla M, Francisco E, Martín Pendás A, Rocha-Rinza T (2015) Dynamical correlation within the Interacting quantum atoms method through coupled cluster theory. *Comput Theor Chem* 1053:90–95
72. Grimme S (2004) Accurate description of van der Waals complexes by density functional theory including empirical corrections. *J Comput Chem* 25:1463–1473
73. Fletcher T, Davie SJ, Popelier PLA (2014) Prediction of intramolecular polarization of aromatic amino acids using kriging machine learning. *J Chem Theory Comput* 10:3708–3719
74. Grimme S, Antony J, Ehrlich S, Krieg H (2010) A consistent and accurate ab initio parametrization of density functional dispersion correction (DFT-D) for the 94 elements H-Pu. *J Chem Phys* 132:154104–154122
75. Badenhoop JK, Weinhold F (1997) Natural bond orbital analysis of steric interactions. *J Chem Phys* 107:5406–5421
76. Verstraelen T, Ayers PW, Van Speybroeck V, Waroquier M (2013) Hirshfeld-E partitioning: AIM charges with an improved trade-off between robustness and accurate electrostatics. *J Chem Theory Comput* 9:2221–2225
77. Hirshfeld FL (1977) Bonded-atom fragments for describing molecular charge densities. *Theor Chem Acta* 44:129–138
78. Rasmussen CE, Williams CKI (2006) *Gaussian processes for machine learning*. The MIT Press, Cambridge
79. Krige DG (1951) A statistical approach to some basic mine valuation problems on the Witwatersran. *J Chem Metall Mining Soc South Africa* 52:119–139

80. Kandathil SM, Fletcher TL, Yuan Y, Knowles J, Popelier PLA (2013) Accuracy and tractability of a Kriging model of intramolecular polarizable multipolar electrostatics and its application to histidine. *J Comput Chem* 34:1850–1861
81. Mills MJL, Popelier PLA (2011) Intramolecular polarisable multipolar electrostatics from the machine learning method Kriging. *Comput Theor Chem* 975:42–51
82. Mills MJL, Popelier PLA (2012) Polarisable multipolar electrostatics from the machine learning method Kriging: an application to alanine. *Theor Chem Acc* 131:1137–1153
83. Mills MJL, Hawe GI, Handley CM, Popelier PLA (2013) Unified approach to multipolar polarisation and charge transfer for ions: microhydrated Na⁺. *Phys Chem Chem Phys* 15:18249–18261
84. Handley CM, Hawe GI, Kell DB, Popelier PLA (2009) Optimal construction of a fast and accurate polarisable water potential based on multipole moments trained by machine learning. *Phys Chem Chem Phys* 11:6365–6376
85. Yuan Y, Mills MJL, Popelier PLA (2014) Multipolar electrostatics based on the Kriging machine learning method: an application to serine. *J Mol Model* 20:2172–2186
86. Hughes TJ, Kandathil SM, Popelier PLA (2015) Accurate prediction of polarised high order electrostatic interactions for hydrogen bonded complexes using the machine learning method kriging. *Spectrochim Acta A* 136:32–41
87. Bader RFW (2009) Bond paths are not chemical bonds. *J Phys Chem A* 113:10391–10396
88. Grimme S, Mück-Lichtenfeld C, Erker G, Kehr G, Wang H, Beckers H, Willner H (2009) When do interacting atoms form a chemical bond? spectroscopic measurements and theoretical analyses of dideuteriophenanthrene. *Angew Chem Int Ed* 48:2592–2595
89. Pendas AM, Blanco MA, Francisco E (2009) Steric repulsions, rotation barriers, and stereoelectronic effects: a real space perspective. *J Comput Chem* 30:98–109
90. Ayers PL, Boyd RJ, Bultinck P, Caffarel M, Carbó-Dorca R, Causá M, Cioslowski J, Contreras-Garcia J, Cooper DL, Coppens P, Gatti C, Grabowsky S, Lazzaretti P, Macchi P, Pendas AM, Popelier PLA, Ruedenberg K, Rzepa H, Savin A, Sax A, Schwarz WEH, Shabbazian S, Silvi S, Solà M, Tsirelson V (2015) Six questions on topology in theoretical chemistry. *Comput Theor Chem* 1053:2–16

Chapter 3

Localization-Delocalization Matrices and Electron Density-Weighted Adjacency/Connectivity Matrices: A Bridge Between the Quantum Theory of Atoms in Molecules and Chemical Graph Theory

Chérif F. Matta, Ismat Sumar, Ronald Cook and Paul W. Ayers

The development of chemistry has both led to, and been made possible by, the evolution of certain primary concepts. These concepts, without which there would be neither correlation nor prediction of the observations of descriptive chemistry, are: (1) the existence of atoms of functional groupings of atoms in molecules as evidenced by characteristic sets of properties; (2) the concept of bonding; and (3) the associated concepts of molecular structure and molecular shape. These concepts logically (but not historically) are consequences of fundamental topological properties of the charge distribution (electronic and nuclear) in a molecular system. In terms of the Born-Oppenheimer approximation the electronic distribution $\rho(\mathbf{r})$ is the scalar field defined in the real three-dimensional space with Euclidean metric. The universal topological properties of $\rho(\mathbf{r})$ are characterized by its gradient field $\nabla\rho(\mathbf{r})$ [1].

I.S. Dmitriev (1981)

C.F. Matta (✉) · I. Sumar
Department of Chemistry and Physics, Mount Saint Vincent University,
Halifax, NS B3M 2J6, Canada
e-mail: cherif.matta@msvu.ca

C.F. Matta
Department of Chemistry, Dalhousie University, Halifax, NS B3H 4J3, Canada

C.F. Matta · I. Sumar
Department of Chemistry, Saint Mary's University, Halifax, NS B3H 3C3, Canada

I. Sumar · P.W. Ayers (✉)
Department of Chemistry, McMaster University, Hamilton, ON L8S 4L8, Canada
e-mail: ayers@mcmaster.ca

R. Cook (✉)
TDA Research, Inc, 12345 W. 52nd Ave, Wheat Ridge, CO 80033, USA
e-mail: rmdcook@gmail.com

Abstract Chemical graph theory (CGT) starts by defining matrices that represent the molecular graph then proceed to extract numbering-independent matrix invariants to be used as molecular descriptors in empirical quantitative structure to activity (or property) relationships (QSAR/QSPR). Two proposed matrix representations of molecular structure are presented in this chapter as alternatives to simple connectivity molecular graphs. Firstly, it is proposed to use a more “nuanced” connectivity matrix by weighing the “ones” entered in a CGT molecular graph matrix by the bond critical point electron densities associated with each bond path to yield what we term the “electron density-weighted adjacency/connectivity matrices (EDWAM/EDWCM)”. In a second approach, it is proposed to use the localization and delocalization indices of the quantum theory of atoms in molecules (QTAIM) to construct a richer representation of the molecular graph, a “fuzzy” graph, whereby an edge exists between any two atoms (measured by the delocalization index between them) whether they share a bond path or not. Such a fuzzy graph is represented by what we term “electron localization-delocalization matrix (LDM)”. We show that the LDM representations of a series of molecules provide a powerful tool for robust QSAR/QSPR modeling.

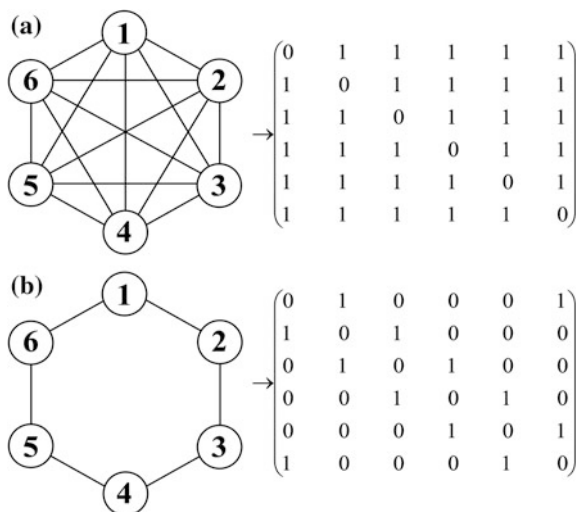
3.1 Introduction

A molecule can be abstracted as a network of points (vertices) connected by lines (edges) and hence constituting a graph. Molecular graphs formed from a set of edges each consisting of what chemists normally call a “chemical bond” can be—but generally are not—*complete*. (A “complete graph” is one in which *every* pair of vertices is connected by an edge, a trivial example being the graph of a diatomic molecule). In contrast, a graph based on any pair-wise property such as inter-nuclear distance, nuclear-nuclear repulsion, or a count of electrons delocalized between any two pairs of atoms in the molecule necessarily constitutes a complete graph.

Molecular graphs, complete or incomplete, can be conveniently represented by connectivity matrices as can be seen in the examples in Fig. 3.1 and in Refs. [1–9]. A complete graph where connectedness is indicated by 1 and disjointedness by 0 will have a non-zero entry for every non-diagonal element of the matrix while an incomplete graph has finite entries only for connected vertices and zero elsewhere in the matrix (Fig. 3.1).

A matrix representative of a complete graph with n vertices whereby connectivity is assigned “1” as in Fig. 3.1a is thus filled with ones except along the diagonal and hence has $n(n - 1)/2$ edges, the number of non-diagonal elements of its matrix representative. In practice, a complete graph such as the delocalization matrix (DM), described below, may have zero (negligible) entries other than along the diagonal when the delocalization index between a given pair of atoms in a molecule has a magnitude below the precision to which the numerical entries are reported.

Fig. 3.1 **a** An example of a complete graph with 6 vertices (K_6) with $(6 \times 5)/2 = 15$ edges along with its matrix representative according to the numbering scheme. **b** An example of an incomplete graph with the same number of vertices and numbering scheme as in (a) along with its matrix representative



Within Bader's Quantum Theory of Atoms in Molecules (QTAIM) [10–12] a molecular graph is defined as the set of connected bond paths found in the molecular electron density. The molecular graph, so defined, is generally incomplete in the graph-theoretic sense since generally not every atom is sharing a bond path with every other atom in the molecule (except in diatomics and possibly a few other exceptions). The same theory, QTAIM, also defines delocalization indices (DIs), *vide infra*, that define a “complete graph” since there is a non-directed DI between every pair of atoms in the molecule whether sharing a bond path or not. As already mentioned, while in principle a DI graph is complete, in numerical practice it may not be so.

3.2 The Localization-Delocalization Matrix (LDM)

3.2.1 Definition of the LDM

Dmitriev, in his introductory book on Chemical Graph Theory (CGT), discusses the relation between molecular topology, graph theory, and what is known today as QTAIM. The author outlines the topological underpinnings of QTAIM in the differential topology and topography of the electron density $\rho(\mathbf{r})$ culminating with the Poincaré-Hopf relationship relating the numbers and types of different critical points (CPs) in the electron density scalar field (points where the gradient of the electron density vanishes, that is, $\nabla\rho_{\text{CP}} = 0$).

QTAIM locates the various critical points in the density and uses each bond critical point (BCP) as a starting point for the search of the inter-atomic surfaces of zero-flux in the gradient vector field of the electron density separated and shared by

pairs of bonded atoms. A BCP is also used in tracing its associated bond path which is a unique line of maximal electron density that links the nuclei of two bonded atoms [13–15] and which characterizes the nature and strength of chemical bonding [16].

The bond path is always found to be accompanied by a shadow graph, the virial path, first discovered by Keith, Bader, and Aray [17]. The virial path is a line of maximally-negative potential energy density in three-dimensional space that links the same pair of atoms that share a bond path and an interatomic surface of zero-flux. No theoretical basis has ever been provided that *requires* the presence of a virial path as a doppelganger of every bond path that links two chemically bonded atoms, however, there is no known computational violation of this observation to date known to the authors. The presence of the virial path links the concept of chemical bonding directly with the concept of energetic stability as amply discussed in literature on QTAIM.

The partitioning of the space into separate non-overlapping atomic basins, exhausting all three-dimensional space, entails the definition of “atomic properties” that add-up to yield the corresponding molecular counterparts. Such atomic properties are obtained by integrating each corresponding property density over the bounded region of real space occupied by the atomic basin.

Figure 3.2 shows the intersection of the atomic basins with the H–C–C(O)–OH plane in ethanoic (acetic) acid. The figure displays isodensity contours of the

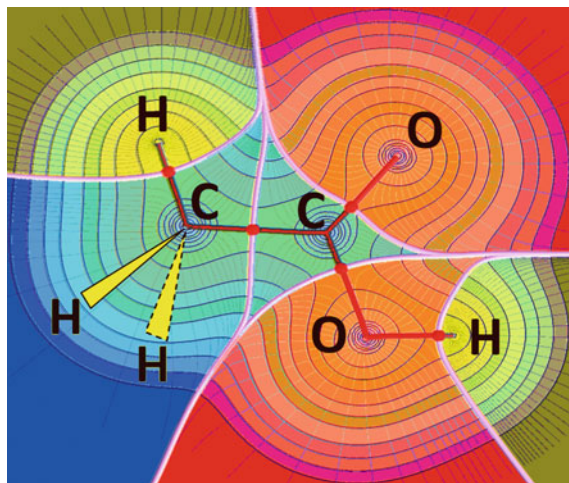


Fig. 3.2 Contours of the electron density in the molecular plane of ethanoic (acetic) acid. The contours from outside inwards have the values (in atomic units (a.u.)): 0.001 au then 2×10^n , 4×10^n , and 8×10^n , n starting at -3 and increasing in steps of unity. Nuclei are linked by bond paths and atomic basins are separated by the intersections of the interatomic surfaces with the molecular plane, every atomic basin being distinguished by an element-specific dominant color. Each BCP appears at the intersection of the associated bond path and interatomic surface and is depicted as a *small red dot*

electron density, a representative set of gradient vector field lines traced by the gradient of the electron density, the intersections of interatomic surfaces (IASs) with the plane of the figure, the set of bond paths that are coplanar with the plane of the figure, and the bond critical points each of which lies simultaneously on the IAS and the associated bond path. For atoms exposed on the molecular surface (and hence that extend to infinity), the atomic basins are usually delimited by the intersections of their IASs with the outer isodensity contour of $\rho_{\text{vdW}} = 0.001$ atomic unit (a.u.), the van der Waals envelope (1 a.u. of electron density = 1 electron per cubic bohr).

As explained above, numerical integration (using readily available robust software such as Keith's AIMAll [18]) yields atomic quantum mechanical averages of properties such as atomic electron populations ($N(\Omega)$), number of electrons localized within the basin ($\Lambda(\Omega)$), and number of electrons delocalized (shared) between one atomic basin and every other basin in the molecule ($\delta(\Omega, \Omega')$).

The number of electrons delocalization (shared) between atomic basins Ω_i and Ω_j can be measured by the delocalization index (DI), $\delta(\Omega_i, \Omega_j)$. For a closed-shell molecule, the DI at the Hartree-Fock level of theory is defined [19]:

$$\delta(\Omega_i, \Omega_j) = 2|F^\alpha(\Omega_i, \Omega_j)| + 2|F^\beta(\Omega_i, \Omega_j)|, \quad (3.1)$$

where

$$F^\sigma(\Omega_i, \Omega_j) = - \sum_k^{\text{occ}} \sum_l^{\text{occ}} \int_{\Omega_i} \int_{\Omega_j} \varphi_k^*(\mathbf{r}_1) \varphi_l(\mathbf{r}_1) \varphi_l^*(\mathbf{r}_2) \varphi_k(\mathbf{r}_2) d\mathbf{r}_1 d\mathbf{r}_2 \quad (3.2)$$

$$= - \sum_k^{\text{occ}} \sum_l^{\text{occ}} S_{kl}(\Omega_i) S_{lk}(\Omega_j) \quad (3.3)$$

is the Fermi correlation, and where $S_{kl}(\Omega_i) = S_{lk}(\Omega_i)$ is the overlap integral of two spin orbitals φ_k and φ_l within Ω_i , and where σ refers to spin (α or β). For single determinantal methods, the first order density matrix—printed in standard electronic structure software—is sufficient to determine all properties since it fixes the second order density matrix. For post-Hartree-Fock methods, the Müller approximation is used by AIMAll, the software used to obtain the LIs and DIs, to obtain an approximate second-order density matrix from the first order density matrix.

If $i = j$ in Eqs. 3.2 and 3.3, ($S_{kl}(\Omega_i) S_{lk}(\Omega_j) \rightarrow [S_{kl}(\Omega_i)]^2$), then both integrals are over the same atomic basin giving the total Fermi correlation for the electrons contained within that basin. At the limit of total localization this double integral approaches $-N^\sigma(\Omega_i)$, the negative of the σ -spin population of Ω_i . This limit is reached only when atoms are infinitely separated since in any molecule electrons in a given atomic basin always exchange with electrons in every other atomic basin

to some extent and $|F^\alpha(\Omega_i, \Omega_i)| \leq N^\alpha(\Omega_i)$. This localization index (LI) is thus defined [19]:

$$\Lambda(\Omega_i, \Omega_i) = |F^\alpha(\Omega_i, \Omega_i)| + |F^\beta(\Omega_i, \Omega_i)|. \quad (3.4)$$

In a molecule, the electron population of an atom is always shared to some extent with other basins, i.e., there always exists a degree of electron sharing or delocalization.

Since electrons can either be localized within a basin or shared with other basins in the molecule, then the LI of an atom plus half of the sum of its $(n - 1)$ DIs shared with the remaining atoms in the molecule (where n is the number of atoms in the molecule), must necessarily equal its electron population $N(\Omega_i)$ [19, 20]:

$$N(\Omega_i) = \Lambda(\Omega_i) + \frac{1}{2} \sum_{j \neq i}^n \delta(\Omega_i, \Omega_j) = \int_{\Omega_i} \rho(\mathbf{r}) d\mathbf{r}. \quad (3.5)$$

The population $N(\Omega_i)$ obtained via the bookkeeping of electrons' whereabouts embodied in the first equality of Eq. (3.5) or through the integration of the electron density over Ω_i (second equality of Eq. 3.5) determines the atomic charge which, given the atomic number Z_{Ω_i} , is defined (in a.u.):

$$q(\Omega_i) = Z_{\Omega_i} - N(\Omega_i). \quad (3.6)$$

Since the total molecular electron population N is the sum of the atomic populations then it is expressible as the sum of two (sub-)populations: The molecular average number of localized electrons (N_{loc}) plus the molecular average of delocalized electrons (N_{deloc}) [20]:

$$N = \sum_{i=1}^n N(\Omega_i) = \sum_{i=1}^n \Lambda(\Omega_i) + \frac{1}{2} \sum_{i=1}^n \sum_{j \neq i}^n \delta(\Omega_i, \Omega_j) = N_{\text{loc}} + N_{\text{deloc}}, \quad (3.7)$$

where

$$N_{\text{loc}} \equiv \sum_{i=1}^n \Lambda(\Omega_i), \quad (3.8)$$

and

$$N_{\text{deloc}} \equiv \frac{1}{2} \sum_{i=1}^n \sum_{j \neq i}^n \delta(\Omega_i, \Omega_j) = N - N_{\text{loc}} = N - \text{tr}(\zeta). \quad (3.9)$$

Further, the full set of molecular LIs and DIs can be organized in a localization-delocalization matrix (LDM, or ζ -matrix) [20–25]:

$$\zeta \equiv \begin{bmatrix} \Lambda(\Omega_1) & \delta(\Omega_1, \Omega_2)/2 & \cdots & \delta(\Omega_1, \Omega_n)/2 \\ \delta(\Omega_2, \Omega_1)/2 & \Lambda(\Omega_2) & \cdots & \delta(\Omega_2, \Omega_n)/2 \\ \vdots & \vdots & \ddots & \vdots \\ \delta(\Omega_n, \Omega_1)/2 & \delta(\Omega_n, \Omega_2)/2 & \cdots & \Lambda(\Omega_n) \end{bmatrix}_{n \times n} \left. \begin{array}{l} \sum_{\text{row}} = N(\Omega_1) \\ = N(\Omega_2) \\ \vdots \\ = N(\Omega_n) \end{array} \right\} \sum_{i=1}^n N(\Omega_i) = N \quad (3.10)$$

$$\underbrace{\sum_{\text{column}} = N(\Omega_1) \quad = N(\Omega_2) \quad = N(\Omega_n)}_{\sum_{i=1}^n N(\Omega_i) = N} \quad \text{tr}(\zeta) = N_{\text{loc}}$$

In the LDM, the sum of the matrix elements in any row or corresponding column equals the atomic population $N(\Omega_i)$ (by the first equality of Eq. 3.5) and hence the sum of the column sums or row sums equals the total molecular electron population. The trace of the LDM is the localized electron population (N_{loc}) of the molecule (Eq. 3.8), and the delocalized electron population can be obtained by difference (Eq. 3.9).

The LDM is a representation of a complete molecular graph where all atoms (vertices) are interconnected by non-directional DI links (edges), and where the diagonals are non-zero giving the number of electrons localized in a given atomic basin. This last point distinguishes the LDM graph from a typical “complete graph” of the type shown in Fig. 3.1a in that vertices are connected back to themselves through their respective LIs.

3.2.2 The LDM as a Molecular Fingerprinting and Similarity Assessment Tool

The distances between the localization-delocalization matrices (LDMs) of different molecules can be used as a measure of their dissimilarity. The greater or smaller the “distance” between two LDMs the lesser or more similar are the molecules they represent.

The inter-molecular distance between two molecules A and B, each represented by an $n \times n$ LDM, is defined as the Frobenius norm of the difference matrix, that is:

$$d(\mathbf{A}, \mathbf{B}) \equiv \|\mathbf{A} - \mathbf{B}\| \equiv \sqrt{\sum_{ij} |\alpha_{ij} - \beta_{ij}|^2}, \quad (3.11)$$

where α_{ij} and β_{ij} are two corresponding matrix elements in the matrices **A** and **B** that represent each molecule in the pair.

After the electronic structure calculation yields a wavefunction file, AIMAll/AIMStudio program [18] is used to calculate the localization and delocalization indices. A Python program (AIMLDM), developed by Sumar et al. [25], extracts the localization and delocalization indices from AIMAll's output and calculates the matrix invariants as well as the Frobenius distances.

3.2.3 Some Limitations of LDMs and Possible Solutions

LDMs share well-known limitations with all matrix representatives of molecular graphs when used as a tool for comparing different molecules. These limitations are briefly outlined along with possible solutions. In this Sect. (3.2.3), only the proposed solutions are outlined leaving examples of their actual usages in a subsequent Sect. (3.4) below.

3.2.3.1 Ambiguity of Atomic Labelling

Any matrix representation of the molecular graph, complete or incomplete, is labelling-dependent since there exists $n!$ ways to label the n -atoms composing a given molecule. Unless all compared molecules have very similar graphs and can be given consistent atomic labelling, e.g. benzoic acids substituted, say, at the *para*-position by monoatomic substituents such as halogens, one must rely on “matrix invariants”.

Labelling-independent invariants extracted from a matrix representation of a molecular graph include, for example, the characteristic polynomial, the eigenvalues, the trace, and the determinant.

LDMs, by being real and symmetric, are diagonalizable by a similar transformation:

$$\mathbf{P}^{-1}\zeta\mathbf{P} = \mathbf{D}, \quad (3.12)$$

where **D** is the diagonalized LDM. The eigenvalues can then be organized as a vector sorted in a consistent order of, say, increasing value.

For example, an LDM- ζ -matrix of methane is:

$$\zeta_{\text{CH}_4} = \begin{array}{c} \text{C1} \\ \text{H2} \\ \text{H3} \\ \text{H4} \\ \text{H4} \\ \Sigma \end{array} \begin{array}{ccccc} \text{C1} & \text{H2} & \text{H3} & \text{H4} & \text{H5} \\ \left(\begin{array}{ccccc} 4.040 & 0.492 & 0.492 & 0.492 & 0.492 \\ 0.492 & 0.444 & 0.021 & 0.021 & 0.021 \\ 0.492 & 0.021 & 0.444 & 0.021 & 0.021 \\ 0.492 & 0.021 & 0.021 & 0.444 & 0.021 \\ 0.492 & 0.021 & 0.021 & 0.021 & 0.444 \end{array} \right)_{5 \times 5} & \Sigma \end{array} \begin{array}{c} 6.007 \\ 0.998 \\ 0.998 \\ 0.998 \\ 0.998 \\ 10.000 \end{array} \quad (3.13)$$

of which the total number of localized electrons is given by its trace, $\text{tr}(\zeta_{\text{CH}_4}) = 5.815$, while its determinant $\det(\zeta_{\text{CH}_4}) \approx 0.082$, and the corresponding \mathbf{D} written either as a matrix or a column vector is:

$$\mathbf{D}_{\text{CH}_4} \begin{array}{c} \left(\begin{array}{ccccc} 0.251 & 0 & 0 & 0 & 0 \\ 0 & 0.423 & 0 & 0 & 0 \\ 0 & 0 & 0.423 & 0 & 0 \\ 0 & 0 & 0 & 0.423 & 0 \\ 0 & 0 & 0 & 0 & 4.295 \end{array} \right)_{5 \times 5} \\ \equiv \left[\begin{array}{c} 0.251 \\ 0.423 \\ 0.423 \\ 0.423 \\ 4.295 \end{array} \right]_{5 \times 1} \\ \Sigma = 5.815 \end{array} \quad (3.14)$$

where the sum of the elements of \mathbf{D} represent the total number of localized electrons since the trace of a matrix is invariant upon diagonalization. The Frobenius distance can be calculated using \mathbf{D} without regard to the arbitrariness of the labelling scheme.

3.2.3.2 Differently-Sized Molecules Are Represented by Unequally-Sized Matrices

Let's suppose we desire now to compare the matrices (3.13) or (3.14) with the corresponding ones for ethane. The Frobenius distance (Eq. 3.11) clearly cannot be evaluated being not defined since the matrix representing ethane is 8×8 while that representing methane is only 5×5 .

Following the lead of White and Wilson [26], a solution to this problem is to enlarge all matrices to equal the size of the *largest* matrix in the set by "padding" the smaller matrices with zeros. The zero padding is, effectively, adding ghost atoms to equalize the sizes of all matrices in the molecular set.

To illustrate how this is achieved, let us write a ζ -matrix representative of ethane:

$$\zeta_{\text{C}_2\text{H}_6} = \begin{array}{l} \text{C1} \\ \text{H2} \\ \text{C3} \\ \text{H4} \\ \text{H5} \\ \text{H6} \\ \text{H7} \\ \text{H8} \\ \Sigma \end{array} \begin{array}{l} \left(\begin{array}{cccccccc} 3.941 & 0.483 & 0.505 & 0.483 & 0.483 & 0.022 & 0.022 & 0.022 \\ 0.483 & 0.456 & 0.022 & 0.021 & 0.021 & 0.007 & 0.002 & 0.002 \\ 0.505 & 0.022 & 3.941 & 0.022 & 0.022 & 0.483 & 0.483 & 0.483 \\ 0.483 & 0.021 & 0.022 & 0.456 & 0.021 & 0.002 & 0.007 & 0.002 \\ 0.483 & 0.021 & 0.022 & 0.021 & 0.456 & 0.002 & 0.002 & 0.007 \\ 0.022 & 0.007 & 0.483 & 0.002 & 0.002 & 0.456 & 0.021 & 0.021 \\ 0.022 & 0.002 & 0.483 & 0.007 & 0.002 & 0.021 & 0.456 & 0.021 \\ 0.022 & 0.002 & 0.483 & 0.002 & 0.007 & 0.021 & 0.021 & 0.456 \end{array} \right) \begin{array}{l} 5.961 \\ 1.013 \\ 5.961 \\ 1.013 \\ 1.013 \\ 1.013 \\ 1.013 \\ 1.013 \\ 18.000 \end{array} \end{array} \quad (3.15)$$

and the corresponding **D**-vector:

$$\mathbf{D}_{\text{C}_2\text{H}_6} = \begin{bmatrix} 0.284 \\ 0.323 \\ 0.430 \\ 0.430 \\ 0.440 \\ 0.440 \\ 3.638 \\ 4.632 \end{bmatrix}_{8 \times 1}, \quad (3.16)$$

In order to compute the Frobenius distance between ethane and methane, we enlarge the matrix representative of methane with ghost atoms to:

$$\zeta'_{\text{CH}_4} = \begin{array}{l} \text{C1} \\ \text{H2} \\ \text{H3} \\ \text{H4} \\ \text{H4} \\ 0 \\ 0 \\ 0 \end{array} \begin{array}{l} \left(\begin{array}{ccccc} \text{C1} & \text{H2} & \text{H3} & \text{H4} & \text{H5} \\ 4.040 & 0.492 & 0.492 & 0.492 & 0.492 & 0 & 0 & 0 \\ 0.492 & 0.444 & 0.021 & 0.021 & 0.021 & 0 & 0 & 0 \\ 0.492 & 0.021 & 0.444 & 0.021 & 0.021 & 0 & 0 & 0 \\ 0.492 & 0.021 & 0.021 & 0.444 & 0.021 & 0 & 0 & 0 \\ 0.492 & 0.021 & 0.021 & 0.021 & 0.444 & 0 & 0 & 0 \\ 0 & 0 & 0 & 0 & 0 & 0 & 0 & 0 \\ 0 & 0 & 0 & 0 & 0 & 0 & 0 & 0 \\ 0 & 0 & 0 & 0 & 0 & 0 & 0 & 0 \end{array} \right)_{8 \times 8} \rightarrow \mathbf{D}'_{\text{CH}_4} = \begin{array}{l} \begin{bmatrix} 0.000 \\ 0.000 \\ 0.000 \\ 0.251 \\ 0.423 \\ 0.423 \\ 0.423 \\ 4.295 \end{bmatrix}_{8 \times 1} \end{array}, \quad (3.17)$$

which, in its **D**-form, can now be compared with the corresponding vector in Eq. (3.16) for ethane (yielding a methane-ethane Frobenius distance of *ca.* 3.294).

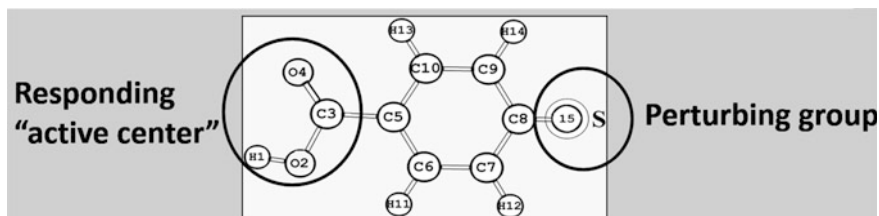


Fig. 3.3 *p*-Benzoic acid viewed as an active centered ($-\text{COOH}$) perturbed by a distant substituent (S) attached at carbon C8

While the padding with zeroes appears ideal for homologous series such as the aliphatic hydrocarbons, other approaches may be more adequate when there exists a “common skeleton” with substituents at a particular location that perturbs the active group of interest. These substituents may or may not have the same number of atoms, but are all attached to the same atom of the common skeleton. An example is provided by the substituted benzoic acids series.

Figure 3.3 represents the series of *para*-substituted benzoic acids, whereby we can consider the carboxylic group as the active center responsible for “activity”, here the $\text{p}K_a$. In this case, the active center is being perturbed through a common skeleton (the aromatic ring) which transmits the perturbation of a substituent S of variable size and nature (in this example, S is at position 15 attached to C8 in Fig. 3.3).

In the example of the substituted benzoic acids, all matrices are equalized in size by condensing all the atoms of S into a “super-atom”, that is a collection of nuclei and their associated atomic basins that are taken as one self-contained group. The idea of a super-atom implements the concept of pruning the branches introduced by Pye and Poirier [27, 28].

The number of localized electrons within the super-atom S is the sum of the localized electrons in each composing atom plus the number of electrons delocalized within the group (that is between the constituent atoms). Thus, we define the localization index of the super atom [21]:

$$\Lambda(\Omega_{\text{super}}) = \sum_{i=1}^{n_{\text{super}}} \Lambda(\Omega_i) + \sum_{\substack{i=1 \\ i \neq j \\ i, j \in \Omega_{\text{super}}}}^{n_{\text{super}}} \delta(\Omega_i, \Omega_j) \quad (3.18)$$

It is non-coincidental that Eq. (3.18) bears a striking resemblance to Eq. (3.7) since at the limit where the super-atom is enlarged to consist of the full molecule

then in this case the number of electrons localized within the bounds of the full super atom (which includes N_{loc} and N_{deloc}) is none else than N , the total number of electrons in the molecule.

On the other hand, the number of electrons shared between the super-atom S and an atom k outside of S is given by the sum of the delocalization indices of every atom within S to that atom [21]:

$$\delta(\Omega_{\text{super}}, \Omega_k) = \sum_{\substack{i=1 \\ i \in \Omega_{\text{super}}}}^{n_{\text{super}}} \delta(\Omega_i, \Omega_k), \quad (3.19)$$

leading to off-diagonal entries of $\frac{1}{2}\delta(\Omega_{\text{super}}, \Omega_k)$ between the super-atom and the k th atom in the molecule.

As an example, and following the numbering scheme in Fig. 3.3, an LDM of p -nitrobenzoic acid is a 17×17 matrix:

	H1	O2	C3	O4	C5	C6	C7	C8	C9	C10	H11	H12	H13	H14	<i>N15</i>	<i>O16</i>	<i>O17</i>
H1	0.07	0.31	0.01	0.01	0.00	0.00	0.00	0.00	0.00	0.00	0.00	0.00	0.00	0.00	<i>0.00</i>	<i>0.00</i>	<i>0.00</i>
O2	0.31	8.10	0.44	0.15	0.04	0.02	0.00	0.00	0.00	0.01	0.02	0.00	0.00	0.00	<i>0.00</i>	<i>0.00</i>	<i>0.00</i>
C3	0.01	0.44	2.83	0.66	0.48	0.02	0.00	0.00	0.00	0.03	0.00	0.00	0.00	0.00	<i>0.00</i>	<i>0.00</i>	<i>0.00</i>
O4	0.01	0.15	0.66	8.20	0.05	0.01	0.00	0.01	0.00	0.02	0.00	0.00	0.02	0.00	<i>0.00</i>	<i>0.00</i>	<i>0.00</i>
C5	0.00	0.04	0.48	0.05	3.91	0.67	0.04	0.04	0.04	0.67	0.02	0.00	0.02	0.00	<i>0.00</i>	<i>0.00</i>	<i>0.00</i>
C6	0.00	0.02	0.02	0.01	0.67	3.94	0.70	0.04	0.05	0.03	0.47	0.02	0.00	0.00	<i>0.01</i>	<i>0.00</i>	<i>0.00</i>
C7	0.00	0.00	0.00	0.00	0.04	0.70	3.93	0.67	0.03	0.05	0.02	0.46	0.00	0.00	<i>0.03</i>	<i>0.02</i>	<i>0.01</i>
C8	0.00	0.00	0.00	0.01	0.04	0.04	0.67	3.77	0.66	0.04	0.00	0.02	0.00	0.02	<i>0.42</i>	<i>0.05</i>	<i>0.05</i>
C9	0.00	0.00	0.00	0.00	0.04	0.05	0.03	0.66	3.93	0.70	0.00	0.00	0.02	0.46	<i>0.03</i>	<i>0.01</i>	<i>0.02</i>
C10	0.00	0.01	0.03	0.02	0.67	0.03	0.05	0.04	0.70	3.94	0.00	0.00	0.47	0.02	<i>0.01</i>	<i>0.00</i>	<i>0.00</i>
H11	0.00	0.02	0.00	0.00	0.02	0.47	0.02	0.00	0.00	0.00	0.38	0.00	0.00	0.00	<i>0.00</i>	<i>0.00</i>	<i>0.00</i>
H12	0.00	0.00	0.00	0.00	0.00	0.02	0.46	0.02	0.00	0.00	0.00	0.36	0.00	0.00	<i>0.00</i>	<i>0.02</i>	<i>0.00</i>
H13	0.00	0.00	0.00	0.02	0.02	0.00	0.00	0.00	0.02	0.47	0.00	0.00	0.37	0.00	<i>0.00</i>	<i>0.00</i>	<i>0.00</i>
H14	0.00	0.00	0.00	0.00	0.00	0.00	0.00	0.02	0.46	0.02	0.00	0.00	0.00	0.36	<i>0.00</i>	<i>0.00</i>	<i>0.02</i>
<i>N15</i>	<i>0.00</i>	<i>0.00</i>	<i>0.00</i>	<i>0.00</i>	<i>0.00</i>	<i>0.01</i>	<i>0.03</i>	<i>0.42</i>	<i>0.03</i>	<i>0.01</i>	<i>0.00</i>	<i>0.00</i>	<i>0.00</i>	<i>0.00</i>	<i>4.44</i>	<i>0.83</i>	<i>0.83</i>
<i>O16</i>	<i>0.00</i>	<i>0.00</i>	<i>0.00</i>	<i>0.00</i>	<i>0.00</i>	<i>0.00</i>	<i>0.02</i>	<i>0.05</i>	<i>0.01</i>	<i>0.00</i>	<i>0.00</i>	<i>0.02</i>	<i>0.00</i>	<i>0.00</i>	<i>0.83</i>	<i>7.30</i>	<i>0.21</i>
<i>O17</i>	<i>0.00</i>	<i>0.00</i>	<i>0.00</i>	<i>0.00</i>	<i>0.00</i>	<i>0.00</i>	<i>0.01</i>	<i>0.05</i>	<i>0.02</i>	<i>0.00</i>	<i>0.00</i>	<i>0.00</i>	<i>0.00</i>	<i>0.02</i>	<i>0.83</i>	<i>0.21</i>	<i>7.30</i>

in which the matrix elements belonging to the atoms composing the super-atom are in *italicized-bold* font for easy distinction. This matrix reduces to a 15×15 matrix

upon treating the $-\text{NO}_2$ group as a super-atom, which, with columns and rows sums explicitly shown, is:

$$\begin{array}{r}
 \begin{array}{cccccccccccccccc}
 & \text{H1} & \text{O2} & \text{C3} & \text{O4} & \text{C5} & \text{C6} & \text{C7} & \text{C8} & \text{C9} & \text{C10} & \text{H11} & \text{H12} & \text{H13} & \text{H14} & \text{NO}_2,15 & \Sigma \\
 \text{H1} & 0.07 & 0.31 & 0.01 & 0.01 & 0.00 & 0.00 & 0.00 & 0.00 & 0.00 & 0.00 & 0.00 & 0.00 & 0.00 & 0.00 & \mathbf{0.00} & 0.41 \\
 \text{O2} & 0.31 & 8.10 & 0.44 & 0.15 & 0.04 & 0.02 & 0.00 & 0.00 & 0.00 & 0.01 & 0.02 & 0.00 & 0.00 & 0.00 & \mathbf{0.00} & 9.09 \\
 \text{C3} & 0.01 & 0.44 & 2.83 & 0.66 & 0.48 & 0.02 & 0.00 & 0.00 & 0.00 & 0.03 & 0.00 & 0.00 & 0.00 & 0.00 & \mathbf{0.00} & 4.49 \\
 \text{O4} & 0.01 & 0.15 & 0.66 & 8.20 & 0.05 & 0.01 & 0.00 & 0.01 & 0.00 & 0.02 & 0.00 & 0.00 & 0.02 & 0.00 & \mathbf{0.00} & 9.13 \\
 \text{C5} & 0.00 & 0.04 & 0.48 & 0.05 & 3.91 & 0.67 & 0.04 & 0.04 & 0.04 & 0.67 & 0.02 & 0.00 & 0.02 & 0.00 & \mathbf{0.01} & 6.00 \\
 \text{C6} & 0.00 & 0.02 & 0.02 & 0.01 & 0.67 & 3.94 & 0.70 & 0.04 & 0.05 & 0.03 & 0.47 & 0.02 & 0.00 & 0.00 & \mathbf{0.01} & 5.99 \\
 \text{C7} & 0.00 & 0.00 & 0.00 & 0.00 & 0.04 & 0.70 & 3.93 & 0.67 & 0.03 & 0.05 & 0.02 & 0.46 & 0.00 & 0.00 & \mathbf{0.07} & 5.98 \\
 \text{C8} & 0.00 & 0.00 & 0.00 & 0.01 & 0.04 & 0.04 & 0.67 & 3.77 & 0.66 & 0.04 & 0.00 & 0.02 & 0.00 & 0.02 & \mathbf{0.52} & 5.80 \\
 \text{C9} & 0.00 & 0.00 & 0.00 & 0.00 & 0.04 & 0.05 & 0.03 & 0.66 & 3.93 & 0.70 & 0.00 & 0.00 & 0.02 & 0.46 & \mathbf{0.07} & 5.98 \\
 \text{C10} & 0.00 & 0.01 & 0.03 & 0.02 & 0.67 & 0.03 & 0.05 & 0.04 & 0.70 & 3.94 & 0.00 & 0.00 & 0.47 & 0.02 & \mathbf{0.01} & 5.98 \\
 \text{H11} & 0.00 & 0.02 & 0.00 & 0.00 & 0.02 & 0.47 & 0.02 & 0.00 & 0.00 & 0.00 & 0.38 & 0.00 & 0.00 & 0.00 & \mathbf{0.00} & 0.93 \\
 \text{H12} & 0.00 & 0.00 & 0.00 & 0.00 & 0.00 & 0.02 & 0.46 & 0.02 & 0.00 & 0.00 & 0.00 & 0.36 & 0.00 & 0.00 & \mathbf{0.02} & 0.91 \\
 \text{H13} & 0.00 & 0.00 & 0.00 & 0.02 & 0.02 & 0.00 & 0.00 & 0.00 & 0.02 & 0.47 & 0.00 & 0.00 & 0.37 & 0.00 & \mathbf{0.00} & 0.92 \\
 \text{H14} & 0.00 & 0.00 & 0.00 & 0.00 & 0.00 & 0.00 & 0.00 & 0.02 & 0.46 & 0.02 & 0.00 & 0.00 & 0.00 & 0.36 & \mathbf{0.02} & 0.91 \\
 \text{NO}_2,15 & \mathbf{0.00} & \mathbf{0.00} & \mathbf{0.00} & \mathbf{0.00} & \mathbf{0.01} & \mathbf{0.01} & \mathbf{0.07} & \mathbf{0.52} & \mathbf{0.07} & \mathbf{0.01} & \mathbf{0.00} & \mathbf{0.02} & \mathbf{0.00} & \mathbf{0.02} & \mathbf{22.76} & 23.50 \\
 \Sigma & 0.41 & 9.09 & 4.49 & 9.13 & 6.00 & 5.99 & 5.98 & 5.80 & 5.98 & 5.98 & 0.93 & 0.91 & 0.92 & 0.91 & 23.50 & 86.00
 \end{array}
 \end{array}
 \tag{3.21}$$

where $N(\text{NO}_2) = 23.50 e^-$ indicating a net electron withdrawal of $0.50 e^-$ from the common skeleton.

3.2.3.3 Other Limitations of LDMs

As discussed in Ref. [20], some matrix invariants within the context of chemical graph theory may occasionally be identical despite being derived from different molecular graphs. A known example is that of the characteristic polynomial of 1,4-divinylbenzene and that of 2-phenylbutadiene which are identical ($x^{10} - 10x^8 + 33x^6 - 44x^4 + 24x^2 - 4$). This problem is extremely unlikely when the molecules are coded not by topological connectivity matrices consisting of ones and zeroes but rather by their respective LDMs (or electron density-weighted adjacency/connectivity matrices, discussed below) since these matrices cannot contain elements that are all of identical magnitudes.

Another common limitation of all known connectivity graphs—complete or incomplete—or of their matrix surrogates is their inherent insensitivity to optical isomerism. This limitation is circumvented if the experimental dataset includes the active isomers.

Finally, and as any other method for use in empirical modeling of experimental data, conformational averaging has to be performed whenever there exists more than one thermally-accessible rotamer that compete significantly for the molecular population as governed by the Boltzman-distribution at the temperature of interest.

3.3 The Electron Density-Weighted Adjacency/Connectivity Matrix (EDWAM/EDWCM)

The LDM requires for its determination a quantum chemical calculation since the calculation of the LIs and DIs requires the electron density and the electron pair density contained in the second order density matrix which is inaccessible from experiment [29].

The usage of matrix representatives of molecules is not restricted to LDMs and can be extended to quantities directly derivable from both theory and experiment such as the matrix of Coulombic nuclear-nuclear repulsion, the distance matrix, or the matrices of bond critical point (BCP) properties such as the electron density-weighted adjacency/connectivity matrix (EDWAM/EDWCM) [22–24, 30].

The chemical graph theoretic hydrogen-suppressed connectivity matrix of ethane is:

$$\begin{array}{cc} & \begin{array}{cc} \text{C1} & \text{C2} \end{array} \\ \begin{array}{c} \text{C1} \\ \text{C2} \end{array} & \begin{pmatrix} 0 & 1 \\ 1 & 0 \end{pmatrix}, \end{array} \quad (3.22)$$

with a determinant of -1 , a vector $\mathbf{D} = (1, -1)$, and the characteristic polynomial:

$$\lambda^2 - 1. \quad (3.23)$$

The unique features and properties of this molecule are captured with a higher fidelity and specificity if (a) the “ones” in the above matrix are multiplied (weighted) by the value of the electron density (in a.u.) at the bond critical point (BCP), and (b) if all atoms are kept including hydrogen atoms to yield an EDWAM representative of this molecule. The idea of EDWAM was first communicated to one of us (CM) by Professor Lou Massa in the form of a private communication [30].

An EDWAM representation of ethane is:

$$\begin{array}{c}
 \begin{array}{cccccccc}
 & \text{C1} & \text{H2} & \text{C3} & \text{H4} & \text{H5} & \text{H6} & \text{H7} & \text{H8} \\
 \text{C1} & \left(\begin{array}{cccccccc}
 0 & 0.273 & 0.238 & 0.273 & 0.273 & 0 & 0 & 0 & 0 \\
 0.273 & 0 & 0 & 0 & 0 & 0 & 0 & 0 & 0 \\
 0.238 & 0 & 0 & 0 & 0 & 0 & 0.273 & 0.273 & 0.273 \\
 0.273 & 0 & 0 & 0 & 0 & 0 & 0 & 0 & 0 \\
 0.273 & 0 & 0 & 0 & 0 & 0 & 0 & 0 & 0 \\
 0 & 0 & 0.273 & 0 & 0 & 0 & 0 & 0 & 0 \\
 0 & 0 & 0.273 & 0 & 0 & 0 & 0 & 0 & 0 \\
 0 & 0 & 0.273 & 0 & 0 & 0 & 0 & 0 & 0
 \end{array} \right) , \\
 \text{H2} \\
 \text{C3} \\
 \text{H4} \\
 \text{H5} \\
 \text{H6} \\
 \text{H7} \\
 \text{H8}
 \end{array}
 \end{array}
 \tag{3.24}$$

which yields a determinant of zero, and $\mathbf{D} = (-0.607, -0.369, 0.000, 0.000, 0.000, 0.000, 0.369, 0.607)$, and a characteristic polynomial:

$$1.000\lambda^8 - 0.504\lambda^6 + 0.050\lambda^4. \tag{3.25}$$

The molecular graph is generally incomplete since not every pair of atoms share a bond path. The EDWAM has the advantage of being accessible from experiment and relatively inexpensive to calculate theoretically since it does not involve any numerical integration over atomic basins. Because of these practical advantages, the EDWAM may be well-suited for quantitative structure activity relationship (QSAR) studies that involve large molecular sets typical of the *in silico* phase of drug design for example.

The limitations and solutions discussed for LDMs in Sect. 3.2.3 apply to the EDWAMs.

3.4 Some Applications of Molecular Fingerprinting Using LDMs in Quantitative Structure-to-Activity/Property Relationships (QSAR/QSPR) Studies

3.4.1 LDMs as Predictors of pK_a 's and λ_{max} 's of Benzoic Acids

LDMs have recently been used to accurately model and predict the pK_a and λ_{max} values of a series of 14 *para*-substituted benzoic acids with the general structure as given in Fig. 3.3 [21]. To obtain a meaningful measure of distance that satisfies, for example, the triangle inequality, one must choose as reference a molecule that extremizes the studied property. The Frobenius distance (Eq. 3.11) between any

given member of the molecular set and this reference is a measure of their dissimilarity and assumed to reflect the dissimilarity of their properties.

The molecule chosen as reference for the property “ pK_a ” is taken to be the most acidic, that is, the molecule exhibiting the lowest pK_a value—which is *p*-nitrobenzoic acid [$pK_a(\text{BANNO}_2) = 3.44$]. In the case of the property “ λ_{\max} ”, the reference is taken to be the unsubstituted benzoic acid as it exhibits the smallest value [$\lambda_{\max}(\text{BA}) = 230 \text{ nm}$].

The diagonal elements of the LDM, the LIs, are usually the matrix elements with the largest magnitudes. The sum of the LIs often represent 70–90 % of the electron population of a molecule and hence the trace of the LDM is a size-sensitive property that can bias properties that are primarily driven electronically (e.g. pK_a). In these cases where the property of interest is clearly determined by electronic properties and is size-independent, the diagonal suppressed LDM, namely the delocalization matrix (or DM), can be a better fingerprinting tool as this example demonstrates [20, 21].

The squared correlation coefficients (r^2) of linear fits of the Frobenius distances to pK_a and λ_{\max} are given in Table 3.1. The values listed in the table show that the strongest correlation of pK_a is with distances calculated from the sub-graph matrix of the $-\text{COOH}$ group, which can be considered as the “active center” with respect to a property such as pK_a . This subgraph yields a marginally stronger correlation with pK_a than the $-\text{OH}$ subgraph, which can be rationalized on the basis that acidity reflects the ability of the entire $-\text{COOH}$ group to accommodate an excess negative charge upon deprotonation. Inclusion of irrelevant regions in the molecule (by including the matrix of the full molecule, rather than the sub-graph of the relevant “active center”) destroys the correlation. This sensitivity to the “important” or “property-determining” region in the molecule indicates a possible inherent ability of the LDM/DM fingerprinting to detect the active center of the property in question automatically.

Table 3.1 Linear squared Pearson correlation coefficients (r^2) from fitting Frobenius distances versus pK_a , and versus λ_{\max}

Property	n	DM			LDM		
		Full	COOH	OH	Full	COOH	OH
pK_a^1	14	0.349	0.986	0.966	0.159	0.970	0.973
$\lambda_{\max} \text{ (nm)}^2$	8	0.757	0.970	0.926	0.445	0.972	0.931

LDM localization delocalization matrices; *DM* delocalization matrices (diagonal suppressed-LDM); *full* matrix calculated for the full molecule; *COOH* and *OH* matrices calculated for these two sub-graphs

Data obtained from Ref. [21]

¹Reference is *p*-nitrobenzoic acid, $pK_a(\text{BA}-\text{NO}_2) = 3.44$

²Reference is unsubstituted benzoic acid, $\lambda_{\max}(\text{BA}) = 230 \text{ nm}$

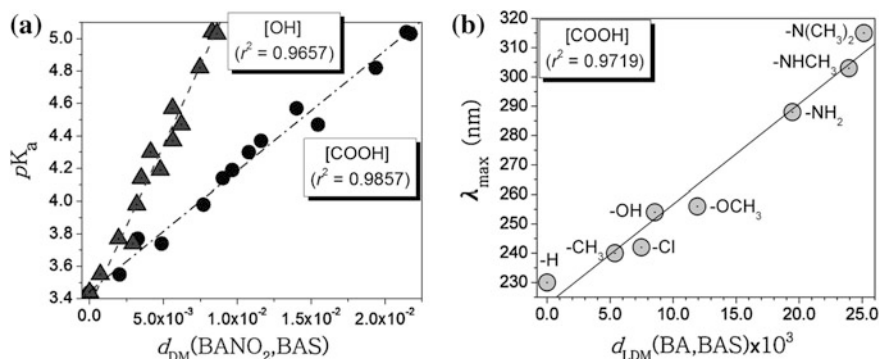


Fig. 3.4 **a** Linear correlations between experimental pK_a and Frobenius distance of the partial delocalization matrices (DMs) from the most acidic molecule in the group (*p*-nitrobenzoic acid, or BANO_2). The partial DMs for the least steep plot include the atoms of the $-\text{COOH}$ group while those of the steepest plot include the $-\text{OH}$ group only. **b** Linear correlations between experimental λ_{max} values and Frobenius distances of the partial localization delocalization matrices (LDMs) calculated for the $-\text{COOH}$ subgraph with (unsubstituted) benzoic acid as reference ($\lambda_{\text{max}}(\text{BA}) = 230$ nm). (Adapted with permission from Ref. [21])

The linear correlations between the calculated Frobenius DM distances of the sub-graphs from that of the reference (*p*-nitrobenzoic acid) are displayed in Fig. 3.4a. Linear regression yields the relation:

$$pK_a = 3.456 + 72.990 \times d_{DM}^{[\text{COOH}]}(\text{BANO}_2, \text{BAS}) \quad (3.26)$$

$$[r^2 = 0.986, q^2 = 0.982, \text{St.Err.} = 0.064, n = 14]$$

where q^2 is the squared leave-one-out cross-validated linear regression coefficient which has an almost identical value as r^2 in this case indicating the absence of over-fitting [31].

The *CRC Handbook of Chemistry and Physics* [32, 33] lists a value of 6.03 for the pK_a of *p*-dimethylaminobenzoic acid (*p*-DMABA). The CRC's pK_a value is inconsistent with the LDM modeling which yields a value of 5.04 [21], the latter agreeing very closely with the value reported in the primary literature ($pK_a = 5.03$) [34]. Further, a calculation based on Hammett σ -constants yields a predicted pK_a of 4.85 for *p*-aminobenzoic acid (*p*-ABA) which is expected to be close to that of *p*-DMABA, and which corroborates that the CRC's entry for *p*-DMABA should be corrected to 5.03 [21].

Electronic spectra remain notoriously difficult to calculate on a large scale by available quantum chemical methods. This is where empirical modeling may provide a practical advantage. The first Hohenberg-Kohn (HK) theorem [35, 36] teaches us that the ground state density, $\rho(\mathbf{r})$, completely specifies the hamiltonian $\hat{H}[\rho(\mathbf{r})]$, and hence it also completely specifies the excited state functions and their properties e.g. energies (the eigenvalues) through the time independent many-particle Schrödinger equation. The mapping of the ground state density to the

energies of the ground and excited states is equivalent to a mapping to the *differences* between these energies and, hence, to UV spectra.

The modeling based on the LDM is also shown capable of the empirical prediction of the substituents effects on the UV absorption surpassing the Hammett constants model in this case. Smith et al. ascribe the inefficiency of modeling spectra with Hammett constants to their calculations from ground state equilibrium constants or bond dissociation energies when the energy gap between a ground and an excited state is what governs UV absorption [37]. One can argue, however, that the ground state equilibrium constants are rooted in the ground-state electron density that fixes the Hamiltonian and the ground and excited eigenstates, as stipulated by the first Hohenberg-Kohn theorem [35, 36]. It appears that it is by virtue of this theorem that our modeling of UV spectra, based on the LDMs/DMs of the *ground* states, can predict electronic excitation energies as described below.

Protonated *para*-benzoic acids exhibit a primary band ~ 230 nm and a secondary weaker band ~ 270 nm [37–39]. The primary band is red-shifted by substitutions in the aromatic ring whether electron donating or withdrawing [38]. Electron withdrawing substituents alter λ_{\max} of the secondary band only if they are $\pi\pi^*$ -chromophores e.g. $-\text{NO}_2$ and $-\text{NHCOCH}_3$ [38], two substituents which we excluded from the correlation for that reason.

Non-chromophoric electron withdrawing groups can red-shift the primary band so much as to overlap and merge with the secondary band sometimes. Electron donors, in contrast, red-shift both the primary and secondary bands [38]. The first band of a series of 8 *para*-substituted benzoic acids, modeled with the Frobenius inter-matrix distances calculated for the $-\text{COOH}$ sub-matrices taking unsubstituted benzoic acid as reference is displayed in Fig. 3.4b and yields the following linear regression equation:

$$\lambda_{\max} = 222.50 + 3.4171 \times 10^3 \times d_{\text{LDM}}^{[\text{COOH}]}(\text{BA}, \text{BAS}) \quad (3.27)$$

$$[r^2 = 0.973, q^2 = 0.944, \text{St.Err.} = 5.74, n = 8]$$

where the closeness of q^2 and r^2 is again indicative of strong predictivity of the model that surpass the modeling with traditional descriptors such as the Hammett σ -constants (see Ref. [21] for details).

3.4.2 LDM-Based Similarity of Rings-in-Molecules (RIMs) to Benzene as a Measure of Local Aromaticity

Aromaticity remains one of the most elusive properties to define in chemistry. It is an abstract term that implies a plethora of properties without being identified with any of these properties. There are several measures of aromaticity that capture one or another of these chemical or physical properties. These measures fall in at least

six broad principal categories: (i) Structural indices of aromaticity such as Krygowski's HOMA index [40–43]; (ii) magnetic properties such as Schleyer's NICS and its variants [44–46], NMR spectra [47, 48], or ring currents [49–51]; (iii) energetic criteria such as resonance energies and aromatic stabilization energies [52–55]; (iv) chemical graph theory criteria as described in detail in Chap. 11 of this book by Professor Ivan Gutman and Dr. Slavko Radenković and references therein; (v) quantum chemical calculated measures of electron delocalization of which the PDI and the FLU are well-known examples among several (see for example Refs. [56–63]); and (vi) aromaticity measures derived from the ring critical point properties, the electrostatic potential, or other properties derived from the electron density (see for example Refs. [49, 64–70]).

These aromaticity measures are generally, but not always, highly correlated and lead at least, but again not always, to a similar ranking of local aromaticity of various rings within molecules [71]. The discrepancies between various indices of aromaticity is not surprising since each of these indices bring to the fore primarily a single aspect of an essentially multi-dimensional multi-faceted phenomenon.

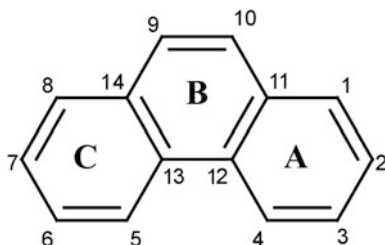
The LDM codes for more than one aspect of the electron distribution in the molecule (one-electron density and pair density) as described in Sect. 3.1 above. Equations (3.5–3.10) show that an LDM contains information on *atomic populations*, *atomic charges*, the *total number of electrons in the molecule (and their localized and delocalized subpopulations)*, and also *two-electron information* derived from the pair density, that is, the full atom-atom delocalization matrix of the system. It is thus *expected* that the LDM codes strongly for aromaticity by virtue of the first Hohenberg-Kohn theorem. The core question is how to get from LDMs to a description of aromaticity?

It is proposed here to approach the problem of quantifying aromatic character from a different angle using LDMs. *Instead of attempting to measure aromaticity directly, the similarity of a given 6-membered carbon ring in a condensed aromatic system to benzene is taken, itself, as a measure of aromaticity.* In a second approach, *the eigenvalues of the LDM of a “ring-in-a-molecule (RIM)” are taken as predictors of the local aromatic character of that ring* [72, 73].

All rings dealt with in this study are exclusively 6-membered carbon rings. Since these rings occur mainly in polycyclic benzenoid hydrocarbons (PBHs), the number of hydrogen atoms that are attached to a given ring varies depending on the neighborhood of the ring in the molecule. To avoid this inconsistency due to the variability of the atoms bonded to the carbon atoms forming the ring, we focus the study exclusively on the carbon skeleton made of the six carbons within a given ring.

When a carbon atom or more is shared between two rings this atom is taken twice, once in evaluating the LDM of one ring and a second time in evaluating the LDM of the second ring. For each molecule, we thus have a number m of LDMs which equals the number of different 6-membered rings in the molecule.

For example, phenanthrene is broken down to three separate LDMs each representing one of its three rings as shown in Scheme 3.1.



Scheme 3.1 Phenanthrene with its atom and ring labeling scheme

The LDMs of the three rings of phenanthrene according to the labeling Scheme 3.1 are [72]:

$$\text{LDM}_A = \begin{matrix} & \begin{matrix} 1 & 2 & 3 & 4 & 12 & 11 \end{matrix} \\ \begin{matrix} 1 \\ 2 \\ 3 \\ 4 \\ 12 \\ 11 \end{matrix} & \begin{pmatrix} 3.957 & 0.746 & 0.036 & 0.048 & 0.031 & 0.637 \\ 0.746 & 3.953 & 0.653 & 0.036 & 0.038 & 0.034 \\ 0.036 & 0.653 & 3.950 & 0.744 & 0.034 & 0.037 \\ 0.048 & 0.036 & 0.744 & 3.951 & 0.640 & 0.031 \\ 0.031 & 0.038 & 0.034 & 0.640 & 3.900 & 0.654 \\ 0.637 & 0.034 & 0.037 & 0.031 & 0.654 & 3.891 \end{pmatrix} \end{matrix}, \quad (3.28)$$

$$\text{LDM}_B = \begin{matrix} & \begin{matrix} 9 & 10 & 11 & 12 & 13 & 14 \end{matrix} \\ \begin{matrix} 9 \\ 10 \\ 11 \\ 12 \\ 13 \\ 14 \end{matrix} & \begin{pmatrix} 3.958 & 0.822 & 0.033 & 0.024 & 0.027 & 0.573 \\ 0.822 & 3.958 & 0.573 & 0.027 & 0.024 & 0.033 \\ 0.033 & 0.573 & 3.891 & 0.654 & 0.026 & 0.017 \\ 0.024 & 0.027 & 0.654 & 3.900 & 0.559 & 0.026 \\ 0.027 & 0.024 & 0.026 & 0.559 & 3.900 & 0.654 \\ 0.573 & 0.033 & 0.017 & 0.026 & 0.654 & 3.891 \end{pmatrix} \end{matrix}, \quad (3.29)$$

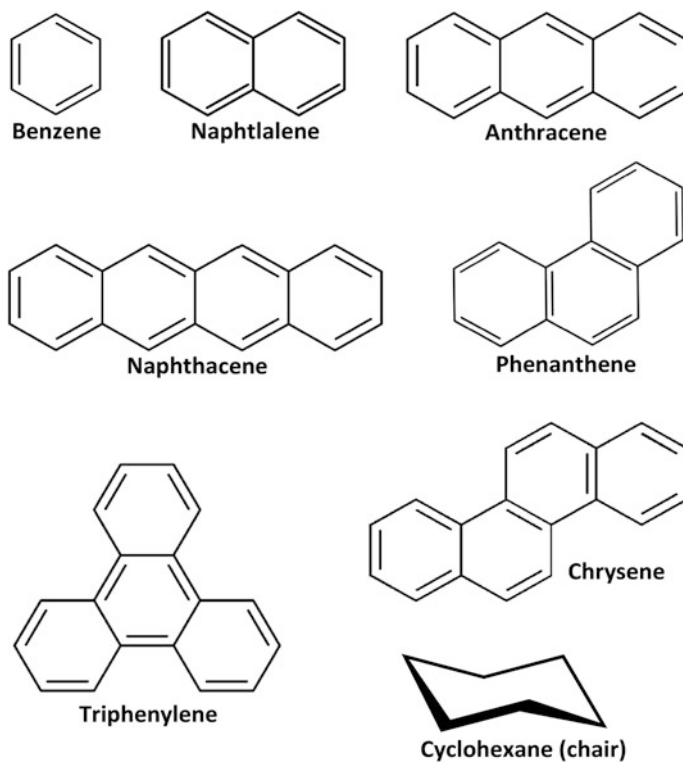
$$\text{LDM}_C = \begin{matrix} & \begin{matrix} 5 & 6 & 7 & 8 & 14 & 13 \end{matrix} \\ \begin{matrix} 5 \\ 6 \\ 7 \\ 8 \\ 14 \\ 13 \end{matrix} & \begin{pmatrix} 3.951 & 0.744 & 0.036 & 0.048 & 0.031 & 0.640 \\ 0.744 & 3.950 & 0.653 & 0.036 & 0.037 & 0.034 \\ 0.036 & 0.653 & 3.953 & 0.746 & 0.034 & 0.038 \\ 0.048 & 0.036 & 0.746 & 3.957 & 0.637 & 0.031 \\ 0.031 & 0.037 & 0.034 & 0.637 & 3.891 & 0.654 \\ 0.640 & 0.034 & 0.038 & 0.031 & 0.654 & 3.900 \end{pmatrix} \end{matrix}. \quad (3.30)$$

Note that unlike the LDM of the full system, a partial LDM such as the ones provided for the individual rings of phenanthrene above will generally *not* sum into an integer number of electrons since the sum of sums now yields the population of

these six carbon atoms within the molecule. This observation reflects the fact that atoms in molecules are open quantum sub-systems exchanging electrons and energy with their neighbours.

If one constructs ring matrices in the same order as that chosen to construct the matrix of the reference, namely, benzene, then the similarity distance measured by the Frobenius distance becomes invariable to the atomic labelling. For example if we choose to construct the benzene reference sub-matrix by listing an *ortho*-carbon atom as the second atom immediately following the *ipso*-carbon atom, the *meta*-carbon attached to it as the third, the *para*- as the fourth, the second *meta*- as the fifth, and the second *ortho*- as the sixth, then the Frobenius distance will be insensitive to what atom we pick as the first in the ring of interest as long as we stick to a nearest neighbour listing of the atoms (whether taken clockwise or anticlockwise is unimportant).

Scheme 3.2 depicts the structures of a selection of aromatic benzenoid hydrocarbons the local aromaticity in which is considered. A comparison with well-known aromaticity criteria such as HOMA (structural), NICS (magnetic), and FLU and PDI (electron delocalization) with the Frobenius distance of local rings



Scheme 3.2 Molecular set considered in the study of “rings-in-molecules (RIMs)” similarity distance from benzene

from benzene reveals striking correlations. The eigenvalues of the LDMs taken as absolute predictors of aromaticity (not compared with benzene) are also highly correlated with these aromaticity measures as well.

The correlations of common aromaticity indices with the Frobenius distance of a ring in a PBH from benzene are generally non-linear except possibly in the case of PDI. Some of these correlations are depicted in Fig. 3.5 and listed in Table 3.2 and discussed in greater detail elsewhere [72, 73]. Cyclohexane is excluded from Fig. 3.5 despite of falling on the general trend lines to improve the resolution of the plot in the region of aromatic rings in PBHs.

3.4.3 LDM-Eigenvalues as Predictors in QSAR

One of the more useful manipulations of a matrix are the linear transformations giving rise to eigenvectors and eigenvalues. One of us (IS) has recently observed that there is a strong correlation between the number of electrons ($N(\Omega)$) in the atomic basins and the eigenvalues of the LDM matrices. The largest eigenvalues are

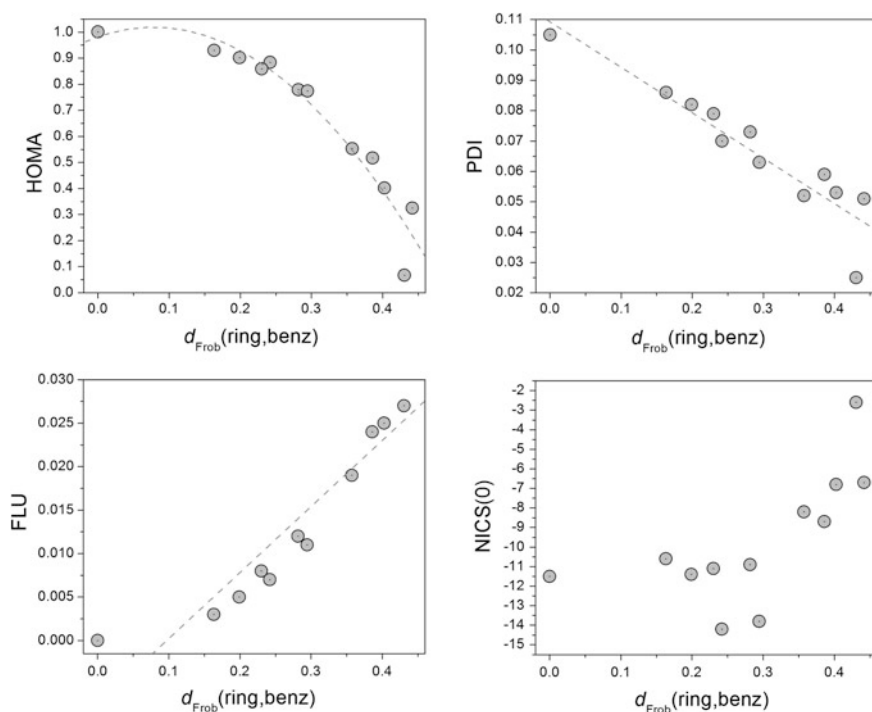


Fig. 3.5 Correlations between the Frobenius distance of various rings listed in Table 3.2 from benzene and four common aromaticity indices: HOMA, PDI, FLU, and NICS(0)

Table 3.2 Aromatic rings sorted in order of their dissimilarity to benzene as measured by the Frobenius distance and four corresponding common indices of aromaticity

Molecule	Ring	d_{Frob}	HOMA	PDI	NICS(0)	FLU
Benzene		0	1.001	0.105	-11.5	0
Triphenylene	Outer	0.1634	0.93	0.086	-10.6	0.003
Phenanthrene	Outer	0.1991	0.902	0.082	-11.4	0.005
Chrysene	Outer	0.2301	0.859	0.079	-11.1	0.008
Anthracene	Inner	0.2420	0.884	0.07	-14.2	0.007
Naphthalene		0.2816	0.779	0.073	-10.9	0.012
Naphthacene	Inner	0.2945	0.774	0.063	-13.8	0.011
Chrysene	Inner	0.3574	0.553	0.052	-8.2	0.019
Anthracene	Outer	0.3859	0.517	0.059	-8.7	0.024
Phenanthrene	Inner	0.4026	0.402	0.053	-6.8	0.025
Triphenylene	Inner	0.4306	0.067	0.025	-2.6	0.027
Naphthacene	Outer	0.4417	0.325	0.051	-6.7	0.031
Cyclohexane	Chair	0.7408	-4.34	0.007	-2.1	0.091

See Scheme 3.2 for the structures of these molecules

associated with the atoms having the most electrons and the smallest eigenvalues being generally associated with the hydrogen atoms. This observation provides a route to reducing the high-dimensional complexity of the LDM to provide a set of molecular descriptors for building quantitative structure property relationships (QSPR) or quantitative structure activity relationships (QSAR).

One of us (RC) has begun to explore the use of Principal Component Analysis (PCA) [74] to reduce the dimensions of the LDM and extract information from it to build robust QSPRs and QSARs. In the PCA approach, a matrix containing entries that may be statistically correlated is converted to an eigenvector, devoid of such correlation between variables, composed of what is termed the “principal components (PCs)”. The PCs may be equal in number to the original variables or can be lesser. The first PC is the one with maximal variance followed by PCs that maximize the variance subject to the constraint of being orthogonal to all previous PCs.

The PCs are, thus, orthogonal (and uncorrelated) by construction and represent the eigenvectors of the (symmetric) covariance matrix. Each of these eigenvectors can be thought of as one of n -axes of an n -D ellipse. Axes of this ellipse that are small mean that the corresponding variance along that axis is also small. We can then neglect axes smaller than a given threshold (and its corresponding PC) from the representation of the LDM without losing much information.

As mentioned above we have observed that there is a strong correlation between the eigenvalues of the LDM and the number of electrons in the atom basins. The hydrogen atoms have the smallest number of electrons and therefore within the dimensionality reducing transformations of the PCA, we will be able to effectively ignore their contributions to the eigenvalues extracted from the LDM by the PCA transformation. Functionally, this is equivalent to the hydrogen suppressed structure used by Kier and Hall to develop their “Atom Level Electrotological State” [75].

As an initial foray into extracting useful information from the LDMs using the PCA transformation we looked at a series of carboxylic acids that extended the set used by Matta et al. [20, 21] to evaluate the potential of LDMs to predict physical properties (e.g. pK_a) of the acids. One of our first observations is that as long as the pair-wise values for the LI (e.g. C1 to C1, O7:O7, etc.) and the DI (C1to O7,O7:H4, etc.) are retained, then the ordering of the LDM does not affect the eigenvalues that are produced from the LDM (Table 3.3).

Table 3.4 shows the largest six eigenvalues extracted using the PCA method. For most of these acids the six largest eigenvalues account for >95 % of the variance in the LDM. Almost all the unaccounted-for variance (especially in the larger molecules) is due to the hydrogen atoms.

As pointed out by Matta [20], a threshold of dissimilarity is assumed between the members of a molecular set for the construction of a QSAR model. Similarity is commonly quantified on the basis of amino acid sequence matching [76], mismatching of 2-dimensional chemical graphs [8], on 3-D molecular skeleton superpositions [77], and on point-by-point comparison of electron density—pioneered by Carbó [78–81] or of the molecular electrostatic potential [82–94]. Through relationships (5) and (6) in Ref. [20], a similarity of $\rho(\mathbf{r})$ necessarily leads to the similarity of all other ground-state properties, and hence the most fundamental molecular comparisons are those effected at the electron density level.

One way to appreciate the similarity of a group of molecules would be to map the molecules in n -dimensional abstract mathematical space and determine if the eigenvalues resulting from the PCA of the LDM coincide with chemical intuition. The visualization of such multi-dimensional data is not feasible beyond three dimensions. Thus even for the 6-dimensional descriptor space that can be constructed from the principal components listed in Table 3.4, the reduction of dimensionality is a must to visualize distance similarity relationships between molecules.

Such dimensional reduction may be achieved by “Multidimensional Scaling (MDS)” techniques. MDS projects the n -dimensional distance in a lower-dimensional space (2- or 3-dimensions) under the constraint of maximizing the retention of the structure of the inter-molecular distance matrix. The representation of the n -dimensional space is optimized in the lower-dimensional projection by minimizing what is known as “stress”. The smaller the stress the better the projection up to the (generally unattainable) limit of zero which is a projection that preserves the distance matrix completely. The quality of the projection can be gleaned from what is known as a “Shepard diagram”.

The Shepard diagram is a scatter plot in which the dissimilarities between the molecules, measured as the distances in the full n -dimensional space, are compared with the corresponding distances in the projected 2-dimensional space. A large spread is an indicator of a poor MDS projection and vice versa up to the unreachable extreme where all points fall on one line which indicates a perfect MDS projection.

Using the data in Table 3.4 and the MDS algorithm in the software package XLSTAT™, the Shepard diagram displayed in Fig. 3.6 is obtained. One can glean

Table 3.3 “Scrambled” LDM for acetic acid and resulting eigenvalues

	C1	C2	H3	H4	H5	O6	O7	H8
C1	4.010	0.464	0.475	0.477	0.477	0.060	0.053	0.004
C2	0.464	2.793	0.017	0.021	0.021	0.654	0.417	0.005
H3	0.475	0.017	0.397	0.017	0.017	0.009	0.007	0.001
H4	0.477	0.021	0.017	0.419	0.018	0.010	0.006	0.001
H5	0.477	0.021	0.017	0.018	0.419	0.010	0.006	0.001
O6	0.060	0.654	0.009	0.010	0.010	8.276	0.143	0.008
O7	0.053	0.417	0.007	0.006	0.006	0.143	8.171	0.321
H8	0.004	0.005	0.001	0.001	0.001	0.008	0.321	0.075
	F1	F2	F3	F4	F5	F6		
Eigen.	3.314	1.816	0.968	0.762	0.559	0.541		
Var.%	41.4	22.7	12.1	9.5	7.0	6.8		
Cum.%	41.4	64.1	76.2	85.8	92.7	99.5		

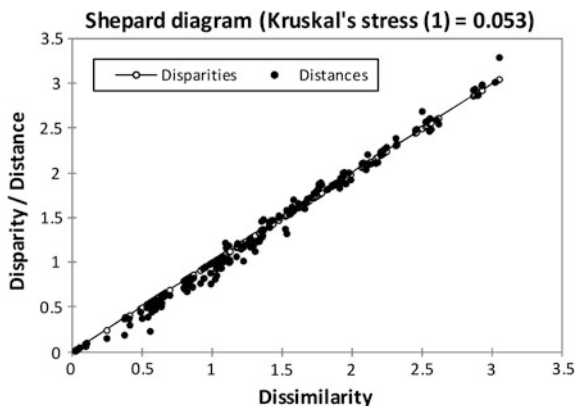
	H3	O7	H4	H5	O6	C1	H8	C2
H3	0.397	0.007	0.017	0.017	0.009	0.475	0.001	0.017
O7	0.007	8.171	0.006	0.006	0.143	0.053	0.321	0.417
H4	0.017	0.006	0.419	0.018	0.010	0.477	0.001	0.021
H5	0.017	0.006	0.018	0.419	0.010	0.477	0.001	0.021
O6	0.009	0.143	0.010	0.010	8.276	0.060	0.008	0.654
C1	0.475	0.053	0.477	0.477	0.060	4.010	0.004	0.464
H8	0.001	0.321	0.001	0.001	0.008	0.004	0.075	0.005
C2	0.017	0.417	0.021	0.021	0.654	0.464	0.005	2.793
	F1	F2	F3	F4	F5	F6		
Eigen.	3.314	1.816	0.968	0.762	0.559	0.541		
Var.%	41.4	22.7	12.1	9.5	7.0	6.8		
Cum.%	41.4	64.1	76.2	85.8	92.7	99.5		

	O6	H4	C2	H3	H5	O7	H8	C1
O6	8.276	0.010	0.654	0.009	0.010	0.143	0.008	0.060
H4	0.010	0.419	0.021	0.017	0.018	0.006	0.001	0.477
C2	0.654	0.021	2.793	0.017	0.021	0.417	0.005	0.464
H3	0.009	0.017	0.017	0.397	0.017	0.007	0.001	0.475
H5	0.010	0.018	0.021	0.017	0.419	0.006	0.001	0.477
O7	0.143	0.006	0.417	0.007	0.006	8.171	0.321	0.053
H8	0.008	0.001	0.005	0.001	0.001	0.321	0.075	0.004
C1	0.060	0.477	0.464	0.475	0.477	0.053	0.004	4.010
	F1	F2	F3	F4	F5	F6		
Eigen.	3.314	1.816	0.968	0.762	0.559	0.541		
Var.%	41.4	22.7	12.1	9.5	7.0	6.8		
Cum.%	41.4	64.1	76.2	85.8	92.7	99.5		

Eigen. eigenvalues, *Var.%* percent variability, *Cum.%* cumulative percentage

Table 3.4 Eigenvalues from PCA of a series of carboxylic acids (non-traditional names are used to highlight the functional groups attached to the C-COOH skeleton)

Compounds	F1	F2	F3	F4	F5	F6	pK _a
Acetic Acid	3.3139	1.8157	0.9681	0.7624	0.5594	0.5410	4.76
Fluoroacetic acid	2.8279	1.7929	1.3095	0.8673	0.5903	0.5444	2.586
Difluoroacetic acid	2.4528	1.6669	1.3705	1.1398	0.8523	0.3994	1.34
Trifluoroacetic acid	2.2115	1.4565	1.1411	1.1403	1.1120	0.7399	0.52
Chloroacetic acid	2.8650	1.8055	1.3091	0.8645	0.5579	0.5375	2.866
Dichloroacetic acid	2.4669	1.6702	1.3612	1.1442	0.8436	0.4083	1.26
Trichloroacetic acid	2.2149	1.4654	1.1462	1.1454	1.0845	0.7442	0.512
Glycine	3.0611	2.6926	1.7311	0.9443	0.7691	0.5314	2.366
N-methylglycine	3.4219	2.4983	2.0691	1.5747	0.8849	0.7399	2.35
N,N-dimethylglycine	3.5031	3.1997	2.3859	1.5197	1.0354	0.8589	2.04
2-hydroxyacetic acid	2.7729	2.2391	1.7063	0.9008	0.7231	0.5576	3.83
2-mercaptoacetic acid	2.7687	2.2753	1.6337	0.8686	0.6791	0.5247	3.55
2-methylacetic acid	3.2949	2.6510	1.6724	0.9231	0.7578	0.5431	4.875
2,2-dimethylacetic acid	3.6229	2.8154	2.0677	1.5495	0.9162	0.7466	4.84
2,2,2-trimethylacetic acid	3.5044	3.4968	2.6103	1.6493	1.1271	0.8440	5.031
2-methoxyacetic acid	3.5054	2.5375	1.6007	1.1461	0.8160	0.6961	3.57
2-cyanoacetic	2.8160	2.2821	1.6958	0.8868	0.7173	0.4891	2.45
2-ethylacetic acid	3.4123	2.6025	2.4643	1.5942	0.9186	0.7470	4.82
2,2-diethyl acetic acid	3.6628	2.9875	2.5368	2.4024	1.9023	1.4590	4.71
2-phenylacetic acid	2.9070	2.3874	2.2992	2.1406	1.6469	1.4845	4.31

Fig. 3.6 Shepard plot of the transformed six dimensional data listed in Table 3.4

from this figure that (a) the Kruskal Stress is low, and that (b) the scatter-plot is highly linear.

The 2-dimensional MDS projection of the 6-dimensional eigenvalue descriptors of the LDM are shown in Fig. 3.7.

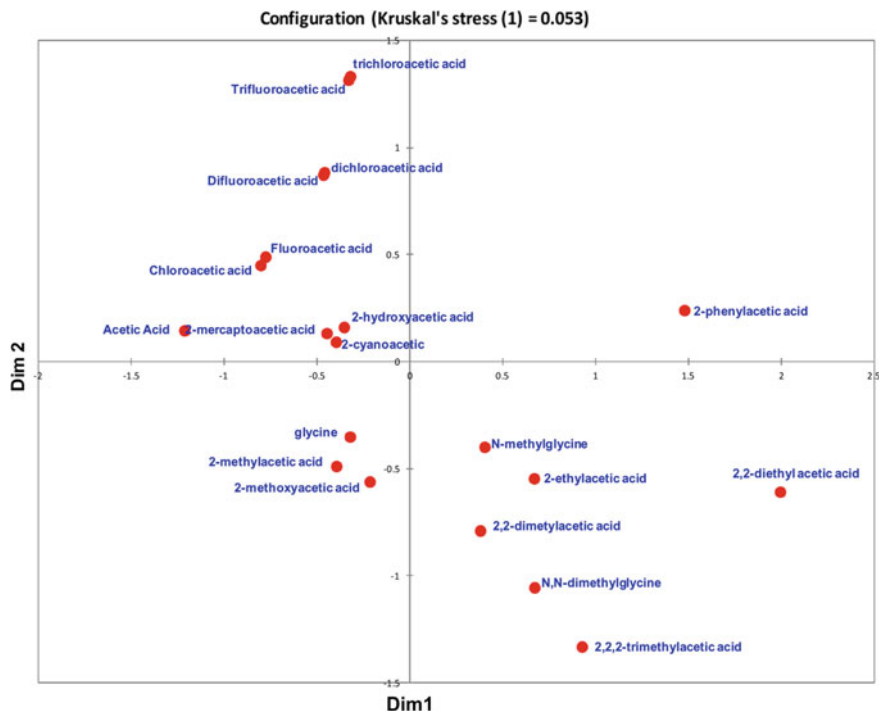


Fig. 3.7 Two-dimensional MDS projection of the 6-dimensional eigenvalue descriptors of the LDM

The mapping of the 6-dimensional eigenvalue descriptors of the LDM to a 2-dimensional space (Fig. 3.7) is in line with our chemical intuition: Electron-withdrawing functional groups are mapped together (upper left quadrant) and electron donating groups are in close proximity and far from the first group (lower right quadrant).

For closely related series of carboxylic acids we might reasonably expect that the positions on the map could scale with physical properties. Matta showed in Fig. 14 of Ref. [20] that a strong correlation exists between the experimental pK_a values of fluorine- and chlorine-substituted acetic acids (SAA) and the Frobenius distance of their localization-suppressed-LDMs (DMs) from that of unsubstituted acetic acid (AA). The data can be closely fit to an exponential model:

$$pK_a(\text{SAA}) \approx -0.588 + 5.415 \exp[-5.066 d_{deloc}(\text{AA}, \text{SAA})] \quad (3.31)$$

$$(r^2 = 0.979, n = 7)$$

Similarly, if we regress the distances (d) of the chlorine and fluorine substituted acids (SAA) from acetic acid taken from the data used to generate the plot in Fig. 3.7 we get the relationship:

$$\begin{aligned} \text{p}K_{\text{a}}(\text{SAA}) &\approx 8.4075 \exp(-0.644 d) \\ (r^2 &= 0.996, n = 7) \end{aligned} \quad (3.32)$$

This suggests that the 2-dimensional projection of the 6-dimensional eigenvalue descriptor set for these molecules retains most of the information of the LDM (and DM) representations of the molecules. We have also shown [95] that the six eigenvalues for the molecules in Table 3.4 can be used to build robust models for multiple physical properties ($\text{p}K_{\text{a}}$, $\text{Log}P$, LD50 (oral:rat), Henry's Law Constants, melting point, boiling point, vapour pressure and the Atmospheric OH rate constant).

In another preliminary evaluation of the use of the 6-dimensional eigenvalues from the LDM as universal descriptors we looked at building a model of the inhibitive properties of heterocyclic diazoles for acidic iron corrosion [96]. Table 3.5 shows the computed eigenvalues and corrosion inhibitor efficiencies (CIE %) for a set of diazoles reported by Babic-Samardzija et al. [96].

From these eigenvalues a relatively simple model can be built:

$$\begin{aligned} \text{CIE}(\%) &= 77.6097 + 703.1552(F4 \times F5) - 261.6683 \times (F4)^2 - 464.9701(F5)^2 \\ (r^2 &= 0.987, \quad q^2 = 0.898, \quad n = 8) \end{aligned} \quad (3.33)$$

with both a high correlation coefficient and a high cross-validation score. A plot of the experimental versus predicted corrosion inhibition efficiencies is shown in Fig. 3.8.

Table 3.5 Eigenvalues and corrosion inhibitor efficiencies (CIE%) for a set of diazoles (CIE% taken from Babic-Samardzija et al. [96])

Compound	F1	F2	F3	F4	F5	F6	CIE%
3-amino-1H-isoindole	3.160	2.854	2.306	1.968	1.566	1.487	90.7
Indazole	2.700	2.432	1.974	1.857	1.540	1.385	83.6
Imidazole	2.608	2.230	1.832	1.081	0.785	0.216	83.4
4-bromoimidazole	2.461	2.140	1.598	1.168	0.847	0.517	83.1
4-methylimidazole	3.471	2.254	1.964	1.262	0.890	0.760	82.8
Pyrazole	2.516	2.321	1.782	1.127	0.799	0.204	79.3
4-nitropyrazole	2.406	2.104	1.981	1.107	1.061	0.990	59.4
4-sulfopyrazole	2.405	2.266	1.993	1.617	1.088	1.069	80.3

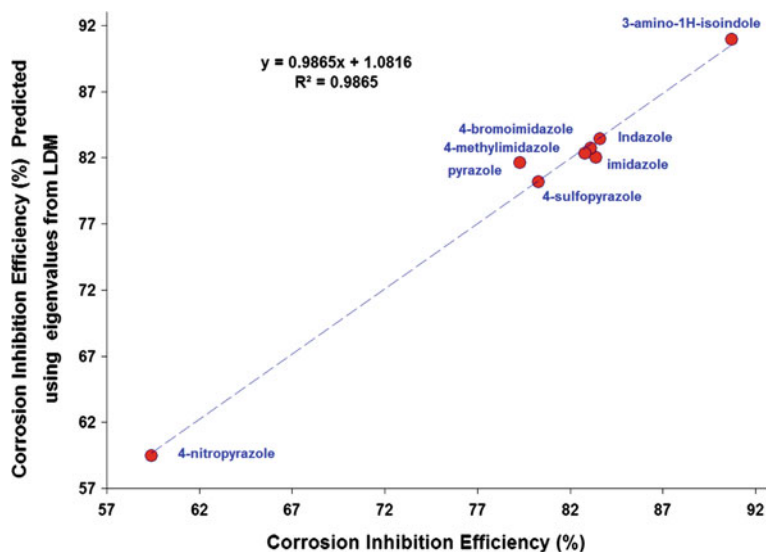


Fig. 3.8 Correlation of observed and predicted CIE (%) where the predicted values are obtained using the eigenvalues extracted by PCA from the LDMs

In summary, preliminary investigations show the potential of the eigenvalues of the LDM extracted from the matrices using the principal component analysis method as “pruned” descriptors of the electron densities contained within the LDM. When compared to the full LDM or DM matrices, the distances of molecules calculated using a combination of PCA and multidimensional scaling produce a simple exponential model between the Euclidian distance separating the molecules of the set and their experimental pK_a . Furthermore, for a more extended group of carboxylic acids, the same set of eigenvalues (Table 3.4) have been used to build physical property models for pK_a , LogP, LD50 (oral:rat), Henry’s Law Constants, melting point, boiling point, vapor pressure and the Atmospheric OH rate constant. For each set of these physical properties, models having both high regression coefficients ($r^2 > 0.95$) and high cross validation scores ($q^2 > 0.90$) could be produced.

Finally, accurate and robust models for corrosion inhibition efficiencies have been found for multiple sets of corrosion inhibition data. This finding is rather remarkable as corrosion inhibition depends on a number of molecular properties such as hydrophobicity (LogP) and Lewis Base strength as well as the solubility of the inhibitor. This corroborates the concept that similarity based on electron density descriptors may in fact capture more than one aspect of the phenomenon being studied.

3.4.4 *LDMs-as a Tool to Evaluate the Quality of Basis Sets and of the Levels of Theory*

Another potential use of the LDM is in assessing the quality of basis sets and/or the different new density functional theory (DFT) functionals, for example. The fundamental assumption is that the closer a given level of theory is to another the closer the corresponding LDMs will be and the smaller the Frobenius distance.

As an exploratory investigation, only Hartree-Fock (HF) results on four small molecules (CH_4 , CH_3OH , H_2O , and NH_3) are considered here in conjunction with a variety of standard basis sets. Since the Hartree-Fock method is variational, the lower the energy the better the quality of the corresponding basis set. In the set of basis sets investigated in this work, the lowest energy is obtained at the HF/cc-pvqz level of theory, which implies that it is the best level of theory used as the comparison standard.

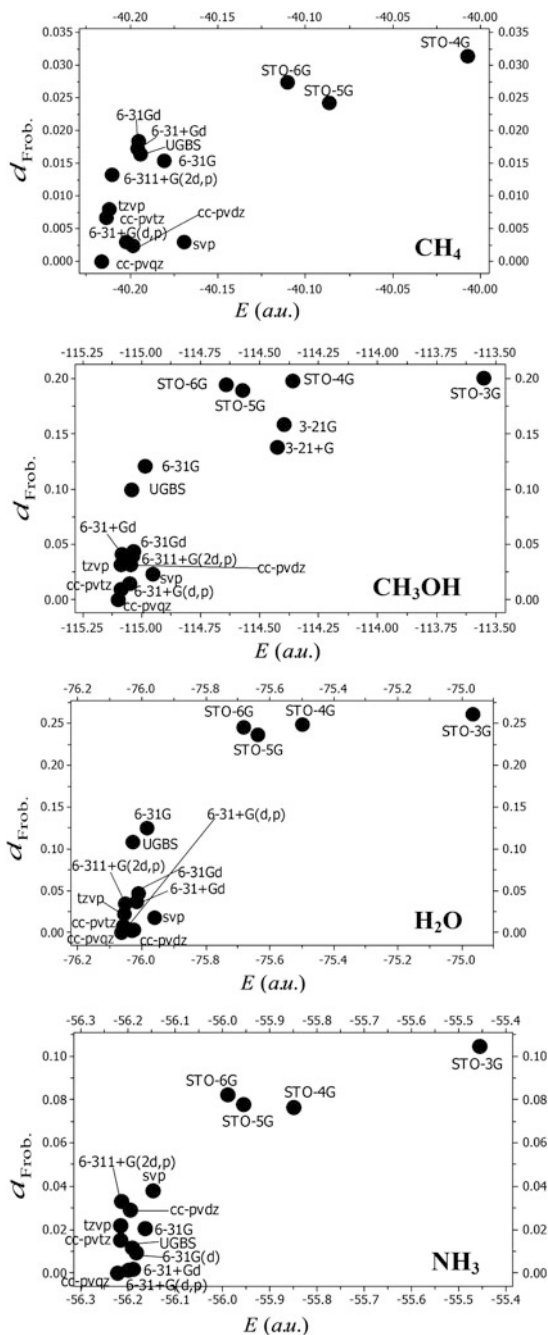
Figure 3.9 displays the correlation between the total energy and the LDM Frobenius distance from the best result (HF/cc-pvqz) for each of the four studied molecules. The plots show that the general trend is that the lower the energy the smaller the distance from the best result.

This new proposal is elaborated in detail elsewhere [25]. Clearly much more numerical corroboration is needed before claiming a definitive usefulness of LDMs in evaluating and comparing the quality of basis sets and/or levels of theory.

3.5 Closing Remarks

As stressed above, the first Hohenberg–Kohn (HK) theorem [35, 36] by establishing a unique functional mapping between the ground-state electron density and both the external potential and the total number of electrons fixes the Hamiltonian. The electron density then, through the intermediacy of the time-independent Schrödinger equation, determines the eigenstates and eigenvalues uniquely. Once the eigenstates are fixed all properties of the ground and excited state are also fixed. It is not surprising then that powerful descriptors can be extracted from the electron density. The pioneering work of Paul Popelier in his Quantum Topological Molecular Similarity (QTMS) approach [97–103], whereby Euclidean similarity distances between molecules in a molecular set are defined on the basis of difference in the sum of their bond critical points properties, led the way for others like us to follow his step. While our approach is different than QTMS, since it rests on a full atomic level description of electron localization and delocalization in each molecule in the set while QTMS is based on a full bond-by-bond level of analysis, what QTMS and the analysis of LDMs have in common is their basis in the topological partitioning of the electron density and its characteristic gradient vector field, as suggested in 1981 by I. Dmitriev in the opening quotation of this chapter. Both QTMS and LDMs analyses are traceable to physical quantities derived from

Fig. 3.9 Correlation of the Frobenius distance with the LDM obtained with the best basis set cc-pvqz versus the total Hartree-Fock energy with datapoints calculated using basis sets of varying quality. The best quality calculations reside in the *lower left side* of each plot and the least accurate ones reside in the *upper-right corner*



or related to the electron density and, in the case of LDM, also to electron delocalization information related to the electron-pair density as well.

In this new approach we draw on the strengths of two sub-fields of theoretical chemistry: Bader's Quantum Theory of Atoms in Molecules (QTAIM) to extract physically meaningful descriptors from the electron density and related properties and Chemical Graph Theory which led the way in abstracting the chemical graph in matrices followed by mathematical treatment to extract matrix invariants for the purpose of correlating with and predicting experimental properties of compounds. This new approach is promising and wide reaching, with possible applications ranging from predicting physicochemical properties of series of molecules to their corrosion protective abilities passing by as diverse problems as quantifying aromaticity to possibly providing a practical tool for assessing the quality of newly developed basis sets of electronic structure calculations such as new DFT functionals.

A book is presently being written by the authors about LDMs and their uses [104]. This book will contain extensive data that support the basic claim of this chapter, that is, that LDMs are a molecular fingerprinting tool that can provide a basis for robust QSAR-type studies.

Acknowledgments The authors thank Dr. Todd A. Keith, Professor Lou Massa, Dr. Nenad Trinajstić, Dr. Sonja Nikolić, and Mr. Matthew J. Timm for helpful discussions. Financial support of this work was provided by the *Natural Sciences and Engineering Research Council of Canada* (NSERC), *Canada Foundation for Innovation* (CFI), *Saint Mary's University*, *McMaster University*, and *Mount Saint Vincent University*.

References

1. Dmitriev IS (1981) *Molecules without chemical bonds* (English Translation). Mir Publishers, Moscow
2. Balaban AT (1976) *Chemical applications of graph theory*. Academic Press, New York
3. Balaban AT (1985) Applications of graph theory in chemistry. *J Chem Inf Comput Sci* 25:334–343
4. Hall LH, Kier LB (1976) *Molecular connectivity in chemistry and drug research*. Academic Press, Boston
5. Bonchev D, Rouvray DH (1991) *Chemical graph theory: introduction and fundamentals*. OPA, Amsterdam
6. Balasubramanian K (1994) Integration of graph theory and quantum chemistry for structure-activity relationship. *SAR & QSAR Environ Res* 2:59–77
7. Diudea MD, Gutman I, Lorentz J (1999) *Molecular topology*. Nova Science Publishers Inc, Hauppauge NY
8. Janezić D, Milicević A, Nikolić S, Trinajstić N (2007) Graph theoretical matrices in chemistry. In: *Mathematical chemistry monographs*, vol 3. University of Kragujevac, Kragujevac
9. Todeschini R, Consonni V (2009) *Molecular descriptors for chemoinformatics*, 2nd Edn, vols. I and II). Wiley-VCH Weinheim, Weinheim
10. Bader RFW (1990) *Atoms in molecules: a quantum theory*. Oxford University Press, Oxford
11. Popelier PLA (2000) *Atoms in molecules: an introduction*. Prentice Hall, London

12. Matta CF, Boyd RJ (eds) (2007) The quantum theory of atoms in molecules: from solid state to DNA and drug design. Wiley-VCH, Weinheim
13. Bader RFW (1998) A bond path: a universal indicator of bonded interactions. *J Phys Chem A* 102:7314–7323
14. Bader RFW (2009) Bond paths are not chemical bonds. *J Phys Chem A* 113:10391–10396
15. Martín-Pendás A, Francisco E, Blanco MA, Gatti C (2007) Bond paths as privileged exchange channels. *Chem Eur J* 13:9362–9371
16. Runtz GR, Bader RFW, Messer RR (1977) Definition of bond paths and bond directions in terms of the molecular charge distribution. *Can J Chem* 55:3040–3045
17. Keith TA, Bader RFW, Aray Y (1996) Structural homeomorphism between the electron density and the virial field. *Int J Quantum Chem* 57:183–198
18. Keith TA (2015) AIMAll/AIMStudio. <http://aim.tkgristmill.com/>
19. Fradera X, Austen MA, Bader RFW (1999) The Lewis model and beyond. *J Phys Chem A* 103:304–314
20. Matta CF (2014) Modeling biophysical and biological properties from the characteristics of the molecular electron density, electron localization and delocalization matrices, and the electrostatic potential. *J Comput Chem* 35:1165–1198
21. Sumar I, Ayers PW, Matta CF (2014) Electron localization and delocalization matrices in the prediction of pK_a 's and UV-wavelengths of maximum absorbance of *p*-benzoic acids and the definition of super-atoms in molecules. *Chem Phys Lett* 612:190–197
22. Timm MJ, Matta CF, Massa L, Huang L (2014) The localization-delocalization matrix and the electron density-weighted connectivity matrix of a finite graphene flake reconstructed from kernel fragments. *J Phys Chem A* 118:11304–11316
23. Matta CF (2014) Localization-delocalization matrices and electron density-weighted adjacency matrices: new electronic fingerprinting tools for medicinal computational chemistry. *Future Med Chem* 6:1475–1479
24. Dittrich B, Matta CF (2014) Contributions of charge-density research to medicinal chemistry. *Int U Cryst J (IUCrJ)* 1:457–469
25. Sumar I, Cook R, Ayers PW, Matta CF (2015) AIMLDM: a program to generate and analyze electron localization–delocalization matrices (LDMs). *Comput Theor Chem* 1070:55–67
26. White D, Wilson RC (2008) Parts-based generative models for graphs. In: 19th International Conference on Pattern Recognition (ICPR 2008), pp 1–4
27. Pye CC, Poirier RA (1998) Graphical approach for defining natural internal coordinates. *J Comput Chem* 19:504–511
28. Pye CC (1997) Applications of optimization to quantum chemistry, PhD Thesis. Memorial University of Newfoundland, Saint John's (NF), Canada
29. Müller AMK (1984) Explicit approximate relation between reduced two- and one-particle density matrices. *Phys Lett A* 105:446–452
30. Massa L (2014) Personal communication
31. Picard RR, Cook RD (1984) Cross-validation of regression models. *J Am Stat Assoc* 79:575–583
32. Lide DR (2007–2008) CRC handbook of chemistry and physics, 88th Edn. CRC Press
33. Lide DR (2006) CRC handbook of chemistry and physics, 87th Edn. CRC Press
34. Jover J, Bosque R, Sales J (2008) QSPR prediction of pK_a for benzoic acids in different solvents. *QSAR Combin Sci* 27:563–581
35. Hohenberg P, Kohn W (1964) Inhomogeneous electron gas. *Phys Rev B* 136:864–871
36. Parr RG, Yang W (1989) Density-functional theory of atoms and molecules. Oxford University Press, Oxford
37. Guo H-B, He F, Gu B, Liang L, Smith JC (2012) Time-dependent density functional theory assessment of UV absorption of benzoic acid derivatives. *J Phys Chem A* 116:11870–11879
38. Pavia DL, Lampman GM, Kriz GS, Vyvyan JR (2009) Introduction to spectroscopy, 4th edn. Brooks/Cole Cengage Learning, Belmont, CA, USA
39. Kamath BV, Mehta JD, Bafna SL (1975) Ultraviolet absorption spectra: some substituted benzoic acids. *J Appl Chem Biotechnol* 25:743–751

40. Krygowski TM, Szatyłowicz H, Stasyuk OA, Dominikowska J, Palusiak M (2014) Aromaticity from the viewpoint of molecular geometry: application to planar systems. *Chem Rev* 114:6383–6422
41. Krygowski TM, Stepien BT (2005) σ - and π -electron delocalization: focus on substituent effects. *Chem Rev* 105:3482–3512
42. Krygowski TM, Cyranski MK (2001) Structural aspect of aromaticity. *Chem Rev* 101:1385–1419
43. Kruszewski J, Krygowski TM (1972) Definition of aromaticity basing on the harmonic oscillator model. *Tetrahedron Lett* 3839–3842
44. Chen Z, Wannere CS, Corminboeuf C, Puchta R, Schleyer PvR (2005) Nucleus-independent chemical shifts (NICS) as an aromaticity criterion. *Chem Rev* 105:3842–3888
45. Schleyer PvR, Manoharan M, Wang Z-X, Kiran B, Jiao H, Puchta R, Hommes NJRVE (2001) Dissected nucleus-independent chemical shift analysis of π -aromaticity and antiaromaticity. *Org Lett* 3:2465–2468
46. Schleyer PvR, Maerker C, Dransfeld A, Jiao H, Hommes NJRVE (1996) Nucleus-Independent chemical shifts: a simple and efficient aromaticity probe. *J Am Chem Soc* 118:6317–6318
47. Memory JD, Wilson NK (1982) *NMR of aromatic compounds*. Wiley, New York
48. Mitchell RH (2001) Measuring aromaticity by NMR. *Chem Rev* 101:1301–1315
49. Gomes JANF, Mallion RB (2001) Aromaticity and ring currents. *Chem Rev* 101:1349–1383
50. Keith TA, Bader RFW (1993) Topological analysis of magnetically induced molecular current distributions. *J Chem Phys* 99:3669–3682
51. Keith TA, Bader RFW (1996) Use of electron charge and current distributions in the determination of atomic contributions to magnetic properties. *Int J Quantum Chem* 60:373–379
52. Badger GM (1969) *Aromatic character and aromaticity*. Cambridge University Press, Cambridge
53. Slayden SW, Liebman JF (2001) The energetics of aromatic hydrocarbons: an experimental thermochemical perspective. *Chem Rev* 101:1541–1566
54. Cyranski MK (2005) Energetic aspects of cyclic & σ -electron delocalization: Evaluation of the methods of estimating aromatic stabilization energies. *Chem Rev* 105:3773–3811
55. Sivaramakrishnan R, Tranter RS, Brezinsky K (2005) Ring conserved isodesmic reactions: a new method for estimating the heats of formation of aromatics and PAHs. *J Phys Chem A* 109:1621–1628
56. Poater J, Fradera X, Duran M, Solà M (2003) The delocalization index as an electronic aromaticity criterion: application to a series of planar polycyclic aromatic hydrocarbons. *Chem Eur J* 9:400–406
57. Poater J, Fradera X, Duran M, Solà M (2003) An insight into local aromaticities of polycyclic aromatic hydrocarbons and fullerenes. *Chem Eur J* 9:1113–1122
58. Matta CF, Hernández-Trujillo J (2005) Bonding in polycyclic aromatic hydrocarbons in terms of the electron density and of electron delocalization. *J Phys Chem A* 107:7496–7504 (Correction: *J Phys Chem A* (2005) 109:10798)
59. Matito E, Duran M, Solà M (2005) The aromatic fluctuation index (FLU): a new aromaticity index based on electron delocalization. *J Chem Phys* 122:014109
60. Poater J, Duran M, Solà M, Silvi B (2005) Theoretical evaluation of electron delocalization in aromatic molecules by means of atoms in molecules (AIM) and electron localization function (ELF) topological approaches. *Chem Rev* 105:3911–3947
61. Portella G, Poater J, Bofill JM, Alemany P, Solà M (2005) Local aromaticity of [*n*]acenes, [*n*]phenacenes, and [*n*]helicenes (*n* = 1–9). *J Org Chem* 70:2509–2521
62. Matito E, Poater J, Solà M (2007) Aromaticity analyses by means of the quantum theory of atoms in molecules. In: Matta CF (ed) *The quantum theory of atoms in molecules: from solid state to DNA and drug design*. Wiley-VCH, Weinheim, pp 399–423
63. Firme CI, Galembeck SE, Antunes OAC, Esteves PM (2007) Density, degeneracy, delocalization-based index of aromaticity (D3BIA). *J Braz Chem Soc* 18:1397–1404

64. Howard ST, Krygowski TM (1997) Benzenoid hydrocarbon aromaticity in terms of charge density descriptors. *Can J Chem* 75:1174–1181
65. Suresh CH, Gadre SR (1999) Clar's aromatic sextet theory revisited via molecular electrostatic potential topography. *J Org Chem* 64:2505–2512
66. Cyranski MK, Stepien BT, Krygowski TM (2000) Global and local aromaticities of linear and angular polyacenes. *Tetrahedron* 56:9663–9667
67. Palusiak M, Krygowski TM (2007) Application of AIM parameters at ring critical points for estimation of π -electron delocalization in six-membered aromatic and quasi-aromatic rings. *Chem Eur J* 13:7996–8006
68. Mandado M, Gonzalez Moa MJ, Mosquera RA (2008) Aromaticity: exploring basic chemical concepts with the quantum theory of atoms in molecules. Nova Science Publishers, Inc., New York
69. Ebrahimi AA, Ghiasi R, Foroutan-Nejad C (2010) Topological characteristics of the ring critical points and the aromaticity of groups IIIA to VIA hetero-benzenes. *J Mol Struct (THEOCHEM)* 941:47–52
70. Nigam S, Majumder C (2011) Aromaticity: from benzene to atomic clusters. In: Aromaticity and metal clusters. Chattaraj PK (Ed.), CRC Press, New York
71. Krygowski TM, Ciesielski A, Bird CW, Kotschy A (1995) Aromatic character of the benzene ring present in various topological environments in benzenoid hydrocarbons. Nonequivalence of indices of aromaticity. *J Chem Inf Comput Sci* 35:203–210
72. Sumar I, Cook R, Ayers PW, Matta CF (2016) Aromaticity of rings-in-molecules (RIMs) from electron localization-delocalization matrices (LDMs). *Phys Scripta* 91:013001 (pp 13)
73. Cook R, Sumar I, Ayers PW, Matta CF (2015) Aromaticity of rings-in-molecules (RIMs) from electron localization-delocalization matrices (LDMs) from self-organized maps. In preparation
74. Mager PP (1984) Multidimensional pharmacology: design of safer drugs. Academic Press Inc, London
75. Kier LB, Hall LH, Frazer JW (1991) An index of electrotopological state for atoms in molecules. *J Math Chem* 7:229–241
76. Attwood TK, Parry-Smith DJ (1999) Introduction to bioinformatics. Prentice Hall, London
77. Doucet J-P, Weber J (1996) Computer-aided molecular design: theory and applications. Academic Press, ltd, London
78. Carbó R, Leyda L, Arnau M (1980) How similar is a molecule to another? an electron density measure of similarity between two molecular structures. *Int J Quantum Chem* 17:1185–1189
79. Carbó-Dorca R, Mezey PGE (1996) Advances in molecular similarity, vol 1. Jai Press Inc, London
80. Carbó-Dorca R, Mezey PGE (1998) Advances in molecular similarity, vol 2. Jai Press Inc, London
81. Carbó-Dorca R, Robert D, Amat L, Gironés X, Besalú E (2000) Molecular quantum similarity in QSAR and drug design. Springer, Berlin
82. Bonaccorsi R, Scrocco E, Tomasi J (1970) Molecular SCF calculations for the ground state of some three-membered ring molecules: $(\text{CH}_2)_3$, $(\text{CH}_2)_2\text{NH}$, $(\text{CH}_2)_2\text{NH}_2^+$, $(\text{CH}_2)_2\text{O}$, $(\text{CH}_2)_2\text{S}$, $(\text{CH})_2\text{CH}_2$, and N_2CH_2 . *J Chem Phys* 52:5270–5284
83. Petrongolo C, Tomasi J (1975) The use of electrostatic molecular potential in quantum pharmacology. 1. Ab initio results. *Int J Quantum Chem Quantum Biol Symp* 2:181–190
84. Bonaccorsi R, Scrocco E, Tomasi J (1976) Group contributions to electrostatic molecular potential. *J Am Chem Soc* 98:4049–4054
85. Tomasi J (1981) Use of the electrostatic potential as a guide to understanding molecular properties. In: Truhlar DG, Politzer P (eds) Chemical applications of atomic and molecular electrostatic potentials. reactivity, structure, scattering, and energetics of organic, inorganic, and biological systems. Plenum Press, New York
86. Tomasi J, Cappelli C, Mennucci B, Cammi R (2010) From molecular electrostatic potentials to solvations models and ending with biomolecular photophysical processes. In: Matta CF

- (ed) Quantum biochemistry: electronic structure and biological activity, vol 1. Wiley-VCH, Weinheim, pp 131–170
87. Truhlar DG, Politzer P (eds) (1981) Chemical applications of atomic and molecular electrostatic potentials. reactivity, structure, scattering, and energetics of organic, inorganic, and biological systems. Plenum Press, New York
 88. Murray JS, Politzer P (1998) Electrostatic potentials: chemical applications. In: Schleyer PvR (ed) Encyclopedia of computational chemistry. Wiley, Chichester, UK
 89. Politzer P, Murray JS (2007) Molecular electrostatic potentials and chemical reactivity. Reviews in computational chemistry. Wiley, Hoboken, NJ
 90. Gadre SR, Kulkarni SA, Suresh CH, Shrivastava IH (1995) Basis set dependence of molecular electrostatic potential topography: a case study of substituted benzenes. Chem Phys Lett 239:273–281
 91. Suresh CH, Gadre SR (1998) Novel electrostatic approach to substituent constants: doubly substituted benzenes. J Am Chem Soc 120:7049–7055
 92. Gadre SR (1999) Topography of atomic and molecular scalar fields. Computational chemistry: reviews of current trends. World Scientific, Singapore, pp 1–53
 93. Gadre SR, Shirsat RN (2000) Electrostatics of atoms and molecules. Universities Press, Hyderabad
 94. Roy D, Balanarayan P, Gadre SR (2008) An appraisal of Poincaré-Hopf relation and application to topography of molecular electrostatic potentials. J Chem Phys 129:174103
 95. Cook R (2015) (in preparation)
 96. Babić-Samardžija K, Lupu C, Hackerman N, Barron AR, Luttge A (2005) Inhibitive properties and surface morphology of a group of heterocyclic diazoles as inhibitors for acidic iron corrosion. Langmuir 21:12187–12196
 97. Popelier PLA (2010) Developing Quantum Topological Molecular Similarity (QTMS). In: Matta CF (ed) Quantum biochemistry: electronic structure and biological activity. Wiley-VCH, Weinheim, pp 669–691
 98. Harding AP, Wedge DC, Popelier PLA (2009) pK_a prediction from “quantum chemical topology” descriptors. J Chem Inf Mod 49:1914–1924
 99. Popelier PLA, Chaudry UA, Smith PJ (2002) Quantum topological molecular similarity. Part 5. Further development with an application to the toxicity of polychlorinated dibenzo-*p*-dioxins (PCDDs). J Chem Soc Perkin Trans 2:1231–1237
 100. O’Brien SE, Popelier PLA (2002) Quantum topological molecular similarity. Part 4. A QSAR study of cell growth inhibitory properties of substituted (*E*)-1-phenylbut-1-en-3-ones. J Chem Soc Perkin Trans 2:478–483
 101. O’Brien SE, Popelier PLA (2001) Quantum molecular similarity. 3. QTMS descriptors. J Chem Inf Comput Sci 41:764–775
 102. O’Brien SE, Popelier PLA (1999) Quantum molecular similarity. Part 2: the relation between properties in BCP space and bond length. Can J Chem 77:28–36
 103. Popelier PLA (1999) Quantum molecular similarity. 1. BCP space. J Phys Chem A 103:2883–2890
 104. Cook R., Sumar I, Ayers PW, Matta CF (2016) Electron localization-delocalization matrices (LDMs): theory and applications. Springer

Chapter 4

Extending the Topological Analysis and Seeking the Real-Space Subsystems in Non-Coulombic Systems with Homogeneous Potential Energy Functions

Shant Shahbazian

Abstract It is customary to conceive the interactions of all the constituents of a molecular system, i.e. electrons and nuclei, as Coulombic. However, in a more detailed analysis one may always find small but non-negligible non-Coulombic interactions in molecular systems originating from the finite size of nuclei, magnetic interactions, etc. While such small modifications of the Coulombic interactions do not seem to alter the nature of a molecular system in real world seriously, they are a serious obstacle for quantum chemical theories and methodologies which their formalism is strictly confined to the Coulombic interactions. Although the quantum theory of atoms in molecules (QTAIM) has been formulated originally for the Coulombic systems, some recent studies have demonstrated that most of its theoretical ingredients are not sensitive to the explicit form of the potential energy operator. However, the Coulombic interactions have been explicitly assumed in the mathematical procedure that is used to introduce the basin energy of an atom in a molecule. In this study it is demonstrated that the mathematical procedure may be extended to encompass the set of the homogeneous potential energy functions thus relegating adherence to the Coulombic interactions to introduce the energy of a real-space subsystem. On the other hand, this extension opens the door for seeking novel real-space subsystems, apart from atoms in molecules, in non-Coulombic systems. These novel real-space subsystems, quite different from the atoms in molecules, call for an extended formalism that goes beyond the orthodox QTAIM. Accordingly, based on a previous proposal the new formalism, which is not confined to the Coulombic systems nor to the atoms in molecules as the sole real-space subsystems, is termed the quantum theory of proper open subsystems (QTPOS) and its potential applications are detailed.

S. Shahbazian (✉)

Faculty of Chemistry, Shahid Beheshti University, G. C., Evin,
P.O. Box 19395-4716, 19839 Tehran, Iran
e-mail: chemist_shant@yahoo.com

The harmonic trap model, containing non-interacting fermions or bosons, is considered as an example for the QTPOS analysis. The QTPOS analysis of the bosonic systems is particularly quite unprecedented not attempted before.

Keywords Quantum theory of atoms in molecules • Topological analysis • Non-Coulombic systems • Homogeneous potentials • Virial theorem

4.1 Introduction

The quantum theory of atoms in molecules (QTAIM) has gained a widespread recognition in the last 20 years in chemistry, molecular and solid-state physics, and even in molecular biology [1–3]. However, all applications of the QTAIM have been confined to the Coulombic systems namely, systems containing electrons and clamped nuclei interacting via the Coulombic potential. Even the recent extension of the QTAIM, termed the multi-component QTAIM (MC-QTAIM) [4–16], which goes beyond the clamped nucleus model and deals with the AIM analysis of certain types of non-Born-Oppenheimer molecular wavefunctions, is also confined to the Coulombic systems. Although it is understandable that the Coulombic systems are of prime interest in most applications in chemistry and physics, there are many non-Coulombic systems which are also interesting to be considered from the viewpoint of the AIM analysis. However, before discussing examples of such systems, it must be emphasized that even for usual molecular systems the Coulombic interactions are just approximate potentials, albeit accurate enough for most practical applications, which are used usually in quantum chemical calculations. For highly accurate quantum description of an atomic or molecular system, various small but non-negligible non-Coulombic terms must be added to the Coulombic potential that weak internal magnetic interactions of electrons, originating from the L-S and the S-S couplings, and modifications originating from the finite size of nuclei are just examples. Accordingly, confining the QTAIM formalism to the Coulombic interactions is “artificial” and certainly against the basic idea that *atoms in molecules* are “real” objects emerging independent from the details of the models used to describe molecular systems [17].

On the other hand, in recent decades a wealth of experimental and theoretical evidence has been accumulated demonstrating molecular-like structure for systems not traditionally considered as molecular systems. One may include in this list the “nuclear molecules” in nuclear physics [18, 19], various “exotic molecules” composed of fundamental particles other than electron, protons and neutrons [20–31], “artificial molecules” in condensed-matter physics [32–35], and the “molecular Bose-Einstein condensates” [36–39]. In considering such molecular-like systems the question emerges whether any underlying AIM structure is derivable from the wavefunctions of these systems. To answer this question one must apply the AIM analysis to these systems however, all such systems are intrinsically non-Coulombic in their nature and the formalism of the orthodox QTAIM must be modified to be

applicable to these systems. Therefore, there is a real demand to extend the formalism of the orthodox QTAIM to non-Coulombic systems.

The programme of reconsidering the QTAIM formalism in the case of non-Coulombic interactions was started sometime ago and it was demonstrated that the subsystem variational procedure and the subsystem hypervirial theorem are both insensitive to the nature of the potential energy operator as far as there is a bound quantum state in the system [40, 41]. This is also true for the local zero-flux equation of the one-particle density which is the equation of deriving the inter-atomic surfaces for both the Coulombic and non-Coulombic systems [40, 41]. However, upon considering the Hookean molecules, i.e. model systems where some of the Coulombic interactions have been replaced with the harmonic potential, it emerged that the AIM structures derived from the topological analysis were not the one expected based on “chemical intuition”, which is rooted in previous experiences with the Coulombic systems [41]. Thus, the use of topological analysis and the local zero-flux equation do not automatically guarantee that the emerging “real-space” subsystems are the usual AIM, also called topological atoms. In present study more examples of exotic real-space subsystems in non-Coulombic systems are presented.

In contrast to the previous studies [40, 41], the focus of this contribution is on the part of the QTAIM formalism that is sensitive to the nature of the potential energy operator namely, the basin energy of an atom in a molecule [1]. Accordingly, the definition of the basin energy is extended beyond the Coulombic potential energy function demonstrating that for the subset of homogeneous potential energy functions the regional virial theorem may be used to derive well-defined, origin-independent, basin energies.

4.2 The Generalized Subsystem Virial Theorem for the Homogeneous Potential Energy Functions

The atomic/regional theorems, emerging from the subsystem hypervirial theorem [9, 42, 43], are insensitive to details of the potential energy operator and are true as far as a system is composed of a single type of quantum particles and there is a bound stationary state emerging from the interaction of quantum particles with each other and the external fields. This insensitivity is compelling since the orthodox formalism may be employed with least modifications for non-Coulombic systems however the regional/basin energies have been derived employing explicitly the properties of the Coulombic potential (see particularly Sect. 6.3 in [1]). In the present section the very definition of the basin energy is extended to include the set of the homogeneous potential energy functions (for an elementary discussion on the homogeneous potential energy functions see Chap. 14 in [44]).

A homogeneous potential energy function for a typical N -particle system has the following property: $\hat{V}(s\vec{r}_1, \dots, s\vec{r}_N) = s^n \hat{V}(\vec{r}_1, \dots, \vec{r}_N)$, where s is an arbitrary scaling parameter and n is the degree of homogeneity [44]. It is straightforward to demonstrate that for this set of potential energy functions the following relation holds: $\hat{V}(\vec{r}_1, \dots, \vec{r}_N) = (1/n) \sum_{k=1}^N \vec{r}_k \cdot \vec{\nabla}_k \hat{V}(\vec{r}_1, \dots, \vec{r}_N)$ [44], where \vec{r}_k are the vectors describing the position of each of the N particles; the Coulombic potential is a special member of this set where $n = -1$ [1]. It is evident that $\sum_{k=1}^N \vec{r}_k \cdot \vec{\nabla}_k$ is a projection operator and it is called the virial operator. It is also straightforward to demonstrate that the virial theorem holds generally for any stationary state of an N -particle system: $2\langle \hat{T} \rangle = \langle \sum_{k=1}^N \vec{r}_k \cdot \vec{\nabla}_k \rangle$ [44], where \hat{T} is the sum of the kinetic energy operators of all quantum particles, $\hat{T} = \sum_{k=1}^N \hat{t}_k = (-\hbar^2/2m) \sum_{k=1}^N \nabla_k^2$, while $\langle \dots \rangle$ is used to denote the mean value of the operators for a stationary state. For systems where the potential energy operator is a homogeneous function the virial theorem simplifies to: $2\langle \hat{T} \rangle = n\langle \hat{V} \rangle$ [44].

The local form of the virial theorem derived from the subsystem hypervirial theorem is as follows [1]:

$$2T(\vec{q}) = -V^T(\vec{q}) + L(\vec{q}) \quad (4.1)$$

In this equation $T(\vec{q})$ is the kinetic energy density introduced as: $T(\vec{q}) = \int d\tau' \Psi^* (\sum_{k=1}^N \hat{t}_k) \Psi = N \int d\tau' \Psi^* \hat{t}_q \Psi = -(1/2) \text{tr} [\bar{\sigma}(\vec{q})] + (1/2)L(\vec{q})$, where the second equality originates from the indistinguishability of quantum particles. $V^T(\vec{q}) = -\vec{q} \cdot (\vec{\nabla} \bullet \bar{\sigma}(\vec{q})) + \vec{\nabla} \cdot (\vec{q} \bullet \bar{\sigma}(\vec{q}))$ is the total virial density (the symbol \bullet is used to emphasize the dyadic nature of the product) while $L(\vec{q}) = (-\hbar^2/4m) \nabla^2 \rho(\vec{q})$ where $\rho(\vec{q}) = N \int d\tau' \Psi^* \Psi$ is the one-particle density of quantum particles ($d\tau'$ implies summing over spin variables of all quantum particles and integrating over spatial coordinates of all quantum particles except a typical particle denoted by \vec{q}). The stress tensor density is the key density that both kinetic and total virial densities are based on while the Schrödinger-Pauli-Epstein variant is used in this study: $\bar{\sigma}(\vec{q}) = \left(\frac{N\hbar^2}{4m}\right) \int d\tau' \left\{ \Psi^* (\vec{\nabla} \vec{\nabla} \Psi) + \Psi (\vec{\nabla} \vec{\nabla} \Psi^*) - (\vec{\nabla} \Psi^*) (\vec{\nabla} \Psi) - (\vec{\nabla} \Psi) (\vec{\nabla} \Psi^*) \right\}$ [1]. It is timely to emphasize that stress tensor density is not unique and the Schrödinger-Pauli-Epstein variant is just one member of the infinitely large family of the stress tensor densities [45]. For a real-space subsystem, e.g. AIM, enclosed by the zero-flux surfaces, Ω , based on Gauss's theorem one derives: $L(\Omega) = (-\hbar^2/4m) \int_{\Omega} d\vec{q} \nabla^2 \rho(\vec{q}) = (-\hbar^2/4m) \oint_{\partial\Omega} dS \vec{\nabla} \rho(\vec{q}) \cdot \vec{n}(\vec{q}) = 0$ ($\vec{n}(\vec{q})$ is the unit vector orthogonal to the zero-flux surface). Also, $T(\Omega) = \int_{\Omega} d\vec{q} T(\vec{q})$ and $V^T(\Omega) = \int_{\Omega} d\vec{q} V^T(\vec{q})$ are basin kinetic and total virial energies, respectively, and the regional/subsystem virial theorem is as follows [1]:

$$2T(\Omega) = -V^T(\Omega) \quad (4.2)$$

It is important to realize that the total virial density is composed of two contribution, one originating directly from the virial operator and called basin virial density: $V^B(\vec{q}) = \int d\tau' \Psi^* \left(-\sum_{k=1}^N \vec{r}_k \cdot \vec{\nabla}_k \right) \Psi = N \int d\tau' \Psi^* \left(-\vec{q} \cdot \vec{\nabla}_q \right) \Psi = -\vec{q} \cdot \left(\vec{\nabla}_q \bullet \vec{\sigma}(\vec{q}) \right)$ and another term originating from the assumed zero-flux surfaces as boundaries of subsystems and called surface virial density: $V^S(\vec{q}) = \oint_{\partial\Omega} dS \left(\vec{q} \bullet \vec{\sigma}(\vec{q}) \right) \cdot \vec{n}(\vec{q})$. It is straightforward to demonstrate that the surface virial is null for the total system and this fact differentiates the virial theorem of total system with that of the real-space subsystems [1].

At the mechanical equilibrium [1], the Hamiltonian of an N -particle system with a homogeneous potential energy is:

$$\hat{H} = \hat{T} + \hat{V} = \sum_{k=1}^N \left(\hat{i}_k + (1/n) \vec{r}_k \cdot \vec{\nabla}_k \right) = \sum_{k=1}^N \hat{h}_k \quad (4.3)$$

Based on this equation the energy density is:

$$\begin{aligned} E(\vec{q}) &= \int d\tau' \Psi^* \left(\sum_{k=1}^N \hat{h}_k \right) \Psi = N \int d\tau' \Psi^* \hat{h}_q \Psi \\ &= N \int d\tau' \Psi^* \left(-(\hbar^2/2m) \nabla_q^2 + (1/n) \vec{q} \cdot \vec{\nabla}_q \right) \Psi = T(\vec{q}) - (1/n) V^B(\vec{q}) \end{aligned} \quad (4.4)$$

Integration of the energy density in the whole space (R^3) yields the total energy of the system: $E = \langle \hat{T} \rangle + \langle \hat{V} \rangle$, while based on the virial theorem for total system one derives: $E = (1 + 2/n) \langle \hat{T} \rangle = (1 + n/2) \langle \hat{V} \rangle$. However it is well-known if the integration is done on a real-space subsystem ($\Omega \subset R^3$), then the resulting basin energy, because of the origin-dependence of the basin virial density, is also origin dependent which is plainly an unpleased feature [1]. To overcome this problem, inspired by the regional virial theorem, Eq. (4.2), the following modified energy density and basin energy are introduced:

$$\begin{aligned} E(\vec{q}) &= T(\vec{q}) - (1/n) V^T(\vec{q}) = T(\vec{q}) - (1/n) (V^B(\vec{q}) + V^S(\vec{q})) \\ E(\Omega) &= \int_{\Omega} d\vec{q} E(\vec{q}) = T(\Omega) - (1/n) V^T(\Omega) \end{aligned} \quad (4.5)$$

Using Eq. (4.2) as the regional virial theorem the basin energy may be expressed just by the regional kinetic or total virial energies:

$$E(\Omega) = (1 + 2/n)T(\Omega) = -(1/2 + 1/n)V^T(\Omega) \quad (4.6)$$

For the special case of the Coulombic potentials Eq. (4.6) recovers the well-known results derived from the orthodox formalism: $E(\Omega) = -T(\Omega) = (1/2)V^T(\Omega)$ [1].

For N -particle systems with one- and two-particle interactions the potential energy operator is: $\hat{V}(\vec{r}_1, \dots, \vec{r}_N) = \sum_{k=1}^N \hat{v}_k(\vec{r}_k) + \sum_{i>j}^N \hat{v}_{ij}(\vec{r}_i, \vec{r}_j)$. The role of the virial operator is the projection of the two-particle terms into “pseudo” one-particle contributions and this is easily seen for a two-particle system: $\hat{v}_{12} = (1/n) (\vec{r}_1 \cdot \vec{\nabla}_1 \hat{v}_{12} + \vec{r}_2 \cdot \vec{\nabla}_2 \hat{v}_{12})$; these “pseudo” one-particle contributions make it possible to introduce the virial density bypassing the need to introduce potential energy density explicitly [1]. For the subset of N -particle systems without two-particle interactions, i.e. non-interacting systems trapped in external potentials, the relation between one-particle interactions and the virial operator is as follows: $\hat{v}_k = (1/n)\vec{r}_k \cdot \vec{\nabla}_k \hat{v}_k$. Accordingly, one may now introduce the potential energy density directly: $V(\vec{q}) = \int d\tau' \Psi^* (\sum_{k=1}^N \hat{v}_k) \Psi = N \int d\tau' \Psi^* \hat{v}_q \Psi$, which is equal to the basin virial density. The local and regional forms of the virial theorem are then transformed as follows:

$$\begin{aligned} 2T(\vec{q}) &= nV(\vec{q}) - V^s(\vec{q}) + L(\vec{q}) \\ 2T(\Omega) &= nV(\Omega) - V^s(\Omega) \end{aligned} \quad (4.7)$$

The energy density and basin energies for the real-space subsystems is then introduced as follows:

$$\begin{aligned} E(\vec{q}) &= T(\vec{q}) + V(\vec{q}) - (1/n)V^s(\vec{q}) \\ E(\Omega) &= \int_{\Omega} d\vec{q} E(\vec{q}) = T(\Omega) + V(\Omega) - (1/n)V^s(\Omega) \\ &= (1 + 2/n)T(\Omega) = (1 + n/2)V(\Omega) - (1/2 + 1/n)V^s(\Omega) \end{aligned} \quad (4.8)$$

These equations vividly demonstrate that apart from the potential energy density originating from the interaction of each quantum particle with the external field, the surface virial also contributes to the basin energy. Assuming $\Omega = R^3$ the surface virial vanishes and the equations are indistinguishable from those derived for the total system independently.

4.3 The Topological Analysis of Non-Coulombic Systems: The Harmonic Trap Model

The topological analysis of the one-particle density yields the topological structure, through identifying critical points (CPs) and the boundaries between real-space subsystems. Particularly, the local zero-flux equation, $\vec{\nabla}\rho(\vec{q}) \cdot \vec{n}(\vec{q}) = 0$, is used to determine the zero-flux surfaces that act as inter-atomic boundaries [1]. However, these surfaces are just a small subset of the zero-flux surfaces emerging from the equation [40, 46, 47]. It has been demonstrated that the zero-flux surfaces that are not acting as the boundaries of topological atoms may found interesting applications; the “morphologies” of the real-space subsystems which they are shaping are different from the topological atoms [48–55], and even more exotic (from the viewpoint of their morphology) real-space subsystems emerge from the net zero-flux equation, $\int_{\Omega} d\vec{q} \nabla^2 \rho(\vec{q}) = 0$, as demonstrated recently [47, 56]. All these studies point to the fact that even for the Coulombic systems the topological analysis may yield a wide spectrum of real-space subsystems apart from the topological atoms. Accordingly, it is tempting to consider what kind of real-space subsystems may emerge from the topological analysis of non-Coulombic systems. In the rest of this section the harmonic trap model is considered for this purpose.

The model of N quantum particles confined in a harmonic trap has been widely used to model the Bose-Einstein condensation in trapped dilute gases [57–68], and more recently in trapped Fermi gases [69–73]. A simplified model of the trap may be constructed assuming a non-interacting system of quantum particles in an external isotropic harmonic trap, as a homogeneous potential, $n = 2$, with the following Hamiltonian: $\hat{H} = \sum_{k=1}^N \hat{h}_k = (-\hbar^2/2m) \sum_{k=1}^N \{ \nabla_k^2 - \alpha^2 (x_k^2 + y_k^2 + z_k^2) \}$, where $\alpha = 2\pi f m / \hbar$ and f is the frequency of mechanical vibration of the particle in the trap [44]. The spectrum of the eigenfunctions and eigenvalues of the one-particle Hamiltonian, $\hat{h}_K \phi_{v_1 v_2 v_3} = \varepsilon_{v_1 v_2 v_3} \phi_{v_1 v_2 v_3}$, is well-known (v_1, v_2, v_3 are the quantum numbers) [44], e.g. $\phi_{000}(x, y, z) = (\alpha/\pi)^{3/4} \text{Exp}[-(\alpha/2)(x^2 + y^2 + z^2)]$, $\varepsilon_{000} = 3\pi\hbar f$ and $\phi_{100}(x, y, z) = (4\alpha^5/\pi^3)^{1/4} x \text{Exp}[-(\alpha/2)(x^2 + y^2 + z^2)]$, $\varepsilon_{100} = 5\pi\hbar f$. The wavefunction of the system may be constructed based on the statistics of the trapped particles. In the ground state of the system filled with non-interacting bosons all particles are at the lowest one-particle energy state, $E_0^{Boson} = N\varepsilon_{000} = 3N\pi\hbar f$, and neglecting the spin variable, the spatial part of the wavefunction is a simple product of the one-particle eigenfunctions associated to the lowest one-particle energy state: $\Psi_{Boson} = \prod_{k=1}^N \phi_{000}(x_k, y_k, z_k) = (\alpha/\pi)^{3N/4} \text{Exp}[-(\alpha/2) \sum_{k=1}^N (x_k^2 + y_k^2 + z_k^2)]$. On the other hand, if the trap is filled with fermions then the spin variable is of pivotal importance and the spin-eigenfunctions, instead of the spatial eigenfunctions, must be used to construct the fermionic wavefunction, $\begin{cases} \psi_{v_1 v_2 v_3} = \phi_{v_1 v_2 v_3} \alpha \\ \bar{\psi}_{v_1 v_2 v_3} = \phi_{v_1 v_2 v_3} \beta \end{cases}$ (α and β are the spin eigenfunctions). The Pauli Exclusion Principle dictates a $N \times N$ determinant, composed of the spin-eigenfunctions, as the ground state wavefunction of the system:

$\Psi_{Fermion} = (N!)^{-1/2} \sum_{i=1}^{N!} (-1)^{p_i} \hat{P}_i [\psi_{000}(x_1, y_1, z_1) \bar{\psi}_{000}(x_2, y_2, z_2) \psi_{100}(x_3, y_3, z_3) \dots]$, where \hat{P}_i is the permutation operator generating all possible permutations of particles within the spin-eigenfunctions while p_i is the number of transpositions/exchanges (the wavefunction is a linear combination of such determinants if the determinants are describing degenerate ground states) [44]. The ground state energy of the fermionic system is: $E_0^{Fermion} = 3N\pi\hbar f + 2\pi\hbar f \sum_{v_1} \sum_{v_2} \sum_{v_3} n_{v_1 v_2 v_3} (v_1 + v_2 + v_3)$, where $n_{v_1 v_2 v_3}$ is the occupation number of the one-particle energy states denoted by the quantum numbers v_1, v_2, v_3 and is always equal to two, one or zero.

The formalism of the QTAIM is insensitive to the statistics of quantum particles however, according to the best of author's knowledge, no previous QTAIM analysis of a bosonic system has been done. This is understandable since only many-electron systems have been considered within the context of the QTAIM [1]. The one-particle density and its gradient vector field for the bosonic system are as follows:

$$\begin{aligned} \rho_{Boson}(x, y, z) &= N(\alpha/\pi)^{3/2} \text{Exp}[-\alpha(x^2 + y^2 + z^2)] \\ \vec{\nabla} \rho_{Boson} &= -N \sqrt{4\alpha^5/\pi^3} \text{Exp}[-\alpha r^2] \vec{r} \end{aligned} \quad (4.9)$$

Since the one-particle density is isotopic, the gradient vector field is written in the spherical polar coordinate system (r, θ, φ) : $r = \sqrt{x^2 + y^2 + z^2}$ and $\vec{r} = r\vec{r}_0$, where $\vec{r}_0 = \vec{i} \sin \theta \cos \varphi + \vec{j} \sin \theta \sin \varphi + \vec{k} \cos \theta$ is the unit vector [44]. It is evident from these equations that the topological structure of the gradient vector field is independent from the number of particles and from the equation: $\vec{\nabla} \rho_{Boson} = 0$, just a single (3, -3) CP emerges at the origin of the coordinate system. The one-particle density monotonically decays from its maximum value at the origin $\rho_{Boson}(0, 0, 0) = N(\alpha/\pi)^{3/2}$ and this pattern is reminiscent of the one-electron density of atoms [1]. This similarity is suggestive that the ground state of the bosonic aggregate, trapped in the external harmonic potential, independent from the number of trapped bosons, is similar to a single atom (a "giant atom" if $N \rightarrow \infty$). Interestingly, this is also in line with the description of the Bose-Einstein condensate at its ground state as a "super-atom" [57]. Evidently, just a single topological atom emerges from the topological analysis and the zero-flux surfaces emerging from the local zero-flux equation are all crossing the CP. In the case of the fermionic system the explicit form of the ground state one-particle density depends on the number of particles and only two cases, $N = 2, 8$, are considered here. For a two-particle system the one-particle density and its gradient vector field for the system are as follows:

$$\rho_{Fermion}^{N=2}(r) = \sqrt{4\alpha^3/\pi^3} \text{Exp}[-\alpha r^2]$$

$$\vec{\nabla} \rho_{Fermion}^{N=2} = -\sqrt{16\alpha^5/\pi^3} \text{Exp}[-\alpha r^2] \vec{r} \quad (4.10)$$

These equations clearly demonstrate that the two-particle fermionic system is quite similar to the bosonic system and the structure of a single atom emerges from the topological analysis. For the eight-particle system, $N = 8$, the Pauli Exclusion Principle dictates the occupation of the three degenerate one-particle lowest energy excited states $\phi_{100}, \phi_{010}, \phi_{001}$ (a “closed-shell” configuration), apart from the ground one-particle ϕ_{000} state which is also occupied for $N = 2$ system. The one-particle density and its gradient vector field for this system are as follows:

$$\begin{aligned} \rho_{Fermion}^{N=8}(r) &= \sqrt{4\alpha^3/\pi^3} (1 + 2\alpha r^2) \text{Exp}[-\alpha r^2] \\ \vec{\nabla} \rho_{Fermion}^{N=8}(r) &= \sqrt{16\alpha^5/\pi^3} (1 - 2\alpha r^2) \text{Exp}[-\alpha r^2] \vec{r} \end{aligned} \quad (4.11)$$

In contrast to the Eqs. (4.9) and (4.10), the one-particle density is not monotonically decaying in this system and from the equation: $\vec{\nabla} \rho_{Fermion}^{N=8} = 0$, two kinds of CPs emerge. A CP is located at the center of the coordinate system and infinite numbers of CPs are all located on a spherical surface around the center of the coordinate system with the radius: $r_{CP} = 1/\sqrt{2\alpha}$. The amount of one-particle density at the central CP is: $\rho_{Fermion}^{N=8}(0) = \sqrt{4\alpha^3/\pi^3}$, while on the spherical surface one finds: $\rho_{Fermion}^{N=8}(1/\sqrt{2\alpha}) = 2\text{Exp}[-1/2] \sqrt{4\alpha^3/\pi^3}$. Evidently, the amount of one-particle density is larger at the spherical shell and the central CP is a global minimum or a (3, +3) CP whereas the CPs on the spherical surface are “non-isolated” (1, -1) CPs that have been rarely observed in molecular systems [74]. Instead of the well-known “point” attractors with rank 3, e.g. (3, -3) or (3, -1), in this system one is faced with a “global” attractor with rank 1, i.e. (1, -1), which is a spherical surface with infinite numbers of degenerate point attractors; a similar global attractor in the one-electron density of the 2S excited state of hydrogen atom also appears [75]. Based on the emerging topological structure, this system also seems to be composed of a single real-space subsystem though it is not a topological atom. Finally one infers from the comparison of the eight-particle bosonic and fermionic systems that statistics of particles has a pivotal role on the topological structure of the one-particle density which does not seem to be noticed previously.

4.4 Conclusion and Prospects

The programme of extending the QTAIM formalism to non-Coulombic systems widens the applications of the theory and in this regard it is similar to the ongoing programme of extending the QTAIM to the multi-component systems. Sometime ago it was proposed that the real-space subsystems emerging from the topological analysis do not need to be similar to the topological atoms and a generalized

framework called Quantum Theory of Proper Open Subsystems (QTPOS) was developed to deal with all types, rather than just the topological atoms, of the real-space subsystems [47]. While in that paper only the Coulombic systems were conceived as targets, the present contribution demonstrates that the QTPOS may be conceived as a general theory that deals with both the Coulombic and non-Coulombic systems composed of a single type of quantum particles interacting with each other and external fields through the homogeneous potentials. Apart from the previously considered examples [41], and those considered in this chapter, a large number of interesting systems, some indicated in the first section, remain to be considered within context of the QTPOS. However, a completely comprehensive theory must encompass also quantum systems containing particles that their interaction potentials are inhomogeneous functions. This is also important in the case of extending the QTAIM analysis further since upon adding new, albeit small, terms to the Coulombic potentials the resulting potential energy operator is inevitably inhomogeneous.

The comparative analysis of the real-space subsystems emerging in fermionic and bosonic systems is another novel aspect of the present study. This is an interesting area for future studies since it may reveal the “local” role of the Pauli Exclusion Principle in molecular systems. Pauli “repulsions” and associated steric interactions are usually invoked in both qualitative and quantitative analysis to rationalize conformational selections, tracing molecular stresses and instabilities. However, most of such analyzes are based on indirect methods and one may hope that a direct comparative QTAIM analysis on a fermionic system and associated bosonic counterpart may reveal a more detailed picture of the role of the statistics on the local interactions in molecular systems.

Acknowledgments The author is grateful to Masume Gharabaghi and Ángel Martín-Pendás for their detailed reading of a previous draft of this paper and helpful suggestions.

References

1. Bader RFW (1990) *Atoms in molecules: a quantum theory*. Oxford University Press, Oxford
2. Popelier PLA (2000) *Atoms in molecules an introduction*. Pearson, London
3. Matta C, Boyd RJ (2007) *Quantum theory of atoms in molecules: from solid state to DNA and drug design*. Wiley, Weinheim
4. Nasertayoob P, Goli M, Shahbazian S (2011) *Int J Quantum Chem* 111:1970–1981
5. Goli M, Shahbazian S (2011) *Int J Quantum Chem* 111:1982–1998
6. Heidar Zadeh F, Shahbazian S (2011) *Int J Quantum Chem* 111:1999–2013
7. Goli M, Shahbazian S (2011) *Theoret Chem Acc* 129:235–245
8. Goli M, Shahbazian S (2012) *Theoret Chem Acc* 131, 1208:1–19
9. Goli M, Shahbazian S (2013) *Theoret Chem Acc* 132, 1362:1–14
10. Goli M, Shahbazian S (2013) *Theoret Chem Acc* 132, 1365:1–17
11. Goli M, Shahbazian S (2013) *Theoret Chem Acc* 132, 1410:1–22
12. Shahbazian S (2013) *Found Chem* 15:287–302
13. Goli M, Shahbazian S (2014) *Phys Chem Chem Phys* 16:6602–6613
14. Goli M, Shahbazian S (2015) *Comput Theoret Chem* 1053:96–105
15. Goli M, Shahbazian S (2015) *Phys Chem Chem Phys* 17:245–255

16. Goli M, Shahbazian S (2015) *Phys Chem Chem Phys* 17:7023–7037
17. Shahbazian S (2014) *Found Chem* 16:77–84
18. von Oertzen W, Freer M, Kanada-En'yo Y (2006) *Phys Rep* 432:43–113
19. Freer M (2007) *Rep Prog Phys* 70:2149–2210
20. Ruijgrok TW, Tjon JA, Wu TT (1983) *Phys Lett B* 129:209–212
21. Singer R, Trautmann D (1989) *Nucl Phys A* 491:525–540
22. Yamazaki T, Akaishi Y (2007) *Phys Rev C* 76, 045201:1–16
23. Yamazaki T (2007) *Prog Theoret Phys Suppl* 170:138–160
24. Gutsche T, Branz T, Faessler A, Lee IW, Lyubovitskij VE (2010) *Chin Phys C* 34:1185–1190
25. Törnqvist NA (1994) *Z Phys C* 61:525–537
26. Wong C-Y (2004) *Phys Rev C* 69, 055202:1–13
27. Suzuki M (2005) *Phys Rev D* 72, 114013:1–13
28. Liu Y-R, Liu X, Deng W-Z, Zhu S-L (2008) *Eur Phys J C* 56:63–73
29. Liu X, Liu Y-R, Deng W-Z, Zhu S-L (2008) *Phys Rev D* 77, 034003:1–9
30. Lee N, Luo Z-G, Chen X-L, Zhu S-L (2011) *Phys Rev D* 84, 114013:1–15
31. Hall JMM, Kamleh W, Leinweber DB, Menadue BJ, Owen BJ, Thomas AW, Young RD (2015) *Phys Rev Lett* 114, 132002:1–5
32. Kastner MA (1993) *Phys Today* 46:24–31
33. Ashoori RC (1996) *Nature* 379:413–419
34. van Loo AF, Federov A, Lalumière K, Sanders BC, Blais A, Wallraff A (2013) *Science* 342:1494–1496
35. Gustafsson MV, Aref T, Kockum AF, Ekström MK, Johansson G, Delsing P (2014) *Science* 346:207–211
36. Pethick CJ, Smith H (2004) *Bose-Einstein condensation in dilute gases*. Cambridge University Press, Cambridge
37. Leggett AJ (2006) *Quantum liquids: Bose condensation and cooper pairing in condensed-matter systems*. Oxford University Press, Oxford
38. Weber T, Herig J, Mark M, Nägerl H-C, Grimm R (2003) *Science* 299:232–235
39. Jochim S, Bartenstein M, Altmeyer A, Hendl G, Ridel S, Chin C, Denschlag JH, Grimm R (2003) *Science* 302:2101–2103
40. Nasertayoob P, Shahbazian S (2010) *Int J Quantum Chem* 110:1188–1196
41. Joypazadeh H, Shahbazian S (2014) *Found Chem* 16:63–75
42. Bader RFW, Popelier PLA (1993) *Int J Quantum Chem* 45:189–207
43. Bader RFW (2007) *J Phys Chem A* 111:7966–7972
44. Levine IN (2006) *Quantum chemistry*, 5th edn. Prentice-Hall, New Delhi
45. Anderson JSM, Ayers PW, Hernandez JIR (2010) *J Phys Chem A* 114:8884–8895
46. Eberhart M (2001) *Philos Mag B* 81:721–729
47. Heidar Zadeh F, Shahbazian S (2011) *Int J Quantum Chem* 111:2788–2801
48. Jones TE, Eberhart ME, Clougherty DP, Woodward C (2008) *Phys Rev Lett* 101, 085505:1–4
49. Jones TE, Eberhart ME, Clougherty DP (2008) *Phys Rev Lett* 101, 017208:1–4
50. Jones TE (2009) *J Chem Phys* 130, 204108:1–5
51. Jones TE, Eberhart ME (2010) *Int J Quantum Chem* 110:1500–1505
52. Jones TE, Eberhart ME, Clougherty DP (2010) *Phys Rev Lett* 105, 265702:1–4
53. Jones TE, Eberhart ME, Imlay S, Mackey C (2011) *J Phys Chem A* 115:12582–12585
54. Jones TE, Eberhart ME, Imlay S, Mackey C, Olson GB (2012) *Phys Rev Lett* 109, 125506:1–5
55. Eberhart ME, Jones TE (2012) *Phys Rev B* 86, 134106:1–7
56. Heidar Zadeh F, Shahbazian S (2011) *Theoret Chem. Acc* 128:175–181
57. Cornell EA, Wieman CE (1998) *Sci Am* 3:40–45
58. Grossmann S, Holthaus M (1995) *Phys Lett A* 208:188–192
59. Ruprecht PA, Holland MJ, Burnett K, Edwards M (1995) *Phys Rev A* 51:4704–4711
60. Edwards M, Burnett K (1995) *Phys Rev A* 51:4704–4711
61. Holland M, Cooper J (1996) *Phys Rev A* 53:R1954–R1957
62. Ketterle W, van Druten NJ (1996) *Phys Rev A* 54:656–660
63. Kirsten K, Toms DJ (1996) *Phys Rev A* 54:4188–4202

64. Haugerud H, Haugset T, Ravndal F (1997) *Phys Lett A* 225:18–22
65. Haugset T, Haugerud H, Andersen JO (1997) *Phys Rev A* 55:2922–2929
66. Pathria PK (1998) *Phys Rev A* 58:1490–1495
67. Ligare M (1998) *Am J Phys* 66, 185–190; 2002 70:76–78
68. Ye J-P, Hu G-X, An S-Q, Dai X-X, Dai J, Evenson WE (2003) *Phys A* 323:357–369
69. DeMarco B, Jin DS (1999) *Science* 285:1703–1706
70. Thomas JE, Gehm ME (2004) *Am Sci* 92:238–245
71. Thomas JE (2006) *Nature Phys* 2:377–378
72. Werner F, Castin Y (2006) *Phys Rev A* 74, 053604:1–10
73. Yin J (2006) *Phys Rep* 430:1–116
74. Bader RFW, Nguyen-Dang TT, Tal Y (1981) *Rep Prog Phys* 44:893–948
75. Bader RFW (2001) *Theoret Chem Acc* 105:276–283

Chapter 5

Exploring Chemistry Through the Source Function for the Electron and the Electron Spin Densities

Carlo Gatti, Ahmed M. Orlando, Emanuele Monza
and Leonardo Lo Presti

Abstract The Source Function, a chemical descriptor introduced by Bader and Gatti in 1998, represents a challenging tool to see the electron density from an unusual perspective. Namely, as caused, at any point in the space, by *source* contributions operating at all other points of space. Summing up the local sources over the atomic basins of a system, enable us to regard the electron density at any system's location as determined by smaller or larger contributions from all the atoms or group of atoms of the system. Such decomposition of sources provides valuable chemical insight and it may be applied, on the same grounds, to theoretically or experimentally derived electron densities. Two recent Source Function developments, specifically its application to detect subtle electron delocalization effects and its extension to the electron spin density sources are reviewed through this chapter. An original application, as viewed through the eyes of the Source Function, then follows each illustrated development. Precisely: (a) the electron delocalization mechanisms in complex and non planar aromatic systems, like the homotropylium cation and the 1,6-methano[10]annulene, and (b) the spin density transferability properties in a series of n-alkyl radicals.

Keywords Source function · Electron density · Electron spin density · Chemical bonding · Electron conjugation · Aromaticity · Non-planar aromatic frameworks · Chemical transferability · Spin density transferability

C. Gatti (✉) · L. Lo Presti
CNR-ISTM, Via Golgi 19, 20133 Milan, Italy
e-mail: c.gatti@cnr.istm.it

L. Lo Presti
e-mail: leonardo.lopresti@unimi.it

C. Gatti · A.M. Orlando · L. Lo Presti
Center for Material Crystallography, Aarhus University, Langelandsgade 140,
8000 Aarhus, Denmark

A.M. Orlando · E. Monza · L. Lo Presti
Chemistry Department, Università degli Studi di Milano, Via Golgi 19,
20133 Milan, Italy

Abbreviations

bcp	Bond critical point
BP	Bond path
CP	Critical point
DI	Delocalization index
ED	Electron density
FHDD	Fermi Hole Delocalization Density index
HOMA	Harmonic Oscillator Model of Aromaticity
LS	Local Source Function
MO	Molecular Orbital
NBCC	Non Bonded Charge Concentration
NICS	Nucleus-Independent Chemical Shift
QTAIM	Quantum Theory of Atoms in Molecules
PAH	Polycyclic Aromatic Hydrocarbons
PDI	Para-Delocalization Index
<i>rp</i>	Reference point
SDD	Electron Spin Density Distribution
SF	Source Function (for the electron density)
SF _S	Source Function (for the electron spin density)
SF%	Percentage Source Function (for the electron density)
SF _S %	Percentage Source Function (for the electron spin density)
SFLAI	Source Function Local Aromaticity Index
3MR	Three-Membered Ring
6MR	Six-Membered Ring
7MR	Seven-Membered Ring
10MR	Ten-Membered Ring

5.1 Introduction

This chapter highlights recent developments and new applications of the Source Function (SF) descriptor, introduced long time ago by Bader and Gatti [1] and later on largely used in several studies (for comprehensive and critical overviews, updated to 2012, see Refs. [2, 3]). The SF enables one to see the properties of a scalar at a given point of the space in terms of *source* contributions from all other points of the space, within an interesting cause-effect relationship. It represents, therefore, a tool profoundly germane to one of the main operative notions of chemistry, that is that any local property and chemical behaviour of a system is to some extent, be it small or large, influenced by the remaining parts of the system. It is also neatly connected to the *Topological methods in molecular chemistry*, one of the main focus of the present book, as the SF relates a local property of a scalar of interest to chemistry, say the electron density, to its local source behaviour in another, far or close, region of space. Analysing such a link between the properties

of two τόποι can be clearly considered as a topological method. Following a general presentation of the SF tool (Sect. 5.2), the present chapter reviews two recent SF developments, specifically its use to detect subtle electron conjugation effects (Sect. 5.3) and its extension to the electron spin density (Sect. 5.4). It is shown that the sources and thus the kind of link existing between two τόποι may largely depend on the function being analysed (electron or electron spin density). The two reviewed developments are then each followed by the presentation of an original application. Namely, the SF analysis of the electron conjugation in non planar systems (Sects. 5.3.1–5.3.3), where σ/π separation is disabled, and the study, through the eye of the SF, of the electron spin density transferability in n-alkyl radicals (Sect. 5.4.1). Section 5.5 concludes.

5.2 The Source Function Descriptor

In the late 1990s, Bader and Gatti [1] showed that the electron density (ED) at any point \mathbf{r} in a closed quantum system with boundary at infinity, may be thought as determined by a *local source* (LS), $LS(\mathbf{r}, \mathbf{r}')$, operating at all other points in space:

$$\rho(\mathbf{r}) = \int LS(\mathbf{r}, \mathbf{r}') d\mathbf{r}' \quad (5.1)$$

The function LS at \mathbf{r} is defined in terms of the Laplacian of the electron density at \mathbf{r}' according to:

$$LS(\mathbf{r}, \mathbf{r}') = -(4\pi \cdot |\mathbf{r} - \mathbf{r}'|)^{-1} \cdot \nabla^2 \rho(\mathbf{r}') \quad (5.2)$$

The factor $(4\pi \cdot |\mathbf{r} - \mathbf{r}'|)^{-1}$ is a Green's function, or an *influence function* [4], which represents the effectiveness of the *cause*, $\nabla^2 \rho(\mathbf{r}')$, in producing the *effect*, $\rho(\mathbf{r})$. By integrating LS over the topological atoms Ω defined by the Quantum Theory of Atoms in Molecules (QTAIM) [5], i.e. over the disjoint and exhaustive regions of space bounded by zero-flux surfaces in the $\nabla \rho(\mathbf{r})$ vector field, $\rho(\mathbf{r})$ is then partitioned into a sum of basin contributions:

$$\rho(\mathbf{r}) = S(\mathbf{r}, \Omega) + \sum_{\Omega' \neq \Omega} S(\mathbf{r}, \Omega') \quad (5.3)$$

In Eq. 5.3, each $S(\mathbf{r}, \Omega)$ addendum is called the *source function* (SF) of atom Ω to $\rho(\mathbf{r})$ at the reference point \mathbf{r} (hereinafter, *rp*) and the summation is conveniently decomposed into a source from the atomic basin Ω hosting the *rp* and a sum of sources from the remaining basins Ω' . Although any mutually exclusive or fuzzy partitioning scheme could be used to subdivide the LS integration over R^3 into convenient contributions, adoption of the QTAIM criterion enables one to provide a rigorous association, rooted in quantum mechanics, of individual Source contributions $S(\mathbf{r}, \Omega)$

to atoms or group of atoms (“functional groups”). In other words, the SF tool brings *quantitative* chemical insight [2, 6], as it allows to quantify the extent to which the various functional groups or atoms in a system contribute to determine the amount of electron density at a given rp . This property holds whether such chemical moieties are or are not linked through a bond path (BP) to the nucleus of the basin hosting the rp . The SF is so able to highlight, in the real space, *nonlocal* quantum effects, provided they have some influence on the ground-state ED and are properly modelled within the adopted computational model.

One relevant feature of the SF descriptor is that its evaluation requires only the knowledge of the ED distribution and it is so also experimentally accessible from single-crystal or powder X-ray diffraction intensity data through the so-called multipole models [7–9]. As a matter of fact, the SF tool provides a true bridge between theory and experiment, allowing one to compare either results on the same grounds [2, 3, 10]. Since the seminal work by Bader and Gatti, the SF descriptor has been extensively and successfully applied to study non-local bonding effects in molecules and crystals [2, 3, 6, 11–17].

When one is dealing with the investigation of the chemical bonding, it is reasonable that bond critical points (bcp’s) be taken as the least biased choices for rp ’s [2, 6]. The relative ability of an atom Ω to determine the ED at the rp is called the Source Function percentage contribution of Ω to rp , $SF\%(rp, \Omega)$:

$$SF\%(rp, \Omega) = \frac{S(rp, \Omega)}{\rho(rp)} \cdot 100 \quad (5.4)$$

The more covalently bonded are two atoms, the higher will be their ability to contribute to the ED value at their intervening bcp and, thus, their related $SF\%$ contribution [2, 6]. For less localized interactions, the SF contributions also become much more delocalised throughout the molecule and individual $SF\%$ values become generally smaller [2, 3, 6, 14]. Such an analysis has been applied to several classes of chemical bonds [2, 3], including hydrogen-bonds, multi-center bonds, metal-metal and metal-ligand bonds in organometallic systems, and it has also been exploited for assessing even more subtle chemical features, like electron delocalization effects [15], the role of substituents [16], and the effect of the environment [18].

5.3 A SF-based Description of Electron Delocalization and Aromaticity

There not exist perhaps in chemistry other concepts besides those of “electron delocalization” and “aromaticity” that, although being cornerstones of chemical understanding and classification, seem at the same time to elude any attempt of being rigorously defined and, thus, uniquely quantified (for a comprehensive and updated bibliography see Ref. [19]). Such intrinsic limit is but a consequence of their not direct association to quantum-mechanical observables.

More than 30 years ago, Bader et al. [20] and Cremer et al. [21] published two seminal papers about the use of electron distributions and bcp properties for describing conjugation, hyperconjugation and homoaromaticity features. Those papers opened the way to the study of the various facets related to electron delocalization through *electron-based* descriptors. One main conclusion was that the electronic effects predicted by orbital models could be mirrored into observable properties of the electron density distribution, along with the important additional pro that being based on an observable, the analysis may be equally applied to non planar systems, where the σ - π separation of the molecular orbital models does no longer apply. In those two studies, descriptors like the electron-density-based bond orders, the bond ellipticity and the degree of the alignment of axes uniquely defining the plane of the π -electron distribution for each CC bond had for the first time been introduced to quantify the extent of electron delocalization (and aromaticity). Successful applications of the method had then concerned several interesting cases, like the assessment of potential homoaromatic conjugation in a series of non planar cations, including the debated case of the homotropylium cation [21, 22] or the characterization of competing electron conjugation pathways in some 11,11-disubstituted 1,6-methano[10]annulenes [23, 24].

Though it had been unequivocally shown that the electron density bears recognizable signatures (of the effects) of electron delocalization, it later on became progressively evident that its very mechanism is immediately related only to the quantum-mechanical correlation among electron pairs. Such correlation had long time before already been discussed, among others, by Mc Weeney [25] and Bader and Stephens [26]. The so called exchange-correlation density, $\rho_{2,xc}(\mathbf{r}_1, \mathbf{r}_2)$, is an useful tool to study such correlation. It measures the deviation between the true pair density of a system and that given by the purely classical description of a product of two independent electron densities, not subject to any Coulomb and Fermi correlation of electron motions. Use of the exchange-correlation density has led through years to the definition of several electron delocalization descriptors, like the so called delocalization indices (DI's) [27], that provide an estimate of the number of electrons pairs delocalized (shared) between two atoms Ω and Ω' , no matter whether they are or they are not directly linked by a bond path. DI's have been largely employed to highlight delocalization effects and to quantify aromaticity, for example through the so-called para-delocalization index PDI [28] or the Fermi Hole Delocalization Density index, FHDD [29], which both represent global measures of electron delocalization non homogeneity. The performance of such global aromaticity indicators has also been extensively compared with that of several other aromaticity measures, less fundamental in nature and based instead on given, indirect consequences of electron delocalization. The HOMA (Harmonic Oscillator Model of Aromaticity) [30, 31] and NICS (Nucleus-Independent Chemical Shift) [32, 33] indices, represent just two popular examples. HOMA exploits the increase of the CC bond length equalization with increasing electron delocalization homogeneity, while NICS the supposedly different magnetic shielding of a magnetic test dipole at the center of a conjugated ring in the presence of a diatropic (aromatic system) or paratropic (antiaromatic system) ring current. Both indices have been

largely used, but also seriously criticised (for a comprehensive and critical review on aromatic indices, the reader is referred to Ref. [34]). Such a plethora of descriptors often disagree even in ranking classical aromatic compounds on an absolute (overall and local) aromaticity scale, sometimes raising even more confusion. According to Bultinck [34] this divergence is not a consequence of a real multidimensional character of aromaticity [35], but it is rather due to “confusion and vagueness of the term (local) aromaticity”.

Recently we showed that the SF descriptor is able to reveal, order and quantify π -electron delocalization effects, despite being defined in terms of the ED and its Laplacian, that is of quantities depending only from the diagonal elements of the first order density matrix. Our analysis [15] was applied to simple benchmark organic systems, such as benzene, biphenyl and polycyclic aromatic hydrocarbons (PAH). The onset of electron delocalization was found to be mirrored into an enhanced capability of determining the density distribution along a given bond by the distant, though through-bonds connected, atomic regions. The SF allows to translate such alteration of sources into an easy-to-catch pictorial representation, consisting of enhanced and reduced atomic SF contributions to the bcp density from, respectively, distant and nearby atoms, and relative to cases where electron delocalization does not realize. Such effects can then be magnified by choosing suitable rp 's lying above (or below) the plane of the carbon-membered rings, so as to sample regions where the π -type molecular orbitals can enter *directly*, and not just indirectly, into the play [2, 15, 20]. Magnification of effects due to electron correlation does not imply, as a prerequisite, a perfect σ/π Molecular Orbital separation. Indeed, the SF analysis is currently performed on the full ED and an analogous outcome would be obtained in terms of an ED sharing the same local density values, but given numerically on a grid, rather than analytically, from separate MO contributions.

Eventually, we proposed an our own index based on the SF descriptor (SFLAI, Source Function Local Aromaticity Index) for quantifying the degree of aromaticity of 6-membered rings (6MRs) in polycyclic systems. Analogously to the SF analysis of electron delocalization, such an index might prove to be particularly useful for application to experimentally-derived ED's, as, at variance with other commonly employed quantum-mechanical (local) aromaticity descriptors, it does not require the knowledge of the pair density.

According with the functional form of the Fermi Hole Delocalization Density (FHDD) index [29], SFLAI is defined as [15]:

$$\text{SFLAI} = 1 - \frac{c}{6} \sqrt{\sum_{A=1}^6 \left(k - \sum_{b=1}^6 \text{SF}_{Ab}^{\%} \right)^2} \quad (5.5)$$

In Eq. (5.5), the summation runs over all $\text{SF}^{\%}$ contributions of the carbon atom A to each b -th C–C bcp in the benzenoid ring, k is the analogue quantity in benzene and c is a normalization constant, such that SFLAI is exactly 0 in cyclohexane. We found that this descriptor correlates well with several other structural and quantum

aromaticity indices and particularly well with those defined through the pair density, like FHDD. Moreover, SFLAI is able to correctly detect the progressive increase of π delocalization on passing from cyclohexane, through cyclohexene and 1,3-cyclohexadiene, to benzene. Eventually, it properly orders the local aromaticity of different rings in simple PAH and in their partially hydrogenated derivatives [15]. In summary, the SF descriptor has proved to be a quite interesting tool to discuss electron delocalization effects, despite its lack of a direct physical link to the very mechanism of electron delocalization, as it is instead the case of the indices based on the exchange correlation density like the delocalization indices. A systematic application of SF analysis on X-ray derived electron densities of benzene and substituted naphthalene crystals has been already discussed some time ago [36, 37] and related publications have appeared [38] or are currently in preparation [39].

In the following paragraph, we extend, instead, our electron delocalization SF study of ab initio EDs to some non-planar and less conventional conjugated systems.

5.3.1 *Non-planar Aromatic Systems*

A long-standing tenet of organic chemistry states that aromaticity requires a planar ring of atoms to be exploited [40]. Accordingly, distortions from planarity imply a (usually slight) loss of aromatic character [41], even though delocalized π systems tend in principle to be preserved due to their high stability. The propensity of aromatic compounds to remain planar arises from the requirement of maximizing the π -symmetry overlap among formally single-occupied p orbitals on adjacent nuclei. Au contraire, significant deviations from planarity are usually associated to antiaromatic systems [42, 43] where the energy cost of achieving an unfavourable electron configuration in molecular π orbitals can be alleviated by a spontaneous distortion of the ring that breaks—or reduces—the π overlap. Cyclooctatetraene is a prototypical example of a compound exhibiting such a distortion [44].

Yet, several classes of non-planar aromatic compounds are also known. In most cases, such compounds contain fused benzene-like ring moieties that are bent out-of-plane by steric constraints. Molecular belts [45], pyrenophane derivatives [46, 47] and contracted porphyrinoids [48] are representative examples of these systems. In general, the study of non-planar aromatic compounds opens new opportunities for developing molecular devices with potential application in materials science. For example, porphyrinoids have recently attracted significant interest, as their curved aromatic structures show concave or convex π surfaces able to interact in various ways with electroactive compounds [48].

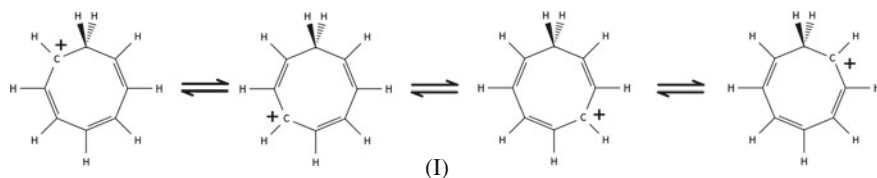
In late 1950s, a novel class of cyclic compounds was discovered, that exhibited aromatic character from a chemical, thermodynamic and spectroscopic viewpoint despite the presence of sp^3 -hybridized atoms within the ring [49]. In his pioneering work, Winstein [49] named such compounds as ‘homoaromatics’ due to their

similarity with homo-conjugated alkenes. According to the IUPAC Compendium of Chemical Terminology [50], "...whereas in an aromatic molecule there is continuous overlap of p-orbitals over a cyclic array of atoms, in an homoaromatic molecule there is a formal discontinuity in this overlap resulting from the presence of a single sp^3 hybridized atom at one or several positions within the ring; p-orbital overlap apparently bridges these sp^3 centres, and features associated with aromaticity are manifest in the properties of the compound".

Great efforts were devoted in the last decades to gain insights into the homoaromatic character, and several new homoaromatic compounds were discovered since then. Some authors have recently claimed to have found neutral homoaromatic molecules [51], even though homoaromatic character in neutral compounds was largely questioned and debated in the past [52]. In fact, homoaromaticity is usually associated to charged moieties exhibiting homoconjugate π network, i.e. a formally conjugated system with an interposed non-conjugate group or a sp^3 -hybridized C atom. From a structural viewpoint, this implies that homoaromaticity is associated with the union of a cyclopropane-like system with an unsaturated linear segment [53–58]. From the ED perspective, homoconjugate patterns may be either distinguished as *through-bond* (if a bcp is present between the sp^2 carbon atoms bonded to the off-plane sp^3 group) or as *through-space* (if a bcp is lacking). Both kinds of interactions have been thoroughly characterized by the topological analysis of the ED scalar field by Childs, Cremer and co-workers [59, 60]. Barzaghi and Gatti [22] have studied the structures, energetics and ED topological features of a series of supposedly 6π electron homoaromatic systems, which differ by the number of basal carbon atoms (from 4 to 7) and the formal charge (-2 to $+1$), i.e. $C_{n+3}H_{n+4}^{(n-4)}$ for $n = 2-5$. They actually found that Möbius aromaticity is preferred over through-bond homoaromaticity, in stabilizing all these structures. In the former, stability is achieved by involving the basis orbitals of the external methylene group, thus effectively ruling out transmission of conjugation along the ring-fused bond. The electron delocalization largely involves the off-plane sp^3 group, leading to a strong enhancement and to a gain of partial π -character of the bonds linking the polyenic fragment with the methylene group. This situation chiefly characterizes the case with $n = 5$, discussed through the SF descriptor in the next paragraph.

5.3.2 Homotropylium Cation

Homotropylium cation (cyclooctatrienylium, (I), $C_8H_9^+$, Scheme 5.1), also called homotropenylium, is the archetype of homoaromatic compounds [61] and belongs to the category of through-space homoconjugate systems [60, 62]. It adopts a boat-shaped conformation, with just the sp^3 C2 atom being significantly off-plane. This system has been thoroughly studied, both recently and in the past [63–65], with the aim of investigating the interplay among its structural, energetics and induced magnetic properties [60, 66] as well as of evaluating energy barriers



Scheme 5.1 Structure of the homotropylium cation, with resonance formulae

involved in carbocation rearrangements [67, 68] and of understanding the role of substituents on the ring chemistry [65, 69].

In this section, we report on the ability of the SF descriptor to investigate electron delocalization in I, taken as a representative test-case for homoaromaticity. The gas-phase optimized geometry of (I) was obtained at the DFT/B3LYP level of theory, with the DZVP2 basis set [70]. Point symmetry (C_s) was exploited while computing the wavefunction. The Gaussian09 program was used throughout [71]. All the topological properties, delocalization indices and atomic SF contributions were evaluated with a modified version [72] of the AIMPACK suite of programs [73]. The accuracy of the numerical integration was checked ensuring that the magnitude of the atomic integrated Lagrangian is lower than 10^{-3} and 10^{-5} au for C and H atoms, respectively, and that the percentage errors (ER%) [14] in the ED reconstruction at the rp 's according to Eq. (5.3) are lower than 1 %.

According with the model of cyclic electron circulation through the sp^2 atoms (Scheme 5.2), bond lengths tend to equalize in the C1–C8–C7–C6–C5–C4–C3 pseudo-7MR (Table 5.1), with small but significant deviation from planarity affecting the whole ring. The C1–C3 distance (2.148 Å), on the other hand, is well larger than $2r_C$, r_C being the covalent radius of an sp^2 carbon (0.73(2) Å) [74]. As expected, a BP is absent between C1 and C3.

Table 5.1 also shows delocalization indices (DI) computed for relevant atom pairs, together with relative Source Function percentage (SF%) contributions from various groups of atoms at each reference point. DI values confirm the delocalized nature of (I) and the limited share of electrons between the bridgehead atoms C1 and C3 [$\delta(C1, C3) = 0.28$]. The percentage SF contributions from bonded atoms, $SF_{ij}\%$, parallel such trend as their values are almost constant in the pseudo-7MR

Scheme 5.2 Homotropylium cation, with atom numbering scheme

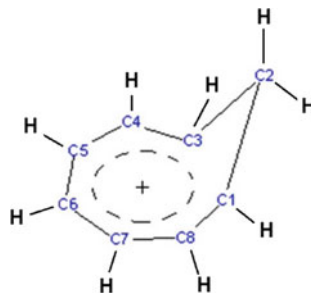


Table 5.1 Bond lengths d , DI's δ and SF% contributions for symmetry-independent C–C bonds in (I)

Bond i–j	$d/\text{\AA}$	ρ_{bcp} , au	$\delta(\text{C}_i, \text{C}_j)$	SF _{ij} %	SF _{nn} %	SF _{others} %	SF%(C2)
C2–C3	1.496	0.251	1.00	78.5	5.9 (3.0; 2.9)	1.5	38.6
C3–C4	1.385	0.311	1.45	85.8	3.9 (1.5;2.4)	0.8	1.5
C4–C5	1.411	0.297	1.33	84.8	5.2 (2.8; 2.4)	0.9	0.3
C5–C6	1.407	0.298	1.38	85.1	4.8 (2.3; 2.5)	1.3	0.1
C1–C3 ^b	2.148	0.087	0.28	32.7	30.0 (18.8, 5.6, 5.6)	2.8	18.8
C=C	1.402	0.301	1.39	84.3	5.2 (2.6; 2.6)	1.4	//

If not otherwise specified, bond critical points (bcp's) in the ED scalar field were taken as rp 's.^a For the sake of comparison, the last line shows the same parameters as computed in benzene (D_{6h})^a 'ij' means contributions from the bonded C atoms i and j, 'nn' implies contributions from the next-neighbour couple of C atoms and 'others' refers to contributions from all the other carbon atoms in the ring. In the case of SF_{nn}%, the separate contribution from the two (or three, for C1–C3) next-neighbour atoms is reported in parenthesis, ordered by increasing carbon atom number^b No bcp found. The midpoint between the C1 and C3 nuclei was chosen as the reference point

and similar to the value in benzene, while the reconstruction of the density at the C1–C3 midpoint reveals a scenario of highly delocalised sources. Only 33 % of this density is determined by the closest atoms C1 and C3 and the apical sp^3 carbon C2 is found to contribute even more (18.8 %) than each of the bridgehead atoms. Relatively high SF_{nn}% and SF_{others}% contributions are observed for the bonds in the pseudo-7MR, though lower than the analogues in benzene [15]. This is likely the consequence of the peculiar (homoconjugative) aromatic character of the π system in this compound. In fact, C2 is an allylic sp^3 atom; therefore, it provides an almost halved SF% contribution to its adjacent bonds with respect to a sp^2 carbon atom within a conventional aromatic network, as may be seen (Table 5.1) from the SF_{nn}% data and their separate contributions from next neighbour atoms, reported in parentheses in this same Table. Interestingly, the SF_{nn}% contributions to the bcp density of the bonds C2–C3 (and C1–C2) linking the polyenic fragment with the methylene group are, instead, even larger than for benzene. The SF descriptor thus neatly reveals the asymmetry of the electron delocalization capability, which, relative to benzene, is definitely lower from the methylenic group to the polyenic fragment and slightly larger, though only in percentage, in the opposite direction.

Both bond distances and DI's in Table 5.1 suggest that the methylene sp^3 group behaves as an allylic carbon, being able to interact with the electron delocalized system within the pseudo-7MR through an allegedly hyperconjugative mechanism. Actually, the percentage contribution of C2 to C3–C4 bcp is comparable to that observed for the allylic C atom C5 in 1,3-cyclohexadiene (Table 5.2). This similarity is conserved even for SF% contribution to distant bonds and it is mirrored by DI's values involving C2 in I and its non bonded atoms C4 and C5 as well as C5 with its non bonded atoms C3 and C2 in 1,3 cyclohexadiene.

Although in non-planar systems the σ/π symmetry labelling of molecular orbitals (and related electrons) is no longer valid, it is still possible to enhance electron

Table 5.2 Comparison of C2 in homotropylium with the allylic carbon atom (C5) in 1,3-cyclohexadiene

Homotropylium		1,3-cyclohexadiene	
SF%(C2, @ bcp C3–C4)	1.4	SF%(C5, @ bcp C3–C4)	1.2
SF%(C2, @ bcp C4–C5)	0.3	SF%(C5, @ bcp C2–C3)	0.2
SF%(C2, @ bcp C5–C6)	0.1	SF%(C5, @ bcp C1–C2)	0.1
δ (C2, C4)	0.054	δ (C5, C3)	0.061
δ (C2, C5)	0.020	δ (C5, C2)	0.014

delocalization effects by suitably choosing reference points other than bcp. According with our previous study on simple aromatic hydrocarbons [15], we located such new *rps* by moving away from the bcp along the *major axis* of the bond (see Fig. 5.1). The major axis is defined in terms of the L_2 eigenvector of the ED Hessian matrix at the bcp, along which the magnitude of the negative curvature of the ED at bcp is a minimum [5, 20]. Bader et al. [20] showed that the L_2 eigenvector points in the direction of the maximum in the π -electron distribution of the molecular orbital theory. The outcomes of such an analysis are collected in Table 5.3.

Data in Table 5.3 nicely confirm the expected enhancement of next-neighbour and other atoms sources and the concomitant decrease of those from atoms the *rp* directly refers to. As concerns the C4–C5 and C5–C6 bonds, no remarkable differences are observed upon choosing the *rp* above (i.e. in *cis*- with respect to C2) or

**Fig. 5.1** Reference points (*rp*'s, red spheres) considered for computing the SF contributions shown in Table 5.3. These *rp*'s were located on the directions determined by the L_2 eigenvectors of the ED Hessian matrix, as evaluated at the corresponding bcp's**Table 5.3** SF % contributions above/below the pseudo-7MR plane at the distance of 1 au from the bcp

Bond i–j	SF _{ij} % ^a	SF _{nn} %	SF _{others} %	SF%(C2)
C2–C3	53.3/55.5	8.4/14.7	2.3/4.7	29.2/27.5
C3–C4	74.1/74.4	6.5/6.8	2.2/0.9	2.4/2.7
C4–C5	71.9/71.7	9.0/9.1	1.9/1.4	0.4/0.7
C5–C6	73.1/72.0	8.1/8.3	2.4/2.5	0.0/0.2

^aThe subscripts 'ij', 'nn' and 'others' have the same meaning as in Table 5.1

below (*trans*-C2) the pseudo-7MR plane.¹ On the other hand, for the C2–C3 bond, the SF contributions are clearly different whether they are evaluated above or below the plane. More in detail, SF_{nn}% and SF_{others}% are greater when the *rp* is chosen in *trans*- with respect to the C2 atom, that is by moving the *rp* towards the interior rather than to the exterior of the ring and thus to a more symmetric position relative to the atoms of the ring. Thanks to the degree of freedom ensured by the choice of the *rp*, the SF descriptor may be a very efficient sensor of electron delocalization magnitude asymmetries.

In conclusion, even for a homoconjugated system, like the homotropylium cation (I), the SF picture nicely fits with that provided by more sophisticated instruments like the delocalization indices. On top of this, due to its mixed local/integral nature (choice of the *rp* and summation of local sources within a region of space), the SF descriptor may reveal relevant asymmetries in the electron delocalization processes. These may be related to different magnitudes of the electron delocalization effects when travelling in opposite directions along a sequence of bonds, or to different magnitudes of such effects when moving perpendicularly to a bond path and in opposite directions relative to a bcp.

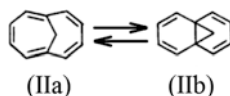
In the next section, a more complex case will be explored, where homoconjugation coexists with aromaticity in a nonbenzenoid 10-membered ring (10MR).

5.3.3 1,6-Methano[10]Annulene

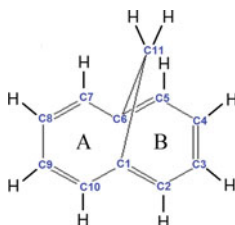
1,6-methano[10]annulene (IIa, C₁₁H₁₀, Scheme 5.3) was the first discovered stable, aromatic cyclodecapentaene. In this respect, it represents a true cornerstone in the history of nonbenzenoid aromatic compounds [75]. Even though the methylene bridge at the C11 carbon (Scheme 5.4) distorts the hydrocarbon backbone from being planar, the 10MR is aromatic, as it can be inferred from the NMR spectrum. Indeed, peripheral H nuclei are deshielded, while the bridging ones are strongly shielded, due to the significant intra-annular diamagnetic ring current induced by the magnetic probe [76]. Moreover, the main ring is prone to electrophilic substitution reactions [77, 78]. Interestingly, (IIa) can exist in equilibrium with its norcaradiene valence tautomer (IIb, Scheme 5.3), that undergoes spontaneous valence tautomerization to the (slightly) more stable (IIa) compound [75, 79]. The equilibrium between these two forms is rather subtle, and it is not surprising that different substituents R, R' at the bridging methylene atom can reverse the stability order, as demonstrated by single-crystal X-ray diffraction experiments [80–83].

In general, bridged methano[10]annulene derivatives are a very attractive class of compounds for investigating non-trivial aromatic systems. Being quite easy to be synthesized and showing a somewhat ‘tunable’ conjugation pattern [84] due to the

¹Actually, the pseudo-7MR system is not rigorously planar. Here we intend the mean least-squares plane passing through the sp² atoms.



Scheme 5.3 1,6-methano[10]annulene



Scheme 5.4 Numbering scheme for atoms and rings in 1,6-methano[10]annulene, compound (IIa)

above sketched tautomerism [79], these compounds allow for a systematic experimental investigation of electron delocalization. Some decades ago, they were extensively studied by Gatti et al. by applying QTAIM topological descriptors to their theoretical ED distributions and using X-ray derived crystalline geometries [23, 24]. Similarly, Bianchi, Destro and Merati lately applied such approach to the accurate experimentally-derived ED distribution of a polybridged annulene derivative [85]. A first attempt of understanding aromaticity (and possibly homoaromaticity) in these compounds using descriptors based on the pair density was carried out far more recently [84].

In their study, Gatti et al. found that when the C₁–C₆ bond length is close to the value of normal CC bonds, i.e. for R = R' = CN or CH₃, the π -like charge distribution of the 3MR system is preserved and the whole cyclopropyl ring behaves as a conjugate π bond. However, when the C₁–C₆ bond lengthens, the 3MR Critical Point (CP) approaches the CP of the C₁–C₆ bond and, for R = R' = H or F, the two points eventually merge, leading to an annulenic structure. Even in such structure, however, besides the presence of the 10- π electronic system, a conjugative coupling of the cyclopropyl ring to the [10]-annulenic framework occurs, similarly to the case of homotropylium cation. The strong involvement of the two external bonds of the 3MR ring in conjugation make them very short and with quite significant ellipticity [23]. Moreover, the overall conjugative mechanism is signalled by the presence of two 7MR ring CPs, largely displaced from the plane of the 10-annulenic framework and pointing towards the bridgehead carbon C₁₁ [23, 24]. The availability of this extra-conjugation mechanism complies with the far better stability of 1,6-methano[10]annulene relative to the extremely reactive π -isoelectronic unbridged [10]annulenes. These latter are in fact characterized by very alternating CC bond lengths and bear few if any signs of aromaticity.

In this section, we extend the SF analysis to 1,6-methano[10]annulene (Schemes 5.3 and 5.4), on the basis of the results found on homotropylium

(Sect. 5.3.2) and naphthalene [15]. The latter compound was considered for the sake of comparison with the annulenic 10MR of (IIa). The level of theory and adopted computer codes are the same as described in Sect. 5.3.2. Computations on IIa have been performed within the C_{2v} symmetry constraint.

There is a certain similarity among bond lengths, DI's and $SF_{ij}\%$ values in the 10MR of (IIa) and naphthalene [15], Table 5.4. However, a closer inspection of the $SF\%$ contributions of distant atoms to each C_i-C_j bond reveals that the nature of their delocalization patterns is markedly different. Actually, the lack of the C1–C6 bond in 1,6-methano[10]annulene ($d = 2.283 \text{ \AA}$, no bcp found) implies that π -delocalized electrons are constrained to flow along the perimeter of the 10MR, i.e. no crossing of the delocalization pattern among the opposite sides of the cyclic chain is allowed through the C1–C6 bridge. In turn, this implies that atoms on opposite branches of the chain partly lose their influence over a given rp . The farther is the atom from the rp , the more significant this effect is.

For example, C1 gives a null contribution to the ED of C4–C5 and C5–C6 bcp's, whereas its influence to C3–C4 is slightly lower than in naphthalene (0.3 vs. 0.4 %). On the other hand, $SF\%$ contribution of C6 to C4–C5 and C5–C6 is slightly higher in 1,6-methano[10]annulene (Table 5.4). This fact reflects also on $SF_{\text{others}}\%$ values, which are always lower than in naphthalene, even when C1 and C6 do not contribute *directly* (but in turn do it *indirectly* through the lack of the C1–C6 bond) to that quantity.

It is instructive to see whether some kind of through-space homoconjugation is also present between the not bonded C1 and C6 atoms. Indeed, atoms C1 and C6 have a significant influence on the ED at their midpoint (see Table 5.4). Moreover, bond distances and DI's of the allylic bonds (C11–C1/C11–C6 in (IIa) and C2–C1/C2–C3 in (I)) are almost the same in 1,6-methano[10]annulene and

Table 5.4 Bond lengths, d , DI's, δ , and $SF\%$ contributions for the symmetry-independent C–C bonds in 1,6-methano[10]annulene (first row) and for corresponding bonds in naphthalene (second row)

Bond	$d/\text{\AA}$	$\delta(C_i, C_j)$	$SF_{ij}\%^b$	$SF_{nn}\%^{b,c}$	$SF_{\text{others}}\%^{b,d}$	$SF\%(C1)$	$SF\%(C6)$
C1–C6 ^a	2.283	0.17	25.2	38.1 (19.1, 0.0, 19.1)	5.0 (2.5, 0.0, 2.5)	12.6	12.6
	1.434	1.22	81.2	9.8 (4.9, 0.0, 4.9)	3.2 (1.6, 0.0, 1.6)	42.7	42.7
C1–C2	1.414	1.29	83.7	6.4 (2.7, 0.0, 2.3)	1.9 (0.8, 0.0, 1.1)	41.5	0.0
	1.427	1.25	82.5	7.3 (3.0, 2.0, 2.3)	3.0 (1.4, 0.0, 1.6)	40.7	2.0
C2–C3	1.398	1.44	85.1	4.4 (2.2, 2.2, 0.0)	1.8 (0.6, 0.0, 1.1)	2.2	0.0
	1.380	1.49	85.3	4.4 (2.4, 2.0, 0.0)	2.3 (0.7, 0.4, 1.2)	2.0	0.4
C3–C4	1.431	1.31	83.5	5.4 (5.4, 0.0, 0.0)	1.4 (0.0, 0.7, 0.8)	0.3	0.3
	1.424	1.29	83.7	5.9 (5.9, 0.0, 0.0)	1.9 (0.0, 0.8, 1.1)	0.4	0.4

^aWhen a bcp is not present, the C⋯C midpoint was selected as rp

^bThe subscripts 'ij', 'nn' and 'others' have the same meaning as in Table 5.1

^cFor a given C_i-C_j bond, the values within parentheses are (from left to right): the $SF\%$ contributions of the nearest neighbour C atoms belonging to the same ring (A) of the bond being analysed and not being shared with the other 6MR; the same contributions from C1 and C6 atoms, common to the two 6MRs; the same contributions from atoms belonging only to the other 6MR (B). Bridging C11 atom is excluded from $SF\%$ contributions

^dAs in (c), but referred to the "other" C atoms. C11 atom is excluded

Table 5.5 Bond lengths, d , DI's, δ , and SF% values for symmetry-independent C1–C11 (1,6-methano[10]annulene, C₁₁H₁₀) and C3–C2 (homotropylium cation, C₈H₉⁺) allylic bonds

System	$d/\text{\AA}$	$\delta(\text{C}_i, \text{C}_j)$	SF _{ij} % ^a	SF _{nn} %	SF _{others} %	SF%(C _{allyl})
C ₁₁ H ₁₀	1.494	0.98	76.8	7.5	3.1	38.0
C ₈ H ₉ ⁺	1.496	1.00	78.5	5.9	1.5	38.6

^aThe subscripts 'ij', 'nn' and 'others' have the same meaning as in Table 5.1

homotropylium cation (Table 5.5). At the C11–C1 bcp in IIa, SF_{nn}% amounts to 7.5, 5.4 % due to C2 and C10 and the remaining 2.1 % to C6. In the homotropylium cation, the SF_{nn}% for the C2–C3 bcp is equal to 5.9, 2.9 % arising from C4 and 3.0 % from C1. The latter value is remarkably greater than 2.1 % from C6 in the annulenic system. This implies that in compound (IIa) C6 is indeed simultaneously involved in the electron delocalization pattern of both the pseudo-6MR's. Thus, its influence to the allylic bond must be lower than in homotropylium cation, that possesses a unique ring of atoms. It should be noted that SF_{others}% at the C11–C1 bcp in 1,6-methano[10]annulene is twice the value detected for the analogue allylic C2–C3 bond in homotropylium, in a sort of additive bis-homoconjugative fashion. A further confirmation of the identical role of C-sp³ atoms (C11 and C2) in both molecules is given by their almost comparable influence to distant bonds, as shown in Table 5.6.

Table 5.7 shows the integral topological descriptors for the through-space bridging C⋯C interactions in the homotropylium cation (C1⋯C3) and in the annulenic system (C1⋯C6). The latter interaction is clearly weaker and more delocalized than its C1⋯C3 analogue in homotropylium. Higher delocalization could be explained by noting that in the 1,6-methano[10]annulene two

Table 5.6 Comparison of C11 in 1,6-methano[10]annulene with C2 in homotropylium

Homotropylium		1,6-methano[10]annulene	
SF%(C2, @ bcp C2–C3)	38.6	SF%(C11, @ bcp C11–C1)	38.0
SF%(C2, @ bcp C3–C4)	1.4	SF%(C11, @ bcp C1–C2)	1.2
SF%(C2, @ bcp C4–C5)	0.3	SF%(C11, @ bcp C2–C3)	0.1
SF%(C2, @ bcp C5–C6)	0.1	SF%(C11, @ bcp C3–C4)	–0.1
$\delta(\text{C2}, \text{C4})$	0.054	$\delta(\text{C11}, \text{C2})$	0.051
$\delta(\text{C2}, \text{C5})$	0.020	$\delta(\text{C11}, \text{C3})$	0.022

Table 5.7 Comparison of C1⋯C6 (1,6-methano[10]annulene) and C1⋯C3 (homotropylium) interactions

System	$d/\text{\AA}$	$\delta(\text{C}_i, \text{C}_j)$	SF _{ij} % ^a	SF _{nn} %	SF _{others} %	SF%(C2(Ia) or C11 (IIa))
C ₁₁ H ₁₀	2.283	0.17	25.2	38.1	5.0	18.9
C ₈ H ₉ ⁺	2.148	0.28	32.7	29.0	2.8	17.8

The midpoint is taken as rp in both systems

^aThe subscripts 'ij', 'nn' and 'others' have the same meaning as in Table 5.1

pseudo-6MR's contribute to the density at the midpoint, instead of just one 7MR as in homotropylium. Indeed, the annulenic 10MR can in principle delocalize electrons *without passing through* C1⋯C6. Therefore, the “through bond”, but not necessarily the “through space” homoconjugative mechanism is expected to be less important than in homotropylium. In this respect, the weakening of C1⋯C6 is a straightforward consequence. As a further proof, each pseudo-6MR in the annulenic system does not show the typical *para* effect of aromatic 6MR [15], as $\delta(\text{C1}, \text{C3}) = 0.07$ is larger and not smaller than $\delta(\text{C1}, \text{C4}) = 0.05$ and $\delta(\text{C1}, \text{C5}) = 0.02$ is much smaller than both $\delta(\text{C1}, \text{C3})$ and $\delta(\text{C1}, \text{C4})$.

5.4 Source Function Applied to Spin-Polarized Systems: A Novel Tool for Gaining Insight into the Transmission of Magnetic Information at the Molecular and Sub-molecular Level

Various cutting-edge research areas, including spintronics [86], advanced sensing [87] and production of porous molecular sieves [88, 89] continuously require the development of novel magnetic networks, often designed at the molecular scale. Different mechanisms, such as direct exchange, ligand-mediated exchange and superexchange are involved in transmitting the magnetic information from a given paramagnetic centre to its neighbouring atoms [90]. Such mechanisms often compete with each other, so it is far from trivial even to accurately understand—saying nothing about predicting—the macroscopic magnetic properties of complex bulk materials. Similarly to the ED scalar field, magnetism is also due to *non-local* effects, which may likewise develop through space or through chemical bonds. In particular, non-locality is crucial in determining magnetic properties, as it inherently concerns far range correlations among unpaired electrons, more or less localized onto different centres.

To achieve a first-principle understanding of magnetism in complex systems, the electron spin density distribution, SDD ($s(\mathbf{r})$), is often analysed. It is defined as:

$$s(\mathbf{r}) = \rho_{\alpha}(\mathbf{r}) - \rho_{\beta}(\mathbf{r}) \quad (5.6)$$

with $\rho_{\alpha}(\mathbf{r})$ and $\rho_{\beta}(\mathbf{r})$ being the spin α and β contributions to the total electron density, $\rho(\mathbf{r})$. The SDD expresses the *local* extent of spin polarization. It is positive (negative) when the ED due to the α electrons at \mathbf{r} exceeds (is lower than) that due to the β electrons, while $s(\mathbf{r}) = 0$ implies local full pairing.

Although SDD is customarily obtained from quantum mechanical simulations, it is also experimentally accessible through magnetic scattering of polarized X-rays [91] and neutrons [92]. The ever increasing availability of intense neutron and synchrotron X-ray sources, along with a recent extension of the standard Hansen-Coppens multipolar model, will largely improve the quality and enhance

the role of experimentally-derived SDD, which might so become soon a key instrument to understand and design specific magnetic interactions in complex solid-state networks [93].

The SDD alone is, however, neither able to provide direct information on the reasons underlying possible spin polarization effects, nor to disentangle different exchange/pairing mechanisms. Of late, we have proposed a novel SDD-based real-space descriptor [94], the spin density Source Function (SF_S), that is able to gain quantitative insight on the relative importance of different atoms or groups of atoms in determining the electron spin density at a given reference point. Due to its own nature, this new tool equally applies to theoretically or experimentally derived SDDs. From Eqs. (5.1)–(5.3), the SF decomposition scheme for the SDD $s(\mathbf{r})$ will read as follows:

$$s(\mathbf{r}) = \int_{R^3} \text{LS}_S(\mathbf{r}, \mathbf{r}') d\mathbf{r}' = \sum_{\Omega} \int_{\Omega} \text{LS}_S(\mathbf{r}, \mathbf{r}') d\mathbf{r}' = \sum_{\Omega} \text{SF}_S(\mathbf{r}, \Omega) \quad (5.7)$$

where the Local Source LS_S is now defined in terms of the spin density Laplacian:

$$\text{LS}_S(\mathbf{r}, \mathbf{r}') = -\frac{1}{4\pi} \frac{\nabla^2 s(\mathbf{r}')}{|\mathbf{r} - \mathbf{r}'|} = -\frac{\nabla^2 [\rho_{\alpha}(\mathbf{r}') - \rho_{\beta}(\mathbf{r}')] }{4\pi |\mathbf{r} - \mathbf{r}'|} = \frac{\nabla^2 \rho_{\beta}(\mathbf{r}') - \nabla^2 \rho_{\alpha}(\mathbf{r}')}{4\pi |\mathbf{r} - \mathbf{r}'|} \quad (5.8)$$

The Green function $(4\pi|\mathbf{r} - \mathbf{r}'|)^{-1}$, being a purely geometrical (effectiveness) factor, is common to both Eqs. 5.2 and 5.8, while the local *cause*, $\nabla^2 s(\mathbf{r}')$, and *effect*, $s(\mathbf{r})$, are now given in terms of the electron spin density, rather than of the total electron density. This implies that SF and SF_S descriptors will in general provide quite different pictures of how the two scalars are determined at a given point, that is of how the electron density and the electron spin density information is transmitted throughout a system. Such a difference is but a consequence of the diverse local condensation ($\nabla^2 u(\mathbf{r}') < 0$, $u = s$ or ρ) or dilution ($\nabla^2 u(\mathbf{r}') > 0$) of the two distributions throughout a system. Finally, note that the integral over the whole space is partitioned, also for SF_S, into disjoint contributions from Bader's topological atoms Ω 's [5], implying that $\nabla^2 s(\mathbf{r}')$ does not generally sum to zero when integrated over a basin Ω .

A full description of the various technical aspects of the SF_S tool is reported in the original paper [94]. Here, we just summarise the effect that the local relative dilution/concentration of α and β densities has on the local source for the spin density. This effect represents a crucial step to correctly interpret the outcomes of the SF_S tool, and it can be easily understood by inspecting at Table 5.8.

When $\nabla^2 s(\mathbf{r}') < 0$, the local source LS_S is positive and the α component of the total electron density, i.e. its α -spin polarization, is increased at a given $r\rho$ \mathbf{r} . Viceversa, when $\nabla^2 s(\mathbf{r}') > 0$, LS_S is negative and it is the β component that turns out to be raised at the $r\rho$. The ability of a given source point \mathbf{r}' to determine an α or

Table 5.8 How the signs and relative magnitudes of $\nabla^2\rho_\alpha$ and $\nabla^2\rho_\beta$ at \mathbf{r}' produce an α or β effect on the spin density $s(\mathbf{r})$ at the rp ^a

Sign($\nabla^2\rho_\alpha(\mathbf{r}')$)	Sign($\nabla^2\rho_\beta(\mathbf{r}')$)	Relative magnitudes	$\nabla^2s(\mathbf{r})$	$LS_S(\mathbf{r},\mathbf{r}')$	Effect on $s(\mathbf{r})$
>0	>0	$\nabla^2\rho_\alpha > \nabla^2\rho_\beta$	>0	<0	β
		$\nabla^2\rho_\alpha < \nabla^2\rho_\beta$	<0	>0	α
>0	<0	Any	>0	<0	β
<0	>0	Any	<0	>0	α
<0	<0	$ \nabla^2\rho_\alpha > \nabla^2\rho_\beta $	<0	>0	α
		$ \nabla^2\rho_\alpha < \nabla^2\rho_\beta $	>0	<0	β

^aThis table is reproduced with permission from Ref. [94], Copyright 2015, The Royal Society of Chemistry (RSC)

β contribution to the electron density at the rp is named as ‘ α ’ or ‘ β effect’, respectively. Clearly, for a given \mathbf{r}' , the magnitude of such effect depends on the distance from the rp , but its α or β nature is only a function of the source point \mathbf{r}' . Table 5.8 illustrates the role played by the local relative magnitudes of the α - and β -density Laplacian values in determining such nature, which eventually depends on which of the two SDD Laplacian contributions prevails (Eq. 5.8). In particular, if either ρ_α or ρ_β is locally concentrated, while the other distribution is locally depleted, the α or β nature of the effect will be necessarily defined by the concentrated distribution, regardless of the relative magnitudes of the ρ_α or ρ_β Laplacians. However, when both ρ_α and ρ_β are locally concentrated or depleted, the sign of $LS_S(\mathbf{r}, \mathbf{r}')$ will depend on whether it is the α or the β distribution that is more concentrated or depleted. What matters is the *relative* concentration or dilution of the two distributions, as having both distributions concentrated or depleted does not guarantee an α or β effect, respectively. As an example, a point \mathbf{r}' where both the α and β distributions are depleted, but $\nabla^2\rho_\alpha(\mathbf{r}') < \nabla^2\rho_\beta(\mathbf{r}')$, will act as α source as ρ_α is locally less depleted than ρ_β .

We also demonstrated that the specific choice of the rp is crucial in determining how the paramagnetic centre influences the non-magnetic centres and *vice versa*. This occurs because of the large anisotropy of the SDD and of its Laplacian distributions. Indeed, it may result that $s(\mathbf{r})$ be significantly determined by atomic basins different from the atomic basin to which the point belongs to, and even so in the case of regions within the basin of the paramagnetic centre [94].

In our first paper on the SF for the spin density [94], we have addressed a very simple test case, 3B_1 water, to exemplify whether an atom or group of atoms concur or oppose the paramagnetic center in determining a given local polarization.

Likewise, in the example reported below, we investigate such a behaviour in n -alkyl radicals, but we also focus, in particular, on their spin density transferability. Use of the SF tool to assess and analyse the transferability of the ED properties in the corresponding n -alkanes was reported long time ago [1]. The present study represents the first case where such an analysis is extended to the electron spin density.

5.4.1 *Electron Density and Electron Spin Density Transferability Viewed Through the Eye of the Source Function Tool: The Case of N-alkyl Radicals*

A cornerstone of chemistry is the atomic group transferability paradigm, deduced from a plethora of experimental facts and corroborated on a firm quantitative basis, for a large variety of group properties, by the Quantum Theory of Atoms in Molecules [5]. The Source Function descriptor may be then conveniently exploited to add further insight. On the one hand, the SF tool is capable to distinguish between *perfect* transferability, implying that the electron density of a group is fully transferable among a series of chemically related compounds, from the case of *compensatory* transferability, where a constant value for a group property is only achieved through compensatory effects [2, 6]. On the other hand, the occurrence of perfect transferability of a group property, say for instance the value of the electron density at a bcp within the group, not only implies a transferable SF contribution from the atoms forming the group, but also that the sum of contributions to that density from the remaining atoms or group of atoms in the system remains constant, no matter the size of the system. This clearly adds further (chemical) information on how perfect transferability realizes.

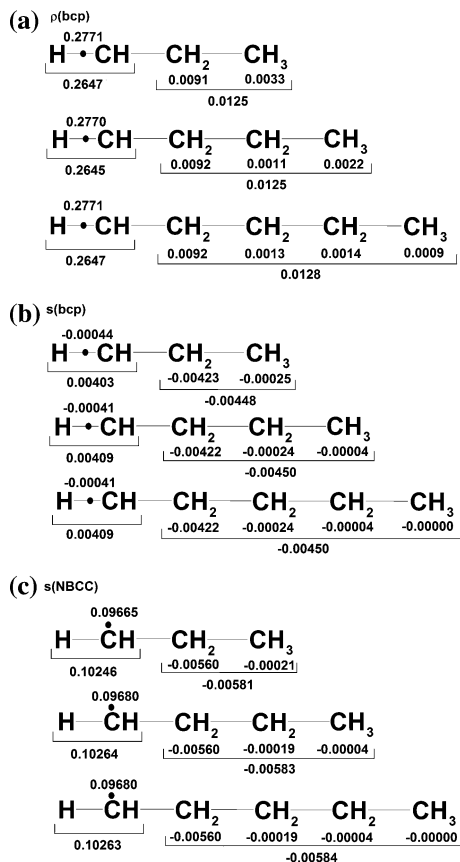
Terminal methyl groups in n-alkanes, past ethane, are known to be fully transferable [5] as they show several properties (energy, electron population, volume and spectroscopic responses) that remain constant regardless the length of the carbon chain. The transferability of the electron distribution in the methyl group is so good that a constant value for the electron density at its unique C–H bcp is also observed, past ethane. Such transferability realizes because of a constant SF contribution from the CH₃ group and a constant SF external contribution from the remaining atoms in the chain, no matter its length [1, 2].

To verify whether this holds true also for SDD, CH₃(CH₂)_nCH₂[•] n-alkyl radicals [95] with n = 1–3, at fully optimized geometries and in their most stable conformations were considered. These correspond for all systems to the C[p] orbital, housing the unpaired electron in the terminal CH₂[•] group, being almost eclipsed with respect to one of its β C–H bonds. Wavefunctions were calculated at the UPBE1PBE/6-311 + G(d,p) level, using the Gaussian-09 code. Spin contamination annihilated wavefunctions [IOP(5/14 = 2), pop = noab] were used for both geometry optimization and SF_S analysis. Integration of the spin density over the basin of the terminal CH₂[•] group typically shows that more than 91 % of the excess α density lies in this group and essentially on the C (90 %), the second most important contribution (6 %) coming from the eclipsed β-hydrogen atom mentioned above.

Figure 5.2 compares the electron density [*top*, (a)] and the electron spin density [*middle*, (b)] transferability at the C–H bcp of the terminal CH₂[•] group for all considered radicals.

The former transferability is confirmed to occur also in the n-alkyl radicals, and with similar mechanisms to those operative in the corresponding alkanes.

Fig. 5.2 Electron density and electron spin density transferability as viewed through the source function, in *n*-alkyl radicals. The electron (a) and electron spin (b) densities at a terminal C–H bcp are reported along with their total SF contributions from the various CH₂ and CH₃ groups in each system, c is the same as (b), but for a (3, +1) $-\nabla^2\rho$ non bonded charge concentration (NBCC) reference point associated to the unpaired electron. All values are given in atomic units (au)



The dominant contribution to the bcp electron density (0.265 au) comes from the terminal group hosting the bcp, while the remaining methyl and methylene bridge groups adjust their SF contributions so as to provide a constant residual density (0.013 au). An almost perfect transferability is then recovered also for the very low value of the spin density, $s = -0.0004$ au, found for all systems at the bcp. However, at variance with the electron density, the overall α SF_S contribution from the terminal CH₂ group, $s = 0.0041$, is more than compensated for by an overall β and constant contribution, $s = -0.0045$, arising from the remaining part of the molecule, regardless of the length of the chain. Spin transferability is thus ensured through a combination of opposing α and β SF_S cumulative effects of similar magnitude. An equally remarkable transferability characterizes the value of the spin density at the (3, +1) $-\nabla^2\rho$ critical point, located above the plane of the terminal CH₂ group, about 1 au far from the C and on the same side of the H eclipsed to the C[p] orbital housing the unpaired electron [Fig. 5.2, bottom (c) and Fig. 5.3]. This (3, +1) CP and the almost symmetric one lying below such plane, but of (3, -1) signature, may be both associated to non-bonded charge concentrations

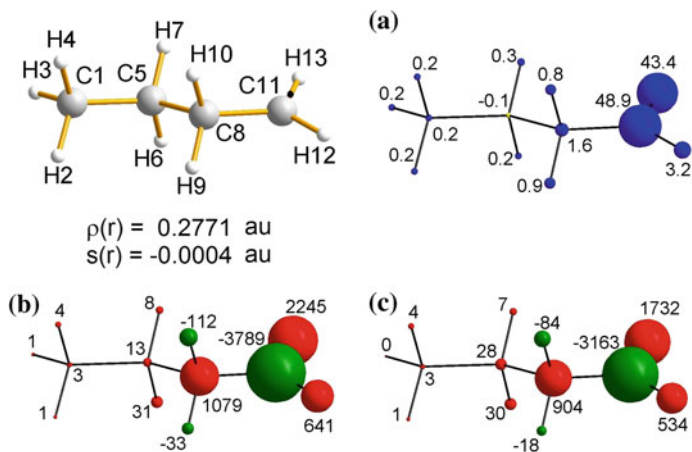


Fig. 5.3 Atomic SF (a) and SF_S (b) percentages at the C₁₁-H₁₃ bond critical point (bcp, shown as a black dot in the upper left ball-and-stick scheme) for the *n*-butyl radical. In (c) the SF_S percentages only due to the magnetic orbital density are displayed. The values of ρ and s at the bcp are given in atomic units. Atoms are portrayed as spheres with volumes proportional to their source function contributions to ρ and s values at the bcp. Colour codes: (a) blue or yellow whether atoms represent positive or negative sources for ρ at the bcp; (b) and (c) green or red whether atoms represent positive (α effect) or negative (β effect) sources for s at bcp. Note, instead, that in (b) and (c) the sign of percentage atomic sources is positive (negative) when the atom concurs (opposes) to the s value at the bcp

(NBCCs). They are largely due to the unpaired electron, although they do not correspond to electron spin density maxima.

At variance with the case of the terminal C-H bcp, the s value is large and positive, $s = 0.0968$ au, at this NBCC. It is larger than half the density value, $\rho = 0.1717$ au, and fully dominated by the overall α effect contribution, $s = 0.1026$, from the terminal CH₂[•] group. The role of the remaining part of the molecule is just that of slightly counteracting such contribution through a comparatively modest overall β effect ($s = -0.0058$) at the NBCC. In summary, though transferability holds true for both the electron and the electron spin density in *n*-alkyl radicals, it realizes in quite different ways and largely dependent on the selected rp .

To add further insight, it is instructive to dissect the SF group contributions, in terms of their atomic components, for one member of the series (*n*-butyl radical, Figs. 5.3 and 5.4, for $rp = \text{bcp}$ and $rp = \text{NBCC}$, respectively). Comparing Fig. 5.3a with Fig. 5.3 b, one notices further differences between the electron density and electron spin density reconstructions at the terminal C-H bcp. First, for $rp = \text{bcp}$, the atoms bonded to each other always oppose themselves in their action, one giving an α and the other a β effect. This typically occurs for through-bond transmission between covalently bonded atoms (“antiferromagnetically” coupled). Secondly, the individual atomic SF_S contributions are very large in magnitude, even forty times as large (C11) as the s value they concur to reconstruct. The overall contributions from the terminal CH₂[•] or from its neighbouring CH₂ group are also

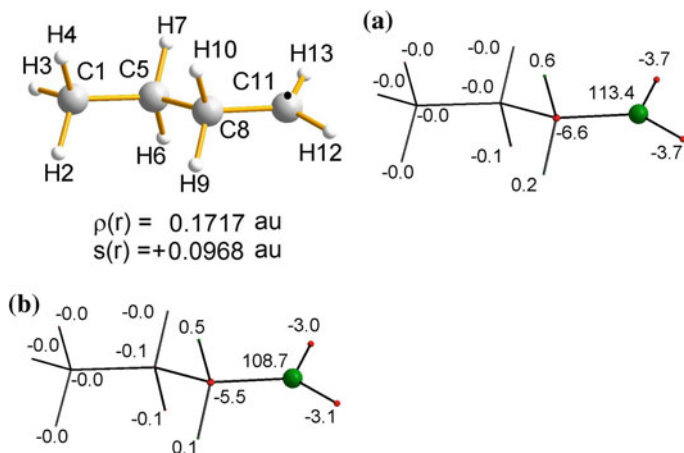


Fig. 5.4 *n*-butyl radical: (a) atomic SF₅ percentages at the (3, +1) $-\nabla^2\rho$ critical point, located above the plane of the terminal CH₂ group, highlighted as a *black dot* in the *upper left* ball-and-stick scheme and associated to non-bonded charge concentrations largely due to the unpaired electron. In (b) the SF₅ percentages only due to the *magnetic* orbital density are displayed. The values of ρ and s at the reference point bcp are shown. Colour codes for atoms and signs of atomic SF₅ percentages bear the same meaning and are defined analogously to Fig. 5.3

much larger in magnitude than the s value at rp , but not as large as the individual atomic contributions because of the opposing contributions from their covalently bonded atoms. At last, while the SF contributions from the H atoms of the terminal CH₂ group to the C11–H13 bcp density markedly differ between each other, and with that from H13 being almost 14 times as large as the one from H12, this is not at all the same for the corresponding SF₅ contributions. The latter are more comparable in magnitude, as that from H13 is only three times as large as that from H12 atom, which is not directly related to the bcp taken as rp . It is clear, from such data, that the spin density at C–H bcp originates from much less local sources than it is for its corresponding electron density.

A quite different scenario characterises the spin density reconstruction at the NBCC located above the plane of the terminal CH₂ group (Fig. 5.4a). The large s value at this rp is essentially determined by the C carrying the unpaired electron, SF₅% (C11) = 113.4, the role of its linked H and C atoms being simply that to neutralize the slight α -effect excess arising from the C11 atom. It emerges that the SF₅% values are able to neatly distinguish the case where the rp characterizes a covalent bonding interaction, with respect to the case where the rp is associated to a NBCC largely due to a fairly localised unpaired electron (see the spin atomic populations reported earlier for such systems). Spin information transmits indeed quite differently in the two cases, if judged from the relative SF₅% values. However, the order of magnitude of the overall SF₅ contributions from the two H of the terminal CH₂ group or the order of magnitude of the cumulative SF₅ contribution from the β -CH₂ group, are similar for the two selected reference points.

The large discrepancy on the SFs percentages arises from the three order of magnitude larger s value at NBCC.

In Ref. [94] we showed that interpretation of SF_S values may be largely enhanced when they are decomposed into a *magnetic* and into a *reaction* or *relaxation* contribution, the former being due to the magnetic natural orbital(s) density and the second one to the remaining natural orbitals density. Magnetic orbital(s) are easily obtained through diagonalization of the first order density matrix and identified by picking up the orbital(s) with occupations equal to or very close to 1. Technical details and a full discussion of the mentioned decomposition scheme are reported in Ref. [94] and in its supplementary information. Interestingly, the magnetic contribution, though being due only to an α -density, does not always lead to an α -effect, but may also result in an overall decrease of the spin density at a given rp . Likewise, the reaction contribution may either concur or counteract the magnetic one in determining the SDD at the rp . For n -alkyl radicals, the situation is very simple as there is only one magnetic natural orbital, whose effect is made visible in Figs. 5.3c and 5.4b for the case of n -butyl radical and for the two examined rps . The role of the reaction contribution may be assessed from the difference of (b) and (c) SF_S values in Fig. 5.3 and, analogously, of (a) and (b) SF_S values in Fig. 5.4. One observes that the magnetic orbital density plays the major role and that the remaining relaxation density moderately (from 5 to 20 % in magnitude) concur to the effects produced by the former density, for both rps . These effects may be either of α or of β nature for both densities, but always agree in their nature in this case, at least for the more significant contributions.

5.5 Concluding Remarks

In this chapter, we reviewed two recent developments of the Source Function analysis and illustrated a couple of novel applications thereof, which emphasize the ability of this descriptor to retrieve interesting and non trivial chemical insights.

We first showed that, analogously to what already reported for planar mono- and polycyclic aromatic hydrocarbons, the Source Function tool is able to detect subtle electron delocalization effects also in the non-planar and less conventional hydrocarbons, like the homotropylium cation and the 1,6-methano[10]annulene, where the usual σ/π separation does no longer apply. The analysis of such systems has been made by dissecting the electron density values at bond critical points in terms of Source Function contributions from the *bonded* atoms, their next neighbouring carbon atoms and the other carbon atoms in the system and by comparing the nature of such dissection with that obtained for more conventional, π -conjugated, planar reference compounds. Clear, quantitative footprints of *through space* and *through bond* homoconjugation mechanisms have been so identified for the homotropylium cation, along with similarities and differences, relative to benzene, in the way electron conjugation realizes in the unsaturated moiety of its C atom linkage. In the case of the 1,6-methano[10]annulene, comparison with source contributions

patterns in naphthalene and homotropylium cation, has enabled us to disentangle the signatures of the ‘classical’ electron delocalization scheme, involving circulation of π electrons along the 10MR hydrocarbon chain, from those due to the homoconjugative mechanism, which takes place essentially through space and largely involves the two allylic, short bridge bonds.

Both discussed cases confirm that the Source Function picture nicely complies with that provided by more sophisticated instruments based on the pair density, like the delocalization indices. But the Source Function has, possibly, an advantage as it may also reveal chemically relevant asymmetries in the electron delocalization processes. It has been shown how these asymmetries disclose the non equivalence of the delocalization effects between two atoms directly or indirectly connected along a sequence of bonds or the different magnitudes of such effects when moving perpendicularly to a bond and in opposite directions relative to the bond critical point.

Secondly, we briefly reviewed the recent extension of the Source Function to the electron spin density. Similarly to the case of the electron density, such development enables one to see the electron spin density at any point in the space in terms of *source* contributions from the remaining points. The influence of each atom or group of atoms in determining the spin polarization at any point can be then quantified by integrating these local sources within atomic basins. It becomes so possible to evaluate whether an atom or group of atoms concurs with or counteracts the paramagnetic centre(s) in determining the local valence spin polarization at a given point and whether it does so in a relevant or negligible measure. At the same time, competing or cooperating spin propagation mechanisms can be disentangled. Decomposition of source function contributions into a *magnetic* and into a *relaxation* term adds further precious chemical insight and largely facilitates their interpretation. The magnetic contribution, though associated to an α -density only, may still result in both an overall increase or decrease of the spin density at a given point. The relaxation contribution may then either concur or counteract the effect of the magnetic term.

We have concluded our chapter by analysing whether the spin density properties are as transferable as are the electron density properties in a series of *n*-alkyl radicals. We have convincingly shown that this is actually the case, but also that the transferability of the two fields realizes in a quite distinct manner and one that strongly depends on where the field is reconstructed through the Source Function contributions. For instance, when the electron density or its spin counterpart are reconstructed at the C–H bcp of a terminal CH_2 group one finds that the electron density at such point is largely determined by the atoms of the terminal group, and with the remaining atoms providing only a small, constant contribution, regardless the length of the chain. Instead, in the case of the spin density, the overall α contribution from the terminal CH_2 group is more than compensated for by an overall β and constant contribution arising from the remaining part of the molecule. Spin transferability at the bcp is thus ensured through a combination of opposing α and β contributions of similar magnitude. Quite different is the case for the spin density reconstruction at the non bonded charge concentration located above the

plane of the terminal CH_2^{\bullet} group, where the very large spin density value is essentially determined by the carbon carrying the unpaired electron and where the role of its linked hydrogen and carbon atoms is just that of neutralize the slight α -effect excess arising from the radicalic carbon.

In general, joint analyses of the spin and electron density source functions provide interesting insights, as the different way the two scalar fields dilute and concentrate in the space lead to reconstructions of these fields which may be totally different. For example, this is the case of the points associated to the lone pair electrons in water triplet [94] or the just mentioned case of the spin density at the terminal C–H bcp in *n*-alkyl radicals.

Being defined in term of observables, the Source Function tool is amenable to experimental determination. This is already a standard practice for the electron density. The latter has become almost routinely accessible, even from microcrystals, due to the impressive advance of the photon source technology and the developments of modern multipole methods (including the availability of pole libraries) [9]. The electron spin density is, however, also becoming more and more within reach, experimentally [96]. The ongoing possibility of an unbiased comparison of ab initio and experimental (polarized neutrons plus X-rays) spin densities is of a paramount importance for the molecular-scale design of novel magnetic materials. Electron spin densities are known to be very sensitive to the adopted theoretical framework [94], while several technical limitations arise when experimental results are considered [9]. The Source Function could be a valuable tool in such regard. It shows how the electron spin density is determined in the various molecular regions and, therefore, it could also neatly disclose the cause behind an observed, significant spin density difference or behind a particular spin density sensitivity to computational and methodological parameters.

Acknowledgments We thank the Danish National Research Foundation for partial funding of this work through the Center for Materials Crystallography (DNRF93).

References

1. Bader RFW, Gatti C (1998) A Green's function for the density. *Chem Phys Lett* 287:233–238
2. Gatti C (2012) The source function descriptor as a tool to extract chemical information from theoretical and experimental electron densities. *Struct Bond* 147:193–286
3. Gatti C (2013) Challenging chemical concepts through charge density of molecules and crystals. *Phys Scripta* 87:048102 (38 pp)
4. Arfken G (1985) *Mathematical methods for physicists*. Academic Press, Orlando
5. Bader RFW (1990) *Atoms in molecules: a quantum theory*. In: International series of monographs on chemistry, vol 22. Oxford Science Publications, Oxford UK
6. Gatti C, Cargnoni F, Bertini L (2003) Chemical information from the source function. *J Comput Chem* 24:422–436
7. Hansen NK, Coppens P (1978) Electron population analysis of accurate diffraction data. 6. testing aspherical atom refinements on small-molecule data sets. *Acta Cryst A* 34:909–921

8. Stewart RF, Bentley J, Goodman B (1975) Generalized X-ray scattering factors in diatomic molecules. *J Chem Phys* 63:3786–3793
9. Gatti C, Macchi P (eds) (2012) *Modern charge density analysis*. Springer, Dordrecht
10. Lo Presti L, Gatti C (2009) Using the source function descriptor to dampen the multipole model bias in charge density studies from X-ray structure factor refinements. *Chem Phys Lett* 476:308–316
11. Farrugia LJ, Cameron E, Tegel M (2006) Chemical bonds without “chemical bonding”? a combined experimental and theoretical charge density study on an iron trimethylenemethane complex. *J Phys Chem A* 110:7952–7961
12. Farrugia LJ, Cameron E, Lenz D et al (2009) The QTAIM approach to chemical bonding between transition metals and carbocyclic rings: a combined experimental and theoretical study of $(\eta^5\text{-C}_5\text{H}_5)\text{Mn}(\text{CO})_3$, $(\eta^6\text{-C}_6\text{H}_6)\text{Cr}(\text{CO})_3$, and $(E)\text{-}\{(\eta^5\text{-C}_5\text{H}_4)\text{CF-CF}(\eta^5\text{-C}_5\text{H}_4)\}(\eta^5\text{-C}_5\text{H}_5)_2\text{Fe}_2$. *J Am Chem Soc* 131:1251–1268
13. McGrady GS, Sirsch P, Chatterton NP et al (2009) Nature of the bonding in metal-silane σ -complexes. *Inorg Chem* 48:1588–1598
14. Gatti C, Lasi D (2007) Source function description of metal–metal bonding in d-block organometallic compounds. *Faraday Discuss* 135:55–78
15. Monza E, Gatti C, Lo Presti L et al (2011) Revealing electron delocalization through the source function. *J Phys Chem A* 115:12864–12878
16. Lo Presti L, Ellern A, Destro R et al (2011) Rationalizing the effect of halogenation on the molecular structure of simple cyclobutene derivatives by topological real-space analysis of their electron density. *J Phys Chem A* 115:12695–12707
17. Schmökel M, Cenedese S, Overgaard J et al (2012) Testing the concept of hypervalency: charge density analysis of K_2SO_4 . *Inorg Chem* 51:8607–8616
18. Engels B, Schmidt TC, Gatti C et al (2012) Challenging problems in charge density determination. *Struct Bond* 147:47–98
19. Cocq K, Lepetit C, Maraval V et al (2015) “Carbo-aromaticity” and novel carbo-aromatic compounds. *Chem Soc Rev* 44:6535–6559. doi:10.1039/c5cs00244c
20. Bader RFW, Slee S, Cremer D et al (1983) Description of conjugation and hyperconjugation in terms of electron distributions. *J Am Chem Soc* 105:5061–5068
21. Cremer D, Kraka E, Slee S et al (1983) Description of homoaromaticity in terms of electron distributions. *J Am Chem Soc* 105:5069–5075
22. Barzaghi M, Gatti C (1987) Homoaromaticity versus Möbius aromaticity. *J Chimie Physique* 84:783–789
23. Gatti C, Barzaghi M, Simonetta M (1985) Charge density topological approach to the Dinorcaradiene \leftrightarrow [10]Annulene equilibrium in some 11, 11-Disubstituted 1,6-Methane[10]annulenes. *J Am Chem Soc* 107:878–887
24. Simonetta M, Barzaghi M, Gatti C (1986) Cyclopropane ring closure in 11,11-Disubstituted 1,6-methano[10]annulenes. *J Mol Struct (THEOCHEM)* 138:39–50
25. Mc Weeney R (1960) Some recent advances in density matrix theory. *Rev Mod Phys* 32:335–369
26. Bader RFW, Stephens ME (1975) Spatial localization of the electronic pair and number distributions in molecules. *J Am Chem Soc* 97:7391–7399
27. Fradera X, Austen MA, Bader RFW (1999) The Lewis model and beyond. *J Phys Chem A* 103:304–314
28. Poater J, Fradera X, Duran M et al (2003) The delocalization index as an electronic aromaticity criterion: application to a series of planar polycyclic aromatic hydrocarbons. *Chem Eur J* 9:400–406
29. Matta CF, Hernández-Trujillo J (2003) Bonding in polycyclic aromatic hydrocarbons in terms of the electron density and of electron delocalization. *J Phys Chem A* 107:7496–7504
30. Kruszewski J, Krygowski TM (1972) Definition of aromaticity basing on the harmonic oscillator model. *Tetrahedron Lett* 13:3839–3842
31. Krygowski TM (1993) Crystallographic studies of inter- and intramolecular interactions reflected in aromatic character of π -electron systems. *J Chem Inf Comput Sci* 33:70–79

32. Elser V, Haddon RC (1987) Icosahedral C₆₀: an aromatic molecule with a vanishingly small ring current magnetic susceptibility. *Nature* 325:792–794
33. Schleyer PVR, Maerker C, Dransfeld A et al (1996) Nucleus-independent chemical shifts: a simple and efficient aromaticity probe. *J Am Chem Soc* 118:6317–6318
34. Bultinck P (2007) Critical analysis of the local aromaticity concept in poly-aromatic hydrocarbons. *Faraday Discuss* 135:347–365 and references therein
35. Katritzky AR, Barczynski Musumarra G et al (1989) Aromaticity as a quantitative concept. 1. A statistical demonstration of the orthogonality of classical and magnetic aromaticity in five- and six-membered heterocycles. *J Am Chem Soc* 111:7–15
36. Gatti C, Saleh G, Lo Presti L et al (2012) Making experiment and theory talking together: electron delocalization effects and non covalent interactions detection *via* the Source Function and the Reduced Density Gradient. In: Abstracts (page 42) of the Sagamore meeting XVII on Charge Spin and Momentum Densities, Daini Meisui Tei, Sapporo, Hokkaido, Japan, 15–20 July 2012
37. Gatti C (2013) New descriptors for an “unbiased” and chemically insightful comparison of ab-initio and X-ray derived charge densities. In: Abstracts of Natta’s Seeds Grow, From the crystallography and modelling of stereoregular polymers to the challenges of complex systems, International symposium on occasion of the 50th anniversary of the award of the Nobel Prize for Chemistry to Giulio Natta and Ziegler, Politecnico di Milano, 21–22 Nov 2013
38. Saleh G (2014) Chemical paradigms seen through charge density descriptor lenses, Ph.D. thesis, Università degli Studi, Milano, Italy
39. Gatti C, Saleh G, Lo Presti L (2015) Source Function applied to experimental densities reveals subtle electron delocalization effects and appraises their transferability properties in crystals. *Acta Cryst B*, invited feature article under review
40. Hendrickson JB, Cram DJ, Hammond GS (1970) *Organic chemistry*, 3rd edn. McGraw-Hill, New York
41. Cysewski P (2011) Influence of thermal vibrations on aromaticity of benzene. *Phys Chem Chem Phys* 13:12998–13008
42. Breslow R (1973) Antiaromaticity. *Acc Chem Res* 6:393–398
43. Pal R, Mukherjee S, Chandrasekhar S et al (2014) Exploring cyclopentadienone antiaromaticity: charge density studies of various tetracyclones. *J Phys Chem A* 118:3479–3489
44. Anslyn EV, Dougherty DA (2006) *Modern physical organic chemistry*. University Science Books
45. Yao T, Yu H, Vermeij RJ et al (2008) Nonplanar aromatic compounds. Part 10: a strategy for the synthesis of aromatic belts—all wrapped up or down the tubes? *Pure Appl Chem* 80:533–546
46. Bodwell GJ, Bridson JN, Cyrański MK et al (2003) Nonplanar aromatic compounds. 8. Synthesis, crystal structures, and aromaticity investigations of the 1, n-Dioxan[n](2,7) pyrenophanes. How does bending affect the cyclic π -electron delocalization of the pyrene system? *J Org Chem* 68:2089–2098
47. Dobrowolski MA, Cyrański MK, Merner BL et al (2008) Interplay of π -electron delocalization and strain in [n](2,7)Pyrenophanes. *J Org Chem* 73:8001–8009
48. Claessens CG, González-Rodríguez D, Rodríguez-Morgade MS et al (2014) Subphthalocyanines, subporphyrines, and subporphyrins: singular nonplanar aromatic systems. *Chem Rev* 114:2192–2277
49. Winstein S, Sonnenberg J, deVries L (1959) The Tris-homocyclopropenyl cation. *J Am Chem Soc* 81:6523–6524
50. IUPAC. Compendium of Chemical Terminology, 2nd ed. (the “Gold Book”). McNaught AD, Wilkinson A (eds) Blackwell Scientific Publications, Oxford (1997). XML on-line corrected version: <http://goldbook.iupac.org> (2006) created by Nic M, Jirat J, Kosata B; updates compiled by Jenkins A. ISBN 0–9678550-9-8. doi:10.1351/goldbook
51. Freeman PK (2005) Neutral homoaromaticity in some heterocyclic systems. *J Org Chem* 70:1998–2001
52. Williams RV, Kurtz HA (1994) Homoaromaticity. *Adv Phys Org Chem* 29:273–331

53. Jorgensen WL (1975) Chemical consequences of orbital interactions. II. Ethylene and butadiene bridged polycyclic hydrocarbons containing three- and four-membered rings. *J Am Chem Soc* 97:3082–3090
54. Jorgensen WL (1976) The energetic impact of monohomoaromaticity. *J Am Chem Soc* 98:6784–6789
55. Haddon RC (1974) Homoaromatic, nonhomoaromatic, antihomoaromatic, and dihomooaromatic character. *Tetrahedron Lett* 2797–2800
56. Haddon RC (1974) The involvement of the cyclobutane ring in homoaromatic conjugation. *Tetrahedron Lett* 15:4303–4304
57. Haddon RC (1975) Perturbational molecular orbital (PMO) theory of homoaromaticity. *J Am Chem Soc* 97:3608–3615
58. Hehre WJ (1973) Homoaromatic stability. *J Am Chem Soc* 95:5807–5809
59. Childs RF, Cremer D, Elia G (1995) Cyclopropyl homoconjugation-experimental facts and interpretations. In: Rappoport Z (ed) *The chemistry of functional groups: the chemistry of the cyclopropyl group*, vol 2. Wiley, Chichester, pp 411–468 and references therein
60. Cremer D, Reichel F, Kraka E (1991) Homotropylium cation: structure, stability, and magnetic properties. *J Am Chem Soc* 113:9459–9466
61. Childs RF (1984) The homotropylium ion and homoaromaticity. *Acc Chem Res* 17:347–352
62. Williams RV (2001) Homoaromaticity. *Chem Rev* 101:1185–1204
63. Minkin VI, Glukhovtsev MN, Simkin BY (1994). Homoaromaticity. Aromaticity and antiaromaticity. Electronic and structural aspects, Chapter 6. Wiley, New York, pp 230–251
64. Reindl B, Clark T, Schleyer PVR (1998) Modern molecular mechanics and ab initio calculations on benzylic and cyclic delocalized cations. *J Phys Chem A* 102:8953–8963
65. Alkorta I, Elguero J, Eckert-Maksič M et al (2004) Influence of the H/F replacement on the homoaromaticity of homotropylium ion: a GIAO/DFT theoretical study. *Tetrahedron* 60:2259–2265
66. Cremer D, Olsson L, Reichel F et al (1993) Calculation of NMR chemical shifts—the third dimension of quantum chemistry. *Isr J Chem* 33:369–385
67. Brown EC, Bader RFW, Werstiuk NH (2009) QTAIM study on the degenerate Cope rearrangements of 1,5-Hexadiene and Semibullvalene. *J Phys Chem A* 113:3254–3265
68. Genaev AM, Sal'nikov GE, Shubin VG (2007) Energy barriers to carousel rearrangements of carbocations: quantum-chemical calculations vs. experiment. *Russ J Org Chem* 43:1134–1138
69. Barzaghi M, Gatti C (1988) Substituent effect on the planarization energy and the relative stability of Winstein and Möbius structures of the homotropylium cation. *J Mol Struct (THEOCHEM)* 167:275–300
70. Godbout N, Salahub DR, Andzelm J et al (1992) Optimization of Gaussian-type basis sets for local spin density functional calculations. Part I. Boron through neon, optimization technique and validation. *Can J Chem* 70:560–571
71. Frisch MJ, Trucks GW, Schlegel HB et al (2009) Gaussian 09, Revision A.1. Gaussian, Inc., Wallingford
72. Gatti C Unpublished result (available upon request)
73. Available from Prof. Bader's RFW Laboratory. McMaster University, Hamilton, Canada L8S 4M1. <http://www.chemistry.mcmaster.ca/aimpac/>
74. Cordero B, Gómez V, Platero-Plats AE et al (2008) Covalent radii revisited. *Dalton Trans* 2832–2838
75. Hill RK, Giberson CB, Silverton JV (1988) Forfeiture of the aromaticity of a Bridged[10] Annulene by benzannulation. *J Am Chem Soc* 110:497–500
76. Mitchell RH (2001) Measuring aromaticity by NMR. *Chem Rev* 101:1301–1316
77. Creary X, Miller KJ (2003) Stabilized and destabilized carbocations in the 1,6-methano[10] annulene series. *J Org Chem* 68:8683–8692
78. Creary X, Miller KJ (2002) 1,6-Methano[10]annulene-stabilized radicals. *Org Lett* 3493–3496
79. Vogel E, Roth HD (1964) Synthese eines cyclodecapentaens. *Angew Chem* 76:145
80. Bianchi R, Pilati T, Simonetta M (1972) A very long carbon-carbon bond in a cyclopropane derivative. *J Chem Soc Chem Commun* 1073–1074

81. Bianchi R, Morosi G, Mugnoli A et al (1973) The influence of substituents on the equilibrium bisnorcaradiene-[10]annulene. The crystal and molecular structure of 11,11-dimethyltricyclo[4,4,1,0^{1,6}]undeca-2,4,7,9-tetraene. *Acta Crystallogr Sect B* 29:1196–1208
82. Bianchi R, Pilati T, Simonetta M (1981) On the equilibrium [10]Annulene \leftrightarrow Bisnorcaradiene. X-ray study of the β -Form of 11-Methyltricyclo[4.4.1.0^{1,6}]undeca-2,4,7,9-tetraene-11-carbonitrile at two temperatures. *J Am Chem Soc* 103:6426–6431
83. Vogel E, Scholl T, Lex J et al (1982) Norcaradiene valence tautomer of a 1,6-Methano[10]annulene:Tricyclo[4.4.1.0^{1,6}]undeca-2,4,7,9-tetraene-11,11-dicarbonitrile. *Angew Chem Int Ed Engl* 21:869–870
84. Caramori GF, Kleber T, Galembeck SE et al (2007) Aromaticity and homoaromaticity in Methano[10]annulenes. *J Org Chem* 72:76–85
85. Bianchi R, Destro R, Merati F (1991) Electrostatic properties and topological analysis of the charge density of syn-1,6:8,13-Biscarbonyl[14]Annulene derived from X-ray diffraction data at 16 K. In: Jeffrey GA, Piniella JF (eds) *The application of charge density research to chemistry and drug design*, vol 250. NATO ASI Series, pp 340–340
86. Ohno H, Chiba D, Matsukura F et al (2000) Electric-field control of ferromagnetism. *Nature* 408:944–946
87. Issadore D, Park YI, Shao H et al (2014) Magnetic sensing technologies for molecular analyses. *Lab Chip* 14:2385–2397
88. Zhang Q, Li B, Chen L (2013) First-principle study of microporous magnets M-MOF-74 (M = Ni Co, Fe, Mn): the role of metal centers. *Inorg Chem* 52:9356–9362
89. Eisenträger A, Vella D, Griffiths IM (2014) Particle capture efficiency in a multi-wire model for high gradient magnetic separation. *Appl Phys Lett* 105:033508
90. Coey JMD (2010) *Magnetism and magnetic materials*. Cambridge University Press, Cambridge
91. Nandi S (2003) Magnetic X-ray scattering. In: *Characterization of materials*. Wiley
92. Shirane G, Shapiro SM, Tranquada JM (2002) *Neutron scattering with a triple-axis spectrometer—basic techniques*. Cambridge University Press, Cambridge
93. Gillon B, Sangregorio C, Caneschi A et al (2007) Experimental spin density in the high spin ground state of the Fe₈pcl cluster. *Inorg Chim Acta* 360:3802–3806
94. Gatti C, Orlando AM, Lo Presti L (2015) Insights on spin polarization through the spin density source function. *Chem. Sci.* 6:3845–3852
95. Pacansky J, Waltman RJ, Barnes RA (1993) Studies on the structure and β -bond scission reactions of primary Alkyl radicals, CH₃(CH₂)_nCH₂O, for n = 1–6. *J Phys Chem* 97:10694–10701
96. Deutsch M, Gillon B, Claiser N et al (2014) First spin-resolved electron distributions in crystals from combined polarized neutron and X-ray diffraction experiments. *IUCrJ* 1:194–199

Chapter 6

Emergent Scalar and Vector Fields in Quantum Chemical Topology

A. Martín Pendás, E. Francisco, A. Gallo Bueno, J.M. Guevara Vela
and A. Costales

Abstract Several potentially useful scalar and vector fields that have been scarcely or even never used to date in Quantum Chemical Topology are defined, computed, and analyzed for a few small molecules. The fields include the Ehrenfest force derived from the second order density matrix, which does not show many of the spurious features encountered when it is computed from the electronic stress tensor, the exchange-correlation (xc) potential, the potential acting on one electron in a molecule, and the additive and effective energy densities. The basic features of the topology of some of these fields are also explored and discussed, paying attention to their possible future interest.

6.1 Introduction

The use of topological approaches in the theory of chemical bonding has become a standard procedure to gain insight on the nature of quantum mechanical binding in all sort of systems, from small molecules to biomolecules or even materials [16, 28, 29]. An outstanding advantage of these techniques over other procedures lies in their invariance under orbital transformations. Being based on quantities derived from real or momentum space density matrices, their physical or chemical interpretation exists

A. Martín Pendás (✉) · E. Francisco · A. Gallo Bueno · J.M. Guevara Vela · A. Costales
University of Oviedo, 33006 Oviedo, Spain
e-mail: angel@fluor.quimica.uniovi.es

E. Francisco
e-mail: evelio@uniovi.es

A. Gallo Bueno
e-mail: gelbehahn@gmail.com

J.M. Guevara Vela
e-mail: jmguevarav@gmail.com

A. Costales
e-mail: costalesmaria@uniovi.es

per se, and does not rely on method-dependent objects, e.g. orbitals. Moreover, topologically derived quantities may be compared smoothly across different levels of theory and, in favourable cases, like when using the electron density as a basic variable, with experiment. Today, it is common to gather all these methods under the umbrella of *Quantum Chemical Topology* (QCT).

Despite the success of these techniques over the years, and the torrent of new information about bonding they have provided, it is our opinion that the vast majority of standard QCT procedures are based on electron probability measures and not on energetically derived properties. In this sense, the electron density itself and its various derivatives (its gradient field or its laplacian), the localization and delocalization indices of the Quantum Theory of Atoms in Molecules (QTAIM) [1], or the source function defined by Bader and Gatti [2] are clear examples. The electron localization function (ELF) of Becke and Edgecombe [3], although reformulated in terms of kinetic energy density excesses by Savin and coworkers [33], was originally introduced in terms of the same spin Fermi hole curvature. Similarly, the restricted space partitioning techniques introduced by Kohout [19–23] leading, for instance, to the Electron Localizability Indicator (ELI), the maximum probability domains (MPD) of Savin and coworkers [6], or the electron distribution functions (EDFs) of Francisco et al. [10, 11, 13, 25] make wide use of first or higher order electron number densities.

In this arena, energetic properties are usually derived by integrating densities over real space domains, and not by examining appropriate scalar or vector fields. Exceptions to this rule exist: the localized orbital locator (LOL) focuses on the topological properties of a kinetic energy density [34], and the QTAIM virial (\mathcal{V}) and energy density (\mathcal{H}) fields are commonly examined at critical points (CPs) of the density. The latter are however computed from the density and its derivatives through the QTAIM's local virial theorem [1], that depends on an arbitrary choice of the kinetic stress tensor [9].

We thus believe that there is still plenty of room to introduce new, or scarcely known, scalar and vector fields in QCT characterized by a solid energetic meaning. We review in this Chapter some possibilities, paying attention to the links that may exist among them as well as with other widely used descriptors. As it will become clear, we will focus on quantities that depend on the two-particle density $\rho_2(\mathbf{r}_1, \mathbf{r}_2)$. This dependence gives rise to implementation and computational difficulties. On the one hand, only wave function methods provide well-defined second order density matrices. This, in principle, leaves density functional theory (DFT) aside, although approximate results obtained with DFT pseudo wave functions have been found to be qualitatively similar to those extracted from costly correlated alternatives. Moreover, the two-particle density is not part of the standard output of conventional electronic structure packages. Given the usefulness that ρ_2 is showing in chemical bonding in the last years [12, 31], we firmly think that this situation should change. On the other hand, quantities based on the pair density intrinsically demand more computing power than those based on the plain electron density. Again, we think that this fact should not preclude their use if they are found to provide unique insights into bonding.

We will consider four scalar and two vector fields that we are starting to explore as potentially useful candidates in QCT studies. The exchange-correlation potential $V_{xc}(\mathbf{r})$, which determines the covalent interaction energy density among electrons at point \mathbf{r} and the rest of the electrons of the system, the potential acting on an electron in a molecule as defined by Zhao and Yang [7, 8] (PAEM), which determines the interaction of an electron belonging to a molecule and the remaining electrons and nuclei, and the additive and effective energy densities $E^{add}(\mathbf{r})$, $E^{eff}(\mathbf{r})$, that provide additive (counting half the interaction of an electron with the rest of the system's particles) and effective (counting them all) energetic contributions of a volume element located at \mathbf{r} to the total energy. All these scalar fields may be subjected to the standard QCT procedure, so their gradients will induce topological partitions of the physical space, providing new sets of critical points, inter-basin surfaces, etc. The vector fields explored are the PAEM force, defined as minus the PAEM gradient, and the Ehrenfest force field, i.e. the force density acting on electrons at \mathbf{r} due to the remaining particles comprising the molecule. Vector fields can also be used to directly determine partitions of the space, as shown in the case of the Ehrenfest field [27].

Since our aim here is presenting the overall features of these quantities, we will focus on their basic properties, showing their basic topological portraits in a small set of archetypal molecules. We will stress the similarities and differences with other known fields, as well as their potential usefulness.

The rest of the Chapter is organized as follows: first we will briefly define all the quantities we will discuss, leaving some technical details for an appendix. Then we will present the behaviour of the scalar and vector fields in a couple of systems, computed at several levels of theory, discussing their similarities and differences. We will end with some conclusions and prospects.

6.2 On QCT Fields Depending on the Pair Density

As shown in the introduction, we have decided to focus in this contribution on some fields that depend on the second order density, $\rho_2(\mathbf{r}_1, \mathbf{r}_2)$. This is an essential ingredient of the molecular energy, entering the electron-electron repulsion. Any total energy index that does not use it relies either on (i) some approximate density functional, or (ii) on a local theorem that allows for a mapping of the two body complexity of the electron-electron interactions onto one body contributions (like the local virial theorem). Since the quantities we will manipulate are related to total energy (or force) components, we will easily recognize in their definitions a set of well known components of the energy: electron-nucleus attraction, electron-electron repulsion, nucleus-nucleus repulsion, and kinetic energy (densities).

In order to ease the comparison among the different quantities that we will introduce, it is instructive to recall two important auxiliary fields that will appear in several of our discussions. The first is the molecular electrostatic potential (MEP),

$V_{\text{mep}}(\mathbf{r})$, widely used in computational chemistry and the theory of chemical reactivity [32]:

$$V_{\text{mep}}(\mathbf{r}) = \sum_B \frac{Z^B}{|\mathbf{r} - \mathbf{R}_B|} - \int \frac{\rho(\mathbf{r}_2)}{|\mathbf{r} - \mathbf{r}_2|} d\mathbf{r}_2, \quad (6.1)$$

where B runs over all the nuclei of the molecule, and Z^B is the nuclear charge of a nucleus at \mathbf{R}_B . It measures the potential energy that a positive test unit charge (not belonging to the molecular system) gains on being transported from infinity to point \mathbf{r} when all geometric and electronic relaxation is quenched. Minus its gradient, the electric field derived from it,

$$\mathbf{E}(\mathbf{r}) = -\nabla V_{\text{mep}}(\mathbf{r}) = \sum_B \frac{Z^B(\mathbf{r} - \mathbf{R}_B)}{|\mathbf{r} - \mathbf{R}_B|^3} - \int \rho(\mathbf{r}_2) \frac{(\mathbf{r} - \mathbf{r}_2)}{|\mathbf{r} - \mathbf{r}_2|^3} d\mathbf{r}_2, \quad (6.2)$$

is equal to the force acting on our test charge at \mathbf{r} .

We will now briefly consider basic notions about the fields we will use, leaving for the Appendix details on the computation of their gradients and/or Hessians which are needed to obtain their topology.

6.2.1 The Exchange-Correlation Potential

The diagonal second-order reduced density matrix (2-RDM) of a molecule, $\rho_2(\mathbf{r}_1, \mathbf{r}_2)$, given by (a summation over the spin variables of all the electrons is implicitly assumed from now on),

$$\rho_2(\mathbf{r}_1, \mathbf{r}_2) = N(N-1) \int d\mathbf{r}_3, \dots, d\mathbf{r}_N \Psi^* \Psi, \quad (6.3)$$

may always be written in the form

$$\rho_2(\mathbf{r}_1, \mathbf{r}_2) = \rho(\mathbf{r}_1)\rho(\mathbf{r}_2) - \rho_{\text{xc}}(\mathbf{r}_1, \mathbf{r}_2), \quad (6.4)$$

where $\rho^C(\mathbf{r}_1, \mathbf{r}_2) = \rho(\mathbf{r}_1)\rho(\mathbf{r}_2)$ is the Coulombic or independent particle part of the pair density and $\rho_{\text{xc}}(\mathbf{r}_1, \mathbf{r}_2)$ defines the exchange-correlation (xc) density. The delocalization index between a pair of real space atoms or fragments A and B of a molecule, δ^{AB} , which is usually taken as the analogous within QCT to the classical covalent bond order used in the molecular orbital paradigm, results from averaging the electrons 1 and 2 of $\rho_{\text{xc}}(\mathbf{r}_1, \mathbf{r}_2)$ over the domains associated to A and B , respectively (Ω_A, Ω_B). Its energetic counterpart, given by an analogous integration

of $-|\mathbf{r}_1 - \mathbf{r}_2|^{-1} \rho_{xc}(\mathbf{r}_1, \mathbf{r}_2)$, is an essential ingredient of the interacting quantum atoms approach (IQA) [5, 15, 26], and has repeatedly been shown to provide a measure of the covalent interaction energy between A and B [14, 17].

Hence, the scalar field $V_{xc}(r)$, defined by

$$V_{xc}(\mathbf{r}) = \int \frac{\rho_{xc}(\mathbf{r}, \mathbf{r}_2)}{|\mathbf{r} - \mathbf{r}_2|} d\mathbf{r}_2, \quad (6.5)$$

and named the xc potential in what follows provides the covalent energy density at \mathbf{r} due to the interaction of the electrons lying in volumen element $d\mathbf{r}$ and the rest of the system. Given that it has been shown that the exchange-correlation energy between two QTAIM domains is clearly linked to the appearance of bond critical points (BCPs) in the ρ field [5, 26], this fact establishing for the first time a direct connection between bond paths and energetic quantities, we expect that the topology of $V_{xc}(\mathbf{r})$ may shed more light on this important problem. To that end, it is also useful to recall that $\int \rho_{xc}(\mathbf{r}, \mathbf{r}_2) d\mathbf{r}_2 = \rho(\mathbf{r})$, so our exchange-correlation potential provides, in a way, a distance weighted density measured in a covalent energy scale.

6.2.2 The Ehrenfest Force

The total potential energy of a molecule, excluding the internuclear repulsion,

$$V = - \sum_i^N \sum_B \frac{Z^B}{|\mathbf{r}_i - \mathbf{R}_B|} + \sum_{i>j}^N \frac{1}{|\mathbf{r}_i - \mathbf{r}_j|}, \quad (6.6)$$

yields the following expression for $-\nabla_I V$, the instantaneous force acting over electron 1,

$$-\nabla_1 V = - \sum_B \frac{Z^B (\mathbf{r}_1 - \mathbf{R}_B)}{|\mathbf{r}_1 - \mathbf{R}_B|^3} + \sum_{i>1} \frac{(\mathbf{r}_1 - \mathbf{r}_i)}{|\mathbf{r}_1 - \mathbf{r}_i|^3}. \quad (6.7)$$

Averaging $-\nabla_1 V$ over the motions (i.e. positions) of electrons 2, 3, ..., N gives

$$\mathbf{F}_e(\mathbf{r}_1) = N \int d\mathbf{r}_2 \dots d\mathbf{r}_N \Psi^\star (-\nabla_1 V) \Psi. \quad (6.8)$$

$\mathbf{F}_e(\mathbf{r}) d\mathbf{r}$ is the force acting over the electrons within the infinitesimal volume $d\mathbf{r}$. It is known as the Ehrenfest force [1], and has been often used within the QTAIM to develop force concepts in chemical bonding studies [18, 30].

The Ehrenfest force owes its popularity to a deep theoretical link with one-body quantities through the electronic stress tensor [1], $\mathbf{F}_e(\mathbf{r}) = -\nabla \cdot \sigma(\mathbf{r})$. The stress

tensor σ may be obtained from the non-diagonal first order density $\rho(\mathbf{r}'; \mathbf{r})$. We have shown, however, that severe errors [27] may be introduced when gaussian basis sets are used to obtain \mathbf{F}_e as a divergence, so direct use of our previous expressions depending on the 2-RDM may alleviate this problem. Be it as it may, there have been scarce studies of the structure and topology of the Ehrenfest field.

Since the probability of finding one and only one of the electrons of the system in volume $d\mathbf{r}$ is $\rho(\mathbf{r})d\mathbf{r}$, $\mathbf{F}_e(\mathbf{r})/\rho(\mathbf{r})$ is a vector field directly comparable with \mathbf{E} , Eq. 6.2. Thus, substituting Eq. 6.7 in Eq. 6.8 and taking into account that the $N - 1$ electrons with $i > 1$ are equivalent to electron 2 gives

$$\mathbf{F}_e(\mathbf{r}_1) = -\rho(\mathbf{r}_1) \sum_B \frac{Z^B(\mathbf{r}_1 - \mathbf{R}_B)}{|\mathbf{r}_1 - \mathbf{R}_B|^3} + \int d\mathbf{r}_2 \frac{\rho_2(\mathbf{r}_1, \mathbf{r}_2)}{|\mathbf{r}_1 - \mathbf{r}_2|^3} (\mathbf{r}_1 - \mathbf{r}_2), \quad (6.9)$$

and using Eq. 6.4

$$\mathbf{F}_e(\mathbf{r}) = \rho(\mathbf{r})\nabla V_{\text{mep}}(\mathbf{r}) + \mathbf{F}_{\text{xc}}(\mathbf{r}) \quad (6.10)$$

$$\mathbf{F}_e(\mathbf{r})/\rho(\mathbf{r}) = -\mathbf{E}(\mathbf{r}) + \frac{\mathbf{F}_{\text{xc}}(\mathbf{r})}{\rho(\mathbf{r})}, \quad \text{where} \quad (6.11)$$

$$\mathbf{F}_{\text{xc}}(\mathbf{r}) = - \int d\mathbf{r}_2 \frac{\rho_{\text{xc}}(\mathbf{r}, \mathbf{r}_2)}{|\mathbf{r} - \mathbf{r}_2|^3} (\mathbf{r} - \mathbf{r}_2). \quad (6.12)$$

Equations 6.10 and 6.11 contain most of the physics of the problem. In the first place, \mathbf{F}_e behaves as $-\mathbf{E}$, since the first is a force over electrons and the second over positive charges. In the second place, the Ehrenfest force is corrected by a term that might be called the xc force, $\mathbf{F}_{\text{xc}}(\mathbf{r})$. The exchange part of this term, as in the case of the exchange energy, serves mainly to eliminate the self-interaction force, i.e. to take properly into account that an electron interacts with the remaining $N - 1$ electrons and not with N electrons. A more direct form to understand this is the following. Given that $\int d\mathbf{r}_2 \rho_{\text{xc}}(\mathbf{r}, \mathbf{r}_2) = \rho(\mathbf{r})$, Eq. 6.12 eliminates, overall, the electron field generated by a single electron. In other words, we add to $-\mathbf{E}(\mathbf{r})$ a term equal to

$$\frac{\mathbf{F}_{\text{xc}}(\mathbf{r})}{\rho(\mathbf{r})} = -\frac{1}{\rho(\mathbf{r})} \int d\mathbf{r}_2 \frac{\rho_{\text{xc}}(\mathbf{r}, \mathbf{r}_2)}{|\mathbf{r} - \mathbf{r}_2|^3} (\mathbf{r} - \mathbf{r}_2) \approx -\frac{(\mathbf{r} - \mathbf{r}_2)}{|\mathbf{r} - \mathbf{r}_2|^3} \quad (6.13)$$

due to a positive charge.

Notice that Eq. 6.12 is not the gradient of Eq. 6.5, contrarily to what we showed between the MEP and the molecular electrostatic field. This is due to the absence of a Hellmann-Feynman-like theorem for the electronic subsystem or, in other words, to the explicit dependence of $\rho_{\text{xc}}(\mathbf{r}, \mathbf{r}_2)$ on \mathbf{r} . This has been the source of some confusion in the past. Similar comments apply to the other quantities that follow.

The Ehrenfest field has already been examined in some test systems, but its relation to \mathbf{E} has been obscure due to the computational problems commented above.

6.2.3 The Potential Acting on an Electron in a Molecule

Zhao and Yang [7, 8] define the potential acting on an electron in a molecule (PAEM) as the interaction energy of a local electron that belongs to the molecule (say electron 1) with all the nuclei and the remaining electrons. The instantaneous Coulomb interaction energy of the first electron at \mathbf{r}_1 with the rest of particles is

$$V_1 = - \sum_B \frac{Z^B}{|\mathbf{r}_1 - \mathbf{R}_B|} + \sum_{i>1}^N \frac{1}{|\mathbf{r}_1 - \mathbf{r}_i|}. \quad (6.14)$$

Averaging $V(\mathbf{r}_1)$ over the positions of all of the remaining electrons in the system gives

$$V'(\mathbf{r}) = \int d\mathbf{r}_2 \dots d\mathbf{r}_N \Psi^* V_1 \Psi, \quad (6.15)$$

which, in terms of $\rho(\mathbf{r})$ and $\rho_2(\mathbf{r}, \mathbf{r}_2)$, reduces to

$$V'(\mathbf{r}) = - \frac{\rho(\mathbf{r})}{N} \sum_B \frac{Z^B}{|\mathbf{r} - \mathbf{R}_B|} + \frac{1}{N} \int \frac{\rho_2(\mathbf{r}, \mathbf{r}_2)}{|\mathbf{r} - \mathbf{r}_2|} d\mathbf{r}_2. \quad (6.16)$$

Since $\rho(\mathbf{r})/N$ measures the probability of finding the first electron at \mathbf{r} and $[N(N-1)]^{-1} \rho_2(\mathbf{r}, \mathbf{r}_2)$ the probability of finding the first electron at \mathbf{r} while the second electron is at \mathbf{r}_2 , the potential acting on an electron at \mathbf{r} is expressed as

$$V_{\text{PAEM}}(\mathbf{r}) = \frac{V'(\mathbf{r})}{\rho(\mathbf{r})/N} = - \sum_B \frac{Z^B}{|\mathbf{r} - \mathbf{R}_B|} + \frac{1}{\rho(\mathbf{r})} \int \frac{\rho_2(\mathbf{r}, \mathbf{r}_2)}{|\mathbf{r} - \mathbf{r}_2|} d\mathbf{r}_2. \quad (6.17)$$

Using again Eq. 6.4 we have

$$V_{\text{PAEM}}(\mathbf{r}) = -V_{\text{mep}}(\mathbf{r}) - \frac{V_{\text{xc}}(\mathbf{r})}{\rho(\mathbf{r})}. \quad (6.18)$$

As pointed out by Zhao et al., the potentials $-V_{\text{mep}}(\mathbf{r})$ and $V_{\text{PAEM}}(\mathbf{r})$ display essential differences. First, $V_{\text{PAEM}}(\mathbf{r})$ describes the interaction energy of an internal electron with the rest of the molecule, while $-V_{\text{mep}}(\mathbf{r})$ represents the interaction

energy of an external unit charge with the whole molecule. Second, $V_{\text{PAEM}}(\mathbf{r})$ contains the xc interaction energy of the target electron with all the other electrons, a quantum effect, while there is no such xc effect in $-V_{\text{mep}}(\mathbf{r})$. Third and finally, the second term in Eq. 6.18 also includes the self-interaction of the considered electron with itself that is canceled by that which is contained in the electronic part of $V_{\text{mep}}(\mathbf{r})$.

Zhao and Yang define the force acting on one electron in a molecule as

$$\mathbf{F}_{\text{PAEM}}(\mathbf{r}) = -\nabla V_{\text{PAEM}}(\mathbf{r}) = \nabla V_{\text{mep}}(\mathbf{r}) + \nabla \left[\frac{V_{\text{xc}}(\mathbf{r})}{\rho(\mathbf{r})} \right]. \quad (6.19)$$

The field $\rho(\mathbf{r})\mathbf{F}_{\text{PAEM}}(\mathbf{r}) \equiv \mathbf{f}_{\text{PAEM}}(\mathbf{r})$ is not equal to the Ehrenfest force given by Eq. 6.10 due to the same Hellmann-Feynman-like problem already put forward, but is closely related to it. A relevant difference between \mathbf{F}_e and \mathbf{F}_{PAEM} is that, while $\mathbf{F}_{\text{PAEM}}(\mathbf{r})$ derives from a potential ($V_{\text{PAEM}}(\mathbf{r})$), $\mathbf{F}_e(\mathbf{r})$ does not. From a physical point of view, the Ehrenfest force is computed by averaging the instantaneous force suffered by one of the electrons over the positions of the remaining electrons, while to obtain $\mathbf{F}_{\text{PAEM}}(\mathbf{r})$ Eq. 6.19 is applied after averaging the potential (Eq. 6.15). For comparative purposes with $V_{\text{mep}}(\mathbf{r})$ and $\mathbf{F}_e(\mathbf{r})$, respectively, the PAEM scalar and vector fields that we will actually compute are $-V_{\text{PAEM}}(\mathbf{r})$ and $\mathbf{f}_{\text{PAEM}}(\mathbf{r})$.

6.2.4 The Additive and Effective Energy Densities

Finally, we will introduce kinetic energy densities to define new scalar fields conveying total energy information. These, as far as we know, have not been used before within QCT, and stem from local forms of IQA global quantities, the atomic (or group) additive and effective energies. The additive energy density (AED) is defined as

$$E^{\text{add}}(\mathbf{r}) = G(\mathbf{r}) - \sum_B \frac{Z^B \rho(\mathbf{r})}{|\mathbf{r} - \mathbf{R}_B|} + \frac{1}{2} \int_{\mathcal{R}^3} \frac{\rho_2(\mathbf{r}_1, \mathbf{r}_2)}{r_{12}} d\mathbf{r}_2 + \frac{1}{2} \sum_{B \neq A} \frac{Z^A Z^B}{R_{AB}} \delta(\mathbf{r} - \mathbf{R}_A), \quad (6.20)$$

where $G(\mathbf{r}) = \frac{\hbar^2}{2m} (\nabla \cdot \nabla') \rho(\mathbf{r}, \mathbf{r}')|_{\mathbf{r}=\mathbf{r}'}$ is the Lagrangian kinetic energy density constructed from $\rho(\mathbf{r}, \mathbf{r}')$, the non-diagonal first-order density matrix, and \mathcal{R}^3 as a subindex in the integral means integration over all the space. The integration of $E^{\text{add}}(\mathbf{r})$ over a region Ω_A containing a single nucleus Z^A at \mathbf{R}_A gives

$$\int_{\Omega_A} E^{\text{add}}(\mathbf{r}) d\mathbf{r} = E^{\text{add}}(\Omega_A) = \int_{\Omega_A} G(\mathbf{r}) - \sum_B Z^B \int_{\Omega_A} \frac{\rho(\mathbf{r})}{|\mathbf{r} - \mathbf{R}_B|} d\mathbf{r} \\ + \frac{1}{2} \int_{\mathcal{R}^3} d\mathbf{r}_2 \int_{\Omega_A} \frac{\rho_2(\mathbf{r}_1, \mathbf{r}_2)}{r_{12}} d\mathbf{r}_1 + \frac{1}{2} \sum_{B \neq A} \frac{Z^A Z^B}{R_{AB}}, \quad (6.21)$$

where $E^{\text{add}}(\Omega_A)$ is the additive energy of region Ω_A within the IQA formalism [5]. The total energy of the system is recovered simply from $E = \sum_A E^{\text{add}}(\Omega_A)$, i.e. by integrating $E^{\text{add}}(\mathbf{r})$ over all space. In other words, $E^{\text{add}}(\mathbf{r}) d\mathbf{r}$ represents the contribution of the volume element $d\mathbf{r}$ at \mathbf{r} to the total energy of the molecule.

The additive energy is constructed to mimic the standard energy density used in the QTAIM, $E_e(\mathbf{r})$, this time without the constraints imposed by the need of the latter to satisfy the virial theorem [1]. It is generally assumed that $E_e(\mathbf{r}) = G(\mathbf{r}) + \mathcal{V}(\mathbf{r})$, where $\mathcal{V}(\mathbf{r})$ is the local virial field, so $E_e(\mathbf{r}) = -K(\mathbf{r})$, the Hamiltonian kinetic energy density.

Closely related to the additive density is the effective energy density, EED, given by Eq. 6.20 where the 1/2 factors that eliminate double counting in the electron–electron and nucleus–nucleus terms have not been taken into account:

$$E^{\text{eff}}(\mathbf{r}) = G(\mathbf{r}) - \sum_B \frac{Z^B \rho(\mathbf{r})}{|\mathbf{r} - \mathbf{R}_B|} + \int_{\mathcal{R}^3} \frac{\rho_2(\mathbf{r}, \mathbf{r}_2)}{|\mathbf{r} - \mathbf{r}_2|} d\mathbf{r}_2 + \sum_{B \neq A} \frac{Z^A Z^B}{R_{AB}} \delta(\mathbf{r} - \mathbf{R}_A) \quad (6.22)$$

The EED is a measure of the local energy density of volume element $d\mathbf{r}$, and plays a role similar to the orbital energy of an electron described by a given spinorbital. Actually, $E^{\text{eff}}(\mathbf{r})/\rho(\mathbf{r})$ is a local orbital energy. It is also clear that EED integrated over an atomic (or fragment) domain will lead to the IQA group effective energy, $E^{\text{eff}}(\Omega_A)$. Differences in atomic group effective energies are key to understand chemical changes, so we expect that changes in local EEDs will give information about local energy reorganizations in chemical processes.

Remembering the definition of the MEP, Eq. 6.1, and using Eq. 6.4, $E^{\text{eff}}(\mathbf{r})$ transforms to

$$E^{\text{eff}}(\mathbf{r}_1) = G(\mathbf{r}_1) - V_{\text{mep}}(\mathbf{r}_1)\rho(\mathbf{r}_1) - V_{\text{xc}}(\mathbf{r}_1) + \sum_{B \neq A} \frac{Z^A Z^B}{R_{AB}} \delta(\mathbf{r}_1 - \mathbf{R}_A). \quad (6.23)$$

As we can see from Eq. 6.18, $\rho(\mathbf{r})V_{\text{PAEM}}(\mathbf{r}) = -V_{\text{mep}}(\mathbf{r})\rho(\mathbf{r}) + V_{\text{xc}}(\mathbf{r})$, so that $E^{\text{eff}}(\mathbf{r})$ can be equally written as

$$E^{\text{eff}}(\mathbf{r}) = G(\mathbf{r}) + \rho(\mathbf{r})V_{\text{PAEM}}(\mathbf{r}) + \sum_{B \neq A} \frac{Z^A Z^B}{R_{AB}} \delta(\mathbf{r} - \mathbf{R}_A). \quad (6.24)$$

The quantity $\int d\mathbf{r} \rho(\mathbf{r})V_{\text{PAEM}}(\mathbf{r})$ represents the total potential energy of the electrons in the volume element $d\mathbf{r}$.

6.3 Computational Details and Studied Systems

We will now turn to show the general properties of the scalar and vector fields presented in the last Section. Our purpose here is not that of systematizing, but just picking some very simple systems where we will compare the fields with each other when relevant, or show their shape and basic topology.

All the scalar and vector fields defined in Sect. 6.2, as well as their gradients and Hessians, were computed with our PROMOLDEN code [24]. All the electronic structure calculations were performed with a domestic version of the GAMESS code [35].

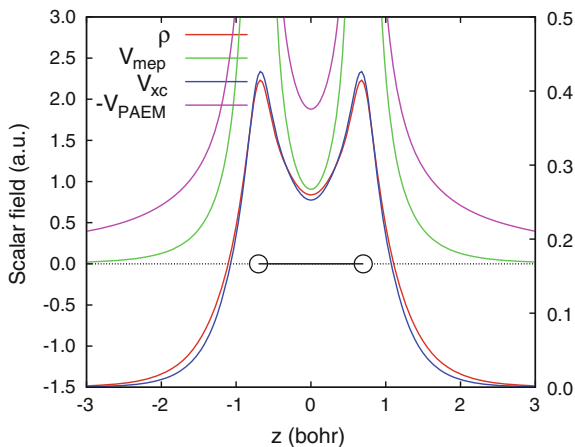
We will start considering a simple correlated description of the H_2 molecule, where the basic features of the fields will be presented. Then we will show to what extent these features are general by examining the ethylene molecule at the Hartree-Fock level.

6.4 Results and Discussion

6.4.1 The Dihydrogen Molecule

We will briefly discuss here the basic structure of the fields in the prototype H_2 molecule, computed at a simple CAS[2,2]//6-311G level. Figure 6.1 shows a comparison of the density, MEP, PAEM and the x_c potentials along the internuclear

Fig. 6.1 Density, MEP, x_c , and PAEM potentials depicted along the internuclear axis for the H_2 molecule computed at the CAS[2,2]//6-311G level. V_{xc} and ρ should be read on the right axis



axis. All these scalars show extrema (which may rise to infinity) at the nuclear positions, so we may topologically consider these as attractors of their gradient fields. We should notice that, as well known, the position of the attractors in the density, and in this case also in the x_c potential, do not exactly coincide with the nuclear positions in the case of H atoms whenever finite gaussian basis sets are used. This are artifacts of the modeling.

Several interesting facts stand out. First, it is rather interesting that ρ and V_{xc} are not only alike, but strikingly similar. Although the relation between the exchange-correlation density and the density has already been pointed out, the role of the r_{12}^{-1} weight seems small. This is a non-trivial result that we have found pretty general. $V_{xc}(\mathbf{r})$, a covalent energy density, is close to quantitatively equal to the density. As we will show below, its critical points are also extremely close to those of the density. Although the validity of these assertions demands further work, we think that these results reinforce the energetic link between the BCPs of the QTAIM and the exchange-correlation channels that was found in our previous work on the interatomic exchange-correlation energies [5, 26].

We must also comment on the (di)similarities between the MEP and the PAEM potentials. As expected the impact of considering the potential felt by an electron of the molecule, or that felt by a test charge is considerable in a two electron system. In both cases, the electron-nucleus interaction dominates, being counteracted by electron-electron contributions of two and one electrons, respectively, as shown in Eqs. 6.1 and 6.17. This leads to similar portraits but larger PAEM values in this system.

Figure 6.2 contains a visual summary of the vector fields along the internuclear axis. In the first place, all of these fields lead to topologically equivalent gradient portraits. Nuclei are attractors, and the only other critical point is the standard $(3, -1)$ BCP of the density, at the midpoint along the nuclear axis. Therefore, all the

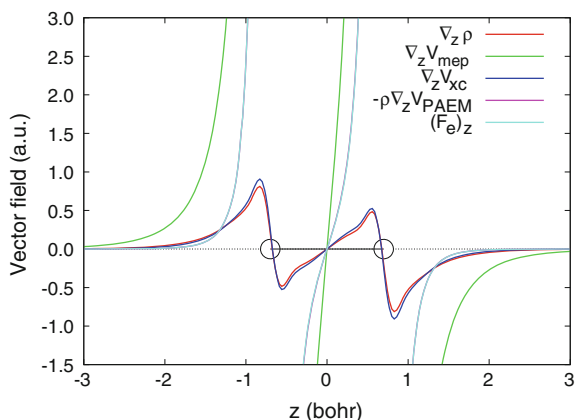
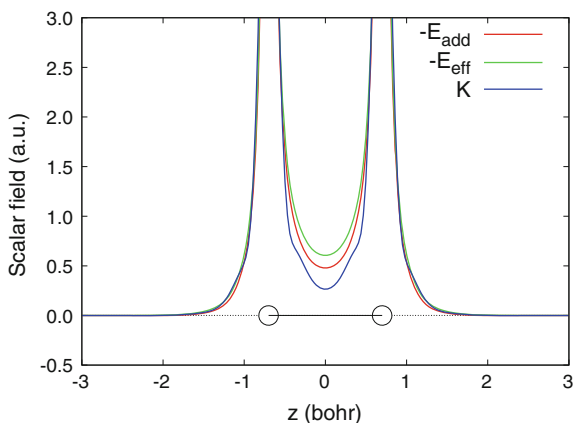


Fig. 6.2 z component of the Density, MEP, x_c , and PAEM gradients together with the Ehrenfest field along the internuclear axis for the H_2 molecule computed at the CAS[2,2]/6-311G level. The $(F_e)_z$ and $-\rho\nabla_z V_{PAEM}$ curves practically coincide

Fig. 6.3 Additive, Effective, and Hamiltonian kinetic energy densities along the internuclear axis for the H_2 molecule computed at the CAS[2,2]/6-311G level



fields provide the same partition of the space. Secondly, the density scaled gradient of the PAEM and the Ehrenfest force are almost coincident. Their difference is due to the Hellmann-Feynman imbalance commented before, very small in this system. This means that although strictly speaking \mathbf{F}_e is not a gradient field, the PAEM potential may be used as an approximate potential for it. Thirdly, both the gradients of the density and the xc potential are again extremely similar.

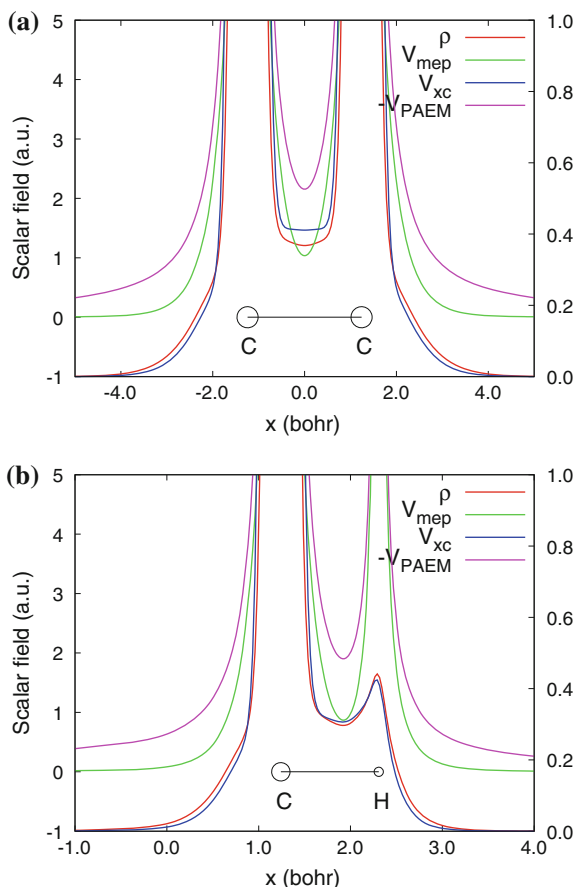
Finally, Fig. 6.3 depicts the additive and effective energy densities together with the Hamiltonian kinetic energy density along the internuclear axis. Although not clear on the figure scale, the three quantities change sign at large distances. Close enough to the nuclei the three energies are stabilizing, and it is clear that the internuclear region boosts binding, since it is in this part where the energy densities are clearly more stabilizing than what we would get from the superposition of free hydrogen atoms. Notice that both the effective energy and $-K(\mathbf{r})$ integrate to the same total electronic molecular energy.

6.4.2 The Ethylene Molecule

In this subsection we will show that the above results are of quite general validity. We have chosen the C_2H_4 system, computed at the HF//TZV(3d,p)++ level. Figure 6.4 contains the density as well as the MEP, xc , and PAEM potentials along the C–C and C–H internuclear axes. Our previous conclusions can be repeated almost exactly here, stressing the similarity between the xc potential and the electron density. The gradient fields show again the great similarity between the Ehrenfest and PAEM forces.

We also show in Fig. 6.5 the gradient field portraits of just two of our fields: the xc gradient and the Ehrenfest field. As it can be seen, both display the same topology, with six attractors at nuclear positions and $(3, -1)$ critical points along the C–C and C–H lines. Both provide an atomic-like partition of the space. Moreover,

Fig. 6.4 Density, MEP, x_c , and PAEM potentials depicted along the C–C (a), and C–H (b) internuclear lines for the C_2H_4 molecule computed at the HF//TZV(3d, p)++ level. V_{xc} and ρ should be read on the right axis



the position of the C–H BCPs (the C–C one is determined by symmetry) hardly varies upon changing the field. This can better be grasped from Table 6.1, where the bonded radius of the C atom is displayed for our fields.

It is perhaps more interesting to examine the effective and additive energy densities. Figure 6.6 shows them along the C–C and C–H lines together with $K(\mathbf{r})$ and $\nabla^2\rho(\mathbf{r})$. First, we should notice that these densities have laplacian-like behavior. This is here a much more clear feature than in the H_2 case, where only one shell exists. It is also notorious that the qualitative behavior of K follows that of E^{add} . The latter shows bonded energy concentrations similar to the bonded charge concentrations of the laplacian field. As before, the generality of these results is to be determined in future works. If confirmed, another energetic-like link, this time between an energy density and the laplacian of the electron density would have been uncovered. Figure 6.7 shows the -1.5 and -0.5 a.u. isosurfaces of E^{add} and $\nabla^2\rho$ in ethylene. Notice that the number and type of the critical points in the valence region coincides for the two fields.

Fig. 6.5 xc (top), and Ehrenfest (bottom) gradient portraits for the C_2H_4 molecule in the molecular plane

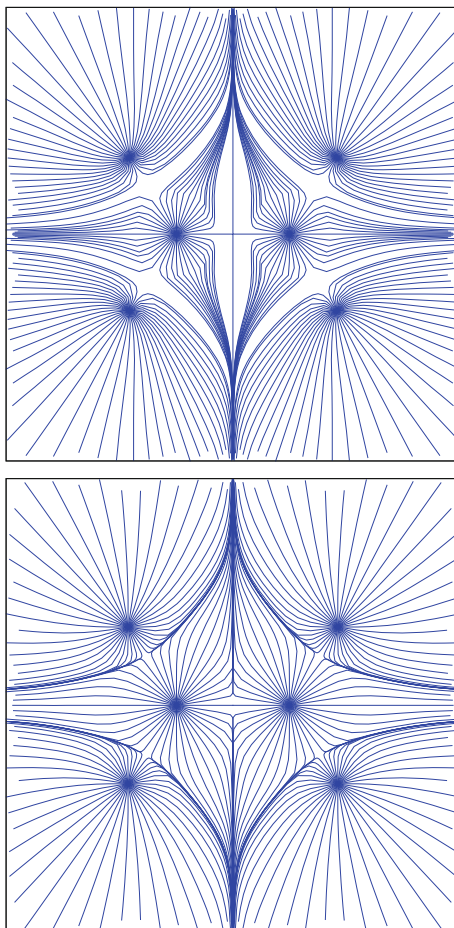


Table 6.1 Carbon bonded radii along the C–H line for different fields in the C_2H_4 molecule

Field	C radius	Vector field	C radius
$\nabla\rho$	1.291	$-\rho\nabla V_{\text{PAEM}}$	1.295
∇V_{mep}	1.297	∇V_{xc}	1.278
F_e^*	1.326	$F_e(\mathbf{r})$	1.293

All the nuclear CPs except the 3, -3 CPs of the hydrogen atoms corresponding to $\nabla\rho(\mathbf{r})$ and $\nabla V_{\text{xc}}(\mathbf{r})$ coincide with the nuclear positions. The latter are displaced 0.033 and 0.018 bohr towards the C nucleus, respectively. $F_e(\mathbf{r})^*$ and $F_e(\mathbf{r})$ are the Ehrenfest force derived from the quantum stress tensor and Eq. 6.10, respectively. All distances in a.u

Fig. 6.6 Additive, Effective, Hamiltonian kinetic energy densities, together with the laplacian of the density along the C–C (a), and C–H (b) internuclear lines for the C_2H_4 molecule computed at the HF/TZV(3d,p)++ level

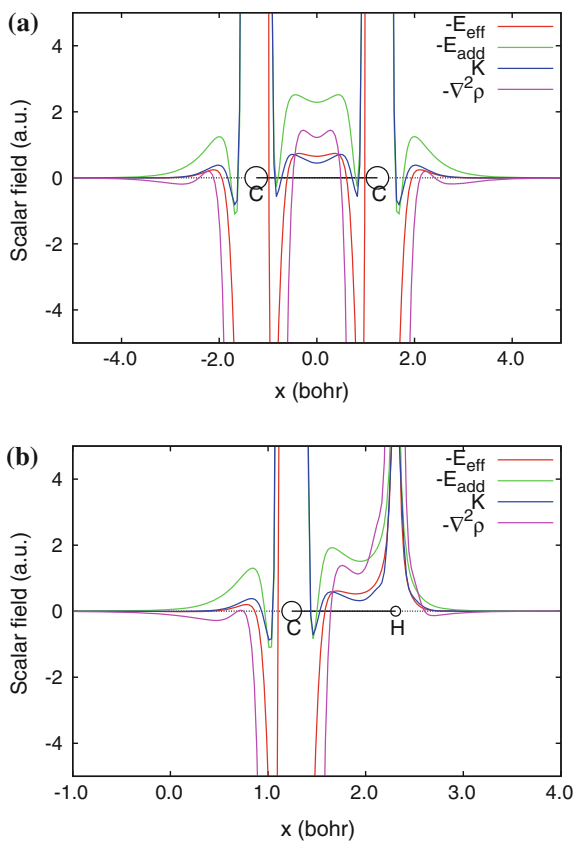
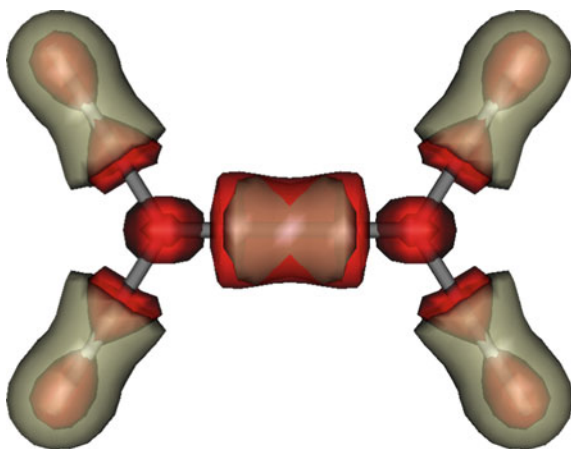


Fig. 6.7 -1.5 and -0.5 a.u. isosurfaces of E^{add} (red) and $\nabla^2\rho$ (greenish) in ethylene



6.5 Summary and Conclusions

We have briefly reviewed here some scalar and vector fields that might play a significant role in future developments of Quantum Chemical Topology. In this contribution we have focused on some scalar densities and forces that depend on the pair density, thus delivering direct information on electron-electron interactions. Several interesting conclusions have emerged. On the one hand, we have shown that the gradient of the potential acting on an electron in a molecule (PAEM) defined by Zhao and Yang is strikingly similar to the Ehrenfest force. This means that the absence of a Hellmann-Feynman link between both does not affect qualitatively their shape. Another potentially important discovery is the semi-quantitative similarity between the exchange-correlation potential and the electron density. We believe that this reinforces the link between covalency and topology, paving the way to future studies that definitively link energetic properties to the electron density topology. Our other energetic scalars, the additive and effective energy densities, have also shown intriguing connections to several well-known fields. The former, for instance, integrates to the total molecular energy, and is locally similar to minus the Hamiltonian kinetic energy density, that does also integrate to E at stationary points on potential energy surfaces. As the exchange-correlation potential mimics the density from the energetic side, the additive energy density mimics the Laplacian. Future works will determine the role that these functions may play in chemical bonding theory.

Acknowledgements The authors acknowledge the financial support from the Spanish MICINN, Project CTQ2012-31174. AGB also acknowledges FICYT for a Ph.D. grant (BP 11-127).

Appendix

Here, we give some details regarding the calculation of the different scalar and vector fields defined in Sect. 6.2, as well as of their gradients and Hessians. In all of the following expressions, $\nabla f(\mathbf{r})$ and $\mathbf{V}^t f(\mathbf{r})$ represent the gradient of the scalar field $f(\mathbf{r})$ in row and column forms, respectively, $\mathbf{V}^t \mathbf{V} f(\mathbf{r})$ is the 3×3 array of the second derivatives of $f(\mathbf{r})$, and $\mathbf{V}^t f(\mathbf{r}) \mathbf{V} g(\mathbf{r})$ is the 3×3 array that results from the matrix product of the column vector $\mathbf{V}^t f(\mathbf{r})$ with the row vector $\mathbf{V} g(\mathbf{r})$. All the integrals involving the molecular orbitals (MOs) were evaluated using the McMurchie-Davidson algorithm as implemented in the PROMOLDEN code.

The xc potential, $\rho^{xc}(\mathbf{r}_1, \mathbf{r}_2)$, can be written in terms of a set of m real MOs φ_i ($i = 1, \dots, m$) in the form

$$\rho^{xc}(\mathbf{r}_1, \mathbf{r}_2) = \sum_{p \geq q} \sum_{r \geq s} \lambda_{pq,rs} \varphi_p(\mathbf{r}_1) \varphi_q(\mathbf{r}_1) \varphi_r(\mathbf{r}_2) \varphi_s(\mathbf{r}_2), \quad (6.25)$$

where the array λ is symmetric in the (pq) and (rs) pairs. To compact the notation, we will collect the pair of indices p and q with $p \geq q$ in a single index i , and the product $\varphi_p(\mathbf{r})\varphi_q(\mathbf{r})$ will be represented as $\phi_i(\mathbf{r})$. Then

$$\rho^{\text{xc}}(\mathbf{r}_1, \mathbf{r}_2) = \sum_{ij} \lambda_{ij} \phi_i(\mathbf{r}_1) \phi_j(\mathbf{r}_2). \quad (6.26)$$

Although it is not strictly necessary, it is convenient for our purposes to diagonalize λ and express $\rho^{\text{xc}}(\mathbf{r}_1, \mathbf{r}_2)$ in the form

$$\rho^{\text{xc}}(\mathbf{r}, \mathbf{r}_2) = \sum_i \eta_i G_i(\mathbf{r}) G_i(\mathbf{r}_2), \quad (6.27)$$

where η_i are the eigenvalues of λ ,

$$G_i(\mathbf{r}) = \sum_j d_{ji} \phi_j(\mathbf{r}), \quad (6.28)$$

and $(d_{1i}, d_{2i}, \dots) \equiv \mathbf{d}_i$ is the i th eigenvector of λ . This is the usual way of proceed in the PROMOLDEN program to facilitate the numerical evaluation of all the integrals that appear within the Interacting Quantum Atoms (IQA) method. Substituting 6.27 into Eq. 6.5 we have

$$V_{\text{xc}}(\mathbf{r}) = \sum_i \eta_i G_i(\mathbf{r}) \int d\mathbf{r}_2 \frac{G_i(\mathbf{r}_2)}{|\mathbf{r} - \mathbf{r}_2|} = \sum_i \eta_i G_i(\mathbf{r}) V_{G_i}(\mathbf{r}). \quad (6.29)$$

The gradient of $V_{\text{xc}}(\mathbf{r})$ is

$$\nabla V_{\text{xc}}(\mathbf{r}) = \sum_i \eta_i G_i(\mathbf{r}) \nabla V_{G_i}(\mathbf{r}) + \sum_i \eta_i V_{G_i}(\mathbf{r}) \nabla G_i(\mathbf{r}) \quad (6.30)$$

The three components of $\nabla G_i(\mathbf{r})$ can be obtained simply by deriving Eq. 6.28. On the other hand, from the definition of $V_{G_i}(\mathbf{r})$ in Eq. 6.29 we have

$$\nabla V_{G_i}(\mathbf{r}) = - \int d\mathbf{r}_2 \frac{G_i(\mathbf{r}_2)(\mathbf{r} - \mathbf{r}_2)}{|\mathbf{r} - \mathbf{r}_2|^3} \quad (6.31)$$

From the definition of $F_{\text{xc}}(\mathbf{r})$ in Eqs. 6.12 and 6.27 we also have

$$\mathbf{F}_{\text{xc}}(\mathbf{r}) = - \sum_i \eta_i G_i(\mathbf{r}) \int d\mathbf{r}_2 \frac{G_i(\mathbf{r}_2)(\mathbf{r} - \mathbf{r}_2)}{|\mathbf{r} - \mathbf{r}_2|^3} = \sum_i \eta_i G_i(\mathbf{r}) \nabla V_{G_i}(\mathbf{r}), \quad (6.32)$$

so that

$$\nabla V_{\text{xc}}(\mathbf{r}) = \mathbf{F}_{\text{xc}}(\mathbf{r}) + \sum_i \eta_i V_{G_i}(\mathbf{r}) \nabla G_i(\mathbf{r}). \quad (6.33)$$

It is important to note that, according to the above equations, $\mathbf{F}_{\text{xc}}(\mathbf{r}) \neq \nabla V_{\text{xc}}(\mathbf{r})$. The Hessian of $V_{\text{xc}}(\mathbf{r})$ is obtained by simply deriving Eq. 6.33:

$$\nabla^t \nabla V_{\text{xc}}(\mathbf{r}) = \mathbf{H}_{\text{xc}}(\mathbf{r}) + \sum_i \eta_i [\nabla^t G_i(\mathbf{r}) \nabla V_{G_i}(\mathbf{r}) + V_{G_i}(\mathbf{r}) \nabla^t \nabla G_i(\mathbf{r})], \quad (6.34)$$

where $(\mathbf{H}_{\text{xc}})_{\alpha\beta} \equiv (\partial F_{\text{xc},\alpha} / \partial \beta)$. From Eq. 6.32 one has

$$\mathbf{H}_{\text{xc}} = \sum_i \eta_i [\nabla^t V_{G_i}(\mathbf{r}) \nabla G_i(\mathbf{r}) + G_i(\mathbf{r}) \nabla^t \nabla V_{G_i}(\mathbf{r})], \quad \text{with} \quad (6.35)$$

$$\nabla^t \nabla V_{G_i}(\mathbf{r}) = \int d\mathbf{r}_2 \frac{G_i(\mathbf{r}_2)}{|\mathbf{r} - \mathbf{r}_2|^5} \left[3(\alpha - \alpha_2)(\beta - \beta_2) - \delta_{\alpha\beta} |\mathbf{r} - \mathbf{r}_2|^2 \right]. \quad (6.36)$$

Regarding the Ehrenfest force, $\mathbf{F}_e(\mathbf{r})$, calling $(\mathbf{H})_{e,\alpha\beta} \equiv H_{e,\alpha\beta} = (\partial F_{e,\alpha} / \partial \beta)$, one easily obtains from Eq. 6.10

$$\mathbf{H}_e(\mathbf{r}) = \rho(\mathbf{r}) \nabla^t \nabla V_{\text{mep}}(\mathbf{r}) + \nabla^t V_{\text{mep}}(\mathbf{r}) \nabla \rho(\mathbf{r}) + \mathbf{H}_{\text{xc}}(\mathbf{r}) \quad (6.37)$$

The exact relationship between $\mathbf{F}_e(\mathbf{r})$ and $\mathbf{f}_{\text{PAEM}}(\mathbf{r}) = \rho(\mathbf{r}) \mathbf{F}_{\text{PAEM}}(\mathbf{r})$, obtained by explicitly computing the gradient $\nabla(V_{\text{xc}}/\rho)$ that appears in Eq. 6.19, is

$$\mathbf{f}_{\text{PAEM}}(\mathbf{r}) = \mathbf{F}_e(\mathbf{r}) - \frac{V_{\text{xc}}(\mathbf{r})}{\rho(\mathbf{r})} \nabla \rho(\mathbf{r}) + \sum_i \eta_i V_{G_i}(\mathbf{r}) \nabla G_i(\mathbf{r}). \quad (6.38)$$

As a consequence of the last term in Eq. 6.38 the expression for \mathbf{H}_{PAEM} , defined as $(\mathbf{H}_{\text{PAEM}})_{\alpha\beta} = (\partial \mathbf{f}_{\alpha, \text{PAEM}}(\mathbf{r}) / \partial \beta)$ is a little bit cumbersome:

$$\begin{aligned} \mathbf{H}_{\text{PAEM}} = & \mathbf{H}_e - \frac{V_{\text{xc}}}{\rho} \nabla^t \nabla \rho - \frac{(\nabla^t \rho) F_{\text{xc}}}{\rho} + \frac{V_{\text{xc}}}{\rho^2} \nabla^t \rho \nabla \rho \\ & - \frac{\nabla^t \rho}{\rho} \sum_i \eta_i V_{G_i} \nabla G_i + \sum_i \eta_i [(\nabla^t G_i)(\nabla V_{G_i}) + V_{G_i} \nabla^t \nabla G_i]. \end{aligned} \quad (6.39)$$

The gradient and Hessian of $E_{\text{eff}}(\mathbf{r})$, Eq. 6.23, are given by

$$\nabla E_{\text{eff}} = \nabla G - \rho \nabla V_{\text{mep}} - V_{\text{mep}} \nabla \rho - \nabla V_{\text{xc}}, \quad (6.40)$$

$$\begin{aligned}\nabla^t \nabla E_{\text{eff}} &= \nabla^t \nabla G - \rho \nabla^t \nabla V_{\text{mep}} - \nabla^t V_{\text{mep}} \nabla \rho - V_{\text{mep}} \nabla^t \nabla \rho \\ &\quad - \nabla^t \rho \nabla V_{\text{mep}} - \nabla^t \nabla V_{\text{xc}}.\end{aligned}\quad (6.41)$$

where $\nabla^t \nabla V_{\text{xc}}(\mathbf{r})$ is given by Eq. 6.34 The gradient and Hessian of $E_{\text{add}}(\mathbf{r})$, Eq. 6.20, are even more complicated:

$$\begin{aligned}\nabla E_{\text{add}} &= \nabla G - \rho \nabla V_{\text{mep}}^{\text{nuc}} - V_{\text{mep}}^{\text{nuc}} \nabla \rho \\ &\quad - \frac{1}{2} \left[\rho \nabla V_{\text{mep}}^{\text{ele}} + V_{\text{mep}}^{\text{ele}} \nabla \rho + \mathbf{F}_{\text{xc}} \right] - \frac{1}{2} \sum_i \eta_i V_{G_i} \nabla G_i,\end{aligned}\quad (6.42)$$

$$\begin{aligned}\nabla^t \nabla E_{\text{add}} &= \nabla^t \nabla G - \rho \nabla^t \nabla V_{\text{mep}}^{\text{nuc}} - \nabla^t V_{\text{mep}}^{\text{nuc}} \nabla \rho - V_{\text{mep}}^{\text{nuc}} \nabla^t \nabla \rho - \nabla^t \rho \nabla V_{\text{mep}}^{\text{nuc}} \\ &\quad - \frac{1}{2} \left[\mathbf{H}_{\text{xc}} + \rho \nabla^t \nabla V_{\text{mep}}^{\text{ele}} + \nabla^t V_{\text{mep}}^{\text{ele}} \nabla \rho + V_{\text{mep}}^{\text{ele}} \nabla^t \nabla \rho + \nabla^t \rho \nabla V_{\text{mep}}^{\text{ele}} \right] \\ &\quad - \frac{1}{2} \sum_i \eta_i [\nabla^t G_i \nabla V_{G_i} + V_{G_i} \nabla^t \nabla G_i].\end{aligned}\quad (6.43)$$

To shorten Eqs. 6.39–6.43, the dependence on \mathbf{r} of every magnitude has been avoided.

References

1. Bader RFW (1990) Atoms in molecules. Oxford University Press, Oxford
2. Bader RFW, Gatti C (1998) Chem Phys Lett 287:233–238
3. Becke AD, Edgecombe KE (1990) A simple measure of electron localization in atomic and molecular systems. J Chem Phys 92:5397–5403
4. Berlin T (1951) J Chem Phys 19:208–213
5. Blanco MA, Martín Pendás A, Francisco E (2005) J Chem Theory Comput 1:1096–1109
6. Cancès E, Keriven R, Lodier F, Savin A (2004) Theoret Chem Acc 111:373–380
7. Dong-Xia Z, Li-Dong G, Zhong-Zhi Y (2005) J Phys Chem 109:10121–10128
8. Dong-Xia Z, Zhong-Zhi Y (2014) J Comput Chem 35:965–977
9. Finzel K (2014) Int J Quantum Chem 114(9):568–576
10. Francisco E, Martín Pendás A, Blanco MA J Chem Phys 126
11. Francisco E, Martín Pendás A, Blanco MA (2008) Comput Phys Commun 178:621–634
12. Francisco E, Martín Pendás A, García-Revilla M (2013) Comput Theoret Chem 1003:71–78
13. Francisco E, Pendás M (2014) Comput Phys Commun 185:2663–2682
14. García-Revilla M, Francisco E, Popelier PLA, Martín Pendás A (2013) Chem Phys Chem 14:1211–1218
15. García-Revilla M, Popelier PLA, Francisco E, Martín Pendás A (2011) J Chem Theory Comput 7:1704–1711
16. Gatti C, Macchi P (eds) (2012) Modern charge-density analysis. Springer, Dordrecht
17. Guevara-Vela JM, Chávez-Calvillo R, García-Revilla M, Hernández-Trujillo J, Christiansen O, Francisco E, Martín Pendás A (2013) Chem Eur J 19, 14:304–14,315
18. Hernandez-Trujillo J, Cortés-Guzman F, Fang DC, Bader RFW (2007) Faraday Discuss 135:79–95
19. Kohout M (2004) A measure of electron localizability. Int J Quantum Chem 97:651–658

20. Kohout M (2007) Bonding indicators from electron pair density functionals. *Faraday Discuss* 135:43–54
21. Kohout M, Pernal K, Wagner FR, Grin Y (2004) Electron localizability indicator for correlated wavefunctions. i. parallel-spin pairs. *Theoret Chem Acc* 112:453–459
22. Kohout M, Pernal K, Wagner FR, Grin Y (2005) Electron localizability indicator for correlated wavefunctions. ii antiparallel-spin pairs. *Theoret Chem Acc* 113:287–293
23. Kohout M, Wagner FR, Grin Y (2008) Electron localizability indicator for correlated wavefunctions. iii: singlet and triplet pairs. *Theoret Chem Acc* 119:413–420
24. Martín Pendás A, Francisco E Promolden. a qtaim/iqa code (unpublished). A QTAIM/IQA code (Unpublished)
25. Martín Pendás A, Francisco E, Blanco MA *J Chem Phys* 127
26. Martín Pendás A, Francisco E, Blanco MA, Gatti C (2007) *Chem Eur J* 13:9362–9371
27. Martín Pendás A, Hernández-Trujillo J (2012) *J Chem Phys* 137, 134:101–1–134,101–9
28. Matta CF (ed) (2010) *Quantum biochemistry*. Wiley-VCH Verlag GmbH & Co. KGaA
29. Matta CF, Boyd RJ (eds): *The Quantum Theory of Atoms in Molecules*. Wiley-VCH Verlag GmbH & Co. KGaA (2007)
30. Maza JR, Jenkins S, Steven RK, Anderson JSM, Ayers PW (2013) *Phys Chem Chem Phys* 15:17823–17836
31. Menéndez M, Álvarez Boto R, Francisco E, Martín Pendás A (2015) *J Comput Chem* xxx, xxxx–xxxx
32. Murray KS, Sen K (eds) (1996) *Molecular electrostatic potentials: concepts and applications*, Elsevier
33. Savin A, Jepsen O, Flad J, Andersen OK, Preuss H, von Schnering HG (1992) *Angew Chem Int Ed Engl* 31:187–188
34. Schmider HL, Becke AD (2002) *J Chem Phys* 116(8):3184–3193
35. Schmidt MW, Baldrige KK, Boatz JA, Elbert ST, Gordon MS, Jensen JH, Koseki S, Matsunaga N, Nguyen KA, Su SJ, Windus TL, Dupuis M, Montgomery JA (1993) *J Comput Chem* 14:1347

Chapter 7

Topology of Quantum Mechanical Current Density Vector Fields Induced in a Molecule by Static Magnetic Perturbations

P. Lazzeretti

Abstract It is shown that the quantum mechanical theory of static magnetic properties can be reformulated in terms of electronic current densities induced by an external magnetic field and permanent magnetic dipole moments at the nuclei. Theoretical relationships are reported to evaluate magnetizability, nuclear magnetic shielding and nuclear spin-spin coupling via the equations of classical electromagnetism, assuming that the current density is evaluated by quantum mechanical methods. Emphasis is placed on the advantage of the proposed formulation, as an alternative to procedures based on perturbation theory, as regards interpretation of response allowing for the ideas of current density tensor and current susceptibility vector. Visualisation of the electronic interaction with a magnetic field and intramolecular perturbations, e.g., nuclear magnetic dipoles, is made possible via current density maps, nuclear shielding density maps and plots of nuclear spin-spin coupling density. Topological analysis of the quantum mechanical current density in terms of Gomes stagnation graphs is shown to yield fundamental information for understanding magnetic response. Examples are given for a few archetypal molecules. A topological definition of delocalized electron currents is proposed.

Keywords Electronic current densities induced by magnetic fields and nuclear magnetic dipoles · Molecular magnetic response · Property densities · Gauge invariance · Charge conservation · Current density vectors and current density tensors · Current susceptibility vectors · Topology of current density vector fields · Bifurcations · Topological definition of ring current

P. Lazzeretti (✉)
Dipartimento di Scienze chimiche e geologiche,
Università degli Studi di Modena e Reggio Emilia,
Via Campi 213/b, 41125 Modena, Italy
e-mail: lazzeret@unimore.it

7.1 Introduction

The magnetic response of diamagnetic atoms, molecules and clusters, i.e., typical quantum mechanical systems, can be effectively interpreted and visualized via the laws of classical electrodynamics, allowing for functions of position \mathbf{r} which describe the electronic charge density $\rho(\mathbf{r})$, a scalar property, and the electronic current density $\mathbf{J}(\mathbf{r})$, a vector field, evaluated by quantum mechanical methods.

An introduction to magnetic properties merging classical relationships with quantum mechanical computational recipes constitutes a *trait d'union* between classical and quantum mechanics rather interesting from the epistemological point of view. In fact, $\rho(\mathbf{r})$ and $\mathbf{J}(\mathbf{r})$ are *subobservables* [1], that is, expectation values of corresponding quantum mechanical operators: if these expectation values are known as functions in \mathbb{R}^3 , a number of molecular electromagnetic properties can be evaluated without the explicit use of electronic wave functions.

The central aim of this chapter is to give a simple, self-contained approach to a set of molecular magnetic properties in terms of induced current densities and related property density maps, via classical relationships combined with quantum mechanical definitions, and computational procedures. Some efforts are made to document the effectiveness of such a theoretical treatment, in the attempt to rationalize the phenomenology and to form a mental image of the mechanisms underlying the electronic interaction with static magnetic perturbations.

Particular prominence is given to $\mathbf{J}^{\mathbf{B}}(\mathbf{r})$ and $\mathbf{J}^{m_I}(\mathbf{r})$, describing respectively the current density induced in the electron cloud by a spatially uniform static magnetic field \mathbf{B} and by a permanent magnetic dipole m_I at nucleus I . Emphasis is placed on the practical advantages arising from the use of functions defined within the 3-dimensional space for interpreting experimental data, e.g., the parameters of nuclear magnetic resonance (NMR) spectroscopy, by means of two-dimensional maps and perspective representations of three-dimensional fields.

Besides, the mathematical properties of $\mathbf{J}^{\mathbf{B}}$ and \mathbf{J}^{m_I} as dynamical systems constitute an object of investigation per se quite appealing from the purely mathematical point of view. The structure of these vector fields can be studied by the tools of differential topology. The phase portraits giving a geometric representation of the trajectories in the vicinity of points at which the modulus of the current density vanishes are particularly interesting.

Terminology and notation adopted in previous papers and reviews [2–5] are used, allowing for standard tensor formalism, e.g., summation over repeated Greek indices is implied according to the Einstein convention.

7.1.1 The Conventional Approach of Perturbation Theory to Magnetic Properties

The magnetic response of atoms and molecules to external static electromagnetic fields and internal perturbations, e.g., nuclear magnetic dipoles and nuclear electric quadrupoles, is usually rationalized within the framework of time-independent Rayleigh-Schrödinger perturbation theory (RSPT) [6, 7] by introducing tensors of increasing rank which describe intrinsic electronic properties. For instance, RSPT is the basic tool used by Van Vleck to study second-rank $\zeta_{\alpha\beta}$ magnetizability tensors [8]. Ramsey implemented an analogous approach to the magnetic shielding [9–11] $\sigma_{\alpha\beta}^I$ of nucleus I and to the electron-mediated interaction between the spins of two nuclei I and J in a molecule via $J_{I,J}$ nuclear spin-spin coupling [12, 13]. These quantities are related to the spectral parameters of high resolution NMR spectroscopy [14]. The components of the chemical shift tensor $\zeta_{\alpha\beta}^I$, which can in principle be obtained experimentally for a molecular species in ordered phase, are related to the absolute shielding tensor components $\sigma_{\alpha\beta}^I$ by the equation

$$\zeta_{\alpha\beta}^I = (\sigma_{\alpha\beta}^{REF} - \sigma_{\alpha\beta}^I) / (\delta_{\alpha\beta} - \sigma_{\alpha\beta}^{REF}) \approx \sigma_{\alpha\beta}^{REF} - \sigma_{\alpha\beta}^I,$$

where $\sigma_{\alpha\beta}^{REF}$ is the absolute shielding of a reference compound and $\delta_{\alpha\beta}$ is the Kronecker tensor.

Within the RSPT computational scheme for nondegenerate systems [7] the eigenvalue problem $H^{(0)}|j\rangle = E_j^{(0)}|j\rangle$ for the unperturbed Hamiltonian $H^{(0)}$ is preliminarily solved, determining the unperturbed energy levels $E_j^{(0)}$ and wavefunctions $|j\rangle$. All over this chapter the reference state eigenvector $|a\rangle$ will assumed to be the ground state of a diamagnetic atom, or a molecule within the Born-Oppenheimer approximation. The wavefunction and the energy of the a -perturbed state correct to a given order are obtained according to a well known scheme [6, 7], assuming a complete set of unperturbed eigenstates. For instance,

$$\Psi_a = \Psi_a^{(0)} + \Psi_a^{(1)} + \dots, \quad (7.1)$$

$$\Psi_a^{(1)} = -\frac{1}{\hbar} \sum_{j \neq a} |j\rangle \langle j | \hat{H}^{(1)} | a \rangle \omega_{ja}^{-1}, \quad (7.2)$$

$$W_a^{(1)} = \langle a | \hat{H}^{(1)} | a \rangle, \quad (7.3)$$

$$W_a^{(2)} = \langle a | \hat{H}^{(2)} | a \rangle - \frac{1}{\hbar} \sum_{j \neq a} \omega_{ja}^{-1} \langle a | \hat{H}^{(1)} | j \rangle \langle j | \hat{H}^{(1)} | a \rangle, \quad (7.4)$$

where $\omega_{ja} = (E_j^{(0)} - E_a^{(0)})/\hbar$ denotes the natural transition frequencies. $\hat{H}^{(1)}$ and $\hat{H}^{(2)}$ are first- and second-order perturbing Hamiltonians.

RSPT formally yields a rapidly convergent series for the interaction energy of a molecule in the presence of external perturbing fields and an easy-to-handle set of computational recipes for related response properties up to fourth-order, which are evaluated by differentiation with respect to perturbation parameters [3]. Nonetheless, the analysis of predictions arrived at by k -th order wavefunctions $\Psi_a^{(k)} = \Psi_a^{(k)}(\mathbf{x}_1, \mathbf{x}_2 \dots \mathbf{x}_n)$ depending on $6n$ space-spin coordinates $\mathbf{x}_i \equiv \mathbf{r}_i \otimes \mathbf{s}_i$, $i = 1, \dots, n$ for an n -electron system [3, 15, 16], may be quite hard, if not impossible, in the majority of cases. Propagator methods [17–20] and coupled cluster theory [21–23] offer appealing alternatives to RSPT for accurate calculations in small and medium-size molecules with ground states characterized by a dominant single electronic configuration [24–27], but, in general, do not make simpler the interpretation of results.

7.1.2 *The Hydrodynamical Approach to Quantum Mechanics*

In 1926 Schrödinger proposed a definition of quantum-mechanical current density, which satisfies a continuity equation formally identical to that of classical electrodynamics, in his fourth paper on quantization as an eigenvalue problem [28]. A few months later, in the same year, Madelung put forward an alternative foundation of quantum theory allowing for a hydrodynamical analogy [29]. Fundamental contributions were given by de Broglie in 1926 [30] and 1927 [31]. Later on, more advanced formulations were elaborated by Landau [32] and by London [33]. Within the hydrodynamical approach to quantum mechanics, the continuity condition and a vector equation, with the same form as the Hamilton-Jacobi equation of motion of classical mechanics, provide a substitute of the wave equation [34–40]. The equation of motion can also be recast as the Newton second law, taking into account a nonlocal quantum potential¹ [34]. Takabayasi investigated a relativistic hydrodynamics, which offers a hydrodynamical model of the Dirac matter [41].

The profound physical meaning [42], the capacity to gain an accurate and deep understanding of the phenomenology and the philosophical implications [43, 44] of the representation of quantum mechanics proposed by Madelung [29], Landau [32], and London [33] (MLL) cannot be overstressed. Bohm showed that the hydrodynamical quantum mechanics is deterministic and provides an interpretation of physical reality alternative to that of the Copenhagen School [34, 35].

¹See Eq. (8a) of Ref. [34]. By combining the first two addenda on the l.h.s. of Eq. (2) of Ref. [36], a quantum-mechanical relationship of the same form as the Newton's second law is obtained for a particle acted upon by the Lorentz force and by the nonlocal Bohm potential, see Eq. (94) of Ref. [15].

In a number of instances, the MLL formulation is quite useful, e.g., it yields powerful tools for studying molecular magnetic response, which can be rationalized via the electronic current density induced by a spatially uniform, time-independent external magnetic field \mathbf{B} and by intramolecular magnetic dipoles \mathbf{m}_I , $I = 1, 2, \dots, N$ at the nuclei. The practical advantages of dealing with a vector function of position in real space, instead of a complex wave function depending on $6n$ space-spin coordinates for an n particle problem, are evident.

As recalled in the Introduction, the charge density and the current density are expectation values of related linear Hermitian operators [1], defined respectively by

$$\hat{\rho}(\mathbf{r}) = -e \sum_{i=1}^n \delta(\mathbf{r} - \mathbf{r}_i), \quad (7.5)$$

$$\hat{\mathbf{J}}(\mathbf{r}) = -\frac{e}{2m_e} \sum_{i=1}^n [\hat{\mathbf{p}}_i \delta(\mathbf{r} - \mathbf{r}_i) + \delta(\mathbf{r} - \mathbf{r}_i) \hat{\mathbf{p}}_i]. \quad (7.6)$$

Therefore, if charge and current density subobservables [1] are available, one can keep apart the quantum mechanical procedure used to get them, and rely on relationships of classical electrodynamics for solving a number of problems quite efficiently. In most cases, a simple representation of the \mathbf{J} -field by a set of arrows is sufficient to visualize essential features of systems responding to magnetic perturbations [24, 25, 45]. Separate plots of streamlines and modulus of the current density field are required to understand topological subtleties [15]. The differential Biot-Savart (BS) law [46] affords simple and clear interpretations of nuclear magnetic shielding [24, 25, 47–50] and nuclear spin-spin coupling [16, 51, 52] via the related concept of property density [3, 53, 54].

However, besides providing powerful interpretative tools, maps of current density field are very interesting by themselves for more general reasons. A few problems of physico-mathematical interest have received much attention. The analysis is carried out by the theory of differential equations and differential topology. Most relevant characteristics are observed in the vicinity of the singularities. A point at which the modulus of the current density vanishes is referred to as “equilibrium” or “stagnation” point (SP). The singularities determine the topological structure of the vector field, which is described in compact form by a “stagnation graph” (SG) conveying essential information [55–57] for understanding magnetic response.

The quantum mechanical theory underlying the present study is outlined in Sect. 7.2. Topological aspects are taken into account in some detail in Sects. 7.3 and 7.4. A few observations on magnetic symmetry [58] are recalled in Sect. 7.5, reporting results obtained for some molecules which deserve a special attention for the peculiarity of their magnetic response. In particular, we considered a few, neutral or charged, mono-cyclic conjugated systems described by the general formula C_nH_n , customarily regarded as “aromatic” on the magnetic criterion, and classified as “diatropic”. They have aroused a major interest in connection with the so-called ring-current model (RCM) [15].

7.2 Electron Current Density Induced by Magnetic Fields and Nuclear Magnetic Dipoles

The expression for the quantum mechanical current density induced in the electron cloud by a homogeneous, static magnetic field $\mathbf{B} = \nabla \times \mathbf{A}^{\mathbf{B}}$, where

$$\mathbf{A}^{\mathbf{B}} = \frac{1}{2} \mathbf{B} \times \mathbf{r} \quad (7.7)$$

is the vector potential in the Coulomb gauge, is obtained as a sum of diamagnetic and paramagnetic contributions by theoretical procedures illustrated by McWeeny [59] and employed in previous Refs. [3, 15, 60], whose notation is used in the following. The diamagnetic contribution,

$$\mathbf{J}_d^{\mathbf{B}}(\mathbf{r}) = -\frac{e^2}{m_e} \mathbf{A}^{\mathbf{B}}(\mathbf{r}) \gamma^{(0)}(\mathbf{r}), \quad (7.8)$$

is related to the probability density of the unperturbed molecule [59],

$$\gamma^{(0)}(\mathbf{r}) = n \int dx_2 \dots dx_n \Psi_a^{(0)}(\mathbf{r}, \mathbf{x}_2, \dots, \mathbf{x}_n) \Psi_a^{(0)*}(\mathbf{r}, \mathbf{x}_2, \dots, \mathbf{x}_n), \quad (7.9)$$

and the paramagnetic contribution, parallel to the canonical momentum vector $\hat{\mathbf{p}}$, is given by

$$\begin{aligned} \mathbf{J}_p^{\mathbf{B}}(\mathbf{r}) = & -\frac{ne}{m_e} \int dx_2 \dots dx_n \\ & \times \left[\mathbf{B} \cdot \Psi_a^{\mathbf{B}*}(\mathbf{r}, \mathbf{x}_2, \dots, \mathbf{x}_n) \hat{\mathbf{p}} \Psi_a^{(0)}(\mathbf{r}, \mathbf{x}_2, \dots, \mathbf{x}_n) \right. \\ & \left. + \Psi_a^{(0)*}(\mathbf{r}, \mathbf{x}_2, \dots, \mathbf{x}_n) \hat{\mathbf{p}} \mathbf{B} \cdot \Psi_a^{\mathbf{B}}(\mathbf{r}, \mathbf{x}_2, \dots, \mathbf{x}_n) \right]. \end{aligned} \quad (7.10)$$

The total current density is obtained by summing,

$$\mathbf{J}^{\mathbf{B}} = \mathbf{J}_d^{\mathbf{B}} + \mathbf{J}_p^{\mathbf{B}}. \quad (7.11)$$

Analogous expressions are found for the current density induced by a nuclear magnetic dipole \mathbf{m}_I via the Ramsey nuclear spin/electron orbit interaction [12, 13, 15, 16, 51, 52, 61–63]. The diamagnetic contribution is connected to the probability density of the unperturbed system [59], Eq. (7.9),

$$\mathbf{J}_d^{\mathbf{m}_I}(\mathbf{r}) = -\frac{e^2}{m_e} \mathbf{A}^{\mathbf{m}_I}(\mathbf{r} - \mathbf{R}_I) \gamma^{(0)}(\mathbf{r}), \quad (7.12)$$

indicating by

$$\mathbf{A}^{\mathbf{m}_I}(\mathbf{r} - \mathbf{R}_I) = \frac{\mu_0}{4\pi} \frac{\mathbf{m}_I \times (\mathbf{r} - \mathbf{R}_I)}{|\mathbf{r} - \mathbf{R}_I|^3}, \quad (7.13)$$

the vector potential associated to the permanent magnetic dipole \mathbf{m}_I at nucleus I . The paramagnetic contribution is obtained by

$$\begin{aligned} \mathbf{J}_p^{\mathbf{m}_I}(\mathbf{r}) &= -\frac{en}{m_e} \int d\mathbf{x}_2 \dots d\mathbf{x}_n \\ &\times \left[\mathbf{m}_I \cdot \Psi_a^{\mathbf{m}_I^*}(\mathbf{r}, \mathbf{x}_2, \dots, \mathbf{x}_n) \hat{\mathbf{p}} \Psi_a^{(0)}(\mathbf{r}, \mathbf{x}_2, \dots, \mathbf{x}_n) \right. \\ &\left. + \Psi_a^{(0)*}(\mathbf{r}, \mathbf{x}_2, \dots, \mathbf{x}_n) \hat{\mathbf{p}} \mathbf{m}_I \cdot \Psi_a^{\mathbf{m}_I}(\mathbf{r}, \mathbf{x}_2, \dots, \mathbf{x}_n) \right]. \end{aligned} \quad (7.14)$$

The total current density induced by the nuclear magnetic dipole is

$$\mathbf{J}^{\mathbf{m}_I} = \mathbf{J}_d^{\mathbf{m}_I} + \mathbf{J}_p^{\mathbf{m}_I}. \quad (7.15)$$

The first-order RSPT functions, Eq. (7.1), $\Psi_a^{\mathbf{B}}$ and $\Psi_a^{\mathbf{m}_I}$ that appear in Eqs. (7.10) and (7.14) are axial vectors with three independent components, that is

$$|\Psi_a^{B_x}\rangle = \frac{1}{\hbar} \sum_{j \neq a} \omega_{ja}^{-1} |j\rangle \langle j | \hat{m}_x | a \rangle, \quad (7.16)$$

$$|\Psi_a^{m_x}\rangle = \frac{1}{\hbar} \sum_{j \neq a} \omega_{ja}^{-1} |j\rangle \langle j | \hat{B}_{I_x}^n | a \rangle, \quad (7.17)$$

denoting by

$$\hat{\mathbf{m}} = -\frac{e}{2m_e} \sum_{i=1}^n \hat{\mathbf{l}}_i, \quad (7.18)$$

the orbital magnetic moment operator related to the angular momentum, and by $\hat{\mathbf{B}}_I^n$ the n -electron operator for the magnetic field at nucleus I . The latter is obtained as a sum,

$$\hat{\mathbf{B}}_I^n = \sum_{i=1}^n \hat{\mathbf{B}}_I^i, \quad (7.19)$$

of operators for the magnetic field exerted by the i -th electron on nucleus I ,

$$\hat{\mathbf{B}}_I^i = -\frac{e}{m_e} \hat{\mathbf{M}}_I^i, \quad (7.20)$$

related to the operator

$$\hat{M}_I^i = \frac{\mu_0}{4\pi} \frac{\mathbf{r}_i - \mathbf{R}_I}{|\mathbf{r}_i - \mathbf{R}_I|^3} \times \hat{\mathbf{p}}_i = \frac{\mu_0}{4\pi} \frac{\hat{\mathbf{l}}_i(\mathbf{R}_I)}{|\mathbf{r}_i - \mathbf{R}_I|^3}. \quad (7.21)$$

The operator $\hat{\mathbf{l}}_i(\mathbf{R}_I)$ represents the angular momentum of electron i with respect to the origin at nucleus I with position \mathbf{R}_I [3].

The spin-dipolar and the Fermi contact terms of the Ramsey theory [12, 13] are obtained from the general expression for the current density

$$\mathbf{J}(\mathbf{r}) = \nabla \times \mathcal{M}(\mathbf{r}), \quad \mathcal{M}(\mathbf{r}) = -\frac{e}{m_e} \mathcal{Q}(\mathbf{r}), \quad (7.22)$$

due to the magnetization density \mathcal{M} associated to the electron spin density defined via the spin density matrix [59, 62],

$$\mathcal{Q}(\mathbf{r}, \mathbf{r}') = \int_{s=s'} \hat{s}\gamma(\mathbf{x}, \mathbf{x}') ds, \quad \mathcal{Q}(\mathbf{r}) = \mathcal{Q}(\mathbf{r}, \mathbf{r}), \quad (7.23)$$

denoting by \hat{s} the spin operator. The corresponding contributions to the current density are [4, 61, 62]

$$\begin{aligned} J_{SD}^{\mathbf{m}_I}(\mathbf{r}) &= -\frac{en}{m_e} \int d\mathbf{x}_2 \dots d\mathbf{x}_n \\ &\times \nabla \times \left\{ \mathbf{m}_I \cdot \Psi_a^{SD*}(\mathbf{r}, \mathbf{x}_2, \dots, \mathbf{x}_n) \hat{s} \Psi_a^{(0)}(\mathbf{r}, \mathbf{x}_2, \dots, \mathbf{x}_n) \right. \\ &\left. + \Psi_a^{(0)*}(\mathbf{r}, \mathbf{x}_2, \dots, \mathbf{x}_n) \hat{s} \Psi_a^{SD}(\mathbf{r}, \mathbf{x}_2, \dots, \mathbf{x}_n) \cdot \mathbf{m}_I \right\}, \end{aligned} \quad (7.24)$$

$$\begin{aligned} J_{FC}^{\mathbf{m}_I}(\mathbf{r}) &= -\frac{en}{m_e} \int d\mathbf{x}_2 \dots d\mathbf{x}_n \\ &\times \nabla \times \left\{ \mathbf{m}_I \cdot \Psi_a^{FC*}(\mathbf{r}, \mathbf{x}_2, \dots, \mathbf{x}_n) \hat{s} \Psi_a^{(0)}(\mathbf{r}, \mathbf{x}_2, \dots, \mathbf{x}_n) \right. \\ &\left. + \Psi_a^{(0)*}(\mathbf{r}, \mathbf{x}_2, \dots, \mathbf{x}_n) \hat{s} \Psi_a^{FC}(\mathbf{r}, \mathbf{x}_2, \dots, \mathbf{x}_n) \cdot \mathbf{m}_I \right\}, \end{aligned} \quad (7.25)$$

In these cases the current field is parallel to $\nabla \times \hat{s}$.

Definitions of the second-order energy alternative to the RSPT's, Eq. (7.4), are obtained in terms of $\mathbf{J}^{\mathbf{B}}$ and $\mathbf{J}^{\mathbf{m}_I}$, via relationships of classical electromagnetism easily applicable to calculate magnetizability, nuclear magnetic shielding, and reduced spin-spin coupling tensors, that is, via the expression

$$W^{\mathbf{B}\mathbf{B}} = -\frac{1}{2} \int \mathbf{A}^{\mathbf{B}} \cdot \mathbf{J}^{\mathbf{B}} d^3r, \quad (7.26)$$

and from either side of the interchange theorems [3, 4]

$$W^{\mathbf{m}_I \mathbf{B}} = - \int \mathbf{A}^{\mathbf{m}_I} \cdot \mathbf{J}^{\mathbf{B}} d^3 r = - \int \mathbf{A}^{\mathbf{B}} \cdot \mathbf{J}^{\mathbf{m}_I} d^3 r, \quad (7.27)$$

$$W^{\mathbf{m}_I \mathbf{m}_J} = - \int \mathbf{A}^{\mathbf{m}_I} \cdot \mathbf{J}^{\mathbf{m}_J} d^3 r = - \int \mathbf{A}^{\mathbf{m}_J} \cdot \mathbf{J}^{\mathbf{m}_I} d^3 r, \quad (7.28)$$

In fact, the quantum mechanical relationships for magnetizability, nuclear magnetic shielding, and nuclear spin-spin coupling arrived at from the derivatives of the second-order energy expressed in the form (7.26)–(7.28) are the same as those obtained via RSPT [2–4],

$$\zeta_{\alpha\beta} = - \frac{\partial^2 W^{\mathbf{B}\mathbf{B}}}{\partial B_\alpha \partial B_\beta}, \quad (7.29)$$

$$\sigma_{\alpha\beta}^I = \frac{\partial^2 W^{\mathbf{m}_I \mathbf{B}}}{\partial m_{I_\alpha} \partial B_\beta}, \quad (7.30)$$

$$\mathcal{K}^{I_\alpha J_\beta} = \frac{\partial^2 W^{\mathbf{m}_I \mathbf{m}_J}}{\partial m_{I_\alpha} \partial m_{J_\beta}}. \quad (7.31)$$

The magnetizability defined via Eq. (7.29) and the reduced indirect nuclear spin-spin coupling, Eq. (7.31), are measured in J T^{-2} and $\text{J}^{-1} \text{T}^2 \equiv \text{NA}^{-2} \text{m}^{-3}$, respectively, within the SI system of units [64]. The dimensionless shielding tensor of nucleus I , Eq. (7.30), is customarily expressed in parts per million, p.p.m.

Equations (7.7) and (7.26) show that the contribution to the interaction energy from the component of $\mathbf{J}^{\mathbf{B}}$ parallel (or antiparallel) to \mathbf{B} vanishes identically. Such a component is only given by the paramagnetic term, Eq. (7.10). Null contributions to the energy, Eq. (7.27), are obtained for $\mathbf{J}^{\mathbf{B}}$ parallel (or antiparallel) to \mathbf{m}_I and $\mathbf{J}^{\mathbf{m}_I}$ parallel (or antiparallel) to \mathbf{B} , according to Eqs. (7.7) and (7.13).

7.2.1 Gauge Invariance of Induced Current Density and Magnetic Properties

In the gauge transformation of the vector potential, Eq. (7.7),

$$\mathbf{A}^{\mathbf{B}} \rightarrow \mathbf{A}^{\mathbf{B}} + \nabla f, \quad (7.32)$$

induced by a generating function² $f(\mathbf{r})$, the first-order Hamiltonian

$$\hat{H}^{\mathbf{B}} = -\hat{\mathbf{m}} \cdot \mathbf{B} \equiv \frac{e}{m_e} \sum_{i=1}^n \mathbf{A}_i^{\mathbf{B}} \cdot \hat{\mathbf{p}}_i, \quad (7.33)$$

undergoes the transformation

$$\hat{H}^{\mathbf{B}} \rightarrow \hat{H}^{\mathbf{B}} + \frac{e}{m_e} (\nabla_{\mathbf{x}} f) \hat{P}_x, \quad (7.34)$$

where $\hat{\mathbf{P}} = \sum_{i=1}^n \hat{\mathbf{p}}_i$ is the n -electron canonical momentum operator. The corresponding transformation of the first-order wavefunction, Eq. (7.16), is given by

$$B_x \Psi_a^{B_x} \rightarrow B_x \Psi_a^{B_x} + \Psi_a^{P_\beta} \nabla_{\beta} f, \quad (7.35)$$

introducing the first-order function

$$\Psi_a^{P_\beta} = -\frac{e}{m_e \hbar} \sum_{j \neq a} \Psi_j^{(0)} \langle j | \hat{P}_\beta | a \rangle \omega_{ja}^{-1} = -\frac{ie}{\hbar} \hat{R}_\beta \Psi_a^{(0)}. \quad (7.36)$$

The second identity in Eq. (7.36) is obtained by the hypervirial relation [65]

$$\langle a | \hat{R}_x | j \rangle = \frac{i}{m_e} \omega_{ja}^{-1} \langle a | \hat{P}_x | j \rangle, \quad (7.37)$$

allowing for the definition of overlined operators, i.e.,

$$\hat{\overline{R}} \equiv \hat{R} - \langle a | \hat{R} | a \rangle. \quad (7.38)$$

Therefore, in the gauge transformation, Eq. (7.32), the change in the diamagnetic and paramagnetic contributions to the current density, Eqs. (7.8) and (7.10), is given by

$$\mathbf{J}_d^{\mathbf{B}} \rightarrow \mathbf{J}_d^{\mathbf{B}} - \frac{e^2}{m_e} \gamma^{(0)} \nabla f, \quad \mathbf{J}_p^{\mathbf{B}} \rightarrow \mathbf{J}_p^{\mathbf{B}} + \frac{e^2}{m_e} \gamma^{(0)} \nabla f, \quad (7.39)$$

so that the total current density, Eq. (7.11), is invariant. A translation of the coordinate system can be assimilated to a gauge transformation, Eq. (7.32), in which the generating function is

²The f function is fully arbitrary, provided it is continuous and has the physical dimensions of a magnetic flux density times the square of length. It is well-behaved for $r \rightarrow \infty$ and satisfies the condition $\nabla^2 f = 0$.

$$f^{\mathbf{B}} \equiv d_{\alpha} A_{\alpha}^{\mathbf{B}} = \frac{1}{2} \epsilon_{\alpha\beta\gamma} d_{\alpha} B_{\beta} r_{\gamma}. \quad (7.40)$$

Therefore, the total electron current density $\mathbf{J}^{\mathbf{B}}$ is origin independent. Explicit formulae expressing the change of diamagnetic and paramagnetic contributions to $\mathbf{J}^{\mathbf{B}}$ are given elsewhere [3, 4].

In the gauge transformation, Eq. (7.32), of the vector potential (7.7), the interaction energy, Eqs. (7.26) and (7.27), the magnetizability and the nuclear shielding, Eqs. (7.29) and (7.30), are invariant for exact [2, 3, 15, 66–71] and optimal variational eigenfunctions [65]. There is a connection between gauge invariance and charge-current conservation [65, 72, 73], as can be easily seen, for instance, from relationship (7.26). In the change of gauge considered above, one gets an additional term on the r.h.s. of Eq. (7.26), which is required to identically vanish for the energy to stay the same, that is,

$$\int \mathbf{J}^{\mathbf{B}} \cdot \nabla f d^3 r = \int \nabla \cdot (f \mathbf{J}^{\mathbf{B}}) d^3 r - \int f \nabla \cdot \mathbf{J}^{\mathbf{B}} d^3 r = 0. \quad (7.41)$$

Allowing for the Gauss theorem, the first volume integral on the r.h.s. of Eq. (7.41) is equivalent to a surface integral, which vanishes due to the boundary conditions $\gamma^{(0)}(\mathbf{r}), \mathbf{J}_{\alpha}^{\mathbf{B}}(\mathbf{r}) \rightarrow 0$ for $\mathbf{r} \rightarrow \infty$. Therefore the integral on the l.h.s. of Eq. (7.41), arising in the gauge transformation induced by the generating function f , vanishes, and the interaction energy, Eq. (7.26), is invariant, if the continuity equation $\nabla \cdot \mathbf{J}^{\mathbf{B}} = \mathbf{0}$ is satisfied. As f is fully arbitrary, one finds in particular, for $f^{\mathbf{B}}$ given by Eq. (7.40), that is, $f \propto x, y, z$, an integral conservation condition for $\mathbf{J}^{\mathbf{B}}$ from Eqs. (7.8) and (7.10) [3, 60],

$$\int \mathbf{J}_{\alpha}^{\mathbf{B}} d^3 r = 0. \quad (7.42)$$

This relationship is equivalent to the Arrighini-Maestro-Moccia (AMM) sum rule [74],

$$\{\hat{P}_{\alpha}, \hat{m}_{\beta}\}_{-1} = \frac{1}{2} \epsilon_{\alpha\beta\gamma} \langle a | \hat{\mu}_{\gamma} | a \rangle, \quad (7.43)$$

which is also a condition for origin independence of total magnetizabilities [2, 3, 15, 68–71, 74]. The operator $\hat{\mu}_{\beta} = -e \sum_{i=1}^n r_{i\beta}$ in Eq. (7.43) denotes the electric dipole of the electrons.

The flux of the current density $\mathbf{J}^{\mathbf{B}}$

$$I^{\mathbf{B}} = \int_S \mathbf{J}^{\mathbf{B}} \cdot d\mathbf{s} \quad (7.44)$$

from a surface S defines the current passing through. The oriented element of S is indicated by ds . If S is closed, $I^{\mathbf{B}}$ vanishes, which constitutes the integral form of the continuity equation

$$\nabla \cdot \mathbf{J}^{\mathbf{B}} = 0.$$

7.2.2 Current Density Tensor and Current Susceptibility Vector

The current density second-rank tensor [3, 15, 71, 75] associated with the magnetic-field induced current density $J_{\alpha}^{\mathbf{B}}$ is a function of position defined all over the molecular domain by the derivative

$$\mathcal{J}_{\alpha}^{B\beta}(\mathbf{r}) = \frac{\partial J_{\alpha}^{\mathbf{B}}(\mathbf{r})}{\partial B_{\beta}}. \quad (7.45)$$

An analogous definition has been proposed for the current density $J_{\alpha}^{m_i}$ induced by a nuclear magnetic dipole [16, 51, 52, 62, 63]

$$\mathcal{J}_{\alpha}^{m_i\beta} = \frac{\partial J_{\alpha}^{m_i}}{\partial m_{i\beta}}. \quad (7.46)$$

The diamagnetic and paramagnetic contributions to $\mathcal{J}_{\alpha}^{B\beta}$, Eq. (7.45), are obtained from Eqs. (7.8) and (7.10), respectively,

$$\mathcal{J}_{d\alpha}^{B\beta}(\mathbf{r}) = -\frac{e^2}{2m_e} \epsilon_{\alpha\beta\gamma} r_{\gamma} \gamma^{(0)}(\mathbf{r}), \quad (7.47)$$

$$\begin{aligned} \mathcal{J}_{p\alpha}^{B\beta}(\mathbf{r}) = & -\frac{ne}{m_e} \int d\mathbf{x}_2 \dots d\mathbf{x}_n \\ & \times \left[\Psi_a^{B\beta*}(\mathbf{r}, \mathbf{x}_2, \dots, \mathbf{x}_n) \hat{p}_{\alpha} \Psi_a^{(0)}(\mathbf{r}, \mathbf{x}_2, \dots, \mathbf{x}_n) \right. \\ & \left. + \Psi_a^{(0)*}(\mathbf{r}, \mathbf{x}_2, \dots, \mathbf{x}_n) \hat{p}_{\alpha} \Psi_a^{B\beta}(\mathbf{r}, \mathbf{x}_2, \dots, \mathbf{x}_n) \right]. \end{aligned} \quad (7.48)$$

The contributions to $\mathcal{J}_{\alpha}^{m_i\beta}$, Eq. (7.46), obtained from current density terms corresponding to a given Ramsey mechanism, e.g., the diamagnetic and paramagnetic contributions from the nuclear spin/electron orbit terms, Eqs. (7.12) and (7.14), are, respectively,

$$\mathcal{J}_{dz}^{m_{I\beta}}(\mathbf{r}) = -\frac{\mu_0 e^2}{4\pi m_e} \epsilon_{\alpha\beta\gamma} \frac{r_\gamma - R_{I_\gamma}}{|\mathbf{r} - \mathbf{R}_I|^3} \gamma^{(0)}(\mathbf{r}), \quad (7.49)$$

$$\begin{aligned} \mathcal{J}_{pz}^{m_{I\beta}}(\mathbf{r}) &= -\frac{ne}{m_e} \int d\mathbf{x}_2 \dots d\mathbf{x}_n \\ &\times \left[\Psi_a^{m_{I\beta}*}(\mathbf{r}, \mathbf{x}_2, \dots, \mathbf{x}_n) \hat{p}_\alpha \Psi_a^{(0)}(\mathbf{r}, \mathbf{x}_2, \dots, \mathbf{x}_n) \right. \\ &\left. + \Psi_a^{(0)*}(\mathbf{r}, \mathbf{x}_2, \dots, \mathbf{x}_n) \hat{p}_\alpha \Psi_a^{m_{I\beta}}(\mathbf{r}, \mathbf{x}_2, \dots, \mathbf{x}_n) \right]. \end{aligned} \quad (7.50)$$

The nonsymmetric current density tensor is an intrinsic molecular property, in terms of which magnetizability and nuclear magnetic shielding are obtained from Eqs. (7.26), (7.27), (7.29), (7.30) and (7.45)–(7.50),

$$\chi_{\alpha\delta} = \frac{1}{2} \epsilon_{\alpha\beta\gamma} \int r_\beta \mathcal{J}_\gamma^{B_\delta}(\mathbf{r}) d^3 r, \quad (7.51)$$

$$\sigma_{\alpha\delta}^I = -\frac{\mu_0}{4\pi} \epsilon_{\alpha\beta\gamma} \int \frac{r_\beta - R_{I_\beta}}{|\mathbf{r} - \mathbf{R}_I|^3} \mathcal{J}_\gamma^{B_\delta}(\mathbf{r}) d^3 r = -\frac{1}{2} \epsilon_{\beta\gamma\delta} \int r_\beta \mathcal{J}_\gamma^{m_{I\alpha}}(\mathbf{r}) d^3 r. \quad (7.52)$$

According to these equations, there is no contribution of $J_x^{\mathbf{B}}$ to χ_{xx} and σ_{xx}^I , nor a contribution to σ_{xx}^I from $J_x^{m_I}$. Analogous statements hold for the y and z directions. All the relevant equations of the theory of magnetic response can be rewritten in terms of current density tensors, e.g., the AMM sum rule, Eq. (7.43), is obtained by integrating the current density tensor, Eq. (7.45),

$$\int \mathcal{J}_\alpha^{B_\beta}(\mathbf{r}) d^3 r = -\frac{e}{m_e} (2\{\hat{P}_\alpha, \hat{m}_\beta\}_{-1} - \epsilon_{\alpha\beta\gamma} \langle a | \hat{\mu}_\gamma | a \rangle) = 0. \quad (7.53)$$

The spin-orbit, spin-dipolar, and Fermi contributions to the reduced spin-spin coupling tensor for two nuclei I and J can be recast in the general form

$$\begin{aligned} \mathcal{K}^{I_\alpha J_\beta} &= -\frac{\mu_0}{4\pi} \epsilon_{\delta\alpha\gamma} \int \frac{(r_\gamma - R_{I_\gamma})}{|\mathbf{r} - \mathbf{R}_I|^3} \mathcal{J}_\delta^{m_{J\beta}}(\mathbf{r}) d^3 r \\ &= -\frac{\mu_0}{4\pi} \epsilon_{\delta\beta\gamma} \int \frac{(r_\gamma - R_{J_\gamma})}{|\mathbf{r} - \mathbf{R}_J|^3} \mathcal{J}_\delta^{m_{I\alpha}}(\mathbf{r}) d^3 r, \end{aligned} \quad (7.54)$$

where differentiation of the vector potential (7.13) and of various current density terms, Eqs. (7.12), (7.14), (7.24) and (7.25), with respect to magnetic dipole components has been formally carried out. Details on the derivation of the spin-dipolar and Fermi contributions have been previously illustrated [4].

A current susceptibility vector is defined via Eq. (7.44),

$$I^{B_x} = \int_S \mathcal{J}_\beta^{B_x}(\mathbf{r}) ds_\beta \quad (7.55)$$

where $ds_\beta = n_\beta dS$ is the element of area orthogonal to $\mathbf{J}^{\mathbf{B}}(\mathbf{r})$, with orientation defined by the orthogonal unit vector \mathbf{n} . I^{B_x} is the electronic current passing through S per unit of magnetic field B_x . It is conveniently expressed in nanoampère/tesla in the SI system [24–27, 76, 77].

A similar definition can be proposed for the current induced by a nuclear magnetic dipole from Eq. (7.46).

7.2.3 Property Density Functions as Maps on the Current Density Field

Noninvertible maps of the current density vector field can be defined to construct second-rank property density tensors quite useful for interpreting the phenomenology of magnetic response. For instance, the electron coupled effects of a perturbing \mathbf{B} on a nuclear magnetic dipole \mathbf{m}_I can be impressively visualized via nuclear magnetic shielding density functions of position \mathbf{r} , with the dimension of the inverse of a volume, which are defined by the second-rank tensor Σ^I [3, 4, 53, 54]. They are directly connected to the magnetic-field induced current-density by the map

$$f : \mathbf{J}^{\mathbf{B}}(\mathbf{r}) \rightarrow \Sigma^I(\mathbf{r})$$

and are immediately obtained from the integrand of the BS law [46]. The Σ^I density function

$$\sum_{\alpha\delta}^I(\mathbf{r}) = -\frac{\mu_0}{4\pi} \epsilon_{\alpha\beta\gamma} \frac{r_\beta - R_{I\beta}}{|\mathbf{r} - \mathbf{R}_I|^3} \mathcal{J}_\gamma^{B_\delta}(\mathbf{r}) \quad (7.56)$$

is useful to determine regions of the molecular basin where shielding-desielding mechanisms take place, and to analyze the contribution provided by different domains of the $\mathbf{J}^{\mathbf{B}}(\mathbf{r})$ field all over the molecular dimensions. Nice representations are obtained by plotting components of $\Sigma_{\alpha\beta}^I$ in a plane specified by fixing one spatial coordinate.

Similarly, visualizations of magnetic-dipole induced current-density, together with maps of the nuclear spin-spin coupling density [4, 16, 51, 52, 62],

$$\kappa^{J\beta I_x}(\mathbf{r}) = -\frac{\mu_0}{4\pi} \epsilon_{\delta\beta\gamma} \frac{(r_\gamma - R_{J_\gamma})}{|\mathbf{r} - \mathbf{R}_J|^3} \mathcal{J}_\delta^{m_{I_x}}(\mathbf{r}), \quad (7.57)$$

(a tensor defined all over the molecular domain, measured in $\text{T}^2 \text{J}^{-1} \text{m}^{-3}$ in the SI system), yield fundamental complementary information on the nuclear coupling phenomenon, transmission paths and electron-nuclear interaction. The κ^{IJ} function can be integrated to obtain the local magnetic field

$$\langle \hat{\mathbf{B}}_{J_\beta}^n \rangle = -\mathcal{K}^{J\beta I_x} m_{I_x},$$

and the coupling constant, Eq. (7.54). These expressions can also be regarded as generalized forms of the integral BS law from classical electrodynamics [46].

7.3 Singularities, Stagnation Lines and Stagnation Graph of a Current Density Field

The current density of an n -electron quantum mechanical system may form $3n - 2$ -dimensional vortices in 3-dimensional configuration space [78–84]. If the system admits a description in terms of density matrices, natural orbitals are obtained by diagonalizing $\gamma^{(0)}(\mathbf{r})$, Eq. (7.9). Then the total current density vector, $\mathbf{J}^{\mathbf{B}}$ or \mathbf{J}^{m_I} , can be analyzed in terms of distinct contributions from each orbital.

The topology of the $\mathbf{J}^{\mathbf{B}}$ vector field deserves a careful and detailed investigation. Its most interesting features are observed in the proximity of an SP at which the modulus $|\mathbf{J}^{\mathbf{B}}|$ vanishes. An SP is classified in terms of *topological index*³ ι [85, 86], and of a (*rank, signature*) label [15, 55–57, 87–90]. A continuous, open or closed, path of SPs is referred to as stagnation line (SL), consisting of either *vortex* points (index $\iota = +1$), or *saddle* points (index $\iota = -1$).

In the vicinity of a stagnation point at \mathbf{r}_0 , the fields $\mathbf{J}^{\mathbf{B}}(\mathbf{r})$ and $\mathbf{J}^{m_I}(\mathbf{r})$ can be described by a truncated Taylor series expansion about \mathbf{r}_0 , e.g.,

$$\begin{aligned} J_\gamma^{\mathbf{B}}(\mathbf{r}) &= (r_\alpha - r_{0\alpha}) \left[\nabla_\alpha J_\gamma^{\mathbf{B}} \right]_{\mathbf{r}=\mathbf{r}_0} \\ &+ \frac{1}{2} (r_\alpha - r_{0\alpha})(r_\beta - r_{0\beta}) \left[\nabla_\alpha \nabla_\beta J_\gamma^{\mathbf{B}} \right]_{\mathbf{r}=\mathbf{r}_0} + \dots \end{aligned} \quad (7.58)$$

³The topological index ι counts the number of times that the current density vector $\mathbf{J}^{\mathbf{B}}$ rotates completely while one walks counterclockwise around a circle of radius ϵ , so small that $\mathbf{J}^{\mathbf{B}}$ has no zeroes inside except the SP at its centre. The topological index ι of a saddle (vortex) line is -1 ($+1$). Both SPs have $(r, s) = (2, 0)$.

The 3×3 transposed Jacobian matrix $\mathfrak{S}_{\alpha\beta}^{\mathbf{B}} = \nabla_{\alpha} \mathbf{J}_{\beta}^{\mathbf{B}}$, evaluated at the stagnation point \mathbf{r}_0 , has real elements. It represents a nonsymmetric tensor in the absence of molecular point group symmetry. Within the linear approximation [91], only the first term in the expansion is considered and the description of the field about a stagnation point amounts to solving a system of three coupled linear differential equations whose corresponding matrix is given by the transposed Jacobian matrix.

Reyn [92] reported a table of all possible phase portraits in the vicinity of a stagnation point in three-dimensional flow and a corresponding classification of canonical forms in connection with the eigenvalues and eigenvectors of the Jacobian $\mathfrak{S}_{\alpha\beta}^{\mathbf{B}}$. Within the classification of stagnation points based on the (*rank, signature*) index [87] proposed in Refs. [55–57] and generally adopted [15, 89, 90], the rank r is defined as the number of nonvanishing eigenvalues of the Jacobian, the signature s is the excess of positive over negative eigenvalues, if they are real or pure imaginary.⁴ Because of the continuity equation $\nabla_{\alpha} \mathbf{J}_{\alpha}^{\mathbf{B}} = 0$ for stationary flow, the Jacobian is traceless all over the definition domain of the $\mathbf{J}^{\mathbf{B}}$ vector field, so that only two eigenvalues are linearly independent. This places a limit on the possible (r, s). The allowed cases are [55–57, 93]

- (3, ± 1) points, which correspond to isolated singularities, referred to as saddle-nodes [92]. Two eigenvalues satisfy the condition $\zeta_3 = -\Re(\zeta_1 + \zeta_2)$ (the symbol \Re denotes the real part of its argument). If ζ_1 and ζ_2 are real (they may also be $\zeta_1 = \zeta_2$), then, in the representation of the flow in the plane of the eigenvectors \mathbf{t}_1 and \mathbf{t}_2 corresponding to ζ_1 and ζ_2 , a node or a saddle point (see Ref. [91] for the nomenclature) is observed; if they are complex conjugate a focus is found.
- (2, 0) points, corresponding to the eigenvalues $\zeta_3 = 0, \zeta_1 = -\zeta_2$. For real $\zeta_{1,2} = \pm a$ (pure imaginary $\zeta_{1,2} = \pm ib$), the phase portrait of a saddle (vortex) is observed. The eigenvectors \mathbf{t}_1 and \mathbf{t}_2 , corresponding to ζ_1 and ζ_2 , are real in the case of a saddle (they give the direction of the asymptotes through the singularity) and imaginary in the case of a vortex. Saddle and vortex stagnation lines are continuous manifolds of (2, 0) points. Usually these SLs are symmetry determined and lie entirely on symmetry planes of a molecule. The eigenvector \mathbf{t}_3 is locally tangent to the SL. (2, 0) points can be open lines—this is the case of an *axial vortex* (AV)—or form close loops. A *toroidal vortex* (TV) flows around a closed vortex line of (2, 0) points [78]. Diamagnetic (paramagnetic) AVs of the electronic current density rotate clockwise (anticlockwise) with respect to an observer placed at the North pole of the \mathbf{B} field. The direction of flow about a vortical line is determined by the *vorticity*, i.e., by the local $\nabla \times \mathbf{J}^{\mathbf{B}}$.
- (0, 0) degenerate points, corresponding to three zero eigenvalues of the Jacobian, which are referred to as *branching* or *transition points*. From the mathematical point of view, the change of regime is related to an exchange

⁴If the eigenvalues are complex one defines the signature as the difference between the number of eigenvalues having a positive real part and the number of eigenvalues having a negative real part.

between different canonical forms of the Jacobian [15]. Since a (0, 0) point corresponds to a transition between pure imaginary and pure real eigenvalues, the branching must necessarily take place at an SP characterized by three zero eigenvalues [55, 56].

The reason for the denomination “branching point” used for (0, 0) singularities is easily understood. Consider, for instance, a molecule of D_{nh} symmetry, in the singlet electronic ground state, in the presence of a magnetic field \mathbf{B} along the highest symmetry axis C_n . According to the general analysis of Sect. 7.5.2, in the outer reaches of the molecular domain, the induced electronic current density is diamagnetic, that is, it flows in planes at right angles to \mathbf{B} , like the Larmor current that takes place in atoms. In the proximity of the North and South poles, at large distance from the molecular plane, the diamagnetic regime is represented by the primary (2, 0) vortical stagnation line parallel to \mathbf{B} and C_n . Transition to different regimes, e.g., from vortex to saddle flow, or vice versa, takes place closer to the centre of charge, i.e., in the regions of higher electron density $\rho(\mathbf{r})$, where the primary vortex line may split up into saddle and vortical lines.

The splitting of a SL into several SLs is regulated by a fundamental topological theorem proved by Gomes [55–57, 93] in the form of an index conservation constraint. Recall that, according to footnote 3, the index of a saddle (vortex) line is -1 ($+1$). When an SL of index l_0 splits into m new lines, the sum of the indices of the SLs which emerge from the branching point must satisfy the condition

$$\sum_{k=1}^m l_k = l_0. \quad (7.59)$$

For instance, a vortex line may bifurcate giving rise to two new vortex lines and one saddle line. This bifurcation conserves the total index $+1$.

7.3.1 The Gomes Flow

A simple model of velocity vector field exhibiting branching of vortex and saddle stagnation lines has been considered by Gomes [56] via the system of differential equations

$$\begin{cases} \dot{x} = y^3 + y(z^2 - z - 2) \\ \dot{y} = -x^3 - x(z^2 + z - 2) \\ \dot{z} = 0 \end{cases} \quad (7.60)$$

describing trajectories everywhere parallel to the xy plane, shown in Figs. 7.1 and 7.2 for some z values. They display the change of regime occurring in different

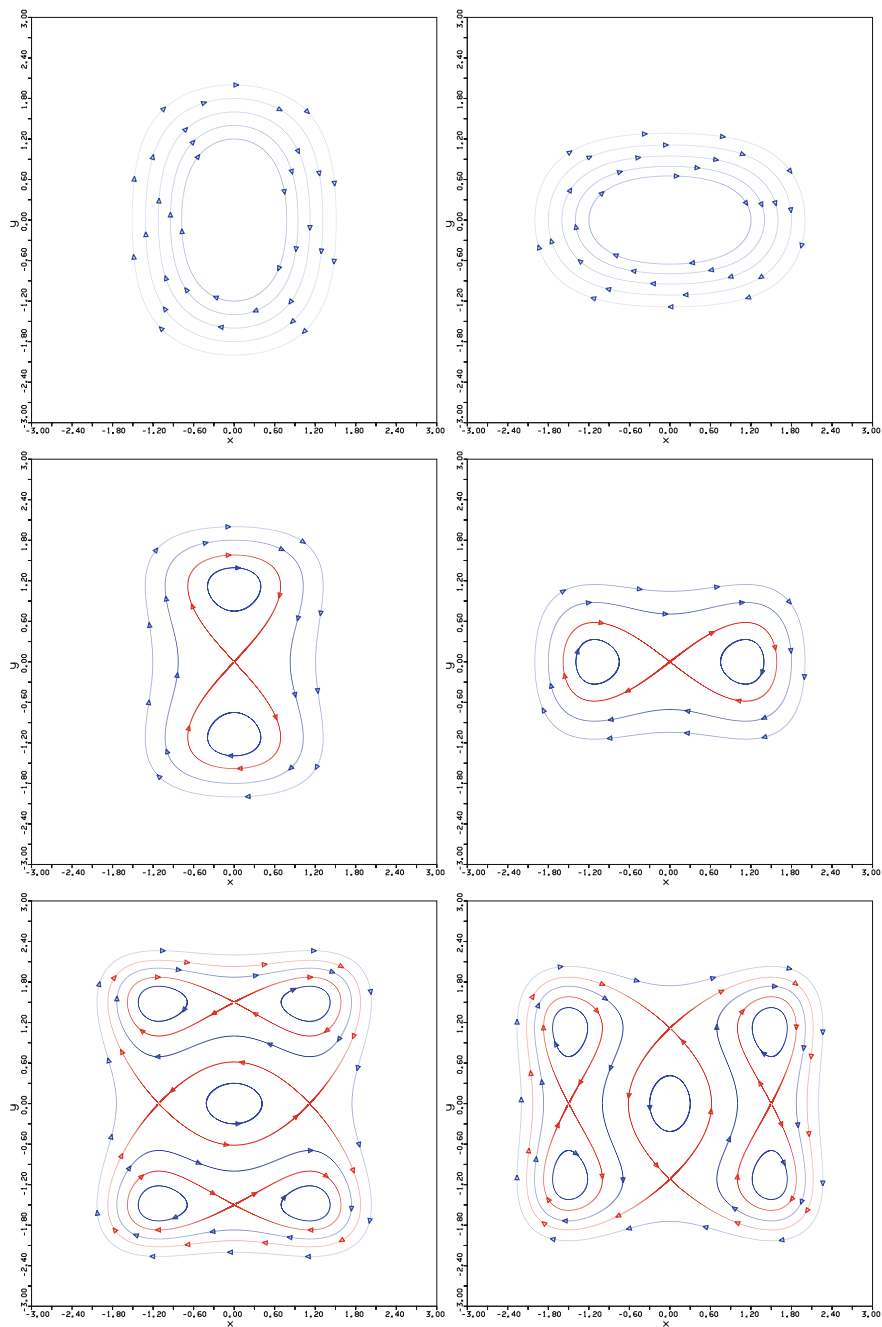


Fig. 7.1 The Gomes flow, Eq. (7.60). On the left [right], from top to bottom $z = +2.5$, $z = +1.5$, $z = +0.5$ [$z = -2.5$, $z = -1.5$, $z = -0.5$]. Regular orbits are blue. The homoclinic trajectories through saddle points are red

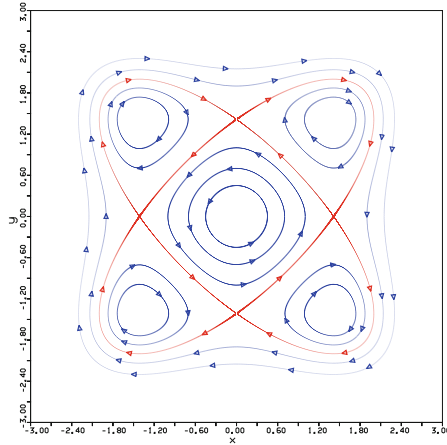
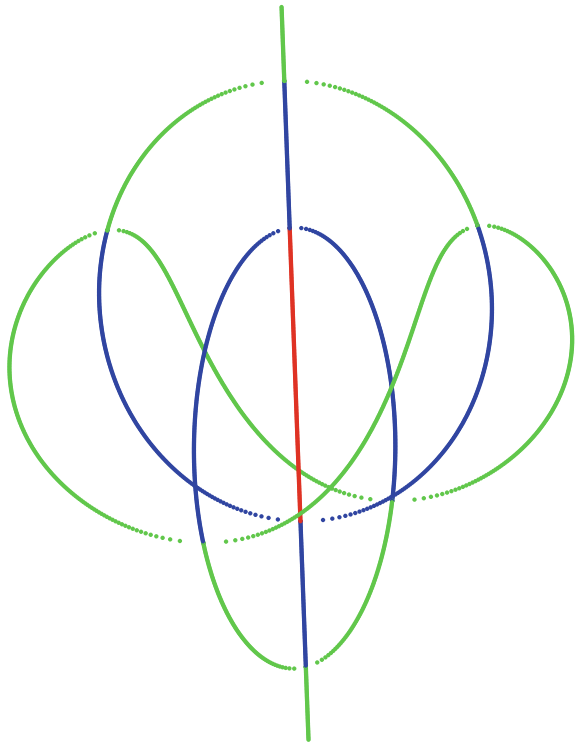


Fig. 7.2 The Gómes flow, Eq. (7.60), on the $z = 0$ plane. The color code is the same as in Fig. 7.1

Fig. 7.3 Perspective view of the stagnation graph of the Gómes flow, Eq. (7.60), for $|z| < 2.5$. The central stagnation line coincides with the z axis. Green (red) lines correspond to clockwise (anticlockwise) vortices in Figs. 7.1 and 7.2, saddle lines are blue



planes. Branching points are found on the central stagnation line at $z = \pm 2.0$ and $z = \pm 1.0$. Branchings conserve the total index +1. The stagnation graph of Fig. 7.3 conveys complete information on the velocity field (7.60) in compact and economical form.

7.4 Bifurcations of a Dynamical System

The splitting of an SL of the quantum mechanical current densities $\mathbf{J}^{\mathbf{B}}$ and $\mathbf{J}^{\mathbf{m}_i}$ at a branching point in \mathbb{R}^3 can be studied within the framework of bifurcation theory of dynamical systems, see [94–96] for an introduction to the subject. Accordingly, let us consider a system of first-order differential equations in matrix form

$$\dot{\mathbf{X}} = F_{\mu}(\mathbf{X}) \quad (7.61)$$

where $\dot{\mathbf{X}} \equiv d\mathbf{X}/dt$, $\mathbf{X} \in \mathbb{R}^3$ and $\mu \in \mathbb{R}^k$. With this notation it is implied that F_{μ} depends on k parameters [94]. The system (7.61) is referred to as a *flow* in three-dimensional space. It will be assumed in the following that F_{μ} does not depend explicitly on time, but only on \mathbf{X} . For $F_{\mu} = F_{\mu}[\mathbf{X}(t)]$, the flow (7.61) is said to be *autonomous*. The solutions to the system of algebraic equations

$$F_{\mu}(\mathbf{X}) = \mathbf{0} \quad (7.62)$$

are referred to as fixed, or equilibrium, or stagnation points of the flow.

The existence of roots of $F_{\mu}(\mathbf{X}) = \mathbf{0}$ can be studied via maps describing their dependence on μ . The solution as a function of the parameter is referred to as a *solution branch* and a *bifurcation point* is a point in \mathbb{R}^k from which a set of branches moves out [94]. The *codimension of a bifurcation* is defined to be the smallest dimension of \mathbb{R}^k in which a bifurcation can take place [94]. In the following we will limit ourselves to studying two-dimensional flows of codimension one, taking into account a few archetypal one-dimensional differential forms listed in Appendix A of Ref. [94]. A second differential equation can be added to consider systems of two types, either

$$\begin{cases} \dot{x} = f_{\mu}(x) \\ \dot{y} = -\alpha y \end{cases} \quad (7.63)$$

or

$$\begin{cases} \dot{x} = -\alpha y \\ \dot{y} = f_{\mu}(x) \end{cases} \quad (7.64)$$

with $\alpha > 0$ an arbitrary constant, which without loss of generality will be taken equal to 1. The continuity equation

$$\nabla_x \dot{x}_x \equiv \frac{\partial \dot{x}}{\partial x} + \frac{\partial \dot{y}}{\partial y} = 0,$$

satisfied by (7.64), is not fulfilled by the flow (7.63). Two classes of bifurcations of codimension 1, satisfying the continuity constraint, i.e., corresponding to the flow (7.64), are considered in the following:

- *supercritical*, or *normal* bifurcations, characterized by opposite sign of the terms appearing in the polynomial expansion of f_μ . In such a case, the nonlinear terms in x^2 or x^3 within this expansion have an effect opposing to the instability generated by the term of the lower order [94, 95].
- *subcritical*, or *inverse* bifurcations, in which the nonlinear term, of the same sign as that of lower order, has also a destabilizing effect.

7.4.1 Supercritical Saddle-Centre Bifurcation

This bifurcation can be modelled by the system of differential equations

$$\begin{cases} \dot{x} = -y \\ \dot{y} = \mu - x^2 \end{cases} \quad (7.65)$$

obtained by adding the first equation to the canonical one-dimensional normal form in Table I, p. 297 of Ref. [94]. The field is characterized by the $C_{2v}(C_s) \equiv \underline{mmm}$ magnetic symmetry, see Sect. 7.5. The transposed Jacobian of (7.65) is

$$\tilde{\mathfrak{S}}_{\alpha\beta} = \begin{pmatrix} 0 & -1 \\ -2x & 0 \end{pmatrix}$$

For $\mu < 0$ the dynamic system has no equilibrium points, for $\mu \geq 0$ there is a couple of equilibrium points (coinciding in a critical degenerate point for $\mu = 0$), respectively in $(\sqrt{\mu}, 0)$ $(-\sqrt{\mu}, 0)$. The corresponding matrices are

$$\tilde{\mathfrak{S}}_{\alpha\beta}(\sqrt{\mu}, 0) = \begin{pmatrix} 0 & -1 \\ -2\sqrt{\mu} & 0 \end{pmatrix}, \quad \tilde{\mathfrak{S}}_{\alpha\beta}(-\sqrt{\mu}, 0) = \begin{pmatrix} 0 & -1 \\ 2\sqrt{\mu} & 0 \end{pmatrix}$$

The eigenvalues are determined by solving the equation $\lambda^2 - 2x = 0$, with roots $\lambda_{1,2} = \pm\sqrt{2x}$. Hence

- for the point $(\sqrt{\mu}, 0)$ the solutions are $\lambda_{1,2} = \pm\sqrt{2\sqrt{\mu}}$, i.e., $\lambda_1 > 0$ and $\lambda_2 < 0$: the equilibrium point is a saddle,
- for the point $(-\sqrt{\mu}, 0)$ the solutions are pure imaginary, $\lambda_{1,2} = \pm i\sqrt{2\sqrt{\mu}}$: the equilibrium point is a centre.

The trajectories on the (x, y) plane do not exhibit equilibrium points for $\mu < 0$, see top left of Fig. 7.4. For $\mu = 0$, a cusp is observed in the proximity of the $(0, 0)$ degenerate point, at which the bifurcation takes place. For $\mu > 0$ the typical phase portraits of a saddle and a vortex are observed. Homoclinic orbits, or trajectories, of the flow of this dynamical system join a saddle equilibrium point to itself.

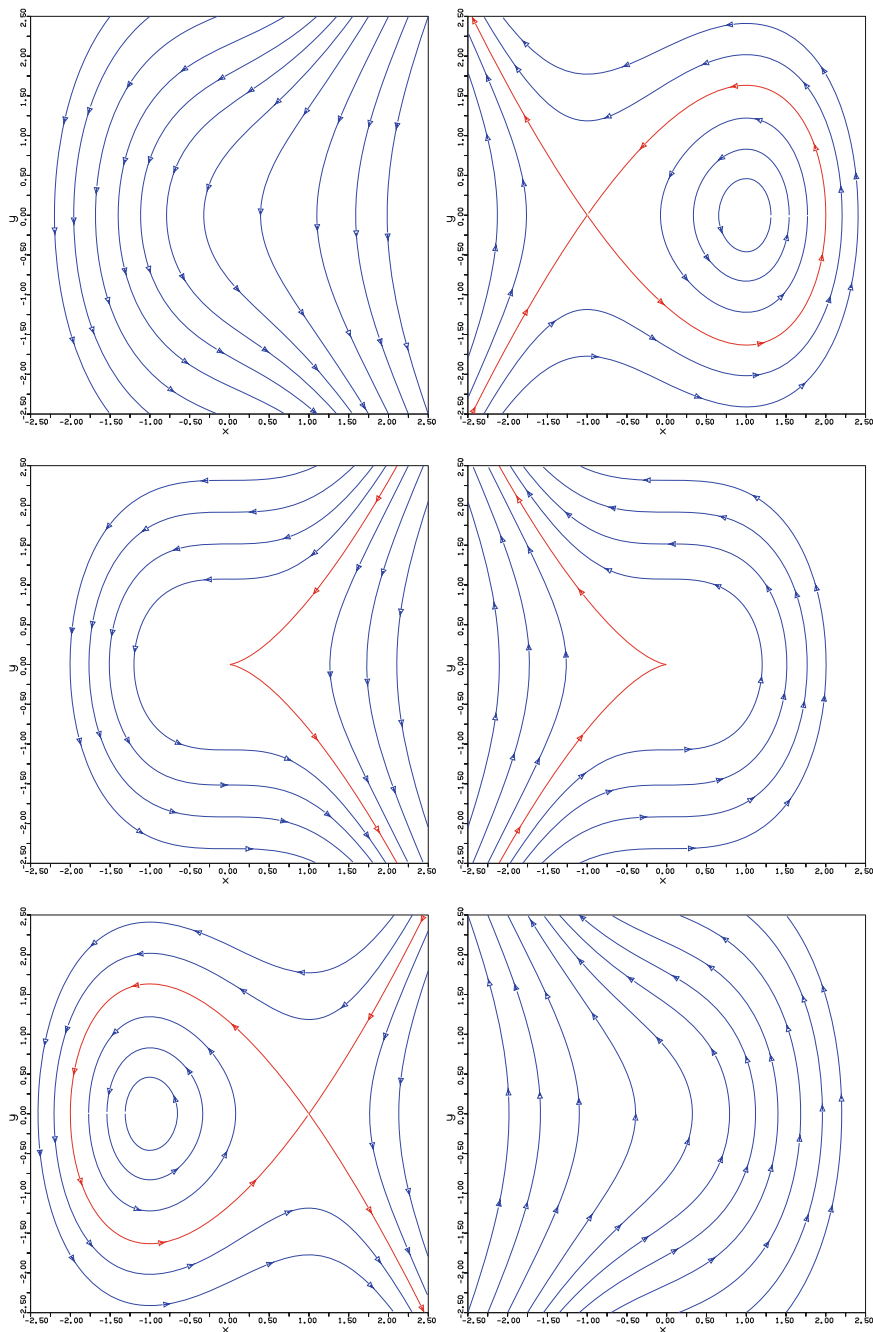


Fig. 7.4 On the *left* [*right*]: supercritical [subcritical] saddle-centre bifurcation, Eq. (7.65) [Eq. (7.66)], for $\mu = -1, 0, +1$, from *top* to *bottom*. Regular orbits are *blue*. The homoclinic trajectories through saddle points and the trajectories joining at the cusp, i.e., at the degenerate critical point corresponding to the bifurcation, are *red*

7.4.2 Subcritical Saddle-Centre Bifurcation

The system of differential equations corresponding to this bifurcation has a form similar to Eq. (7.65), except for the sign of x^2 in the second equation:

$$\begin{cases} \dot{x} = -y \\ \dot{y} = \mu + x^2 \end{cases} \quad (7.66)$$

The transposed Jacobian of (7.66) is

$$\tilde{\mathfrak{S}}_{\alpha\beta} = \begin{pmatrix} 0 & -1 \\ +2x & 0 \end{pmatrix}$$

Accordingly, there are two equilibrium points for $\mu \leq 0$, respectively in $(\sqrt{|\mu|}, 0)$ and $(-\sqrt{|\mu|}, 0)$ (coalescing at a degenerate critical point for $\mu = 0$). The corresponding matrices are

$$\tilde{\mathfrak{S}}_{\alpha\beta}(\sqrt{|\mu|}, 0) = \begin{pmatrix} 0 & -1 \\ 2\sqrt{|\mu|} & 0 \end{pmatrix}, \quad \tilde{\mathfrak{S}}_{\alpha\beta}(-\sqrt{|\mu|}, 0) = \begin{pmatrix} 0 & -1 \\ -2\sqrt{|\mu|} & 0 \end{pmatrix}$$

Hence

- the point $(\sqrt{|\mu|}, 0)$, with corresponding pure imaginary eigenvalues $\lambda_{1,2} = \pm\sqrt{-2\sqrt{|\mu|}}$ is a centre,
- the point $(-\sqrt{|\mu|}, 0)$, with corresponding real eigenvalues of opposite sign, $\lambda_{1,2} = \pm\sqrt{2\sqrt{|\mu|}}$, is a saddle.

The scenario is inverted with respect to that of the supercritical bifurcation of Sect. 7.4.1, see the right column of Fig. 7.4.

7.4.3 Transcritical Saddle-Centre Bifurcation (Supercritical)

This bifurcation corresponds to the system

$$\begin{cases} \dot{x} = -y \\ \dot{y} = \mu x - x^2 \end{cases} \quad (7.67)$$

The transposed Jacobian of (7.67) is

$$\tilde{\mathfrak{S}}_{\alpha\beta} = \begin{pmatrix} 0 & -1 \\ \mu - 2x & 0 \end{pmatrix}$$

There are two equilibrium points, $(0, 0)$ and $(\mu, 0)$, with corresponding Jacobians

$$\tilde{\mathfrak{S}}_{\alpha\beta}(0, 0) = \begin{pmatrix} 0 & -1 \\ \mu & 0 \end{pmatrix}, \quad \tilde{\mathfrak{S}}_{\alpha\beta}(\mu, 0) = \begin{pmatrix} 0 & -1 \\ -\mu & 0 \end{pmatrix}$$

The eigenvalues are $\lambda_{1,2} = \pm\sqrt{-\mu}$ and $\lambda_{1,2} = \pm\sqrt{\mu}$. Hence,

- the $(0, 0)$ point is respectively a saddle for $\mu < 0$ and a centre for $\mu > 0$,
- the $(\mu, 0)$ point is a centre for $\mu < 0$ and a saddle for $\mu > 0$.

Therefore, on varying the value of the parameter from negative to positive within the interval $-1 \leq \mu \leq 1$, an inversion of the bifurcation scenario with exchange of stability [94] is observed. The bifurcation occurs at the degenerate critical point for $\mu = 0$. The trajectories are displayed on the left of Fig. 7.5. The flow is characterized by the $C_{2v}(C_s) \equiv \underline{2mm}$ magnetic symmetry, see Sect. 7.5.

7.4.4 Transcritical Saddle-Centre Bifurcation (Subcritical)

The system of differential equations is

$$\begin{cases} \dot{x} = -y \\ \dot{y} = \mu x + x^2 \end{cases} \quad (7.68)$$

The transposed Jacobian has the form

$$\tilde{\mathfrak{S}} = \begin{pmatrix} 0 & -1 \\ \mu + 2x & 0 \end{pmatrix}$$

The equilibrium points are $(0, 0)$ and $(-\mu, 0)$. Hence,

- the eigenvalues at $(0, 0)$ are $\lambda_{1,2} = \pm\sqrt{-\mu}$: a saddle and a centre are observed for $\mu < 0$ and $\mu > 0$, respectively,
- the eigenvalues at $(-\mu, 0)$ are $\lambda_{1,2} = \pm\sqrt{\mu}$: a saddle and a centre are observed for $\mu > 0$ and $\mu < 0$, respectively.

The trajectories are displayed on the right column of Fig. 7.5. Also in this case, on varying the parameter within the interval $-1 \leq \mu \leq 1$ there is an inversion of the bifurcation scenario with exchange of stability.

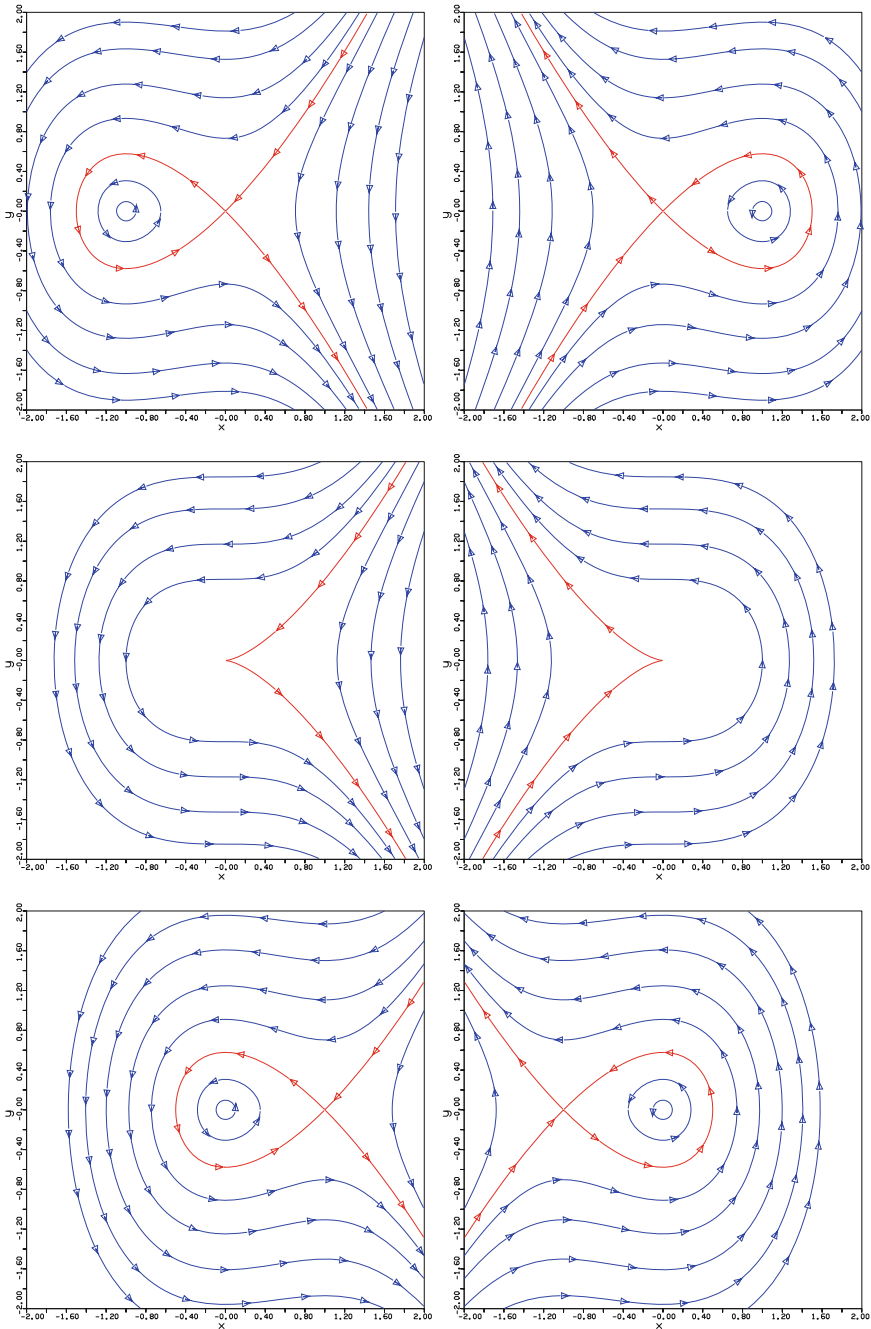


Fig. 7.5 On the *left* [*right*]: supercritical [subcritical] transcritical saddle-vortex bifurcation, Eq. (7.67) [Eq. (7.68)], for $\mu = -1, 0, +1$. Colour conventions are the same as in Fig. 7.4

7.4.5 *Supercritical Pitchfork Bifurcation*

This bifurcation pattern is more complex than the previous ones. In fact, on varying the parameter, we pass from one equilibrium point for $\mu < 0$ to three equilibrium points for $\mu > 0$. The autonomous system is

$$\begin{cases} \dot{x} = -y \\ \dot{y} = \mu x - x^3 \end{cases} \quad (7.69)$$

The corresponding transposed Jacobian is

$$\tilde{\mathfrak{J}} = \begin{pmatrix} 0 & -1 \\ \mu - 3x^2 & 0 \end{pmatrix}$$

For $\mu < 0$ there is only the $(0, 0)$ equilibrium point, for $0 < \mu < +1$ also the solutions $(\pm\sqrt{\mu}, 0)$ emerge. Hence the phase portraits are

- a saddle for $\mu < 0$ and a centre for $\mu > 0$ at point $(0, 0)$;
- two saddles at points $(\pm\sqrt{\mu}, 0)$ (only for $\mu > 0$).

Within this scenario the saddle flow bifurcates into a centre and two adjacent saddles. This happens at the critical degenerate point corresponding to $\mu = 0$, at which the unique solution of the differential system starts splitting into three solutions. The phase portrait is neither a saddle nor a centre. The orbits are shown in the left column of Fig. 7.6.

The Gomes theorem [56] is fulfilled. In fact, using the index $+1$ (-1) for a centre (saddle), Eq. (7.59) is satisfied passing from top to bottom of the left column of Fig. 7.6: the index value -1 is conserved.

7.4.6 *Subcritical Pitchfork Bifurcation*

This is analogous to the previous one, except for the sign of the nonlinear term,

$$\begin{cases} \dot{x} = -y \\ \dot{y} = \mu x + x^3 \end{cases} \quad (7.70)$$

The transposed Jacobian is

$$\tilde{\mathfrak{J}} = \begin{pmatrix} 0 & -1 \\ \mu + 3x^2 & 0 \end{pmatrix}$$

Hence,

- the root $(0, 0)$ corresponds to a centre for $\mu > 0$ and a saddle for $\mu < 0$,
- the roots $(\pm\sqrt{|\mu|}, 0)$ correspond to centres for $\mu < 0$.

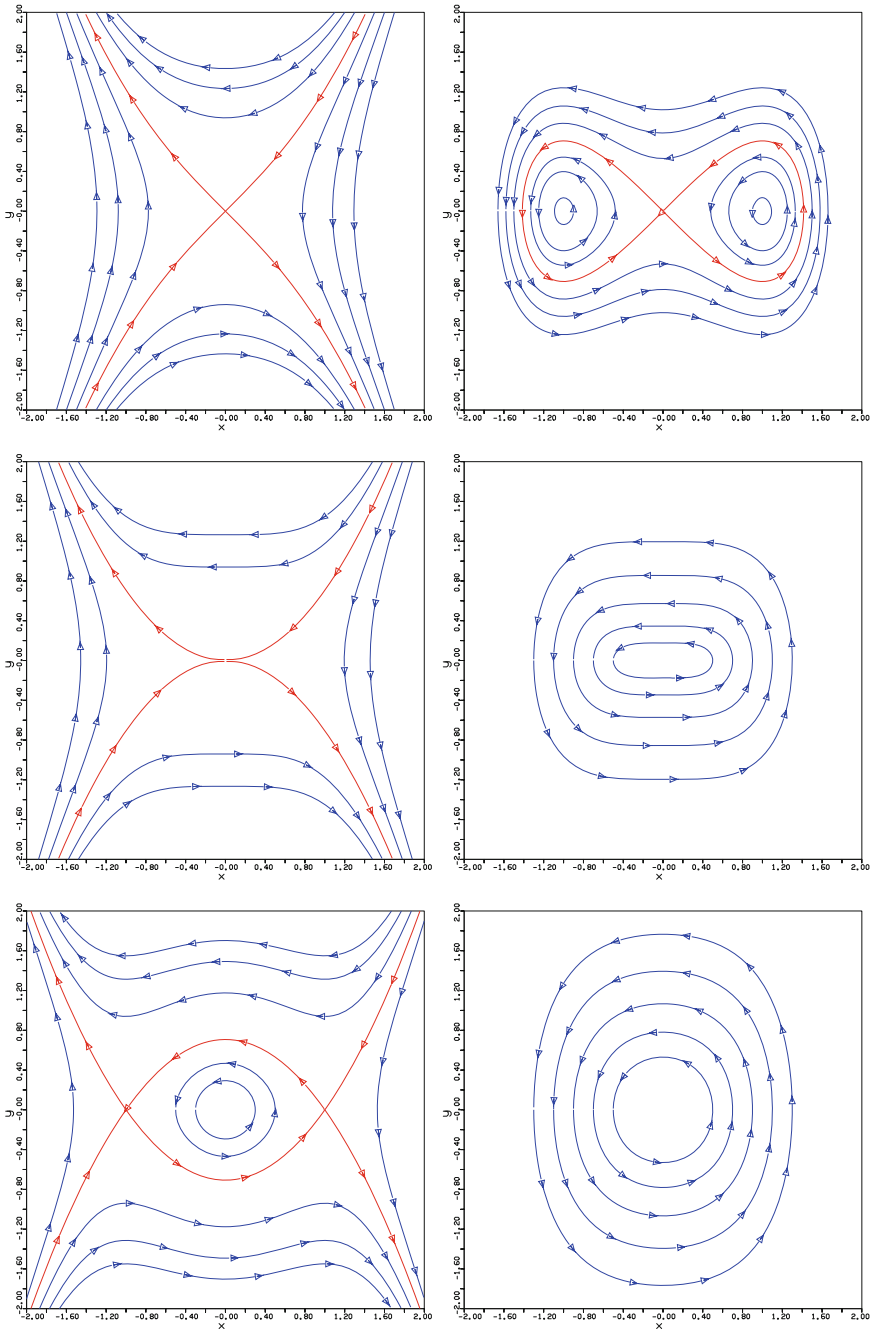


Fig. 7.6 On the *left* [*right*]: supercritical [subcritical] pitchfork bifurcation, Eq. (7.69) [Eq. (7.70)], for $\mu = -1, 0, +1$. Colour conventions are the same as in Fig. 7.4. The magnetic symmetry is given by Eq. (7.74)

Within this scenario two centres and the saddle in between, corresponding to three different fixed points, reduce to a single centre, see the right column of Fig. 7.6. Also in this case the Gomes theorem is satisfied, as shown by adding the indices, $(+1 + 1 - 1 = +1)$.

7.5 Magnetic Symmetry of a Molecule in an External Magnetic Field

The point group symmetry of a molecule in a field \mathbf{B} and the local symmetry at the site of nucleus I , carrying the permanent magnetic dipole \mathbf{m}_I , determine the essential features of $\mathbf{J}^{\mathbf{B}}(\mathbf{r})$ and $\mathbf{J}^{\mathbf{m}_I}(\mathbf{r})$ fields and of their SGs. In the absence of magnetic perturbations, one can take into account the 32 point groups describing the symmetry of the time-averaged charge density $\varrho(\mathbf{r})$ of a molecule in the equilibrium state. In the presence of magnetic field, or intramolecular magnetic dipoles at the nuclei, the analysis of stationary electron current densities $\mathbf{J}^{\mathbf{B}}$ and $\mathbf{J}^{\mathbf{m}_I}(\mathbf{r})$ becomes an essential tool. Since the equilibrium state is unchanged if the sign of these vectors is reversed, it is expedient to introduce the time-reversal operator T [97], which changes the sign of the current at each point in space, but does not act on the spatial coordinates. T commutes with the spatial rotations and reflections and satisfies the cyclic condition $T^2 = E$, but it cannot itself be regarded as an element of a group. It always appears as a combination TG_i for any operator G_i in a group G , but TC_3 cannot occur as a separate symmetry transformation, since $(TC_3)^3 = TE = T$.

By introducing T in the 32 finite point symmetry groups, 58 new symmetry groups can be constructed via the Tavger-Zaitsev algorithm [58, 98, 99]. The procedure can be summarized in the following terms. For any of the 32 groups, $G \equiv \{G_i\}$, $i = 1, 2, \dots, n$, a subgroup \mathcal{H} of index 2 in G is selected. The elements A_i of the set $G - \mathcal{H}$, such that $G = \mathcal{H} + A_i\mathcal{H}$, are used to obtain a magnetic group G' , isomorphic to G , by the recipe

$$G' = \mathcal{H} + TA_i\mathcal{H}. \quad (7.71)$$

In the Schönflies notation we denote this magnetic group as $G'(\mathcal{H})$. The corresponding notations in the Shubnikov system and in the *international system* are also used [58].

The magnetic groups of a few relevant molecules in the presence of a magnetic field are considered hereafter to discuss the main features of the $\mathbf{J}^{\mathbf{B}}$ field. Hamermesh [58] and Mulliken conventions [100, 101] are used.

Orthorhombic system

$$\begin{aligned} D_2 &\equiv \{ E \quad C_2(z) \quad C_2(y) \quad C_2(x) \} \equiv 222 \\ C_2 &\equiv \{ E \quad C_2(z) \} \equiv 2 \\ D_2(C_2) &\equiv \{ E \quad C_2(z) \quad TC_2(y) \quad TC_2(x) \} \equiv \underline{222} \end{aligned} \quad (7.72)$$

$$\begin{aligned}
C_{2v} &\equiv \{ E \ C_2(z) \ \sigma_v(xz) \ \sigma_v(yz) \} \equiv 2mm \\
C_2 &\equiv \{ E \ C_2(z) \} \equiv 2 \\
C_{2v}(C_2) &\equiv \{ E \ C_2(z) \ T\sigma_v(xz) \ T\sigma'_v(yz) \} \equiv \underline{2mm}
\end{aligned} \tag{7.73}$$

$$\begin{aligned}
D_{2h} &\equiv \{ E \ C_2(z) \ C_2(y) \ C_2(x) \ i \ \sigma_v(xy) \ \sigma_v(zx) \ \sigma_h(zy) \} \\
&\equiv mmm \\
C_{2h} &\equiv \{ E \ C_2 \ i \ \sigma_h \} \equiv 2/m \\
D_{2h}(C_{2h}) &\equiv \{ E \ C_2(z) \ TC_2(y) \ TC_2(x) \ i \ \sigma(xy) \ T\sigma(zx) \ T\sigma(yz) \} \\
&\equiv \underline{mmm}
\end{aligned} \tag{7.74}$$

Tetragonal system

$$\begin{aligned}
D_{2d} &\equiv \{ E \ 2S_4(z) \ C_2(z) \ C'_2(x) \ C'_2(y) \ 2\sigma_d \} \equiv \bar{4}2m \\
S_4 &\equiv \{ E \ S_4(z) \ C_2(z) \ S_4^3(z) \} \equiv \bar{4} \\
D_{2d}(S_4) &\equiv \{ E \ 2S_4(z) \ C_2(z) \ TC'_2(x) \ TC'_2(y) \ 2T\sigma_d \} \equiv \bar{4}\underline{2m} \\
D_{4h} &\equiv \{ E \ 2C_4 \ C_2 \ 2C'_2 \ 2C''_2 \ i \ 2S_4 \ \sigma_h \ 2\sigma_v \ 2\sigma_d \} \equiv 4/mmm \\
C_{4h} &\equiv \{ E \ C_4 \ C_2 \ C_4^3 \ i \ S_4^3 \ \sigma_h \ S_4 \} \equiv 4/m \\
D_{4h}(C_{4h}) &\equiv \{ E \ C_4 \ C_2 \ C_4^3 \ 2RC'_2 \ 2RC''_2 \ i \ S_4^3 \ \sigma_h \ S_4 \ 2R\sigma_v \ 2R\sigma_d \} \\
&\equiv 4/\underline{mmm}
\end{aligned} \tag{7.75}$$

Trigonal system

$$\begin{aligned}
D_3 &\equiv \{ E \ 2C_3 \ 3C_2 \} \equiv 32 \\
C_3 &\equiv \{ E \ 2C_3 \} \equiv 3 \\
D_3(C_3) &\equiv \{ E \ 2C_3 \ 3TC_2 \} \equiv \underline{32} \\
C_{3v} &\equiv \{ E \ 2C_3 \ 3\sigma_v \} \equiv 3m \\
C_3 &\equiv \{ E \ 2C_3 \} \equiv 3 \\
C_{3v}(C_3) &\equiv \{ E \ 2C_3 \ 3T\sigma_v \} \equiv \underline{3m}
\end{aligned} \tag{7.77}$$

Hexagonal system

$$\begin{aligned}
D_{3h} &\equiv \{ E \ 2C_3 \ 3C_2 \ \sigma_h \ 2S_3 \ 3\sigma_v \} \equiv \bar{6}m2 \\
C_{3h} &\equiv \{ E \ 2C_3 \ \sigma_h \ 2S_3 \} \equiv \bar{6} \\
D_{3h}(C_{3h}) &\equiv \{ E \ 2C_3 \ 3TC_2 \ \sigma_h \ 2S_3 \ 3T\sigma_v \} \equiv \bar{6}\underline{m2}
\end{aligned} \tag{7.79}$$

$$\begin{aligned}
 D_{6h} &\equiv \{ E \quad 2C_6 \quad 2C_3 \quad C_2 \quad 3C'_2 \quad 3C''_2 \quad i \quad 2S_3 \quad 2S_6 \quad \sigma_h \quad 3\sigma_d \quad 3\sigma_v \} \\
 &\equiv 6/mmm \\
 C_{6h} &\equiv 6/m \equiv \{ E \quad 2C_6 \quad 2C_3 \quad C_2 \quad i \quad 2S_3 \quad 2S_6 \quad \sigma_h \} \\
 D_{6h}(C_{6h}) &\equiv \{ E \quad 2C_6 \quad 2C_3 \quad C_2 \quad 3TC'_2 \quad 3TC''_2 \quad i \quad 2S_3 \quad 2S_6 \quad \sigma_h \quad 3T\sigma_d \quad 3T\sigma_v \} \\
 &\equiv 6/\underline{mmm}
 \end{aligned}
 \tag{7.80}$$

A series of simple rules is obtained taking magnetic symmetry into account:

- A symmetry plane orthogonal to \mathbf{B} (usually a σ_h plane) cannot be crossed by the trajectories
- $T\sigma_v$ and $T\sigma_d$ planes can be crossed only by streamlines normal to them in the typical case of vortical regime. If a streamline approaches a $T\sigma_{v,d}$ plane forming an angle different from $\pi/2$, it is scattered away, and a saddle is found. Therefore any open or closed, vortex or saddle, SL may lie on, but not pass through, a $T\sigma_{v,d}$ plane, and pass through perpendicularly, but not lie on, a σ_h plane. In most of the systems considered in this chapter, the SLs are determined by symmetry and are entirely contained in $T\sigma_{v,d}$ planes.
- As the in-plane components of the $\mathbf{J}^{\mathbf{B}}$ vector vanish all over $T\sigma_{v,d}$ planes by symmetry, the continuity equation for stationary flow, $\nabla \cdot \mathbf{J}^{\mathbf{B}} = 0$ is necessarily fulfilled for the perpendicular component, even if $\mathbf{J}^{\mathbf{B}}$ has been evaluated via approximate quantum mechanical methods.
- The C_n symmetry axes parallel to the inducing magnetic field \mathbf{B} , lying on $T\sigma_v$ planes, are necessarily SLs.
- In the absence of $T\sigma_{v,d}$ planes, e.g., for chiral molecules, the electron flow spirals about a C_n symmetry axis, and only isolated (3, ± 1) isolated points are observed in the SG.

These rules are useful to analyze the main features of the SGs in connection with the point group symmetry of a molecule perturbed by magnetic fields and nuclear dipole moments. They have been applied to a large series of compounds [102]. A few examples are considered in the following Sect. 7.5.1.

7.5.1 The Stagnation Graph of Some Small Molecules

Spatial models of magnetic-field induced electronic currents have been constructed via stagnation graphs and current density maps displayed in Figs. 7.7, 7.8, 7.9, 7.10, 7.11, 7.12, 7.13, 7.14, 7.15, 7.16, 7.17, 7.18, and 7.19, which provide fundamental help for rationalizing magnetizability and nuclear magnetic shielding. A number of interesting features has been observed [102]. A perspective view of the SG of the $\mathbf{J}^{\mathbf{B}}$ current density in trans-difluoro ethene $C_2H_2F_2$, in a uniform external magnetic field \mathbf{B} perpendicular to the molecular plane (a system with magnetic symmetry

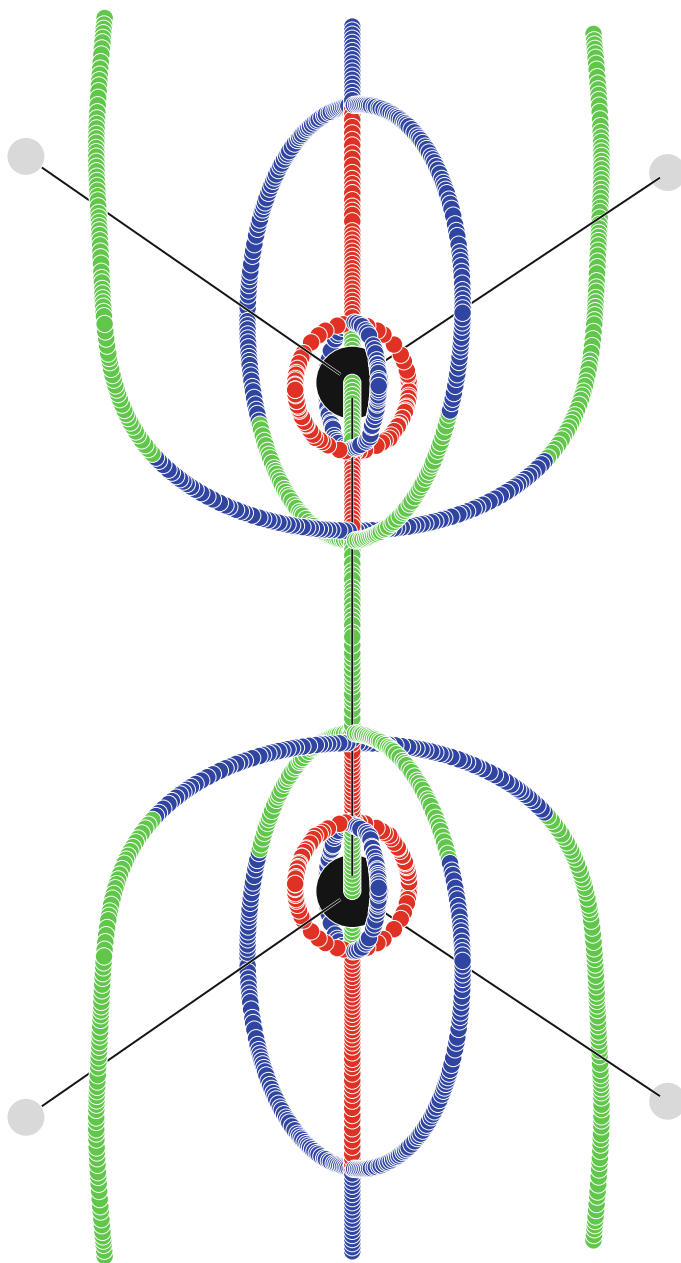


Fig. 7.7 Perspective view of the stagnation graph of the current density vector field in planar ethene C_2H_4 , with magnetic symmetry $D_{2h}(C_{2h})$. The uniform external magnetic field \mathbf{B} is applied in the direction of the C–C bond, coincident with the z axis. Here and in the following figures, *green (red) lines* denote diamagnetic (paramagnetic) vortices, saddle lines are *blue*

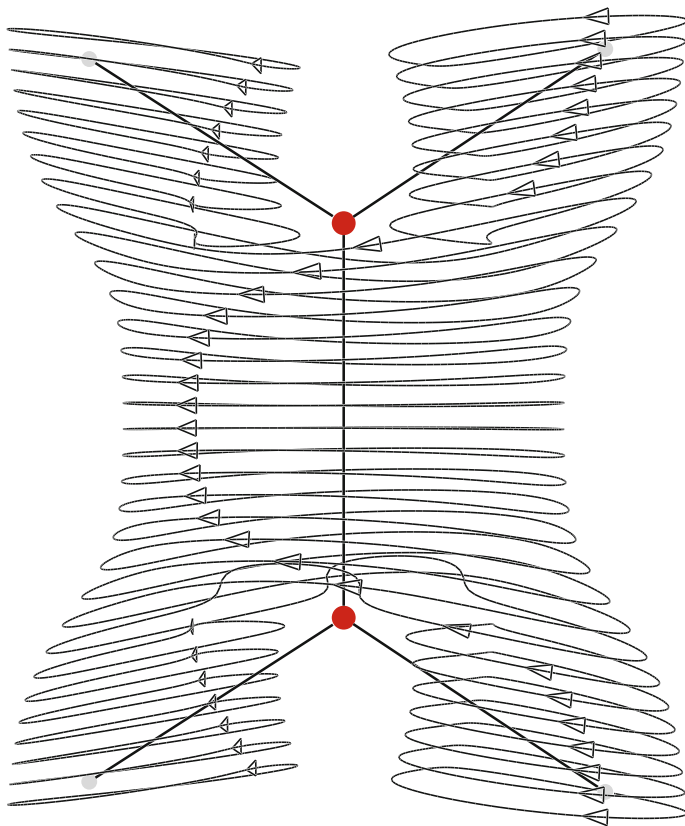


Fig. 7.8 Perspective view of an intermediate portion of the current density vector field in ethene C_2H_4 , with magnetic symmetry $D_{2h}(C_{2h})$, showing the bifurcation at points $P_{\pm 2}$ of the central diamagnetic vortex into two vortices flowing about the C–H bonds. The uniform external magnetic field \mathbf{B} is applied in the direction of the C–C bond, coincident with the z axis. The sequence of vortex-saddle splittings documented by the SG of Fig. 7.7 is fully contained within the streamline surface, and is not visible

C_{2h} , the same as in the absence of field), shows a “dust” of $(3, \pm 1)$ stagnation points: as there is no $T\sigma_v$ plane, SLs do not occur. These isolated SPs correspond to local saddle-nodes and diamagnetic or paramagnetic foci, see Figs. 1 and 2 of Ref. [102]. An analogous situation was found for planar H_3BO_3 , with C_{3h} magnetic symmetry: the stagnation graph consists of isolated stagnation points because of the absence of $T\sigma_v$ planes, see Figs. 3 and 4 of Ref. [102]. Also the stagnation graph of the current density vector field in distorted ethene C_2H_4 , with magnetic symmetry $D_2(C_2)$ consists of a “dust” of $(3, \pm 1)$ SPs. Accordingly, plots of the current density vector field contain only two symmetry-connected spiralling streamlines, see Figs. 5 and 6 of Ref. [102].

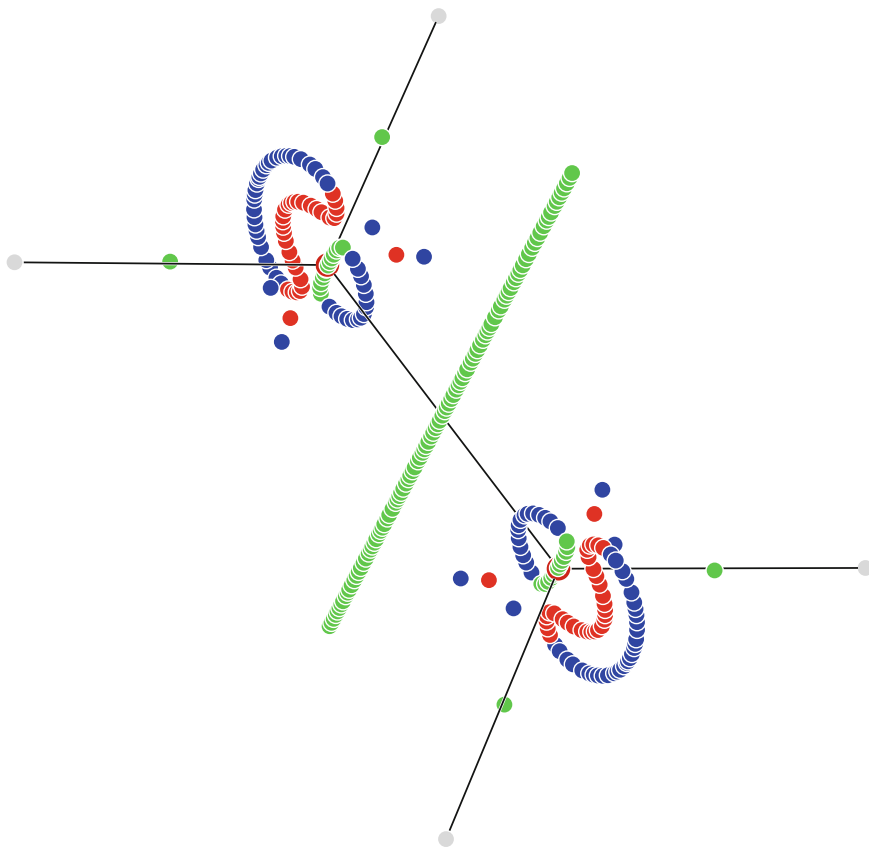


Fig. 7.9 Perspective view of the stagnation graph of the current density vector field induced by a magnetic field $\mathbf{B} \equiv B\mathbf{e}_1$ normal to the yz plane of the nuclei of ethylene. *Green (red) lines* denote diamagnetic (paramagnetic) vortices, saddle lines are *blue*. *Isolated blue points* mark $(3, \pm 1)$ saddle-nodes, *isolated green (red) points* denote $(3, \pm 1)$ diamagnetic (paramagnetic) foci

Ten $(0, 0)$ critical points lying on the C–C bond direction are found in the SG of the energetically stable rotamer with $D_{2h}(C_{2h})$ symmetry in Fig. 7.7. The current density vector field is shown in Fig. 7.8. Denoting by $P_{\pm i}$, $i = 1, 2 \dots 5$, branching points on opposite sides of, and equally spaced from, the origin in the centre of mass (CM), they are $P_{\pm 1}$ at ± 0.47 , $P_{\pm 2}$ at ± 0.52 , $P_{\pm 3}$ at ± 0.92 , $P_{\pm 4}$ at ± 1.54 , and $P_{\pm 5}$ at ± 2.60 , with distances in bohr. The C nuclei are located at ± 1.24 bohr from CM. The $P_{\pm 1}$ and $P_{\pm 2}$ SPs are separated by a short segment (0.05 bohr) of saddle-type SL, which can be observed by magnifying the figure [102].

The primary diatropic vortex SL branches out at two $(0, 0)$ critical points (too far to be seen in Fig. 7.7) into a set of three SLs on the plane of the nuclei: a central (blue) saddle SL and two (green) vortical SLs crossing the C–H bonds. These vortex lines become saddle-type at points with coordinates $(x = 0, y = \pm 1.05, z = \pm 0.86)$ bohr, where the ι topological index changes from -1 to $+1$. The saddle SLs merge at

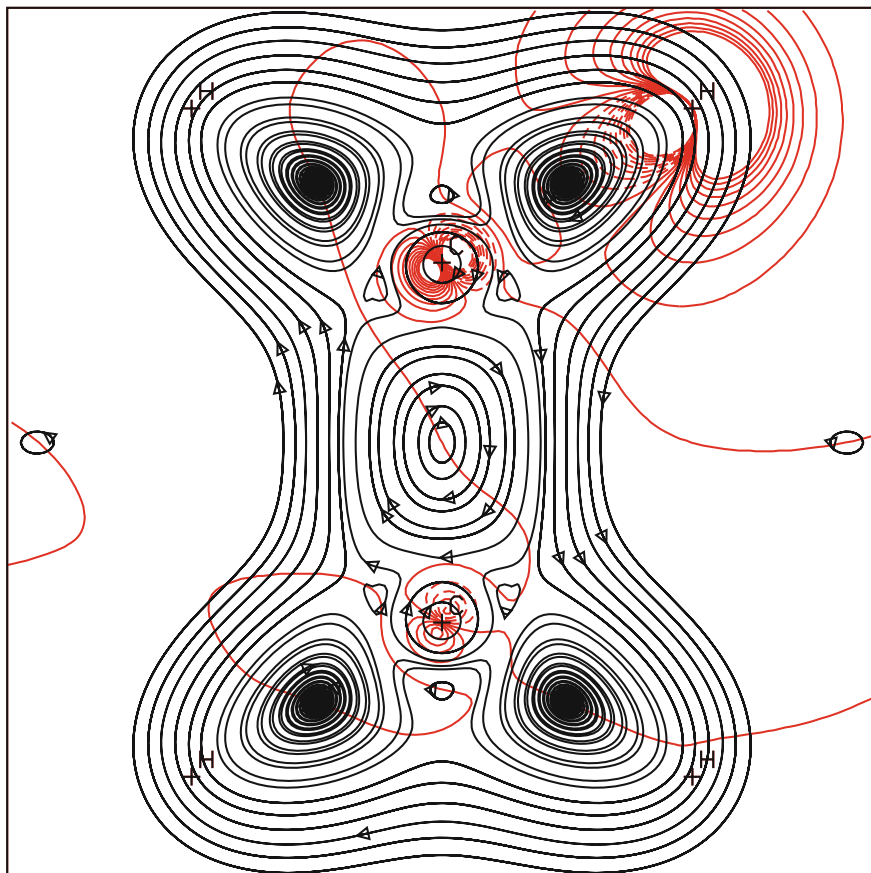


Fig. 7.10 Display of the current density vector in the plane containing the nuclei of ethylene. The applied magnetic field is orthogonal to the plot plane and directed outward. Atom positions are marked by crosses. The maximum modulus is 1.84 (cut to 0.25) au and the step between two consecutive contours is 0.025 au. Contours of the magnetic shielding density Σ_{xx}^H , Eq. (7.81), of hydrogen nucleus on the molecular plane of ethylene are represented in red. Solid (dashed) red lines denote positive (negative) values

$P_{\pm 2}$. At $P_{\pm 5}$ the central saddle SL splits into a central (red) paratropic vortical SL, and two saddle SLs lying on the $T\sigma_v(xz)$ plane orthogonal to that of the molecule. These saddle SLs change index sign at two points with coordinates $(x = \pm 1.10, y = 0, z = \pm 1.07)$ bohr, and the emerging diatropic vortex lines end up at $P_{\pm 1}$. Two cages are found, each about one C nucleus. These patterns consist of a set of SLs merging at $P_{\pm 3}$ and $P_{\pm 4}$ (two paratropic vortical, two saddle SLs, and a central portion of diatropic vortical SL). All the branchings fulfill the Gomes theorem, Eq. (7.59).

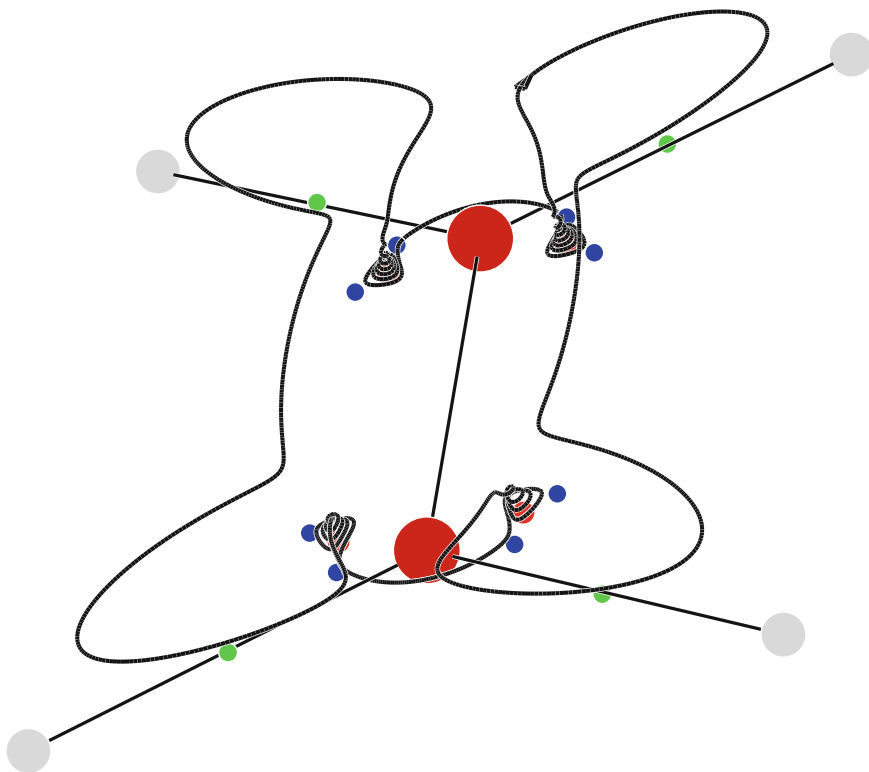


Fig. 7.11 Spiralling paratropic trajectories of current density above the plane containing the nuclei of ethylene for a field perpendicularly pointing outward. The mirror image of this pattern is observed below the plane of the nuclei. *Isolated blue points* mark (3 ± 1) saddle-nodes, *isolated green (red) points* denote (3 ± 1) diamagnetic (paramagnetic) foci

The SG for $\mathbf{J}^{\mathbf{B}}$ induced by a field orthogonal to the molecular plane of ethene is displayed in Fig. 7.9 and the corresponding streamlines are plotted in Fig. 7.10. A contour map (in red) of the shielding density

$$\sum_{xx}^I(\mathbf{r}) = -\frac{\mu_0}{4\pi} \epsilon_{x\beta\gamma} \frac{r_\beta - R_{I\beta}}{|\mathbf{r} - \mathbf{R}_I|^3} \mathcal{J}_\gamma^{B_x}(\mathbf{r}), \quad (7.81)$$

defined via Eq. (7.81) for $I = \text{H}$ is shown in Fig. 7.10 on the plane of the nuclei of $\text{CH}_2\text{-CH}_2$. Red contours superimposed to the streamlines of the $\mathbf{J}^{\mathbf{B}}(\mathbf{r})$ field provide visual understanding of the local (shielding or deshielding) contributions at points \mathbf{r} on the plot plane [103]. Figure 7.10 shows that the largest proton shielding component, $\sigma_{xx}^{\text{H}} = 29.9$ ppm, is essentially determined by local flow. Nearly vanishing contributions of opposite sign arise from closest and furthest portions of distant current loops. An interesting set of phase portraits was observed for the

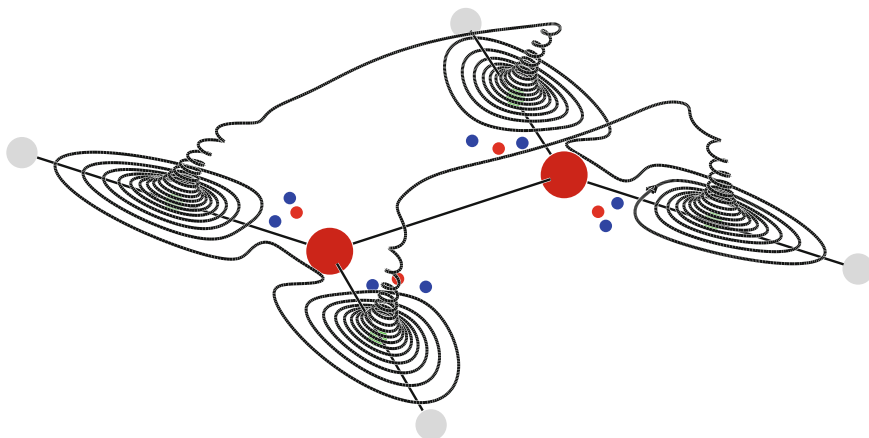


Fig. 7.12 Spiralling diatropic trajectories of current density above the plane containing the nuclei of ethylene for a field perpendicularly pointing outward. The mirror image of this pattern is observed below the plane of the nuclei. The isolated $(3, \pm 1)$ stagnation points are represented with the *colour* convention of Fig. 7.11

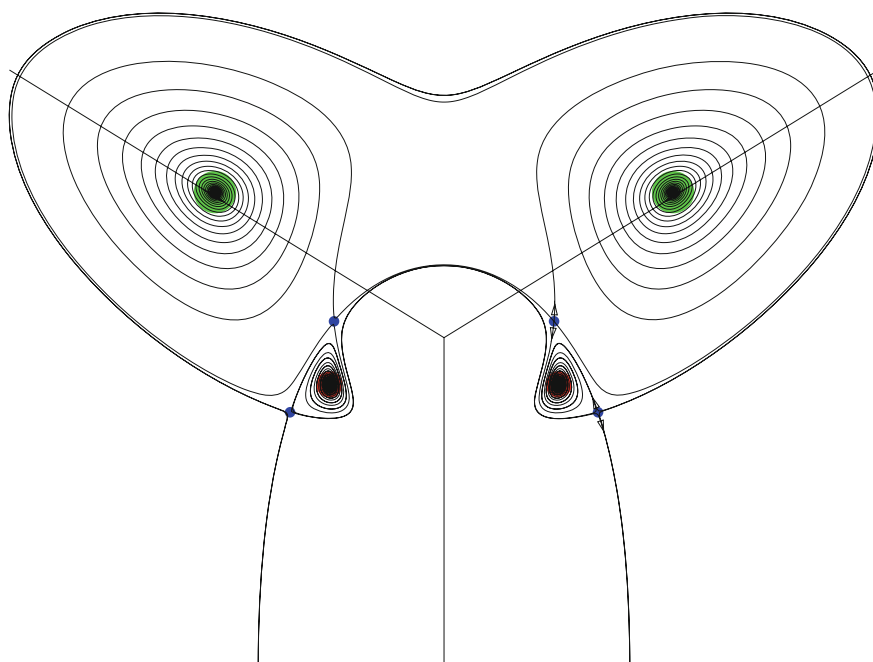
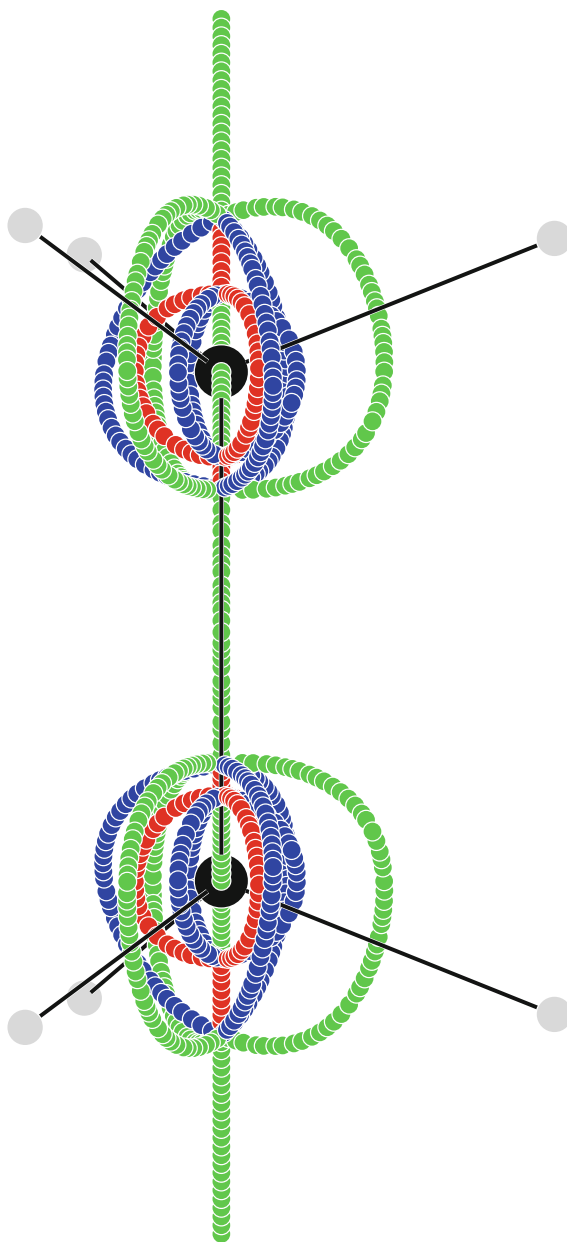


Fig. 7.13 Asymptotic lines of current density on the plane containing the nuclei of ethylene. The magnetic field, applied at right angles to the plot plane, points outwards. *Blue points* denote $(3, \pm 1)$ saddle-nodes, *green (red) spots* mark regions of diamagnetic (paramagnetic) spiral flow about $(3, \pm 1)$ foci

Fig. 7.14 Perspective view of the stagnation graph of the current density vector field in eclipsed ethane C_2H_6 , with magnetic symmetry $D_{3h}(C_{3h})$. The uniform external magnetic field \mathbf{B} is parallel to the C–C bond axis



trajectories spiralling about the red $(3, \pm 1)$ foci. All of them are connected by asymptotic streamlines, starting and ending at each focus, as shown in the perspective spatial view of Figs. 7.11 and 7.12. Homoclinic lines on the σ_h plane are displayed in Fig. 7.13.

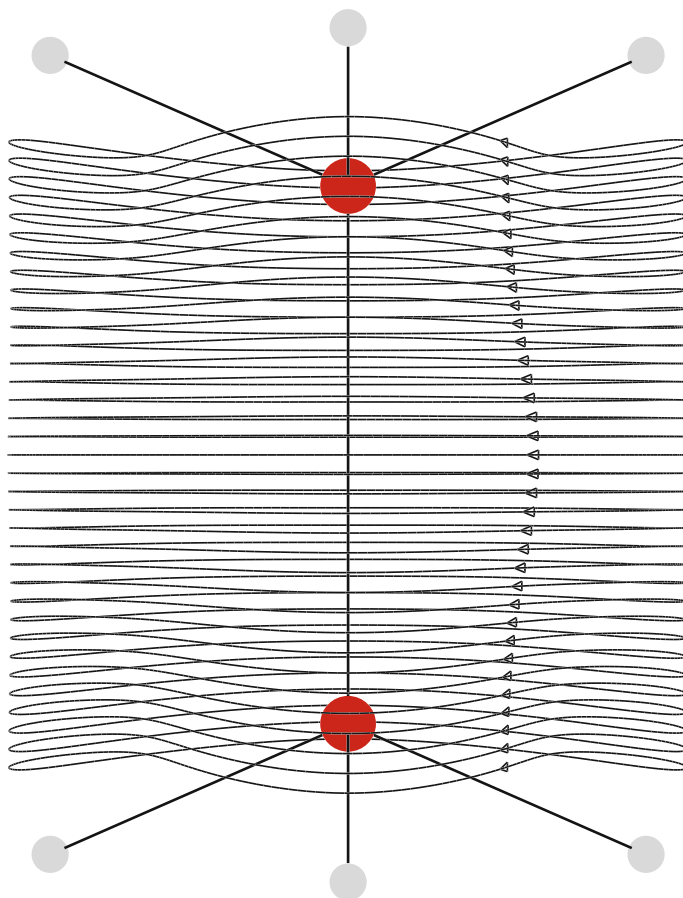
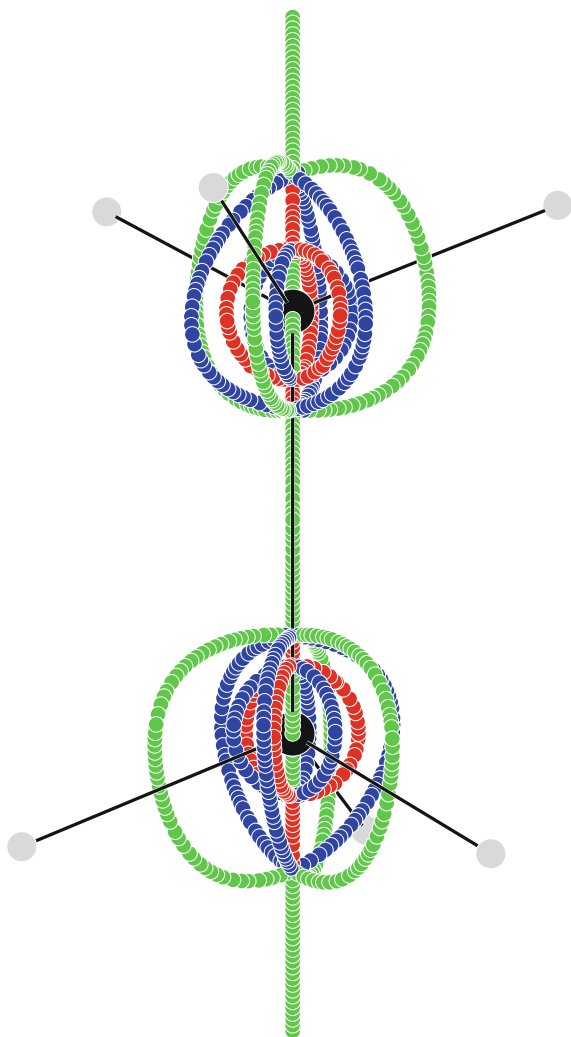


Fig. 7.15 Perspective view of the current density vector field in ethane C_2H_6 , with magnetic symmetry $D_{3h}(C_{3h})$. The uniform external magnetic field \mathbf{B} is parallel to the C–C bond axis

A perspective view of the stagnation graph of the current density vector field of methane CH_4 in a uniform external magnetic field \mathbf{B} parallel to a C_2 symmetry axis bisecting HCH angles (a system with $D_{2d}(S_4)$ magnetic symmetry isomorphic to D_{2d}) shows branching points occurring at a short distance ($\approx \pm 0.4$ bohr) from the C nucleus, see Fig. 9 of Ref. [102]. An analogous representation of the SG of \mathbf{J}^B of a distorted ethane molecule C_2H_6 , in the presence of uniform external magnetic field parallel to the C–C bond axis, with magnetic symmetry $D_3(C_3)$, contains eight ($3, \pm 1$) foci along the threefold symmetry axis, which indicates that the diatropic electron flow spirals about it and that closed current density loops are absent. This is confirmed by the corresponding streamline map, showing a single diatropic trajectory spiralling about the C_3 symmetry axis [102]. This pattern can be compared

Fig. 7.16 Perspective view of the stagnation graph of the current density vector field in staggered ethane C_2H_6 , with magnetic symmetry $D_{3d}(S_6)$. The uniform external magnetic field \mathbf{B} is parallel to the C–C bond axis



with the series of distinct closed loops in Fig. 7.15 for a flow with $D_{3h}(C_{3h})$ magnetic symmetry and Fig. 7.17 for a flow with $D_{3d}(S_6)$ magnetic symmetry. The corresponding SGs are shown in Figs. 7.14 and 7.16.

The $C_{3v}(C_3)$ magnetic subsymmetry, Eq. 7.78, is observed in methane for \mathbf{B} along a C–H bond, taken to lie in the z direction. The corresponding SG is reported in Fig. 7.18. The cage of SLs about a C nucleus is a transferable pattern, compare for that observed for ethane in Figs. 7.14 and 7.16. Four $(0, 0)$ branching points occur along the threefold axis, at $P_{\pm 1} = \pm 0.66$, $P_{\pm 2} = \pm 0.50$ bohr from the origin on the C nucleus [102]. The corresponding streamline map is displayed in Fig. 7.19.

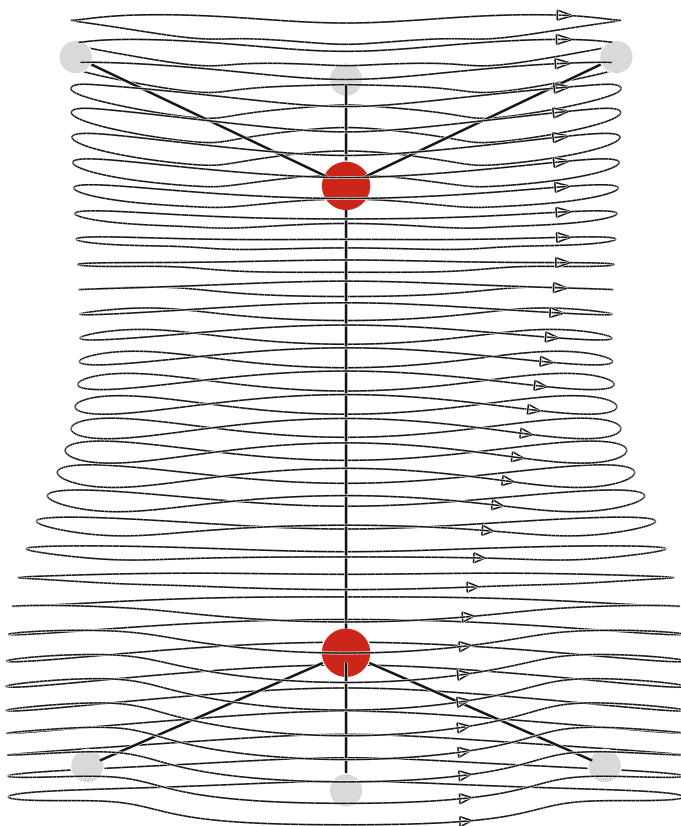
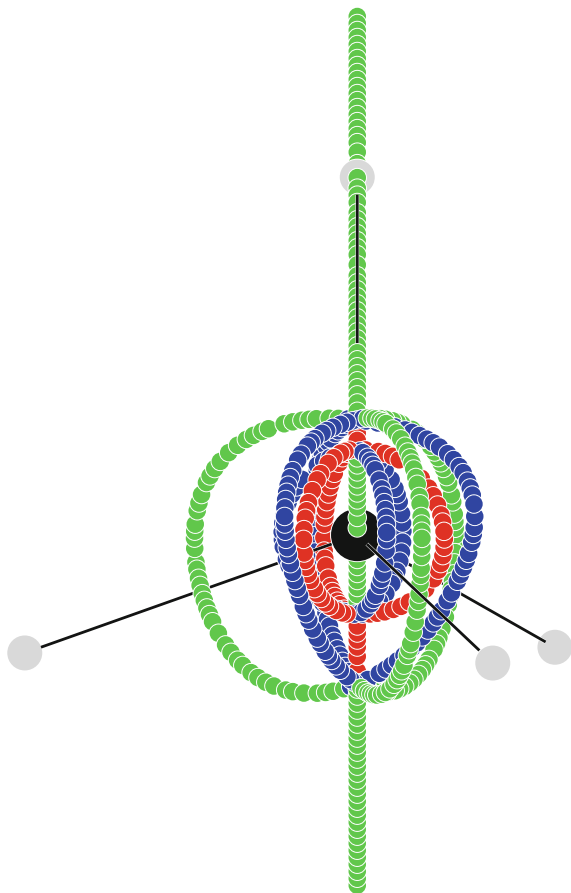


Fig. 7.17 Perspective view of the current density vector field in ethane C_2H_6 , with magnetic symmetry $D_{3d}(S_6)$. The uniform external magnetic field \mathbf{B} is parallel to the C–C bond axis

7.5.2 *Magnetic Symmetry, Stagnation Graph and Induced Current Density of Mono-cyclic Neutral and Charged C_nH_n Systems in a Magnetic Field*

Several attempts have been made to achieve reliable representations of the \mathbf{J}^B current density field in neutral and charged cyclic conjugated compounds with chemical formula C_nH_n in the presence of a static magnetic field orthogonal to the molecular σ_h plane, in connection with their magnetotropy [15]. The molecular point group symmetry of these unsaturated systems determines the essential features of the induced current density field and relative SG. $D_{nh}(C_{nh})$ magnetic groups [58, 98, 99] were considered to discuss the symmetry of conjugated cyclic molecules [104].

Fig. 7.18 Perspective view of the stagnation graph of the current density vector field in methane CH_4 . The uniform external magnetic field \mathbf{B} is parallel to a C_3 symmetry axis along a CH bond



For instance, assuming \mathbf{B} along the C_n axis, parallel to the z direction, the magnetic group of benzene, the archetypal aromatic molecule, contains the symmetry elements listed in Eq. (7.80), that of cyclopropenyl cation, with $n = 3$, is given by Eq. (7.79), and that of the cyclobutadienyl dication, $\text{C}_4\text{H}_4^{2+}$, by Eq. (7.76). Other interesting cyclic systems are the cyclopentadienyl anion, C_5H_5^- , belonging to the symmetry group $D_{5h}(C_{5h})$, and the tropylium cation C_7H_7^+ . These systems are regarded as aromatic on the magnetic criterion [15]. Using the nomenclature of Eqs. (7.72)–(7.80),

$$\begin{aligned}
 D_{5h} &\equiv \{ E \quad 2C_5 \quad 2C_5^2 \quad 5C_2 \quad \sigma_h \quad 2S_5 \quad 2S_5^3 \quad 5\sigma_v \} \\
 C_{5h} &\equiv \{ E \quad C_5 \quad C_5^2 \quad C_5^3 \quad C_5^4 \quad \sigma_h \quad S_5 \quad S_5^2 \quad S_5^3 \quad S_5^4 \} \\
 D_{5h}(C_{5h}) &\equiv \{ E \quad C_5 \quad C_5^2 \quad C_5^3 \quad C_5^4 \quad 5TC_2 \quad \sigma_h \quad S_5 \quad S_5^2 \quad S_5^3 \quad S_5^4 \quad 5T\sigma_v \}
 \end{aligned}
 \tag{7.82}$$

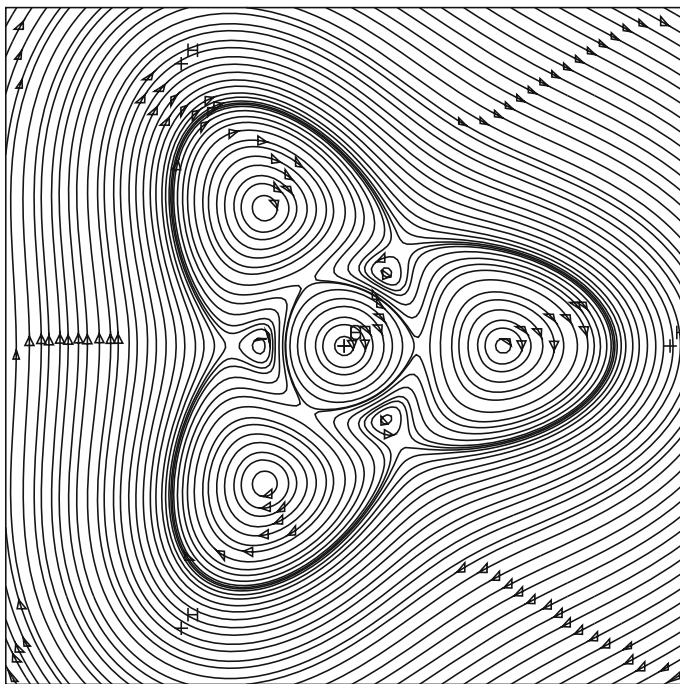


Fig. 7.19 Streamlines of the current density vector field in methane CH_4 on a plane through the C nucleus, normal to the uniform external magnetic field \mathbf{B} parallel to the C_3 symmetry axis along a CH bond. The (2, 0) stagnation points are identified via the stagnation graph of Fig. 7.18

The magnetic point groups for the tropilium cation, $D_{7h}(C_{7h})$, and cyclo-octatetraenyl di-cation and di-anion, $D_{8h}(C_{8h})$, can also be constructed by the Tavger-Zaitsev recipe [58, 98, 99], Eq. (7.71).

The electronic wavefunction of neutral and charged C_nH_n cyclic conjugated molecules is characterized by sigma/pi separability for symmetry reasons, see, for instance Ref. [15] and references therein. This feature is only preserved in the presence of magnetic field perpendicular to the molecular σ_h plane. In these conditions, the magnetic response properties, e.g., magnetizability and nuclear magnetic shieldings, can be partitioned into separate contributions from σ - and π -electrons. Analogously, the current density field $\mathbf{J}^{\mathbf{B}}$ induced in neutral and charged C_nH_n cyclic systems by a magnetic field \mathbf{B} perpendicular to the molecular σ_h plane, can be represented by the superposition of disjointed σ - and π -contributions. Accordingly, total properties can be rationalized in terms of separate pieces [15]. On the other hand, for \mathbf{B} parallel to the molecular plane, σ - and π -electron flow is inextricably mixed.

A general quantum-mechanical procedure, referred to as *continuous transformation of origin of the current density-diamagnetic zero* (CTOCD-DZ) [3, 15, 71, 105], within the damped DZ2 variant [106, 107], has been employed, at the

Hartree-Fock level of accuracy, to obtain the stagnation graph of $D_{nh}(C_{nh})$ compounds. The third-order linear autonomous system for the flow was integrated using Runge-Kutta procedures [108].

Stagnation graphs of unsaturated C_nH_n hydrocarbons in a magnetic field orthogonal to the σ_h molecular plane are displayed in Fig. 7.20. It can be observed that the SGs of the \mathbf{J}^B field, characterized by the symmetry elements of the magnetic groups $D_{nh}(C_{nh})$, show common features. In the outer reaches of the molecular domain the flow is diamagnetic. It is represented in Fig. 7.20 by a green open vortical line, coinciding with the highest symmetry axis and extending to the boundaries of configuration space. A pair of (0, 0) transition points, at the same distance above and below the plane of the carbon nuclei, is found for all systems. The distance of the (0, 0) SPs increases from ≈ 1.3 bohr for $n = 3$ to ≈ 2.0 bohr for $n = 4$, and to ≈ 2.5 bohr for $n = 5$. Approximately the same values were found for higher n , i.e., ≈ 2.5 bohr for $n = 6$, ≈ 2.4 bohr for $n = 7$, and ≈ 2.13 bohr for $n = 8$.

The $2n + 1$ SLs originating at the north (0, 0) point merge at the other; n of the southbound lines are saddle lines and n are diamagnetic vortical lines. In Fig. 7.20, the former are represented in blue, the latter in green. Each diamagnetic vortex crosses the molecular plane in the region of a C–C bond, close to its midpoint, each saddle line passes through a point of σ_h in the proximity of the carbon nucleus [104]. The conservation condition (Gomes theorem) [55–57, 93], Eq. (7.59), is satisfied. All the SLs lie on a topological surface with the shape of an oval ball, referred to as *separatrix* [56], encasing domains of localized flow and a central paramagnetic vortex represented by a red line in Fig. 7.20. All over this surface, the element of electric current, Eq. (7.44), $d\mathbf{I}^B = \mathbf{J}^B \cdot d\mathbf{s}$ vanishes, since no current density streamline can cross the separatrix.

Quite remarkably, the topological index of each of the $2n$ SLs constituting the skeleton of the separatrix does not stay the same on moving south (north) from the north (south) branching point, which can be observed in Fig. 7.20 as a colour change corresponding to a change of local regime—from saddle to vortex and viceversa. The change takes place at points lying on a same plane for every SL. One can ask if such a change implies a violation of the index conservation theorem, Eq. (7.59). The question is answered in the negative if it is assumed that, for each SL, the scenario is modelled by the pitchfork bifurcations of Eqs. (7.69) and (7.70), visualized in Fig. 7.6.

The corresponding maps for the streamlines of the current density flowing on the σ_h plane displayed in Fig. 7.21 show patterns of vortex and saddle regime which are elucidated by the SGs of Fig. 7.20. The existence of a central paramagnetic vortex, documented for the first time in 1982 by Lazzeretti and Zanasi [109], is the distinctive feature of all diatropic systems with $D_{nh}(C_{nh})$ magnetic symmetry. It must exist as required by the index conservation constraint proven by Gomes, Eq. (7.59) [55–57, 93]. The analysis of proton magnetic shielding in cyclic compounds [110] is consistent with these results.

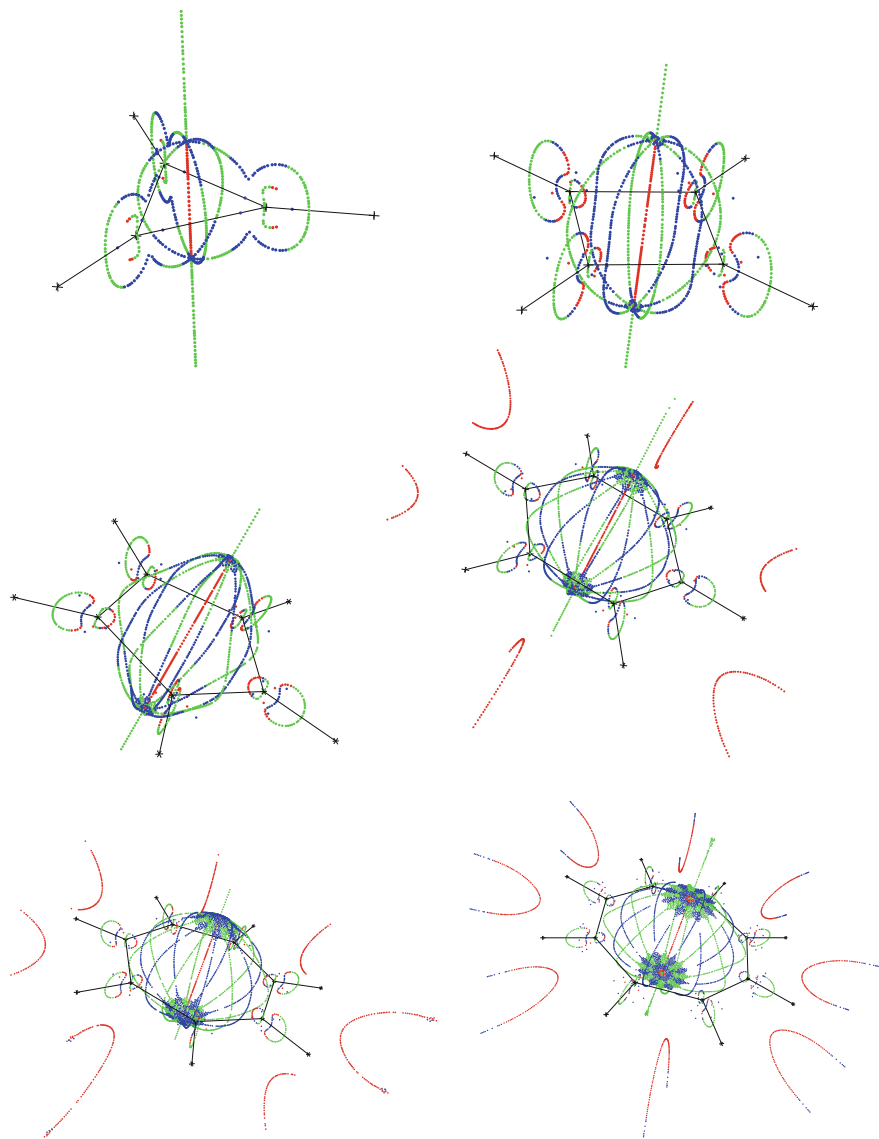


Fig. 7.20 The stagnation graph of the \mathbf{J}^B current density in cyclic systems C_nH_n for $n = 3, 4, \dots, 8$. Green (red) SLs denote diamagnetic (paramagnetic) vortices, saddle SLs are blue

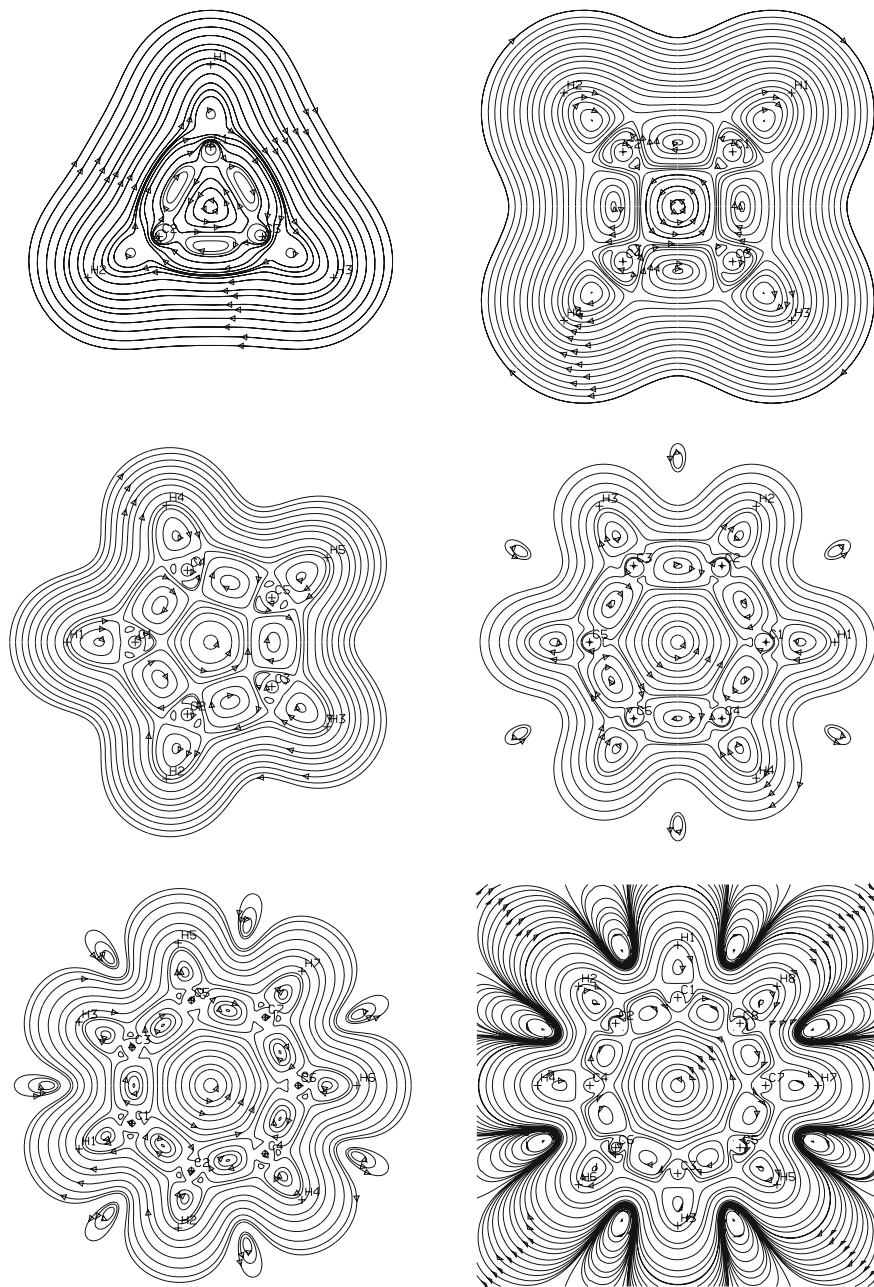


Fig. 7.21 Streamlines of the J^B current density vector field induced by a static, uniform magnetic field at right angles to the molecular plane of C_nH_n cyclic systems for $n = 3, 4, \dots, 8$. Diamagnetic flow is clockwise

7.5.3 Five-Membered Heterocyclic Molecules

The stagnation graphs of 1,3-cyclopentadiene, furan, pyrrole, and thiophene, in the presence of a magnetic field perpendicular to the molecular plane [111], are displayed in Fig. 7.22. They show that the electron flow induced by a perpendicular magnetic field in pentatomic cyclic molecules with $C_{2v}(C_s) \equiv \{E, TC_2, T\sigma_v, \sigma'_v\}$ symmetry is characterized by a regime remarkably different from that of $D_{nh}(C_{nh})$ compounds discussed in Sect. 7.5.2. An analogous consideration was made for

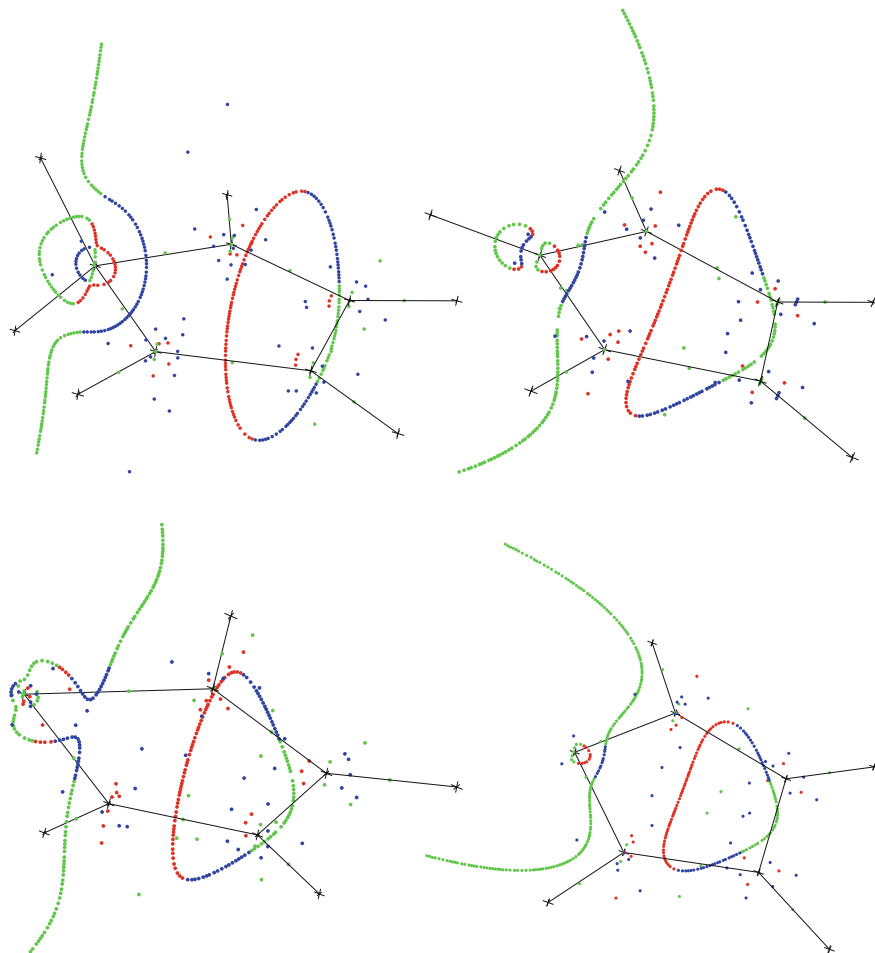


Fig. 7.22 The stagnation graph of five-membered cyclic compounds. Clockwise from *top left*: 1,3-cyclopentadiene, pyrrole, furan, and thiophene in the presence of a magnetic field perpendicular to the molecular plane. Diamagnetic (paramagnetic) vortices are represented by *green (red) lines*, and saddle lines are *blue*. All the stagnation lines lie on the $T\sigma_v$ plane of magnetic symmetry

phosphole and arsole [111, 112], with lower $C_s(C_1) \equiv \{E T\sigma\}$ magnetic symmetry.

The stagnation graphs of 1,3-cyclopentadiene, furan, pyrrole, and thiophene is characterized by a similar pattern in the proximity of the CH_2 group or the heterotom, i.e., the green truncated vortex line, denoting diamagnetic flow which extends to the tail regions of the molecular domain. On crossing the plane of the nuclei, for the first three compounds, this SL corresponds to saddle flow. A small closed loop corresponding to two vortices flowing in opposite directions, which characterizes a TV, is observed in front of it in pyrrole and thiophene. More complicated patterns were found in the vicinity of the CH_2 moiety of 1,3-cyclopentadiene and nearby the oxygen atom in furan.

Another common feature constitutes the hallmark of all the five-membered cyclic molecules in Fig. 7.22 and characterizes their peculiar magnetic response, that is, the closed stagnation loop disconnected from the rest of the SG, passing nearby the midpoint of the pentagon side opposite to the CH_2 group or the heteroatom. The green diamagnetic vortex line crossing the C–C bond and the red paramagnetic vortex line, flowing in the vicinity of its centre of mass, are connected to blue saddle lines by (0, 0) points, at which change of regime takes place. The Gomes index of this disconnected piece is 0, as two lines with opposite ± 1 index emerge at each branching point.

The red portion of the stagnation loop crossing the molecular plane indicates, according to the colour code of Fig. 7.22, the presence of a paramagnetic vortex, which is actually observed in the streamline maps [111]. Its substantial difference from that typical of $D_{nh}(C_{nh})$ aromatics, corresponding to a vortical SL in between two (0, 0) degenerate points on the main symmetry axis, i.e., belonging to a connected set of SLs, can hardly be overemphasized. Therefore, the disconnected stagnation loop is the topological signature distinguishing five-membered heterocyclic molecules from the cyclic C_nH_n molecules to which they are frequently associated. An analysis of diatropicity of pentatomic cyclic molecules, and a comparison of their aromaticity (on the magnetic criterion) with benzene's, should not put aside these findings.

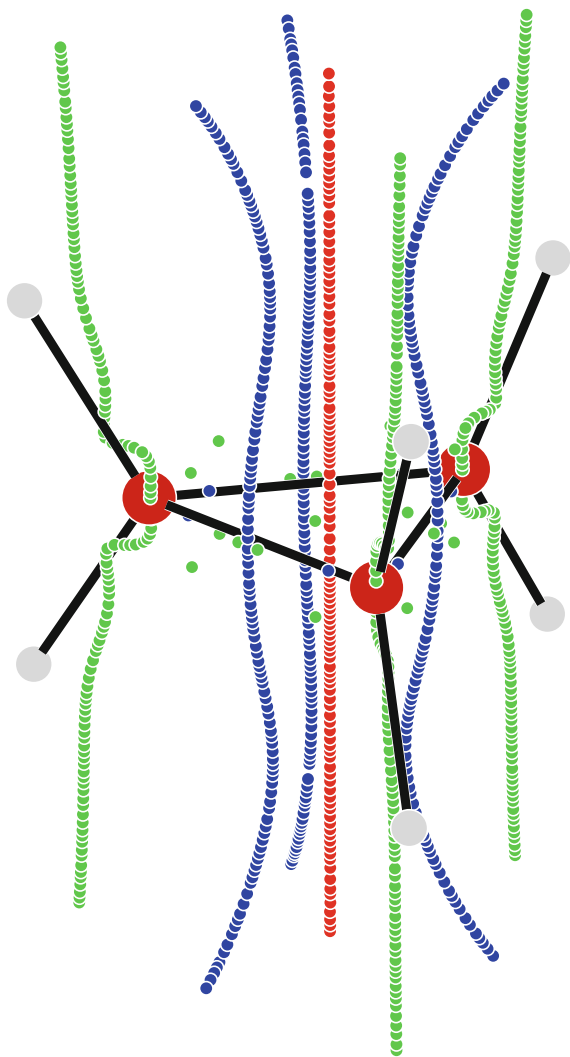
7.5.4 Cyclopropane

Chemists traditionally assumed that cyclopropane enjoys a peculiar combination of properties referred to as σ -aromaticity, which would be determined by σ -electron delocalization related to resonance and to strained geometry. In fact, the experimental average magnetizability ξ_{av} of C_3H_6 is much larger than that calculated from additive Pascalian schemes. The enhanced anisotropy of $\xi_{\alpha\beta}$ has been attributed to the presence of σ -electron ring currents induced by a magnetic field perpendicular to the molecular plane, which would also cause upfield chemical shift in proton magnetic resonance. This interpretation has been seriously questioned in recent

papers [113, 114] via near Hartree-Fock representations of magnetic-field induced current density field. No proof for strong diatropism was found for the cyclopropane molecule in a magnetic field normal to the carbon plane.

The essential features of $\mathbf{J}^{\mathbf{B}}$ are understood by the SG shown in Fig. 7.23 and by the current density maps of Fig. 7.24. The SG is very different from that of π -aromatic C_nH_n cyclic system analyzed in Sect. 7.5.2. It shows that the primary vortical SL branches out into four vortical and three saddle SLs. Two far-off (0, 0) critical points, not visible in the figure, lie on the C_3 axis, at a distance of more than 10 bohr from the centre of mass. The Gomes theorem, Eq. (7.59), is fulfilled: three diamagnetic vortical SLs, each lying on a $T\sigma_v$ symmetry plane, pass through the C nuclei, then they bend outward at some

Fig. 7.23 Perspective view of the stagnation graph of the current density vector field in cyclopropane. The uniform external magnetic field, $\mathbf{B} \equiv B\epsilon_3$, is parallel to the z axis. *Green (red) lines* denote diamagnetic (paramagnetic) vortices, saddle lines are *blue*



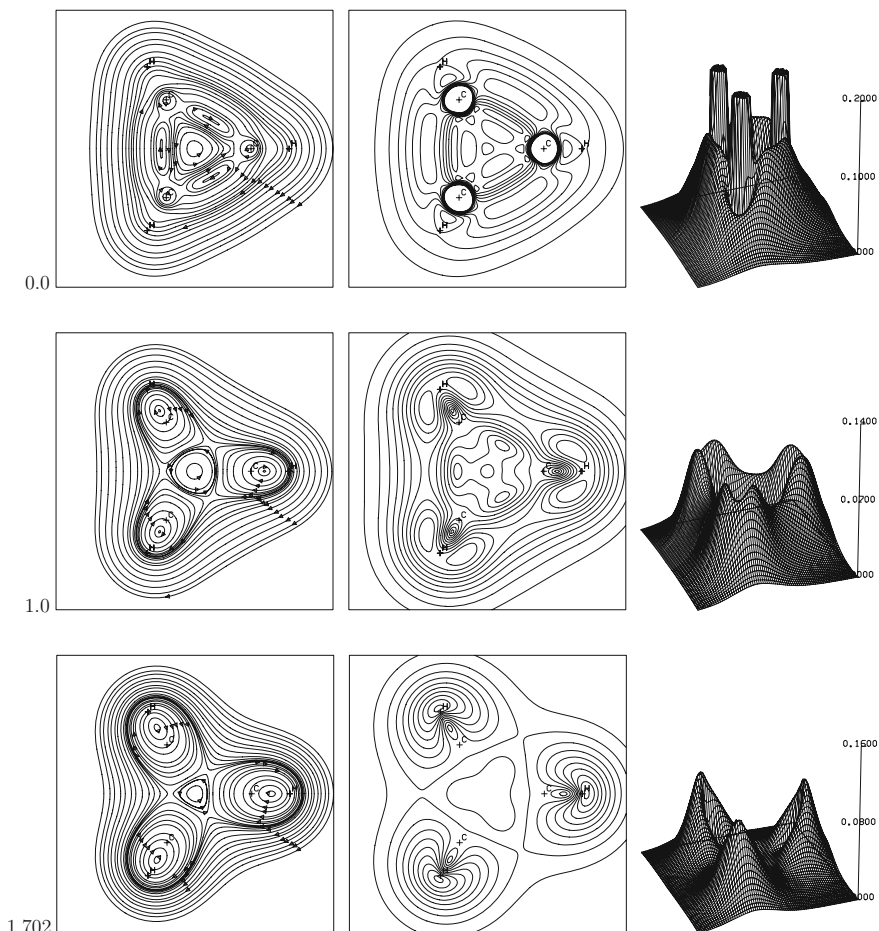


Fig. 7.24 Streamlines and modulus of the current density vector field induced by a magnetic field of unit magnitude, normal to the molecular plane of cyclopropane and directed outward. The distance in bohr from the origin is specified by a number on the *down-left corner*. Atom positions are marked by *crosses*. Maximum modulus (step between two consecutive contours) in au: 2.22 (0.02) at 0.0, 0.0872 (0.009) at 1.0, and 0.0916 (0.009) at 1.702

distance above and below the σ_h plane. The fourth paramagnetic vortex rotates about an SL that coincides with the C_3 axis. The streamlines in Fig. 7.24 show the extension of the paramagnetic vortex about the centre of the molecule. The corresponding contours and three-dimensional perspective view accounting for the intensity of the current field indicate that the central paratropic whirlpool is as weak as the diamagnetic flow in the tail regions. There is no evidence of strong delocalized currents and of σ -aromaticity on the magnetic criterion [113, 114].

An interesting comparison is offered by the prismane molecule, a polycyclic hydrocarbon with formula C_6H_6 , whose carbon and hydrogen atoms are arranged in the shape of a six-atom triangular prism. The magnetic symmetry is the same as cyclopropane's $D_{3h}(C_{3h})$. It is a valence isomer of benzene, far less stable than the archetypal aromatic molecule. A spatial ring current model for this molecule has been reported [115].

7.5.5 *Cubane and Pentaprismane*

Cubane is a Platonic hydrocarbon with chemical formula C_8H_8 , possessing octahedral O_h symmetry. Its special magnetic properties have been investigated by some authors, whose work was reviewed in a recent paper [116]. A compact spatial model for the electronic current density vector field induced in the cubane molecule by a magnetic field perpendicular to a face has been proposed to interpret its magnetic response.

A perspective view of the SG of the cubane molecule is shown in Fig. 7.25. It conveys the essential information needed to understand the maps the \mathbf{J}^B field, Figs. 7.26 and 7.27. The central vortical SL coincides with the $C_4(z)$ symmetry axis. Branching of this SL takes place at a pair of far-off critical points, where transition occurs from diamagnetic flow in the tail regions to paratropic regime.

The central paramagnetic axial vortex is represented in Fig. 7.25 by a red line extending to great lengths in the direction of the \mathbf{B} field. Four green diamagnetic vortical lines lie on the $T\sigma_d$ planes intersecting along the z axis and containing HCC bonds, and four blue saddle SLs are situated on the $T\sigma_v$ planes bisecting CC bonds. The Gomes theorem, Eq. (7.59), is obeyed: by counting the ι indices of the SLs one has $+5 - 4 = +1$, i.e., the overall circulation is vortical.

On crossing the faces of the carbon cage parallel to the xy plane, short green segments, representing diamagnetic vortical flow embedded in the blue saddle SLs, are observed. This feature is similar to that observed in aromatic compounds examined in Sect. 7.5.2 and it can tentatively be interpreted in terms of pitchfork bifurcations taking place on a same plane parallel to σ_h .

Maps of \mathbf{J}^B field, Figs. 7.26 and 7.27, on planes orthogonal to \mathbf{B} constitute a basic model useful to describe the magnetic properties of cubane. They show the diamagnetic circulation in the tail regions of the molecule, typical of all diamagnetic systems, and the set of vortex and saddle SPs at the intersection of corresponding SLs with the plot plane.

To sum up, the magnetic response of the C_8H_8 molecule to a magnetic field applied at right angles to a face of the cube is characterized by a strong paratropic AV flowing inside the lateral surface of the cube. The intensity of the paratropic ring currents sustained by σ -electrons in cubane is higher than that induced in the π -electrons of benzene. Therefore, even if overall diamagnetism prevails, as proven

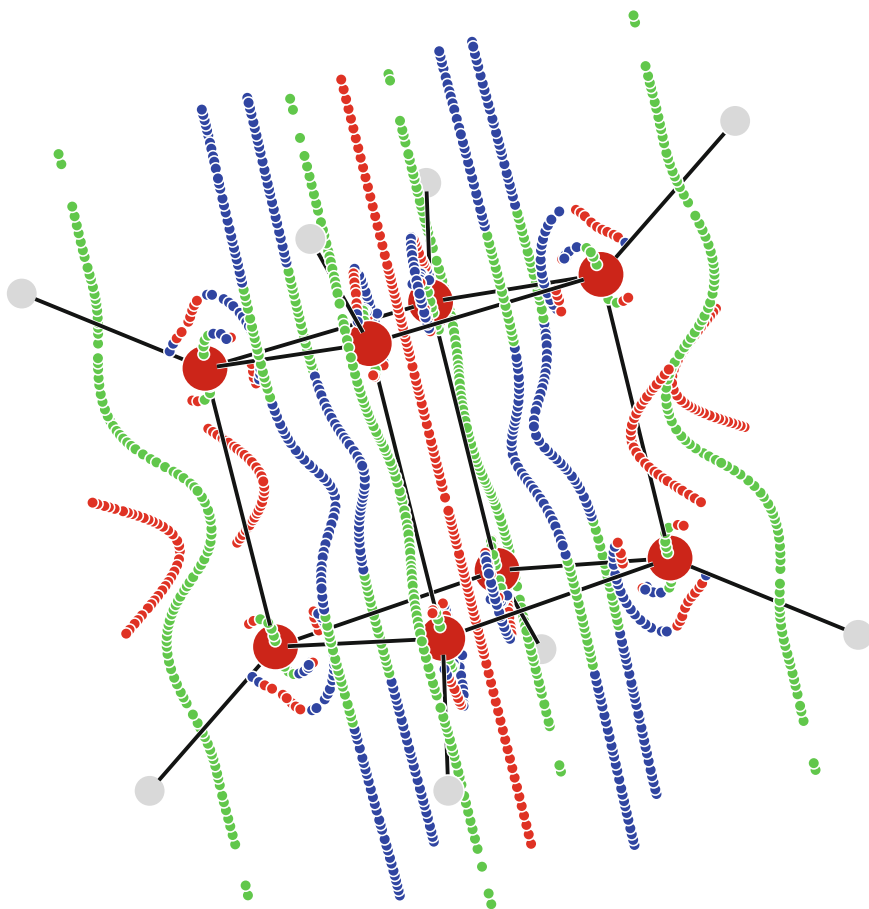


Fig. 7.25 Perspective view of the stagnation graph of the current density vector field in cubane C_8H_8 . The uniform external magnetic field $\mathbf{B} = \epsilon_3 B_z$ is perpendicular to opposite square faces of the C_8H_8 cage (ϵ_3 is the unit vector in the direction of the z axis through the centre). *Green (red) lines* denote diatropic (paratropic) vortices, saddle lines are *blue*

by the calculated average magnetizability $\xi_{av} = -86.5 \times 10^{-29} \text{ J T}^{-2}$, the cubane cage can be considered a hallmark of face-centred paramagnetism [116].

Pentaprismane constitutes another example of molecules designed and synthesized by chemists to give pleasure through their abstract beauty. Besides, it is endowed with noticeable magnetic properties, interpretable [117] via the theoretical tools outlined in this chapter. A perspective view of the SG of the pentaprismane molecule in a spatially uniform magnetic field parallel to the C_5 symmetry axis, i.e., at right angles to the five-membered face, is shown in Fig. 7.28. The magnetic symmetry is $D_{5h}(C_{5h})$, Eq. (7.82).

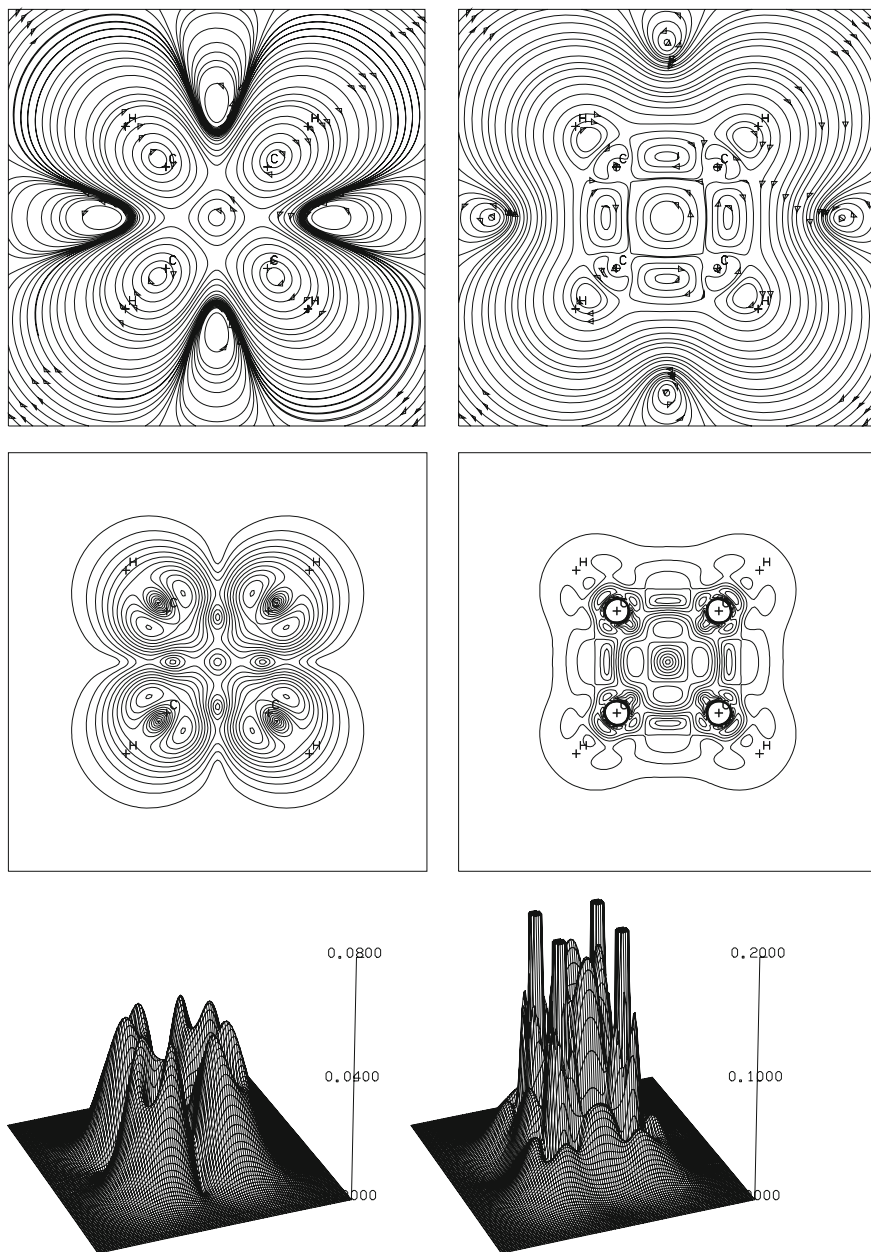


Fig. 7.26 Streamlines and modulus of the current density vector field induced in cubane by a magnetic field B_z with magnitude 1 au normal to a face of the cube and directed outward, plotted (*left*) in the xy plane through the centre of the molecule; (*right*) in the plane of a face. The projection of atom positions is marked by a *cross*. The maximum modulus (step between two consecutive contours) in au is 4.8×10^{-2} (4×10^{-3}) on the *left*, 1.93, cut at 0.2, (2×10^{-2}) on the *right*

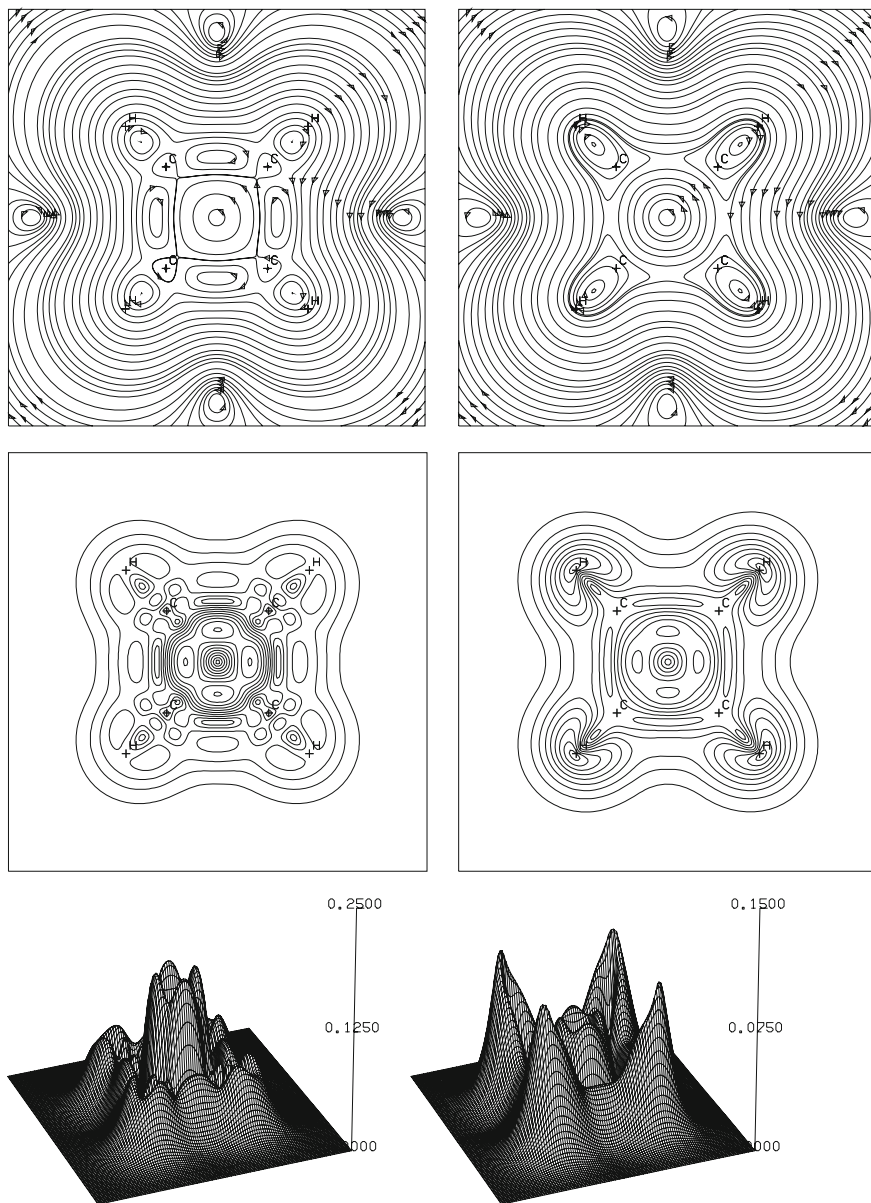


Fig. 7.27 Streamlines and modulus of the J^B field. The graphical conventions are the same as in Fig. 7.2. The plot planes are (*left*) parallel to a face at a distance $z = 2$ bohr; (*right*) parallel to the plane of the H nuclei, at $z = 2.62896$ bohr. The maximum modulus (step between two consecutive contours) in au is 0.15 (1.5×10^{-2}) on the *left*, and 9.3×10^{-2} (1×10^{-3}) on the *right*

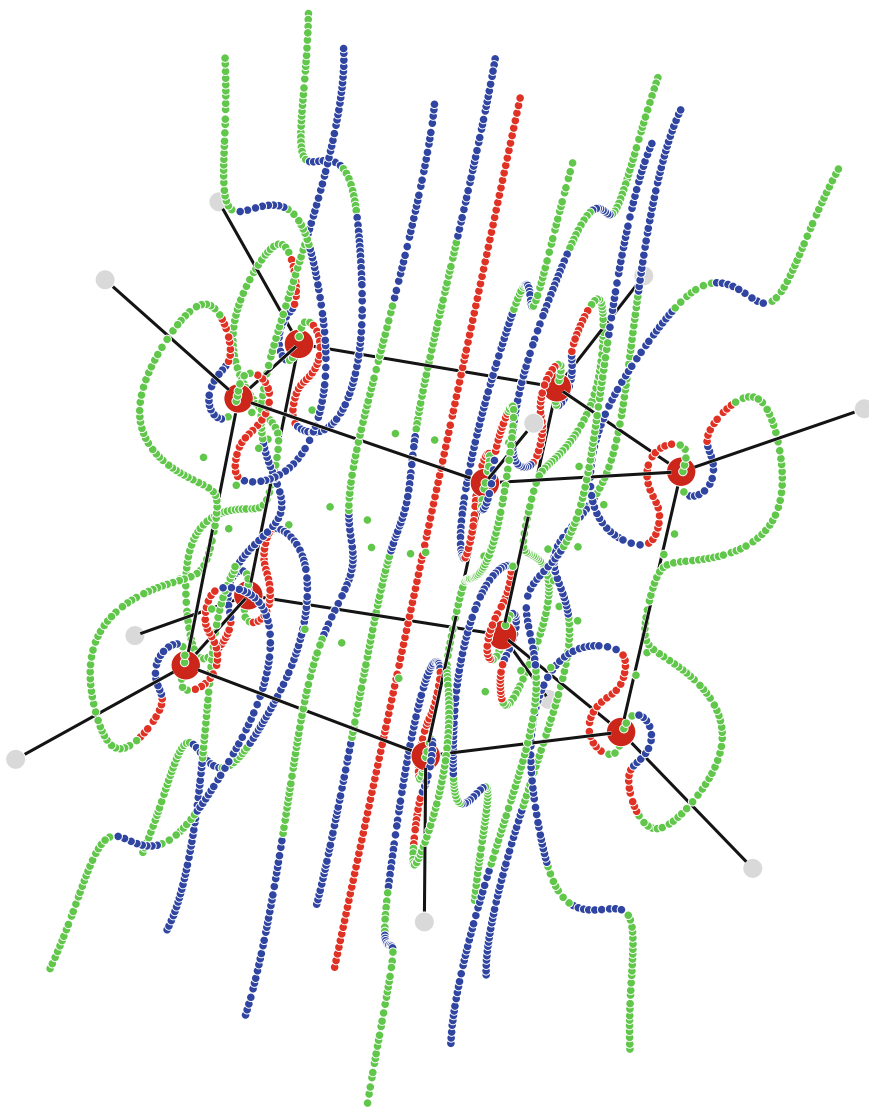


Fig. 7.28 Perspective view of the stagnation graph of the current density vector field in pentaprismane $C_{10}H_{10}$. The uniform external magnetic field $\mathbf{B} = \epsilon_3 B_z$ is perpendicular to the pentagonal faces of the C-cage (ϵ_3 is the unit vector in the direction of the $C_5 \equiv z$ axis through the centre). *Green (red) points* denote diatropic (paratropic) vortices, or foci; saddle points are *blue*

The topological features of the SG and the associated representations of the \mathbf{J}^B field, Figs. 7.29 and 7.30, are analogous to those reported for prismane [115] and outlined above for cubane. A similar structure characterizes the set of vortex- and saddle-SLs which emerge from a pair of remote $(0, 0)$ branching points, at which

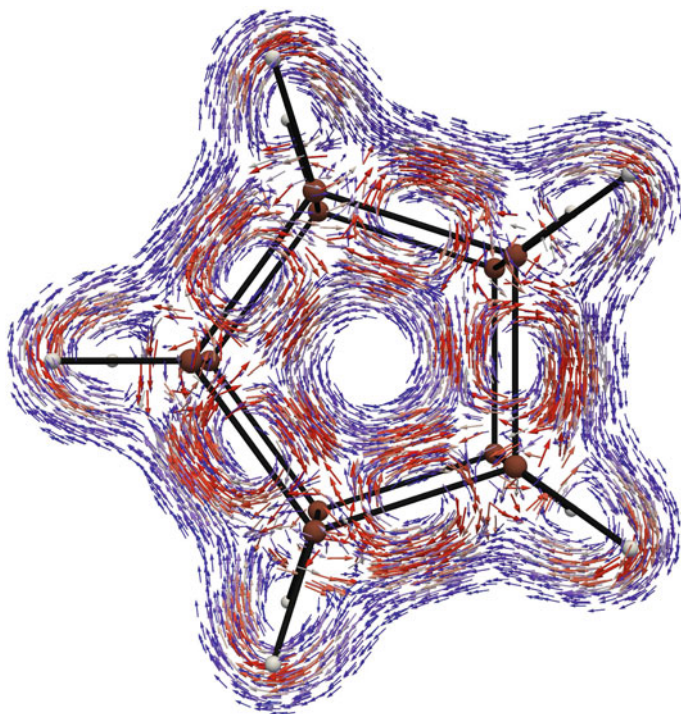


Fig. 7.29 Perspective view of the $\mathbf{J}^{\mathbf{B}}$ field in pentaprismane in a uniform external magnetic field $\mathbf{B} = B_z \varepsilon_3$, of magnitude 1 au, perpendicular to the pentagonal faces. Only current densities with $|\mathbf{J}^{\mathbf{B}}|$ between 0.05 (blue arrows) and 0.1 au (red arrows) are plotted. The figure shows the peripheral regions of delocalized diatropic flow, the central paratropic vortex and the local diatropic vortices about the midpoint of the C–C bonds

transition occurs from diamagnetic vortical flow in the outer reaches of the molecule to the internal region of the current density field, enclosed within the grey surface observable in Fig. 7.31. This surface is a two-dimensional manifold of points \mathbf{r} at which the zz component of the shielding density, Eq. (7.56),

$$\sum_{zz}^I(\mathbf{r}) = -\frac{\mu_0}{4\pi} \varepsilon_{z\beta\gamma} \frac{r^\beta - R_{I\beta}}{|\mathbf{r} - \mathbf{R}_I|^3} \mathcal{J}_\gamma^{B_z}(\mathbf{r}) \quad (7.83)$$

vanishes for any dummy atom I all along the C_5 symmetry axis, in a magnetic field \mathbf{B} parallel to it. It surrounds the central paratropic vortex, indicated by a red line, and five diatropic vortices indicated by green lines, separated by the five saddle blue lines, but it does not coincide with the separatrix. The line branching of Fig. 7.28 is consistent with the Gomes theorem, Eq. (7.59). Planar visualisations of the density function, Eq. (7.83), for $I = \text{H}$, are displayed in Fig. 7.30.

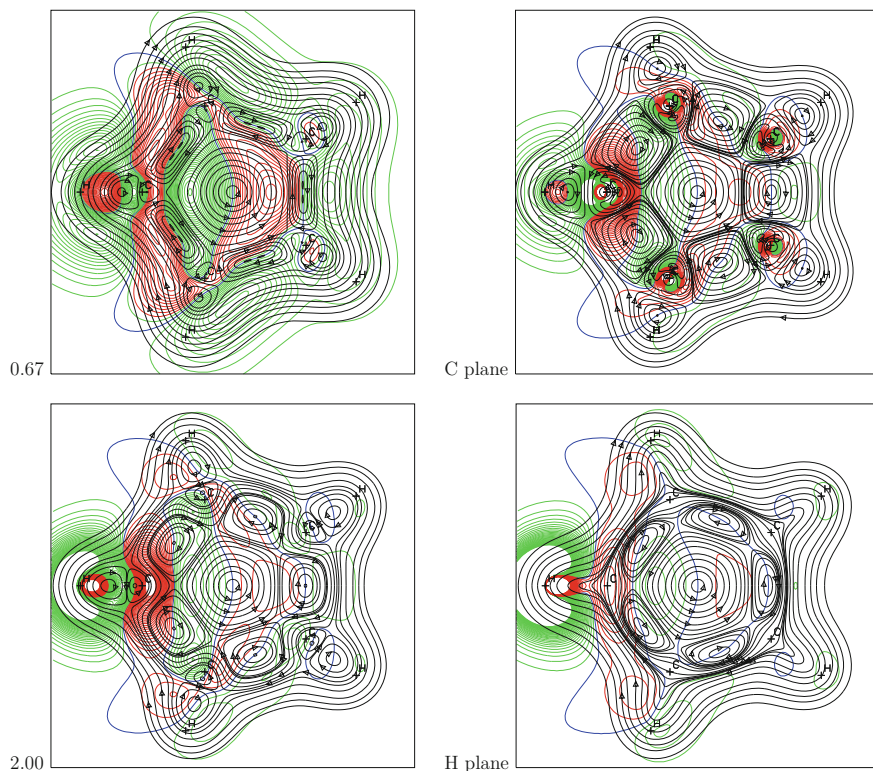
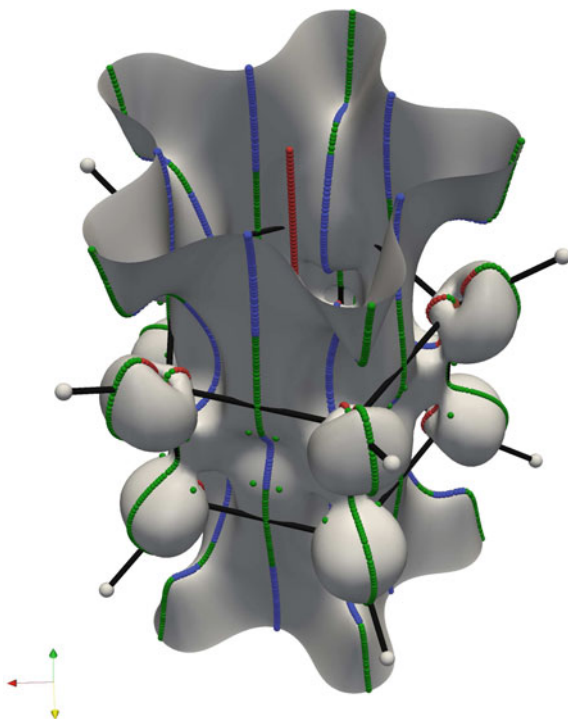


Fig. 7.30 Streamlines of J^B and corresponding contours of the magnetic shielding density Σ_{zz}^H , in au, in pentaprismane $C_{10}H_{10}$, for an applied field of 1 au directed outward, parallel to the C_5 symmetry axis, on four parallel planes, at distance (in bohr) $Z = 0.67$ (min = -2.1×10^{-3} , max = 2.3×10^{-3}), $Z = 1.47$ (the plane of the C nuclei, min = -2.4×10^{-1} , max = 4.0×10^{-1} , truncated at $\pm 3.0 \times 10^{-2}$), $Z = 2.00$ (min = -5.0×10^{-2} , max = 6.3×10^{-2} , truncated at $\pm 3.0 \times 10^{-2}$), and $Z = 2.59$ (the plane of the H nuclei, min = -6.0×10^2 , max = 2.0×10^3 , truncated at $\pm 3.0 \times 10^{-2}$). In all the maps the step is 1.0×10^{-3} . *Green (red)* contours denote shielding (deshielding). The shielding contributions which arise from the ring currents sustained by σ -electrons of the carbon atoms on the plane of the nearest pentagonal face are very small, those provided by the delocalised currents increase on the plane at 2.00 bohr. A major shielding contribution to σ_{zz}^H arises from delocalised flow on the plane of the hydrogen nuclei. The plot at 0.67 documents the local deshielding operated by the σ -currents flowing below the 5-membered carbon ring

7.6 Toroidal Flow and Associated Anapole Moment

As shown by Hirschfelder and coworkers, one is left with the possibility of either AVs, rotating around nodal manifolds which extend to the boundaries of space, or TVs flowing up through the centre and down around the sides of a closed nodal line [37–40, 78, 118].

Fig. 7.31 Isoshielding density surfaces $\Sigma_{zz}^I(r) = 0.0$ au (represented in grey) for any dummy atom I lying on the C_5 symmetry axis of pentaprismane in a magnetic field $\mathbf{B} \parallel C_5$. Vortex and saddle SLs of the SG in Fig. 7.28 lie on this surface, which separates the inner part of the $\mathbf{J}^{\mathbf{B}}$ field from the peripheral region of delocalized currents



Toroidal flow, see Fig. 7.32, is characterized by remarkable properties: vanishing induced magnetic dipole moment, induced magnetic field with the shape of a topological circumference confined inside the torus surface, and induced anapole moment [119]. The presence of TVs in maps of $\mathbf{J}^{\mathbf{B}}$ has been detected in some molecules [103, 120–122].

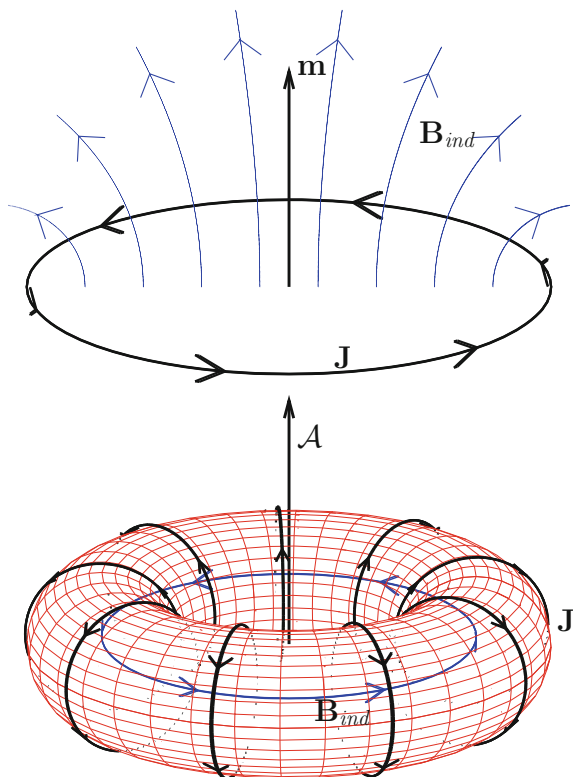
The anapole moment can be expressed [118] via the current density $\mathbf{J}^{\mathbf{B}}$ induced by a uniform magnetic field \mathbf{B} ,

$$\mathcal{A}_\alpha = -\frac{1}{6} \int (r^2 \delta_{\alpha\beta} - r_\alpha r_\beta) J_\beta^{\mathbf{B}} d^3 r. \quad (7.84)$$

The anapole susceptibility is a nonsymmetric second-rank tensor [123, 124] defined by

$$a_{\alpha\beta} = \frac{\partial \mathcal{A}_\alpha}{\partial B_\beta}. \quad (7.85)$$

Fig. 7.32 Above Ampère magnetic dipole \mathbf{m} and BS magnetic field \mathbf{B}_{ind} induced by the current density flowing in a loop. Below Anapole moment \mathbf{A} and confined magnetic field \mathbf{B}_{ind} induced by the current density \mathbf{J} flowing on the surface of a torus



Whereas the components of the anapole vector are origin dependent, the trace $a_{av} = (1/3)a_{zz}$ is invariant, so that the anapole moment induced in a freely tumbling molecule

$$\mathbf{A} = a_{av}\mathbf{B} \quad (7.86)$$

is also invariant of the origin. The sign of a_{av} and \mathbf{A} is opposite for two enantiomers and these properties can therefore be considered markers for chiral discrimination [123, 124].

Toroidal vortices are easily recognized from current density maps and corresponding stagnation graph. A spatial current model for LiH [121] is described in Figs. 7.33, 7.34, 7.35, and 7.36. The stagnation graph for a field B_x applied perpendicular to the z bond axis, shown in Fig. 7.33, contains a set of (2, 0) SLs lying on the $T\sigma_v(zx)$ symmetry plane i.e., a green line, crossing the bond in the vicinity of the hydrogen nucleus, extending to the limits of the molecular domain, and a closed loop constituted by green and red portions, corresponding to opposite vorticity,

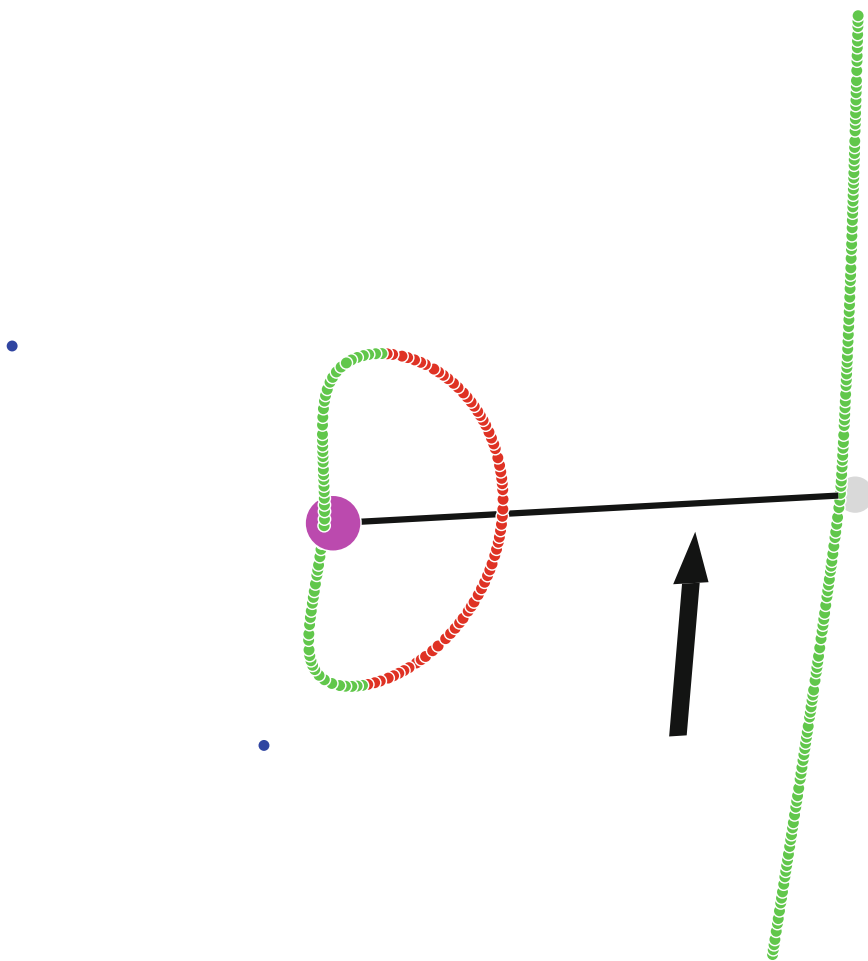


Fig. 7.33 Perspective view of the stagnation graph of the LiH molecule in a magnetic field, represented by a *big black arrow*, perpendicular to the bond. *Green (red)* SLs denote diamagnetic (paramagnetic) vortices. The stagnation loop and two off-axis conjugated saddle-node $(3, \pm 1)$ stagnation points (represented in *blue*) indicate toroidal flow in the basin of Li atom

in the basin of the Li atom. The former indicates a diamagnetic AV, the latter is typical of a TV [78], whose presence is confirmed by a pair of blue $(3, \pm 1)$ conjugated SPs on either side of the bond direction. These points are classified as stable and unstable saddle-nodes in the terminology of Reyn [92]. An observer in front of the nodal loop in Fig. 7.34 would see currents coming out from the $(3, +1)$ source point in the proximity of its centre, flowing through the centre around the sides of this loop, and entering through the $(3, -1)$ sink behind the nodal loop.

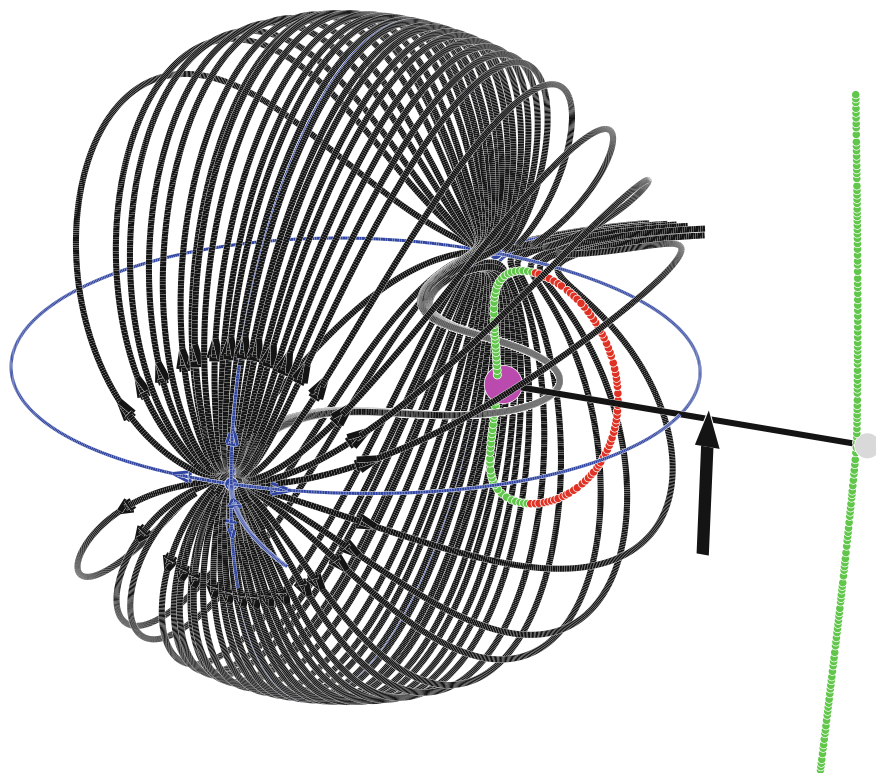


Fig. 7.34 Perspective view of the toroidal flow in the basin of the Li atom within the LiH molecule in a magnetic field perpendicular to the bond. All the streamlines flow through the centre and down around the sides of the stagnation loop containing one *green* and one *red* segment. The $(3, +1)$ saddle-node, observed in the foreground as a source, is connected by *black* trajectories to its conjugated $(3, -1)$ (sink) partner lying behind the torus. A *blue* closed asymptotic line defines the intersection of the separatrix containing the torus with the plane of the nuclei perpendicular to the applied field. On this plane, the $(3, \pm 1)$ points look like saddles. The other homoclinic blue line joining the $(3, \pm 1)$ points lies on a plane normal to the bond axis. A wavy asymptotic line, which connects the $(3, \pm 1)$ points passing inside the stagnation loop, is best observed in Fig. 7.35

The TV looks like a doughnut with a very small central hole, completely enclosed within an S^2 surface, that is, a separatrix with the shape of a topological sphere, which forms a boundary marking the limits to the rest of the vector field. This separatrix is filled by asymptotic paths, referred to as homoclinic trajectories [57], see Fig. 7.35. In the streamline plot of Fig. 7.36, the toroidal flow is represented by two juxtaposed vortices, one diamagnetic and one paramagnetic. Their centres are found at the intersection of the green and red SLs of the stagnation loop of the TV with the $\sigma_h(yz)$ plane.

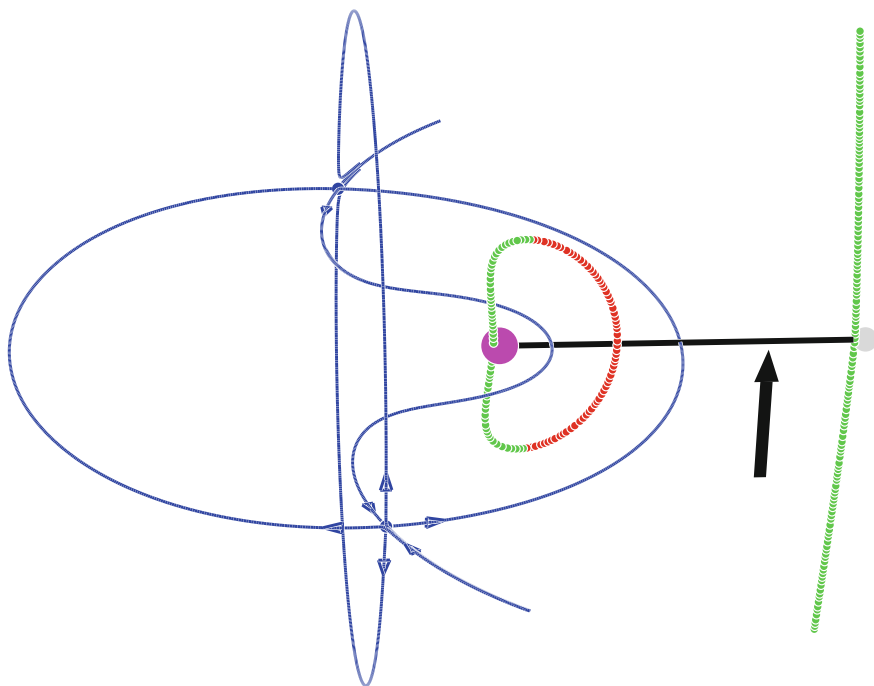


Fig. 7.35 Homoclinic trajectories connecting the $(3, \pm 1)$ saddle-nodes on the separatrix of the torus about the Li atom in the LiH molecule. The *arrows* indicate the direction of the eigenvectors of the transposed Jacobian matrix $\mathbf{VJ}^{\mathbf{B}}$ at the stagnation points. An asymptotic wavy line flows across the stagnation loop, about its centre

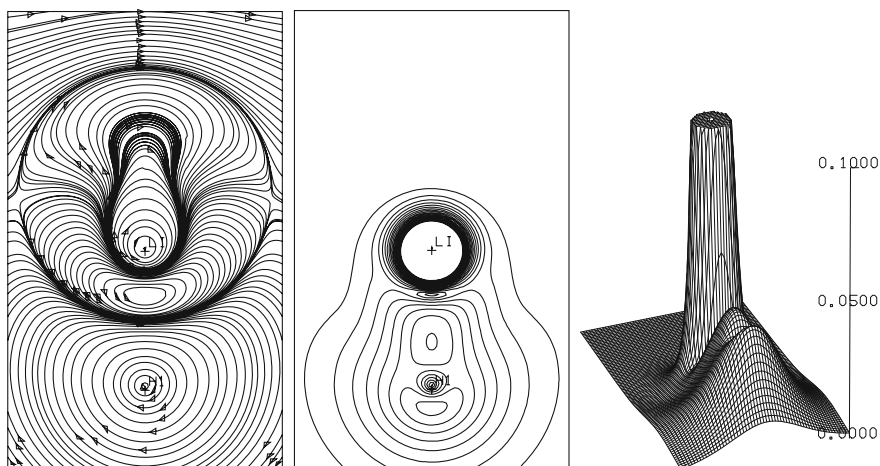


Fig. 7.36 The current density field for LiH in a field perpendicular to the plane containing the nuclei, with $|\mathbf{B}| = 1$ au. Diatropic (paratropic) current density is clockwise (anti-clockwise). The maximum intensity of the $\mathbf{J}^{\mathbf{B}}$ field is 0.58 au, truncated to 0.10 in the perspective view on the *right*. Corresponding contours start at 5.0×10^{-3} au and are 5.0×10^{-3} apart

Analogous topological models of magnetic-field induced current densities are shown in Figs. 7.37, 7.38, and 7.39 for the CO_2 molecule [121] and in Figs. 7.40, 7.41, 7.42, and 7.43 for the CH-CH molecule [103].

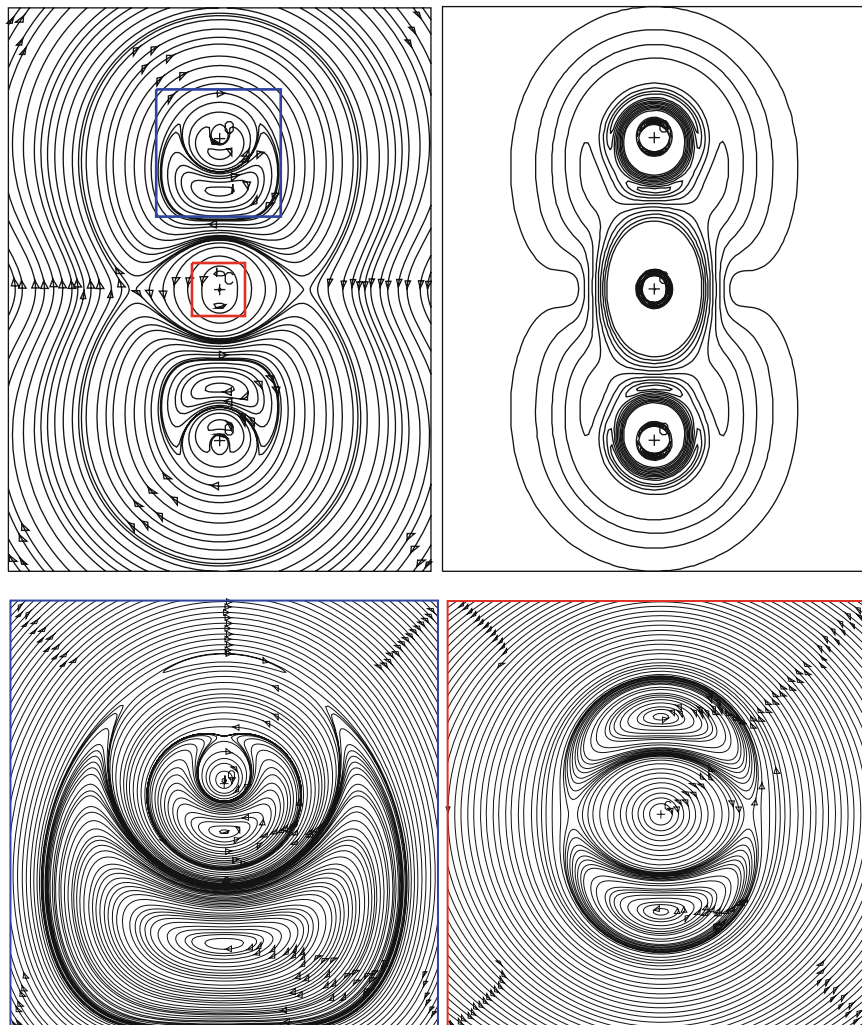


Fig. 7.37 The current density field for CO_2 in a field perpendicular to a plane containing the nuclei, with $|\mathbf{B}| = 1$ au. Cross-sections of the flow in the basin of an oxygen atom, showing the TV, and about the central carbon nucleus—*insets* with *blue* and *red* frame, respectively—are magnified in the *bottom*. The maximum intensity of the $\mathbf{J}^{\mathbf{B}}$ field is 3.55 au, truncated to 0.30 in the *top-right* contour map, which start at 0.03 au and are 0.03 apart

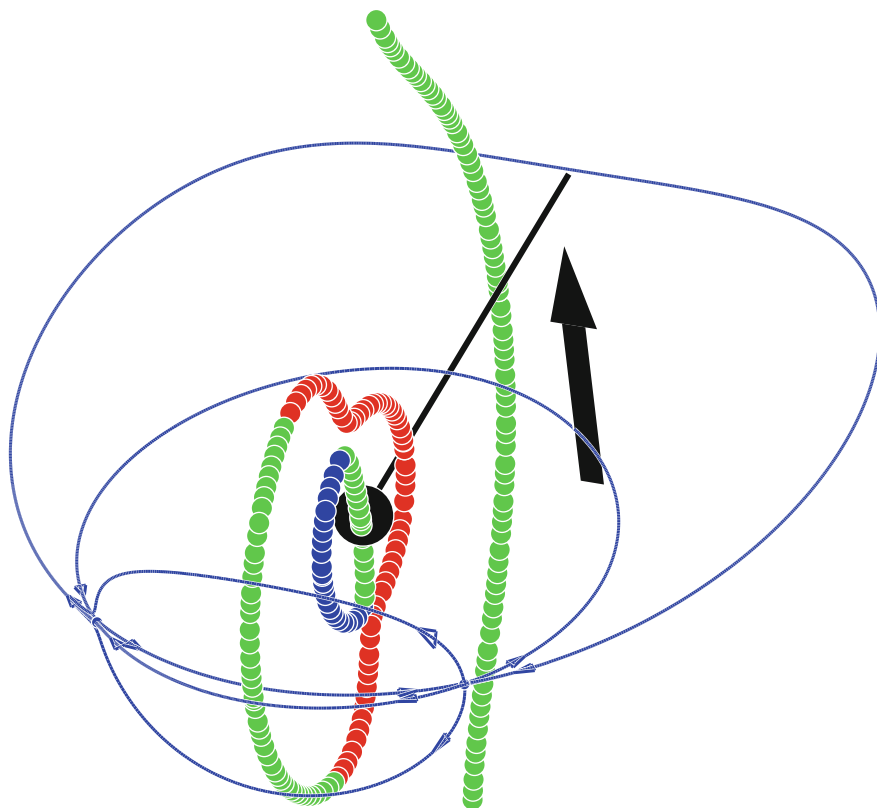


Fig. 7.38 Asymptotic lines connecting the $(3, \pm 1)$ points in the CO₂ molecule

7.7 The Topological Definition of Ring Currents

Several efforts have been made by many chemists to come to grips with universally acceptable notions of aromaticity, antiaromaticity and non-aromaticity as molecular properties. The results arrived at so far are at times rather frustrating, indicating the difficulty, if not the impossibility, of ascribing a consistent set of common distinguishing features to aromatic compounds [15]. Rules of aromaticity have been proposed by a number of researchers, see the chapter “Rules of Aromaticity”, by Feixas et al. in this book [125], assuming a basic connection between aromatic character and electron delocalization.

Electron delocalization is typical of systems whose structure is characterized by resonance hybrids according to the valence-bond theory. Delocalized electrons do not have a specific location; they cannot be drawn in a simple Lewis structure. Allowing for a visualization reported in the IUPAC Gold Book [126], they are spread across a moiety including *three or more atoms* of a molecule. Examples

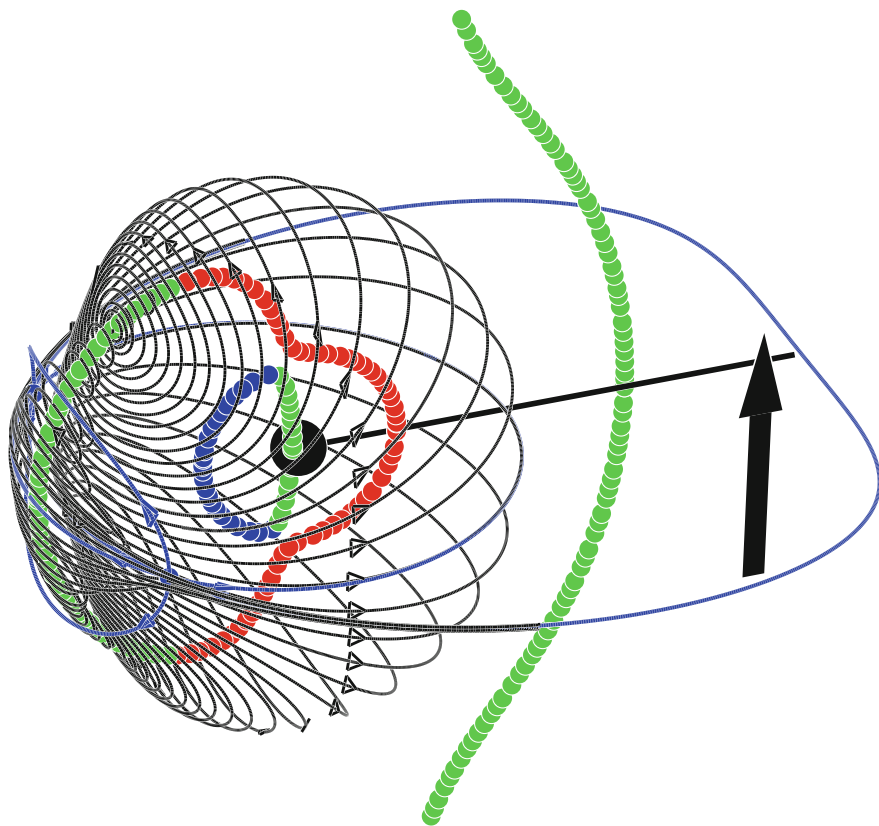


Fig. 7.39 Toroidal regime in the neighbourhood of an oxygen atom in the CO_2 molecule. The figure shows the small size of the diamagnetic portion

[126] illustrate the peculiar delocalization of charge in ionic conjugated systems, e.g., R-CO_2^- , $\text{CH}(\text{CH}_2)_2^+$. Attempts have been made at rationalizing electron delocalization in recent papers citing previous relevant literature [27, 127–130].

On the other hand, practical and clearcut definitions, well-suited to reconcile diverging views [131–133], are not available for the related concept of *delocalized current* induced in the electrons of a molecule by an applied magnetic field \mathbf{B} . In general it is merely assumed that delocalized π -electrons are quite free to move. There is a general accord that they sustain diatropic [104, 134–136] “ring currents” in conjugated planar cyclic molecules, e.g., the “aromatic” benzene [15, 137, 138], in the presence of \mathbf{B} orthogonal to the molecular plane. On the same ground it is assumed that the π -electrons of “anti-aromatic” systems, e.g., cyclobutadiene and the flattened cyclo-octatetraene model molecule, support paratropic currents delocalized all over the carbon ring [49, 139]. The SG of the latter presents quite remarkable features, see Fig. 5 of Ref. [139].

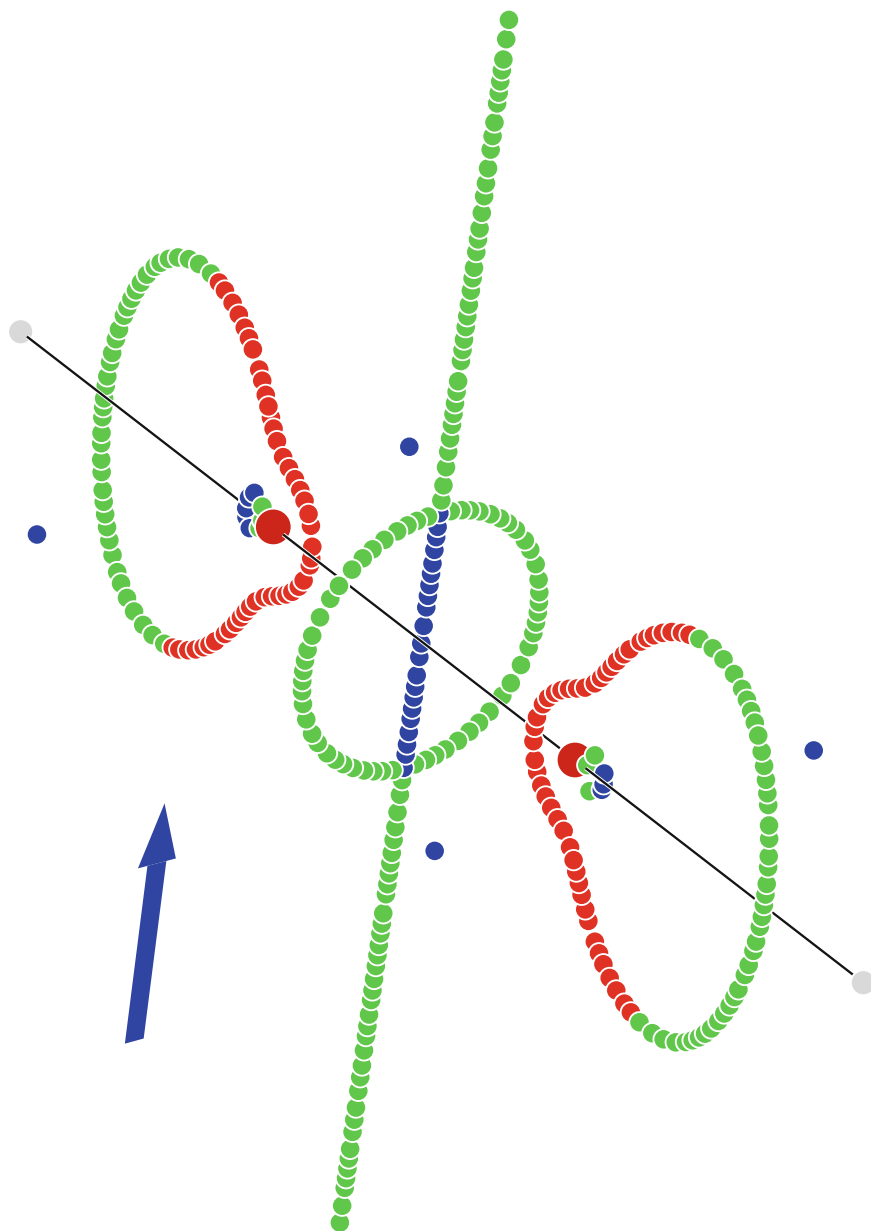


Fig. 7.40 Perspective view of the stagnation graph of the current density vector field induced by a magnetic field $\mathbf{B} \equiv B\epsilon_1$ normal to the bond axis of acetylene. Here and in Figs. 7.41 and 7.42 the direction of \mathbf{B} is represented by a fat blue arrow. Green (red) lines denote diamagnetic (paramagnetic) vortices, saddle lines are blue. Isolated blue points mark (3 ± 1) saddle-nodes, isolated green (red) points denote (3 ± 1) diamagnetic (paramagnetic) foci

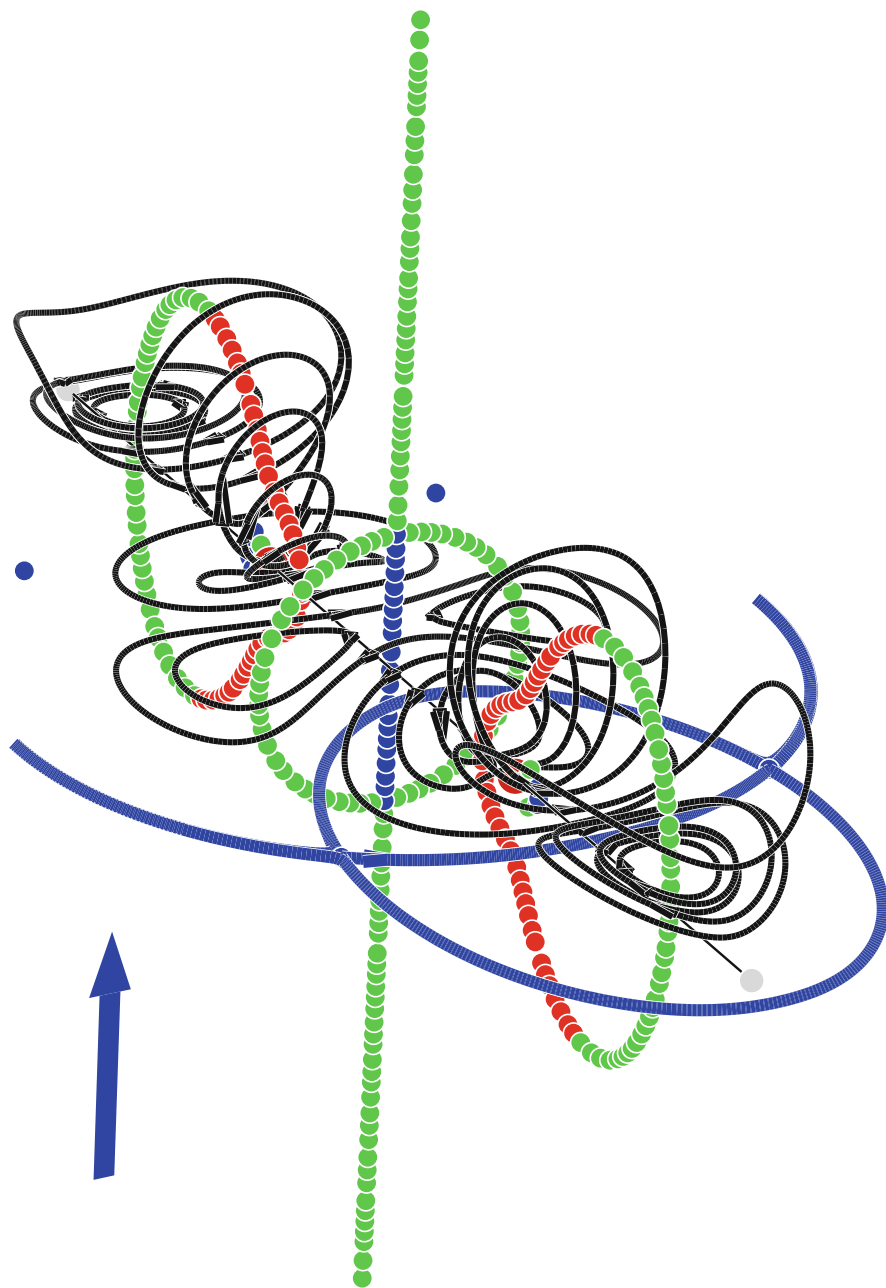


Fig. 7.41 Splitting of the central diamagnetic vortex into a central saddle line and two diamagnetic vortical lines in acetylene. The asymptotic *blue* trajectories passing through (3 ± 1) saddle-node points mark the intersection of the separatrices containing the TVs with the yz plane. The truncated *blue* line is connected to the symmetrical pattern about the other C–H bond. The diamagnetic (paramagnetic) portions of the TV are observed around *green* (*red*) SLs

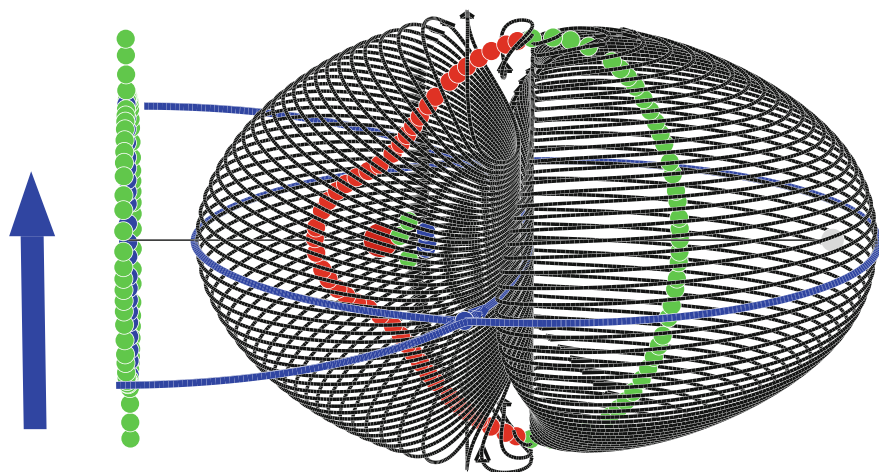


Fig. 7.42 Magnification of the TV about a C–H bond of acetylene

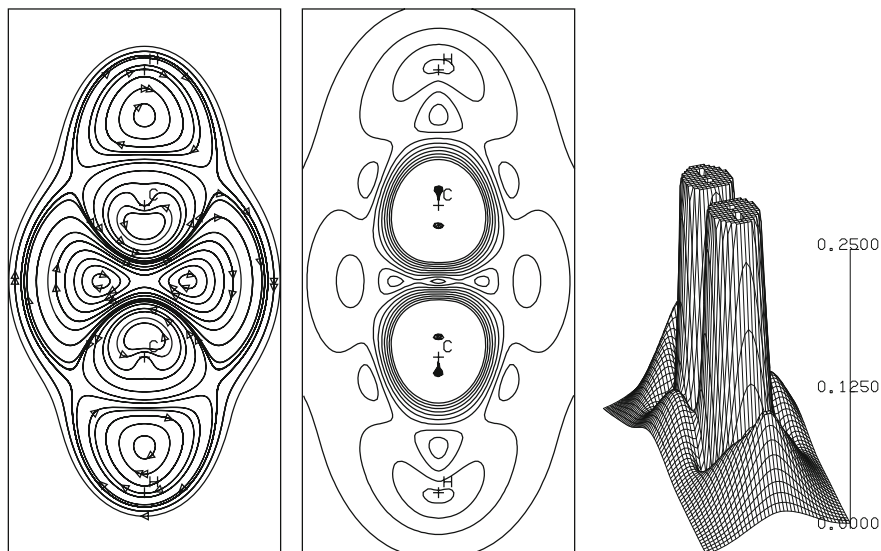


Fig. 7.43 Display of the vector current density (streamlines on the *left*, modulus contours in the *centre*, and related 3-dimensional view on the *right*) on a plane containing the bonds of the acetylene molecule. The applied magnetic field is directed out, and perpendicular to, the plot plane. Atom positions are marked by *crosses*. The maximum modulus is 3.54 (cut to 0.25) au, and the step between two consecutive contour levels is 0.025 au

The existence of magnetic-field induced electronic “ring currents” in benzene and other unsaturated planar molecules was the object of a forceful dispute, opposing Musher [131, 132] to Gaidis and West [133]. Musher restated his point in an extended review article [140]. At any rate, after nearly half a century, and despite

several attempts at ironing out rough spots, the question still appears partially unsettled [15, 137, 138].

In particular, a common agreement about the notion of interatomic current has not been reached and fundamental questions remain unanswered, e.g., are delocalized currents a distinguishing prerogative of planar unsaturated molecules, or rather the ubiquitous feature [131, 132] of any molecule? To what extent are the electrons of noncyclic compounds capable of sustaining delocalized flow in the presence of a magnetic field? Are π - and σ -electrons characterized by comparable mobility? What about a practical intensity measure of the induced currents? Are ring-shaped molecules carriers of stronger currents compared with noncyclic ones? Is there an indisputable quantifier of current delocalization?

Delocalized σ -electron currents were found in planar saturated molecules. A paradigmatic example is provided by H_6 , the cyclic arrangement of three juxtaposed hydrogen molecules with D_{6h} symmetry [141–143], first studied by London [144]. Noticeably, a delocalized pattern was observed also in ethylene, another noncyclic system which sustains an annular current (with maximum modulus 0.075 au, for $|\mathbf{B}| = 1$ au) orthogonal to the molecular plane, see Fig. 7.10 and a recent paper [103]. Delocalization of electron flow takes place on the plane of the hydrogen nuclei of the CH_3 -group in D_{3d} or D_{3h} conformations of ethane in the presence of a magnetic field parallel to the C_3 symmetry axis, see Figs. 7.15 and 7.17.

The existence of fairly large delocalized electron flow was demonstrated in H_2O , BH_3 , NH_3 , CH_4 , CH_3-CH_3 , H_3O^+ , CH_3^+ , and NH_4^+ , by plots of quantum mechanical current density and by current susceptibilities, Eq. (7.55), calculated by accurate ab initio methods [102, 145]. The latter, also referred to as “current strengths” measured in nano ampère per tesla, are defined via flux integrals evaluated over suitably chosen molecular domains [76]. Simple procedures, allowing for ideal current models based on the BS law [46], have been applied to predict the ability of a certain molecule to support magnetic-field induced electron currents flowing through an interatomic circuit [77, 141–143].

According to the conclusions expounded in a recent paper [145] one can reasonably claim that the delocalized patterns observed in the current density maps actually prove the existence of “ring currents without a ring”. These results would seem to lend support to the paradoxical statement made by Musher, “... the hydrogen atom also... sustains a ring current.” [131]. Since electron currents flowing over wide portions of a molecular domain are not the exclusive property of cyclic conjugated systems, rigorous and comprehensive definitions of “delocalized current” seem therefore to be necessary.

In the light of the findings discussed above, a *definition of delocalized current* was tentatively proposed [145] as *a current flowing along a closed loop containing three or more atoms*. It appears consistent with the IUPAC acceptance of delocalized charge [126]. Such a definition would seem appropriate for CH_3^+ and BH_3 , as well as NH_3 , H_3O^+ , and NH_4^+ . However, the intriguing case of H_2O in a field \mathbf{B} parallel to the C_2 axis shows that only two atoms may be sufficient to give rise to an intense delocalized current, moving around in a loop of sufficiently large size [145].

A falsifiable definition of “ring currents” [15] as a synonym of delocalized currents in a molecule may be attempted within the lexicon of topology, *delocalized currents are those flowing in the domain which extends beyond the separatrix surrounding the nuclear skeleton*. This formulation would seem ad hoc for cyclic, neutral or charged, planar molecules C_nH_n in the presence of a magnetic field orthogonal to the molecular plane, i.e., compounds with $D_{nh}(C_{nh})$ magnetic symmetry, see Sect. 7.5.2, in which the separatrix is defined by the surface containing n vortical and n saddle stagnation lines: delocalized currents flow on the outside for a great enough distance to reach the tail regions of the electron cloud. It seems appropriate also to the case of cyclopropane and prismane discussed in Sect. 7.5.4, cubane and pentaprismene, Sect. 7.5.5.

However, the same definition would apply to the case of π -electron currents in the same molecules, in which the separatrix coincides with the single vortical line through the centre of the molecule. It would be also applicable to diamagnetic atoms, in which the delocalized flow beyond the nucleus consists of concentric circular streamlines about a vortical stagnation axis identifiable with the separatrix [60].

7.8 Current Density Induced by a Pair of Magnetic Dipole Moments and Nuclear Spin-Spin Coupling

The Ramsey theory of indirect nuclear spin-spin coupling [12, 13] can be reformulated in terms of linear superposition of two current density fields, \mathbf{J}^{m_I} and \mathbf{J}^{m_J} , induced in the electrons of a molecule by nuclear magnetic dipoles \mathbf{m}_I and \mathbf{m}_J [3, 51, 52, 61]. Graphical representations of the interference pattern within the total current density vector field, together with corresponding density maps, Eq. (7.57), are very useful to elucidate coupling pathways and to rationalize the exchange of spin information between coupled nuclei.

A paradigmatic application has been reported for ethane [16]. It shows that the Fermi contact contributions to experimental nuclear spin-spin coupling constant are easy to explain in terms of current densities (7.25), which transport spin polarization along the coupling pathway, and associated plots of property density, Eq. (7.57). Same-spin electron correlation, the only kind of correlation recovered by the Hartree Fock wavefunction considered in Ref. [16], determines the alignment of the nuclear dipoles at its ends, as shown in the current-density maps reported for ethane, Fig. 7.44.

According to experimental and theoretical results, the magnetic dipoles of the vicinal protons are anti-parallel, in the configuration of lower energy. Therefore, the physically acceptable magnetic symmetries are C_{2v} for the eclipsed, and $C_{2h}(C_s)$ for the staggered ethane. The current density fields induced in the electrons by two anti-parallel and parallel nuclear magnetic dipoles at vicinal protons of the eclipsed ethane, are shown respectively on the left and on the right of Fig. 7.44.

The streamlines in Fig. 7.44a cannot cross the σ_v plane. At a vanishingly small distance from this plane, the trajectories flow parallel. In Fig. 7.44d, the $T\sigma_v$ plane

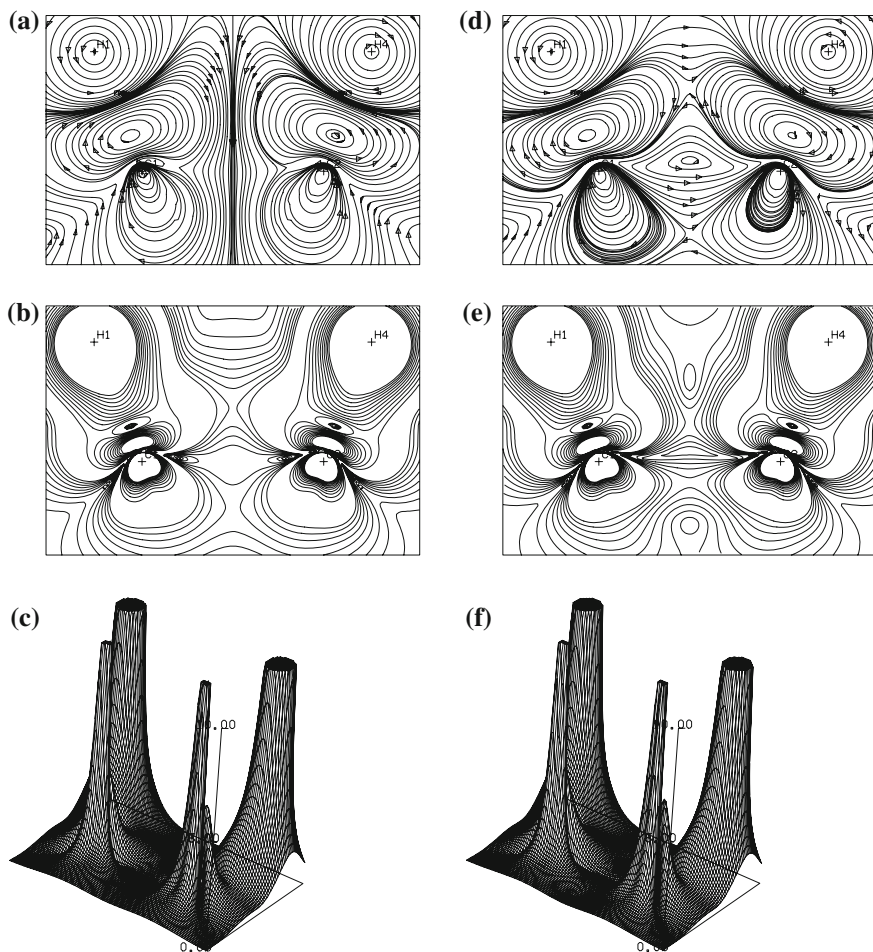


Fig. 7.44 Current density field induced via the Fermi contact interaction by two magnetic dipoles at the vicinal protons of eclipsed ethane. The coupling pattern, for anti-parallel (parallel) dipoles, is represented on the *left* (*right*). The streamlines are shown in **(a)** and **(d)**; **b** and **e** are contour levels for the intensity, in au; the values of the *solid* (*dashed*) lines increase (decrease) in steps of 5×10^{-2} from the 0-contour, up to 0.5 au; **c** and **f** are the corresponding 3-dimensional perspective views. The position of the nuclei is marked by a *cross*; a corresponding symbol can be seen in the contour maps

can be crossed only by streamlines perpendicular to it, according to the discussion in Sect. 7.3. Orbits approaching this plane with an angle different from $\pi/2$ are scattered. Actually, the phase portraits of two saddle SPs lying on $T\sigma_v$ are observed in Fig. 7.44d.

A representation of the Dirac-Van Vleck vector model [16, 51, 52, 146] for the experimental vicinal coupling in $\text{CH}_3\text{-CH}_3$ is given by Fig. 7.44a. Within the

plotting conventions of this figure, the anti-clockwise flow about the H1 nucleus is supported by β -polarised electrons [16, 51, 52, 146]. Two clockwise whirlpools, supported by opposite α polarisation, are observed in the H1–C1 bond and about the C1 nucleus. The regime is reversed on the right of the σ_v plane, as required by the C_{2v} magnetic symmetry. At the end of the coupling path, all over the H4 nucleus, the circulation is clockwise, corresponding to local α -electron distribution. The contour plots, (b) and (e), and the three-dimensional perspective views, (c) and (f), show local maxima of modulus of the current density field about the nuclei.

The Fermi-contact coupling density, Eq. (7.57), for vicinal protons in the eclipsed and staggered conformations of ethane is shown in Fig. 7.45. Analogous

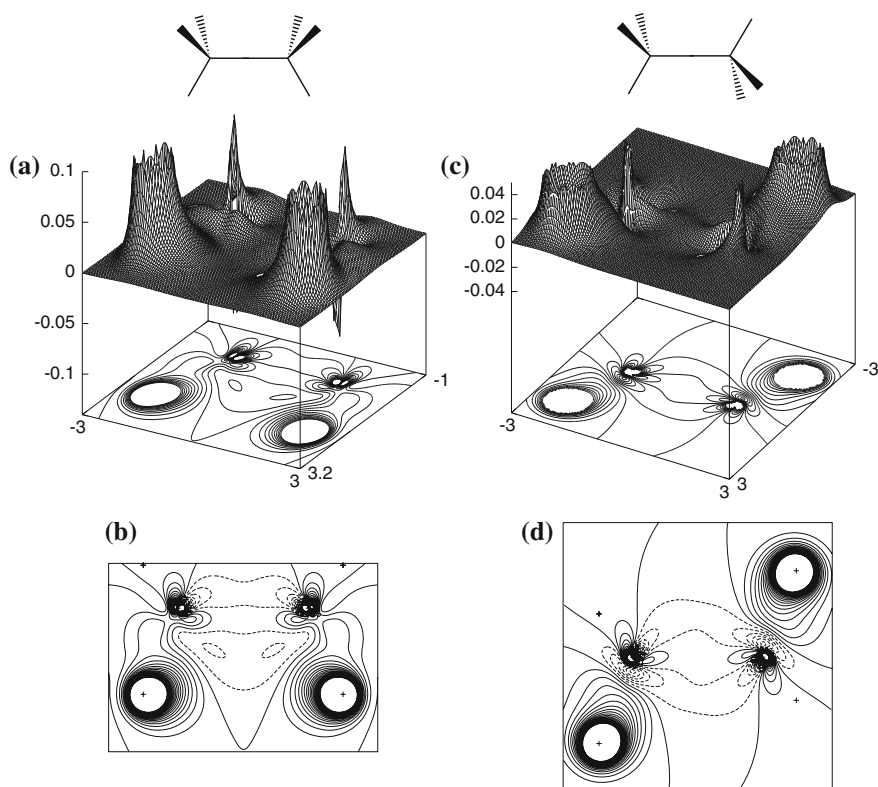


Fig. 7.45 a and c Three-dimensional perspective view of the average Fermi coupling density $(1/3)\kappa_{zz}^I(\mathbf{r})$, Eq. (7.57), in au, for the vicinal protons $I \equiv \text{H1}$ and $J \equiv \text{H4}$, for the eclipsed and staggered conformations of ethane, in au. The corresponding contour plots are shown in (b) and (d). The H1–C1–C2–H4 pathways lie over the plot plane. Absolute values larger than 0.10 and 0.04 au, respectively for eclipsed and staggered conformations, were truncated. In (b) and (d), the position of the hydrogen nuclei is marked by crosses. Solid (dashed) lines mean positive (negative) values. In (b) the values of the dashed (solid) lines increase (decrease) in steps of 5×10^{-3} au from the 0-contour. In (d) the step is 10^{-2} au

considerations can be made for both conformations of ethane. However, since the geometry of the former corresponds to higher molecular energy, its contribution to the experimental coupling constant is smaller than that attributable to the latter. The three-dimensional perspective view clearly defines the H1–C1–C2–H4 coupling pathway through the bonds as a sequence of up-spikes in the proximity of the nuclei. The spike pattern indicates that, in the eclipsed conformation, through-space H1–H4 coupling takes place to a little extent, see Fig. 7.45a, b, where down-spikes connected with the current vortex about the H1–C1 bond are observed. These down-spikes are absent in Fig. 7.45c, d for the staggered conformation, in which through-space vicinal coupling is unimportant. Although the up-spikes about the carbon nuclei are much lower than those over the coupled protons, they indicate the essential role of the charge distribution in these regions for transporting spin information.

The interpretation of the coupling density maps of Fig. 7.45 via the approaches of Refs. [51, 52] is facilitated by models of the interference pattern of current densities induced by the pair of interacting nuclear magnetic dipoles. Thus, for a reference electron of given spin close to H1, the Fermi correlation precludes same-spin polarization in its proximity, gives rise to alternating opposite spin densities along the coupling pathway, and determines the indirect spin-spin interaction for two nuclei at its ends.

7.9 Conclusions

The response of diamagnetic molecules to an external homogeneous static magnetic field \mathbf{B} and to intramolecular permanent nuclear magnetic dipoles \mathbf{m}_I is effectively rationalized via maps of streamlines and modulus of quantum mechanical induced current densities $\mathbf{J}^{\mathbf{B}}$ and $\mathbf{J}^{\mathbf{m}_I}$. In this chapter it is shown that the essential features of intrinsic tensor properties, magnetizability $\chi_{\alpha\beta}$, magnetic shielding $\sigma_{\alpha\beta}^I$ at nucleus I , and spin-spin coupling $\mathcal{K}^{I,J\beta}$ between nuclei I and J , are nicely explained by analyzing contributions which arise from different molecular domains. In particular, $\sigma_{\alpha\beta}^I$ and $\mathcal{K}^{I,J\beta}$ can be related to property-density functions $\Sigma_{\alpha\beta}^I$ and $\kappa^{I,J\beta}$ via non-invertible maps, $f : \mathbf{J}^{\mathbf{B}}(\mathbf{r}) \rightarrow \Sigma^I(\mathbf{r})$ and $f : \mathbf{J}^{\mathbf{m}_I}(\mathbf{r}) \rightarrow \kappa^{IJ}(\mathbf{r})$, which clearly visualize the local phenomenology. The topological analysis of singularities, stagnation lines and stagnation graph of $\mathbf{J}^{\mathbf{B}}$ and $\mathbf{J}^{\mathbf{m}_I}$ current density vector fields provides powerful interpretative tools, as shown in a number of examples. A definition of magnetic-field induced delocalized electron currents (ring currents) can be proposed on a topological criterion.

References

1. Hirschfelder JO (1978) *J Chem Phys* 68:5151
2. Lazzeretti P (1989) *Adv Chem Phys* 75:507
3. Lazzeretti P (2003) Electric and magnetic properties of molecules. In: Wilson S (ed) *Handbook of molecular physics and quantum chemistry*, vol 3, Part 1, Chapter 3. Wiley, Chichester, pp 53–145
4. Lazzeretti P (2013) Electronic current densities induced by magnetic fields and nuclear magnetic dipoles. Theory and computation of NMR spectral parameters, volume 3 of *High resolution NMR spectroscopy, science and technology of atomic, molecular, condensed matter and biological systems*. Elsevier, New York
5. Lazzeretti P (2014) *Int J Quantum Chem* 114:1364
6. Landau LD, Lifshitz EM (1981) *Quantum mechanics*. Pergamon Press, Oxford
7. Hirschfelder JO, Brown WB, Epstein S (1964) *Adv Quantum Chem* 1:255
8. Van Vleck JH (1932) *The theory of electric and magnetic susceptibilities*. Oxford University Press, Oxford
9. Ramsey NF (1950) *Phys Rev* 78:699
10. Ramsey NF (1951) *Phys Rev* 83:540
11. Ramsey NF (1952) *Phys Rev* 86:243
12. Ramsey NF, Purcell EM (1952) *Phys Rev* 85:143
13. Ramsey NF (1953) *Phys Rev* 91:303
14. Emsley JW, Feeney J, Sutcliffe LH (1967) *High resolution nuclear magnetic resonance spectroscopy*. Pergamon Press, Oxford, pp 10–13
15. Lazzeretti P (2000) Ring currents. In: Emsley JW, Feeney J, Sutcliffe LH (eds) *Progress in nuclear magnetic resonance spectroscopy*, vol 36. Elsevier, pp 1–88
16. Soncini A, Lazzeretti P (2005) *Chem Phys Lett* 409:177
17. Zubarev DN (1974) *Nonequilibrium statistical thermodynamics*. Consultants Bureau, New York
18. Jørgensen P, Simons J (1981) *Second quantization-based method in quantum chemistry*. Academic Press, New York
19. Helgaker T, Jørgensen P, Olsen J (2000) *Molecular electronic structure theory*. Wiley, Chichester
20. Sauer SPA (2011) *Molecular electromagnetism: a computational chemistry approach*. Oxford University Press, Oxford
21. Taylor PR (1994) Lecture notes in quantum chemistry, European summer school in quantum chemistry. In: Roos BO (ed). Springer, Berlin
22. Bartlett RJ (1995) *Modern electronic structure theory*. In: Yarkony DR (ed). World Scientific, Singapore
23. Bartlett RJ, Musiał M (2007) *Rev Mod Phys* 79:291
24. Jusélius J, Sundholm D, Gauss J (2004) *J Chem Phys* 121:3952
25. Lin Y-C, Jusélius J, Sundholm D, Gauss J (2005) *J Chem Phys* 122:214308
26. Fliegl H, Sundholm D, Taubert S, Jusélius J, Klopper W (2009) *J Phys Chem A* 113:8668
27. Fliegl H, Taubert S, Lehtonen O, Sundholm D (2011) *Phys Chem Chem Phys* 13:20500
28. Schrödinger E (1926) *Ann Phys (Leipzig)* 81:109
29. Madelung E (1926) *Z Phys* 40:322
30. de Broglie L (1926) *C R Acad Sci (Paris)* 183:447
31. de Broglie L (1927) *C R Acad Sci (Paris)* 184:273
32. Landau L (1941) *J Phys USSR* 5:71
33. London F (1945) *Rev Mod Phys* 17:310
34. Bohm D (1952) *Phys Rev* 85:166
35. Bohm D (1952) *Phys Rev* 85:180
36. Bialynicki-Birula I, Bialynicka-Birula Z (1971) *Phys Rev D* 3:2410
37. Hirschfelder JO, Christoph AC (1974) *J Chem Phys* 61:5435

38. Hirschfelder JO, Goebel CJ, Bruch LW (1974) *J Chem Phys* 61:5456
39. Hirschfelder JO, Tang KT (1976) *J Chem Phys* 64:760
40. Hirschfelder JO, Tang KT (1976) *J Chem Phys* 65:470
41. Takabayasi T (1957) *Progress Theor Phys Suppl* 4:1
42. Holland PR (1993) *The quantum theory of motion*. Cambridge University Press, New York
43. Bohm D, Hiley BJ, Kaloyerou PN (1987) *Phys Rep* 144:321
44. Cushing JT, Fine A, Goldstein S (eds) (1996) *Bohmian mechanics: an appraisal*. Kluwer, Boston
45. Faglioni F, Ligabue L, Pelloni S, Soncini A, Viglione RG, Ferraro MB, Zanasi R, Lazzeretti P (2005) *Org Lett* 7:3457
46. Jackson JD (1998) *Classical electrodynamics*, 3rd edn. Wiley, New York, pp 175–178
47. Ferraro MB, Lazzeretti P, Viglione RG, Zanasi R (2004) *Chem Phys Lett* 390:268
48. Pelloni S, Ligabue A, Lazzeretti P (2004) *Org Lett* 6:4451
49. Soncini A, Fowler PW, Lazzeretti P, Zanasi R (2005) *Chem Phys Lett* 401:164
50. Ferraro MB, Faglioni F, Ligabue A, Pelloni S, Lazzeretti P (2005) *Magn Res Chem* 43:316
51. Soncini A, Lazzeretti P (2003) *J Chem Phys* 118:7165
52. Soncini A, Lazzeretti P (2003) *J Chem Phys* 119:1343
53. Jameson CJ, Buckingham AD (1979) *J Phys Chem* 83:3366
54. Jameson CJ, Buckingham AD (1980) *J Chem Phys* 73:5684
55. Gomes JANF (1983) *J Chem Phys* 78:4585
56. Gomes JANF (1983) *Phys Rev A* 28:559
57. Gomes JANF (1983) *J Mol Struct (THEOCHEM)* 93:111
58. Hamermesh M (1972) *Group theory and its applications to physical problems*. Addison-Wesley, London
59. McWeeny R (1989) *Methods of molecular quantum mechanics*. Academic Press, London
60. Pelloni S, Lazzeretti P (2012) *J Chem Phys* 136:164110
61. Lazzeretti P, Malagoli M, Zanasi R (1994) *J Mol Struct (Theochem)* 313:299
62. Soncini A, Lazzeretti P (2006) *ChemPhysChem* 7:679
63. Lazzeretti P (2012) *J Chem Phys* 137:074108
64. Raynes WT (1992) *Magn Reson Chem* 30:686
65. Epstein ST (1974) *The variation method in quantum chemistry*. Academic Press, New York
66. Arrighini GP, Maestro M, Moccia R (1970) *J Chem Phys* 52:6411
67. Arrighini G, Maestro M, Moccia R (1970) *Chem Phys Lett* 7:351
68. Lazzeretti P, Zanasi R (1980) *J Chem Phys* 72:6768
69. Lazzeretti P, Zanasi R (1977) *Int J Quantum Chem* 12:93
70. Lazzeretti P, Malagoli M, Zanasi R (1991) *Chem Phys* 150:173
71. Lazzeretti P, Malagoli M, Zanasi R (1994) *Chem Phys Lett* 220:299
72. Epstein ST (1973) *J Chem Phys* 58:1592
73. Landau LD, Lifshitz EM (1979) *The classical theory of fields*, 4th edn. Pergamon Press, Oxford
74. Arrighini GP, Maestro M, Moccia R (1968) *J Chem Phys* 49:882
75. Lazzeretti P (2012) *Theor Chem Acc* 131:1 (and references therein)
76. Monaco G, Zanasi R, Pelloni S, Lazzeretti P (2010) *J Chem Theor Comput* 6:3343
77. Pelloni S, Lazzeretti P (2011) *J Phys Chem A* 115:4553
78. Hirschfelder JO (1977) *J Chem Phys* 67:5477
79. Takabayasi T (1952) *Progress Theoret Phys* 8:143
80. Takabayasi T (1953) *Progress Theoret Phys* 9:187
81. Riess J, Primas H (1968) *Chem Phys Lett* 1:545
82. Riess J (1970) *Ann Phys* 57:301
83. Riess J (1971) *Ann Phys* 67:346
84. Riess J (1970) *Phys Rev D* 2:647
85. Milnor JW (1997) *Topology from the differentiable viewpoint*. University of Virginia Press, Charlottesville
86. Guillemin V, Pollack A (1974) *Differential topology*. Prentice-Hall, Englewood Cliffs

87. Collard K, Hall GG (1977) *Int J Quantum Chem* XII:623
88. Bader RFW (1990) *Atoms in molecules-a quantum theory*. Oxford University Press, Oxford
89. Keith TA, Bader RFW (1993) *J Chem Phys* 99:3669
90. Bader RFW, Keith TA (1993) *J Chem Phys* 99:3683
91. Coddington EA, Levinson N (1955) *Theory of ordinary differential equations*. Mc Graw-Hill, New York
92. Reyn JW, Angew Z (1964) *Math Physik* 15:540
93. Gomes JANF (1983) *J Chem Phys* 78:3133
94. Bergé P, Pomeau Y, Vidal C (1998) *L'ordre dans le Chaos - vers une approche déterministe de la turbulence*, cinquième édition. Hermann, New York
95. Abraham RH, Shaw CD (1992) *Dynamics—the geometry of behavior*, 2nd edn. Addison-Wesley, Redwood City
96. Gilmore R (1993) *Catastrophe theory for scientist and engineers*. Dover Publications Inc., New York
97. Sachs RG (1987) *The physics of time reversal*. The University of Chicago Press, Chicago, p 12, 21, 24
98. Tavger BA, Zaitsev VM (1956) *Sov Phys JETP* 3:430
99. Bradley CJ, Davies BL (1968) *Rev Mod Phys* 40:359
100. (1955) *J Chem Phys* 23:1997
101. Mulliken RS (1956) *J Chem Phys* 24:1118
102. Pelloni S, Lazzeretti P (2011) *Int J Quantum Chem* 111:356
103. Pelloni S, Lazzeretti P (2009) *Chem Phys* 356:153
104. Pelloni S, Faglioni F, Zanasi R, Lazzeretti P (2006) *Phys Rev A* 74:012506
105. Coriani S, Lazzeretti P, Malagoli M, Zanasi R (1994) *Theor Chim Acta* 89:181
106. Keith TA, Bader RFW (1993) *Chem Phys Lett* 210:223
107. Zanasi R (1996) *J Chem Phys* 105:1460
108. Parker TS, Chua LO (1986) *Practical numerical algorithms for chaotic systems*. Springer, New York
109. Lazzeretti P, Zanasi R (1982) *J Chem Phys* 77:3129
110. Viglione RG, Zanasi R, Lazzeretti P (2004) *Org Lett* 6:2265
111. Pelloni S, Lazzeretti P (2007) *Theor Chem Acc* 117:903
112. Pelloni S, Lazzeretti P (2007) *Theor Chem Acc* 118:89
113. Pelloni S, Lazzeretti P, Zanasi R (2007) *J Phys Chem A* 111:8163
114. Carion R, Champagne B, Monaco G, Zanasi R, Pelloni S, Lazzeretti P (2010) *J Chem Theor Comput* 6:2002
115. Pelloni S, Lazzeretti P (2008) *J Phys Chem A* 112:5175
116. Pelloni S, Lazzeretti P (2008) *J Chem Phys* 128:194305
117. Pelloni S, Carion R, Liégeois V, Lazzeretti P (2011) *J Comput Chem* 32:1599
118. Faglioni F, Ligabue A, Pelloni S, Soncini A, Lazzeretti P (2004) *Chem Phys* 304:289
119. Khriplovich IB (1991) *Parity nonconservation in atomic phenomena*. Gordon and Breach, Oxford
120. Pelloni S, Faglioni F, Soncini A, Ligabue A, Lazzeretti P (2003) *Chem Phys Lett* 375:583
121. Pelloni S, Lazzeretti P, Zanasi R (2009) *Theor Chem Acc* 123:353
122. Pelloni S, Lazzeretti P, Monaco G, Zanasi R (2011) *Rend Lincei* 22:105
123. Provasi PF, Pagola GI, Ferraro MB, Pelloni S, Lazzeretti P (2014) *J Phys Chem A* 118:6333
124. Pagola GI, Ferraro MB, Provasi PF, Pelloni S, Lazzeretti P (2014) *J Chem Phys* 141
125. Feixas F, Matito E, Poater J, Solà M (2015) Chapter “Rules of aromaticity”, this book
126. IUPAC Gold Book. <http://goldbook.iupac.org/D01583.html>
127. Omelchenko IV et al (2011) *Phys Chem Chem Phys* 13:20536
128. Steinmann SN, Mo Y, Corminboeuf C (2011) *Phys Chem Chem Phys* 13:20584
129. Feixas F, Vandenbussche J, Bultinck P, Matito E, Solà M (2011) *Phys Chem Chem Phys* 13:20690
130. Feixas F, Matito E, Poater J, Solà M (2015) *Chem Soc Rev* 44:6434
131. Musher JI (1965) *J Chem Phys* 43:4081

132. Musher JI (1967) *J Chem Phys* 46:1219
133. Gaidis JM, West R (1967) *J Chem Phys* 46:1218
134. Garrat PJ (1986) *Aromaticity*. Wiley, New York
135. Sondheimer F (1972) *Acc Chem Res* 5:81
136. Haigh CW, Mallion RB (1979) Ring current theories in nuclear magnetic resonance. In: Emsley JW, Feeney J, Sutcliffe LH (eds) *Progress in nuclear magnetic resonance spectroscopy*, vol 13. Pergamon Press, Oxford, pp 303–344
137. von Ragué Schleyer P (2001) *Chem Rev* 101:1115 (and articles therein)
138. Gomes JANF, Mallion RB (2001) *Chem Rev* 101:1349
139. Pelloni S, Lazzeretti P, Zanasi R (2009) *J Phys Chem A* 113:14465
140. Musher JI (1966) Theory of the chemical shift. In: Waugh JS (ed) *Advances in magnetic resonance*, vol 2. Academic Press, New York, pp 177–224
141. Pelloni S, Monaco G, Lazzeretti P, Zanasi R (2011) *Phys Chem Chem Phys* 13:20666
142. Pelloni S, Monaco G, Zanasi R, Lazzeretti P (2012) *AIP Conf Proc* 1456:114
143. Pelloni S, Lazzeretti P (2013) *J Phys Chem A* 117:9083
144. London F (1937) *J Phys Radium* 8:397 (7ème Série)
145. Pelloni S, Monaco G, Della Porta P, Zanasi R, Lazzeretti P (2014) *J Phys Chem A* 118:3367
146. Van Vleck JH, Sherman A (1935) *Rev Mod Phys* 7:167

Chapter 8

Topological Analysis of the Fukui Function

P. Fuentealba, C. Cardenas, R. Pino-Rios and W. Tiznado

Abstract In this work, the Fukui function will be analyzed using the framework of the topological analysis. First, the Fukui function will be introduced as part of the Density Functional Theory of Chemical Reactivity, and its chemical interpretation will be discussed. Then, some applications showing the importance of the topological analysis will be presented. The applications cover from acids and basis of Lewis, substituted benzenes and as an orientation predictor for the most favorable interaction between clusters (used as building blocks) to form larger structures.

8.1 Introduction

All the chemical and physical processes we are interested in occur in real space (a three dimensional space). Therefore, it is obviously necessary to have three-dimensional mathematical functions in order to adequately describe them. The calculation and analysis of three-dimensional functions are very well known. However, the global graphical representation and visualization of a three dimensional function is not as easy as the one for one- or two-dimensional functions.

P. Fuentealba (✉) · C. Cardenas
Departamento de Física, Facultad de Ciencias, Universidad de Chile,
653 Santiago, Chile
e-mail: pfuentea@hotmail.es

P. Fuentealba · C. Cardenas
Centro para el desarrollo de la Nanociencias y Nanotecnología,
CEDENNA, 3493 Av. Ecuador, Santiago, Chile

R. Pino-Rios · W. Tiznado
Doctorado en Físicoquímica Molecular, Facultad de Ciencias Exactas,
Universidad Andres Bello, República 275, Santiago, Chile
e-mail: tiznado@unab.cl

R. Pino-Rios · W. Tiznado
Departamento de Ciencias Químicas, Facultad de Ciencias Exactas,
Universidad Andres Bello, República 275, Santiago, Chile

Thus one resorts to contour maps or isosurface plots to represent them. Unfortunately, they show only a part of the information contained in the function, since they depend on the contour (or isosurface) value choice one decides to plot. In order to have a more unambiguous way to analyze a three-dimensional (or higher dimension) function, one could use the framework of the topological analysis. In theoretical chemistry, this has already been done in the pioneer works of Bader, which originated the Quantum Theory of Atoms in Molecules (QTAIM) [1]. Later this topological analysis was applied to interpret the Electron Localization Function [2–4], and lately it has been applied to the study of the Fukui function [5–7], which is namely the object of this chapter.

We will start with the presentation of the Fukui function in the framework of the Density Functional Reactivity Theory and its chemical interpretation, [8–14] followed by a brief account of the different ways to analyze it and ending with its topological analysis. Finally, several applications of this analysis will be shown, and some open problems will be discussed.

8.2 Fukui Function

Density Functional Theory is based on the existence of a functional of the electron density, $\rho(r)$, which gives the ground state energy:

$$E[\rho] = F[\rho] + \int v(r)\rho(r)dr \quad (8.1)$$

where $F[\rho]$ is the universal functional of Hohenberg and Kohn [15], and $v(r)$ is the external potential. Besides, there is a variational principle, which yields the following Euler-Lagrange equation:

$$\mu = \frac{\delta F[\rho]}{\delta \rho(r)} + v(r) \quad (8.2)$$

where μ is the chemical potential present in the equation as the Lagrange parameter. It can be demonstrated that the chemical potential is the derivative of the energy with respect to the electron number N [16]

$$\mu = \left(\frac{\partial E}{\partial N} \right)_v \quad (8.3)$$

The derivative is well defined only for open systems and presents a discontinuity at integer number of electrons [17–24]. Therefore, the derivative at integer number of electrons has different values whether it is taken either by the right or the left.

Parr and Yang defined the Fukui function, $f(r)$, as the functional derivative of the chemical potential with respect to the external potential at constant number of electrons [5, 6]

$$f(r) = \left[\frac{\delta\mu}{\delta v(r)} \right]_N \quad (8.4)$$

Note that because of Eq. 8.3, the Fukui function is really the second derivative of the energy with respect to the electron number and the external potential. Assuming that the energy is an exact differential, the crossed second order derivatives are equal, and

$$f(r) = \left(\frac{\partial \rho(r)}{\partial N} \right)_v \quad (8.5)$$

As for the chemical potential, the Fukui function has different values if the derivative is taken from the right or the left. It can be demonstrated that, in the canonical ensemble at zero temperature, the Fukui function is given by

$$f^+(r) = \rho_{N+1}(r) - \rho_N(r) \quad (8.6)$$

When the derivative is taken by the right, and

$$f^-(r) = \rho_N(r) - \rho_{N-1}(r) \quad (8.7)$$

when the derivative is taken by the left.

Equations 8.5–8.7 are not valid if the ground state or its vertical anions are degenerate states. In such cases, the functional derivative of Eq. 8.4 is ill-defined and, a proper perturbation theory for degenerate states must be used to define Fukui function analogues [25–27]. The Fukui function, approximated using the Eq. 8.6, represents the molecular reactivity as an electron acceptor; whereas the Fukui function, approximated using the Eq. 8.7, plays the same role in the reactivity of electron donors. In a frozen orbital approximation Eqs. 8.6 and 8.7 are just the square of the frontier orbitals, LUMO and HOMO, respectively. In this way, they recover all the frontier orbital reactivity developed by Fukui [5, 28], making their chemical interpretation clear. The regions of the molecule where the Fukui function has a big value are the most prone to accept or donate electrons.

Hence, both Fukui functions are useful reactivity descriptors especially for orbital controlled reactions. Considering the Eqs. 8.6 and 8.7, it is easy to see that the Fukui function integrates to one:

$$\int f(r) dr = 1 \quad (8.8)$$

On the other side, there are many numerical evidences that the Fukui function can have negative values [29–33]. Therefore, it cannot be interpreted as a distribution function.

In chemistry, it is important to know the local preference inside a molecule to make or break bonds (For instance, in regioselectivity and stereoselectivity). Then, it is desirable to describe this preference by assigning a number to each atom, which was carried out in the early days of the Fukui function. Yang and Mortier [34] had the brilliant idea of “condensing” the Fukui function through a simple protocol, in order to assign a number to the Fukui function on each atom of the molecule. This was done in analogy with the Mulliken atomic population analysis. Considering Eqs. (8.6 and 8.7), they proposed to condense both, the electron acceptor Fukui function in atom k in the molecule as:

$$f_k = q_k(N + 1) - q_k(N) \quad (8.9)$$

and, the electron donor Fukui function as:

$$f_k = q_k(N) - q_k(N - 1) \quad (8.10)$$

where $q_k(N)$ is the charge assigned to atom k in the molecule with N electrons, whereas $q_k(N - 1)$ and $q_k(N + 1)$ are the charges of its vertical cation and anion, respectively. Until today, this is the most traditional way to present the Fukui function. In the original version, the charges were calculated using the Mulliken population analysis. However, nowadays it is clear that this analysis fails greatly when basis sets with diffuse functions are used. To address this problem, some authors propose the use of net atomic charges computed using modern methods, such as electrostatic potential analysis and natural population analysis, and the results can differ in a significant way [35–37]. Fortunately, the Fukui function is usually used to compare the relative reactivity of different atoms of a molecule. Therefore, the adequate description of the local reactivity preferences is more important than the numbers themselves. Other methodologies to calculate the charges are also in use; the Bader’s partition of atoms in molecules (AIM) and the Hirschfeld’s population analysis [38–42]. They differ from the Mulliken approximation because they do not use the molecular orbitals.

8.3 Topological Analysis and Condensed Fukui Function

The last two methodologies mentioned above directly divide the whole space into various regions assigning the volume Ω_k to atom k in the molecule; and the integration of the density in this region is used for computing the charge of atom k . In this way, one can generalize the proposed condensed Fukui function as:

$$f_k = \int_{\Omega_k} f(r) dr \quad (8.11)$$

The way to choose those regions is still arbitrary. It is possible to further generalize the condensed Fukui function as:

$$f_k = \int \omega(r) f(r) dr \quad (8.12)$$

where $\omega(r)$ is a somewhat arbitrary weight function. For instance, one choice is:

$$\omega(r) = \begin{cases} q_k & \text{if } r \in \Omega_k \\ 0 & \text{otherwise} \end{cases} \quad (8.13)$$

The charges q_k can be chosen from any of the previously mentioned population analyses. Equation 8.12 shows even another ambiguity: every population analysis is understood as the charge obtained after the integration of the density in a determined region of the space:

$$q_k = \int \omega(r) \rho(r) dr \quad (8.14)$$

and the condensed Fukui function is calculated using these charges. However, this is not exactly the same as Eq. 8.12. The Fukui function is the difference between the densities of the neutral and charged systems, but the weight function $\omega(r)$ is not necessarily the same for both neutral and charged systems. If the weight function of a system with M electrons ($M = N - 1, N, N + 1$) is denoted as $\omega_M(r)$, then Eq. 8.12 reads as:

$$f^-(r) = \int \omega_N(r) (\rho_N(r) - \rho_{N-1}(r)) dr \quad (8.15)$$

with a similar equation for $f^+(r)$. This is different from:

$$f^-(r) = \int (\omega_N(r) \rho_N(r) - \omega_{N-1}(r) \rho_{N-1}(r)) dr \quad (8.16)$$

which comes from Eq. 8.9. Most works have used the last equation because the definitions of the different population analyses carry it out in such a way. The differences between both versions have been recently exposed [41, 43]. From a formal point of view, the correct way to condense the Fukui function is through Eq. 8.15 [43].

In order to keep its practical advantages and avoid these mentioned ambiguities, one can use a well-studied mathematical tool (the topological analysis) to characterize the Fukui function [44]. This has been applied before to analyze both the

electron density (AIM) and the Electron Localization Function (ELF) [3, 4, 35, 45]. The Fukui function, being a scalar field in \mathbb{R}^3 itself, can also be analyzed topologically. In this case, the critical points correspond to maxima, minima and saddle points. They can be located by the analysis of its gradient fields. The maxima are called attractors, which many times have a physical interpretation. For instance, the Fukui function, like the electron density, has a cusp condition at the nuclei positions. Therefore, it will always have an attractor at the atomic positions. However, it can also have attractors in other positions. We will see that this characteristic has an interesting chemical interpretation. It is useful to define the f -localization domains as the volumes enclosed by the isosurface $f(r) = f$ involving all the points for which $f(r) \geq f$. They are called reducible when they contain more than one attractor and, irreducible when they contain only one attractor. Each attractor is characterized by its basin, which is the set of points lying on the trajectories ending in this attractor. The basins are irreducible domains (they do not overlap) and the set of all basins fills the complete space. Hence, the whole space is partitioned into basins of attractors, and any observable physical property can be defined in those regions. For instance, for a basin Ω_k , one can calculate the number of electrons contained in this basin as:

$$N_k = \int_{\Omega_k} \rho(r) dr \quad (8.17)$$

The overall sum of the N_k naturally results in the total number of electrons. One can also define the condensed Fukui function as its integration over each basin as:

$$f_k^\pm = \int_{\Omega_k^\pm} f^\pm(r) dr \quad (8.18)$$

The interpretation remains the same. Note that the basins of the Fukui function f^+ and f^- will be different.

8.4 Some Selected Applications

In this section we present some representative examples to show how the topological analysis of the Fukui function works. Accordingly with the literature [44, 46, 47] the results are commonly reported in two ways: the first involves a 3D-representation of $f(r)$ where one isosurface is selected to plot in a way that can represent all the Fukui basins. Accompanying these isosurfaces are the values of the Fukui function condensed in the corresponding basins. The second way makes it simple to compare with other methods used to condense the Fukui function, due to the fact that all atomic contributions are reported as a single value over each atom k . The geometrical optimization and electronic structure calculation have been

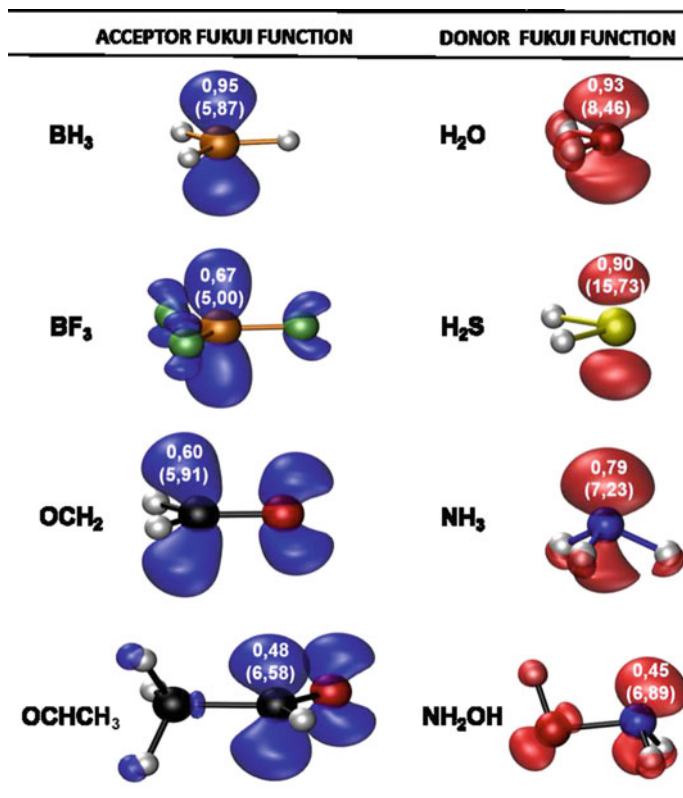


Fig. 8.1 Acceptor and donor Fukui functions (f^+ and f^-) isosurfaces with $f(r) = 0.01$ a.u. The values of condensed Fukui function (Eq. 8.18), and the condensed electron density (Eq. 8.17) (in parenthesis above) are also shown next to each domain

performed using the PBE0 [48] functional and the 6-311G* basis set implemented in the G09 package of programs [49]. For topological analysis, we have used the Multiwfn program [50] and the isosurfaces have been plotted with VMD 1.9.1 visualization software [51].

Figure 8.1 shows the condensed Fukui function for a set of Lewis acids (LAs) and Lewis bases (LBs), which are classic examples of electrophilic (electron acceptors) and nucleophilic (electron donors) reagents, respectively. The shapes of isosurfaces evidence the contribution of the p atomic orbitals to the frontier molecular orbitals (FMOs) and, therefore, to the Fukui function. The LAs (**BH₃**, **BF₃**, **OCH₂**, **OCHCH₃**) are expected to accept electrons through the p_z orbital of the reactive atom, whereas the LBs (**H₂O**, **H₂S**, **NH₃**, **NH₂OH**) are expected to donate charge from the lone-pairs; the reactive atoms are highlighted in bold. The condensed values obtained with Eqs. 8.17 and 8.18 allow us to identify the most reactive atom of the molecule. However, in contrast to the classical methods, the topological analysis provides two basins associated to each of the reactive atoms.

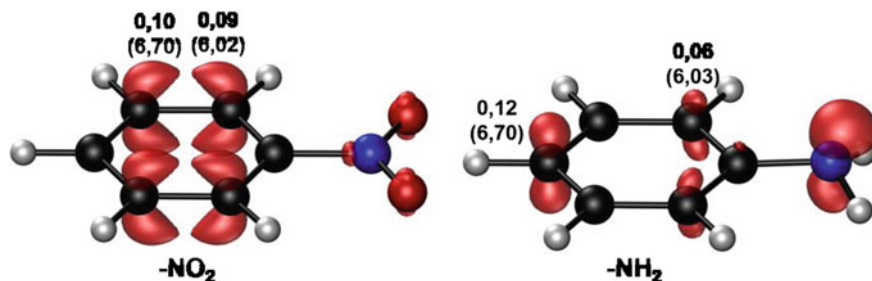


Fig. 8.2 Donor (nucleophilic) Fukui functions isosurfaces, with $f^-(r) = 0.01a.u.$ The values of condensed Fukui function (Eq. 8.18), and the condensed electron density (Eq. 8.17) (in parenthesis above) are also shown next to each domain

In the complete set of LAs these basins are symmetric and located above and below the atom, perpendicular to the molecular plane. This reactivity description predicts equal probability of being attacked by a nucleophile from above or below. The same could be extrapolated for LBs H_2O and H_2S , but in these cases the reactivity should describe an electrophilic attack. In cases where this does not happen, as in NH_3 and $HONH_2$, there is a clear chemical interpretation: it is expected that nucleophiles will primarily be attacked in the lone pair of the N.

Electrophilic aromatic substitution (EAS) reactions are among the most thoroughly studied classes of organic reactions from a mechanistic point of view. Therefore, even though they are classic and widely used as reference, they are still an adequate starting point for evaluate any local descriptor of reactivity. Such reactions have been rationalized using empirical reactivity rules derived from resonance theory [52], methods based on the frontier molecular orbitals (FMOs) theory, and electrostatic potentials [53]. The isosurfaces and condensed values for two representative molecules, aniline ($C_6H_5NH_2$ (*ortho-para* reactivity)), and nitrobenzene ($C_6H_5NO_2$ (*meta* reactivity)) are shown in Fig. 8.2. For $C_6H_5NH_2$, carbons in position *ortho* and *para* have the highest condensed values and the *para* position is predicted as the most reactive between the two. This is in agreement with the experimental observations. In contrast, for $C_6H_5NO_2$ (*meta* reactivity), the condensed values suggest the same preference for *ortho* and *meta* positions, which disagrees with the experimentally observed *meta* preference. This inconsistency has also been noted in earlier studies based in FMOs analysis [54]. In the last time has been demonstrated that all the response functions based in perturbation theory should be completely different in the case of degenerate states [25–27]. In the case of $C_6H_5NO_2$, eventhough it is not strictly degenerate, there is a quasidegeneracy which could be the explanation of the wrong result. However, in this chapter, we are only interested in presenting the topological analysis of the Fukui function obtained by finite differences (Eq. 8.9).

Figure 8.3 shows the condensed values of the Fukui for a set of monosubstituted benzenes (C_6H_5X , $X = CH_3$, NH_2 , OH , and OCH_3 (electron-releasing groups (ERGs)) and $X = CF_3$, CN , and NO_2 (electron withdrawing group (EWGs)). The

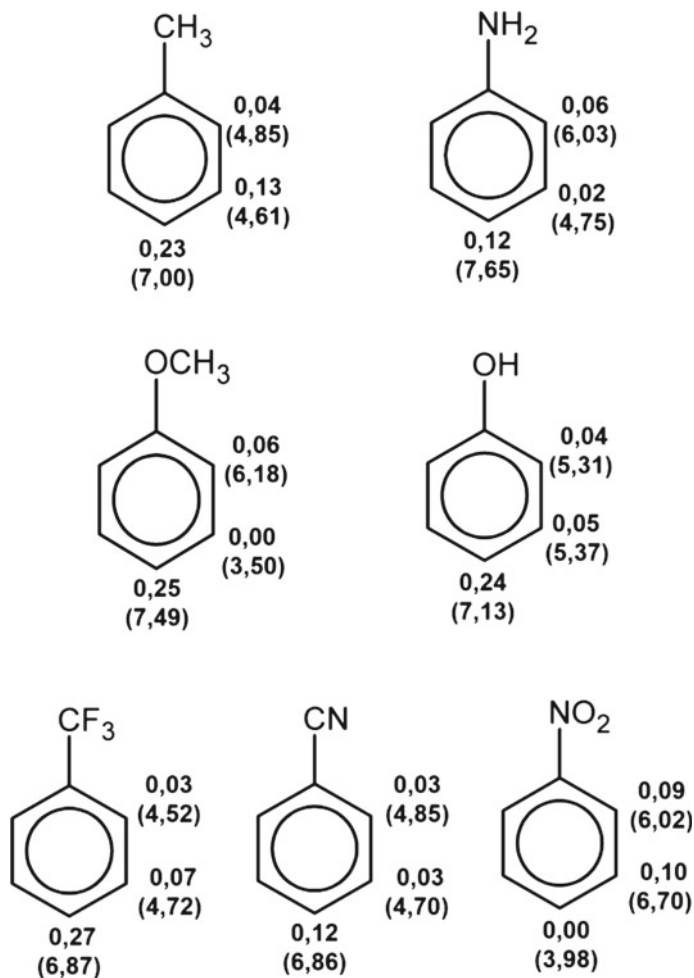


Fig. 8.3 Condensed values of the Fukui function (Eq. 8.18) and the electron density (Eq. 8.17) (in parenthesis) integrated in the basins of the donor (nucleophilic) Fukui function (f^-). The values have been obtained by summing the entire basin associated to each atom

ortho-para reactivity induced by ERGs is adequately described. However, it is predicted that EWGs favor *ortho-meta* (in the case of X = NO₂) and *para* reactivity for the rest, which disagrees with the experimental evidence where only *meta* position is favored. The results presented in Figs. 8.1, 8.2 and 8.3 are similar to those previously reported in Ref. [44] at B3LYP/6-311G* level of theory.

Another instance, where the methodology has been used is to predict the most favorable orientation between two small clusters to produce a larger one, according to the “maximum matching” criteria of the Fukui function [55]. The proposal was tested in the formation of a series of clusters Si_n (n = 4 – 8) using a set of small Si_n (n = 2 – 6)

clusters, in singlet and triplet ground state multiplicities, as building blocks. The reasoning of this strategy is simple; the integral of the Fukui function in each basin is a measure of the “abundance” of it around the attractor associated to the basin. It is therefore reasonable to assume that at a given distance between the fragments, an assembling of them that makes small the total distance between the attractors corresponding to the more populated basins (f_k large) translates into a large overlap of the Fukui functions. We have selected two hypothetical reactions to show in this section, the interaction between two Si_3 fragments to produce Si_6 (Fig. 8.4 panel (a)) and the interaction between two Si_4 fragments to produce Si_8 (Fig. 8.4 panel (b)).

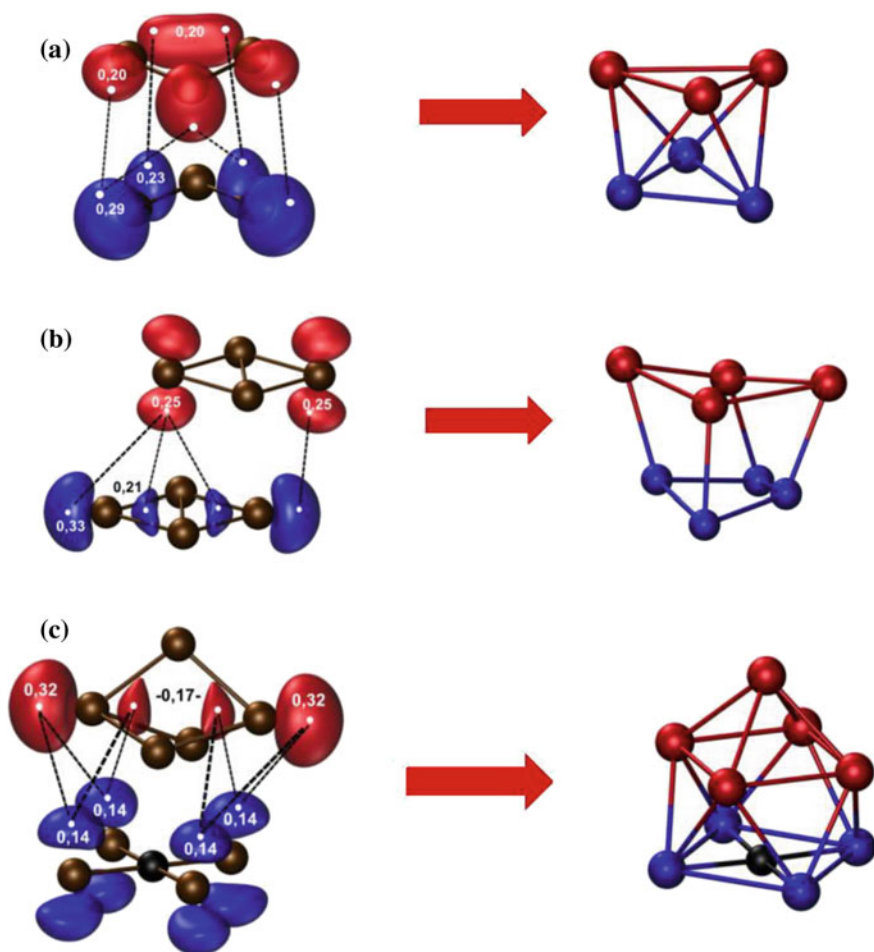


Fig. 8.4 Best orientation to maximize the matching of the Fukui functions of two small clusters. f^- and f^+ are identified in red and blue, respectively. Next to each attractor (white dots) the value of the condensed Fukui function is also shown. **a** $\text{Si}_3 + \text{Si}_3 \rightarrow \text{Si}_6$, **b** $\text{Si}_4 + \text{Si}_4 \rightarrow \text{Si}_8$, **c** $\text{Si}_4\text{C} + \text{Si}_5^{2-} \rightarrow \text{Si}_9\text{C}$

Blue and red isosurfaces correspond to acceptor and donor Fukui functions respectively. In the product the atoms corresponding to the original fragments are differentiated in red and blue. We obtained the same results as those previously reported at B3LYP/6-311 +G(d, p) level of theory [55]. As an additional example of the strategy applied to predict the most favorable interaction in clusters assemble, we present the hypothetical reaction between the planar (D_{4h}) Si_4C^{2+} cation and the tridimensional (D_{3h}) Si_5^{2-} anion, to form the neutral Si_9C cluster. This possibility was suggested by Ngan and Tam [56], who based their proposal on the higher stability of the fragments. They showed that the structural patterns of the fragments persist in the global minimum structure of Si_9C . The confrontation of the two fragments guided by the Fukui function information allow us to obtain the global minimum conformation of Si_9C , as it can be seen in the panel (c) of the Fig. 8.4.

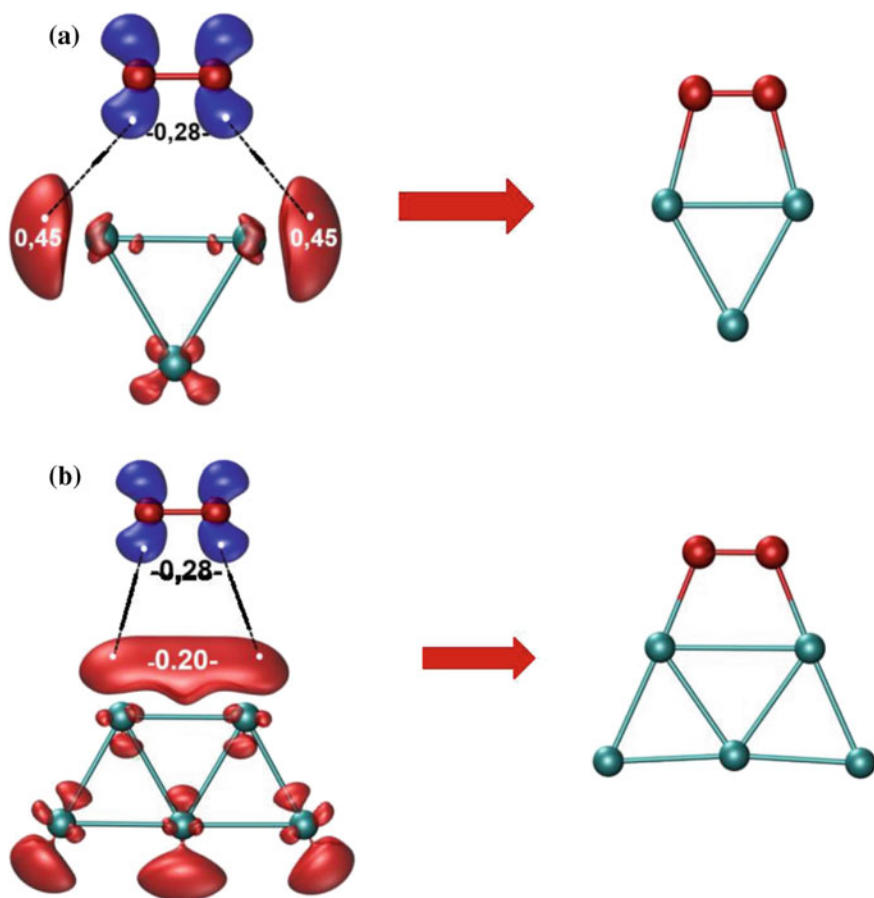


Fig. 8.5 Condensed values of the Fukui function (using Eq. 8.18) into the basins of the donor (f^-) (for Cu_3 (a) and Cu_5^- (b)) and acceptor (f^+) (for O_2) Fukui functions, respectively

In the last example, although the reaction would be dominated by the electrostatic attraction, the Fukui function is able to predict the matching of the fragments.

Finally, we would like to show two examples where this approximation was used to predict the interaction of molecular oxygen with metallic copper clusters. It has been shown that one can make useful predictions of the binding sites, based on the knowledge of the donor local reactivity of the cluster, by using the condensed Fukui function, f_k^- . In this way, it was reported that Cu_3 , Cu_5 , and Cu_5^- have the highest reactivity toward molecular oxygen. In Fig. 8.5, the results for Cu_3 (panel a) and for Cu_5^- (panel b) are shown. These results are similar to those reported in Ref. [57].

8.5 Conclusions

This chapter has provided an introduction to the topological analysis of the Fukui function, a strategy that allows for a theoretical expression of the chemical concepts of local reactivity, and enables one to employ these concepts in a quantitative manner to predict and understand chemical problems. The applicability of the method is presented through different examples, involving acids and bases of Lewis, substituted benzenes, and as an orientation predictor for the most favorable interaction between clusters (used as building blocks) to form larger structures. We hope that by using the remarkable on-going software developments, and processor technology, the applicability of this method increase further in both scope and reliability, for the different areas of chemistry.

Acknowledgments CC and PF acknowledges financial support from FONDECYT through projects No 11090013 and 1130202, and also by Millennium Nucleus CILIS, Project ICM-P10-003-F. WT and RP acknowledge financial support from FONDECYT through project No 1140358.

References

1. Bader RFW (1990) *Atoms in molecules: a quantum theory*. Clarendon, Oxford
2. Becke AD, Edgecombe KE (1990) A simple measure of electron localization in atomic and molecular-systems. *J Chem Phys* 92(9):5397–5403
3. Silvi B, Savin A (1994) Classification of chemical-bonds based on topological analysis of electron localization functions. *Nature* 371(6499):683–686
4. Savin A, Nesper R, Wengert S, Fassler TF (1997) ELF: the electron localization function. *Angew Chem* 36(17):1809–1832
5. Parr RG, Yang WT (1984) Density functional approach to the frontier-electron theory of chemical reactivity. *J Am Chem Soc* 106:4049–4050
6. Yang WT, Parr RG, Pucci R (1984) Electron density, Kohn-Sham frontier orbitals, and Fukui functions. *J Chem Phys* 81:2862–2863
7. Yang WT, Parr RG (1985) Hardness, softness, and the Fukui function in the electron theory of metals and catalysis. *PNAS* 82:6723–6726

8. Parr RG, Yang W (1989) Density-functional theory of atoms and molecules. Oxford UP, New York
9. Ayers PW, Anderson JSM, Bartolotti LJ (2005) Perturbative perspectives on the chemical reaction prediction problem. *Int J Quantum Chem* 101:520–534
10. Chattaraj PK, Sarkar U, Roy DR (2006) Electrophilicity index. *Chem Rev* 106:2065–2091
11. Gazquez J (2008) Perspectives on density functional theory of chemical reactivity. *J Mex Chem Soc* 52(1):3–10
12. Liu S-B (2009) Conceptual density functional theory and some recent developments. *Acta Phys-Chim Sinica* 25(03):590–600
13. Fuentealba P, Cardenas C (2015) Density functional theory of chemical reactivity. In: *Chemical modelling: volume 11, vol 11*. The Royal Society of Chemistry, pp 151–174
14. Geerlings P, De Proft F, Langenaeker W (2003) Conceptual density functional theory. *Chem Rev* 103:1793–1873
15. Hohenberg P, Kohn W (1964) Inhomogeneous electron gas. *Phys Rev* 136:B864–B871
16. Parr RG, Donnelly RA, Levy M, Palke WE (1978) Electronegativity: the density functional viewpoint. *J Chem Phys* 68:3801–3807
17. Perdew JP, Parr RG, Levy M, Balduz JL Jr (1982) Density-functional theory for fractional particle number: derivative discontinuities of the energy. *Phys Rev Lett* 49:1691–1694
18. Chan GKL (1999) A fresh look at ensembles: derivative discontinuities in density functional theory. *J Chem Phys* 110:4710–4723
19. Yang WT, Zhang YK, Ayers PW (2000) Degenerate ground states and fractional number of electrons in density and reduced density matrix functional theory. *Phys Rev Lett* 84:5172–5175
20. Cohen MH, Wasserman A (2003) Revisiting N-continuous density-functional theory: chemical reactivity and “atoms” in “molecules”. *Isr J Chem* 43:219–227
21. Cohen MH, Wasserman A (2007) On the foundations of chemical reactivity theory. *J Phys Chem A* 111:2229–2242
22. Ayers PW (2008) The continuity of the energy and other molecular properties with respect to the number of electrons. *J Math Chem* 43(1):285–303
23. Cohen AJ, Mori-Sanchez P, Yang WT (2008) Insights into current limitations of density functional theory. *Science* 321(5890):792–794
24. Fuentealba P, Cardenas C (2013) On the exponential model for energy with respect to number of electrons. *J Mol Model* 19:2849–2853
25. Bultinck P, Cardenas C, Fuentealba P, Johnson PA, Ayers PW (2013) How to compute the Fukui matrix and function for systems with (quasi-)degenerate states. *J Chem Theory Comput* 10(1):202–210
26. Bultinck P, Cardenas C, Fuentealba P, Johnson PA, Ayers PW (2013) Atomic charges and the electrostatic potential are ill-defined in degenerate ground states. *J Chem Theory Comput* 9(11):4779–4788
27. Cardenas C, Ayers PW, As Cedillo (2011) Reactivity indicators for degenerate states in the density-functional theoretic chemical reactivity theory. *J Chem Phys* 134(17):174103
28. Ayers PW, Levy M (2000) Perspective on “density functional approach to the frontier-electron theory of chemical reactivity” by Parr RG, Yang W (1984). *Theor Chem Acc* 103:353–360
29. Echegaray E, Rabi S, Cárdenas C, Zadeh FH, Rabi N, Lee S, Anderson JS, Toro-Labbe A, Ayers PW (2014) In pursuit of negative Fukui functions: molecules with very small band gaps. *J Mol Model* 20(3):1–7
30. Bultinck P, Carbo-Dorca R, Langenaeker W (2003) Negative Fukui functions: new insights based on electronegativity equalization. *J Chem Phys* 118:4349–4356
31. Melin J, Ayers PW, Ortiz JV (2007) Removing electrons can increase the electron density: a computational study of negative Fukui functions. *J Phys Chem A* 111:10017–10019
32. Bultinck P, Clarisse D, Ayers PW, Carbo-Dorca R (2011) The Fukui matrix: a simple approach to the analysis of the Fukui function and its positive character. *Phys Chem Chem Phys* 13(13):6110–6115

33. Echegaray E, Cardenas C, Rabi S, Rabi N, Lee S, Heidar Zadeh F, Toro-Labbe A, Anderson JSM, Ayers PW (2013) In pursuit of negative Fukui functions: examples where the highest occupied molecular orbital fails to dominate the chemical reactivity. *J Mol Model* 19:2779–2783
34. Yang WT, Mortier WJ (1986) The use of global and local molecular parameters for the analysis of the gas-phase basicity of amines. *J Am Chem Soc* 108:5708–5711
35. Chamorro E, Duque M, Cardenas C, Santos C, Tiznado W, Fuentealba P (2005) Condensation of the highest occupied molecular orbital within the electron localization function domains. *J Chem Sci* 117:419–424
36. Zielinski F, Tognetti V, Joubert L (2012) Condensed descriptors for reactivity: a methodological study. *Chem Phys Lett* 527:67–72
37. Bultinck P, Fias S, Alsenoy CV, Ayers PW, Carbo-Dorca R (2007) Critical thoughts on computing atom condensed Fukui functions. *J Chem Phys* 127:034102
38. Hirshfeld FL (1977) *Theor Chim Act* 44:129–138
39. Nalewajski RF (2003) Information principles in the theory of electronic structure. *Chem Phys Lett* 372(1–2):28–34
40. Ayers PW (2006) Information theory, the shape function, and the Hirshfeld atom. *Theor Chem Acc* 115:370–378
41. Bultinck P, Van Alsenoy C, Ayers PW, Carbo-Dorca R (2007) Critical analysis and extension of the Hirshfeld atoms in molecules. *J Chem Phys* 126:144111
42. Verstraelen T, Ayers PW, Van Speybroeck V, Waroquier M (2013) Hirshfeld-E partitioning: AIM charges with an improved trade-off between robustness and accurate electrostatics. *J Chem Theory Comput* 9:2221–2225
43. Bultinck P, Fias S, Van Alsenoy C, Ayers PW, Carbo-Dorca R (2007) Critical thoughts on computing atom condensed Fukui functions. *J Chem Phys* 127(3):11
44. Fuentealba P, Florez E, Tiznado W (2010) Topological analysis of the Fukui function. *J Chem Theory Comput* 6(5):1470–1478
45. Savin A, Becke AD, Flad J, Nesper R, Preuss H, Vonscherner HG (1991) A new look at electron localization. *Angew Chem* 30(4):409–412
46. Tiznado W, Chamorro E, Contreras R, Fuentealba P (2005) Comparison among four different ways to condense the Fukui function. *J Phys Chem A* 109(14):3220–3224
47. Osorio E, Ferraro MB, Oña OB, Cárdenas C, Fuentealba P, Tiznado W (2011) Assembling small silicon clusters using criteria of maximum mismatch of the Fukui functions. *J Chem Theory Comput* 7:3995–4001
48. Levy M (1983) The constrained search approach, mappings to external potentials, and virial-like theorems for electron-density and one-matrix energy-functional theories. In: Keller J, Gazquez JL (eds) *Density functional theory*, vol 187, *Lecture Notes in Physics* Springer, Heidelberg, pp 9–35
49. Frisch MJ, Trucks GW, Schlegel HB, Scuseria GE, Robb MA, Cheeseman JR, Scalmani G, Barone V, Mennucci B, Petersson GA, Nakatsuji H, Caricato M, Li X, Hratchian HP, Izmaylov AF, Bloino J, Zheng G, Sonnenberg JL, Hada M, Ehara M, Toyota K, Fukuda R, Hasegawa J, Ishida M, Nakajima T, Honda Y, Kitao O, Nakai H, Vreven T, Montgomery JA, Peralta JE, Ogliaro F, Bearpark M, Heyd JJ, Brothers E, Kudin KN, Staroverov VN, Kobayashi R, Normand J, Raghavachari K, Rendell A, Burant JC, Iyengar SS, Tomasi J, Cossi M, Rega N, Millam JM, Klene M, Knox JE, Cross JB, Bakken V, Adamo C, Jaramillo J, Gomperts R, Stratmann RE, Yazyev O, Austin AJ, Cammi R, Pomelli C, Ochterski JW, Martin RL, Morokuma K, Zakrzewski VG, Voth GA, Salvador P, Dannenberg JJ, Dapprich S, Daniels AD, Farkas, Foresman JB, Ortiz JV, Cioslowski J, Fox DJ (2009) *Gaussian 09*, Revision B.01. Gaussian 09, Revision B.01, Gaussian, Inc., Wallingford CT
50. Lu T, Chen F (2012) Multiwfn: a multifunctional wavefunction analyzer. *J Comput Chem* 33(5):580–592. doi:10.1002/jcc.22885
51. Humphrey W, Dalke A, Schulten K (1996) VMD: visual molecular dynamics. *J Mol Graph* 14(1):33–38

52. Pauling L, Wheland GW (1933) The nature of the chemical bond. V. The quantum mechanical calculation of the resonance energy of benzene and naphthalene and the hydrocarbon free radicals. *J Chem Phys* 1(6):362–374
53. Murray JS, Politzer P (2011) The electrostatic potential: an overview. *Wiley Interdisc Rev.: Comput Mol Science* 1(2):153–163
54. Hehre WJ, Radom L, Pople JA (1972) Molecular orbital theory of the electronic structure of organic compounds. XII. conformations, stabilities, and charge distributions in monosubstituted benzenes. *J Am Chem Soc* 94(5):1496–1504. doi:[10.1021/ja00760a011](https://doi.org/10.1021/ja00760a011)
55. Osorio E, Ferraro MB, Oña OB, Cardenas C, Fuentealba P, Tiznado W (2011) Assembling small silicon clusters using criteria of maximum matching of the Fukui functions. *J Chem Theory Comp* 7(12):3995–4001
56. Tam NM, Ngan VT, Nguyen MT (2014) Planar tetracoordinate carbon stabilized by heavier congener cages: the Si_9C and Ge_9C clusters. *Chem Phys Lett* 595–596:272–276
57. Florez E, Tiznado W, Mondragón F, Fuentealba P (2005) Theoretical study of the interaction of molecular oxygen with copper clusters. *J Phys Chem A* 109(34):7815–7821

Chapter 9

Topological Tools for the Study of Families of Reaction Mechanisms: The Fundamental Groups of Potential Surfaces in the Universal Molecule Context

Paul G. Mezey

Abstract Two types of the main topological properties of potential energy surfaces are compared, where the first types are related to the chemical processes, conformational changes and chemical reactions along the potential energy surface, and where the second types are describing the presence, interrelations, structural variability, and shape variations of identifiable chemical species associated with the potential surface. Some new relations are obtained when the families of topologically equivalent reaction paths representing reaction mechanisms at some energy bound, and the algebraic structure of the fundamental group of reaction mechanisms for a given collection of atoms (that is, for a given stoichiometry) are constrained by the collection of “catchment regions” of the potential surface, representing chemical species. These relations, providing additional detail when they are compared to the more traditional, unconstrained cases, are phrased in terms of potential energy surface level set relations and the originally integer, but “unquantized” continuous variables of the Universal Molecule model.

9.1 Introduction

Topological methods, especially those of algebraic and differential topology [1, 2], provide very powerful tools for the description of chemical problems, far beyond the “skeletal models” provided by graph theory. Molecules are better described by topology than by geometry, since a whole range of possible geometries of a given molecule preserves the chemical identity of the molecule, that is, the topological

P.G. Mezey (✉)

Department of Chemistry, and Department of Physics and Physical Oceanography,
Memorial University of Newfoundland, 283 Prince Philip Drive,

St. John's, NL A1B 3X7, Canada

e-mail: pmezey@mun.ca; paul.mezey@gmail.com

URL: <http://www.mun.ca/research/chairs/mezey.php>

features are far more significant than some specific geometrical features of our models, especially, if one considers the Heisenberg uncertainty relation, where no precise geometrical features are compatible with the typically available momentum information. The inherent fuzziness of molecular electron density clouds is far more compatible with a topological analysis than with some rigid geometrical description. In particular, linking classical concepts with quantum chemical reality, and providing computational, algorithmic approaches as well as algebraic frameworks, such as the fundamental group of reaction mechanisms discussed here, algebraic topology and differential topology have an increasingly important role in theoretical and computational chemistry.

The reaction path model on a potential energy surface is based on an essentially classical mechanical concept. In reality, the actual displacements of atomic nuclei in chemical reactions do not follow a formal path, just as electronic rearrangements do not follow any formal path, either in a molecule when the molecular electron density changes due to some interaction, or in some change of the electronic state. This follows from the fact that the Heisenberg uncertainty relation and the wave-particle duality apply to both electrons and nuclei. Nevertheless, nuclei are certainly more “particle-like” than electrons within any given molecule. Consequently, the concept of nuclear positions in a molecule, although not strictly valid, is still a useful approximate concept, whereas the concept of electronic “positions” within a molecule is far too crude to have much use beyond very simplistic models. In the above sense, a formal reaction path, describing some essential aspects of the geometrical displacements of the nuclei in a reaction has a useful role as a practical approximation in many instances.

It is evident though that a single reaction path cannot faithfully represent the quantum mechanical process of a chemical reaction, and some broadening of this concept may serve as an improvement of the approximation. In this contribution a topological approach is discussed, using certain equivalence classes of formal reaction paths on potential energy surfaces to describe a quantum chemical concept of reaction mechanisms. These reaction mechanisms are dependent on an energy bound A over the actual potential energy surface. The family of all reaction mechanisms has a group-theoretical algebraic structure, called the “Fundamental Group of Reaction Mechanisms”, defined as the one-dimensional homotopy group of the potential energy surface (actually a hypersurface) truncated at some energy bound A . A brief review is given here for relevant earlier results in this field [3], as well as their relations to the global and local shape problems of molecules [4–7], where topological methods also play a dominant role. As a current development, this model of the complete set of reaction mechanisms on a given potential energy surface is now combined with some topological features of the Universal Molecule model [8–11] for the actual common stoichiometry of the family of nuclei associated with the same potential energy surface.

9.2 From Reaction Path to Reaction Mechanism

The collection of all possible arrangements of a given set of N atomic nuclei forms the relevant nuclear configuration space, that can be chosen as a metric space M , with a well-defined distance function $d(K, K')$ for any pair of nuclear configurations K and K' , where the dimension of this space is $3N - 6$ for $N > 2$ (diatomic and monoatomic cases are special with respect to internal coordinates).

What is less well-known, although it can be shown easily [3], that a nuclear configuration space M of internal coordinates can never be a vector space, and this fact is a frequent source of Euclidean-geometry-based misinterpretations of potential energy surface (in fact, potential energy hypersurface) problems.

Nevertheless, M being a metric space, it allows the use of many tools of abstract geometry as well as topology, and a reasonably detailed description of formal reaction paths and reaction mechanisms is possible [3].

The potential energy surface $E(K)$ is an energy function where the variables are the internal nuclear coordinates, collected into the symbol K of the nuclear configuration. Note, that different electronic states are associated to different potential energy surfaces.

If energy E is regarded as one additional variable beyond the $3N-6$ internal coordinates of the nuclear configurations (the dimension of space M), then the total dimension is $3N-5$, and the energy function is in fact a $(3N-6)$ -dimensional hypersurface; an object that has one dimension less than the dimension of the complete space. Note, however, that for brevity, the term “potential energy surface” is used more often.

It is customary to think of a reaction path as a line in configuration space M , for example, one leading from some “reactant configuration” K_{reactant} to some “product configuration” K_{product} , through some intermediate K configurations. One may associate the energy value of each configuration to the corresponding point along the path in configuration space, and by taking these values measured along an extra “energy” dimension, another line is obtained, a “relief path”, or “relief reaction path” along the potential energy surface. It is also customary to regard energy E as a “vertical” dimension, and one may think that the “relief reaction path” on the potential energy surface $E(K)$ runs “above” the reaction path within the configuration space M . One may also think that the reaction path in the configuration space M is the “shadow at high noon” of the relief reaction path along the potential energy surface $E(K)$.

For the purposes of a consistent mathematical treatment in the following topological description, one may regard a path not as the collection of points in some space, but as a formal, continuous function $p(u)$, assigning points in the actual space M to values u of the unit interval, $[0,1]$. In our case, a path $p(u)$ is regarded as a continuous mapping from the closed interval $[0,1]$ to space M , describing a continuous change of nuclear configurations K , represented by a displacement in M .

From such a parametrization by the unit interval, with the choice of

$$u = 0, \quad p(0) = K_{\text{orig}}$$

this point is referred to as the *origin*, and with the choice of

$$u = 1, \quad p(1) = K_{\text{extr}}$$

this point is referred to as the *extremity* of the given path $p(u)$.

A path $p(u)$ is called a *constant path*, if the image of each u is the same point K of M :

$$p(u) = K \text{ for every } u.$$

Beyond the conditions shown above and the requirement of continuity in terms of the metric $d(K, K')$ of the nuclear configuration space M , there is no additional restriction on these functions, and many *different* actual parametrizations may generate the *same point set* in the configuration space M , and all these different parametrizations are regarded as *different paths*.

Specifically, the *inverse path* $p^{-1}(u)$ of path $p(u)$ has the very same point set image as the path $p(u)$, however, these paths are considered different, and the inverse path $p^{-1}(u)$ is defined by the “opposite” parametrization:

$$p^{-1}(u) = p(1 - u);$$

for example, the roles of origin and extremity are interchanged.

Clearly, as point sets, the path $p(u)$, and the inverse path $p^{-1}(u)$ are the same, but as paths, they are different, as long as $p(u)$ is not a constant path.

If a path $p(u)$ is such that its origin coincides with its extremity,

$$p(0) = p(1),$$

then p is called a *closed path*, or a *loop*.

If a path $p_1(u)$ can be continued by path $p_2(u)$, that is, if the $p_1(1)$ extremity of path $p_1(u)$ coincides with the origin $p_2(0)$, of path $p_2(u)$,

$$p_1(1) = p_2(0),$$

than paths p_1 and p_2 have a *product path* p_3 defined for them, indicated by the equation

$$P_3 = P_1P_2$$

where this *product path* p_3 is actually defined by a specific parametrization as

$$p_3(u) = p_1(2u), \quad \text{if } 0 \leq u \leq 1/2,$$

and

$$p_3(u) = p_2(2u - 1), \quad \text{if } 1/2 \leq u \leq 1$$

Evidently, the sufficient and necessary condition for the existence of the product path $p_3(u)$ is the coincidence of $p_1(1)$ and $p_2(0)$.

The first physical constraint one may want to introduce is the elimination of highly unrealistic, very high energy nuclear arrangements for the species considered along the potential energy surface $E(K)$.

Instead of considering all possible paths in M , it is useful to apply an energy constraint, in terms of a “level set” $F(A)$, that is, by taking only those nuclear configurations, that is, points K of M with reference to a given potential energy surface $E(K)$, where the energy value $E(K)$ is less than some bound A :

$$F(A) = \{K : E(K) < A\}$$

The next step of simplification is suggested by the recognition that two different but very similar reaction paths are likely to describe essentially the same formal chemical process. Here, the degree of similarity is treated not exclusively by geometrical means, but also by using the tools of topology. This is an important aspect, since even those paths which are rather different geometrically, may still show essentially the same chemically relevant outcomes, and it is topology that provides the means to exploit this.

Within a level set $F(A)$ we consider two paths $p_1(u)$ and $p_2(u)$ to be *homotopically equivalent* relative to $F(A)$, if they have coincident origins, as well as coincident extremities,

$$p_1(0) = p_2(0),$$

$$p_1(1) = p_2(1),$$

all within $F(A)$, and if $p_1(u)$ can be continuously deformed into $p_2(u)$ within the level set $F(A)$. Clearly, this condition is energy dependent; at a higher energy bound value A , more paths can become homotopically equivalent relative to $F(A)$. We shall use the \sim symbol to express this homotopical equivalence:

$$p_1(u) \sim p_2(u).$$

Those paths which are homotopic to one another within level set $F(A)$, form a *homotopy equivalence class*, denoted by $[p]$, where the path p explicitly shown in the notation is any one member of this equivalence class:

$$[p] = \{p' : p' \sim p\}.$$

The use of homotopy equivalence classes at some energy bound A is the key step in the simplification of dealing with infinitely many possible individual reaction paths, and reducing the problem to dealing with reaction mechanisms.

In order to achieve this, one should first realize that each and every path can be regarded as a segment of a loop path, hence, one may consider only loop paths and their homotopy classes within the energy-dependent level set $F(A)$.

The analogy of boat trips on a flooded hilly terrain comes to mind, where the energy bound A corresponds to the height of the water level, and any actual boat trip can be regarded as a part of a circular boat trip. If the destination of the trip is important, than the actual geometrical path of the boat is not the most important, and many actual paths would qualify as essentially representing the same boat trip. Evidently, if the water level changes, the equivalence classes of various actual paths of boat trips may also change: for example, if a small island is flooded, some previously non-equivalent paths for the boat trips can become equivalent, since the actual paths of the boat trips can be deformed into one another without carrying the boat over any land, an effort that would have been necessary before the flooding of the island.

Returning now to the problems of reaction mechanism modelling, one may take an arbitrary choice for a constant path $p_0(u) = K_0$ within $F(A)$, and take all loop paths with origin at K_0 .

By this choice of origin at K_0 , the product path necessarily exists for each and every pair of such paths. Specifically, a path multiplied by its inverse path does always exist. We note that a product of an algebraic entity with its inverse usually provides some connection to a formal unit element. In our case, however, there are many such, non-unique products, so, as it is, this choice of multiplication does not lead yet to a unique unit element, consequently, this non-unique result does not lead yet to a group-theoretical structure.

If, however, one takes the homotopy equivalence classes of these loop paths, and if one takes an appropriate definition for the product of these equivalence classes, all properties of groups can be identified, and one ends up with a group theoretical structure not for the paths but for their homotopy equivalence classes, that is, for all loop-like reaction mechanisms, constrained by some energy bound A .

For such a definition, the product homotopy equivalence class $[p_3]$ of two $F(A)$ -relative homotopy equivalence classes $[p_1]$ and $[p_2]$ generated by all loop paths in $F(A)$, with common origin K_0 , is defined as the homotopy equivalence class $[p_3]$

that contains as element the path-product of any path p'_1 from $[p_1]$ and any path p'_2 from $[p_2]$:

$$p'_3 = p'_1 p'_2$$

where p'_3 is a member of homotopy equivalence class $[p_3]$. Note that this product path p'_3 must always exist, since all loop paths considered have their origins and extremities at the common point K_0 .

Then, we may write the product for the homotopy equivalence classes as

$$[p_3] = [p_1] [p_2],$$

and for all the loop-path homotopy equivalence classes this product also necessarily exists.

The unit element $[K_0]$ for these homotopy classes is defined as the homotopy equivalence class that contains the constant path $p(u) = K_0$. Since all these loop paths, when multiplied by their inverse paths, generate a loop path that is homotopically contractible to K_0 , therefore, these path-products are all homotopically equivalent to the constant path $p(u) = K_0$, so they must all belong to the same, and unique, homotopy equivalence class.

The inverse of homotopy class $[p]$ is the class $[p]^{-1} = [p^{-1}]$, since pp^{-1} must be homotopically equivalent to the origin K_0 of p , therefore,

$$[p] [p]^{-1} = [p] [p^{-1}] = [K_0].$$

For a group-theoretical structure one also needs that the product has the associativity property, and, again, this is not necessarily fulfilled for the product of the loop-paths themselves. The associativity property does not necessarily hold for all choices of three paths, p_1 , p_2 , and p_3 , even if the products exist, that is,

$$p_A = (p_1 p_2) p_3 \neq p_1 (p_2 p_3) = p_B$$

is possible.

For example, if one applies the product parametrization by u for paths $p_A(u)$ and $p_B(u)$, differing only in the way the parentheses are placed, and by picking the parameter value of $u = 0.48$, then, by simple application of the product rule one obtains that

$$\begin{aligned} p_A(0.48) &= p_2(0.92) \\ p_B(0.48) &= p_1(0.96), \end{aligned}$$

which are, evidently, not in general identical points of $F(A)$.

Hence, the associativity condition for the path product is not in general fulfilled.

However, in all instances, the paths $p_A = (p_1 p_2) p_3$ and $p_B = p_1 (p_2 p_3)$ are homotopically equivalent. Consequently, for the products of loop homotopy equivalence classes, the associativity condition applies:

$$([p_1][p_2])[p_3] = [p_1]([p_2][p_3]).$$

Since all four conditions required for a group hold, these energy constrained homotopy equivalence classes of loop paths form a group, denoted by $\pi_1(F(A), K_0)$.

In summary, we have the necessary group properties:

1. Closure property: each pair of homotopy classes have a product defined for them that is also a homotopy class
2. There exists a unique unit element, $[K_0]$.
3. Each homotopy equivalence class $[p]$ has a unique inverse $[p]^{-1}$
4. The associativity condition holds, $([p_1][p_2])[p_3] = [p_1]([p_2][p_3])$.

This group $\pi_1(F(A), K_0)$ is of relevance to the reaction mechanism problem on $F(A)$, however, as it stands, it has some apparent shortcomings. We can show, though, that these shortcomings are of no significance, and, indeed, the group so derived describes the most essential algebraic structure of all reaction mechanisms on $E(K)$, subject to the energy bound A .

Specifically, for the given energy constraint expressed by the level set $F(A)$, this group $\pi_1(F(A), K_0)$ appears highly restricted in one aspect: group $\pi_1(F(A), K_0)$ refers to a specific point K_0 and the associated unit element $[K_0]$. However, it can be easily shown, that this group $\pi_1(F(A), K_0)$ is isomorphic with any other analogous group $\pi_1(F(A), K'_0)$ using a different reference point K'_0 and the associated unit element $[K'_0]$.

This can be demonstrated as follows. By considering any path $p_{00'}$ (u) connecting point K_0 to point K'_0 , every loop path $p(u)$ with origin at K_0 can be extended by the two paths, $p_{00'}$ (u) and $p_{00'}^{-1}$ (u) into a loop path q with the new origin K'_0

$$q = p_{00'}^{-1} p p_{00'}$$

For each choice of p , the two loops, p and q are clearly continuously deformable into one another within $F(A)$, in fact, the continuous deformation may occur within the very point set represented by the path $p_{00'}$ (u), hence p and q are necessarily members of the same homotopy equivalence class. That is, as abstract group, the group $\pi_1(F(A), K_0)$, formed by homotopy equivalence classes with unit element $[K_0]$ is isomorphic with the group $\pi_1(F(A), K'_0)$ of homotopy equivalence classes with unit element $[K'_0]$.

That is, there is only one such abstract group, and its algebraic structure is independent of the choice of the actual realization of the unit element $[K_0]$, hence, for this abstract group, the reference to any specific point K_0 can be omitted, and one may simply write $\pi_1(F(A))$.

In the terminology of algebraic topology, the lower index 1 in the notation $\pi_1(F(A))$ refers to dimension, and such a group is called the one-dimensional homotopy group of the given $F(A)$ set (since the objects related to one another by continuous deformations are one-dimensional paths, as opposed to deformations of two-dimensional sheets, or higher-dimensional objects).

Alternatively, such a group is called the Fundamental Group of the relevant set, in our case, $\pi_1(F(A))$ is the fundamental group of the $F(A)$ level set of the metric nuclear configuration space M , with respect to the actual potential energy surface $E(K)$. Since the elements of this group $\pi_1(F(A))$ are equivalence classes of loop reaction paths, which can be regarded as the relevant circular (loop) reaction mechanisms on $F(A)$, and since these circular reaction mechanisms contain, as parts, all non-circular reaction mechanisms as well, these groups have been named the Fundamental Groups of Reaction Mechanisms [3].

9.3 Generalizations of Transformations Between Molecules: The Universal Molecule Model

A chemical reaction can be regarded as a transformation between molecules: typically, a change of the nuclear coordinates serves as an indication of this transformation, and the nuclear configuration space and potential energy surface models with the associated reaction path and reaction mechanism approaches provide a useful description.

Of course, in the process of a chemical reaction other important changes, most importantly, changes of the bonding pattern and the associated changes in the shape of the electron density [4–7] also occur, where the latter changes are those which are most directly detected by other, neighboring molecules. Even local changes of molecular electron densities encode important information: based on the holographic electron density theorem [7], any small positive volume part of the ground-state molecular electron density cloud contains the complete information about the entire molecule.

If some common trends can be found in a family of molecules, then those trends can be exploited in a predictive manner for any additional molecules which may fit some aspects of this trend. In fact, such models involve some, often abstract “interpolations” and “extrapolations” among molecules, although in some instances, the actual variables along which these, often inexact transformations occur, are not necessarily clearly defined.

One model, the “Universal Molecule” model explicitly allows for such transformations: all parameters describing the molecules are considered as abstract, continuous variables, even those, which in the physical reality are restricted to be integers, such as the case for the nuclear charges [8–11]. Using nuclear charges as examples, a model where these integer values are replaced by continuous variables describes reality only in specific cases, when the variables become integers. However, just as

integration on the complex plane, using imaginary values, is advantageous in deriving new relations for problems involving only real numbers, this additional freedom of using continuous nuclear charges in the Universal Molecule models can also lead to new relations between real molecules.

As one of the simplest examples, a continuous nuclear charge variation between isoelectronic molecules N_2 and CO provides quantum chemically rigorous electronic energy inequalities, universally valid for every common bond length value [10]. Note that, far more complicated energy relations can also be derived by this approach [8–11].

9.4 The Extent of Identity-Preserving Deformations of Chemical Species

A somewhat simpler aspect of the Universal Molecule model is exploited if one considers a specific stoichiometry, that is, a given set of nuclei, as a single “super-entity”, and all the possible molecular species which can be obtained from this set of nuclei and a fixed number of electrons are regarded only as variants of the same Universal Molecule. In fact, this, somewhat simplified version of the Universal Molecule model is the closest to the potential energy surface model: if the electronic state is also restricted, then, in fact, all realizations of this Universal Molecule are actual species along the potential energy surface.

It is of some interest to link this model to more conventional models of chemical species. Traditionally, molecular deformations are often considered in the context of shape changes, for example, shape changes of the bonding pattern and the nuclear skeleton, or the shape changes of the actual electron density cloud [4]. Shape changes are often studied in terms of symmetry, or in terms of deformations relative to some symmetry [5–7], and the relations between local and global similarities among molecular species are relevant [7, 12]. One rather general model, as a part of the Universal Molecule approach [8–11] that has been applied, for example, for transformations between molecules by nuclear charge variations, as well as in combinatorial quantum chemistry approaches [8], also describes deformations which often go beyond those which preserve chemical identity.

For a given electronic state, associated with a specified potential energy surface $E(K)$, the simplest model to describe identity-preserving deformations is based on the concept of *catchment regions* [3]: all distorted conformations K from where an infinitely slow, vibrationless relaxation would lead to a common critical point on the potential energy surface, belong to the same catchment region. Note that catchment regions can have different dimensions: for a $(3N-6)$ -dimensional nuclear configuration space M , the catchment region of an energy minimum is also $(3N-6)$ -dimensional, yet the catchment regions of various saddle points have dimensions less than $(3N-6)$.

For catchment regions of energy minima, that is, for $(3N-6)$ -dimensional catchment regions of nuclear configuration space M with respect to a given potential energy surface $E(K)$, an intuitively attractive analogy can be drawn with actual watersheds taken as the set of all locations from where rain is collecting in a common sinkhole [3].

Critical points on a potential energy surface all have vanishing energy gradients, and are characterized by the second derivatives of the energy function $E(K)$ according to the local nuclear coordinates. The Hessian matrix of second energy derivatives provides curvature information, and the eigenvalues of the Hessian matrix are important clues concerning the importance of these critical points. For simplicity in the discussion, here we ignore the cases of degenerate critical points, where the Hessian matrix has one or more zero eigenvalues; these special cases are discussed in [3], and will not modify the essential conclusions in this section.

Index λ is the number of negative eigenvalues of the Hessian matrix at the given critical point, where $\lambda = 0$ corresponds to energy minima, whereas $\lambda = 1$ corresponds to saddle points of transition structures (often referred to as transition “states”). Other critical points of higher index, $\lambda > 1$, are usually avoided by minimum energy paths, that is, by the “most likely” ideal reaction paths (which are, of course, strictly speaking, unrealistic, even classically, showing no vibrational contributions).

This preference for critical points of indices 0 and 1 suggests a modification of the fundamental group approach for reaction mechanisms described in the previous section.

From the level set $F(A)$ of all parts of the given potential energy surface below energy bound A , one may consider to eliminate all points of most lower-dimensional catchments regions, except the points of those catchment regions which belong to energy minima and transition structures, that is, to identity-preserving distortions of energy minima, and identity-preserving distortions of transition structures of chemical reactions. In other words, one may decide to eliminate all those points K where the energy $E(K)$ does not fall below the energy bound A , and also all points which fall within a catchment region of index 2 or higher.

This λ —constrained level set, denoted by

$$F_{\lambda=0,1}(A),$$

can then replace the original level set $F(A)$ in the derivation of the conditions and properties of the fundamental group of reaction mechanisms, and a new, somewhat more distinguishing and more revealing algebraic structure is obtained. All formal steps of the development of the fundamental group of reaction mechanisms on $F(A)$ can be repeated for this new set $F_{\lambda=0,1}(A)$, and the resulting fundamental group,

$$\pi_1(F_{\lambda=0,1}(A))$$

provides more chemically relevant detail describing the most important part of potential energy surface $E(K)$.

For example, in most potential energy surfaces there are likely regions where the energy falls below some bound A , yet, in these regions there are some neighborhoods of critical points of index $\lambda > 1$, typically avoided by trajectories which take into account some classically-described dynamic features of molecular transformations. These neighborhoods contain points of M which are present in $F(A)$ but are eliminated from $F_{\lambda=0,1}(A)$, hence these “missing” points serve as barriers to some continuous deformations of formal reaction paths. Consequently, if this happens, then the homotopy equivalence classes of $F(A)$ and $F_{\lambda=0,1}(A)$ can be different, typically, the equivalence classes of $F_{\lambda=0,1}(A)$ are more numerous, hence the fundamental group of reaction mechanisms $\pi_1(F_{\lambda=0,1}(A))$ for the modified level set $F_{\lambda=0,1}(A)$ is richer, providing more chemically relevant detail than the fundamental group $\pi_1(F(A))$ of reaction mechanisms for the original level set $F(A)$ of energy bound A .

9.5 Summary

By combining some of the topological techniques used for the study of reaction mechanisms and the determination of the extent of chemical-identity-preserving deformations and shape changes of molecular species, the framework provided by the Universal Molecule model leads to a more detailed and more revealing variant of the fundamental group of reaction mechanisms, describing some essential features of the algebraic structure of all reactions on the potential surface $E(K)$ below some energy bound A .

Acknowledgement The original studies leading to the basic results reviewed, and the initial developments serving as the basis for the novel aspects of this study have been supported by the Canada Research Chair Program, the Canadian Foundation for Innovation, the Natural Sciences and Engineering Research Council of Canada, and the Albert Szent-Györgyi Award of Hungary.

References

1. Spanier EH (1966) Algebraic topology. McGraw-Hill, New York
2. Guillemin V, Pollack A (1974) Differential topology. Prentice Hall, Englewood Cliffs
3. Mezey PG (1987) Potential energy hypersurfaces. Elsevier, Amsterdam
4. Mezey PG (1993) Shape in chemistry: an introduction to molecular shape and topology. VCH Publishers, New York
5. Mezey PG (1990) A global approach to molecular symmetry: theorems on symmetry relations between ground and excited state configurations. *J Am Chem Soc* 112:3791–3802

6. Mezey PG (1992) On the allowed symmetries of all distorted forms of conformers, molecules, and transition structures. *Canad J Chem* 70:343–347
7. Mezey PG (1999) The holographic electron density theorem and quantum similarity measures. *Mol Phys* 96:169–178
8. Mezey PG (2009) Discrete skeletons of continua in the universal molecule model. In: Proceedings of the conference on computation in modern science and engineering: AIP (American Institute of Physics), vol 1504, pp 725–728
9. Mezey PG (2013) On Discrete to Continuum Transformations and the Universal Molecule Model—A Mathematical Chemistry Perspective of Molecular Families. In: Proceedings of the conference on Computation in Modern Science and Engineering: AIP (American Institute of Physics), vol 963/2, parts A and B, pp 513–516
10. Mezey PG (1981) Electronic energy inequalities for isoelectronic molecular systems. *Theor Chim Acta* 59:321–332
11. Mezey PG (2015) Compensation Effects in Molecular Interactions and the Quantum Chemical le Chatelier Principle. *J Phys Chem* 119:5305–5312 (volume dedicated to Prof. Tomasi J)
12. Mezey PG (2014) Fuzzy Electron Density Fragments in Macromolecular Quantum Chemistry, Combinatorial Quantum Chemistry, Functional Group Analysis, and Shape—Activity Relations. *Acc Chem Res* 47:2821–2827

Chapter 10

Quantum Chemical Topology Approach for Dissecting Chemical Structure and Reactivity

Juan Andrés, Lourdes Gracia, Patricio González-Navarrete and Vicent S. Safont

Abstract Chemical structure and bonding are key features and concepts in chemical systems which are used in deriving structure–property relationships, and hence in predicting physical and chemical properties of compounds. Even though the contemporary high standards in determination using theoretical methods and experimental techniques, questions of chemical bonds as well as their evolution along a reaction pathway are still highly controversial. We present a conceptionally approach to dissect chemical structure and reactivity (bond formation and breaking processes) in the nucleation and formation of Ag on AgVO_3 provoked in this crystal by the electron-beam irradiation, and glycolic acid decomposition using concepts from quantum chemical topology. The electronic activity that drives the structure and the molecular mechanism of the reaction was identified, fully characterized, and associated with specific chemical events, bond forming/breaking processes.

10.1 The Concept of Chemical Bond in Chemistry

The chemical structure and reactivity are deeply anchored in the mind of chemists, due to the physical and chemical properties of a molecule are related with its structure, i.e. by the arrangement of atoms and bonds. These bonds and the making and breaking bond processes determine chemical reactivity and the achievement of their mechanistic understanding depends on knowing the geometric structure and the nature of the bonds in the molecules. It is also (arguably) the most challenging problem within the discipline.

Structural elucidation both by experiments and quantum-chemical computations has seen tremendous progress in the last decades to rationalize the chemical and physical properties of molecules. Experimental techniques such as X-ray diffraction, electron diffraction, and nuclear magnetic resonance have been extensively

J. Andrés (✉) · L. Gracia · P. González-Navarrete · V.S. Safont
Departament de Química Física i Analítica, Universitat Jaume I,
Avda. Sos Baynat s/n, 12071 Castelló, Spain
e-mail: andres@qfa.uji.es

© Springer International Publishing Switzerland 2016
R. Chauvin et al. (eds.), *Applications of Topological Methods in Molecular Chemistry*, Challenges and Advances in Computational Chemistry and Physics 22, DOI 10.1007/978-3-319-29022-5_10

developed to attain this knowledge by obtaining three dimensional structures. These techniques, however, do not provide a direct view of the molecules in real space. To overcome this drawback, atomic force microscope and inelastic tunneling probe based on the scanning tunneling microscope are used to obtain real-space images of the molecular structures and chemical bonds of mostly planar molecules [1, 2], and adsorbed molecules [3, 4], respectively. Very recently, Bredtmann et al. [5] demonstrate how the chemically active valence electron densities can be directly accessed from the full scattering patterns in order to reach information of how a chemical reaction takes place and hence electronic bond-to-bond fluxes. The degenerate Cope rearrangement of semibullvalene is selected as a working example. In addition, Kössl et al. [6] have followed the progress of the alcoholysis reaction of phenylisocyanate with cyclohexanol and of 2,4-toluene-diisocyanate with chloralhydrate, by means of infrared absorption spectroscopy in combination with anharmonic frequency calculations using density functional theory. The measured infrared marker bands in the isocyanate NCO and alcohol OH stretching region have been employed to in situ characterization of these reactions and in particular for determination of Arrhenius activation energies. Bratos et al. [7], describe the X-ray filming of the I_2 re-association in CCl_4 , comparing the experimental data with standard reaction rate theories. These authors emphasized that the atomic motions must be followed even after the first “touch” of the reacting atoms must, and by studying the earliest stages of a reaction process, designated collectively by the generic term “elementary chemical act”, is definitely becoming possible. Very recently, an international team, involving experimental and theoretical researchers, has reported what it believes are the first direct measurements of transition states where separate atoms can form a bond. In this work, fired X-rays at molecules and atoms adsorbed onto a surface in a *vacuum* chamber are used, and from the energy of a select portion of the X-rays scattered back, it is possible to track how the electronic structure of each adsorbed atom changed as the reaction progressed. The authors studied carbon monoxide oxidation on ruthenium as a well known chemical reaction taking place in automobile catalytic converters [8]. In addition, another team have also directly observed the formation of chemical bonds using a femtosecond X-ray laser. The group used similar techniques to study the formation of a gold trimer complex ($[Au(CN)_2^-]_3$) from dissolving $Au(CN)_2^-$ in water. Both sets of researchers believe that analysing chemical bonds on such small timescales will provide scientists with a tool to study the dynamics of complex chemical and biological systems [9].

From the theoretical point of view, the emergence of molecular structure from the complete molecular Hamiltonian is a very complex topic and interesting papers on this subject have been published [10–16]. It is, with our present mathematical understanding of quantum mechanics, impossible to solve any system which is more complex than the hydrogen atom analytically in the sense of Schrödinger’s quantum theory. Slightly larger systems may be solved to numerical accuracy, but there is no hope to obtain the complete wave function for a chemically relevant molecule. The problem of solving the quantum mechanical description of a number

of interacting particles, known as the many-body problem [17, 18] has stimulated the development of a number of general approximation techniques.

As it was emphasized by Löwdin [19] “Quantum chemistry deals particularly with the electronic structure of atoms, molecules, and condensed matter, and describes it in terms of electronic wave patterns of standing waves. It deals also with collisions between atoms and molecules and with the study of chemical reactivity”. In quantum chemistry, the fundamental model of chemical bond is based on one-determinant electronic structure methods like Hartree-Fock or Kohn-Sham density functional theory (DFT). However, despite the contemporary high standards in determination of geometrical parameters, questions of chemical bond are still highly controversial. This problem can be traced back to the lack of a clear and unambiguous definition of a bond in quantum mechanics. Therefore, a chemical bond together with other essential concepts such as electron shells, lone pairs, aromaticity, atomic charges, (hyper-) conjugation, strain, etc. have been getting fuzzier over time, yet invaluablely useful concepts [20–23], which are of essential importance for practical chemistry leading to constructive ideas and developments when appropriately used and defined, have been developed. In the Faraday Discussions 135 [24], which took place in September 2006 in Manchester, a number of methods have been suggested (Chemical Concepts from Quantum Mechanics) without laying an end to the debate. Many concepts, including chemical bond, cannot be derived from theory reduction from the principles of quantum mechanics, because they were introduced heuristically as ordering criteria, as it was remarked by Primas [25].

What is a chemical bond? and how should we define chemical bond? are still a critical questions for chemical community, and remain as an active area of research [26–43]. For example, the controversy about the existence of a sextuple bond or not in Cr_2 , and more recently the existence or not of a quadruple bond in C_2 [44–46], as well as the nature of hydrogen bonding [47, 48]. In this sense, chemical bonds have even been compared to unicorns: mythical creatures of which everyone knows how they look, despite nobody ever having seen one [49]. Very recently, the different methods of defining and describing chemical bonds have been highlighted in a two-volume book dedicated to the chemical bond [50]. But it is important to remark, as noted by Frenking and Caramori [48]: “The physical nature of chemical bonding is quite complicated [51]. It is in most cases not necessary for a synthetic chemist to engage in elaborate quantum-chemical investigations. Standard calculations will usually provide sufficient information to classify a new compound and design new experiments”.

10.2 Electron Density

The electron density is related to the molecular Hamiltonian, and hence is the ultimate source of all properties in the ground- and excited states. In addition, descriptors and/or indexes derived from the electron density possess physical and

chemical meanings, and can be obtained both experimentally and by means of theoretical calculations, except for properties that require the full density matrix obtainable only from quantum mechanical calculations. Combined experimental and theoretical charge density studies rely on the analysis of electron density distributions obtained from quantum chemical calculations, $\rho_{\text{calc}}(\mathbf{r})$, and from experimental X-ray diffraction data, $\rho_{\text{exp}}(\mathbf{r})$ [52–55]. The comparison of the topological parameters of $\rho_{\text{calc}}(\mathbf{r})$ and $\rho_{\text{exp}}(\mathbf{r})$ provides important information for the interpretation of experimental results and allows to evaluate the accuracy of the experimental data. A direct comparison between both electron density distributions is biased because they are subjected to different sources of errors. The electron density $\rho_{\text{exp}}(\mathbf{r})$ is, for example, affected by systematic experimental errors and the model ambiguities introduced during the reconstruction of a static electron density distribution from the measured X-ray scattering factors.

Recently, Gavezzotti [56] has reviewed the physical principles of chemical bonding from the Feynman perspective. The answer of this question: What binds atoms together? was provided by Feynman [57]: “The force on a nucleus in an atomic system is shown to be just the classical electrostatic force that would be exerted on this nucleus by other nuclei and by the electrons’ charge distribution”. Being that the electron density is the observable common to both the experimental and theoretical approaches, it has become logical to focus on the observable itself, rather than on a model density, to confront and mutually validate them and their densities [58]. But the most important reason for studying the total density has been the increasing popularity of the so-called topological studies of bonding, that is, those made in terms of the study of the gradient vector field of a scalar function containing information on bonding [58]. Accurate X-ray diffraction experiments allow for a reconstruction of the electron density distribution of solids and molecules in a crystal.

The concept of molecular orbitals [59], the valence bond theory [60], related natural bond orbitals approach [61] and the valence shell electron pair repulsion concept [62] have provided quite reliable predictions of chemical structures, i.e. molecular geometries, while Woodward–Hoffmann rules [63], Fukui’s frontier molecular orbital theory [64], analysis based on valence bond theory [65] or Marcus theory [66] have been helpful for our current understanding of chemical reactivity. Advanced theories in science, as chemistry and/or physics, to be sustainable need to have a mathematical support to give basic concepts of the theory. Furthermore, the scalar fields based on electron density are experimentally amenable and thereby provide a clear-cut bridge between theory and experiment. Collar and Hall [67], and Bader [68] have provided the foundations of the topological analysis of one-electron charge densities. The path-breaking works due to Bader and co-workers have generated an active research area based on the study of the topology of molecular scalar fields. It is aimed at providing an understanding of molecular structure and reactivity [69]. Likewise, Nasertayoob and Shahbazian [70] have presented the mathematical foundations of the dynamical aspects of topological analysis of the electronic charge densities.

“Thomas [71] and Dirac [72] imagined that the kinetic and exchange energies of systems of many electrons could be *locally* modeled by their *uniform electron gas energy densities*”. The electron density is a scalar field that can be experimentally accessed [55] in principle and contains all necessary information for the ground state of the molecular system, according to the Hohenberg–Kohn [73, 74] theorems of DFT [75]. There is growing interest in explaining chemical phenomena arising from the structure of the charge density. One branch of this developing research field is the so-called conceptual DFT [76, 77], which has provided rigorous definitions for various chemical concepts such as electronegativity [78] and hardness, [79] as well as relating changes within the density to frontier orbital concepts through the Fukui function [80]. Calculations based on the seminal idea of Kohn [81] are now an integral component of almost all areas of chemistry, physics and materials sciences [82–84]. Although the exact functional form of the quantum mechanical part of the electron–electron interaction (also referred to as the exchange–correlation interaction) is not known, our ability to derive reasonable approximations to this functional has made DFT an enormously practical tool [85, 86].

10.3 Quantum Chemical Topology Analysis

In recent years, the topological analysis of the three-dimensional scalar fields [87–95], such as electron density [55, 67, 92, 95–97], the Laplacian of the electron density [68, 92], the electron localization function (ELF) [94, 98], and molecular electrostatic potential, have been widely used to discern chemical structure and reactivity. This procedure, named quantum chemical topology (QCT) [99] has been utilized for the study of chemical structure and reactivity [100–106]. Since its origins, the well-known approach of the “atoms in molecules” quantum theory (QTAIM), has evolved to be an invaluable tool for the chemical interpretation of quantum mechanical data, which relies on the properties of the electron density $\rho(\mathbf{r})$ when atoms interact. Excellent reviews on QTAIM methods have been published elsewhere [69, 96, 107–109].

QTAIM starts from a particular division of real space into atomic basins. Given the appropriate operator density, any quantum mechanical observable can be integrated within the atomic basins, giving rise to the partition of properties into additive atomic contributions. QTAIM represents molecular structure and bonding as consequence of the charge-density topology and geometry. However, it is important to note that there is some controversy on the applicability of QTAIM [110–120]. Basically, their criticisms are focused on the arbitrariness of the theory, the ambiguity of the topological construction and lack of predictive capabilities. For such reason, more complex topologies such as the topology of the electron localization function (ELF) have been used [98, 121–124]. ELF performs a topological

analysis of the same-spin pair probability density and thus generates basins of localized electron pairs [125–127]. The integration of the electron density over the ELF basin yields the basin population, that is, the amount of electron density in the chemical bond [128–130].

As Silvi et al. [131] stated: "... the ELF topological analysis provides a mathematical bridge between quantum mechanics and chemistry which relies on the one hand on the statistical interpretation and on the other hand on the theory of dynamical system. This approach shares the dynamical system theory as common mathematical method with the Atoms in Molecules theory, the difference being the nature of the potential function and therefore the nature of the investigated properties. The QTAIM theory is rightly claimed to be rooted in physics rather than in chemistry and its partition scheme aims accordingly to define open quantum systems within which the virial theorem holds."

10.4 The Bonding Evolution Theory

The analysis of the electronic structure at the stationary points concomitantly with the description of the possible reaction pathways associated with the chemical rearrangements are undoubtedly one of the most relevant applications of modern computational chemistry; nevertheless accurate geometries, energies, as well as other observables properties cannot always be guaranteed from quantum chemical calculations. Likewise, there is no physical observable corresponding to the chemical bond and their rearrangement along a given chemical reaction (which corresponds to the essence of the chemical reactivity). Such concepts cannot be unambiguously defined in pure quantum theory, and therefore, qualitative concepts are of essential importance for practical chemistry.

In spite of Hohenberg–Kohn theorem guarantees that all the molecular information is encoded in the electron density, the physical description of chemical systems requires additional postulates for extracting observable information in terms of atomic contributions. This is achieved by the QTAIM introduced by Bader, providing a quantum topological partitioning of the molecular space into chemically transferable molecular fragments for which the energy and all other measurable properties can be precisely defined [132]. The introduction of concepts such as bond path in the framework of QTAIM allows the description of the evolution of the electronic structure along a reaction pathway, and hence, to understand a given chemical rearrangement following the redistribution of the electron density along the reaction pathway connecting the stationary points. Thus, Bader and co-workers pioneered the study of the evolution of the electron density in chemical reactions considering the structural changes in this scalar field according to the Thom's catastrophes theory (CT) [97, 133, 134].

However, the applicability of the Thom's CT in the framework of the QTAIM has been found to be limited to intramolecular chemical processes since no topological changes are found in the electron density when two atoms separate. Subsequently Silvi and Krokidis [135], as a generalization of Bader's work, have developed the joint use of electronic localization function ELF and Thom's CT. In this context, the mechanism of a given chemical reactions can be rationalized in terms of chemical events, namely: bond forming or breaking processes, creation and annihilation of electron pairs. This analysis allows us to understand the electronic structure and related properties of the reactants as the reaction takes place, providing a nice guide to elucidate the mechanism of chemical reactions and further understanding of the chemical reactivity. This methodology proposed is known as bonding evolution theory (BET). Changes in the control parameters defining the reaction pathway (such as the nuclear coordinates and the electronic state) can lead to different topologies of the ELF. Therefore, according to the theory of dynamical systems, a system can be considered structurally stable if a small perturbation is only possible for values of the control parameters comprised into well-defined ranges, namely structural stability domains (SSDs), where all the critical points are hyperbolic and separated by catastrophic points in which at least one critical point is non-hyperbolic. Therefore, according to the BET, the reaction pathway of a given chemical system goes from a given ELF-SSD to another by means of bifurcation catastrophes occurring at the turning points. The bifurcation catastrophes occurring at these turning points are identified according to Thom's classification [133, 134]. In this way, a chemical reaction can be understood as a sequence of chemical events (ELF-SSDs) and separated by bifurcation points. Only three types of bifurcation catastrophes have been found in chemical reactivity: (i) the fold catastrophe, corresponding to the creation or annihilation of two critical points of different parity; (ii) the cusp catastrophe, which transforms one critical point into three (and viceversa) such as in the formation or the breaking of a covalent bond; (iii) the elliptic umbilic, in which the index of a critical point changes by two. The identification of the turning points connecting the ELF-SSDs along the reaction pathway allows a rigorous characterization of the sequence of electron pair rearrangements taking place during a chemical transformation, such as multiple bond forming/breaking processes, creation/annihilation of lone pairs, transformations of double bonds into single ones or vice versa, and other electronic rearrangements. Details of the Thom's classification in chemical reactions have been described in detail elsewhere [103]. A plethora of chemical rearrangements have been studied by BET: cycloadditions [103, 136–139], cyclization [140–142], S_N2 reaction [143], Nazarov reaction [144], Cope reaction [145], Cope rearrangement of semibullvalene [146], the reaction of uranium ions with N_2O in the gas phase [147], the reaction of Mn^+ with small molecules [148], or inorganic reactions involving Mo complexes [149, 150]. Also, some reviews on the applicability of BET to understand and rationalize chemical reactivity have been published [138, 151–153], including the study of the bonding changes along solid-solid phase transitions [154].

10.5 Examples

We have selected two examples: (i) QTAIM study on the AgVO_3 , for the simulation of Ag nucleation and formation on AgVO_3 provoked in this crystal by the electron-beam irradiation. (ii) An ELF and Thom's catastrophe theory (BET) study for different reaction pathways associated with the decomposition of glycolic acid decomposition.

10.5.1 AgVO_3

Silver vanadium oxide nanomaterials such as AgVO_3 , have attracted extensive attention owing to their potential applications in rechargeable high-energy density lithium batteries [155] and sensors [156]. AgVO_3 has scarcely been studied in morphologies, but two phases $\alpha\text{-AgVO}_3$ and $\beta\text{-AgVO}_3$ are known. Both structures are monoclinic and $\alpha\text{-AgVO}_3$ is irreversibly transformed into $\beta\text{-AgVO}_3$ at around 200 °C [157]. $\beta\text{-AgVO}_3$ demonstrates a narrowband gap fit for visible light, showing a high potential as an effective photocatalyst. However, the photocatalytic activity of $\beta\text{-AgVO}_3$ is still insignificant because of its low capability to separate electro-hole pairs, which significantly limits its practical extensive application. Thus, further study is necessary to enhance its photo-catalytic performance for the practical application. Recently, experimental and theoretical studies have reported that surface modification such as Ag nanoparticles (with excellent conductivity and strong electron trapping ability) on surfaces could enhance the separation rate of photogenerated holes and electrons [158–160].

This investigation's motivation essentially arises from a discovery of an unwanted real-time in situ nucleation and growth of Ag filaments on $\alpha\text{-Ag}_2\text{WO}_4$, Ag_3PO_4 , and Ag_2MoO_4 crystals which was driven by an accelerated electron beam from an electronic microscope under high vacuum [161–165].

First-principles total-energy calculations were carried out within the periodic DFT framework using the VASP program [166]. In the calculations, electrons were introduced one by one up to four in the monoclinic unit cells of $\alpha\text{-AgVO}_3$ and $\beta\text{-AgVO}_3$ and the distribution of these extra electrons takes place by means of a simultaneously geometry optimization on both the lattice parameters and the atomic positions. The Kohn-Sham equations have been solved by means of the Perdew, Burke, and Ernzerhof exchange-correlation functional, and the electron-ion interaction described by the projector-augmented-wave pseudopotentials [167, 168]. The plane-wave expansion was truncated at a cut-off energy of 520 eV and the Brillouin zones have been sampled through Monkhorst-Pack special k -points grids that assure geometrical and energetic convergence for the AgVO_3 structures considered in this work.

A graphical representation of $\alpha\text{-AgVO}_3$ and $\beta\text{-AgVO}_3$ structures using polyhedra is presented in Fig. 10.1a, b, respectively. The number of oxygen atoms coordinating to a vanadium atom in $\alpha\text{-AgVO}_3$ is four while that of $\beta\text{-AgVO}_3$ is five.

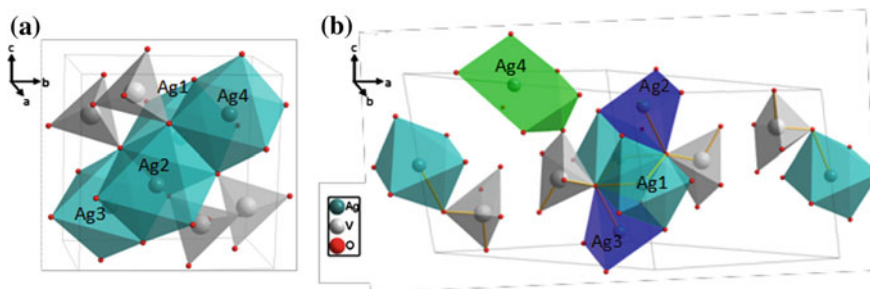


Fig. 10.1 Bulk structure of **a** α - AgVO_3 and **b** β - AgVO_3 , in terms of its constituent polyhedra

Moreover, only one type of V site is present in the α - AgVO_3 , forming an almost regular tetrahedron with O atoms. This is in contrast to the four types of distorted octahedral coordinated ones for the β - AgVO_3 . The smaller the coordination number of polyhedral of vanadates, the larger the interaction between a vanadium and oxygen atoms, and the average bond length between V and O in four coordination is shorter than that in five coordination. It also results in an increase in the energy gap between the HOMO and LUMO consisting of O 2p and V 3d orbitals, respectively, and the band gap of α - AgVO_3 is larger than that of β - AgVO_3 in spite of the same composition [169]. There are two types of Ag sites in the α - AgVO_3 , coordinated by distorted octahedra of O atoms, which are expanded to the c -direction by sharing the edges. The zigzag chains of $[\text{VO}_4]$ tetrahedra which are sandwiched between the sheets of octahedra form the smaller atomic packing compared with the octahedra as found in many vanadate bronzes, especially with the β - AgVO_3 in which 5-, 6- and 7-coordinated polyhedra formed by O atoms are occupied by four types of Ag atoms. The computed unit-cell parameters of α - AgVO_3 structure, space group $C2/c$, are $a = 10.619 \text{ \AA}$, $b = 10.070 \text{ \AA}$, $c = 5.574 \text{ \AA}$, and $\beta = 100.41^\circ$. β - AgVO_3 belongs to the Cm space group, with $a = 18.677 \text{ \AA}$, $b = 3.692 \text{ \AA}$, $c = 8.148 \text{ \AA}$, and $\beta = 105.04^\circ$. Geometrical data for both structures are in agreement with previous reported studies [170].

In Table 10.1, the values of the bond distances of Ag–O and V–O in $[\text{AgO}_6]$ and $[\text{VO}_4]$ clusters for α - AgVO_3 are shown as a function of electrons added. An

Table 10.1 Values of Ag–O and V–O, in Å , in the two types of $[\text{AgO}_6]$ and $[\text{VO}_4]$ clusters for α - AgVO_3 as a function of electrons added (N)

N	$[\text{AgO}_6]_1$			$[\text{AgO}_6]_2$			$[\text{VO}_4]$	
	(2)	(2)	(2)	(2)	(2)	(2)	(2)	(2)
0	2.422	2.478	2.528	2.430	2.461	2.674	1.668	1.820
1	2.210	2.740	3.042	2.233	2.554	–	1.694	1.807
2	2.429	–	–	2.506	2.596	–	1.660	1.815
3	2.298	–	–	2.406	–	–	1.673	1.818
4	2.333	–	–	2.548	–	–	1.666	1.829

The multiplicity of the bond is placed in parenthesis

analysis and a comparison of the geometries for a neutral ($N = 0$) and charged ($N = 4$) structures show a pronounced increase in the corresponding Ag–O distances with the addition of electrons. There are two types of $[\text{AgO}_6]$, $[\text{AgO}_6]_1$ centered by Ag1/Ag2 and $[\text{AgO}_6]_2$ centered by Ag3/Ag4 (see Fig. 10.1a). $[\text{AgO}_6]_1$ cluster when $N = 0$ pass to $[\text{AgO}_4]$ for $N = 1$, while $[\text{AgO}_6]_2$ appears as an octahedron more distorted with three different Ag–O distances. For $N = 2$, each Ag is surrounded by four O atoms at the same time that the Ag1–Ag3 and Ag2–Ag4 contact distance is noticeably shortened. For $N = 3$ and $N = 4$ each Ag is surrounded only by two O atoms. Ag1–Ag3 and Ag2–Ag4 distances are shortened to 2.65 Å. For the $[\text{VO}_4]$ clusters we find that the V–O distances remain almost unaltered.

In Table 10.2, the values of the bond distances of Ag–O in $[\text{AgO}_x]$ clusters for $x = 5, 6$ and 7 for $\beta\text{-AgVO}_3$, are presented as a function of the number of electrons added. There are two types of $[\text{AgO}_5]$, centered by Ag2 and Ag3 (see Fig. 10.1b) but are very similar, so in Table 10.2 the averaged distances for both are provided. For $N = 2$ and $N = 3$, the two types of $[\text{AgO}_5]$ are disappeared and both Ag atoms are surrounded by three and two O atoms, respectively. This fact can be explained due to an approaching of Ag2 and Ag3 centers of adjacent cells at distances of 2.645 and 2.713 Å for $N = 2$ and $N = 3$, respectively. However, for $N = 4$ one type of $[\text{AgO}_5]$ formed by Ag2 is maintained, while Ag3 is only coordinated to two O atoms at 2.494 Å. Ag1 and Ag4 forms the $[\text{AgO}_6]$ and $[\text{AgO}_7]$ clusters, respectively. Ag–O distances corresponding to $[\text{AgO}_6]$ cluster show a pronounced increase in passing from $N = 0$ to $N = 2$. However, for $N = 3$ and $N = 4$, Ag1 is only bonded to two O atoms at the same time that the Ag1–Ag3 distance of adjacent cells is noticeably shortened to 2.741 and 2.745 Å, respectively. Finally, Ag4 forms a $[\text{AgO}_7]$ cluster only for $N = 0$; when electrons are added, there is a notable increase of the unit cell distortion as well as of the constitutive polyhedra and Ag4 is coordinated to 3, 4, 5 and 5 O atoms for $N = 1, 2, 3$ and 4 , respectively. For the four types of $[\text{VO}_4]$ clusters, we find that the five V–O distances remain almost unaltered.

The electronic charge of each atom is evaluated using Bader charge analysis within the QTAIM framework, which is a way of dividing molecules or solids into atoms on the basis of electronic charge density. Finding zero flux surfaces between two atoms allows the atomic charge to be calculated, using integrations of the charge density within the atomic basins, Ω , and subtracting the nuclear charge, Z , of the corresponding atom.

Table 10.2 Values of Ag–O, in Å, in the three types of $[\text{AgO}_x]$ clusters for $x = 5, 6$ and 7 for $\beta\text{-AgVO}_3$, in Å, as a function of the number of electrons added (N)

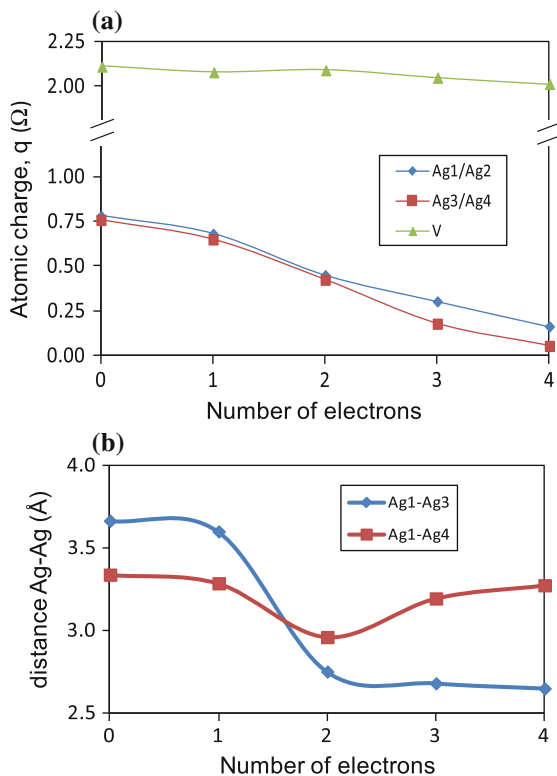
N	$[\text{AgO}_5]$			$[\text{AgO}_6]$			$[\text{AgO}_7]$			
	(2)	(2)	(1)	(2)	(2)	(2)	(2)	(2)	(2)	(1)
0	2.375	2.404	2.500	2.418	2.420	2.457	2.254	2.360	2.587	2.974
1	2.385	2.465	2.517	2.392	2.397	2.498	2.207(1)	–	2.341	–
2	2.345	–	2.775	2.245	2.629	2.795	2.305	2.366(1)	–	2.389
3	2.340	–	–	2.363	–	–	2.320	2.460	2.69(1)	3.152
4	2.243	2.460	2.931	2.408	–	–	2.316	2.590	2.72(1)	3.198

The multiplicity of the bond is placed in parenthesis

$$q(\Omega) = Z_{\Omega} - N(\Omega) \quad \text{with } N(\Omega) = \int_{\Omega} \rho(\Omega) dr \quad (10.1)$$

In Fig. 10.2a, the charge density of the Ag and V centers of the $[\text{AgO}_6]_1$, $[\text{AgO}_6]_2$, and $[\text{VO}_4]$ clusters is depicted as a function of the number of electrons added to $\alpha\text{-AgVO}_3$. The average bond distances of Ag–Ag as a function of the number of electrons added are presented in Fig. 10.2b. An analysis of the results presented in Fig. 10.2 shows that the Ag atoms of the $[\text{AgO}_6]$ clusters are more prone to be reduced than V atoms (that form $[\text{VO}_4]$ clusters), since the Ag coordination changes to 4 at $N = 2$ and to 2 at $N = 3$ and 4. Above $N = 2$, charge density differences between $[\text{AgO}_6]_1$ and $[\text{AgO}_6]_2$ start to be sensed, being Ag3/Ag4 more prone to be reduced than Ag1/Ag2 (by 0.12 units). This result is related to the major Ag–O distance obtained for the completely reduced Ag3/Ag4 (2.548 Å) compared to the Ag1/Ag2 (2.333 Å) for $N = 4$ (see Table 10.1). In addition, Ag1–Ag3

Fig. 10.2 **a** Charge density of the Ag and V centers in $[\text{AgO}_6]_1$, $[\text{AgO}_6]_2$, and $[\text{VO}_4]$ clusters, **b** average Ag–Ag distances, as a function of the number of electrons added for $\alpha\text{-AgVO}_3$



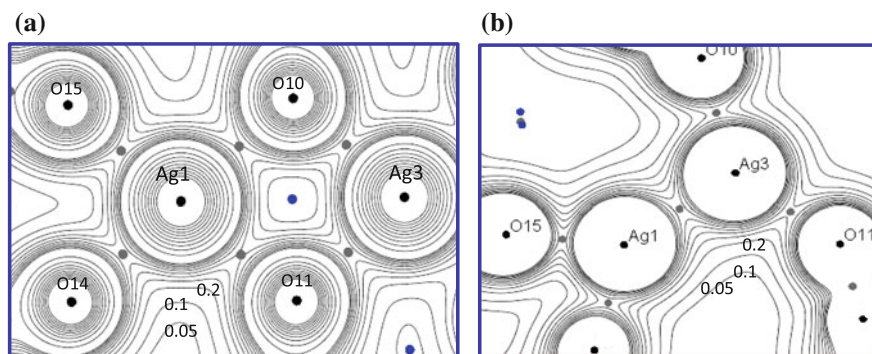


Fig. 10.3 Electron density contours for **a** neutral ($N = 0$) and **b** charged ($N = 4$) α - AgVO_3 structure, on a plane containing the two types of Ag atoms

distances are reduced from 3.66 to 2.65 Å, while Ag2–Ag3 distances are practically maintained its initial value.

Figure 10.3a, b show 2D charge density maps associated to the interaction of $[\text{AgO}_6]_1$ – $[\text{AgO}_6]_2$ clusters, considering a neutral state ($N = 0$) and addition of four electrons ($N = 4$), respectively. The zones with high and low charge densities are specified by the concentration of charge lines around the atoms. A comparison of the two pictures reveal that the electron density distribution is enhanced between Ag1 and Ag3 for $N = 4$, at the same time that the Ag1–Ag3 contact distance is shortened, since the two Ag atoms are twofold-coordinated. On the other hand, Fig. 10.3a shows the equatorial plane of octahedral $[\text{AgO}_6]$ clusters.

The calculations of the charge density, ρ_{bcp} , at the (3,–1) bond critical points (BCP) as well as its Laplacian, $\nabla^2\rho_{\text{bcp}}$, in Ag–O bonds for $[\text{AgO}_6]$ units are presented in Table 10.3. The effect of adding electrons to the material produces striking differences in the values of the Laplacian and charge density at the (3,–1) BCP. Thus, it is worth noting that the Ag–O bonds considerably reduce their Laplacian and charge density values as the number of electrons are added increase, indicating that these bonds become less strong in favor of the formation of metallic Ag.

In Fig. 10.4, the charge density of the Ag centers of the $[\text{AgO}_x]$ clusters for $x = 5, 6$ and 7, as a function of the number of electrons added is depicted for β - AgVO_3 . The zones with high and low charge densities are specified by the

Table 10.3 Laplacian and charge density at the (3,–1) BCPs in Ag–O bonds for $[\text{AgO}_6]$ clusters as a function of the number of electrons added, N

N	BCP $[\text{AgO}_6]$	
	Ag–O	
	ρ_{bcp}	$\nabla^2\rho_{\text{bcp}}$
0	0.54	6.98
2	0.46	5.68
4	0.42	5.32

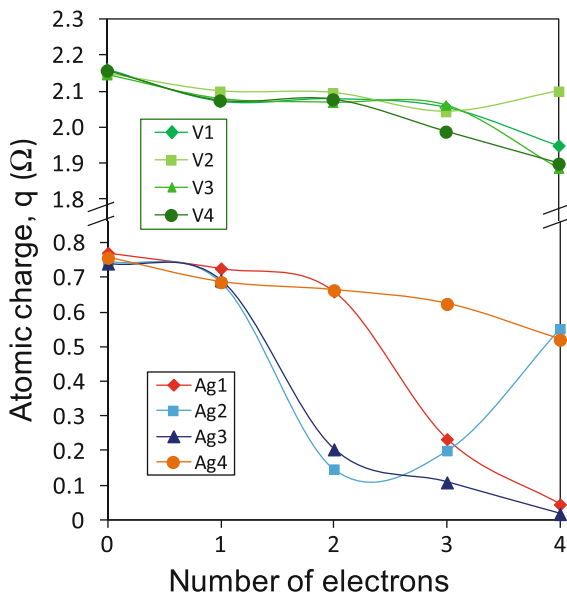


Fig. 10.4 Charge density of the Ag centers of the $[\text{AgO}_x]$ clusters for $x = 5, 6$ and 7 , as a function of the number of electrons added for $\beta\text{-AgVO}_3$. $q(\Omega)$ represents the number of valence

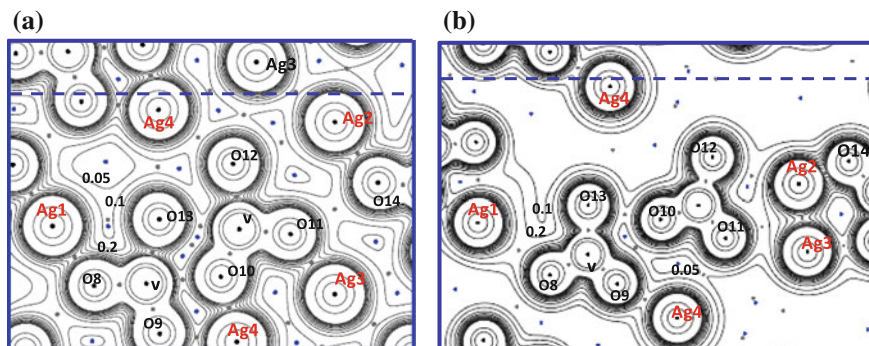


Fig. 10.5 Electron density contours for **a** neutral ($N = 0$) and **b** charged ($N = 4$) $\beta\text{-AgVO}_3$ structure, on a plane containing the four types of Ag atoms

concentration of charge lines around the atoms. Figure 10.5a, b show 2D charge density maps for neutral $\beta\text{-AgVO}_3$ structure and for ($N = 4$), respectively.

An analysis of Fig. 10.4 shows that the charge density of the Ag_2 and Ag_3 centers that initially forms $[\text{AgO}_5]$ clusters are very similar till $N = 2$, in which they are threefold-coordinated. As more electrons are added, Ag_3 is more prone to be reduced than Ag_2 . This fact is related to Ag-O , since Ag_3 is coordinated to two O

atoms while Ag2 recover the five coordination at $N = 4$. Simultaneously, in passing from $N = 0$ to $N = 4$ Ag2–Ag3 distance decreases from 5.725 to 4.853 Å. In addition, a comparison of the two pictures of Fig. 10.5 reveals that the electron density distribution is enhanced between Ag2 and Ag3 for $N = 4$.

Ag1 center, that forms the $[\text{AgO}_6]$ clusters, shows a pronounced charge density decrease up to $N = 2$, according to the change of the coordination number from 6 to 2. Therefore, Fig. 10.4 reveals that the extra electron density added to the material is transferred from one cluster to another through the lattice network, in particular between Ag1 and Ag3 arrangements, which behave similarly. At $N = 4$ both are practically reduced and are coordinated only to two O atoms, being Ag1–Ag3 distance of adjacent cells is reduced to 2.745 Å.

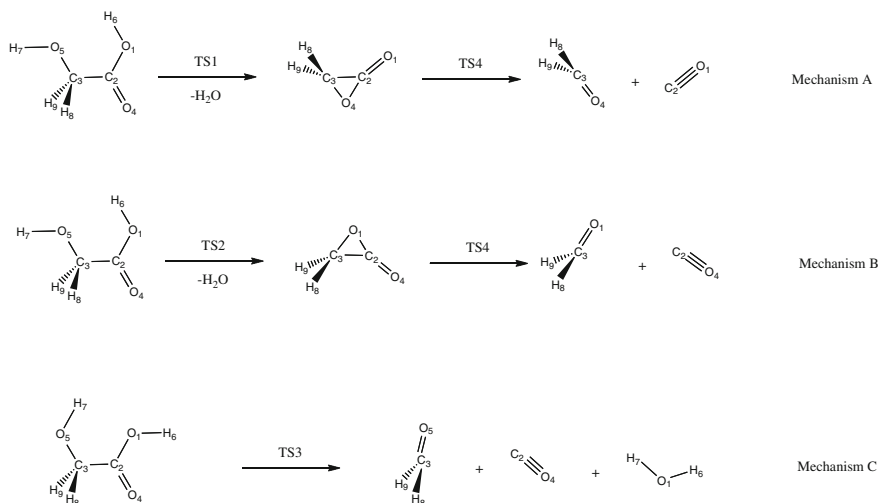
Finally it is worth noting that the charge density for the Ag4, that forms $[\text{AgO}_7]$ cluster, as well as for V atoms remains almost unaltered.

10.5.2 Glycolic acid decomposition

The gas phase decompositions of several carboxylic acids and related compounds have been theoretically characterized by us in the past [171–176], reproducing the experimentally observed kinetics of such processes. In particular, the decomposition of glycolic acid takes place through a homogeneous, unimolecular reaction following a first order rate law. We demonstrated [177] that three competitive reaction mechanisms could exist, being a two-step process the more favorable reaction pathway. For this pathway, the first step was associated with the water elimination, thus giving rise to the formation of an α -lactone intermediate by means of the nucleophilic attack of the carbonyl oxygen atom. The second step was the ring opening to obtain carbon monoxide and formaldehyde (mechanism A). A second two-step mechanism was found to be also possible, with a first step also describing the water elimination with formation of the α -lactone intermediate, but in this case by means of the nucleophilic attack of the hydroxylic oxygen atom of the carboxyl group (mechanism B, which shares the second step with mechanism A). Finally, a third pathway was also described, consisting on a one-step process in which the decomposition of the glycolic acid would take place in a concerted fashion to form carbon monoxide, water and formaldehyde in a unique step (mechanism C). The three proposed mechanisms are sketched in Scheme 10.1 along with the atom numbering used.

In the present work, we revisited that study by using a topological approach, as an example of the usefulness of this methodology to describe chemical reactions, and in particular to characterize in detail the chemical events that make possible the glycolic acid decomposition. The study has been done by using the Gaussian 09 program [178] at the MP2/6-31++G** theoretical level, that has previously proven to be adequate to reproduce the experimental values of the rate constants [177].

To gain a deeper insight in the description of the decomposition process we have used the TopMod package [87] to obtain the ELF function values. We have used a



Scheme 10.1 The three mechanisms studied and the atom numbering used

cubical grid of step size smaller than 0.1 bohr. In this framework, the reaction mechanism can be rationalized in terms of chemical events (bond forming or breaking processes, creation and annihilation of electron pairs) that drive the chemical rearrangement. This analysis allows us to understand the electronic structure and related properties of the reactants as the reaction takes place, providing a further understanding of the chemical reactivity. Starting from the TS, the reaction path has been traced following the intrinsic reaction coordinate (IRC) [179, 180] using a Rx in mass-weighted step of $0.1 \text{ amu}^{1/2} \text{ bohr}$ until reaching the minimum or until a maximum of 100 steps have been done.

10.5.2.1 Mechanism A, First Step

As explained above, the mechanism A is a stepwise process, whose first step accounts for the water elimination from glycolic acid to form the α -lactone intermediate. The energy profile along the IRC path down from TS1 to the glycolic acid in one side, and to the α -lactone intermediate in the other side, is reported in Fig. 10.6, together with the structural stability domains (SSD) found.

For the process leading from glycolic acid to the α -lactone intermediate through TS1, seven SSDs have been characterized, and they are indicated in Fig. 10.6.

The series of SSDs found can be viewed as a sequence of chemical events depicted in Scheme 10.2, which has been represented according to the perspective of the ELF analysis. In Scheme 10.2 the full lines and the points represent disynaptic and monosynaptic basins, respectively, and the hydrogenated basins have been represented with ellipses.

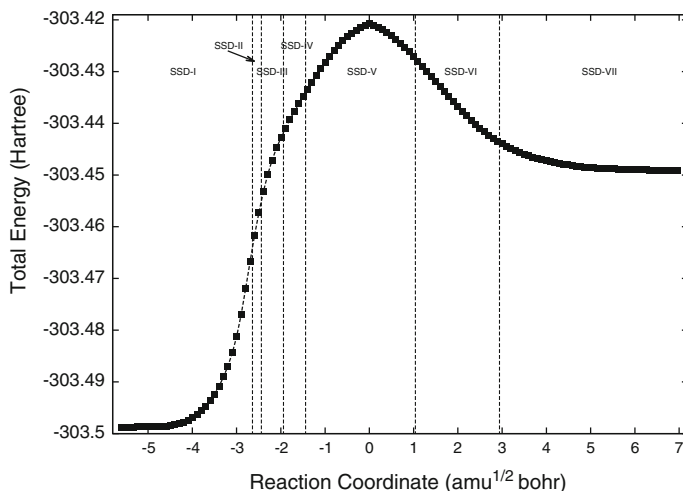
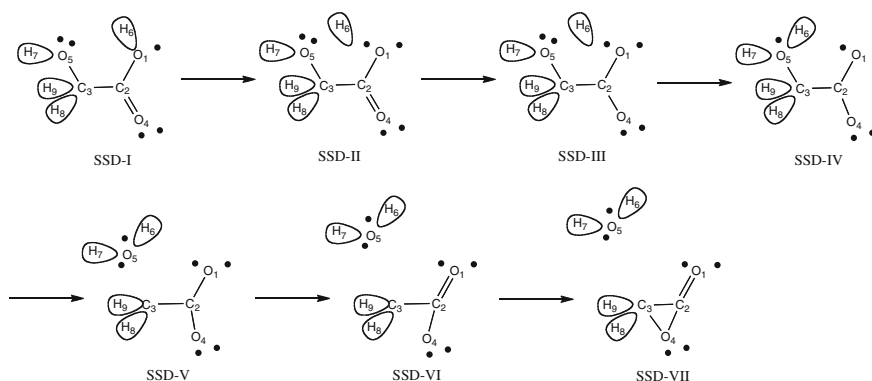


Fig. 10.6 Energy profile for the water elimination from glycolic acid (*left side*) to obtain the α -lactone intermediate through TS1, calculated by means of the IRC method. The SSDs found are indicated



Scheme 10.2 Representation of the first step of the glycolic acid decomposition through the mechanism A, depicted from the ELF viewpoint

At the glycolic acid, the first point of the SSD-I, nineteen basins can be found, corresponding to the five core basins, five disynaptic basins (accounting for the C–C bond, the two C–O bonds and two basins for the C=O double bond), four hydrogenated basins, and five monosynaptic basins associated with the oxygen atoms lone pairs. In particular, we have found two monosynaptic basins corresponding to the O4 atom, also two monosynaptic basins for the O5 oxygen atom, and only one monosynaptic basin corresponding to the O1 atom.

The first topological change connecting SSD-I and SSD-II is associated with a cusp-type catastrophe. The disynaptic basin $V(O1, H6)$ splits in two monosynaptic

basins, $V_2(O1)$ and $V(H6)$. The creation of the monosynaptic basin $V(H6)$ involves an intermediate structure in which the hydrogen is detached, and transfers electron density (dressed proton) toward one of the lone pairs of O5. It is worth noting that the presence of the $V(H6)$ is observed in both SSD-II and SSD-III. Later, the passage from SSD-II to SSD-III reveals another cusp-type catastrophe. The disynaptic basins $V_{1,2}(C2,O4)$ associated with the double bond $C2=O4$ are transformed into single disynaptic basin $V(C2,O4)$. Subsequently, when the system reaches the SSD-IV, the monosynaptic basins $V(H6)$ and $V_1(O5)$ are replaced by a single disynaptic basin $V(O5,H6)$ (cusp-type of catastrophe). The latter topological change allows thus the formation of a water molecule which is coordinated to C3. Next, the turning point between SSD-IV and SSD-V is associated with a fold-type catastrophe. Herein, the disynaptic basin $V(C3,O5)$ becomes monosynaptic $V(O5)$. Thus, the water molecule coordinated to C3 and formed by O5, H6 and H7 departs from the rest of the system. It is important to remark that according to the ELF topological point of view when the system reaches the TS1, no breaking/forming processes are observed. After TS1, when the system reaches the SSD-VI, the disynaptic basin $V(C2,O1)$ is replaced by a pair of disynaptic basins $V_{1,2}(C2,O1)$. From a chemical point of view, this cusp-type of catastrophe may be interpreted as a change of topological signature of the single bond $C2-O1$ to double bond $C2=O1$. Finally, when SSD-VII is reached, the ELF scalar field undergoes a fold-type catastrophe and the creation of the disynaptic basin $V(C3,O4)$ is observed giving rise to the formation of the lactone intermediate.

Snapshots of the ELF basins for some selected points along the IRC, representing the different SSDs found, are depicted in Fig. 10.7.

The snapshots (a), (b), (c) and (d) of Fig. 10.2 clearly describe the proton transfer from O1 to O5. The snapshots (d) and (e) show the changes taking place between C3 and O5: at SSD-IV there is a disynaptic $V(C3,O5)$ basin (see the green basin between these two atoms in Fig. 10.2d) while when the turning point between SSD-IV and SSD-V is reached the disynaptic basin $V(C3,O5)$ becomes monosynaptic $V(O5)$ (see the red basin in Fig. 10.2e). Subsequently, the water molecule release precedes the final cyclization of the intermediate while the last chemical event accounts for the lactone closure. In Fig. 10.7g the small bonding basin $V(C3,O4)$ between C3 and O4 is observed.

To complete the topological description of the process, an analysis of the population evolution of the basins directly related with the changes taking place can be done. These data are reported in Fig. 10.8.

As can be seen in Fig. 10.8, by the end of SSD-I the population of the disynaptic basin $V(O1,H6)$ diminishes concomitantly with an increase in the population of the disynaptic basin $V(C2,O1)$. Therefore, the departure of the H6 from O1 initially makes the population of the basin corresponding to the $C2-O1$ bond increase. However, when the basin $V(O1,H6)$ disappears at the turning point between SSD-I and SSD-II, its population is not assumed by the disynaptic basin $V(C2,O1)$, but principally by a new monosynaptic basin $V(O1)$. In Fig. 10.8 we have represented the population of the monosynaptic basins on O1 as a whole, and therefore a sudden increase in the $V(O1)$ populations is noticed when the new

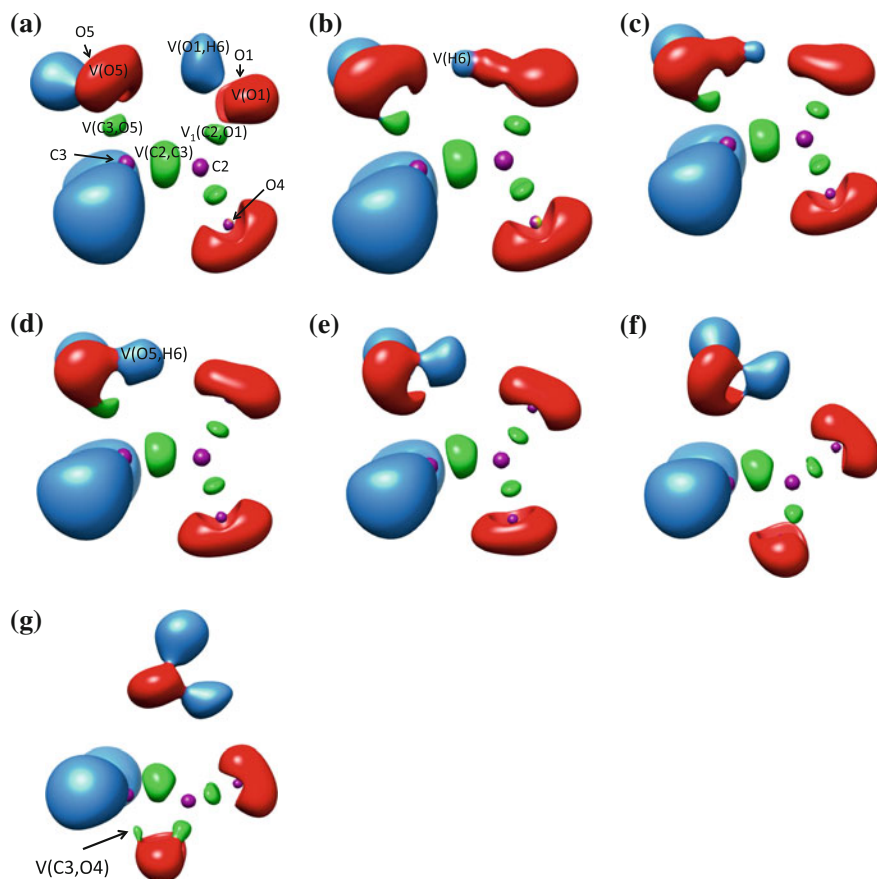


Fig. 10.7 Snapshots of the ELF localization domains ($\eta = 0.829$ isosurface) for selected points along the IRC from TS1: **a** glycolic acid, belonging to SSD-I, with indication of some atoms positions **b** point at $s \approx -2.596 \text{ amu}^{1/2} \text{ bohr}$ belonging to SSD-II, **c** point at $s \approx -2.196 \text{ amu}^{1/2} \text{ bohr}$ belonging to SSD-III, **d** point at $s \approx -1.696 \text{ amu}^{1/2} \text{ bohr}$ belonging to SSD-IV, **e** TS belonging to SSD-V, **f** point at $s \approx +1.997 \text{ amu}^{1/2} \text{ bohr}$ belonging to SSD-VI, **g** last point of the IRC, corresponding to the α -lactone species plus water, belonging to SSD-VII. The color code is as follow: *purple*, core basins; *red*, monosynaptic basins; *green*, disynaptic basins; *blue*, hydrogenated basins. Some basins are labeled throughout the figure

monosynaptic basin appears on O1. Along SSD-II and also SSD-III the monosynaptic basin $V(\text{H6})$ briefly appears, as explained, and as can be seen in Fig. 10.8 its population is scarce. On the other hand, the two bonding basins $V_{1,2}(\text{C2},\text{O4})$ accounting for the double bond character of the $\text{C2}-\text{O4}$ bond, merge in a unique disynaptic basin $V(\text{C2},\text{O4})$ in the turning point between SSD-II and SSD-III. Therefore its population suddenly increases at this point, and from this point on its population decreases along the reaction coordinate.

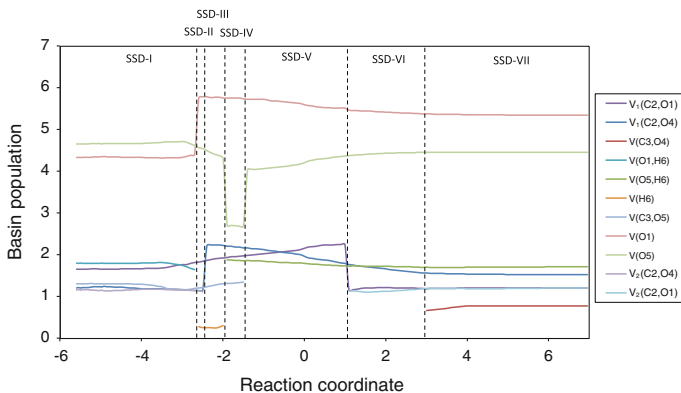


Fig. 10.8 Population evolution of some selected basins along the IRC path from TS1. *Dashed lines* separate the structural stability domains found, which are indicated. $V(O1)$ and $V(O5)$ account for the total population of the monosynaptic basins on the O1 and O5 atoms, respectively

As explained above, the cusp-type catastrophe between SSD-III and SSD-IV accounts for the $V(H6)$ and $V_1(O5)$ monosynaptic basins being replaced by a single disynaptic basin $V(O5,H6)$, while the turning point between SSD-IV and SSD-V accounts for the change in the synaptic order of the disynaptic $V(C3,O5)$ basin to a new monosynaptic $V_3(O5)$ basin. Hence, the whole population of the monosynaptic basins on O5, represented as $V(O5)$ in Fig. 10.8, decreases in the SSD-III to SSD-IV passage and increases back in the SSD-IV to SSD-V turning point.

The topological change between SSD-V and SSD-VI corresponds to the splitting of the $V(C2,O1)$ basin, whose population was increasing from the very beginning of the process. From this turning point onwards, two disynaptic basins, $V_1(C2,O1)$ and $V_2(C2,O1)$ are observed between C2 and O1 accounting for its double bond character. Finally, when SSD-VII is reached, the new $V(C3,O4)$ basin appears accounting for the closure of the lactone ring. The population of this new disynaptic basin is quite low: slightly increases at the beginning of the SSD-VII, but soon its population stabilizes around a 0.78 e value.

10.5.2.2 Mechanism A, Second Step

As explained above, the second step of the mechanism A accounts for the lactone intermediate opening to form carbon monoxide and formaldehyde. The energy profile along the IRC path down from TS4 to the α -lactone intermediate in one side, and to carbon monoxide plus formaldehyde in the other side, is reported in Fig. 10.9, together with the SSDs found. These have been shown in Scheme 10.3, which as explained has been depicted from the perspective of the ELF analysis, following the same code.

At the α -lactone, the first point of the SSD-I, fifteen basins have been found, corresponding with the four core basins, five disynaptic basins accounting for the

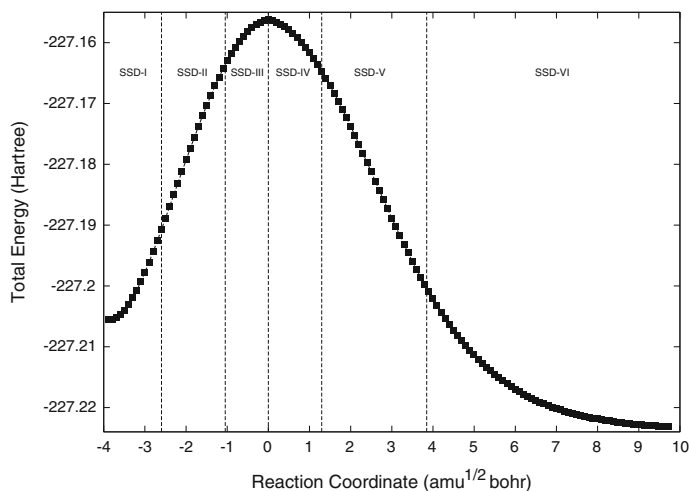
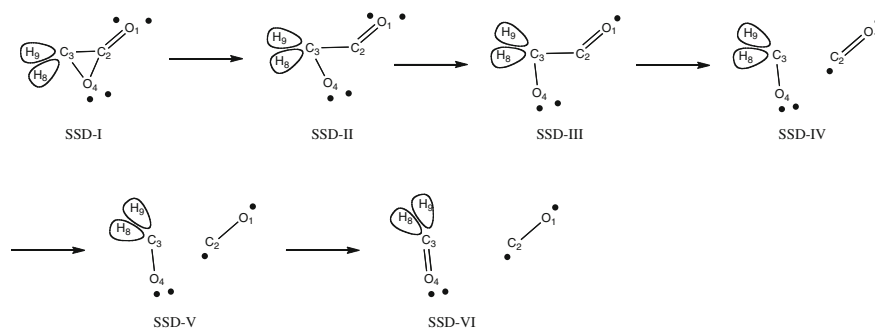


Fig. 10.9 Energy profile for the α -lactone (*left side*) decomposition to obtain carbon monoxide plus formaldehyde through TS4, calculated by means of the IRC method. The SSDs found are indicated



Scheme 10.3 Representation of the second step of the glycolic acid decomposition through the mechanism A, depicted from the ELF viewpoint

double and the three single bonds, two hydrogenated basins and four monosynaptic basins, located two on each oxygen atom. The annihilation of the disynaptic basin V (C2,O4) is observed in the turning point between SSD-I and SSD-II by means of a fold-type catastrophe, and in this way the topological analysis describes the beginning of the three-membered ring opening. The second topological change of the ELF field connecting SSD-II and SSD-III corresponds to a cusp-type catastrophe where two monosynaptic basins $V_{1,2}(O1)$ merging to form a unique V(O1) monosynaptic basin. Then the bonding basin V(C2,C3) becomes monosynaptic V(C2) by means of a fold-type catastrophe (just at the TS of the process, as can be seen in Fig. 10.9) and the SSD-IV is reached. From that point on, the two fragments separate from each

other along the IRC, and the changes that can be noticed are the merging of the two disynaptic basins $V_{1,2}(C2,O1)$ into a unique disynaptic basin $V(C2,O1)$ (cusp-type catastrophe) when the system reaches the SSD-V. Finally the system reaches the SSD-VI, the splitting of the $V_1(C3,O4)$ disynaptic basin into two disynaptic basins $V_{1,2}(C3,O4)$ (cusp-type catastrophe) accounting for the newer double bond formation

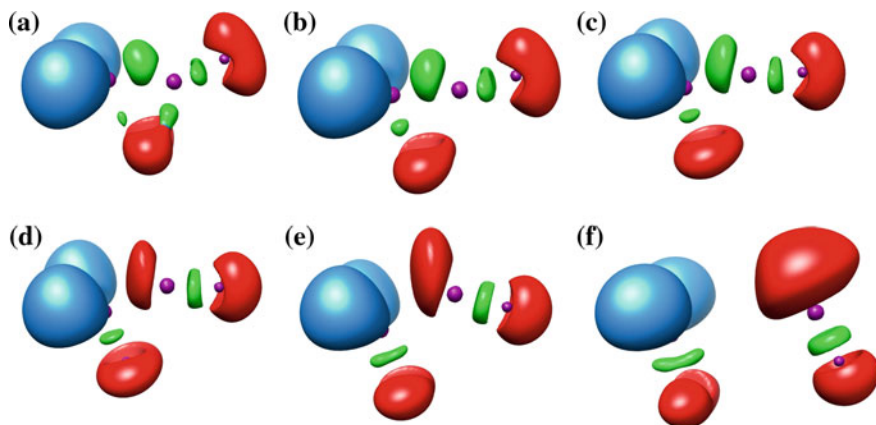


Fig. 10.10 Snapshots of the ELF localization domains ($\eta = 0.819$ isosurface) for selected points along the IRC from TS4: **a** α -lactone intermediate, belonging to SSD-I, **b** point at $s \approx -1.998$ $\text{amu}^{1/2}$ bohr belonging to SSD-II, **c** point at $s \approx -0.498$ $\text{amu}^{1/2}$ bohr belonging to SSD-III, **d** point at $s \approx 0.498$ $\text{amu}^{1/2}$ bohr belonging to SSD-IV, **e** point at $s \approx 1.998$ $\text{amu}^{1/2}$ bohr belonging to SSD-V, **f** last point of the IRC, corresponding to carbon monoxide plus formaldehyde, belonging to SSD-VI

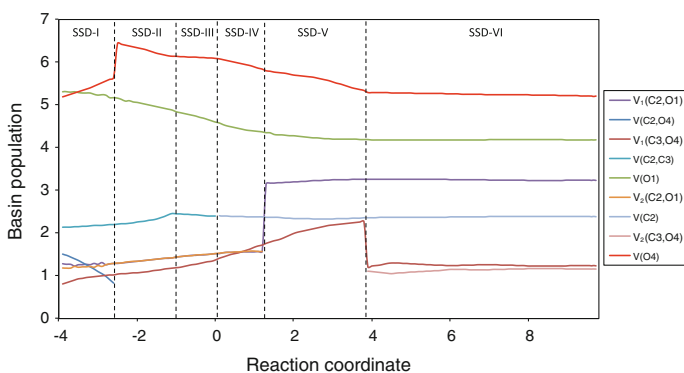


Fig. 10.11 Population evolution of some selected basins along the IRC path from TS4. *Dashed lines* separate the structural stability domains found, which are indicated. $V(O1)$ and $V(O4)$ account for the total population of the monosynaptic basins on the O1 and O4 atoms, respectively

between C3 and O4 that is observed. Snapshots of the ELF basins for some selected points along the IRC are shown in Fig. 10.10.

The population evolution of some basins directly related with the changes taking place in the reaction is reported in Fig. 10.11. As can be seen, the reaction begins with a very acute diminution of the population of the V(C2,O4) disynaptic basin, that very soon disappears in the catastrophe between SSD-I and SSD-II, thus making apparent that the ring opening process begins in this bond, taking place the breaking of the C2–C3 bond at a later stage. The population of this disappearing basin is assumed by the monosynaptic basins V(O4), represented as a whole in Fig. 10.11, whose population increase as the V(C2,C3) population decrease, and suddenly increases at the turning point between SSD-I and SSD-II. The populations of the monosynaptic basins on O1 (initially two basins, only one after the turning point between SSD-II and SSD-III is reached) are also represented as a whole in Fig. 10.11, and labeled V(O1). As can be seen, either the V(O4) population as well as the V(O1) one constantly decrease from the SSD-I to SSD-II turning point on, until stable values of *ca* 5.22 and *ca* 4.18 e, respectively, are reached. Concomitantly, the population of V₁(C3,O4) disynaptic basin constantly increases until it is splitted in the turning point between SSD-V and SSD-VI, into two disynaptic basins accounting for the double C3–O4 bond character. It can also be noticed that the V(C2,C3) disynaptic basin at the end of SSD-III becomes monosynaptic V(C2), with the same population that had the V(C2,C3) basin, when the turning point between SSD-III and SSD-IV is reached. On the other hand, the populations of the disynaptic basins V_{1,2}(C2,O1) slightly increase and finally merge in the turning point between SSD-IV and SSD-V.

As can be seen, there is only one basin between the C2 and the O1 atoms by the end of the process, and the populations of the basins V(C2), V(O1) and V(C2,O1) at the last point of the IRC are 2.39, 4.18 and 3.23 e, respectively. Therefore, the topological description of the carbon monoxide moiety shows that the ten valence electrons are greatly displaced towards the oxygen atom, and in fact the populations of the V(O1) basins are greater than the population of the V(C2,O1) bonding basin, thus reflecting the electronic displacement due to the large oxygen electronegativity.

10.5.2.3 Mechanism B, First Step

As explained above, an alternative mechanism was suggested for the water elimination from glycolic acid to yield the α -lactone intermediate, by means of the nucleophilic attack of the hydroxylic oxygen (O1) of the carboxyl group on the α -carbon atom (C3). The energy profile along the IRC path down from TS2 to the glycolic acid in one side and to the α -lactone intermediate on the other is reported in Fig. 10.12, along with the SSDs found. In Scheme 10.4 these domains have been sketched following the same aforementioned code.

The beginning of the reaction takes place in the same way as already explained when studying the mechanism A: starting at the glycolic acid, with nineteen basins,

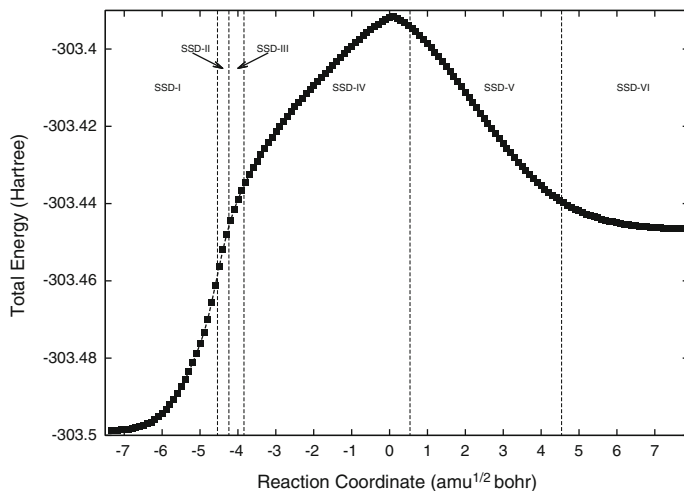
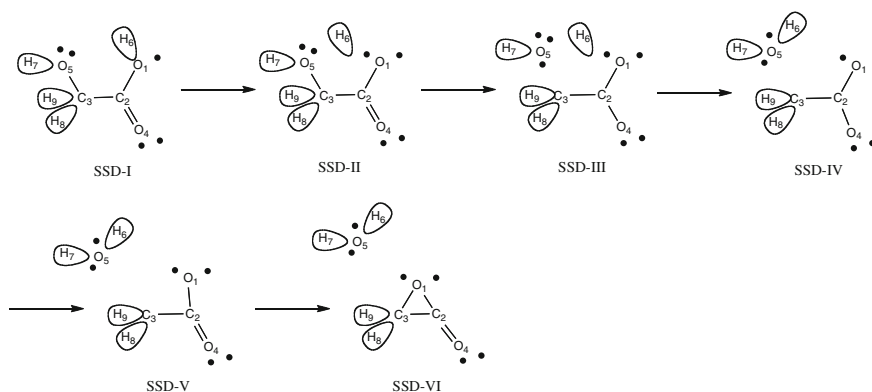


Fig. 10.12 Energy profile for the water elimination from glycolic acid (*left side*) to obtain the α -lactone intermediate through TS2, calculated by means of the IRC method. The SSDs found are indicated



Scheme 10.4 Representation of the first step of the glycolic acid decomposition through the mechanism B, depicted from the ELF viewpoint

the SSD-I ends up with the departure of the H6 from O1, where the bonding basin $V(O1, H6)$ splits into two monosynaptic basins $V(O1)$ and $V(H6)$. After that, the proton is located between the monosynaptic basins of O1 and O5 along SSD-II and SSD-III, finally reaching the O5 atom at SSD-IV. However, in the mechanism B the breaking of the C3–O5 bond takes place earlier than in the mechanism A according to the BET description: in the turning point between SSD-II and SSD-III the $V(C3, O5)$ disynaptic basin is replaced by a new $V(O5)$ monosynaptic basin. In the mechanism A this change took place once the H6 had reached the O5 atom,

whereas in the mechanism B the C3–O5 bond breaks before the H6–O5 bond has developed. From a topological point of view this is the main difference between the two mechanisms, and might explain why the mechanism A is favored over the mechanism B. As can be seen in Fig. 10.6, the turning point between SSD-IV and SSD-V (namely, the breaking of the C3–O5 bond according to the ELF description) is ca 8.5 kcal/mol below the TS, so that the water departure is not very much energy demanding. However, as can be seen in Fig. 10.12, the turning point between SSD-II and SSD-III (where the C3–O5 breaks in this case) is ca 20.5 kcal/mol under the TS, and therefore the OH departure with the H6 proton surrounding O1, is in this case much more energy demanding until the TS is found with the water molecule formed far from the rest of the system. This would explain why the mechanism A is favored over the mechanism B.

The latter steps of the mechanism B can be described analogously to the description of the mechanism A: the double bond is developed, now between C2 and O4, when SSD-V is reached, and the last change corresponds to the ring closure.

Snapshots of the ELF basins for some selected points along the IRC representing the different SSD's found are depicted in Fig. 10.13.

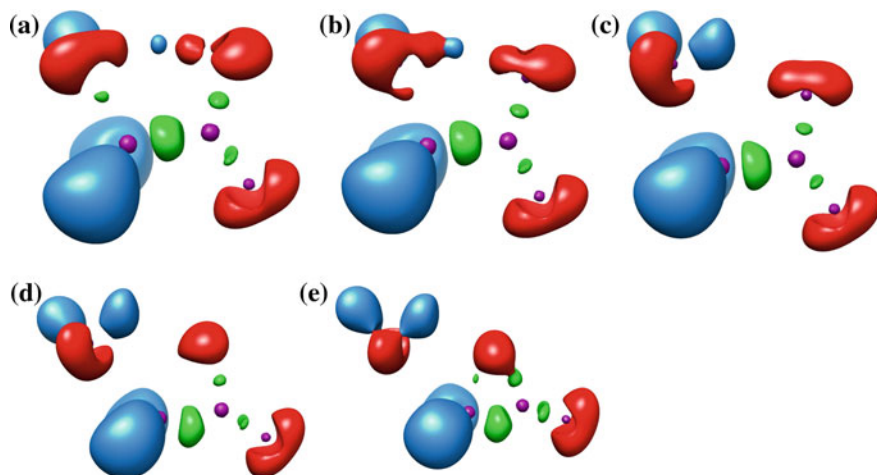


Fig. 10.13 Snapshots of the ELF localization domains ($\eta = 0.85$ isosurface, except when indicated) for selected points along the IRC from TS2 (see in Fig. 10.7a the domains corresponding to glycolic acid, belonging to SSD-I, and the atoms and basins labels there): **a** point at $s \approx -4.396 \text{ amu}^{1/2} \text{ bohr}$ belonging to SSD-II, **b** point at $s \approx -3.996 \text{ amu}^{1/2} \text{ bohr}$ belonging to SSD-III, **c** TS belonging to SSD-IV, **d** point at $s \approx +2.497 \text{ amu}^{1/2} \text{ bohr}$ belonging to SSD-V, **e** last point of the IRC, corresponding to the α -lactone species plus water, belonging to SSD-VI ($\eta = 0.825$ isosurface)

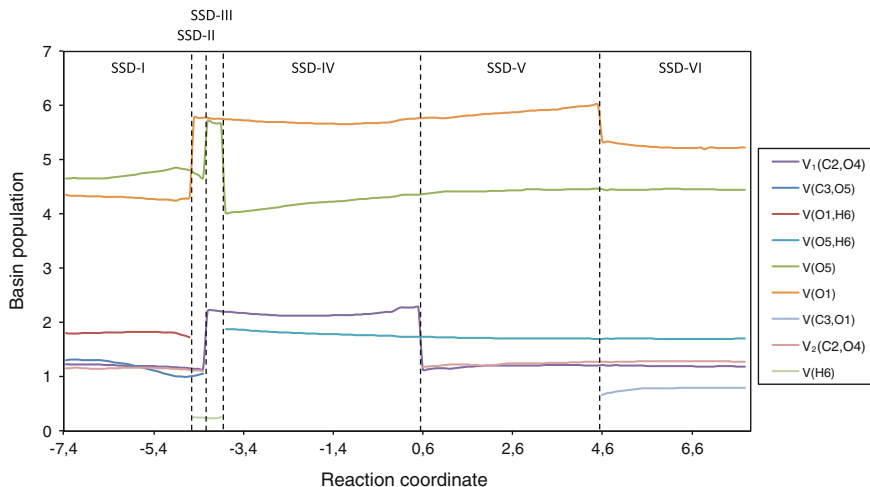


Fig. 10.14 Population evolution of some selected basins along the IRC path from TS2. *Dashed lines* separate the structural stability domains found, which are indicated. $V(O1)$ and $V(O5)$ account for the total populations of the monosynaptic basins on the O1 and O5 atoms, respectively

As can be seen the snapshots in Fig. 10.7a and in Fig. 10.13a–c, clearly describe the proton transfer from O1 to O5. Also the disappearance of the disynaptic basin between C3 and O5 can be followed comparing the snapshots (a) and (b) of Fig. 10.13, since the green $V(C3,O5)$ disynaptic basin in (a) disappears in (b). As already mentioned, the closure of the lactone ring is the last step, and the small green bonding basin between C3 and O1 cannot be seen until SSD-VI is reached, snapshot (e) in Fig. 10.13.

The process can also be followed with the aid of the population evolution of some selected basins along the process. Such evolution is reported graphically in Fig. 10.14, in which $V(O1)$ and $V(O5)$ account for the whole population of the monosynaptic basins on these two atoms.

As can be seen, along SSD-I the basin populations do not change significantly, with the exception of the $V(C3,O5)$ population diminution anticipating the breaking of this bond soon after SSD-I finishes. The first turning point reflects the sudden increase on the $V(O1)$ monosynaptic basins population, due to the appearance of a new $V(O1)$ basin concomitant with the $V(O1,H6)$ hydrogenated basin disappearance at this point. Then two very short domains, SSD-II and SSD-III, are reached, in which a scarcely populated $V(H6)$ basin briefly appears, accounting for the dressed proton travel from O1 to O5. Also in the turning point between these two domains, the whole population of the $V(O5)$ basins increases because the former $V(C3,O5)$ basins changes to a new $V(O5)$ monosynaptic basin. Soon after that the

whole population of the V(O5) basins decreases back because the V(O5,H6) basin appears replacing one of the V(O5) monosynaptic basins and taking its population, at the turning point between of SSD-III to SSD-IV. On the other hand, the two bonding basins $V_{1,2}(C2,O4)$ merge to each other in the SSD-II to SSD-III change, and the resulting basin has got the sum of the populations until it is again splitted in the SSD-IV to SSD-V turning point. The final appearance of the V(C3,O1)

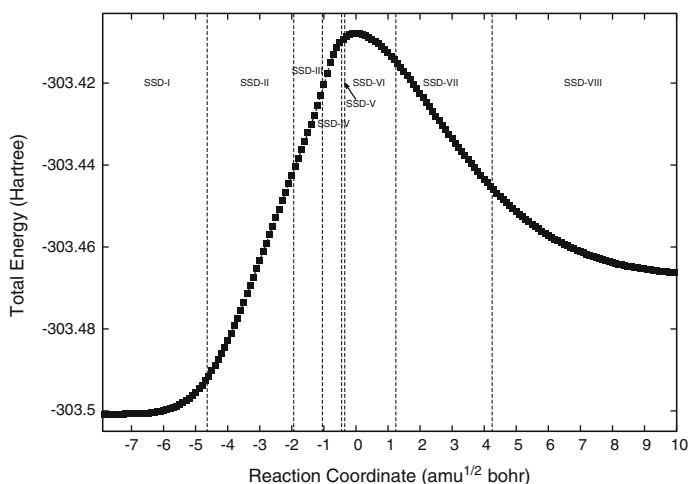
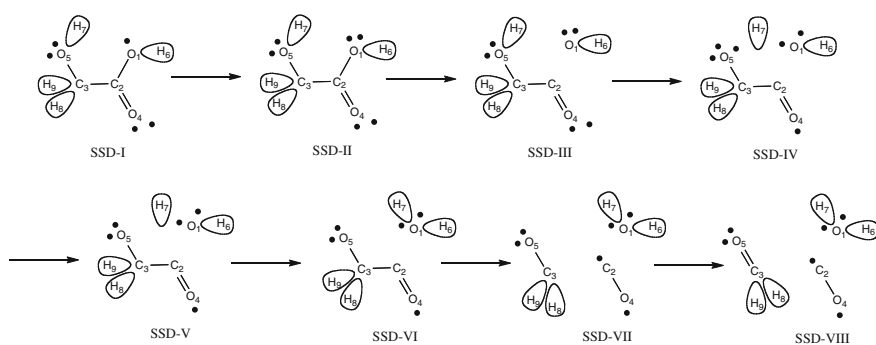


Fig. 10.15 Energy profile for the decomposition glycolic acid (*left side*) through TS3 to obtain carbon monoxide, water and formaldehyde, calculated by means of the IRC method. The SSDs found are indicated



Scheme 10.5 Representation of the glycolic acid decomposition through the mechanism C, depicted from the ELF viewpoint

disynaptic basin accounting for the ring closure is accompanied by a diminution of the $V(O1)$ monosynaptic basins population.

10.5.2.4 Mechanism C

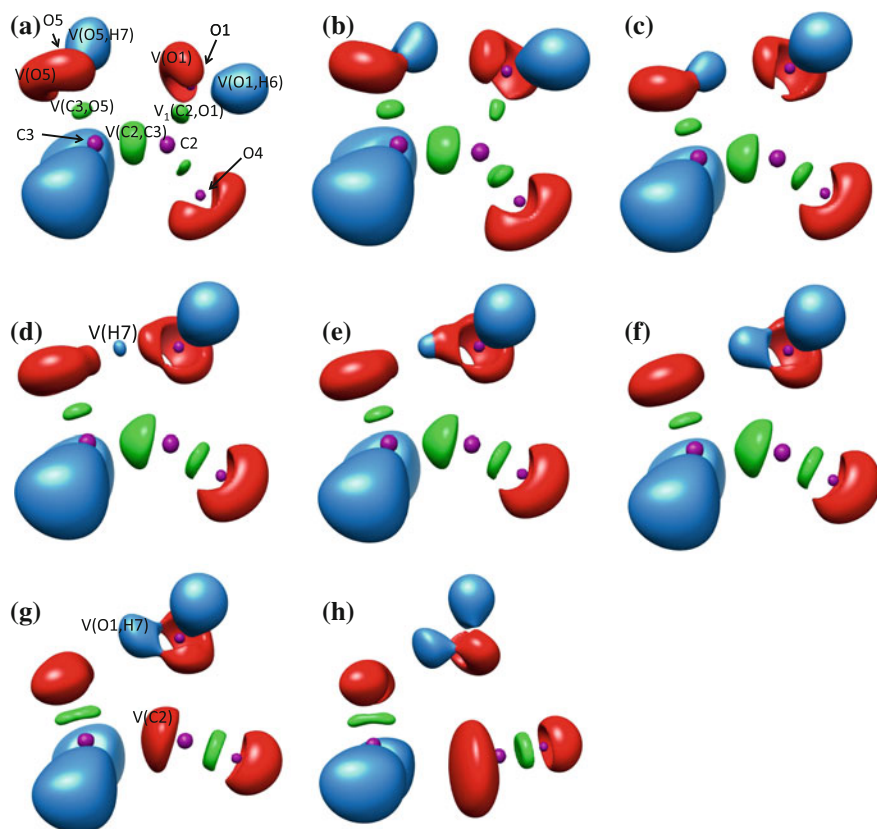


Fig. 10.16 Snapshots of the ELF localization domains ($\eta = 0.825$ isosurface, except when indicated) for selected points along the IRC from TS3: **a** glycolic acid, belonging to SSD-I ($\eta = 0.85$ isosurface), with recall of some atom positions and basin labels, **b** point at $s \approx -2.996$ $\text{amu}^{1/2}$ bohr belonging to SSD-II **c** point at $s \approx -1.496$ $\text{amu}^{1/2}$ bohr belonging to SSD-III, **d** point at $s \approx -0.698$ $\text{amu}^{1/2}$ bohr belonging to SSD-IV, **e** point at $s \approx -0.398$ $\text{amu}^{1/2}$ bohr belonging to SSD-V, **f** TS belonging to SSD-VI, **g** point at $s \approx +2.496$ $\text{amu}^{1/2}$ bohr belonging to SSD-VII, **h** last point of the IRC, corresponding to carbon monoxide plus water and formaldehyde, belonging to SSD-VIII

A third pathway was found to compete with the already explained mechanisms. The third pathway is a one-step process directly leading from the glycolic acid to the

reaction products, namely, carbon monoxide, water and formaldehyde. In Fig. 10.15 we report the energy profile along the IRC path down from TS3 to the glycolic acid on one side, and to the reaction products in the other side. The SSDs found are indicated and sketched in Scheme 10.5.

As can be seen, the process begins in a different way than in the A and B mechanisms: although the first topological change also corresponds to a new V(O1) monosynaptic basin appearance, the proton transfer does not begin neither in the first stage of the process nor in the second or the third. It is not until SSD-IV is reached that the V(O5,H7) splits into two monosynaptic basins V(O5) and V(H7). This can also be viewed in Fig. 10.16, in which the snapshots of the ELF basins for some selected points along the IRC for the decomposition of the glycolic acid by means of the mechanism C are reported. As can be seen, the snapshots (a), (b) and (c) do not show any proton transfer.

The breaking of the C2–O1 bond can be sensed by comparing the snapshots (b) and (c) in Fig. 10.16: the green disynaptic basin between C2 and O1 cannot be detected at SSD-III. The proton transfer can be followed in the snapshots (c), (d), (e), and (f) in Fig. 10.16. The C2–C3 breaking is reflected by the red monosynaptic V(C2) basin that can be seen at Fig. 10.16g instead of the former disynaptic V(C2, C3) green basin between these two atoms that can still be viewed at Fig. 10.16f.

Therefore, the series of chemical events taking place according to the ELF description is rather different in the mechanism C with respect the other two mechanisms: in the mechanism C the C2–O1 bond breaks first, forming an OH moiety. After that, at the turning point between SSD-III and SSD-IV, the V(H7) appears accounting from the proton migration from O5 to O1 while at the turning point between SSD-V and SSD-VI the bonding basin V(O1,H7) appears. After that, going down from the TS to the final products, the chemical events taking place are: (i) the C2–C3 breaking, (the disynaptic basin V(C2,C3) becomes monosynaptic V(C2)) (ii) the disynaptic basin $V_1(C3,O5)$ splits into two disynaptic basins $V_{1,2}(C3, O5)$ accounting for the double bond formation.

In the mechanism A the H6 transfer from O1 to O5 was the first chemical event taking place, followed by the C3–O5 breaking (water departure), lactone ring closure through C3–O4 bond formation, and decomposition of the lactone intermediate via C2–O4 bond breaking followed by C2–C3 breaking and final C3–O4 double bond formation. On the other hand, in the mechanism B the series of events begun with the H6 departure from O1 followed by the C3–O5 breaking (OH departure), water formation via O5–H6 bond, closure of the lactone ring through C3–O1 bond formation, and decomposition of the lactone intermediate via C2–O1 bond breaking followed by C2–C3 breaking and final C3–O1 double bond formation.

The population evolution of several basins, related with the advance of the process along the mechanism C, have been represented as a function of the reaction coordinate in Fig. 10.17, in which the SSDs found are also indicated.

Along SSD-I only a diminution of the V(C2,O1) population concomitant with an increase in the V(O1) basins population is sensed. At the turning point between SSD-I and SSD-II a new monosynaptic basin appears on O1, and this is reflected in

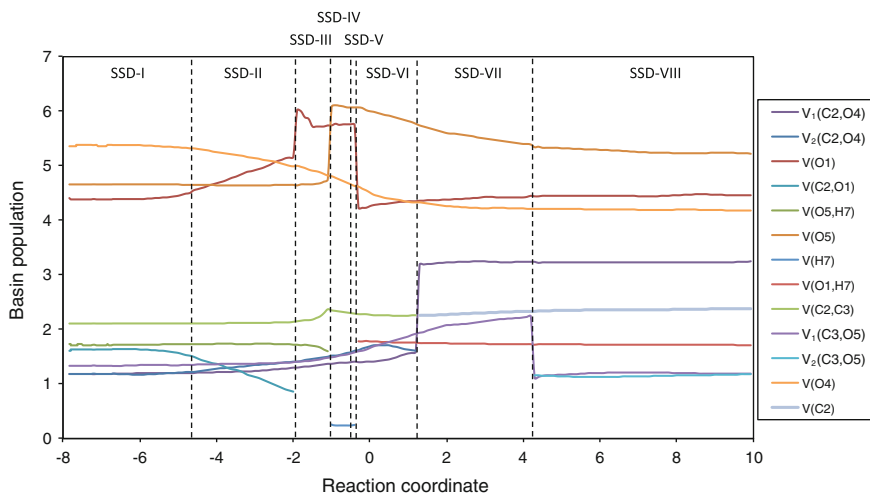


Fig. 10.17 Population evolution of some selected basins along the IRC path from TS3. *Dashed lines* separate the structural stability domains found, which are indicated. $V(O1)$, $V(O4)$ and $V(O5)$ account for the total populations of the monosynaptic basins on the O1, O4 and O5 atoms, respectively

a continuous increase in the total population of the monosynaptic basins on this atom, represented as a whole in Fig. 10.17 under the $V(O1)$ label. Along SSD-II the diminution in the $V(C2,O1)$ population continues, as well as the increase in the $V(O1)$ population. Also, the diminution of the populations of the monosynaptic basins $V(O4)$ can be sensed. The population of these basins will continue reducing until half SSD-VII is reached.

The turning point between SSD-II and SSD-III represents the breaking of the C2–O1 bond (the corresponding disynaptic basin disappears) with a concomitant sudden increase of the $V(O1)$ basins population. After that, three very short domains (SSD-III, SSD-IV and SSD-V) can be found, accounting for the H7 departure from O5 and a monosynaptic basin on O5 appearing in the turning point between SSD-III and SSD-IV, reflected in the sudden increase in its population observed in Fig. 10.17. Also, a scarcely populated $V(H7)$ basin briefly appears along SSD-IV and SSD-V. When SSD-VI is reached, the new $V(O1,H7)$ basin appears with the corresponding population diminution of the $V(O1)$ monosynaptic basins. The next catastrophe between SSD-VI and SSD-VII accounts for the C2–C3 bond breaking. The last turning point is related with the splitting of the $V(C3,O5)$ basin into two disynaptic basins accounting for the double bond character of the C3–O5 bond in formaldehyde.

10.6 Conclusions

As recently noted by Alvarez “But we must not forget that chemistry is all about connecting and disconnecting atoms to form new molecular or supramolecular objects. So understanding the ways in which atoms and molecules can be held together should play an important role in developing new chemistries” [181]. Our analysis demonstrates that concepts from quantum chemical topology constitute a promising tool to investigate chemical structure and reactivity.

In this work we review how these advances, have led to interesting and important new insights into the physical chemistry of materials and molecules and is a clear example of how overcome the sentence by Sutcliffe: “It is at least arguable that, from the point of view of quantum chemistry as usually practiced, the supercomputer has dissolved the bond” [182]. We then review in detail a few specific applications that highlight some of these quantum chemical topology capabilities. Two working examples have been selected: (i) the Ag nucleation and formation on AgVO_3 material provoked by the electron-beam irradiation, has been investigated by means of a QTAIM study, (ii) the decomposition of glycolic acid has been analyzed by the joint use of ELF plus CT (BET).

We conclude this chapter by quoting the Dirac’s statement [183] “It therefore becomes desirable that approximate practical methods of applying quantum mechanics should be developed, which can lead to an explanation of the main features of complex atomic systems without too much computation”

Acknowledgements The authors are grateful to Generalitat Valenciana for *PrometeoIII/2014/022* and *ACOMP/2014/270* projects, Ministerio de Economía y Competitividad (Spain) for project *CTQ-2012-36253-C03-02*, and Universitat Jaume I for project *P1·1B2013-40*. The authors are also grateful to the Servei d’Informàtica, Universitat Jaume I for generous allocation of computer time.

References

1. Gross L, Mohn F, Moll N, Liljeroth P, Meyer G (2009) The chemical structure of a molecule resolved by atomic force microscopy. *Science* 325:1110–1114
2. Gross L, Mohn F, Moll N, Schuler B, Criado A, Guitian E, Pena D, Gourdon A, Meyer G (2012) Bond-order discrimination by atomic force microscopy. *Science* 337:1326–1329
3. Lu J, Loh KP (2013) Single-molecule chemical reactions tracked at the atomic-bond level. *Angew Chem Int Ed* 52:13521–13523
4. Chiang C-L, Xu C, Han Z, Ho W (2014) Real-space imaging of molecular structure and chemical bonding by single-molecule inelastic tunneling probe. *Science* 344:885–888
5. Bredtmann T, Ivanov M, Dixit G (2014) X-ray imaging of chemically active valence electrons during a pericyclic reaction. *Nat Commun* 5:5509
6. Kössl F, Lisaj M, Kozich V, Heyne K, Kühn O (2015) Monitoring the alcoholysis of isocyanates with infrared spectroscopy. *Chem Phys Lett* 621:41–45
7. Bratos S, Wulff M, Leicknam JC, Kong Q (2015) Ultrafast chemical kinetics: elementary chemical act. *Chem Phys Lett* 619:88–91

8. Öström H, Öberg H, Xin H, LaRue J, Beye M, Dell'Angela M, Gladh J, Ng ML, Sellberg JA, Kaya S, Mercurio G, Nordlund D, Hantschmann M, Hieke F, Kühn D, Schlotter WF, Dakovski GL, Turner JJ, Minitti MP, Mitra A, Moeller SP, Föhlich A, Wolf M, Wurth W, Persson M, Nørskov JK, Abild-Pedersen F, Ogasawara H, Pettersson LGM, Nilsson A (2015) Probing the transition state region in catalytic CO oxidation on Ru. *Science* 347:978–982
9. Kim KH, Kim JG, Nozawa S, Sato T, Oang KY, Kim TW, Ki H, Jo J, Park S, Song C, Sato T, Ogawa K, Togashi T, Tono K, Yabashi M, Ishikawa T, Kim J, Ryoo R, Kim J, Ihee H, Adachi S-I (2015) Direct observation of bond formation in solution with femtosecond X-ray scattering. *Nature* 518:385–389
10. Cafiero M, Adamowicz L (2004) Molecular structure in non-Born-Oppenheimer quantum mechanics. *Chem Phys Lett* 387:136–141
11. Lowdin PO (1989) on the long way from the Coulombic Hamiltonian to the electronic-structure of molecules. *Pure Appl Chem* 61:2065–2074
12. Sutcliffe BT, Woolley RG (2005) Comment on 'Molecular structure in non-Born-Oppenheimer quantum mechanics'. *Chem Phys Lett* 408:445–447
13. Woolley RG (1976) Quantum-theory and molecular-structure. *Adv Phys* 25:27–52
14. Woolley RG (1986) Molecular shapes and molecular-structures. *Chem Phys Lett* 125:200–205
15. Woolley RG (1991) Quantum-chemistry beyond the Born-Oppenheimer approximation. *Theochem-J Mol Struct* 76:17–46
16. Woolley RG (1998) Is there a quantum definition of a molecule? *J Math Chem* 23:3–12
17. Fetter AL, Walecka JD (2003) Quantum theory of many-particle systems, 1st edn. Dover Publications, Mineola (New York)
18. Mattuck RD (1992) A guide to Feynman diagrams in the many-body problem, 2nd edn. Dover Publications, New York
19. Lowdin PO (1991) On the importance of theory in the future development of chemistry. *Theochem* 76:1–3
20. Schleyer PV (2005) Introduction: delocalization—Pi and Sigma. *Chem Rev* 105:3433–3435
21. Popelier PLA (2007) Chemical concepts from quantum mechanics—University of Manchester, UK 4–6 Sept 2006—Preface. *Faraday Dis* 135:3–5
22. Alabugin IV, Gilmore KM, Peterson PW (2011) Hyperconjugation. *Wiley Interdiscip Rev Comput Mol Sci* 1:109–141
23. Gonthier JF, Steinmann SN, Wodrich MD, Corminboeuf C (2012) Quantification of “fuzzy” chemical concepts: a computational perspective. *Chem Soc Rev* 41:4671–4687
24. Earis P (ed) (2007) Chemical concepts from quantum mechanics: Faraday discussions, vol 135. The Royal Society of Chemistry, Cambridge
25. Primas H (1985) Can chemistry in physics be reduced. *Chem unserer Zeit* 19:109–119
26. Wilson CW Jr, Goddard WA III (1970) Exchange kinetic energy, contragradience, and chemical binding. *Chem Phys Lett* 5:45–49
27. Kutzelnigg W (1990) The physical origin of the chemical bond. In: Maksic ZB (ed) Theoretical models of chemical bonding: Part 2. Springer, Berlin, pp 1–43
28. Ruedenberg K (1962) Physical nature of chemical bond. *Rev Mod Phys* 34:326–376
29. Vieira FS, Fantuzzi F, Cardozo TM, Chaer MA (2013) Nascimento, Interference energy in C-H and C-C bonds of saturated hydrocarbons: dependence on the type of chain and relationship to bond dissociation energy. *J Phys Chem A* 117:4025–4034
30. Bader RFW, Henneker WH (1965) Ionic bond. *J Am Chem Soc* 87:3063–000
31. Sini G, Maitre P, Hiberty PC, Shaik SS (1991) Covalent, ionic and resonating single bonds. *Theochem J Mol Struct* 75:163–188
32. Chesnut DB (2008) A simple definition of ionic bond order. *J Chem Theory Comput* 4:1637–1642
33. Shaik S, Danovich D, Wu W, Hiberty PC (2009) Charge-shift bonding and its manifestations in chemistry. *Nat Chem* 1:443–449

34. Gamez JA, Yanez M (2013) FAAF (-) (A = O, S, Se, Te) or how electrostatic interactions influence the nature of the chemical bond. *J Chem Theory Comput* 9:5211–5215
35. Goddard WA III, Harding LB (1978) The description of chemical bonding from ab initio calculations. *Ann Rev Phys Chem* 29:363–396
36. Kovacs A, Esterhuysen C, Frenking G (2005) The nature of the chemical bond revisited: an energy-partitioning analysis of nonpolar bonds. *Chem Eur J* 11:1813–1825
37. Ponec R, Cooper DL (2007) Anatomy of bond formation. Bond length dependence of the extent of electron sharing in chemical bonds from the analysis of domain-averaged Fermi holes. *Faraday Dis* 135:31–42
38. Ponec R (2007) Anatomy of bond formation. domain-averaged fermi holes as a tool for the study of the nature of the chemical bonding in Li(2), Li(4), and F(2). *J Phys Chem A* 111:11294–11301
39. Bitter T, Ruedenberg K, Schwarz WHE (2007) Toward a physical understanding of electron-sharing two-center bonds. I. General aspects. *J Comput Chem* 28:411–422
40. Ruedenberg K, Schmidt MW (2009) Physical understanding through variational reasoning: electron sharing and covalent bonding. *J Phys Chem A* 113:1954–1968
41. Ando K (2012) Electron wave packet modeling of chemical bonding: Floating and breathing minimal packets with perfect-pairing valence-bond spin coupling. *Chem Phys Lett* 523:134–138
42. Jacobsen H (2013) Bond descriptors based on kinetic energy densities reveal regions of slow electrons—another look at aromaticity. *Chem Phys Lett* 582:144–147
43. Mayer I (2014) Covalent bonding: the role of exchange effects. *J Phys Chem A* 118:2543–2546
44. Shaik S, Rzepa HS, Hoffmann R (2013) One molecule, two atoms, three views, four bonds? *Angew Chem Int Ed Engl* 52:3020–3033
45. Frenking G, Hermann M (2013) Critical comments on “One molecule, two atoms, three views, four bonds?”. *Angew Chem Int Ed* 52:5922–5925
46. Danovich D, Shaik S, Rzepa HS, Hoffmann R (2013) A response to the critical comments on “One molecule, two atoms, three views, four bonds?”. *Angew Chem Int Ed* 52:5926–5928
47. Weinhold F, Klein RA (2014) Anti-electrostatic hydrogen bonds. *Angew Chem Int Ed* 53:11214–11217
48. Frenking G, Caramori GF (2015) No need for a re-examination of the electrostatic notation of the hydrogen bonding: a comment. *Angew Chem Int Ed* 54:2596–2599
49. Frenking G, Krapp A (2007) Unicorns in the world of chemical bonding models. *J Comput Chem* 28:15–24
50. Frenking G, Shaik S (eds) (2014) *The chemical bond, vol 2*. Wiley VCH, Weinheim. ISBN 978-3-527-33318-9
51. Schmidt MW, Ivanić J, Ruedenberg K (2014) The physical origin of covalent bonding, the chemical bond. Wiley-VCH Verlag GmbH & Co. KGaA2014, pp 1–68
52. Coppens P (2013) The interaction between theory and experiment in charge density analysis. *Phys Scr* 87:048104
53. Volkov A, Abramov Y, Coppens P, Gatti C (2000) On the origin of topological differences between experimental and theoretical crystal charge densities. *Acta Cryst Sect A* 56:332–339
54. Chopra D (2012) Advances in understanding of chemical bonding: inputs from experimental and theoretical charge density analysis. *J Phys Chem A* 116:9791–9801
55. Koritsanszky TS, Coppens P (2001) Chemical applications of X-ray charge-density analysis. *Chem Rev* 101:1583–1628
56. Gavezzotti A (2013) Crystal formation and stability: physical principles and molecular simulation. *Cryst Res Technol* 48:793–810
57. Feynman RP (1939) Forces in molecules. *Phys Rev* 56:340–343
58. Gatti C (2005) Chemical bonding in crystals: new directions. *Zeitschrift Fur Kristallographie* 220:399–457
59. Mulliken RS (1928) Assignment of quantum numbers for electrons in molecules. I. *Phys Rev* 32:186–222

60. Heitler W, London F (1927) Reciprocal action of neutral atoms and homopolar combination according to quantum mechanics. *Z Angew Phys* 44:455–472
61. Foster JP, Weinhold F (1980) Natural hybrid orbitals. *J Am Chem Soc* 102:7211–7218
62. Gillespie RJ, Nyholm RS (1957) Inorganic stereochemistry. *Quart Rev* 11:339–380
63. Woodward RB, Hoffmann R (1970) The conservation of orbital symmetry. Verlag Chemie GmbH, Academic Press, Weinheim New York
64. Fukui K (1971) Recognition of stereochemical paths by orbital interaction. *Acc Chem Res* 4:57–64
65. Shaik SS, Hiberty PC (2008) A chemist's guide to valence bond theory. Wiley-Interscience, Hoboken
66. Marcus RA (1964) Chemical + electrochemical electron-transfer theory. *Annu Rev Phys Chem* 15:155–196
67. Collard K, Hall GG (1977) Orthogonal trajectories of the electron density. *Int J Quantum Chem* 12:623–637
68. Bader RFW (1975) Molecular fragments or chemical bonds. *Acc Chem Res* 8:34–40
69. Matta CF, Boyd RJ (2007) The Quantum theory of atoms in molecules: from solid state to DNA and drug design. Wiley-VCH, Weinheim
70. Nasertayob P, Shahbazian S (2008) The topological analysis of electronic charge densities: a reassessment of foundations. *J Mol Struct Theochem* 869:53–58
71. Thomas LH (1927) Calculation of atomic fields. *Proc Camb Philos Soc* 33:542–548
72. Dirac PAM (1930) Exchange phenomena in the Thomas atom. *Proc Camb Philos Soc* 26:376–385
73. Hohenberg PC, Kohn W (1964) Inhomogeneous electron gas. *Phys Rev* 136:B864–B871
74. Kohn W, Sham LJ (1965) Self-consistent equations including exchange and correlation effects. *Phys Rev* 140:1133–000
75. Parr RG, Yang W (1989) Density-functional theory of atoms and molecules. Oxford University Press, New York
76. Parr RG, Yang WT (1995) Density-functional theory of the electronic-structure of molecules. *Annu Rev Phys Chem* 46:701–728
77. Geerlings P, Fias S, Boisdenghien Z, De Proft F (2014) Conceptual DFT: chemistry from the linear response function. *Chem Soc Rev* 43:4989–5008
78. Parr RG, Donnelly RA, Levy M, Palke WE (1978) Electronegativity—density functional viewpoint. *J Chem Phys* 68:3801–3807
79. Parr RG, Pearson RG (1983) Absolute hardness—companion parameter to absolute electronegativity. *J Am Chem Soc* 105:7512–7516
80. Parr RG, Yang WT (1984) Density functional-approach to the frontier-electron theory of chemical-reactivity. *J Am Chem Soc* 106:4049–4050
81. A tale of many electrons. *Nat Mater* (2014) 13:913–913
82. Jain A, Hautier G, Moore CJ, Ong SP, Fischer CC, Mueller T, Persson KA, Ceder G (2011) A high-throughput infrastructure for density functional theory calculations. *Comput Mater Sci* 50:2295–2310
83. Lejaeghere K, Van Speybroeck V, Van Oost G, Cottenier S (2014) Error estimates for solid-state density-functional theory predictions: an overview by means of the ground-state elemental crystals. *Crit Rev Solid State Mater Sci* 39:1–24
84. Neugebauer J, Hickel T (2013) Density functional theory in materials science. *Wiley Interdiscip Rev Comput Mol Sci* 3:438–448
85. Burke K (2012) Perspective on density functional theory. *J Chem Phys* 136:150901
86. Cohen AJ, Mori-Sánchez P, Yang W (2008) Insights into current limitations of density functional theory. *Science* 321:792–794
87. Noury S, Krokidis X, Fuster F, Silvi B (1999) Computational tools for the electron localization function topological analysis. *Comput Chem* 23:597–604
88. Popelier PLA (1996) MORPHY, a program for an automated “atoms in molecules” analysis. *Comput Phys Commun* 93:212–240
89. Kohout M (2002) Chemical bonding analysis in direct space. <http://www.cpfs.mpg.de/ELF>

90. Biegler-König F, Schönbohm J, Bayles D (2001) Software news and updates—AIM2000—a program to analyze and visualize atoms in molecules. *J Comput Chem* 22:545–559
91. Otero-de-la-Roza A, Blanco MA, Pendas AM, Luana V (2009) Critic: a new program for the topological analysis of solid-state electron densities. *Comput Phys Commun* 180:157–166
92. Bader RFW (1990) *Atoms in molecules: a quantum theory*. Oxford University Press, Oxford
93. Gillespie RJ, Popelier PLA (2001) *Chemical bonding and molecular geometry: from Lewis to electron densities*. Oxford University Press, New York
94. Silvi B (1994) Importance of electrostatic interactions between nonbonded molecules in ice. *Phys Rev Lett* 73:842–845
95. Merino G, Vela A, Heine T (2005) Description of electron delocalization via the analysis of molecular fields. *Chem Rev* 105:3812–3841
96. Bader RFW (1991) A quantum theory of molecular structure and its applications. *Chem Rev* 91:893–928
97. Bader RFW (1985) Atoms In Molecules. *Acc Chem Res* 18:9–15
98. Becke AD, Edgecombe KE (1990) A simple measure of electron localization in atomic and molecular systems. *J. Chem. Phys.* 92:5397–5403
99. Popelier PLA, Bremond EAG (2009) Geometrically faithful homeomorphisms between the electron density and the bare nuclear potential. *Int J Quantum Chem* 109:2542–2553
100. de Courcy B, Pedersen LG, Parisel O, Gresh N, Silvi B, Pilme J, Piquemal JP (2010) Understanding selectivity of hard and soft metal cations within biological systems using the subvalence concept. 1. Application to blood coagulation: direct cation-protein electronic effects versus indirect interactions through water networks. *J Chem Theory Comput* 6:1048–1063
101. Pilme J, Berthoumieux H, Robert V, Fleurat-Lessard P (2007) Unusual bond formation in aspartic protease inhibitors: a theoretical study. *Chem Eur J* 13:5388–5393
102. De La Lande A, Salahub DR, Maddaluno J, Scemama A, Pilme J, Parisel O, Gerard H, Caffarel M, Piquemal J-P (2011) Rapid communication spin-driven activation of dioxygen in various metalloenzymes and their inspired models. *J Comput Chem* 32:1178–1182
103. Berski S, Andrés J, Silvi B, Domingo LR (2006) New findings on the Diels–Alder Reactions. An analysis based on the bonding evolution theory. *J Phys Chem A* 110:13939–13947
104. Poater J, Duran M, Sola M, Silvi B (2005) Theoretical evaluation of electron delocalization in aromatic molecules by means of atoms in molecules (AIM) and electron localization function (ELF) topological approaches. *Chem Rev* 105:3911–3947
105. Pauzat F, Pilme J, Toulouse J, Ellinger Y (2010) About the collapse of the 3.3 μm CH stretching band with ionization in polycyclic aromatic hydrocarbons: configuration interaction and quantum Monte Carlo studies of the CH fragment. *J Chem Phys* 133:054301
106. Rivera-Fuentes P, Aonso-Gomez JL, Petrovic AG, Seiler P, Santoro F, Harada N, Berova N, Rzepa HS, Diederich F (2010) Enantiomerically pure alleno-acetylenic macrocycles: synthesis, solid-state structures, chiroptical properties, and electron localization function analysis. *Chem Eur J* 16:9796–9807
107. Popelier PL (2000) *Atoms in molecules: an introduction*. Pearson Education, Harlow
108. Bader RFW (2007) Everyman’s derivation of the theory of atoms in molecules. *J Phys Chem A* 111:7966–7972
109. Bader RFW (2005) The quantum mechanical basis of conceptual chemistry. *Monatshefte Fur Chemie* 136:819–854
110. Cerpa E, Krapp A, Vela A, Merino G (2008) The implications of symmetry of the external potential on bond paths. *Chem Eur J* 14:10232–10234
111. Krapp A, Frenking G (2007) Is this a chemical bond? A theoretical study of $\text{Ng}(2)@\text{C}-60$ ($\text{Ng} = \text{He, Ne, Ar, Kr, Xe}$). *Chem Eur J* 13:8256–8270
112. Cioslowski J, Edgington L, Stefanov BB (1995) Steric Overcrowding In Perhalogenated Cyclohexanes, Dodecahedranes, And 60 Fullerenes. *J Am Chem Soc* 117:10381–10384
113. Matta CF, Hernandez-Trujillo J, Tang TH, Bader RFW (2003) Hydrogen-hydrogen bonding: a stabilizing interaction in molecules and crystals. *Chem Eur J* 9:1940–1951

114. Hernandez-Trujillo J, Matta CF (2007) Hydrogen-hydrogen bonding in biphenyl revisited. *Struct Chem* 18:849–857
115. Sulway SA, Girshfeld R, Solomon SA, Muryr CA, Poater J, Sola M, Bickelhaupt FM, Layfield RA (2009) Alkali metal complexes of silyl-substituted ansa-(tris)allyl ligands: metal-, co-ligand- and substituent-dependent stereochemistry. *Eur J Inorg Chem* 4157–4167
116. Bader RFW (2009) Bond paths are not chemical bonds. *J Phys Chem A* 113:10391–10396
117. Bader RFW (2006) Pauli repulsions exist only in the eye of the beholder. *Chem Eur J* 12:2896–2901
118. Matta CF, Bader RFW (2006) An experimentalist's reply to "What is an atom in a molecule?". *J Phys Chem A* 110:6365–6371
119. Bader RFW (2002) A comment on "some fundamental problems with zero-flux partitioning of electron densities". *Theoret Chem Acc* 107:381–382
120. Shahbazian S (2011) The mathematical soundness and the physical content of the subsystem variational procedure of the QTAIM. *Int J Quantum Chem* 111:4497–4500
121. Savin A, Nesper R, Wengert S, Fässler TF (1997) ELF: The electron localization function. *Angew Chem Int Ed Engl* 36:1808–1832
122. Silvi B (2003) The spin-pair compositions as local indicators of the nature of the bonding. *J Phys Chem A* 107:3081–3085
123. Matito E, Silvi B, Duran M, Sola M (2006) Electron localization function at the correlated level. *J Chem Phys* 125:2736
124. Feixas F, Matito E, Duran M, Sola M, Silvi B (2010) Electron localization function at the correlated level: a natural orbital formulation. *J Chem Theory Comput* 6:2736–2742
125. Chevreau H, Fuster F, Silvi B (2001) Chemical bond: myth or reality? Topological methods of bond description. *Actualite Chimique* 15–22
126. Savin A (2005) The electron localization function (ELF) and its relatives: interpretations and difficulties. *J Mol Struct Theochem* 727:127–131
127. Kohout M, Wagner FR, Grin Y (2002) Electron localization function for transition-metal compounds. *Theoret Chem Acc* 108:150–156
128. Savin A, Silvi B, Colonna F (1996) Topological analysis of the electron localization function applied to delocalized bonds. *Can J Chem-Revue Canadienne De Chimie* 74:1088–1096
129. Kohout M, Savin A (1996) Atomic shell structure and electron numbers. *Int J Quantum Chem* 60:875–882
130. Kohout M, Savin A (1997) Influence of core-valence separation of electron localization function. *J Comput Chem* 18:1431–1439
131. Silvi B, Fourre I, Alikhani ME (2005) The topological analysis of the electron localization function. A key for a position space representation of chemical bonds. *Monatshefte Fur Chemie* 136:855–879
132. Bader RFW (1994) Principle of stationary action and the definition of a proper open system. *Phys. Rev. B* 49:13348–13356
133. Thom R (1976) Structural stability and morphogenesis. W. A. Benjamin Inc., Redding
134. Thom R (1977) Catastrophe theory. *Nature* 270:658
135. Krokidis X, Noury S, Silvi B (1997) Characterization of elementary chemical processes by Catastrophe theory. *J Phys Chem A* 101:7277–7282
136. Berski S, Andres J, Silvi B, Domingo LR (2003) The joint use of catastrophe theory and electron localization function to characterize molecular mechanisms. A density functional study of the Diels-Alder reaction between ethylene and 1,3-butadiene. *J Phys Chem A* 107:6014–6024
137. Polo V, Andrés J, Castillo R, Berski S, Silvi B (2004) Understanding the molecular mechanism of the 1,3-dipolar cycloaddition between fulminic acid and acetylene in terms of the electron localization function and catastrophe theory. *Chem Eur J* 10:5165–5172

138. Polo V, Andres J, Berskit S, Domingo LR, Silvi B (2008) Understanding reaction mechanisms in organic chemistry from catastrophe theory applied to the electron localization function topology. *J Phys Chem A* 112:7128–7136
139. González-Navarrete P, Domingo LR, Andrés J, Berski S, Silvi B (2012) Electronic fluxes during diels-alder reactions involving 1,2-benzoquinones: mechanistic insights from the analysis of electron localization function and catastrophe theory. *J Comput Chem* 33:2400–2411
140. Santos JC, Andres J, Aizman A, Fuentealba P, Polo V (2005) A theoretical study on the reaction mechanism for the Bergman cyclization from the perspective of the electron localization function and catastrophe theory. *J Phys Chem A* 109:3687–3693
141. Andres J, Berski S, Domingo LR, Gonzalez-Navarrete P (2012) Nature of the ring-closure process along the rearrangement of octa-1,3,5,7-tetraene to cycloocta-1,3,5-triene from the perspective of the electron localization function and catastrophe theory. *J Comput Chem* 33:748–756
142. Santos JC, Polo V, Andres J (2005) An electron localization function study of the trimerization of acetylene: reaction mechanism and development of aromaticity. *Chem Phys Lett* 406:393–397
143. Polo V, Gonzalez-Navarrete P, Silvi B, Andres J (2008) An electron localization function and catastrophe theory analysis on the molecular mechanism of gas-phase identity S(N)2 reactions. *Theoret Chem Acc* 120:341–349
144. Polo V, Andres J (2007) Lewis acid and substituent effects on the molecular mechanism for the nazarov reaction of penta-1,4-dien-3-one and derivatives. A topological analysis based on the combined use of electron localization function and catastrophe theory. *J Chem Theory Comput* 3:816–823
145. Polo V, Andres J (2005) A joint study based on the electron localization function and catastrophe theory of the chameleonic and centauric models for the cope rearrangement of 1,5-hexadiene and its cyano derivatives. *J Comput Chem* 26:1427–1437
146. González-Navarrete P, Andrés J, Berski S (2012) How a quantum chemical topology analysis enables prediction of electron density transfers in chemical reactions. The degenerated cope rearrangement of semibullvalene. *J Phys Chem Lett* 3:2500–2505
147. Alikhani ME, Michelini MC, Russo N, Silvi B (2008) Topological analysis of the reaction of uranium ions (U+, U2+) with N2O in the gas phase. *J Phys Chem A* 112:12966–12974
148. Michelini MD, Sicilia E, Russo N, Alikhani ME, Silvi B (2003) Topological analysis of the reaction of Mn+ (S-7, S-5) with H2O, NH3, and CH4 molecules. *J Phys Chem A* 107:4862–4868
149. Berski S, Sensato FR, Polo V, Andres J, Safont VS (2011) Olefin epoxidation by molybdenum peroxo compound: molecular mechanism characterized by the electron localization function and catastrophe theory. *J Phys Chem A* 115:514–522
150. Gonzalez-Navarrete P, Sensato F, Andrés J, Longo E (2014) Oxygen atom transfer reactions from mimoun complexes to sulfides and sulfoxides. A bonding evolution theory analysis. *J Phys Chem A*
151. Andres J, Berski S, Domingo LR, Polo V, Silvi B (2011) Describing the molecular mechanism of organic reactions by using topological analysis of electronic localization function. *Curr Org Chem* 15:3566–3575
152. Andrés J, González-Navarrete P, Safont VS (2014) Unraveling reaction mechanisms by means of Quantum Chemical Topology Analysis. *Int J Quantum Chem* 114:1239–1252
153. Andres J, Gracia L, Gonzalez-Navarrete P, Safont VS (1053) Chemical structure and reactivity by means of quantum chemical topology analysis. *Computational and Theoretical Chemistry* 2015:17–30
154. Contreras-García J, Marqués M, Silvi B, Recio JM (2012) Bonding changes along solid-solid phase transitions using the electron localization function approach. In: Gatti C, Macchi P (eds) *Modern charge-density analysis*. Springer, Netherlands, pp 625–658

155. Chen Z, Gao S, Li R, Wei M, Wei K, Zhou H (2008) Lithium insertion in ultra-thin nanobelts of Ag₂V₄O₁₁/Ag. *Electrochim Acta* 53:8134–8137
156. Mai L, Xu L, Gao Q, Han C, Hu B, Pi Y (2010) Single beta-AgVO₃ Nanowire H₂S Sensor. *Nano Lett* 10:2604–2608
157. Kittaka S, Matsuno K, Akashi H (1999) Crystal structure of alpha-AgVO₃ and phase relation of AgVO₃. *J Solid State Chem* 142:360–367
158. Ren J, Wang W, Sun S, Zhang L, Chang J (2009) Enhanced photocatalytic activity of Bi₂WO₆ loaded with Ag nanoparticles under visible light irradiation. *Appl Catal B-Environ* 92:50–55
159. Zhao W, Guo Y, Faiz Y, Yuan W-T, Sun C, Wang S-M, Deng Y-H, Zhuang Y, Li Y, Wang X-M, He H, Yang S-G (2015) Facile in-situ synthesis of Ag/AgVO₃ one-dimensional hybrid nanoribbons with enhanced performance of plasmonic visible-light photocatalysis. *Appl Catal B* 163:288–297
160. Zhao W, Liang F, Jin Z-M, Shi X-B, Yin P-H, Wang X-R, Sun C, Gao Z-Q, Liao L-S (2014) Efficient plasmonic photocatalytic activity on silver-nanoparticle-decorated AgVO₃ nanoribbons. *J Mater Chem A* 2:13226–13231
161. Andres J, Gracia L, Gonzalez-Navarrete P, Longo VM, Avansi W Jr, Volanti DP, Ferrer MM, Lemos PS, La Porta FA, Hernandez AC, Longo E (2014) Structural and electronic analysis of the atomic scale nucleation of Ag on alpha-Ag₂WO₄ induced by electron irradiation. *Sci Rep* 4:5391–5391
162. Pereira WS, Andres J, Gracia L, San-Miguel MA, da Silva EZ, Longo E, Longo VM (2015) Elucidating the real-time Ag nanoparticle growth on [small alpha]-Ag₂WO₄ during electron beam irradiation: experimental evidence and theoretical insights. *Phys Chem Chem Phys* 17:5352–5359
163. Andrés J, Ferrer MM, Gracia L, Beltran A, Longo VM, Cruvinel GH, Tranquilin RL, Longo E (2015) A combined experimental and theoretical study on the formation of Ag filaments on beta-Ag₂MoO₄ induced by electron irradiation. *Part Part Syst Charact*. doi:10.1002/ppsc.201400162
164. Longo E, Cavalcante LS, Volanti DP, Gouveia AF, Longo VM, Varela JA, Orlandi MO, Andres J (2013) Direct in situ observation of the electron-driven synthesis of Ag filaments on alpha-Ag₂WO₄ crystals. *Sci Rep* 3:1676
165. Botelho G, Sczancoski JC, Andres J, Gracia L, Longo E (2015) Experimental and theoretical study on the structure, optical properties and growth of metallic silver nanostructures in Ag₃PO₄. *J Phys Chem C* 119:6293–6306
166. Kresse G, Hafner J (1994) Ab-initio molecular-dynamics simulation of the liquid-metal amorphous-semiconductor transition in germanium. *Phys Rev B* 49:14251–14269
167. Perdew JP, Burke K, Ernzerhof M (1996) Generalized gradient approximation made simple. *Phys Rev Lett* 77:3865–3868
168. Kresse G, Joubert D (1999) From ultrasoft pseudopotentials to the projector augmented-wave method. *Phys Rev B* 59:1758–1775
169. Konta R, Kato H, Kobayashi H, Kudo A (2003) Photophysical properties and photocatalytic activities under visible light irradiation of silver vanadates. *Phys Chem Chem Phys* 5:3061–3065
170. Zhang S, Li W, Li C, Chen J (2006) Synthesis, characterization, and electrochemical properties of Ag₂V₄O₁₁ and AgVO₃ 1-D nano/microstructures. *J Phys Chem B* 110:24855–24863
171. Safont VS, Moliner V, Andres J, Domingo LR (1997) Theoretical study of the elimination kinetics of carboxylic acid derivatives in the gas phase. Decomposition of 2-chloropropionic acid. *J Phys Chem A* 101:1859–1865
172. Safont VS, Andres J, Domingo LR (1998) A theoretical study on the decomposition mechanism of beta-propiolactone and beta-butyrolactone. *Chem Phys Lett* 288:261–269

173. Rotinov A, Chuchani G, Andres J, Domingo LR, Safont VS (1999) A combined experimental and theoretical study of the unimolecular elimination kinetics of 2-alkoxypropionic acids in the gas phase. *Chem Phys* 246:1–12
174. Domingo LR, Picher MT, Safont VS, Andres J, Chuchani G (1999) Theoretical study of the mechanisms for the alkoxyacetic acids decomposition. *J Phys Chem A* 103:3935–3943
175. Chuchani G, Rotinov A, Andres J, Domingo LR, Safont VS (2001) A combined experimental and theoretical study of the homogeneous, unimolecular decomposition kinetics of 3-chloropivalic acid in the gas phase. *J Phys Chem A* 105:1869–1875
176. Safont VS, Andres J, Castillo R, Chuchani G, Rotinov A, Dominguez RM, Herize A (2004) A joint experimental and theoretical study on the mechanisms of methyl 2-hydroxypropionate and methyl 2-hydroxyisobutyrate decomposition in the gas phase. *J Phys Chem A* 108:996–1007
177. Domingo LR, Andres J, Moliner V, Safont VS (1997) Theoretical study of the gas phase decomposition of glycolic, lactic, and 2-hydroxyisobutyric acids. *J Am Chem Soc* 119:6415–6422
178. Gaussian 09, Frisch MJ, Schlegel HB, Scuseria GE, Robb JRCMA, Scalmani G, Barone V, Mennucci B, Petersson HNGA, Caricato M, Li X, Hratchian HP, Izmaylov JBAF, Zheng G, Sonnenberg JL, Hada M, Ehara KTM, Fukuda R, Hasegawa J, Ishida M, Nakajima T, Honda OKY, Nakai H, Vreven T, Montgomery Jr JA, Peralta FOJE, Bearpark M, Heyd JJ, Brothers E, Kudin VNSKN, Keith T, Kobayashi R, Normand J, Raghavachari ARK, Burant JC, Iyengar SS, Tomasi J, Cossi NRM, Millam JM, Klene M, Knox JE, Cross JB, Bakken CAV, Jaramillo J, Gomperts R, Stratmann RE, Yazyev AJAO, Cammi R, Pomelli C, Ochterski JW, Martin KMRL, Zakrzewski VG, Voth GA, Salvador JJDP, Dapprich S, Daniels AD, Farkas JBFO, Ortiz JV, Cioslowski J, Fox DJ, Wallingford CT (2010)
179. Fukui K (1970) A formulation of reaction coordinate. *J Phys Chem* 74:4161–4163
180. Fukui K (1981) The path of chemical-reactions—the IRC approach. *Acc Chem Res* 14:363–368
181. Alvarez S (2015) What we mean when we talk about bonds. *Chemistry World*, 29 January 2015
182. Sutcliffe BT (1996) The development of the idea of a chemical bond. *Int J Quant Chem* 58:645–655
183. Dirac PAM (1929) Quantum mechanics of many-electron systems. *Proc R Soc Lond* 123:714–733

Part II
Topological Methods for the
Characterization of Π -Electron
Delocalization and Aromaticity

Chapter 11

Paradise Lost— π -Electron Conjugation in Homologs and Derivatives of Perylene

Ivan Gutman and Slavko Radenković

Abstract Various Kekulé–structure–based models, aimed at describing π -electron conjugation in polycyclic aromatic compounds are briefly described. Our main concern are benzenoid hydrocarbons, π -electron systems in which the Kekulé–structure–based approaches are expected to yield the best results. Although there are numerous examples in which reasonings based on Kekulé structures render correct results, there exist cases in which significant violations are encountered. Perylene, its homologs, and derivatives are characteristic representatives of such “anomalous” conjugated systems. Violations from the predictions of the Kekulé–structure–based models are verified by means of a variety of Kekulé–structure–independent theoretical methods.

11.1 Introduction

The way how August Kekulé discovered the structural formula of benzene is one of the legends of the history of chemistry [1, 2]. In 1865/6, Kekulé proposed for benzene the hexagonal formula **1** shown in Fig. 11.1, according to which the carbon atoms would be three-valent (or, in more modern terminology: three-coordinate). In order to make the carbon atoms four-valent, in 1872 Kekulé inserted three double bonds into his benzene formula, which can be done in two distinct ways—formulas **2** and **3** shown in Fig. 11.1. Nowadays, these are referred to as the *Kekulé structures* or the *Kekulé structural formulas* of benzene.

It soon became evident that not only benzene, but the whole class of polycyclic aromatic compounds (benzenoid hydrocarbons in particular), possess a non-unique

I. Gutman (✉) · S. Radenković
Faculty of Science, University of Kragujevac, Kragujevac, Serbia
e-mail: gutman@kg.ac.rs

S. Radenković
e-mail: slavko.radenkovic@gmail.com

I. Gutman
State University of Novi Pazar, Novi Pazar, Serbia

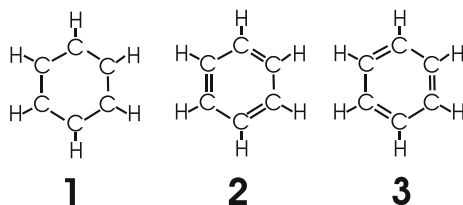


Fig. 11.1 Structural formulas for benzene proposed by Kekulé in 1865/66 (1) and in 1872 (2 and 3). Note that benzene was the first chemical compound for which a cyclic structure was postulated. Note also that in his first paper on the structure of benzene, Kekulé proposed several different structural formulas, only one of which is the nowadays accepted one, having the form of a regular hexagon

classical structural formula, i.e., that for such compounds several distinct Kekulé structures can be drawn. A characteristic example is depicted in Fig. 11.2.

The fact that there may exist several equally plausible Kekulé-type structural formulas for a chemical compound, has long pt there may exist several equally plausibleuzzled the chemical community. A more-or-less acceptable solution was found only after quantum-theoretical arguments were used for the description and explanation of chemical bonding [3–8]. One direction of development of quantum chemistry (usually referred to as “valence bond theory”) explicitly used mathematical objects resembling Kekulé structural formulas.

Strictly speaking, Kekulé structures provide only a small fraction of the diagrams used in valence bond theory for constructing the wave function. (For example, of 42 non-ionic Rumer diagrams of naphthalene, only three pertain to Kekulé structures.) Nevertheless, it was a compelling idea (especially for scholars with a chemistry background) to try to describe the physical and chemical properties of polycyclic conjugated molecules by employing only their Kekulé structures. This is usually referred to as “resonance theory”, for details see [9–12].

A noteworthy early attempt along these lines was a paper by Pauling and coworkers [13], who used the quantity

$$P(ij) = \frac{K_{ij}}{K} \quad (11.1)$$

for rationalizing the variation of the carbon–carbon bond lengths in benzenoid hydrocarbons; here K is the number of Kekulé structures, whereas K_{ij} is the number of Kekulé structures in which the bond ij is double. Nowadays, $P(ij)$ is referred to as the *Pauling bond order*.

Kekulé structures gained much on their popularity in the 1950s, when it was discovered that

- (1) if $K = 0$, then the respective conjugated hydrocarbon has non-bonding π -electron molecular orbitals and an open-shell π -electron configuration, and is thus highly unstable [14], and

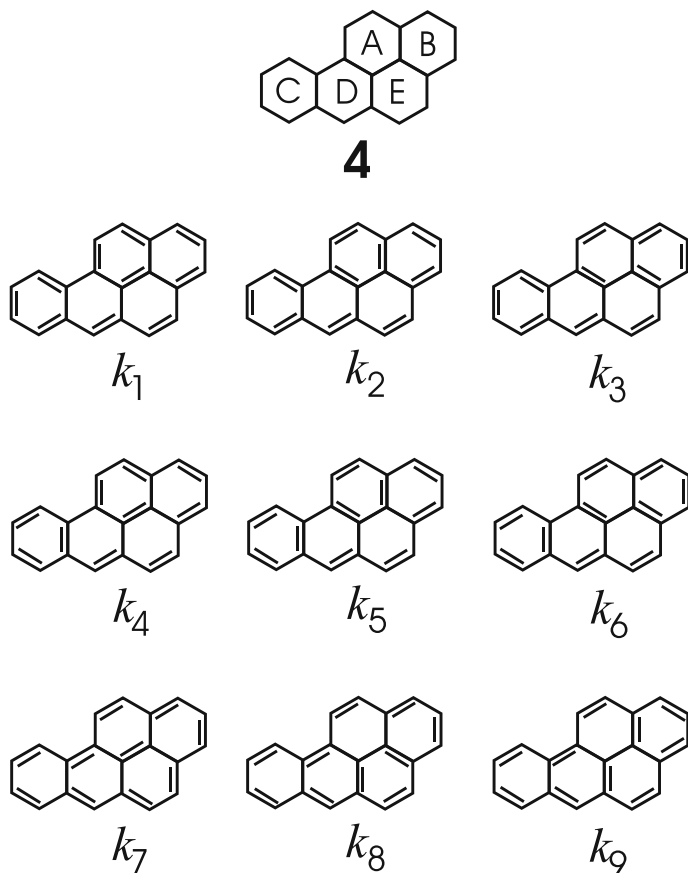


Fig. 11.2 Benzo[*a*]pyrene (4) and its nine Kekulé structures. The Kekulé structure count is traditionally denoted by K . Thus, for benzo[*a*]pyrene, $K = 9$

- (2) the determinant of the Hamiltonian matrix in Hückel molecular orbital (HMO) theory (after setting $\alpha = 0$ and $\beta = 1$), is equal to K^2 [15].

Eventually, other Kekulé–structure–based relations between valence bond and molecular orbital theories were discovered [16–21].

Already in the seminal paper by Dewar and Longuet–Higgins [15], it was established that the K^2 -regularity does not hold for all polycyclic conjugated π -electron systems, and that corrections for the “parity” of Kekulé structures need to be taken into account. This became the concept of “algebraic structure count” [22, 23], which was later shown to be not applicable to all non-alternant conjugated hydrocarbons [24, 25]. The fortunate fact is that all Kekulé structures of benzenoid hydrocarbons have the same “parity” [20], which has the consequences that all Kekulé–structure–based models work best for benzenoid systems. Also in this

survey, the conjugated π -electron systems considered (mainly benzenoid hydrocarbons) belong to the class of species whose Kekulé structures have equal “parity”.

Another reason for the increase of interest to Kekulé–structure–based studies was the recognition that in mathematics there exists a fully equivalent notion, namely the concept of *perfect matching* (or, in an earlier terminology, of *1-factor*) [26–28]. This soon resulted in various mathematics–oriented researches on Kekulé structures, see e.g. [29, 30] (which are not the concern of the present survey).

Anyway, beginning with the 1970s, a number of approaches was put forward, all based on counting or examination of Kekulé structures (and only Kekulé structures!), all offering reasonably good quantitative prediction of various molecular properties. We provide a short survey of these methods in the subsequent section.

11.2 Kekulé–Structure–Based Approaches: Success

11.2.1 Resonance Theory

In 1973 William Herndon put forward a resonance–theoretical model, according to which he was able to calculate the resonance energies of benzenoid hydrocarbons with accuracy tantamount to the best (in that time) molecular–orbital theories [31]. Let it be mentioned that similar ideas were proposed by Simpson in 1953 [32], but in that time had little impact.

In Herndon’s resonance theory, the basic assumption is that Kekulé structures alone suffice to describe the π -electron configuration of the ground state of a conjugated hydrocarbon. The respective wave function is of the form

$$|\Psi\rangle = \frac{1}{\sqrt{K}} \sum_{i=1}^K |k_i\rangle \quad (11.2)$$

where $|k_i\rangle$ is the wave function associated to the Kekulé structure k_i , $i = 1, 2, \dots, K$. The resonance energy is then calculated as

$$RE = \frac{2}{K} \sum_{1 \leq i < j \leq K} \langle k_i | \hat{H} | k_j \rangle \quad (11.3)$$

where \hat{H} is a formal Hamiltonian operator and $\langle k_i | \hat{H} | k_j \rangle$ are the corresponding matrix elements. In Herndon’s model

$$\langle k_i | \hat{H} | k_j \rangle = \gamma_1 = 0.841 \text{ eV}$$

if the Kekulé structures k_i and k_j differ in the position of exactly three double bonds,

$$\langle k_i | \hat{H} | k_j \rangle = \gamma_2 = 0.336 \text{ eV}$$

if the Kekulé structures k_i and k_j differ in the position of exactly five double bonds, and

$$\langle k_i | \hat{H} | k_j \rangle = 0$$

if the Kekulé structures k_i and k_j differ in the position of more than five double bonds.

For example, in the case of benzo[*a*]pyrene, with notation defined in Fig. 11.2, $\langle k_1 | \hat{H} | k_4 \rangle = \langle k_4 | \hat{H} | k_5 \rangle = \gamma_1$, $\langle k_1 | \hat{H} | k_3 \rangle = \langle k_3 | \hat{H} | k_8 \rangle = \gamma_2$, $\langle k_1 | \hat{H} | k_5 \rangle = \langle k_1 | \hat{H} | k_9 \rangle = 0$.

For more details on Herndon resonance theory see [33–37] and in the book [38, pp. 66–70].

Instead of the abstract and chemists–unfriendly expressions of the kind (11.2) and (11.3), simplified resonance–theoretical approaches became popular, based only on counting of Kekulé structures, i.e., on the number K .

Relating resonance energy and aromaticity of benzenoid molecules directly with the number of Kekulé structures has a long history [9, 39, 40]. It was generally believed (and accepted as self-evident) that among benzenoid isomers, stability/aromaticity increases with their K -values [41]. Of a variety of K -dependent expressions for resonance energy, we mention here that of Swinborne–Sheldrake [42]

$$RE = 1.185 \ln K \text{ (eV)} \quad (11.4)$$

similar to a much older formula by Carter [43], and the countless works on K -dependence of HMO total π -electron energy, e.g. [44–49], the reviews [50, 51] and the book [38, pp. 70–73].

A strong argument in favor of K -based considerations is the fact that no benzenoid hydrocarbon without Kekulé structure has ever been obtained, in spite of several synthetic attempts [52, 53]; for more details on the $K = 0$ case see [38, pp. 62–66].

By using Kekulé structure count, it was attempted to rationalize thermochemical parameters of benzenoid hydrocarbons [54–56], as well as their reactivities [57–62] and ionization potentials [63, 64].

11.2.2 Conjugated Circuits

The fact that different parts of a polycyclic conjugated molecule may possess different degrees of aromaticity, motivated Milan Randić to propose a simple criterion for “local aromaticity” [65]. His “index of local aromaticity” is defined as

$$ILA(R) = \frac{2K(BH - R)}{K(BH)} \quad (11.5)$$

where BH is a benzenoid molecule and $BH - R$ is the fragment obtained by deleting the ring R from BH . The ring R is usually assumed to be 6-membered.

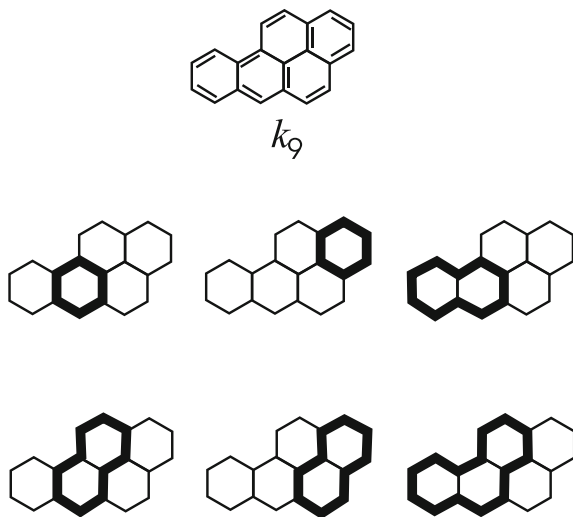
It can be easily seen that $2K(BH - R)$ is just the number of Kekulé structures of BH in which the ring R possesses three double bonds. For example, for the five rings of benzo[*a*]pyrene (see Fig. 11.2), $ILA(A) = 4/9$, $ILA(B) = 6/9$, $ILA(C) = 6/9$, $ILA(D) = 4/9$, and $ILA(E) = 2/9$. Consequently, the ring E would be the least aromatic domain of benzo[*a*]pyrene, whereas the rings B and C would have the greatest aromatic character.

The simple ILA -approach was eventually extended to the “conjugated circuit model” [66–70].

A “conjugated circuit” is a cyclic arrangement of single and double bonds in a Kekulé structure, such that each single bond is followed by a double bond, and vice versa. (In mathematics, this is called an alternating cycle of a perfect matching [28]). In Kekulé structures of benzenoid hydrocarbons, only conjugated circuits of size $4n + 2$ (i.e., 6, 10, 14, 18, ...) may occur [71]. For example, the Kekulé structure k_9 of benzo[*a*]pyrene (see Fig. 11.2) has 2 conjugated circuits of size 6, three conjugated circuits of size 10, and one conjugated circuit of size 14. These are shown in Fig. 11.3.

According to the conjugated circuit model, for $n = 1, 2, 3, \dots$, one has to determine the number ρ_n of conjugated circuits of size $4n + 2$ in all Kekulé structures of the underlying benzenoid system, and compute the resonance energy as

Fig. 11.3 A Kekulé structure of benzo[*a*]pyrene (denoted by k_9 in Fig. 11.2), and the conjugated circuits contained in it



$$RE = \frac{1}{K} \sum_{n \geq 1} \rho_n R_n \quad (11.6)$$

where R_n , $n = 1, 2, 3, \dots$ are parameters whose values are adjusted so as to best reproduce molecular-orbital resonance energies. In [72], the following values were recommended:

$$R_1 = 0.869 \text{ eV}, R_2 = 0.247 \text{ eV}, R_3 = 0.100 \text{ eV}$$

and $R_k = 0$ for $k \geq 4$ (see also [73]). More details on the conjugated circuits model and on its relation to Herndon and Clar resonance theory can be found in [38, pp. 79–91] and [74].

11.2.3 π -Electron Content of Rings

In a series of papers published in 2004 [75–78], Milan Randić and Alexandru Balaban elaborated a Kekulé-structure-based method for partitioning the π -electrons into individual rings of a polycyclic conjugated molecule. Their method is quite simple: If a double bond in a Kekulé structure belongs solely to a particular ring, then two π -electrons are assumed to belong to this ring. If a double bond is shared between two rings, then one π -electron is assumed to belong to each ring. By this, an “algebraic Kekulé structure” is generated [79, 80]. The actual partition of π -electron is then obtained as an arithmetic average over all Kekulé structures.

In Fig. 11.4 the concept of algebraic Kekulé structures is illustrated by two examples. In Fig. 11.5 we show how the π -electrons are partitioned in phenanthrene. It is convenient to interpret the thus obtained numbers as the π -electron

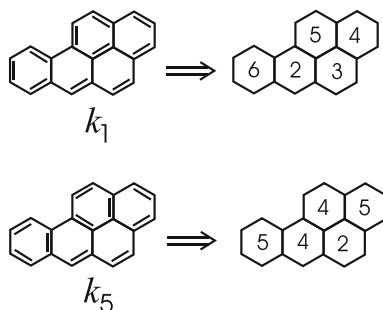


Fig. 11.4 Two Kekulé structures of benzo[*a*]pyrene (denoted by k_1 and k_5 in Fig. 11.2), and the algebraic Kekulé structures associated to them. Note that the correspondence between Kekulé structures and algebraic Kekulé structures is not one-to-one [80]

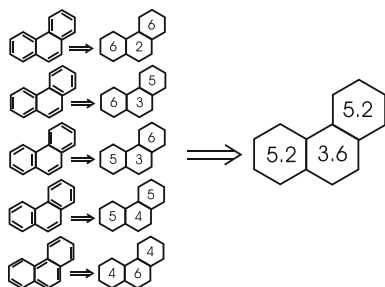


Fig. 11.5 Calculation of π -electron content of rings of phenanthrene. Note that $\frac{1}{5}(6 + 5 + 6 + 5 + 4) = 5.2$, $\frac{1}{5}(2 + 3 + 3 + 4 + 6) = 3.6$, and $\frac{1}{5}(6 + 6 + 5 + 5 + 4) = 5.2$

content of the respective rings [81]. In most cases, their values excellently agree with other measures of local aromaticity [82–84].

At this point it is worth mentioning that recent studies showed that in the case of very large polycyclic π -electron systems (graphenes), one needs to distinguish between local and global features of aromaticity [85].

11.2.4 Carbon–Carbon Bond Lengths

Although Pauling, Brockway and Beach [13] used Kekulé structures for calculating carbon–carbon bond lengths in conjugated molecules already in the 1930s, the true beginning of this approach was in 1970s, when Herndon published his papers [33, 86, 87]. In these and subsequent works, e.g. [88–91], numerous examples have been offered, supporting the claim that by means of Pauling bond orders, Eq. (11.1), one can predict bond lengths with an accuracy equal to the accuracy of experimental data (of that time). For what follows, it is only important that carbon–carbon bond lengths are expected to be a monotonically decreasing function of the respective Pauling bond order. Several such functional dependencies were proposed, for example, the length r_{ij} of the bond ij can be calculated as [89]

$$r_{ij} = r_s - (r_s - r_d) \frac{1.84 P(ij)}{0.84 P(ij) + 1} \text{ (pm)} \quad (11.7)$$

where r_s and r_d are the lengths of a single and double bond, respectively, between sp^2 -hybridized carbon atoms, $r_s = 150.4$ pm, $r_d = 133.4$ pm.

For more details on the Pauling bond order see [38, pp. 73–76].

11.2.5 Induced π -Electron Currents

As a relatively recent Kekulé–structure–based application, a method for calculating induced currents of π -electrons in a polycyclic conjugated molecule placed in a magnetic field was proposed by Randić [92]. Such “ring currents” [93] are traditionally related with aromaticity of the underlying π -electron system [94–99]. For benzenoid hydrocarbons, the procedure proposed by Randić proceeds as follows:

- (1) All Kekulé structures have to be constructed.
- (2) All conjugated circuits in all Kekulé structures have to be recognized.
- (3) The edges in each conjugated circuit have to be directed in an anti-clockwise manner, representing a “current”.
- (4) The “currents” thus obtained have to be superimposed over all conjugated circuits of all Kekulé structures.

Randić and his coworkers have offered a number of examples [92, 100–104] in which their results appear to be in a reasonably good agreement with π -electron current densities obtained by *ab initio* quantum chemical computations.

11.2.6 Comments

The Kekulé–structure–based models briefly outlined in the previous parts of this section, have been corroborated by numerous examples (mainly benzenoid hydrocarbons) and—statistically speaking—give chemically satisfactory results. In the subsequent section we will show that there exist cases in which these models fail, sometimes completely disagreeing with experimental findings.

At this point we call the reader’s attention to a detail that sometimes is overlooked. All models described above give equal importance to each Kekulé structure. This is explicitly visible from Eqs. (11.2), (11.3), and (11.6), and implicitly from any approach in which the simple count of Kekulé structures (i.e., K) or averaging over all Kekulé structures is encountered.

On the other hand, it was recognized quite early [105] that some Kekulé structures give a better description of the actual molecule than others. Attempts to incorporate this feature into resonance theoretical models [106–108] did not gain much popularity. It may be that such distinguishing between Kekulé structures is not at all justified. When the Pauling bond order concept was modified, by giving different weights to different Kekulé structures (in line with the “Fries rule”), the accuracy of the calculated bond lengths did not significantly improve [108].

Here must be mentioned the “aromatic sextet theory” developed by Erich Clar [109], within which some Kekulé structures are represented via “Clar formulas” whereas some are fully ignored. Details of Clar’s theory can be found in [38, pp. 93–116] and [109, 110], but cannot be further elaborated in this survey.

11.3 Kekulé–Structure–Based Approaches: Failures

11.3.1 Minor Violations

In the 1970s, George Hall noticed that the HMO total π -electron energy of isomeric benzenoid hydrocarbons is remarkably well linearly correlated with their K -values [44, 111]. This, so-called “Hall rule” is just what chemists would expect from the dependence of thermodynamic stability of benzenoids on the number of Kekulé structures. Eventually, it was shown that this dependence is not linear [49, 112, 113], and that it is violated in numerous cases [114]. Along the same lines, Cioslowski and Dobrowolski established that there is a complete lack of correlation between the ab initio π -electron energy and Kekulé structure count of benzenoid isomers [115].

There exist polycyclic conjugated systems possessing many fixed single and double bonds, i.e., bonds that are single (resp. double) in all Kekulé structures [116–118]; examples are depicted in Fig. 11.6.

The pattern of cyclic conjugation in such molecules was found to be far from what their Kekulé structures would infer [119]. The Pauling bond orders of fixed single and double bonds are, respectively, zero and unity, and one might expect that the carbon–carbon bond lengths in such conjugated systems would alternate between ca. 150 pm (for single) and ca. 133 pm (for double). The geometries of such molecules, determined by ab initio DFT calculations [120, 121] completely disagreed from this Kekulé–structure–based prediction. Moreover, some molecules of this kind were shown to have diradical character and a triplet ground state [122, 123].

The above examples may be understood as an indication that theoretical models based on Kekulé structures fail in some exceptional, sporadic, borderline cases. In the subsequent sections were point out some more serious, systematic shortcomings of Kekulé–structure–based models.

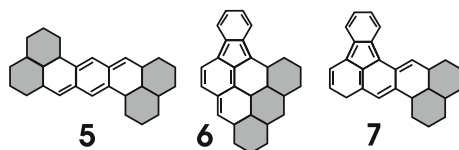


Fig. 11.6 Examples of polycyclic conjugated systems with large number of fixed double bonds. The part of the molecule where the double bonds are not fixed is indicated by shading. The compounds **5**, **6**, and **7** have 9, 4, and 3 Kekulé structures, respectively

11.3.2 The Perylene Anomaly

Perylene (compound **8** in Fig. 11.7) is the simplest benzenoid hydrocarbon with fixed single carbon–carbon bonds. These are the two vertical bonds belonging to the ring E of **8**. The fact that these are fixed single bonds can be verified by inspecting the Kekulé structures of perylene, depicted in Fig. 11.8.

In Fig. 11.8 is also shown the general form of a benzenoid system **P** with fixed carbon–carbon bonds. Such systems are obtained by joining two benzenoid fragments **X** and **Y** which both must possess Kekulé structures. (In case of perylene, **X** = **Y** = naphthalene, and $n = 1$.) Then the bonds drawn vertically in the diagram **P**, belonging to the rings E_1, E_2, \dots, E_n , are single in all Kekulé structures of **P**.

All Kekulé–structure–based theoretical models predict that there is no π -electron conjugation in the rings E_1, E_2, \dots, E_n . In particular, $ILA(E_i) = 0$, $i = 1, 2, \dots, n$,

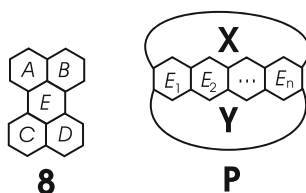
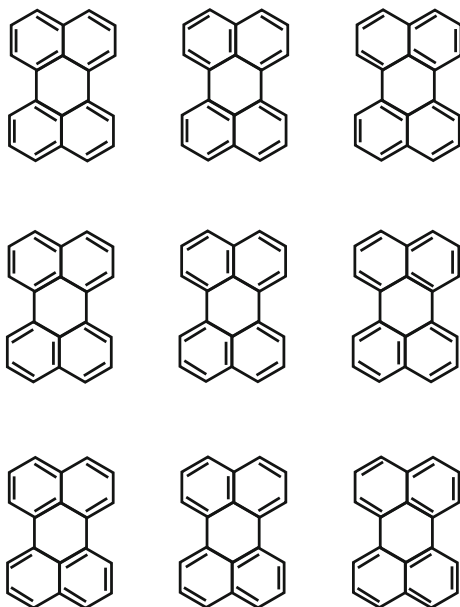


Fig. 11.7 Perylene (**8**) and the general formula **P** of a benzenoid system with fixed single bonds, $K(\mathbf{X}) > 0$, $K(\mathbf{Y}) > 0$

Fig. 11.8 The Kekulé structures of perylene. By direct calculation (cf. Fig. 11.5) one gets that the π -electron content of each of the four peripheral rings is $42/9 = 4.67$, whereas the central ring contains in average only $12/9 = 1.67$ π -electrons



cf. Eq. (11.5). These rings do not contain, and are not embraced by any, conjugated circuit. Their π -electron contents are small (but non-zero), never exceeding 2.00. For both Herndon resonance energy, Eq. (11.3), Swinborne–Sheldarke resonance energy, Eq. (11.4), and conjugated–circuits resonance energy, Eq. (11.6),

$$RE(\mathbf{P}) = RE(\mathbf{X}) + RE(\mathbf{Y}).$$

In addition, it can be easily verified [116] that $K(\mathbf{P}) = K(\mathbf{X}) \cdot K(\mathbf{Y})$.

Randić's model of induced π -electron currents predicts zero current through the “vertical” bonds of the rings E_1, E_2, \dots, E_n .

Of course, a sober chemist would never consider the above stated “predictions” of properties of the benzenoid systems \mathbf{P} as something absolutely true, but rather as a more-or-less plausible approximation. Thus, the above Kekulé–structure–based claims should be understood as follows:

- (1) The local aromaticity of the rings E_1, E_2, \dots, E_n is small, significantly smaller than that of other rings of \mathbf{P} .
- (2) The extent of cyclic conjugation in these rings is small, significantly smaller than that in other rings of \mathbf{P} .
- (3) The π -electron contents of these rings is small, significantly smaller than that of other rings of \mathbf{P} .
- (4) The difference of resonance energies

$$RE(\mathbf{P}) - [RE(\mathbf{X}) + RE(\mathbf{Y})]$$

is small, but non-zero.

- (5) The induced π -electron current through the fixed single bonds of \mathbf{P} is small but non-zero.

The statements (1)–(5) can be checked by other, Kekulé–structure–independent, theoretical methods. By this, the Kekulé–structure–based models can be tested, and their general applicability either verified or refuted.

We begin with a good news.

The extent of cyclic conjugation can be estimated by a molecular–orbital–based method, whose details are described elsewhere (see the survey [124], the recent papers [125–128], and the references cited therein). This method renders the π -electron energy–effect $ef(BH, R)$ of the rings R of a polycyclic conjugated hydrocarbon BH . The greater the (positive) ef -value, the greater is the thermodynamic stabilization caused by cyclic conjugation in the underlying ring R . The ef -values may be viewed as a measure of local aromaticity [129–132].

Now, the ef -method gives the following results for perylene (with rings labeled as in Fig. 11.8): $ef(\mathbf{8}, A) = ef(\mathbf{8}, B) = ef(\mathbf{8}, C) = ef(\mathbf{8}, D) = 0.1093$ and $ef(\mathbf{8}, E) = 0.0218$ [133]. These are in a fairly good agreement with the Kekulé–structure–based predictions: the extent of cyclic conjugation in the central ring of perylene is found to be ca. five times weaker than in its four peripheral rings.

Table 11.1 HOMA values of the rings of the first seven members of the perylene/bisanthrene series (\mathbf{P}_n) [142]

n	E_1	E_2	E_3	E_4	F_1	F_2	F_3	F_4
1	0.0125				0.7735			
2	0.2675				0.7031	0.6966		
3	0.3271	0.5777			0.6981	0.6539		
4	0.3333	0.6398			0.7199	0.6431	0.6090	
5	0.3253	0.6358	0.6358		0.7352	0.6508	0.5928	
6	0.3377	0.6259	0.7202		0.7687	0.6634	0.5886	0.5681
7	0.3311	0.6134	0.6864	0.7053	0.7482	0.6653	0.6010	0.5770

The labeling of the rings is indicated in Fig. 11.10. Only the data for symmetry-nonequivalent rings are given. The greater HOMA is, the higher is the local aromaticity and cyclic conjugation in the underlying ring. Observe that the HOMA values of some E -type rings exceed those of F -type rings, contrary to what Kekulé–structure–based models would predict

Other, DFT-based, calculations also indicate that the properties of perylene are in good agreement with the predictions inferred from their Kekulé structures; see the data for \mathbf{P}_1 given in Tables 11.1, 11.2, 11.3 and in Fig. 11.11.

In the case of monobenzo-annulated perylenes, the situation is similar: in benzo[a]perylene (**9**) and benzo[b]perylene (**10**), the ef -values of the central ring have been only slightly changed relative to perylene, see Fig. 11.9. (The decrease and increase of the magnitude of cyclic conjugation caused, respectively, by a - and b -type benzo-annulation, was later found to be a general regularity [134–138].)

Now the bad news start.

The extent of cyclic conjugation in the central “empty” ring of benzo[b]perylene is somewhat greater than in non-annulated perylene. Because perylene has three additional annulation sites symmetry-equivalent to position b , namely, positions f, k, o , the effect observed at benzo[b]perylene can be magnified by considering tetra-benzo[b, f, k, o]perylene (**11**, Fig. 11.9). In this derivative of perylene, cyclic conjugation in the central “empty” ring, $ef(\mathbf{11}, E) = 0.0522$, exceeds that of the normal, naphthalene-like rings, $ef(\mathbf{11}, A) = ef(\mathbf{11}, B) = ef(\mathbf{11}, C) = ef(\mathbf{11}, D) = 0.0437$,

Table 11.2 NICS values (with virtual charge located 1 Å above the center of the ring) for the same molecules/rings as in Table 11.1 [142]

n	E_1	E_2	E_3	E_4	F_1	F_2	F_3	F_4
1	+2.77				−8.38			
2	+2.71				−7.32	−7.60		
3	+2.14	−0.04			−7.11	−5.95		
4	+2.25	−2.82			−7.58	−5.27	−3.16	
5	+2.81	−3.69	−7.09		−8.30	−5.73	−2.00	
6	−1.17	−9.48	−15.65		−10.04	−9.13	−5.57	−4.01
7	+0.09	−7.35	−13.55	−15.76	−9.95	−9.66	−6.65	−4.67

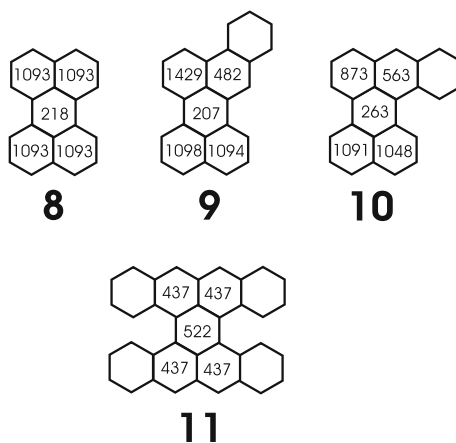
The more negative NICS is, the higher is the local aromaticity and cyclic conjugation in the underlying ring. Observe that the NICS values of some E -type rings are more negative than those of F -type rings, contrary to what Kekulé–structure–based models would predict

Table 11.3 SCI values for the same molecules/rings as in Table 11.1 [142]

n	E_1	E_2	E_3	E_4	F_1	F_2	F_3	F_4
1	0.0033				0.0237			
2	0.0050				0.0196	0.0148		
3	0.0058	0.0080			0.0190	0.0121		
4	0.0060	0.0092			0.0196	0.0114	0.0094	
5	0.0057	0.0092	0.0105		0.0201	0.0116	0.0088	
6	0.0051	0.0087	0.0112		0.0212	0.0117	0.0083	0.0074
7	0.0052	0.0084	0.0102	0.0108	0.0206	0.0120	0.0089	0.0079

The greater SCI is, the higher is the local aromaticity and cyclic conjugation in the underlying ring. Observe that the SCI values of some E -type rings exceed those of F -type rings, contrary to what Kekulé–structure–based models would predict

Fig. 11.9 Energy effects of the rings of perylene (**8**), benzo[*a*]perylene (**9**), benzo[*b*]perylene (**10**), and tetrabenzo[*b,f,k,o*]perylene (**11**). For the sake of simplicity, the ef -values are multiplied by 10,000



and is by no means “significantly smaller”, as expected from the softened interpretation of Kekulé–structure–based models [133].

Analogous violations of the Kekulé–structure–based modes of cyclic conjugation were found also at other *b,f,k,o*-annelated perylenes [139].

The “anomaly” of local aromaticity of the central ring in benzo-annelated perylenes was eventually confirmed by other quantum chemical (DFT) calculations [140]. For additional studies along these lines see [126].

11.3.3 Anomalies in the Perylene/Bisanthrene Homologous Series

An obvious argument against exemplifying the shortcomings of the Kekulé–structure–based models by means of *b,f,k,o*-annelated perylenes is that these are

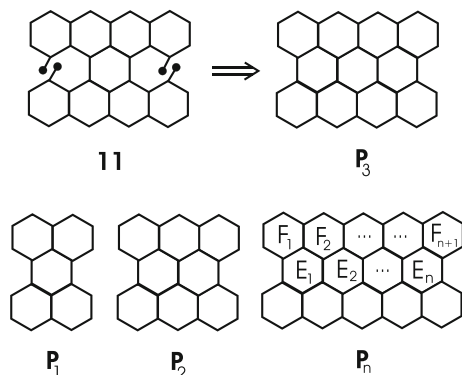


Fig. 11.10 Transforming tetrabenzo[*b,f,k,o*]perylene (**11**) into the third member (**P₃**) of the perylene/bisanthrene homologous series. Here **P₁** = perylene, and **P₂** = bisanthrene. The benzenoid molecules **P_n**, $n = 1, 2, 3, \dots$, are the simplest representatives of the conjugated π -electron system **P**, depicted in Fig. 11.7

highly strained, non-planar molecules, the consequence of repulsion between four near-lying hydrogen atoms (see diagram **11** in Fig. 11.10). A direct formal way to overcome this problem is to eliminate the overcrowded *H*-atoms by introducing two new carbon–carbon bonds, see Fig. 11.10. This leads to the perylene/bisanthrene homologous series, whose π -electron properties have been studied in due detail [141–143]. For these benzenoid species, whose geometries are strictly planar, a number of remarkable deviations from the Kekulé–structure–inferred picture could be established.

In addition to the *ef*-method, other criteria of cyclic conjugation and local aromaticity have also been utilized, all based on accurate DFT calculations. These were the “harmonic oscillator model of aromaticity”, HOMA [144–146], “nucleus-independent chemical shifts”, NICS [147, 148], and “six-center indices”, SCI [149, 150]. (For details on multi-center indices of aromaticity, see [99].)

Results pertaining to the “empty” rings E_1, E_2, \dots, E_n and the “full” rings F_1, F_2, \dots, F_{n+1} of **P_n** (see Fig. 11.10), for $n = 1, 2, \dots, 7$ are shown in Tables 11.1, 11.2 and 11.3. The data in Tables 11.1, 11.2 and 11.3 were obtained by using the Gaussian 09 W package, version 0.1, at the B3LYP/6-311+(G(d,p) level of theory [142].

Induced currents densities in the perylene/bisanthrene family were also calculated [143] (see also [151]); characteristic results are depicted in Fig. 11.11. The respective geometries were optimized by the B3LYP/6-311+G(d,p) method, using Gaussian 03. Current densities were computed by means of coupled HF theory, using the diamagnetic-zero variant of the CTOCD method [143].

From the data shown in Tables 11.1, 11.2, 11.3 and Fig. 11.11 one concludes the following:

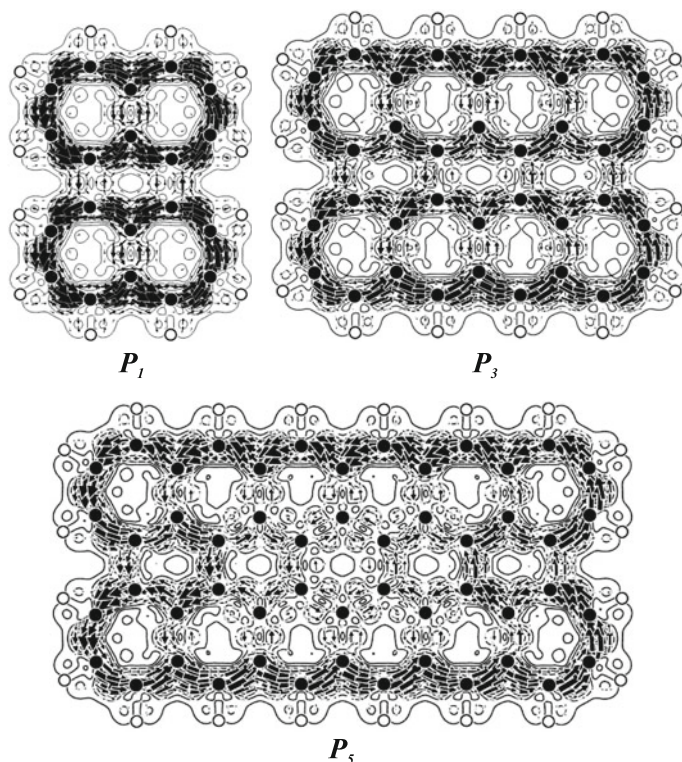


Fig. 11.11 Current density maps of three members of the perylene/bisanthrene homologous series, cf. Fig. 11.10. Whereas the currents in perylene (\mathbf{P}_1) are localized mainly in the two naphthalene fragments, in the case of \mathbf{P}_5 the dominating part of the current goes through some fixed single bonds, forming a peculiar pattern that embraces the “empty” rings E_1 and E_5 . The case of \mathbf{P}_3 is borderline

- (1) The predictions of Kekulé–structure–based models are reasonably correct in case of the first few members of the perylene/bisanthrene family \mathbf{P}_n , especially for $n = 1$ and $n = 2$.
- (2) In the case of higher member of this family, \mathbf{P}_n , $n \geq 5$, there are significant violations of the Kekulé–structure–based predictions. The magnitude of cyclic conjugation in the rings lying near the center of the “empty” ring-system E_1, E_2, \dots, E_n is high and surpasses the cyclic conjugation of some of the rings belonging to the “full” ring-system F_1, F_2, \dots, F_{n+1} .
- (3) The central domain of the higher members of the perylene/bisanthrene series has a pronounced degree of local aromaticity, not anticipated by any of the Kekulé–structure–based models.
- (4) The behavior of the members of the \mathbf{P}_n series for $n = 3$ and $n = 4$ is borderline.

11.3.4 Chevrons—the Ultimate Anomaly

The partisans of Kekulé–structure–based models may argue that all examples considered in the previous subsections contain fixed single and double bonds, and that their models actually work only if such fixed bonds are absent. To their dismay, we now describe a case of “anomalous” behavior in benzenoid systems in which no carbon–carbon bond is fixed.

In this subsection we focus our attention to a class of benzenoid molecules called “chevrons” (see in the book [116, pp. 110–120], in [152, 153], and in Fig. 11.12).

The chevron \mathbf{Ch}_n has $\frac{1}{6}(n+1)(n+2)(2n+3)$ Kekulé structures, and none of its carbon–carbon bonds is fixed. In other words, the Pauling bond orders, Eq. (11.1), satisfy the condition $0 < P(ij) < 1$, i.e., for no bond ij is the Pauling bond order equal to zero or to unity.

For the rung carbon–carbon bonds $b_0, b_1, b_2, \dots, b_{n-1}, b_n$, as indicated in Fig. 11.12, direct calculation yields for the Pauling bond order [153]:

$$P(b_i) = \frac{6(n+1-i)^2}{(n+1)(n+2)(2n+3)}. \quad (11.8)$$

The right–hand side of Eq. (11.8) is a monotonically decreasing function of the parameter i , implying

$$P(b_0) > P(b_1) > P(b_2) > \dots > P(b_{n-1}) > P(b_n)$$

from which Kekulé–structure–based reasoning predicts that the lengths r_i of the rung carbon–carbon bonds $b_0, b_1, b_2, \dots, b_{n-1}, b_n$ should satisfy the conditions

$$r_0 < r_1 < r_2 < \dots < r_{n-1} < r_n. \quad (11.9)$$

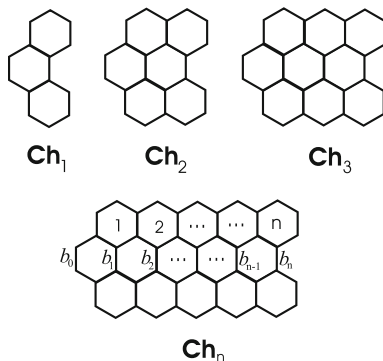


Fig. 11.12 The chevron homologous series. Formally, these are related to the perylene/bisanthrene series: \mathbf{Ch}_2 may be viewed as benzo[*cde*]perylene, \mathbf{Ch}_3 as benzo[*cde*]bisanthrene, etc.

Table 11.4 Length (in pm) of the rung carbon–carbon bonds in the first few members of the chevron homologous series Ch_n [153]

n	r_0	r_1	r_2	r_3	r_4	r_5	r_6	r_7	r_8
2	137.2	142.6	146.8						
3	138.3	142.2	142.2	147.1					
4	138.8	142.5	143.2	144.1	147.2				
5	139.0	142.8	143.3	143.3	144.1	147.2			
6	138.9	142.9	143.4	143.4	143.3	144.2	147.2		
7	138.9	142.9	143.6	143.5	143.4	143.4	144.2	147.2	
8	138.8	142.9	143.6	143.6	143.5	143.4	143.4	144.2	147.2

Observe that the ordering $r_i < r_{i+1}$, required by the Kekulé–structure–inferred Eq. (11.9), is obeyed for $n = 2, 3, 4, 5$, but is violated for $n = 7$ and $n = 8$, whereas the case $n = 6$ is borderline

The validity of inequalities (11.9) can be checked by Kekulé–structure–independent approaches. In [153], the geometries of the chevron molecules Ch_n , $n = 2, 3, \dots, 8$, were calculated by means of the B3LYP/6-311G(d,p) method. The optimized geometries of all studied molecules were found to be perfectly planar and to correspond to minima on the potential energy hypersurface. The lengths of the rung carbon–carbon bonds are collected in Table 11.4. As seen, the ordering (11.9) is violated, beginning at $n = 6$.

To be on the safe side, corrections for the effect of strain caused by the two near-lying hydrogen atoms were made [153], but these did not change our main conclusion:

Because of the perfect planarity of the molecules and negligible steric strain, the chevron homologous series appears to be completely suitable for applying any of the Kekulé–structure–based models. According to Pauling–bond–order considerations, the lengths of the rung bonds should monotonically increase, Eq. (11.9). This, indeed, is the case only for the first members of the series, but it is evidently violated for the higher members, where the bond lengths first increase, then decrease reaching a minimum around the center of the chain, and then increase again.

Thus the breakdown of the Kekulé–structure–based arguments could happen also within a class of “good”, fully conjugated benzenoid hydrocarbons.

11.4 Conclusion

The results outlined in this chapter suggest that the Kekulé–structure–based approaches in the theory of polycyclic conjugated compounds, and benzenoid hydrocarbons in particular, although leading to acceptable conclusions in many cases, are not generally valid and fail in some cases. Therefore, if such approaches will continue to be used in the future, this should be done with a great deal of care and caution.

References

1. Wizinger-Aust R, Gillis JB, Helferich B, Wurster C (1966) Kekulé und seine Benzolformel. Verlag Chemie, Weinheim
2. Bugge G (1979) Das Buch der Grossen Chemiker II. Verlag Chemie, Weinheim, pp 200–216
3. Hückel E (1931) Quantentheoretische Beiträge zum Benzolproblem I. Die Elektronenkonfiguration des Benzols und verwandter Verbindungen. *Z Phys* 70:204–286
4. Hückel E (1940) Grundzüge der Theorie ungesättigter und aromatischer Verbindungen. Verlag Chemie, Berlin
5. Pauling L, Wheland GW (1933) The nature of the chemical bond. V. The quantum-mechanical calculation of the resonance energy of benzene and naphthalene and the hydrocarbon free radicals. *J Chem Phys* 1:362–374
6. Pauling L, Sherman J (1933) The nature of the chemical bond. VI. The calculation from thermochemical data of the energy of resonance of molecules among several electronic structures. *J Chem Phys* 1:606–617
7. Pauling L (1945) The nature of the chemical bond. Cornell Univ. Press, Ithaca
8. Gallup GA (2002) A short history of valence bond theory. In: Cooper DL (ed) Valence bond theory. Elsevier, Amsterdam, pp 1–37
9. Wheland GW (1955) Resonance in organic chemistry. Wiley, New York
11. Klein DJ (1983) Valence bond theory for conjugated hydrocarbons. *Pure Appl Chem* 55:299–306
11. Klein DJ, Seitz WA (1988) Pauling-Wheland resonance theory of benzenoid hydrocarbons. *J Mol Struct (Theochem)* 169:167–181
12. Klein DJ (1990) Semiempirical valence bond views for benzenoid hydrocarbons. *Topics Curr Chem* 153:57–83
13. Pauling L, Brockway LO, Beach JY (1935) The dependence of interatomic distance on single bond—double bond resonance. *J Am Chem Soc* 57:2705–2709
14. Longuet-Higgins HC (1950) Resonance structures and MO in unsaturated hydrocarbons. *J Chem Phys* 18:265–274
15. Dewar MSJ, Longuet-Higgins HC (1952) The correspondence between the resonance and molecular orbital theories. *Proc Roy Soc Lond A* 214:482–493
16. Ham NS (1958) Mobile bond orders in the resonance and molecular orbital theories. *J Chem Phys* 29:1229–1231
17. Ham NS, Ruedenberg K (1958) Mobile bond orders in conjugated systems. *J Chem Phys* 29:1215–1223
18. Heilbronner E (1962) Über einen graphentheoretischen Zusammenhang zwischen dem Hückel'schen MO-Verfahren und dem Formalismus der Resonanztheorie. *Helv Chim Acta* 50:1722–1725
19. Herndon WC (1973) Enumeration of resonance structures. *Tetrahedron* 29:3–12
20. Cvetković D, Gutman I, Trinajstić N (1974) Graph theory and molecular orbitals. VII. The role of resonance structures. *J Chem Phys* 61:2700–2706
21. Kiang YS (1980) Determinant of adjacency matrix and Kekulé structures. *Int J Quantum Chem Quantum Chem Symp* 14:541–547
22. Wilcox CF (1968) Stability of molecules containing $(4n)$ -rings. *Tetrahedron Lett* 9:795–800
23. Wilcox CF (1969) Stability of molecules containing nonalternant rings. *J Am Chem Soc* 91:2732–2736
24. Gutman I, Trinajstić N (1975) On the parity of Kekulé structures. *Croat Chem Acta* 47:35–39
25. Gutman I, Randić M, Trinajstić N (1978) Kekulé structures and topology. III. On inseparability of Kekulé structures. *Rev Roum Chim* 23:383–395
26. Cvetković D, Gutman I, Trinajstić N (1972) Kekulé structures and topology. *Chem Phys Lett* 16:614–616
27. Graovac A, Gutman I, Trinajstić N (1977) Topological approach to the chemistry of conjugated molecules. Springer, Berlin

28. Lovász L, Plummer MD (1986) Matching theory. North-Holland, Amsterdam
29. Zhang H (2006) Z-Transformation graphs of perfect matchings of plane bipartite graphs: a survey. MATCH Commun Math Comput Chem 56:457–476
30. Vukičević D (2011) Applications of perfect matchings in chemistry. In: Dehmer M (ed) Structural analysis of complex networks. Birkhäuser, Dordrecht, pp 463–482
31. Herndon WC (1973) Resonance energies of aromatic hydrocarbons. A quantitative test of resonance theory. J Am Chem Soc 95:2404–2406
32. Simpson WT (1953) On the use of structures as an aid in understanding π -electron spectra. J Am Chem Soc 75:597–603
33. Herndon WC (1974) Resonance theory and the enumeration of Kekulé structures. J Chem Educ 51:10–15
34. Herndon WC, Ellzey ML (1974) Resonance theory. V. Resonance energies of benzenoid and nonbenzenoid π systems. J Am Chem Soc 96:6631–6642
35. Herndon WC (1980) Structure–resonance theory—A review of applications to π -hydrocarbon systems. Israel J Chem 20:270–275
36. Herndon WC (1981) Notes on valence bond theory, structure–resonance theory, and graph theory. MATCH Commun Math Comput Chem 11:3–11
37. Klein DJ, Schmalz TG (1989) Exact ground state for a Herndon-Simpson model in resonance–theoretic cluster expansion. Int J Quantum Chem 35:373–383
38. Gutman I, Cyvin SJ (1989) Introduction to the theory of benzenoid hydrocarbons. Springer, Berlin
39. Hall GG (1991) Aromaticity measured by Kekulé structures. Int J Quantum Chem 39:605–613
40. Randić M (2003) Aromaticity of polycyclic conjugated hydrocarbons. Chem Rev 103:3449–3606
41. Gutman I, Stanković S (2007) Why is phenanthrene more stable than anthracene? Maced J Chem Chem Engin 26:111–114
42. Swinborne-Sheldrake R, Herndon WC, Gutman I (1975) Kekulé structures and resonance energies of benzenoid hydrocarbons. Tetrahedron Lett 16:755–758
43. Carter PC (1949) An empirical equation for the resonance energy of polycyclic aromatic hydrocarbons. Trans Faraday Soc 45:597–602
44. Hall GG (1973) A graphical model of a class of molecules. Int J Math Educ Sci Technol 4:233–240
45. Gutman I, Trinajstić N, Wilcox CF (1975) Graph theory and molecular orbitals—X. The number of Kekulé structures and the thermodynamic stability of conjugated systems. Tetrahedron 31:143–146
46. Cioslowski J (1987) A unified theory of the stability of benzenoid hydrocarbons. Int J Quantum Chem 31:581–590
47. Cioslowski J (1990) A final solution of the problem concerning the (N, M, K) -dependence of the total π -electron energy of conjugated systems. MATCH Commun Math Comput Chem 25:83–93
48. Gutman I, Hall GG (1992) Linear dependence of total π -electron energy of benzenoid hydrocarbons on Kekulé structure count. Int J Quantum Chem 41:667–672
49. Gutman I (1999) On the Hall rule in the theory of benzenoid hydrocarbons. Int J Quantum Chem 74:627–632
50. Gutman I (1992) Total π -electron energy of benzenoid hydrocarbons. Topics Curr Chem 162:29–63
51. Gutman I (2005) Topology and stability of conjugated hydrocarbons. The dependence of total π -electron energy on molecular topology. J Serb Chem Soc 70:441–456
52. Clar E, Stewart DG (1953) Aromatic hydrocarbons. XLV. Triangulene derivatives. J Am Chem Soc 75:2667–2672
53. Clar E, Kemp W, Stewart DG (1958) The significance of Kekulé structures for the stability of aromatic systems. Tetrahedron 3:325–333

54. Herndon WC (1974) Thermochemical parameters for benzenoid hydrocarbons. *Thermochim Acta* 8:225–237
55. Herndon WC, Biedermann PU, Agranat I (1998) Molecular structure parameters and predictions of enthalpies of formation for catacondensed and pericondensed polycyclic aromatic hydrocarbons. *J Org Chem* 63:7445–7448
56. Herndon WC, Connor DA, Li P (1990) Structure–enthalpy relationships in polycyclic cata-condensed aromatic hydrocarbons. *Pure Appl Chem* 62:435–444
57. Herndon WC (1975) Resonance theory. VIII. Reactivities of benzenoid hydrocarbons. *J Org Chem* 40:3583–3586
58. Wilcox CF, Gutman I, Trinajstić N (1975) Graph theory and molecular orbitals—XI. Aromatic substitution. *Tetrahedron* 31:147–152
59. Biermann D, Schmidt W (1980) Diels-Alder reactivity of polycyclic aromatic hydrocarbons. 1. Acenes and benzologs. *J Am Chem Soc* 102:3163–3173
60. Biermann D, Schmidt W (1980) Diels-Alder reactivity of polycyclic aromatic hydrocarbons. 2. Phenols and starphenols. *J Am Chem Soc* 102:3173–3181
61. Hall GG (1988) Resonance and reactivity. *J Mol Struct (Theochem)* 169:233–244
62. Gutman I (1998) Topologically activated sites in benzenoid hydrocarbons. Polyacenes and benzo–annulated polyacenes. *J Serb Chem Soc* 63:987–993
63. Herndon WC (1976) Ionization potentials of π -molecular hydrocarbons. *J Am Chem Soc* 98:887–889
64. Eilfeld P, Schmidt W (1981) Resonance theoretical approach to the calculation of the first IP's of polycyclic aromatics. *J Electron Spectr Rel Phenom* 24:101–120
65. Randić M (1974) On the characterization of local aromatic properties of benzenoid hydrocarbons. *Tetrahedron* 30:2067–2074
66. Randić M (1975) Graph theoretical approach to local and overall aromaticity of benzenoid hydrocarbons. *Tetrahedron* 31:1477–1481
67. Randić M (1976) Conjugated circuits and resonance energies of benzenoid hydrocarbons. *Chem Phys Lett* 38:68–70
68. Randić M (1977) Aromaticity and conjugation. *J Am Chem Soc* 99:444–450
69. Randić M (1977) A graph theoretical approach to conjugation and resonance energies of hydrocarbons. *Tetrahedron* 33:1905–1920
70. Klein DJ (1992) Aromaticity via Kekulé structures and conjugated circuits. *J Chem Educ* 69:691–694
71. Gutman I, Cyvin SJ (1989) Conjugated circuits in benzenoid hydrocarbons. *J Mol Struct (Theochem)* 184:159–163
72. Randić M, Nikolić S, Trinajstić N (1987) The conjugated circuit model: on the selection of parameters for computing the resonance energies. In: King RB, Rouvray DH (eds) *Graph theory and topology in chemistry*. Elsevier, Amsterdam, pp 429–447
73. Randić M, Trinajstić N (1987) Critical test for resonance energies. *J Am Chem Soc* 109:6923–6926
74. Ciesielski A, Krygowski TM, Cyrański MK, Balaban AT (2011) Defining rules of aromaticity: a unified approach to the Hückel, Clar and Randić concepts. *Phys Chem Chem Phys* 13:3737–3747
75. Randić M, Balaban AT (2004) Partitioning of π -electrons in rings of polycyclic conjugated hydrocarbons. Part 1: catacondensed benzenoids. *Polyc Arom Comp* 24:173–193
76. Balaban AT, Randić M (2004) Partitioning of π -electrons in rings of polycyclic benzenoid hydrocarbons. 2. Catacondensed coronoids. *J Chem Inf Comput Sci* 44:50–59
77. Balaban AT, Randić M (2004) Partitioning of π -electrons in rings of polycyclic conjugated hydrocarbons. Part 3. Perifusenes. *New J Chem* 28:800–806
78. Balaban AT, Randić M (2004) Partitioning of π -electrons in rings of polycyclic conjugated hydrocarbons. 5. Nonalternant hydrocarbons. *J Chem Inf Comput Sci* 44:1701–1707
79. Randić M (2004) Algebraic Kekulé formulas for benzenoid hydrocarbons. *J Chem Inf Comput Sci* 44:365–372

80. Gutman I, Vukičević D, Graovac A, Randić M (2004) Algebraic Kekulé structures of benzenoid hydrocarbons. *J Chem Inf Comput Sci* 44:296–299
81. Gutman I, Morikawa T, Narita S (2004) On π -electron content of bonds and rings in benzenoid hydrocarbons. *Z Naturforsch* 59a:295–298
82. Balaban AT, Randić M (2005) Partitioning of π -electrons in rings of polycyclic conjugated hydrocarbons. 6. Comparisons with other methods for estimating the local aromaticity of rings in polycyclic benzenoids. *J Math Chem* 37:443–453
83. Randić M, Balaban AT (2006) Partitioning of π -electrons in rings for Clar structures of benzenoid hydrocarbons. *J Chem Inf Model* 46:57–64
84. Balaban AT, Randić M (2008) Correlations between various ways of accounting for the distribution of π -electrons in benzenoids. *New J Chem* 32:1071–1078
85. Zubarev DY, Frenklach DY, Lester WA (2012) From aromaticity to self-organized criticality in graphene. *Phys Chem Chem Phys* 14:12075–12078
86. Herndon WC (1974) Resonance theory. VI. Bond orders. *J Am Chem Soc* 96:7605–7614
87. Herndon WC, Párkányi C (1976) π -Bond orders and bond lengths. *J Chem Educ* 53:689–692
88. Párkányi C, Herndon WC (1978) Bond lengths and bond orders in π -electron heterocycles. *Phosphorus Sulphur* 4:1–7
89. Pauling L (1980) Bond numbers and bond lengths in tetrabenzo[*de, no, st, cl, dl*]heptacene and other condensed aromatic hydrocarbons: a valence-bond treatment. *Acta Cryst B* 36:1898–1901
90. Goddard R, Haenel MW, Herndon WC, Krüger C, Zander M (1995) Crystallization of large planar polycyclic aromatic hydrocarbons: the molecular and crystal structures of hexabenzo [*bc, ef, hi, kl, no, qr*]coronene and benzo[*1,2,3-bc:4,5,6-b'c'*]dicononene. *J Am Chem Soc* 117:30–41
91. Narita S, Morikawa T, Shibuya T (2000) Linear relationship between the bond lengths and the Pauling bond orders in fullerene molecules. *J Mol Struct (Theochem)* 532:37–40
92. Randić M (2010) Graph theoretical approach to π -electron currents in polycyclic conjugated hydrocarbons. *Chem Phys Lett* 500:123–127
93. Gomes JANF, Mallion RB (2001) Aromaticity and ring currents. *Chem Rev* 101:1349–1383
94. Minkin VI, Glukhovtsev MN, Simkin BY (1994) Aromaticity and antiaromaticity. Electronic and structural aspects. Wiley, New York
95. Aihara J (2006) Circuit resonance energy: a key quantity that links energetic and magnetic criteria of aromaticity. *J Am Chem Soc* 128:2873–2879
96. Bultinck P, Fias S, Ponec R (2006) Local aromaticity in polycyclic aromatic hydrocarbons: electron delocalization versus magnetic indices. *Chem Eur J* 12:8813–8818
97. Stanger A (2009) What is aromaticity: a critique of the concept of aromaticity—can it really be defined?. *Chem Commun* 1939–1947
98. Ciesielski A, Krigowski TM, Cyrański MK, Dobrowolski MA, Aihara J (2009) Graph-topological approach to magnetic properties of benzenoid hydrocarbons. *Phys Chem Chem Phys* 11:11447–11455
99. Solá M, Feixas F, Jiménez-Halla JOC, Matito E, Poater J (2010) A critical assessment of the performance of magnetic and electronic indices of aromaticity. *Symmetry* 2:1156–1179
100. Randić M, Plavšić D, Vukičević D (2011) π -Electron currents in fully aromatic benzenoids. *J Indian Chem Soc* 88(2011):13–23
101. Randić M, Novič M, Vračko M, Plavšić D (2012) π -Electron currents in polycyclic conjugated hydrocarbons: coronene and its isomers having five and seven member rings. *Int J Quantum Chem* 112:972–985
102. Randić M, Vukivcević D, Novič M, Plavšić D (2012) π -Electron currents in large fully aromatic benzenoids. *Int J Quantum Chem* 112:2456–2462
103. Randić M, Novič M, Plavšić D (2012) π -Electron currents in fixed π -sextet aromatic benzenoids. *J Math Chem* 50:2755–2774
104. Randić M, Vukičević D, Balaban AT, Vračko M, Plavšić D (2012) Conjugated circuits currents in hexabenzocoronene and its derivatives formed by joining proximal carbons. *J Comput Chem* 33:1111–1122

105. Fries K (1927) Über bicyclische Verbindungen und ihren Vergleich mit dem Naphthalin, III Mitteilung. *Ann Chem* 454:121–324
106. Gründler W (1982) Signifikante Elektronenstrukturen für benzenoide Kohlenwasserstoffe. *Wiss Z Univ Halle* 31:97–116
107. Graovac A, Gutman I, Randić M, Trinajstić N (1973) Kekulé index for valence bond structures of conjugated polycyclic systems. *J Am Chem Soc* 95:6267–6273
108. Sedlar J, Anđelić I, Gutman I, Vukičević D, Graovac A (2006) Vindicating the Pauling–bond–order concept. *Chem Phys Lett* 427:418–420
109. Clar E (1972) The aromatic sextet. Wiley, London
110. Solá M (2013) Forty years of Clar’s aromatic π -sextet rule. *Frontiers Chem* 1(22):1–8
111. Hall GG (1977) On the eigenvalues of molecular graphs. *Mol Phys* 33:551–557
112. Gutman I, Marković S, Hall GG (1995) Revisiting a simple regularity for benzenoid hydrocarbons: total π -electron energy versus the number of Kekulé structures. *Chem Phys Lett* 234:21–24
113. Gutman Radenković (2006) Extending and modifying the Hall rule. *Chem Phys Lett* 423:382–385
114. Radenković S, Gutman I (2009) Stability order of isomeric benzenoid hydrocarbons and Kekulé structure count. *J Serb Chem Soc* 74:155–158
115. Cioslowski J, Dobrowolski JC (2003) Structural dependence of thermodynamic stability of unbranched catacondensed benzenoid hydrocarbons. *Chem Phys Lett* 371:317–320
116. Cyvin SJ, Gutman I (1988) Kekulé Structures in Benzenoid Hydrocarbons. Springer, Berlin
117. Gutman I (1990) Nonaromatic benzenoid hydrocarbons. *Pure Appl Chem* 62:429–434
118. Gutman I (2010) Kekulé structures in fluoranthenes. *Z Naturforsch* 65a:473–476
119. Gutman I, Stanković S, Kovačević R, Đurđević J, Furtula B (2005) Anomalous cyclic conjugation in benzenoid molecules with a small number of Kekulé structures. *Indian J Chem* 44A:1751–1755
120. Gutman I, Marković S, Jeremić S (2010) A case of breakdown of the Kekulé–structure model. *Polyc Arom Comp* 30:240–246
121. Vukičević D, Đurđević J, Gutman I (2012) Limitations of Pauling bond order concept. *Polyc Arom Comp* 32:36–47
122. Marković S, Đurđević J, Jeremić S, Gutman I (2010) Diradical character of some fluoranthenes. *J Serb Chem Soc* 75:1241–1249
123. Marković, S., Đurđević, J., Jeremić, J., Gutman, I.: triplet fluoranthenes: aromaticity versus unpaired electrons, *J Mol Model* 17, 805–810 (2011)
124. Gutman I (2005) Cyclic conjugation energy effects in polycyclic π -electron systems. *Monatsh Chem* 136:1055–1069
125. Gutman I (2010) Theory of the PCP effect and related phenomena. *J Math Chem* 47:1309–1312
126. Gutman I, Radenković S, Linert W (2010) Pairwise energy effect of cyclic conjugation in benzo–annelated perylene. *Monatsh Chem* 141:401–407
127. Balaban AT, Gutman I, Jeremić S, Đurđević J (2011) Effect of benzo–annulation on cyclic conjugation. *Monatsh Chem* 142:53–57
128. Fatoohchahi, H., Gutman, I., Abolghasemi, H. (in press) A combined technique for computation of energy–effect of cycles in conjugated molecules. *J Math Chem*
129. Aihara J (2006) Circuit resonance energy: a key quantity that links energetic and magnetic criteria of aromaticity. *J Am Chem Soc* 128:2873–2879
130. Aihara J (2008) Topological resonance energy, bond resonance energy, and circuit resonance energy. *J Phys Org Chem* 21:79–85
131. Chauvin R, Lepetit C, Fowler PW, Malrieu JP (2010) The chemical roots of the matching polynomial. *Phys Chem Chem Phys* 12:5295–5306
132. Chauvin R, Lepetit C (2013) The fundamental chemical equation of aromaticity. *Phys Chem Chem Phys* 15:3855–3860
133. Gutman I, Turković N, Jovičić J (2004) Cyclic conjugation in benzo–annelated perylenes: how empty is the “empty” ring? *Monatsh Chem* 135:1389–1394

134. Gutman I, Balaban AT (2011) Simple mathematical model for the effect of benzo-annellation on cyclic conjugation. *J Serb Chem Soc* 76:1505–1511
135. Radenković S, Đurđević J, Bultinck P (2012) Local aromaticity of the five-membered rings in acenaphthylene derivatives. *Phys Chem Chem Phys* 14:14067–14078
136. Đurđević J, Gutman I (2012) Phenyl–cyclopentadienyl rule. *Maced J Chem Chem Engin* 31:1–15
137. Radenković S, Gutman I, Bultinck P (2012) A comparative study of aromaticity in tetraoxa [8] circulenes. *J Phys Chem A* 116:9421–9430
138. Radenković S, Kojić J, Petronijević J, Antić M (2014) Effect of benzo-annellation on local aromaticity in heterocyclic conjugated compounds. *J Phys Chem A* 118:11591–11601
139. Gutman I, Furtula B, Đurđević J, Kovačević R, Stanković S (2005) Annellated perylenes: benzenoid molecules violating the Kekulé-structure-based cyclic conjugation models. *J Serb Chem Soc* 70:1023–1031
140. Radenković S, Linert W, Gutman I, Jeremić S (2009) Pairwise energy effects of rings in benzo-annellated perylenes. *Indian J Chem* 48A:1657–1661
141. Gutman I, Đurđević J, Matović Z, Marković M (2012) Verifying the modes of cyclic conjugation in tetrabenzo[bc,ef,op,rs]circumanthracene. *J Serb Chem Soc* 77:1401–1408
142. Gutman I, Đurđević J, Radenković S, Matović Z (2012) Anomalous cyclic conjugation in the perylene/bisanthrene homologous series. *Monatsh Chem* 143:1649–1653
143. Radenković S, Bultinck P, Gutman I, Đurđević J (2012) On induced current density in the perylene/bisanthrene homologous series. *Chem Phys Lett* 552:151–155
144. Krygowski TM (1993) Crystallographic studies of inter- and intramolecular interactions reflected in aromatic character of π -electron systems. *J Chem Inf Comput Sci* 33:70–78
145. Krygowski TM, Cyrański MK (1996) Separation of the energetic and geometric contributions to the aromaticity of π -electron carbocyclics. *Tetrahedron* 52:1713–1722
146. Krygowski TM, Cyrański MK (2001) Structural aspects of aromaticity. *Chem Rev* 101:1385–1419
147. Ragué von Schleyer P, Jiao H (1996) What is aromaticity. *Pure Appl Chem* 68:209–218 (1996)
148. Ragué von Schleyer P, Maerker C, Drausfeld A, Jiao H, van Eikema Hommes JNR (1996) Nucleus-independent chemical shifts: a simple and efficient aromaticity probe. *J Am Chem Soc* 118:6317–6318 (1996)
149. Giambiagi M, de Giambiagi MS, dos Santos Silva CD, de Figueiredo AP (2000) Multicenter bond indices as a measure of aromaticity. *Phys Chem Chem Phys* 2:3381–3392
150. Bultinck P, Ponec R, Van Damme S (2005) Multicenter bond indices as a new measure of aromaticity in polycyclic aromatic hydrocarbons. *J Phys Org Chem* 18:706–718
151. Aihara J, Sekine R, Ishida T (2011) Electronic and magnetic characteristics of polycyclic aromatic hydrocarbons with factorizable Kekulé structure counts. *J Phys Chem A* 115:9314–9321
152. Gutman I, Radenković S, Antić M, Đurđević J (2013) A test of Clar aromatic sextet theory. *J Serb Chem Soc* 78:1539–1546
153. Radenković S, Gutman I, Antić M (2014) A case of breakdown of the Pauling bond order concept. *Chem Phys Lett* 614:104–109

Chapter 12

Rules of Aromaticity

Ferran Feixas, Eduard Matito, Jordi Poater and Miquel Solà

Abstract The concept of aromaticity is elusive; it is not directly observable. Somewhat surprisingly, given the fuzzy character of this concept, there exist a number of very simple mathematical rules that can account for the aromaticity of a large number of organic and inorganic molecules. Among them we can mention Hückel's, Baird's, Wade-Mingos', and Hirsch's rules. In this chapter we summarize recent advances carried out in our group in the study of these aromaticity rules.

12.1 Introduction

The field of aromaticity is in constant evolution and the variety of molecules that present properties related to aromaticity is growing exponentially. Over the last two decades there has been a remarkable expansion in the number of different types of aromatic systems and in our understanding of aromaticity. In 2001 Boldyrev, Wang, and coworkers [1] detected a series of bimetallic clusters containing Al_4^{2-} , the first all-metal aromatic cluster known, face-capped by an M^+ cation ($M = Li, Na, Cu$). Six years later the same group identified $Ta_3O_3^-$ [2], the first discovered metallic cluster with δ -aromaticity. From these and many other studies [3–5], it is now recognized that the aromaticity concept can be applied to the entire periodic table. It is also widely accepted that there is not a unique type of aromaticity (the classical π -aromaticity) but chemical compounds can also have σ -, δ -, and even ϕ -aromaticity, together with combinations of these different types (multifold aromaticity) [3–5]. From a theoretical point of view, the last two decades also brought several important advances. More powerful tools to quantify aromaticity have been

F. Feixas · E. Matito · M. Solà (✉)

Institut de Química Computacional i Catàlisi and Departament de Química,
Universitat de Girona, Campus de Montilivi, 17071 Girona, Catalonia, Spain
e-mail: miquel.sola@udg.edu

J. Poater

Department of Theoretical Chemistry and Amsterdam Center for Multiscale Modeling,
Vrije Universiteit, De Boelelaan 1083, NL-1081HV Amsterdam, The Netherlands

developed. Among them we can mention some refined NICS measures (such as the NICS profiles [6, 7] or NICS _{π zz} values [8]) and new defined indices of aromaticity based on electron delocalization measures such as PDI [9], FLU [10], I_{ring} [11], and MCI [12] and the normalized versions of the last two, I_{NG} and I_{NB} [13].

Many of the novel aromatic compounds found present high symmetry. Symmetry is one of the usual features of aromatic compounds. Although not all aromatic species are symmetric, the most archetypal aromatic compounds are highly symmetric and possess degenerate highest-occupied molecular orbitals. These orbitals can be fully occupied resulting in a closed-shell structure or can be same-spin half-filled. This is the case of paradigmatic aromatic species, namely, benzene, B₆H₆²⁻ closo borane cluster, C₆₀¹⁰⁺, Al₄²⁻, but also of triplet C₅H₅⁺ or C₆₀¹⁻ with a spin of 11/2. The closed-shell or same-spin half-filled electronic structure is the origin of several rules of aromaticity such as the $4n + 2$ Hückel [14], $4n$ Baird [15], $2n + 2$ Wade-Mingos [16, 17], $2(n + 1)^2$ Hirsch [18] or the $2n^2 + 2n + 1$ [19] rules.

In this chapter we review the results of our recent investigations on the abovementioned rules of aromaticity. It is worth noting that extension of these rules to aromatic polycyclic hydrocarbons (PAH) has led to the Clar π -sextet rule [20, 21] and the Glidewell-Lloyd [22] extension of Clar's rule. These extensions will not be discussed in the present chapter. Neither we will comment on the $4n$ rule for Möbius aromaticity [23, 24] nor on its extension by Rzepa in what is known as the linking number rule [25].

12.2 Hückel's $4n + 2$ Rule

The classification of molecules into groups based on similar molecular properties, structure, or reactivity has been one of the goals of chemistry from the very beginning. Benzene and related compounds attracted a lot of attention because of their peculiar stability and reactivity and were gathered to form the group of aromatic molecules. Understanding the peculiarities of aromatic molecules and the features that a molecule should display to join the group of aromatic compounds became a goal of chemistry. Since aromaticity is not directly observable, theoretical calculations have played a key role in classifying molecules as aromatic. In 1931, Hückel put forward the importance of delocalized electrons (π -electrons) to rationalize molecular properties of conjugated molecules [26]. According to Hückel molecular orbital (HMO) theory, the topology of the molecule and the number of π -electrons determines the stability of the molecule. An outcome of the HMO theory applied to cyclic conjugated hydrocarbons was the well-known $4n + 2$ stability rule [14]. Its connection to the concepts of aromaticity and antiaromaticity has played a central role in organic chemistry.

Hückel's rule of aromaticity states that monocyclic conjugated hydrocarbons with $4n + 2$ π -electrons are aromatic, whereas systems with $4n$ π -electrons are antiaromatic. Consequently, the number of π -electrons is crucial to determine stability, structure, and reactivity of aromatic and antiaromatic systems. In 1954, Doering and

Knox synthesized cycloheptatrienyl cation ($C_7H_7^+$), a molecule with six π -electrons which represents the first experimental support to Hückel's rule [27]. Although the original formulation of the $4n + 2$ rule was limited to monocycles, Clar and later on Glidewell and Lloyd generalized the concept to characterize the aromaticity of polycyclic aromatic hydrocarbons (PAH) [20, 22]. In addition, the $4n + 2$ rule has been used to rationalize multifold aromaticity in all-metal clusters [3]. More recently, Mayer derived the $4n + 2$ rule analytically to determine the energetic effects of the ring closure [28]. As mentioned above, important advances in the field of aromaticity has led to the definition of a number of versatile descriptors based on the measurement of structural, magnetic, energetic or electronic properties. Before applying these indicators to complex molecular systems, the performance of such descriptors is usually assessed for a set of annulenes and PAH that obey $4n + 2$ and $4n$ aromaticity rules. One of the first aromaticity criteria was suggested by Breslow who proposed to estimate the aromatic character of a ring by comparing the π -energy of a cyclic π -conjugated system with respect to the corresponding iso- π -electronic linear compound [29]. A decrease of energy upon cyclization is related to aromaticity while an increase points out antiaromaticity. In 1972, Hobe demonstrated that Breslow's proposal is connected to the $4n + 2$ Hückel's rule [30]. The $4n + 2$ rule has also been assessed by means of other energetic and magnetic indicators, including aromatic stabilization energy (ASE) calculations, nucleus independent chemical shifts (NICS) [31] and ring currents [32] among many others.

The concept of aromaticity is strongly related to molecular topology and cyclic π -electron delocalization. The aim of this section is to explore the nature of π -electron delocalization patterns in simple aromatic and antiaromatic compounds that are in agreement with the $4n + 2$ and $4n$ rules respectively. To this end, we selected a set of neutral annulenes and their respective dianions and dication. Electronic delocalization is usually studied by computing the so-called electron sharing indices (ESI) or through the calculation of the electron localization function (ELF) [33]. In this work we made use of ESI calculated in the framework of the quantum theory of atoms in molecules (QTAIM) [34]. The sum of all ESI gives the total delocalization of the system, δ_{TOT} . Interestingly, for planar systems the total electronic delocalization can be exactly split into σ and π contributions, $\delta_{TOT} = \delta_\sigma + \delta_\pi$. To analyze the differences on electronic delocalization between aromatic and antiaromatic systems, we studied how δ_π changes when two π -electrons are either added or removed from a set of $4n + 2$ aromatic and $4n$ antiaromatic systems [35]. Let us consider an aromatic $4n + 2$ system such as benzene (see Scheme 12.1). If we add two electrons to benzene (N electrons), we obtain a $4n$ system ($C_6H_6^{2-}$ with $N + 2$ electrons), which should be antiaromatic according to Hückel's rule. Therefore, we expect these two added electrons will be mainly localized and the value of δ_π will be barely affected with respect to C_6H_6 . As Table 12.1 shows, δ_π is 3.369 e for C_6H_6 whereas the total electronic delocalization in $C_6H_6^{2-}$ is 3.482 e. We added a pair of π -electrons but only an increment of 0.113 e is observed. Thus, a net change on electronic delocalization close to zero is expected when going from N to $N + 2$ species if N is an aromatic $4n + 2$ system. On the other hand, if we subtract two π -electrons from C_6H_6 to obtain the antiaromatic $C_6H_6^{2+}$ (with $N - 2$ electrons) one expects a significant

Table 12.1 Total electronic delocalization (δ_{TOT}), total π electronic delocalization (δ_π), and the corresponding crossed contributions to this latter ($\delta_\pi^{1,x}$) for C_4H_4 and C_8H_8 antiaromatic compounds

	$N - 2$	N	$N + 2$	Δ^2
C_6H_6				
δ_{TOT}	14.863	15.618	15.731	
δ_π	2.614	3.369	3.482	0.642
$\delta_\pi^{1,2}$	0.288	0.427	0.385	0.181
$\delta_\pi^{1,3}$	0.087	0.037	0.083	-0.096
$\delta_\pi^{1,4}$	0.059	0.094	0.051	0.078
C_8H_8				
δ_{TOT}	20.344	20.866	21.172	
δ_π	3.955	4.477	4.783	0.216
$\delta_\pi^{1,2}$	0.338	0.432	0.414	0.112
$\delta_\pi^{1,3}$	0.074	0.029	0.061	-0.077
$\delta_\pi^{1,4}$	0.018	0.040	0.025	0.037
$\delta_\pi^{1,5}$	0.054	0.007	0.044	-0.084

Units are electrons

decrease of δ_π as Table 12.1 indicates (from 3.369 to 2.614 e). Therefore, when a pair of electrons are added to a $4n$ antiaromatic system these electrons are mainly delocalized as shown by the increment of 0.75e observed when going from an antiaromatic $C_6H_6^{2+}$ to an aromatic C_6H_6 . In general, we observed an increment of about one electron when going from an $N - 2$ antiaromatic molecule to an N aromatic system. To simplify the analysis, we calculated the difference between the two steps ($N - 2$ to N and N to $N + 2$) as $\Delta^2 = [2\delta_{\pi N} - \delta_{\pi(N-2)} - \delta_{\pi(N+2)}]$, which comprises the sum of changes when going from N to $N + 2$ and from N to $N - 2$ species and it is proportional to the numerical second derivative of δ_π . The value of Δ^2 for benzene is 0.642. We also studied the changes on π -electronic delocalization for a series of typical antiaromatic systems. In contrast to aromatic species, the differences in δ_π are less conclusive. In Table 12.1, we gathered the results obtained when adding and subtracting two π -electrons to a $4n$ C_8H_8 system. The value of δ_π shows a similar increase when going from $N - 2$ to N and from N to $N + 2$, i.e. 0.522 and 0.306 e respectively to give a Δ^2 of 0.216. Therefore, a clear frontier between aromatic and antiaromatic systems cannot be established by only analyzing the changes in the total π -electronic delocalization.

To gain more insight into the nature of electron delocalization in aromatic and antiaromatic systems, we split the total π -electron delocalization into *ortho* ($\delta_\pi^{1,2}$), *meta* ($\delta_\pi^{1,3}$), *para* ($\delta_\pi^{1,4}$), and successive contributions (crossed terms, see Fig. 12.1) and we analyzed the changes on the so-called delocalization crossed terms when two electrons are added or removed from systems with $4n + 2$ or $4n$ π -electrons [36]. For benzene, when two electrons are added to the antiaromatic $C_6H_6^{2+}$ to get the aromatic C_6H_6 system, the *ortho* and *para* contributions significantly increase while the *meta* component of the total π -electronic delocalization decreases

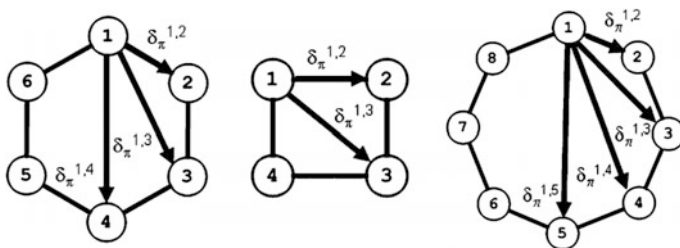
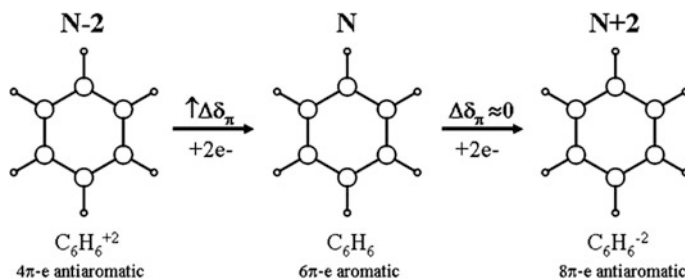


Fig. 12.1 Decomposition of electron delocalization in crossed-terms $\delta_{\pi}^{1,x}$ for C_6H_6 , C_4H_4 , and C_8H_8

(see Table 12.1). The opposite effect is observed when adding two electrons to C_6H_6 to reach $C_6H_6^{2-}$, that is, *meta* increases whereas *ortho* and *para* components decrease. This alternation is also captured by Δ^2 which takes positive values for $\delta_{\pi}^{1,2}$ and $\delta_{\pi}^{1,4}$ components, i.e. 0.181 and 0.078 respectively, while gives negative values for $\delta_{\pi}^{1,3}$ contribution, i.e. -0.096 . For antiaromatic C_8H_8 , $\delta_{\pi}^{1,2}$ and $\delta_{\pi}^{1,4}$ increase and $\delta_{\pi}^{1,3}$ and $\delta_{\pi}^{1,5}$ decrease when going from $N \pm 2$ to N , which corresponds to positive Δ^2 for $\delta_{\pi}^{1,2}$ and $\delta_{\pi}^{1,4}$ components and negative Δ^2 for $\delta_{\pi}^{1,3}$ and $\delta_{\pi}^{1,5}$. In general, we observed that the Δ^2 value of the crossed term corresponding to the two farthest atoms in the ring (i.e. $\delta_{\pi}^{1,4}$ in C_6H_6 or $\delta_{\pi}^{1,5}$ in C_8H_8) gives positive values when two electrons are added or removed from an aromatic system, whereas the opposite is true for antiaromatic species (see Table 12.1). Interestingly, the crossed terms represent a kind of electronic footprints that clearly capture the differences between aromatic and antiaromatic species. To sum up, we have shown the differences of electronic delocalization patterns between systems that are catalogued as aromatic and antiaromatic according to the Hückel $4n + 2$ rule.



Scheme 12.1 Expected changes in δ_{π} when moving from $C_6H_6^{+2}$ to C_6H_6 and to $C_6H_6^{-2}$ by adding two electrons each time

12.3 Baird's 4n Rule

Hückel's rule has shown the importance of molecular topology in order to determine the aromaticity of molecular systems. In this section, we will show that the electronic state also plays an important role and actually gives rise to a different counting rule. The number of studies devoted to the aromaticity of excited states is scarce when compared with the ground-state literature, but the importance of excited-state aromaticity is very well highlighted in the excellent recent review of Ottosson and coworkers [37], which puts forward how this property can be used to rationalize a number of photophysical and photochemical reactions. For instance, the design of appropriate antiaromatic olefins could lead to excited triplet-state species suitable for adiabatic Z/E photoisomerization [38] and triplet-state aromaticity was used to explain the stability of substituted fulvenes [39] and the dipole moments of fulvenes, fulvalenes, and azulene [40]. One of the first evidences of excited-states aromaticity is due to Baird [15], who used perturbation molecular orbital theory and Dewar resonance energy arguments to show that aromatic singlet annulenes were antiaromatic in the lowest-energy excited triplet state (T_1), and vice versa. Baird's rule states that $4n\pi$ monocycles are aromatic in the T_1 but it is also generally accepted that these compounds are also aromatic in the lowest-lying excited singlet states (S_1). In 2008, Soncini and Fowler generalized Baird's rule stating that open-shell $4n + 2$ ($4n$) annulenes with even (odd) total spin are aromatic, whereas odd (even) total spin monocyclic compounds are antiaromatic [41]. The same year, Mandado and coworkers concluded that all these rules are particular cases of a more general rule applying separately to α and β electrons [42].

In the following we will focus on analyzing the changing patterns of electron delocalization and the aromaticity of different vertical excited states of benzene, cyclobutadiene (CBD) and planar cyclooctatetraene (COT).¹ To this aim, we will use electron sharing indices (ESI) and multicenter (MCI) aromaticity indices (see Table 12.2). Interestingly, the ESIs reveal the true symmetry of the excited state without the need of optimizing the geometry, as they do not depend on the symmetry of the ground state. For instance, benzene's S_1 keeps the D_{6h} electronic distribution but there is small reduction of the ESIs of the peripheral CC bond that goes with the corresponding decrease of aromaticity. On the contrary, the next two lowest-energy singlet states, S_2 and S_3 , show the symmetry break to D_{2h} and a substantial reduction of aromaticity as compared to S_1 . T_1 exhibits a more evident symmetry break (ESIs that differ by 0.33 e) and a significant reduction of aromaticity, thus confirming Baird's rule. According to Soncini and Fowler's extension of the latter, the lowest-lying quintet state (Q_1) should be also aromatic. This rule cannot be fully confirmed by our calculations as B3LYP assigns a clear

¹The ground-state minimal energy structure of COT is a non-aromatic and non-planar species that is not so interesting from Baird's rule perspective. For this reason, we have chosen the planar D_{4h} COT, which is not an energy minimum but is a stationary point of the potential energy surface with bond-length alternation and well-known antiaromatic character.

Table 12.2 MCI and ESI (in electrons) and vertical excitation energies (AE in eV) of several excited states of benzene, cyclobutadiene, and octatetraene

Molecule	State	MCI (B3LYP) ^a	$\delta(C_1, C_2)$, $\delta(C_2, C_3)$	AE
C ₆ H ₆ <i>D</i> _{6h}	S ₀	43.5 (72.1)	1.288, 1.288	0.00
	S ₁	4.1	1.189, 1.189	5.00
	S ₂	0.8	1.092, 1.203	8.17
	S ₃	0.8	1.266, 1.116	8.17
	T ₁	2.3 (-1.5)	1.429, 1.100	3.55
	Q ₁	2.0 (45.1)	1.126, 1.126	7.88
C ₄ H ₄ <i>D</i> _{4h}	S ₀	9.2 (10.1)	1.480, 1.002	0.00
	T ₁	36.1 (127.1)	1.231, 1.126	0.75
C ₈ H ₈ <i>D</i> _{4h}	S ₀	5.0 (-0.5)	1.482, 1.083	0.00
	T ₁	4.7 (27.1)	1.313, 1.199	1.60
	Q ₁	0.2 (1.3)	1.221, 1.122	8.26
	Septet ₁	0.1 (17.8)	1.158, 1.097	13.80

^aMCI values multiplied by 1000 obtained at the CASSCF level (in parenthesis B3LYP values)

aromatic character to Q₁, but CASSCF value suggests an important reduction of aromaticity.

CBD and COT are antiaromatic in their ground state geometries according to Hückel's rule. Both molecules show alternating ESI pattern with one single bond adjacent to one double and large aromaticity values, thus corroborating this fact. Despite the inherent *D*_{2h} geometry, the vertical excitation of CBD to the T₁ state completely changes the electron distribution affording a symmetric electron delocalization along the ring, with only 0.11e ESI difference between adjacent bonds. In addition, according to all electronic aromaticity indices, T₁ is an aromatic species as predicted by Baird's rule. These results are in agreement with NICS calculations performed by Karadakov [43, 44]. The same situation is found for the T₁ state of COT, although the effect is far much less obvious. The study of Q₁ and the lowest-energy septet state at the B3LYP level indicates that these molecules are antiaromatic and aromatic, respectively, in agreement with Soncini-Fowler's extension of Baird's rule. However, CASSCF calculation reduces the value of MCI for the lowest-lying septet state suggesting, once again, that this rule might not be fully attained upon inclusion of electron correlation. The systematic reduction of delocalization indices due to the inclusion of electron correlation² suggests that the failure of MCI indices to reproduce Soncini-Fowler's rule might not be completely relevant.

²B3LYP also includes some electron correlation effects in the calculation of the energy but it is a well-documented fact that the use of Kohn-Sham wavefunction to calculate the electron delocalization indices provides results close to the Hartree-Fock ones and, therefore, they do not include electron correlation [45].

12.4 Rules of Spherical Aromaticity

In 2000, Hirsch's $2(n + 1)^2$ rule of aromaticity for spherical compounds [18, 46, 47] was introduced as the spherical analog of Hückel's $4n + 2$ rule. Hirsch's rule is based on the fact that the π -electron system of an icosahedral fullerene can be, in a first approximation, considered as a spherical electron gas surrounding the surface of a sphere. The corresponding wave functions of this electron gas are characterized by the angular momentum quantum number l ($l = 0, 1, 2, \dots$), with each energy level $2l + 1$ times degenerated, and thus all π -shells are completely filled when we have $2(n + 1)^2$ electrons. For such reason, spherical species with $2(n + 1)^2$ π -electrons are aromatic, like icosahedral C_{20}^{2+} , C_{60}^{10+} or C_{80}^{8+} .

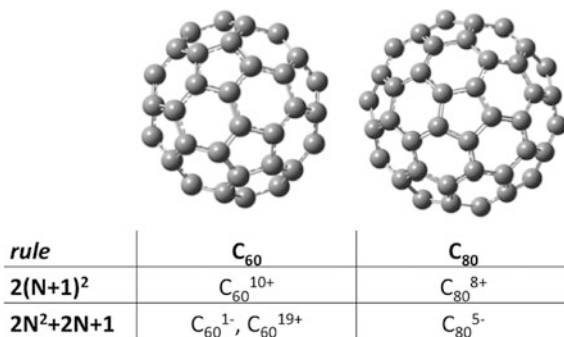
In the same way that Baird's $4n$ rule represented the extension of Hückel's $4n + 2$ rule to triplet state systems, those spherical systems having a same-spin half-filled last energy level with the rest of the levels being fully filled should be aromatic. Thus, recently Poater and Solà proved that the spherical compounds with $2n^2 + 2n + 1$ electrons and with a spin $S = n + 1/2$ accomplish this latter statement [19].

Table 12.3 includes a series of C_{60} and C_{80} derivatives with the aim to prove both $2(n + 1)^2$ and $2n^2 + 2n + 1$ rules for closed- and open-shell spherical compounds, respectively (see Scheme 12.2) [19]. The aromaticity analysis is performed by means of the magnetic NICS(1)_{zz}, the electronic MCI, and the bond length

Table 12.3 NICS(1)_{zz} (in ppm) and MCI (in electrons) values for C_{60} and C_{80} derivatives

System	Symmetry	Ring	NICS(1) _{zz}	MCI ^a	BLA	Spin
C_{60}	I_h	6-MR	0.8	18	0.058	S = 0
		5-MR	21.5	11		
C_{60}^{1-}	I_h	6-MR	-1.4	17	0.002	S = 11/2
		5-MR	-19.9	49		
C_{60}^{19+}	I_h	6-MR	-14.9	19	0.013	S = 9/2
		5-MR	-25.3	41		
C_{60}^{10+}	I_h	6-MR	-18.6	11	0.030	S = 0
		5-MR	-29.5	17		
C_{80}	S_6	5-MR	10.7	19	0.025	S = 0
		6-MR	-5.2	12		
		5-MR	26.3	18		
		6-MR	11.3	14		
		6-MR	-5.1	12		
C_{80}^{8+}	I_h	6-MR	-7.2	11	0.015	S = 0
		5-MR	-4.0	17		
C_{80}^{5-}	I_h	6-MR	-20.8	19	0.012	S = 13/2
		5-MR	-5.5	34		

^aMCI values multiplied by 1000



Scheme 12.2 Examples of charged C_{60} and C_{80} fullerenes which are particularly aromatic according to $2(n+1)^2$ and $2n^2+2n+1$ rules

alternation (BLA) indicators. First, for C_{60} , which does not obey any of the two rules, all measures point out that it has a non-aromatic or only slightly aromatic character. On the other hand, C_{60}^{10+} appears to be more aromatic than C_{60} with more negative NICS and smaller BLA, in line with Hirsch's rule for a system with 50 electrons. Next, C_{60}^{19+} and C_{60}^{1-} with $S = 9/2$ and $11/2$, respectively, thus following the $2n^2+2n+1$ rule, appear to be the most aromatic. For larger C_{80} , the different aromaticity criteria show a non-aromatic or slightly aromatic character of this system. However, C_{80}^{8+} , which obeys the $2(n+1)^2$ rule, presents higher aromaticity. Finally, C_{80}^{5-} with $S = 13/2$, thus following the $2n^2+2n+1$ rule, is found to be the most aromatic with more negative NICS(1)_{zz}, larger MCI, and smaller BLA values.

It is worth noting that NICS calculations for open-shell systems are approximate since they contain only the contributions arising from the perturbation of the wavefunction due to the external magnetic field [44, 49]. Moreover, we have to warn the reader on the use of NICS alone to draw conclusions on aromaticity. Although in many cases one gets reasonable results, NICS results can be unsafe for several reasons: first, NICS indicator of aromaticity can potentially incorporate some spurious information arising from the electron ring currents not related with aromaticity [50, 51]; second, they are biased by a spurious geometrical dependence on the ring size, incorrectly exalting aromaticity in cyclic systems of small ring size [52–54]; and, third, coupling of magnetic fields from different rings can lead to wrong conclusions [55–58]. However, we consider that the combined results of the NICS(1)_{zz}, MCI, and BLA descriptors provide strong evidence in favor of the $2n^2+2n+1$ rule.

Just to conclude, Hirsch et al. [18] already pointed out that the rule should be universally applicable to all conjugated π -systems, including inorganic compounds that present the nuclei distributed symmetrically over the spherical surface. This point has been supported by Ge_{12} spherene derivatives, with Ge_{12}^{4+} ($2(n+1)^2$) and Ge_{12}^{1-} with $S = 5/2$ ($2n^2+2n+1$), being more aromatic than Ge_{12}^{2-} [19].

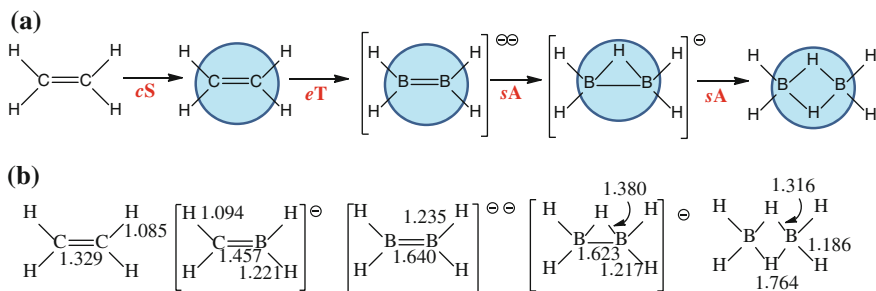
12.5 Equivalence Between Wade-Mingos' and Hückel's Rules

Closo boron hydride clusters are anions with the general formula $[\text{B}_n\text{H}_n]^{2-}$ that have the structure of a polyhedron with triangular faces [59]. They are very stable and unreactive and because of that they are considered aromatic. They obey the $2n + 2$ Wade rule [17, 60], in which n are the vertexes of the polyhedron, or Mingos' $4n + 2$ rule [16, 61]. Both rules are equivalent: Wade's rule refers to the cage electron pairs whereas Mingos' rule incorporates also the exo electron pairs corresponding to the B–H bonds, thus referring to the total number of valence electrons.

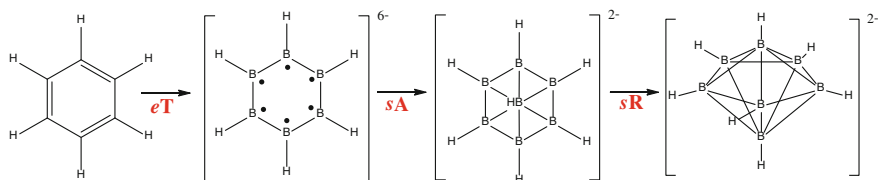
In a recent work [62], some of us have established a link between the hydrocarbon and boron hydride chemistries by showing that hydrocarbons and boron hydrides have a common root regulated by the number of valence electrons in a confined space. Application of the so-called electronic confined space analogy (ECSA) method to archetypal hydrocarbons leads to well-known boron hydrides and, even more importantly, it allows the design of new interesting molecules that can be a source of inspiration for synthetic chemists. In addition, application of ECSA also allows to reach the conclusion that the $4n + 2$ Wade-Mingos rule for three-dimensional closo boranes is equivalent to the $(4n + 2)\pi$ Hückel rule for bidimensional PAHs [63].

The steps followed to apply the ECSA method are the following: (1) first we state the model organic compound; (2) next we define its confined space (**cS**) as the molecular space occupied by the molecule; (3) we transmute each C atom into a B atom and one electron (**eT**); (4) these extra electrons are replaced by sacrificial atoms (**sA**); (5) and finally (if necessary) we generate the new boronhydride compound by structural relaxation (**sR**). During the whole process, the number of valence electrons in the corresponding confined space remains unaltered. As sacrificial atoms we use H^+ , B^{3+} or $[\text{BH}]^{4+}$ among others. These cations have empty valence orbitals perfectly suited to form multicenter bonds. As an example of the procedure, in Scheme 12.3 we apply the ECSA method in the case of ethene. ECSA links ethene with diborane (Scheme 12.3a). However, it also links ethene with known dianionic diboranes ($\text{B}_2\text{R}_4^{2-}$) [64–69] and yet to be discovered $\text{R}_2\text{CBR}_2^{2-}$, B_2HR_4^- or $\text{R}_2\text{CHBR}_2^{2-}$ species (Scheme 12.3b).

When the ECSA method is applied to aromatic molecules, a connection between the aromatic closo boranes following the Wade-Mingos rule and the classical organic molecules that obey Hückel's rule emerges [63]. As an example, let us consider benzene that is the archetype of the aromatic molecules (see Scheme 12.4). In this case 36 electrons is the total number of valence electrons in the confined space. The electronic transmutation with B^- drives us to $[\text{B}_6\text{H}_6]^{6-}$ with chair-like structure. The sacrificial group we add is $[\text{BH}]^{4+}$ leading to hexagonal pyramid $[\text{B}_7\text{H}_7]^{2-}$ that is not a minimum, but relaxes to a pentagonal bipyramid $[\text{B}_7\text{H}_7]^{2-}$, as experimentally found [70]. The NICS(0) of -22.8 ppm points out that $[\text{B}_7\text{H}_7]^{2-}$ is at least as aromatic as benzene [63]. The relatively low bond length alternation



Scheme 12.3 **a** Link established by ECSA between ethene and diborane. The total number of valence electrons in the confined space in *blue* remains constant and equal to 12. **b** A number of species derived from the application of ECSA to ethene (bond lengths in Å)



Scheme 12.4 Link established by ECSA between benzene and $[\text{B}_7\text{H}_7]^{2-}$. The total number of valence electrons in the confined space remains constant and equal to 30

value of 0.17 Å seems to confirm the aromatic character of this closo borane. Resonance energies per face calculated by Aihara [48] indicate that $[\text{B}_7\text{H}_7]^{2-}$ is the most aromatic closo borane $[\text{B}_n\text{H}_n]^{2-}$ ($n = 5-12$) after $[\text{B}_6\text{H}_6]^{2-}$. Similar links are found for $\text{C}_4\text{H}_4^{2-}$, C_5H_5^- and C_7H_7^+ with $[\text{B}_5\text{H}_5]^{2-}$, $[\text{B}_6\text{H}_6]^{2-}$, and $[\text{B}_8\text{H}_8]^{2-}$, respectively [63]. As a summary, the ECSA method links highly stable monocyclic hydrocarbon reference compounds fulfilling $(4n + 2)\pi$ Hückel's electron rule with the corresponding monodeltahedral closo borane clusters that obey the $4n + 2$ Wade-Mingos rule. Noticeably the value of n has not the same meaning in one equation and the other. In $(4n + 2)\pi$ Hückel's rule n can be any integer and has no direct relationship with the structure; conversely in $4n + 2$ Wade-Mingos' rule n is structure dependent and refers to the number of vertexes occupied by boron atoms.

12.6 Conclusions

One of the main difficulties faced by researchers interested in aromaticity characterization is the lack of a physical basis for this property, which makes its quantification difficult. The existence of rules of aromaticity that provide the magical numbers of electrons that are required to reach this property helps to characterize

aromatic compounds. In this chapter, we have shown that it is possible to differentiate between aromatic and antiaromatic planar conjugated rings by analyzing how the crossed delocalization terms changes when adding or removing a pair of electrons. Using multicenter electron delocalization measures, we have verified the $4n$ Baird rule, although our results have been inconclusive about the validity of Soncini-Fowler's extension of Baird's rule. We have also confirmed the validity of the $2(n + 1)^2$ and $2n^2 + 2n + 1$ ($S = n + 1/2$) rules of spherical aromaticity for closed and open-shell species, respectively. Finally, we have shown the existence of a connection between the $4n + 2$ Hückel rule for two-dimensional aromaticity in planar conjugated rings and the $4n + 2$ Wade-Mingos rule for three-dimensional aromaticity in boranes.

Acknowledgments This work has been supported by the Ministerio de Economía y Competitividad (MINECO) of Spain (Projects CTQ2014-54306-P and CTQ2013-41236-ERC) and the Generalitat de Catalunya (project 2014SGR931, Xarxa de Referència en Química Teòrica i Computacional, and ICREA Academia 2014 prize for M.S.). F.F. acknowledges financial support of the Beatriu de Pinós programme from AGAUR for the postdoctoral grants BP_A_00339 and BP_A2_00022. The EU under the Marie Curie Career Integration grant PCI09-GA-2011-294240 (E.M.) and the FEDER grant UNGI10-4E-801 (European Fund for Regional Development) have also funded this research.

References

1. Li X, Kuznetsov AE, Zhang H-F, Boldyrev A, Wang L-S (2001) Observation of all-metal aromatic molecules. *Science* 291:859–861
2. Zhai H-J, Averkiev BB, Zubarev DY, Wang L-S, Boldyrev AI (2007) δ Aromaticity in $[\text{Ta}_3\text{O}_3]^-$. *Angew Chem Int Ed* 46:4277–4280
3. Boldyrev AI, Wang L-S (2005) All-metal aromaticity and antiaromaticity. *Chem Rev* 105:3716–3757
4. Feixas F, Matito E, Poater J, Solà M (2013) Metalloaromaticity. *WIREs Comput Mol Sci* 3:105–122
5. Tsipis CA (2005) DFT study of “all-metal” aromatic compounds. *Coord Chem Rev* 249:2740–2762
6. Jiménez-Halla JOC, Matito E, Robles J, Solà M (2006) Nucleus-independent chemical shift (NICS) profiles in a series of monocyclic planar inorganic compounds. *J Organomet Chem* 691:4359–4366
7. Stanger A (2006) Nucleus-independent chemical shifts (NICS): distance dependence and revised criteria for aromaticity and antiaromaticity. *J Org Chem* 71:883–893
8. Schleyer PvR, Manoharan M, Wang ZX, Kiran B, Jiao HJ, Puchta R, van Eikema Hommes NJR (2001) Dissected nucleus-independent chemical shift analysis of π -aromaticity and antiaromaticity. *Org Lett* 3:2465–2468
9. Poater J, Fradera X, Duran M, Solà M (2003) The delocalization index as an electronic aromaticity criterion. Application to a series of planar polycyclic aromatic hydrocarbons. *Chem Eur J* 9:400–406
10. Matito E, Duran M, Solà M (2005) The aromatic fluctuation index (FLU): a new aromaticity index based on electron delocalization. *J Chem Phys* 122:014109; Erratum *ibid.*(2006) 125:059901

11. Giambiagi M, de Giambiagi MS, dos Santos CD, de Figueiredo AP (2000) Multicenter bond indices as a measure of aromaticity. *Phys Chem Chem Phys* 2:3381–3392
12. Bultinck P, Ponec R, Van Damme S (2005) Multicenter bond indices as a new measure of aromaticity in polycyclic aromatic hydrocarbons. *J Phys Org Chem* 18:706–718
13. Cioslowski J, Matito E, Solà M (2007) Properties of aromaticity indices based on the one-electron density matrix. *J Phys Chem A* 111:6521–6525
14. Hückel E (1937) The theory of unsaturated and aromatic compounds. *Z Elektrochem* 43(752–788):827–849
15. Baird NC (1972) Quantum organic photochemistry. II. Resonance and aromaticity in the lowest $^3\pi\pi^*$ state of cyclic hydrocarbons. *J Am Chem Soc* 94:4941–4948
16. Mingos DMP (1984) Polyhedral skeletal electron pair approach. *Acc Chem Res* 17:311–319
17. Wade K (1971) The structural significance of the number of skeletal bonding electron-pairs in carboranes, the higher boranes and borane anions, and various transition-metal carbonyl cluster compounds. *J Chem Soc D Chem Commun* (15):792–793
18. Hirsch A, Chen Z, Jiao H (2000) Spherical aromaticity in icosahedral fullerenes: the $2(N + 1)^2$ rule. *Angew Chem Int Ed* 39:3915–3917
19. Poater J, Solà M (2011) Open-shell spherical aromaticity: the $2N^2 + 2N + 1$ (with $S = N + 1/2$) rule. *Chem Commun* 47:11647–11649
20. Clar E (1972) *The aromatic sextet*. Wiley, New York
21. Solà M (2013) Forty years of Clar's aromatic pi-sextet rule. *Front Chem* 1:22
22. Glidewell C, Lloyd D (1984) MNDO study of bond orders in some conjugated bi- and tri-cyclic hydrocarbons. *Tetrahedron* 40:4455–4472
23. Herges R (2006) Topology in chemistry: designing Möbius molecules. *Chem Rev* 106:4820–4842
24. Rzepa HS (2005) Möbius aromaticity and delocalization. *Chem Rev* 105:3697–3715
25. Rappaport SM, Rzepa HS (2008) Intrinsically chiral aromaticity. Rules incorporating linking number, twist, and writhe for higher-twist Möbius annulenes. *J Am Chem Soc* 130:7613–7619
26. Hückel E (1931) Quantentheoretische Beiträge zum Benzolproblem I. Die Elektronenkonfiguration des Benzols und verwandter Verbindungen. *Z Physik* 70:104–186
27. Doering WVE, Knox LH (1954) The cycloheptatrienylium (tropylium) ion. *J Am Chem Soc* 76: 3203–3206
28. Mayer I (2010) Analytical derivation of the Hückel “ $4n + 2$ rule”. *Theoret Chem Acc* 125:203–206
29. Breslow R (1968) Small antiaromatic rings. *Angew Chem Int Ed Engl* 7:565–570
30. Hoberg WD (1972) Free-electron molecular-orbital model of aromaticity. *J Org Chem* 37:1137–1141
31. Jiao H, Schleyer PVR, Mo Y, McAllister MA, Tidwell TT (1997) Magnetic evidence for the aromaticity and antiaromaticity of charged fluorenyl, indenyl, and cyclopentadienyl systems. *J Am Chem Soc* 119:7075–7083
32. Fowler PW, Steiner E, Jenneskens LW (2003) Ring-current aromaticity in triplet states of $4n\pi$ electron monocycles. *Chem Phys Lett* 371:719–723
33. Poater J, Duran M, Solà M, Silvi B (2005) Theoretical evaluation of electron delocalization in aromatic molecules by means of atoms in molecules (AIM) and electron localization function (ELF) topological approaches. *Chem Rev* 105:3911–3947
34. Bader RFW (1991) A quantum theory of molecular structure and its applications. *Chem Rev* 91:893–928
35. Feixas F, Matito E, Solà M, Poater J (2008) Analysis of Hückel's $[4n + 2]$ rule through electronic delocalization measures. *J Phys Chem A* 112:13231–13238
36. Feixas F, Matito E, Solà M, Poater J (2010) Patterns of π -electron delocalization in aromatic and antiaromatic organic compounds in the light of the Hückel's $4n + 2$ rule. *Phys Chem Chem Phys* 12:7126–7137
37. Rosenberg M, Dahlstrand C, Kilsa K, Ottosson H (2014) Excited state aromaticity and antiaromaticity: opportunities for physical and photochemical rationalizations. *Chem Rev* 114:5379–5425

38. Zhu J, Fogarty HA, Möllerstedt H, Brink M, Ottosson H (2013) Aromaticity effects on the profiles of the lowest triplet-state potential-energy surfaces for rotation about the C=C bonds of olefins with five-membered ring substituents: an example of the impact of Baird's rule. *Chem Eur J* 19:10698–10707
39. Ottosson H, Kilså K, Chajara K, Piqueras MC, Crespo R, Kato H, Muthas D (2007) Scope and limitations of the Baird's theory on triplet state aromaticity: application to the tuning of singlet-triplet energy gaps in fulvene. *Chem Eur J* 13:6998–7005
40. Möllerstedt H, Piqueras MC, Crespo R, Ottosson H (2004) Fulvenes, fulvalenes, and azulene: are they aromatic chameleons? *J Am Chem Soc* 126:13938–13939
41. Soncini A, Fowler PW (2008) Ring-current aromaticity in open-shell systems. *Chem Phys Lett* 450:431–436
42. Mandado M, Graña AM, Pérez-Juste I (2008) Aromaticity in spin-polarized systems: can rings be simultaneously alpha aromatic and beta antiaromatic? *J Chem Phys* 129:164114
43. Karadakov PB (2008) Aromaticity and antiaromaticity in low-lying electronic states of cyclooctatetraene. *J Phys Chem A* 112:12707–12713
44. Karadakov PB (2008) Ground- and excited-state aromaticity and antiaromaticity in benzene and cyclobutadiene. *J Phys Chem A* 112:7303–7309
45. Matito E, Solà M, Salvador P, Duran M (2007) Electron sharing indexes at the correlated level. application to aromaticity measures. *Faraday Discuss* 135:325–345
46. Chen Z, Jiao H, Hirsch A, Thiel W (2001) The $2(N + 1)^2$ rule for spherical aromaticity: further validation. *J Mol Model* 7:161–163
47. Chen ZF, King R (2005) Spherical aromaticity: recent work on fullerenes, polyhedral boranes, and related structures. *Chem Rev* 105:3613–3642
48. Aihara J (1978) Three-dimensional aromaticity of polyhedral boranes. *J Am Chem Soc* 100:3339–3342
49. Gogonea V, Schleyer PvR, Schreiner PR (1998) Consequences of triplet aromaticity in $4n\pi$ -electron annulenes: calculation of magnetic shieldings for open-shell species. *Angew Chem Int Ed* 37:1945–1948
50. Lazzarretti P (2000) Ring currents. In: Emsley JW, Feeney J, Sutcliffe LH (eds) *Progress in nuclear magnetic resonance spectroscopy*, vol 36. Elsevier, Amsterdam, pp 1–88
51. Lazzarretti P (2004) Assessment of aromaticity via molecular response properties. *Phys Chem Chem Phys* 6:217–223
52. Pelloni S, Lazzarretti P (2011) Correlation between the out-of-plane components of magnetizability and central magnetic shielding in unsaturated cyclic molecules. *J Phys Chem A* 115:4553–4557
53. Pelloni S, Lazzarretti P (2013) Polygonal current model: an effective quantifier of aromaticity on the magnetic criterion. *J Phys Chem A* 117:9083–9092
54. Pelloni S, Monaco G, Lazzarretti P, Zanasi R (2011) Beyond NICS: estimation of the magnetotropy of inorganic unsaturated planar rings. *Phys Chem Chem Phys* 13:20666–20672
55. Feixas F, Jiménez-Halla JOC, Matito E, Poater J, Solà M (2007) Is the aromaticity of the benzene ring in the $(\eta^6\text{-C}_6\text{H}_6)\text{Cr}(\text{CO})_3$ complex larger than that of the isolated benzene molecule? *Polish J Chem* 81:783–797
56. Osuna S, Poater J, Bofill JM, Alemany P, Solà M (2006) Are nucleus-independent (NICS) and ^1N NMR chemical shifts good indicators of aromaticity in π -stacked polyfluorenes? *Chem Phys Lett* 428:191–195
57. Poater J, Bofill JM, Alemany P, Solà M (2006) The role of electron density and magnetic couplings on the NICS profiles of [2.2] paracyclophane and related species. *J Org Chem* 71:1700–1702
58. Poater J, Solà M, Viglione RG, Zanasi R (2004) The local aromaticity of the six-membered rings in pyracylene. A difficult case for the NICS indicator of aromaticity. *J Org Chem* 69:7537–7542
59. Lipscomb WN (1963) *Boron hydrides*. W. A. Benjamin, New York
60. Welch AJ (2013) The significance and impact of Wade's rules. *Chem Commun* 49:3615–3616

61. Mingos DMP (1972) A general theory for cluster and ring compounds of the main group and transition elements. *Nature Phys Sci* 236:99–102
62. Poater J, Solà M, Viñas C, Teixidor F (2013) A simple link between hydrocarbon and borohydride chemistries. *Chem Eur J* 19:4169–4175
63. Poater J, Solà M, Viñas C, Teixidor F (2014) π Aromaticity and three-dimensional aromaticity: two sides of the same coin? *Angew Chem Int Ed* 53:12191–12195
64. Moezzi A, Bartlett RA, Power PP (1992) Reduction of a boron–nitrogen 1,3-butadiene analogue: evidence for a strong B–B π -bond. *Angew Chem Int Ed Engl* 31:1082–1083
65. Moezzi A, Olmstead MM, Power PP (1992) Boron–boron double bonding in the species $[\text{B}_2\text{R}_4]^{2-}$: synthesis and structure of $\{[(\text{Et}_2\text{O})\text{Li}]_2\{\text{Mes}_2\text{BB}(\text{Mes})\text{Ph}\}\}$, a diborane(4) dianion analog of a substituted ethylene. *J Am Chem Soc* 114:2715–2717
66. Nöth H, Knizek J, Ponikvar W (1999) A boron–boron double bond in the dianions of tetra (amino)diborates. *Eur J Inorg Chem* 1999:1931–1937
67. Shoji Y, Matsuo T, Hashizume D, Fueno H, Tanaka K, Tamao K (2010) A stable doubly hydrogen-bridged butterfly-shaped diborane(4) compound. *J Am Chem Soc* 132:8258–8260
68. Grigsby WJ, Power P (1997) One-electron reductions of organodiborane(4) compounds: singly reduced anions and rearrangement reactions. *Chem Eur J* 3:368–375
69. Grigsby WJ, Power PP (1996) Comparison of B–B π -bonding in singly reduced and neutral diborane (4) derivatives: isolation and structure of $\{[\text{Li}(\text{Et}_2\text{O})_2]\{\text{MeO}(\text{mes})\text{BB}(\text{mes})\text{OMe}\}\}$. *Chem Commun* 19:2235–2236
70. Klanberg F, Eaton DR, Guggenberger LJ, Muetterties EL (1967) Chemistry of boranes. XXVIII. New polyhedral borane anions, $\text{B}_8\text{H}_8^{2-}$, B_8H_8^- , and $\text{B}_7\text{H}_7^{2-}$. *Inorg Chem* 6: 1271–1281

Chapter 13

Localized Structures at the Hückel Level, a Hückel-Derived Valence Bond Method

Yannick Carissan, Nicolas Goudard, Denis Hagebaum-Reignier
and Stéphane Humbel

Abstract A simple Hückel Hamiltonian is used and modified to describe localized states, where the electron pairs are confined to bonds between two atoms, or to lone pairs. The electronic delocalization can be considered either as a mixture of these localized states, or through a standard Hückel calculation. The two Hückel-Lewis methods described here attempt to find the coefficients of the mixture, based on energy or overlap consistence with the standard Hückel results. After the description of the two methods, test examples are used to show advantages and drawbacks of the different approaches. In any case, the results are compared to the NBO-NRT approach which is used on the electronic density obtained from standard DFT hybrids calculations such as B3LYP/6-31+G(d). This chapter ends with an introduction to the HuLiS program in which the two methods are implemented.

This contribution is concerned with two approaches, called the Hückel-Lewis (HuLiS) family of methods, that aim at associating a weight to a topological envision of the electronic structure of a molecule. These methods are embedded in the HuLiS code, which will also be briefly described. HuLiS targets primarily at a classroom use, and is limited to planar π -conjugated systems. Our approach has proved to be consistent with more elaborated methods such as the Natural Bond Orbital (NBO)-based methods using Density Functional Theory (DFT) electronic densities, or Valence Bond (VB) approaches [1]. It also has an appreciable

Y. Carissan (✉) · N. Goudard · D. Hagebaum-Reignier · S. Humbel
Aix Marseille Université, Centrale Marseille, CNRS, iSm2, UMR 7313,
13397 Marseille, France
e-mail: yannick.carissan@univ-amu.fr

N. Goudard
e-mail: nicolas.goudard@univ-amu.fr

D. Hagebaum-Reignier
e-mail: denis.hagebaum-reignier@univ-amu.fr

S. Humbel
e-mail: stephane.humbel@univ-amu.fr

simplicity due to the underlying Hückel approximations, and its failures are easy to understand. Finally, it conveys some clear understanding of the electronic delocalization.

13.1 Understanding Delocalization: Lewis Drawings and Mesomerism Versus Molecular Orbitals (Hückel) Method

This section introduces the context and the notation of the Hückel-Lewis (HL) methods. The notations that follow can be found in Table 13.1.

13.1.1 Definition of a Ground State Reference Wave Function

In the following, we shall discuss the status of the objects we use in this chapter. By application of the superposition principle of quantum mechanics, for any system, the exact ground state wave function, Ψ_{exact} , can be written as a linear combination of an infinite number of wave functions. In the framework of a molecule with π electrons, Ψ_{exact} can be separated into two wave functions with the understanding that these wave functions are written on an infinite basis as well:

$$\Psi_{exact} = c_{exact}^{\pi} \Psi_{exact}^{\pi} + c_{exact}^{non-\pi} \Psi_{exact}^{non-\pi} \quad (13.1)$$

The assumption is done here that the space spanned by Ψ_{exact} is the direct sum of the π and the $non-\pi$ spaces. In this chapter, we are interested in treating π systems only, thus we shall not consider $\Psi_{exact}^{non-\pi}$. As mentioned above, Ψ_{exact}^{π} is written on an infinite basis set. With no loss of generality, this basis set can be made of localized wave functions. By local, we mean that single electrons or electron pairs occupy orbitals, which are written on atomic basis functions that are carried by a few number of atoms. If this number is one or two, we shall define these local

Table 13.1 Wave function and energy notations

Ψ_{ref}, E_{ref}	Wave function and energy of the ground state when it is described with the reference method, here Hückel, see (13.9)
Ψ_i, E_i	Wave function and energy of a Lewis structure. They will be described also within the Hückel framework
$\tilde{\Psi}, \tilde{E}$	Truncated description of the wave function and energy of the ground state, expressed on a limited set of N Lewis structures, as defined in (13.6)

structures as Lewis structures. For higher numbers, they would be called non-Lewis:

$$\Psi_{exact}^{\pi} = \Psi_{exact}^{\pi/Lewis} + \Psi_{exact}^{\pi/non-Lewis} \quad (13.2)$$

with:

$$\Psi_{exact}^{\pi/Lewis} = \sum_{i=1}^{\infty} c_i^{\pi/Lewis} \Psi_i^{\pi/Lewis} \quad (13.3)$$

$$\Psi_{exact}^{\pi/non-Lewis} = \sum_{i=1}^{\infty} c_i^{\pi/non-Lewis} \Psi_i^{\pi/non-Lewis} \quad (13.4)$$

The infinite sum comes from the fact that the atomic basis function set is infinite. Yet, we shall focus on valence orbitals only. Furthermore, as we will use the Hückel formalism, we will restrict ourselves to the parametrized basis set of one p orbital per atom, $\{p_i\}_{i=1,n}$. So, we can rewrite (13.3) as:

$$\Psi_{exact}^{\pi/Lewis} = \sum_{i=1}^{N_{MAX}} c_i^{\pi/Lewis} \Psi_i^{\pi/Lewis} + \sum_{i=N_{MAX}+1}^{\infty} c_i^{\pi/Lewis} \Psi_i^{\pi/Lewis} \quad (13.5)$$

The $\{\Psi_i^{\pi/Lewis}\}_{i=1,N_{MAX}}$ is the full set of Lewis structures that can be written in the Hückel basis set. The size of this set, N_{MAX} is usually very large and we shall restrict this set to the N meaningful structures only. In this work, we attempt to approximate $\Psi_{exact}^{\pi/Lewis}$ by a linear combination of $\Psi_i^{\pi/Lewis}$, called $\tilde{\Psi}$. For the sake of simplicity, the label $\pi/Lewis$ will systematically be dropped:

$$\Psi_{exact}^{\pi/Lewis} \approx \tilde{\Psi} = \sum_i^N c_i \Psi_i \quad (13.6)$$

The choice of a set of local wave functions is arbitrary and other choices could be done. For instance, instead of using Lewis and non-Lewis wave functions, one could rewrite Ψ_{exact}^{π} on a set of Slater determinants $\{D_i\}_{i=0,\infty}$, written on delocalized molecular orbitals of occupation number 0, 1 or 2. In some cases, Ψ_{exact}^{π} can be approximated by one determinant D_0 . Thus:

$$\Psi_{exact}^{\pi} = C_0 D_0 + \underbrace{\sum_{i=1}^{\infty} C_i D_i}_{\rightarrow 0} \quad (13.7)$$

In the Hückel framework, D_0 is projected onto the Hückel basis set by the projector operator:

$$\hat{P} = \sum_i^n \sum_j^n |p_i\rangle \langle p_j| \quad (13.8)$$

The delocalized wave function of the ground state can be written as:

$$\Psi_{exact}^\pi \approx \Psi_{ref} = C_0 \sum_i^n \sum_j^n |p_i\rangle \langle p_j| D_0 \quad (13.9)$$

As C_0 is not meaningful in this context, Ψ_{ref} can be normalized without loss of information.

13.1.2 Lewis Structures

In the process of understanding chemistry, Lewis structures have a prominent position. A Lewis structure is often a good approximated answer to the question “how is the electronic structure of this molecule?”. Besides, whenever a unique Lewis structure does not suffice, that is when some delocalization occurs, mesomerism is invoked. With mesomerism, a set of Lewis structures is defined, and a weight is attributed to each of them (w_i for the i th structure). This weight represents the importance of the structure. The larger w_i , the more significant the i th structure will be. Such a weight can be computed in Valence Bond-like formalisms [2, 3], but it is usually only estimated with the following qualitative rules, by decreasing priority:

- Is the octet rule fulfilled?
- Are there charge separations?
- Is the charge distribution consistent with the electronegativity?

Whenever the answer to one of these questions is no, the weight of the considered structure gets smaller, and the corresponding structure gets less likely. This qualitative estimate leads to the following labeling: two or more structures can be equivalent, or a major structure can be found, together with one or more minor structures.¹ Hence the weights can be somehow ordered.

They can also be estimated numerically from $\tilde{\Psi}$, (13.6). As local structures may overlap, $S_{ij} \neq 0$ in (13.10), in a resonant scheme that involves N structures, the

¹Two structures are equivalent when they behave the same and/or when one can be deduced from the other by symmetry.

weight (w_i) can be calculated according to the Coulson-Chirgwin's definition (13.11) [4].

$$S_{ij} = \langle \Psi_i | \Psi_j \rangle \quad (13.10)$$

$$w_i = c_i \sum_j^N c_j S_{ij} \quad (13.11)$$

Unfortunately, the computation of the Ψ_i is usually not straightforward because localized orbitals are in principle non orthogonal, and these overlapping orbitals bring computational difficulties. Hence, Valence Bond computations have remarkably been superseded by methods based on Molecular Orbitals (MO) [5], where the orbitals are orthogonal to each other. Density functional theory has also provided interesting alternatives for efficient computations [6]. However, by these methods the electronic localization is lost and topological analysis have to be settled a posteriori [7–14]. Here we make use of the special features of the Hückel approximations to get the Ψ_i , and to evaluate the c_i and w_i in a straightforward way.

13.1.3 Hückel in a Nutshell

The Hückel method is based on two $n \times n$ matrices, where n is the number of π orbitals: the overlap matrix \mathbf{S} and the Hamiltonian matrix \mathbf{H} , which are expressed on the basis of the atomic orbitals that are involved in the so-called π system. In the Hückel approximation, \mathbf{S} is simply equal to the identity matrix: the atomic orbitals of two atoms A and B are considered orthogonal ($S_{AB} = \delta_{AB}$). To compensate for the fact that the method deals with non-overlapping orbitals, topological information is embedded in \mathbf{H} , for instance for a linear system see (13.12). The \mathbf{H} matrix is also called the topological matrix of the system. Remind that if A is a carbon atom, the diagonal term $H_{AA} = \alpha_A = \alpha$. Formally, α is negative as it is the energy of the occupied $2p_z$ orbital of a sp^2 hybridized carbon atom. When two such carbon atoms are bonded, the off-diagonal term H_{AB} is set to β which is negative as the low lying orbital is an in-phase interaction.

The relative electronegativity of an heteroatom B with respect to carbon is taken into account by a shift of the diagonal term in β unit: $H_{BB} = \alpha_B = \alpha + \beta \times h_B$. Since $\beta < 0$, when B is more electronegative than a carbon, $h_B > 0$.

The off-diagonal terms H_{AB} are negative and are relative to the strength of the interaction between the two atoms ($H_{AB} = k_{AB} \times \beta$, with $k_{AB} \geq 0$ because $\beta < 0$). The values of the k_{AB} are related to the nature of the atoms A and B , and to their coordination number [15]. We used the values proposed by Van-Catledge throughout [16]. It is noteworthy that non-bonded atoms (A and B) have a zero interatomic Hamiltonian parameters ($H_{AB} = 0$).

$$\mathbf{H} = \begin{pmatrix} \alpha_A & k_{AB}\beta & 0 & \dots & 0 \\ k_{AB}\beta & \alpha_B & \ddots & 0 & 0 \\ 0 & \ddots & \alpha_C & \ddots & \\ \vdots & 0 & \ddots & \ddots & \ddots \\ 0 & 0 & & \ddots & \alpha_n \end{pmatrix} \quad (13.12)$$

Orbital energies are obtained by solving:

$$\det(\mathbf{H} - \varepsilon\mathbf{S}) = 0 \quad (13.13)$$

The vector ε contains the energies (ε_j) of all the molecular orbitals (say π_j) of the molecule. In order to solve (13.13), it is of common use to write the determinant as a function of a reduced dimensionless variable $x = \frac{\alpha - \varepsilon}{\beta}$:

$$\det(\mathbf{H} - \varepsilon\mathbf{S}) = \begin{vmatrix} x + h_A & k_{AB} & 0 & \dots & 0 \\ k_{AB} & x + h_B & \ddots & 0 & 0 \\ 0 & \ddots & x + h_C & \ddots & \\ \vdots & 0 & \ddots & \ddots & \ddots \\ 0 & 0 & & \ddots & x + h_n \end{vmatrix} \quad (13.14)$$

$$= P_n(x) \quad (13.15)$$

This determinant is a polynomial of x , called the characteristic polynomial of the system. Its roots x_i lead to the eigenvalues of the molecular orbitals $\varepsilon_i = \alpha - x_i\beta$. Thus, one can compute the total energy of the system either by finding the solutions of (13.13), or by finding the roots of the characteristic polynomial $P_n(x)$. This polynomial expression will be used in Sect. 13.4.3 to define the topological resonance energy.

The molecular orbitals obtained by the Hückel method are delocalized over the molecule, and are used in a Slater determinant to build the reference wave function (Ψ_{ref}) of our Hückel-Lewis family of methods. Hence, for ethylene $\Psi_{ref} = |\pi\bar{\pi}|$ and for a four- π -electron molecule like acrolein, it reads $\Psi_{ref} = |\pi_1\bar{\pi}_1\pi_2\bar{\pi}_2|$. Thus, we consider that a single determinantal wave function adequately describes the system at hand. Radicals are considered in a restricted formalism: two electrons of opposite spin share the same spatial part. Higher spin states are not considered in our implementation.

The energy of a configuration is the sum of the energies of the occupied orbitals: $E_{ref} = \sum_j^{n_{occ}} n_j \varepsilon_j$, where n_j is the occupation number of the j th orbital. Hence, the bielectronic part that would differentiate an open shell singlet from the triplet is obviously missing.

13.1.4 From Hückel Molecular Orbital to Lewis Structures

In the Hückel-Lewis family of methods, we use the fact that the Hückel Hamiltonian is versatile, so electrons can be localized by simply zeroing out some terms in a modified Hamiltonian matrix. This terms are those that correspond to single bonds in a Lewis structure. The new Hamiltonian leads to eigenvectors that correspond to local orbitals, and corresponding eigenvalues are also obtained. The wave function Ψ_i , that describes the i th structure, is again a Slater determinant, obtained by distributing the electrons in the appropriate local orbitals.

Acrolein can be used as an example (Fig. 13.1). The major structure is evidently structure **I**, and structure **II** is a reasonable structure involved in the electronic delocalization because of the oxygen's larger electronegativity compared to carbons. For the same reason, structure **III** has a priori less chemical relevance. The Hückel-Lewis methods can compute the weights of each structure and help to determine if a structure is important.

To describe structure **III**, the four π electrons must be located as follows: the carbon C_1 (on the left) must have two electrons in its p_π orbital, and two other electrons must be in the central double bond. We shall emphasize that the oxygen must have an empty atomic orbital. These localized orbitals are obtained by using a modified Hamiltonian that somehow isolates the different electronic parts of the molecule: left carbon, central C–C bond, and right oxygen. It is noteworthy that such a modified Hamiltonian applies to either structure **II** or structure **III**. The eigenvectors and eigenvalues are thus the same for both (Fig. 13.2), but the electronic distribution differentiates the two structures. Hence the electronic configuration $(\pi)^2(p_O)^0(p_C)^2(\pi^*)^0$, with a filled orbital centered on carbon C_1 , corresponds to **III**, while $(\pi)^2(p_O)^2(p_C)^0(\pi^*)^0$, with a filled orbital centered on the oxygen, corresponds to structure **II**.

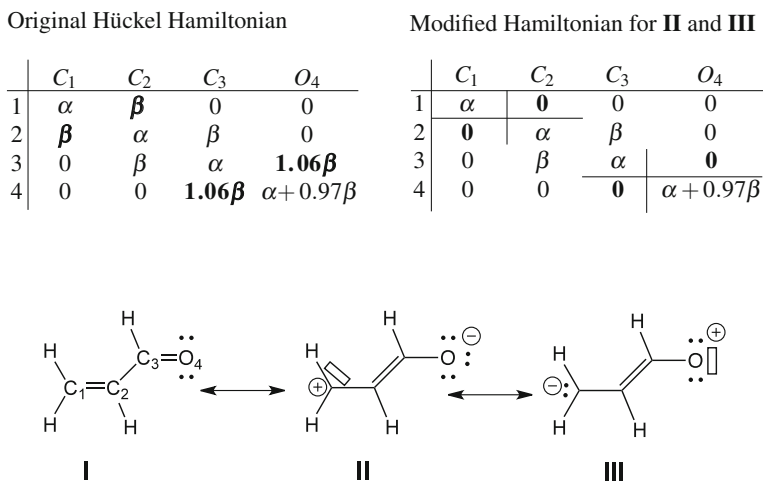
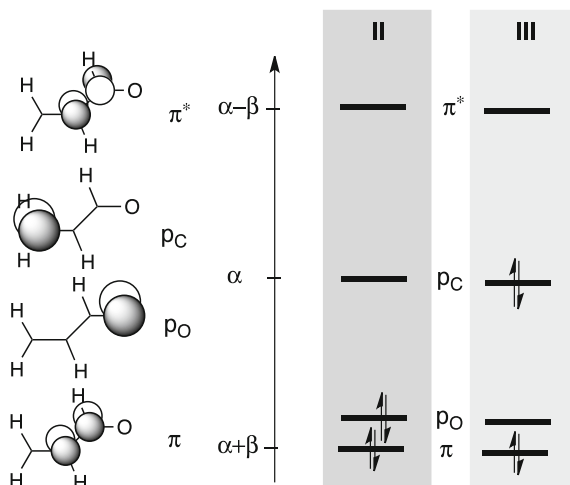


Fig. 13.1 Acrolein's mesomeric structures. The atoms are numbered from the left to the right

Fig. 13.2 Acrolein's localized orbitals for structures **II** and **III**, and corresponding orbital occupation



This zeroing-out technique is straightforward to use and de facto isolates any double bond or lone pair in a molecule. The Lewis structures can then be characterized both with a wave function Ψ_i and an energy E_i . Delocalization energies are obtained by energy difference between the energy of a localized structure, and E_{ref} , which is the Hückel energy of the molecule.

One shall notice that contrary to *ab initio* calculations, where fully localized orbitals are necessarily non-orthogonal and lead to heavy calculations, Hückel orbital localization does not bring any complication, neither to the code, nor to the computational effort. The only slight complication arises from open shell covalently paired electrons, when the two electrons are not in the same π orbital but belong to two different orbitals, say a and b . We shall represent such a singlet coupling with a plain arc that links the two electrons' dots (Fig. 13.3). The wave function associated to such a case contains the determinants $|a\bar{b}| + |b\bar{a}|$.



Fig. 13.3 Convention for covalently paired electrons. Three representative cases

13.2 Two Different Hückel-Lewis Schemes to Define a Configuration Interaction in the Hückel Framework

The Hückel framework defines the reference wave function, Ψ_{ref} and its energy, E_{ref} . It is possible to extract information from this structure in the same way it is done at high level of calculations. The Hückel solution should be seen as a quantum chemistry calculation done in a minimal basis. If one tries to write the reference wave function on a set of localized structures, many approaches can be defined. These approaches are a posteriori analysis of the reference wave function and help to understand the nature of its electronic structure. We defined the following schemes:

HL-CI: The Hückel Lewis Configuration Interaction (CI) is formally equivalent to the Hückel method for the interaction between several localized structures: one can diagonalize a Hamiltonian in the basis of localized Lewis structures. In the following, this will be referred to as the *energy based scheme*.

HL-P: The Hückel Lewis Projection is a CI expansion based on the overlap between Ψ_{ref} and each of the chosen localized structures Ψ_i . This will be referred to as the *space based scheme*.

13.2.1 Energy Based Scheme

The HL-CI method is an analog of the Hückel method in the multiconfigurational framework [17–20]. It is based on the assumption that the delocalized wave function, which has the lowest possible energy, results from the interaction of all local structures of higher energy. Let Ψ_{ref} be a delocalized wave function of energy E_{ref} to be written on the basis of N local structures $\{\Psi_i\}_{i=1,N}$ of energy E_i . One searches $\tilde{\Psi}$, of energy \tilde{E} :

$$\tilde{\Psi} = \sum_i^N c_i \Psi_i \quad (13.16)$$

such that:

$$\tilde{E} = E_{ref}. \quad (13.17)$$

In Hückel theory, atomic basis functions are assumed to be orthonormal. The interaction between neighbouring functions is included in the off-diagonal term of the Hamiltonian. In the HL-CI framework, these two approximations are done among the local structures.

$$S_{ij} = \delta_{ij} \quad (13.18)$$

$$H_{ij}|_{i \neq j} = B < 0 \quad (13.19)$$

$$H_{ii} = E_i \quad (13.20)$$

Yet, there is no way to determine a vicinity between structures: there is no topological matrix in the localized structures space. Thus, we add the approximation that the local structures interact in the same manner between each other. This term is called B by analogy with the β Hückel constant (13.19). It is worth noting that for any system with more than one localized structure, the B value will assure that the condition (13.17) is fulfilled. The choice $B < 0$ implies that the lowest eigenvalue corresponds to a linear combination in which all c_i are positive. This means that the approximate solution $\tilde{\Psi}$ will always be an in-phase interaction between the Ψ_i contributors. Thus, HL-CI will not be able to give the appropriate solution when out-of-phase interactions are required, that is when symmetry will require such an interaction. This shortcoming will be illustrated in Sect. 13.3.1 with the allyl radical case. HL-CI weights are computed using the Coulson-Chirgwin definition. As $S_{ij} = \delta_{ij}$ (13.18), the weight of a structure is the square of its coefficient.

13.2.2 Space Based Scheme

The HL-P method focuses on the overlap between the localized structures and the reference wave function. The wave function is written as a linear combination of localized structures (13.16). Only the optimization criterion changes: instead on focusing on the energy, it is the overlap between the linear combination of localized structures and the reference wave function, τ which is aimed at being maximized by improving the $\{\Psi_i\}_{i=1,N}$ set. This is done either by increasing N , or by choosing more significant Ψ_i structures. Let us assume that $\langle \Psi_{ref} | \Psi_{ref} \rangle = 1$. Then we define the quantity to be improved as:

$$\tau = \langle \Psi_{ref} | \tilde{\Psi} \rangle \rightarrow 1 \quad (13.21)$$

The overlap matrix of the localized structures, \mathbf{S} is computed, as well as, \mathbf{S}_{ref} , the vector which contains the overlap between each localized structure, Ψ_i , and Ψ_{ref} . The wave functions, localized or not, are written as single Slater determinants. Let Ψ_i be a local structure written on a set of non orthogonal spin orbitals $\{\phi_k^i\}_{k=1,n_{el}}$ and Ψ_j another local structure written on a set of non orthogonal spin orbitals $\{\phi_l^j\}_{l=1,n_{el}}$. Then, S_{ij} as defined in (13.10), is computed as the determinant of the overlap matrix of the non orthogonal occupied spin orbitals [21, 22]:

$$S_{ij} = \det(\langle \phi_k^i | \phi_l^j \rangle) \quad (13.22)$$

To find the c_i coefficients (elements of vector \mathbf{C}), one solves the following linear system of equations:

$$\langle \Psi_i | \Psi_{ref} \rangle = \sum_j^N c_j S_{ij}; \quad i = 1, N \quad (13.23)$$

$$\Leftrightarrow \mathbf{S}_{ref} = \mathbf{S}\mathbf{C} \quad (13.24)$$

At this stage, the norm of $\tilde{\Psi}$ is a direct measurement of its quality: the closer to one, the better. As it is custom in quantum chemistry and in order to be able to extract meaningful information from $\tilde{\Psi}$, in the rest of this chapter, it is normalized.

The Coulson-Chirgwin weights (13.11) are not defined positive. If a negative weight is computed, it means that the set of localized Lewis structures, $\{\Psi_i\}_{i=1,N}$, is over complete. This can be detected by checking that eigenvalues of \mathbf{S} are close to zero. This is an indicator of redundancy in the $\{\Psi_i\}_{i=1,N}$ set: the structures were not adequately chosen and other choices should be done.

In HL-P, the trust parameter, τ (13.21), is a measure of the completeness of the set $\{\Psi_i\}_{i=1,N}$ in the space spanned by Ψ_{ref} . It shall be used as well in the HL-CI framework as safeguard. In the context of calculating τ , the exact overlap matrix must be used (13.22). In the HL-CI framework, the B constant was arbitrarily chosen to be negative as it models an in-phase interaction. Any system which requires out-of-phase interaction will exhibit a much lower τ with HL-CI than with HL-P. It contains also implicitly the overlap of a given structure with the reference wave function, which is assumed to be positive.²

13.3 Comparison of the Two Hückel-Lewis Schemes: Pros and Cons Through Examples

In this section, we compare the two Hückel-Lewis schemes previously defined with NBO-NRT calculations [9, 13, 14] on typical examples.

We first show in Sect. 13.3.1 that the space-based HL-P and energy-based HL-CI methods give comparable results in the description of the resonance of the allylic systems (cation, radical and anion), except for the radical case, where the HL-P method is more reliable as it respects symmetry.

In Sect. 13.3.2, we discuss the butadiene and benzene cases by examining how the trust parameter τ of the HL-P method is modified when Lewis structures are

²It is the same in the Hückel method: β is negative because the low energy solution is an in-phase interaction and because two adjacent p orbitals overlap positively.

added or removed in a given mesomerism scheme and how this parameter helps choosing the important structures that best describe the resonance in these systems.

All NRT calculations have been performed using the NBO 6.0 program [23]. Unless otherwise mentioned, the geometries of the systems studied in this section have been optimized at the B3LYP/6-31+G(d) level of calculation, using the G09 Gaussian [24] package. The values of the trust parameter τ differ from previously published work [1], the values published here corresponding to a normalized $\tilde{\Psi}$.

13.3.1 Resonance in the Allyl Series: Cation, Radical and Anion

Let us examine in this section the mesomerism in the three allylic systems: the cation, radical and anion. Such molecules have served as model systems in numerous theoretical studies on π delocalization [25–29].

In the following, the Hückel reference wave functions for the cation, radical and anion will be noted Ψ^+ , Ψ^\bullet and Ψ^- , respectively (see Fig. 13.4). For each system, three Lewis structures are considered: the left (Ψ_L) and right (Ψ_R) structures, whereby the positive/negative charge or radical is located on the left and on the right of the molecule skeleton, respectively. In the third structure (Ψ_C), the positive/negative charge or radical is located on the central carbon atom, whereas the electrons on opposite carbons are covalently paired (see Fig. 13.3). The mesomerism scheme for the allyl radical is represented in Fig. 13.5, as an example.

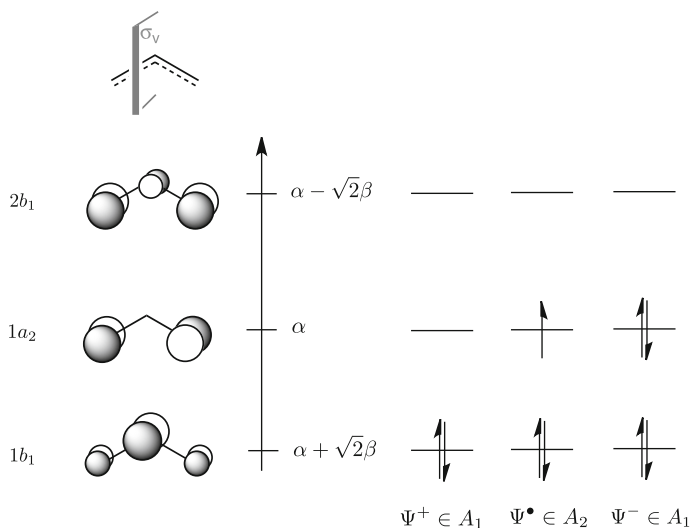


Fig. 13.4 Hückel molecular orbital diagram and symmetries of the ground state of the allyl cation (Ψ^+), radical (Ψ^\bullet) and anion (Ψ^-)

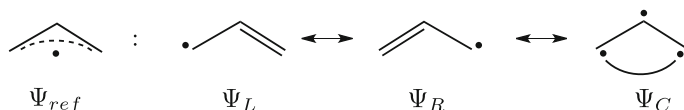


Fig. 13.5 Mesomerism scheme for the allyl radical: the delocalized Hückel wave function Ψ_{ref} is represented as a linear combination of resonating Lewis structures Ψ_L , Ψ_R and Ψ_C

Table 13.2 Weights w_i of resonant Lewis structures for the cationic, radical and anionic allyl molecules obtained with the two schemes HL-CI and HL-P and compared with the standard NRT (B3LYP/6-31+G(d)) weights

Molecule	HL-CI		HL-P		NRT	
	w_i	τ	w_i	τ	w_i	τ
+ Allyl	50/50/	92	50/50/	92	50/50/	97
	46/46/8	98	44/44/12	99	45/45/10	97.5
• Allyl	50/50/	0	50/50	92	50/50/	96
	39/39/22	0	50/50/0	92	50/50/0	–
- Allyl	50/50/	92	50/50/	92	50/50	94
	46/46/8	98	44/44/12	99	44/44/12	96.5

The weights w_i (in %) are given in the order $\Psi_L/\Psi_R/\Psi_C$ and gathered along with the trust parameters τ (in %) for each method

We want to compare here the weights of each Lewis structure given by the two different Hückel-Lewis schemes (HL-CI and HL-P) discussed in Sect. 13.2 with those obtained by the NRT method [9, 13, 14] (see Table 13.2).

In the two-structure mesomerism, the weights for Ψ_L and Ψ_R are equal to 50 % for the allyl series, as expected. The trust parameters given by the two schemes are equal and agree well with the NRT method (from about 92–99 %).³

There is however a notable exception for the allyl radical: the trust parameter, $\tau = 0\%$, indicates an incorrect HL-CI wave function. This surprising result can be traced back in the assumption $B < 0$ (13.19) and inspection of the symmetry of the allyl radical state provides an explanation. As mentioned earlier in Sect. 13.2.1, this assumption implies an in-phase interaction between the Lewis structures (positive c_i coefficients in (13.16)). As pointed out by Goddard [25], this actually corresponds to an excited state. In the allyl radical case, the ground state space symmetry is A_2 (C_{2v} point group), as can be seen from Fig. 13.4. The Hückel wave function is antisymmetric with respect to the σ_v plane perpendicular to the molecular plane. Thus, only an out-of-phase combination of the resonant structures Ψ_L and Ψ_R can account for the correct symmetry of the ground state, since each structure Ψ_L and

³Note here that the τ value for the NRT results is defined as the sum of the weights of the π /Lewis resonant structures built from the NBO analysis of the molecular density. The NRT weights given here are renormalized so that the sum of the weights of all considered contributors is equal to 100 %. The same definition will apply in Sect. 13.3.2.

Ψ_R are symmetric to each other with respect to the σ_v plane. The in-phase approximate wave function $\tilde{\Psi} = \Psi_L + \Psi_R$ is of B_1 symmetry and has thus a zero overlap ($\tau = 0\%$) with the reference state Ψ_{ref} (A_2 symmetry).

As a summary for the two-structure mesomerism, we have learned that the HL-CI method, by its construction, can not account for an out-of-phase combination of resonant structures that would be required by the symmetry of the reference state Ψ_{ref} and the trust parameter is a good indicator for this shortcoming.

Let us now examine the three-structure mesomerism scheme. First, one can see that the weights for the allyl cation and allyl anion are the same. This stems from the fact that the Hückel molecular orbitals are the same for the neutral, cationic or anionic systems, the different values for the neutral being due to symmetry.

The HL-CI and HL-P methods give similar weights, which compare very well with the NRT weights, in the case of the cation and anion. The trust parameters are improved compared to those of the two-structure mesomerism by about 10 %. Regarding the radical, the HL-CI method gives an incorrect non-zero weight of 22 % for Ψ_C , as a direct consequence of the symmetry problem of the HL-CI method previously discussed. The third structure Ψ_C is namely symmetric with respect to the σ_v plane and cannot improve the description of the reference state. Its weight should be zero and the quality of the mesomerism given by τ remains unchanged when this structure is included. This can be seen in Table 13.2 for the HL-P method. This method gives the correct weight for Ψ_C as it intrinsically relies on the overlap of each Lewis structure with the Hückel reference wave function and thus indirectly accounts for the correct symmetry.

As a short summary on this study of the allyl series, both HL-CI and HL-P methods provides reliable weights for the resonant structures of the ionic allyl species compared to the weights given by the NRT method. For the allyl radical, only the HL-P method gives the correct weight of the minor structure. The trust parameter τ is a good safeguard to identify symmetry problems in the HL-CI method. In the following section, we will only compare results obtained with the HL-P method with the NRT calculations.

13.3.2 *Measuring the Quality of a Mesomerism Scheme: The Butadiene and Benzene Cases*


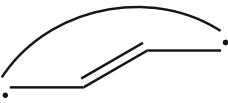
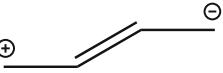
We want to show here that the trust parameter is a good indicator of the completeness of a given mesomerism scheme, that is, how relevant the chosen resonant Lewis structures are, in quality and number. We illustrate this point with two typical examples: the butadiene and benzene molecules, where we compare the HL-P method with the reference NRT calculations.

13.3.2.1 The Butadiene Case

The butadiene molecule is the simplest conjugated diene in which electron delocalization occurs. As can be seen from Table 13.3, the major neutral Lewis structure of butadiene describes well the Hückel reference wave function Ψ_{ref} as it spans 90 % of the space. The description is gradually improved when including the diradical structure (case 2a: $\tau = 92$ %) along with the two ionic structures (case 3: $\tau = 95$ %). The comparison of case 2a with case 2b ($\tau = 92$ %) tells us that the two ionic structures and the diradical contribute the same amount to the description of Ψ_{ref} , i.e. they overlap similarly with Ψ_{ref} . But they do not overlap with each other, so that the trust parameter increases when both are added.

Regarding the weights of the best set (case 3), the HL-P method confirms the dominance of the purely neutral Lewis structure (81 %) over the diradical structure (9 %), which weight is equivalent to the weight of the two ionic structures together (2×5 % = 10 %). This is in good agreement with the NRT results, which shows the same tendency. In the NRT calculations, the major structure came along with four zwitterionic structures having adjacent charges (overall weight of 16 %, each weighting 4 %). Two of these zwitterionic structures have charges on carbon 1 and 2 and a double bond between carbon 3 and 4. In the two others, charges and double bond are permuted. They complete the description of each double bond of this major structure. This behavior of the NRT method will also be encountered in the benzene case.

Table 13.3 Comparison of the HL-P weights w_i (in %) and trust parameter τ (in %) for the butadiene resonance scheme with their NRT counterparts

				τ
	(1)	(1)	(2)	
HL-P				
Case 1	100	–	–	90
Case 2a	91	9	–	92
Case 2b	90	–	5	92
Case 3	81	9	5	95
NRT	70(+16) ^a	8	3	95

The number of equivalent contributors are indicated in parenthesis. The highlighted line corresponds to the best set of contributors

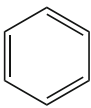
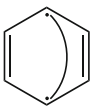
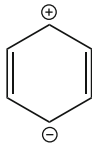
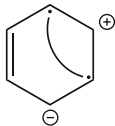
^aThe weights of the purely covalent Lewis structure account for 70 % and those of the four ionic structures with adjacent charges for 16 %. See text for explanation

13.3.2.2 The Benzene Case

The benzene molecule is an archetype for the study of π delocalization and aromaticity (see e.g. the reviews [30, 31] and references therein). In standard chemistry textbooks, the resonance in the benzene molecule involves only the two major Kekule structures (see Table 13.4). However this two-structure scheme is by far incomplete to describe the π delocalization of benzene. It is well recognized in the VB community that about 175 VB structures are needed in order to grasp the resonance in the benzene molecule [32].

In Table 13.4, we illustrate nicely with the HL-P method the need of numerous structures in order to obtain a good description of the resonance, that is, a high value of τ . When only the two Kekule structures are considered (case 1), the HL-P trust parameter is rather low (77 %). When this set is augmented with the three Dewar structures (case 2), τ slightly increases to 80 %, which is obviously still not satisfactory. One has to add six equivalent para ionic structures to gain almost 10 % from the initial Kekule set (case 3), and another 24 extra meta ionic/covalent contributors to reach 97 % of the spanned space (case 4). The resulting 35-structure set corresponds to 145 among the 175 VB structures. The major importance of the Kekule

Table 13.4 Comparison of the weights w_i (in %) and trust parameter τ (in %) for the benzene resonance scheme between the HL-P and NRT methods

	 Kekule (2)	 Dewar (3)	 para ionic (6)	 meta ionic/cov. (24)	τ
HL-P					
Case 1	50	–	–	–	77
Case 2	40	7	–	–	80
Case 3	28	7	4	–	85
Case 4	22	5	3	1	97
Case 5	–	12	6	1	86
Case 6	–	–	9	2	70
NRT	19.5(+20) ^a	5	1	0	90

The number of equivalent contributors are indicated in parenthesis. The highlighted line corresponds to the best set of contributors

^aThe weights of the two Kekule structures account for 19.5 % and those of the 12 ionic Lewis structures with adjacent charges for 20 %. See text for explanation

and Dewar structures among the full set of case 4 can be evaluated when one removes them: the quality of the resonance scheme drops to 86 % when removing only the Kekule structures (case 5) and 70 %, when removing both (case 6).

The NRT results reported in Table 13.4 were obtained with the full set of 35 structures (case 4) as initial structures, so that we can compare both methods with the same mesomerism scheme. They indicate an overall good description of the density of benzene ($\tau = 90\%$). The best HL-P set of contributors (highlighted line corresponding to $\tau = 97\%$ in Table 13.4) compares well with the NRT results as it provides the same tendency regarding the relative importance of the structures: the Kekule structures are dominant (weight of 22 % in HL-P against 19.5 % in NRT) over the Dewar structures (weight of 5 % in both methods), and over the para ionic structures (weight of 3 % in HL-P against 1 % in NRT). In the HL-P scheme, the 24 meta ionic/covalent structures have a small weight of 1 % each and contribute to the resonance scheme (τ is improved by 12 % when they are included) but are absent in NRT. One has to keep in mind that the HL-P method relies on a Hückel wave function and does not have as much flexibility as the NRT method to describe the resonance of benzene. This explains the small discrepancies between both methods. Moreover, as in the butadiene case, the major Kekule structures came along with 12 zwitterionic structures having adjacent charges. Two of these zwitterionic structures have charges on carbon 1 and 2 and double bonds elsewhere, which leads to six structures per initial Kekule structure when permuting charges and double bonds (two such structures per double bond for the six double bonds of the Kekule structures) and account for an overall weight of 20 %. Their weights are added to the weight of the Kekule structures, as they contribute to their description.

As a summary of the two examples discussed in this section, the trust parameter τ designed in the HL-P method provides an excellent means of measuring how good a given set of contributors is, to mimic the reference wave function.

13.4 HuLiS: An Easy-to-Use Code to Link Hückel to Lewis Concepts

HuLiS started as a Java applet and evolves to a javascript/HTML5 script to increase the ease of use [33]. The program is available as a web application at <http://ism2.univ-amu.fr/hulis>,⁴ and can also be downloaded as a standalone java applet. The mobile version is available from the same address. In addition to the simple Hückel method, HuLiS implements the two methods described herein and the topological resonance module described in this section.

⁴Note to the referee: at the moment HuLiS is at <http://www.hulis.free.fr> but it will migrate soon.

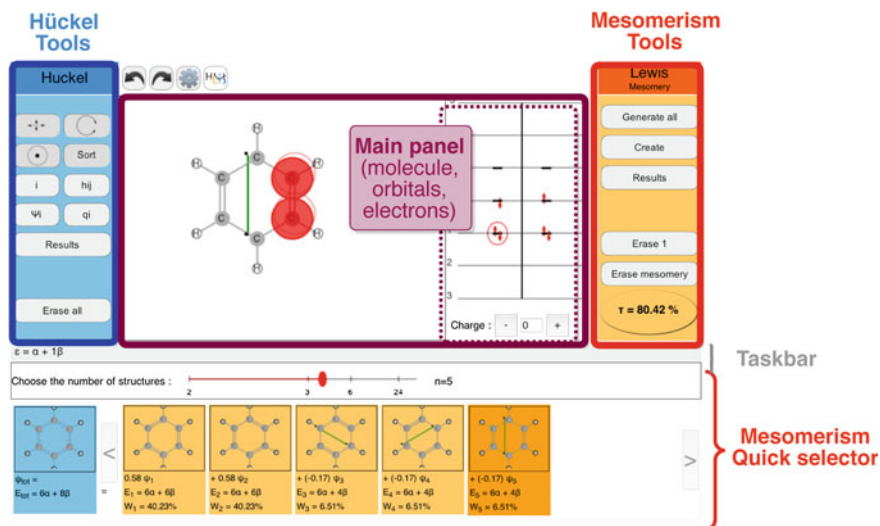


Fig. 13.6 HuLiS's screenshot of the mobile version

13.4.1 Overview of the HuLiS Program

The user can build a structure, and the Lewis structures can be generated and their weights are evaluated almost instantaneously. All the process is graphical.

The interface (Fig. 13.6) differentiates the tools that concern the delocalized wave function (Hückel tools on the left, in blue) and the tools for mesomerism (Mesomerism, on the right, in orange). The central panel contains the drawings and displays the molecule, and possibly the orbitals, charges, atom numbering, parameters. In the upper part, close to the <Undo>/<Redo> buttons, the user finds the <preference> and the <about> buttons.

The user starts by the left-hand side part: the molecule has to be defined through the types of atoms and their connectivity, which produces the Hamiltonian matrix. This Hückel Hamiltonian is solved “on the fly”. Neat outputs can be viewed with the left-hand side <results> button. The right-hand side part can then be used to study the mesomerism. Again, tidy outputs can pop up with the right-hand side <results> button. In the results panel, the program generates inputs for use in gaussian [24], with the NBO strings that correspond to the Lewis structures. Similarly, HuLiS can read xyz coordinates and NBO input strings using copy/paste or via the Files Reading menu.⁵

⁵The molecule has however to be Hückel-compatible i.e. essentially flat. Methyl substituents are allowed.

13.4.2 Automatic Generation of Localized Structures

The automatic generation of localized structures is a two-step procedure, Fig. 13.7. In the following, we shall illustrate this procedure with the $C_5H_7^\bullet$ radical species.

The starting point is a structure in which each atom carries its own π electrons. This is stored as a n dimension array, called Γ , filled with integers equal to the number of π electrons on each atom. In our example, at this point, the only structure is such that $\Gamma = [1|1|1|1|1]$. From this structure one generates all other possible structures under the following constraints:

- do not exceed a maximum number of charge separation;
- do not exceed a maximum number of radical centers;
- do not put more than two electrons on one center.

These constraints are set up by the user in the preferences. The first step of the procedure keeps the array unchanged, $\Gamma = [1|1|1|1|1]$ (Fig. 13.7, Path 1), or leads for instance to $\Gamma = [0|1|1|2|1]$ (Path 2). Additionally, structures with adjacent charges are removed. Thus, $\Gamma = [0|2|1|1|1]$ is discarded (Path 3). From these structures, in a second step, one generates the final set by coupling the radical centers if necessary. The coupling of two adjacent radical centers leads to a double bond. The number of remaining radicals is computed. Each structure with a larger number of radical centers than the maximum allowed is discarded. In the current version (3.1.2c) this number is limited to three. Thus, $\Gamma = [1|1|1|1|1]$ is not accepted as such (i.e. with no singlet coupling). Furthermore, the number of charge

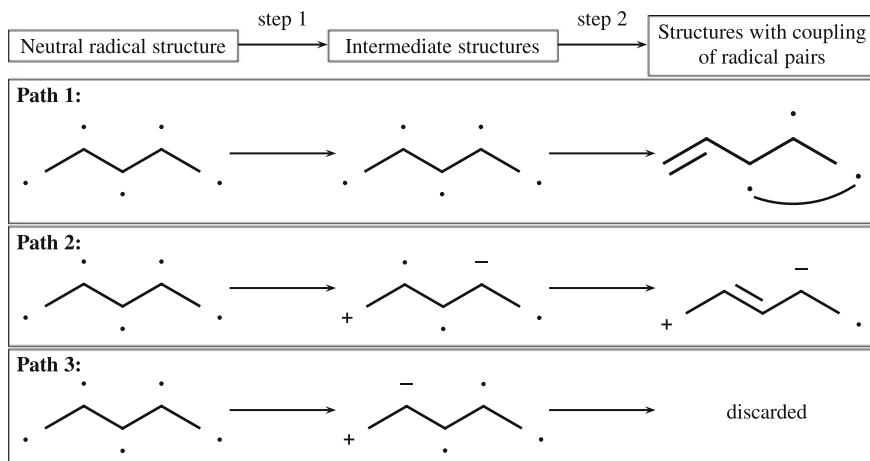


Fig. 13.7 Example of two possible paths which generate relevant Lewis structures for the $C_5H_7^\bullet$ species. In such a way, 39 structures can be generated which respect the conditions defined in the text

separations is by default set to one, i.e. one positive charge and one negative charge on two different atoms. We believe it is a wise choice as it could be hard to give a chemical meaning to structures with more charge separation.

13.4.3 Topological Resonance Energy

The Topological Resonance Energy (TRE) is a measurement of the resonance energy based on the topology of the molecule [34–36]. It is defined as the difference between the energy of the considered molecule and its acyclic counterpart. The latter is a fictitious yet well defined system in which aromaticity is lost. A way to suppress aromaticity is to consider the mixture with an anti-aromatic system. It was recently shown that the characteristic polynomial (13.15) of the acyclic system is the average of the characteristic polynomial of the real molecule and its anti-aromatic Möbius counterpart [37]. In the framework of cyclic species with π electrons, the fictitious Möbius molecule is obtained by rotating along the n -fold cycle the p orbital of the i^{th} vertex by $\frac{(i-1)\pi}{n}$. This leads to an out-of-phase interaction between the p orbitals of the first and the n th vertices. In other words, the p axis rotates by π radians along the cycle, like the Möbius ribbon. This rotation is equivalent to setting all interactions equal between adjacent centers except for the last one which is multiplied by -1 .

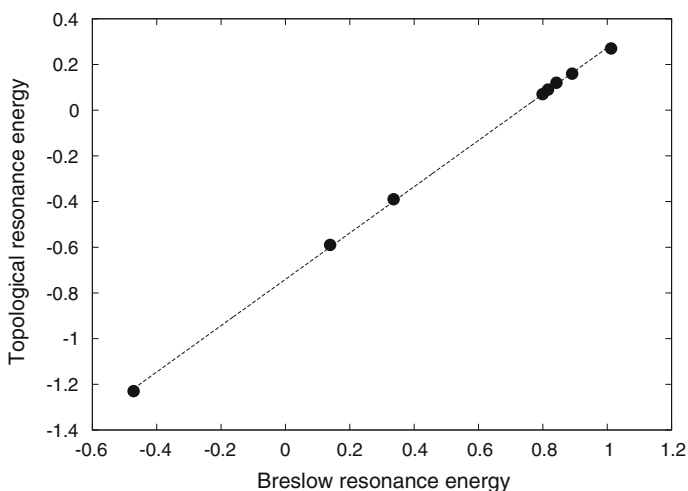
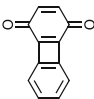
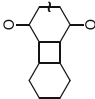
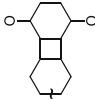
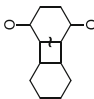
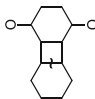
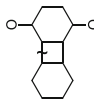
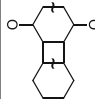


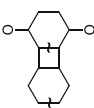
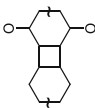
Fig. 13.8 Agreement between Breslow resonance energy [40] and topological resonance energy for cyclic species $C_n H_n$ for $n = 4, 6, 8, 10, 12, 14, 18, 22$. The fit on the function $P^n(x) = 1.0138 \times x - 0.7404$ is excellent: $\chi^2 = 10^{-4}$

Table 13.5 1,4-Biphenylene/dione and its decomposition into Möbius structures

	$P_0(x) = x^{14} - 1.9400x^{13} - 15.3063x^{12} + 29.3398x^{11} + 84.0563x^{10} - 160.0174x^9 - 209.5683x^8 + 403.3896x^7 + 236.0142x^6 - 488.6627x^5 - 86.6499x^4 + 255.2086x^3 - 17.0579x^2 - 37.0781x + 7.2056$	$E_0 = 20.87\beta$
	$P_1(x) = x^{14} - 1.9400x^{13} - 15.3063x^{12} + 29.3398x^{11} + 84.0563x^{10} - 160.0174x^9 - 205.5683x^8 + 395.6296x^7 + 219.7778x^6 - 449.8627x^5 - 81.4679x^4 + 208.6486x^3 - 2.4763x^2 - 21.5581x - 0.3216$	$E_1 = 21.06\beta$
	$P_2(x) = x^{14} - 1.9400x^{13} - 15.3063x^{12} + 29.3398x^{11} + 84.0563x^{10} - 160.0174x^9 - 205.5683x^8 + 395.6296x^7 + 210.7890x^6 - 441.1436x^5 - 49.4516x^4 + 182.4911x^3 - 16.5150x^2 - 12.8389x - 0.3216$	$E_2 = 20.92\beta$
	$P_3(x) = x^{14} - 1.9400x^{13} - 15.3063x^{12} + 29.3398x^{11} + 88.0563x^{10} - 167.7774x^9 - 234.7935x^8 + 450.9088x^7 + 291.1901x^6 - 578.8184x^5 - 156.1784x^4 + 324.9616x^3 + 36.1468x^2 - 56.4346x - 10.4214$	$E_3 = 21.71\beta$
	$P_4(x) = x^{14} - 1.9400x^{13} - 15.3063x^{12} + 29.3398x^{11} + 88.0563x^{10} - 167.7774x^9 - 234.7935x^8 + 450.9088x^7 + 282.2013x^6 - 570.0993x^5 - 106.1844x^4 + 281.3660x^3 - 23.9469x^2 - 12.8389x - 0.3216$	$E_4 = 21.20\beta$
	$P_5(x) = x^{14} - 1.9400x^{13} - 15.3063x^{12} + 29.3398x^{11} + 88.0563x^{10} - 167.7774x^9 - 238.7935x^8 + 458.6688x^7 + 315.4265x^6 - 633.1384x^5 - 177.8332x^4 + 418.0816x^3 + 14.9836x^2 - 102.9946x + 12.1602$	$E_5 = 21.64\beta$
	$P_6(x) = x^{14} - 1.9400x^{13} - 15.3063x^{12} + 29.3398x^{11} + 88.0563x^{10} - 167.7774x^9 - 230.7935x^8 + 443.1488x^7 + 257.9649x^6 - 515.7793x^5 - 84.5296x^4 + 188.2460x^3 + 21.2163x^2 - 12.8389x - 0.3216$	$E_6 = 21.09\beta$

(continued)

Table 13.5 (continued)

	$P_7(x) = x^{14} - 1.9400x^{13} - 15.3063x^{12} + 29.3398x^{11} + 88.0563x^{10} - 167.7774x^9 - 230.7935x^8 + 443.1488x^7 + 257.9649x^6 - 515.7793x^5 - 84.5296x^4 + 188.2460x^3 + 21.2163x^2 - 12.8389x - 0.3216$	$E_7 = 21.09\beta$
	$P_8(x) = x^{14} - 1.9400x^{13} - 15.3063x^{12} + 29.3398x^{11} + 84.0563x^{10} - 160.0174x^9 - 201.5683x^8 + 387.8696x^7 + 194.5526x^6 - 402.3436x^5 - 44.2696x^4 + 135.9311x^3 + 6.0666x^2 - 12.8389x - 0.3216$	$E_8 = 20.84\beta$
	$P_{ac}(x) = \frac{1}{10}(P_0(x) + P_1(x) + P_2(x) + P_3(x) + P_4(x) + 2 \times P_5(x) + P_6(x) + P_7(x) + P_8(x))$ $P_{ac}(x) = x^{14} - 1.9400x^{13} - 15.3063x^{12} + 29.3398x^{11} + 86.4563x^{10} - 164.6734x^9 - 223.1034x^8 + 428.7971x^7 + 258.1308x^6 - 522.8766x^5 - 104.8927x^4 + 260.1262x^3 + 5.4617x^2 - 38.5255x + 1.9175$	$E_{ac} = 21.27\beta$

$$TRE = 21.27\beta - 20.87\beta = 0.40\beta$$

For each structure the polynomial and total energy is given. To calculate $P_{ac}(x)$, $P_5(x)$ is taken into account twice for symmetry reasons. The calculation of the TRE energy of the molecule is detailed in the last line. The tilde sign indicates on which bond, the interaction was multiple by -1 to get the Möbius energy

In the HuLiS application, the characteristic polynomial $P_n(x)$ of any molecule is computed using the Balasubramanian algorithm [38]:

$$P_n(x) = \sum_{k=0}^n d_k x^{n-k} \quad (13.25)$$

$$d_k = \frac{1}{k} \text{tr}(\mathbf{B}_{k-1}); d_0 = -1 \quad (13.26)$$

$$\mathbf{B}_k = \mathbf{B}\mathbf{A}(\mathbf{B}_{k-1} - d_k \mathbf{I}); \mathbf{B}_0 = \mathbf{A} \quad (13.27)$$

with \mathbf{A} the topological matrix of the molecule (13.14) and \mathbf{I} the identity matrix both of $n \times n$ dimension. The $n \times n$ \mathbf{B}_k matrices and the d_k coefficients are completely defined in the recursive algorithm. The roots of $P_n(x)$ are the energies of the molecular orbitals of the molecule.

The topological resonance energy can be easily computed for one ring species: the acyclic polynomial is the average of the Hückel and the Möbius system. As an example, let us compare the topological resonance energies and the Breslow resonance energies, defined as the difference in energy between the cyclic and the open molecule [39], Fig. 13.8. The agreement between both definitions is excellent.

Discussion about the status of different resonance energies is beyond the scope of this work. The interested reader will find more information in [39, 40].

For polycyclic systems, one follows Ref. [41] and as an application, we can compute the TRE of 1,4-Biphenylenedione. The decomposition shown in Table 13.5 is easily done in HuLiS as a polynomial calculator is available in the software. This calculator allows any linear combination of characteristic polynomials and searches for their roots. The calculation of TRE is thus at hand for any molecule which HuLiS is able to treat.

References

1. Carissan Y, Hagebaum-Reignier D, Goudard N, Humbel S (2008) *J Phys Chem A* 112 (50):13256
2. Shaik SS, Hiberty PC (2008) *A chemist's guide to valence bond theory*. Wiley-Interscience, Hoboken
3. Cooper DL (ed) (2002) *Valence bond theory*. Elsevier Science
4. Chirgwin BH, Coulson CA (1950) *Proc R Soc Lond Math Phys Eng Sci* 201(1065):196
5. Jensen F (2006) *Introduction to computational chemistry*. Wiley
6. Deglmann P, Schäfer A, Lennartz C (2015) *Int J Quantum Chem* 115(3):107
7. Hirao K, Nakano H, Nakayama K, Dupuis M (1996) *J Chem Phys* 105(20):9227
8. Thorsteinsson T, Cooper D, Gerratt J, Karadakov P, Raimondi M (1996) *Theor Chim Acta* 93 (6):343
9. Glendening ED, Weinhold F (1998) *J Comput Chem* 19(6):593
10. Bader RF (1994) *Atoms in molecules: a quantum theory*. Oxford University Press, Oxford
11. Shaik S, Danovich D, Silvi B, Lauvergnat D, Hiberty P (2005) *Chem Eur J* 11(21):6358

12. Rahm M, Christe KO (2013) *ChemPhysChem* 14(16):3714
13. Glendening ED, Weinhold F (1998) *J Comput Chem* 19(6):610
14. Glendening ED, Badenhop JK, Weinhold F (1998) *J Comput Chem* 19(6):628
15. Rauk A (2001) *Orbital interaction theory of organic chemistry*, 2nd edn. Wiley
16. Van-Catledge F (1980) *J Org Chem* 45:4801
17. Hückel E (1957) *Z Für Elektrochem. Berichte Bunsenges. Für Phys Chem* 61(8):866
18. Kutzelnigg W (2007) *J Comput Chem* 28(1):25
19. Humbel S (2007) *J Chem Educ* 84(8):1277
20. Hagebaum-Reignier D, Girardi R, Carissan Y, Humbel S (2007) *J Mol Struct Theochem* 817 (1–3):99
21. Löwdin PO (1955) *Phys Rev* 97(6):1474
22. Leasure SC, Balint-Kurti GG (1985) *Phys Rev A* 31(4):2107
23. Glendening ED, Landis CR, Weinhold F (2013) *J Comput Chem* 34(16):1429
24. Frisch MJ, Trucks GW, Schlegel HB, Scuseria GE, Robb MA, Cheeseman JR, Scalmani G, Barone V, Mennucci B, Petersson GA, Nakatsuji H, Caricato M, Li X, Hratchian HP, Izmaylov AF, Bloino J, Zheng G, Sonnenberg JL, Hada M, Ehara M, Toyota K, Fukuda R, Hasegawa J, Ishida M, Nakajima T, Honda Y, Kitao O, Nakai H, Vreven T, Montgomery Jr JA, Peralta JE, Ogliaro F, Bearpark M, Heyd JJ, Brothers E, Kudin KN, Staroverov VN, Kobayashi R, Normand J, Raghavachari K, Rendell A, Burant JC, Iyengar SS, Tomasi J, Cossi M, Rega N, Millam JM, Klene M, Knox JE, Cross JB, Bakken V, Adamo C, Jaramillo J, Gomperts R, Stratmann RE, Yazyev O, Austin AJ, Cammi R, Pomelli C, Ochterski JW, Martin RL, Morokuma K, Zakrzewski VG, Voth GA, Salvador P, Dannenberg JJ, Dapprich S, Daniels AD, Farkas O, Foresman JB, Ortiz JV, Cioslowski J, Fox DJ, Gaussian Inc. Wallingford CT (2009)
25. Levin G, Goddard WA (1975) *J Am Chem Soc* 97(7):1649
26. Levin G, Goddard WA (1975) *Theoret Chim Acta* 37(4):253
27. Shaik SS, Hiberty PC, Lefour JM, Ohanessian G (1987) *J Am Chem Soc* 109(2):363
28. Mach TJ, King RA, Crawford TD (2010) *J Phys Chem A* 114(33):8852
29. Olsen S, McKenzie RH (2012) *J Chem Phys* 136(23):234313
30. Schleyer PR (2001) *Chem Rev* 101(5):1115
31. Krygowski TM, Szatyłowicz H, Stasyuk OA, Dominikowska J, Palusiak M (2014) *Chem Rev* 114(12):6383
32. Norbeck JM, Gallup GA (1974) *J Am Chem Soc* 96(11):3386
33. Goudard N, Carissan Y, Hagebaum-Reignier D, Humbel S (2014) <http://ism2.univ-amu.fr/hulis> or mobile version: <http://ism2.univ-amu.fr/m-hulis>
34. Aihara J (1976) *J Am Chem Soc* 98(10):2750
35. Gutman I, Milun M, Trinajstić N (1977) *J Am Chem Soc* 99(6):1692
36. Gutman I, Milun M, Trinajstić N (1976) *Croat Chem Acta* 48:87
37. Chauvin R, Lepetit C (2013) *Phys Chem Chem Phys* 15(11):3855
38. Balasubramanian K (1991) *J Math Chem* 7(1):353
39. Schaad LJ, Hess BA (2001) *Chem Rev* 101(5):1465
40. Malrieu JP, Gicquel M, Fowler PW, Lepetit C, Heully JL, Chauvin R (2008) *J Phys Chem A* 112(50):13203
41. Chauvin R, Lepetit C, Fowler PW, Malrieu JP (2010) *Phys Chem Chem Phys* 12(20):5295

Chapter 14

Magnetic Properties of Conjugated Hydrocarbons from Topological Hamiltonians

Jean-Paul Malrieu, Nicolas Ferré and Nathalie Guihéry

Abstract The present chapter shows first that the topological Hückel Hamiltonian provides an analytical expression of both the singly occupied Molecular Orbitals and the spin density distribution of mono- and poly-radical conjugated hydrocarbons. It permits a new derivation of the Ovchinnikov's rule (first established from a magnetic model Hamiltonian), which predicts the preferred ground state spin multiplicity from the topology of the molecule. From the Hubbard simplified representation of the bi-electronic Hamiltonian one obtains directly, without any matrix diagonalization, a reasonable evaluation of the singlet-triplet energy difference. For singlet di-radicals the method enables one to predict whether the $M_s = 0$ single-determinant solution is subject to a spin-symmetry breaking. The spin polarization of the closed shells, which is a different phenomenon, of bi-electronic origin, increases the value of the magnetic coupling in these systems, contrasts the spin densities between negative and positive values and spatially extends the spin distribution. Numerical Unrestricted Density Functional Theory calculations illustrate the relevance of the predictions of the topological model.

14.1 Introduction

The occurrence of open shells (or singly occupied MOs) is more common in coordination chemistry than in organic chemistry. The metal ions which usually bear the unpaired electrons exhibit a local spin momentum responsible for magnetic properties. The field of molecular magnetism [1–9] and its extension to periodic lattices are key areas of coordination chemistry because of their potential applica-

J.-P. Malrieu (✉) · N. Guihéry
Laboratoire de Chimie et Physique Quantiques, UMR 5626 (CNRS), IRSAMC,
Université P. Sabatier, 118 Rte de Narbonne, 31062 Toulouse Cedex, France
e-mail: jean-paul.malrieu@irsamc.ups-tlse.fr

N. Ferré
Aix-Marseille Université, CNRS, Institut de Chimie Radicalaire,
13397 Marseille Cedex 20, France

tions. One may mention ferro- (or ferri-) magnetic lattices, commutable spin-cross-over systems, single molecule magnets or spintronic devices. In these systems the metal ions are connected by closed-shell ligands which mediate the interactions between the localized spins. Theoreticians have made great efforts in understanding the mechanisms of the magnetic interactions between magnetic sites and have developed appropriate computational tools for their study, either based on wave-function based methods or on density functional theory (DFT) [10–13].

The magnetism of organic compounds receives more and more attention, and the idea that one might conceive the organic counterpart of the magnetic devices developed by coordination chemists attracts more and more attention from researchers [14–17]. Several works deal with famous stable radicals such as nitroxides and parent compounds [18]. Nevertheless purely carbon-based magnetic polyradical architectures, using for instance the meta-xylylene unit as a building block, have been conceived and even synthesized [19]. These architectures are conjugated hydrocarbons and the present contribution focuses on these systems. Conjugated hydrocarbons have the advantage of presenting a high homogeneity (same sp^2 carbons, similar CC bond lengths) and their description may take benefit from the topological models developed in the early days of Quantum Chemistry [20]. We shall concentrate here our attention on open-shell hydrocarbons. In contrast to what happens in coordination chemistry, the unpaired electrons may be strongly delocalized, as manifest from the shapes of the singly occupied molecular orbitals (SOMOs). Actually when one branches a (CH_2) group on a closed-shell moiety, such as a benzene ring or a fused polycyclic hydrocarbon, the spin density is no longer concentrated on the added methylene group, it spreads over the whole π systems. This phenomenon is the spin delocalization, and Sect. 14.2 focuses on its study in free radicals. The topological rules governing its extension are derived from the Hückel Hamiltonian and confirmed by DFT calculations. In Sect. 14.3, fully conjugated di- or poly-radicals are considered. They are frequently seen as resulting from the attachment of two (or more) radical groups on a closed-shell moiety. It is shown that spin delocalization can also be easily predicted from the Hückel model and that the topology governs the ground state spin multiplicity (singlet or triplet) owing to the Ovchinnikov's rule [21]. This rule has been originally established from a magnetic model Hamiltonian, which is in principle valid for strongly-correlated systems, while the π electronic population is usually considered as weakly correlated. The same rule is here derived from a mixed Hückel-Hubbard picture, which simply considers the effect of on-site bi-electronic repulsion as a first-order perturbation to the energies. This procedure avoids any self-consistent mean-field calculation of the Hubbard Hamiltonian. On a series of examples, it is shown that the energy gaps between the lowest triplet and singlet states estimated from elementary analytical calculations compare well with the quantitative DFT predictions reported in Sect. 14.4.

Often confused with spin delocalization, spin polarization, discussed in Sect. 14.5, is a different phenomenon. It introduces spin densities in orbitals of different symmetries than the SOMOs, for instance in the σ system of π radicals. While spin delocalization is well described by restricted open-shell formalisms, spin

polarization involves the bi-electronic operator of the Hamiltonian and requires using either unrestricted mean-field formalisms or preferably multi-determinant descriptions. This section briefly recalls the physics of this phenomenon and illustrates its signatures.

In this chapter the molecular architectures, quantities and functions relative to the free radicals will not receive ‘ nor “ upper symbols, those relative to ferromagnetic systems will be affected by the symbol ‘, and those concerning the antiferromagnetic systems will be marked by “.

14.2 Spin Delocalization in Conjugated Free Radical Hydrocarbons

14.2.1 Recall of Elementary Features

Hereafter, as we try to reach analytic conclusions, the π electrons of a conjugated hydrocarbon are described by the Hückel Hamiltonian. The on-site energies are assumed to be equal and define the zero of energy:

$$H = \sum_{(p,q)\text{bonded}} t_{pq}(a_p^+ a_q + a_q^+ a_p) \quad (14.1)$$

where the hopping integrals t_{pq} on the bonds p - q are negative but may be of different amplitudes, depending on the bond strength. The description makes also use of a Hubbard Hamiltonian

$$H' = \sum_{(p,q)\text{bonded}} t_{pq}(a_p^+ a_q + a_q^+ a_p) + \sum_p U_p n_{p\uparrow} n_{p\downarrow} \quad (14.2)$$

where the second term accounts for the repulsion of two electrons occupying the same site p . This simplified representation of the bi-electronic part of the Hamiltonian keeps its leading qualitative effects.

In the strongly-correlated limit, when the electron delocalization (i.e. the t_{pq} terms) becomes smaller than the electron repulsion U , an appropriate description of the lowest states is provided by the neutral VB determinants only, i.e. those in which each carbon p bears one unpaired electron in its π atomic orbital (AO, hereafter labelled χ_p). The π electron systems behaves as a pure spin system, obeying a Heisenberg Hamiltonian [22, 23]. The inter-atomic delocalization, i.e. the interaction between the neutral VB distributions and the ionic ones, results in an antiferromagnetic spin coupling on each bond. One of the below-discussed rules, known as the Ovchinnikov's rule [21], has been derived from this magnetic approach. Numerous works [24] have shown the relevance of magnetic descriptions

of conjugated hydrocarbons, despite the fact that the delocalization prevails over bi-electronic repulsion. In the present work we shall enter the problem from the opposite side, considering first the delocalization only and later the electronic repulsion as a first-order perturbation.

Let us consider “alternant conjugated hydrocarbons” for which the molecular graph, defined by the conjugated carbons, does not present odd-membered rings. As a consequence the conjugate carbons can be separated in two classes to which one may attribute “colors”, say red and blue. Each red atom is chemically linked to blue atoms and vice versa. These graphs are also called “bipartite” by solid state physicists. If one identifies the colors to spins, α or β , one may say that an alternant hydrocarbon is a spin non-frustrated graph, in the sense that it accepts at least one and at most two spin distributions for which each chemical bond presents a spin alternation, and the determinants of lowest energy are the fully spin-alternant distributions (called Néel function in Solid State Physics). For sake of simplicity we shall label p, q, \dots the atoms of a given color and p', q', \dots the atoms of the other color.

A basic theorem has been established in the early days of Quantum Chemistry, when it focused on the study of conjugated hydrocarbons. It is the so-called “mirror theorem” [25], which says that for any alternant graph of $2n$ sites the $2n$ eigenvalues of the Hückel Hamiltonian are in a mirror correspondence, namely to each bonding MO φ_k , of negative eigenvalue ε_k one may associate an antibonding MO φ_{k^*} of eigenvalue

$$\varepsilon_{k^*} = -\varepsilon_k \quad (14.3)$$

and the values of the coefficients in the corresponding eigenvectors on the atomic orbitals χ_p obeying

$$H\varphi_k = \varepsilon_k \varphi_k, \quad \varphi_k = \sum_p c_{kp} \chi_p \quad (14.4)$$

$$H\varphi_{k^*} = \varepsilon_{k^*} \varphi_{k^*}, \quad \varphi_{k^*} = \sum_p c_{k^*p} \chi_p \quad (14.5)$$

are equal on the atoms p of a given color and opposite on the atoms q' of the other color

$$c_{k^*p} = c_{kp}, \quad \text{and} \quad c_{k^*q'} = -c_{kq'}. \quad (14.6)$$

The proof is straightforward and consists in projecting the eigenequations relative to φ_k and φ_{k^*} on χ_p and on $\chi_{q'}$. As an important point one should notice that the theorem is satisfied whatever the values of the hopping integrals are, they do not need to be equal. The key condition is the fact that one atom of a color only interacts with atoms of the other color.

14.2.2 *The Singly Occupied Molecular Orbital and Spin Density Distribution in Free Radicals of Conjugated Systems*

The other important theorem [25] is relative to the systems with an odd $(2n + 1)$ number of sites, i.e. concerns the free radicals. Let us consider that the graph implies $n + 1$ red atoms and n blue atoms. Then the theorem tells that the $(n + 1)$ th eigenenergy is zero,

$$\varepsilon_{n+1} = 0 \quad (14.7)$$

and that the corresponding coefficients are zero on the minor (blue) color sites:

$$c_{n+1,q'} = 0. \quad (14.8)$$

The SOMO exhibits nodes on minor (blue) atoms. The proof follows the same logics. The non-zero coefficients on the major (red) sites satisfy the following equations (one for each atom q' of minor color):

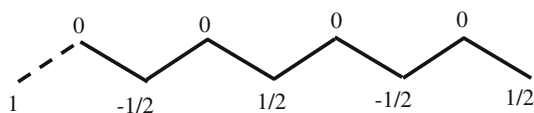
$$\sum_p t_{pq'} c_{n+1,p} = 0, \quad (14.9)$$

where p and q are bonded atoms and $n + 1$ is the number of the non-bonding MO. If the molecule is neutral, the MO φ_{n+1} is singly occupied (SOMO). The distribution of the spin density is given by the squared coefficients of this MO on the various atoms

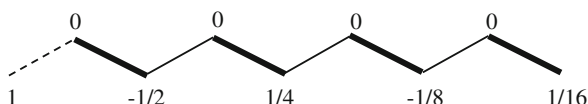
$$\rho_p = (c_{n+1,p})^2 \quad (14.10)$$

$$\rho_{q'} = 0. \quad (14.11)$$

From the eigenequation $H|\varphi_{n+1}\rangle = 0$ or Eq. (14.9) one can easily determine the coefficients of the SOMO and the spin densities. The relative amplitudes of the SOMO on the different atoms may be obtained directly, on the back of an envelope. The so-obtained SOMO is not normalized. The norm is the sum of the squares of the amplitudes, and the atomic spin density is the square of the coefficient divided by the norm. Giving for instance a coefficient 1 to the most isolated (less connected) atom of major color, one satisfies Eq. (14.9) for each minor color atom q' successively. Let us start with an even regular 1D chain (with equal hopping integrals t) to which an external atom is attached through a weak bond of hopping integral τ . This atom receives an arbitrary coefficient 1. Then atom 2 of the chain has a coefficient $c_2 = -\tau/t$. The amplitudes on the even numbered atom are the same all along the chain $c_2 = -c_4 = c_6 \dots$. The external spin introduces a *non-damped* spin wave in the chain, whatever the weakness of the hopping integral τ , as illustrated below when $\tau/t = 1/2$.



For an alternated chain with hopping integrals $t_{2n+1,2n} = t$ for strong bonds and $t_{2n-1,2n} = t'$ for weak bonds. The application of Eq. (14.9) leads to $c_4/c_2 = -t'/t = c_4/c_6 = c_{2n+2}/c_{2n}$. The spin density wave is *exponentially damped*, as illustrated below for the case $\tau/t = 1/2 = t'/t$.



The comparison between these two cases suggests that the spin density wave introduced by an external magnetic site on a conjugated hydrocarbon has a long range spatial extent when the bonds of the conjugated system are weakly contrasted. This is the case in fused polycyclic hydrocarbons.

Let us consider series of examples which will be studied by mean of DFT calculations in Sect. 14.5. They are represented in Fig. 14.1 with specific labels combining the number of 6-membered rings and a letter which refer to the various series **a**, **b** and **c**. One should note that some molecules belong to several series and

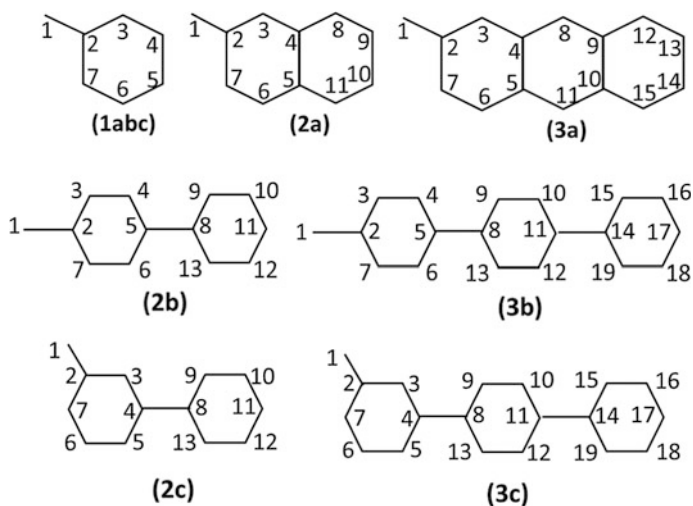
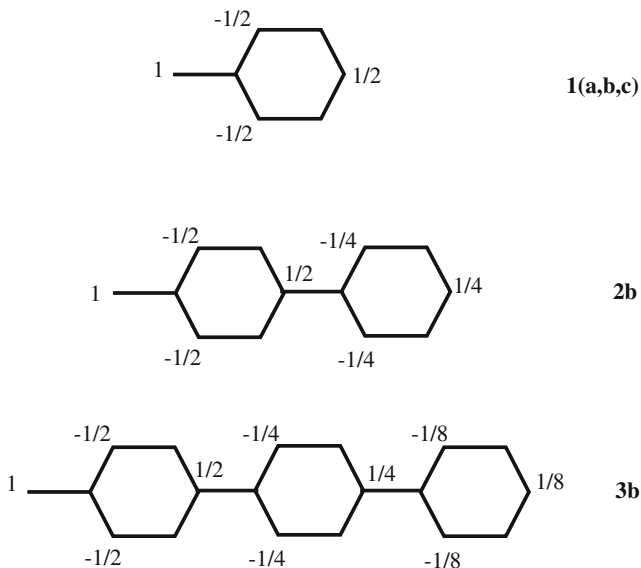
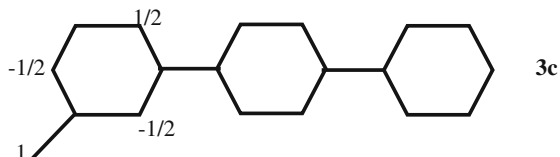


Fig. 14.1 Atom labelling for the 3 series of free radicals

may have two different labels. The first series noted **b** concern the phenylene and longer analogs obtained by adding 6-membered rings to the phenylene in various topologies. A coefficient 1 is attributed to the extracyclic atom. If the additional benzene rings are fixed in para position, the value of the coefficients of the SOMO decreases *exponentially* along the chain.



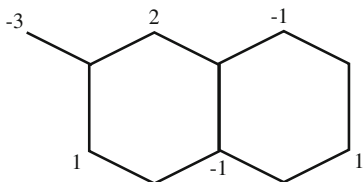
It is interesting to note that the decrease is the same when the CH_2 group is attached in ortho position of the polyphenyl chain. At variance, for a meta position of this group (series **c**, see for instance **3c** below) the SOMO is not delocalized on the chain as the chain is attached on an atom of minor color. This is a general property: *The SOMO does not exhibit delocalization tails on fragments of the conjugated system having an equal number of atoms of the two colors which are connected to a minor atom.* This result again is independent of the magnitude of the hopping integrals.



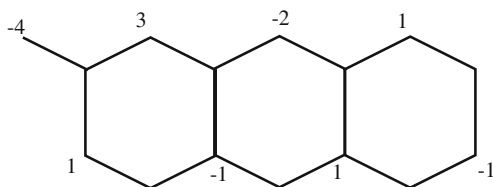
Let us now consider radicals obtained by adding an extra site on a polyacene or fused polycyclic hydrocarbons.

In series **a**, the second system **2a** (note that the first system **1a,b,c** has already been considered) is a naphthalene molecule connected to a CH_2 group by one of the outermost carbon atoms. The value 1 is attributed to the closest carbon of major color in the lower part of the molecule. The values of the coefficients of all the atoms in the lower part are therefore ± 1 . This imposes an alternant *arithmetic* progression of the magnitude of the coefficients on the atoms located in the upper part of the molecule. For a system constituted of n rings and if one numbers the rings starting from the external CH_2 group, the absolute values of the coefficients on an atom belonging to the upper part of the chain decrease as $(n - p + 1)$ while those of the lower part are all equal to 1. The norm can be expressed as a function of the number of rings of the acene: $\text{Norm}(n) = (n + 1)(1 + (n + 2)(2n + 3)/6)$ which asymptotically behaves as $n^3/3$.

As a qualitative result one may notice that the largest spin density is carried by the outer carbon atom and decreases as n^{-1} with the number of rings. The spin densities on the atoms of the lower part of the skeleton decrease as n^{-3} . The spin densities do not follow an exponential decrease with their distance to the external magnetic site. A strong (long range) delocalization of the unpaired electron occurs in fused ring hydrocarbons.



2a : Norm=17



3a : Norm=34

14.3 Diradicals and Polyradicals and Their Preferred Spin Multiplicity

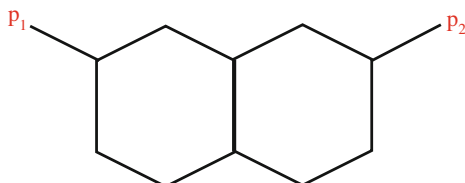
This section shows how the SOMOs of diradicals can be generated from the SOMOs of two single radicals. Then the energy difference between the lowest triplet and singlet states may be analytically estimated from the values of the coefficients of the SOMOs of the diradical.

14.3.1 Ferromagnetic Di- and Poly-radicals

Organic diradicals have been intensively studied by ab initio treatments [26–33]. We concentrate here on a simple and deductive approach.

(a) From radicals to diradicals: analytic derivation

First let us consider systems constituted of $n + 2$ sites of red color and n sites of blue color. It is easy to show that such systems accept two non-bonding MOs, of energy zero. Deleting hypothetically the atom p_1 of major color which is expected to bear the largest spin density, for instance located on an external CH_2 group, would lead to a free radical.



The SOMO $|\varphi_{(-p_1)}\rangle$ of this radical is of energy zero as well, as discussed previously. The atom p_1 is connected to atoms of minor color, so the coefficients on these atoms are zero in this SOMO. Complementing the SOMO $|\varphi_{(-p_1)}\rangle$ of the single radical on the atom p_1 with a zero coefficient gives a vector $|\varphi'_{(p_1)}\rangle$ which still satisfies the equation

$$H|\varphi'_{(p_1)}\rangle = 0 \quad (14.12)$$

i.e. is an eigenvector for the whole molecule.

One may repeat the same procedure for the atom p_2 on which one may also expect a large spin density and get a second SOMO of the diradical,

$$H|\varphi'_{(p_2)}\rangle = 0. \quad (14.13)$$

These two eigenvectors are linearly independent as the first one has amplitude on the p_2 atom while the second one has not. They both have non-zero coefficients on the same red atoms and zero coefficients on the blue ones. One may note that they are not orthogonal. Using their overlap

$$\langle \varphi'_{(p_1)} | \varphi'_{(p_2)} \rangle = \langle \varphi_{(-p_1)} | \varphi_{(-p_2)} \rangle = S_{12} \quad (14.14)$$

they may be orthogonalized through the $S^{-1/2}$ procedure.

(b) Illustrations

One may consider first the series of meta-para dimethylene polyphenylenes, appearing as **2'bc** and **3'bc** in Fig. 14.2. The overlap between the two radical SOMOs generated respectively from the two CH_2 groups is very small $(1/217)^{1/2}$ for **2'bc** and $(1/889)^{1/2}$ for **3'bc** due to the decrease of the coefficients.

The second series is obtained by adding two CH_2 groups on acenes, for instance in the dimethylene naphthalene **2'a** or longer analogs. From the values of the coefficients obtained in radical **2'a**, the overlap between the two SOMOs of **2'a** is $1/17$. As the overlap is small the orthogonal localized SOMOs of the di-radical are almost identical to those of the mono-radicals. The coefficients on the various centers of the diradical SOMO of major amplitude on p_1 are very similar to those (in parenthesis) of the SOMO of the corresponding mono-radical: $c_{p_1} = c_1 = 0.73$ (0.73), $c_7 = -0.48$ (-0.49), $c_5 = 0.23$ (0.24), $c_3 = -0.25$ (-0.24) and $c_{p_2} = c_{10} = 0.02$ (0.0). The overlap between the radical SOMOs is larger ($3/17$) for the dimethylene anthracene, appearing as **3'a** in Fig. 14.2.

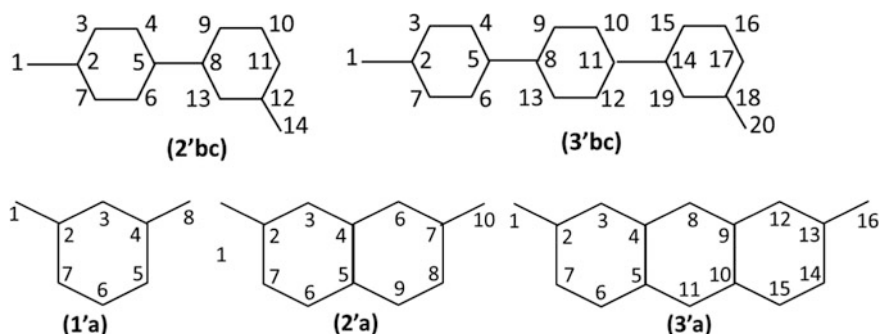
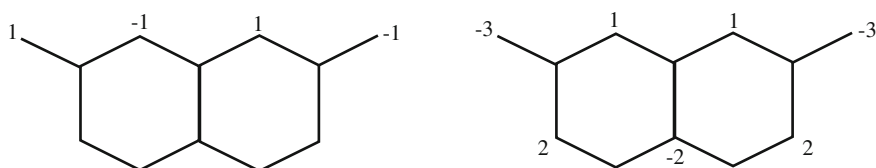


Fig. 14.2 Atom labelling for the two series of ferromagnetic diradicals

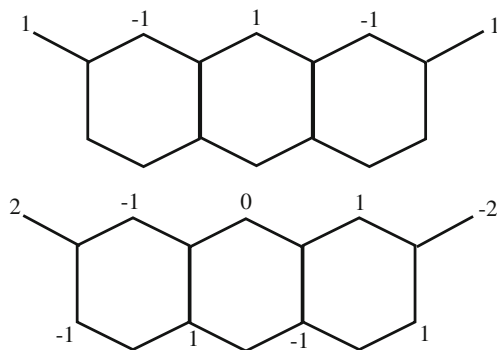
The symmetrically orthogonalized MOs

$$|\tilde{\varphi}'_1\rangle = |\varphi'_{(p_2)}\rangle - S_{12}/2|\varphi'_{(p_1)}\rangle \quad \text{and} \quad |\tilde{\varphi}'_2\rangle = |\varphi'_{(p_1)}\rangle - S_{12}/2|\varphi'_{(p_2)}\rangle \quad (14.15)$$

keep their largest amplitudes on atoms p_1 and p_2 respectively. In such symmetrical systems one may use symmetry arguments to obtain directly the coefficients of the symmetry-adapted SOMOs. One of them is antisymmetric with respect to the reflection plane, and attributing a coefficient 1 on the less connected atoms of major color one obtains one SOMO located on the upper side atoms with alternant values. The symmetrical one second one has larger amplitudes on the lower side atoms. The generalization to longer acenes is straightforward. The symmetries of these SOMO depend on the parity of the number of rings. For **2'a** they are



and the following ones for **3'a**



From these symmetry-adapted SOMOs φ'_g and φ'_u , which are the canonical (symmetry-adapted) SOMOs of the Hückel Hamiltonian, again obtained without diagonalization, one may define the localized SOMOs

$$\begin{aligned}
|\tilde{\varphi}'_1\rangle &= (|\varphi'_g\rangle + |\varphi'_u\rangle)/\sqrt{2}, \\
|\tilde{\varphi}'_2\rangle &= (|\varphi'_g\rangle - |\varphi'_u\rangle)/\sqrt{2}, \\
|\tilde{\varphi}'_g\rangle &= (|\varphi'_{(-p1)}\rangle + |\varphi'_{(-p2)}\rangle)/\sqrt{2(1+S_{12})} \\
|\tilde{\varphi}'_u\rangle &= (|\varphi'_{(-p1)}\rangle - |\varphi'_{(-p2)}\rangle)/\sqrt{2(1-S_{12})}.
\end{aligned} \tag{14.16}$$

From the two symmetry-adapted SOMOs one may build a triplet and a singlet state

$$\Psi_T = \left| \text{core} \cdot (\tilde{\varphi}'_1 \tilde{\varphi}'_2 - \tilde{\varphi}'_2 \tilde{\varphi}'_1) / \sqrt{2} \right| \tag{14.17}$$

$$\Psi_S = \left| \text{core} \cdot (\tilde{\varphi}'_1 \tilde{\varphi}'_2 + \tilde{\varphi}'_2 \tilde{\varphi}'_1) / \sqrt{2} \right| \tag{14.18}$$

It is important to notice that in this case there is no ionic component in the singlet state. As $|\tilde{\varphi}'_1\rangle$ and $|\tilde{\varphi}'_2\rangle$ are eigenfunctions of H , the term which would couple the neutral and ionic forms is null

$$\langle \tilde{\varphi}'_1 | H | \tilde{\varphi}'_2 \rangle = 0. \tag{14.19}$$

There is no Anderson's antiferromagnetic mechanism (or "kinetic exchange") in such magnetic systems.

The triplet state is the lowest state and the energy difference between the two states is given by the direct exchange integral

$$E_S - E_T = 2K_{12} = 2\langle \tilde{\varphi}'_1 \tilde{\varphi}'_2 | r_{12}^{-1} | \tilde{\varphi}'_2 \tilde{\varphi}'_1 \rangle. \tag{14.20}$$

This integral is easily calculated in the Hubbard approximation through a summation on the atoms of the major color,

$$2K_{12} = 2U \sum_p \tilde{c}'_{1p}{}^2 \tilde{c}'_{2p}{}^2 \tag{14.21}$$

where \tilde{c}'_{1p} and \tilde{c}'_{2p} are the coefficients on the atom p of the SOMOs $|\tilde{\varphi}'_1\rangle$ and $|\tilde{\varphi}'_2\rangle$ respectively. Notice that the so calculated value of the energy gap between the triplet and the singlet is necessarily a rational number, as long as the bonds have equal hopping integrals.

If one prefers to use the symmetry-adapted SOMOs one may write as well

$$2K_{12} = (J_{gg} + J_{uu} - 2J_{gu})/2 = (U/2) \sum_p (c_{gp}^2 - c_{up}^2)^2 \tag{14.22}$$

where the symbols J refer to coulomb integrals ($J_{ij} = \langle \varphi_i \varphi_j | r_{12}^{-1} | \varphi_i \varphi_j \rangle$) and where c'_{gp} and c'_{up} refer to the coefficients of the symmetry-adapted SOMOs on the atom p . For the more sophisticated Pariser-Parr-Pople Hamiltonian which accounts for repulsion integrals γ_{pq} between the electrons on site p and q , one gets:

$$2K_{12} = 2 \sum_{p \leq q} \tilde{c}'_{1p} \tilde{c}'_{2p} \tilde{c}'_{1q} \tilde{c}'_{2q} \gamma_{pq}. \quad (14.23)$$

In this sum the contribution from the nearest-neighbor atoms p and q is zero because one of them is necessarily a node in the SOMOs. If one neglects the repulsion integrals between next-nearest neighbor (NNN) atoms, U should take a value close to γ_{pp} . A typical value of U^{eff} is generally taken around 5 eV. In the above examples we get the following estimates of the triplet to singlet gaps:

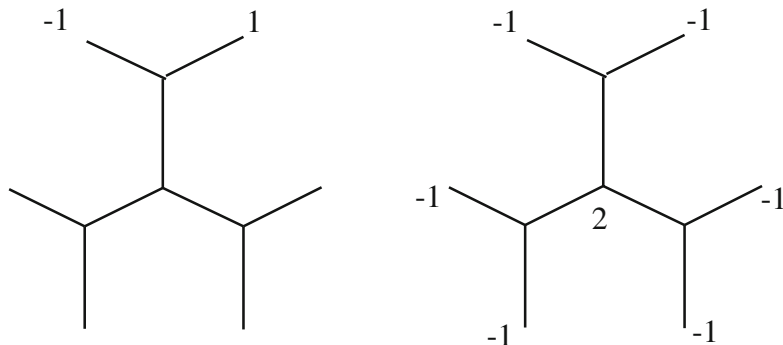
- $U/8 = 0.55$ eV for the metaxylylene (**1'a,b,c**),
- $22U/(17)^2 = 0.38$ eV for the dimethylene naphthalene (**2'a**)
- $72U/(34)^2 = 0.31$ eV for di-methylene anthracene (**3'a**)
- $6U/217 = 0.137$ eV for **2'bc**
- $6U/889 = 0.033$ eV for **3'bc**.

One sees that a Hückel approach may be used to predict, even without any diagonalization of the Hamiltonian matrix, the amplitude of the Triplet-Singlet gap in symmetric diradicals where the difference between the numbers of atoms of different colors is equal to 2.

(c) Ferromagnetic polyradicals

One may generalize the previous demonstration to any difference between the number $n + p$ of atoms of the red color and the number n of atoms of the blue color. One must define a set of p "external" sites of the dominant color such that by subtracting them from the molecular graph one gets a connected "residual" alternant graph of $2n$ sites. Again one may consider successively the p free radicals where one adds one of the p "external" sites to the "residual" graph. When extended on the other external sites with zero coefficients on these sites, the SOMOs of the p free radicals are eigenfunctions of the total graph, with a zero eigenenergy. They are linearly independent and thus one gets p non-bonding MOs. They must be orthogonalized, but they necessarily have coefficients on the same major color sites and zero coefficients on the minor color atoms. The exchange integrals between the SOMOs are positive and the ground state has the highest spin multiplicity. The exchange integrals between the SOMOs may be calculated from their coefficients, which give access to the entire low-energy spectrum.

Let us consider the tri-allyl methylene as an example of polyradical. Its ground state is a quintet, since it has 4 SOMOs, three of them being located on different allyl groups, while the 4th one is centered on the center of the molecule. The relative coefficients are depicted below:



These SOMOs are orthogonal. The exchange integrals between the allyl moieties are zero since they are spread on disjoint sets of atoms while the exchange integral between the central SOMO and the peripheral ones is equal to $U/10$. For U (5 eV) one gets $K = 0.25$ eV, which is close to the value (0.33 eV) obtained from sophisticated *ab initio* calculations [34] on a parent compound in which the outer conjugated carbons are bridged by CH_2 groups, in order to maintain the planarity of the conjugated skeleton.

(d) The Ovchinnikov's rule rederived

Almost 40 years ago Ovchinnikov established that in an alternant hydrocarbon with n^* carbon atoms of one color and n carbon atoms of the other color the spin multiplicity of the ground state is

$$S = |n^* - n| + 1 \quad (14.24)$$

The demonstration made use of a Heisenberg Hamiltonian

$$H_H = 2 \sum_{\langle i,j \rangle} J_{ij} (\vec{S}_i \cdot \vec{S}_j - I/4) \quad (14.25)$$

where the sites i and j are nearest neighbors, J_{ij} is the magnetic coupling between these sites, assumed to be antiferromagnetic, i.e. positive. This Hamiltonian works in the space of the neutral Valence Bond distributions, with one and only one electron per site. It only plays with spins. The diagonal energy of a determinant $|I\rangle$ is given by

$$\langle I|H_H|I\rangle = 2 \sum_{\langle i,j \rangle} J_{ij} (\langle I|S_{zi} \cdot S_{zj} - 1/4|I\rangle), \quad (14.26)$$

which gives a negative contribution on all the bonds presenting a spin alternation. Thus the determinant of lower energy is the one presenting a spin alternation on all bonds. If N_b is the number of bonds and if the magnetic couplings are equal to a

common value J , its energy is $-N_b J$. Moreover this determinant interacts with N_b determinants obtained by a spin exchange on the various bonds, which is the maximum number of interactions which one may find on a line of the Hamiltonian. Therefore this determinant only belongs to the lowest eigenvector which necessarily has an $M_s = |n^* - n|$ value, and an $S = |n^* - n| + 1$ spin multiplicity.

Of course the Heisenberg Hamiltonian is supposed to be valid for systems where the electron-electron repulsion prevails on the electron delocalization. It may be established as an effective Hamiltonian from the Hubbard Hamiltonian by a second-order expansion, using the quasi degenerate perturbation theory, provided that the ratio $|2t/U| < 1$, which results in a value of $J = 2t^2/U$. This inequality is hardly satisfied in conjugated hydrocarbons, which are typically considered as strongly delocalized (almost metallic) or weakly correlated. The validity of magnetic treatments of half-filled bands actually extends beyond the perturbative limit. Using a non-perturbative estimate of the magnetic coupling obtained from the exact solution of the two-center problem, the Heisenberg Hamiltonian has proved to be extremely efficient in the treatment of the ground state and lowest excited states of conjugated hydrocarbons, especially when the Hamiltonian adds a scalar potential to reproduce the effect of the sigma bonds and when the magnetic coupling, extracted from accurate ab initio calculations on the ethylene molecule, is geometry-dependent [35]. Nevertheless it is desirable to produce a demonstration valid whatever the value of the $|t/U|$ ratio, and especially when U tends to zero.

Starting from the Hubbard Hamiltonian Lieb has given a general proof of the same theorem (called Lieb's theorem [36] in Solid State Physics community) for regular alternant lattices. Our approach is different, it rests on the identification of $n^* - n$ linearly independent non-bonding MOs, defined on the atoms of major color, from the Hückel ($U = 0$) limit. Their existence does not depend on the values of the inter-site hopping integrals. Then the interaction between the electrons in these non-bonding MOs is purely ferromagnetic. As the exchange integrals between the orthogonalized SOMOs are necessarily positive, the ground state is of major spin multiplicity, which demonstrates the Ovchinnikov's statement. Notice that the exchange integrals between the SOMOs are necessarily positive, even for disjoint diradicals, where it falls to zero in the crude Hubbard approximation. Then in full generality the spin multiplicity of the ground state is necessarily equal to the number $n^* - n$ of SOMOs plus one.

To summarize this section we may say that

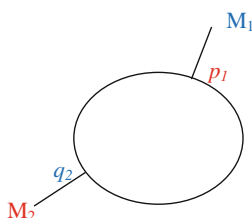
- we have demonstrated the Ovchinnikov's rule regarding the preferred spin multiplicity of alternant graphs starting from the strong delocalization limit, rather than from the strong correlation limit and an Heisenberg Hamiltonian, as originally done. Our demonstrations are valid even when the $|U/t|$ ratio tends to zero,
- the Hückel picture enables us to predict the spin densities from back-of-an-envelope calculations, while the solution of the Heisenberg Hamiltonian are not accessible in such an easy manner (not to speak of ab initio computations!),

- introducing the inter-electronic repulsion in its simplest form, through the Hubbard Hamiltonian, this approach also gives access to a straightforward evaluation of the energy gap between the lowest eigenstate and the other states of the same spatial configuration.

14.3.2 Antiferromagnetic Coupling in Singlet Diradicals

(a) Analytic derivation

Let us now consider the alternant graphs having the same number of atoms of both colors. Most of them are in principle closed-shell systems since they do not have degenerate non-bonding MOs. The $4n$ -membered rings represent an exception to this statement but a Jahn-Teller distortion removes this degeneracy and stabilizes a closed-shell ground state. However it is worth considering first some systems where two radical centers are weakly coupled, in an antiferromagnetic manner, through a conjugated ligand of $2n$ sites, with n sites of each color. Many complexes in coordination chemistry belong to this category, i.e. they may be written M_1-L-M_2 .



In the antiferromagnetic complexes the magnetic sites M_1 and M_2 are respectively attached to two atoms, p_1 and q_2 , which are now of opposite colors, so that in the total graph one has $n + 1$ sites of each color. If the hopping integrals between the external magnetic sites and the atoms p_1 and q_2 are weak, one may clearly consider the system as a diradical and try to analyze the physics of the magnetic coupling between the external sites through the ligand. One may again consider the SOMOs of the parent free-radicals (M_1-L) and ($L-M_2$). The delocalization follows the same laws as before, but now the magnetic orbital issued from M_1 has amplitudes on the atoms q_i , of the same color as M_1 , while the magnetic orbital issued from M_2 takes coefficients on the atoms p_j , of the other color. The $2p_z$ Atomic orbitals on atoms M_1 and M_2 will be labelled m_1 and m_2 respectively. The two SOMOs $|\varphi''_{m_1}\rangle$ and $|\varphi''_{m_2}\rangle$ of the free radicals are orthogonal since defined on two disjoint sets of atomic orbitals. The coefficients of these MOs are governed by Eq. (14.9), and topologically determined if the hopping integrals are the same for all bonds.

These two orbitals $|\varphi''_{m1}\rangle$ and $|\varphi''_{m2}\rangle$ are not eigenfunctions of the diradical, since they interact. The hopping integrals between the red and blue atoms, p and q, induce an interaction between these two MOs

$$t'' = \langle \varphi''_{m1} | H | \varphi''_{m2} \rangle = \sum_{\langle p,q \rangle} t_{pq} c''_{m1,p} c''_{m2,q}, \quad (14.27)$$

where the atoms p and q are bonded. This interaction results in a splitting of the energies of an in-phase MO

$$\varphi''_g = (\varphi''_{m1} + \varphi''_{m2}) / \sqrt{2} \quad (14.28)$$

$$\varepsilon_g = t'' \quad (14.29)$$

and of an out-of-phase MO

$$\varphi''_u = (\varphi''_{m1} - \varphi''_{m2}) / \sqrt{2} \quad (14.30)$$

$$\varepsilon_u = -t'' \quad (14.31)$$

It is interesting at this stage to compare these MOs to the HOMO and the LUMO of the whole molecule. Actually they are somewhat different. The action of the Hückel Hamiltonian on $|\varphi''_{m1}\rangle$ is given by

$$H|\varphi''_{m1}\rangle = c_{m'_1,q_2} |q_2\rangle. \quad (14.32)$$

The norm of this vector is small if the coefficient of the vector $|\varphi''_{m1}\rangle$ on the atom to which the second radical group is attached is small. In this case the two functions $|\varphi''_g\rangle$ and $|\varphi''_u\rangle$ are very close to the HOMO and the LUMO. The quantity t'' (Eq. 14.29) should be close to the energy of the HOMO if it is negative (of that of the LUMO in the opposite case). The difference between the exact energy of the HOMO and the energy ε_g is an indication of the diradical character of the molecule, the smaller this difference, the stronger the diradical character of the molecule. If this difference is small one may assimilate the HOMO and LUMO to the MOs $|\varphi''_g\rangle$ and $|\varphi''_u\rangle$, and since the amplitudes of these radical SOMOs are obtained analytically, this approach offers an access to the shape of the HOMO (and LUMO) without any diagonalization, from a purely topological logic.

What is the spin multiplicity of the ground state? One faces again the well-known problem of two electrons in two MOs, which is the basic training ground of the theory of magnetism [1–10, 53, 54]. One may treat it either from the orthogonal magnetic orbitals $|\varphi''_{m1}\rangle$ and $|\varphi''_{m2}\rangle$, which are centered on the external

sites but have tails on the ligand, or from the delocalized orbitals $|\varphi_g''\rangle$ and $|\varphi_u''\rangle$, which are the in-phase and out-of-phase combinations of $|\varphi_{m1}''\rangle$ and $|\varphi_{m2}''\rangle$. Let us take the first path. As a first remark one may notice that since the two MOs $|\varphi_{m1}''\rangle$ and $|\varphi_{m2}''\rangle$ are defined on different subsets of atomic orbitals the exchange integral is null, at least for the Hubbard Hamiltonian,

$$K_{12} = K_{m_1''m_2''} = 0. \quad (14.33)$$

This nullity remains valid for the more realistic Pariser-Parr-Pople Hamiltonian, which still neglects the differential overlap distributions. If one considers the exact bi-electronic operator, this strict cancellation does not occur, but the exchange integral, i.e. the ferromagnetic contribution to the magnetic coupling, remains weak. On the contrary the antiferromagnetic mixing of the neutral

$$\Psi_N = \left| \text{core.}(\varphi_{m1}''\bar{\varphi}_{m2}'' + \varphi_{m2}''\bar{\varphi}_{m1}'')/\sqrt{2} \right| \quad (14.34)$$

singlet configuration, and the ionic one

$$\Psi_I = \left| \text{core.}(\varphi_{m1}''\bar{\varphi}_{m1}'' + \varphi_{m2}''\bar{\varphi}_{m2}'')/\sqrt{2} \right| \quad (14.35)$$

stabilizes the singlet state. Let us call U' the energy difference between the ionic and neutral configurations

$$U'' = \langle \Psi_I | H | \Psi_I \rangle - \langle \Psi_N | H | \Psi_N \rangle \quad (14.36)$$

This quantity is easily calculated from the knowledge of the coefficients of the MOs $|\varphi_{m1}''\rangle$ and $|\varphi_{m2}''\rangle$ on the ligand AOs

$$U'' = (J_{m_1''m_1''} + J_{m_2''m_2''})/2 - J_{m_1''m_2''} \quad (14.37)$$

In the Hubbard approximation the last coulomb integral is zero, since $|\varphi_{m1}''\rangle$ and $|\varphi_{m2}''\rangle$ are defined on different subsets of atoms, and anyway the quantity U'' is large. For the Hubbard Hamiltonian

$$J_{m_1''m_1''} = \sum_{q_i} U_{q_i} c_{m_1''q_i}^A \quad (14.38)$$

As

$$\langle \Psi_N | H | \Psi_I \rangle = 2t'' \quad (14.39)$$

the energy stabilization of the ground state singlet is equal to

$$E_S = (U'' - \sqrt{U''^2 + 16t''^2})/2, \quad (14.40)$$

which can be approximated by

$$E_S = -4t''^2/U'' \quad (14.41)$$

if $|t''|$ is sufficiently small in front of U'' . This is the famous Anderson's mechanism, sometimes called "kinetic exchange". The final gap between the singlet and the triplet

$$E_S - E_T = -4t''^2/U'' \quad (14.42)$$

may be estimated from the amplitudes of the SOMOs of the two free radicals on the ligand according to Eqs. (14.27) and (14.38).

This way of thinking belongs to the magnetism point of view. Of course the more traditional point of view consists in using a closed-shell description of the singlet, with double occupancy of the HOMO,

$$\Phi_0 = \left| \text{core} \cdot \varphi_g'' \bar{\varphi}_g'' \right| \quad (14.43)$$

and taking into account its interaction with the (nearly degenerate) doubly excited configuration,

$$\Phi_* = \left| \text{core} \cdot \varphi_u'' \bar{\varphi}_u'' \right| \quad (14.44)$$

The two configurations interact through the integral $K_{gu} = U''/2$. The two approaches are equivalent and lead to Eq. (14.40).

Notice that the crucial quantities may also be calculated from the exact energy of the HOMO, replacing t'' by E_{HOMO} and evaluating U'' from Eq. (14.38) using the exact coefficients of the HOMO.

(b) Spin symmetry breaking condition

This derivation also enables us to predict whether the single-determinant description of the Singlet state is subject to a spin-symmetry breaking of the $M_s = 0$ single-determinant description, i.e. whether the lowest-energy single-determinant description presents a spin and space symmetry breaking, the α - and β -spin MOs being spatially different, or whether it keeps a closed-shell character [37]. In the here-considered systems the broken-symmetry singly occupied MOs tend to localize on the above-introduced MOs $|\varphi_{m1}''\rangle$ and $|\varphi_{m2}''\rangle$. The broken symmetry function takes the form

$$\Phi_{BS} = \left| \text{core.} \tilde{\varphi}_{m1}'' \bar{\varphi}_{m2}'' \right| \quad (14.45)$$

where the magnetic MOs are linear combinations of $|\varphi_{m1}''\rangle$ and $|\varphi_{m2}''\rangle$,

$$\begin{aligned} \tilde{\varphi}_{m1}'' &= \varphi_{m1}'' \cos \theta + \varphi_{m2}'' \sin \theta \\ \bar{\varphi}_{m2}'' &= \varphi_{m2}'' \cos \theta + \varphi_{m1}'' \sin \theta \end{aligned} \quad (14.46)$$

The rotation angle is given by the relation

$$\sin 2\theta = -\frac{2t''}{U''} \quad (14.47)$$

which requires that $|2t''| < U''$. This is the so-called instability condition. If it is not satisfied the lowest energy single determinant is a closed shell. This analysis therefore enables one to predict, from the direct calculation of t'' and U'' , whether a symmetry-breaking takes place in the mean-field calculation of the $M_s = 0$ single-determinant description of an antiferromagnetic diradical. In our topological approach $t'' = \lambda t$ and $U'' = \mu U$, where λ and μ are rational numbers and t and U are the parameters of the Hubbard Hamiltonian. In the ratio

$$\frac{t''}{U''} = \frac{\lambda}{\mu} \cdot \frac{t}{U} \quad (14.48)$$

the first factor is topologically determined, the second one depends on the local physics of the system. These comments are relevant for both Hartree-Fock (HF) and Kohn-Sham DFT calculations. It is known that in DFT the effective $|t|/U$ ratio is larger than when using the exact Hamiltonian, so that in a homogeneous series, for instance those discussed in the next section, the symmetry breaking takes place for less extended systems in HF calculations than for DFT calculations.

(c) Illustrations

This approach will be illustrated on three series of compounds pictured in Fig. 14.3, namely the dimethylene-polyphenylenes, dimethylene-polyacenes where the two CH_2 groups are attached in remote para positions. In the following t and U are assumed to take the typical values $t = -3.5$ eV and $U = 5$ eV.

Let us consider first the paradigmatic series of para dimethylene-polyphenylenes [38–43], (series **1''a,b,c**, **2''b**, **3''b** of Fig. 14.3) the first member of which is the para-xylylene. This molecule has a closed shell ground state. The topological approach gives $t' = 2t/7$ and $U' = 19U/49$, the ratio $t''/U'' = 0.73 t/U$ is larger than 0.5 in absolute value, there is no spin symmetry breaking. The value of t'' (0.29t), agrees well with the energy of the HOMO (0.32t). The calculated singlet to triplet gap is 1.25 eV. The larger analog, **2''b**, with two phenyl rings, have been shown [43] to be border line regarding the spin-symmetry breaking. In the optimized geometry of the triplet the $M_s = 0$ solution of BL3LYP DFT calculation is

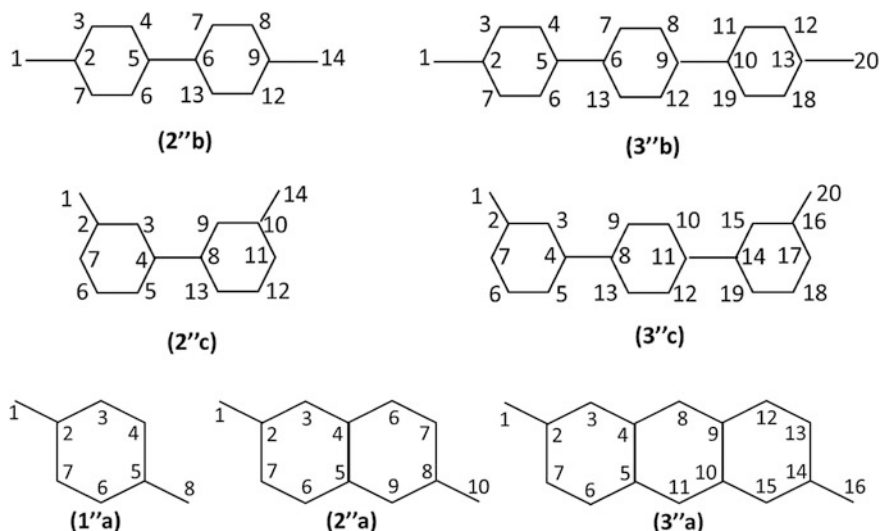


Fig. 14.3 Atom labelling for the three series of antiferromagnetic diradicals

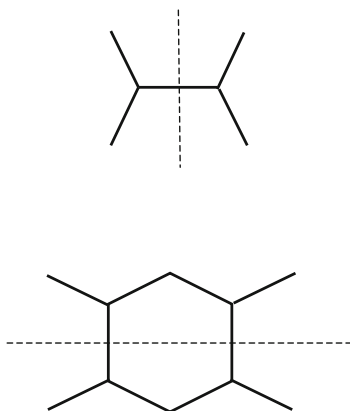
symmetry broken, while the geometry optimization of the $M_s = 0$ solution converges to a closed shell. The spin-decontaminated optimized geometry exhibits a moderate symmetry breaking. The topological model gives $t'' = 0.129t$ (to be compared with the HOMO energy, $0.135t$) and $U'' = 0.319U$, which leads to a spin symmetry breaking. The singlet to triplet energy gap is calculated to be 0.40 eV for the accepted values of t and U . The $M_s = 0$ solutions of longer analogs have an $\langle S^2 \rangle$ value close to 1, i.e. are half-and-half mixtures of singlet and triplet states. For the larger analogs the diradical view gets closer and closer to the exact Hückel + Hubbard approach, the difference between t'' and the HOMO energy tends to zero and so does the two evaluations of U'' . For **3''b** $t'' = 0.063t$ (exact energy of the HOMO = $0.64t$) while $U'' = 0.305U$. The singlet to triplet gap is evaluated to be 0.118 eV .

The dimethylene naphthalene molecule **2''a** is the first member of a series of branched polyacenes which are expected to be singlet and which accept a unique Kékulé bond pairing. Suppressing successively one of the two extra methylene groups one generates two free radical SOMOs a and b, the shape of which was given in Sect. 14.2. For **2''a** the hopping integral between the a and b SOMOs is easily calculated to be equal to $t'' = 3t/17 = 0.176t$, close to the Hückel HOMO energy ($0.188t$). The quantity U'' is also easily calculated to be equal to $101U/289$. In this case, according to Eq. (14.38), the singlet to triplet excitation energy is found to be 0.63 eV .

(d) “Undecidable” spin multiplicity

It is worth mentioning a family of graphs for which the ground state multiplicity cannot be assessed without accurate calculations, despite the fact that they are alternant with equal numbers of sites of both colors. These graphs are such that they may be seen as resulting from the interaction between two disjoint free radicals connected by one or several atoms which are nodal positions of the SOMOs of these radicals [44]. Consider a molecular graph with $2n$ sites, n red and n blue sites. If the graph may be divided into a fragment A with $2p + 1$ sites, $p + 1$ of red color, p of blue color, and a fragment B with $2q - 1$ sites, $q - 1$ of red color, and q of blue color ($p + q = n$), and if the atoms connecting the fragments A and B are the minor color atoms of both fragments, i.e. blue color atoms of fragment A and red color atoms of fragment B, then one may define a non-bonding SOMO m_A on A and a non-bonding SOMO m_B on B, and the hopping integral between them, according to Eq. (14.4) is zero, $t_{m_A m_B} = 0$.

As the two MOs are defined in disjoint fragments the exchange integral $K_{m_A m_B}$ is also null or very weak and one cannot decide about the ground state multiplicity from topological arguments. The simplest example is the famous tetra-methylene ethene, which can be divided into two allyl fragments connected by their nodal central atom, and which has been intensively studied by theoreticians [45–47].



The 1-3-4-6 tetra-methylene benzene may be seen as the interaction between two pentadienyl radicals through their nodal sites. So would be the longer tetra-substituted polyacenes, where a polyacene would replace the benzene ring in the preceding graph. One may show that the spin polarization mechanism actually fixes the preferred spin multiplicity of such graphs. This situation has already been noticed in Sect. 14.3 (b) for ferromagnetic systems ($n^* = n + 2$) where the two radical groups are connected through minor color sites. The compounds **2''c** and **3''c** of Fig. 14.3 appear as disjoint diradicals and their singlet to triplet gap is equal to zero in the topological approach.

14.4 The Spin Polarization Mechanism and Its Impact

The most frequently used single-determinant descriptions of the magnetic systems incorporate spin polarization effects through spin-symmetry breaking of the molecular orbitals. Since the next section is devoted to comparisons between the predictions of the topological approaches and the results of non-empirical calculations, which are performed along the Unrestricted Density Functional Theory (UDFT) approximation, it is worth recalling briefly the main features of the spin polarization phenomenon.

The spin polarization effect was first identified in free radicals, and in particular in conjugated hydrocarbons [48, 49]. In such radicals (the simplest one being the planar CH_3 molecule), where the unpaired electron is supposed to occupy a π type MO, the EPR (Electron Paramagnetic Resonance) experiment evidenced the existence of spin density on the nuclei of the hydrogen atoms. This seems in contradiction with the nullity of the SOMO in the plane of the molecule and thus on the H atom nuclei. This observation could be interpreted only if one leaves the closed-shell description of the “core”,

$$\Phi_0 = |\Pi_i \bar{i}i a| \quad (14.49)$$

The orbitals are supposed to have been optimized by a self-consistent field through a common Fock operator for α and β electrons, which averages the effect of the exchange with the unpaired electron. This exchange effect is actually different and it was suggested that one might accept, although remaining in a single-determinant description, to give different space parts to α and β spin MOs of the previously closed shell core. The resulting function

$$\Phi'_0 = |\Pi_i i_\alpha \bar{i}_\beta a| \quad (14.50)$$

introduces spin densities through the spatial differences between the α and β spin MOs, and in particular in the MOs describing the σ bonds. In the so-called Unrestricted Hartree-Fock or Unrestricted DFT the energy of such a single determinant wave function may be optimized, using different Fock operators for the α and β spin MOs. The spin polarized MOs are

$$\begin{aligned} i_\alpha &= i - \sum_r \lambda_{ir} r \\ i_\beta &= i + \sum_r \lambda_{ir} r \end{aligned} \quad (14.51)$$

where the r 's are virtual MOs and where, according to a perturbative expansion,

$$\lambda_{ir} = -\frac{\langle i|\mathbf{K}_a|r\rangle}{2\Delta E^3(i\rightarrow r)}. \quad (14.52)$$

One sees there that, contrarily to the spin delocalization, the spin polarization phenomenon is governed by the bi-electronic part of the Hamiltonian. In the Hubbard approximation one may write

$$\langle i|\mathbf{K}_a|r\rangle = \sum_p c_{ip}c_{rp}(c_{ap})^2 U_p \quad (14.53)$$

This integral is important when the MOs i and r have important coefficients on the atoms where the magnetic MO has important amplitudes. This phenomenon may introduce spin densities in MOs which are of different symmetries than the magnetic MOs and in regions of the molecule where the spin density was (almost) null in the restricted description.

The unrestricted single-determinant description is of course approximate. This single determinant is no longer an eigenfunction of the S^2 operator, i.e. is not a spin eigenstate, a pure doublet, it is contaminated by components of Quartet spin multiplicity. Nevertheless this approach is extremely simple, makes easy geometry optimizations and is very popular.

The method can be applied to the ferromagnetic diradicals (or polyradicals of higher spin multiplicity ground state), writing the wave function of largest M_s value, for instance for a diradical, as

$$\Phi'_{M_s=1} = |\Pi_i i_\alpha \bar{i}_\beta a b| \quad (14.54)$$

where the two unpaired electrons occupy the magnetic MOs a and b , and where the core MOs are spin polarized. Since the energy difference between the high spin-multiplicity ground state and the excited states of lower spin multiplicity is the crucial observable, a consistent description of these open-shell states was highly desirable. From first principle constraints, they cannot be described as single determinants. A convenient strategy has been employed, which consists in minimizing the energy of a determinant of lower M_s value, for instance for a diradical,

$$\Phi'_{M_s=0} = |\Pi_i i'_\alpha \bar{i}'_\beta a' \bar{b}'| \quad (14.55)$$

This function introduces eventually ionic VB components, through the overlap between the magnetic MOs a' and b' , and specific spin polarization effects. But it is not a spin eigenfunction, and if the overlap between a' and b' remains small it is an almost equal mixing of singlet and triplet functions. The energy of the singlet state must be evaluated through some approximate spin decontamination techniques [50–52]. This strategy is actually applied to all diradicals, whatever their preferred ground state multiplicity. Moreover, as already mentioned for the monoradicals, the spin polarization correction introduced by the unrestricted single-determinant

treatment is only one half of the total one [10, 53, 54]. Nevertheless it is possible to estimate the contributions of the various physical effects entering in the energy difference between the triplet and the singlet states from the unrestricted single-determinant approaches [55, 56].

Exploiting the mirror theorem and the Hubbard Hamiltonian it is possible to reach some qualitative conclusions from the analytic treatment of the spin polarization effect, which apply to conjugated hydrocarbons. We do not give here the explicit derivations. They may be summarized as follows:

- in radicals and in ferromagnetic diradicals the spin polarization increases the positive spin densities on the π orbitals of major color sites,
- it introduces negative spin densities on the π orbitals of minor color sites,
- this effect is non-local, the spin polarization introduces spin densities in regions of the molecule where they were zero at the topological description level,
- the spin polarization usually contributes to increase the singlet triplet energy gap, whatever its sign,
- the spin polarization of the doubly occupied π and σ MO fixes the preferred spin multiplicity of the “undecidable” diradicals through the parity of the number of Carbon atoms separating the disjoint radicalar regions. The ground state is singlet when this number is even, triplet when it is odd.

All these statements will be illustrated in the next section.

14.5 Comparison Between Topological Assessments and Numerical DFT Calculations

In order to assess the validity of our topological predictions, concerning both energy differences and spin distributions, we decided to perform DFT calculations on the previously introduced series of hydrocarbons. To make closer the comparison with topological Hamiltonians we used ideal geometries with equal CC (1.40 Å) and CH (1.05 Å) bond lengths, planar geometries and 120° angles. The basis set was of triple zeta plus polarization quality, and the exchange correlation potential was the B3LYP one. Both restricted and unrestricted calculations will be reported. We did not compare with Hartree-Fock calculations since they are known [57–60] to give a spurious concentration of the unpaired electron on the external site. Full Configuration Interaction of the π electrons in the π valence MOs are usually necessary to obtain reliable spin densities. The resulting natural MO, obtained at a high computational cost, are close to the Hückel MOs and to the DFT MOs. The numerical calculations used the B3LYP exchange correlation potential in the Gaussian package [61]. The decomposition of the energy difference between the singlet and the triplet has been performed according to the recently proposed method [55, 56].

Table 14.1 Spin polarization energy (in a.u.) (difference between the RDFT and UDFT solutions) and $\langle S^2 \rangle$ of the UDFT solution of the monoradicals

Compound	1a,b	2a	3a	2b	3b	2c	3c
ΔE	-0.077	-0.084	-0.104	-0.081	-0.081	-0.079	-0.079
$\langle S^2 \rangle$	0.7785	0.7896	0.8229	0.7859	0.7880	0.7829	0.7836

One may first discuss the amplitude of the impact of the spin polarization on the energies. As seen from Tables 14.1 and 14.5 this effect is not extremely sensitive to the extent of the spin delocalization. It only increases slightly when going from **1a** to **3a**. One may notice that this energy is almost constant in the series **1a**, **2c**, **3c**, which is in line with the localized character of the SOMO in the series, as predicted by Hückel calculation.

Tables 14.2, 14.3 and 14.4 compare the Hückel spin densities of the monoradicals of Fig. 14.1 with those obtained by the RODFT calculations [55, 56]. A general comment concerns the delocalization of the unpaired electron from the external CH₂ group to the benzene rings. It is larger in the Hückel calculation, by a factor close to 1.2. A good fit with the RODFT values would be obtained by fixing the value of the extra-cyclic CC hopping integral t' to 0.8 t , which would only change the ratios between the spin density of the extra cyclic carbon and those of the rings. Actually the relative amplitudes in the rings given by the RODFT calculations are in good agreement with those of the topological approach, in the series **2b**, **4b**, they are divided by a factor 4 when going from a ring to the next one. The

Table 14.2 Mulliken spin densities on the various atoms of the series **a** monoradicals for the RDFT and UDFT solutions

Atoms number	1a,b			2a			3a		
	Hückel	RDFT	UDFT	Hückel	RDFT	UDFT	Hückel	RDFT	UDFT
1	0.571	0.652	0.813	0.529	0.616	0.783	0.471	0.549	0.729
2	–	0.009	-0.185	–	0.010	-0.192	–	0.010	-0.203
3	0.143	0.104	0.237	0.253	0.181	0.363	0.264	0.228	0.422
4	–	0.003	-0.128	–	0.004	-0.104	–	0.005	-0.127
5	0.143	0.111	0.259	0.059	0.047	0.130	0.029	0.027	0.107
6	–	–	–	–	0.001	-0.116	–	0.001	-0.123
7	–	–	–	0.059	0.041	0.139	–	0.019	0.125
8	–	–	–	–	0.039	0.134	0.117	0.078	0.247
9	–	–	–	–	0.001	-0.082	–	0.002	-0.081
10	–	–	–	0.056	0.046	0.142	0.029	0.025	0.096
11	–	–	–	–	0.001	-0.094	–	0.001	-0.136
12	–	–	–	–	–	–	0.029	0.017	0.099
13	–	–	–	–	–	–	–	0.001	-0.073
14	–	–	–	–	–	–	0.029	0.023	0.102
15	–	–	–	–	–	–	–	0.001	-0.082

Table 14.3 Mulliken spin densities on the various atoms of the series **b** monoradicals for the RDFT and UDFT solutions

Atoms number	2b			3b		
	Hückel	RDFT	UDFT	Hückel	RDFT	UDFT
1	0.516	0.600	0.767	0.504	0.590	0.758
2	–	0.009	–0.185	–	0.009	–0.184
3	0.129	0.099	0.225	0.125	0.098	0.222
4	–	0.003	–0.133	–	0.003	–0.133
5	0.129	0.104	0.244	0.125	0.102	0.240
8	–	0.002	–0.073	–	0.002	–0.078
9	0.032	0.022	0.081	0.031	0.022	0.080
10	–	0.001	–0.043	–	0.001	–0.048
11	0.032	0.024	0.084	0.031	0.022	0.083
14	–	–	–	–	0.001	–0.025
15	–	–	–	0.008	0.005	0.027
16	–	–	–	–	<10 ^{–3}	–0.015
17	–	–	–	0.008	0.006	0.029

Table 14.4 Mulliken spin densities on the various atoms of the series **c** monoradicals for the RDFT and UDFT solutions

Atoms number	2c			3c		
	Hückel	RDFT	UDFT	Hückel	RDFT	UDFT
1	0.571	0.650	0.812	0.571	0.650	0.813
2	–	0.009	–0.188	–	0.009	–0.188
3	0.143	0.106	0.248	0.143	0.106	0.249
4	–	0.004	–0.125	–	0.004	–0.124
5	0.143	0.109	0.268	0.143	0.109	0.268
6	–	0.003	–0.130	–	0.003	–0.130
7	0.143	0.102	0.242	0.143	0.102	0.243
8	–	<10 ^{–3}	0.030	–	<10 ^{–3}	0.033
9	–	<10 ^{–3}	–0.027	–	<10 ^{–3}	–0.027
10	–	0.001	0.017	–	0.001	0.018
11	–	<10 ^{–3}	–0.026	–	<10 ^{–3}	–0.025
12	–	0.001	0.017	–	0.001	0.019
13	–	<10 ^{–3}	–0.029	–	<10 ^{–3}	–0.029
14	–	–	–	–	<10 ^{–3}	0.008
15	–	–	–	–	<10 ^{–3}	–0.008
16	–	–	–	–	<10 ^{–3}	0.004
17	–	–	–	–	<10 ^{–3}	–0.008
18	–	–	–	–	<10 ^{–3}	0.004
19	–	–	–	–	<10 ^{–3}	–0.009

Table 14.5 Energies in a.u. of the RDFT and UDFT $M_s = 1$ and $M_s = 0$ solutions, $\langle S^2 \rangle$ of the UDFT solutions and triplet to singlet gaps in eV of the ferromagnetic diradicals

Compound	1'a,b,c	2'a	3'a	2'bc	3'bc
Reference energy	-309.0	-463.0	-616.0	-540.0	-771.0
RDFT $M_s = 0$	-0.601613	-0.280669	-0.951045	-0.703328	-0.796909
UDFT $M_s = 0$	-0.644094	-0.319110	-0.987935	-0.742861	-0.837638
$\langle S^2 \rangle$	1.0114	1.0233	1.0384	1.0408	1.0563
RDFT $M_s = 1$	-0.646196	-0.318504	-0.985469	-0.739320	-0.832446
UDFT $M_s = 1$	-0.653264	-0.326077	-0.994091	-0.746086	-0.838730
$\langle S^2 \rangle$	2.0614	2.0909	2.1395	2.0815	2.0824
Spin polar energy	-0.0070	-0.00757	-0.00862	-0.00676	-0.00628
$U\Delta E_{TS}$ (eV)	0.500	0.379	0.335	0.175	0.029
Topol ΔE_{TS} (eV)	0.55	0.375	0.325	0.137	0.033
$2K_{ab}$ (eV)	0.378	0.210	0.162	0.080	0.018

The topological estimates are based on a value $U = 5$ eV of the on-site repulsion

ratios between the spin densities on the ring atoms of the series **1a**, **2a**, **3a** are very close to those predicted from the topology. The local character of the SOMO in **2c** and **3c**, predicted by this Hamiltonian, is confirmed at this level. These tables also report the values obtained from Unrestricted DFT (UDFT) calculations. The spin polarization does not change significantly the ratios between the spin densities of the atoms which bear large positive spin densities at the RODFT level, but it introduces large values on atoms which are far from the extra-cyclic CH_2 group. The spin polarization introduces long range effects, especially in the acene series (Cf. **3a** in Table 14.2), as previously commented. The effect is much less pronounced in **2c** and **3c**, due to the localization of the SOMO. One sees that despite the neglect of the spin polarization important information can be obtained from the topological Hamiltonian (Table 14.5).

The same comments are valid concerning the spin densities of ferromagnetic diradicals, reported in Table 14.6 for the series **1'a**, **2'a** and **3'a**, and in Table 14.7 for the series **2'c**, **3'c**. The extra-cyclic spin densities are too large in the Hückel approach but the ratios in the six-membered rings are in excellent agreement with those given by the RODFT (Restricted Open-shell DFT) calculations.

The crucial point concerns the triplet to singlet energy gaps. Table 14.5 first gives the estimates from RODFT, calculating the exchange integral K_{ab} from the RODFT SOMOs, then from the UDFT $M_s = 1$ and $M_s = 0$ solutions, using a spin decontamination factor equal to 2 (the Yamaguchi's correction being practically the same). At the RODFT level the energy differences, i.e. the $2K_{ab}$ quantities, are somewhat smaller than the values obtained at the UDFT level, which confirms the fact that the spin polarization increases the energy difference. These values must be compared to those of the topological derivation, which only depend on the value of U , the on-site repulsion of the Hubbard Hamiltonian. The here-reported values are

Table 14.6 Mulliken spin densities on the various atoms of the ferromagnetic diradicals for the triplet RDFT and UDFT solutions of series **a**

Atoms number	1'a,b,c			2'a			3'a		
	Hückel	RDFT	UDFT	Hückel	RDFT	UDFT	Hückel	RDFT	UDFT
1	0.583	0.627	0.804	0.531	0.594	0.770	0.485	0.545	0.735
2	–	0.014	–0.245	–	0.011	–0.223	–	0.011	–0.217
3	0.333	0.259	0.481	0.281	0.225	0.435	0.274	0.234	0.432
4	–	–	–	–	0.009	–0.183	–	0.007	–0.169
5	0.250	0.213	0.416	0.125	0.104	0.253	0.071	0.061	0.192
6	–	0.006	–0.214	–	0.003	–0.181	–	0.002	–0.164
7	–	–	–	0.125	0.098	0.268	0.071	0.052	0.208
8	–	–	–	–	–	–	0.200	0.152	0.372
11	–	–	–	–	–	–	–	0.002	–0.202

Table 14.7 Mulliken spin densities on the various atoms of the ferromagnetic diradicals for the triplet RDFT and UDFT solutions of series **b**

Atoms number	2'bc			3'bc		
	Hückel	RDFT	UDFT	Hückel	RDFT	UDFT
1	0.519	0.587	0.756	0.504	0.586	0.753
2	–	0.009	–0.191	–	0.009	–0.186
3	0.130	0.102	0.235	0.126	0.098	0.223
4	–	0.004	–0.150	–	0.003	–0.137
5	0.130	0.107	0.264	0.126	0.098	0.233
6	–	0.004	–0.148	–	0.003	–0.137
7	0.130	0.099	0.229	0.126	0.103	0.244
8	–	0.006	–0.180	–	0.002	–0.099
9	0.166	0.133	0.323	0.031	0.024	0.098
10	–	0.004	–0.160	–	0.001	–0.074
11	0.166	0.128	0.301	0.031	0.023	0.095
12	–	0.010	–0.208	–	0.001	–0.072
13	0.185	0.138	0.328	0.031	0.023	0.113
14	0.573	0.644	0.808	–	0.004	–0.145
15	–	–	–	0.149	0.115	0.288
16	–	–	–	–	0.004	–0.141
17	–	–	–	0.149	0.114	0.277
18	–	–	–	–	0.009	–0.195
19	–	–	–	0.153	0.108	0.263
20	–	–	–	0.571	0.648	0.811

based on $U = 5$ eV, a commonly accepted value. This agreement between a topological analytic estimate and the results of black box calculations is rather surprising.

The agreement is similar regarding the antiferromagnetic diradicals, reported in Table 14.8, although we may only compare the topological model to the UDFT calculations, which incorporate spin polarization effects. In these cases the approximate spin-decontamination process of Yamaguchi was used [50, 51]. The first striking result is the smallness of the K_{ab} exchange integral, calculated at the RODFT level, using the magnetic MOs of the triplet and localizing them. This result is in agreement with the topological analysis. One may see a dramatic contrast between the values of the exchange integral in meta- versus para-dimethylene acenes (series **1'a**, **2'a**, **3'a** in Table 14.5, versus series **1''a**, **2''a**, **3''a** in Table 14.8). While the distances between the methylene groups are similar the exchange integral almost vanishes in the antiferromagnetic series. The order of magnitude of the singlet to triplet energy gap is again correctly predicted by the topological model. Of course this model predicts a zero value for the disjoint diradicals **2''c** and **3''c**, but the DFT calculations confirm the extremely low value of the corresponding excitation energies (0.078 and 0.018 eV respectively).

The quantitative impact of the spin polarization on the energy difference between the singlet and the triplet states is significant but it is not directly accessible in DFT calculations. One may of course compare the restricted DFT and unrestricted DFT gaps, for instance in the dimethylene naphthalene **2'a** which has a triplet ground state. The RDFT values of the excitation energies are 1.0 eV while the UDFT calculation (corrected for the spin contamination) gives 0.38 eV. This overestimation is essentially due to the closed-shell constraint imposed to the restricted DFT calculation of the Singlet, which is not physical in these ferromagnetic systems, rather than to the spin polarization itself. The core spin-polarization free description should be the two-electron in two-orbital CASSCF solution. This description properly reduces the ionic component of the wave function which is exceedingly large in the restricted $M_s = 0$ wave function.

It is interesting at this point to return to the cases which appeared as unpredictable from the spin-delocalization only, such as the tetra-methylene ethylene (TME). The spin polarization contribution of the π doubly occupied MOs acts in favor of the singlet, according to the preceding arguments, despite the fact that the kinetic exchange was not decisive, due to the smallness of the hopping integral between the localized singly occupied MOs. The spin-polarization contribution strictly obeys the parity determinism expressed by the Ovchinnikov's rule. This is observed in compounds **2''c** and **3''c** (Table 14.8). It is worth noticing that the σ bond spin polarization works in the same direction as that of the π system, the CC σ bond connecting the two allyl groups in TME prefers a complete spin alternation in the π system. Notice that the spin-polarization mechanism represents a step in the MO picture toward the Heisenberg description. Both treatments introduce for instance negative spin densities in the triplet state.

Table 14.8 Energies in a.u. of the RDFT and UDFT Ms = 0 and Ms = 1 solutions and $\langle S^2 \rangle$ of the UDFT solutions of the antiferromagnetic diradicals

Compound	1''a,b	2''a	3''a	2''b	3''b	2''c	3''c
Reference energy	-309.0	-463.0	-16.0	-540.0	-771.0	-540.0	-771.0
RDFT Ms = 0	-0.673114	-0.329564	-0.988158	-0.746159	-0.826039	-0.708732	-0.790704
UDFT Ms = 0	-	-0.334033	-0.997662	-0.753867	-0.843252	-0.742907	-0.835563
$\langle S^2 \rangle$	-	0.6274	0.8716	0.7852	0.9997	1.0710	1.0749
RDFT Ms = 1	-0.631792	-0.310551	-0.980389	-0.737305	-0.833894	-0.736221	-0.829573
UDFT Ms = 1	-0.634368	-0.314293	-0.994091	-0.741692	-0.8391199	-0.741469	-0.835243
$\langle S^2 \rangle$	2.0076	2.0225	2.1395	2.0361	2.0530	2.0465	2.0587
U ΔE_{ST} (eV)	1.054	0.767	0.154	0.543	0.224	0.078	0.018
Topol ΔE_{ST} (eV)	1.250	0.990	0.356	0.406	0.118	0.0	0.0
2Kab (eV)	0.015	0.008	<10 ⁻³	0.005	0.002	<10 ⁻³	<10 ⁻³

The topological estimates are based on $t = 3.5$ eV and $U = 5$ eV

14.6 Conclusion

This work has shown how one may exploit the analytical properties of the Hückel Hamiltonian to predict many properties of monoradicals, diradicals or polyradicals. This topological model enables one to establish analytically the coefficients of the singly occupied MOs on the different conjugated carbons of radicals. When the molecule has an open-shell singlet ground state, it is possible to determine the HOMO and LUMO energies from the coefficients of the SOMOs of the monoradicals obtained by subtracting from the graph successively the two atoms which are expected to bear the unpaired electrons with major spin densities. Then introducing the bi-electronic repulsion through the Hubbard Hamiltonian, the ground-state spin multiplicity is predicted by simply considering the topology. This model affords a derivation of the Ovchinnikov's rule in the weak correlation limit, consistent with the physics of conjugated hydrocarbon ($|t/U|$ is larger than $1/2$). One can note that this rule was originally derived from the Heisenberg Hamiltonian, i.e. in the strong correlation limit.

Another advantage of this approach is that it provides a direct analytical estimate of both singlet-triplet gaps of polyradicals and the coefficients of the SOMOs. Estimates of both direct exchange integrals for ferromagnetic systems and kinetic exchange contributions for antiferromagnetic systems are easily obtained. One may note that at variance, the estimation of singlet-triplet gaps from the topological Heisenberg Hamiltonian requires a matrix diagonalization. Moreover this analysis gives a direct access to the spin-instability condition (broken-symmetry solution lower in energy than the spin-restricted one). The reader may play with various architectures, involving other branching of methylene groups on polyphenylene, acenes or fused polycyclic aromatic hydrocarbons. Let us mention that these analysis have been recently used to predict the conductance properties of polycyclic hydrocarbons, as function of the sites of attachments to conducting sources [62]. Finally we would like to mention that the present topological analysis can be used to rationalize the spin-symmetry breaking occurring in the series of polyacenes, their diradical character, which is a matter of debate in the recent literature [63–67], and the length dependence of the singlet-triplet energy gap.

The proofs of the here-formulated theorems and rules do not require equal hopping integrals. As a consequence the conclusions may be relevant to systems where the conjugated hydrocarbon is either weakly or strongly bonded to external magnetic sites, such as open-shell metal ion complexes or organic radicals like nitroxides [68] or nitrenes [69]. The topological conclusions remain valid, as far as the on-site energies of the external magnetic sites are not too different from those of the sp^2 carbons. Some of the conclusions are applicable to the dinuclear complexes of Cu(II) or Ni(II) where the two magnetic ions are connected by long conjugated hydrocarbons [70, 71]. Such architectures attract more and more attention in the field of spintronic. Among the bridging ligands commonly used to connect transition metal ions, those which exhibit strong bond alternations (like polyenes or chains of phenyls) are bad spin linkers. At variance, fused aromatic polybenzenic

systems are good spin linkers. Indeed, our analysis shows that the spin delocalization extent in the ligand is severely damped by bond alternation and therefore reduces the interference effects between the spin waves of remote magnetic sites. One should note that the spin-polarizability of hydrocarbon bridging ligands increases with the near degeneracy of the lowest spin states. These ligands might finally behave as non-innocent ligands.

From a conceptual point of view, this chapter also recalls the essential difference between the spin delocalization and spin polarization mechanisms [71, 72]. The former is governed by mono-electronic operators while the latter is a bi-electronic. This is a matter of frequent confusion. Indeed one sometimes unduly speaks of spin polarization of the ligand as soon as its atoms bear some spin densities [68–70]. In most cases this is simply a delocalization effect as the magnetic orbitals have delocalization tails on the ligand. Happily enough the spin delocalization and the spin polarization quite often work in the same direction, regarding the sign and magnitude of the magnetic couplings. The spin polarization may concern subsets of orbitals which, for symmetry reasons, are not affected by the spin delocalization, for instance the σ MOs of π radicals. When it affects the subsystems of MOs already concerned by the spin delocalization (for instance the π MOs of π radicals) the spin polarization reinforces the contrast in the spin density distribution on the ligand, increasing the positive spin densities and introducing negative spin densities on the atoms which were on nodal positions of the Hückel SOMOs.

References

1. Gatteschi D, Kahn O, Miller JS, Palacio F (eds) (1991) *Magnetic molecular materials*. Kluwer, Dordrecht
2. Kahn O (1993) *Molecular magnetism*. VCH, Weinheim
3. Gatteschi D (1994) *Adv Mater* 6:635–645
4. Miller JS, Epstein AJ (1994) *Angew Chem Int Ed Engl* 33:385–415
5. (1996) *Molecule-based magnetic materials*. ACS Symposium series, vol 644
6. Itoh K, Kinoshita M (2000) *Molecular magnetism*. Gordon and Breach, Tokyo
7. Long J (2003) In: Yang P (ed) *Chemistry of nanostructured materials*. World Scientific Publishing, Hong Kong
8. (2005) *Coord Chem Rev* 249. Special issue “Molecular magnetism”
9. Gatteschi D, Bogani L, Cornia A, Mannini M, Sorace L, Sessoli R (2008) *Solid State Sci* 10:1701–1709
10. Malrieu J-P, Caballol R, Calzado CJ, de Graaf C, Guihéry N (2014) *Chem Rev* 114:429
11. Moreira I de PR, Illas F (2006) *Phys Chem Chem Phys* 8:1645
12. Bencini V (2008) *Inorg Chim Acta* 361:3820
13. Neese F (2009) *Coord Chem Rev* 253:526
14. Iwamura H (2013) *Polyhedron* 66:3–14
15. Makarova TL, Palacio F (eds) (2006) *Carbon-based magnetism: an overview of metal-free carbon-based compounds and materials*. Elsevier, Amsterdam
16. Nakano M, Fukui H, Minami T, Yoneda K, Shigeta Y, Kishi R, Champagne B, Botek E, Kubo T, Ohta K, Kamada K (2011) *Theor Chem Acc* 130:711–724

17. Motomura S, Nakano M, Fukui H, Yoneda K, Kubo T, Carion R, Champagne B (2011) *Phys Chem Chem Phys* 13:20575–20583 and references therein
18. Landolt-Bornstein (2005) Nitroxide radicals and nitroxide based high-spin systems, vol 26. Springer, Berlin
19. Rajca S, Rajca A, Wongsriratanakul J, Butler P, Choi S-M (2004) *J Am Chem Soc* 126:6972–6986
20. Salem L (1966) The molecular orbital theory of conjugated systems. Benjamin Inc, New York
21. Ovchinnikov AA (1978) *Theor Chim Acta* 47:297–304
22. Malrieu J-P, Maynau D (1982) *J Amer Chem Soc* 104:3021–3029
23. Malrieu J-P (1982) D Maynau *J Amer Chem Soc* 104:3029–3034
24. Said M, Maynau D, Malrieu J-P, Garcia-Bach M-A (1984) *J Am Chem Soc* 106:571–579
25. Longuet-Higgins HC (1950) *J Chem Phys* 18:265
26. Borden WT (1982) *Diradicals*. Wiley-Interscience, New York
27. Du P, Borden WT (1987) *J Am Chem Soc* 109:930–931
28. Nicolaidis A, Borden WT (1993) *J Am Chem Soc* 115:11951–11957
29. Borden WT, Iwamura H, Berson JA (1994) *Acc Chem Res* 27:109–116
30. Hrovat DA, Borden WT (1994) *J Am Chem Soc* 116:6327–6331
31. Fang S, Lee M-S, Hrovat DA, Borden WT (1995) *J Am Chem Soc* 117:6727–6731
32. Bally T, Borden WT (1993) In: Lipkowitz KB, Boyd DB (eds) *Reviews in computational chemistry*, vol 13. Wiley-VCH, New York, pp 1–97
33. Lineberger WC, Borden WT (2011) *Phys Chem Chem Phys* 13:11792–11813
34. Trinquier G, Suaud N, Malrieu J-P (2010) *Chem Eur J* 16:8762–8772
35. Said M, Maynau D, Malrieu J-P (1984) *J Am Chem Soc* 106:580
36. Lieb EH (1989) *Phys Rev Lett* 62:1201–1204
37. Caballol R, Castell O, Illas F, de Moeira IPR, Malrieu J-P (1997) *J Phys Chem A* 101:7860–7866
38. Thiele J, Balhorn H (1904) *Chem Ber* 37:1463–1470
39. Chichibabin AE (1907) *Chem Ber* 40:1810–1819
40. Montgomery LK, Huffman JC, Jurczak EA, Grendze MP (1986) *J Am Chem Soc* 108:6004–6011
41. Muller E, Pfanz H (1941) *Chem Ber* 74:1051
42. Shishlov NM, Asfandiarov NL (2000) *Russ Chem Bull Int Ed* 40:1676–1681
43. For a recent theoretical study of the series see, Trinquier G, Malrieu J-P (2015) *Chem Eur J* 21:814–828
44. Abe M (2013) *Chem Rev* 113:7011–7088
45. Filatov M, Shaik S (1999) *J Phys Chem A* 103:8885–8889
46. Rodríguez E, Reguero M, Caballol R (2000) *J Phys Chem A* 104:6253–6258
47. Pozun ZD, Su X, Jordan KD (2013) *J Am Chem Soc* 135:13862–13869
48. McConnell HM (1956) *J Chem Phys* 24:764
49. Bernsohn R (1956) *J Chem Phys* 24:1066
50. Yamaguchi K, Takahara Y, Fueno T (1986) In: Smith VH (ed) *Applied quantum chemistry*. Reidel, Dordrecht, p 155
51. Soda T, Kitagawa Y, Onishi T, Takano T, Shigeta Y, Nagao H, Yoshioka Y, Yamaguchi K (2000) *Chem Phys Lett* 319:223–230
52. Malrieu J-P, Ferré N, Guihéry N (2015) *Phys Chem Chem Phys* 17:14375
53. De Loth P, Cassoux P, Daudey J-P, Malrieu J-P (1981) *J Amer Chem Soc* 103:4007
54. Calzado CJ, Cabrero J, Malrieu J-P, Caballol R (2002) *J Chem Phys* 116:2728
55. Coulaud E, Guihéry N, Malrieu J-P, Hagenbaum-Reignier D, Siri D, Ferré N (2012) *J Chem Phys* 137:114106
56. Coulaud E, Malrieu J-P, Guihéry N, Ferré N (2013) *J Comput Theory Chem* 9:3429
57. Borden WT, Davidson ER, Feller D (1982) *Tetraedron* 38:737–739
58. Borden WT, Davidson ER (1996) *Acc Chem Res* 29:67–75
59. Suaud N, Ruamps R, Guihéry N, Malrieu J-P (2012) *J Chem Theory Comput* 8:4127–4137
60. Suaud N, Ruamps R, Malrieu J-P, Guihéry N (2014) *J Phys Chem A* 118:5876

61. Frisch MJ, Trucks GW, Schlegel HB, Scuseria GE, Robb MA, Cheeseman JR, Scalmani G, Barone V, Mennucci B, Petersson GA, Nakatsuji H, Caricato M, Li X, Hratchian HP, Izmaylov AF, Bloino J, Zheng G, Sonnenberg JL, Hada M, Ehara M, Toyota K, Fukuda R, Hasegawa J, Ishida M, Nakajima T, Honda Y, Kitao O, Nakai H, Vreven T, Montgomery Jr JA, Peralta JE, Ogliaro F, Bearpark M, Heyd JJ, Brothers E, Kudin KN, Staroverov VN, Kobayashi R, Normand J, Raghavachari K, Rendell A, Burant JC, Iyengar SS, Tomasi J, Cossi M, Rega N, Millam JM, Klene M, Knox JE, Cross JB, Bakken V, Adamo C, Jaramillo J, Gomperts R, Stratmann RE, Yazyev O, Austin AJ, Cammi R, Pomelli C, Ochterski JW, Martin RL, Morokuma K, Zakrzewski VG, Voth GA, Salvador P, Dannenberg JJ, Dapprich S, Daniels AD, Farkas O, Foresman JB, Ortiz JV, Cioslowski J, Fox DJ, Gaussian 09 Revision A.02. (2009) Gaussian Inc. Wallingford CT
62. Mayou D, Zhou Y, Ernzerhof M (2013) *J Phys Chem C* 117:7870
63. Bendikov M, Duong HM, Starkey K, Houk KN, Carter EA, Wudl F (2004) *J Am Chem Soc* 126:7416–7417
64. Dos Santos MC (2006) *Phys Rev B* 74:045426–045429
65. Jiang D, Dai S (2008) *J Phys Chem A* 112:332–335
66. Hachmann J, Dorando JJ, Avilés M, Chan GK-L (2007) *J Chem Phys* 127:134309
67. Hajgato B, Huzak M, Deleuze MS (2011) *J Phys Chem A* 115:9282
68. Ali ME, Datta SN (2006) *J Phys Chem A* 110:2776, 13232
69. Lahti PM, Ichimura S, Sanborn JA (2001) *J Phys Chem A* 105:151
70. Pardo E, Carrasco R, Ruiz-Garcia R, Julve M, Lloret F, Munoz MC, Journaux Y, Ruiz E, Cano J (2008) *J Amer Chem Soc* 130:576
71. Ferrando-Soria J, Castellano M, Yuste C, Lloret F, Julve M, Fabelo O, Ruiz-Perez C, Stiriba SE, Ruiz-Garcia R, Cano J (2010) *Inorg Chim Acta* 363:1666
72. Terencio T, Bastardis R, Suaid N, Maynau D, Bonvoisin J, Calzado CJ, Malrieu J-P, Guihéry N (2011) *Phys Chem Chem Phys* 13:12314

Part III
Topological Methods for the
Characterization of Weak Bonding
Interactions

Chapter 15

What Can Be Learnt from a Location of Bond Paths and from Electron Density Distribution

Slawomir J. Grabowski

Abstract A bond path being a line of maximum electron density linking attractors of two atoms is often applied in various studies as a criterion of the existence of numerous interactions such as for example hydrogen, halogen or pnicoen bond. It covers cases of atom-atom energetically stabilized links, from weak van der Waals interactions, through stronger Lewis acid–Lewis base interactions up to covalent bonds. The location of bond paths also allows interpreting mechanisms of interactions and, in general, of chemical reactions. The Quantum Theory of Atoms in Molecules (QTAIM) results are mainly presented here; however they are supported by other approaches as, for example, the Natural Bond Orbitals (NBO) method or the σ -hole concept. The most important orbital-orbital interactions determined from the NBO method and characterizing different types of interactions are presented. The analysis of the distribution of the electron charge density is also performed here for numerous systems; this is shown that the regions of the concentration and depletion of the electron density coincide with the regions of the negative and positive regions of the electrostatic potential. The role of the analysis of the laplacian of the electron density is shown on the basis of numerous interactions.

Keywords Bond path • Bond critical point • Laplacian of the electron density • Hydrogen bond • Halogen bond • Pnicogen bond • Lewis acid–Lewis base interaction • Quantum Theory of Atoms in Molecules (QTAIM) • Natural Bond Orbitals (NBO) method • σ -hole concept • Electrostatic potential

S.J. Grabowski (✉)

Kimika Fakultatea, Euskal Herriko Unibertsitatea UPV/EHU, and Donostia International Physics Center (DIPC), P.K. 1072, 20080 Donostia, Euskadi, Spain
e-mail: s.grabowski@ikerbasque.org

S.J. Grabowski

Basque Foundation for Science, IKERBASQUE, Maria Diaz de Haro 3,
48013 Bilbao, Spain

15.1 Introduction

The analysis of the electron charge density is one of the most often applied and standard approaches to describe the system investigated; molecule, ion, greater cluster or even crystal [1–3]. This is why the Quantum Theory of Atoms in Molecules (QTAIM) seems to be a useful tool for such analysis since it concerns directly the electron charge density distribution of the system analyzed [4, 5]. One of ideas of the QTAIM approach is the partitioning of 3D electron charge density space into fragments attributed to atoms (atomic basins); the properties of those fragments are often transferable from one system to another one. In such a way it is possible to consider volumes of atoms or to calculate charges integrated over those volumes. This is important that the mentioned here theoretically calculated volumes and charges may have experimental equivalents since it is possible to perform the crystal structure determination to have the experimental electron charge density distribution in crystal and further apply the QTAIM approach [1–3].

However that is not all; the detailed properties of the electron density, $\rho(r)$, of the system considered may be analyzed [5–7]. The critical points (CPs) denoted by the coordinates r_C , are those where the gradient of the electron density, $\nabla\rho(r_C)$, vanishes and they correspond to minima, maxima or saddle points of the electron density. The CP is labeled by giving the duo of values (ω, σ) , where ω is the rank of CP while σ is its signature. There are the following critical points; $(3, -3)$ —the local maximum often named as attractor is attributed to the position of atom, $(3, -1)$ —the saddle point which often is called the bond critical point (BCP), $(3, +1)$ —the saddle point which is called the ring critical point (RCP) and $(3, +3)$ —the local minimum, i.e. the cage critical point (CCP). The physical interpretation of critical points mentioned here is very well known and it is discussed in numerous monographs and review articles. This is important to announce here that the positions of $(3, -3)$ critical points (attractors) are attributed to the positions of atoms. However there is an excellent agreement between the positions of non-hydrogen attractors and the corresponding nuclei (at least the differences are much smaller than the experimental or theoretical errors) but there is noticeable disagreement between the positions of hydrogen atom attractors (local maxima of the electron density) and their nuclei [8]. This is later discussed in this chapter.

There is another important term useful to describe the distribution of the electron density—the bond path which links pair of attractors [9, 10]. The two gradient paths which originate at the bond critical point and terminate at each of the two attractors define the bond path [11]. In other words the bond path (BP) is a line of the maximum electron density linking the nuclei (more precisely attractors) of two atoms. The bond critical point is that one at the bond path where the electron density attains the minimum value. There are numerous studies on properties and physical meaning of the bond path. It was pointed out that every bond path is accompanied by a virial path [12]. The latter one is a line linking the same nuclei as those connected by the bond path. The virial path is characterized by the maximally negative potential electron energy density thus it is maximally stabilizing with

respect to any other neighboring lines. Bader has pointed out that “one may define a bond path operator as a Dirac observable, making the bond path the measurable expectation value of a quantum mechanical operator” [10]. The bond path denotes two atoms are bonded and it is not equivalent to the chemical bond [10]. The former term can describe the complete range of bonded interactions and is attributed to the electron charge accumulation between the pair of atoms, on the other hand the latter term—bond is limited and dominated by the pair-electron concept of Lewis. This is why the term “bond path” at least should be considered as an alternative way to describe the arrangement of atoms in the species analyzed. This is discussed in the next section.

The molecular graph is defined as a set of bond paths and critical points [6, 7]. Figure 15.1 shows the molecular graph of the complex of water with fluorobenzene. One can observe here the bond paths indicating covalent bonds (solid lines) of the fluorobenzene and water molecules as well as two bond paths indicating intermolecular interactions (broken lines); i.e. the H...F and H...O contacts corresponding to the O–H...F and C–H...O hydrogen bonds, respectively. The isolines of the laplacian of electron density, $\nabla^2\rho^2(r)$, are also presented in this figure and it is

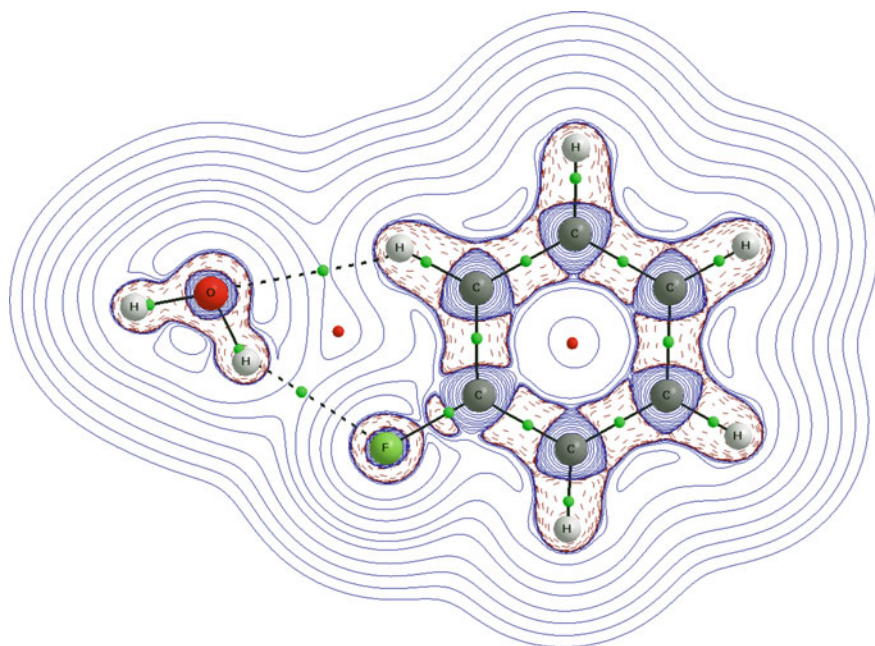


Fig. 15.1 The molecular graph of the $C_6FH_5-H_2O$ complex, solid and broken lines correspond to bond paths, big circles to attractors and small circles to critical points (green—bond critical points, red—ring critical points), the isolines of laplacian of electron density are also presented; positive values are depicted in solid lines and negative values in broken lines (this is the rule for the other figures of this chapter); the laplacian isodensity lines in the plane of the complex; based on the MP2/aug-cc-pVTZ results of calculations

indicated where the laplacian value is negative or positive. The latter indication is useful to describe different characteristics of the system analyzed such as the Lewis acid and Lewis base sites, the nature of interatomic contacts (bonds or intermolecular contacts), the regions of the concentration and depletion of electron charge density—the latter often leads to the location of unshared electron pairs, to the identification if the bond is ionic or covalent in nature, etc. [13–15]. For numerous molecular graphs analyzed hereafter these laplacian isolines or the reactive surfaces ($\nabla\rho^2(r) = 0$ isosurfaces) are also presented to deepen the understanding of the nature of interactions.

There is no difference if, from classical point of view, the intermolecular interaction or the chemical bond is considered. For both cases the bond path is created what means that two atoms are bonded (but it does not mean that necessarily there is the bond between them). Sometimes the characteristics of the bond critical point (BCP) related to the bond path considered are analyzed, the negative value of the laplacian of the electron density at BCP, $\nabla^2\rho_{\text{BCP}}$, indicates the concentration of the electron charge density in the inter-atomic region what is typical for covalent bonds. If the positive value of $\nabla^2\rho_{\text{BCP}}$ is observed thus there is the closed-shell interaction like in a case of an ionic bond, a van der Waals interaction or a hydrogen bond. However the above classification is not always a rule. Sometimes for strong hydrogen bonds the total electron energy density at BCP, H_{BCP} , is negative or even for very strong hydrogen bonds the $\nabla^2\rho_{\text{BCP}}$ value is negative like for the typical covalent bonds [16, 17]. It was stated that the interaction is covalent in nature or at least it is characterized by the partial covalency if H_{BCP} for the analyzed interatomic contact is negative, there is no requirement of the negative value of $\nabla^2\rho_{\text{BCP}}$ [18, 19]. One can mention here well known relationships between energetic topological parameters and the laplacian of the electron density at BCP (expressed in atomic units, see Eq. 15.1) [5, 6].

$$1/4\nabla^2\rho_{\text{BCP}} = 2G_{\text{BCP}} + V_{\text{BCP}}, \quad \text{where } H_{\text{BCP}} = V_{\text{BCP}} + G_{\text{BCP}} \quad (15.1)$$

G_{BCP} and V_{BCP} are the components of the mentioned above H_{BCP} energy density and represent the kinetic electron energy density and the potential electron energy density, respectively. G_{BCP} is always a positive value while V_{BCP} is always negative.

For the $\text{C}_6\text{FH}_5\text{-H}_2\text{O}$ complex presented here the typical medium in strength or weak hydrogen bonds are created where both H_{BCP} and $\nabla^2\rho_{\text{BCP}}$ values are positive. The electron density at the $\text{H}\dots\text{F}$ BCP, ρ_{BCP} , corresponding to the $\text{O-H}\dots\text{F}$ hydrogen bond is equal to 0.014 au while the ρ_{BCP} value for the $\text{H}\dots\text{O}$ contact of the $\text{C-H}\dots\text{O}$ hydrogen bond is equal to 0.009 au. The electron density at BCP corresponding to intermolecular contact, especially in a case of hydrogen bonds, is often treated as the measure of the strength of interaction [16, 17]. The presented values of ρ_{BCP} indicate that the hydrogen bonds considered here are rather weak, for example the ρ_{BCP} for the $\text{H}\dots\text{O}$ intermolecular contact for water dimer linked through the medium in strength $\text{O-H}\dots\text{O}$ hydrogen bond amounts ~ 0.02 au (this value depends slightly on a level of calculations) [20].

It was pointed out that the $n(\text{B}) \rightarrow \sigma_{\text{AH}}^*$ orbital-orbital interaction may be treated as a signature of the $\text{A}\cdots\text{H}\cdots\text{B}$ hydrogen bond since it corresponds to the $\text{H}\cdots\text{B}$ contact [21–24]. For the hydrogen bonds the latter orbital-orbital interaction energy is the most important contribution to the charge transfer energy term. For two $\text{O}\cdots\text{H}\cdots\text{F}$ and $\text{C}\cdots\text{H}\cdots\text{O}$ hydrogen bonds presented in Fig. 15.1 there are the $n(\text{F}) \rightarrow \sigma_{\text{OH}}^*$ and $n(\text{O}) \rightarrow \sigma_{\text{CH}}^*$ orbital-orbital interactions, respectively, with the corresponding energies amounting 1.7 and 0.8 kcal/mol (HF/aug-cc-pVTZ//MP2/aug-cc-pVTZ level). The corresponding $n(\text{O}) \rightarrow \sigma_{\text{OH}}^*$ orbital-orbital interaction for the mentioned above water dimer is equal to ~ 6 kcal/mol (depending on the level of calculation).

One can see two ring critical points (RCPs, red small circles in Fig. 15.1) attributed to the benzene ring and to the ring created by covalent bonds and two $\text{H}\cdots\text{F}$ and $\text{H}\cdots\text{O}$ contacts; i.e. the latter RCP corresponds to the $\text{O}\cdots\text{H}\cdots\text{F}\cdots\text{C}\cdots\text{H}\cdots\text{O}$ ring. Figure 15.1 shows also the isolines of the laplacian of electron density with the regions of the concentration of the electron density at O and F proton acceptor centers. Those regions correspond to the lone electron pairs which are responsible for the existence of the negative electrostatic potentials (EPs) at the oxygen and fluorine atoms. The hydrogen atoms of the $(\text{C})\text{H}\cdots\text{O}$ and $(\text{O})\text{H}\cdots\text{F}$ contacts are characterized by the positive EPs due to the significant outflow of the electron density from the hydrogen atoms to the carbon and oxygen atoms and to the $\text{C}\cdots\text{H}$ and $\text{O}\cdots\text{H}$ inter-atomic regions. Figure 15.2 presents maps of the

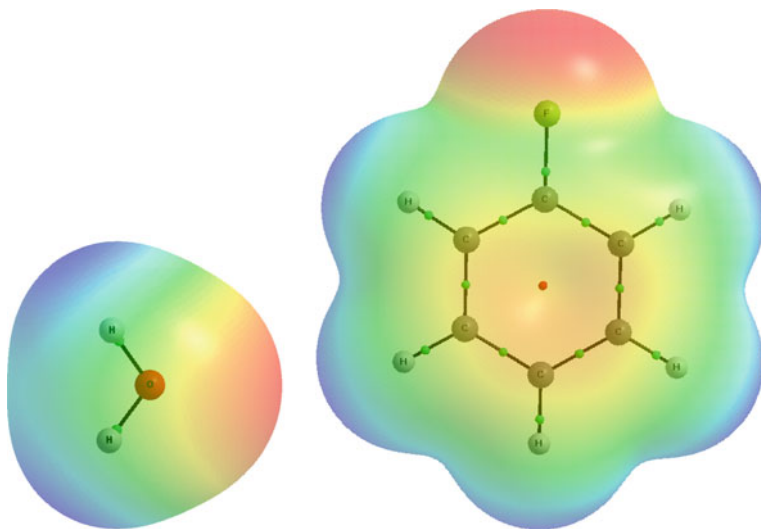


Fig. 15.2 The maps of the electrostatic potential calculated at the 0.001 au molecular electron density surfaces for H_2O (*left*) and $\text{C}_6\text{H}_5\text{F}$ (*right*) molecules; *red* and *blue* colors correspond to negative and positive EP, respectively. The maximum and minimum EP-values for H_2O are equal to +0.0709 au (H-atoms) and -0.0514 au (O-atom), respectively; such values for $\text{C}_6\text{H}_5\text{F}$ are equal to +0.0296 au (H-atoms) and -0.0259 au (F-atom); MP2/aug-cc-pVTZ level of calculations

electrostatic potential for the H_2O and $\text{C}_6\text{H}_5\text{F}$ molecules calculated separately at 0.001 au electron density molecular surfaces. The distributions of the EP for both species are in line with the observations presented earlier here and concerning the electron charge distribution.

There is another interesting observation for the $\text{C}_6\text{H}_5\text{F}-\text{H}_2\text{O}$ complex (Fig. 15.1). For all O–H, C–H and C–C covalent bonds one can see the continuous regions of the negative laplacian surrounding the corresponding bond critical points; with one exception of the C–F bond where there is the region of positive laplacian between two corresponding nuclei; even the positive $\nabla^2\rho_{\text{BCP}}$ value is detected for the C–F bond critical point. This may indicate that the C–F bond is mostly ionic in nature and that there is the polarization of C–F bond with the concentration of the electron charge density at the fluorine centre. The polarization of C–F bond (the percentage of the electron charge density calculated at F-centre) evaluated within NBO approach is equal to 72.8 %. The QTAIM integrated charges of carbon and fluorine in this bond are equal to +0.472 au and –0.714 au, respectively.

The aim of this chapter is to show, on the basis of several examples, how the location of the bond path may be useful to characterize, define and/or verify the specific, considered interaction. Mainly the QTAIM approach [4–7] is considered here; however sometimes there are also references to other methods and concepts as for example; the Natural Bond Orbitals (NBO) method [21, 22] or the σ -hole concept [25–27]. This is worth to note that the results presented hereafter are mainly based on the MP2/aug-cc-pVTZ level of calculations; those results are taken from earlier studies or the calculations were carried out especially for the purposes of this chapter. Consequently the QTAIM calculations were performed on the MP2/aug-cc-pVTZ wave functions. The binding energies (E_{bin} 's) were calculated as differences between the energy of the complex and the sum of energies of monomers optimized separately and they were corrected for the basis set superposition error (BSSE) by the counterpoise method [28]. Since the NBO method is based on the Hartree-Fock method thus the corresponding NBO results, i.e. orbital-orbital interactions or atomic charges, if presented, are based on the HF/aug-cc-pVTZ//MP2/aug-cc-pVTZ level. Hence there is rather not indicated the level of calculations for the next systems discussed hereafter; unless the results presented were obtained within other levels of calculations.

15.2 The Case of Halogen Bond

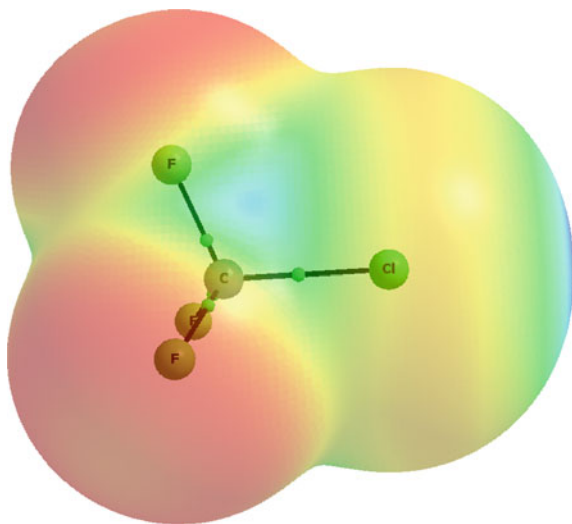
The halogen bond interaction is one of the most interesting phenomena analyzed during the last few decades. It was found that the halogen atoms (designated later here as X), especially if connected with carbon (in C–X bonds), often play a role of electron acceptors (Lewis acid centers) interacting with the Lewis bases, i.e. with the electron rich species. This seems to be strange since halogen atoms are commonly known as the electronegative centers. There were various trials to explain

this phenomenon. One can mention concepts of the anisotropy of the van der Waals radii of halogens [29] or of the anisotropy of the electron charge distribution around the halogen atoms [30]. According to the latter concept the electron density distribution of the halogen atom is characterized approximately by the ellipsoid shape, the major axis of the ellipsoid is perpendicular to the C–X bond while the minor axis belongs to the C–X bond line. This is why the X-centre interacts with nucleophiles in the direction being the elongation of the C–X bond while electrophiles interact with halogens in the direction perpendicular to the C–X bond or nearly so. The latter direction is rich in electron density while the elongation of the C–X bond is characterized by the deficiency of the electron density. These explanations are in line with experimental findings; especially those based on the crystal structures determinations [31].

It seems that more recent σ -hole concept [25–27], being in line with explanations based on the anisotropy of the electron charge distribution, explains additionally the source of such anisotropy as well as this concept explains sufficiently the phenomena of numerous other interactions, not only of the halogen bond. The σ -hole concept of Clark, Murray and Politzer is based on simple models of electron configurations and hybridizations [32, 33]. For example, in a case of the CF_3X molecules ($\text{X} = \text{Cl}, \text{Br}$ and I) the approximate $s^2p_x^2p_y^2p_z^1$ configuration is observed for X-atoms, where the Z-axis is along the C–X bond. The unshared electron pairs are responsible for the existence of the negative electrostatic potential (EP) around the X-atom in the direction approximately perpendicular to the C–X bond while the single p_z^1 electron is involved in the C–X σ -bond what results in the loss of the electron density on the outermost portion of the halogen surface, in the elongation of the C–X bond. This is why this region (σ -hole) is characterized by the positive EP.

Figure 15.3 presents the map of EP for the CF_3Cl molecule. One can see here regions of the negative EP attributed to the fluorine atoms (red color in Fig. 15.3) as

Fig. 15.3 The map of the electrostatic potential calculated at the 0.001 au molecular electron density surface for CF_3Cl molecule; red and blue colors correspond to negative and positive EP, respectively



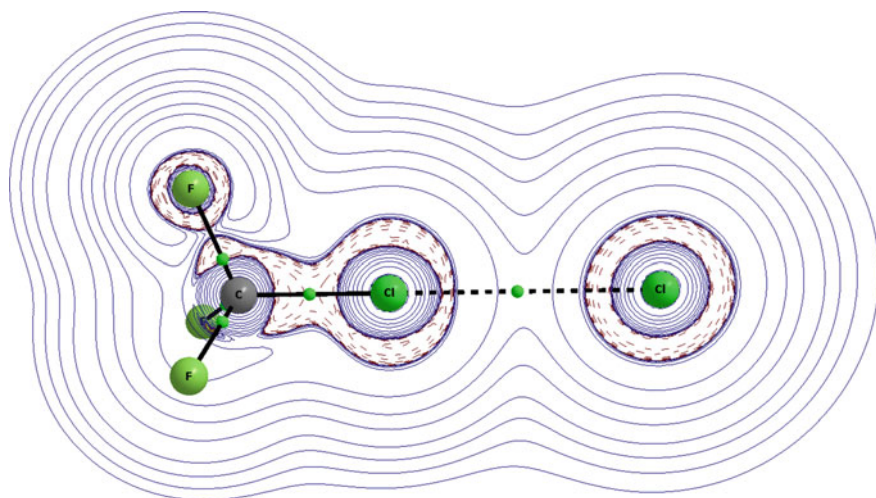


Fig. 15.4 The molecular graph of the $\text{CF}_3\text{Cl}\dots\text{Cl}^-$ complex, solid and broken lines correspond to bond paths, big circles to attractors and small green circles to BCPs, the isolines of laplacian of electron density are also presented; the laplacian isodensity lines in the plane containing CFCl atoms of the CF_3Cl molecule and Cl^- anion

well as less negative region of EP around the Cl-atom (orange color in Fig. 15.3) being the consequence of the existence of unshared electron pairs. The positive region of EP in the elongation of the C–Cl bond is observed (blue color). This is interesting that there are also regions of the positive EP in the elongation of F–C and Cl–C bonds, attributed to the carbon which may also act as the Lewis acid sites. Such regions are also nicely explained in terms of the σ -hole concept.

In general the σ -hole concept explains satisfactory why the halogen centers possess the dual character; they may act as the Lewis acid and as the Lewis base. In the former case the corresponding interaction is named as the halogen bond and it is usually linear or nearly so due to the location of the restricted area of the positive EP in the elongation of C–X bond.

Different complexes of the CF_3Cl moiety were analyzed recently and the dual character of the chlorine centre was also investigated. Figure 15.4 shows the molecular graph of the $\text{CF}_3\text{Cl}\dots\text{Cl}^-$ complex where the chlorine anion is directed to the positive EP region of the Cl-centre in the CF_3Cl molecule. The linear C–Cl...Cl⁻ link is observed what is in line with the σ -hole concept and the earlier explanations presented here. The bond path linking chlorines with the corresponding BCP is observed. The isolines of laplacian of the electron density are also presented showing the anisotropic concentration of the electron density around the (C)Cl chlorine centre while the unperturbed spherical concentration of the electron density is observed for chlorine anion. One can also see the regions corresponding to other σ -holes, attributed to the carbon, i.e. to the elongations of the F–C and Cl–C bonds.

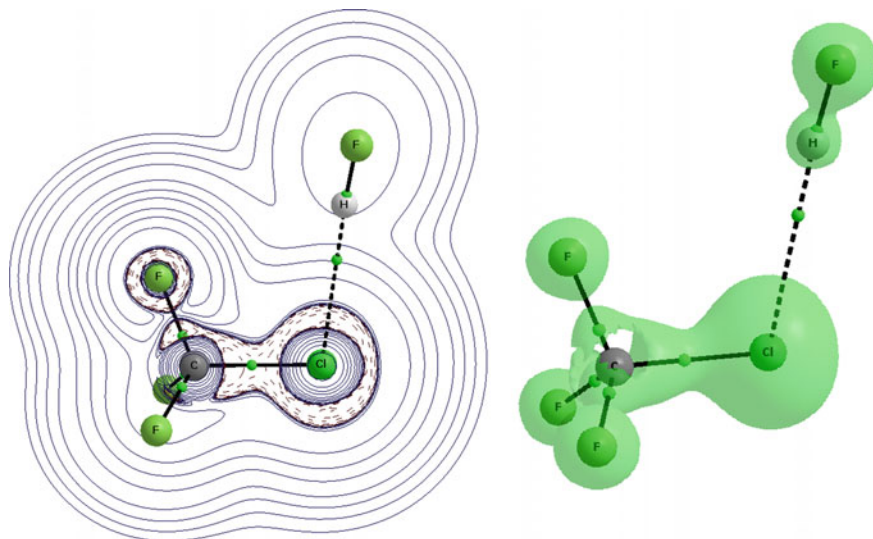


Fig. 15.5 The molecular graph of the $\text{CF}_3\text{Cl}\cdots\text{HF}$ complex, *solid and broken lines* correspond to bond paths, *big circles* to attractors and *small green circles* to BCPs, the isolines of laplacian of electron density are also presented (the laplacian isodensity lines in the plane containing CFCI atoms of the CF_3Cl molecule); the reactive surface ($\nabla^2\rho(r) = 0$ isosurface) is presented in the *right* part of the figure

Figure 15.5 presents the molecular graph of the $\text{CF}_3\text{Cl}\cdots\text{HF}$ complex where the positively charged and characterized by the positive EP hydrogen atom of HF is directed to the “belt” of the negative EP around chlorine atom; this “belt” is visible from the map of the laplacian isolines performed in the plane containing CFCI atoms of the CF_3Cl molecule. In other words the Cl-centre plays the role of the Lewis base in this complex. There are other interesting findings here. The HF molecule is situated outside of the mentioned above CFCI plane. This is why the 2D map with laplacian isolines do not show the negative regions of the laplacian for the HF molecule since the latter species is situated outside the molecular graph projection. Probably such a configuration of the complex is observed because of the repulsion between the fluorine atoms of CF_3Cl and the fluorine atom of HF molecule. Figure 15.5 presents also the reactive surface ($\nabla^2\rho(r) = 0$ isosurface); this picture may be read in the following way, the areas closed by those lines are characterized by the negative values of the laplacian of electron density thus they correspond to the concentration of the electron charge.

It was explained in terms of the σ -hole concept that the fluorine usually does not possess the regions of positive EP since the high electronegativity of F-centre as well as the sp -hybridization cause that the σ -hole usually occurring in the outermost part of C–F bond is neutralized [32, 33]. Additionally the Lewis acid strength for halogen atoms increases in the following order, $\text{F} < \text{Cl} < \text{Br} < \text{I}$ what is connected with the increase of the polarization of the corresponding C–X bonds (% of the

electron density calculated at the carbon atom increases). For example, the HCCX halogen derivatives of acetylene were analyzed and it was found that the maximum EP at X center is equal to +2.3, +20.4 and +27.0 kcal/mol for X = F, Cl and Br, respectively (B3PW92/6-31G(d,p) level of calculations) [34]. There are similar findings of an increase of the positive EP for heavier X-center for other species, like for example H_3CX , F_3CX or C_6H_5X [34].

Figure 15.6 presents the molecular graphs of HCCCl and HCCBr molecules with the isolines of the laplacian of electron density. One can see the anisotropic

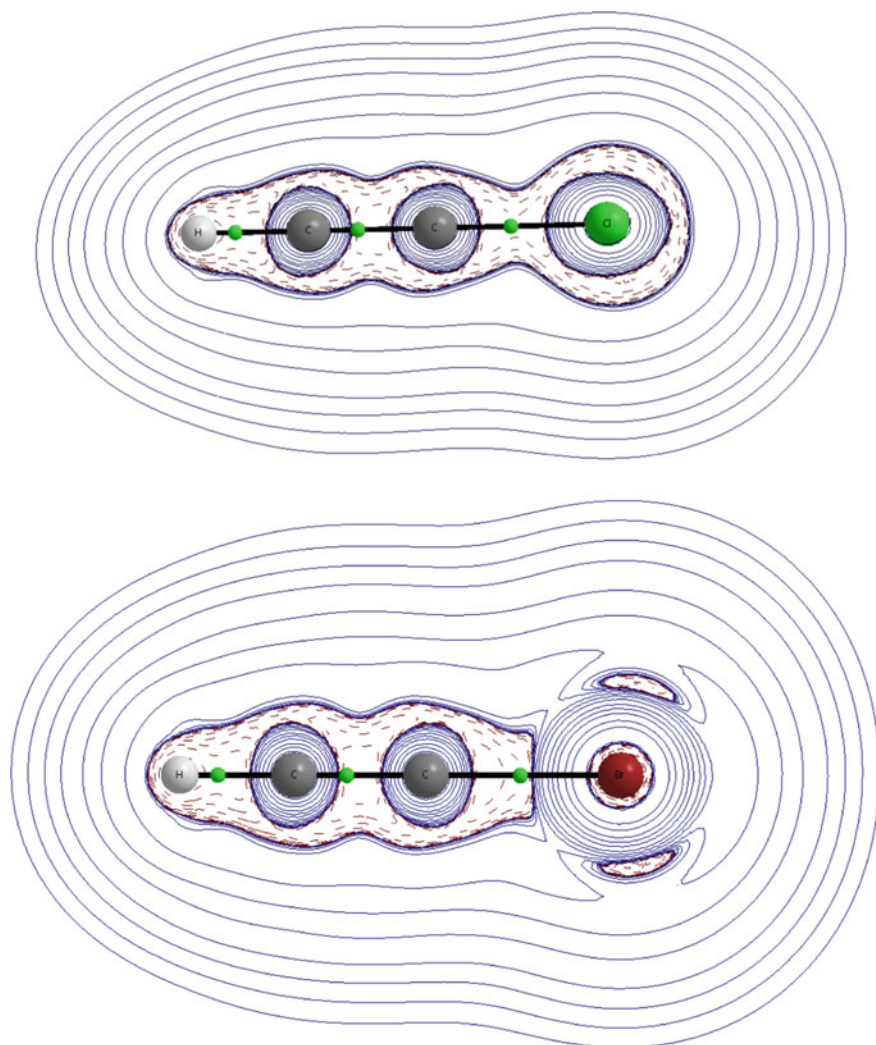


Fig. 15.6 The molecular graphs of the HCCCl (*up*) and HCCBr (*down*) molecule, *solid and broken lines* correspond to bond paths, *big circles* to attractors and *small green circles* to BCPs, the isolines of Laplacian of electron density are also presented

concentration of the electron charge density around chlorine for the HCCCl molecule, with its “thin” concentration in the elongation of C–Cl bond and wider concentration in the direction perpendicular to this bond; the latter corresponds to the lone unshared electron pairs. In a case of HCCBr molecule there is no the concentration of the electron density in the C–Br bond line! This is why the more positive EP is observed for the bromine derivative of acetylene than for the chlorine derivative.

In a case of halogen bond the monovalent halogen center is usually analyzed while there are only few studies on that kind of interaction with multivalent halogen atoms. One can mention the study on Ph_2IX complexes with XF_3 ($\text{X} = \text{Cl}, \text{Br}, \text{I}$) [35] or the study where the complexes of XF_3 are compared with their XF analogues ($\text{X} = \text{Br}$ or Cl) [36]. Very recently the complexes of BrF_3 and BrF_5 with N_2 and HCN species acting as Lewis bases were analyzed [37]. The situation for the bromine center in BrF_3 and BrF_5 is different than in a case of monovalent halogens. First of all, the whole hemispheres of multivalent bromines are characterized by the positive electrostatic potential. It means that bromine should play the role of the Lewis acid only and not of the Lewis base. For the BrF_3 moiety characterized by the C_{2v} symmetry the maximum positive EP occurs for the Br center in the elongation of the F–Br equatorial bond (Fig. 15.7). Slightly different situation is observed for the C_{4v} symmetry BrF_5 molecule where four equivalent maxima of EP are observed at Br-center, around the fourfold symmetry axis of the molecule (Fig. 15.7).

The distribution of the electrostatic potential for two bromine species has further consequences; particularly the location of the maxima of EP shows the most probable nucleophilic attacks here. This is why the liner halogen bonds are formed with BrF_3 while bent ones for the BrF_5 molecule. Figure 15.8 shows the molecular graph of the $\text{BrF}_3\text{--NCH}$ complex with the reactive surface corresponding to the laplacian of the electron density equal to zero. The straight bond path connecting the bromine atom with the nitrogen Lewis base center of HCN molecule is observed

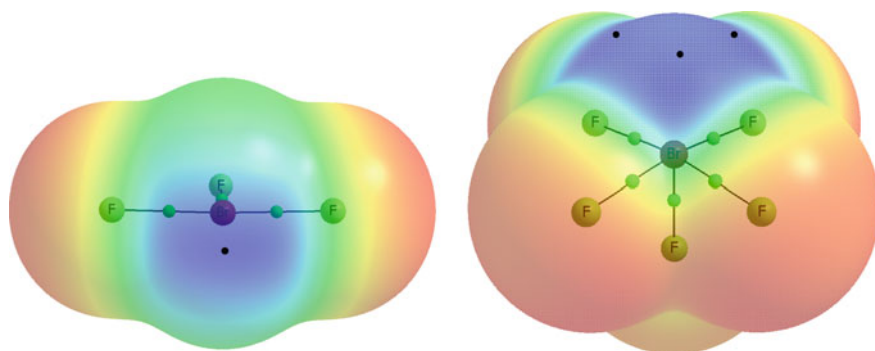


Fig. 15.7 The map of the electrostatic potential calculated at the 0.001 au molecular electron density surfaces for BrF_3 (left) and BrF_5 (right) molecules; red and blue colors correspond to negative and positive EP, respectively. Black points designate the maxima of EP, one local maximum for BrF_3 and 4 local maxima for BrF_5 (only 3 maxima are visible in the figure)

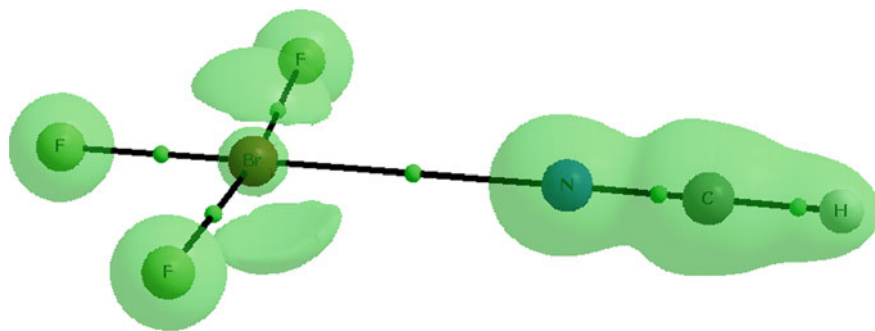


Fig. 15.8 The molecular graph of the $\text{BrF}_3 \dots \text{NCH}$ complex, *solid lines* correspond to bond paths, *big circles* to attractors and *small green circles* to BCPs, the reactive surface ($\nabla^2 \rho(r) = 0$ isosurface) is also presented

here; one can say that the bond path crosses the maximum of EP of the bromine atom. It is worth to mention that the BrF_3 molecule displays a T-shaped molecular structure and a trigonal bipyramidal electronic structure. Two lone unshared electron pairs are located symmetrically to the mirror plane containing the BrF_3 molecule. This picture is in line with the chemical intuition and with the NBO results. The latter approach confirms the existence of two unshared electron pairs for bromine which is also characterized by 14 core orbitals (28 electrons); 3 remaining bromine electrons are involved in Br–F bonds. The electron configurations for bromine in the isolated BrF_3 molecule and in the $\text{BrF}_3\text{--NCH}$ complex are practically the same according to the NBO approach, only there are negligible differences in the occupancies of orbitals.

As it was pointed out earlier here, the different situation is observed for the BrF_5 moiety. For example, for the $\text{BrF}_5\text{--N}_2$ complex the Lewis base N-center of molecular nitrogen is directed to one of the BrF_5 EP maxima. Figure 15.9 presents the corresponding molecular graph of that complex with the Br...N bond path crossing the local EP maximum and partly avoiding the unshared electron pair of bromine. The bromine electron configuration derived from NBO for the BrF_5 moiety is as follows, 28 core electrons, 1 lone electron pair and 5 remaining electrons are involved in 5 F–Br σ -bonds. This means that for the square pyramidal BrF_5 molecular structure observed here there are 12 electrons in the valence shell. The latter is often named as hypervalency in the literature [38] since the octet rule is not obeyed here. The electron configuration of bromine in the $\text{BrF}_5\text{--N}_2$ complex is practically the same as in the BrF_5 moiety not involved in any interaction, similarly as it was observed in a case of the BrF_3 species and its complexes.

Very interesting situation is observed for the $\text{BrF}_5\text{--Cl}^-$ complex (Fig. 15.10). This complex is characterized by a very strong interaction since the binding energy amounts here -37.8 kcal/mol while for the complexes of BrF_5 with HCN and N_2 the binding energy is equal to -5.1 and -1.7 kcal/mol, respectively [37]. The laplacian of the electron density, $\nabla^2 \rho_{\text{BCP}}$, at Br–Cl BCP is positive; however the

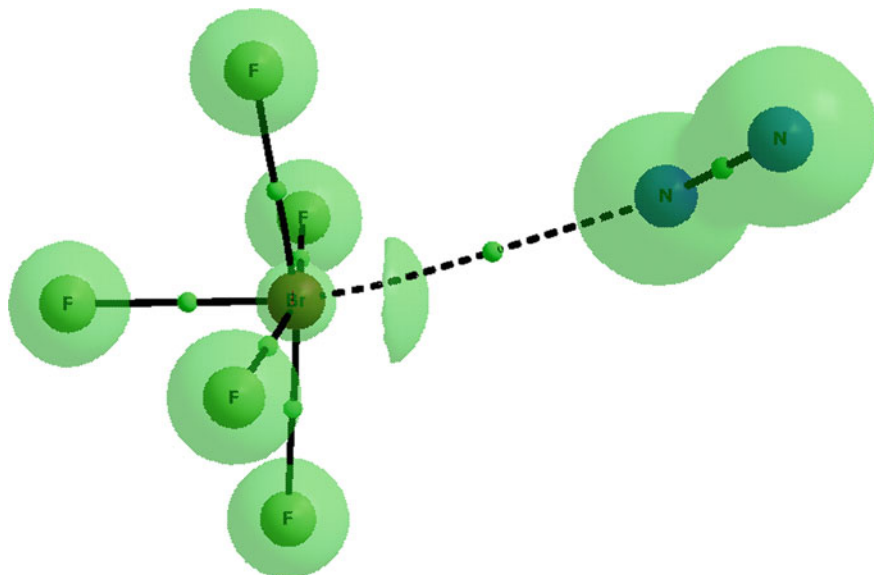


Fig. 15.9 The molecular graph of the $\text{BrF}_5 \dots \text{N}_2$ complex, solid and broken lines correspond to bond paths, big circles to attractors and small green circles to BCPs, the reactive surface ($\nabla^2 \rho(r) = 0$ isosurface) is presented

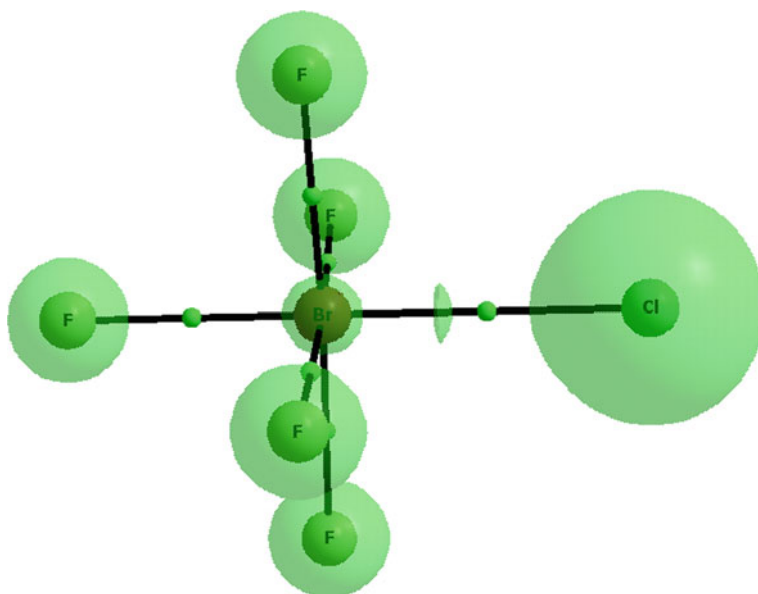


Fig. 15.10 The molecular graph of the $\text{BrF}_5 \dots \text{Cl}^-$ complex, solid lines correspond to bond paths, big circles to attractors and small green circles to BCPs, the reactive surface ($\nabla^2 \rho(r) = 0$ isosurface) is presented

total electron energy density at BCP, H_{BCP} , is negative what means that the interaction is at least partly covalent in nature. The similar situation is observed for all five Br–F connections—the positive $\nabla^2\rho_{\text{BCP}}$ values and the negative H_{BCP} ones. It seems that the strong interaction of the BrF_5 species with the Cl^- anion extorts the greater electron density changes in the complex, particularly in the BF_5 moiety. One lone electron pair of bromine is observed in the complex within the NBO approach, similarly as in the isolated BrF_5 species; however the lone pairs in the complex possesses s-character in 99.2 %. This is confirmed by the QTAIM approach since Fig. 15.10 shows the spherical electron charge density concentration around bromine center. The change of the location of the bromine electron lone pair results in the existence of the straight bond path linking the Br and Cl centers in contrary to the interactions of the BrF_5 molecule with weak Lewis bases (see Fig. 15.9).

The positive values of the laplacian of electron density at all BCPs corresponding to the Br–F and Br–Cl links in the $\text{BrF}_5\text{--Cl}^-$ complex may indicate the ionic character of interactions since it was pointed out that such values are typical for the closed-shell interactions [5–7]. This means that in the latter complex all bonds (links) are strongly polarized; the NBO approach shows that the polarization for the Br–F bonds is equal to 23.2 % and it amounts 33.6 % for the Br–Cl bond (% of the electron density at the Br center). The Br atomic charge calculated within NBO and QTAIM approaches is equal to +2.25 au and +2.32 au, respectively. Figure 15.10 clearly shows the concentration of the electron density at attractors and not at interatomic regions; the similar situation is observed for all BrF_3 and BrF_5 complexes.

There is another interesting finding for the $\text{BrF}_5\text{--Cl}^-$ complex; the NBO approach shows that there are tri-center four-electron (3c-4e) linear bonds here. They concern the following linear triads in the BF_5Cl^- moiety; two F–Br–F triads and one F–Br–Cl triad. Such 3c-4e bonds were analyzed earlier in literature; for example Weinhold and Landis analyzed numerous hypervalent centers [21] and they extended the 3c-4e concept of Pimentel and Rundle [39, 40].

15.3 Lewis Acid–Lewis Base Interactions

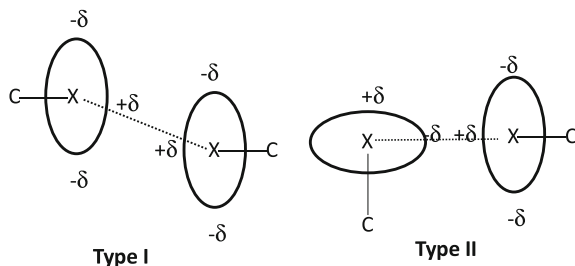
The σ -hole concept mentioned in the previous section which explains the mechanisms of formation of the halogen bond is also useful to analyze other Lewis acid–Lewis base interactions [26, 27, 41]. One can mention tetrel [42–45], pnictogen [46–50] and chalcogen bonds [51–53] where the elements of Groups IV, V and VI, respectively, play the role of the Lewis acid centers. The mechanism of the formation of those bonds is practically the same as that one of the halogen bond; a region of positive electrostatic potential (designated as σ -hole) on the extension of the bond to the atom being the acidic center is an effect of the electron charge shift from the outermost part of this center. These centers possessing σ -holes are usually characterized by the unshared electron pairs thus they may act simultaneously as the Lewis acids and the Lewis bases. The situation is slightly different for the tetrel

atoms which are characterized by the sp^3 hybridization and do not possess free electron pairs. That rather excludes their potential basicity. Similarly, as it was mentioned earlier here in the previous section, multivalent halogens may be characterized only by acidity properties but in that case the halogen centers possess lone electron pairs.

The dual character mentioned few times here results in important consequences that the same elements may be involved in the stabilization interaction; i.e. that halogen-halogen, chalcogen-chalcogen, etc. interactions are possible. That is not all since at least two different in nature connections may be mentioned here. For example, the X halogen center may interact by its Lewis acid region (σ -hole) with the Lewis base region (unshared electron pairs) of the X-center of another molecule or both halogen centers being in the X...X contact may play the dual role, both may act simultaneously as Lewis acid and Lewis base. Both cases of C-X...X-C halogen-halogen interactions were described in early study of Fourmigue and Batali [31] and they are presented in Scheme 15.1. In a case of the interaction designated as I, the halogen atoms act simultaneously as Lewis acid and Lewis base centers. Such centers may be sometimes related by symmetry, for example, in the crystal structures such halogen atoms may belong to symmetry equivalent molecules. In a case of the type II interaction one of halogens acts as the Lewis base and the second one as the Lewis acid in spite of the fact that potentially both possess dual character.

Similar types of interactions are observed for other σ -hole bonds. For example, P...P pnictogen interactions were analyzed in numerous complexes [54, 55]. For the FH_2P-PH_3 complex the σ -hole of the FH_2P moiety situated in the elongation of the F-P bond interacts with the lone electron pair of the PH_3 species; this corresponds to the $n(P) \rightarrow \sigma_{PF}^*$ orbital-orbital interaction within the NBO approach; in other words the FH_2P species reveals here the Lewis acid properties while the PH_3 molecule the Lewis base properties. One can expect the reverse situation, where the FH_2P and PH_3 molecules act as the Lewis base and the Lewis acid, respectively with the corresponding $n(P) \rightarrow \sigma_{PH}^*$ orbital-orbital interaction. However the P center possesses the stronger Lewis acid properties in the FH_2P molecule than in the PH_3 species since the $n(P) \rightarrow \sigma_{PF}^*$ and $n(P) \rightarrow \sigma_{PH}^*$ energies of interactions in the FH_2P-PH_3 complex are equal to 8.9 and 2.7 kcal/mol, respectively. Besides the FH_2P σ -hole (elongation of the F-P bond) is characterized by the more positive EP than the PH_3 σ -hole (elongation of H-P bond) [54, 55]. Figure 15.11 presents the molecular graph of this complex with the reactive surface ($\nabla\rho^2(r) = 0$ isosurface). One can see that two molecules of the complex are oriented in such a way that lone electron pair (the electron charge density concentration) is directed to the σ -hole region.

On the other hand the $(FH_2P)_2$ dimer represents the situation of the equivalent phosphorus atoms, both acting simultaneously as the Lewis acid and as the Lewis base what corresponds to two equivalent $n(P) \rightarrow \sigma_{PF}^*$ orbital-orbital interactions (each characterized by the energy of 29.5 kcal/mol). Figure 15.12 presents the molecular graph of this complex. The authors described also P...P interactions in other complexes [55]; for example for the $FH_2P...P(OH)H_2$ complex there are two important orbital-orbital interactions: $n(P) \rightarrow \sigma_{PF}^*$ and $n(P) \rightarrow \sigma_{P-OH}^*$; however the



Scheme 15.1 Two types of C-X...X-C halogen-halogen interactions; this figure is based on the scheme presented in Ref. [31]; the ellipsoids represent here the non-spherical distribution of the electron charge density

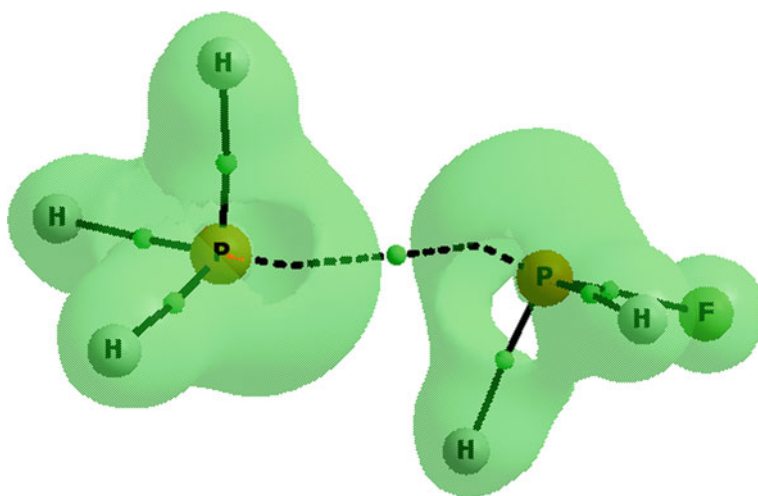


Fig. 15.11 The molecular graph of the $\text{FH}_2\text{P}\dots\text{PH}_3$ complex, solid and broken lines correspond to bond paths, big circles to attractors and small green circles to BCPs, the reactive surface ($\nabla^2\rho(r) = 0$ isosurface) is presented

former one is stronger than the latter one what means that the P center is more acidic in the PFH_2 moiety than in the P(OH)H_2 one.

The results presented here show that for the pnictogen-pnictogen contacts there is no clear border between type I and II configurations as it was found for halogen-halogen interactions (Scheme 15.1). It seems that an orientation corresponding exactly to the II type orientation found for the X...X contacts cannot be formed for the P...P interaction. It probably comes from the existence of three σ -holes for trivalent P centers while in a case of monovalent halogens there is only one σ -hole characterized by the acidic properties.

This is worth mentioning that in both cases of pnictogen-pnictogen interaction there is only one bond path linking the corresponding attractors (see Figs. 15.11 and

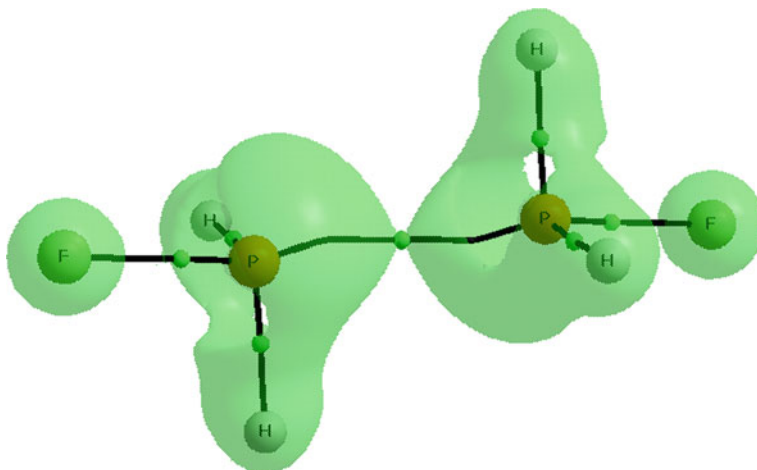


Fig. 15.12 The molecular graph of the $(\text{FH}_2\text{P})_2$ dimer, solid lines correspond to bond paths, big circles to attractors and small green circles to BCPs, the reactive surface ($\nabla^2\rho(r) = 0$ isosurface) is presented

15.12). It seems that this situation may be generalized for interactions between the same kind centers, i.e. for the chalcogen-chalcogen or halogen-halogen (dihalogen) bonds. The results presented here show that the molecular graph does not reflect more complex situation, i.e. differences between those two cases. Such difference is reflected within the NBO analysis. However it seems that the QTAIM approach provides the tools to describe that more complex situation. The σ -hole bonds, i.e. halogen and pnictogen bonds, were analyzed recently by Eskandari and co-workers [56, 57]. They have shown that the P...P, P...N and N...N interactions [56], as well as halogen bonds [57], may be categorized as lump-hole interactions where the hole is a region of charge depletion and the excess of the kinetic energy while the lump is a region of the electron charge concentration and an excess of the potential energy. In such a way the authors have found one hole-lump interaction for the $\text{FH}_2\text{P}\dots\text{PH}_3$ complex and two equivalent hole-lump interactions for the $(\text{FH}_2\text{P})_2$ dimer [56] what corresponds to one dominant or two equivalent orbital-orbital interactions, respectively.

There is a very interesting case of tetrel bonds where the Group IV element plays the role of the Lewis acid center. The tetrel bonds were analyzed recently as a kind of σ -hole bonds [42–45]; however such interactions were known early on as the preliminary stages of the $\text{S}_{\text{N}}2$ reactions [58, 59]. For example, the methane species may be treated as a very weak acid interacting through the H-atom with the Lewis base centre; H-atoms of methane are characterized by the positive EP (+0.015 au at 0.001 au molecular surface) while C-centre by slightly negative EP (−0.004 au). Figure 15.13 presents the molecular graph of the $\text{CH}_4\dots\text{NCH}$ complex corresponding to this situation where the H...N bond path corresponding to the C–H...N hydrogen bond is observed. However for the CH_3Cl derivative there is the region of

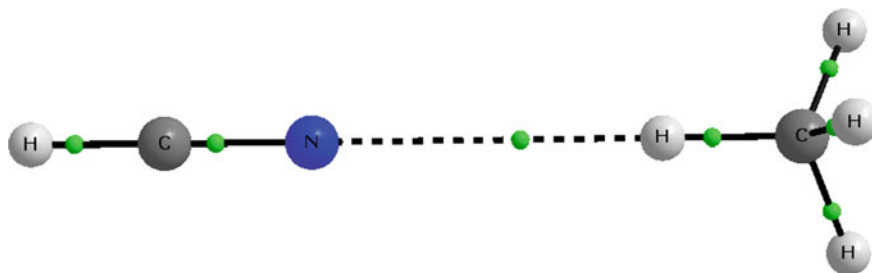


Fig. 15.13 The molecular graph of the $\text{CH}_4 \dots \text{NCH}$ complex, solid and broken lines correspond to bond paths, big circles to attractors and small green circles to BCPs

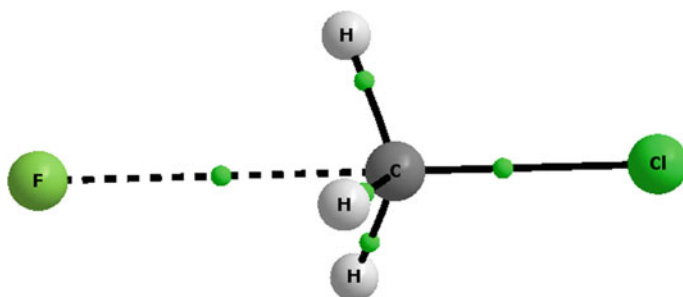


Fig. 15.14 The molecular graph of the $\text{CH}_3\text{Cl} \dots \text{F}^-$ complex, solid and broken lines correspond to bond paths, big circles to attractors and small green circles to BCPs

the positive EP (+0.032 au) at the C-center in the elongation of the Cl–C bond, this is the σ -hole which plays the role of the Lewis acid in interactions with electron rich species. Figure 15.14 presents the molecular graph of such situation; this is the $\text{CH}_3\text{Cl} \dots \text{F}^-$ complex which may be treated as the preliminary stage of the $\text{CH}_3\text{Cl} + \text{F}^- \rightarrow \text{CH}_3\text{F} + \text{Cl}^-$ reaction governed by the $\text{S}_{\text{N}}2$ mechanism.

Let us look at few experimental studies; the addition reactions of methyl(halogeno)tin and methyl(halogeno)germanium compounds to electron-rich platinum(II) complexes were analyzed [60]. These studies clearly point to an $\text{S}_{\text{N}}2$ mechanism for the interactions considered. It was found that methylhalotin species, Me_3SnX ($\text{X} = \text{Cl}, \text{Br}, \text{I}$), react by an $\text{S}_{\text{N}}2$ pathway. The germanium analogues were also analyzed. For example, the variable temperature NMR spectral series for Me_3GeCl shows the rate decrease of the $\text{S}_{\text{N}}2$ reaction in comparison with the analogues tin species and the authors explain that this is partly due to a size effect. This is in line with the σ -hole concept as well as with the topology of complexes linked through the tetrel bonds. It was found that for the tetrel atoms as well as for the other Groups centers the positive EP increases in the Group if the atomic number of the center

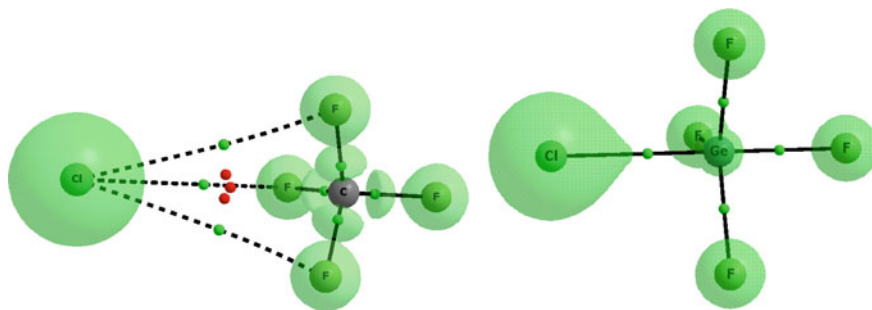


Fig. 15.15 The molecular graphs of the $\text{CF}_4 \dots \text{Cl}^-$ (left) and $\text{GeF}_4 \dots \text{Cl}^-$ (right) complexes, solid and broken lines correspond to bond paths, big circles to attractors and small green circles to BCPs (red ones—RCPs), the reactive surface ($\nabla^2 \rho(r) = 0$ isosurface) is presented

increases. For example, for the CH_3F , SiH_3F and GeH_3F series the maximum EP at tetrel atom, in the elongation of fluorine—tetrel center bond, is equal to +0.033, +0.062 and +0.068 au, respectively [45]. Hence the $\text{S}_{\text{N}}2$ reaction mentioned earlier here and preceded by the tetrel bond is more probable for the tin species than for the germanium one. There is also the influence of the size effect. It was claimed that the methyl groups are more important to block the tetrel center if the latter one is characterized by the smaller size [60]. Figure 15.15 presents a similar situation of the influence of fluorine substituents for the $\text{CF}_4 \dots \text{Cl}^-$ and $\text{GeF}_4 \dots \text{Cl}^-$ complexes. For the carbon species the Cl-attractor is linked by the bond paths with the fluorine attractors of CF_4 species; in a case of the germanium complex there is the Cl...Ge intermolecular bond path what means that for the germanium complex the $\text{S}_{\text{N}}2$ reaction is more probable.

The similar situation occurs for ammonium cation, NH_4^+ and its analogues, PH_4^+ and AsH_4^+ [50]. However for those cations the whole molecular surfaces are characterized by the positive EP thus they do not act as Lewis bases. For the NH_4^+ ion the maximum EP amounts +0.286 au and it is attributed to the H-atoms while the minimum to the nitrogen center, +0.263 au. This is why for the complexes with hydrogen cyanide (through N-center) as well as with the other Lewis base centers [61], firstly the H-atoms of ammonia cation are involved in interactions and next the links are formed with the nitrogen center of NH_4^+ . For example, for the $\text{NH}_4^+ \dots (\text{NCH})_n$ clusters, the N—H...N hydrogen bonds are formed for $n \leq 4$ and next, when all H-atoms are saturated by the hydrogen bonds the N...N links are created. The latter ones correspond to the σ -hole bonds. Figure 15.16 presents the $\text{NH}_4^+ \dots (\text{NCH})_5$ cluster where one can observe four N—H...N hydrogen bonds and one N...N interaction; for all interactions the corresponding bond paths exist.

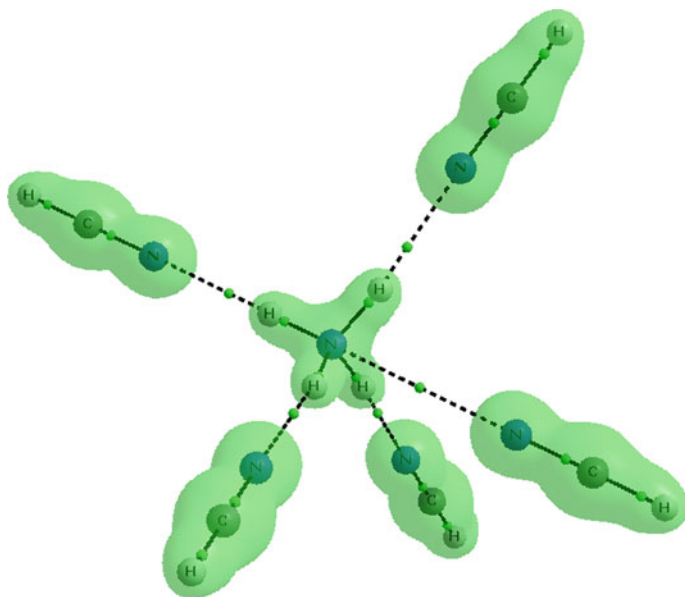


Fig. 15.16 The molecular graph of the $\text{NH}_4^+ \dots (\text{NCH})_5$ complex, solid and broken lines correspond to bond paths, big circles to attractors and small green circles to BCPs, the reactive surface ($\nabla^2 \rho(r) = 0$ isosurface) is presented

15.4 The Case of Hydrogen Bond

It was discussed that the A–H...B hydrogen bond may be classified as a case of the σ -hole bond [33, 62]. For the A–H bond, similarly as for other covalent bonds where the σ -hole is observed, there is the electron charge density shift from H-atom to the A-center. However the mechanism of the σ -hole formation is different for the H-atom than for the other heavier atoms [33, 63]. In a case of pnictogen, chalcogen and halogen atoms p-electron is involved in the σ -bond what results in the depletion of the electron density in outermost part of the center considered and a small area of the increased electrostatic potential, often up to the positive value [26, 27]. Such a region of the positive EP, if exists, is surrounded by areas of the negative EP. There are exceptions, as for example for the tetrel atoms or multivalent halogens described earlier here, where the whole centers are characterized by the positive EP. For the H-atom the whole hemisphere is characterized by the positive EP and there is the single s-type electron involved in the A–H bond, the polarization of this bond results in the additional increase of the EP at the hydrogen atom.

This is interesting that for the protic H-atom in A–H bond there is the detectable shift of its electron density maximum towards the A-center. This effect is not observed for halogen, chalcogen or any others heavier atoms. That may be calculated within the QTAIM approach since the positions of attractors correspond to the

Table 15.1 A–H bonds of selected molecules and cations (A designates heavy atom); r—the distance between A and H attractors; R—the distance between A and H nuclei; $\Delta R\%$ is equal to $[(R-r)/R]*100\%$; ϵ —electronegativity of the A heavy atom in the Pauling scale; distances in Å

Species	r	R	R-r	$\Delta R\%$	ϵ
H ₂ O	0.934	0.961	0.027	2.8	3.44
H ₂ S	1.321	1.336	0.015	1.1	2.58
HF	0.888	0.922	0.034	3.7	3.98
HCl	1.256	1.274	0.018	1.4	3.16
NH ₃	0.990	1.012	0.022	2.2	3.04
PH ₃	1.401	1.413	0.012	0.9	2.19
CH ₄	1.070	1.086	0.016	1.5	2.55
SiH ₄	1.467	1.477	0.010	0.7	1.9
H ₃ O ⁺	0.947	0.980	0.032	3.3	3.44
H ₃ S ⁺	1.334	1.351	0.017	1.3	2.58
NH ₄ ⁺	0.997	1.022	0.025	2.5	3.04
PH ₄ ⁺	1.377	1.392	0.015	1.1	2.19

positions of the local maxima of the electron density; they may be attributed to the positions of atoms. However if one assumes that the atoms' positions correspond to nuclei thus this is not the same. Table 15.1 presents MP2/aug-cc-pVTZ results for the selected molecules and cations containing hydrogen atoms. One can see that for all systems considered, for A–H bonds (A = C, N, O, F, Si, P, S, Cl) the distance between the attractors (r) is shorter than the distance between corresponding nuclei (R). Since the positions of attractors and nuclei for heavy (non-hydrogen) atoms are practically the same thus the R-r difference is exactly the shift of the electron density maximum of H-atom from the corresponding nucleus to the A-atom. The R-r difference may be also read as the distance between the nucleus of H-atom and its attractor. The range of those differences is between 0.01 Å and 0.03 Å (Table 15.1), the greatest values are observed for the HF molecule and H₃O⁺ cation, 0.034 Å and 0.032 Å, respectively. The $\Delta R\%$ values relate those differences to the R distances (between nuclei) since $\Delta R\% = [(R-r)/R]100\%$.

It seems that the greatest R-r differences occur for the more electronegative A-atoms; this seems to be natural since the more electronegative center withdraws easier the electron density. Figure 15.17 presents the dependence between the electron charge density shift (expressed as the $\Delta R\%$ value) and the electronegativity of the non-hydrogen A-atom. The results for molecules and cations are included. One can see correlations within the periods, i.e. if the A-atom belongs to the same period and only the neutral species are considered. In a case of cations there is the greater electron charge density shift if one compares it with the neutral molecules. For example, the R-r value for the NH₃ molecule is equal to 0.022 Å while for the NH₄⁺ cation it amounts 0.025 Å; for H₂O and H₃O⁺ species it is equal to 0.027 Å and 0.032 Å, respectively.

Figure 15.18 presents the O–H bond length histograms based on results from Cambridge Structural Database (CSD) [64]; X-ray and neutron diffraction results are presented separately. The CSD searches were performed for all derivatives of benzene containing OH group, this means that not only phenol is considered but

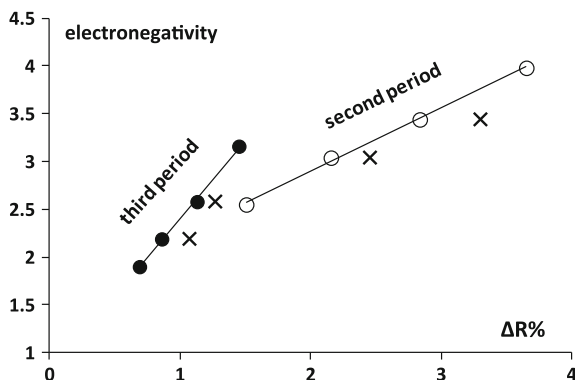


Fig. 15.17 The relationship between $\Delta R\%$ value (for species collected in Table 15.1) and the electronegativity of the A non-hydrogen atom, circles correspond to neutral molecules while crosses to cations

also species where other H-atoms of benzene are substituted. Of course such substituents may influence on the electron density distribution including the hydroxyl group. However the aim of those searches was only to evaluate briefly the differences between the neutron and X-ray diffraction results if the covalent bond containing H-atom is considered. In a case of the neutron diffraction the positions of atoms in the crystal correspond to the positions of nuclei while for the X-ray measurements these are the positions of the local maxima of electron density; in other words in the latter case we have the positions of attractors. This is why the QTAIM approach may be applied for the crystal structures' results [1–3] and for numerous crystal structures the topological analysis based on the experimental electron density is performed. The mentioned above searches on the phenol derivatives were carried out for high quality measurements since the following search criteria were applied: no disordered structures, no structures with unresolved errors, no powder structures, no polymeric structures, e.s.d.'s for C–C bonds $\leq 0.005 \text{ \AA}$ and the discrepancy index $R \leq 7 \%$.

The precision of the determination of the positions of the maxima of electron density for H-atoms in X-ray diffraction measurements is much lower than the precision of determination of hydrogen nuclei positions in the neutron diffraction [8] but one can see that statistically the X-ray O–H bonds are much shorter than the neutron diffraction counterparts (Fig. 15.18); the mean OH bond length for X-ray experiments is equal to 0.871 \AA while this value for neutron diffraction amounts 0.990 \AA ; the corresponding median values are equal to 0.841 \AA and 0.984 \AA , respectively. The median values are presented here since the bond length distributions are not the normal ones. The number of the OH bonds included in the histograms (Fig. 15.18) for the X-ray and neutron diffraction is equal to 3798 and 12, respectively. This is because, in general, the number of X-ray observations collected in CSD is large in comparison with the neutron diffraction ones; the total number of crystal structures stored into Cambridge Structural Database is equal to

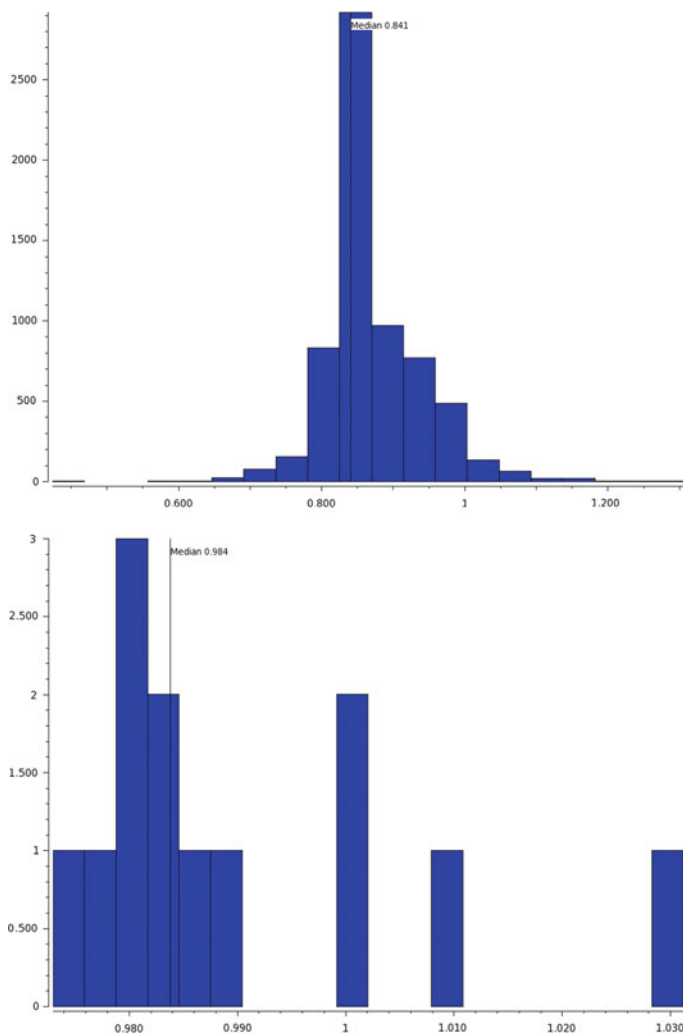


Fig. 15.18 Histograms of the O-H bond length for O-H groups connected with benzene ring detected in crystal structures, neutron diffraction (*down*) and X-ray diffraction results (*up*) are presented. The *horizontal* axes correspond to O-H bonds (length in Å), the *vertical* axes to number of observations, based on the results from the Cambridge Structural Database [64]

686 944 while only 1616 of them are the neutron diffraction measurements (CSD summary statistics—6 January 2014 [65]). It is worth mentioning that the total number of crystal structures deposited in CSD at the end of 2014 reached 750 200. In spite of the great disproportion between the number of neutron diffraction and X-ray results one can see that the experimental results clearly show that there is the electron charge density shift from H-atom to the bonded center, in the case considered here (Fig. 15.18) to the oxygen atom.

In view of those results one may say that the positive EP at hydrogen atom is enhanced owing to the electron density shift and that the links of H-atom with Lewis base centers, i.e. hydrogen bonds, may be classified as the σ -hole bonds. An example of the complex connected through two hydrogen bonds, O–H...F and C–H...O, was considered in the introduction (see Fig. 15.1). These are the classical examples of 3c-4e (3 center—4 electron) A–H...B hydrogen bonds since there are A, H and B centers, 2 electrons of the A–H σ -bond and the lone electron pair of the proton acceptor (B). However the A–H... π interactions, where it is difficult to indicate the single B-center, are also classified as hydrogen bonds. It is commonly accepted that for those interactions π -electrons play the role of the Lewis base.

Figure 15.19 shows the molecular graphs of the $C_2H_2...HF$ T-shaped complex; two graphs with the isolines of the laplacian of electron density corresponding to two levels of calculations (MP2/aug-cc-pVTZ and MP2/aug-cc-pVQZ) are presented. In both cases there is the bond path linking the H-atom attractor of HF molecule with the π -electron system of acetylene; in the case of aug-cc-pVTZ basis set there is the link between H-attractor and the non-nuclear attractor (NNA) situated between carbon atoms, in a case of the aug-cc-pVQZ basis set there is the hydrogen-bond critical point (H...BCP) link. Practically there is no the significant difference between those results, one may say that both NNA and BCP mimic the one-center π -electron Lewis base. This is worth to mention that such H... π bond paths for hydrogen bonded systems were analyzed before [66]. The characteristics of the BCP corresponding to the H... π bond path are practically the same for both levels (ρ_{BCP} and $\nabla^2\rho_{BCP}$ are equal to 0.021 au and 0.049 au,

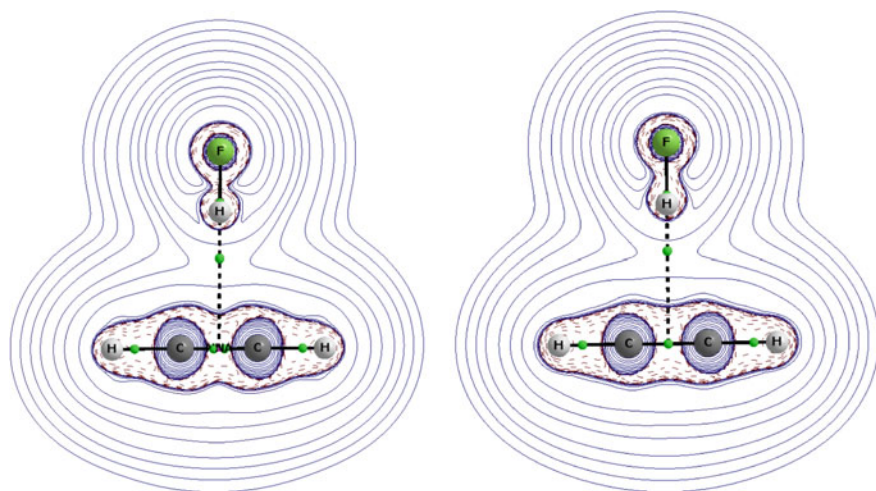


Fig. 15.19 The molecular graphs of the $C_2H_2...HF$ complex, the MP2/aug-cc-pVTZ (left) and MP2/aug-cc-pVQZ (right) levels, solid and broken lines correspond to bond paths, big circles to attractors and small green circles to BCPs, the isolines of Laplacian of electron density are also presented; there is non-nuclear attractor (small red circle) between carbon atoms (left) for the MP2/aug-cc-pVTZ level

respectively; the remaining characteristics differ only slightly). The characteristics of BCP situated between carbon atoms for the aug-cc-pVQZ basis set are as follows; $\rho_{\text{BCP}} = 0.416$ au and $\nabla^2\rho_{\text{BCP}} = -1.274$ au while for the aug-cc-pVTZ basis set there are two BCPs between carbon attractors for which $\rho_{\text{BCP}} = 0.411$ au and $\nabla^2\rho_{\text{BCP}} = -1.278$ au, there is also NNA situated between latter BCPs where $\rho_{\text{BCP}} = 0.411$ au and $\nabla^2\rho_{\text{BCP}} = -1.370$ au.

The situation is more complicated if the multicenter (more than 2 centers) π -electron system plays the role of proton acceptor in hydrogen bond interaction. It is often stated in the literature that aromatic systems or other closed-ring π -electron systems may play the role of proton acceptors in hydrogen bonds [67]; such species as benzene, antracene, cyclopentadienyl anion and their derivatives as well as other moieties are often considered. This means that π -electrons as a whole are treated as the Lewis base center. The hydrogen bonds with the multicenter π -electron systems were analyzed recently (the calculations were performed at the MP2/6-311 ++G(d, p) level) and it was found that at least few sub-classes of the A–H... π hydrogen bonds may be considered [68]. Figure 15.20 presents the molecular graphs of the $\text{C}_6\text{H}_6\text{...HCCH}$, $\text{C}_6\text{H}_6\text{...HF}$ and $\text{C}_5\text{H}_5^-\text{...HF}$ complexes. The binding energy for the $\text{C}_6\text{H}_6\text{...HCCH}$ complex amounts -2.1 kcal/mol (BSSE correction included), the complex is characterized by the C_{6v} symmetry and the molecular graph (Fig. 15.20) reflects this symmetry since six H...C bond paths between the hydrogen of acetylene and the carbon attractors of benzene are observed. For the BCPs of those bond paths the following characteristics were found; $\rho_{\text{BCP}} = 0.007$ au and $\nabla^2\rho_{\text{BCP}} = 0.023$ au. One may say that the C–H... π hydrogen bond is classified here as rather weak interaction and that all C-atoms of the benzene ring are involved equivalently in that interaction. On the other hand one may say that there are six equivalent C–H...C interactions for the $\text{C}_6\text{H}_6\text{...HCCH}$ complex (bifurcated hydrogen bond); this situation is different than for the $\text{C}_2\text{H}_2\text{...HF}$ complex presented earlier here where the H...BCP (or H...NNA) bond path was observed and where

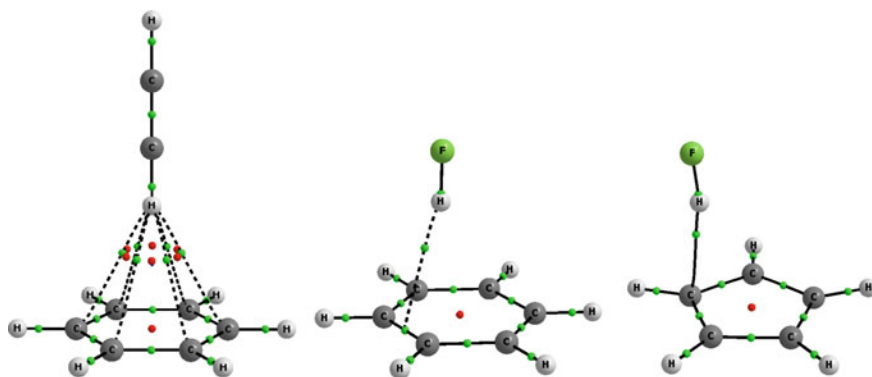


Fig. 15.20 The molecular graphs of the $\text{C}_6\text{H}_6\text{...HCCH}$, $\text{C}_6\text{H}_6\text{...HF}$ and $\text{C}_5\text{H}_5^-\text{...HF}$ complexes (from left to right), the MP2/6-311 ++G(d,p) level, solid and broken lines correspond to bond paths, big circles to attractors and small circles to critical points (green—BCPs, red—RCPs)

the BCP (or NNA) of the triple $C \equiv C$ bond mimics the one-center Lewis base. Since within the NBO approach the Lewis type structures are considered thus three $\pi_{CC} \rightarrow \sigma_{CH}^*$ intermolecular orbital-orbital interactions were found here, each of the energy amounting 0.4 kcal/mol and each corresponding to the overlap of CC π -bond orbital of benzene and the antibonding CH orbital of acetylene. The high C_{6v} structure symmetry results in the same electron charge distribution symmetry thus as it was pointed out earlier here, there are six equivalent C...H bond paths between acetylene and benzene as well as the equivalent charges for benzene atoms are detected (NBO charges for C and H atoms are equal to -0.208 au and $+0.209$ au, respectively; the corresponding charges for isolated benzene are equal to -0.204 au and $+0.204$ au).

For the $C_6H_6 \dots HF$ complex there is the H...BCP bond path between the HF molecule and the BCP of the CC bond of benzene; thus it is the similar situation to that one occurring for the $C_2H_2 \dots HF$ complex. The interaction is stronger here than for the complex of benzene with acetylene since the binding energy is equal to -3.3 kcal/mol; the following characteristics were found for the BCP of the mentioned above H...BCP bond path; $\rho_{BCP} = 0.010$ au and $\nabla^2 \rho_{BCP} = 0.031$ au. One can see that the C_{6v} symmetry is broken here; two carbon atoms are distinguished since the BCP of the path between them mimics the one-center Lewis base for this complex. The charges of those carbon atoms in the C_6H_6-HF complex are the most negative ones since they are equal to -0.225 au while the remaining C-charges amount -0.204 au; besides the intermolecular H...C distances are smallest for these carbons, 2.503 Å, while the remaining H...C (HF-benzene) distances amount $2.724-2.929$ Å. This means that the bond path between HF and C_6H_6 molecules shows the preferable H...C interactions. What is the reason of such an orientation of the HF molecule in the C_6H_6-HF complex? Probably for this structure the electrostatic interactions between benzene and HF are more attractive than in a case of the C_{6v} symmetry complex. However the difference is not significant; the MP2/aug-cc-pVTZ calculations show that the transition state C_{6v} symmetry C_6H_6-HF complex is higher in energy than the corresponding complex being in the energetic minimum only by 0.1 kcal/mol. The single $\pi_{CC} \rightarrow \sigma_{CH}^*$ orbital-orbital interaction is observed for the C_6H_6-HF complex with the interaction energy of 1.1 kcal/mol; the CC bond π -orbital corresponds here to the CC BCP which is connected with the H-atom attractor of HF molecule (see Fig. 15.20).

Figure 15.20 presents also the $C_5H_5^- \dots HF$ complex where the F-H... π hydrogen bond is assisted by the negative charge. It results in the stronger $C_5H_5^- - HF$ interaction since the binding energy is equal to -16.3 kcal/mol. The molecular graph shows the single H...C bond path where the following characteristic of the corresponding BCP were calculated; $\rho_{BCP} = 0.028$ au and $\nabla^2 \rho_{BCP} = 0.056$ au. The total electron energy density, H_{BCP} , at this bond critical point is equal to -0.002 au what may be explained by the partly covalent in nature corresponding H...C interaction. Also in this case, similarly as it was found for the C_6H_6-HF complex, the bond path shows the preferable H...C interaction since the charge of the corresponding C-atom of the $C_5H_5^-$ anion is equal to -0.433 au while for the remaining carbons of the anion this charge is situated in a range between -0.350 au

and -0.353 au. The H...C distance corresponding to the bond path is equal to 2.007 Å while the remaining distances amount 2.395 – 2.902 Å. This is worth to mention that for the $C_5H_5^- \dots HF$ complex a lone electron pair orbital within the NBO approach is detected for the carbon atom of $C_5H_5^-$ and that this orbital is involved in the most important $n(C) \rightarrow \sigma_{CH}^*$ orbital-orbital overlap for which the energy of interaction amounts 9.7 kcal/mol; this orbital is located at the C-atom connected by the bond path with HF molecule.

One can see that for the A–H... π hydrogen bonds presented here there are significant structural differences between them; those differences are reflected in the geometry as well as in the electron charge distributions. One can observe hydrogen bonds where the protic H-atom is linked with the Lewis base by atom-atom bond path (in $C_5H_5^- \dots HF$), by the atom-BCP bond path (in $C_6H_6 \dots HF$ or $C_2H_2 \dots HF$) and by the few equivalent atom-atom bond paths (in the $C_6H_6 \dots HCCH$ complex). In such a situation the question arises if the meaning of the term A–H... π hydrogen bonds should be revised. For example, maybe for the $C_5H_5^- \dots HF$ complex the term F–H...C hydrogen bond is more proper than the F–H... π one and maybe for the $C_6H_6 \dots HCCH$ complex the bifurcated hydrogen bond (six F–H...C intermolecular contacts) should be applied.

It is interesting that also σ -electrons may play a role of the proton acceptor in the hydrogen bonds; they are designated as the A–H... σ interactions. Such systems were analyzed theoretically for the $FH \dots H_2$, $H_3O^+ \dots H_2$, $NH_4^+ \dots H_2$ and other complexes where the molecular hydrogen acts as the Lewis base [69–72]. For all of them the situation is similar to that one occurring for the $C_2H_2 \dots HF$ complex; i.e. there is the bond path linking the hydrogen protic atom of the Lewis acid unit with the bond critical point of H–H molecular hydrogen bond. Figure 15.21 presents the molecular graph of the $NH_4^+ \dots H_2$ complex where one may observe this type of the bond path. One can see that for this complex the N–H bond of ammonia cation is located perpendicularly (or nearly so) to the H_2 molecule. Such T-shaped structures are observed for other complexes mentioned here, where the σ -electrons of the molecular hydrogen are the proton acceptor in hydrogen bonds [71]. For the $NH_4^+ \dots H_2$ complex the binding energy is equal to -2.3 kcal/mol (MP2/6-311 ++ (3df,3pd) level, BSSE included), the ρ_{BCP} and $\nabla^2\rho_{BCP}$ values for the BCP corresponding to the H...BCP bond path linking ammonia cation with H_2 molecule are equal to 0.013 au and 0.041 au, respectively. This is interesting that the most important orbital-orbital interaction corresponds here to the $\sigma_{H-H} \rightarrow \sigma_{N-H}^*$ overlap where σ_{H-H} is the σ -bond orbital of molecular hydrogen while σ_{N-H}^* is the anti-bonding N–H orbital of ammonia cation, the corresponding energy of interaction is equal to 3.6 kcal/mol (HF/6-311 ++G(d,p)//MP2/6-311 ++G(d,p) level).

The existence of the A–H... σ hydrogen bonds was confirmed by experiment. For example, gas phase measurements of dipole moment and vibrational predissociation lifetimes as well as the determination of rotational constants performed for the F–H... H_2 complex [73] confirmed its T-shaped structure. The high-resolution infrared spectra were analyzed for the H_2 –HF, D_2 –HF and HD–HF complexes solvated in helium nanodroplets and also for those species the T-shaped structure was confirmed [74–76]. The infrared vibrational predissociation spectra

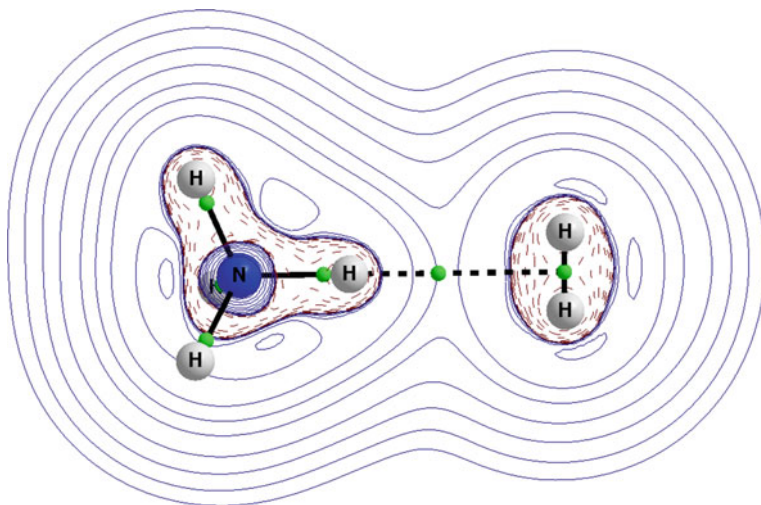


Fig. 15.21 The molecular graph of the $\text{NH}_4^+ \dots \text{H}_2$ complex, solid and broken lines correspond to bond paths, big circles to attractors and small green circles to BCPs, the isolines of Laplacian of electron density are presented; the projection in the plane containing H_2 molecule and HNH atoms of NH_4^+ cation

measurements were carried out for the $\text{H}_2\text{-HCO}^+$ complex linked through $\text{C-H} \dots \sigma$ interaction, where the σ -electrons of the molecular hydrogen act as the Lewis base [77]. The authors did not consider the $\text{C-H} \dots \sigma$ interaction as the hydrogen bond; however the results of experiment clearly show that this arrangement possesses characteristics typical for the latter kind of interaction.

Finally it is worth mentioning that the clusters of ammonia cation, NH_4^+ , with H_2 molecules— $(\text{NH}_4^+)(\text{H}_2)_n$ (n up to 8) were calculated [69, 78]. It was also found that the whole molecular surface of ammonia cation (0.001 au electron density surface was considered) is characterized by the positive EP; however the EP maxima are attributed to H-atoms [50]. Hence the increase of the number of molecular hydrogen molecules surrounding ammonia cation results in the $\text{N-H} \dots \sigma$ hydrogen bonds formation and when all N-H bonds are saturated by those interactions (for $n = 4$) thus next H_2 molecules (for clusters with $n \geq 5$) are linked with the nitrogen center of the cation, however all H_2 molecules for those clusters act as Lewis bases through their σ -electrons. The situation is very similar to that one occurring for the $(\text{NH}_4^+)(\text{HCN})_n$ clusters [61] mentioned earlier here (see also Fig. 15.16).

This is interesting that the molecular hydrogen possesses the properties of Lewis base (σ -electrons) and of the Lewis acid what is reflected in the distribution of electrostatic potential which is negative along the H-H σ -bond and it is positive at the outermost parts of H-atoms [79]. One may expect that the interaction of the H_2 molecule with Lewis acids should result in its connection through H-H BCP while the interaction with Lewis bases should result in the connection of the H_2 species by

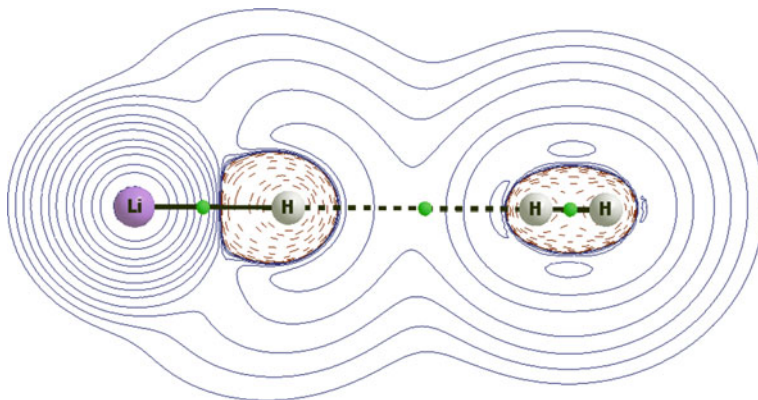


Fig. 15.22 The molecular graph of the LiH...H₂ complex, solid and broken lines correspond to bond paths, big circles to attractors and small green circles to BCPs, the isolines of Laplacian of electron density are also presented

one of its H-attractors. Figure 15.22 presents the latter situation where H₂ interacts as the Lewis acid with the hydride Lewis base center of LiH species. Figure 15.22 clearly shows the H...H bond path linking basic (of LiH) and acidic (of H₂) hydrogen atoms. This kind of interaction is known as the dihydrogen bond [80–83] and really, early on the LiH...H–H system was classified as linked by this type of interaction [84].

The distribution of the laplacian of electron density (Fig. 15.22) shows the vertical to the H–H σ -bond concentration of the electron density and this density depletion at the edges of H-atoms of hydrogen molecule. There is a very interesting distribution for the LiH species where it is clear that hydride anion interacts with the electron density deprived Li cation. The most important orbital-orbital interaction corresponds here to the $\sigma_{\text{Li-H}}^* \rightarrow \sigma_{\text{H-H}}^*$ overlap where $\sigma_{\text{Li-H}}$ is the σ -bond orbital of LiH molecule while $\sigma_{\text{H-H}}^*$ is the antibonding H–H orbital of dihydrogen, the corresponding energy of interaction is equal to 1.7 kcal/mol. The polarization of the H₂ molecule is observed here since the NBO atomic charges are equal to +0.031 au and –0.036 au (the positively charged H-atom is in contact with the negatively charged H-atom of the LiH species). One can see that the whole H₂ molecule is slightly negatively charged, this is because of the acidic properties of H₂ in this complex what results in the electron density shift from the LiH species to the dihydrogen. This is worth mentioning that such polarization does not occur for the dihydrogen in the NH₄⁺...H₂ complex considered earlier here since atomic charges of H-atoms in the dihydrogen are both equal to +0.007 au. In the latter complex the H₂ molecule is slightly positively charged since there is outflow of the electron density from that species due to its Lewis base characteristics.

The analysis of interactions of dihydrogen with other species seems to be very important to understand the mechanisms of numerous reactions and processes such as for example, the activation of molecular hydrogen and next its splitting at

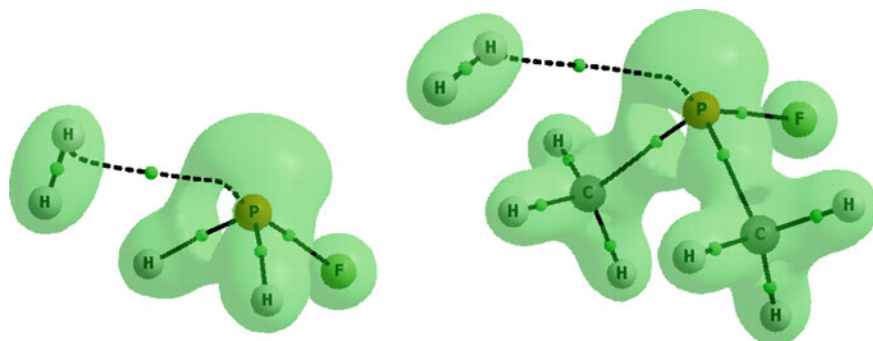


Fig. 15.23 The molecular graphs of the $\text{PFH}_2\dots\text{H}_2$ (left) and $\text{PF}(\text{CH}_3)_2\dots\text{H}_2$ (right) complexes, solid and broken lines correspond to bond paths, big circles to attractors and small green circles to BCPs, the reactive surface ($\nabla^2\rho(r) = 0$ isosurface) is presented

reaction center [85]; usually the metallic center is considered both experimentally [86] and theoretically [87].

Figure 15.23 presents molecular graphs of two complexes where dihydrogen interacts with the phosphorus (non-metallic) center, i.e. the $\text{PFH}_2\dots\text{H}_2$ and $\text{PF}(\text{CH}_3)_2\dots\text{H}_2$ complexes are considered. In both cases the P-center is characterized by the Lewis acid properties due to the existence of the σ -hole since the regions of the positive EP situated in the elongation of F–P bond are observed. The σ -holes located at the P-centers are characterized by the positive EPs which amount 0.060 au and 0.037 au for the PFH_2 and $\text{PF}(\text{CH}_3)_2$ monomers, respectively. The binding energies for the $\text{PFH}_2\text{--H}_2$ and $\text{PF}(\text{CH}_3)_2\text{--H}_2$ systems are equal to -1.2 kcal/mol and -0.7 kcal/mol, respectively (not corrected for BSSE).

There is an interesting issue if the dihydrogen in those complexes reveals its Lewis acid or Lewis base properties. Figure 15.23 shows that for the $\text{PFH}_2\text{--H}_2$ complex the P–dihydrogen intermolecular bond path crosses the region of the σ -hole but very close to the region of the electron charge concentration corresponding to the unshared P electron pair and next this bond path is aimed to the BCP of dihydrogen; however finally it ends at the H-atom attractor. The non-linear trajectory of the bond path does not show ambiguously the nature of centers being in contact; one may rather expect that the dihydrogen interacts as the Lewis base with the Lewis acid region of phosphorus. Two most important orbital-orbital interactions are detected for this complex; $\sigma(\text{H}_2) \rightarrow \sigma^*(\text{P--F})$ and $n(\text{P}) \rightarrow \sigma^*(\text{H}_2)$ which correspond to the Lewis base and Lewis acid properties of dihydrogen, respectively. The energy of interaction for the former overlap is equal to 1.5 kcal/mol while it amounts 0.6 kcal/mol for the latter overlap. Thus according to the NBO approach, the dihydrogen reveals stronger Lewis base properties than the Lewis acid ones in the $\text{PFH}_2\dots\text{H}_2$ complex.

The different picture is observed for the $\text{PF}(\text{CH}_3)_2\text{--H}_2$ complex where the trajectory of the P...dihydrogen bond path prompts the Lewis acid properties of H_2 and Lewis base properties of the phosphorus species since the bond path crosses the

lone electron pair region of P-center and it clearly ends at one of H-atoms of the dihydrogen. The NBO results confirm that since the $\sigma(\text{H}_2) \rightarrow \sigma^*(\text{P-F})$ and $n(\text{P}) \rightarrow \sigma^*(\text{H}_2)$ orbital-orbital energies of interactions are equal to 0.2 kcal/mol and 0.6 kcal/mol, respectively showing the stronger Lewis acid properties of the dihydrogen in that complex.

The interactions of molecular hydrogen with the $\text{PF}(\text{CH}_3)_2$ and PFH_2 species are classified as weak ones thus there are only slight electron density shifts for the corresponding complexes, -0.002 au and +0.008 au for the $\text{PFH}_2\text{-H}_2$ and $\text{PF}(\text{CH}_3)_2\text{-H}_2$ complexes, respectively (NBO results). This means that for the $\text{PFH}_2\text{-H}_2$ complex there is the shift from the H_2 molecule while for the $\text{PF}(\text{CH}_3)_2\text{-H}_2$ complex the shift to the dihydrogen is observed. Those shifts clearly confirm the results presented earlier here of the Lewis base or Lewis acid properties of the molecular hydrogen.

15.5 Summary

The analysis of the location of bond paths, of their trajectories and the distribution of the electron density in species analyzed, especially if such a distribution is discussed on the basis of the laplacian of the electron density, are very useful tools to deepen the understanding of the nature of interactions. This is also important that the analysis of the molecular graphs is often in line with the results of other approaches. This is worth mentioning that the molecular graph may be treated as a source of information on the location of atomic attractors (positions of atoms) and on the location of bond paths corresponding to the preferable stabilizing interactions.

Let us look at examples presented in this chapter; it is evident, that very often for weak interactions the atom-atom contacts correspond to Lewis acid-Lewis base centers' contacts characterized by the opposite electrostatic potentials. The hydrogen bonded systems are examples of such a situation, or even more generally, the σ -hole bonds. This is interesting that the bond paths, for weak interactions, usually connect the local maximum of EP with the minimum of EP. The complexes of the BrF_5 characterized by the pentavalent bromine center are examples of that situation; there are four equivalent local maxima of EP at the Br center situated symmetrically around the fourfold axis of symmetry of the BrF_5 molecule. This is why the complexes of BrF_5 with weak Lewis bases are not linear since the bond path crosses one of the local maxima of bromine. However the interactions with stronger Lewis bases like F^- or Cl^- anions lead to the meaningful changes in the electron charge distribution what results in the formation of BrF_6^- and BrF_5Cl^- complexes with the $\text{F-Br}\dots\text{F}^-$ and $\text{F-Br}\dots\text{Cl}^-$ linear arrangements, respectively.

One can enumerate other examples where the molecular graphs inform of the kinds and of the nature of interactions. The complexes of molecular hydrogen may be mentioned here. The dihydrogen possesses Lewis acid and Lewis base characteristics since the positive electrostatic potential is observed at the H-atoms, at edges

of the H–H bond while the negative EP is connected with the σ -bond. This is why the H₂ molecule interacts with Lewis acid centers through its σ -electrons and in the corresponding molecular graphs the bond paths between the Lewis acid center and the bond critical point of the H–H σ -bond are observed. On the other hand if the H₂ molecule reveals their Lewis acid properties thus the bond paths between H-atom of molecular hydrogen and the Lewis base center may be observed.

In general the contour maps of the laplacian of the electron density nicely show the links between the regions of the electron density depletion with the regions of its concentration; this was rationalized recently by Eskandari and coworkers in terms of the lump-hole interactions concept [55, 56].

Acknowledgments Financial support comes from Eusko Jauraritza (GIC 07/85 IT-330-07) and the Spanish Office for Scientific Research (CTQ2011-27374). Technical and human support provided by Informatikako Zerbitzu Orokorra - Servicio General de Informatica de la Universidad del Pais Vasco (SGI/IZO-SGIker UPV/EHU), Ministerio de Ciencia e Innovación (MICINN), Gobierno Vasco Eusko Jauranitza (GV/EJ), European Social Fund (ESF) is gratefully acknowledged. The QTAIM calculations as well as the corresponding figures were performed with the use of the AIMAll program [88].

References

1. Tsirelson VG, Ozerov RP (1996) Electron density and bonding in crystals. Institute of Physics, Bristol, Philadelphia
2. Coppens P (1997) X-Ray charge densities and chemical bonding. Oxford University Press, IUCr
3. Koritszansky TS, Coppens P (2001) Chemical applications of X-ray charge density analysis. Chem Rev 101:1583–1638
4. Bader RFW (1985) Atoms in molecules. Acc Chem Res 18:9–15
5. Bader RFW (1990) Atoms in molecules, a quantum theory. Oxford University Press, Oxford
6. Popelier P (2000) Atoms in molecules. an introduction. Prentice Hall, Pearson Education Limited, Harlow
7. Matta C, Boyd RJ (ed) (2007) Quantum theory of atoms in molecules: recent progress in theory and application. Wiley-VCH
8. Dunitz JD (1979) X-Ray analysis and the structure of organic molecules. Cornell University Press, Ithaca, p 395
9. Bader RFW (1998) A bond path: a universal indicator of bonded interactions. J Phys Chem A 102:7314–7323
10. Bader RFW (2009) Bond paths are not chemical bonds. J Phys Chem A 113:10391–10396
11. Runtz GR, Bader RFW, Messer RR (1977) Definition of bond paths and bond directions in terms of the molecular charge distribution. Can J Chem 55:3040–3045
12. Keith TA, Bader RFW, Aray Y (1996) Structural homeomorphism between the electron density and the virial field. Int J Quantum Chem 57:183–198
13. Gatti C, Cargnoni F, Bertini L (2003) Chemical information from the source function. J Comput Chem 24:422–436
14. Gatti C (2005) Chemical bonding in crystals: new directions. Z Kristallogr 220:399–457
15. Stalke D (2011) Meaningful structural descriptors from charge density. Chem Eur J 17:9264–9278

16. Rozas I, Alkorta I, Elguero J (2000) Behavior of ylides containing N, O, and C atoms as hydrogen bond acceptors. *J Am Chem Soc* 122:1154–11161
17. Grabowski SJ (2011) What is the covalency of hydrogen bonding? *Chem Rev* 11:2597–2625
18. Cremer D, Kraka E (1984) A description of the chemical-bond in terms of local properties of electrodensity and energy. *Croat Chem Acta* 57:1259–1281
19. Jenkins S, Morrison I (2000) The chemical character of the intermolecular bonds of seven phases of ice as revealed by ab initio calculation of electron densities. *Chem Phys Lett* 317:97–102
20. Grabowski SJ (2001) Ab initio calculations on conventional and unconventional hydrogen bonds—study of the hydrogen bond strength. *J Phys Chem A* 105:10739–10746
21. Weinhold F, Landis C (2005) Valency and bonding, a natural bond orbital donor—acceptor perspective. Cambridge University Press
22. Reed AE, Curtiss LA, Weinhold F (1988) Intermolecular Interactions from a natural bond orbital, donor-acceptor viewpoint. *Chem Rev* 88:899–926
23. Alabugin IV, Manoharan M, Peabody S, Weinhold F (2003) Electronic basis of improper hydrogen bonding: a subtle balance of hyperconjugation and rehybridization. *J Am Chem Soc* 125:5973–5987
24. Weinhold F, Klein R (2012) What is a hydrogen bond? mutually consistent theoretical and experimental criteria for characterizing H-bonding interactions. *Mol Phys* 110:565–579
25. Murray JS, Lane P, Politzer P (2009) Expansion of the σ -hole concept. *J Mol Model* 15:723–729
26. Politzer P, Murray JS, Clark T (2010) Halogen bonding: an electrostatically-driven highly directional noncovalent interaction. *Phys Chem Chem Phys* 12:7748–7758
27. Politzer P, Murray JS, Clark T (2013) Halogen bonding and other σ -hole interactions: a perspective. *Phys Chem Chem Phys* 15:11178–11189
28. Boys SF, Bernardi F (1970) The calculation of small molecular interactions by the differences of separate total energies. Some procedures with reduced errors. *Mol Phys* 19:553–566
29. Nyburg SC, Faerman CH (1985) A revision of van der Waals atomic radii for molecular crystals: nitrogen, oxygen, fluorine, sulfur, chlorine, selenium, bromine, and iodine bonded to carbon. *Acta Crystallogr B* 41:274–279
30. Zordan F, Brammer L, Sherwood P (2005) Supramolecular chemistry of halogens: complementary features of inorganic (M-X) and organic (C-X') halogens applied to M-X... X'-C halogen bond formations. *J Am Chem Soc* 127:5979–5989
31. Formigué M, Batail P (2004) Activation of hydrogen- and halogen-bonding interactions in tetrathiafulvalene-based crystalline molecular conductors. *Chem Rev* 104:5379–5418
32. Clark T, Hennemann M, Murray JS, Politzer P (2007) Halogen bonding: the σ -hole. *J Mol Model* 13:291–296
33. Clark T (2013) σ -Holes. *Wires Comput Mol Sci* 3:13–20
34. Politzer P, Murray JS, Concha MC (2007) Halogen bonding and the design of new materials: organic bromides, chlorides and perhaps even fluorides as donors. *J Mol Model* 13:643–650
35. Landrum GA, Goldberg N, Hoffmann R, Minyaev RM (1998) Intermolecular interactions between hypervalent molecules: Ph2IX and XF3 (X = Cl, Br, I) dimers. *New J Chem* 22:883–890
36. Wang W (2011) Halogen bond involving hypervalent halogen: CSD search and theoretical study. *J Phys Chem A* 115:9294–9299
37. Grabowski SJ (2014) Halogen bond with the multivalent halogen acting as the Lewis acid center. *Chem Phys Lett* 605–606:131–136
38. Weinhold F, Landis C (2005) Valency and bonding, a natural bond orbital donor—acceptor perspective. Cambridge University Press, pp 275–306
39. Pimentel GC (1951) The bonding of trihalide and bifluoride ions by the molecular-orbital method. *J Chem Phys* 19:446–448
40. Rundle RE (1947) Electron deficient compounds. *J Am Chem Soc* 69:1327–1331
41. Politzer P, Murray JS (2013) Halogen bonding: an interim discussion. *ChemPhysChem* 14:2145–2151

42. Bundhun A, Ramasami P, Murray JS, Politzer P (2012) Trends in σ -hole strengths and interactions of F3MX molecules (M = C, Si, Ge and X = F, Cl, Br, I). *J Mol Mod* 19:2739–2746
43. Bauzá A, Mooibroek TJ, Frontera A (2013) Tetrel-bonding interaction rediscovered supramolecular force? *Angew Chem Int Ed Engl* 52:12317–12321
44. Mani D, Arunan E (2013) The X-C...Y (X = O/F, Y = O/S/F/Cl/Br/N/P) ‘carbon bond’ and hydrophobic interactions. *Phys Chem Chem Phys* 15:14377–14383
45. Grabowski SJ (2014) Tetrel bond— σ -hole bond as a preliminary stage of the S_N2 reaction. *Phys Chem Chem Phys* 16:1824–1834
46. Sundberg MR, Uggla R, Viñas C, Teixidor F, Paavola S, Kivekäs R (2007) Nature of intramolecular interactions in hypercoordinate C-substituted 1,2-dicarba-*closo*-dodecaboranes with short P...P distances. *Inorg Chem Commun* 10:713–716
47. Bauer S, Tschirschwitz S, Lönnecke P, Franck R, Kirchner B, Clark ML, Hey-Hawkins E (2009) Enantiomerically Pure Bis(phosphanyl)carbaborane(12) Compounds. *Eur J Inorg Chem* 2776–2788
48. Del Bene JE, Alkorta I, Sanchez-Sanz G, Elguero J (2011) Structures, energies, bonding, and NMR properties of pnictogen complexes $H_2XP:NXH_2$ (X = H, CH_3 , NH_2 , OH, F, Cl). *J Phys Chem A* 115:13724–13731
49. Scheiner S (2011) Can two trivalent N atoms engage in a direct N...N noncovalent interaction? *Chem Phys Lett* 514:32–35
50. Grabowski SJ (2013) σ -Hole bond versus hydrogen bond: from tetravalent to pentavalent N, P, and as atoms. *Chem Eur J* 19:14600–14611
51. Sanz P, Yañez M, MÓ O (2002) Competition between X...H...Y intramolecular hydrogen bonds and X...Y (X = O, S, and Y = Se, Te) chalcogen-chalcogen interactions. *J Phys Chem A* 106:4661–4668
52. Wang W, Ji B, Zhang Y (2009) Chalcogen bond: a sister noncovalent bond to halogen bond. *J Phys Chem A* 113:8132–8135
53. Alikhani E, Fuster F, Madebene B, Grabowski SJ (2014) Topological reaction sites—very strong chalcogen bonds. *Phys Chem Chem Phys* 16:2430–2442
54. Del Bene JE, Alkorta I, Sánchez-Sanz G, Elguero J (2011) ^{31}P - ^{31}P Spin-Spin coupling constants for pnictogen homodimers. *Chem Phys Lett* 512:184–187
55. Del Bene JE, Alkorta I, Elguero J (2015) Substituent effects on the properties of pnictogen-bonded complexes $H_2XP:PYH_2$, for X, Y = F, Cl, OH, NC, CCH, CH_3 , CN, and H. *J Phys Chem A* 119:224–233
56. Eskandari K, Mahmoodabadi N (2013) Pnictogen bonds: a theoretical study based on the laplacian of electron density. *J Phys Chem A* 117:13018–13024
57. Eskandari K, Zariny H (2010) Halogen bonding: a lump-hole interaction. *Chem Phys Lett* 492:9–13
58. Bento AP, Solà M, Bickelhaupt FM (2005) *Ab initio* and DFT benchmark study for nucleophilic substitution at carbon ($S_N2@C$) and silicon ($S_N2@Si$). *J Comput Chem* 26:1497–1504
59. Pierrefixe SCAH, Guerra CF, Bickelhaupt FM (2008) Hypervalent silicon versus carbon: ball-in-a-box model. *Chem Eur J* 14:819–828
60. Levy CJ, Puddephatt RJ (1997) Rapid reversible oxidative addition of group 14-halide bonds to platinum(ii): rates, equilibria, and bond energies. *J Am Chem Soc* 119:10127–10136
61. Grabowski SJ (2014) Clusters of ammonium cation–hydrogen bond versus σ -hole bond. *ChemPhysChem* 15:876–884
62. Murray JS, Riley KE, Politzer P, Clark T (2010) Directional weak intermolecular interactions: σ -hole bonding. *Aust J Chem* 63:1598–1607
63. Lipkowski P, Grabowski SJ (2014) Could the lithium bond be classified as the σ -hole bond?—QTAIM and NBO analysis. *Chem Phys Lett* 591:113–118
64. Allen FH (2002) The cambridge structural database: a quarter of a million crystal structures and rising. *Acta Cryst B* 58:380–388
65. http://www.ccdc.cam.ac.uk/Lists/ResourceFileList/2014_stats_entries.pdf

66. Domagała M, Grabowski SJ (2009) X-H... π and X-H...N hydrogen bonds—acetylene and hydrogen cyanide as proton acceptors. *Chem Phys* 363:42–48
67. Nishio M, Hirota M, Umezawa Y (1998) The CH/ π interaction, evidence, nature, and consequences. Wiley-VCH, New York
68. Grabowski SJ, Ugalde JM (2010) Bond paths show preferable interactions: ab initio and QTAIM studies on the X-H... π hydrogen bond. *J Phys Chem A* 114:7223–7229
69. Szymczak JJ, Grabowski SJ, Roszak S, Leszczynski J (2004) H... σ interactions—an ab initio and ‘atoms in molecules’ study. *Chem Phys Lett* 393:81–86
70. Grabowski SJ, Sokalski WA, Leszczynski J (2006) Can H... σ , π ...H + ... σ and σ ...H + ... σ interactions be classified as H-bonded? *Chem Phys Lett* 432:33–39
71. Grabowski SJ (2007) Hydrogen bonds with π and σ electrons as the multicenter proton acceptors: high level ab initio calculations. *J Phys Chem A* 111:3387–3393
72. Grabowski SJ (2013) Dihydrogen bond and X-H... σ interaction as sub-classes of hydrogen bond. *J Phys Org Chem* 26:452–459
73. Jucks KW, Miller RE (1987) Infrared stark spectroscopy on the hydrogen-HF binary complex. *J Chem Phys* 87:5629–5633
74. Moore DT, Miller RE (2003) Dynamics of hydrogen–HF complexes in helium nanodroplets. *J Chem Phys* 118:9629–9636
75. Moore DT, Miller RE (2003) Solvation of HF by molecular hydrogen: helium nanodroplet vibrational spectroscopy. *J Phys Chem A* 107:10805–10812
76. Moore DT, Miller RE (2004) Rotationally resolved infrared laser spectroscopy of (H₂)_n-HF and (D₂)_n-HF (n = 2–6) in helium nanodroplets. *J Phys Chem A* 108:1930–1937
77. Bieske EJ, Nizkorodov SA, Bennett FR, Maier JP (1996) The infrared spectrum of the H₂–HCO complex. *J Chem Phys* 102:5152–5164
78. Urban J, Roszak S, Leszczynski J (2001) Shellvation of the ammonium cation by molecular hydrogen: a theoretical study. *Chem Phys Lett* 346:512–518
79. Grabowski SJ, Alkorta I, Elguero J (2013) Complexes between dihydrogen and amine, phosphine, and arsine derivatives. hydrogen bond versus pnictogen interaction. *J Phys Chem A* 117:3243–3251
80. Richardson TB, de Gala S, Crabtree RH (1995) Unconventional hydrogen bonds: intermolecular B-H...H-N interactions. *J Am Chem Soc* 117:12875–12876
81. Wessel J, Lee JC Jr, Peris E, Yap GPA, Fortin JB, Ricci JS, Sini G, Albinati A, Koetzle TF, Eisenstein O, Rheingold AL, Crabtree RH (1995) An unconventional intermolecular three-center N-H...H₂Re hydrogen bond in crystalline [ReH₅(PPh₃)₃]-indole-C₆H₆. *Angew Chem Int Ed Engl* 34:2507–2509
82. Crabtree RH, Siegbahn PEM, Eisenstein O, Rheingold AL, Koetzle TFA (1996) A new intermolecular interaction: unconventional hydrogen bonds with element-hydride bonds as proton acceptor. *Acc Chem Res* 29:348–354
83. Crabtree RH, Eisenstein O, Sini G, Peris E (1998) New types of hydrogen bonds. *J Organomet Chem* 567:7–11
84. Cybulski H, Pecul M, Sadlej J (2003) Characterization of dihydrogen-bonded D-H...H–A complexes on the basis of infrared and magnetic resonance spectroscopic parameters. *J Chem Phys* 119:5094–5104
85. Kubas GJ (2001) Metal dihydrogen and σ -bond complexes. Kluwer, Academic, New York
86. Stephan DW, Erker G (2010) Frustrated Lewis pairs: metal-free hydrogen activation and more. *Angew Chem Int Ed* 49:46–76
87. Rokob TA, Bakó I, Stirling A, Hamza A, Pápai I (2013) Reactivity models of hydrogen activation by frustrated Lewis pairs: synergistic electron transfers or polarization by electric field? *J Am Chem Soc* 135:4425–4437
88. Todd A, Keith TK (2011) AIMAll (Version 11.08.23). Gristmill Software, Overland Park KS, USA (aim.tkgristmill.com)

Chapter 16

Following Halogen Bonds Formation with Bader's Atoms-in-Molecules Theory

Vincent Tognetti and Laurent Joubert

Abstract In this chapter, we will show how Bader's atoms-in-molecules theory enables to unravel the main physicochemical factors that drive the formation of halogen bonds, which are intriguing and fascinating noncovalent interactions at work as well as in crystals, biological and chemical systems, and which have found numerous applications in, among other fields, drug design and supramolecular chemistry. In particular, the use of Pendás and coworkers' interacting quantum atoms scheme will cast the light on the nature of such interactions (more or less electrostatic, more or less covalent) and will provide useful hints to account for the existence or absence of energy minima in the corresponding potential energy surface. Importantly, such a rationalizing approach can be carried out whatever the system and also possesses predictive power.

Keywords Halogen bonds · Bader's atoms-in-molecules theory · Energy decomposition · Interacting quantum atoms scheme · Electrostatic interactions · Electronic quantum exchange

16.1 Introduction

Halogen bonds [1–7] have generated for the last years a considerable amount of experimental and theoretical works because they are ubiquitous in biology (involved in molecular folding, ligand binding) [8–15], material science (in particular in crystal engineering, supramolecular scaffolds) [16–24], nanoparticles chemistry [25], organo- and organometallics catalysis [26–38], the number of their applications being

V. Tognetti (✉) · L. Joubert (✉)
Normandy University, COBRA UMR 6014 & FR 3038, Université de Rouen, INSA Rouen,
CNRS, 1 rue Tesnière, 76821 Cedex, Mont St Aignan, France
e-mail: vincent.tognetti@univ-rouen.fr

L. Joubert
e-mail: laurent.joubert@univ-rouen.fr

constantly and endlessly growing in almost all these related fields, so that the bibliography for this chapter cannot obviously be exhaustive.

Experimentally, they can be characterized using all flavours of spectroscopy [29–38], while an equal huge number of papers [39–60] has been devoted to the theoretical understanding and rationalization of these particular interactions, using the whole computational and analysis arsenal developed over the past decades (density functional theory (DFT), post Hartree-Fock methods, molecular orbital theory, conceptual DFT, valence bond theory, energy decomposition, quantum chemical topology...). For the very same reasons as those when dealing with experimental progress, our references list about theoretical advances is far from being comprehensive.

All these plethoric works have been in particular instrumental in the advent of the retained definition of the halogen bond by the International Union of Pure and Applied Chemistry (IUPAC): “A halogen bond occurs when there is evidence of a net attractive interaction between an electrophilic region associated with a halogen atom in a molecular entity and a nucleophilic region in another, or the same, molecular entity” [1].

In a series of recent articles, we notably investigated the properties of halogen bonds, and more generically of interactions between halogens and electronegative atoms, whatever in intramolecular or intermolecular fashion [61–68], from the electron density point of view (through conceptual DFT or Bader’s atoms-in-molecules theory (QTAIM) [69, 70], which are complementary approaches, grounded on the same key-ingredient). Let us recall that the electron density is the primary and fundamental observable of any chemical system and that it can be obtained not only from theoretical calculations but also experimentally thanks to X-ray diffraction. In this chapter, we will mainly focus on the QTAIM description of halogen bond formation, that-is-to say we will follow selected QTAIM descriptors along the reaction path leading to possible halogen-bond stabilized complexes.

16.2 Theory

16.2.1 *Basics of QTAIM: Atomic Basins and Energy Decomposition*

Bader’s atoms-in-molecules theory [69, 70] is based on the topology of the electron density $\rho(\vec{r})$ and enables to partition the three-dimensional real space into non-overlapping domains called “basins”. To achieve such separation, one looks at the so-called gradient paths (GPs), which are the equivalent of field lines in classical electromagnetism. A GP is defined as a curve C such that the electron density gradient $\vec{\nabla}\rho(\vec{r})$ (which can stem from theoretical calculations as well as from X-ray diffraction experiments) is tangent to C at every C point. In general (non-nuclear

attractors will not be considered here), these GPs end at a nucleus. The collection of all GPs terminating at the same nucleus then forms a 3D volume that is called the atomic basin (denoted Ω_A) related to nucleus A. The corresponding quantum atom is subsequently simply defined as the union of nucleus A and basin Ω_A .

Once this partition is determined, many atomic properties can be evaluated by integrating the proper real space function over the considered basin (whose frontiers, called interatomic surfaces (IASs), obey the celebrated zero density gradient flux condition). For instance, the atomic electronic population (average number of electrons inside a given basin) is calculated according to:

$$N(A) = \int_{\Omega_A} \rho(\vec{r}) d^3r. \quad (16.1)$$

The corresponding atomic charge is then univocally defined by:

$$q(A) = Z_A - N(A), \quad (16.2)$$

where Z_A denotes the charge (in atomic units) of the nucleus (located at \vec{R}_A).

Besides, one could show [71–73] that the molecular energy can be exactly decomposed by:

$$E_{mol} = \sum_A E_A^{intra} + \sum_A \sum_{B>A} E_{AB}^{inter}, \quad (16.3)$$

where E_A^{intra} represents the intraatomic (also called “self” or “monobasin”) energy of each atom, while E_{AB}^{inter} stands for the interaction energy between each pair of atoms A and B. More specifically,

$$E_A^{intra} = T_A + E_A^{ne} + E_A^{ee}. \quad (16.4)$$

where T_A represents the atomic kinetic energy, E_A^{ne} the attraction energy of the electrons inside basin Ω_A by nucleus A, and E_A^{ee} the electron-electron repulsion energy between the electrons inside the same basin.

Similarly, the pair interaction terms can be decomposed following:

$$E_{AB}^{inter} = E_{AB}^{nn} + E_{AB}^{ne} + E_{AB}^{en} + E_{AB}^{ee}, \quad (16.5)$$

where E_{AB}^{nn} is the repulsion energy between nuclei A and B, E_{AB}^{ne} (respectively E_{AB}^{en}) the attraction energy of the electrons in basin Ω_B (resp. Ω_A) by nucleus A (resp. B), and E_{AB}^{ee} the energy due to the repulsion between electrons in Ω_B with those inside Ω_A .

Using perturbation theory, this last term can be rigorously split into pure Coulombic classical and exchange-correlation (“pure quantum”) contributions:

$$E_{AB}^{ee} = \underbrace{\int_{\Omega_A} \int_{\Omega_B} \frac{\rho(\vec{r}_A)\rho(\vec{r}_B)}{\|\vec{r}_A - \vec{r}_B\|} d^3r_A d^3r_B}_{E_{AB}^{ee,cl}} + E_{AB}^{ee,xc}. \quad (16.6)$$

Equation 16.5 can thus be rewritten:

$$E_{AB}^{inter} = \underbrace{E_{AB}^{nm} + E_{AB}^{ne} + E_{AB}^{en} + E_{AB}^{ee,cl}}_{E_{AB}^{cl}} + E_{AB}^{ee,xc} \equiv E_{AB}^{cl} + E_{AB}^{ee,xc}, \quad (16.7)$$

where E_{AB}^{cl} is the so-called total Coulombic classical part of the interaction energy between the two considered atoms (note however that it may indirectly include quantum effects since the integral in Eq. 16.6 may involve the electron density obtained through quantum calculations). Obviously, the very same decomposition can be made for the intraatomic electron-electron repulsion energy:

$$E_A^{ee} = E_A^{ee,cl} + E_A^{ee,xc}. \quad (16.8)$$

One can go further by using the following expansion in terms of regular $R_{l,m}$ and irregular $I_{l,m}$ normalized spherical harmonics [74–76]:

$$\frac{1}{\|(\vec{R}_B - \vec{R}_A) - (\vec{r}_A - \vec{r}_B)\|} = \sum_{l=0}^{+\infty} \sum_{m=-l}^{+l} (-1)^m I_{l,m}(\vec{R}_B - \vec{R}_A) R_{l,-m}(\vec{r}_A - \vec{r}_B), \quad (16.9)$$

so that the classical Coulombic interaction between any atom pair reads:

$$E_{AB}^{cl} = \sum_{l_A, l_B, m_A, m_B} G_{l_A, l_B, m_A, m_B}(\vec{R}_B - \vec{R}_A) Q_{l_A, m_A}(A) Q_{l_B, m_B}(B), \quad (16.10)$$

where G is a pure geometric tensor and $Q_{l,m}$ are the so-called atomic multipole moments. In particular, the first term is given by point charges interaction (in atomic units):

$$E_{AB}^{cl} = \frac{q(A)q(B)}{\|\vec{R}_B - \vec{R}_A\|} + \text{higher terms}, \quad (16.11)$$

the higher terms including the interaction between atomic charge-atomic dipole, atomic dipole-atomic dipole etc., and being essential for a correct description of electrostatics, notably in biological systems [77]. One of the peculiarities of QTAIM is indeed that it defines atomic dipole: as the electron density is anisotropic inside a basin due to its environment, the barycentre of the negative charge inside the basin is thus not anymore confounded with the nucleus position, creating a dipole inside the atom. This fruitful concept notably explains the very small dipole

moment of carbon monoxide (via counterpolarization) [78] and can be also used to characterize charge transfers and repolarization upon light absorption [79, 80].

Finally, it should be stressed that this full energetic decomposition, coined “interacting quantum atoms” (IQA) by Pendás and coworkers (who have applied it to very different systems, proving its versatility [81–87]), is in principle exact. However, as it is grounded on the partition of the first-order reduced density matrix (RDM) for the kinetic part and of the second-order RDM to decompose the total electron-electron repulsion energy, it should a priori be used only in conjunction with (post Hartree-Fock) wavefunction theory. We will mark this fact by explicitly writing these energetic terms as functionals of the wavefunction ($E = E[\psi]$).

Indeed, density functional theory (DFT) in principle provides (in the Hohenberg-Kohn as well as in its Kohn-Sham (KS) formulation) only the exact electron density, but does not afford direct ways to evaluate the first and second-order RDMs, and this would remain true even if the exact density functional was known in analytical form. Nevertheless, the IQA approach can be used in a KS framework in an approximate way. In practice, the intraatomic contributions will be evaluated using:

$$E_{A,KS}^{\text{intra}} = T_A^{KS} [\{\psi_i^{KS}\}] + E_{A,KS}^{ne}[\rho] + E_{A,KS}^{ee,cl}[\rho] + E_{A,KS}^{ee,x}[\{\psi_i^{KS}\}], \quad (16.12)$$

where T^{KS} denotes the kinetic energy of the fictitious KS non-interacting system and $\{\psi_i^{KS}\}$ are the KS orbitals. When dealing with functionals, one should distinguish between two different concepts: the functional itself (that-is-to-say its mathematical expression) and the numerical value it gives in the calculation. A given functional $A[f]$ can give inaccurate numbers for two reasons (that might occur simultaneously): (1) the exact f function is unknown; (2) the A functional is only approximated. As an example, we can consider $E_{A,KS}^{ne}[\rho]$. The functional is exactly known ($\int_{\Omega_A} \rho(\vec{r}) v_{ext}(\vec{r}) dr$, where $v_{ext}(\vec{r})$ is the external potential created by the nuclei), but it will be evaluated in practice on an approximate density ($E_{A,KS}^{ne}[\rho_{approx}]$).

Actually, all functionals in Eq. 16.12 are exact in the sense that they would provide the exact KS value if the exact density and KS orbitals were used. Note that the exchange part is exact in this perspective as a functional of the KS orbitals, but that it is not exactly known as a functional of the electron density. However, as the first-order RDM based on KS orbitals is not in general (even if the exact KS orbitals were determined) equal to that of the real system (only their diagonal element, namely the electron density, must be in principle equal), one has:

$$E_{A,KS}^{ee,x} [\{\psi_{i,exact}^{KS}\}] \neq E_A^{ee,x} [\psi_{exact}]. \quad (16.13)$$

Moreover, Eq. 16.12 lacks the so-called correlation kinetic energy, so that:

$$T_A^{KS} \left[\left\{ \psi_{i,exact}^{KS} \right\} \right] \neq T_A[\psi]. \quad (16.14)$$

The same analysis could be done for the interatomic energies. In this approach, we will have:

$$E_{AB,KS}^{ee} = E_{AB,KS}^{ee,cl}[\rho] + E_{AB,KS}^{ee,x} \left[\left\{ \psi_i^{KS} \right\} \right], \quad (16.15)$$

with:

$$\begin{cases} E_{AB,KS}^{ee,cl}[\rho_{exact}] = E_{AB}^{ee,cl}[\psi_{exact}] \\ E_{AB,KS}^{ee,x} \left[\left\{ \psi_{i,exact}^{KS} \right\} \right] \neq E_{AB}^{ee,x}[\psi]. \end{cases} \quad (16.16)$$

Such possible discrepancies between wavefunction-IQA and KS-IQA could make us think that KS-IQA is unwarranted. Interestingly, the very same question has arisen for the evaluation of delocalization indexes [88] and for the atomic energies derived from the virial theorem. Matta and coworkers have discussed it in great detail from the theoretical point of view in the annex of Ref. [89], and also provided, in the same paper, definitive numerical evidence that KS virial energies could be effectively used as surrogates for the real atomic energies, in particular when one is interested in energy differences.

Similarly, we recently gave numerical proofs [61, 65] that the differences between wavefunction-IQA and KS-IQA are numerically small, so that KS-IQA can be safely used for semi-quantitative purposes. Accordingly, we will use it throughout this chapter (for sake of clarity, the KS and *ee* subscript and superscript will now be omitted).

It must be however remarked that electron-electron correlation effects are missing in Eq. 16.12. For weak interactions like halogen bonds, the correlation effects mainly manifest through dispersion. It has notably been proved that some halogen-bonded complexes exhibit important dispersion [90]. From a pragmatic point of view, it can be approximated within DFT by the addition of pair-potentials, as pioneered by Grimme. In the so-called D2 scheme [91], one evaluates the dispersion correction between two atoms solely based on internuclei distance and C_6 atomic coefficients:

$$E_{AB}^{disp} = -s_6 f_{dmp}(R_{AB}) \frac{\sqrt{C_6(A)C_6(B)}}{R_{AB}^6}, \quad (16.17)$$

where f_{dmp} denotes a damping factor (here of the Fermi-Dirac type) that switches the interaction off at small interaction distances. Note that a priori these C_6 coefficients should be calculated for the atom inside the considered molecule. Nevertheless, tabulated constant atomic values can be used as a first step.

It must be emphasized that this D2 procedure actually provides a correction to the DFT approximations in order to recover the correct interaction energies for reference van der Waals systems, and not a direct evaluation of the dispersion energy. Indeed, some DFT approximations can partly (and often fortuitously) include dispersion effects [92]. Nonetheless, in case of functionals that are known to fully miss dispersion (typically B3LYP), it is reasonable to presume that the correction will be close to the real dispersion energy. In consequence, the dispersion interaction energy between any atom pair will be evaluated by the B3LYP-D2 correction.

16.2.2 Basics of QTAIM: Critical Points

QTAIM also includes a complementary local approach to atomic interactions, by focusing on the so-called critical points (CPs), defined as points in real space where the electron density gradient vanishes. CPs can be classified by their rank r and their signature s , this last number being the sum of the signs of the density Hessian eigenvalues. For instance, in this (r, s) nomenclature, $(3, -3)$ CPs correspond to attractors (in general nuclei). The Poincaré-Hopf (PH) relationship imposes that the numbers of the different BCP types are linked according to (for a non-periodic system):

$$n_{(3,-3)} - n_{(3,-1)} + n_{(3,+1)} + n_{(3,-3)} = 1. \quad (16.18)$$

Of particular importance are $(3, -1)$ CPs. They correspond to a minimum of density along a direction and to a maximum in the two perpendicular directions. At a molecular equilibrium geometry, they are called “bond critical points” (BCPs) and then enable to determine which atoms are bonded in the orthodox QTAIM sense: two atoms are bonded if and only if a BCP is present between them, the union of the two GPs linking the BCP to each nucleus being named the “bond path”. Note that such a characterization has raised some controversies in the last decades (see Ref. [93] for a recent discussion). However, the existence of a bond path is a fundamental feature that has been explicitly mentioned in the IUPAC definition [1] of halogen bonds.

Noteworthy, BCPs properties usually provide valuable information about the bond itself. For instance, covalent bonds are characterized by high electron density values (ρ_c) at BCPs, while ρ_c is typically very low for non-covalent bonds like hydrogen, agostic, halogen, and van der Waals ones [94–97]. Another important descriptor is the BCP density laplacian value that quantifies the electron accumulation (negative values) or depletion (positive values) at the BCP. Thus, very negative values are observed for covalent bonds (“shared interactions” in Bader’s vocabulary), while ionic (“closed-shell” interactions) ones feature positive values. Many relationships between interaction energies and $(\rho_c, \nabla^2 \rho_c)$ have been reported in the literature.

For completeness, one can mention that others local descriptors have been designed over the years (ellipticity, various density energies like the G_c and K_c kinetic, potential V_c , Hamiltonian H_c ones at BCP, reduced density gradient variation rates [98], DFT-based local descriptors [99]...). Besides, following the appearance and disappearance of critical points also constitutes an efficient way of describing the mechanism of chemical transformations (see Ref. [100] for a recent example).

16.2.3 Computational Details

Consistently with our previous works, and as recommended by Kozuch and Martin [101], the ω B97X-D exchange-correlation functional [102] was used in conjunction with the triple- ζ aug-cc-pVTZ basis set. Potential energy surfaces were explored through relaxed energy scans on the X...N (X being any halogen) distance with a stepsize equal to 0.07 Å. All DFT calculations were carried out using the Gaussian 09 software [103], while Keith's AIMAll program [104] was used for the whole topological analysis.

16.3 Unravelling Halogen Bond Formation with the QTAIM-IQA Approach

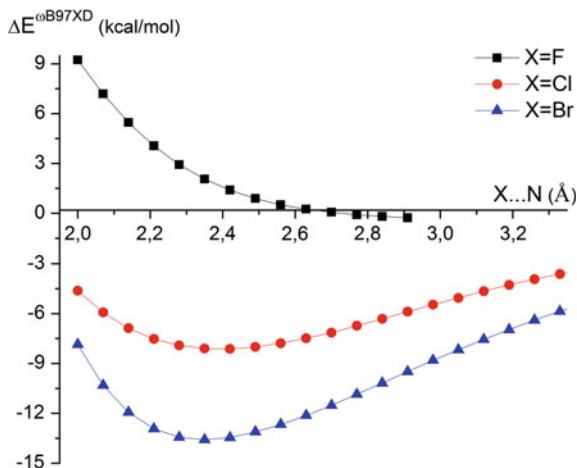
As first examples, we will consider the $\text{Cl}_3\text{COX}\dots\text{NH}_3$ complexes (X = F, Cl, and Br) that belong to the $\text{R}_3\text{COX}\dots\text{NH}_3$ family, which was studied by Politzer [56] and recently revisited by us within the framework of conceptual DFT [67] and density Laplacian maps [68].

16.3.1 Potential Energy Surfaces

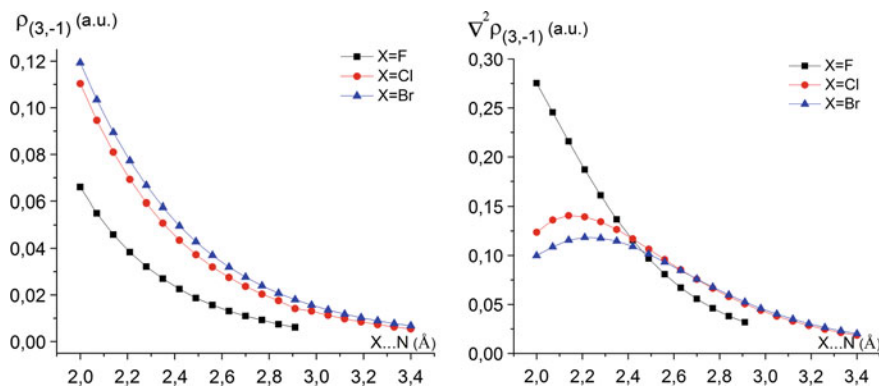
The potential energy surface along the X...N distance coordinate for the three complexes is represented in Graph 16.1.

It clearly appears that an energy minimum (from the SCF energy point of view) is located in the chlorine and bromine cases, while the curve exhibits an overall repulsive interaction between the two moieties for X = F.¹ Consistently with the higher bromine electrophilicity and its higher polarizability, the complexation energy is larger for Br than for Cl. Noticeably, while bromine is in general a bigger atom than chlorine, the equilibrium distance for the bromine complex is slightly smaller than that for the chlorine one: the contraction due to the halogen bond formation is thus larger.

¹Very small negative values for large separation distances are due to basis set superposition errors.



Graph 16.1 Relative energies (with respect to the optimized free fragments) for the $\text{Cl}_3\text{COX}\dots\text{NH}_3$ complexes as a function of the $\text{X}\dots\text{N}$ distance



Graph 16.2 Variations of $\rho_{(3,-1)}$ (left) and $\nabla^2\rho_{(3,-1)}$ (right) as a function of the $\text{X}\dots\text{N}$ distance for the $\text{Cl}_3\text{COX}\dots\text{NH}_3$ complexes

16.3.2 Electron Density Topology

The same topology is observed at any distance for the three systems: a $(3, -1)$ CP is present between the two moieties.² This is actually expected from the Poincaré-Hopf (PH) relationship, as derived in Ref. [105]. Indeed, the two fragments keep

²It is fundamental to notice that this critical point is a BCP at the equilibrium geometry for the chlorine and bromine complexes, while no BCP is present along the fluorine pathway since it does not feature any equilibrium geometry.

their promolecular essence in the complex since they still fulfil the PH equality given by Eq. 16.18. Thus, in order that the total complex also respects PH at the molecular level, at least one (3, -1) or one (3, -3) must be created, a pure mathematical effect, independent of the nature of the interactions between the moieties (as also discussed in Ref. [65]). Graph 16.2 shows the variations of the electron density and laplacian values at this (3, -1) CP.

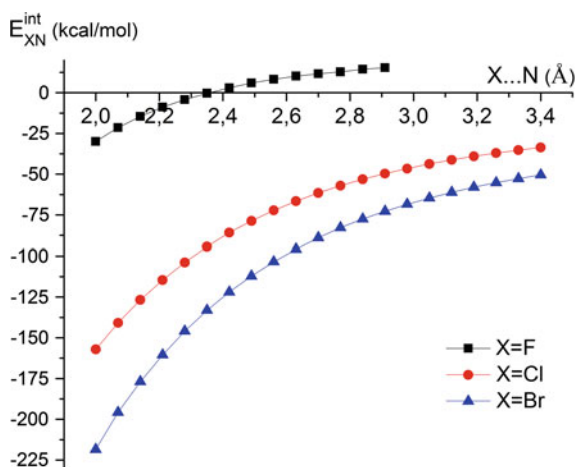
The curves are all similar in the attractive part of the potential energy surface: the electron density and laplacian values increase, but $\rho_{(3,-1)}$ remains small (consistently with the assumed non-covalent nature of the interactions), and $\nabla^2\rho_{(3,-1)}$ is still positive (in accordance with their expected noncovalent character). However, these (3, -1) CP properties do not enable to discriminate between stable and unstable complexes (that is between X = Br, Cl on one hand, and X = F on the other hand).

It can be added that neither do some other local real space approaches like the noncovalent interactions index (NCI) [106], which will predict attraction in all cases due to the presence of this (3, -1) CP, as also revealed for similar systems by Cormanich et al. [107]. Such local approaches should thus be complemented by integrated ones. To this aim, the IQA scheme is certainly particularly appealing.

16.3.3 Energy Decomposition of the Primary X...N Interaction

As discussed in the theory section, these DFT relative energies include both intraatomic and interatomic contributions. We will firstly examine the primary interatomic interaction between atoms X and N within the KS-IQA formalism (Eqs. 16.5 and 16.16) as represented in Graph 16.3.

Graph 16.3 IQA interaction energies between atoms X and N (primary interaction) as a function of the X...N distance for the $\text{Cl}_3\text{COX}\dots\text{NH}_3$ complexes



It is found negative at any distance for Cl and Br (more stabilizing in that case), being larger and larger as the distance decreases. On the contrary, it is noteworthy that the F...N interaction, which is destabilizing at long range, becomes slightly negative in energy when the distance is lower than about 2.3 Å (but not enough to overcome the other factors of destabilization, which will be discussed later).

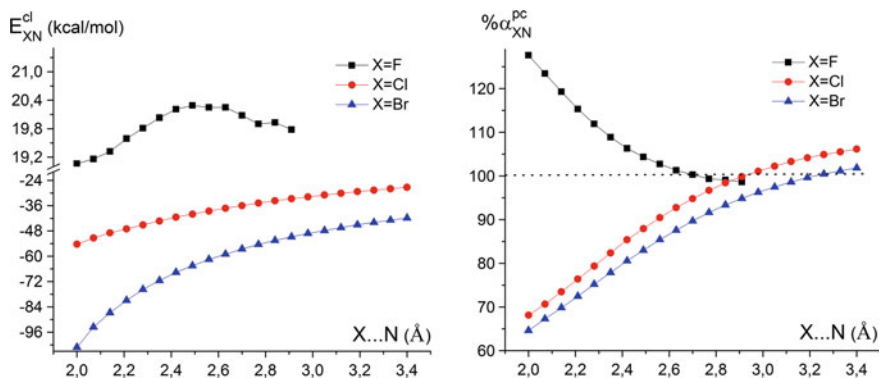
The nature of these diatomic interactions can be further elucidated by decomposing them into their classical electrostatic and exchange-correlation (in fact, exchange in our KS-IQA treatment, see Eq. 16.16) counterparts. As evidenced by the left part of Graph 16.4, the interaction is stabilizing from a classical electrostatic point of view at any distance for Cl and Br complexes, while it is destabilizing whatever the F...N separation.

It is instructive to investigate the weight of the atomic point charges interaction by defining the following ratio:

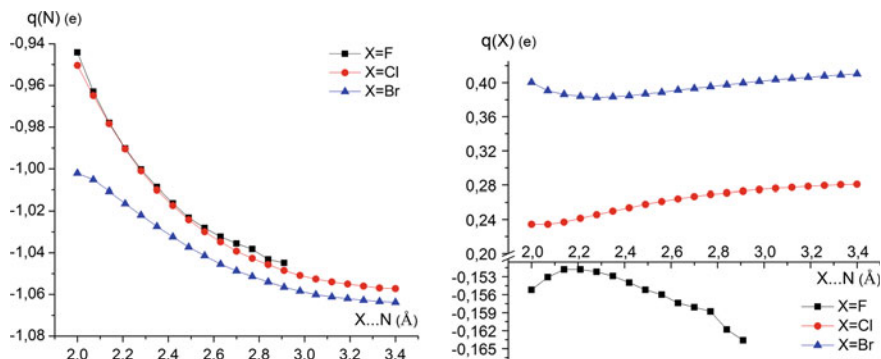
$$\% \alpha_{XN}^{pc} = 100 \frac{q(N)q(X)}{R_{XN} E_{XN}^{cl}}. \quad (16.19)$$

The corresponding curves are plotted in the right part of Graph 16.4.

As the point charges interaction is the most long-range one (since it decreases in $1/R$, while the other terms in the multipolar expansion behave like $1/R^n$), it is intuitive that $\% \alpha_{XN}^{pc}$ is close to 100 when the fragments are sufficiently remote. For smaller distances, a clear dichotomy appears: $\% \alpha_{XN}^{pc}$ increases, becoming larger than 100 for fluorine, whereas it decreases for the two other systems. In other words, the higher multipolar effects tend to be opposite (stabilizing the interaction) to the point charges ones for fluorine, while they become of the same magnitude and of the same sign for chlorine and bromine (see also Ref. [108] for another study of multipolar effects in halogen bonds). Such competitions can be accounted for by



Graph 16.4 Classical electrostatic energy component (*left*) and weight of the corresponding point charges contribution to it (*right*, $\% \alpha_{XN}^{pc} = 100 \frac{q(F)q(X)}{r_{FX} E_{XN}^{cl}}$ ratio) for the X...N primary interaction as a function of the X...N distance for the $\text{Cl}_3\text{COX}\dots\text{NH}_3$ complexes. Please note the break at the middle of the y-axis with two different scales



Graph 16.5 Selected atomic charges variations as a function of the X...N distance for the $\text{Cl}_3\text{COX}\dots\text{NH}_3$ complexes. Please note the break in the y-axis for the right part with two different scales

looking at the evolution of the atomic charges along the formation path, as represented in Graph 16.5.

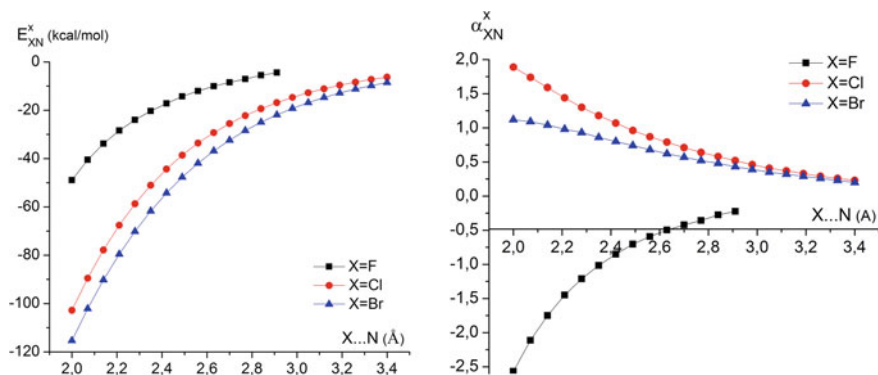
For the three complexes, the atomic charge on nitrogen is strongly negative (about $-1.0 e$). As the distance becomes smaller, it loses in any case some electrons (at most $0.1 e$ for chlorine when $\text{Cl}\dots\text{N} = 2.0 \text{ \AA}$). It can be then expected that the charge on X will decrease due this direct charge transfer. As shown in the right part of Graph 16.5, this is partly true for bromine and chlorine (it can be noticed that not the whole charge lost by N is recovered by Cl and Br, due to the presence of another electron acceptor atom (O) in the molecule), but the charge can be considered as remaining constant for fluorine (the variation only amounting to $0.01 e$).

More importantly, the charges on Br and Cl are always positive, while it is negative at any scan point on fluorine owing to its strong electronegativity. As a consequence, along the studied pathways, $q(F)q(X)/R_{FX}$ is negative for the Br and Cl complexes, and positive for the F one, precluding, in this last case, the formation of halogen bond from the classical electrostatic point of view.

However, this is not the only contribution to the interaction energy. One should in particular scrutinize exchange counterpart (that is negative by definition), which is plotted in the left part of Graph 16.6.

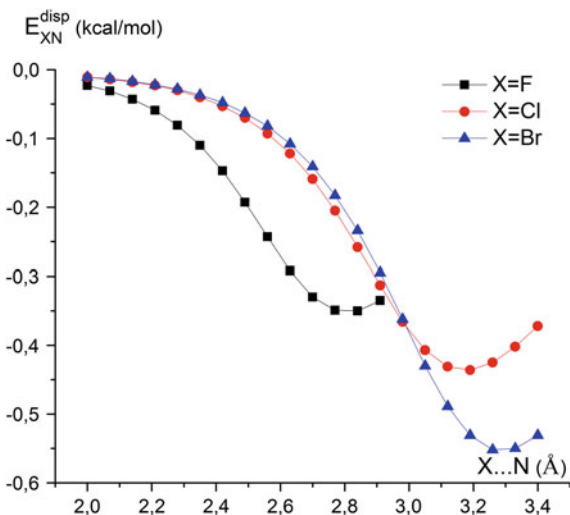
In all cases, it is higher in absolute value when the interaction distance is small. Nevertheless, while it reaches the -100 kcal/mol value for Br and Cl (the two curves being very similar), it is considerably lower in absolute value in $\text{Cl}_3\text{COF}\dots\text{NH}_3$ (less than 50 kcal/mol at the smallest studied distance), but, in this case, it is enough high to overcome the classical electrostatic destabilization. Thus, in order to have more insight on the influence of exchange in bonding, it is valuable to introduce the following ratio (see the right part of Graph 16.6).

$$\alpha_{XN}^x = \frac{E_{XN}^x}{E_{XN}^{\text{cl}}}. \quad (16.20)$$



Graph 16.6 Interaction exchange energy (left) and $\alpha_{XN}^x = \frac{E_{XN}^x}{E_{XN}^{cl}}$ ratio (right) for the X...N primary interaction as a function of the X...N distance for the $\text{Cl}_3\text{COX}\dots\text{NH}_3$ complexes

Graph 16.7 Interaction energy due to dispersion for the X...N primary interaction as a function of the X...N distance for the $\text{Cl}_3\text{COX}\dots\text{NH}_3$ complexes



As exchange is usually less long-range than classical electrostatics, it is not surprising that α_{XN}^x tends toward 0 for large separation distances. Conversely, it becomes predominant at small distances (smaller than approximately 2.4 Å, corresponding to $|\alpha_{XN}^x| > 1$). For instance, for $\text{F}\dots\text{N} = 2.0$ Å, $E_{FN}^x = -48.9$ kcal/mol (while $E_{FN}^{cl} = +19.6$ kcal/mol). This hierarchy also holds for the other halogens, as exemplified by the bromine case: $E_{BrN}^x = -115.3$ kcal/mol (while $E_{BrN}^{cl} = -103.1$ kcal/mol for $\text{Br}\dots\text{N} = 2.0$ Å).

At such distances, the use, as an interpretative tool, of the molecular electrostatic potential (which is simply the Gâteaux derivative of the molecular classical electrostatic energy functional with respect to the electron density) becomes arguable since classical electrostatics does not exclusively drive the studied interactions. This

is in particular the case at the equilibrium distances for the Cl and Br complexes for which $\alpha_{Cl,BrN}^x \approx 0.9 - 1.1$. This dual character of the formed halogen bond (classical electrostatics and exchange are comparable) is also reflected in the delocalization indexes values that lie in the [0.4; 0.5] range in the bonding part of the potential energy surfaces (note that these values still remain far from 1.0 (reached for instance by the C–C bond in ethane), so that these bonds cannot be considered covalent).

Lastly, as recalled in the theory section, our KS-IQA treatment does not enable to properly extract pure correlation effects, but we proposed to use the B3LYP-D2 approach to evaluate dispersion (see Eq. 16.17). Graph 16.7 thus shows the corresponding estimated X...N dispersion energy:

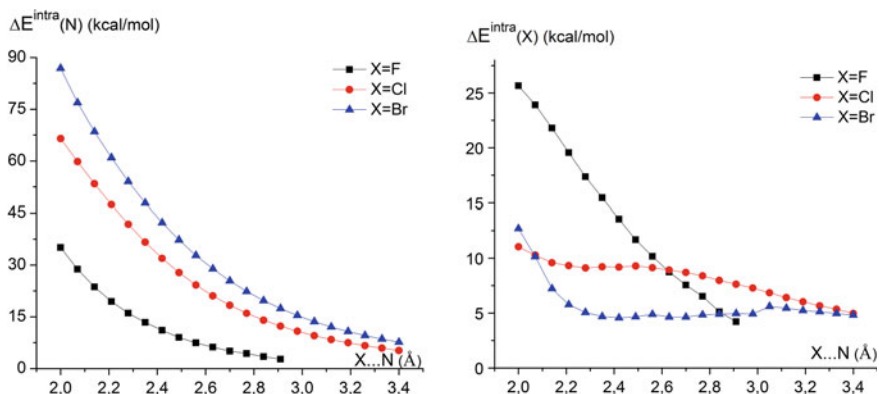
As the C_6 coefficients mainly depend on the atomic polarizability (cf. London's model), dispersion is more important for bromine, then chlorine, and remains small for fluorine. Yet, in any case, it is smaller than 0.6 kcal/mol in absolute value, so that its contribution to the primary interaction is negligible with respect to classical electrostatic and exchange in the three studied complexes. It can also be noticed that if dispersion between X and N was the main factor driving the formation of these halogen bonds, then the equilibrium distance would be significantly larger (about 3.0 Å).

16.3.4 Role of the Intraatomic Energies

Up to now, it should be remarked that none of the presented curves for the primary halogen...nitrogen interaction energies parallels those for the molecular energy. There is however no contradiction, since, as investigated in details in Ref. [63], secondary interactions and intraatomic (i.e. monobasin or "self") energetic components are important contributions to take into account in order to recover the total molecular interaction energies.

We illustrate this last point by inspecting the variation of the monobasin nitrogen and halogen self energies, plotted in Graph 16.8.

For all adducts, $E^{intra}(N)$ is increasing when the distance decreases, the nitrogen atom being more and more destabilized, which is in line with the observation that it loses electrons. For instance, at 2.0 Å, it is equal to +35.1 kcal/mol for the fluorine complex, a value that is higher in absolute value than the F...N interaction energy (−29.8 kcal/mol), impeding the formation of a stable species. The variations for the halogen atoms are more difficult to interpret. For Br and Cl, the halogen intraatomic energy is rather constant in the (2.2; 3.0 Å) range, certainly due to the fact that these atoms partly get electrons lost by nitrogen. On the contrary, as the fluorine population only varies little, there is no electron transfer to prevail on the destabilization induced by the density reorganization (and the concomitant rise of the atomic kinetic energy) inside the basin.



Graph 16.8 Variations of intraatomic (“self”) energies with respect to the X...N distance (the origin corresponding to the self energies inside the isolated optimized fragment) for the $\text{Cl}_3\text{COX} \dots \text{NH}_3$ complexes

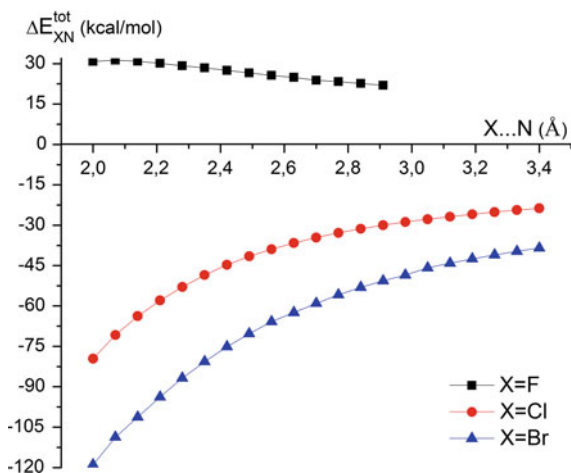
From all these previous considerations, it seems judicious to define the following descriptor that involves the main energetic components linked to the primary atoms:

$$\Delta E_{\text{XN}}^{\text{tot}} = E_{\text{XN}}^{\text{QA}} + E_{\text{XN}}^{\text{disp}} + \Delta E_{\text{IQA}}^{\text{intra}}(X) + \Delta E_{\text{IQA}}^{\text{intra}}(N), \quad (16.21)$$

where ΔE^{intra} is calculated with respect to the intraatomic energy in the relevant free isolated fragment. The evolutions of this quantity are depicted in Graph 16.9.

A clear dichotomy is then revealed: $\Delta E_{\text{FN}}^{\text{tot}}$ is always positive and is increasing when the distance F...N is decreased, in concordance with the absence of an equilibrium geometry, whereas $\Delta E_{\text{BrN}}^{\text{tot}}$ and $\Delta E_{\text{ClN}}^{\text{tot}}$ are negative and decreasing when the two moieties get closer, the effect being enhanced for bromine. Obviously,

Graph 16.9 $\Delta E_{\text{XN}}^{\text{tot}}$ (as defined by Eq. 16.21) variations with respect to the X...N distance for the $\text{Cl}_3\text{COX} \dots \text{NH}_3$ complexes



ΔE_{XN}^{tot} does not enable to retrieve the full molecular energy since the secondary interactions and the intraatomic energies of the secondary atoms, whose evaluation can be very time-consuming for large systems (there are about N^2 atoms pairs and IQA implies 6D-integrations), are not included. However, ΔE_{XN}^{tot} provides an expeditious semi-quantitative view of analysing the fundamental role of the primary atoms for the formation of halogen bonds.

16.3.5 The Case of the Fluorine Bond

It was long thought that fluorine cannot be engaged in halogen bonds. Nevertheless, both experimental and theoretical evidence was given that, when F is linked to very electronegative groups, a σ -hole could appear on the outer part of it, so that it can form a stable complex with a Lewis base [109, 110]. Such a case is epitomized by the F_2 molecule, where the σ -hole (developed in the F–F axis) can be visualized (see Ref. [111] for the corresponding figures) by both the electrostatic potential and the first-state specific dual descriptor [112]. As a consequence, a minimum on the potential energy surface is obtained when F_2 interacts with $NCCH_3$,³ featuring the F...N distance equal to 3.07 Å, while the molecular complexation energy is equal to –0.70 kcal/mol.

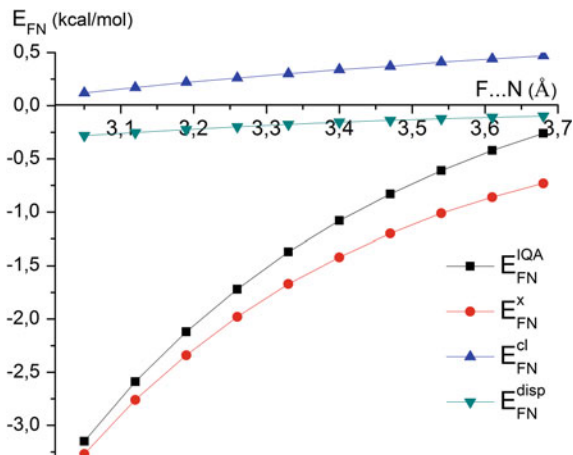
The primary interaction energy decomposition is presented in Graph 16.10 for the attractive part of the potential energy surface.

At variance with the $Cl_3COF...NH_3$ complex, E_{FN}^{IQA} is negative whatever the distance, and increasing in absolute value when the two fragments come closer. This curve is parallel to that for exchange. The classical electrostatic part is also decreasing, but remains positive at any point of the potential energy surface. In other words, it is destabilizing, which seems to contradict the σ -hole paradigm. To have more insight on this electrostatic component, atomic charges are represented in Graph 16.11.

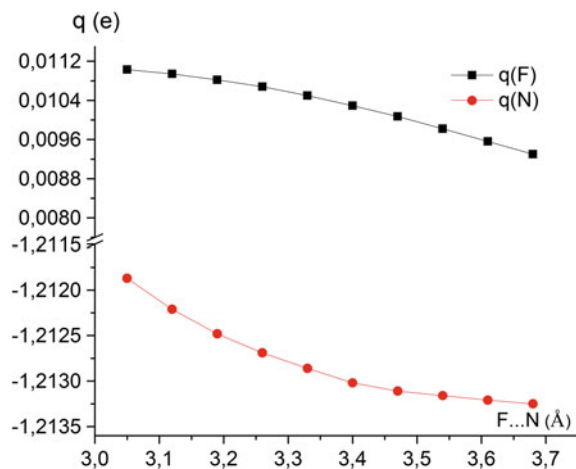
As previously noticed, nitrogen is negatively charged and loses electrons when the distance decreases, but the variation is here one order of magnitude smaller than in $Cl_3OF...NH_3$ (about 0.01 e with respect to around 0.1 e). On the contrary, fluorine is now positively charged (we recall that for the isolated fragment it is exactly neutral) and its charge increases when the interaction distance decreases. These results may seem paradoxical since nitrogen also loses electrons. One thus may have expected this fluorine atom to gain them. To illustrate the electronic distribution between atoms, one finds at the equilibrium position, $q(N) = -1.212 e$, while $q(F) = 0.011 e$. Interestingly, for the secondary fluorine atom: $q(F') = -0.018$

³We use this partner instead of NH_3 because, with ammonia, the creation of a F...H–N hydrogen bond is largely favoured; besides, the $F_2...NCCH_3$ complex has been already studied by Politzer and coworkers [109], so that comparisons of the different theoretical approaches are possible.

Graph 16.10 Analysis of the interaction energy between F and N atoms as a function of the F...N distance in the F₂...NCCH₃ complex

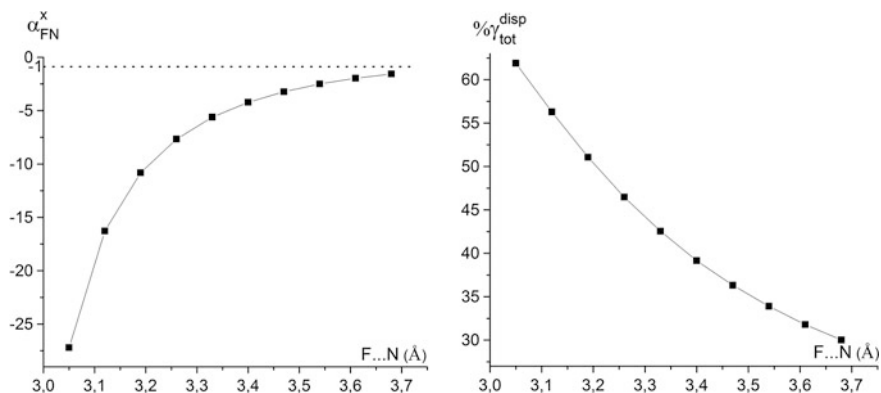


Graph 16.11 Variation of the atomic charges for F and N as a function of the F...N distance in the F₂...NCCH₃ complex. Please note the break in the y-axis



e. It follows that the electrons lost by nitrogen are actually captured by the other (secondary) fluorine atom.

It also results from these charges signs that the pure point charges contributions, E_{FN}^{pc} , to the classical electrostatic interaction is always stabilizing, contrarily to the total classical electrostatic part. When going from F...N = 3.68 to F...N = 3.05 Å, E_{FN}^{pc} varies from -1.02 to -1.45 kcal/mol, while E_{FN}^{cl} goes from +0.47 to +0.12 kcal/mol, which implies that the atomic charges are not enough high to fully overcome the destabilization induced by the higher multipolar moments. In summary, even if fluorine is not a much polarizable atom and accordingly generates rather small atomic multipoles, the sum of these quantities dominates the small positive monopole.



Graph 16.12 $\alpha_{FN}^x = \frac{E_{FN}^x}{E_{FN}^{tot}}$ (left) and $\% \gamma_{tot}^{disp}$ (right, see Eq. 16.22 for definition) ratios with respect to the F...N distance for the $F_2 \dots NCCH_3$ complex

As previously done, the classical electrostatic contribution can be compared to that of exchange through the α_{FN}^x descriptor, as shown in the left part of Graph 16.12.

Its negative sign is plain from our preceding remarks. The weight of exchange considerably increases as the two partners come closer. Importantly, even for the largest studied distance (3.68 Å), it is higher than 1.5 in absolute value, indicating that exchange is already preponderant at this separation (below the horizontal dotted line at $y = -1$ in Graph 16.12). This is thus exchange that mainly describes the F...N interaction.

As for the intraatomic contributions, as expected, both F and N ones decrease in absolute value when the F...N distance is reduced. These destabilizing factors are thus once again in competition with the stabilizing interaction energy (mainly due to exchange). All these effects can be gathered in ΔE_{FN}^{tot} (Eq. 16.21). We found that within the (3.05; 3.68 Å) range, it is monotonically decreasing from 4.1 to 3.0 kcal/mol. The curve is henceforth very flat, in strong contrast to the $Cl_3COF \dots NH_3$ complex (for which the ΔE_{FN}^{tot} variation inside the studied F...N distance range was almost equal to 20 kcal/mol). Fluorine and nitrogen are thus considerably less “reluctant” to halogen bond formation.

It is also enlightening to look at the secondary interactions. As an example, Fig. 16.1 reports selected interaction energies between atoms of the two fragments.

It shows, for instance, that the interaction energy, E'_1 , between the other fluorine atom (labelled F8 in Fig. 16.1) and nitrogen is not at all negligible with respect to the primary interaction (−1.9 kcal/mol to be compared with −2.9 kcal/mol). However, this secondary interaction is partly compensated by another one, E'_2 , between the same secondary fluorine and the carbon atom adjacent to the nitrogen (+1.1 kcal/mol), so that $E'_1 + E'_2$ equals −0.8 kcal/mol. Please note that we refer the interested reader to our recent paper [63] for a closer and more systematic look at all

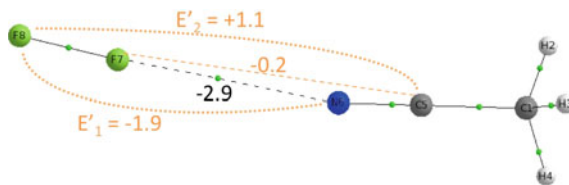


Fig. 16.1 Selected IQA interaction energies (which does not include dispersion correction) for the $F_2 \dots NCCH_3$ complex at its equilibrium geometry. All values in kcal/mol

these secondary contributions that very often compensate between themselves or with the primary ones.

We have not yet discussed the role of dispersion. From Graph 16.7, it appears to be a negligible contribution to the interaction between F and N (about -0.3 kcal/mol). However, contrary to electrostatics, dispersion between the two fragments (evaluated using the B3LYP-D2 correction) is cumulative: all atomic pairs contribute to the stabilization of the complex without compensation due to sign changes (contrarily to the classical electrostatic contribution). It is thus informative to consider the following ratio that evaluates the total contribution of dispersion to the complexation energy:

$$\begin{aligned} \% \gamma_{tot}^{disp} &= 100 \frac{\Delta E^{disp}}{\Delta E_{\omega B97XD}} \\ &= 100 \frac{E_{B3LYPD2}^{disp}(F_2 \dots NCCH_3) - E_{B3LYPD2}^{disp}(F_2) - E_{B3LYPD2}^{disp}(NCCH_3)}{E_{\omega B97XD}^{SCF}(F_2 \dots NCCH_3) - E_{\omega B97XD}^{SCF}(F_2) - E_{\omega B97XD}^{SCF}(NCCH_3)}. \end{aligned} \quad (16.22)$$

As shown in the right part of Graph 16.12, the weight of dispersion increases when the distance decreases, reaching more than 60 % at the equilibrium distance, while the contribution of dispersion to the primary interaction energy is negligible. It is thus clear from this simple example that distinguishing total complexation energy from the primary interaction energy is pivotal to a physical analysis of any halogen bond.

16.4 Conclusions

In this chapter, we provided evidence that Bader's atoms-in-molecules provides deep physical insight into the formation mechanism of halogen bonds. Within this framework, the interacting quantum atoms decomposition enables to cure the deficiencies of the local approach based on critical points, and to rigorously assess the importance of classical electrostatics and quantum effects in terms of energetic quantities. It was notably shown that even if classical electrostatics (that can be further decomposed into charge points and multipolar components) generally

predominates at long range, exchange becomes an important contribution around the equilibrium position. Furthermore, the role of atomic destabilization was also discussed, as well as that of secondary interactions, proving that the stabilization energy of a halogen-bonded complex is the sum of competing effects, and does not reduce to the interaction energy between the halogen atom and the nucleophilic atom of the Lewis base. This is conversely the subtle combination of various factors that make such interactions challenging and incentivizing for both experimentalists and theoreticians.

Acknowledgements V.T. and L.J. gratefully acknowledge the CRIHAN computational centre for providing computational resources, the Centre National de la Recherche Scientifique (CNRS) for a “Chaire d’Excellence” at the University of Rouen, and the Labex SynOrg (ANR-11-LABX-0029).

References

1. Desiraju RG, Ho PS, Kloo L, Legon AC, Marquardt E, Metrangolo P, Politzer P, Resnati G, Rissanen K (2013) Definition of the halogen bond (IUPAC recommendations 2013). *Pure Appl Chem* 85:1711–1713
2. Metrangolo P, Pilati T, Resnati G (2006) Halogen bonding and other noncovalent interactions involving halogens: a terminology issue. *Cryst Eng Comm* 8:946–947
3. Metrangolo P, Resnati G (eds) (2008) *Halogen bonding: fundamentals and applications, structure and bonding*. Struct Bond 126. Springer, Berlin
4. Metrangolo P, Resnati G (2012) Halogen bonding: where we are and where we are going. *Cryst Growth Des* 12:5835–5838
5. Legon AC (2010) The halogen bond: an interim perspective. *Phys Chem Chem Phys* 12:7736–7747
6. Fourmigué M (2009) Halogen bonding: recent advances. *Curr Opin Solid State Mater Sci* 13:36–45
7. Cavallo G, Metrangolo P, Pilati T, Resnati G, Terraneo G (2015) Halogen bond: a long overlooked interaction. *Top Curr Chem*, Top Curr Chem 358:1–17
8. Scholfield MR, Zanden CM, Carter M, Ho PS (2013) Halogen bonding (X-bonding): a biological perspective. *Protein Sci* 22:139–152
9. Lu Y, Wang Y, Zhu W (2010) Nonbonding interactions of organic halogens in biological systems: implications for drug discovery and biomolecular design. *Phys Chem Chem Phys* 12:4543–4551
10. Auffinger P, Hays FA, Westhof E, Ho S (2004) Halogen bonds in biological molecules. *Proc Natl Acad Sci USA* 101:16789–167945
11. Hardegger L-A, Kuhn B, Spinnler B, Anselm L, Ecabert R, Stihle M, Gsell B, Thoma R, Diez J, Benz J, Plancher J-M, Hartmann G, Banner DW, Haap W, Diederich F (2011) Systematic investigation of halogen bonding in protein-ligand interactions. *Angew Chem Int Ed* 50:314–318
12. Jentzsch AV, Matile S (2013) Transmembrane halogen-bonding cascades. *J Am Chem Soc* 135:5302–5303
13. Wilcken R, Zimmermann MO, Lange A, Joerger AC, Boeckler FM (2013) Principles and applications of halogen bonding in medicinal chemistry and chemical biology. *J Med Chem* 56:1363–1388
14. Parisini E, Metrangolo P, Pilati T, Resnati G, Terraneo G (2011) Halogen bonding in halocarbon-protein complexes: a structural survey. *Chem Soc Rev* 40:2267–2278

15. Lu Y, Shi T, Wang Y, Yang H, Yan X, Luo X, Jiang H, Zhu W (2009) Halogen bonding—a novel interaction for rational drug design? *J Med Chem* 52:2854–2862
16. Priimagi A, Cavallo G, Metrangolo P, Resnati G (2013) The halogen bond in the design of functional supramolecular materials: recent advances. *Acc Chem Res* 46:2686–2695
17. Metrangolo P, Resnati G, Pilati T, Biella S (2008) Halogen bonding in crystal engineering. *Struct Bonding (Berlin)* 126:105–136
18. Meyer F, Dubois P (2013) Halogen bonding at work: recent applications in synthetic chemistry and materials science. *Cryst Eng Comm* 15:3058–3071
19. Metrangolo P, Resnati G, Pilati T, Liantonio R, Meyer F (2007) Engineering functional materials by halogen bonding. *J Polym Sci Part A Polym Chem* 45:1–15
20. Metrangolo P, Meyer F, Pilati T, Resnati G, Terraneo G (2008) Halogen bonding in supramolecular chemistry. *Angew Chem Int Ed* 47:6114–6127
21. Metrangolo P, Resnati G (2001) Halogen bonding: a paradigm in supramolecular chemistry. *Chem Eur J* 7:2511–2519
22. Voth AR, Hays FA, Ho PS (2007) Directing macromolecular conformation through halogen bonds. *Proc Natl Acad Sci USA* 104:6188–6193
23. Nguyen HL, Horton PN, Hursthouse MB, Legon AC, Bruce DW (2004) Halogen bonding: a new interaction for liquid crystal formation. *J Am Chem Soc* 126:16–17
24. Ueda K, Oguna M, Asaji T (2014) Halogen bond as controlling the crystal structure of 4-amino-3,5-dihalogenobenzoic acid and its effect on the positional ordering/disordering of acid protons. *Cryst Growth Des* 14:6189–6196
25. Shirman T, Kaminker R, Freeman D, van der Boom ME (2011) Halogen-bonding mediated stepwise assembly of gold nanoparticles onto planar surfaces. *ACS Nano* 5:6553–6563
26. Kniep F, Jungbauer SH, Zhang Q, Walter SM, Schindler S, Schnapperelle I, Herdtweck E, Huber SM (2013) Organocatalysis by neutral multidentate halogen-bond donors. *Angew Chem Int Ed* 52:7028–7032
27. Takeda Y, Hisakuni D, Lin C-H, Minataka S (2015) 2-Halogenoimidazolium salt catalyzed Aza-diels–alder reaction through halogen-bond formation. *Org Lett* 17:318–321
28. Lefèvre G, Franc G, Adamo C, Jutand A, Ciofini I (2012) Influence of the formation of the halogen bond ArX.N on the mechanism of diketone ligated copper-catalyzed amination of aromatic halides. *Organometallics* 31:914–920
29. Benesi HA, Hildebrand JH (1948) Ultraviolet absorption bands of iodine in aromatic hydrocarbons. *J Am Chem Soc* 70:2832–2833
30. Novick SE, Janda KC, Klempner W (1976) HFCIF: structure and bonding. *J Chem Phys* 65:5115–5121
31. Stephens SL, Walker NR, Legon AC (2011) Internal rotation and halogen bonds in CF₃⋯NH₃ and CF₃⋯N(CH₃)₃ probed by broadband rotational spectroscopy. *Phys Chem Chem Phys* 13:20736–20744
32. Stephens SL, Mizukami W, Tew DP, Walker NR, Legon AC (2012) The halogen bond between ethene and a simple perfluoroiodoalkane: C₂H₄⋯ICF₃ identified by broadband rotational spectroscopy. *J Mol Spectrosc* 280:47–53
33. Weingarth M, Raouafi N, Jouvelet B, Duma L, Bodenhausen G, Boujlel K, Scöllhorn B, Tekley P (2008) Revealing molecular self-assembly and geometry of non-covalent halogen bonding by solid-state NMR spectroscopy. *Chem Commun* 45:5981–5983
34. Chudzinski MG, McClary CA, Taylor MS (2011) Anion receptors composed of hydrogen- and halogen-bond donor groups: modulating selectivity with combinations of distinct noncovalent interactions. *J Am Chem Soc* 133:10559–10567
35. Hauchecorne D, Szostak R, Herrebout WA, van der Vekken BJ (2009) CX⋯O Halogen bonding: interactions of trifluoro- methyl halides with dimethyl ether. *Chem Phys Chem* 10:2105–2115
36. Cappelletti D, Candori P, Pirano F, Belpassi L, Tarantelli F (2011) Nature and stability of weak halogen bonds in the gas phase: molecular beam scattering experiments and ab initio charge displacement calculations. *Cryst Growth Des* 11:4279–4283

37. Hassel O, Hvorslev J (1954) The structure of bromine 1,4-dioxanate. *Acta Chem Scand* 8:873–873
38. Erdélyi M (2012) Halogen bonding in solution. *Chem Soc Rev* 41:3547–3557
39. McAllister LJ, Bruce DW, Karadakov PB (2012) Quantum chemical investigation of attractive non-covalent interactions between halomethanes and rare gases. *J Phys Chem A* 116:10621–10628
40. Riley KE, Hobza P (2011) Strength and character of halogen bonds in protein-ligand complexes. *Cryst Growth Des* 11:4272–4278
41. Grabowski SJ (2012) QTAIM characteristics of halogen bond and related interactions. *J Phys Chem A* 116:1838–1845
42. Grabowski SJ (2011) Halogen bond and its counterparts: Bent's rule explains the formation of nonbonding interactions. *J Phys Chem A* 115:12340–12347
43. Grabowski SJ (2012) Non-covalent interactions—QTAIM and NBO analysis. *J Mol Model* 19:4713–4721
44. Grabowski SJ (2013) Hydrogen and halogen bonds are ruled by the same mechanisms. *Phys Chem Chem Phys* 15:7249–7259
45. Domagała M, Matczak P, Palusiak M (2012) Halogen bond, hydrogen bond and N...C interaction—on interrelation among these three noncovalent interactions. *Comp Theor Chem* 998:26–33
46. Palusiak M (2010) On the nature of halogen bond—the Kohn-Sham molecular orbital approach. *J Mol Struct (Theochem)* 945:89–92
47. Xu L, Lv J, Sang P, Zou JW, Yu QS, Xu MB (2011) Comparative insight into the halogen bonding of 4-chloropyridine and its metal [CuI, ZnII] coordinations with halide ions: a theoretical study on M-C-X...XO. *Chem Phys* 379:66–72
48. Riley KE, Hobza P (2008) Investigations into the nature of halogen bonding including symmetry adapted perturbation theory analyses. *J Chem Theory Comput* 4:232–242
49. Wang Z, Liu Z, Ding X, Yu X, Hou B, Yi P (2012) Comparisons of the halogen-bonded and hydrogen-bonded complexes of furan, thiophene and pyridine with Lewis acids (ClF, HCl). *Comp Theor Chem* 981:1–6
50. Wang C, Danovich D, Mo Y, Shaik S (2014) On the nature of the halogen bond. *J Chem Theory Comput* 10:3726–3737
51. Solomon RV, Vedha SA, Venuvanalingam P (2014) A new turn in codon-anticodon selection through halogen bonds. *Phys Chem Chem Phys* 16:7430–7440
52. Politzer P, Murray JS (2013) Halogen bonding: an interim discussion. *Chem Phys Chem* 14:278–294
53. Politzer P, Murray JS, Clark T (2013) Halogen bonding and other σ -hole interactions: a perspective. *Phys Chem Chem Phys* 15:11178–11189
54. Politzer P, Riley KE, Bulat FA, Murray JS (2012) Perspectives on halogen bonding and other σ -hole interactions: *lex parsimoniae* (Occam's Razor). *Comp Theor Chem* 998:2–8
55. Politzer P, Murray JS, Clark T (2010) Halogen bonding: an electrostatically-driven highly directional noncovalent interaction. *Phys Chem Chem Phys* 12:7748–7757
56. Brinck T, Murray JS, Politzer P (1992) Surface electrostatic potentials of halogenated methanes as indicators of directional intermolecular interactions. *Int J Quantum Chem* 44:57–64
57. Johansson MP, Swart M (2013) Intramolecular halogen–halogen bonds? *Phys Chem Chem Phys* 15:11543–11553
58. Bartashevich EV, Troitskaya EA, Tsirelson VG (2014) The N...I halogen bond in substituted pyridines as viewed by the source function and delocalization indices. *Chem Phys Lett* 601:144–148
59. Bartashevich EV, Troitskaya EA, Pendás AM, Tsirelson VG (2016) Understanding the bifurcated halogen bonding N...Hal...N in bidentate diazaheterocyclic compounds. *Comput Theor Chem* 1053:229–237

60. Bartashevich EV, Yushina ID, Stash AI, Tsirelson VG (2014) Halogen bonding and other iodine interactions in crystals of dihydrothiazolo(oxazino)quinolinium oligoiodides from the electron-density viewpoint. *Cryst Growth Des* 14:5674–5684
61. Tognetti V, Joubert L (2013) On the physical role of exchange in the formation of an intramolecular bond path between two electronegative atoms. *J Chem Phys* 138:024102
62. Tognetti V, Joubert L (2013) On critical points and exchange-related properties of intramolecular bonds between two electronegative atoms. *Chem Phys Lett* 579:122–125
63. Syzgantseva OA, Tognetti V, Joubert L (2013) On the physical nature of Halogen bonds: a QTAIM study. *J Phys Chem A* 117:8969–8980
64. Tognetti V, Joubert L (2014) Density functional theory and Bader's atoms-in-molecules theory: towards a vivid dialogue. *Phys Chem Chem Phys* 16:14539–14550
65. Tognetti V, Yahia-Ouahmed M, Joubert L (2014) Comment on "analysis of CF...FC interactions on cyclohexane and naphthalene frameworks". *J Phys Chem A* 118:9791–9792
66. Yahia-Ouahmed M, Tognetti V, Joubert L (2015) Halogen–halogen interactions in perhalogenated ethanes: an interacting quantum atoms study. *Comput Theor Chem* 1053:254–262
67. Tognetti V, Morell C, Joubert L (2015) Quantifying electro/nucleophilicity by partitioning the dual descriptor. *J Comput Chem* 36:649–659
68. Tognetti V, Joubert L (2015) Electron density Laplacian and halogen bonds. *Theor Chem Acc* 134:90
69. Bader RFW (1990) *Atoms in molecules: a quantum theory. the international series of monographs on chemistry: no. 22*, Oxford University Press, New York
70. Popelier PLA (2000) *Atoms in molecules: an introduction*. Pearson Education, Harlow
71. Pendás AM, Blanco MA, Francisco E (2004) Two-electron integrations in the quantum theory of atoms in molecules. *J Chem Phys* 120:4581–4592
72. Blanco MA, Pendás AM, Francisco E (2005) Interacting quantum atoms: a correlated energy decomposition scheme based on the quantum theory of atoms in molecules. *J Chem Theory Comput* 1:1096–1109
73. Pendás AM, Blanco MA, Francisco E (2006) Molecular energy decomposition scheme for atoms in molecules. *J Chem Theory Comput* 2:90–102
74. Popelier PLA, Joubert L, Kosov DS (2001) Convergence of the electrostatic interaction based on topological atoms. *J Phys Chem A* 105:8254–8261
75. Popelier PLA, Kosov DS (2001) Atom–atom partitioning of intramolecular and intermolecular Coulomb energy. *J Chem Phys* 114:6539–6547
76. Solano CJF, Pendás AM, Francisco E, Blanco MA, Popelier PLA (2010) Convergence of the multipole expansion for 1,2 Coulomb interactions: the modified multipole shifting algorithm. *J Chem Phys* 132:194110
77. Popelier PLA (2012) Quantum chemical topology: knowledgeable atoms in peptides. *AIP Conf Proc* 1456:261–268
78. Bader RFW, Matta CF (2004) Atomic charges are measurable quantum expectation values: a rebuttal of criticisms of QTAIM charges. *J Phys Chem A* 108:8385–8394
79. Tognetti V, Joubert L (2013) On the use of Bader's atomic charges for the evaluation of charge transfers between ground and excited states. *Chem Phys Lett* 557:150–153
80. Syzgantseva OA, Tognetti V, Boulangé A, Peixoto PA, Leleu S, Franck X, Joubert L (2014) Evaluating charge transfer in epicocconone analogues: toward a targeted design of fluorophores. *J Phys Chem A* 118(2014):757–764
81. Pendás AM, Blanco MA, Francisco E (2006) The nature of the hydrogen bond: a synthesis from the interacting quantum atoms picture. *J Chem Phys* 125:184112
82. Pendás AM, Francisco E, Blanco MA (2006) Binding energies of first row diatomics in the light of the interacting quantum atoms approach. *J Phys Chem A* 110:12864–12869
83. Tiana D, Francisco E, Blanco MA, Pendás AM (2009) Using pseudopotentials within the interacting quantum atoms approach. *J Phys Chem A* 113:7963–7971

84. Tiana D, Francisco E, Blanco MA, Macchi P, Sironi A, Pendás AM (2010) Bonding in classical and non-classical transition metal carbonyls: the interacting quantum atoms perspective. *J Chem Theory Comput* 6:1064–1074
85. Bartashevich EV, Pendás AM, Tsirelson VG (2014) An anatomy of intramolecular atomic interactions in halogen-substituted trinitromethanes. *Phys Chem Chem Phys* 16:16780–16789
86. Popov AA, Avdoshenko SM, Pendás AM, Dunsch L (2012) Bonding between strongly repulsive metal atoms: an oxymoron made real in a confined space of endohedral metallofullerenes. *Chem Commun* 48:8031–8050
87. Ferro-Costas D, Pendás AM, González Mosquera RA (2014) Beyond the molecular orbital conception of electronically excited states through the quantum theory of atoms in molecules. *Phys Chem Chem Phys* 16:9249–9258
88. Matta CF (2010) How dependent are molecular and atomic properties on the electronic structure method? comparison of Hartree-Fock, DFT, and MP2 on a biologically relevant set of molecules. *J Comput Chem* 31:1297–1311
89. Matta CF, Arabi AA, Keith TA (2007) Atomic partitioning of the dissociation energy of the PO(H) bond in hydrogen phosphate anion (HPO₄²⁻): disentangling the effect of Mg²⁺. *J Phys Chem A* 111:8864–8872
90. Riley KE, Murray JS, Fanfrlík J, Rezáč J, Solá RJ, Concha MC, Ramos FM, Politzer P (2013) Halogen bond tunability II: the varying roles of electrostatic and dispersion contributions to attraction in halogen bonds. *J Mol Model* 19:4651–4659
91. Grimme S (2006) Semiempirical GGA-type density functional constructed with a long-range dispersion correction. *J Comput Chem* 27:1787–1799
92. Cooper VR (2010) Van der Waals density functional: an appropriate exchange functional. *Phys Rev B* 81:161104
93. Foroutan-Nejad C, Shahbazian S, Marek R (2014) Toward a consistent interpretation of the QTAIM: tortuous link between chemical bonds, interactions and bond/line paths. *Chem Eur J* 20:10140–10152
94. Koch U, Popelier PLA (1995) Characterization of C–H–O hydrogen bonds on the basis of the charge density. *J Phys Chem* 99:9747–9754
95. Popelier P, Logothetis G (1998) Characterization of an agostic bond on the basis of the electron density. *J Organomet Chem* 555:101–111
96. Tognetti V, Joubert L, Raucoules R, De Bruin T, Adamo C (2012) Characterizing agosticity using the quantum theory of atoms in molecules: bond critical points and their local properties. *J Phys Chem A* 116:5472–5479
97. Sahi A, Arunan E (2014) Hydrogen bonding, halogen bonding and lithium bonding: an atoms in molecules and natural bond orbital perspective towards conservation of total bond order, inter- and intra-molecular bonding. *Phys Chem Chem Phys* 26:22935–22952
98. Tognetti V, Joubert L, Cortona P, Adamo A (2009) Towards a combined DFT/QTAIM description of agostic bonds: the critical case of a Nb(III) complex. *J Phys Chem A* 113:12322–12327
99. Tognetti V, Joubert L, Adamo C (2010) Making density functional theory and the quantum theory of atoms in molecules converse: a local approach. *J Chem Phys* 132:211101
100. Bonnet ML, Tognetti V (2011) The influence of density functional approximations on the description of LiH + NH₃ → LiNH₂ + H₂ reaction. *Chem Phys Lett* 511:427–433
101. Kozuch S, Martin JML (2013) Halogen bonds: benchmarks and theoretical analysis. *J Chem Theor Comput* 9:1918–1931
102. Chai JD, Head-Gordon M (2008) Long-range corrected hybrid density functionals with damped atom-atom dispersion corrections. *Phys Chem Chem Phys* 10:6615–6620
103. Frisch MJ, Trucks GW, Schlegel HB, Scuseria GE, Robb MA, Cheeseman JR, Scalmani G, Barone V, Mennucci B, Petersson GA, Nakatsuji H, Caricato M, Li X, Hratchian HP, Izmaylov AF, Bloino J, Zheng G, Sonnenberg JL, Hada M, Ehara M, Toyota K, Fukuda R, Hasegawa J, Ishida M, Nakajima T, Honda Y, Kitao O, Nakai H, Vreven T, Montgomery JA, Peralta JE, Ogliaro F, Bearpark M, Heyd JJ, Brothers E, Kudin KN, Staroverov VN,

- Keith TA, Kobayashi R, Normand J, Raghavachari K, Rendell A, Burant JC, Iyengar SS, Tomasi J, Cossi M, Rega N, Millam JM, Klene M, Knox JE, Cross JB, Bakken V, Adamo C, Jaramillo J, Gomperts R, Stratmann RE, Yazyev O, Austin AJ, Cammi R, Pomelli C, Ochterski JW, Martin RL, Morokuma K, Zakrzewski VG, Voth GA, Salvador P, Dannenberg JJ, Dapprich S, Daniels AD, Farkas, Foresman JB, Ortiz JV, Cioslowski J, Fox DJ (2009). Gaussian 09, revision D.01. Wallingford
104. Keith TA (2014) AIMAll software, version 14.04.17 professional, <http://aim.tkgristmill.com>
105. Tognetti V, Joubert L (2011) On the influence of density functional approximations on some local Bader's atoms-in-molecules properties. *J Phys Chem A* 115:5505–5515
106. Johnson ER, Kelnan S, Mori-Sánchez P, Contreras-García J, Cohen AJ, Yang W (2010) Revealing noncovalent interactions. *J Am Chem Soc* 132:6498–6506
107. Cormanich RA, Rittner R, O'Hagan D, Bühl M (2014) Analysis of CF \cdots FC interactions on cyclohexane and naphthalene frameworks. *J Phys Chem A* 118:7901–7910
108. Jaharomi HJ, Eskanderi K (2013) Halogen bonding: a theoretical study based on atomic multipoles derived from quantum theory of atoms in molecules. *Struct Chem* 24:1281–1287
109. Metrangolo P, Murray JS, Pilati T, Politzer P, Resnati G, Terraneao T (2011) The fluorine atom as a halogen bond donor, viz. a positive site. *Cryst Eng Comm* 13:6593–6596
110. Metrangolo P, Murray JS, Pilati T, Politzer P, Resnati G, Terraneao G (2011) Fluorine-centered halogen bonding: a factor in recognition phenomena and reactivity. *Cryst Growth Des* 11:4238–4246
111. Guégan F, Mignon P, Tognetti V, Joubert L, Morell C (2014) Dual descriptor and molecular electrostatic potential: complementary tools for the study of the coordination chemistry of amphiphilic ligands. *Phys Chem Chem Phys* 16:15558–15569
112. Tognetti V, Morell C, Ayers PW, Joubert L, Chermette H (2013) A proposal for an extended dual descriptor: a possible solution when frontier molecular orbital theory fails. *Phys Chem Chem Phys* 15:14465–14475

Chapter 17

Charge Transfer in Beryllium Bonds and Cooperativity of Beryllium and Halogen Bonds. A New Perspective

Kateryna Mykolayivna Lemishko, Giovanni Bistoni,
Leonardo Belpassi, Francesco Tarantelli,
M. Merced Montero-Campillo and Manuel Yáñez

Abstract The main characteristics of beryllium bonds formed by the interaction of different Lewis bases with BeX_2 ($X = \text{H}, \text{F}$) moieties have been analyzed by means of the Charge Displacement (CD) function. This analysis is systematically compared with that provided by other approaches based on the topology of the electron density, namely the quantum theory of atoms in molecules (QTAIM) and the electron localization function (ELF). The CD scheme provides a quantitative description of the charge transfer that gives rise to the formation of beryllium bonds. For systems of suitable symmetry, its decomposition into symmetry contributions allows to easily identify the mechanisms involved in the charge transfer process, as well as to quantify possible back-donations. The CD function analysis also provides a clear quantitative description of cooperativity between the beryllium and halogen bonds in ternary $\text{F}_2\text{Be}:\text{FCI}:\text{N-base}$ (N-base = NH_3 , NHCH_2 , NCH) complexes, confirming the trends obtained by the QTAIM and ELF methods. The different viewpoints each of these methodologies provide are clearly complementary, the CD being the only one that permits to quantify the charge transfer from the Lewis base to the Lewis acid.

Keywords Charge-Displacement function · QTAIM · ELF · Beryllium bonds · Halogen bonds · Cooperativity

K. Mykolayivna Lemishko · M. Merced Montero-Campillo · M. Yáñez (✉)
Departamento de Química, Facultad de Ciencias, Módulo 13,
Universidad Autónoma de Madrid, Campus de Excelencia UAM-CSIC, Cantoblanco,
28049 Madrid, Spain
e-mail: manuel.yanez@uam.es

G. Bistoni · F. Tarantelli
Dipartimento di Chimica, Biologia e Biotecnologie, Università di Perugia,
via Elce di Sotto 8, 06123 Perugia, Italy

G. Bistoni · L. Belpassi · F. Tarantelli
Istituto di Scienze e Tecnologie Molecolari del CNR (ISTM-CNR),
via Elce di Sotto 8, 06123 Perugia, Italy

17.1 Introduction

Non-covalent interactions play a crucial role in nature, because they are responsible for the organization of practically all molecular assemblies, either of natural origin like DNA, or of artificial origin, such as the so-called metal-organic-frameworks (MOFs) [1]. They hold together the so-called “soft materials”, characterized by binding energies of the order of the thermal energy. This definition includes polymers, colloids and surfactants [1, 2]. Hence, not surprisingly, the detailed characterization of the noncovalent interactions turns out to be essential for the development of new molecular materials. In particular, the last two decades have witnessed a massive development of new materials of potential interest for technological applications based on molecular assemblies [3, 4]. Over the same period, the interest on non-covalent interactions has continuously increased, leading to the characterization of a large variety of them, differing in energy or nature [5]. Remarkably enough, some of them are almost as strong as conventional covalent linkages [6], thus going beyond the conventional view which describes the non-covalent interactions as weak interactions between closed-shell systems with no electron sharing. The most paradigmatic example is the inter- and intramolecular hydrogen bond; but after its early recognition, similar closed-shell interactions, such as the dihydrogen [6, 7], halogen [8–10], pnictogen [11–16], chalcogen [17, 18], beryllium bonds [19, 20] or tetrel interactions [21–23] have been found to contribute to the stability of different molecular assemblies.

It is worth noting that, in this astonishing development, modeling based on the use of quantum chemistry techniques has played a crucial role. Modeling helps to save huge amounts of money by providing clues to understand the mechanisms involved in the material activity and opens the possibility of designing new materials, with better performances, in very powerful synergy with experiment [24–35].

One of the signatures of the non-covalent interactions mentioned above is the polarization of the electron density of the closed-shell system behaving as a Lewis base towards the closed-shell moiety which acts as a Lewis acid. Again hydrogen bonds $AH\cdots B$ constitute a paradigmatic example, in which there is an interaction between the lone-pair of the hydrogen bond acceptor B towards the σ_{AH}^* antibonding molecular orbital of the hydrogen bond donor [36]. This electronic density redistribution is mirrored in the lengthening of the A–H bond and the red shift of the A–H stretching frequency, which characterize this kind of non-covalent interactions [37]. This mechanism reaches its maximum intensity in the so-called dative bonds, in which a significant charge transfer from the Lewis base towards the Lewis acid takes place. The difference between dative bonds and the other much weaker non-covalent interactions mentioned above is essentially quantitative rather than qualitative.

These electron density redistributions lead to one of the most interesting characteristics that non-covalent interactions evidenced in recent years: their capability to modulate the intrinsic properties of the interacting subunits by changing their donor or acceptor electron capacities [38–40]. In general, the Lewis base has its intrinsic acidity increased after the formation of the complex, due to the charge transfer towards the Lewis acid, whose basicity concomitantly increases too. Depending on the intensity of this charge transfer mechanism, the increase of the intrinsic acidity of the base can be dramatic. Typical bases like aniline, for instance, become stronger Bronsted acids than phosphoric acid, whereas 1H-tetrazole becomes a nitrogen Bronsted acid stronger than perchloric acid [39]. One important consequence of these acidity enhancements is the possibility of having spontaneous proton transfers between a Lewis base and a Lewis acid, with the spontaneous formation of an ion-pair in the gas phase [41, 42], or the formation of polymeric structures for ditopic monomer presenting one end that acts as a Lewis base whereas the other acts a Lewis acid [43]. Another signature of the non-covalent interactions is cooperativity (or anticooperativity), that is the reinforcement (or weakening) of non-covalent interactions when two or more functionalities coincide within the same molecular assembly, and is closely related with the aforementioned electron density redistributions [44–75].

Therefore, the analysis of the electron density distribution of the molecular aggregates held together through non-covalent interaction can provide valuable information on both their properties and how these change with respect to the isolated building blocks. This analysis can be carried out by means of different techniques, the most popular of which are the Quantum Theory of Atoms in Molecules (QTAIM) theory [76, 77], the Electron Localization Function (ELF) [78–80] and the Natural Bond Orbital (NBO) method [81].

The QTAIM approach relies on a topological analysis of the electron density, $\rho(\mathbf{r})$, allowing to build up the molecular graphs as the ensemble of the critical points of $\rho(\mathbf{r})$. These include maxima associated with the position of the nuclei, bond and ring critical points associated with the existence of a bond between two atoms or a ring, and the bond paths, defined as lines of maximum density which connect two maxima through a first-order saddle point called bond critical point (BCP). In general, the electron density at the BCPs offers direct information on the strength of the bond and the values of the so-called energy density provides information about the covalent or electrostatic nature of the interaction.

The ELF theory allows one to divide the physical space into regions dominated by an opposite spin pair or by a single electron. These electronic domains can be seen as a generalization of the ideas of Lewis, so that the valence shell of a molecule consists of two types of basin: disynaptic (or polysynaptic) basins, which belong to two (or more) atomic valence shells and the monosynaptic ones (typically lone-pairs), which belong to only one valence shell, and therefore correspond to nonbonding valence density. The basin populations also offer interesting information on the strength and characteristics of the bonds.

The NBO method is particularly well suited to analyze charge transfer mechanisms between two interacting systems through the NBO second order perturbation analysis between the occupied orbitals of the base and the empty orbitals of the acid [36]. These “localized hybrids” are obtained as local block eigenvectors of the one-particle density matrix.

An alternative approach to specifically investigate the charge transfer between the interacting subunits of a molecular complex is the Charge Displacement (CD) function, introduced by Belpassi et al. [82] to study the chemical bond between gold and the noble gases, and later on successfully employed to study the charge transfer in noncovalent interactions [83–86] and in coordination chemistry [87–91]. This theoretical scheme permits a quantitative analysis of the actual electronic charge fluctuation and allows to measure the exact amount of electron charge that, upon formation of an adduct from two constituting fragments, is transferred across a plane perpendicular to the bond axis.

In the present study, we used this method to investigate cooperativity between different non-covalent interactions. For sake of comparison, we also carried out a parallel analysis using the QTAIM, ELF and NBO approaches. In particular, we have chosen as suitable benchmark cases complexes stabilized simultaneously by beryllium bonds, which lead usually to rather strong linkages, and halogen bonds, which conversely are rather weak non-covalent interactions. As prototypes of halogen bond, we have considered the complexes that FCl may form with nitrogen bases in which the hybridization of the basic site changes from sp_3 , ammonia, to sp_2 , methanimine, to sp , hydrogen cyanide. Then these complexes were allowed to interact, through the fluorine atom of the FCl subunit, with beryllium difluoride, to form the corresponding beryllium bond.

Since beryllium bonds have attracted much attention in recent years, the first part of this study will focus on the information that the CD scheme provides on these kind of linkages, when the base that interacts with the beryllium derivative presents as basic sites first or second-row atoms. In particular, we have studied the beryllium bond between BeH_2 or BeF_2 and H_2O , SH_2 , NH_3 and PH_3 .

17.2 Computational Details

Geometries and electron densities were calculated at the DFT level with the B3LYP functional, that combines the Becke’s three-parameter non-local hybrid exchange functional [92] with non-local correlation function of Lee et al. [93]. DFT calculations have been carried out with Gaussian 09 [94] program using aug-cc-pVTZ basis set [95] and with ADF suite of programs in combination with TZ2P basis set [96]. The good performance of the B3LYP method to describe the structure of both beryllium and halogen bonds has been previously assessed in the literature [19, 75].

The QTAIM and the ELF calculations have been carried out by using the AIMAll [97] and the TopMod [98] program packages, respectively. The NBO

analysis was carried out by means of the NBO 3.1 suite of programs [99]. The Charge Displacement (CD) function:

$$\Delta q(z) = \int_{-\infty}^z dz' \int_{-\infty}^{\infty} \int_{-\infty}^{\infty} \Delta \rho(x, y, z') dx dy \quad (17.1)$$

is defined as a progressive partial integration along a chosen z axis (usually chosen to be the bond axis between the fragments) of the difference $\Delta \rho(x, y, z)$ between the electron density of the complex and that of its constituting fragments, placed exactly in the same position they occupy in the adduct.

The CD function reflects the electron rearrangement in the boundary region arising from the formation of the complex in a very effective and visual manner. When measuring the amount of charge transferred from the donor to the acceptor with this method, the most common option is to choose as reference the so called “isodensity point” on the z axis, the point where the electron densities of the interacting species are equal and tangent. This point is usually close to the BCP provided by QTAIM.

In studying the $\text{Be} \cdots \text{X}$ ($\text{X} = \text{H}_2\text{O}$, SH_2 , NH_3 , PH_3) bond, we used as fragments BeH_2 or BeF_2 and the Lewis base X . When dealing with triads involving BeF_2 , FCl and the nitrogen base, the fragment will be the BeF_2 and the remaining FCl:N -base moiety and as z axis the one joining the Be and the F atom of FCl . Conversely, in studying the $\text{Cl} \cdots \text{N}$ bond, we used as fragments the N -base and the remaining $\text{BeF}_2\text{:FCl}$ moiety and as integration axis, z , the one joining the Cl and the N atom.

17.3 Characterization of Beryllium Bonds

As mentioned in the Introduction, an extensive list of non-covalent interactions have been successfully characterized by topological methods [100], i.e., hydrogen bonds, halogen bonds, dihydrogen bonds or pnictogen bonds, but only few of these in the light of the CD analysis. As beryllium bonds share many common features with other weak interactions that involve a certain amount of charge transfer [19], the CD analysis should provide interesting information on the nature of bonding in beryllium complexes, and in particular on the amount of charge transfer accompanying the beryllium bond formation. Therefore, the aim of this section is to discuss the results of this analysis, trying at the same time to establish the possible relationships with topological approaches as QTAIM and ELF, and with the descriptions obtained with the NBO method.

The optimized geometries of the binary complexes under scrutiny, indicating the corresponding beryllium bond distances, are represented in Fig. 17.1.

The 3D contour plots of the electron density changes accompanying the beryllium bond formation in $\text{H}_2\text{Be-OH}_2$ and $\text{F}_2\text{Be-OH}_2$ are reported in Fig. 17.2, as a suitable example. Beryllium bonds for both the complexes are characterized by significant electron density rearrangements all over the whole molecular region of

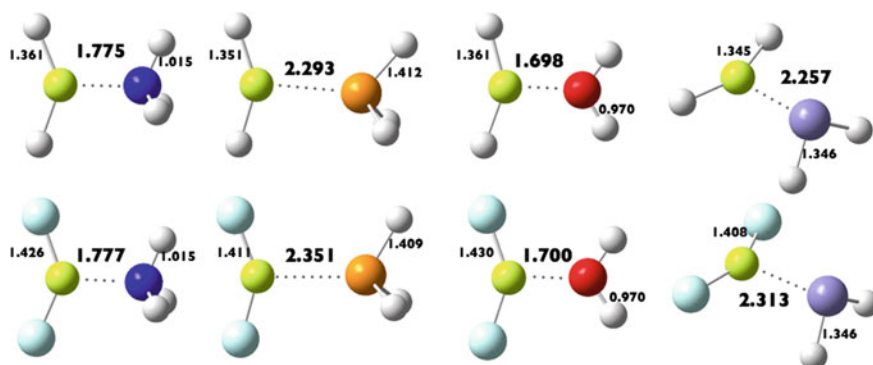


Fig. 17.1 Optimized structures for complexes between BeX_2 ($X = \text{H}, \text{F}$) and different Lewis basis B ($B = \text{NH}_3, \text{PH}_3, \text{H}_2\text{O}, \text{SH}_2$ from left to right) at B3LYP/aug-cc-pVTZ level of theory. The Be-X bond length in free BeX_2 is 1.332 Å and 1.379 Å for $X = \text{H}$ and $X = \text{F}$, respectively

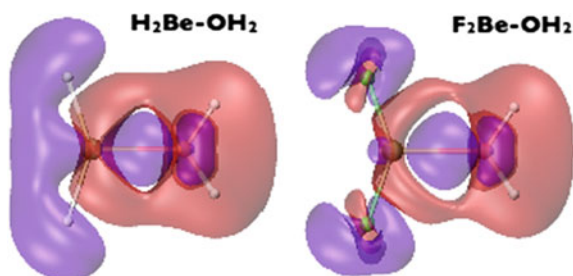


Fig. 17.2 3D isodensity surfaces ($\pm 0.0001 \text{ e/a.u.}^3$) of for $\text{H}_2\text{Be-OH}_2$ and $\text{F}_2\text{Be-OH}_2$ complexes. Red surface (negative values) identify charge depletion areas, violet surfaces (positive values) identify charge accumulation areas

these systems, contour plots of $\Delta\rho$ evidencing wide regions of charge accumulation in the area between BeX_2 and water, and in the area around the X substituents (positive $\Delta\rho$) whereas the density is depleted from the water region (negative $\Delta\rho$).

There is also a non-negligible electron density depletion at the Be-X bonding regions in both cases. This is consistent with the significant lengthening of the Be-X ($X = \text{H}, \text{F}$) bond on going from the isolated BeX_2 derivatives to the binary complexes with the different bases considered. As we will discuss later this finding is also consistent with the characteristics of the corresponding molecular graphs. It is also worth noting that, upon the formation of the binary complexes, the BeX_2 moiety becomes significantly distorted and it is not linear anymore. We will come back later to this point when analyzing the NBO description of these systems.

The charge displacement curves for all BeH_2 complexes are shown in Fig. 17.3.

This corresponds to the electronic charge that, upon the formation of the complex, is transferred from positive to negative values of a chosen axis, that in our case coincides with the Be-Y ($Y = \text{O}, \text{S}, \text{N}, \text{P}$) bond, through a plane perpendicular to

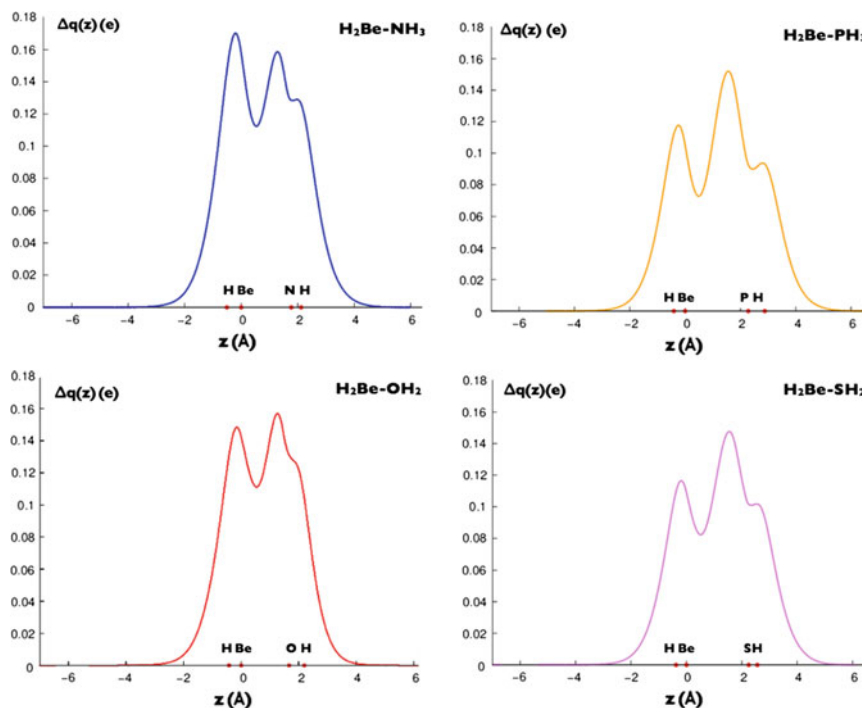


Fig. 17.3 CD curves for $\text{H}_2\text{Be-NH}_3$, $\text{H}_2\text{Be-PH}_3$, $\text{H}_2\text{Be-OH}_2$ and $\text{H}_2\text{Be-SH}_2$ complexes

this axis at point z . Thus, a positive value of $\Delta q(z)$ means that the charge passes from positive to negative values of z . It can be observed that $\Delta q(z)$ is positive all over the molecular region, thus showing in an unambiguous manner the presence of charge transfer from the Lewis base to the beryllium moiety. At the boundary, the total charge transfer (in e) for BeH_2 complexes is 0.115 (NH_3), 0.076 (PH_3), 0.111 (H_2O) and 0.084 (H_2S). It is remarkable that the amount of charge transferred is higher in BeH_2 complexes than in BeF_2 (see Fig. 17.4), for which total charge transfer (e) is 0.075 (NH_3), 0.063 (PH_3), 0.078 (H_2O) and 0.063 (H_2S).

In principle, one would expect that the greater is the electronegativity of the X substituent, the greater would become the ability of the beryllium bond to accept charge. However, though fluorine is more electronegative than chlorine and much more electronegative than hydrogen, the amount of charge that beryllium atom accepts in BeF_2 is lower than in the BeH_2 case. This apparent contradiction has been explained for both boron derivatives and beryllium derivatives as a consequence of the deformation undergone by the Lewis acid, which significantly modifies its electron acceptor capacity changing the aforementioned trend. In contrast with what could be expected from the electronegativity increase by substituting a H atom by a F atom, it was proved that due to the deformation effects BH_2F and BHF_2 are weaker Lewis acids than BH_3 and only BF_3 is slightly stronger [101]. Similarly, BeHF was found to be a weaker Lewis acid than BeH_2 [102].

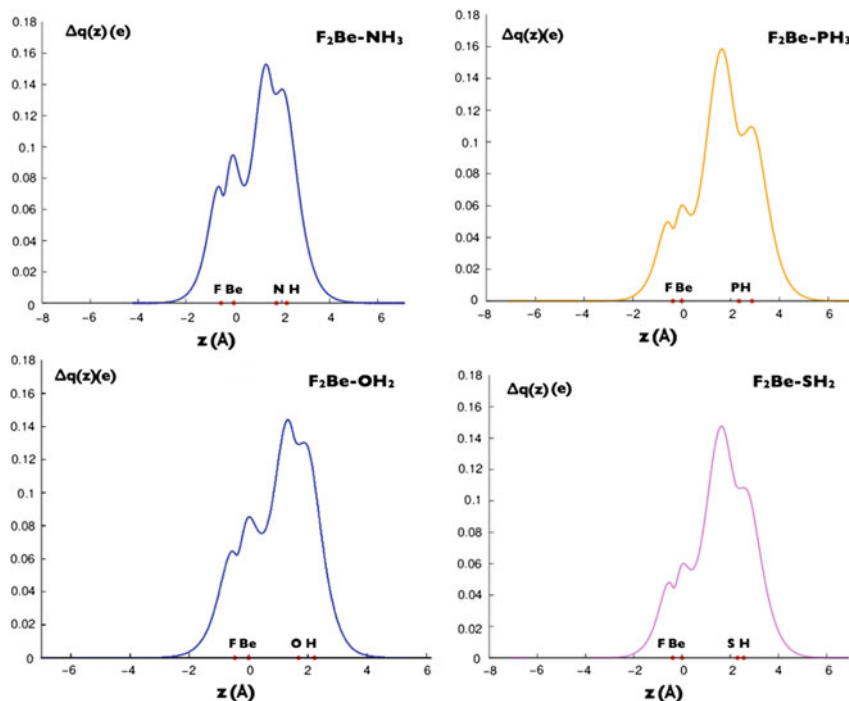


Fig. 17.4 CD curve for F_2Be-NH_3 , F_2Be-PH_3 , F_2Be-OH_2 and F_2Be-SH_2 complexes

Interestingly, the QTAIM comparison (Figs. 17.5 and 17.6) between beryllium bonds is less straightforward. Electron density values at the BCPs are of course significantly higher in NH_3 and H_2O complexes than in the PH_3 or SH_2 ones, because in the latter case more voluminous second-row atoms are involved, so no direct conclusions can be extracted from these facts with respect to the strength of the beryllium bond. It should be noted, however that very similar values are found if we compare BeH_2/BeF_2 results: 0.061/0.062 (NH_3), 0.037/0.034 (PH_3), 0.055/0.057 (H_2O) and 0.034/0.032 (H_2S), showing that the strength of the beryllium bond is not necessarily smaller when BeF_2 is involved. Further information can be obtained when looking at the laplacian of the electron density ($\nabla^2\rho$) as Eskandari did studying our set of complexes [103]. The L-function, defined as the negative of $\nabla^2\rho$, presents positive values in regions of charge concentration (lump) and negative values on regions of charge depletion (hole). As our CD analysis shows quantitatively, contour maps of the L-function show qualitatively beryllium bonds as a lump-hole interaction. We looked at the L-function value on the BCP of the beryllium bond and larger negative values are found for BeH_2 complexes than for the BeF_2 ones in all cases: $-0.339/-0.323$ (NH_3), $-0.114/-0.087$ (PH_3), $-0.455/-0.429$ (H_2O), $-0.138/-0.099$ (SH_2).

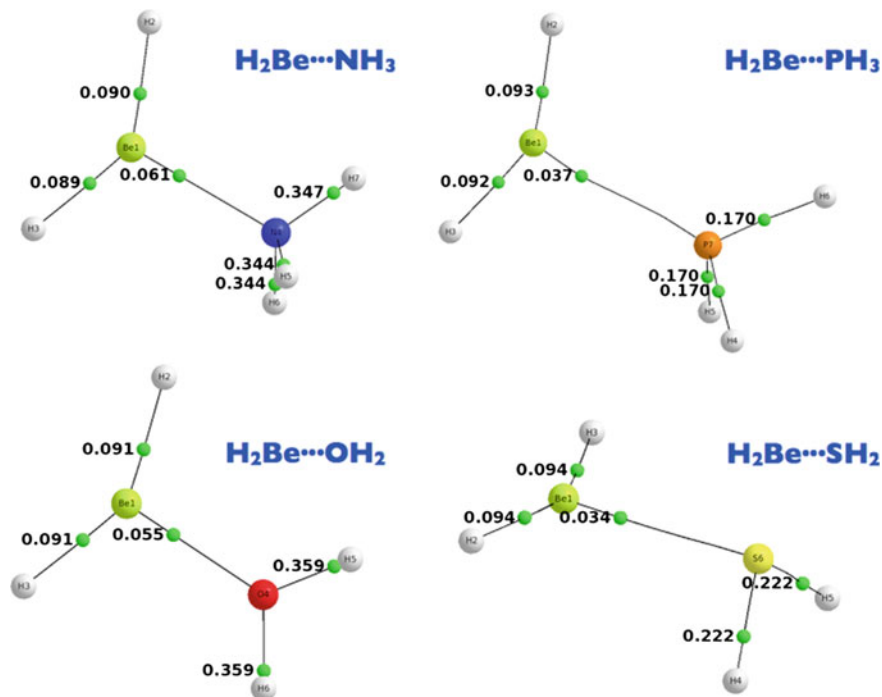


Fig. 17.5 Molecular graphs of $\text{H}_2\text{Be}\cdots\text{NH}_3$, $\text{H}_2\text{Be}\cdots\text{PH}_3$, $\text{H}_2\text{Be}\cdots\text{OH}_2$ and $\text{H}_2\text{Be}\cdots\text{SH}_2$ complexes. Green points correspond to BCPs along with their electron densities

QTAIM is however well suited to provide a good picture of the electron density re-distributions triggered by the non-covalent interaction. For instance, in Fig. 17.6 is apparent the significant decrease of the electron density at the Be-X (X = H, F) BCP, which is mirrored in the lengthening of the corresponding bonds on going from the isolated BeX_2 to the binary complexes, as already mentioned. Opposite changes, although quantitatively smaller, are observed for the electron density at the BCPs of the bonds between the basic site and the H atoms of the different bases. Also consistently, the corresponding bonds shrink on going from the isolated base to the base in the binary complex. This effect is a consequence of the electronegativity enhancement undergone by the basic site. As indicated by the CD function, a significant charge transfer takes place from the lone-pairs of the base towards the Be moiety. Consequently, the basic site tries to recover the charge transferred by polarizing the valence charge of the hydrogen atoms bonded to it, with the result that the electron density increases in the internuclear region and concomitantly the hydrogen atoms become more acidic, as also reflected by the increase of their natural charge.

Electron sharing becomes much clearer when dealing with ELF results (Figs. 17.7 and 17.8). In all BeH_2 complexes (Fig. 17.7), disynaptic basins $V(\text{Be},\text{N})$, $V(\text{Be},\text{P})$, $V(\text{Be},\text{O})$ and $V(\text{Be},\text{S})$ are found. Lone pairs originally from N and O atoms are now

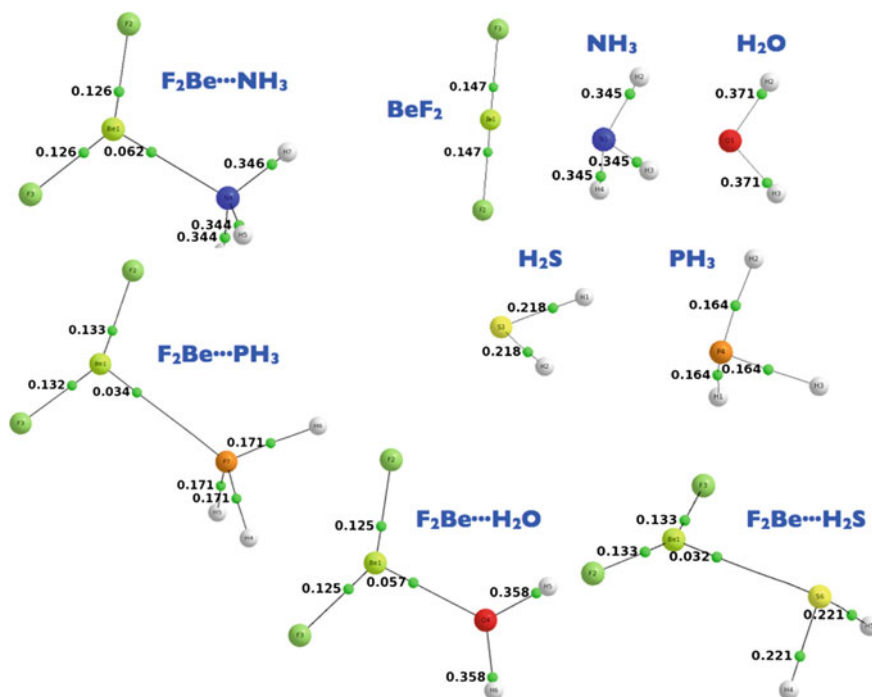
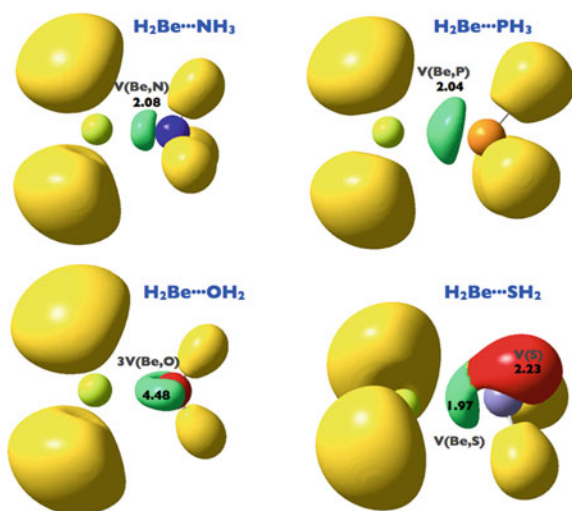


Fig. 17.6 Molecular graphs of F_2Be-NH_3 , F_2Be-PH_3 , F_2Be-OH_2 and F_2Be-SH_2 complexes, and of the monomers they involved. Green points correspond to BCPs along with their electron densities

Fig. 17.7 Three-dimensional ELF plots (ELF = 0.85) of H_2Be-NH_3 , H_2Be-PH_3 , H_2Be-OH_2 and H_2Be-SH_2 complexes with the population of the basins in e



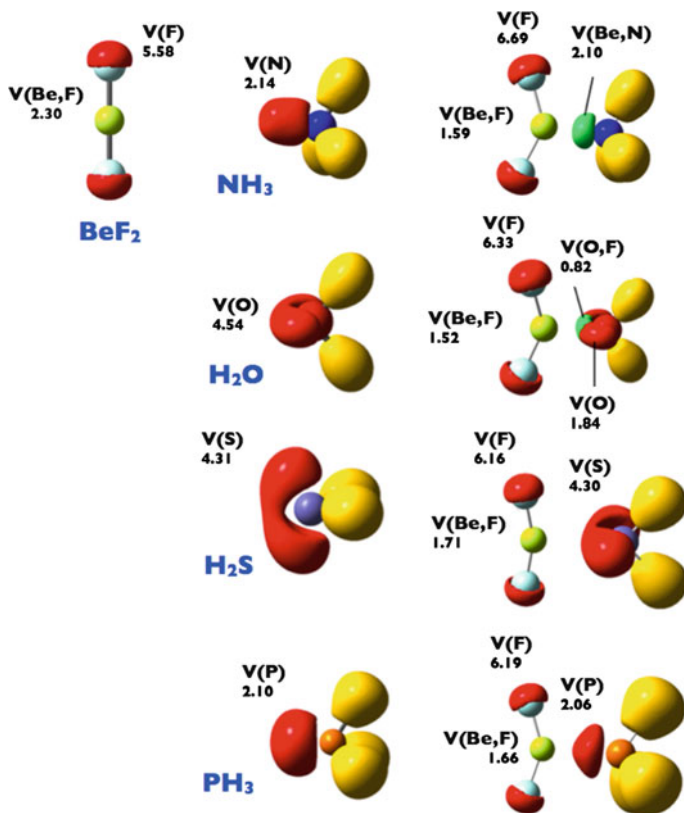


Fig. 17.8 Three-dimensional ELF plots (ELF = 0.85) of F₂Be–NH₃, F₂Be–PH₃, F₂Be–OH₂ and F₂Be–SH₂ complexes and of the corresponding monomers. *Yellow, red, green and blue lobes* correspond to disynaptic basins involving H atoms, monosynaptic lone pair basins, to disynaptic basins between two bonded atoms, and to monosynaptic atomic cores, respectively. The population of the different basins is given in e⁻

strongly interacting with the empty beryllium orbitals in such a way that those pairs appear as shared by the atoms involved in the beryllium bond. Phosphine complex behaves similar to ammonia, whereas BeH₂–SH₂ complex is different from the water one: both hydrogens from H₂S are not co-planar with BeH₂, and lone pairs of sulfur are split into two contributions: a V(Be,S) disynaptic basin and a monosynaptic V(S) basin located over the BeH₂ plane. We will return later on this BeH₂–SH₂ complex, as CD analysis can provide more detailed information.

If we pay attention to ELF results for BeF₂ complexes (Fig. 17.8), there are many interesting changes with respect to the previous picture. The disynaptic basin V(Be,P) becomes a monosynaptic V(P) pair, whereas the three V(Be,O) basins summing 4.48 e split in two V(O) basins (3.68 e) and one basin V(Be,O) with less than one electron (0.82 e). Regarding sulfur, all basins around this atom are now

monosynaptic. ELF and CD clearly show how charge donation towards beryllium is less effective with BeF_2 with respect to BeH_2 and offer a much unambiguous interpretation than QTAIM.

There are other interesting features in Fig. 17.7. For instance, when the $\text{BeF}_2:\text{NH}_3$ complex is formed, not only the $V(\text{N})$ monosynaptic basin on ammonia changes into a $V(\text{Be},\text{N})$ disynaptic basin, but also undergoes a significant volume contraction, in spite of the fact that its total population decreases only slightly. This is a direct consequence of the strength of the interaction leading to a very short $\text{Be}\cdots\text{N}$ distance and therefore the volume of the basin becomes almost 1/3 the one in the isolated base. Similar changes are observed for the other complexes. It can also be noted in agreement with our previous CD and QTAIM analysis that the population of the $V(\text{Be},\text{F})$ disynaptic basin decreases quite significantly in the binary complexes with respect to the isolated BeF_2 molecule, leading to a weaker and longer $\text{Be}-\text{F}$ bond. In addition, the net population at the F lone pairs increases.

The description of the NBO is in line with that obtained by means of these approaches, showing that the formation of a beryllium bond involves the interaction of the lone-pair of the base with both the empty $2p$ orbitals of Be and the σBeX^* antibonding orbitals. The latter interaction is directly responsible of the lengthening of the $\text{Be}-\text{X}$ linkages already discussed, whereas the former accounts for the bending of the BeX_2 moiety, because the population of the initially empty p orbital of Be, changes its hybridization from sp to sp^n , n being greater than one [19].

It is now interesting to look at the information that CD scheme can provide in the quantification of the different charge flows associated with the bond formation. As a suitable example, we will study the beryllium bond formation in the complexes of H_2O and H_2S , taking advantage of the symmetry of these complexes. Indeed, the electron density difference can be partitioned according to the irreducible representation of the point group to which both the molecule and the fragments belong [87]. This permits the separation of the electron density difference into symmetry components, according to the following equations:

$$\Delta\rho = \sum_p \Delta\rho_p \quad (17.2)$$

$$\Delta\rho = \sum_{i \in p} |\phi_i(\text{AB})|^2 - \sum_{i \in p} |\phi_i(\text{A})|^2 - \sum_{i \in p} |\phi_i(\text{B})|^2 \quad (17.3)$$

where p labels the different irreducible representations. A, B and AB represent the two monomers and the complex, respectively, while ϕ_i are Kohn-Sham orbitals. This decomposition permits the separation of the overall CD function into additive symmetry component.

The $\text{H}_2\text{Be}-\text{OH}_2$ complex belongs to the C_{2v} symmetry point group with all nuclei laying in the $\sigma_v(yz)$ plane. The other symmetry plane $\sigma_v(xz)$, containing the Be and O nuclei, cut in half both the $\text{H}-\text{Be}-\text{H}$, and the $\text{H}-\text{O}-\text{H}$ angles. Accordingly, the A_1 component is expected to correlate with the donation from occupied lone pairs of water to unoccupied spz orbital (of beryllium atom) and σ^* (of the $\text{Be}-\text{H}$ bond) of BeH_2 . The B_1 symmetry correlates with the donation to the out-of-plane unoccupied px orbital of Be and B_2 corresponds to the backdonation

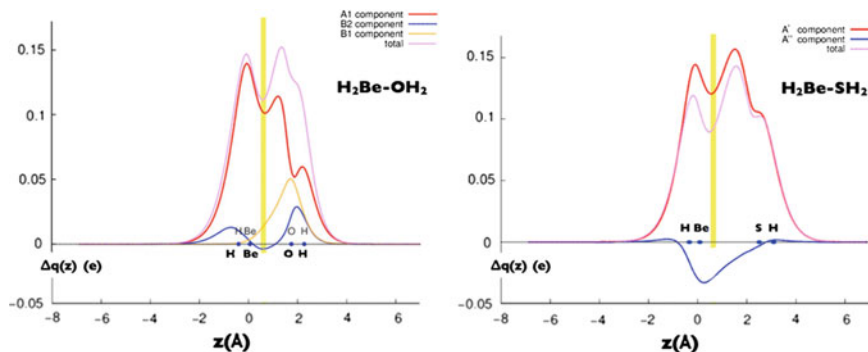


Fig. 17.9 CD curve for $\text{H}_2\text{Be-OH}_2$ and $\text{H}_2\text{Be-SH}_2$ complexes according to their irreducible representations

from the σ bonding orbitals (Be–H bond) to the empty orbitals of the Lewis base of suitable symmetry. The A2 component does not represent any important contribution.

The corresponding CD functions are reported in Fig. 17.9 (left panel). The major contribution to the total charge transfer has the A1 symmetry component that correlates with the spz orbital of the beryllium atom, whereas the donation to the formally empty p_x orbital (of beryllium in the Be– H_2 moiety) amounts to only the 12 % of the total charge transfer taken at the isodensity boundary (the center of the yellow wide line). No significant backdonation is present in this case (the curve labeled as B2 is indeed very small in the interfragment region where it crosses the zero axis).

The $\text{H}_2\text{Be-SH}_2$ complex belongs to C_s symmetry and symmetry plane (σ_h) cuts in half both the H–Be–H and the H–S–H bond. Consequently, the A' symmetry correlates with the donation into formally empty p_x , spz (of Be) and σ^* (of Be–H) orbitals while the A'' symmetry correlates to the backdonation from the occupied orbitals of Be– H_2 (i.e. the σ orbitals of the two Be–H bonds) to the unoccupied orbitals of the SH_2 molecule of suitable symmetry.

As clearly emerges from the analysis of the corresponding CD functions (right panel Fig. 17.9), the situation in this case is markedly different from the H_2O case. In particular, the curve referred to as A'' is always negative, thus indicating the presence of a significant amount of back-donation from the Be–H bonding orbitals to the empty orbitals of H_2S . The CD curve varies significantly along the intermolecular region, reaching its minimum near the isodensity boundary. At this point, the amount of charge back-donated from beryllium to the Lewis base reaches 0.037 e, which is around 45 % of the total amount of charge transfer taken at the isodensity point (0.084 e). Even if 0.121 e are donated from the H_2S moiety to the Lewis acid, the back-donation decreases the overall amount of charge transfer from the basic site to the acid site, making it significantly lower than in the $\text{H}_2\text{Be-OH}_2$ case. The difference between H_2S and H_2O complexes could, at least partially, be imputed to the different mutual orientation of the molecules. This is something also

Table 17.1 Charge transfer (CT), interaction energies (E_{int}) and X–Be–X angles obtained at the B3LYP/aug-cc-pVTZ level of theory

Complex	CT (e)	E_{int} (kJ/mol)	$\angle\text{X–Be–X}$ (deg)
H ₂ Be–NH ₃	0.115	–133.0	138.8
H ₂ Be–PH ₃	0.076	–57.8	145.8
H ₂ Be–OH ₂	0.111	–106.2	145.4
H ₂ Be–OH ₂	0.084	–32.2	147.8
F ₂ Be–NH ₃	0.075	–159.7	137.4
F ₂ Be–PH ₃	0.063	–69.9	144.8
F ₂ Be–OH ₂	0.078	–128.3	142.6
F ₂ Be–SH ₂	0.063	–37.4	146.4

evidenced by the shape and position of basins around S atom in ELF pics of these complexes in Fig. 17.7.

We thought it was interesting to investigate whether there is some correlation between the charge transfer (CT) and the interaction energies (E_{int}) in the binary complexes defined as the difference between the electronic energy of the complex and the monomers with the same geometry they have in the complex. Similarly, we have also analyzed the possible correlation between CT and the deformation of the BeX₂ unit as measured by the value of the X–Be–X angle. The results obtained have been summarized in Table 17.1.

Although a rough correlation seems to exist between the interaction energy and the distortion of the BeX₂ moiety, no correlation seems to exist at all when the interaction energy is replaced by CT. Consistently, no correlation between charge transfer and interaction energies is found either. For instance, the amount of charge transfer in H₂Be–NH₃ is 0.040 e higher than in F₂Be–NH₃ although interaction energy in the latter complex is more than 26 kJ/mol higher (see Table 17.1). The presence of some other components (like the electrostatic one) should play a non-negligible role. Interestingly, ELF shows that, on passing from BeH₂ (Fig. 17.7) to BeF₂ (Fig. 17.8), the basins in the boundary region gain some average population (0.02 e), although some of these basins become lone pairs. In other words, the interboundary region is slightly more populated in BeF₂ complexes but less shared, what seems to be related with the increase in the interaction energies but a decrease of the total amount of CT.

In summary, topological tools as QTAIM, ELF and CD can offer a complementary and very complete description of beryllium bonds. These bonds, taking into account their energetic and the amount of charge transferred from donor to acceptor, go clearly beyond the typical definition of non-covalent interactions (i.e. weak interactions between closed-shell systems with no electron sharing). They present some clear features: (i) interaction energies range within 10–40 kcal/mol, typical of weak covalent bonds; (ii) the net contribution of charge transfer from donor to acceptor is significantly larger than the one usually found in hydrogen bonds (for example, CT in water dimer is of 0.014–0.015 e [104], about five times smaller than we found here for BeX₂–OH₂); (iii) for suitable interfragment

orientation and Lewis bases, beryllium bond may present a certain amount of CT in direction going from the beryllium moiety to the base (i.e. non-negligible back-donation), as typically occurs for transition metals in coordination bonding.

17.4 Cooperativity Between Beryllium Bonds and Halogen Bonds. The $F_2Be:FCl:NCH$ Complex

In this section we study the cooperativity of halogen and beryllium bonds by comparing the electronic structure of $F_2Be:FCl$ and $FCl:NCH$ with the one of the corresponding ternary complex, namely $F_2Be:FCl:NCH$. Our aim is to quantify the effect of the base on the $Be\cdots F$ bonding features and, at the same time, to understand how the $Cl\cdots N$ bond is affected by the presence of the BeF_2 moiety.

We start comparing the $Be\cdots F$ (FCl) bonding features between $F_2Be:FCl$ and $F_2Be:FCl:NCH$. The corresponding CD curves are reported in Fig. 17.10 as black and green solid lines, for $F_2Be:FCl:NCH$ and $F_2Be:FCl$, respectively. Each curve provides a quantitative picture of the charge flow associated to the formation of the beryllium bond in the corresponding system, while the comparison between them gives information on the cooperative effect. Remarkably enough, both curves are positive in the $Be-F$ region, demonstrating the presence of a significant $Be \leftarrow F$ charge transfer in both cases. Moreover, at a given z point, the curve of the ternary complex always assumes greater values with respect to the binary complex, indicating that the presence of the base enhances the $Be \leftarrow F$ charge flow.

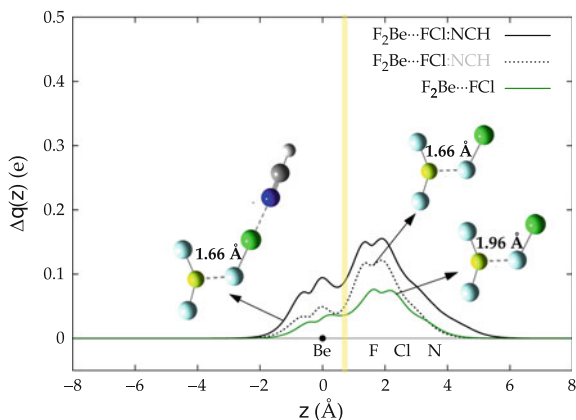


Fig. 17.10 Solid lines are the CD functions for the formation of the $Be\cdots F$ bond in $F_2Be:FCl:NCH$ (black) and $F_2Be:FCl$ (green). The dotted black line corresponds to the formation of the beryllium bond in the binary complex when atomic positions are frozen to the ones of the ternary complex. In all cases, the z -axis is the one joining the beryllium and the fluorine atom (FCl) and the Be atom lies in the origin (black dot in the z axis). The vertical line identifies the isodensity boundary of the ternary complex

As a standard, we use the value of the CD function at the point along the z-axis where equal-valued isodensity surfaces of the isolated fragments become tangent (vertical band in the Figures, see caption for details) to estimate the charge transfer (CT) between the fragments. This indicates that the CT associated to the formation of the $\text{Be}\cdots\text{F}$ bond is amplified through cooperative effect by 130 %, going from the 0.036 e transferred ($\text{Be} \leftarrow \text{F}$) in $\text{F}_2\text{Be}:\text{FCl}$ to the 0.082 e transferred in the ternary $\text{F}_2\text{Be}:\text{FCl}:\text{NCH}$ complex.

The next step of our investigation is the study of the electron density rearrangement upon $\text{Cl}\cdots\text{N}$ bond formation in both the ternary complex $\text{F}_2\text{Be}:\text{FCl}:\text{NCH}$ and the binary complex $\text{FCl}:\text{NCH}$. The corresponding CD curves are shown in Fig. 17.11 (again, the black solid line refers to the ternary complex and the green solid line to the binary one). Similarly to what we have found in the case of the beryllium bond, the curve of the ternary complex is always above to the one of the binary complex, indicating an increased $\text{Cl} \leftarrow \text{N}$ charge flow. The CT associated to the formation of the $\text{Cl}\cdots\text{N}$ bond goes from the 0.038 e ($\text{Cl} \leftarrow \text{N}$) of $\text{FCl}\cdots\text{NCH}$ to the 0.171 e of the ternary $\text{F}_2\text{Be}:\text{FCl}:\text{NCH}$ complex (+350 %).

It is interesting to notice that the $\text{FCl} \leftarrow \text{NCH}$ and the $\text{F}_2\text{Be} \leftarrow \text{FCl}$ charge transfers are of very similar magnitude in the isolated binary complexes, while the situation dramatically changes in the ternary complex, with the $\text{F}_2\text{Be}:\text{FCl} \leftarrow \text{NCH}$ CT becoming about twice as large as that of $\text{F}_2\text{Be} \leftarrow \text{FCl}:\text{NCH}$. However, at least part of this difference has to be attributed to the different shortening of the corresponding bonds on going from the binary complex to the ternary one, that is of 0.3 Å for $\text{Be}\cdots\text{F}$ and 0.5 Å for $\text{Cl}\cdots\text{N}$.

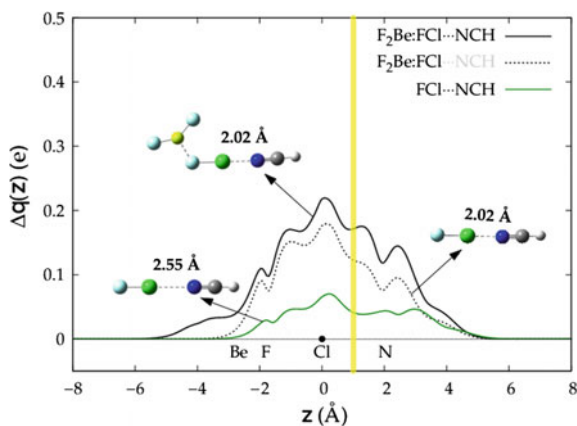


Fig. 17.11 Solid lines are the CD functions for the formation of the $\text{Cl}\cdots\text{N}$ bond in $\text{F}_2\text{Be}:\text{FCl}:\text{NCH}$ (black) and $\text{FCl}:\text{NCH}$ (green). The dotted black line corresponds to the formation of the halogen bond in the binary complex when atomic positions are frozen to the ones of the ternary complex. In all cases, the z-axis is the one joining the chlorine and the nitrogen atoms and the Cl atom being at the origin (black dot in the z axis). The vertical line identifies the isodensity boundary of the ternary complex

The significant differences in the bonding distances between the binary and ternary complexes led us to study the beryllium and the halogen bonds in the geometry obtained by freezing the binary complex atoms at the position they occupy in the ternary complex. By comparing the bonding features of these systems with the ones of the ternary complex, we want to estimate the net electronic effect due to cooperativity, leaving out effects due to the geometry relaxation.

Before discussing cooperativity, it is necessary to compare the $\text{Be}\cdots\text{F}$ and $\text{Cl}\cdots\text{N}$ bonds when binary complexes are on their minimum configuration with the ones of the “frozen” binary complexes. The CD curve for the $\text{Be}\cdots\text{F}$ bond in the geometry obtained by removing the NCH atoms from the ternary complex structure while keeping the remaining atoms frozen at the same position is the black dotted line of Fig. 17.10. In this case, we observed a CT of 0.039 e, only 0.003 e larger than the one of the relaxed binary complex, despite the significant shortening of the $\text{Be}\cdots\text{F}$ bond. Conversely, the CD associated with the formation of the $\text{Cl}\cdots\text{N}$ bond in the structure obtained by removing the BeF_2 molecule from the ternary complex (black dotted line of Fig. 17.13) shows the presence of net charge transfer between the fragments of 0.127 e, significantly higher than the 0.038 e transferred when the binary complex is on its relaxed configuration. This behavior is consistent with the shortening observed in the presence of a single, σ component of the interaction.

It is remarkable that, if we use the frozen binary complex as reference, the $\text{Cl} \leftarrow \text{N}$ charge transfer increases in the ternary complex ($\text{F}_2\text{Be}:\text{FCl}:\text{NCH}$) by 0.044 e, that is similar to the increment of 0.041 e observed in the case of the $\text{Be} \leftarrow \text{F}$ charge transfer upon inclusion of the NCH group.

It is worth noting that the description provided by the QTAIM theory is qualitatively similar, but with some quantitative differences. As shown in Fig. 17.12, the electron density at the $\text{F}_2\text{Be}\cdots\text{FCl}$ BCP for the complex in its equilibrium conformation is smaller than when the complex has the same geometry as in the $\text{F}_2\text{Be}:\text{FCl}:\text{NCH}$ ternary complex. The same finding is observed as far as the $\text{FCl}\cdots\text{NCH}$ interaction is concerned. This trend is in agreement with the increasing CT observed on going from the relaxed dimer to the frozen dimer extracted by our CD analysis, which is expected to be closely related to the electron density at the BCP. However, quantitatively speaking, whereas the change in the $\text{Cl}\cdots\text{N}$ BCP is twice as large as

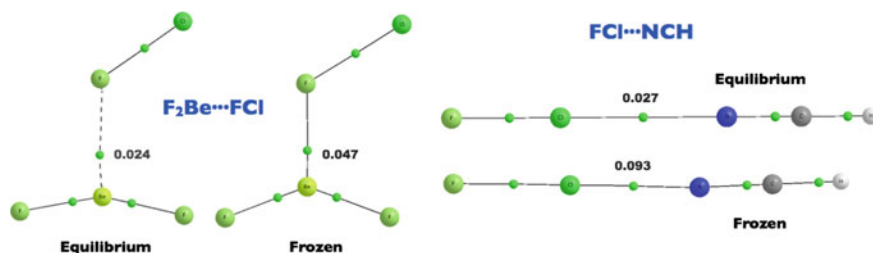


Fig. 17.12 Molecular graphs of the $\text{BeF}_2:\text{FCl}$ and $\text{FCl}:\text{NCH}$ complexes in their equilibrium conformation and with the geometries (*frozen*) they have at the corresponding ternary $\text{F}_2\text{Be}:\text{FCl}:\text{NCH}$ complex. *Green dots* denote BCPs. Electron densities are in a.u.

that at the $\text{Be}\cdots\text{F}$ BCP, the corresponding difference in the CT component is much bigger. This points to the fact that the electron densities at the BCP do not depend only by the amount of charge transferred but also on the physical volume in which it is accommodated.

17.5 Effect of the Nature of the Basic Site on Cooperativity. Comparison of $\text{F}_2\text{Be}:\text{FCl}:\text{Nbase}$ (N-Base = NCH , NHCH_2 , NH_3) Ternary Complexes

In this section we extend our study by including different ternary complexes. In particular, we study complexes of formula $\text{F}_2\text{Be}:\text{FCl}:\text{N-base}$, where the N-base are the sp , sp^2 and sp^3 hybridized bases NCH , NHCH_2 and NH_3 , respectively. We focused here on the comparison between the beryllium/halogen bonds in the ternary complex and in the binary ones frozen at the same positions they occupy in the ternary complex.

The CD curves associated to the formation of the $\text{Be}\cdots\text{F}$ bond in these three systems are shown in Fig. 17.13 as black, blue and red solid lines, respectively for N-base = NCH , NHCH_2 and NH_3 . Remarkably enough, all curves are positive in the $\text{Be}-\text{F}$ (FCl) region, demonstrating the presence of a significant $\text{Be} \leftarrow \text{F}$ charge transfer. In the $\text{Be}-\text{F}$ region, the black curve always assumes smaller values,

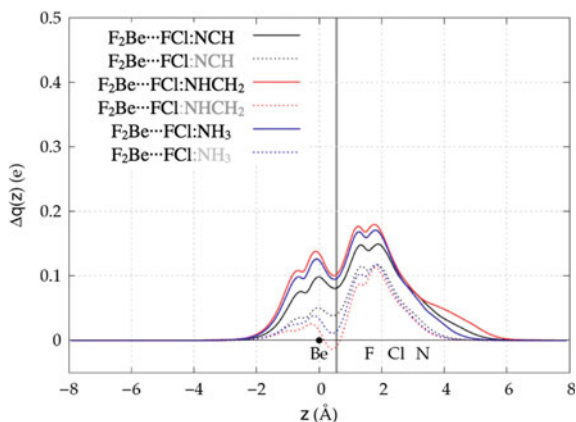


Fig. 17.13 Solid lines are the CD functions for the formation of the $\text{Be}\cdots\text{F}$ bond in $\text{F}_2\text{Be}:\text{FCl}:\text{N-base}$ (black line for NCH , red for NHCH_2 and blue for NH_3). Their analogues for the binary complexes $\text{F}_2\text{Be}\cdots\text{FCl}$ obtained by removing the N-base fragment (all atoms are frozen at the same positions they occupy in the ternary complex) are also reported for comparison as dotted lines with the same color. In all cases, the z -axis is the one joining the beryllium and the fluorine atoms (FCl) the Be atom being at the origin (black dot in the z axis). The vertical band contains the isodensity boundary of the ternary complexes

indicating that the CT component is smaller in $F_2Be:FCl:NCH$ than in $F_2Be:FCl:NHCH_2$ and $F_2Be:FCl:NH_3$. These latter show very similar curves all over the molecular region. The total CT extracted at the isodensity boundary are 0.082 e, 0.101 e and 0.095 e, for N-base = NCH, $NHCH_2$ and NH_3 , respectively.

The CD functions associated to the formation of beryllium bond in the structure obtained by removing the N-base fragment from the ternary complex are reported in Fig. 17.13 as black, blue and red dotted lines for NCH, $NHCH_2$ and NH_3 , respectively. Therefore, the differences between the dotted lines are due to the different geometry of each $F_2Be:FCl:N$ -base system, while the difference between a solid and a dotted line of the same color can be used to estimate the net electronic effect due to cooperativity, as we previously did in the case of $F_2Be:FCl:NCH$. As clearly emerges from the figure, the difference between solid and dotted lines changes from color to color, indicating that different bases affect differently the $Be \cdots F$ bond. In particular, the difference taken at the isodensity boundary is of +0.041, +0.112 and +0.077, for the sp , sp_2 and sp_3 hybridized bases, respectively. This shows that the cooperativity effect in enhancing the $Be \leftarrow F$ CT strongly depends even on the nature of the base.

Figure 17.14 exhibits the CD functions associated to the formation of the $Cl \cdots N$ bond. As revealed by this Figure, changing the N-base strongly affects the $Cl-N$ interaction, with the sp hybridized NCH showing the smallest $Cl \leftarrow N$ CT. $F_2Be:FCl:NHCH_2$ and $F_2Be:FCl:NH_3$ show very similar curves all over the molecular region. The total CT is now 0.171, 0.369 and 0.352 e, for N-base = NCH, $NHCH_2$ and NH_3 , respectively. Indeed, the charge donated from the sp^2 and sp^3 bases is

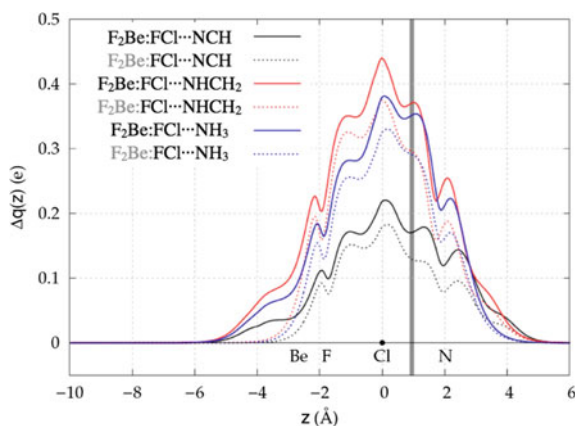


Fig. 17.14 Solid lines are the CD functions for the formation of the $Cl \cdots N$ bond in $F_2Be:FCl:N$ -base (black line for NCH, red for $NHCH_2$ and blue for NH_3). Their analogues for the binary complexes $FCl \cdots N$ -base obtained by removing the N-base fragment (all atoms are frozen at the same positions they occupy in the ternary complex) are also reported for comparison as dotted lines with the same color. In all cases, the z -axis is the one joining the chlorine atom (FCl) and the N atom. Chlorine lies in the origin (black dot in the z axis). The vertical band contains the isodensity boundary of the ternary complexes

more than twice the one donated by NCH. In order to study which is the effect of the beryllium bond on the halogen bonding features, we have also reported in Fig. 17.14 the CD functions associated to the formation of the halogen bond in the structure obtained by removing the BeF_2 fragment from the ternary complex (black, blue and red dotted lines for NCH, NHCH_2 and NH_3 , respectively). As one might expect, the difference between a solid and a dotted line of the same color shows smaller variations along the series if compared with the $\text{Be}\cdots\text{F}$ case. At the inter-fragment boundary, these differences are $+0.044$, $+0.072$ and $+0.061$ e, for NCH, NHCH_2 and NH_3 , respectively. These smaller variations are expected on the basis we are not changing the nature of the beryllium fragment and this results in a systematic enhancement of the $\text{Cl} \leftarrow \text{N}$ charge flow.

The mutual effect of beryllium and halogen bonds that is apparent when the CD functions are analyzed is also seen when comparing the molecular graphs of the ternary complexes with those of the binary ones (See Fig. 17.15), since both the

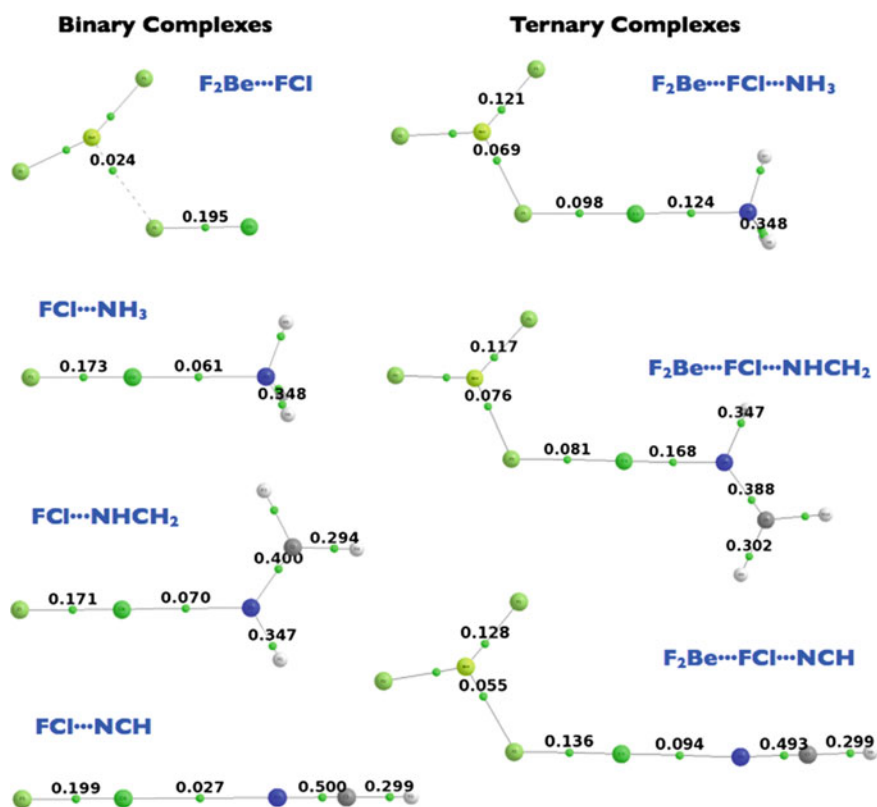


Fig. 17.15 Molecular graphs of the binary complexes, $\text{BeF}_2:\text{FCl}$ and $\text{FCl}:\text{N-base}$ (N-base = NH_3 , NHCH_2 , NCH) complexes and the ternary complexes, $\text{BeF}_2:\text{FCl}:\text{N-base}$ (N-base = NH_3 , NHCH_2 , NCH). Green dots denote BCPs. Electron densities are in a.u.

beryllium and the halogen bonds exhibit a significantly larger electron density in the ternary complexes.

Remarkably enough, there are rather good linear correlations between the electron density at the beryllium and halogen BCPs and the CT calculated by means of the CD function. Similarly good correlations are found when comparing the increase of the electron density at these BCPs, by subtracting from the value of the ternary complex the value of the binary one, with the variation of the calculated CT when the N base is removed from the ternary complex (see Fig. 17.16).

The good linear correlations of Fig. 17.16 show that, similarly to what was found when analyzing the CT, the stronger the interaction with the N-base, the larger the changes in the electron densities. Note that the QTAIM analysis also indicates that the reinforcement of both the beryllium and the halogen bonds are accompanied by a significant weakening of the F–Cl bond, whose electron density at the BCP decreases also following the order $\text{NHCH}_2 > \text{NH}_3 > \text{NCH}$. Consistently, the F–Cl bond length increases from 1.649 Å to 1.817, 1.955, 2.034 Å on going from the isolated F–Cl molecule to the ternary $\text{BeF}_2\text{:FCI:N-Base}$ complexes where N-Base is NCH, NH_3 and NHCH_2 , respectively.

The bonding changes on going from binary to ternary complexes is also mirrored in the plots of the corresponding ELF (See Fig. 17.17).

In the $\text{BeF}_2\text{:FCI}$ binary complex, the formation of the Be bond leads to a distortion of the torus associated with the disynaptic F–Cl basins of the isolated molecule. This distortion, due to the polarization effects associated with the beryllium bond, increases on going from the $\text{BeF}_2\text{:FCI}$ binary complex to the $\text{BeF}_2\text{:FCI:N-base}$ ternary ones. Note that for the particular case of NHCH_2 , where cooperativity is stronger, the ELF shows the formation of a Be–F disynaptic basin.

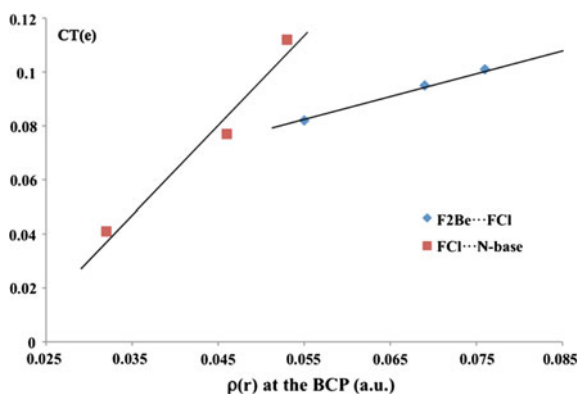


Fig. 17.16 Linear relationship between the $\text{Be} \rightarrow \text{F}$ and the $\text{Cl} \rightarrow \text{N}$ charge transferred (CT(e)) and the electron density at the BCP of the $\text{Be}\cdots\text{F}$ and the $\text{Cl}\cdots\text{N}$ linkages for ternary complexes $\text{BeF}_2\text{:FCI:N-base}$ (N-base = NH_3 , NHCH_2 , NCH)

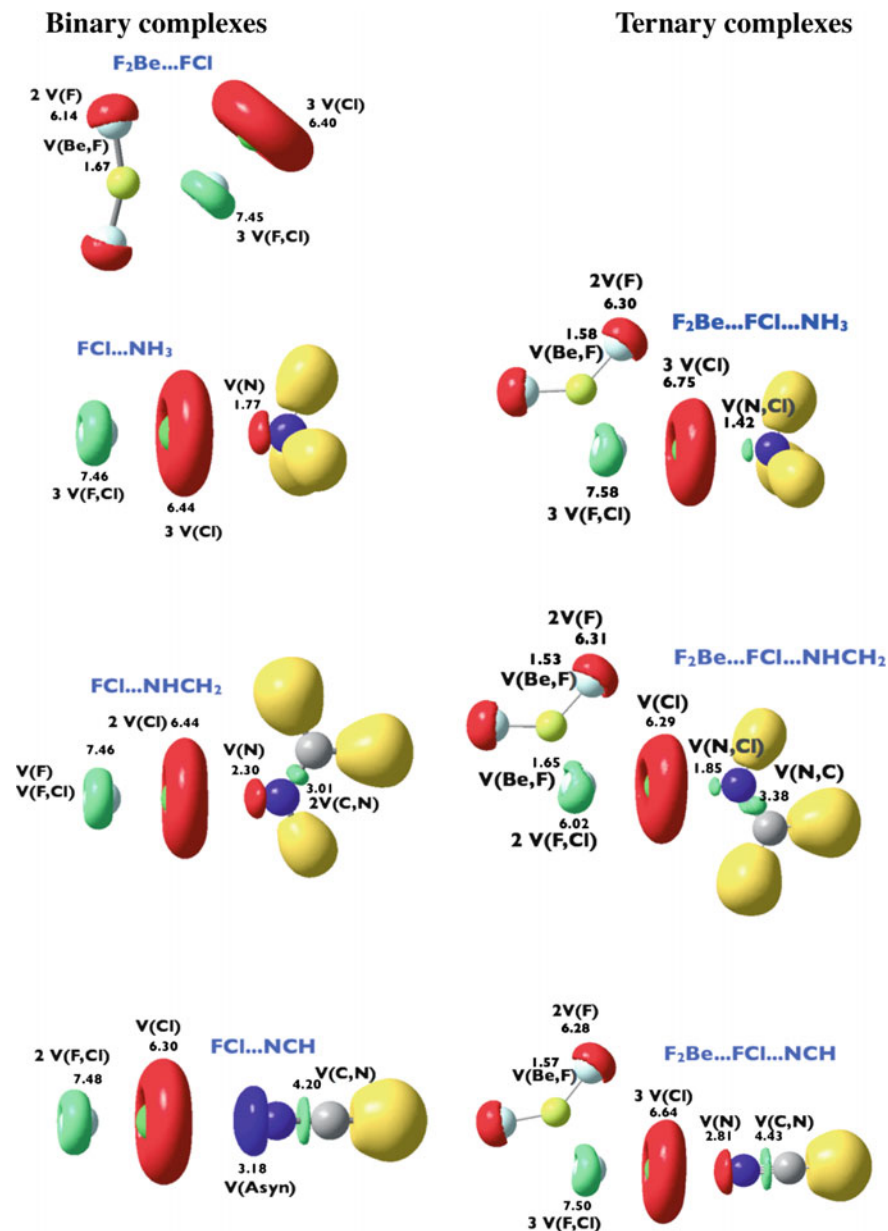


Fig. 17.17 Three-dimensional representations of ELF isosurfaces with ELF = 0.85 for binary complexes, $BeF_2:FCl$ and $FCl:N$ -base (N -base = NH_3 , $NHCH_2$, NCH) complexes and the ternary complexes, $BeF_2:FCl:N$ -base (N -base = NH_3 , $NHCH_2$, NCH). *Yellow, red, green and blue lobes* correspond to disynaptic basins involving H atoms, monosynaptic lone-pair basins, to disynaptic basins between two bonded atoms, and to monosynaptic atomic cores, respectively. The population of the different basins is given in e

The notorious reinforcement of the Cl \cdots N halogen bond in the triads is reflected in the change of a N-monosynaptic basin in the binary complex into a Cl–N disynaptic in the triad. However, for the ternary complexes involving NH₃ and NCH the ELF approach does not provide a clear picture of the weakening of the F–Cl chemical bond since the population of the F–Cl disynaptic basins remains practically unchanged or is a little larger in the triad. Only for the complex involving NHCH₂ this weakening is rather obvious since the formation of a new Be–F disynaptic basin reduces the F–Cl ones to only two.

17.6 Conclusions

The CD approach provides a quantitative description of the charge transfer occurring upon the formation of a beryllium bond between the Lewis base and the BeX₂ moiety. For systems of suitable symmetry, the CD function can be easily decomposed into additive contributions correlating with the different irreducible representations of the molecular point group to which both the molecule and its constituting fragments belong. This allows for the identification of the mechanisms involved in the charge-transfer process and permits the quantification of possible back-donations. Very importantly, this approach also provides a clear description of cooperativity. This has been shown by the study of a series of ternary complexes stabilized through beryllium and halogen bonds. By comparing the CD function of the triads with that of the two binary complexes in which it can be decomposed, we have shown that, in the former, the synergistic effect of halogen and beryllium bond enhances the charge transfer associated with both these non-covalent interactions. The comparison of the results obtained with the CD analysis with those provided by QTAIM and ELF theories, shows a clear agreement as far as the analysis of qualitative trends is concerned. This is well reflected for instance in the good correlations between the amount of charge transferred calculated with the CD approach and the electron density at the BCP of the linkages formed, calculated accordingly to the QTAIM theory. However, the different viewpoints each of these methodologies provide are clearly complementary, the CD being the only one that permits to quantify the charge transfer from the Lewis base to the Lewis acid.

Acknowledgments This work has been also partially supported by the Ministerio de Economía y Competitividad (Projects No. CTQ2012-35513-C02-01 and CTQ2013-43698-P), by the STSM COST Action CM1204, by the Project FOTOCARBON-CM S2013/MIT- 2841 of the Comunidad Autónoma de Madrid and by grants from MIUR (Rome, Italy) with the program FIRB-Futuro in ricerca (RBFR1022UQ). Computational time at Centro de Computación Científica (CCC) of the Universidad Autónoma de Madrid is also acknowledged.

References

1. Yakhmi JV (2011) Soft matter: a perspective. *J Mat Educ* 33(3–4):149–160
2. Whittell GR, Hager MD, Schubert US, Manners I (2011) Nature Mater. Functional Soft materials from metallopolymers and metallosupramolecular polymers 10:176–188
3. Ball P (2004) Nanomaterials—jagged edge. *Nature* 427(6974):497–497. doi:[10.1038/427497a](https://doi.org/10.1038/427497a)
4. Forro L (2006) Nanomaterials—display of flexibility. *Nature* 441(7092):414–415. doi:[10.1038/441414a](https://doi.org/10.1038/441414a)
5. Hobza P, Zahradník R, Müller-Dethlefs K (2006) The world of non-covalent interactions: 2006. *Collect Czech Chem Commun* 71:443–531
6. Custelcean R, Jackson JE (2001) Dihydrogen bonding: structures, energetics, and dynamics. *Chem Rev* 101(7):1963–1980. doi:[10.1021/cr000021b](https://doi.org/10.1021/cr000021b)
7. Bakhmutov VI (2008) Dihydrogen bonds: principles, experiments and applications. Wiley, Hoboken, NJ
8. Metrangolo P, Resnati G (2001) Halogen bonding: a paradigm in supramolecular chemistry. *Chem-Eur J* 7(12):2511–2519. doi:[10.1002/1521-3765\(20010618\)7:12<2511:aid-chem25110>3.0.co;2-t](https://doi.org/10.1002/1521-3765(20010618)7:12<2511:aid-chem25110>3.0.co;2-t)
9. Politzer P, Lane P, Concha MC, Ma Y, Murray JS (2007) An overview of halogen bonding. *J Mol Mod* 13(2):305–311. doi:[10.1007/s00894-006-0154-7](https://doi.org/10.1007/s00894-006-0154-7)
10. Politzer P, Murray JS, Clark T (2013) Halogen bonding and other sigma-hole interactions: a perspective. *Phys Chem Chem Phys* 15(27):11178–11189. doi:[10.1039/c3cp00054k](https://doi.org/10.1039/c3cp00054k)
11. Del Bene JE, Alkorta I, Sanchez-Sanz G, Elguero J (2011) Structures, energies, bonding, and NMR properties of pnictogen complexes H₂XP:NXH₂ (X = H, CH₃, NH₂, OH, F, Cl). *J Phys Chem A* 115(46):13724–13731. doi:[10.1021/jp2094164](https://doi.org/10.1021/jp2094164)
12. Moilanen J, Ganesamoorthy C, Balakrishna MS, Tuononen HM (2009) Weak interactions between trivalent pnictogen centers: computational analysis of bonding in dimers X₃E···EX₃ (E = Pnictogen, X = Halogen). *Inorg Chem* 48(14):6740–6747. doi:[10.1021/ic900635f](https://doi.org/10.1021/ic900635f)
13. Zahn S, Frank R, Hey-Hawkins E, Kirchner B (2011) Pnictogen bonds: a new molecular linker? *Chem Eur J* 17(22):6034–6038. doi:[10.1002/chem.201002146](https://doi.org/10.1002/chem.201002146)
14. Scheiner S (2011) Weak H-bonds. Comparisons of CH···O to NH···O in proteins and PH···N to direct P···N interactions. *Phys Chem Chem Phys* 13(31):13860–13872. doi:[10.1039/c1cp20427k](https://doi.org/10.1039/c1cp20427k)
15. Scheiner S (2013) The pnictogen bond: its relation to hydrogen, halogen, and other noncovalent bonds. *Acc Chem Res* 46(2):280–288. doi:[10.1021/ar3001316](https://doi.org/10.1021/ar3001316)
16. Guan LY, Mo YR (2014) Electron transfer in pnictogen bonds. *J Phys Chem A* 118(39):8911–8921. doi:[10.1021/jp500775m](https://doi.org/10.1021/jp500775m)
17. Wang WZ, Ji BM, Zhang Y (2009) Chalcogen bond: a sister noncovalent bond to halogen bond. *J Phys Chem A* 113(28):8132–8135. doi:[10.1021/jp904128b](https://doi.org/10.1021/jp904128b)
18. Scheiner S (2013) Detailed comparison of the pnictogen bond with chalcogen, halogen, and hydrogen bonds. *Int J Quant Chem* 113(11):1609–1620. doi:[10.1002/qua.24357](https://doi.org/10.1002/qua.24357)
19. Yáñez M, Sanz P, Mó O, Alkorta I, Elguero J (2009) Beryllium bonds, do they exist? *J Chem Theor Comput* 5:2763–2771
20. Fernández Villanueva E, Mó O, Yáñez M (2014) On the existence and characteristics of pi-beryllium bonds. *Phys Chem Chem Phys* 16:17531–17536
21. Bauza A, Mooibroek TJ, Frontera A (2013) Tetrel-bonding interaction: rediscovered supramolecular force? *Angew Chem Int Ed* 52(47):12317–12321. doi:[10.1002/anie.201306501](https://doi.org/10.1002/anie.201306501)
22. Li QZ, Guo X, Yang X, Li WZ, Cheng JB, Li HB (2014) A sigma-hole interaction with radical species as electron donors: does single-electron tetrel bonding exist? *Phys Chem Chem Phys* 16(23):11617–11625. doi:[10.1039/c4cp01209g](https://doi.org/10.1039/c4cp01209g)

23. Azofra LM, Scheiner S (2015) Tetrel, chalcogen, and CH \cdots O hydrogen bonds in complexes pairing carbonyl-containing molecules with 1, 2, and 3 molecules of CO $_2$. *J Chem Phys* 142(3):034307–034309. doi:[10.1063/1.4905899](https://doi.org/10.1063/1.4905899)
24. Lundberg JK, Field RW, Sherrill CD, Seidl ET, Xie Y, Schaefer HF (1993) Acetylene—synergy between theory and experiment. *J Chem Phys* 98(11):8384–8391. doi:[10.1063/1.464496](https://doi.org/10.1063/1.464496)
25. Ladurner AG, Itzhaki LS, Daggett V, Fersht AR (1998) Synergy between simulation and experiment in describing the energy landscape of protein folding. *Proc Nat Acad Sci USA* 95(15):8473–8478. doi:[10.1073/pnas.95.15.8473](https://doi.org/10.1073/pnas.95.15.8473)
26. Shoeib T, Hopkinson AC, Siu KWM (2001) Collision-induced dissociation of the Ag + proline complex: fragmentation pathways and reaction mechanisms—a synergy between experiment and theory. *J Phys Chem B* 105(49):12399–12409. doi:[10.1021/jp012335o](https://doi.org/10.1021/jp012335o)
27. Alcamí M, Mó O, Yáñez M (2001) Computational chemistry. a useful (some times mandatory) tool in mass spectrometry studies. *Mass Spectrom Rev* 20:195–245
28. Medina AS, Claessens CG, Rahman GMA, Lamsabhi AM, Mó O, Yáñez M, Guldi DM, Torres T (2008) Accelerating charge transfer in a triphenylaminesubphthalocyanine donor-acceptor system. *Chem Commun* 15:1759–1761
29. McGrady J (2009) The synergy between theory and experiment. *Dalton Trans* (30):5819–5819. doi:[10.1039/b912487j](https://doi.org/10.1039/b912487j)
30. Mu WH, Chasse GA, Fang DC (2009) A synergy between experiment and theory for the formation of pyridine and pyrrole derivatives from selected butadienes and organolithium reagents: mechanism, solvent, and substituent effect. *Organometallics* 28(20):5848–5856. doi:[10.1021/om900242g](https://doi.org/10.1021/om900242g)
31. Sierka M (2010) Synergy between theory and experiment in structure resolution of low-dimensional oxides. *Prog Surf Sci* 85(9–12):398–434. doi:[10.1016/j.progsurf.2010.07.004](https://doi.org/10.1016/j.progsurf.2010.07.004)
32. Faza ON, Feldman KS, Lopez CS (2010) Cyclization cascade of allenyl azides: synergy between theory and experiment. *Curr Org Chem* 14(15):1646–1657
33. Pettersson L, Nilsson A (2014) A molecular perspective on the d-band model: synergy between experiment and theory. *Top Catal* 57(1–4):2–13. doi:[10.1007/s11244-013-0157-4](https://doi.org/10.1007/s11244-013-0157-4)
34. Lupp D, Christensen NJ, Fristrup P (2014) Synergy between experimental and theoretical methods in the exploration of homogeneous transition metal catalysis. *Dalton Trans* 43(29):11093–11105. doi:[10.1039/c4dt00342j](https://doi.org/10.1039/c4dt00342j)
35. Clot E (2014) Synergy between experiment and theory. *Dalton Trans* 43(29):11092–11092. doi:[10.1039/c4dt90087a](https://doi.org/10.1039/c4dt90087a)
36. Reed AE, Curtiss LA, Weinhold F (1988) Intermolecular interactions from a natural bond orbital, donor-acceptor viewpoint. *Chem Rev* 88(6):899–926. doi:[10.1021/cr00088a005](https://doi.org/10.1021/cr00088a005)
37. Rozenberg M, Loewenschuss A, Marcus Y (2000) An empirical correlation between stretching vibration redshift and hydrogen bond length. *Phys Chem Chem Phys* 2(12):2699–2702. doi:[10.1039/b002216k](https://doi.org/10.1039/b002216k)
38. Mó O, Yáñez M, Alkorta I, Elguero J (2012) Modulating the strength of hydrogen bonds through beryllium bonds. *J Chem Theory Comput* 8:2293–2300
39. Yáñez M, Mó O, Alkorta I, Elguero J (2013) Can conventional bases and unsaturated hydrocarbons be changed into gas-phase superacids stronger than most of the known oxyacids? the role of Beryllium bonds. *Chem Eur J* 35:11637–11643. doi:[10.1002/chem.201300808](https://doi.org/10.1002/chem.201300808)
40. Montero-Campillo MM, Lamsabhi AM, Mó O, Yáñez M (2013) Modulating weak intramolecular interactions through the formation of beryllium bonds: complexes between squaric acid and BeH $_2$. *J Mol Model* 19(7):2759–2766. doi:[10.1007/s00894-012-1603-0](https://doi.org/10.1007/s00894-012-1603-0)
41. Yáñez M, Mó O, Alkorta I, Elguero J (2013) Spontaneous ion-pair formation in the gas phase induced by Beryllium bonds. *Chem Phys Lett* 590:22–26
42. Mó O, Yáñez M, Alkorta I, Elguero J (2014) Spontaneous proton transfers induced by Beryllium bonds. *Mol Phys* 112:592–600

43. Alkorta I, Elguero J, Yáñez M, Mó O (2014) Cooperativity in Beryllium bonds. *Phys Chem Chem Phys* 16:4305–4312
44. Kleeberg H, Klein D, Luck WAP (1987) Quantitative infrared spectroscopic investigations of hydrogen-bond cooperativity. *J Phys Chem* 91(12):3200–3203. doi:[10.1021/j100296a019](https://doi.org/10.1021/j100296a019)
45. Mó O, Yáñez M, Elguero J (1992) Cooperative (nonpairwise) effects in water trimers: an ab initio molecular orbital study. *J Chem Phys* 97(9):6628–6638
46. Hannachi Y, Silvi B, Bouteiller Y (1992) Ab initio study of the structure, cooperativity, and vibrational properties of the H₂O(HF)₂ hydrogen-bonded complex. *J Chem Phys* 97(3):1911–1918. doi:[10.1063/1.463127](https://doi.org/10.1063/1.463127)
47. Karpfen A, Yanovitskii O (1994) Cooperativity in hydrogen-bonded clusters—an improved ab-initio SCF study on the structure and energetics of neutral, protonated and deprotonated chains and of neutral, cyclic hydrogen-fluoride oligomers. *J Mol Struct Theochem* 314(1–2):211–227
48. Mó O, Yáñez M, Elguero J (1994) Cooperative effects in the cyclic trimer of methanol. An ab initio molecular orbital study. *J Mol Struct Theochem* 314(1–2):73–81
49. Suhai S (1994) Cooperativity and electron correlation effects on hydrogen-bonding in infinite systems. *Int J Quantum Chem* 52(2):395–412. doi:[10.1002/qua.560520213](https://doi.org/10.1002/qua.560520213)
50. Latajka Z, Scheiner S (1997) Structure, energetics and vibrational spectra of dimers, trimers, and tetramers of HX (X = Cl, Br, I). *Chem Phys* 216(1–2):37–52. doi:[10.1016/s0301-0104\(97\)00012-8](https://doi.org/10.1016/s0301-0104(97)00012-8)
51. Bryce RA, Vincent MA, Malcolm NOJ, Hillier IH, Burton NA (1998) Cooperative effects in the structuring of fluoride water clusters: ab initio hybrid quantum mechanical/molecular mechanical model incorporating polarizable fluctuating charge solvent. *J Chem Phys* 109(8):3077–3085. doi:[10.1063/1.476900](https://doi.org/10.1063/1.476900)
52. González L, Mó O, Yáñez M (1998) High level ab initio and density functional theory studies on methanol-water dimers and cyclic methanol(water)₂ trimer. *J Chem Phys* 109(1):139–150
53. Masella M, Flament JP (1998) Relation between cooperative effects in cyclic water, methanol/water, and methanol trimers and hydrogen bonds in methanol/water, ethanol/water, and dimethylether/water heterodimers. *J Chem Phys* 108(17):7141–7151. doi:[10.1063/1.476131](https://doi.org/10.1063/1.476131)
54. Philp D, Robinson JMA (1998) A computational investigation of cooperativity in weakly hydrogen-bonded assemblies. *J Chem Soc-Perkin Trans* 2(7):1643–1650. doi:[10.1039/a800931g](https://doi.org/10.1039/a800931g)
55. Cabaleiro-Lago EM, Ríos MA (2000) Ab initio study of interactions in methylamine clusters. The significance of cooperative effects. *J Chem Phys* 112(5):2155–2163. doi:[10.1063/1.480781](https://doi.org/10.1063/1.480781)
56. Parra RD, Gong B, Zeng XC (2001) Energetics and cooperativity in three-center hydrogen bonding interactions. II. Intramolecular hydrogen bonding systems. *J Chem Phys* 115(13):6036–6041. doi:[10.1063/1.1400142](https://doi.org/10.1063/1.1400142)
57. Dannenberg JJ (2002) Cooperativity in hydrogen bonded aggregates. Models for crystals and peptides. *J Mol Struct* 615(1–3):219–226. doi:[10.1016/s0022-2860\(02\)00220-x](https://doi.org/10.1016/s0022-2860(02)00220-x)
58. Karpfen A (2002) Cooperative effects in hydrogen bonding. In: Prigogine I, Rice SA (eds) *Advances in chemical physics*, vol 123, pp 469–510. Wiley, New York. doi:[10.1002/0471231509.ch8](https://doi.org/10.1002/0471231509.ch8)
59. Wieczorek R, Dannenberg JJ (2003) Hydrogen-bond cooperativity, vibrational coupling, and dependence of helix stability on changes in amino acid sequence in small 3(10)-helical peptides. A density functional theory study. *J Am Chem Soc* 125(46):14065–14071. doi:[10.1021/ja034034t](https://doi.org/10.1021/ja034034t)
60. Viswanathan R, Asensio A, Dannenberg JJ (2004) Cooperative hydrogen-bonding in models of antiparallel beta-sheets. *J Phys Chem A* 108(42):9205–9212. doi:[10.1021/jp047404o](https://doi.org/10.1021/jp047404o)
61. Kriz J, Dybal J (2005) Cooperative H-bonds of macromolecules. 1. Binding of low-molecular-weight ligands to polymers. *J Phys Chem B* 109(28):13436–13444. doi:[10.1021/jp051373v](https://doi.org/10.1021/jp051373v)

62. Mó O, Yáñez M, Del Bene JE, Alkorta L, Elguero J (2005) Cooperativity and proton transfer in hydrogen-bonded triads. *ChemPhysChem* 6(7):1411–1418
63. Alkorta I, Elguero J, Solimannejad M (2008) Dihydrogen bond cooperativity in (HCCBeH)(n) clusters. *J Chem Phys* 129(6):064115. doi:[10.1063/1.2966007](https://doi.org/10.1063/1.2966007)
64. Alkorta I, Blanco F, Elguero J (2009) A computational study of the cooperativity in clusters of interhalogen derivatives. *Struct Chem* 20(1):63–71. doi:[10.1007/s11224-008-9392-x](https://doi.org/10.1007/s11224-008-9392-x)
65. Grabowski SJ, Leszczynski J (2009) The enhancement of X-H center dot center dot center dot pi hydrogen bond by cooperativity effects—Ab initio and QTAIM calculations. *Chem Phys* 355(2–3):169–176. doi:[10.1016/j.chemphys.2008.12.011](https://doi.org/10.1016/j.chemphys.2008.12.011)
66. Alkorta I, Blanco F, Deya PM, Elguero J, Estarellas C, Frontera A, Quiñonero D (2010) Cooperativity in multiple unusual weak bonds. *Theor Chem Acc* 126(1–2):1–14. doi:[10.1007/s00214-009-0690-1](https://doi.org/10.1007/s00214-009-0690-1)
67. Alkorta I, Blanco F, Elguero J (2010) Dihydrogen bond cooperativity in azaborane derivatives. *J Phys Chem A* 114(32):8457–8462. doi:[10.1021/jp1046694](https://doi.org/10.1021/jp1046694)
68. Solimannejad M, Malekani M, Alkorta I (2011) Cooperativity between the hydrogen bonding and halogen bonding in F₃CX center dot center dot center dot NCH(CNH)center dot center dot center dot NCH(CNH) complexes (X = Cl, Br). *Mol Phys* 109(13):1641–1648. doi:[10.1080/00268976.2011.582050](https://doi.org/10.1080/00268976.2011.582050)
69. Del Bene JE, Alkorta I, Elguero J (2011) An ab initio study of cooperative effects in ternary complexes X:CNH: Z with X, Z = CNH, FH, ClH, FCl, and HLI: structures, binding energies, and spin-spin coupling constants across intermolecular bonds. *Phys Chem Chem Phys* 13(31):13951–13961. doi:[10.1039/c1cp20480g](https://doi.org/10.1039/c1cp20480g)
70. Parra RD, Streu K (2011) Hydrogen bond cooperativity in polyols: a DFT and AIM study. *Comput Theor Chem* 967(1):12–18. doi:[10.1016/j.comptc.2011.03.027](https://doi.org/10.1016/j.comptc.2011.03.027)
71. Albrecht L, Boyd RJ, Mó O, Yáñez M (2012) Cooperativity between hydrogen bonds and beryllium bonds in (H₂O)(n)BeX₂ (n = 1–3, X = H, F) complexes. A new perspective. *Phys Chem Chem Phys* 14(42):14540–14547. doi:[10.1039/c2cp42534c](https://doi.org/10.1039/c2cp42534c)
72. Karthikeyan S, Nagase S (2012) Origins of the stability of imidazole & imidazole, benzene&imidazole, and benzene&indole dimers: CCSD(T)/CBS and SAPT calculations. *J Phys Chem A* 116:1694–1700
73. Li QZ, Liu XF, Li R, Cheng JB, Li WZ (2012) Competition between dihydrogen bond and beryllium bond in complexes between HBeH and HArF: a huge blue shift of distant H-Ar stretch. *Spectrosc Acta Pt A-Molec Biomolec Spectr* 90:135–140. doi:[10.1016/j.saa.2012.01.022](https://doi.org/10.1016/j.saa.2012.01.022)
74. Vallejos MM, Lamsabhi A, Peruchena NM, Mó O, Yáñez M (2012) Microsolvation of morpholine, a bidentate base—the importance of cooperativity. *J Phys Org Chem* 25(12):1380–1390. doi:[10.1002/poc.3053](https://doi.org/10.1002/poc.3053)
75. Albrecht L, Boyd RJ, Mó O, Yáñez M (2014) Changing weak halogen bonds into strong ones through cooperativity with beryllium bonds. *J Phys Chem A* 118:4205–4213
76. Bader RFW (1990) *Atoms in molecules. A quantum theory*. Clarendon Press, Oxford
77. Matta CF, Boyd RJ (2007) *The quantum theory of atoms in molecules*. Wiley-VCH, Weinheim
78. Becke AD, Edgecombe KE (1990) A simple measure of electron localization in atomic and molecular systems. *J Chem Phys* 92(9):5397–5403
79. Silvi B, Savin A (1994) Classification of chemical-bonds based on topological analysis of electron localization functions. *Nature* 371(6499):683–686
80. Savin A, Nesper R, Wengert S, Fäsler TF (1997) ELF: the electron localization function. *Angew Chem Int Ed Engl* 36:1808–1832
81. Reed AE, Weinhold F (1985) Natural localized molecular-orbitals. *J Chem Phys* 83(4):1736–1740. doi:[10.1063/1.449360](https://doi.org/10.1063/1.449360)
82. Belpassi L, Infante I, Tarantelli F, Visscher L (2008) The chemical bond between Au(I) and the noble gases. Comparative study of NgAuF and NgAu(+) (Ng = Ar, Kr, Xe) by density functional and coupled cluster methods. *J Am Chem Soc* 130(3):1048–1060. doi:[10.1021/ja0772647](https://doi.org/10.1021/ja0772647)

83. Belpassi L, Reza ML, Tarantelli F, Roncaratti LF, Pirani F, Cappelletti D, Faure A, Scribano Y (2010) Charge-transfer energy in the water-hydrogen molecular aggregate revealed by molecular-beam scattering experiments, charge displacement analysis, and ab initio calculations. *J Am Chem Soc* 132(37):13046–13058. doi:[10.1021/ja1056642](https://doi.org/10.1021/ja1056642)
84. Bistoni G, Belpassi L, Tarantelli F, Pirani F, Cappelletti D (2011) Charge-displacement analysis of the interaction in the ammonia-noble gas complexes. *J Phys Chem A* 115(51):14657–14666. doi:[10.1021/jp208859x](https://doi.org/10.1021/jp208859x)
85. Cappelletti D, Ronca E, Belpassi L, Tarantelli F, Pirani F (2012) Revealing charge-transfer effects in gas-phase water chemistry. *Acc Chem Res* 45(9):1571–1580. doi:[10.1021/ar3000635](https://doi.org/10.1021/ar3000635)
86. Bartocci A, Cappelletti D, Pirani F, Tarantelli F, Belpassi L (2014) Intermolecular interaction in the H₂S-H₂ complex: molecular beam scattering experiments and ab-initio calculations. *J Phys Chem A* 118(33):6440–6450. doi:[10.1021/jp502170g](https://doi.org/10.1021/jp502170g)
87. Salvi N, Belpassi L, Tarantelli F (2010) On the Dewar-Chatt-Duncanson model for catalytic gold(I) complexes. *Chem-Eur J* 16(24):7231–7240. doi:[10.1002/chem.201000608](https://doi.org/10.1002/chem.201000608)
88. Bistoni G, Belpassi L, Tarantelli F (2013) Disentanglement of donation and back-donation effects on experimental observables: a case study of gold-ethyne complexes. *Angew Chem Int Ed* 52(44):11599–11602. doi:[10.1002/anie.201305505](https://doi.org/10.1002/anie.201305505)
89. Ciancaleoni G, Scafuri N, Bistoni G, Macchioni A, Tarantelli F, Zuccaccia D, Belpassi L (2014) When the Tolman electronic parameter fails: a comparative DFT and charge displacement study of (L)Ni(CO)(3) (0/-) and (L)Au(CO)(0/+). *Inorg Chem* 53(18):9907–9916. doi:[10.1021/ic501574e](https://doi.org/10.1021/ic501574e)
90. Marchione D, Belpassi L, Bistoni G, Macchioni A, Tarantelli F, Zuccaccia D (2014) The chemical bond in gold(I) complexes with N-heterocyclic carbenes. *Organometallics* 33(16):4200–4208. doi:[10.1021/om5003667](https://doi.org/10.1021/om5003667)
91. Ciancaleoni G, Biasiolo L, Bistoni G, Macchioni A, Tarantelli F, Zuccaccia D, Belpassi L (2015) Selectively measuring pi back-Donation in gold(I) Complexes by NMR spectroscopy. *Chem-Eur J* 21(6):2467–2473. doi:[10.1002/chem.201406049](https://doi.org/10.1002/chem.201406049)
92. Becke AD (1993) *J Chem Phys* 98:5648–5652
93. Lee C, Yang W, Parr RG (1988) *Phys Rev B* 37:785–789.
94. Frisch MJ, Trucks GW, Schlegel HB, Scuseria GE, Robb MA, Cheeseman JR, Scalmani G, Barone V, Mennucci B, Petersson GA, Nakatsuji H, Caricato M, Li X, Hratchian HP, Izmaylov AF, Bloino J, Zheng G, Sonnenberg JL, Hada M, Ehara M, Toyota K, Fukuda R, Hasegawa J, Ishida M, Nakajima T, Honda Y, Kitao O, Nakai H, Vreven T, Montgomery Jr. JA, Peralta JE, Ogliaro F, Bearpark M, Heyd JJ, Brothers E, Kudin KN, Staroverov VN, Kobayashi R, Normand J, Raghavachari K, Rendell A, Burant JC, Iyengar SS, Tomasi J, Cossi M, Rega N, Millam JM, Klene M, Knox JE, Cross JB, Bakken V, Adamo C, Jaramillo J, Gomperts R, Stratmann RE, Yazyev O, Austin AJ, Cammi R, Pomelli C, Ochterski JW, Martin RL, Morokuma K, Zakrzewski VG, Voth GA, Salvador P, Dannenberg JJ, Dapprich S, Daniels AD, Farkas O, Foresman JB, Ortiz JV, Cioslowski J, Fox DJ (2009) Gaussian09, Revision A.02. Gaussian09, Revision A.02 edn. Gaussian, Inc., Wallingford CT
95. Dunning TH (1989) Gaussian-basis sets for use in correlated molecular calculations. 1. the atoms boron through neon and hydrogen. *J Chem Phys* 90(2):1007–1023
96. Velde G, Bickelhaupt FM, Baerends EJ, Guerra CF, Van Gisbergen SJA, Snijders JG, Ziegler T (2001) Chemistry with ADF. *J Comput Chem* 22(9):931–967. doi:[10.1002/jcc.1056](https://doi.org/10.1002/jcc.1056)
97. Keith TA (2013) AIMAll (Version 13.05.06). AIMAll (Version 13.05.06) Gristmill Software, Overland Park, KS, 2013. aim.tkgristmill.com
98. Noury S, Krokidis X, Fuster F, Silvi B (1999) Computational tools for the electron localization function topological analysis. *Comput Chem* 23(6):597–604
99. Glendening ED, Badenhoop JK, Reed AE, Carpenter JE, Bohmann JA, Morales CM, Weinhold F (2004) NBO 5.G. <http://www.chem.wisc.edu/~nbo5> edn. Theoretical Chemistry Institute, University of Wisconsin, Madison, WI

100. Martín-Sómer A, Montero-Campillo MM, Mó O, Yáñez M, Alkorta I, Elguero J (2014) Some interesting features of non-covalent interactions. *Croat Chem Acta* 87:291–306
101. Alkorta I, Elguero J, Del Bene JE, Mó O, Yáñez M (2010) New insights into factors influencing B-N bonding in X:BH₃-nFn and X:BH₃-nCln for X = N-2, HCN, LiCN, H₂CNH, NF₃, NH₃ and n = 0-3: the importance of deformation. *Chem-Eur J* 16(39):11897–11905. doi:[10.1002/chem.201001254](https://doi.org/10.1002/chem.201001254)
102. Martín-Sómer A, Lamsabhi A, Mó O, Yáñez M (2012) The importance of deformation on the strength of beryllium bonds. *Comput Theor Chem* 998:74–79. doi:[10.1016/j.comptc.2012.06.009](https://doi.org/10.1016/j.comptc.2012.06.009)
103. Eskandari K (2012) Characteristics of beryllium bonds; a QTAIM study. *J Mol Mod* 18:3481–3487
104. Ronca E, Belpassi L, Tarantelli F (2014) A quantitative view of charge transfer in the hydrogen bond: the water dimer case. *ChemPhysChem* 15(13):2682–2687. doi:[10.1002/cphc.201402321](https://doi.org/10.1002/cphc.201402321)

Chapter 18

A Complete NCI Perspective: From New Bonds to Reactivity

**Christophe Narth, Zeina Maroun, Roberto A. Boto,
Robin Chaudret, Marie-Laure Bonnet, Jean-Philip Piquemal
and Julia Contreras-García**

Abstract The Non-Covalent Interaction (NCI) index is a new topological tool that has recently been added to the theoretical chemist's arsenal. NCI fills a gap that existed within topological methods for the visualization of non-covalent interactions. Based on the electron density and its derivatives, it is able to reveal both attractive and repulsive interactions in the shape of isosurfaces, whose color code reveals the nature of the interaction. It is interesting to note that NCI can even be calculated at the promolecular level, making it a suitable tool for big systems, such as proteins or DNA. Within this chapter we will review the main characteristics of NCI, its similarities with and differences from previous approaches. Special attention will be paid to the visualization of new interaction types. Being based on the electron density, NCI is not only very stable with respect to the calculation method, but it is also a suitable tool for detecting new bonding mechanisms, since all such mechanisms should have a detectable effect on the electron density. This type of approach overcomes the limitations of bond definition, revealing all

Zeina Maroun can be contacted at zema@topsoe.dk

C. Narth · R.A. Boto · J.-P. Piquemal · J. Contreras-García
Laboratoire de Chimie Théorique, UPMC Univ Paris 06, UMR 7616, 75005 Paris, France
e-mail: christophe.narth@lct.jussieu.fr

R.A. Boto
e-mail: alboto@lct.jussieu.fr

J.-P. Piquemal
e-mail: jpp@lct.jussieu.fr

C. Narth · R.A. Boto · J.-P. Piquemal · J. Contreras-García (✉)
Laboratoire de Chimie Théorique, CNRS, UMR 7616, 75005 Paris, France
e-mail: contrera@lct.jussieu.fr

Z. Maroun
Department of Chemistry, University of Copenhagen, Universitetsparken 5, 2100
Copenhagen, Denmark
e-mail: zeina@chem.ku.dk

interaction types, irrespective of whether they have a name or have previously been identified. Finally, we will show how this tool can be used to understand chemical change along a chemical reaction. We will show an example of *torquoselectivity* and put forward an explanation of selectivity based on secondary interactions which is complementary to the historical orbital approach.

18.1 Introduction

As defined by Linus Pauling, “Chemistry is the science of substances: their structure, their properties, and the reactions that change them into other substances” [1]. The first aspects, structure and properties, are clearly associated with the arrangement of atoms in a molecule, i.e. the chemical bond. These bonds determine Pauling’s third aspect, chemical reactivity. In other words, chemical bonds are the undisputed foundation of chemistry and their visualization should allow chemists to understand how molecules behave at the most fundamental level.

Achievement of a mechanistic understanding of chemical and biological functions as well as the structure of solid materials depends on knowing the geometric structure and the nature of bonds. But, despite the chemical bond being a fundamental concept in chemistry, “**what is a chemical bond?**” **still remains a critical question** for the chemical community because of the lack of a unique definition as well as an unclear understanding of its physical nature.

Successful numerical solution of the Schrödinger equation has yielded energies and properties of atoms and molecules, but not yet a clear physical explanation of chemical bonding. There is even a controversy on the mechanistic origin of the most “simple” chemical bond, covalent bonding, as it was remarked by Burdett in his classical book [2].

As recently as in 2007, a special issue was devoted to the “90 Years of Chemical Bonding” [3]. In this issue, the chemical bond was compared to a unicorn, “a mythical but useful creature, which brings law and order [...] in an otherwise

R. Chaudret
Scienomics, 16 rue de l’Arcade, 75008 Paris, France
e-mail: Robin.Chaudret@scienomics.com

M.-L. Bonnet
Institut de Recherche de Chimie Paris, ENSCP, Ecole Nationale Supérieure de Chimie de Paris Chimie ParisTech, UMR 8247, 75231 Paris, France
e-mail: marie-laure.bonnet@chimie-paristech.fr

M.-L. Bonnet
Institut de Recherche de Chimie Paris, CNRS, UMR 8247, 75231 Paris, France

R.A. Boto
Institut du Calcul et de la Simulation (ICS), Université Pierre et Marie Curie (UPMC), Paris VI, 75005 Paris, France

chaotic and disordered world” [4]. Everyone knows how it looks despite nobody ever having seen one [4–6]. This line of reasoning is similar to Coulson’s comment: “Sometimes it seems to me that a bond between two atoms has become so real, so tangible, so friendly, that I can almost see it. Then I awake with a little shock, for a chemical bond is not a real thing. It does not exist. No one has ever seen one. No one ever can. It is a figment of our own imagination” [7]. Even chemical bonds have been described as “noumena” rather than “phenomena” [8–10].

Chemical bonds together with other concepts such as atomic orbitals, electron shells, lone pairs, aromaticity, atomic charges, (hyper-) conjugation, strain, etc. do not correspond to physical observables. Such concepts therefore cannot be unambiguously defined in pure quantum theory, but constitute a rich set of “fuzzy”, yet invaluable useful concepts [11–14]. They lead to constructive ideas and developments when appropriately used and defined.

In chemistry as well as in physics, advanced theories are held by two milestones: (i) a mathematical structure/formalism disclosing the basic entities of the theory and their mathematical relationships, and (ii) an “interpretative” recipe of basic entities of the theory. The latter discloses the qualitative meaning of the basic entities and their relation to other known entities within and beyond the theory. It is important to highlight that the connection between the mathematical formalism and its interpretation is always subtle. This problem can be traced back to the lack of a clear and unambiguous definition of a bond in quantum mechanics and the plethora of interpretations that have been introduced with various “meanings” of the “mathematical symbols/entities” of the theory [15].

In front of this quandary, two opposite attitudes can be envisaged. On the one hand, the old and negative statement of the French mathematician R. Thom: “Il me faut cependant avouer que la chimie proprement dite ne m’a jamais beaucoup intéressée. Pourquoi? Peut-être parce que des notions telles que celles de valence, de liaison chimique etc., m’ont toujours semblé peu claires du point de vue conceptuel.” (I should admit that chemistry never really interested me. Why? Perhaps because notions such as those of valence, chemical bond, etc., always appeared unclear to me from the conceptual point of view). On the other hand, the more recent and pragmatic comment of Alvarez et al.: “Chemistry has done more than well in a universe of structure and function on the molecular level with just this imperfectly defined concept of a chemical bond. Or maybe it has done so well precisely because the concept is flexible and fuzzy” [16].

However, it is important to note that scientific arguments, debates, and controversies are at the heart of chemistry. This situation has been clearly stated in the very recent paper entitled “The Nature of the Fourth Bond in the Ground State of C₂: The Quadruple Bond Conundrum” by Danovich et al. [17] in which these authors recognize that they are in front of a “Rashomon effect”, in which the bonding picture is becoming too fuzzy to be constructive anymore.

In trying to overcome this dichotomy, topological analysis has become one of the most useful tools to characterize chemical interactions. Visualization of bonding interactions between atoms and molecules is a long-standing quest in theoretical and computational chemistry. The main interest lies in creating a tool that enables

not only to see the interaction, but also to interpret its character and properties. Different types of bonding can be revealed by various topological methods, each based on different scalar fields [18]. This chapter deals with a new interpretative tool, NCI (standing for Non-Covalent Interactions), for revealing non-covalent interactions, which tries to bring some intuitive order into this fuzzy set of ideas.

18.1.1 *Historical Framework*

Over the years, different approaches have been developed to reveal chemical bonds. Covalent bonds are intuitively represented using conventional Lewis structures [19]. Molecular Orbital (MO) theory has been very useful and successful for the theoretical analysis of chemical reactions and chemical reactivity. The frontier orbital theory [20] and the orbital symmetry rules of Woodward and Hoffman [21] are paradigmatic examples of the possibilities of quantum chemistry within the MO theory.

To reduce the dimensionality of the problem, three-dimensional interpretative approaches have been introduced. The conceptual density functional theory pioneered by Parr et al. [22] has been at the origin of very useful reactivity descriptors. Another low dimensional approach has originally been developed by Bader: [23–25] the topological approach. Within these approaches, 3D space is divided following the gradient of a scalar function into mutually disjoint regions. Bader's QTAIM (Quantum Theory of Atoms In Molecules) theory is based on the topological analysis of the density and provides an atomic picture of the system. Chemical bonds and the underlying molecular graph may be traced by the analysis of its bond critical points (BCPs, first order saddle points). Following the same philosophy, ELF [26, 27] (Electron Localization Function) topological analysis divides the space into chemically intuitive regions associated with electron pairs so that electronic shells, bonds, and lone pairs are revealed. Also, purely electrostatic interactions can be analyzed using electrostatic potential maps [28].

18.1.2 *Weak Interactions*

Chemical interactions between a protein and a drug, or a catalyst and its substrate, self-assembly of nanomaterials [29, 30], and even some chemical reactions [31, 32], are dominated by non-covalent interactions. This class of interactions spans a wide range of binding energies, and encompasses hydrogen bonding, dipole-dipole interactions and London dispersion [33] as well as more up to date interactions such as halogen bonds, $\text{CH}\cdots\pi$ and $\pi\cdots\pi$ interactions. Repulsive interactions, also known as steric clashes, should not be disregarded either.

More specifically, non-covalent interactions are of paramount importance in chemistry and especially in bio-disciplines [34, 35], since they set up the force field scenario through which chemical species interact with each other without a significant electron sharing between them. They represent, in fact, the machinery

through which molecules recognize themselves and establish how molecules will approach and eventually pack together.

During the last decade, non-covalent interactions have also raised a great deal of interest in the context of self-assembly [36] and crystallization [37], whose underlying general rules are at the moment too far away to be fully rationalized and understood [38]. Knowledge of such rules would in principle allow to build from scratch (even complex) materials exhibiting the desired properties [29, 39, 40]. Although it can not be ignored that a given observed structure is generally the outcome of a “drawing” among a plethora of energetically similar, but structurally dissimilar options [41], understanding intermolecular non-covalent interactions and their mutual interplay in the supramolecular assemblies is nonetheless a fundamental step in making progress in structural prediction and evolution.

18.1.2.1 Weak Interactions: The Need for a New Approach

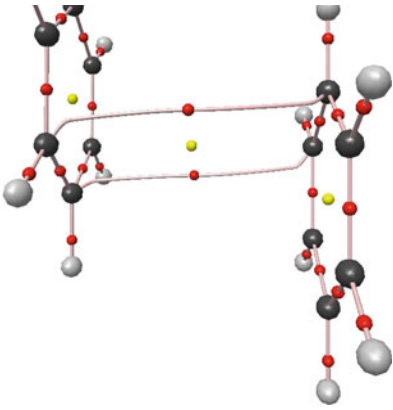
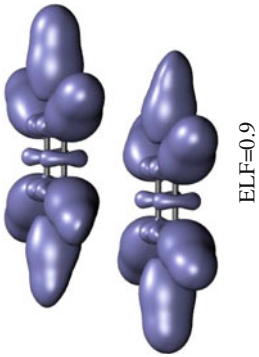
Non-covalent interactions are frequently visualized using distance-dependent contacts, generally without consideration of hydrogen atoms [42–44]. Hydrogen-bonds can be identified from the molecular geometry [45] and from ELF [46], while grid-based calculations from classical force fields are used to model van der Waals interactions [47]. The crucial role of weak interactions can also be analyzed in an indirect manner through property computations (from population to electrostatic moments) [48]. However, these fluctuations are not easily visualized. In other words, a visual quantum chemical approach was conspicuously missing in this scenario.

Let’s look at an example to clearly pinpoint the state of the art of topological approaches to weak interactions. The image provided by QTAIM and ELF of benzene dimer is provided in Table 18.1. Let’s first focus on a given benzene molecule: The electron density shows maxima (cusps) for the C and H atoms, whereas C–H and C–C bonds are represented by BCPs (in red). ELF, instead, provides a picture based on electron localization, so that isosurfaces appear around nuclei and bonds. In both cases the chemical structure is revealed as expected from chemical intuition. However, the ELF picture is obviously more intuitive thanks to the isosurfaces.

Now, if we take a look at the complete system, the stacking dimer, we can see that intermolecular BCPs appear along with a ring critical point (second order saddle point, in yellow). The fact that interactions are related to saddle points, locates them on the interatomic surfaces, so that they highlight interatomic contact, but they do not have an associated region within this approach. Moreover, the critical points unite pairs of C atoms, which is not the chemical picture we have of a stacking interaction: it should appear as a benzene to benzene interaction. The VSEPR regions of benzene dimer are clearly identified by ELF, but nothing is seen for the inter-benzene stacking interaction.

In other words, both approaches fail to correctly provide a picture of delocalized interactions. Thus, it is the aim of this chapter to introduce such a tool, show its advantages over previous theories and its ability to provide a complete and holistic vision of non-covalent interactions and their changes directly from the electron density.

Table 18.1 Comparison between QTAIM and ELF topologies in benzene dimer

Method	QTAIM	ELF
Function	Electron density	Pauli kinetic energy density
Partition	Atoms	Lewis pairs
Example		 ELF=0.9

18.2 NCI: Non-covalent Interaction Index

The electron density has a fundamental advantage over MO-based descriptors because it is an experimentally accessible local function defined within the exact many-body theory, also supported by the Hohenberg-Kohn theorem [49]. The relationship between electron density and physical/chemical properties can be understood from the Hohenberg-Kohn theorem, which asserts that a system's ground-state properties are a consequence of its electron density. Furthermore since chemical reactions proceed by $\rho(\mathbf{r})$ redistributions, methods that analyze $\rho(\mathbf{r})$ distributions should help to understand the electron structure of molecules and thus chemical reactivity (see Sect. 18.8).

Our approach, introduced in the coming sections, uses the density and its derivatives, allowing simultaneous analysis and visualization of all non-covalent interaction types as real-space surfaces, thus adding an important tool to the chemist's arsenal [50–52].

18.2.1 The Reduced Density Gradient

The reduced density gradient, s or RDG, is a fundamental dimensionless quantity in DFT used to describe the deviation from a homogeneous electron distribution [49, 53, 54]. Properties of the reduced gradient have been investigated in depth in the process of developing increasingly accurate functionals [55].

The origin of the reduced density gradient can be traced to the generalized gradient contribution to the GGA exchange energy, E_X^{GGA} , from density-functional theory:

$$E_X^{GGA} - E_X^{LDA} = - \sum \int F(s) \rho^{4/3}(\mathbf{r}) d\mathbf{r}, \quad (18.1)$$

where $F(s)$ is a function of s for a given spin with

$$s = \frac{1}{C_S} \frac{|\nabla\rho|}{\rho^{4/3}}, \quad (18.2)$$

Small values of s occur close to the nuclei, due to $C_S = 2(3\pi^2)^{1/3}$ and the 4/3 exponent of the density ensuring that s is a dimensionless quantity.

s accounts for local density inhomogeneities due to its differential behavior depending on the chemical region of the molecule. The reduced density gradient assumes large values in the exponentially-decaying density tails far from the nuclei, where the density denominator approaches zero more rapidly than the gradient numerator. Small values of s occur close to the nuclei, due to the combination of

large densities and small density gradients. The lower bound on the reduced density gradient is zero, as occurs throughout a homogeneous electron gas and at BCPs.

The effect of bonding on the reduced density gradient is especially easy to visualize when s is plotted as a function of the density. When ρ is given by a single Slater Type Orbital (STO), graphs of $s(\rho)$ assume the form $f(x) = ax^{-1/3}$, where a is a constant (see Appendix, Table 18.2). This can easily be proven from a Slater Type Orbital (STO) model density. For a single atomic orbital $\psi = e^{-ar}$, the density is $\rho = e^{-2ar}$ and the gradient is $\nabla\rho = -2a\rho$, such that

$$s(\rho) = \frac{1}{C_S} \frac{2\alpha\rho}{\rho^{4/3}} = \frac{2\alpha}{C_S} \rho^{-1/3}. \quad (18.3)$$

When there is overlap between atomic orbitals, a spike in the $s(\rho)$ diagram appears (Fig. 18.1). The points forming this spike can identify the interaction location when they are mapped back to real space. This procedure is able to reveal non-covalent interactions.

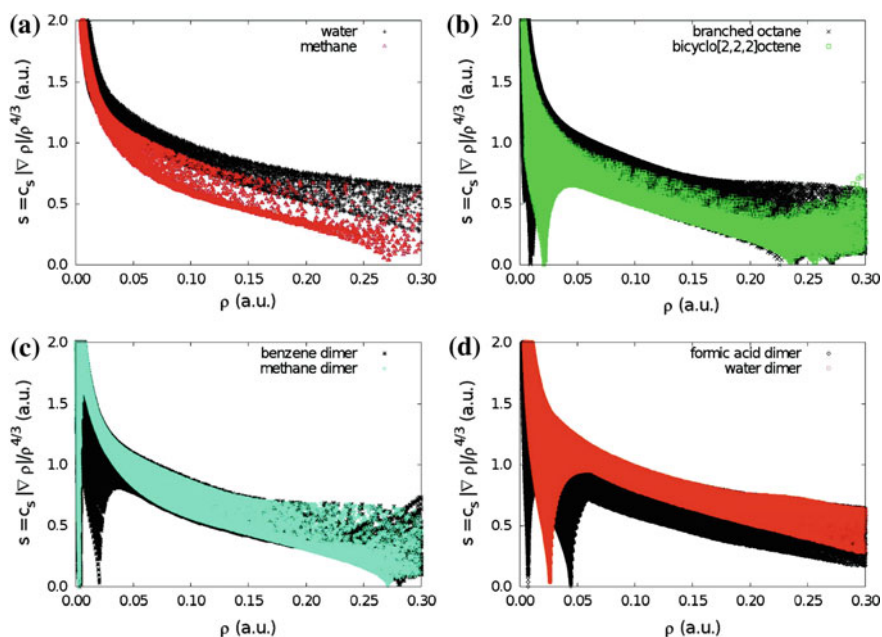


Fig. 18.1 Plots of the electron density and its reduced gradient for methane, water, branched octane, bicyclo [2,2,2]octene, and the homomolecular dimers of methane, benzene, water, and formic acid. The data was obtained by evaluating B3LYP/6-31G* density and gradient values on cuboid grids. Reprinted with permission from Ref. [50]. Copyright 2010 American Chemical Society

To explore the features associated with small reduced gradients, we first examine plots of s versus ρ (Fig. 18.1). These plots were generated by evaluating the B3LYP [56, 57] density and reduced gradients on cuboid grids, with a 0.1 a.u. step size, for each molecule or dimer. To provide even more sampling of the small low-density, low-gradient regions in hydrogen-bonded complexes, additional calculations were performed for water and formic acid dimers with a much denser 0.025 a.u. step size.

Plotting s versus ρ , as in Fig. 18.1, reveals the basic pattern of intramolecular interactions. Methane (Fig. 18.1a) illustrates the typical covalent bond pattern. The top left-side points (small density and large reduced gradient) correspond to the exponentially-decaying tail regions of the density, far from the nuclei. The points on the bottom right side (density values of ca. 0.25 a.u. and low reduced density gradient) correspond to the C–H covalent bonds. Covalent bonds have their characteristic BCP in the electron density, corresponding to $s = 0$. Regions near the nuclei have larger density values and appear beyond the right edge of the plot. The plot has an overall shape of the form $a\rho^{-1/3}$ because atomic and molecular densities are piecewise exponential. The results for water are very similar, the only difference being that the covalent bonds lie at higher density values, past the edge of the plot. In Fig. 18.1b–d, we consider six examples of chemical systems displaying various types of non-covalent interactions. Plots of s versus ρ for these systems all exhibit a new feature: one or more spikes in the low-density, low-gradient region, a signature of non-covalent interactions. This is the basis of NCI.

18.2.2 The Density Second Eigenvalue

According to the divergence theorem [58], the sign of the Laplacian of the density, $\nabla^2\rho$, indicates whether the net gradient flux is entering, $\nabla^2\rho < 0$, or leaving, $\nabla^2\rho > 0$, an infinitesimal volume around a reference point. Hence, it highlights whether the density is concentrated or depleted at that point, relative to the surrounding environment. To differentiate between different types of weak interactions one cannot resort to the sign of the Laplacian itself (as is common within AIM theory) since it is dominated by the principle axis of variation and is positive for all closed-shell interactions [59].

To understand bonding in more detail, it is often useful to decompose the Laplacian into the contributions along the three particular axes of maximal variation. These components are the three eigenvalues, λ_i of the electron-density Hessian matrix, such that, $\nabla^2\rho = \lambda_1 + \lambda_2 + \lambda_3$, ($\lambda_1 < \lambda_2 < \lambda_3$). At points with zero gradient, analysis of the Hessian eigenvalues is analogous to determining the signature of the critical point. Thus, at nuclei (cusps interpreted as maxima of ρ), all the eigenvalues are negative, while at the center of cages or holes (minima of ρ) all the eigenvalues are positive. In the remaining points of space $\lambda_3 > 0$, $\lambda_1 < 0$, and λ_2 can be either

positive or negative. Within the NCI framework, the sign of λ_2 (i.e. the perpendicular plane) enables identification of the interaction type. Attractive interactions appear at $\lambda_2 < 0$ whereas in the cases where λ_2 is positive (as in rings or cages), usually several atoms interact but are not bonded, which corresponds to steric crowding according to classical chemistry.

Both van der Waals interactions and hydrogen bonds show negative values of λ_2 at the critical point (with $\lambda_2 \simeq 0$ for van der Waals interactions and even $\lambda_2 \geq 0$ on the surface). This can be attributed to the homomorphic virial path associated with the bonding direction, which defines a line along which the potential-energy density is maximally negative. Conversely, non-bonding interactions, such as steric crowding, result in density depletion, such that $\lambda_2 > 0$. Analogously, the homeomorphism ensures that these critical points (both ring and cages points) identify lines of minimally-negative potential-energy density.

18.3 Interpreting NCI

18.3.1 *The 2D Plot*

Once the second eigenvalue has been introduced to separate attractive from repulsive interactions, it is necessary to categorize the interactions by their strength. This can be done thanks to the properties of the corresponding critical points. Characteristic densities of van der Waals interactions are much smaller than densities at which hydrogen bonds appear. However, steric clashes and hydrogen bonds (HBs) span similar density ranges and overlap in plots of $s(\rho)$. This is illustrated for the phenol dimer in Fig. 18.2a, b. This is a hydrogen-bonded complex that exhibits non-bonding interactions within each benzene ring and a stacking interaction between the benzene rings. We thus have the three main types of interactions: van der Waals, HB and steric clashes. Whereas van der Waals is well-differentiated because it appears at smaller densities, the steric clash and the hydrogen bond spikes overlap in Fig. 18.2a.

The interaction type can be distinguished if the $s(\rho)$ diagrams are modified by plotting $\text{sign}(\lambda_2)\rho$ as the abscissa. Analysis of the sign of λ_2 thus helps to discern between the different types of weak interactions, whereas the density itself provides information about their strength; both are combined in the value of $\text{sign}(\lambda_2)\rho$. When the Hessian eigenvalues are considered, the different nature of these interactions is made clear: the benzene-ring interactions remain at positive values, whereas the hydrogen bond now lies at negative values, within the attractive regime. The NCI spikes nearest zero density correspond to weakly-attractive dispersion interactions between the phenyl rings.

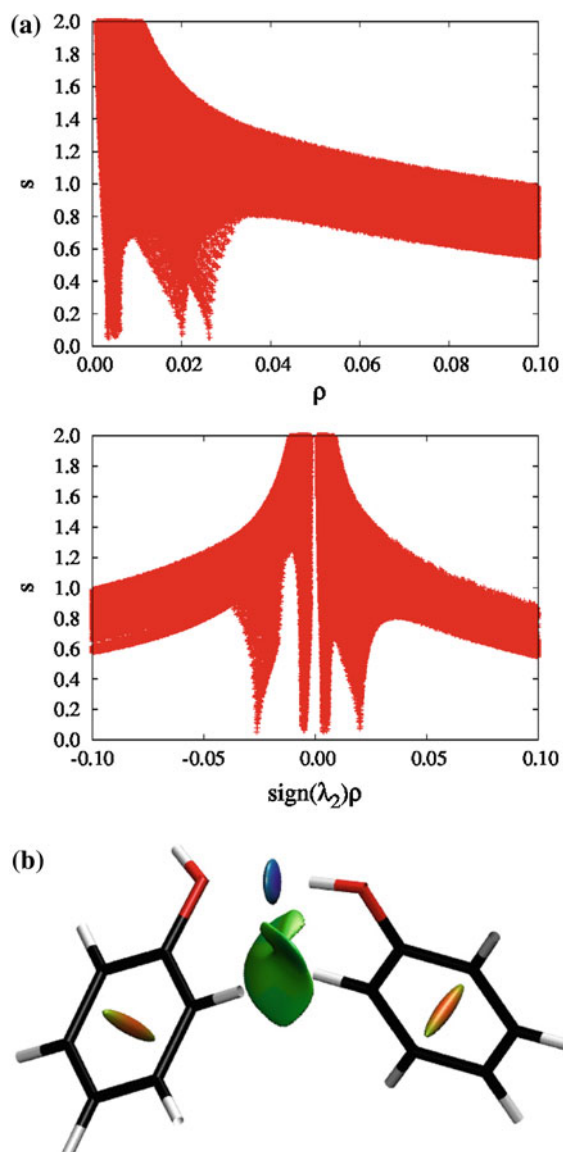


Fig. 18.2 Plots of **a** $s(\rho)$, **b** NCI isosurface, for the phenol dimer. The $s = 0.6$ a.u. isosurface is colored over the range $-0.03 < \text{sign}(\lambda_2)\rho < +0.03$ a.u.

18.3.2 3D Plot

18.3.2.1 3D Visualization

The 3D spatial visualization of the non-covalent interactions as defined above is done using the data from the 2D plots as input to construct 3D plots composed of reduced density gradient isosurfaces.

In a nutshell, a cut-off value of s close to zero, typically $s < 0.5$, is chosen in order to recover all the non-covalent interactions in the system, i.e. all the spikes of the 2D plots. The corresponding reduced density gradient isosurfaces give rise to closed domains in the molecular space which highlight the spatial localization of the interactions within the system (see Fig. 18.2c). Since 3D isosurfaces are, by definition, regions of low reduced gradient, the density is nearly constant within these.

At this stage, however, the types of interaction corresponding to the various isosurfaces are not apparent. In order to discriminate between them, the density oriented by the sign of λ_2 is further used (as in the 2D plot). A RGB (red-green-blue) coloring scheme is chosen to rank interactions, where red is used for destabilizing interactions, blue for stabilizing interactions and green for delocalized weak interactions. The intensity of these colors is associated with a higher local density and therefore with a stronger interaction.

The isovalue (or cut-off) of $s(\rho)$ chosen for plotting the 3D isosurface determines which features will appear in the NCI plot as well as their spatial extension. On the one hand, all NCI spikes do not strictly achieve $s = 0$, so that a too low isovalue might miss some of the interactions of interest [60]. On the other hand, too high isovalues would disclose atomic tails of the density [61]. The cut-off is therefore chosen from the 2D plot so that all spikes, but only spikes, are captured to render a meaningful picture which recovers both attractive and repulsive interactions.

18.3.2.2 2D and 3D Shapes

Topological features of the electron density are very stable with respect to the calculation method. The main effect of different methods on the s versus ρ diagram is a shift of spikes. The only rule of thumb seems that the same s value should be used when comparing to each other the various NCI, both in the same or in different systems, provided a single method was employed to obtain the various electron densities. This not being the case, different s values are seemingly required to compare on similar grounds the s -based results for differently computed electron density (e.g. from wavefunction, multipolar). In other words, a shift of cut-offs is needed to obtain comparable images. This can be related to the fact that s roughly behaves like $\rho^{-1/3}$ (see Eq. 18.3), so that the effect of the method on the density is directly followed by the s -value. This information is crucial when moving towards bigger systems (see Sect. 18.6).

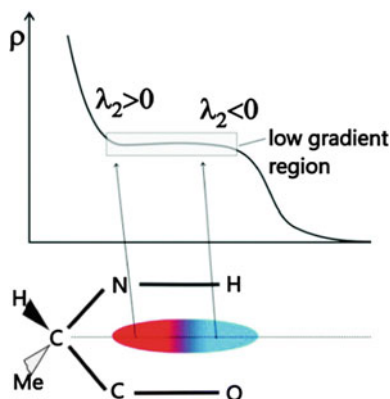


Fig. 18.3 Scheme of a mixed color isosurface in a C5 ring formed in the groove between a carbonyl and a NH group within a peptide residue. Within this isosurface, the curvature varies sign, leading to two well-differentiated parts. A *blue* external part illustrates the directional NH \cdots O interaction and a *red* part is indicative of the strain in the 5-membered ring resulting from a multicentric density in the inner region close to the backbone. In the *top panel* the variation of the density and the sign of λ_2 is depicted. Reproduced from Ref. [62] with permission from the PCCP Owner Societies

It emerges that a one-to-one inverse correlation seems to exist among the directionality (and the strength) of specific non-covalent interactions and the surface/volume ratio of the corresponding s isosurface. In particular, the stronger the interaction is, the smaller and more disc-shaped the s surface appears in real space (and the more negative the ρ sign(λ_2) values are).

In some cases, noticeably in ring closings, bicolored isosurfaces appear (see Fig. 18.3). They result from stabilizing features (revealed by the blue color), counterbalanced by destabilizing interactions due to steric crowding (revealed by the red color), such as ring closure [62].

18.4 Small Molecules

To explore the features associated with small reduced gradients, we first examine 3D NCI plots in representative small molecules.

Figure 18.4 displays NCI isosurfaces for branched octane, bicyclo[2,2,2]octene, and the homomolecular dimers of methane, benzene, water, and formic acid. These isosurfaces provide a rich visualization of non-covalent interactions as broad areas of real space, rather than simple pairwise contacts between atoms. We first consider the sterically-crowded molecules bicyclo[2,2,2]octene (Fig. 18.4a) and the branched octane isomer (Fig. 18.4b). In the first case, the low-density, low-gradient

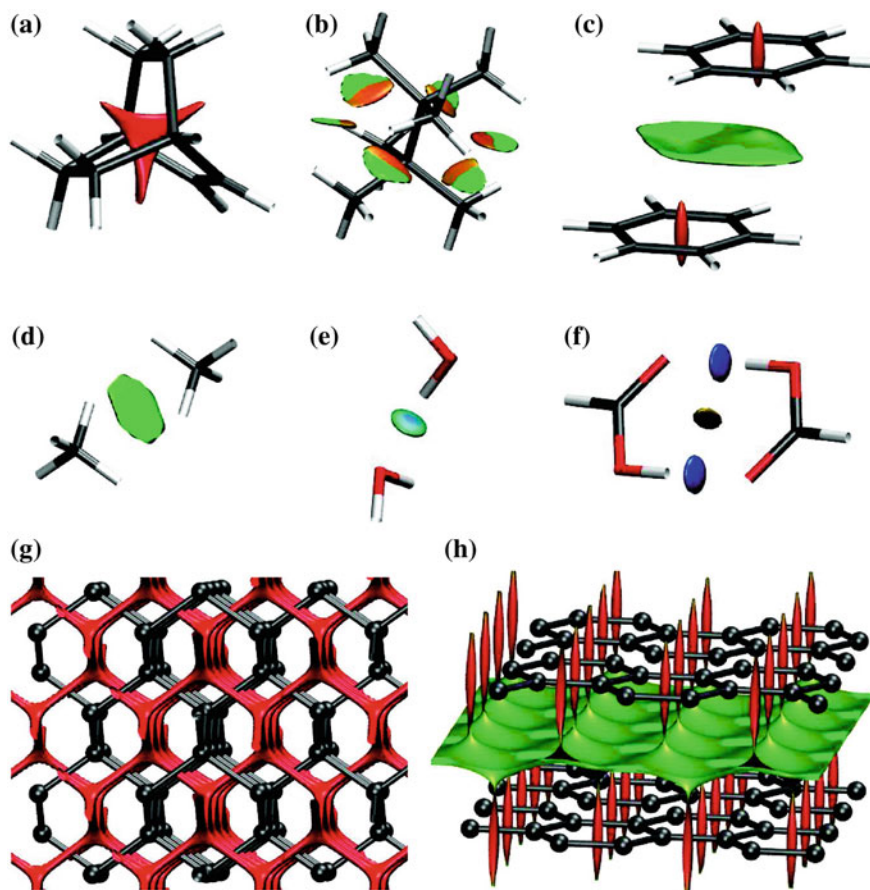


Fig. 18.4 NCI isosurfaces ($s = 0.5$) for **a** branched octane, **b** bicyclo[2,2,2]octane, and the homomolecular dimers of **c** benzene, **d** methane, **e** water, and **f** formic acid. Gradient isosurfaces are also shown for cuboid sections of **g** diamond and **h** graphite. Color coding in the range $-0.04 < \text{sign}(\lambda_2)\rho < +0.02$ a.u. Reprinted with permission from Ref. [50]. Copyright 2010 American Chemical Society

region corresponds to the center of the cage, where steric repulsion between the bridgehead carbons is expected. For the branched octane isomer, the isosurface lies between the closely-interacting methyl groups on opposite sides of the central C–C bond. The interactions are repulsive nearer the C–C bond and weakly attractive between the hydrogen atoms. Dispersion and hydrogen bonding can also be clearly detected. In the dispersion-bound methane dimer (Fig. 18.4d), the isosurface forms a disc between the individual monomers. For the water dimer (Fig. 18.4e), the isosurface lies between a hydrogen donor and oxygen acceptor, characteristic of

hydrogen bonds. The formic acid dimer (Fig. 18.4f) reveals stronger HBs than in the water dimer, and also weak van der Waals interactions between the two closely-interacting acidic hydrogens.

Finally, in the benzene dimer (Fig. 18.4c), there is an area of non-bonded overlap located at the center of each benzene ring, resembling the isosurface for bicyclo[2,2,2]octene. There is another lower-density surface between the overlapping portions of the benzenes, where π -stacking is expected. It is important to compare this image to the ones displayed in Table 18.1. The intermolecular interaction in benzene dimer appears very clearly with NCI as a surface that highlights the benzene to benzene stacking interaction, well beyond the pair interactions found with AIM.

18.5 Solids

As we saw in the Introduction, non-covalent interactions in solid state have raised a great deal of interest lately, due to their relevance for self-assembly [36] and crystallization [37] processes.

Indeed, crystalline solids exhibit rich and challenging bonding patterns. We consider the prototypical examples of carbon in the diamond (Fig. 18.4g) and graphite (Fig. 18.4h) phases at their equilibrium geometries. In diamond, the carbon atoms are sp^3 hybridized and are connected by strong covalent bonds that form a tridimensional, tetrahedral network. Figure 18.4g shows an NCI isosurface for a cuboid section of the diamond crystal. The non-covalent surface extends through the voids of the structure, creating a network similar to that of the covalent bonds.

Graphite in its α form (Fig. 18.4h) has a bidimensional, hexagonal lattice, with the carbon atoms sp^2 hybridized and covalently bonded to their three nearest neighbors. The NCI isosurface shows areas of non-bonded overlap at the center of the hexagonal rings, as seen previously in benzene. π - π stacking interactions between the graphene sheets are clearly manifested by the isosurfaces filling the interlayer spaces.

18.6 Biological Systems

Understanding of non-covalent interactions is crucial for the comprehension of the 3D structure and, thus, of the activity of biosystems [65, 66]. However, the calculation of the electron density in these systems is totally unbearable. Approximations need thus to be sought.

18.6.1 Promolecular Densities

Densities are stable (see Sect. 18.3.2.2) to such an extent that NCI characteristics are already contained in the sum of atomic densities, ρ_i^{at} [63, 64]. The resulting molecular density, also known as promolecular density, ρ^{pro} , is then given by:

$$\rho^{pro} = \sum_i \rho_i^{at} \quad (18.4)$$

A promolecular density obtained from simple exponential atomic pieces is able to qualitatively predict low-density, low-reduced-gradient regions similar to density-functional results. The free atomic densities used in these calculations consist of one Slater-type function for each electron shell, fit to closely reproduce spherically-averaged, density-functional atomic densities (see Appendix, Fig. 18.19).

Approximate promolecular densities were constructed by summing exponential atomic densities for bicyclo[2,2,2]octene, and the homomolecular dimers of methane and water.

Resultant plots of s^{pro} versus ρ^{pro} for these species show the same 2D features seen in Fig. 18.1. Also, 3D isosurfaces generated from the promolecular density are very similar to those obtained previously with self-consistent DFT and even MP2 densities (Fig. 18.5). For all cases considered, results at the self-consistent and promolecular level are qualitatively equivalent. Only slight quantitative differences are introduced by density relaxation that, as expected, shift the s versus ρ spikes to more bonding regimes. Specifically, a large shift towards smaller density values is observed in the spikes corresponding to non-bonded overlap, introducing less repulsion and greater stability. Taking this shift into account in the choice of isosurfaces, results at the self-consistent and promolecular level are qualitatively equivalent for all cases considered (see Fig. 18.5 bottom). For example, lower cut-offs on the gradient (0.25–0.35) and higher cut-offs on the density (0.08–0.09 a.u.) were required in order to generate the isosurface for bicyclo[2,2,2]octene.

18.6.2 Examples

Promolecular densities obviously lack relaxation; however, the promolecular densities are extremely useful in biomolecular systems, such as proteins or DNA. Because the calculation of the electron density in these systems becomes extremely computationally expensive, the promolecular density becomes an attractive option: non-covalent interactions can be analyzed with only the molecular geometry required as input.

We first consider two model polypeptides: an α -helix consisting of 15 alanine residues and an anti-parallel β -sheet consisting of 17 glycine residues. Geometries of the polypeptides were obtained with the MMFF force field using the spartan

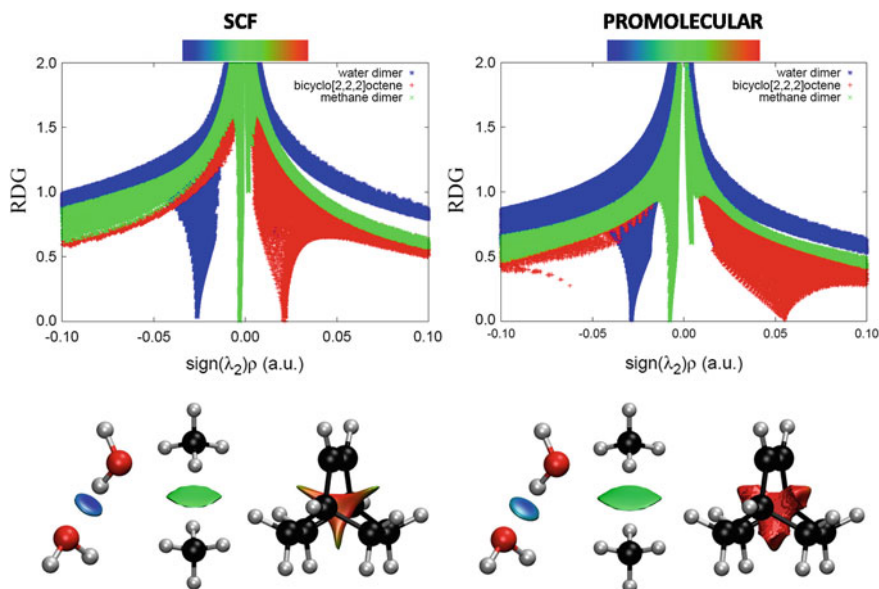


Fig. 18.5 Comparison between SCF and promolecular NCI results. The same $s(\rho)$ features are obtained using self-consistent (left) and promolecular (right) calculations, with a shift toward negative (stabilizing) regimes. *Bottom* Taking the shift in spikes into account (i.e., changing the cut-off), the isosurface shapes remain qualitatively unaltered for selected small molecules. Figures are shown for both SCF (left) and promolecular densities (right). NCI surfaces correspond to $s = 0.6$ and a color scale of $-0.03 < \rho \text{ sign}(\lambda_2) < +0.03$ a.u. for SCF densities. For promolecular densities, $s = 0.5$ (water and methane dimers) or $s = 0.35$ (bicyclo[2,2,2]octene), and the color scale is $-0.04 < \rho \text{ sign}(\lambda_2) < +0.04$ a.u. Reprinted with permission from Ref. [51]. Copyright 2011 American Chemical Society

program [67]. Both were capped with COCH_3 and NHCH_3 groups. Figure 18.6 displays low-gradient isosurfaces for cuboid regions at the center of these polypeptides, colored according to the corresponding density values. For the β -sheet, the lowest-density portions of the gradient isosurface arise from hydrophobic, dispersion-dominated interactions, primarily involving the CH_2 groups of the glycines. The higher-density regions correspond to inter-residue hydrogen-bonds and repulsive interactions between the adjacent $\text{C}=\text{O}$ and $\text{N}-\text{H}$ groups. For the α -helix, the isosurface has a large, low-density region within the helix and between the side-chain methyl groups. The higher-density portions of the isosurface correspond to inter-residue hydrogen-bonds along the helix and repulsive interactions between adjacent $\text{N}-\text{H}$ groups.

We also considered the non-covalent interactions between nucleobases in the B-form of double-strand, six-base-pair (TGTGTG) DNA. The structure was obtained using the X3DNA program [68] with ideal geometry parameters [69]. Figure 18.6c displays the low-gradient isosurface for a cuboid section in the center of the DNA helix, colored according to the $\text{sign}(\lambda_2)\rho$ values. The calculated isosurface resembles

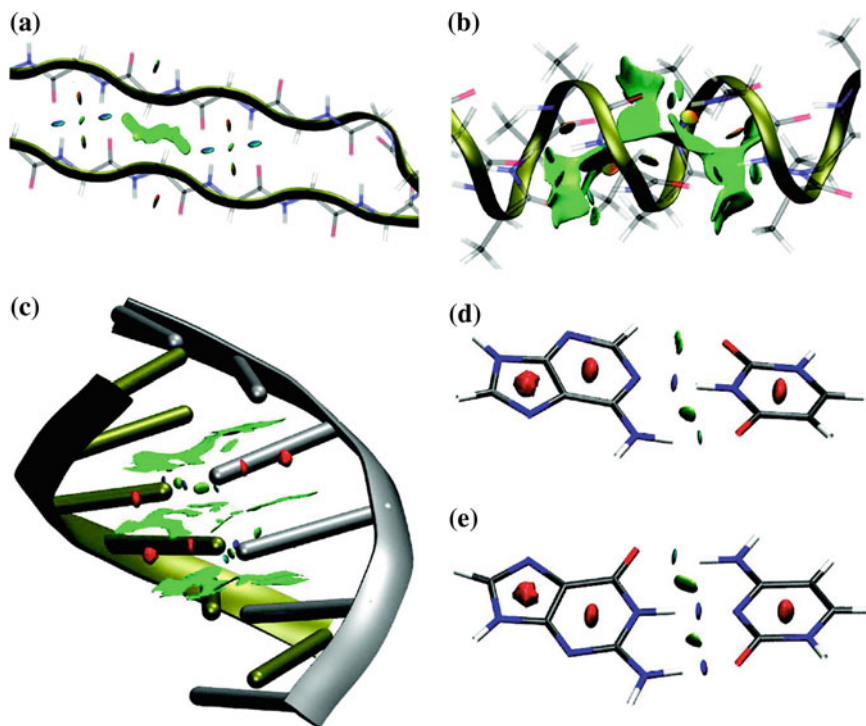


Fig. 18.6 Gradient isosurfaces ($s^{pro} = 0.35$) for cuboid sections of the **a** β -sheet and **b** α -helix polypeptides. Gradient isosurfaces ($s^{pro} = 0.25$) are also shown for the **c** B-form of DNA, and the **d** A-T and **e** C-G base pairs. The surfaces are colored according to values of $\text{sign}(\lambda_2)\rho$, ranging from -0.06 to +0.05 a.u. Reprinted with permission from Ref. [50]. Copyright 2010 American Chemical Society

that of graphite, with broad, low-density regions indicative of π -stacking between base-steps. The interactions between individual deoxyadenosine-deoxythymidine and deoxycytidine-deoxyguanosine pairs are shown in Fig. 18.6d, e. The isosurfaces show non-bonded overlap within the nucleobase rings, as in benzene and graphite, and hydrogen-bonding motifs similar to the formic acid dimer. The strong N-H \cdots O and N-H \cdots N hydrogen bonds can be clearly distinguished from the weaker, attractive C-H \cdots O interaction by the density values, as shown in different colors.

The hydrogen-bonding surfaces in the DNA model have density values of ca. 0.065 a.u., compared to density values of ca. 0.035 a.u. for the polypeptide hydrogen bonds. This is evident from the degree of blue shading for the hydrogen bonds in Fig. 18.6. Since density values at hydrogen-BCPs correlate with the interaction strength [25, 70], our results indicate that the hydrogen bonds between nucleobase pairs are substantially stronger than between amino acids, in agreement with literature data [71–73].

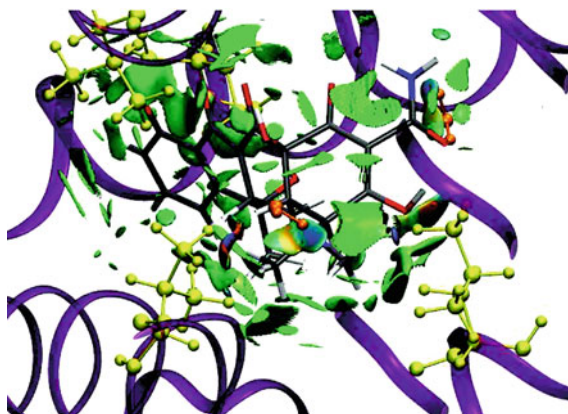


Fig. 18.7 Gradient isosurfaces ($s_{pro} = 0.35$) for interaction between the tetR protein and tetracycline inhibitor. Surfaces colored in the $\text{sign}(\lambda_2)\rho$ range from -0.06 to $+0.05$ a.u. Reprinted with permission from Ref. [50]. Copyright 2010 American Chemical Society

Let us now consider the interaction between a ligand and a protein active site. The low-gradient isosurface for a tetracycline inhibitor bound to the tetR protein in Fig. 18.7 shows a complex web of non-covalent interactions between the ligand and the active site. When analyzing non-covalent interactions in protein-ligand complexes, it is usually assumed that these interactions are due to a specific contact between two atoms [44]. However, it is clearly seen in Fig. 18.7 that this assumption is only partly correct. Hydrogen bonds, such as those between the tetracycline amine groups and two water molecules (atoms shown in orange), are directional and specific. Conversely, van der Waals, dipole-dipole, and hydrophobic interactions, such as those between the tetracycline and the Leu61, Val91, Ile136, and Val166 residues (atoms shown in yellow), are not atom-specific and occupy broader regions in space. The figure reveals some steric clashes (orange and red regions of the isosurface) that must be offset by stronger, attractive interactions to give binding in this crystal structure. A ligand “fits” the geometry of the active site, and the interaction energy between the ligand and protein is comprised of many small contributions. When trying to design a new ligand to fit a specific active site, one should consider all such interactions.

18.7 New Bonds: Do We Really Need to Name Them All?

Hydrogen bonding was postulated in the early twentieth century based on the stunning macroscopic differences between the first and second row hydrides, i.e. water is a high boiling liquid without, which there would be no life, and hydrogen sulphide is a stinking gas, under ambient conditions [1].

With the advent of molecular beam and cryogenic experimental methods as well as the ever advancing theoretical methods, HBs have been proved to exist in H_2S as well [74]. But things go even further. About a century later, chemists have identified a wealth of new bonding types along the periodic table. Halogen bonds (XBs) (group 17) are frequently exploited for crystal engineering [75]. Recently, similar bonding mechanisms have been proposed for adjacent main-group elements, and non-covalent “chalcogen bonds” (group 16) [76] and “pnictogen bonds” (group 15) [77] have also been identified in crystal structures. Recently, even carbon bonding (group 14) [78] has been proposed as a stabilizing interaction.

One of the most interesting features of NCI is that it is based on the density. Thus, it is expected to be able to reveal any type of bonding. Before and beyond its corresponding identification and characterization, the signature on the electron density will be present. In the coming sections we briefly show some representatives of the new bonds series, highlighting the possibility to reveal interactions all along the periodic table from just the fast analysis of NCI.

18.7.1 Halogen Bonding

Halogen bonds (XBs) occur between a halogen atom, playing the role of Lewis acid, and a Lewis base. This non-covalent interaction is analog to hydrogen bonding in the sense that in both cases, an atom or group of atoms with high electron density donates charge to an acceptor which is electron poor. Similar to HBs, XBs are also anisotropic and involved in various fields, such as supramolecular chemistry or even materials chemistry. Moreover, halogenated compounds are often encountered in medicinal chemistry [79] and drug discovery [80]. Quantum Chemistry approaches have revealed a sigma-hole along the axis defined by the halogen atom and the acceptor. This can be studied thanks to the Molecular Electrostatic Potentials, showing the charge distribution as well as the nature of the interaction as electrostatics and charge transfer driven.

We have analyzed NCI in a series of trifluoromethyl halides, CF_3X , where $\text{X} = \text{Cl}, \text{Br}, \text{I}$ with dimethyl ether (DME), dimethyl sulfide (DMS), trimethyl phosphine (TMP) and imidazolin-2-ylidene (NHC). All systems were optimized using second-order Møller-Plesset perturbation theory with the aug-cc-pVDZ(-PP) basis set [81]. The wavefunctions were obtained at DFT level using the B3LYP functional and the 6-31++G** basis set except for iodine, where the pseudopotential LANL2DZ was used.

In the first four cases, the 2D plots (Fig. 18.8) clearly show a spike at very low density, corresponding to a typical van der Waals interaction. In Fig. 18.8b, a second spike arises, exhibiting non bonding interactions between the chlorine atom and DMS hydrogens. They are closer to the halogen than the sulfide atom and benefit from the high electron density at the halogen.

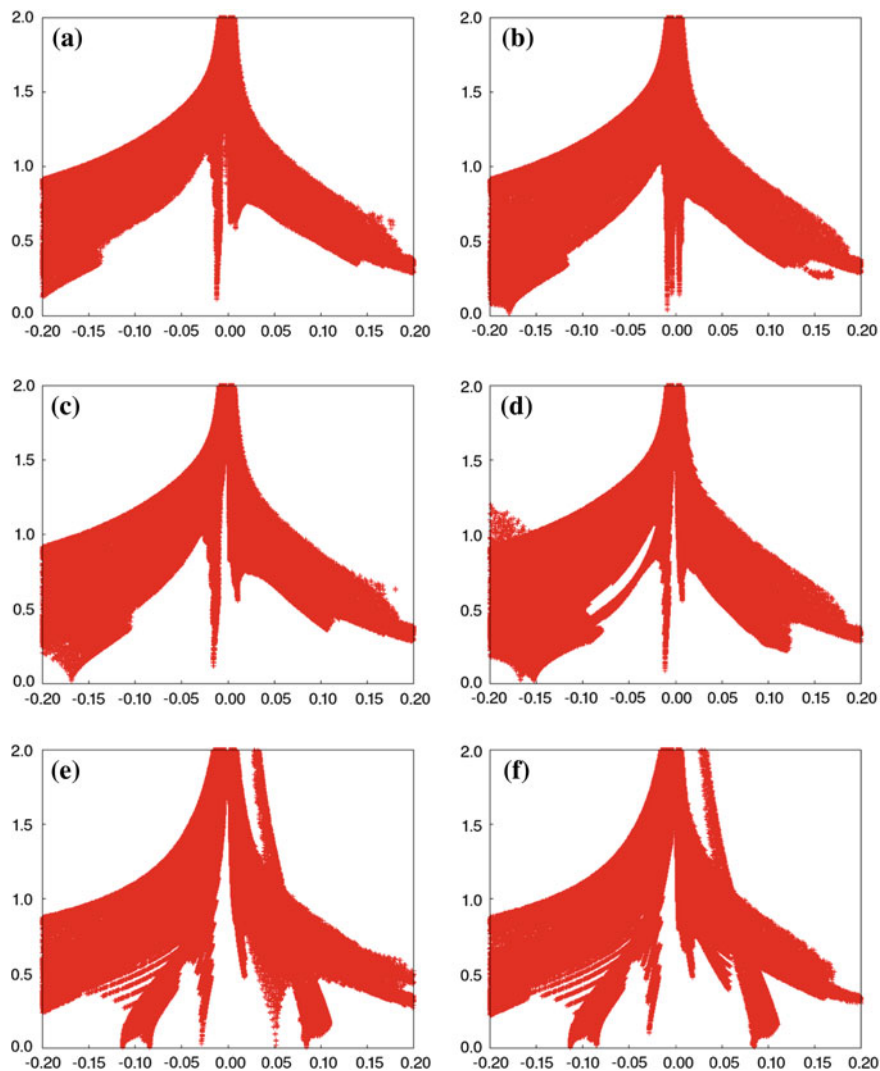


Fig. 18.8 2D plots for halogen bonded complexes: **a** CF_3Cl –DME, **b** CF_3Cl –DMS, **c** CF_3Br –DME, **d** CF_3Br –TMP, **e** CF_3I –NHC, **f** CF_3I –TMA. See Sect. 18.7.5.2 for an interpretation of iodine compounds extra peaks

In agreement with previous studies, the prominent spike is shifted to larger electron densities (left) for iodine, reflecting a stronger non bonding interaction (see Fig. 18.8e, f) as X molecular weight increases (Fig. 18.9).

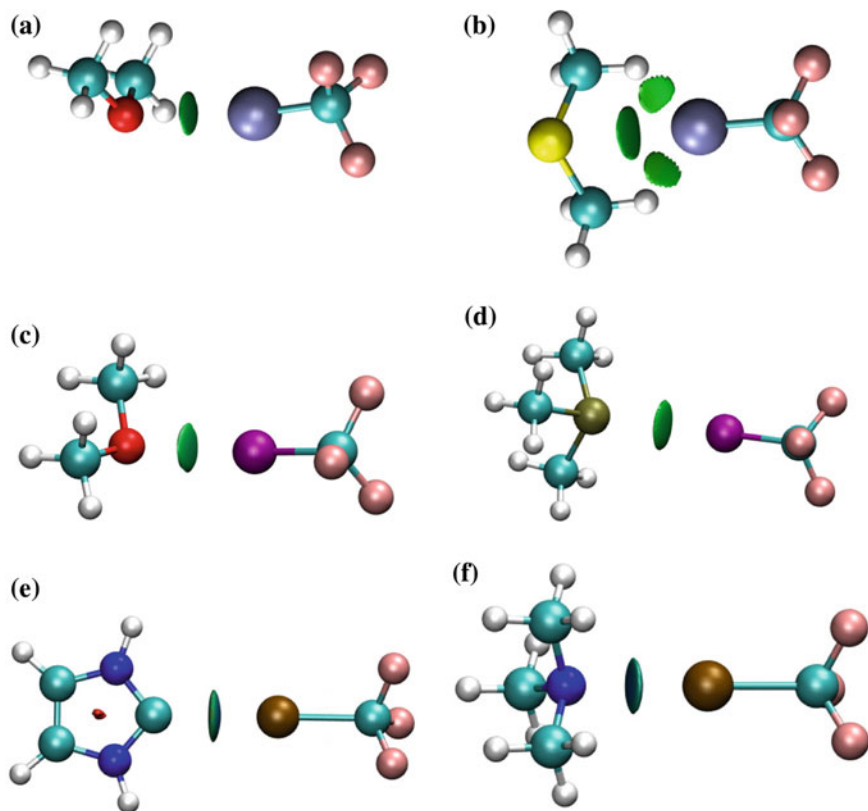


Fig. 18.9 3D plots for halogen bonded complexes: **a** CF_3Cl -DME, **b** CF_3Cl -DMS, **c** CF_3Br -DME, **d** CF_3Br -TMP, **e** CF_3I -NHC, **f** CF_3I -TMA. NCI isosurfaces correspond to $s = 0.5$ a.u. and a color scale of $-0.04 < \text{sign}(\lambda_2)\rho < +0.04$ a.u.

18.7.2 Pnictogen Bonding

Pnictogen bonding is a weak non-covalent bonding involving group 15 elements as electron density acceptors. Similar to halogens, the pnictogen atoms possess a sigma-hole: a region of positive electrostatic potential in the direction of the bond, which is attracted to a lone pair on a nucleophile with an outer negative electrostatic potential [82, 83].

Pnictogen bonding is present in the complex between NH_3 and PH_3 (Fig. 18.10a) [77] where the N atom is the donor of electron density. The sigma-hole gives rise to the equilibrium geometries: the two molecules are oriented such that the P and N atoms face one another directly, without the intermediacy of an H atom. This attraction is due in part to the transfer of electron density from the lone pair of the N atom to the σ^* antibonding orbital of the P-H covalent bond. Unlike in hydrogen bonds, the pertinent hydrogen is oriented about 180° away from the N (instead of

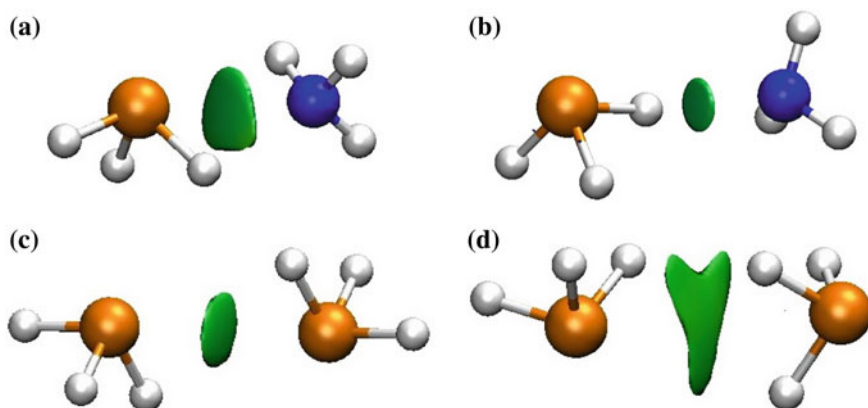


Fig. 18.10 Pnictogen bond examples: **a–b** $\text{NH}_3\text{--PH}_3$, **c–d** $\text{PH}_3\text{--PH}_3$. 3D isosurface was produced using the cut-off values of $s = 0.5$ a.u. and $-0.05 < \rho < 0.05$ a.u.

toward), and the N lone pair overlaps with the lobe of the P–H σ^* orbital that is closest to the P. The calculated binding energy of this pnictogen-bonded complex is larger than the one of the hydrogen-bonded complex that is formed between the same two molecules where the N atom is the proton acceptor (Fig. 18.10b).

We have optimized the $\text{NH}_3\text{--PH}_3$ and $\text{PH}_3\text{--PH}_3$ pairs at the ω B97X-D/6-31+G* level of theory. The NCI analysis of the $\text{NH}_3\text{--PH}_3$ complexes shows the presence of non-covalent bonding and this is illustrated by the 3D isosurfaces of both complexes (Fig. 18.10a, b). The green color of both interactions indicates that the two types of bonding have similar bonding strengths corresponding to that of van der Waals interactions. Whereas in the H-mediated complex, a typical picture of HB is obtained (Fig. 18.10b), a thick surface is obtained in the case of the pnictogen bonding (Fig. 18.10a), which is extended like in the case of van der Waals, but thick like HB ones.

It is interesting to note that in contrast to halogen bonds, there is no requirement of a sigma-hole of positive electrostatic potential on the P atom, nor it is necessary for the two interacting atoms to be of differing potential. In fact, the two atoms can be identical, as the global minimum of the PH_3 homodimer has the same structure, characterized by a $\text{P} \cdots \text{P}$ attraction. Indeed, for the complex between PH_3 and PH_3 , the P atoms possess a partial positive charge and none of the located minima found on the potential energy surface correspond to a hydrogen-bonded complex [77]. The two minima that were located correspond to complexes where the P atoms approach one another (Fig. 18.10c, d). The complex with the symmetric geometry (Fig. 18.10c) was found to be dominated by electrostatic interactions, corresponding to pnictogen bonding, whereas the second structure (Fig. 18.10d) was found to be dominated by dispersion. This shows in the NCI isosurfaces where the interaction region in Fig. 18.10d occupies a larger volume than that of Fig. 18.10c. This is in agreement with the more diffuse character of the dispersion interaction compared to the pnictogen bond which is more concentrated along the bonding direction.

18.7.3 Carbon Bonding

Recently, inspired by the identification of halogen, chalcogen and pnictogen bonding, Mani et al. [78] investigated whether carbon, being a positive centre, can accept electron density. Indeed, both experimental and theoretical studies agree that the tetrahedral face of methane can act as a hydrogen bond acceptor. Rotational spectra of complexes like $\text{CH}_4 \cdots \text{HF}$, $\text{CH}_4 \cdots \text{HCl}$, $\text{CH}_4 \cdots \text{HCN}$ and $\text{CH}_4 \cdots \text{H}_2\text{O}$ further confirm this fact [84]. While tetrahedral faces of methane has an electron rich centre and can act as a hydrogen bond acceptor, substitution of one of its hydrogens with some electron withdrawing group (such as $-\text{F}/\text{OH}$) can make the opposite face electron deficient. The complex between CH_3F and H_2O has a potential energy minimum with water oxygen pointing towards the tetrahedral face of CH_3 . Similar interactions are also found for several methanol complexes in which the electron deficient atom (oxygen) interacts with one of the water's lone pair.

Four examples of complexes, which represent minima on the potential energy surface, are shown in Fig. 18.11a–d. All complexes were optimized at the ω B97X-D/6-31+G* level of theory. In these complexes, the electron density donors (O, P, S and F atoms) are oriented towards the CH_3 face of methanol. Through NCI analysis, the presence of intermolecular interactions are evident in all the complexes. The weak nature of this type of interaction is indicated by the green color of the NCI-isosurfaces that corresponds to van der Waals interactions.

It should be noted that, in spite of the weakness of this type of interactions, they are extremely relevant, since these and similar interactions could give an enthalpic contribution to the so called “hydrophobic interactions” [78].

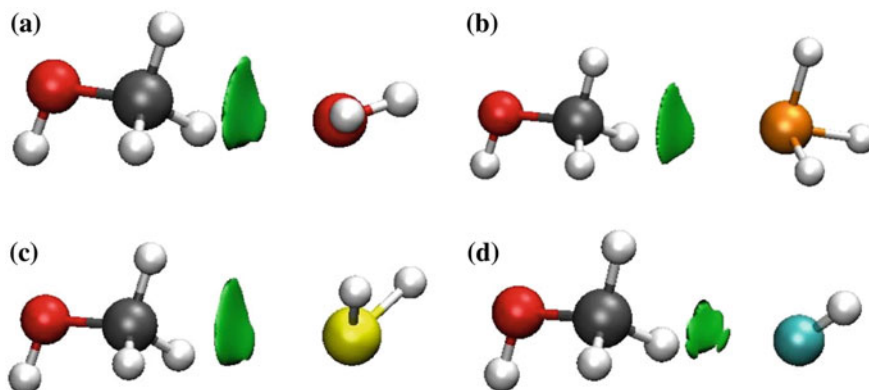


Fig. 18.11 Carbon bond examples for several electron donors (O, P, S and F): **a** $\text{MeOH}-\text{H}_2\text{O}$, **b** $\text{MeOH}-\text{PH}_3$, **c** $\text{MeOH}-\text{SH}_2$, **d** $\text{MeOH}-\text{FH}$. 3D isosurface was produced using the cut-off values of $s = 0.5$ a.u. and $-0.05 < \rho < 0.05$ a.u.

18.7.4 The Di-hydrogen Bond

The term di-hydrogen bond was coined to describe an interaction of the type $D-H\cdots H-E$, where D is a typical hydrogen donor such as N or O. The interesting thing about this type of bond, is that the acceptor atom is also a hydrogen.

Thus, the accepting hydrogen atom must be hydride-like and E has to be an atom capable of accommodating a hydridic hydrogen. Transition metals and boron are some known examples of atoms occurring at position E. Within di-hydrogen bonded complexes, BH_3NH_3 is perhaps the most widely studied [86–88]. We have analyzed the tetramer $(BH_3NH_3)_4$, whose geometry has been derived from the solid state. Figure 18.12 shows the NCI results for $(BH_3NH_3)_4$. It can be seen that each BH_3NH_3 molecule interacts with the surrounding ones establishing one di-hydrogen bond with each, and numerous van der Waals contacts. The surfaces obtained are, in all cases, completely analogous to those obtained in previous examples for hydrogen bonds.

We have also studied a series of nine complexes presenting di-hydrogen bonds ($LiH-HCCH$, $LiH-HCN$, $LiH-HCF_3$, $NaH-HCCH$, $NaH-HCN$, $NaH-HCF_3$, $HBeH-HCCH$, $HBeH-HCN$, $HBeH-HCF_3$) to check the ability of NCI to detect new types of bonds even at the promolecular level. After using the MAPS Platform [89] to set up the initial systems, the complexes were optimized at the MP2/aug-cc-pVDZ level with NWChem [90]. The optimized coordinates were used to perform NCI promolecular analysis. The results are displayed in Fig. 18.13.

Even at this rough level, NCI allows to follow the evolution of the interaction strength for the different systems. The interaction isosurfaces appear similar to those from strong hydrogen bonds. They also seem to be stronger than the di-hydrogen

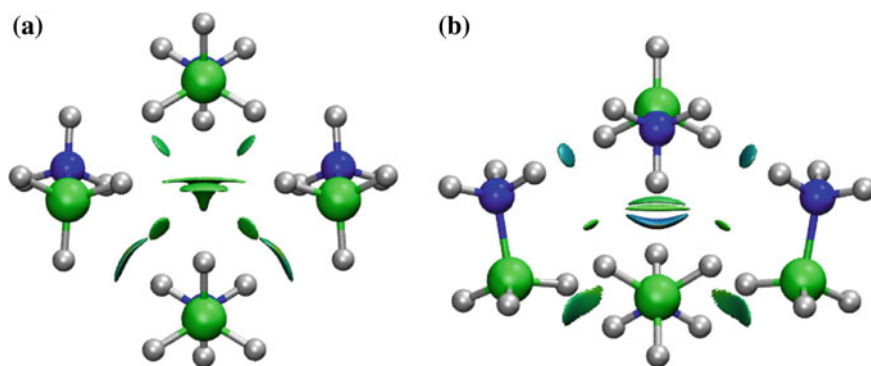


Fig. 18.12 Dihydrogen interactions in a BH_3NH_3 tetramer in **a** the fully optimized gas-phase geometry and **b** the solid-state geometry. NCI surfaces correspond to $s = 0.4$ a.u. and a color scale of $-0.03 < \text{sign}(\lambda_2)\rho < +0.03$ a.u. Reprinted with permission from Ref. [51]. Copyright 2011 American Chemical Society. **a** Gaseous phase. **b** Crystal structure

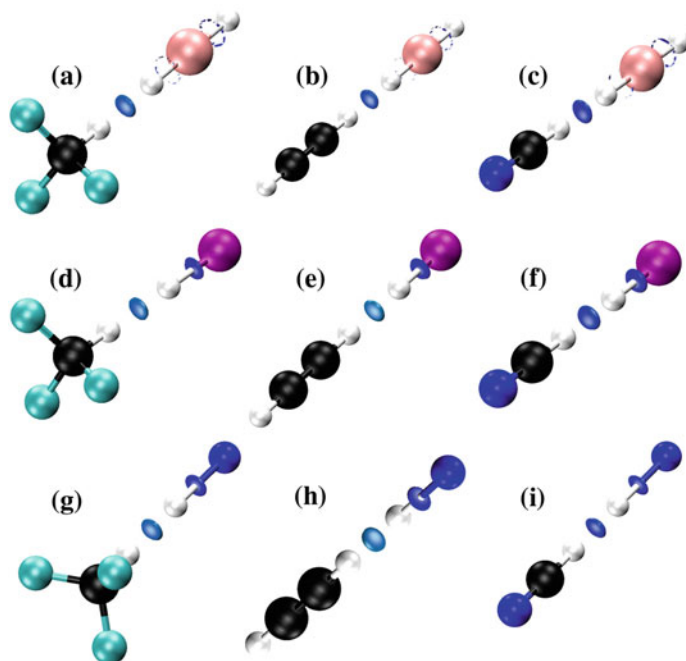


Fig. 18.13 NCI surfaces for several di-hydrogen complexes: **a** HBeH-HCF₃, **b** HBeH-HCCH, **c** HBeH-HCN, **d** LiH-HCF₃, **e** LiH-HCCH, **f** LiH-HCN, **g** NaH-HCF₃, **h** NaH-HCCH, **i** NaH-HCN. The NCI isosurfaces were plotted for $s = 0.3$ a.u. and a color scale of $-0.03 < \text{sign}(\lambda_2)\rho < +0.03$ a.u.

bond in the BH₃NH₃ complex. It should be noted that this agrees with the fact that di-hydrogen bonds have been attributed very variable strengths. Crabtree et al. [91] have placed the NH...HB contact at the upper end of the energy range quoted for hydrogen bonds. Popelier instead, has found it to be in the range of normal HB strengths [86] and Morrison and Siddick [87] assigned it towards the lower end of the hydrogen bond strength spectrum. Our results show that the range of energies covered go (at least) from the strong to the medium HB-type of strength.

18.7.5 Metal Driven Interactions

Although NCI is usually used for weak interactions, its basis does not limit the tool to only weak interactions. Indeed, it can be used for covalent and ionic interactions, as well (see S.I. in Refs. [50] and [61]). Most commonly, it is also used within metallorganic frameworks to detect interactions with metals. We will analyze several model examples relevant to solvation and protein structure. It should be noted that in these cases the default cutoff value of the density needs to be increased.

18.7.5.1 Hg²⁺ Complexation

Understanding the complexation of ions and their preferential ligands is of prime relevance when studying their bioactivity. As an example, their absorbance and transport through the body is extremely dependent on their complexation. It would then be extremely interesting to be able to identify the main series as well as the potential substitution sites. In addition Mercury(II) is a heavy metal cation which is especially challenging for quantum mechanical treatment as both correlation and relativistic effects play a crucial role in modeling its complexes.

Figure 18.14a–d illustrates the ability of NCI to visualize in a fast and efficient manner the complexation sites of Hg and to discriminate the strength of the binding energies between the cation and its ligands. Figure 18.14a shows the $[\text{Hg}(\text{H}_2\text{O})_3]^{2+}$ complex and suggests that the three waters bound to Hg are not equivalent, one of the water molecules being more weakly bound than the others. In order to corroborate this observation, it is possible to perform a decomposition of the interaction energy of such a complex using the RVS [85] (Reduced Variational Space) procedure. Both polarization and charge transfer are significantly weaker for one water molecule: whereas two of the water molecules show a polarization energy of ca. -15 kcal/mol, and a charge transfer energy of -10 kcal/mol, the third water shows a stabilization due to polarization and charge transfer by only -12.7 kcal/mol and -6.2 kcal/mol, respectively.

The ability of NCI to recover the ordering of ligands is also applicable when different ligand series are analyzed. Figure 18.14b–d shows $[\text{Hg}(\text{X})_3]$ complexes

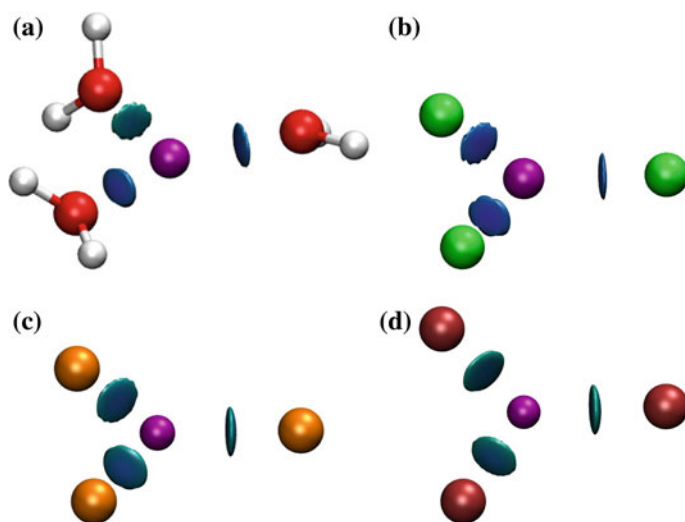


Fig. 18.14 Complexation of Hg. **a** $[\text{Hg}(\text{H}_2\text{O})_3]^{2+}$, **b** $[\text{Hg}(\text{F})_3]^-$, **c** $[\text{Hg}(\text{Cl})_3]^-$, **d** $[\text{Hg}(\text{Br})_3]^-$. Reprinted with permission from Ref. [51]. Copyright 2011 American Chemical Society

(X standing for F, Cl and Br). It is clearly seen that F is more strongly bonded than Cl and Br. This result is in agreement with their binding energies, which are -632.8 , -571.0 and -562.6 kcal/mol, respectively.

18.7.5.2 Zn^{2+} Fingers

Metals play a decisive role in many protein active sites as cofactors. The zinc finger is a small protein structural motif that can be found in many biological systems. It is characterized by the fact that one or more zinc ions can stabilize the fold of a protein. One or two Zn(II) cations [100] are often tetrahedrally coordinated to four or six amino acids such as cysteine (Cys) or histidine (His) forming four major cores: ZnCys_4 , ZnCys_3His , $\text{ZnCys}_2\text{His}_2$ and ZnCys_6 [101].

Starting from the ZnCys_4 core, its modeling can be carried out by substitution of Cys by methyl thiolate, CH_3S^- [101]. In order to analyze the effect of the environment within the HSAB theory, we have analyzed the series $\text{M}^{2+} [\text{SCH}_3]_4^{2-}$, with $\text{M} = \text{Mg}, \text{Zn}, \text{Pd}$ (from hard to soft Lewis acids). All complexes were optimized at the $\omega\text{B3LYP}/6\text{-31++G}^{**}$ level of theory except for Pd, which was optimized with the pseudopotential LANL2DZ.

In all cases, the tetracoordination of the metal to the XMe ligands clearly stands out as a strong interaction (deep blue in Fig. 18.15). It is interesting to note that the interaction spike shifts from ca. $\text{sign}(\lambda_2)\rho = -0.03$ a.u. to $\text{sign}(\lambda_2)\rho = -0.06$ a.u. when passing from Mg(II) , which is a hard cation, to Zn(II) and Pd(II) , which are intermediate and soft cations, respectively. This is in agreement to what is expected from the nature of the sulfur bridge (soft) with the ligands within the HSAB theory.

Spikes appear at very low densities which correspond to secondary interactions in between the ligands, which stabilize the whole structure. As a final note, the big

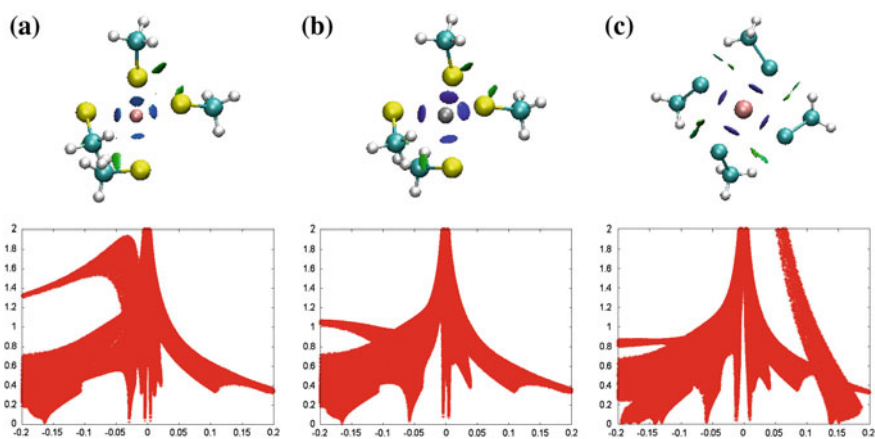


Fig. 18.15 NCI plots for Zn finger model: **a** $[\text{Mg}(\text{SMe})_4]^{2-}$, **b** $[\text{Zn}(\text{SMe})_4]^{2-}$, **c** $[\text{Pd}(\text{SMe})_4]^{2-}$. *Top* 3D NCI plot. *Bottom* 2D NCI plot

spikes appearing for Pd at ca. $\rho = 0.1$ a.u., along with the peaks appearing for the iodine compounds in Sect. 18.7.1, are an artifact from the pseudopotential, and as such, should be disregarded.

18.8 Reactivity

Understanding and predicting chemical reactivity are some of the achievements of quantum chemistry. In this regard, the Woodward-Hoffmann rules [21] for pericyclic reactions have become a classical reference. By definition, pericyclic reactions evolve via a cyclic aromatic transition state of delocalized electrons where bond making and bond breaking occur simultaneously in a cyclic array. Using the orbital symmetry conservation, Woodward-Hoffmann proposed a list of rules of thumb able to predict the mechanism and, hence the stereoselectivity of pericyclic reactions. Examples include cycloadditions, electrocyclizations, sigmatropic rearrangements, and chelotropic reactions. Much work has been devoted to show that electron circulation on the pericyclic transition states may be smartly characterized by the topology of the electron localization function (ELF) [92]. Recently, it was shown how the combined analysis of the NCI method and ELF may be employed as a visual tool to understand the electron reorganization along an intrinsic reaction path (IRC) [93]. Contrary to ELF, the reduced density gradient does not suffer from catastrophes (sudden creation and/or destruction of critical points), being possible to preclude the bonding formation from the first stages of the reaction.

One example of application of NCI to predict the outcome of pericyclic reactions is provided by the two possible ring-openings of *trans*-1,2,3,4-tetrafluoro-3,4-bis(pentafluorosulfanyl)cyclobutene (see Fig. 18.16). As a thermal, $4n$ electron process, the Woodward-Hoffmann rules predict that the conrotatory opening is more favorable than the disrotatory one [21, 94]. Additionally, a given terminal substituent may either rotate “outward”, leading to (*out,out*)-1,2,3,4-tetrafluoro-1,3-bis(pentafluorosulfanyl)butadiene or “inward” to yield (*in,in*)-1,2,3,4-tetrafluoro-1,3-bis(pentafluorosulfanyl)butadiene. Activation energies obtained at the ω B97X-D/6-311G** level for

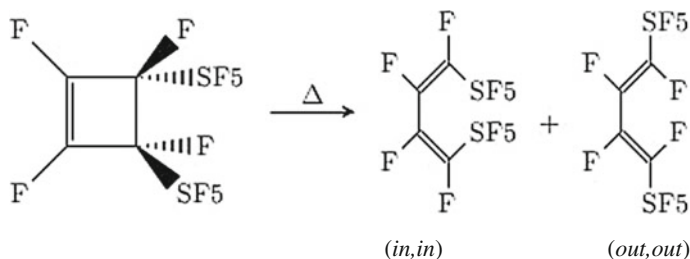


Fig. 18.16 “Outward” (*out*) and “inward” (*in*) conrotatory processes for the thermal ring opening of *trans*-1,2,3,4-tetrafluoro-1,4-bis(pentafluorosulfanyl)cyclobutene

(*out,out*) and (*in,in*) transition states are 41.55 kcal/mol and 21.12 kcal/mol, respectively. Because this kind of stereoselectivity is related to the direction of the twist, it was named *torquoselectivity* by Houk and co-workers [95].

Rondan and Houk proposed in 1984 a widely accepted orbital model able to explain *torquoselectivity* [96, 97]. In a nutshell, this model states that electron donor substituents at C₃ and C₄ preferentially rotate outward in order to maximize the stabilizing interaction with the HOMO of the breaking C₃–C₄ bond and to minimize the repulsive interaction with the LUMO of the same bond. Electron acceptor substituents undergo the opposite effect, and, consequently, inward rotation is preferred. Since only certain orbitals are included in the model, a wrong selection of the interacting orbitals leads to wrong predictions. This disadvantage is common for all theories based on a selected group of orbitals, such as the frontier orbital theory [98]. To avoid this flaw, Ponec decided to reinvestigate the problem in terms of an electron density based indicator, such as the molecular similarity approach [99]. He showed that the origin of the *torquoselectivity* comes from the low electron reorganization required to convert reactants into products.

Additionally, NCI analyses of both (*in,in*) and (*out,out*) transition states provide us with topological arguments to understand this differential selectivity. As seen in Fig. 18.17, out of the breaking carbon-carbon covalent interaction (blue isosurface) and its repulsive counterpart ring tension (red isosurface), we can differentiate three types of non-covalent interactions (green isosurfaces):

- Type 1 Fluor-fluor interaction between pentafluorosulfanyl groups
- Type 2 Pentafluorosulfanyl-carbon interaction
- Type 3 Fluor-fluor interaction between pentafluorosulfanyl and fluoro groups

All of them are present in the (*in,in*) transition state, whereas only interactions of type 3 are found in the (*out,out*) one (see Fig. 18.18). Thus, dispersion interactions between pentafluorosulfanyl groups and those with the carbon cycle should be the driving force of the process. Thus, *torquoselectivity* can also be understood in terms of secondary interactions as revealed by NCI: within this approach products are

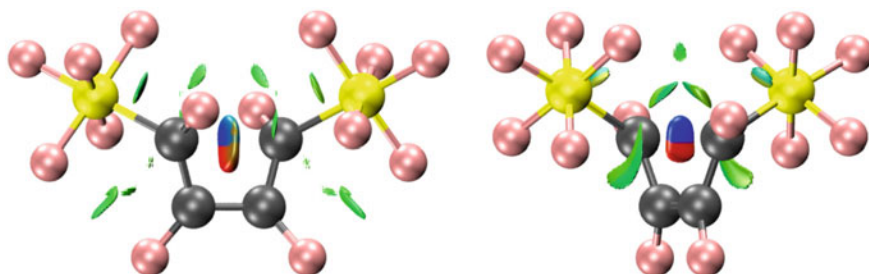


Fig. 18.17 NCI isosurfaces of (*out,out*) (left) and (*in,in*) (right) transition states

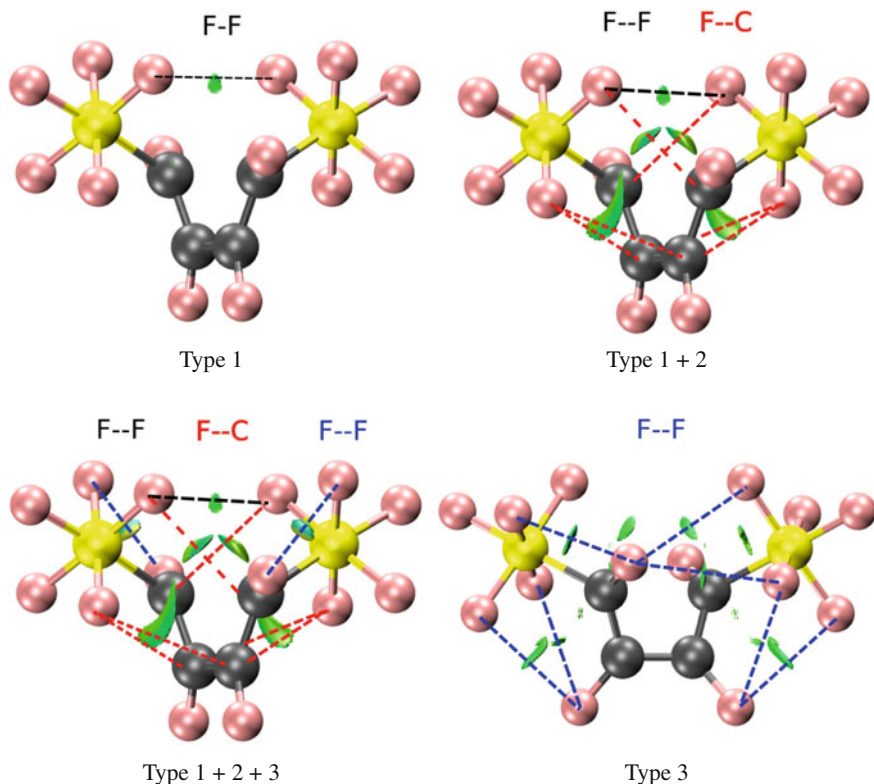


Fig. 18.18 Non-covalent interactions types in (*in, in*) (top left, top right and bottom left) and (*out, out*) (bottom, right) transition states. Black, red and blue dashed lines represent type 1, type 2 and type 3 interactions respectively

driven by the accumulation of non-covalent interactions in the transition state. This is in agreement with the secondary interactions proposed by Hook. However, it should be noted that the different substituents give rise to a different deformation, leading to barriers as high as ca. 20 kcal/mol that can not be strictly attributed to non-covalent interactions.

18.9 Summary and Conclusions

In conclusion, non-covalent interactions have a unique signature and their presence can be revealed solely from the electron density. Non-covalent interactions are highly nonlocal and manifest in real space thanks to the NCI analysis: in other words, as low-gradient isosurfaces with low densities. The sign of the second

Hessian eigenvalue is used to give the type of interaction, and its strength can be derived from the density on the non-covalent interaction surface.

NCI provides a rapid and rich representation of van der Waals interactions, hydrogen bonds, and steric clashes. For large systems, such as proteins or DNA, NCI can be approximated from atomic densities.

Since it is based in the electron density, it is applicable to all types of chemical bonds. We have reviewed here several such examples along the periodic table: halogen bonds, pnictogenic bonds, di-hydrogen bonds. We have even gone to higher densities to show that NCI is also able to reveal and characterize interactions in organometallic systems. Finally, we have also looked at the change of chemical interactions along a reaction path, reformulating orbital rules in the *torquoselectivity*.

In summary, we have shown that the electron density and its derivatives contain all the information to characterize all chemical bonds and their change, making NCI a holistic tool in the analysis of weak interactions.

Acknowledgments This work undertaken (partially) in the framework of CALSIMLAB is supported by the public grant ANR-11-LABX-0037-01 overseen by the French National Research Agency (ANR) as part of the “Investissements d’Avenir” program (reference: ANR-11-IDEX-0004-02).

Behavior of Model Densities

See Fig. 18.19.

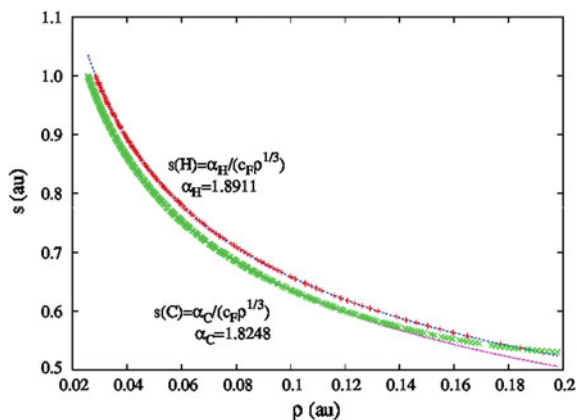


Fig. 18.19 Behavior of $s(\rho)$ for model densities $\rho = e^{-ar}$ for hydrogen and carbon

Parameters for Promolecular Calculations

See Table 18.2.

Table 18.2 Parameterized exponents (η_i) and coefficients (c_i) of sphericalize averaged atomic densities, in atomic units

Atom	c_1	η_1	c_2	η_2	c_3	η_3
H	0.2815	0.5288	–	–	–	–
He	2.437	0.3379	–	–	–	–
Li	11.84	0.1912	0.06332	0.9992	–	–
Be	31.34	0.1390	0.3694	0.6945	–	–
B	67.82	0.1059	0.8527	0.5300	–	–
C	120.2	0.0884	1.172	0.5480	–	–
N	190.9	0.0767	2.247	0.4532	–	–
O	289.5	0.0669	2.879	0.3974	–	–
F	406.3	0.0608	3.049	0.3994	–	–
Ne	561.3	0.0549	6.984	0.3447	–	–
Na	760.8	0.0496	22.42	0.2511	0.06358	1.0236
Mg	1016	0.0449	37.17	0.2150	0.3331	0.7753
Al	1319	0.0411	57.95	0.1874	0.8878	0.5962
Si	1658	0.0382	87.16	0.1654	0.7888	0.6995
P	2042	0.0358	115.7	0.1509	1.465	0.5851
S	2501	0.0335	158.0	0.1369	2.170	0.5149
Cl	3024	0.0315	205.5	0.1259	3.369	0.4974
Ar	3625	0.0296	260.0	0.1168	5.211	0.4412

References

1. Pauling L (1947) General chemistry. Dover Publications Inc, New York
2. Burdett JK (1997) Chemical bonds—a dialog. Wiley, Chichester, England
3. Frenking G, Shaik S (eds) (2007) Special issue: 90 years of chemical bonding. *J Comput Chem* 28:1–466
4. Frenking G, Krapp A (2007) Unicorns in the world of chemical bonding models. *J Comput Chem* 28:15–24
5. Shaik S, Rzepa HS, Hoffmann R (2013) One molecule, two atoms, three views, four bonds? *Angew Chem Int Ed* 52:3020–3033
6. Frenking G, Hermann M (2013) *Angew Chem Int Ed* 52:5922–5925
7. Coulson CA (1953) The spirit of applied mathematics. Clarendon Press, pp 20–21
8. Jacobsen H (2010) Kinetic energy density and covalent bonding—a complementary analysis at the border of bond and no bond. *Dalton Trans* 39:5426–5428
9. Parr RG, Ayers PW, Nalewajski RF (2005) What is an atom in a molecule? *J Phys Chem A* 109:3957–3959

10. Jacobsen H (2013) Topology maps of bond descriptors based on the kinetic energy density and the essence of chemical bonding. *Phys Chem Chem Phys* 15:5057–5066
11. Schleyer PvR (2005) Introduction: delocalization pi and sigma. *Chem Rev* 105:3433–3435
12. Popelier PLA (2007) Preface. *Faraday Discuss* 135:1–3
13. Alabugin IV, Gilmore KM, Peterson PW (2011) Hyperconjugation. *Wiley interdisciplinary reviews: computational molecular science* 1:109–141
14. Gonthier JF, Steinmann SN, Wodrich MD, Corminboeuf C (2012) Quantification of “fuzzy” chemical concepts: a computational perspective. *Chem Soc Rev* 41:4671–4687
15. Whitaker A (1996) Einstein, bohr and the quantum dilemma. Cambridge University Press, Cambridge
16. Alvarez S, Hoffmann R, Mealli C (2009) A bonding quandary—or—a demonstration of the fact that scientists are not born with logic. *Chem Eur J* 15:8358–8373
17. Danovich D, Hiberty PC, Wu W, Rzepa HS, Shaik S (2014) The nature of the fourth bond in the ground state of C-2: the quadruple bond conundrum. *Chem Eur J* 20:6214–6220
18. Ayers PL, Boyd RJ et al (2015) Six questions on topology in theoretical chemistry. *Comput Theor Chem* 1053:2–16
19. Lewis GN (1916) The atom and the molecule. *J Am Chem Soc* 38:762–786
20. Fukui K, Yonezawa T, Shingu H (1952) A molecular orbital theory of reactivity in aromatic hydrocarbons. *J Chem Phys* 20:722–725
21. Woodward RB, Hoffmann R (1969) The conservation of orbital symmetry. *Angew Chem Int Ed Engl* 8:781–932
22. Parr RG, Donnelly RA, Levy M, Palke WE (1978) Electronegativity: the density functional viewpoint. *J Chem Phys* 68:3801
23. Bader RFW (1991) A quantum theory of molecular structure and its applications. *Chem Rev* 91:893–928
24. Bader RFW (1990) Atoms in molecules: a quantum theory. In: *International series of monographs on chemistry*, vol 22. Oxford Science Publications, Oxford
25. Matta CF, Boyd RJ (2007) In the quantum theory of atoms in molecules. Wiley-VCH, New York, pp 1–34
26. Becke AD, Edgecombe KEJ (1990) A simple measure of electron localization in atomic and molecular systems. *J Chem Phys* 92:5397–5403
27. Silvi B, Savin A (1994) Classification of chemical bonds based on topological analysis of electron localization functions. *Nature* 371:683–686
28. Honig B, Nicholls A (1995) Classical electrostatics in biology and chemistry. *Science* 268:1144–1149
29. Fenniri H, Packiarajan M, Vidale KL, Sherman DM, Hallenga K, Wood KV, Stowell JG (2001) Helical rosette nanotubes: design, self-assembly, and characterization. *J Am Chem Soc* 123:3854–3855
30. Kruse P, Johnson ER, DiLabio GA, Wolkow RA (2002) Patterning of vinylferrocene on H-Si (100) via self-directed growth of molecular lines and STM-induced decomposition. *Nano Lett* 2:807–810
31. Sheiko SS, Sun FC, Randall A, Shirvanyants D, Rubinstein M, Lee H, Matyjaszewski K (2006) Adsorption-induced scission of carbon-carbon bonds. *Nature* 440:191–194
32. DiLabio GA, Piva PG, Kruse P, Wolkow RA (2004) Dispersion interactions enable the self-directed growth of linear alkane nanostructures covalently bound to silicon. *J Am Chem Soc* 126:16048–16050
33. Kollman PA (1977) Noncovalent interactions. *Chem Rev* 10:365–371
34. Cerniy J, Hobza P (2007) Non-covalent interactions in biomacromolecules. *Phys Chem Chem Phys* 9:5291–5303
35. Lehninger AL, Nelson DL, Cox MM (1993) *Principles of biochemistry*, 2nd edn. Worth Publishers, Inc
36. Krishnamoorthy N, Yacoub MH, Yaliraki SN (2011) A computational modeling approach for enhancing self-assembly and biofunctionalisation of collagen biomimetic peptides. *Biomaterials* 32:7275–7285

37. Dutta A, Jana AD, Gangopadhyay S, Kumar Das K, Marek J, Marek R, Brus J, Ali M (2011) Unprecedented $\pi\pi$ interaction between an aromatic ring and a pseudo-aromatic ring formed through intramolecular H-bonding in a bidentate Schiff base ligand: crystal structure and DFT calculations. *Phys Chem Chem Phys* 13:15845–15853
38. Gavezzotti A (2007) Molecular aggregation. Structure analysis and molecular simulation of crystals and liquids. In: IUCr monographs on crystallography, vol 19. Oxford University Press, Oxford
39. Keinan S, Ratner MA, Marks TJ (2004) Molecular zippers—designing a supramolecular system. *J Chem Phys Lett* 392:291–296
40. Desiraju GR (1989) Crystal engineering. The design of organic solids. Elsevier, Amsterdam
41. Day GM, Cooper TG, Cruz-Cabeza AJ, Hejczyk KE, Ammon HL, Boerrigter SXM, Tan JS, Della Valle RG, Venuti E et al (2009) *Acta Cryst B* 65:107–125
42. Word JM, Lovell SC, LaBean TH, Taylor HC, Zalis ME, Presley BK, Richardson JS, Richardson DC (1999) Asparagine and glutamine: using hydrogen atom contacts in the choice of side-chain amide orientation. *J Mol Biol* 285:1735–1747
43. Davis IW, Leaver-Fay A, Chen VB, Block JN, Kapral GJ, Wang X, Murray LW, Arendall WB III, Snoeyink J, Richardson JS, Richardson DC (2007) MolProbity: all-atom contacts and structure validation for proteins and nucleic acids. *Nucleic Acids Res* 35:W375–W383
44. Sobolev V, Sorokine A, Prilusky J, Abola EE, Edelman M (1999) Automated analysis of interatomic contacts in proteins. *Bioinformatics* 15:327–332
45. McDonald IK, Thornton JM (1994) Satisfying hydrogen bonding potential in proteins. *J Mol Biol* 238:777–793
46. Alikhani ME, Fuster F, Silvi B (2005) What can tell the topological analysis of ELF on hydrogen bonding? *Struct Chem* 16:203–210
47. Cramer RD III, Patterson DE, Bunce JD (1988) Comparative molecular field analysis (CoMFA). 1. Effect of shape on binding of steroids to carrier proteins. *J Am Chem Soc* 110:5959–5967
48. Pilmé J, Piquemal J-P (2008) Advancing beyond charge analysis using the electronic localization function: chemically intuitive distribution of electrostatic moments. *J Comput Chem* 29:1440–1449
49. Hohenberg P, Kohn W (1964) Inhomogeneous electron gas. *Phys Rev B* 136:B864
50. Johnson ER, Keinan S, Mori-Sánchez P, Contreras-García J, Cohen AJ, Yang W (2010) Revealing noncovalent interactions. *J Am Chem Soc* 132:6498–6506
51. Contreras-García J, Johnson E, Keinan S, Chaudret R, Piquemal J-P, Beratan D, Yang W (2011) NCIPLOT: a program for plotting non-covalent interaction regions. *J Chem Theor Comp* 7:625–632
52. Contreras-García J, Johnson ER, Yang W (2011) Analysis of hydrogen-bond interaction potentials from the electron density: integration of noncovalent interaction regions. *J Phys Chem A* 115:12983–12990
53. Becke AD (1995) Modern electronic structure theory. World Scientific, Yarkony
54. Cohen AJ, Mori-Sánchez P, Yang W (2008) Insights into current limitations of density functional theory. *Science* 321:792–794
55. Zupan A, Burke K, Ernzerhof M, Perdew JP (1997) Distributions and averages of electron density parameters: explaining the effects of gradient corrections. *J Chem Phys* 106:10184–10193
56. Becke AD (1993) Density-functional thermochemistry. III. The role of exact exchange. *J Chem Phys* 98:5648–5652
57. Lee C, Yang W, Parr RG (1988) Development of the Colle-Salvetti correlation-energy formula into a functional of the electron density. *Phys Rev B* 37:785
58. Arfken G (1985) Mathematical methods for physicists. Orlando Academic Press
59. Bader RFW, Essén H (1984) The characterization of atomic interactions. *J Chem Phys* 80:1943–1960

60. Lane JR, Contreras-García J, Piquemal J-P, Miller BJ, Kjaergaard HG (2013) Are bond critical points really critical for hydrogen bonding? *J Chem Theory Comp* 9:3263–3266
61. Contreras-García J, Calatayud M, Piquemal J-P, Recio JM (2012) Ionic interactions: comparative topological approach. *Comp Theo Chem* 998:193–201
62. Chaudret R, de Courcy B, Contreras-García J, Gloaguen E, Zehnacker-Rentien A, Mons M, Piquemal J-P (2013) Unraveling non covalent interactions within flexible biomolecules: from electron density topology to gas phase spectroscopy. *Phys Chem Chem Phys* 16:9876–9891
63. Spackman MA, Maslen EN (1986) Chemical properties from the promolecule. *J Phys Chem* 90:2020–2027
64. Martín Pendás A, Luaña V, Pueyo L, Francisco E, Mori-Sánchez P (2002) Hirshfeld surfaces as approximations to interatomic surfaces. *J Chem Phys* 117:1017–1023
65. Fiedler S, Broecker J, Keller S (2010) Protein folding in membranes. *Cell Mol Life Sci* 67:1779–1798
66. Dill KA (1990) Dominant forces in protein folding. *Biochemistry* 29:7133–7155
67. Deppmeier BJ, Driessen AJ, Hehre W, Johnson JA, Klunzinger PE, Watanabe W (2002) Spartan ES 1.0.2. Wavefunction Inc., Irvine
68. Lu X-J, Olson WK 3DNA: a software package for the analysis, rebuilding and visualization of three-dimensional nucleic acid structures. *Nucleic Acids Res* 31:5108–121
69. <http://rutchem.rutgers.edu/olson/Tsukuba/>
70. Espinosa E, Molins E, Lecomte C (1988) Hydrogen bond strengths revealed by topological analyses of experimentally observed electron densities. *Chem Phys Lett* 285:170–173
71. Wiczorek R, Dannenberg JJ (2004) Comparison of fully optimized α - and β -helices with extended β -strands. An oniom density functional theory study. *J Am Chem Soc* 126:14198–14205
72. Viswanathan R, Asensio A, Dannenberg JJ (2004) Cooperative hydrogen-bonding in models of antiparallel β -sheets. *J Phys Chem A* 108:9205–9212
73. Jurecka P, Hobza P (2003) True stabilization energies for the optimal planar hydrogen-bonded and stacked structures of guanine, cytosine, adenine, thymine, and their 9- and 1-methyl derivatives: complete basis set calculations at the MP2 and CCSD (T) levels and comparison with experiment. *J Am Chem Soc* 125:15608–15613
74. Arunan E, Desiraju GR, Klein RA, Sadlej J, Scheiner S, Alkorta I, Clary DC, Crabtree RH, Dannenberg JJ, Hobza P, Kjaergaard HG, Legon AC, Mennucci B, Nesbitt DJ (2011) Definition of the hydrogen bond (IUPAC Recommendations 2011). *Pure Appl Chem* 83:1637–1641
75. Metrangolo P, Resnati G (2001) Halogen bonding: a paradigm in supramolecular chemistry. *Chem Eur J* 7:2511–2519
76. Manna D, Mughesh G (2012) Regioselective deiodination of thyroxine by iodothyronine deiodinase mimics: an unusual mechanistic pathway involving cooperative chalcogen and halogen bonding. *J Am Chem Soc* 134:4269–4279
77. Scheiner S (2011) A new noncovalent force: comparison of P \cdots N interaction with hydrogen and halogen bonds. *J Chem Phys* 134:094315–094319
78. Mani D, Arunan E (2013) The X-C \cdots Y (X = O/F, Y = O/S/F/Cl/Br/N/P) ‘carbon bond’ and hydrophobic interactions. *Phys Chem Chem Phys* 15:14377–14383
79. Matter H, Nazaré M, Güssregen S, Will DW, Schreuder H, Bauer A, Urmann M, Ritter K, Wagner M, Wehner V (2009) Evidence for C-Cl/C-Br π interactions as an important contribution to protein-ligand binding affinity. *Angew Chem* 121:2955–2960
80. Hardegger LA, Kuhn B, Spinnler B, Anselm L, Ecabert R, Stihle M, Gsell B, Thoma R, Diez J, Benz J et al (2011) Systematic investigation of halogen bonding in protein-ligand interactions. *Angew Chem Int Ed* 50:314–318
81. Peterson KA, Shepler BC, Figgen D, Stoll H (2006) On the spectroscopic and thermochemical properties of ClO, BrO, IO, and their anions. *J Phys Chem A* 110:13877–13883
82. Murray J, Lane P, Politzer P (2007) A predicted new type of directional noncovalent interaction. *Int J Quantum Chem* 107:2286–2292

83. George J, Deringer VL, Dronskowski R (2014) Cooperativity of halogen, chalcogen, and pnictogen bonds in infinite molecular chains by electronic structure theory. *J Phys Chem A* 118:3193–3200
84. Legon AC, Roberts BP, Wallwork AL (1990) Rotational spectra and geometries of the gas-phase dimers (CH₄, HF) and (CH₄, HCl). *Chem. Phys Lett* 173:107–114
85. Stevens WJ, Fink WH (1987) Frozen fragment reduced variational space analysis of hydrogen bonding interactions. Application to the water dimer. *Chem Phys Lett* 139:15–22
86. Popelier PLA (1998) Characterization of a dihydrogen bond on the basis of the electron density. *J Phys Chem A* 102:1873–1878
87. Morrison CA, Siddick MM (2004) Dihydrogen bonds in solid BH₃NH₃. *Angew Chem Int Ed* 116:4780–4782
88. Matta CF, Hernández-Trujillo J, Tang T, Bader RFW (2003) Hydrogen–hydrogen bonding: a stabilizing interaction in molecules and crystals. *Chem Eur J* 9:1940–1951
89. Scienomics (2014) MAPS platform, version 3.4, France
90. Valiev M, Bylaska EJ, Govind N, Kowalski K, Straatsma TP, van Dam HJJ, Wang D, Nieplocha J, Apra E, Windus TL, de Jong WA (2010) NWChem: a comprehensive and scalable open-source solution for large scale molecular simulations. *Comput Phys Commun* 181:1477–1489
91. Richardson TB, de Gala S, Crabtree PE, Siegbahn MRH (1995) Unconventional hydrogen bonds: intermolecular B-H···H-N interactions. *J Am Chem Soc* 117:12875–12876
92. Matito E, Poater J, Duran M, Solà M (2006) Electron fluctuation in pericyclic and pseudopericyclic reactions. *Eur J Chem Phys Phys Chem* 7:111–113
93. Gillet N, Chaudret R, Contreras-Garcia J, Yang W, Silvi B, Piquemal J-P (2012) Coupling quantum interpretative techniques: another look at chemical mechanism in organic reactions. *J Chem Theory Comput* 8:3993–3997
94. Woodward RB, Hoffmann RJ (1965) Selection rules for concerted cycloaddition reactions. *J Am Chem Soc* 87:2046–2048
95. Houk KN, Li Y, Evansck JD (1992) Transition structures of hydrocarbon pericyclic reactions. *Angew Chim Int Ed* 31:682–708
96. Kirmse W, Rondan NG, Houk KN (1984) Stereoselective substituent effects on conrotatory electrocyclic reaction of cyclobutenes. *J Am Chem Soc* 106:7989–7991
97. Rondan NG, Houk KN (1984) Theory of stereoselection in conrotatory electrocyclic reactions of substituted cyclobutenes. *J Am Chem Soc* 107:2099–2111
98. Deward MJS (1989) A critique of frontier orbital theory. *J Mol Struct (Theochem)* 200:301–323
99. Ponec R, Yuzhakov G, Pecka J (1996) Similarity approach to chemical reactivity. Torquoselectivity in pericyclic reactions. *J Math Chem* 20:301–310
100. De Courcy B, Dognon J-P, Clavaguéra C, Gresh N, Piquemal J-P (2011) Interactions within the Alcohol Dehydrogenase (ADH) Zn(II)-metalloenzyme active site: interplay between subvalence, electron correlation/dispersion and charge transfer/induction effects. *Int J Quantum Chem* 111:1213–1221
101. Lee Y-M, Lim C (2011) Factors controlling the reactivity of zinc finger cores. *J Am Chem Soc* 133:8691–8703

Chapter 19

Diversity of the Nature of the Nitrogen-Oxygen Bond in Inorganic and Organic Nitrites in the Light of Topological Analysis of Electron Localisation Function (ELF)

Slawomir Berski and Agnieszka J. Gordon

Abstract The electronic structure of nitrite group ($-\text{ONO}$) has been studied for 21 inorganic and organic nitrites using topological analysis of Electron Localisation Function (ELF) for the DFT(B2PLYP)/aug-cc-pVTZ and DFT(B3LYP)/aug-cc-pVTZ optimised geometrical structures. The N–O bonds exhibit populations smaller than $2e$, thus including the N^+O^- , N^-O^+ Lewis-type structures in the description of electron density delocalisation is of great importance. The main focus of the ELF analysis was formally single N–O bond in the nitrite group ($-\text{O}-\text{NO}$). The results have yielded four different types of local topology: (a) single local maximum $V(\text{N},\text{O})$ with the disynaptic bonding basin, (b) two local maxima $V(\text{N})$, $V(\text{O})$ with monosynaptic non-bonding basins, (c) single local maximum $V(\text{N})$ with monosynaptic non-bonding basin, (d) absence of the local maxima in the N–O bond. Analysis of relationships between basin population values, calculated for the $V(\text{N},\text{O})$, $V(\text{N})$ and $V(\text{O})$ basins, and the N–O bond length, has shown overall trends that can be qualitatively described by the catastrophe theory.

19.1 Introduction

Electronic structure of compounds, containing the nitrite group ($-\text{ONO}$), namely inorganic ($\text{M}-\text{ONO}$, $\text{X}-\text{ONO}$) and organic nitrites ($\text{R}-\text{ONO}$) is interesting as they can serve as NO donors in various chemical and biological systems [1]. Many organic nitrites act as nitrovasodilators [2, 3] and have been used both clinically [4] and recreationally [5]. Inorganic nitrites i.e. alkaline nitrites have been studied in the context of inhibition of steel corrosion process in cement environments [6] or in

S. Berski (✉) · A.J. Gordon
Faculty of Chemistry, University of Wrocław, F. Joliot-Curie 14,
50-383 Wrocław, Poland
e-mail: slawomir.berski@chem.uni.wroc.pl

© Springer International Publishing Switzerland 2016
R. Chauvin et al. (eds.), *Applications of Topological Methods in Molecular Chemistry*, Challenges and Advances in Computational Chemistry and Physics 22, DOI 10.1007/978-3-319-29022-5_19

meat curing. Nitrites in plant food have also been subject of research since their presence in food has been thought to be associated with an increased risk of gastrointestinal cancer and methemoglobinemia in infants [7].

Physico-chemical properties of the nitrite group are associated with the nature of the chemical bonds binding the O atom to NO group and detailed knowledge of their electronic structure is very important. The nature of chemical bonds is usually studied in the Hilbert space within the molecular orbital theory. A more sophisticated approach, Quantum Chemical Topology [8], performed in the real space, invokes such concepts of gradient dynamical theory as gradient path, critical point, attractor and its basin. The most popular applications are: topological analysis of electron density, $\rho(\mathbf{r})$ proposed by Bader [9], topological analysis of Electron Localisation Function (ELF), $\eta(\mathbf{r})$ [10–15] and topological analysis of Electron Localizability Indicator (ELI), $Y^\sigma(\mathbf{r})$ [16, 17]. Our previous studies [18–28] have shown that topological analysis is an effective tool for studying the nature of the N–O (N–O1) bond in the –ONO (–O1–N=O2) group.

In order to understand diverse nature of N–O bonds in nitrites, a detailed information about changes in bond topological structure during the N–O bond dissociation is essential. Analysis of evolution of ELF field using topological approach, during dissociation of covalent homopolar C–C bond in C_2H_6 and covalent dative N–B bond in H_3BNH_3 , was reported by Krokidis et al. [29]. On the basis of his research the Bonding Evolution Theory (BET) was formulated [30–32]. This methodology combines topological analysis of ELF and catastrophe theory of Thom [33]. The reaction mechanism is analysed along the energy profile connecting the stationary points on PES using the intrinsic reaction coordinate (IRC) of Fukui [34]. Along reaction pathway, a system experiences a series of structural stability domains (SSDs) within all the critical points are hyperbolic and separated by catastrophes where at least one critical point is non hyperbolic. The bifurcation catastrophes are identified according to Thom's classification [33] which gives access to their unfolding, a compact polynomial expression which contains all the information about how ELF may change as the control parameters change. This way, a chemical reaction is viewed as a sequence of SSDs connected by catastrophes describing chemical events such as bond forming/breaking processes, creation/annihilation of lone pairs and other types of electron pair rearrangements.

The results of BET analysis for FONO show four SSDs (I–IV), characterised by different number of the local maxima (attractors) of ELF field. For example, the N–O1 bond dissociation of the F–O1–N=O2 (syn) molecule studied at the CCSD/aug-cc-pVTZ//CCSD(T)/aug-cc-pVTZ shows the topologies as presented in Fig. 19.1. For short N–O1 distances only the bonding disynaptic attractor and basin $V(N,O1)$ are observed. Such an ELF-topology (I) corresponds to the 'normal' covalent bond. 'Normal' covalent bond is a chemical bond A–B, represented by the disynaptic attractor $V(A,B)$ in topological analysis of ELF, with any value of its basin population. Further elongation of the N–O1 bond results in electron density redistribution and the change of local properties of ELF in the region of valence interaction between the N and O1 atoms. As a result, two non-bonding monosynaptic attractors are observed, instead of the single $V(N,O1)$ attractor. These are: the

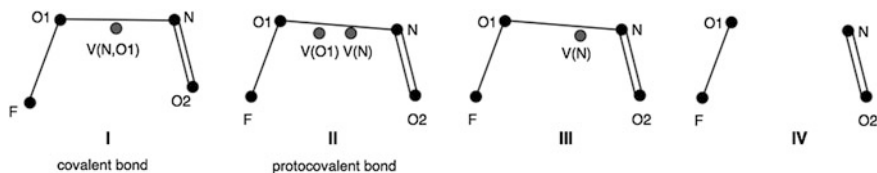


Fig. 19.1 Four types of topology of ELF field observed for the FO–N=O molecule during dissociation of the N–O bond

V(O1) attractor located in the proximity of the C(O1) core attractor and the V(N) attractor in proximity of C(N) core attractor (II). Similar ELF-topology has been first described by Llusar et al. [35] for the molecular fluorine, F₂ and labelled protocovalent bond. This type of bonding occurs in electron density depleted bonds between pnictogen, chalcogen and halogen elements bearing lone pairs. It manifests in the ELF approach through presence of two attractors close to one another determining two monosynaptic basins instead of a single disynaptic one for a standard covalent single bond. The population of each of those monosynaptic basins is less than one. It has been described as protocovalent because its SSD looks like that of two approaching fragments during covalent bond formation. In the valence-bond community this kind of bonding is known as charge-shift bond [36]. Further dissociation of the N–O1 bond and redistribution of the electron density from the N···O1 region to the adjacent bonding regions (F–O, N=O₂) and the regions of lone pairs results in vanishing of the V(O1) attractor and basin. The N–O1 bonding described by such an ELF-topology (III) is characterised by a single non-bonding basin V(N). Finally, when the distance between the N and O1 atoms is very long, the V(N) attractor and basin disappear and no local maxima of ELF field between C(N) and C(O1) core attractors are observed (IV). The ELF-topology corresponds to the situation where two molecules, FO and NO, are separated and no covalent bond N–O exist anymore.

Detailed analysis of a number and types of critical points (attractors) of the ELF field enables a characterisation of quantitative changes of ELF, as well as the electronic structure of the N–O1 bond, within the catastrophe theory. For FOINO₂, three catastrophes observed during dissociation of the N–O1 bond, one cusp and two fold catastrophes, are shown in Fig. 19.2. The V(N,O1) attractor is annihilated in the cusp catastrophe and the protocovalent bond is created by two attractors, V(N) and V(O1). Subsequently the V(N) and V(O1) attractors are annihilated in the fold catastrophes.

In the present study, we wanted to show that all four types of ELF-topology described above, (I–IV) can be found using topological analysis of ELF for the optimised geometrical structures of the nitrites including N–O bond. Such result confirms the nitrogen-oxygen bond diverse nature. We performed comparative analysis of the electronic structure of the nitrite group (–ONO) in various inorganic and organic moieties (X = H, F, Cl, Br, I, OH; M = Li, Na, K, Rb; R = CH₃, C₂H₅, C₃H₇, i-C₃H₇, C₄H₉, i-C₄H₉, C₅H₁₁, C₆H₁₁ (cyclohexyl), C₆H₅C(O), (CF₃)₂N,

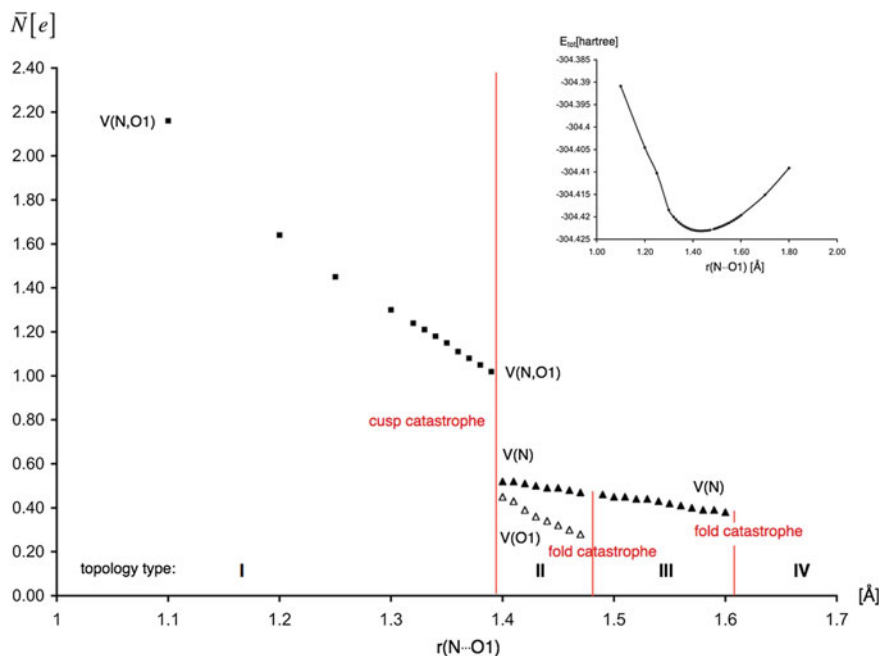


Fig. 19.2 The evolution of the basin population calculated for the $V(\text{N},\text{O1})$, $V(\text{N})$ and $V(\text{O1})$ attractors localised for the N–O1 bond in the FO1–N=O2 molecule during the process of the N–O1 bond dissociation. The plot of the total energy versus the N–O1 bond length

(CH_3)₂N). In order to ensure consistency of results, the wave functions approximation for all studied molecules was performed using the DFT(B2PLYP) method [37]. Only for the (CF_3)₂NONO and (CH_3)₂NONO molecules previously published the DFT(B3LYP) results [27] were used.

19.2 Computational Details

Full geometry optimisations have been performed using the Gaussian 09 program [38]. The minima on the potential energy surface have been confirmed by non-imaginary vibrational frequencies. The DFT(B2PLYP) functional [37] has been used as implemented in G09 programme. Unless otherwise stated, calculations have been carried out using aug-cc-pVTZ basis sets as proposed by Dunning et al. [39, 40]. For the RbONO molecule, the geometrical structure has been optimised using def2-TZVPPD basis set [41] on the O, N atoms and respective pseudopotential (ecp-28) and valence orbitals for the rubidium atom [42] has been applied. The molecular orbitals, necessary for the ELF calculations have been obtained using single-point DFT(B2PLYP) calculations and all-electron TZVall basis set

[43] from the Turbomole programme library. IONO molecule has been optimized using the aug-cc-pVTZ-PP pseudopotential [44] for the core electrons of the iodine atom (ecp-28). Other atoms have been described using the aug-cc-pVTZ basis set. In order to obtain the values of iodine molecular orbitals, the single-point calculations have been carried out using TZVPPall basis set for I atom from the Turbomole programme library. Other atoms have been described with the aug-cc-pVTZ basis set. An energy difference between the conformational isomers of the studied molecules (ΔE) has been corrected by $\Delta ZPVE$.

Topological analysis of the Electron Localization Function (ELF) has been carried out using TopMod09 suite [45, 46]. The wave function has been obtained using approximation for the DFT(B2PLYP) method proposed by Feixas et al. [47], including the natural orbitals and their occupancies only. The ELF functions have been calculated over a rectangular parallelepipedic grid with a step of 0.05 bohr. Graphical representations have been obtained by ChemCraft [48], the UCSF Chimera package [49] and VMD [50] programs.

In the plot showing the relationship between basin populations, \bar{N} and N–O1 bond lengths for all HONO, MONO, XONO and RONO nitrites, the values for IONO have been omitted. In case of the alkaline nitrites both N–O1 and N–O2 bonds have been taken into account.

19.3 Results and Discussion

19.3.1 Nitrous Acid

All compounds chosen for the study are derivatives of the simplest molecule containing the nitrite group, nitrous acid, HONO (HO1NO2). Two conformers of HONO are known (C_s symmetry), one syn (cis) and one anti (trans) characterising the H–O1 bond position in relation to the terminal N=O2 bond. The DFT (B2PLYP)/aug-cc-pVTZ optimised geometrical structure of the anti conformer is 0.63 kcal/mol more stable than the syn conformer. The single N–O1 bond in the syn conformer (1.397 Å) is 0.043 Å shorter than the length of the equivalent bond in the anti conformer. The terminal N=O2 bond, described as formally double bond in the Lewis formula, is 0.013 Å shorter in the syn conformer than in the anti conformer. Since the double N=O2 bond is shorter than the single N–O1 bond, the difference in their electronic structures can be anticipated.

The results of the N–O1 bond electronic structure, studied in the real space using topological analysis of ELF, will vary depending on the computational method used. At the DFT(B2PLYP)/aug-cc-pVTZ computational level, the N–O1 bonds in both conformers are described by two monosynaptic attractors, V(O1) and V(N). Such ELF-topology is characteristic for the protocovalent bond. The core and valence attractors in the syn and anti conformer of the nitrous acid are shown in Fig. 19.3. Similar analysis, carried out using the B3LYP hybrid electron density

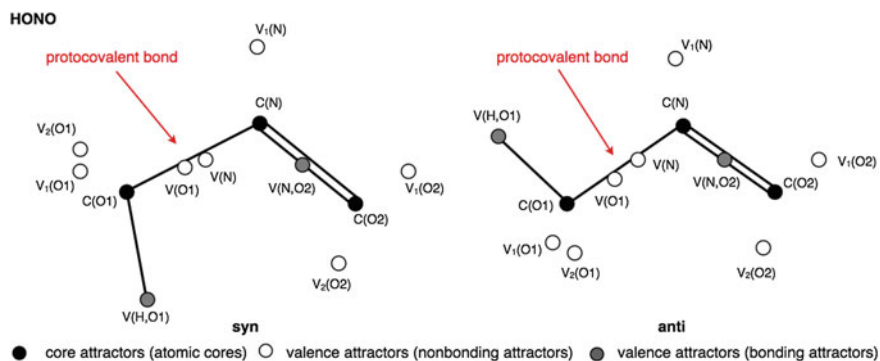


Fig. 19.3 The core and valence attractors in the nitrous acid molecule, HONO

functional and variety of basis sets, ranging from 6-311G(d,p) to aug-cc-pVQZ also concluded the protovalent N–O1 bond [18]. This result has been confirmed by a topological analysis for the ELI-D scalar field with the correlated wave function obtained from the CASSCF(12,10)/6-311++G(2d,2p)//B3LYP/6-311++G(2d,2p) calculations [18]. On the other hand, the topological analysis of ELF, with correlated wave function obtained from the CCSD/aug-cc-pVTZ calculations and the CCSD(T)/aug-cc-pVTZ optimised geometrical structures, showed the bonding disynaptic basin $V(N,O1)$ for the syn conformer ($r_{N-O1} = 1.396 \text{ \AA}$) and the protovalent bond with $V(N)$, $V(O1)$ basins for the anti conformer ($r_{N-O1} = 1.432 \text{ \AA}$) [25].

The basin populations calculated at three computational levels for the syn and anti conformers of HONO are collected in Table 19.1. The $V(N)$ and $V(O1)$ basin populations of the protovalent N–O1 bond, obtained with the wave function

Table 19.1 Mean electron populations, \bar{N} , for the localisation basins in the syn and anti conformers of nitrous acid, HONO (HO1–NO2)

Method	CCSD		B2PLYP		B3LYP	
	syn	anti	syn	anti	syn	anti
$V(N)$	–	0.58	0.60	0.51	0.61	0.53
$V(O1)$	–	0.44	0.51	0.40	0.51	0.42
$V(H,O1)$	1.78	1.79	1.81	1.82	1.81	1.82
$V(N,O1)$	1.15	–	–	–	–	–
$V(N,O2)$	2.06	2.13	2.02	2.09	2.03	2.11
$V_1(N)$	2.67	2.73	2.75	2.82	2.74	2.80
$V_1(O2)$	2.67	2.60	2.68	2.62	2.68	2.61
$V_2(O2)$	2.61	2.59	2.62	2.59	2.63	2.60
$V_1(O1)$	2.35	2.40	2.34	2.38	2.33	2.39
$V_2(O1)$	2.35	2.39	2.33	2.38	2.33	2.39

The topological analysis performed at the CCSD/aug-cc-pVTZ, B2PLYP/aug-cc-pVTZ and B3LYP/aug-cc-pVTZ computational levels

approximated from DFT(B2PLYP)/aug-cc-pVTZ calculations, are 0.60e, 0.51e for syn conformer and 0.51e, 0.40e for anti conformer. In both cases the basin describing the less electronegative atom yields a larger value of \bar{N} . This can be related to the annihilation of the V(O1) attractor at the first stage of the dissociation of the N–O1 bond (as explained above). Furthermore, larger values of \bar{N} obtained for the V(O1) and V(N) basins for the syn conformer correspond to its shorter N–O1 bond. This can be a result of the larger value of electron density associated with the shorter N–O1 bond. It is worth emphasizing, that the amount of electron density found in the N–O1 region describing the N–O1 chemical bond is much smaller than a formal value of 2e. In the light of topological analysis of ELF the N–O1 bond does not have a typical covalent character when a single electron pair is shared between N and O1 atoms. The bond nature is determined by highly delocalised electron density, represented by Lewis structures with the $\text{N}^+\text{O1}^-$ and $\text{N}^-\text{O1}^+$ bonds. Delocalisation of the electron density among ELF-basins is quantitatively described by the values of covariance matrix [51]. For the V(O1) and V(N) basins of the protocovalent bond, the electron density is delocalised mainly with large valence basins that are located in close proximity, namely non-bonding basins $V_{i=1,2}(\text{O1})$ and $V_1(\text{N})$. The magnitude of the covariance for V(O1) with two $V_{i=1,2}(\text{O1})$ lone pairs is 0.10 (each lone pair) and this value is larger than the value of 0.07 for delocalisation with the V(N) basin (within protocovalent bond). In the case of the V(N) basin the largest covariance value has been obtained for delocalisation with the non-bonding basin $V_1(\text{N})$ and is 0.11.

At the CCSD level of calculations [25] similar values of the basin population have been obtained. The value of \bar{N} for the V(N,O1) basin is 1.15e (syn) and 0.58e, 0.44e (anti) for the V(N), V(O1) basins, respectively. These results confirm less covalent character of the longer N–O1 bond and more covalent character of the N–O1 bond for the syn conformer than predicted by DFT calculations. Nevertheless, the comparison of the CCSD, DFT(B2PLYP) and DFT(B3LYP) results (see Table 19.1) shows that classification of the nature of the N–O1 bond is strongly method dependent. The double bond, N=O2, in both molecules and using all computational methods, is described by the single disynaptic bonding basin V(N,O2) with the basin population varying from 2.02e to 2.13e. This value does not correspond to that characteristic of a classical double N=O2 bond as predicted by the Lewis formula (4e). Similarly, formally single H–O1 bond exhibits basin populations in the range between 1.78e and 1.82e, smaller than formal value of 2e.

19.3.2 Alkaline Nitrites

The nature of bonding in inorganic nitrites, MONO (alkaline nitrites, MO1NO2), has been studied for four molecules: LiONO, NaONO, KONO and RbONO. Two stable conformers have been identified with the syn and anti configuration of the formal M–O1 bond in respect to the terminal NO2 bond (see Fig. 19.4). The NO1

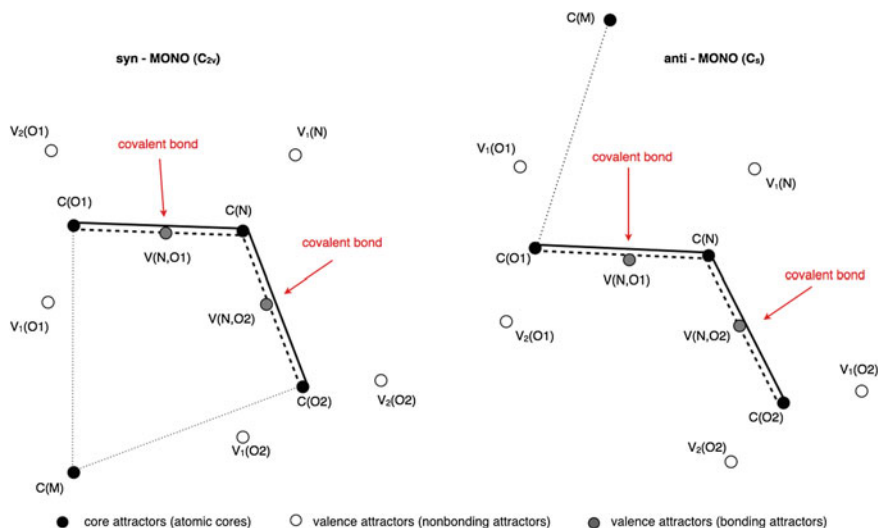


Fig. 19.4 The core and valence attractors in the alkaline nitrites, MONO ($M = \text{Li, Na, K, Rb}$)

and NO2 bonds in the syn conformer (C_{2v}) are longest for the LiONO (1.272 Å) molecule and gradually shorten in length which is reflected in much shorter value (1.216 Å) for RbONO. For the anti conformer (C_s) the NO1 bond is longer than the terminal NO2 bond. The difference between both bond lengths is 0.099 Å for LiONO, 0.082 Å for NaONO, 0.063 Å for KONO and 0.060 Å for RbONO. The values of the bond lengths are shown in Table 19.2.

The spatial organisation of the core and valence attractors in the MONO series ($M = \text{Li, Na, K, Rb}$) obtained from topological analysis of ELF are compared in

Table 19.2 N–O bond lengths and mean electron populations, \bar{N} , for the localisation basins for the N–O bond in alkaline metal nitrites $M\text{--ONO}$ ($M\text{OINO}_2$, $M = \text{Li, Na, K, Rb}$)

No	Molecule	Conformer	$r(\text{N--O1})$ [Å]	$V(\text{N,O1})$ [e]	$r(\text{N--O2})$ [Å]	$V(\text{N,O2})$ [e]
1	LiONO	syn	1.272	1.56	1.272	1.56
		anti	1.310	1.37	1.211	1.83
2	NaONO	syn	1.272	1.51	1.272	1.51
		anti	1.302	1.41	1.220	1.77
3	KONO	syn	1.266	1.55	1.266	1.55
		anti	1.289	1.43	1.226	1.72
4	RbONO	syn	1.261	1.55	1.261	1.55
		anti	1.288	1.44	1.228	1.71

The topological analysis of ELF performed at the B2PLYP/aug-cc-pVTZ (LiONO, NaONO, KONO) and B2PLYP/def2-TZVPPD(N,O),TZVall(Rb)//B2PLYP/def2-TZVPPD (RbONO) computational levels

Fig. 19.4 (both for syn and anti conformers of LiONO). The electronic structure of MONO molecules is relatively simple, because it consists only of four core basins, C(M), C(O1), C(N), C(O2), corresponding to core electron densities of the alkali metal, oxygen and nitrogen; two bonding disynaptic basins $V(N,O1)$, $V(N,O2)$ in the valence space corresponding to the NO1 and NO2 bonds and five nonbonding basins corresponding to non-bonding electrons of oxygen $V_1(O1)$, $V_2(O1)$, $V_1(O2)$, $V_2(O2)$ and nitrogen $V_1(N)$. In the region between the metal atom and the ONO group no valence bonding attractor can be found, thus the metal-oxygen interaction has no covalent character. The ELF analysis supports the $M^{\delta+}[ONO]^{\delta-}$ representation of studied molecules. Very similar result has been obtained previously for LiONO, NaONO and KONO using the DFT(B3LYP) optimised wave function and topological analysis of Electron Localizability Indicator (ELI-D) with the CASSCF (12,10)//MP2/aug-cc-pVTZ wave function and various basis sets [19].

The mean electron populations for the $V(N,O1)$, $V(N,O2)$ basins are collected in Table 19.2. All values are smaller than 1.9e thus the electronic structure of the bonds can be attributed to the delocalisation between structures containing formal N–O bonds and those where the N^+O^- , N^-O^+ bonds are present. As can be seen from Fig. 19.5, where the basin populations are plot versus the lengths of the NO1 and NO2 bonds, three groups of bonds can be distinguished. The largest and the smallest values of \bar{N} have been obtained for the terminal NO2 and NO1 bonds in the anti conformer, respectively. Basin populations for the terminal NO2 bond are in the range between 1.71e (Rb) and 1.83e (Li). Populations for the NO1 bonds are essentially smaller and range between 1.37e (Li) and 1.44e (Rb). These results confirm different characters of the NO1 and NO2 bonds. Contribution of the structures with the N^+O^- , N^-O^+ bonds in electron delocalisation is larger for the

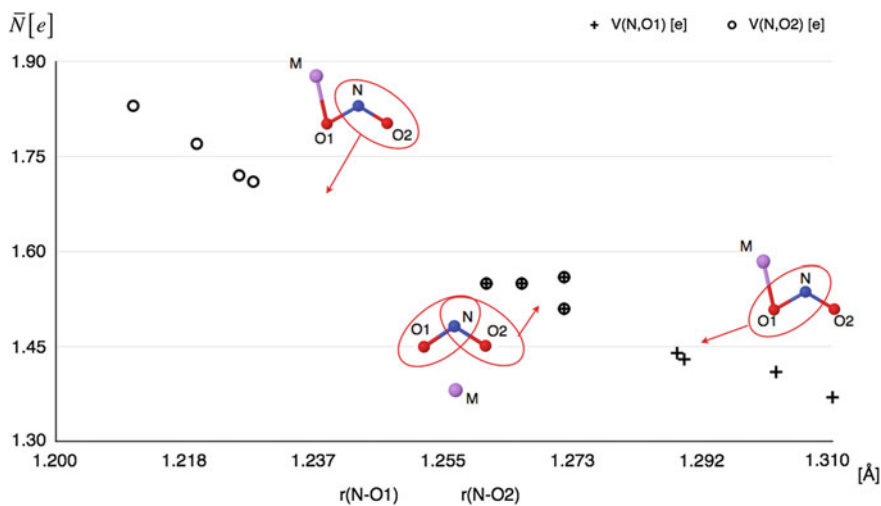


Fig. 19.5 The correlation between the population of $V(N,O1)$, $V(N,O2)$ basins and the $r(N-O1)$, $r(N-O2)$ bond lengths in the alkaline nitrites, MONO

NO1 bond than for the NO2 bond. For the syn isomer of MONO, with two equal NO1 and NO2 bonds, the transient values of \bar{N} have been calculated within a very narrow range i.e. 1.51e (Na)–1.56e (Li, Rb).

The highly polarised structure of $M^{\delta+}[\text{ONO}]^{\delta-}$ yields the question about the nature of the bonding in isolated $[\text{ONO}]^{1-}$ anion and its similarity to the $[\text{ONO}]^{\delta-}$ group in the alkaline nitrites. Topological analysis of ELF performed for the C_{2v} optimised structure ($r(\text{N}-\text{O}) = 1.263 \text{ \AA}$, $\angle(\text{O}-\text{N}-\text{O}) = 117^\circ$) has shown the same core and valence attractors as those observed in MONO. The basin populations for $V(\text{N},\text{O}1)$ and $V(\text{N},\text{O}2)$ equal 1.58e thus they are very similar to the values obtained for MONO (C_{2v}). It supports the observation that alkaline nitrites consist of a metal cation and nitrite anion.

The alkaline nitrites are examples of molecules with the nitrite group characterised by a single disynaptic $V(\text{N},\text{O}1)$ and $V(\text{N},\text{O}2)$ basins, typical for the ‘normal’ covalent bonds. It is worth noting that the bond lengths are smaller than 1.32 \AA thus these bonds are essentially shorter than a formally single N–O1 bond in the nitrous acid molecule, where the protocovalent bond has been identified.

19.3.3 Halogen Nitrites and Peroxynitrous Acid

The electronic structure has been studied for four halogen nitrites XONO (XO1NO2 , X = F, Cl, Br, I) and peroxynitrous acid, HOONO (HOO1NO2). For the XONO molecules, two conformers with syn and anti orientation of the X–O bond in respect to the terminal N=O bond have been found. For the HOONO molecule, three conformers have been investigated: syn-syn, syn-perp and anti-perp.

The B2PLYP/aug-cc-pVTZ optimised geometrical structure of the syn conformer of XONO is 2.99 kcal/mol (F), 3.29 kcal/mol (Cl), 3.89 (Br) and 4.66 kcal/mol (I) more stable than the anti conformer. The results for the HOONO molecule show the syn-syn isomer as the most stable, but the syn-perp and anti-perp conformers are only 0.92 and 3.15 kcal/mol less stable, respectively.

Comparison of the N–O1 bond lengths, collected in Table 19.3, shows longer N–O1 bond in the less stable anti conformer of all XONO molecules. The difference between the N–O1 bond length in the syn and anti isomers is 0.04 \AA (F), 0.06 \AA (Cl), 0.15 \AA (Br) and 0.16 \AA (I), respectively. Similarly, the N–O1 bond length for the less stable syn-perp and anti-perp conformers of HOONO are 0.11 and 0.10 \AA longer than in the most stable syn-syn conformer. In the case of the syn conformers of XONO, the shortest N–O1 bond is observed for IONO (1.348 \AA) and the longest for ClONO (1.496 \AA). For the anti conformers, the shortest N–O1 bond is obtained for IONO (1.504 \AA) and the longest for ClONO (1.554 \AA). With such differences in the bond lengths, significant differences in the topological structure of ELF-field can be expected. It needs to be stressed, however, that the geometrical structure of IONO has been optimised using pseudopotential approximation for the core electrons of iodine, while for other halogen atoms the all-electron basis set has been

Table 19.3 N–O bond lengths and mean electron populations, \bar{N} , for the localisation basins for the N–O1 bond in halogen nitrites XONO (XO1–NO2; X = F, Cl, Br, I) and peroxyxynitrous acid HOONO (HOO1–NO2)

No	Molecule	Conformer	r(N–O1) [Å]	V(O1) [e]	V(N) [e]	V(N,O1) [e]
1	FONO	syn	1.490	–	0.41	–
		anti	1.533	–	0.37	–
2	ClONO	syn	1.496	–	0.42	–
		anti	1.554	–	0.33	–
3	BrONO	syn	1.403	0.33	0.52	–
		anti	1.533	–	0.37	–
4	IONO	syn	1.348	0.50	0.62	–
		anti	1.504	–	0.43	–
5	HOONO	syn-syn	1.393	–	–	0.91
		syn-perp	1.505	–	0.46	–
		anti-perp	1.498	–	0.46	–

The topological analysis of ELF performed at the B2PLYP/aug-cc-pVTZ level for XONO (X = F, Cl, Br) and HOONO molecule and the B2PLYP/aug-cc-pVTZ(H,N,O),TZVPPall(I)//B2PLYP/aug-cc-pVTZ-PP level for IONO

used (see Computational details). This is bound to be reflected in the results of ELF-analysis.

Topological analysis of ELF performed for XO1NO2 molecules shows an interesting topological structures. Only single local maximum, the non-bonding V(N) attractor, in the N–O1 bonding region can be been found for both conformers of FONO and ClONO and for anti isomers of BrONO and IONO (see Table 19.3). The V(N) attractor is situated in the vicinity of the C(N) core attractor. This position of the single V(N) attractor supports ELF-topology of type III for the N–O bond as described above. The DFT(B2PLYP)/aug-cc-pVTZ results for the syn conformers of BrONO and IONO show the protocovalent N–O1 bond with two non-bonding attractors, V(O1) and V(N).

Our previous studies [20, 28] related to FONO where a correlated wave function from the CCSD/aug-cc-pVTZ//CCSD(T)/aug-cc-pVTZ was used [28], showed the protocovalent N–O1 bond for syn isomer ($r(\text{N–O1}) = 1.467 \text{ \AA}$) and only single V(N) attractor for anti conformer ($r(\text{N–O1}) = 1.500 \text{ \AA}$). Analysis of ELF-topology evolution for the N–O1 bond during dissociation process confirmed that only the V(N) attractor is observed at equilibrium. The V(N,O1) attractor expected for ‘normal’ covalent bond and two attractors V(N), V(O1) of the protocovalent bond are observed for shorter distances than that optimised for the equilibrium structure. The discrepancy between the DFT(B2PLYP) and CCSD results for FONO shows that the level of calculations plays important role in the study of the nature of the N–O1 bond in XO1NO2. Similar conclusion can be drawn from topological analysis of ELF performed for the ClONO and BrONO molecules using the various wave functions [23].

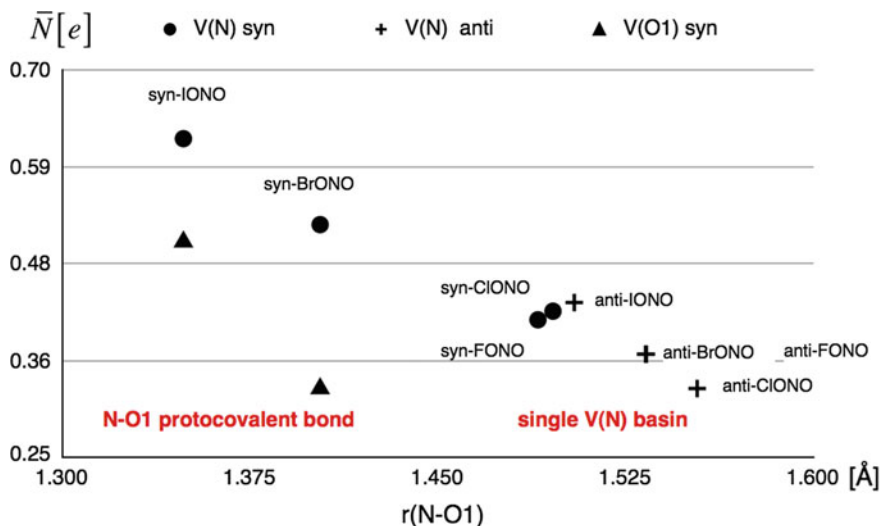


Fig. 19.6 The correlation between the population of V(N), V(O1) basins and the $r(\text{N-O1})$ bond length in the halogen nitrites, XO1NO2

The relationship between the population of the V(N), V(O1) basins and the N–O1 bond length is shown in Fig. 19.6. The protovalent bond is observed for two shortest N–O1 bonds in IONO (syn, 1.348 Å) and BrONO (syn, 1.403 Å). For much longer N–O1 bonds in the syn forms of FONO and CIONO ($r(\text{N}, \text{O1}) > 1.48$ Å) also for all anti conformers of FONO, CIONO, BrONO and IONO ($r(\text{N}, \text{O1}) > 1.50$ Å), the V(O) nonbonding attractor is no longer observed. Two types of ELF-topology (II and III), identified for the N–O1 bond are in agreement with the expected evolution of the V(N,O1) bonding basin in a process of the N–O1 bond dissociation. In such process the V(N,O1) bonding basin is annihilated first and then two non-bonding basins are observed V(N), V(O1). Further elongation of the N–O1 bond results in annihilation of V(O1) and subsequently the V(N) basin.

The core and valence attractors localised in three conformers of the peroxy-nitrous acid molecule are shown in Fig. 19.7. Values of the basin populations can be found in Table 19.3. Comparison of the N–O1 bond lengths show relatively short bond for the syn-syn conformer (1.393 Å), which is 0.112 and 0.105 Å shorter than in the syn-perp and anti-perp conformers. Topological analysis of ELF shows single valence attractor between the C(N) and C(O1) core attractors for all conformers. In the syn-perp and anti-perp isomers with longer N–O1 bond, only the V(N) attractor is observed. The basin populations are 0.46e for both isomers. The same population value is a result of a very small difference between the N–O1 bond lengths (0.007 Å). For the syn-syn conformer, a single valence attractor is found in the vicinity of the O1 atom whereas the single V(N) attractor is observed in the vicinity of N atom. It is classified as disynaptic bonding attractor, V(N,O1). The basin population of 0.91e is much larger than the one calculated for the single V(N) basin

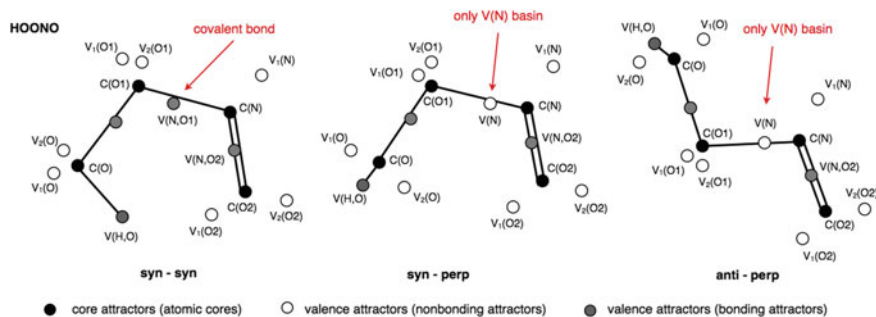


Fig. 19.7 The core and valence attractors in the peroxyntrous acid molecule, HOONO

(0.46e). This result can be associated with the N–O1 bond in the syn-syn conformer, much shorter than the equivalent bonds in the syn-perp and anti-perp isomers. Our previous calculations [25] performed at the CCSD(T)/aug-cc-pVTZ computational level yielded optimised bond lengths (1.388 Å (syn-syn), 1.473 Å (syn-perp), 1.476 Å (anti-perp)) shorter than those obtained from the DFT (B2PLYP)/aug-cpVTZ calculations. The shorter bonds have different ELF-topology and the topological analysis of ELF showed protovalent bonds with the basin population values of: 0.60, 0.48e (syn-syn), 0.54, 0.29e (syn-perp) and 0.53, 0.29e (anti-perp) for V(N), V(O1), respectively. This confirms topological structure of ELF field for the N–O1 bond dependency on the computational level.

Electronic nature of the N–O1 bond in halogen nitrites and peroxyntrous acid exhibits large diversity of ELF-topological structure characterised by types I, II and III. They are represented by the disynaptic bonding attractor V(N,O1), the protovalent bond with monosynaptic non-bonding attractors V(N), V(O1) and only single monosynaptic non-bonding attractor V(N). The III type characterises relatively long N–O1 bonds and has not been observed for HONO and MONO nitrites. The nature of the nitrogen-oxygen interaction in XONO depends strongly on the computational method used for geometry optimisation.

19.3.4 Organic Nitrites

The bonding in the organic nitrites, R–ONO, has been studied for eleven molecules: methyl nitrite, CH₃ONO, ethyl nitrite, C₂H₅ONO, propyl nitrite, C₃H₇ONO, iso-propyl nitrite, i-C₃H₇ONO, butyl nitrite, C₄H₉ONO, iso-butyl nitrite, i-C₄H₉ONO, amyl nitrite (3-methylbutyl nitrite) C₅H₁₁ONO, cyclohexyl nitrite, C₆H₁₁ONO and benzoyl nitrite, C₆H₅C(O)ONO. For CH₃ONO and C₂H₅ONO molecules all known conformers have been investigated, while for the other nitrites only the syn and anti conformers have been considered (see Fig. 19.8). Benzoyl nitrite molecule has been studied only for one stable isomer [52]. The most

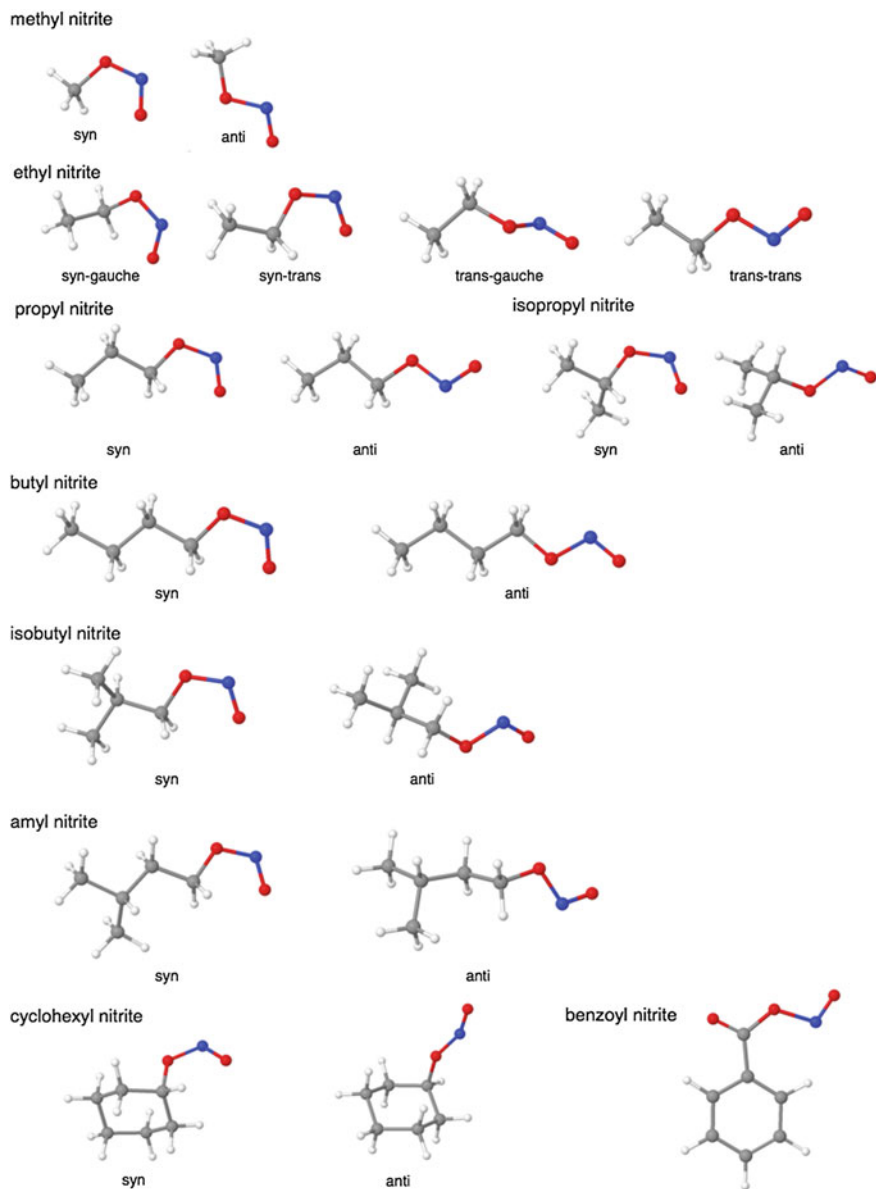


Fig. 19.8 The DFT(B2PLYP)/aug-cc-pVTZ optimised geometrical structures of the organic nitrites, RONO

interesting molecule in organic nitrites group is O-nitrosobis(trifluoromethyl)hydroxylamine, $(\text{CF}_3)_2\text{NONO}$, studied by Ang et al. [53]. Experimental studies (gas electron diffraction, X-ray diffraction) have shown unusually long N–O bond, 1.572

Table 19.4 N–O1 bond lengths and mean electron populations, \bar{N} for the localisation basins for the N–O1 bond in a series of organic nitrites, RONO (RO1–NO2)

No	Molecule	Conformer	r(N–O1) [Å]	V(O1) [e]	V(N) [e]	V(N,O1) [e]
1	CH ₃ O1NO	syn	1.408	0.50	0.57	–
		anti	1.432	0.35	0.52	–
2	C ₂ H ₅ O1NO	syn-gauche	1.404	0.51	0.58	–
		syn-trans	1.411	0.48	0.57	–
		trans-gauche	1.419	0.43	0.55	–
		trans-trans	1.426	0.37	0.53	–
3	C ₃ H ₇ O1NO	syn	1.405	0.50	0.58	–
		anti	1.421	0.42	0.55	–
4	i-C ₃ H ₇ O1NO	syn	1.408	0.49	0.58	–
		anti	1.422	0.38	0.53	–
5	C ₄ H ₉ O1NO	syn	1.405	0.50	0.58	–
		anti	1.421	0.42	0.55	–
6	i-C ₄ H ₉ O1NO	syn	1.406	0.50	0.57	–
		anti	1.428	0.37	0.53	–
7	C ₅ H ₁₁ O1NO	syn	1.405	0.38	0.53	–
		anti	1.425	0.51	0.58	–
8	(CF ₃) ₂ NO1NO ¹⁾	t-s	1.632	–	–	–
		t-a	1.583	–	0.35	–
		c-a	1.617	–	–	–
9	(CH ₃) ₂ NO1NO	t-s	1.503	–	0.52	–
		t-a	1.459	0.29	0.52	–
		c-a	1.466	0.19	0.58	–
		c-s	1.460	0.29	0.59	–

The topological analysis of ELF performed at the B2PLYP/aug-cc-pVTZ level and B3LYP/aug-cc-pVTZ level for (CH₃)₂NO1NO and (CF₃)₂NO1NO molecules

CH₃ONO—methyl nitrite, C₂H₅ONO—ethyl nitrite, C₃H₇ONO—propyl nitrite, i-C₃H₇ONO—
isopropyl nitrite, C₄H₉ONO—butylnitrite, i-C₄H₉ONO—isobutylnitrite, C₅H₁₁ONO—amyl nitrite
(3-methylbutyl) nitrite

(21) Å (gas phase) and 1.669(3) Å (in crystal), respectively. In addition to the (CF₃)₂NONO molecule, its simpler analogue, the (CH₃)₂NONO molecule has also been studied.

The DFT(B2PLYP) optimised lengths of the N–O1 bonds are presented in Tables 19.4 and 19.5. For the (CF₃)₂NONO and (CH₃)₂NONO molecules the DFT (B3LYP)/aug-cc-pVTZ optimised parameters have been used [27]. The N–O1 bond length varies between 1.404 Å for C₂H₅ONO (s-g) and 1.632 Å for (CF₃)₂NONO (t-a). As the N–O1 bond length in (CF₃)₂NO1NO₂ is exceptionally long, it is bound to exhibit interesting topological features for the N–O1 interaction.

Topological analysis of ELF has not shown any bonding disynaptic basin V(N,O1) for the interaction between the N and O1 atoms for all studied organic nitrites. Thus,

Table 19.5 N–O1 bond lengths and mean electron populations, \bar{N} for the localisation basins for the N–O1 bond in organic nitrites with the aliphatic $C_6H_{11}O1-NO$ and aromatic six-membered carbon ring $C_6H_5C(O)O1-NO$

No	Molecule	Conformer	$r(N-O1)$ [Å]	$V(O1)$ [e]	$V(N)$ [e]	$V(N,O1)$ [e]
1	$C_6H_{11}ONO$	syn	1.409	0.49	0.57	–
		anti	1.421	0.39	0.53	–
2	$C_6H_5C(O)ONO$	anti	1.547	–	0.34	–

The topological analysis of ELF performed at the B2PLYP/aug-cc-pVTZ level
 $C_6H_{11}O1NO$ —cyclohexyl nitrite, $C_6H_5C(O)O1NO$ —benzoyl nitrite

the formally single N–O1 bonding in organic nitrites cannot be classified as a standard covalent type. All the N–O1 bonds, with the lengths in the range between 1.404 and 1.466 Å, are described by two non-bonding monosynaptic attractors $V(N)$, $V(O1)$. Thus the N–O1 bonds in methyl, ethyl, propyl, butyl, amyl, cyclohexyl nitrites and $(CH_3)_2NONO$ belong to the protovalent type. Similar results have been obtained for the methyl and ethyl nitrite at the DFT(B3LYP)/aug-cc-pVTZ computational level [21]. The core and valence attractors in the exemplary cyclohexyl nitrite are shown in Fig. 19.9. In the case of longer N–O1 bonds, where the bond lengths range from 1.503 Å ($(CH_3)_2NONO$) to 1.583 Å ($(CF_3)_2NONO$), only one valence non-bonding attractor is observed $V(N)$. Similar ELF-topology has also been found for benzoyl nitrite with the N–O1 bond length of 1.547 Å. The core and valence attractors in benzoyl nitrite are presented in Fig. 19.10. The ELF topology with single $V(N)$ attractor resembles the one observed for the XONO molecules. For the longest N–O1

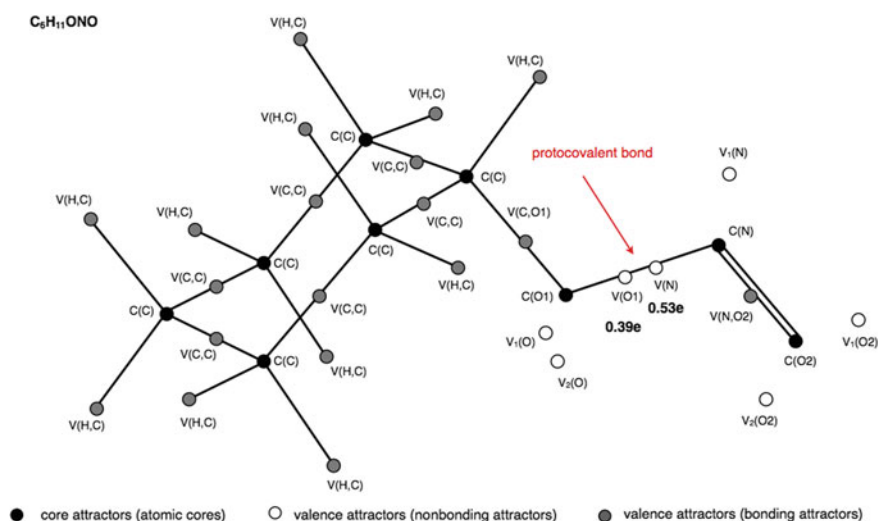


Fig. 19.9 The core and valence attractors in the cyclohexyl nitrite molecule, $C_6H_{11}ONO$

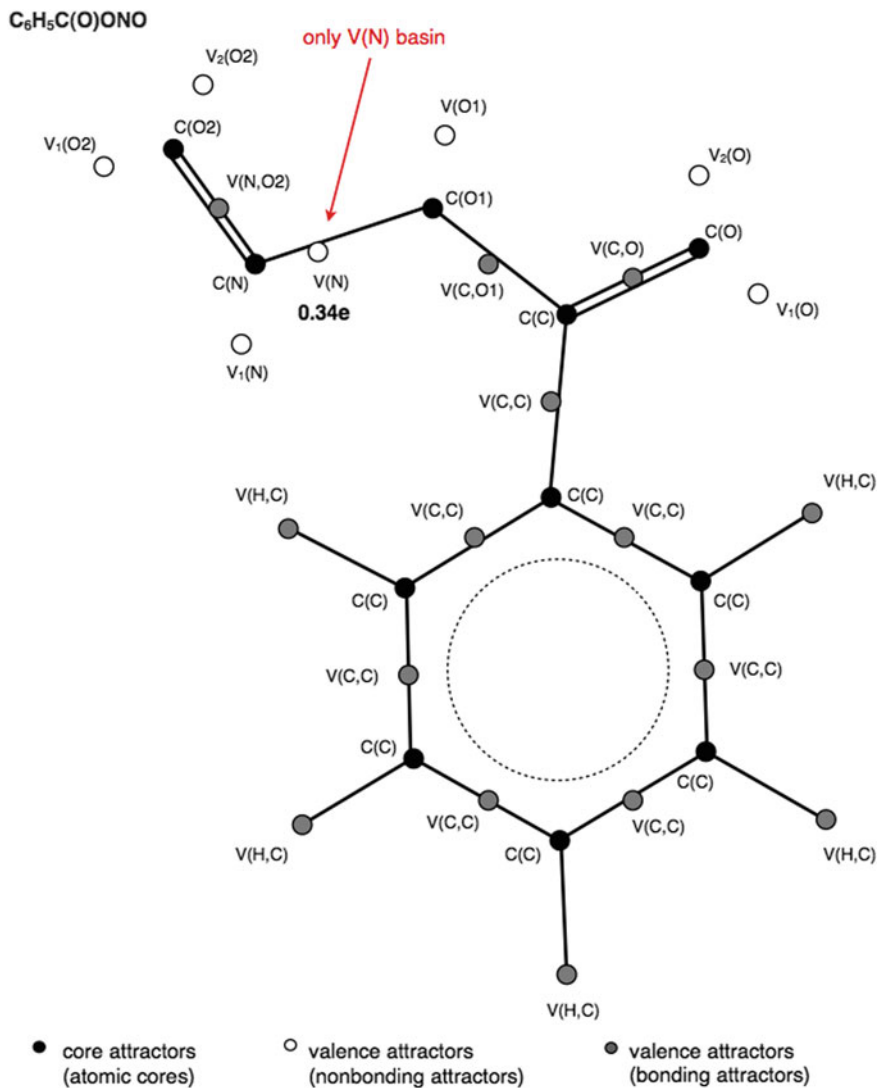


Fig. 19.10 The core and valence attractors in the benzoyl nitrite molecule, C₆H₅C(O)ONO

bond, obtained for (CF₃)₂NONO (t-s) with the length of 1.632 Å, neither bonding nor non-bonding attractors are found. The electron density in the interaction region between the N and O1 atoms is characterised by attractors of the ELF field corresponding to the lone pairs on the N and O1 atoms, V(N), V(O1). The 2D map of ELF function is shown in Fig. 19.11. From ELF-topological point of view the (CF₃)₂NONO molecule consists of the (CF₃)₂NO and NO fragments and type IV of ELF-topology is confirmed. No covalent bond can be identified, even ‘broken’

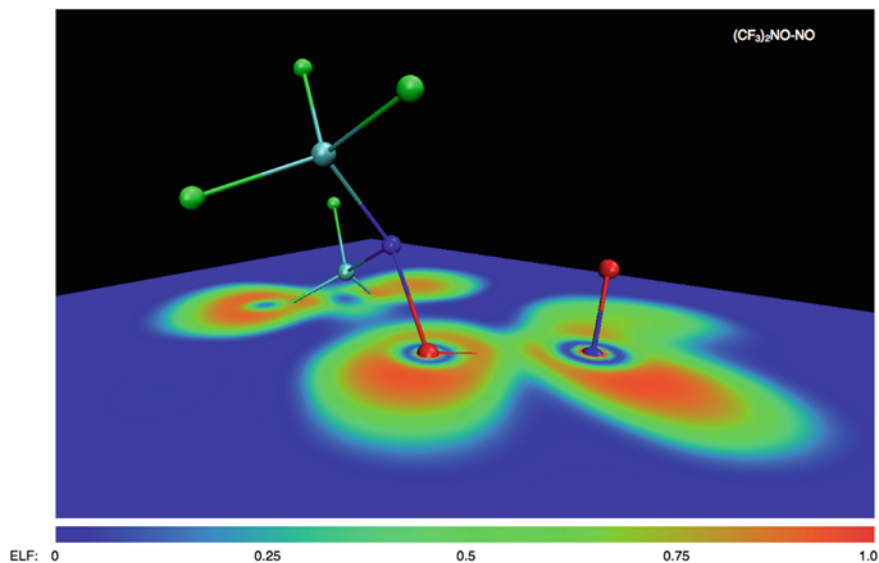


Fig. 19.11 The 2D plot of the ELF function in the plane crossing the N–O1 bond of the nitrite group. Notice the lack of any local maxima of ELF between the domains of core regions of the N and O1 atoms

covalent bond as represented by the protovalent bond or the single $V(N)$ attractor. The results obtained for the $(CF_3)_2NONO$ molecule supports our hypothesis of nitrite existing in an equilibrium configuration, where no valence attractors can be found in the N–O1 bond region.

The mean electron populations, calculated for the ELF-basins in the N–O1 bond for all RONO molecules are collected in Tables 19.4 and 19.5. The values calculated for the $V(O1)$ basin of the protovalent N–O1 bond range from 0.19e ($(CH_3)_2NONO$) to 0.51e (C_2H_5ONO , $C_5H_{11}ONO$). The results for the $V(N)$ basin lie between 0.52e (CH_3ONO , $(CH_3)_2NONO$) and 0.59e ($(CH_3)_2NONO$). The values of \bar{N} for the less electronegative element (nitrogen) are larger than the ones obtained for the more electronegative element (oxygen). The differences $\bar{N} [V(N)] - \bar{N} [V(O1)]$ are between 0.07e and 0.39e. Smaller values of \bar{N} for the $V(O1)$ basin can be associated with the fact that during dissociation of the N–O1 bond (see Fig. 19.2) the $V(O1)$ basin is annihilated first. For the single $V(N)$ basins, found in the $(CF_3)_2NONO$ (t-a), $(CH_3)_2NONO$ (t-s) and benzoyl nitrite molecules the basin population are 0.35e, 0.52e and 0.34e, respectively.

The relationship between the $V(N)$ and $V(O1)$ population values and N–O1 bond length is shown in Fig. 19.12. The simple linear regression model applied to the population values shows a negative slope along with the elongation of the $r(N-O1)$ distance. The longer N–O1 bond has smaller amount of electron density

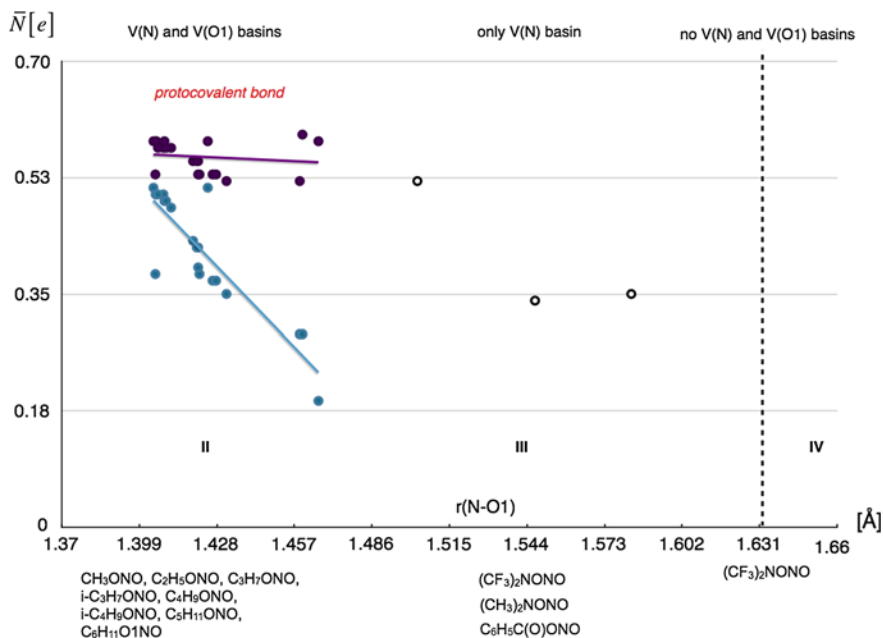


Fig. 19.12 The correlation between the population of V(N), V(O1) basins and the $r(\text{N}-\text{O}1)$ bond length in organic nitrites, RONO

‘concentrated’ on the respective ELF basins. The regression line is steeper for the V(O1) basin than for the V(N) basin. This corresponds to a much faster disappearance of V(O1) during dissociation of the N–O1 bond.

19.4 Conclusions

In this chapter the electronic structure of nitrous acid (HONO), alkaline nitrites (MONO), halogen nitrites (XONO), peroxyntrous acid (HOONO) and a range of organic nitrites (RONO), have been studied using the topological analysis of Electron Localisation Function for the DFT(B2PLYP)/aug-cc-pVTZ and DFT(B3LYP)/aug-cc-pVTZ approximated wave function.

The nitrogen-oxygen bond in the nitrite group shows four types (I–IV) of ELF-topologies. Those different topological structures of the ELF field can arise from various stages of dissociation of the N–O bond. Our study confirms that the first type (I) represented by the bonding disynaptic basin V(N,O) is observed for alkaline nitrites and one of the HOONO conformers. The second type (II) of ELF-topology that corresponds to the protocovalent N–O bond, represented by two non-bonding basins V(N), V(O), is found for HONO, the halogen nitrites BrONO, IONO and a majority of the organic nitrites. The third topological type (III),

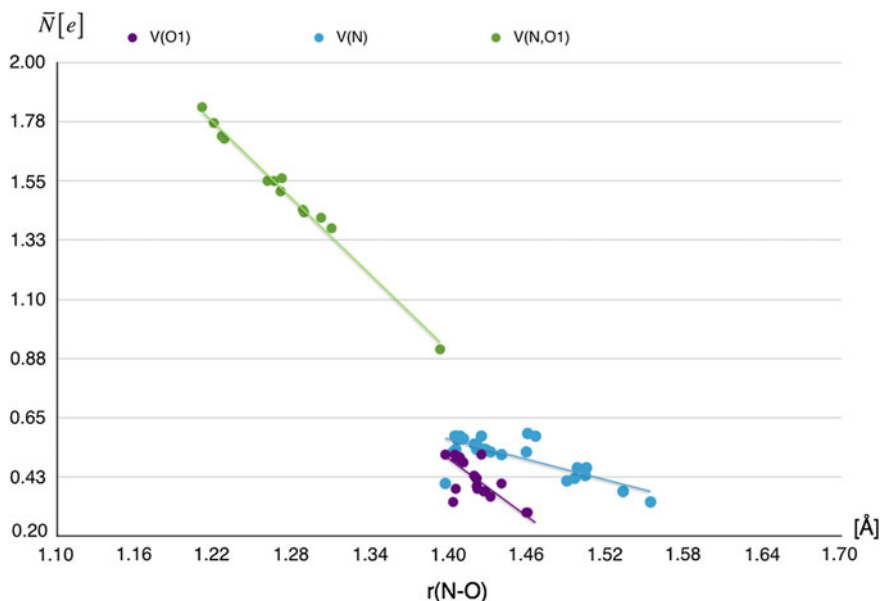


Fig. 19.13 The correlation between the population of the V(N,O1), V(N), V(O1) basins and the $r(\text{N-O})$ bond length for all inorganic and organic nitrites

characterised by single nonbonding basin V(N) is observed for the halogen nitrites FONO, ClONO, HOONO, $(\text{CH}_3)_2\text{NONO}$ and benzoyl nitrite. Finally, for the very long N–O bond, found in the $(\text{CF}_3)_2\text{NO-NO}$ molecule, the fourth type (IV) of ELF-topology is observed. This type is characterised by an absence of local maxima of the ELF field.

The mean electron populations for the basins describing types I–IV of ELF-topology for the N–O bond are compared in Fig. 19.13 (see Computational Details). All calculated values of \bar{N} are smaller than $2e$, thus the electronic nature of the N–O bond is different from a standard single covalent bond formed by two atoms of similar electronegativity with shared electron pair. From the point of view of electron density delocalisation, the nature of the binding is dominated by structures with the bonding pair localised on the N or O atoms, N^+O^- , N^-O^+ . Only in the alkaline nitrites, MONO, the N–O bond shows relatively large values of the basin population ($\bar{N} > 1.3e$). Relationship between the N–O1 bond length and basin population values calculated for the V(N,O1), V(N) and V(O1) basins shows their global evolution in agreement with a picture of the cusp and fold catastrophes (see Fig. 19.2). At the $r(\text{N-O1})$ distances in the range between 1.22 and 1.39 Å, the disynaptic bonding basin V(N,O1) is observed. Around 1.40 Å a cusp catastrophe occurs and the V(N) and V(O1) basins appear at further distances only. The V(O1) is observed in the nitrites until about 1.46 Å and V(N) basin until about 1.55 Å.

Topological analysis of ELF yields large diversity of the the nitrogen-oxygen interactions in contrast to an uniform single covalent bond, predicted by the Lewis

formula N–O. Such diversity of bonding, represented by different SSDs of ELF field, can be quantitatively distinguished and described using topological concepts and the catastrophe theory.

Finally, interesting question arises: what is the driving force behind the N–O bond length variation. The answer is not straightforward as the studies on FONO and HOONO show that the topology of ELF depends on the quality of wave function used for analysis. Furthermore, different conformers can exhibit different number and type of attractors in the N–O bond as has been shown for example for HOONO, $(\text{CF}_3)_2\text{NO}-\text{NO}$ and $(\text{CH}_3)_2\text{NO}-\text{NO}$. Nevertheless some generalisations are possible.

Analysis of the $V(\text{N})$ and $V(\text{O1})$ covariances for the protovalent bond shows that electron density exchange with the nearby large basins of the lone pairs $V_1(\text{N})$ and $V_{i=1,2}(\text{O1})$ is larger than mutual delocalisation between the $V(\text{N})$ and $V(\text{O1})$ basins. Thus the nature of the N–O bond can result from dispersive interaction through instantaneous atomic dipole-dipole interactions $-\text{N}^+ -\text{O}^+$, $+\text{N}^- +\text{O}^-$ yielding energetic stabilisation. Formation of atomic dipoles would arise from large delocalisation of electron density with the lone pairs, $V_1(\text{N})$ and $V_{i=1,2}(\text{O1})$. In that case, polarizability of the central O1 atom, dependent on electronegativity/polarizability of the M, X and R groups bonded to O1 is essential.

Based on the concept of hard and soft acids and bases [54], the electronic structure of the N–O bond in alkaline nitrites (bonding type I) is a consequence of bonding between the O1 atom and a hard acid type atom M: Li^+ , Na^+ , K^+ , Rb^+ . Similar bonding type can be expected for the MO–NO bond, formed by soft acid type M atoms (Ag^+). The bonding types II, III and IV with two $V(\text{N})$, $V(\text{O1})$ basins, single $V(\text{N})$ basin and those without valence basins in the N–O1 bond, respectively are effect of the interaction of the H, X, OH, R, $(\text{CF}_3)_2\text{N}$ and $(\text{CH}_3)_2\text{N}$ groups with O1 atom. Those groups are characterised as either hard or soft bases. The protovalent N–O1 bond (type II) is observed mainly for large group of the organic nitrites with the alkyl group R (including cyclohexyl group), $(\text{CH}_3)_2\text{N}$, BrONO and IONO. The alkyl and Br^- , I^- groups are highly polarisable, therefore they do not significantly perturb the O1 valence electrons. This enables delocalisation between $V(\text{O1})$ and $V_{i=1,2}(\text{O1})$ basins. When weakly polarisable groups, F^- , Cl^- and OH^- i.e. hard bases are bound to O1 atom, the polarising effect on O1 atom is intensified withdrawing electron density from the N–O1 bond and weakening it. This can be associated with the $V(\text{O1})$ basin disappearance (type III). Finally, a very strong polarising effect is expected for the $(\text{CF}_3)_2\text{N}$ group due to the lack of valence basins (type IV) caused by large withdrawal of electron density from the N–O1 bond, diminishing further the O1 atom delocalisation in the valence shell and decreasing the stabilising dispersion-like interaction.

Acknowledgments The authors are grateful to the Wrocław Centre for Networking and Supercomputing for generous allocation of computer time.

References

1. Burgaud JL, Ongini E, Del Soldato P (2002) *Ann N Y Acad Sci* 962:360–371
2. Nicolescu AC, Reynolds JN, Barclay LRC, Thatcher GRJ (2004) *Chem Res Toxicol* 17:185–196
3. Artz JD, Thatcher GR (1998) *Chem Res Toxicol* 11:1393–1397
4. Brunton TL (1867) *Lancet* 2:97
5. Bradberry SM, Whittington RM, Parry DA, Vale JA (1994) *J Toxicol Clin Toxicol* 32:179–184
6. Song H, Saraswathy V, Muralidharan C-HL, Thangavelu K (2009) *J Appl Electrochem* 39 (1):15–22
7. Hord NG, Tang Y, Brayn NS (2009) *Am J Clin Nutr* 90(1):1–10
8. Popelier PLA (2005) *Structure and Bonding. Intermolecular forces and clusters I* 115:1–56
9. Bader RFW (1994) *Atoms in molecules: a quantum theory*. Oxford University Press, Oxford
10. Becke AD, Edgecombe KE (1990) *J Chem Phys* 92:5397–5403
11. Silvi B, Savin A (1994) *Nature* 371:683–686
12. Chevreau H, Fuster F, Silvi B (2001) *L'Actualité Chimique* 240:15–22
13. Silvi B, Fourré I, Alikhani ME (2005) *Monatsh Chem* 136:855–879
14. Silvi B (2002) *J Mol Struct* 614:3–10
15. Savin A, Silvi B, Colonna F (1996) *Can J Chem* 74:1088–1096
16. Kohout M (2004) *Int J Quantum Chem* 97:651–658
17. Kohout M (2007) *Faraday Discuss* 135:43–54
18. Berski S, Mierzwicki K, Bil A, Latajka Z (2008) *Chem Phys Lett* 460:559–562
19. Berski S, Latajka Z (2010) *Int J Quantum Chem* 110:1890–1900
20. Berski S, Latajka Z, Gordon AJ (2010) *J Chem Phys* 133:034304–034313
21. Berski S, Latajka Z, Gordon AJ (2010) *Chem Phys Lett* 493:392–398
22. Berski S, Latajka Z, Gordon AJ (2010) *J Comput Chem* 31:2555–2567
23. Berski S, Gordon AJ (2011) *J Chem Phys* 135:094303–094316
24. Berski S, Latajka Z, Gordon AJ (2011) *Chem Phys Lett* 506:15–21
25. Berski S, Latajka Z, Gordon AJ (2011) *J Comput Chem* 32:1528–1540
26. Berski S, Latajka Z (2011) *Int J Quantum Chem* 111:2378–2389
27. Berski S, Gordon AJ (2012) *Chem Phys Lett* 525–526:24–31
28. Berski S, Gordon AJ, Latajka Z (2013) *J Chem Phys* 138:134313–134322
29. Krokidis X, Noury S, Silvi B (1997) *J Phys Chem A* 101:7277–7282
30. Krokidis X, Silvi B, Alikhani ME (1998) *Chem Phys Lett* 292:35–45
31. Krokidis X, Silvi B, Dezarnaud-Dandine C, Sevin A (1998) *New J Chem* 22:1341–1350
32. Krokidis X, Vuilleumier R, Borgis D, Silvi B (1999) *Mol Phys* 96:265–273
33. Thom R (1972) *Stabilité Structurale et Morphogénèse*. Interéditions, Paris
34. Fukui K (1981) *Acc Chem Res* 14:363–368
35. Llusar R, Beltrán A, Andrés J, Noury S, Silvi B (1999) *J Comput Chem* 20:1517–1526
36. Shaik S, Maitre P, Sini G, Hiberty PC (1992) *J Am Chem Soc* 114:7861–7866
37. Grimme S (2006) *J Chem Phys* 124:034108–034122
38. Gaussian 09, Revision D.01, Frisch MJ, Trucks GW, Schlegel HB, Scuseria GE, Robb MA, Cheeseman JR, Scalmani G, Barone V, Mennucci B, Petersson GA, Nakatsuji H, Caricato M, Li X, Hratchian HP, Izmaylov AF, Bloino J, Zheng G, Sonnenberg JL, Hada M, Ehara M, Toyota K, Fukuda R, Hasegawa J, Ishida M, Nakajima T, Honda Y, Kitao O, Nakai H, Vreven T, Montgomery Jr JA, Peralta JE, Ogliaro F, Bearpark M, Heyd JJ, Brothers E, Kudin KN, Staroverov VN, Kobayashi R, Normand J, Raghavachari K, Rendell A, Burant JC, Iyengar SS, Tomasi J, Cossi M, Rega N, Millam MJ, Klene M, Knox JE, Cross JB, Bakken V, Adamo C, Jaramillo J, Gomperts R, Stratmann RE, Yazyev O, Austin AJ, Cammi R, Pomelli C, Ochterski JW, Martin RL, Morokuma K, Zakrzewski VG, Voth GA, Salvador P, Dannenberg JJ, Dapprich S, Daniels AD, Farkas Ö, Foresman JB, Ortiz JV, Cioslowski J, Fox DJ, Gaussian, Inc., Wallingford CT (2009)

39. Dunning Jr TH (1989) *J Chem Phys.* 90:1007–1023
40. Kendall RA, Dunning Jr TH, Harrison RJ (1992) *J Chem Phys* 96:6797–6806
41. Weigend F, Ahlrichs R (2005) *Phys Chem Chem Phys* 7:3297–3305
42. Leininger T, Nicklass A, Kuechle W, Stoll H, Dolg M, Bergner A (1996) *Chem Phys Lett* 255:274–280
43. Ahlrichs R, May K (2000) *Phys Chem Chem Phys* 2:943–945
44. Peterson KA, Figgen D, Goll E, Stoll H, Dolg M (2003) *J Chem Phys* 119:11113–111123
45. Noury S, Krokidis X, Fuster F, Silvi B (1997) *TopMod*; Paris
46. Noury S, Krokidis X, Fuster F, Silvi B (1999) *Comput Chem* 23:597–604
47. Feixas F, Matito E, Duran M, Solá M, Silvi B (2010) *J Chem Theory Comput* 6:2736–2742
48. Andrienko GA *ChemCraft*. <http://www.chemcraftprog.com>
49. Pettersen EF, Goddard TD, Huang CC, Couch GS, Greenblatt DM, Meng EC, Ferrin TE (2004) *J Comput Chem* 25:1605–1612
50. Humphrey W, Dalke A, Schulten K (1996) *J Mol Graph* 14:33–38
51. Silvi B (2004) *Phys Chem Chem Phys* 6:256–260
52. Du L, Zeng X-Q, Ge M-F, Sun Z, Wang D-X (2008) *J Mol Struct* 878:26–31
53. Ang HG, Klapdor MF, Kwik WL, Lee YW, Mack HG, Mootz D, Poll W, Oberhammer H (1993) *J Am Chem Soc* 115:6929–6933
54. Pearson RG (1963) *J Am Chem Soc* 85:3533–3539

Chapter 20

Quantum Chemical Topology in the Field of Quasirelativistic Quantum Calculations

Mohamed Amaouch, Eric Renault, Gilles Montavon, Nicolas Galland and Julien Pilmé

Abstract This chapter aims to present QTAIM and ELF topological analyzes in the framework of two-component relativistic computations. Attention is focused on spin-orbit coupling (SOC) effects on the chemical bond in systems containing heavy atoms. The emblematic At₂ and uranyl species have been studied as a relevant test set. The presented methodology appears particularly suitable for evidencing relativistic effects on bonding schemes. The influence of SOC was found to depend, not only of the involved heavy atoms, but also of the bond nature. Furthermore, the robustness of QTAIM and ELF for analyzing wave functions built from spinors has been verified.

Keywords QTAIM · ELF · Topological analysis · Relativistic effects · Spin-orbit coupling · Astatine · Uranyl

M. Amaouch · J. Pilmé (✉)
Laboratoire de Chimie Théorique, Sorbonne Universités,
UPMC Université Paris 06, UMR 7616, 75005 Paris, France
e-mail: pilme@lct.jussieu.fr

M. Amaouch · J. Pilmé
CNRS UMR 7616, Laboratoire de Chimie Théorique, 75005 Paris, France

E. Renault · N. Galland (✉)
CEISAM, UMR CNRS 6230, Université de Nantes, 2 Rue de la Houssinière,
BP 92208, 44322 Nantes Cedex 3, France
e-mail: nicolas.galland@univ-nantes.fr

G. Montavon
SUBATECH, UMR CNRS 6457, IN2P3/EMN Nantes/Université de Nantes,
4 rue a. Kastler, BP 20722, 44307 Nantes Cedex 3, France

20.1 Introduction

Since chemists began to draw formulas of chemical compounds where atoms are linked by electron pairs [1, 2], simple concepts such as single and multiple bonds or covalent and ionic bonds, appear as the cornerstone of the molecular structure understanding. They notably have demonstrated their indisputable utility for helping chemists in the rational design of systems with desired properties. However, the bonding in many systems containing heavy atoms is still unclear to chemists, especially because of relativistic effects and in particular the spin-orbit coupling (SOC). One may distinguish electron spin-independent (scalar) effects from spin-dependent relativistic effects. The scalar effects are associated with the relativistic mass increase of electrons, resulting essentially from their high speed in the vicinity of heavy nuclei. The main spin-dependent effect is the coupling between electron spin and electron orbital momentum (SOC). The latter complicates the possibility of imagining a bridge between the complex electronic structure of systems containing heavy atoms (e.g. actinides and heavy *p*-elements) and simple concepts, which can be used by chemists to understand the outcomes of experimental observations as well as the results of state-of-the-art electronic structure calculations. Indeed, a proper description of systems containing actinides or heavy *p*-elements requires including SOC in the quantum mechanical calculations. While computational chemists have been developing tools to bridge quantum mechanical calculations to chemist's views for decades [3–8], this has only been done thoroughly in the framework of non-relativistic or scalar-relativistic methods, since scalar-relativistic effects can be incorporated into existing non-relativistic programs with minimum extra code developments. The situation is deeply contrasting when looking at available tools for scrutinizing SOC effects on traditional pictures of the chemical bond. A fundamental problem is that chemists are not familiar with spinors which are single-particle functions usually used to expand SOC wave functions. Since spinors are complex vector functions of two- or four-component, they do not lend themselves easily to visualization. An illustration is displayed on Fig. 20.1 in the case of one singly occupied two-component (2c) spinor of the At_2 species.

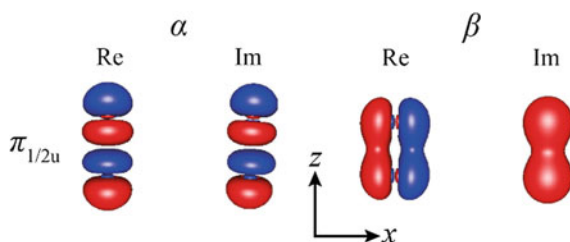


Fig. 20.1 One of $\pi_{1/2u}$ occupied 2c (pseudo)spinors calculated at 2c-B3LYP/aug-cc-pVTZ-PP-2c level of theory for the At_2 species. Notable mixing between σ antibonding characters (α component) and π bonding characters (β component) is evidenced

While seminal works intended to reveal SOC effects on the bonding schemes were discussed in term of spinors [9–13], canonical molecular spinors are not suited for the bonding analysis in complex systems, as opposed to small and/or symmetric model systems. Some have promoted the use of localized spinors [14], and in order to recover some chemical significance in terms of bonding, lone pairs and core orbitals, natural spinors similar to natural orbitals in the non-relativistic frameworks have been derived and implemented [15, 16]. It is worth noting that the concept of bond order in the context of multiconfigurational wave functions have been extended recently to two-step spin-orbit coupling approaches [17].

Alternative strategies belonging to the Quantum Chemical Topology (QCT) methodology are known for a long time in the field of non-relativistic quantum calculations. They aim to answer general questions about the nature of chemical bonds, the characterization of bonding schemes, reactivity and chemical reactions. Among them, both the *Quantum Theory of Atoms In Molecules* (QTAIM) and the topological analysis of the *Electron Localization Function* (ELF) have been reviewed in numerous articles and books [3, 18–23]. Recently, some of us have notably extended ELF and QTAIM analyzes in the field of quasirelativistic quantum calculations [24, 25]. These tools should allow computational chemists to study complex molecular systems for which the consideration of SOC is crucial. The current chapter aims to demonstrate their power for probing the bonding in heavy-atom systems. It is not only of fundamental interest, but it is also crucial for applications of societal interest (e.g. nuclear medicine, energy production), or may be related to environmental issues (e.g. in the context of nuclear waste management). Indeed, in order to illustrate the originality of the proposed methodology, two emblematic test cases have been selected: the At_2 species and the uranyl dication. Astatine (At, $Z = 85$) is the heaviest naturally occurring halogen and one of its longest-lived isotopes, ^{211}At , is of considerable interest in oncology as a radiotherapeutic agent for targeted alpha therapy [26]. While hypothetical, the At_2 species is known for displaying spectacular SOC effects [9, 27–29]. In contrast, the second selected At-species, $\text{AtO}(\text{OH})$ [30], might be involved in some of the labeling protocols, if one looks closely at the experimental conditions (pH , E_h) [31], which are currently developed for using ^{211}At in alpha-immunotherapy. Others interesting systems are actinides complexes and especially those involving multiple bonds [32–37]. The chemistry of the uranyl dication, UO_2^{2+} , is to date more widely studied by computational chemists than that of any other actinide. Indeed, the crucial role of the uranyl dication during the uranium conversion stage in the nuclear fuel cycle has brought for some decades the researchers attention on this species. Nevertheless, much remains to be said about the bonding in UO_2^{2+} . Among the various questions that arise, regarding the selected systems, we focus especially on the following:

- (1) What types of bond tend to establish heavy atoms and what are the factors affecting the chemical bonding?
- (2) How are depicted the SOC effects by means of QCT methodology?
- (3) What is the influence of the selected computational model (methods, basis sets) on QCT results when wave functions are built from spinors?

20.2 The Theoretical Frame

20.2.1 Computational Strategy

The proper treatment of molecular systems containing heavy atoms needs to perform four-component (4c) relativistic calculations based on the exact Hamiltonian. The most straightforward way to construct the relativistic many-electron Hamiltonian is to augment the one-electron Dirac operator with the Coulomb or Breit operator as a two-electron term [38]. However, the applicability of this approach is limited to rather small systems owing to unaffordable computational costs [39]. Either founded on an exact or an approximate formalism, several quasirelativistic approaches are often employed as efficient alternatives [40, 41]. Accurate descriptions of relativistic effects could be obtained with the exact two-component (X2C) Hamiltonians, the familiar Douglas-Kroll (DK*n*) approach, or using the *n*th order regular approximation (ZORA, FORA) of the exact relativistic Hamiltonian. The relativistic effective core potential (RECP), and in particular pseudopotential (PP), as an approximate quasirelativistic method has gained popularity as it makes possible to study systems of increasing size while preserving a high degree of reliability comparable to the all-electron calculations [42]. Good efficiency is ensured by replacing inner-core electrons, which leads to significant reductions in the number of basis functions, and the simpler forms of the Hamiltonian employed. Indeed, 2c effective valence-only Hamiltonians for *n* valence electrons and *N* nuclei can be expressed as follows:

$$\hat{H}_n = \sum_i^n (\hat{h}_i) + \sum_{i<j}^n (\hat{g}_{ij}) + V_{cc} \quad (20.1)$$

where \hat{h}_i and \hat{g}_{ij} represent effective one and two-electron operators, respectively. V_{cc} is the nuclear repulsion energy. In PP approach, it is generally assumed that the kinetic energy operator and the Coulomb interaction between electrons could be used in their non-relativistic forms, \hat{h}_i and \hat{g}_{ij} are expressed as:

$$\hat{h}_i = -\frac{1}{2}\Delta_i + \hat{V}_{PP}(i); \quad \hat{g}_{ij} = \frac{1}{r_{ij}} \quad (20.2)$$

All relativistic contributions can be folded into the Hamiltonian by means of the parametrization of \hat{V}_{PP} . The current form of PPs used in this work is:

$$\hat{V}_{PP}(i) = \sum_A^N \left(-\frac{Z_{\text{eff}}(A)}{r_{Ai}} + \sum_k^N B_{ij}^k e^{(-\beta_{ij}^k r_{Ai}^2)} \hat{P}_{ij} \right) \quad (20.3)$$

where the first sum runs over the *N* nuclei (index *A*) with respective effective charge Z_{eff} . The second sum runs over a gaussian expansion (index *k*) of semi-local

short-range radial potentials which are different for different orbital angular-momentum quantum numbers l and, for a given l , for the two total one-electron angular-momentum quantum numbers $j = l \pm 1/2$ (\widehat{P}_{lj} is the 2c projector onto the complete space of functions with angular symmetry l, j around the core under study). The parameters B_{ij}^k and β_{ij}^k are adjusted so that \widehat{V}_{PP} in 2c valence-only atomic calculations reproduces, as closely as possible, a set of all-electron 4c multiconfiguration Dirac-Hartree-Fock (MCDHF) energies. Note that a transcription of such kind of PP into a scalar-relativistic spin-averaged part (averaged relativistic potential \widehat{V}_{AREP}) and an effective one-electron spin-orbit operator (\widehat{V}_{SO}) is easily possible [43, 44]. The omission of \widehat{V}_{SO} in the calculation leads to one-component (1c) scalar-relativistic approach (in a non-relativistic formalism). Hence, SOC effects can readily be quantified via the difference between calculations with and without \widehat{V}_{SO} included in PPs. The action of \widehat{V}_{SO} generates a wave function built of single-particle functions known as (pseudo)spinors, $\varphi_i(\mathbf{r})$, that are no longer of pure α or β character but have both a α and a β complex component, and hence, two-component. Usually, $\varphi_i(\mathbf{r})$ are expanded using atom-centered gaussian basis functions, $\chi_\mu(\mathbf{r})$, and the expansion coefficients c_i are complex:

$$\varphi_i(\mathbf{r}) = \begin{pmatrix} \varphi_{i\alpha}(\mathbf{r}) \\ \varphi_{i\beta}(\mathbf{r}) \end{pmatrix} = \begin{pmatrix} \sum_{\mu} c_{i\mu}^{\alpha} \chi_{\mu}(\mathbf{r}) \\ \sum_{\mu} c_{i\mu}^{\beta} \chi_{\mu}(\mathbf{r}) \end{pmatrix} \quad (20.4)$$

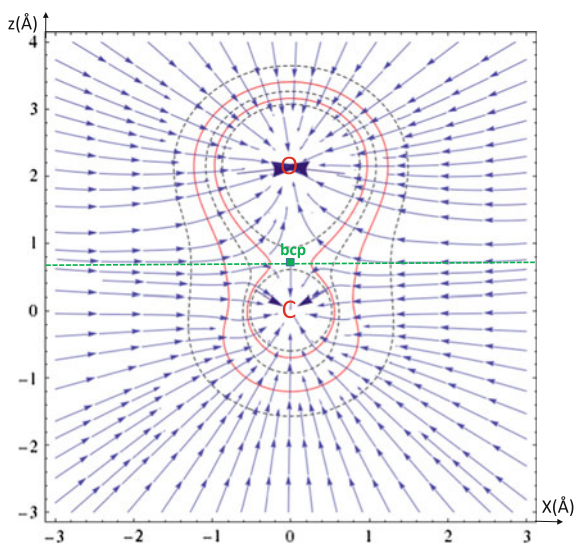
Application of the density functional theory (DFT) appears particularly attractive due to the computational expediency and the implicit inclusion of electron correlation effects. The quasirelativistic spin-orbit DFT (SODFT) method, implemented in the NWChem programs package [44], takes advantage of 2c PPs. The inclusion of spin-dependent terms into the variational treatment of the one-electron operator ensures that scalar-relativistic and SOC effects are treated on an equal footing. Note that special care has to be taken when SOC is planned to be included in calculations with small-core PPs: standard basis sets must be supplemented with few steep functions so that the expansions for the semi-core orbitals become flexible enough to account for the radial differences of the spinors with $j = l \pm 1/2$. This was found especially relevant for the 6p elements (split of the 5p-shell to an energetically lower lying more compact $p_{1/2}$ subshell and a higher lying less compact $p_{3/2}$ subshell), and to a less extent for the 5p and 5d ones [27, 45]. *In fine*, it comes out that the SODFT method allows chemists to perform geometry optimizations and calculations of vibrational spectra at moderate computational costs for systems composed of several tens of atoms.

20.2.2 Sketch of the QTAIM Analysis

Of all the possible ways to partition the electron density in a molecule [46, 47], the QTAIM theory [3, 18] is probably the most used for discussing the nature of chemical bonding in molecules and solids. The pioneering works due to Bader and coworkers in the 70s [48–50] were motivated by the generalization of the quantum mechanical principle of stationary action to a molecular subsystem. Based on the theory of gradient dynamical systems [51, 52], they have led to an original topological partition of the electron density (so-called virial partitioning) into non-overlapping atomic regions [48, 50, 53]. These regions are termed atomic basins (noted Ω) and are stable manifolds of the attractors (maxima) of the density. Then, topological atoms can be defined as the union of a nucleus and of its atomic basin. However, non-nuclear attractors (flat maxima) can be exceptionally found in internuclear regions of metal clusters [54]. Interestingly, the QTAIM approach can be applied to both experimental [55] and calculated electron densities. The basins of the density gradient field $\nabla\rho(\mathbf{r})$ are either circumscribed by interatomic separatrix surfaces, i.e. zero-flux surfaces, or extend to infinity [56] as illustrated on Fig. 20.2.

The ability to use a Lagrangian formulation of quantum mechanics is an important outcome of this partitioning, because the integrated kinetic positive energy density $G[\Omega]$ in the basin volume has a definite value. This allows the derivation of many theorems, such as the atomic force theorem [57, 58] and the atomic virial theorem [57]. The topology of the gradient field is characterized by critical points (where $\nabla\rho(\mathbf{r}) = \mathbf{0}$) and their connectivity. Critical points can be either local maxima (attractor), minima or saddle points of the gradient field. Usually, critical points are single points, but exceptions can occur if the system belongs to a

Fig. 20.2 2D view of the charge density gradient vector field for the CO molecule calculated at the B3LYP/6-31G level of theory. Isovalue curves of the density are in red and in green, both the location of the bond critical point and the interatomic surface between the two atoms (carbon domain at the bottom and oxygen domain at the top)



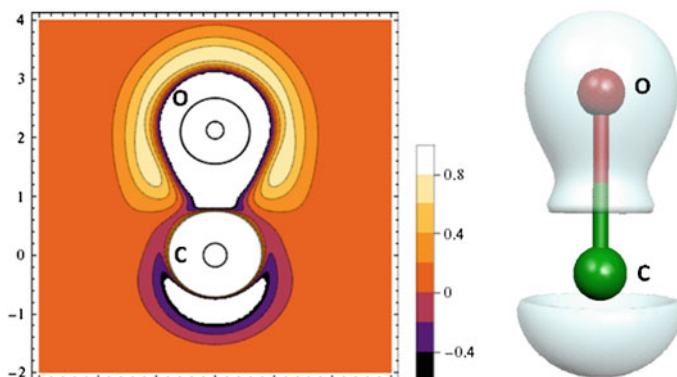


Fig. 20.3 $\nabla^2\rho(\mathbf{r})$ isovalue curves of the CO molecule (left) calculated at the B3LYP/6-31G level of theory, showing VSCCs domains, and 3D view of $\nabla^2\rho(\mathbf{r})$ (right)

continuous symmetry group ($C_{\infty v}$ for instance). Among the saddle points, a *bond critical point* (BCP) plays an essential role in QTAIM theory (see Fig. 20.2). A BCP is only connected to two attractors by the trajectory of the gradient field (bond path) and, at the BCP, the values of some descriptors are distinctly related to the nature of the chemical bond. In molecules and crystals, the Laplacian of the density $\nabla^2\rho(\mathbf{r})$ reveals spatial regions where the electron density is locally concentrated ($\nabla^2\rho(\mathbf{r}) < 0$) or depleted ($\nabla^2\rho(\mathbf{r}) > 0$). Regions of charge concentration, namely the Valence Shell Charge Concentrations (VSCCs), are found in both bonding and non-bonding regions (see Fig. 20.3). It has been shown that the number, size and location of VSCCs are often in agreement with the electron-pair domains of the VSEPR model [59], providing an interesting physical support to the model [60–62].

A clear homeomorphism relationship between $\nabla^2\rho(\mathbf{r})$ and the conditional pair probability have been established by Bader and Heard [63]. Thereby strengthening the link between the $\nabla^2\rho(\mathbf{r})$ probe and the chemical bond. It is worth noting that, although the topology of $\nabla^2\rho(\mathbf{r})$ remains a powerful tool for investigating chemical bonds, its ability for rationalizing other important concepts in chemistry, such as interpreting electronegativity effects, has been questioned [64].

Electron density from 2c-spinors. Most of the time, the N -electron ground state wave functions are approximated by an antisymmetrized product of N orthonormal single-electron functions (spin-orbitals) and are expressed in terms of a Slater determinant $|\psi\rangle$. The electron density is then the expectation value of the one-electron density operator:

$$\hat{\rho}(\mathbf{r}) = \sum_i^N \delta(\mathbf{r}_i - \mathbf{r}) \quad (20.5)$$

Using the variational principle under the only constraints of the single or double occupation for each spatial orbital $\varphi_i(\mathbf{r})$ (Hartree-Fock or Kohn-Sham formalisms), the electron density becomes:

$$\rho(\mathbf{r}) = \langle \Psi | \hat{\rho}(\mathbf{r}) | \Psi \rangle = \sum_i^{\text{occ}} n_i \varphi_i^*(\mathbf{r}) \varphi_i(\mathbf{r}) = \sum_{\mu} \sum_{\nu} P_{\mu\nu} \chi_{\mu}(\mathbf{r}) \chi_{\nu}(\mathbf{r}) \quad (20.6)$$

where $\varphi_i(\mathbf{r})$ are expanded using atom-centered gaussian basis functions, $\chi_{\mu}(\mathbf{r})$, and $P_{\mu\nu}$ are elements of the total one-electron density matrix defined as follows:

$$P_{\mu\nu} = \sum_i^{\text{occ}} n_i c_{i\mu} (c_{i\nu})^* \quad (20.7)$$

n_i is the occupation of the $\varphi_i(\mathbf{r})$ orbital and $c_{i\mu}$ and $c_{i\nu}$ are the real expansion coefficients. Most of topological analyzes of the electron density are performed in case of non-relativistic all-electron calculations but, if heavy elements ($Z > 36$) are involved, RECPs including scalar-relativistic effects are generally used. Recently, the transferability of the QTAIM formalism has been studied in a context of all-electron scalar-relativistic calculations [65], more precisely scalar-relativistic ZORA calculations [66]. Within ZORA Hamiltonians, the kinetic energy operator differs from the non-relativistic operator. This leads to the following boundary condition for QTAIM basins:

$$\left[\frac{c^2}{2mc^2 - V_{\text{KS}}(\mathbf{r})} \right] \nabla \rho(\mathbf{r}) \cdot \mathbf{n}(\mathbf{r}) = 0 \quad (20.8)$$

where m is the electron mass, c is the speed of light and $V_{\text{KS}}(\mathbf{r})$ is the Kohn-Sham potential. Anderson et al. [65] have shown that the definition of the topological atom in the ZORA framework is unchanged. Consequently, QTAIM can be used without any modifications in its current form: this theory is enough robust to resist to modifications of the kinetic energy operator. Beyond the spin-free calculations, the need to include spin-dependent relativistic effects in quantum calculations has been demonstrated for heavy-elements. However, most studies where spin-dependent effects are included report only a crude analysis of their impact on the bonding. Some authors have studied the spin-dependent relativistic effects on the electron density, through 4c, 2c and scalar-relativistic all-electron calculations, but few is said regarding QTAIM analyzes [67–69]. Recently, some of us have extended the QTAIM tools in the framework of quasirelativistic calculations, where both the scalar and SOC effects are taken into account through PPs [25]. In this context, the QTAIM theory can be used without any modifications (notably boundary conditions). The non-relativistic formalism operating with Kohn-Sham (KS) orbitals represented by real numbers is extended to a 2c formalism where the wave function is constructed from complex single-particle functions known as spinors, $\varphi_i(\mathbf{r})$. These later are expanded using atom-centered gaussian basis

functions, $\chi_\mu(\mathbf{r})$, and the expansion coefficients c_i are complex and determined within the SCF procedure (Eq. 20.9). The electron density is then defined as:

$$\begin{aligned} \rho(\mathbf{r}) &= \sum_i^{\text{occ}} \varphi_i^\dagger(\mathbf{r}) \varphi_i(\mathbf{r}) = \sum_i^{\text{occ}} \left(\varphi_{i\alpha}^*(\mathbf{r}) \varphi_{i\alpha}(\mathbf{r}) + \varphi_{i\beta}^*(\mathbf{r}) \varphi_{i\beta}(\mathbf{r}) \right) \\ &= \sum_\mu \sum_\nu P_{\mu\nu} \chi_\mu(\mathbf{r}) \chi_\nu(\mathbf{r}) \end{aligned} \quad (20.9)$$

where $P_{\mu\nu}$ is the total density matrix element obtained from the expansion coefficients, c_i^α and c_i^β , which are here complex for each component α and β :

$$P_{\mu\nu} = \sum_i^{\text{occ}} n_i \left(c_{i\mu}^\alpha (c_{i\nu}^\alpha)^* + c_{i\mu}^\beta (c_{i\nu}^\beta)^* \right) \quad (20.10)$$

In the 2c formalism, functions of the density such as $\nabla^2\rho(\mathbf{r})$, can be easily evaluated from the primitive functions χ_μ and the density matrix elements $P_{\mu\nu}$ [25].

QTAIM charges and classification of interactions at the BCP. The QTAIM theory predicts that several local indicators calculated at the BCP are closely related to the nature of the interactions between atoms [18, 19, 53, 70]. This prediction relies notably on the local definition of the virial theorem:

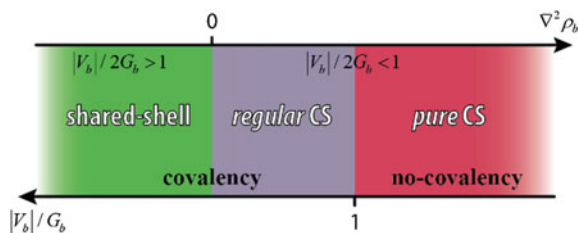
$$\frac{1}{4} \nabla^2 \rho(\mathbf{r}) = 2G(\mathbf{r}) + V(\mathbf{r}) \quad (20.11)$$

where $V(\mathbf{r})$ is the potential energy density (negative) and $G(\mathbf{r})$ is the positive definite kinetic energy density (also referred as $T_s(\mathbf{r})$ in the literature). $G(\mathbf{r})$ is expressed as follows in the 2c formalism:

$$\begin{aligned} G(\mathbf{r}) &= \frac{1}{2} \sum_\mu \sum_\nu P_{\mu\nu} \left(\frac{\partial \chi_\mu(\mathbf{r})}{\partial x} \frac{\partial \nu(\mathbf{r})}{\partial x} + \frac{\partial \chi_\mu(\mathbf{r})}{\partial y} \frac{\partial \nu(\mathbf{r})}{\partial y} \right. \\ &\quad \left. + \frac{\partial \chi_\mu(\mathbf{r})}{\partial z} \frac{\partial \nu(\mathbf{r})}{\partial z} \right) \end{aligned} \quad (20.12)$$

$V(\mathbf{r})$ is then readily obtained by differentiation using Eq. (20.11). The electron density at the BCP, ρ_b , is in general larger than 0.20 e bohr^{-3} in *shared-shell* interactions, in other words, covalent bonds, and smaller than 0.10 e bohr^{-3} in *closed-shell* interactions (e.g. ionic, van der Waals, hydrogen bonding). It is also acknowledged that if the Laplacian of the density at the BCP, $\nabla^2\rho_b$, is negative, the local concentration of charge indicates a shared-shell interaction. In contrast, if $\nabla^2\rho_b$ is positive there is a depletion of charge which characterizes closed-shell interactions. These indicators have been extensively used to classify chemical bonds. Note that one can define the ratio $|V_b|/(2G_b)$, based on the potential energy density (V_b)

Fig. 20.4 Typical QTAIM classification of interactions following calculated indicators at the BCP



and the kinetic energy density (G_b) at the BCP. This ratio is larger than 1 when $\nabla^2\rho_b < 0$, while it is smaller than 1 when $\nabla^2\rho_b > 0$. Another energetic descriptor is often used to differentiate two categories of closed-shell bonding: the $|V_b|/G_b$ ratio that reflects the covalency magnitude of the interaction [71–73]. If the latter ratio is smaller than 1, the kinetic energy density is the leading term and electrons are destabilized close to the BCP, no covalency is expected (for example pure ionic or van der Waals bonding). The interactions are called *pure* closed-shell interactions (*pure CS*). The second category of closed-shell bonding, with some sharing of electrons ($|V_b|/G_b > 1$, i.e. the potential energy density is large and electrons are stabilized at the BCP), is called after Nakanishi et al. *regular* closed-shell (*regular CS*) [74]. Thus, the analysis of the ρ_b , $\nabla^2\rho_b$, V_b and G_b values provide information about the bonding schemes, as summarized in Fig. 20.4.

The integration of the electron density over the atomic basins provides an atomic population. The atomic charge of a topological atom Ω , $q(\Omega)$, is calculated by subtracting the atomic population from the atomic number, $Z(\Omega)$. Note that, due to the use of PPs for heavy atoms, the calculation of their atomic charge involves Z_{eff} , the charge of the inner-core, rather than the atomic number. In contrast to other models of atomic charge [75, 76], the QTAIM charges take into account the anisotropy of the charge distribution in the atomic basins [18, 77]. Thus, QTAIM charges are generally larger with respect to other charge models that implicitly consider a density distributed within spherical atomic basins (obviously not realistic) [78].

20.2.3 Sketch of the ELF Topological Analysis

Since the last 20 years, the ELF topological analysis [4] has been intensively used for studying of the bonding schemes in molecules and solids, or for rationalizing the chemical reactivity [19]. The original ELF formulation of Becke and Edgecombe [5] was built on a HF determinant. The function relies on the Laplacian of the conditional same spin pair probability scaled by the homogeneous electron gas kinetic energy density. ELF is generally interpreted as a signature of the electron-pair distribution. A few years later, this formulation has been generalized to the DFT theory by Kohout and Savin [79], and rationalized in terms of the local

excess kinetic energy due to the Pauli repulsion. Thus, ELF can be defined as follows:

$$\eta(\mathbf{r}) = \left[1 + \left(\frac{T_s(\mathbf{r}) - T_w(\mathbf{r})}{\frac{3}{10}(3\pi^2)^{2/3}\rho(\mathbf{r})^{5/3}} \right)^2 \right]^{-1} \quad (20.13)$$

where $T_s(\mathbf{r})$ is the kinetic energy density and $T_w(\mathbf{r})$ is the von Weizsäcker kinetic energy density. Note that from a rigorous point of view, the expression of ELF (Eq. 20.13) is only valid for closed-shell systems described by a single determinant. Some of us have recently extended the ELF formulation to the 2c relativistic formalism [24]. The present formulation of ELF, based on the total electron density, can readily be calculated from occupied 2c spinors and is safe for practical use on closed-shell species where the spin polarization is small (i.e. the two components differ slightly, which leads to a Kramers-restricted closed-shell configuration resembling to a scalar-relativistic singlet). In addition to the electron density (Eq. 20.9), the different quantities appearing in ELF are evaluated from the $\varphi_i(\mathbf{r})$ spinors and $P_{\mu\nu}$ elements of the total electron density (Eq. 20.10). For instance, the von Weizsäcker kinetic energy density involves first derivatives of the 2c electron density such as:

$$\frac{\partial\rho(\mathbf{r})}{\partial x} = \sum_{\mu} \sum_{\nu} P_{\mu\nu} \left[\frac{\partial\chi_{\mu}(\mathbf{r})}{\partial x} \chi_{\nu}(\mathbf{r}) + \frac{\partial\chi_{\nu}(\mathbf{r})}{\partial x} \chi_{\mu}(\mathbf{r}) \right] \quad (20.14)$$

The ELF topological analysis was proposed several years ago as a bridge between the traditional pictures of the chemical bond derived from the Lewis theory, and first principles quantum-mechanical methodologies [4, 19, 80]. As stated by Gillespie and Robinson [81]: *This function (ELF) exhibits maxima at the most probable positions of localized electron pairs and each maximum is surrounded by a basin in which there is an increased probability of finding an electron pair.* As QTAIM analysis, the ELF topological analysis makes possible a partitioning of the physical space into volumes. This is achieved by applying the theory of dynamical systems. However, ELF attractors (maxima) can be distributed between the atoms. The basins are localized around attractors and are separated by zero-flux surfaces. Generally, the topology of the ELF gradient field [4] shows punctual attractors but, according to the molecular symmetry, it also displays circular (off axis attractors for linear molecules) and spherical attractors (off center attractors for atoms). Thus, in addition to core basins surrounding nuclei with atomic number $Z > 2$, non-atomic valence basins are found. These basins are characterized by the number of core basins with which they share a common boundary (zero-flux surface). This number is called the synaptic order [82, 83]. Each valence basin is presented with a chemical meaning in agreement with the Lewis theory: monosynaptic basin, labeled V(A), in the lone-pair region of A atom; disynaptic basin, labeled V(A, B), of two-center A-B bonds. Overall, the spatial

distribution of the valence basins closely matches the non-bonding and bonding domains of the VSEPR model [61].

Hierarchy of the ELF basins. The f localization domain ($\text{ELF}(\mathbf{r}) = f$) is a volume limited by one or more closed isosurfaces. Initially proposed for visualizing the ELF basins, interestingly it provides a hierarchy of basins in relation with the nature of the chemical bond [84]. The localization domain is called irreducible if it surrounds one attractor or reducible if it contains several attractors. When increasing the $\text{ELF}(\mathbf{r})$ value, a reducible domain splits into several domains, each containing fewer attractors than the parent domain. The first reduction provides useful information on the nature of bonds because the reduction yields two composite domains corresponding to the interacting moieties. For example, the first reduction in a molecule $A-B$ splits usually for covalent bonds into core domains and a single valence domain that contains all the valence attractors. In contrast, for an ionic pair $A^+ B^-$, the first reduction yields domains corresponding to the cation and to the anion fragments.

Integrated properties. As in the QTAIM theory, the ELF basin population is calculated by integrating the electron density over the basin volume. The populations must be understood as arising from Lewis resonant structures and it is possible to calculate some weights of formal Lewis structures [85]. Moreover, a statistical analysis of the basin populations enables one, through the definitions of the variance and the covariance matrix, to obtain information about the electron delocalization between basins [86]. Indeed, the variance of a basin is interpreted as a measure of the electron density fluctuation with all other basins. The covariance matrix elements are measures of the correlation between populations of two given basins. These statistical quantities are useful for characterizing some particular bonding schemes, such as the charge-shift bonding that recently emerged in the literature [87], for which a stabilizing contribution is the resonance energy caused by the covalent-ionic mixing.

The combination of ELF and QTAIM topologies has led Raub and Jansen [88] to introduce a bond polarity index defined for a disynaptic basin $V(A, B)$:

$$p_{AB} = \frac{\overline{N}[V(A, B)|A] - \overline{N}[V(A, B)|B]}{\overline{N}[V(A, B)]} \quad (20.15)$$

where $\overline{N}[V(A, B)|A]$ and $\overline{N}[V(A, B)|B]$ give the contributions of A and B QTAIM basins, respectively, to the $\overline{N}[V(A, B)]$ total population. By definition, a strong polarity of the bond (i.e. mainly ionic bond) yields an index close to 1. This index measures the polarity of the ELF basin. Note that this index can also be calculated for a monosynaptic $V(A)$ basin considering any contribution of a B atomic basin towards the $V(A)$ basin population [19].

20.2.4 Computer Implementation in a 2c Context

The QTAIM and ELF topological analyzes, extended for the treatment of 2c wave functions from the NWChem software, have been implemented in a modified version of the TopMod program package [24, 89]. The program, written in Fortran 90, containing three separated modules *grid_so*, *bas_so* and *pop_so*. Figure 20.5 displays the program structure.

The *grid_so* program generate a 3D-grid containing the values of the function ($\rho(\mathbf{r})$, $\eta(\mathbf{r})$ or $\nabla^2\rho(\mathbf{r})$) for each point \mathbf{r} of a rectangular parallelepipedic grid of dimension $N_x*N_y*N_z$. The *bas_so* module looks for attractors of the function into the grid and assigns each grid point to basins, in the spirit of the original TopMod algorithm where the grid points are assigned following a steepest ascent process (using analytical gradient vectors) [89]. The last program, *pop_so*, provides integrated populations, charges, local dipole moments and the molecular dipole. In this implementation, the basin populations are calculated from partial overlaps over the basins searches for which are themselves the sum of the overlaps over the cells centered on the grid points belonging to the given basin. Using a step of 0.07 bohr between each point of the grid, this method converges to stable values and ensures a numerical complexity scaling as $N \ln(N)$, N being the total number of grid points. The package (Fortran sources, Makefiles for 32 and 64 bit computer architectures running Linux operating system and an user's manual) is available as freeware upon request.

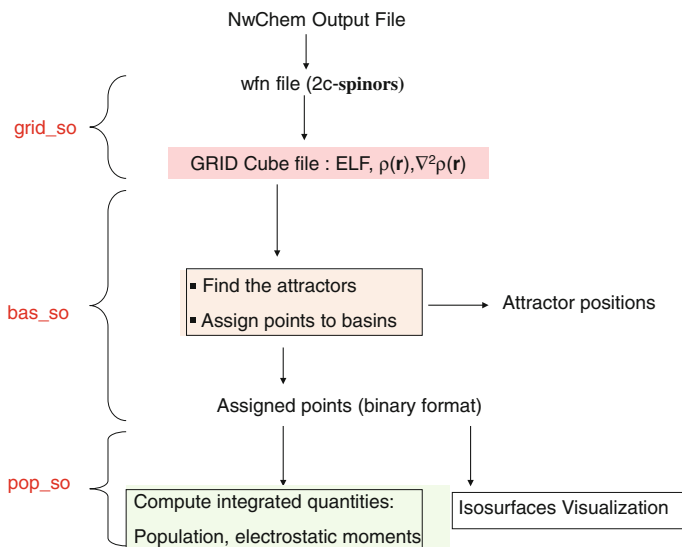


Fig. 20.5 Flow diagram of the organization of TopMod-2c modules

20.2.5 Computational Details

Geometry optimizations and frequency calculations have been performed using the quasirelativistic SODFT method, implemented in the NWChem program package [44], prior to the topological analyzes. Energy-consistent relativistic PPs generated by the Stuttgart/Cologne group for At and U atoms, namely ECP60MDF [90, 91], were used for replacing the 60 core electrons. The explicit treatment of the remaining electrons involved the aug-cc-pVXZ-PP-2c ($X = T, Q$) basis sets, described in Ref. [92], for At and the quadruple zeta ANO basis set, described in Ref. [91], for U. For the lighter atoms, H and O, we opted for the aug-cc-pVXZ basis sets [93, 94]. The ANO and aug-cc-pVQZ basis sets were left fully uncontracted in computations on UO_2^{2+} species to ensure proper description of the semi-core atomic spinors. The applied density-functional approximations were the popular PBE0 and B3LYP hybrid functionals, and the widely used M06-2X meta-hybrid functional. For the sake of simplicity, the results of B3LYP calculations are first discussed and, if necessary, the deviations with respect to the two other functionals are highlighted. In order to evaluate SOC effects on the studied species, geometry optimizations (and frequency calculations) have been also done at scalar-relativistic level through DFT calculations, in the absence of spin-dependent potentials (\hat{V}_{SO}) into PPs. Afterward, new QTAIM and ELF topological analyzes have been carried out. The SOC effects, ΔSO , are defined as the difference between quasirelativistic and scalar-relativistic computed values. Note that for all computations on linear species, the latters are aligned with the z -axis. All the topological analyses here presented have been carried out using modified versions of the NWChem [44] and TopMod [89] program packages. Isovalue curves and surfaces have been drawn using Molekel [95].

20.3 Probing the Nature of At-X Bonds ($X = \text{At}, \text{O}$)

20.3.1 At_2 Species

The At_2 species and other species containing At atom have brought the attention mainly for testing the reliability of relativistic quantum mechanical methods [9, 28, 29, 92, 96, 97]. It came out notably that SOC strongly affects the properties of the closed-shell At_2 species. Spectroscopic constants calculated at CCSD(T) level using either the 4c Dirac-Coulomb Hamiltonian or an X2C Hamiltonian [9, 98], are presented in Table 20.1.

The performances of our 2c-B3LYP/aug-cc-pVTZ-PP-2c computations seem rather good: the calculated bond length (R_e), harmonic frequency (ω_e) and dissociation energy (D_e) deviate from the ones calculated at 4c-CCSD(T) level by less than 1.5 % on average. A lesser agreement appears with 2c-CCSD(T) results and mainly regarding the D_e value, but the latter corresponds to an extrapolation to the

Table 20.1 Spectroscopic constants of the At₂ (X¹Σ_g⁺) species computed at various levels of theory

	R_e (Å)	ω_e (cm ⁻¹)	D_e (eV)
2c-B3LYP/aug-cc-pVTZ-PP-2c	3.048	109	0.65
ΔSO	0.167	-44	-1.06
2c-CCSD(T)/acv3z [98]	3.006	110	0.79 ^a
4c-CCSD(T)/pVTZ [9]	3.046	108	0.63

^aExtrapolation to the complete basis set limit

complete basis set limit. In addition, the B3LYP results reported in Table 20.1 clearly show that SOC effects (ΔSO defined as the difference between quasirelativistic and scalar-relativistic values) strongly weaken the bond. For instance, the dissociation energy is reduced by more than 60 % and the reduction due to SOC on the stretching frequency exceeds 40 % of the final value. These findings are in full agreement with previous results [27–29, 97]. Using the language of molecular orbitals/spinors, the weakening of the bond can be rationalized as follows: [9, 28, 29] scalar-relativistic effects strongly stabilize the 6s valence shell of At atom which forms an inert pair (often termed the “inert pair” effect). The 6p valence electrons give rise to a $\sigma_g^2 \pi_u^4 \pi_g^4$ configuration for At₂ and only the occupied σ_g orbital has a net bonding contribution. When SOC is taken into account, the two pairs of π orbitals are split into their $j_z = \pm 1/2$ and $j_z = \pm 3/2$ components. The resultant configuration can formally be written as $\sigma_{1/2g}^2 \pi_{1/2u}^2 \pi_{1/2g}^2 \pi_{3/2u}^2 \pi_{3/2g}^2$. SOC allows the orbitals with the same j_z quantum number and parity to mix. Two major mechanisms may come into play. On one hand, the $j_z = \pm 1/2$ components of the antibonding π_g orbital can mix with the σ_g one, which clearly shows that SOC weakens the bond. On the other hand, the $j_z = \pm 1/2$ components of π_u can mix with the (unoccupied) antibonding σ_u orbital. The latter mixing again reduces the bond strength.

Further insights into the chemical bond and the role of SOC can be gained by means of topological tools. As expected for most of homonuclear diatomics, the ELF topology of the At₂ species, displayed on Fig. 20.6, is split into two equivalent core basins, C(At₁) and C(At₂), two equivalent nonbonding valence basins, V(At₁) and V(At₂), and one disynaptic basin V(At₁, At₂). The ELF population analysis is given in Table 20.2. The latter reveals a depleted population of the V(At₁, At₂) basin, 0.54 e, which deviates significantly from the expected bonding population, 2 electrons, for a purely covalent single bond. In contrast, the V(At₁) and V(At₂) populations, 6.96 e, are notably higher to what is strictly expected for three halogen lone pairs (6 electrons). A large and negative covariance value of -0.30 between the populations of monosynaptic basins V(At) has been found at B3LYP level. As shown in Table 20.3, the QTAIM analysis strengthens the ELF results: the electron density computed at the BCP (ρ_b) is notably weak, 0.046 e bohr⁻³, and the Laplacian of the density ($\nabla^2 \rho_b$) exhibits a (small) positive value. This features are commonly associated with closed-shell interactions. As previously discussed [25], the bond in At₂ definitively does not fit the shared-shell category (dominant covalent bonding) but it also cannot be classified as ionic (for homonuclear bonds,

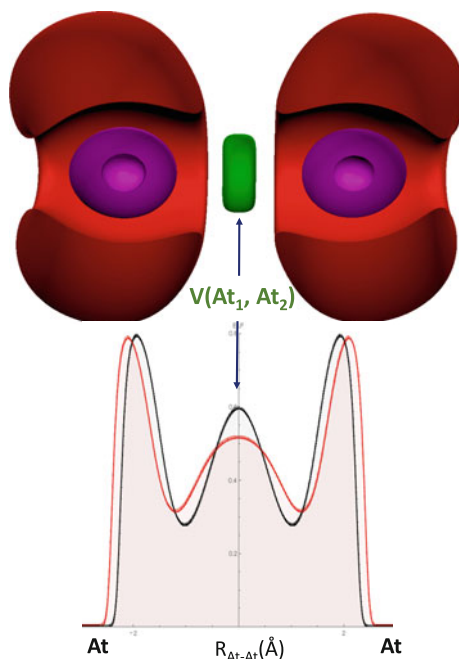


Fig. 20.6 *Top* Split of the ELF localization domains (ELF = 0.7) of the At_2 species calculated at the 2c-B3LYP/aug-cc-pVTZ-PP-2c level of theory. Color code *magenta* for core $\text{C}(\text{At})$ basins, *red* for nonbonding $\text{V}(\text{At})$ basins and *green* for the bonding $\text{V}(\text{At}_1, \text{At}_2)$ basin. *Bottom* ELF profile along the z axis, the *black line* corresponds to B3LYP/aug-cc-pVTZ-PP-2c calculations while the *red* one to 2c-B3LYP/aug-cc-pVTZ-PP-2c calculations

Table 20.2 The ELF population analysis (electrons) of the At_2 species calculated at various levels of theory

ELF basin	$\text{C}(\text{At})$	$\text{V}(\text{At})$	$\text{V}(\text{At}_1, \text{At}_2)$
2c-B3LYP/aug-cc-pVTZ-PP-2c	17.77	6.96	0.54
ΔSO	+0.02	+0.16 (+0.76) ^a	-0.36
2c-B3LYP/aug-cc-pVQZ-PP-2c	17.77	6.92	0.62
ΔSO	+0.01	+0.16 (+0.42) ^a	-0.34
2c-M06-2X/aug-cc-pVTZ-PP-2c	17.91	6.77	0.64
ΔSO	+0.02	+0.13 (+0.74) ^a	-0.30
2c-PBE0/aug-cc-pVTZ-PP-2c	17.93	6.72	0.68
ΔSO	+0.03	+0.12 (+0.76) ^a	-0.31

^a ΔSO π populations of $\text{V}(\text{At})$ is reported between parenthesis, π populations are evaluated by taking into account only the expansion coefficients of the p_x and p_y Gaussian basis functions during the integration of the electron density over the basin volumes

Table 20.3 QTAIM descriptors of the At₂ species calculated at various levels of theory

	$\rho_b(\text{e bohr}^{-3})$	$\nabla^2\rho_b(\text{e bohr}^{-5})$	$ V_b /G_b$	$ V_b /2G_b$
2c-B3LYP/aug-cc-pVTZ-PP-2c	0.046	0.030	1.54	0.77
ΔSO	-0.015	+0.008	-0.21	-0.11
2c-B3LYP/aug-cc-pVQZ-PP-2c	0.047	0.027	1.60	0.80
ΔSO	-0.015	+0.006	-0.16	-0.09
2c-M06-2X/aug-cc-pVTZ-PP-2c	0.054	0.028	1.66	0.83
ΔSO	-0.013	+0.008	-0.15	-0.08
2c-PBE0/aug-cc-pVTZ-PP-2c	0.065	0.017	1.82	0.91
ΔSO	-0.013	+0.010	-0.18	-0.09

electrostatic interactions between static charge distributions should be unimportant) or ruled by van der Waals interactions ($|V_b|/G_b > 1$ at 2c-B3LYP/aug-cc-pVTZ-PP-2c level of theory). Hence, this bond does not satisfy the standard QTAIM classification.

Nevertheless, two specific signatures have emerged: a depleted electron density at the BCP and a small negative or positive $\nabla^2\rho_b$ value which are characteristics of charge-shift bonding (CSB) [99]. CSB stands for a family of bonds that exists along with the classical electron-pair bond families, namely the covalent and the ionic ones, and which originated from valence bond theory [100]. CSB is related to significant fluctuations of the electron-pair resulting from ionic-covalent mixing, hence a notable quantity of electronic density fluctuates back and forth from one atom to the other. Most of the bonds belonging to CSB family are homopolar bonds of compact electronegative and/or lone pair-rich elements, and heteropolar bonds of these elements [101]. Typical signature of CSB exist also regarding the ELF topological analysis: the disynaptic attractor has a depleted population, usually less than 1 e, and in some systems there is not such a disynaptic basin, which is often replaced by a protovalent pair of monosynaptic basins [102]. Furthermore, the large value of the covariance of -0.30 between the populations of both $V(\text{At})$ basins indicates dynamical delocalization of the density between At lone pairs and is characteristic of CSB [87].

At this stage, the fundamental question of the bond weakening by SOC deserves a special attention. The quantum topology tools are able to provide a fine evaluation of spin-dependent effects on the bond. Indeed, Fig. 20.6 (bottom) shows that the ELF value at the bonding punctual attractor appears strongly weakened by SOC. This result is further reinforced by the ELF population analysis in Table 20.2. When comparing scalar-relativistic and quasirelativistic B3LYP/aug-cc-pVTZ-PP-2c calculations, the $V(\text{At}_1, \text{At}_2)$ basin population decreases strongly with SOC, from 0.90 to 0.54 e, in favor of $V(\text{At})$ nonbonding basins [24]. One can notice the spectacular increase of 0.76 e for the π population of each $V(\text{At})$ nonbonding basin. Hence, the redistribution of the electron density due to SOC shall be regarded as an electron withdrawal from the covalent σ bond to the valence π system that is essentially located in the lone pair regions. This behavior is clearly in line with the *lone pair bond weakening effect* (LPBWE) postulated by Sanderson [103], i.e. the

repulsion between the bonding electrons and the lone pairs, adjacent to the bond, that have the same symmetry (σ in dihalogen molecules). It has been rationalized that CSB originates primarily from LPBWE [99, 100]. Therefore, SOC leads to a rise of CSB in the At_2 bond. The QTAIM analysis at the BCP provided in Table 20.3 confirms these findings. When comparing scalar-relativistic and quasirelativistic B3LYP/aug-cc-pVTZ-PP-2c calculations, ρ_b is lowered by SOC ($-0.015 \text{ e bohr}^{-3}$), $\nabla^2\rho_b$ is slightly increased ($+0.008 \text{ e bohr}^{-5}$) and the $|V_b|/G_b$ ratio decreases (-0.21). Each of these observations supports a weakening of the magnitude of covalency in the At_2 bond. Another striking example is the experimentally identified AtCH_3 compound where spin-orbit coupling effects are able to increase the CSB character of the At-C bond [25].

The robustness of QCT analyzes of the 2c-B3LYP/aug-cc-pVTZ-PP-2c wave function has also been checked. Basis set incompleteness effects have been evaluated by replacing the aug-cc-pVTZ-PP-2c basis set by the much more flexible aug-cc-pVQZ-PP-2c one. The effects related to the description of the electron correlation have also been tested by changing the DFT functional for the M06-2X and PBE0 ones. At first, we notice that the equilibrium distance, R_e , is not much modified (at most 3 % with M06-2X functional). Regarding the calculated values reported in Tables 20.2 and 20.3, it is obvious that the populations of ELF basins and QTAIM indicators are quite similar and the SOC effects on these properties (i.e. ΔSO values) appear especially stable regardless of the computational model (functional, basis set) used. No exception has been noticed. But more importantly are the trends drawn from the numbers. Whatever is the retained level of theory, previously outlined trends regarding the bond in At_2 are not changed at all by the results of the further ELF and QTAIM analyzes. Thus, all our results lead to non-ambiguous conclusions: the QCT methodology appears quite suitable to underline SOC effects on the At_2 electronic structure.

20.3.2 *AtO(OH) Species*

At is a rare radioelement, i.e. it has no stable isotopes, and the longest-lived isotopes can only be produced in trace quantities ($<10^{-8} \text{ g}$). Therefore, no spectroscopic tools can be used and structural information lack in the literature for characterizing the nature of At-bonds. Thus, quantum chemical methods represent a valuable tool to shed light, at the molecular scale, on the chemistry of this “invisible” element. The case of the closed-shell AtO(OH) species highlights this situation. This species was recently identified as the product of the hydrolysis reaction of the AtO^+ cation. The measured equilibrium constant, $10^{-1.9}$ [30], is particularly impressive (indicating a strong interaction between AtO^+ and the involved water molecule). As previously discussed [30], the hydrolysis constants published for other mono-charged cations appear, in comparison, very weak. For instance, the values range from $10^{-13.21}$ for the spherical Tl^+ cation to $10^{-4.65}$ for the much bigger MeHg^+ molecular cation. Does the bonding scheme in AtO(OH) can disclose strong

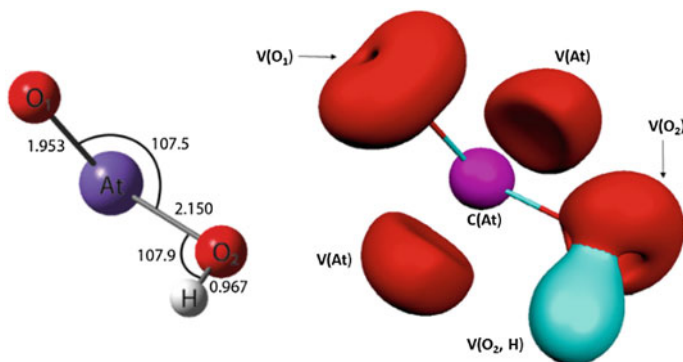


Fig. 20.7 Optimized structure (*left*, distances in angstroms and angle in degrees) and ELF localization domains (*right*, ELF = 0.8) of the AtO(OH) species at the 2c-B3LYP/aug-cc-pVTZ-PP-2c level of theory. Color code *magenta* for core C(At) basin, *red* for valence V(At) and V(O) basins and *cyan* for the protonated bonding V(O, H) basin

interactions which can explain the peculiarity of the AtO^+ hydrolysis constant. The structure of the AtO(OH) species, optimized at the 2c-B3LYP/aug-cc-pVTZ-PP-2c level of theory, is presented in Fig. 20.7.

The At-O₁ distance, 1.953 Å, is close to the predicted bond length in the bare AtO⁺ cation, 1.930 Å [104], while the At-O₂ distance, 2.150 Å, is notably longer and closer to the AtO bond length calculated for the AtOH species, 2.156 Å [25]. The At atom seems divalent and the $\alpha(\text{O}_1\text{AtO}_2)$ valence angle, about 107.5°, argue for a AX₂E₂ type in VSEPR theory. Figure 20.7 also displays the ELF localization domains. In addition to core basins, the ELF topology yields seven valence basins, two V(At) basins accounting for At lone pairs, four V(O) valence basins and one protonated basin, V(O, H). As in the case of the AtOH species [25], no V(At, O) bonding basins were found. This outcome is usual for mainly ionic bonds. The integrated ELF and QTAIM properties are presented in Table 20.4.

$q(\text{At})$ and $q(\text{O})$ atomic charges deserve a special attention: they are large (about one unity or larger) and of opposite signs, as it could be expected for mainly ionic bonds. The QTAIM descriptors at At-O BCPs, reported in Table 20.5, shows large positive $\nabla^2\rho_b$ values consistent with closed-shell interactions between At and O atoms.

Table 20.4 ELF population analysis and QTAIM charges (e) calculated at various levels of theory for the AtO(OH) species

	C(At) + V(At)	V(O ₁)	V(O ₂)	V(O ₂ , H)	q(At)	q(O ₁)	q(O ₂)
2c-B3LYP/aug-cc-pVTZ-PP-2c	23.18	7.07	5.66	1.80	1.46	-0.91	-1.15
ΔSO	+0.08	-0.08	-0.08	+0.06	+0.01	0.00	-0.01
2c-B3LYP/aug-cc-pVQZ-PP-2c	23.07	7.17	5.65	1.82	1.49	-0.95	-1.13
2c-M06-2X/aug-cc-pVTZ-PP-2c	22.91	7.22	5.77	1.80	1.61	-1.01	-1.22
2c-PBE0/aug-cc-pVTZ-PP-2c	23.09	7.16	5.63	1.83	1.53	-0.97	-1.17

Table 20.5 QTAIM descriptors calculated at various levels of theory at the At-O1 and At-O2 BCPs of the AtO(OH) species

At-O ₁	$\rho_b(\text{e bohr}^{-3})$	$\nabla^2\rho_b(\text{e bohr}^{-5})$	$ V_b /G_b$	$ V_b /2G_b$
2c-B3LYP/aug-cc-pVTZ-PP-2c	0.157	0.336	1.50	0.75
Δ SO	-0.007	0.001	-0.02	-0.01
2c-B3LYP/aug-cc-pVQZ-PP-2c	0.164	0.341	1.51	0.75
2c-M06-2X/aug-cc-pVTZ-PP-2c	0.167	0.315	1.55	0.77
2c-PBE0/aug-cc-pVTZ-PP-2c	0.166	0.354	1.52	0.76
At-O ₂	$\rho_b(\text{e bohr}^{-3})$	$\nabla^2\rho_b(\text{e bohr}^{-5})$	$ V_b /G_b$	$ V_b /2G_b$
2c-B3LYP/aug-cc-pVTZ-PP-2c	0.105	0.227	1.40	0.70
Δ SO	-0.011	-0.015	-0.04	-0.02
2c-B3LYP/aug-cc-pVQZ-PP-2c	0.110	0.215	1.44	0.72
2c-M06-2X/aug-cc-pVTZ-PP-2c	0.119	0.253	1.45	0.73
2c-PBE0/aug-cc-pVTZ-PP-2c	0.114	0.247	1.43	0.71

Nevertheless, the associated $|V_b|/G_b$ ratios are larger than 1 and disclose some covalency. Following the QTAIM approach, the bonding in At-O falls in the *regular* CS category (not purely ionic bond), as it was previously found for the AtOH species.

The statements drawn from ELF and QTAIM analyzes are unaffected by the computational model (method, basis sets) used to generate the 2c wave function. Indeed, it appears unnecessary to specify, from Tables 20.4 and 20.5, which set of results is used for supporting the above discussion. The influence of SOC on the bonding scheme in AtO(OH) has also been evaluated. When comparing scalar-relativistic and quasirelativistic B3LYP/aug-cc-pVTZ-PP-2c calculations, ELF populations, QTAIM charges and QTAIM descriptors at BCPs appear almost unchanged. This feature was already observed for the AtOH species. We conclude that the hydrolysis reaction of AtO⁺ cation leads to the formation of an iono-covalent bond with the O atom of one water molecule, resulting in a high equilibrium constant.

20.4 Probing the Nature of the U-O Bond in the Uranyl Species

Many theoretical studies have examined the properties of the uranyl cation, UO₂²⁺ [36, 105, 106]. Regarding its bonding properties, a nominal bond order of three emerges from the analysis of the highest filled MOs, $\pi_g^4\pi_u^4\sigma_g^2\sigma_u^2$ [35], of the ground state electronic configuration [33, 107]. The short length of U-O bonds was attributed notably to the participation of uranium 5f orbitals [108]. More recently, the covalent character of these bonds have been probed by means of QTAIM analyzes [109, 110]. But to date, the theoretical investigations on the chemical bond

Table 20.6 Equilibrium distance and harmonic frequencies of UO_2^{2+} ($X^1\Sigma_g^+$) species computed at various levels of theory

	$R_{\text{U-O}}$ (Å)	ω_{bending} (cm^{-1})	$\omega_{\text{s.stretching}}$ (cm^{-1})	$\omega_{\text{a.stretching}}$ (cm^{-1})
2c-B3LYP/ANO	1.701	163	1043	1131
ΔSO	0.000	-2	+8	+5
4c-CCSD(T) [36]	1.703	-	1016	-
4c-CCSD(T) [108]	1.715	-	974	-

in UO_2^{2+} have been limited to the scalar-relativistic framework, i.e. in the absence of spin-dependent effects. Hence, applying to the bare uranyl cation our QCT methodology, which takes into account SOC, stands for the earliest effort to tackle this issue. The calculated bond length and harmonic frequencies at the 2c-B3LYP/ANO level of theory are shown in Table 20.6.

It is a general experience that the B3LYP functional accurately describes UO_2^{2+} ground state properties [105, 109, 111]. Indeed, the equilibrium distance and symmetric stretching vibration are predicted in fairly good agreement with reference values [36, 108]. The differences between our 2c-B3LYP results and the 4c-CCSD(T) ones of Réal et al. [36] are even lower than the differences between the 4c-CCSD(T) results of Réal et al. and the older 4c-CCSD(T) results of de Jong et al. [108] SOC effects are known to be of little importance regarding the spectroscopic constants of UO_2^{2+} ground state [37, 105]. Calculated ΔSO values, displayed in Table 20.6, show that the bond length is unchanged and the harmonic frequencies are modified by less than 1 %. The rather limited influence of SOC has to be checked regarding the uranyl electronic structure and the topological analysis appears well suited for that.

Figure 20.8a displays the ELF localization domains of the UO_2^{2+} species at the 2c-B3LYP/ANO level of theory. The ELF topology yields six basins: three core basins, $C(\text{U})$, $C(\text{O}_1)$ and $C(\text{O}_2)$, two valence basins associated to oxygen atoms, $V(\text{O}_1)$ and $V(\text{O}_2)$, and a free valence basin for uranium, $V(\text{U})$. The hierarchy of ELF domains can be used to get deeper insights into the nature of U-O interactions. The reduction diagram displays a unique pattern, as shown in Fig. 20.9. It reveals that U-O interactions cannot be understood as a pure ionic pairing picture [$\text{O}^{2-} \text{U}^{6+} \text{O}^{2-}$] because the separation of $V(\text{O})$ domains from the $C(\text{U})$ one occurs once $V(\text{U})$ is separated. Indeed, if a ionic pair $\text{O}^{2-} \text{U}^{6+}$ exists, the reducible domain encompassing $C(\text{U})$ and $V(\text{U})$ must first split into an uranium reducible domain and an oxygen reducible valence domains. The current pattern is rather consistent with bonds having a noticeable covalent character, although the oxygen basins do not split into free valence $V(\text{O})$ basins and bonding $V(\text{U}, \text{O})$ basins as is usually expected for covalent bonds. This finding can be explained by a strong polarization of U-O bonds where the oxygen atoms provide leading contributions to the bonds. This scheme is supported by the ELF population analysis provided in Table 20.7. The populations obtained from 2c-B3LYP/ANO computations are close to 27 electrons for $C(\text{U}) + V(\text{U})$ and larger than 7.30 electrons for each $V(\text{O})$ basins, in

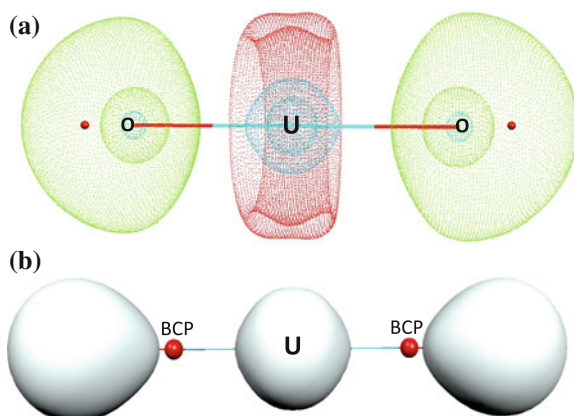


Fig. 20.8 **a** ELF localization domains (ELF = 0.7) of the UO_2^{2+} species calculated at the 2c-B3LYP/ANO level of theory. Color code *cyan* for core $C(\text{U})$ and $C(\text{O})$ basins, *red* for valence $V(\text{U})$ basin and *green* for valence $V(\text{O})$ basins; the $V(\text{O})$ basin's attractor locations are displayed in *red*. **b** VSSCs of Laplacian of the electron density ($\nabla^2\rho_b = 0.05 \text{ e bohr}^{-5}$) calculated at the 2c-B3LYP/ANO level of theory (BCPs locations are displayed in *red*)

Fig. 20.9 Reduction diagram of UO_2^{2+} obtained at the 2c-B3LYP/ANO level of theory

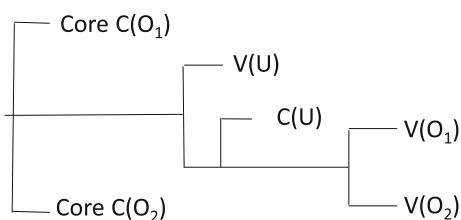


Table 20.7 ELF population analysis (electrons) of the uranyl cation calculated at various levels of theory

ELF basin	$C(\text{U}) + V(\text{U})$	$V(\text{O})$	$p_{\text{VO}}V(\text{O})^a$
2c-B3LYP/ANO	27.10	7.36	0.79
ΔSO	-0.08	0.04	0.00
2c-M06-2X/ANO	26.88	7.41	0.78
ΔSO	-0.04	0.02	0.00
2c-PBE0/ANO	26.95	7.39	0.78
ΔSO	-0.02	0.01	0.00

^aBond polarity index of $V(\text{O})$ basin

agreement with previous results [112]. A noticeable atomic contribution of uranium to the population of $V(\text{O})$ basins is found, about 8 %. The large population of $V(\text{O})$ gathers not only the integrated density corresponding to the oxygen lone pairs but also the bonding population. The bond polarity index p_{UO} for $V(\text{O})$ is 0.79, which is

Table 20.8 QTAIM descriptors of the uranyl cation calculated at various levels of theory

	q(U)	q(O)	$\rho_b(\text{e bohr}^{-3})$	$\nabla^2\rho_b(\text{e bohr}^{-5})$	$ V_b /G_b$	$ V_b /2G_b$
2c-B3LYP/ANO	3.38	-0.69	0.378	0.282	1.86	0.93
Δ SO	0.01	-0.02	-0.001	0.030	-0.01	0.00
2c-M06-2X/ANO	3.45	-0.72	0.394	0.379	1.83	0.91
Δ SO	0.00	-0.01	-0.002	0.042	-0.01	-0.01
2c-PBE0/ANO	3.40	-0.70	0.394	0.245	1.88	0.94
Δ SO	-0.01	-0.01	-0.002	0.033	-0.01	-0.01

consistent with highly polar donor-acceptor U-O bond. This finding mirrors the bonding scheme previously identified in Xe-O bonds for XeO₃ and XeO₄ complexes [19]. The QTAIM analyzes strengthen the conclusions drawn from the ELF results.

The QTAIM descriptors calculated from the 2c-B3LYP/ANO electron density are presented in Table 20.8. A large positive charge, beyond 3.3 e, is found for uranium atom while typical features of covalent bonds are also evidenced. In general, the density at the BCP is greater than 0.20 e bohr⁻³ in shared (covalent) bonding [70]. Here, ρ_b was found equal to 0.35 e bohr⁻³ for the U-O bonds. The covalency magnitude of these bonds is also confirmed by the $|V_b|/G_b$ ratio which exceeds the 1.8 value (i.e. electrons are stabilized at BCPs). In addition, large non-spherical VSCCs have been localized in the oxygen regions, as shown in Fig. 20.8b. Note that for multiple bonds, $\nabla^2\rho_b$ is generally calculated positive at the BCP. The value of $\nabla^2\rho_b$, about 0.28 e bohr⁻⁵, is consistent with results of previous QTAIM studies on uranyl species [109, 110]. Thus, the U-O bonds belong to the electron shared picture which can be rationalized as highly polarized multiple bonds.

We have noticed, when comparing scalar-relativistic and quasirelativistic B3LYP/ANO calculations, that ELF and QTAIM descriptors are similar. The most affected one by SOC is the Laplacian of the density: $\nabla^2\rho_b$ is increased by 10 % (see Δ SO values in Table 20.8), showing a more depleted electron density at the BCP. Nevertheless, the bond polarity is unaffected by SOC since only trifling modifications on atomic charges occur and p_{UO} for V(O) is unchanged (see Table 20.8). In the uranyl cation, the QCT tools reveal a weak influence of the spin-dependent effects on the bonding scheme. The multiple character of U-O bonds is also supported by scalar-relativistic computations. Introduced by *Fradera* et al. in the context of QTAIM analyzes [113], the delocalization index (DI) is a measure of the electron-sharing between two atoms and can be compared to other bond order indices. The DI calculated for U-O bonds at B3LYP/ANO level of theory, 2.25, is in reasonable agreement with previous results [109] and the triple bond yield by MOs analyzes [33, 107]. In the ELF framework, covalent bonds are often characterized by disynaptic basins with a population related to the formal bond order (the basin population decreases while the ionic or CSB contributions to the bond character increase). In the case of U-O bonds, no disynaptic V(U, O)

Table 20.9 Contributions of the bonding MOs to the ELF population of each V(O) basin calculated at the B3LYP/ANO level of theory

Bonding MOs contributing to V(O)	Total	d^a	f^a
π_g	1.70	0.16	0.04
π_u	1.44	0.00	0.22
σ_g	0.87	0.05	0.06
σ_u	0.42	0.01	0.32
Total bonding population ^b	4.43e		
Bond order ^c	2.21		

^aMain AO components of MO contributions integrated over the whole V(O) basin

^bBased on the six highest bonding MOs

^cHalf the total bonding population

basins were found but some of the bonding population contributes to the V(O) basins. Nevertheless, it is not possible to evaluate the bond order using the total population of V(O) basins since the latter encompass also the oxygen lone pairs. MOs contributions to the V(O) basins may provide indications regarding the bond order by summing the contributions of bonding MOs to the V(O) basin population, as shown in Table 20.9. The resulting value, 2.21, is consistent with a highly polarized triple bond. Note that the individual contributions of the uranium 5f and 6d AOs to V(O) populations are in line with the well-known, important involvement of those AOs in the frontier MOs of UO_2^{2+} [35].

The robustness of ELF and QAIM analyzes with respect to the choice of the DFT functional has again been tested. At first, the calculated bond lengths using M06-2X and PBE0 functionals are slightly shorter (1.679 and 1.685 Å, respectively) and therefore, the symmetric stretching vibration appears at higher frequencies ($>1090 \text{ cm}^{-1}$). Regarding the ELF and QAIM indicators, quite similar values are obtained. $\nabla^2\rho_b$ is the most affected one, it changes from 0.379 e bohr⁻⁵ at 2c-M06-2X/ANO level of theory to 0.245 e bohr⁻⁵ at 2c-PBE0/ANO level of theory (35 % decrease). However, this discrepancy as well as all the others observed from one functional to another will never change any of the conclusions stated above.

20.5 Conclusions and Ongoing Developments

In this chapter, we have shown that the QCT approach is a suitable alternative to a crude analysis of 2c wave functions which is generally hampered by technical as well as conceptual difficulties. The presented methodology is particularly effective for evidencing relativistic effects on bonding schemes. Indeed, for the puzzling At_2 species where it is mandatory to consider SOC effects, a much deeper understanding of the nature of the bond was gained. It has been uncovered the propensity of SOC to boost the CSB character of the bond. If chemists truly expect important spin-dependent effects in species containing At atoms, due to this element position in the periodic table (heavy p -element), we have also shown that SOC effects on

chemical bonds may vanish depending on the nature of the bonds. Here, trifling effects were noticed on the mainly ionic At-O bonds of the AtO(OH) species, while it was previously found in the AtCH₃ species that spin-orbit coupling effects are able to increase the CSB character of the At-C bond [25]. Furthermore, the simplicity of the methodology is highlighted via another emblematic case. It is acknowledged that all relativistic contributions must be included into calculations on systems like the uranyl cation (i.e. containing heavy elements), but currently all investigations on the UO₂²⁺ chemical bonding are at best switched to a scalar-relativistic level. This inconsistency is now over.

Beyond practical considerations regarding the understanding of heavy-elements chemistry, this study has also demonstrated the robustness of QTAIM and ELF topological analyzes in the quasirelativistic framework. Only small modifications on the investigated descriptors, among which ELF basin populations, QTAIM atomic charges, ρ_b and $\nabla^2\rho_b$, were found when changing between B3LYP, PBE0 and M06-2X functionals, or when moving from triple zeta basis sets to quadruple ones. Future works will focus on extending the topological analyzes of other functions of the electron density (Fukui functions, Non Covalent Index), as well as the distributed electrostatic moments based on the ELF partition (DEMESP) analysis [114], to the field of quasirelativistic quantum calculations.

Acknowledgements This work has been supported by grants funded by the French National Agency for Research (ANR-2010-BLAN-0807), with “Investissements d’Avenir” (ANR-11-EQPX-0004, ANR-11-LABX-0018).

References

1. Lewis GN (1916) The atom and the molecule. *J Am Chem Soc* 38(4):762–785
2. Linnett JW (1961) A modification of the Lewis-Langmuir octet rule. *J Am Chem Soc* 83(12):2643–2653
3. Bader RFW (1991) A quantum theory of molecular structure and its applications. *Chem Rev* 91(5):893–928
4. Silvi B, Savin A (1994) Classification of chemical bonds based on topological analysis of electron localization functions. *Nature* 371(6499):683–686
5. Becke AD, Edgecombe KE (1990) A simple measure of electron localization in atomic and molecular systems. *J Chem Phys* 92(9):5397–5403
6. Weinhold F (2002) Natural bond orbital methods. In: *Encyclopedia of computational chemistry*, John Wiley & Sons, Ltd
7. Gillespie RJ, Bayles D, Platts J, Heard GL, Bader RFW (1998) The Lennard-Jones function: a quantitative description of the spatial correlation of electrons as determined by the exclusion principle. *J Phys Chem A* 102(19):3407–3414
8. Roos BO, Borin AC, Gagliardi L (2007) Reaching the maximum multiplicity of the covalent chemical bond. *Angew Chem Int Ed Engl* 46(9):1469–1472
9. Visscher L, Dyall KG (1996) Relativistic and correlation effects on molecular properties. I. The dihalogens F₂, Cl₂, Br₂, I₂, and At₂. *J Chem Phys* 104(22):9040–9046
10. Saue T, Faegri K, Gropen O (1996) Relativistic effects on the bonding of heavy and superheavy hydrogen halides. *Chem Phys Lett* 263(3–4):360–366

11. van Lenthe E, Snijders JG, Baerends EJ (1996) The zero-order regular approximation for relativistic effects: The effect of spin-orbit coupling in closed shell molecules. *J Chem Phys* 105(15):6505–6516
12. Nash CS, Bursten BE (1999) Spin-orbit coupling versus the VSEPR method: on the possibility of a nonplanar structure for the super-heavy noble gas tetrafluoride (118)F₄. *Angew Chem Int Ed Engl* 38(1–2):151–153
13. Han Y-K, Lee YS (1999) Structures of RgFn (Rg = Xe, Rn, and Element 118. n = 2, 4.) calculated by two-component spin-orbit methods. A spin-orbit induced isomer of (118)F₄. *J Phys Chem A* 103(8):1104–1108
14. Dubillard S, Rota JB, Saue T, Faegri K (2006) Bonding analysis using localized relativistic orbitals: water, the ultrarelativistic case and the heavy homologues H₂X (X = Te, Po, eka-Po). *J Chem Phys* 124(15):154307
15. TURBOMOLE, v6.3.1 (2011) A development of University of Karlsruhe and Forschungszentrum Karlsruhe GmbH, TURBOMOLE GmbH: Karlsruhe, Germany
16. Zeng T, Fedorov DG, Schmidt MW, Klobukowski M (2011) Effects of spin-orbit coupling on covalent bonding and the Jahn-Teller effect are revealed with the natural language of spinors. *J Chem Theory Comput* 7(9):2864–2875
17. Maurice R, Réal F, Gomes ASP, Vallet V, Montavon G et al (2015) Effective bond orders from two-step spin-orbit coupling approaches: The I₂, At₂, IO⁺, and AtO⁺ case studies. *J Chem Phys* 142:094305–094309
18. Bader RFW (1994) *Atoms in molecules: a quantum theory*. Oxford University Press, New York
19. Silvi B, Gillespie RJ, Gatti C (2013) 9.07—electron density analysis. In: Poeppelemeier KR (ed) *Comprehensive inorganic chemistry II*, 2nd edn, Elsevier, Amsterdam, pp 187–226
20. Piquemal JP, Pilmé J, Parisel O, Gérard H, Fourré I et al (2008) What can be learnt on biologically relevant systems from the topological analysis of the electron localization function? *Int J Quantum Chem* 108(11):1951–1969
21. Causá M, Savin A, Silvi B (2014) Atoms and bonds in molecules and chemical explanations. *Found Chem* 16(1):3–26
22. Ayers PL, Boyd RJ, Bultinck P, Caffarel M, Carbó-Dorca R et al (2015) Six questions on topology in theoretical chemistry. *Comput Theoret Chem* 1053:2–16
23. Silvi B, Pilmé J, Fuster F, Alikhani ME (2003) What can tell topological approaches on the bonding in transition metal compounds. In: Russo N, Salahub DR, Witko M (eds) *Metal-ligand interactions: molecular, nano-, micro-, and macro-systems in complex environments*, NATO ASI Series, vol 116, pp 241–284
24. Pilmé J, Renault E, Ayed T, Montavon G, Galland N (2012) Introducing the ELF topological analysis in the field of quasirelativistic quantum calculations. *J Chem Theory Comput* 8(9):2985–2990
25. Pilmé J, Renault E, Bassal F, Amaouch M, Montavon G et al (2014) QTAIM analysis in the context of quasirelativistic quantum calculations. *J Chem Theory Comput* 10(11):4830–4841
26. Wilbur DS (2013) Enigmatic astatine. *Nature Chem* 5(3):246–246
27. Champion J, Seydou M, Sabatie-Gogova A, Renault E, Montavon G et al (2011) Assessment of an effective quasirelativistic methodology designed to study astatine chemistry in aqueous solution. *Phys Chem Chem Phys* 13(33):14984–14992
28. Mitin A (2006) V., C. van Wullen Two-component relativistic density-functional calculations of the dimers of the halogens from bromine through element 117 using effective core potential and all-electron methods. *J Chem Phys* 124(6):64305
29. Peng D, Liu W, Xiao Y, Cheng L (2007) Making four- and two-component relativistic density functional methods fully equivalent based on the idea of “from atoms to molecule”. *J Chem Phys* 127(10):104106
30. Champion J, Sabatie-Gogova A, Bassal F, Ayed T, Alliot C et al (2013) Investigation of astatine (III) hydrolyzed species: experiments and relativistic calculations. *J Phys Chem A* 117(9):1983–1990

31. Wilbur DS, Chyan M-K, Nakamae H, Chen Y, Hamlin DK et al (2012) Reagents for astatination of biomolecules. 6. An intact antibody conjugated with a maleimido-closo-decaborate(2-) reagent via sulphydryl groups had considerably higher kidney concentrations than the same antibody conjugated with an isothiocyanato-closo-decaborate(2-) reagent via lysine amines. *Bioconjug Chem* 23(3):409–420
32. Szabó Z, Toraiishi T, Vallet V, Grenthe I (2006) Solution coordination chemistry of actinides: thermodynamics, structure and reaction mechanisms. *Coord Chem Rev* 250(7–8):784–815
33. Denning RG (2007) Electronic structure and bonding in actinyl ions and their analogs. *J Phys Chem A* 111(20):4125–4143
34. Schreckenbach G, Shamov GA (2009) Theoretical actinide molecular science. *Acc Chem Res* 43(1):19–29
35. Kaltsoyannis N (2000) Computational study of analogues of the uranyl ion containing the –NUN– unit: density functional theory calculations on UO_2^{2+} , UON^+ , UN_2 , $\text{UO}(\text{NPH}_3)^{3+}$, $\text{U}(\text{NPH}_3)_2^{4+}$, $[\text{UCl}_4\{\text{NPR}_3\}_2]$ (R = H, Me), and $[\text{UOCl}_4\{\text{NP}(\text{C}_6\text{H}_5)_3\}]$. *Inorg Chem* 39(26):6009–6017
36. Réal F, Gomes ASP, Visscher L, Vallet V, Eliav E (2009) Benchmarking electronic structure calculations on the bare UO_2^{2+} ion: How different are single and multireference electron correlation methods? *J Phys Chem A* 113(45):12504–12511
37. García-Hernández M, Lauterbach C, Krüger S, Matveev A, Rösch N (2002) Comparative study of relativistic density functional methods applied to actinide species AcO_2^{2+} and AcF_6 for Ac = U, Np. *J Comput Chem* 23(8):834–846
38. Saue T (2011) Relativistic hamiltonians for chemistry: a primer. *Chem Phys Chem* 12(17):3077–3094
39. Fleig T (2012) Invited review: relativistic wave-function based electron correlation methods. *Chem Phys* 395:2–15
40. Autschbach J (2012) Perspective: relativistic effects. *J Chem Phys* 136(15):150902
41. Liu W (2010) Ideas of relativistic quantum chemistry. *Mol Phys* 108(13):1679–1706
42. Dolg M, Cao X (2011) Relativistic pseudopotentials: their development and scope of applications. *Chem Rev* 112(1):403–480
43. Ermler WC, Lee YS, Christiansen PA, Pitzer KS (1981) AB initio effective core potentials including relativistic effects. A procedure for the inclusion of spin-orbit coupling in molecular wavefunctions. *Chem Phys Lett* 81(1):70–74
44. Straatsma TP, Aprà E, Windus TL, Bylaska EJ, de Jong W et al (2008) NWChem, a computational chemistry package for parallel computers, version 5.1.1. Pacific Northwest National Laboratory, Richland, Washington
45. Armbruster MK, Klopffer W, Weigend F (2006) Basis-set extensions for two-component spin-orbit treatments of heavy elements. *Phys Chem Chem Phys* 8(42):4862–4865
46. Fonseca Guerra C, Handgraaf J-W, Baerends EJ, Bickelhaupt FM (2004) Voronoi deformation density (VDD) charges: assessment of the Mulliken, Bader, Hirshfeld, Weinhold, and VDD methods for charge analysis. *J Comput Chem* 25(2):189–210
47. Hirshfeld FL (1977) Bonded-atom fragments for describing molecular charge densities. *Theoret Chim Acta* 44(2):129–138
48. Bader RFW, Beddall PM (1973) Virial partitioning of charge distributions and properties of diatomic hydrides. *J Am Chem Soc* 95(2):305–315
49. Bader RFW, Anderson SG, Duke AJ (1979) Quantum topology of molecular charge distributions. 1. *J Am Chem Soc* 101(6):1389–1395
50. Bader RFW, Beddall PM, Cade PE (1971) Partitioning and characterization of molecular charge distributions. *J Am Chem Soc* 93(13):3095–3107
51. Abraham RH, Shaw CD (1992) Dynamics: the geometry of behavior. Addison Wesley, Redwood City
52. Abraham RHM, Marsden JE (1994) Foundations of mechanics. Addison Wesley, Redwood City
53. Bader RFW, Essén H (1984) The characterization of atomic interactions. *J Chem Phys* 80(5):1943–1960

54. Mei C, Edgecombe KE, Smith VH, Heilingbrunner A (1993) Topological analysis of the charge density of solids: bcc sodium and lithium. *Int J Quantum Chem* 48(5):287–293
55. Weyrich W (1996) One-electron density matrices and related observables. In: Pisani C (ed) *Quantum-mechanical Ab-initio calculation of the properties of crystalline materials*, vol 67, Springer, Berlin, pp 245–272
56. Collard K, Hall GG (1977) Orthogonal trajectories of the electron density. *Int J Quantum Chem* 12(4):623–637
57. Bader RFW (1994) Principle of stationary action and the definition of a proper open system. *Phys Rev B* 49(19):13348–13356
58. Bader RFW (2007) *The lagrangian approach to chemistry*, Boyd R, Matta CF (ed). Wiley-VCH, Germany
59. Gillespie RJ, Nyholm RS (1957) Inorganic stereochemistry. *Q Rev Chem Soc* 11(4):339–380
60. Bader RFW, Gillespie RJ, MacDougall PJ (1988) A physical basis for the VSEPR model of molecular geometry. *J Am Chem Soc* 110(22):7329–7336
61. Gillespie RJ (2008) Fifty years of the VSEPR model. *Coord Chem Rev* 252(12–14):1315–1327
62. Bader RFW, MacDougall PJ, Lau CDH (1984) Bonded and nonbonded charge concentrations and their relation to molecular geometry and reactivity. *J Am Chem Soc* 106(6):1594–1605
63. Bader RFW, Heard GL (1999) The mapping of the conditional pair density onto the electron density. *J Chem Phys* 111(19):8789–8798
64. Malcolm NOJ, Popelier PLA (2003) The full topology of the Laplacian of the electron density: scrutinising a physical basis for the VSEPR model. *Faraday Discuss* 124:353–363
65. Anderson JSM, Ayers PW (2011) Quantum theory of atoms in molecules: results for the SR-ZORA Hamiltonian. *J Phys Chem A* 115(45):13001–13006
66. Filatov M, Cremer D (2003) On the physical meaning of the ZORA Hamiltonian. *Mol Phys* 101(14):2295–2302
67. Eicklerling G, Mastalerz R, Herz V, Scherer W, Himmel H-J et al (2007) Relativistic effects on the topology of the electron density. *J Chem Theory Comput* 3(6):2182–2197
68. Matito E, Salvador P, Styszynski J (2013) Benchmark calculations of metal carbonyl cations: relativistic vs. electron correlation effects. *Phys Chem Chem Phys* 15(46):20080–20090
69. Bučinský L, Kucková L, Malček M, Kožíšek J, Biskupič S et al (2014) Picture change error in quasirelativistic electron/spin density, Laplacian and bond critical points. *Chem Phys* 438:37–47
70. Matta CF, Boyd RJ (2007) An introduction to the quantum theory of atoms in molecules: from solid state to DNA and drug design. In: Matta CF, Boyd RJ (eds) *The quantum theory of atoms in molecules*. Wiley-VCH Verlag GmbH & Co. KGaA, Weinheim, pp 1–34
71. Cremer D, Kraka E (1984) Chemical bonds without bonding electron density—Does the difference electron-density analysis suffice for a description of the chemical bond? *Angew Chem Int Ed Engl* 23(8):627–628
72. Bianchi R, Gervasio G, Marabello D (2000) Experimental electron density analysis of $\text{Mn}_2(\text{CO})_{10}$: Metal–Metal and Metal–Ligand bond characterization. *Inorg Chem* 39(11):2360–2366
73. Espinosa E, Alkorta I, Elguero J, Molins E (2002) From weak to strong interactions: A comprehensive analysis of the topological and energetic properties of the electron density distribution involving X–H···F–Y systems. *J Chem Phys* 117(12):5529–5542
74. Nakanishi W, Hayashi S (2013) Role of dG/dw and dV/dw in AIM analysis: an approach to the nature of weak to strong interactions. *J Phys Chem A* 117(8):1795–1803
75. Mulliken RS (1955) Electronic population analysis on LCAO–MO molecular wave functions. I. *J Chem Phys* 23(10):1833–1840
76. Reed AE, Weinstock RB, Weinhold F (1985) Natural population analysis. *J Chem Phys* 83(2):735–746
77. Slee T, Larouche A, Bader RFW (1988) Properties of atoms in molecules: dipole moments and substituent effects in ethyl and carbonyl compounds. *J Phys Chem* 92(22):6219–6227

78. Bader RFW, Matta CF (2004) Atomic charges are measurable quantum expectation values: a rebuttal of criticisms of QTAIM charges. *J Phys Chem A* 108(40):8385–8394
79. Savin A, Jepsen O, Flad J, Andersen OK, Preuss H, von Schnering HG (1992) Electron localization in solid-state structures of the elements: the diamond structure. *Angew Chem Int* 31(2):187–188
80. Savin A, Nesper R, Wengert S, Fässler TF (1997) ELF: the electron localization function. *Angew Chem Int Ed Engl* 36(17):1808–1832
81. Gillespie RJ, Robinson EA (2007) Gilbert N. Lewis and the chemical bond: The electron pair and the octet rule from 1916 to the present day. *J Comput Chem* 28(1):87–97
82. Silvi B (2002) The synaptic order: a key concept to understand multicenter bonding. *J Mol Struct* 614(1–3):3–10
83. Häussermann U, Wengert S, Hofmann P, Savin A, Jepsen O et al (1994) Localization of electrons in intermetallic phases containing aluminum. *Angew Chem Int Ed Engl* 33(20):2069–2073
84. Silvi B, Pilme J, Fuster F, Alikhani ME (2003) What can tell topological approaches on the bonding in transition metal compounds. In: Russo N, Salahub D, Witko M (ed) *Metal-Ligand interactions*, vol 116. Springer, Netherlands, pp 241–284
85. Pilme J, Silvi B, Alikhani ME (2005) Comparative study of the bonding in the first series of transition metal 1:1 complexes M–L (M = Sc, ..., Cu; L = CO, N₂, C₂H₂, CN⁻, NH₃, H₂O, and F⁻). *J Phys Chem A* 109(44):10028–10037
86. Silvi B (2004) How topological partitions of the electron distributions reveal delocalization. *Phys Chem Chem Phys* 6(2):256–260
87. Shaik S, Danovich D, Silvi B, Lauvergnat DL, Hiberty PC (2005) Charge-shift bonding-A class of electron-pair bonds that emerges from valence bond theory and is supported by the electron localization function approach. *Chem A Eur J* 11(21):6358–6371
88. Raub S, Jansen G (2001) A quantitative measure of bond polarity from the electron localization function and the theory of atoms in molecules. *Theoret Chem Acc* 106(3):223–232
89. Noury S, Krokidis X, Fuster F, Silvi B (1999) Computational tools for the electron localization function topological analysis. *Comput Chem* 23(6):597–604
90. Peterson KA, Figgen D, Goll E, Stoll H, Dolg M (2003) Systematically convergent basis sets with relativistic pseudopotentials. II. Small-core pseudopotentials and correlation consistent basis sets for the post-d group 16–18 elements. *J Chem Phys* 119(21):11113–11123
91. Dolg M, Cao X (2009) Accurate relativistic small-core pseudopotentials for actinides. Energy adjustment for uranium and first applications to uranium hydride. *J Phys Chem A* 113(45):12573–12581
92. Bischoff FA, Klopper W (2010) Second-order electron-correlation and self-consistent spin-orbit treatment of heavy molecules at the basis-set limit. *J Chem Phys* 132(9):094108
93. Dunning TH Jr (1989) Gaussian basis sets for use in correlated molecular calculations. I. The atoms boron through neon and hydrogen. *J Chem Phys* 90(2):1007–1023
94. Kendall RA, Dunning TH Jr, Harrison RJ (1992) Electron affinities of the first-row atoms revisited. systematic basis sets and wave functions. *J Chem Phys* 96(9):6796–6806
95. Flukiger P, Luthi HP, Portmann S, Weber J (2002) *Molekel*, version 4.3; Swiss Center for Scientific Computing; Manno, Switzerland
96. Dolg M (1996) Accuracy of energy-adjusted quasirelativistic pseudopotentials: a calibration study of XH and X₂ (X = F, Cl, Br, I, At). *Mol Phys* 88(6):1645–1655
97. Wang Z, Wang F (2013) Spin-orbit coupling and electron correlation at various coupled-cluster levels for closed-shell diatomic molecules. *Phys Chem Chem Phys* 15(41):17922–17928
98. Höfener S, Ahlrichs R, Knecht S, Visscher L (2012) Relativistic and non-relativistic electronic molecular-structure calculations for dimers of 4p-, 5p-, and 6p-block elements. *Chem Phys Chem* 13(17):3952–3957

99. Zhang L, Ying F, Wu W, Hiberty PC, Shaik S (2009) Topology of electron charge density for chemical bonds from valence bond theory: a probe of bonding types. *Chem A Eur J* 15(12):2979–2989
100. Shaik S, Maitre P, Sini G, Hiberty PC (1992) The charge-shift bonding concept. Electron-pair bonds with very large ionic-covalent resonance energies. *J Am Chem Soc* 114(20):7861–7866
101. Shaik S, Danovich D, Wu W, Hiberty PC (2009) Charge-shift bonding and its manifestations in chemistry. *Nature Chem* 1(6):443–449
102. Llusar R, Beltrán A, Andrés J, Noury S, Silvi B (1999) Topological analysis of electron density in depleted homopolar chemical bonds. *J Comput Chem* 20(14):1517–1526
103. Sanderson RT (1983) Polar covalence. Academic Press, New York
104. Gomes ASP, Real F, Galland N, Angeli C, Cimiraglia R et al (2014) Electronic structure investigation of the evanescent AtO^+ ion. *Phys Chem Chem Phys* 16(20):9238–9248
105. Ismail N, Heully J-L, Saue T, Daudey J-P, Marsden CJ (1999) Theoretical studies of the actinides: method calibration for the UO_2^{2+} and PuO_2^{2+} ions. *Chem Phys Lett* 300(3–4):296–302
106. Pierloot K, van Besien E (2005) Electronic structure and spectrum of UO_2^{2+} and $\text{UO}_2\text{Cl}_4^{2-}$. *J Chem Phys* 123(20):204309
107. Clark AE, Sonnenberg JL, Hay PJ, Martin RL (2004) Density and wave function analysis of actinide complexes: What can fuzzy atom, atoms-in-molecules, Mulliken, Löwdin, and natural population analysis tell us? *J Chem Phys* 121(6):2563–2570
108. de Jong WA, Visscher L, Nieuwpoort WC (1998) On the bonding and the electric field gradient of the uranyl ion. *J Mol Struct* 458(1–2):41–52
109. Vallet V, Wahlgren U, Grenthe I (2012) Probing the nature of chemical bonding in uranyl (VI) complexes with quantum chemical methods. *J Phys Chem A* 116(50):12373–12380
110. Zhurov VV, Zhurova EA, Stash AI, Pinkerton AA (2011) Characterization of bonding in cesium uranyl chloride: topological analysis of the experimental charge density. *J Phys Chem A* 115(45):13016–13023
111. Wählin P, Danilo C, Vallet V, Réal F, Flament J-P et al (2008) An investigation of the accuracy of different DFT functionals on the water exchange reaction in hydrated uranyl(VI) in the ground state and the first excited state. *J Chem Theory Comput* 4(4):569–577
112. Alikhani ME, Michelini MC, Russo N, Silvi B (2008) Topological analysis of the reaction of uranium ions (U^+ , U^{2+}) with N_2O in the gas phase. *J Phys Chem A* 112(50):12966–12974
113. Fradera X, Austen MA, Bader RFW (1998) The Lewis model and beyond. *J Phys Chem A* 103(2):304–314
114. Pilmé J, Piquemal J-P (2008) Advancing beyond charge analysis using the electronic localization function: chemically intuitive distribution of electrostatic moments. *J Comput Chem* 29(9):1440–1449

Index

A

Acetylene, 215–217, 408, 409, 422, 424
Acrolein, 343, 344
Allyl cation, 348, 350
[n]Annulenes (C_nH_n), 105
Antiaromaticity, 213, 322, 323
Antiferromagnetic, 121, 363, 372, 374, 376,
378, 380, 381, 390, 392
Anthracene, 370, 373
Aromatic Fluctuation Index (FLU), 71, 73–75,
322
Aromaticity, 7, 17, 48, 70, 71, 73–75,
104–108, 112, 113, 197, 199, 213, 259,
301, 304, 305, 308–312, 321, 322, 323,
326–329, 331, 332, 356, 493
 δ -Aromaticity, 321
 σ -Aromaticity, 197, 199
Astatine, 555

B

Baird's rule, 326, 327, 332
Benzene, 3, 70, 71, 73–75, 106, 107, 110, 123,
191, 200, 217, 297, 298, 322–324, 326,
327, 330, 331, 347, 350–353, 362, 367,
382, 386, 403, 419–421, 423, 424, 495,
498, 500, 503–505, 508
Benzenoid, 71, 73, 106, 297–302, 305–308,
311, 313, 314
Benzoic acid, 63, 68–70
Benzopyrene, 299, 301–303
Beryllium bond, 464, 465, 467, 468, 471, 472,
475, 476, 479, 480, 481, 483
Bifurcations, 170, 171, 193, 200
Binary complexes, 465, 466, 469, 472,
476–480, 482, 483
Biphenyl, 106
1,4-Biphenylenedione, 357, 359

Bisanthrene, 309–313

Bond Critical Point (BCP), 28–30, 33, 37, 54,
66, 400, 404, 422, 424, 425, 430, 463
Bond path, 16, 28, 54–57, 67, 104, 105, 112,
262, 400–402, 404, 406, 409, 410, 412,
414, 415, 417, 422–425, 427–429, 441, 559
Butadiene, 347, 350, 351, 353, 519

C

Carbon bonding, 514
Carbon dioxide (CO_2), 212, 213
Catastrophe theory, 32, 530, 531, 549
Catchment region, 252, 253
Charge Displacement Function (CD), 464, 465,
468, 469, 471–483
Chemical graph, 17, 55, 66, 71, 84
Chemical transferability, 262
Chevron, 313, 314
Conjugated circuit, 302, 305
Connectivity matrix, 54, 66
Continuous chemical topology, 8
Cooperativity, 463, 464, 475, 477–479, 481,
483
Cubane, 200–202, 204, 219
Current density, 17, 152, 154, 155–167, 180,
182, 188, 190, 192, 193, 200, 205, 207,
208, 218, 219, 221
Current susceptibility, 162, 164
Cyclobutadiene, 214, 326, 327
Cyclobutene, 519
Cyclopropane, 108, 197, 198, 219

D

Delocalization Index (DI), 54, 57, 105, 134,
575
Deoxyribonucleic Acid (DNA), 426, 506–508,
522

- Diborane, 45, 46, 330, 331
 Dihydrogen, 427, 428, 429, 462, 465
 Dihydrogen bond, 427, 428, 465
 Discrete chemical topology, 6
- E**
 Ehrenfest force, 33, 133, 135, 136, 138, 142, 146, 148
 Electronic quantum exchange, 437
 Electronic stress tensor, 135
 Electron Localization-Delocalization Matrix (LDM), 54, 55, 59–84
 Electron Localization Function (ELF), 2, 12, 33, 132, 228, 232, 261, 323, 463, 494, 519, 533, 555
 Electrostatic interactions, 513, 569
 Electrostatic potential, 13, 33, 38, 39, 71, 76, 133, 230, 234, 261, 403–405, 409, 412, 418, 426, 429, 450, 494, 510, 512, 513
 Energy decomposition, 9, 436, 444, 450
 Ethane, 61, 62, 66, 67, 105, 119, 189, 218, 219, 221, 222, 415, 448, 499, 503, 504, 506, 507, 514
 Ethene, Ethylene, 140, 142, 143, 180, 182, 185, 218, 330, 331, 342, 375, 382
- F**
 Ferromagnetic, 369, 370, 373, 375, 378, 382, 384, 385, 388, 390
 Fluorine bond, 450
 Fluorobenzene, 401
 Fukui function, 228–238, 261
 Fuzzy graph, 54
- G**
 Gauge invariance, 159, 161
 Glycolic acid, 270, 271, 272, 278–284
 Gomes flow, 167–169
 Gradient field analysis, 232
 Graph theory, 6, 7, 8, 17, 31, 55, 65, 71, 84, 243
- H**
 Halogen bonds, 404–406, 409, 412, 415, 435, 436, 440–442, 445, 446, 448, 450, 452–454, 464, 465, 477, 478, 480, 481, 483, 494, 510, 513, 522
 Harmonic Oscillator Model of Aromaticity (HOMA), 71, 73, 105, 311
 Heisenberg Hamiltonian, 363, 374, 375, 392
 HF Complex, 407, 422–425
 Hirsch's rule, 328, 329
 H₂O Complex, 401, 402, 404
- σ -Hole, 404–407, 412–418, 422, 428, 450
 Homoaromaticity, 105, 108, 109, 113
 Homogeneous potential, 91–93, 95, 98
 Homotropylium, 105, 108, 109, 112, 113, 115, 116, 123, 124
 Hubbard Hamiltonian, 362, 363, 375, 376, 378, 380, 385, 388, 392
 Hückel Hamiltonian, 17, 354, 362–364, 371, 377
 Hückel-Lewis methods, 338, 342, 343, 345, 349
 Huckel rule, 330, 332
 HuLiS program, 354
 Hydrate, H₂O complex, 402, 404, 468, 473
 Hydrogen bond, 104, 259, 401, 402, 403, 415, 417, 418, 422–428, 462, 465, 494, 495, 499, 500, 504, 505, 507, 508, 509, 513–516, 522, 561
 Hyperconjugation, 105
 Hypervalence, hypervalency, 410
- I**
 Interacting Quantum Atoms (IQA), 33, 135, 147, 435, 439, 453
- K**
 Kekule structure, 297–307, 313, 352, 353
- L**
 Laplacian of the electron density, 11, 35, 36, 103, 143, 261, 399, 402, 406, 409, 410, 429, 430, 468, 574
 Lewis acid, 233, 399, 404, 406, 409, 412, 413, 416, 425–429, 461–463, 467, 473, 483
 Lewis base, 412, 413, 428, 429, 461, 463, 483
 Lithium iodide (LiI), 208, 427
- M**
 Magnetic coupling, 374–376, 378, 393
 Magnetic field, 155–157, 162, 164, 165, 167, 178, 180, 188, 190, 192, 193, 196–198, 200, 201, 205, 207, 212, 214, 218, 219, 222, 305, 329
 Magnetic response, 152, 153, 155, 163, 164, 192, 197, 200
 Mesomery, 3, 354
 Metal driven interaction, 516
 Methane, 61, 62, 105, 188, 189, 415, 499, 503, 504, 506, 514
 1,6-Methano[10]annulene, 112–115, 123
 Methylene, 108, 110, 112, 120, 362, 390, 392
 Möbius ribbon, Möbius strip, 356

- Molecular graph, 4, 6–8, 15, 16, 46, 54, 55, 59, 60, 65, 67, 373, 382, 401, 402, 406–408, 410, 413, 415, 416, 422, 423, 425, 428, 429, 463, 466, 469, 480, 494
- N**
- Natural Bond Orbital (NBO), 42, 399, 404, 463
- Natural Resonance Theory (NRT), 348–353
- Nitrite, 530, 531, 533, 548
- Nitrous acid, 533, 534, 547
- NH₃ Complex, 450, 452, 472
- Non-Coulombic systems, 89–91, 95, 97, 98
- Non-Covalent Interaction (NCI), 18, 462–465, 469, 474, 483, 491, 494, 495, 497–499, 502, 503, 505–507, 509, 510, 520, 521
- Non-planar aromatic frameworks, 107
- Non-question concept, 23, 47
- Nucleus-Independent Chemical Shift (NICS), 105, 311
- O**
- Orientation predictor, 227, 238
- Ovchinnikov's rule, 374
- P**
- Para-Delocalization Index (PDI), 71, 73, 74, 105, 322
- Pentaprismane, 200, 201, 204–207, 219
- Perylene, 17, 297, 307–313
- Phenanthrene, 45, 71, 72, 75, 304
- Phenol (dimer), 500, 501
- Pnictogen bond, 513
- Polycyclic Aromatic Hydrocarbon (PAH), 106, 123, 297, 323, 392
- Polyphenyl, 367
- Polyradical, 362, 373
- Potential energy profile, 530
- Promolecule, 9
- Protocovalent bond, 531, 533, 535, 538–541, 546, 549
- Pyrrrole, 196, 197
- Q**
- Quantitative Structure-Activity Relationship (QSAR), 6, 67, 75
- Quantitative Structure-Property Relationship (QSPR), 67, 75
- Quantum chemical topology, 23, 24, 48, 131, 132, 146, 257, 261, 286, 530, 555
- Quantum Chemical Topology Force Field (QCTFF), 38
- Quantum Theory of Atoms in Molecules (QTAIM), 14, 23, 54, 55, 84, 90, 119, 132, 228, 399, 400, 461, 463, 494, 555
- Quantum Theory of Proper Open Subsystems (QTPOS), 89, 90, 98
- R**
- Radical, 119, 342, 347–350, 355, 362, 368, 369, 383, 385, 392, 393
- Reaction path(way), 257, 262–264, 270, 530
- Relativistic effects, 18, 517, 553, 554, 556
- Ring current, 71, 213, 214, 217, 219, 222, 305, 323
- Ring-In-Molecule (RIM), 70, 73
- S**
- Scalar field, 125, 133, 135, 138, 146, 232, 260–262, 494
- Silver oxides, 264
- Source function, 101, 103, 116, 124, 125, 132
- Spherical aromaticity, 328, 332
- Spin delocalization, 362, 363, 384, 386, 390, 393
- Spin density, 101, 118–120, 122–125, 362, 365, 368–370, 383, 384, 386
- Spin multiplicity, 362, 373, 375, 377, 382, 384, 392
- Spin-orbit coupling, 553, 555, 570, 577
- Spin polarization, 116, 117, 124, 222, 362, 382–386, 388, 390, 393, 563
- Stagnation graph, 165, 169, 180–183, 187–194, 196–198, 201, 204, 208, 209, 215, 222
- Synapticity, 5
- T**
- Ternary complexes, 477, 478–483
- Topological atom, 23, 25, 28, 30, 31, 34, 37, 38, 41, 42, 48, 91, 95, 97, 98, 103, 558, 562
- Topological manifold, 5
- Topological resonance energy, 7, 356, 359
- Torqueselectivity, 492, 520, 522
- U**
- Universal molecule model, 243, 244, 251, 252, 254
- Uranyl, 553, 555, 572, 575
- V**
- Valence bond method, 18, 23

Valence Shell Electron Pair Repulsion
(VSEPR), 4, 14, 260, 495, 559, 564, 571
Vanadium oxide, 264
Vector field, 13, 17, 32, 103, 131–133, 136,
138, 140, 141, 146, 152, 155, 165, 166
Virial theorem, 38, 91–94, 133, 139, 262, 440,
561

W

Wade-Mingos' rule, 321, 322, 330–332
Water, 34, 44, 248, 258, 270, 282, 284, 466,
472, 498, 499, 503, 504, 506, 507, 509